Vibration, Control and Stability of Dynamical Systems

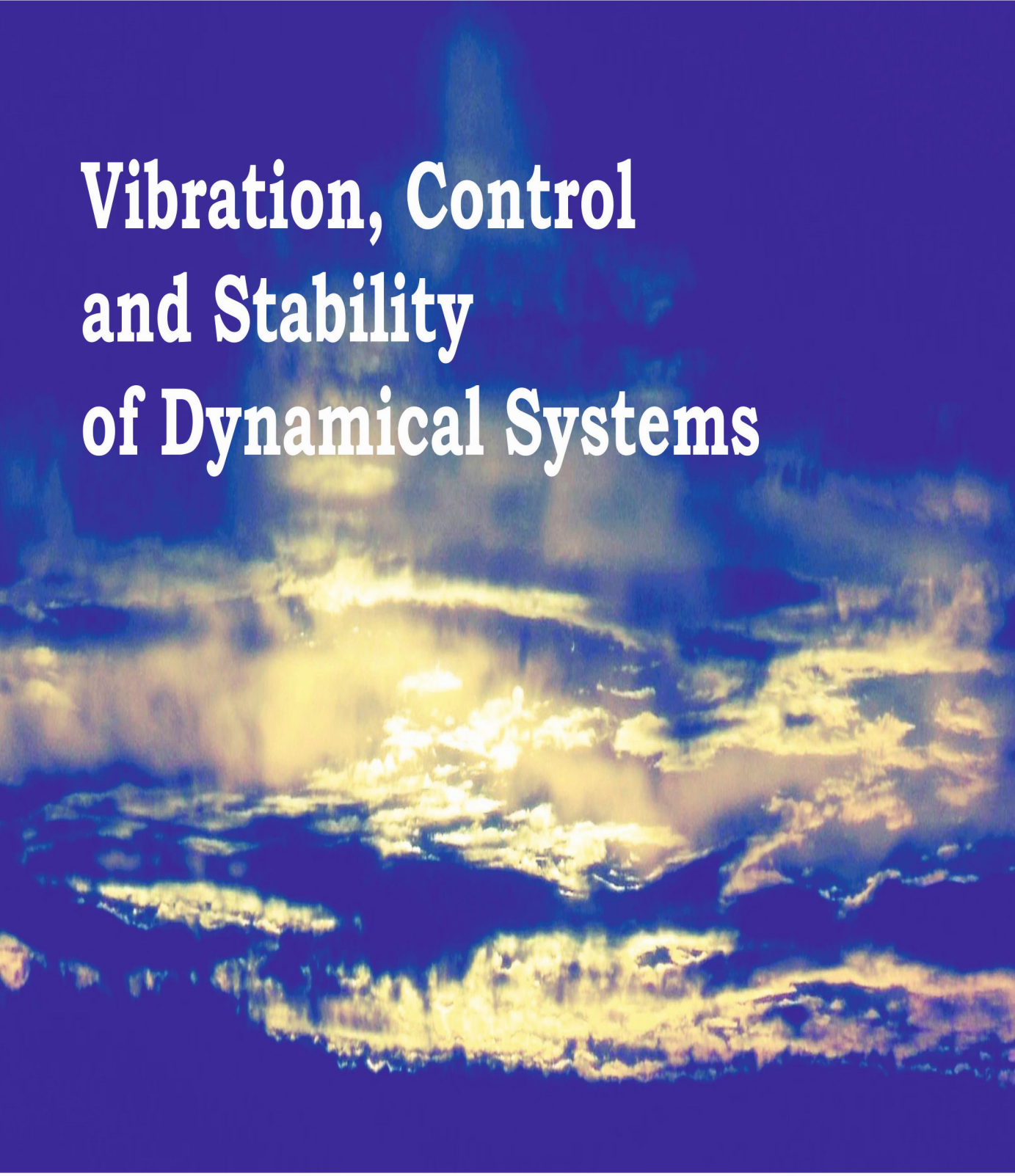

Editors
J. AWREJCEWICZ
M. KAŹMIERCZAK
J. MROZOWSKI
P. OLEJNIK

DSTA 2017

Vibration, Control and Stability of Dynamical Systems

Editors

JAN AWREJCEWICZ, MAREK KAŹMIERCZAK
JERZY MROZOWSKI, PAWEŁ OLEJNIK

ISBN 978-83-935312-5-7
10.34658/9788393531257
https://doi.org/10.34658/9788393531257

Cover design: Marek Kaźmierczak
Technical editor: Marek Kaźmierczak

Printed by:
ARSA Druk i Reklama
90-270 Łódź, ul. Piotrkowska 4
tel./fax (042) 633 02 52
marta@arsa.net.pl
www.arsa.net.pl

PREFACE

This is the fourteenth time when the conference “Dynamical Systems: Theory and Applications” gathers a numerous group of outstanding scientists and engineers, who deal with widely understood problems of theoretical and applied dynamics.

Organization of the conference would not have been possible without a great effort of the staff of the Department of Automation, Biomechanics and Mechatronics. The patronage over the conference has been taken by the Committee of Mechanics of the Polish Academy of Sciences and Ministry of Science and Higher Education of Poland.

It is a great pleasure that our invitation has been accepted by recording in the history of our conference number of people, including good colleagues and friends as well as a large group of researchers and scientists, who decided to participate in the conference for the first time. With proud and satisfaction we welcomed over **180** persons from **31** countries all over the world. They decided to share the results of their research and many years experiences in a discipline of dynamical systems by submitting many very interesting papers.

This year, the DSTA Conference Proceedings were split into three volumes entitled “Dynamical Systems” with respective subtitles: *Vibration, Control and Stability of Dynamical Systems*; *Mathematical and Numerical Aspects of Dynamical System Analysis* and *Engineering Dynamics and Life Sciences*. Additionally, there will be also published two volumes of Springer Proceedings in Mathematics and Statistics entitled “*Dynamical Systems in Theoretical Perspective”* and *“Dynamical Systems in Applications”.*

These books include the invited and regular papers covering the following topics:

- asymptotic methods in nonlinear dynamics,
- bifurcation and chaos in dynamical systems,
- control in dynamical systems,
- dynamics in life sciences and bioengineering,
- engineering systems and differential equations,
- non-smooth systems
- mathematical approaches to dynamical systems
- original numerical methods of vibration analysis,
- stability of dynamical systems,
- vibrations of lumped and continuous systems,
- other problems.

Proceedings of the 14th Conference „Dynamical Systems - Theory and Applications" summarize **168** and the Springer Proceedings summarize **80** best papers of university teachers and students, researchers and engineers from all over the world. The papers were chosen by the International Scientific Committee from **370** papers submitted to the conference. The reader thus obtains an overview of the recent developments of dynamical systems and can study the most progressive tendencies in this field of science.

Our previous experience shows that an extensive thematic scope comprising dynamical systems stimulates a wide exchange of opinions among researchers dealing with different branches of dynamics. We think that vivid discussions will influence positively the creativity and will result in effective solutions of many problems of dynamical systems in mechanics and physics, both in terms of theory and applications.

We do hope that DSTA 2017 will contribute to the same extent as all the previous conferences to establishing a new and tightening the already existing relations and scientific and technological cooperation between both Polish and foreign institutions.

On behalf of both
Scientific and Organizing Committees

Chairman
Professor Jan Awrejcewicz

CONTENTS

Oliver **Alber**, Ulrich **Ehehalt**, Richard **Markert**, Georg **Wegener**
Experimental observations on rotor-to-stator contact **9**

Panagiotis **Alevras**, Stephanos **Theodossiades**, Homer **Rahnejat**, Tim **Saunders**
Torsional vibration energy harvesting through transverse vibrations of a passively tuned beam **25**

Igor V. **Andrianov**, Jan **Awrejcewicz**, Alexander A. **Diskovsky**
Natutral oscillations of rectangular plates with holes: using Reissner's approach **35**

Rafael **Avanço**, Angelo **Tusset**, Marcelo **Suetake**, Helio **Navarro**, José **Balthazar**, Airton **Nabarrete**
The pendulum dynamic analysis with DC motors and generators for sea waves energy harvest **41**

Jan **Awrejcewicz**, Nikolay P. **Erofeev**, Vitalyi **Dobriyan**, Vadim A. **Krysko**
Dissipative dynamics of a geometrically nonlinear Bernoulli-Euler beam under the action of a transverse load and control noises **53**

Jan **Awrejcewicz**, Nataliya **Losyeva**, Volodymyr **Puzyrov**
Gyroscopic forces and asymptotic stability for mechanical systems with partial energy dissipation **61**

Ersin **Aydin**, Baki **Öztürk**, Maciej **Dutkiewicz**
Control of vibrations of multistorey buildings with use of passive dampers **71**

Włodzimierz **Bielski**, Ryszard **Wojnar**
Stokes flow through a tube with wavy wall **83**

Rafał **Burdzik**, Łukasz **Konieczny**, Bogusław **Nowak**, Jakub **Młyńczak**, Jacek **Rozmus**
Analysis of the propagation of the vibration of the rail vehicle while driving with and without locomotive wheel slip **95**

Michał **Ciszewski**, Tomasz **Buratowski**, Mariusz **Giergiel**
Modeling, simulation and control of a pipe inspection mobile robot with an active adaptation system **105**

Nathan Paul **Craig**, Harriet **Grigg**
Effect of anisotropy on surface wave attenuation through fluid medium: a comparison between Rayleigh and Love type waves **115**

Carlos D. **Díaz-Marín,** Alejandro **Jenkins**
Irreversibility of mechanical and hydrodynamic instabilities **127**

Guilherme Pacheco **Dos Santos**, Jose Manoel **Balthazar**, Frederic Conrad **Janzen**, Rodrigo Tumolin **Rocha**, Airton **Nabarrete**, Angelo Marcelo **Tusset**
Nonlinear dynamics and control applied to an aircraft in a longitudinal flight considering gusts of wind in flight **139**

Larysa **Dzyubak**, Atul **Bhaskar**
Transient dynamics of impacting beams with lost connection **151**

Jan **Freundlich**
Vibrations of a cantilevered viscoelastic beam of a fractional derivative type with a tip mass and subjected to the base motion **161**

Mirosław **Gidlewski**, Leszek **Jemioł**, Dariusz **Żardecki**
Sensitivity investigations of the lane change manoeuvre with an automatic control system **173**

Piotr **Kędzia**, Krzysztof **Magnucki**, Mikołaj **Smyczyński**, Iwona **Wstawska**
Stability of a rectangular plate under dynamic load generated by unhomogeneous magnetic field **183**

Tomasz **Kik**, Bernard **Wyględacz**
Application of numerical simulation in thermal cycle acquisition errors identification **193**

Zbigniew **Koruba**
The control of the artillery-rocket set in conditions of random interferences **203**

Angelika **Kosińska**, Dariusz **Grzelczyk**, Jan **Awrejcewicz**
Non-linear dynamics of flexibly suspended spring pendulum embedded in gravity and electric fields **215**

Izabela **Krzysztofik**
Sliding control of a gyroscopic scanning and tracking system mounted on a moveable base **223**

Grzegorz **Kudra**, Michał **Szewc**, Michał **Ludwicki**, Krzysztof **Witkowski**, Jan **Awrejcewicz**
Modelling of rigid body dynamics with spatial frictional contacts **231**

Juliana **Lacerda**, Celso **Freitas**, Elbert **Macau**
Remote synchronization and multistability in a star-like network of oscillators **241**

Jeremy **Laflin**, Kurt **Anderson**
Geometrically exact beam equations in the adaptive DCA-framework **253**

Claude Henri **Lamarque,** Alireza **Ture Savadkoohi**, Simon **Charlemagne**
Passive control of linear structure nonlinear oscillators in series **269**

Wagner Barth **Lenz**, Angelo Marcelo **Tusset**, Rodrigo Tumolin **Rocha**, Frederic Conrad **Janzen**, Adriano **Kossoski**, Jose Manoel **Balthazar**, Airton **Nabarrete**
The influence of anti-roll bar in the dynamics of full-car control **279**

Grzegorz **Litak,** Piotr **Wolszczak,** Krystian **Łygas**
Dynamical response of a bistable system with clearance **291**

Olga **Mazur**, Atul **Bhaskar**
Thermal buckling of triangular plates **299**

Tomasz **Mirosław**, Jan **Szlagowski**, Adam **Zawadzki,** Zbigniew **Zebrowski**
Off-road 4-wheel drive vehicle dynamics and control **311**

Airton **Nabarrete**, Vinicius Yoshida **de Melo**, José Manoel **Balthazar**,
Angelo Marcelo **Tusset**
Nonlinear analysis of rotors with rigid coupling misalignment **323**

Milan **Naď**, Lenka **Kolíková**, Ladislav **Rolník, Radislav Ďuriš**
Analysis of vibration effects on edge-chipping occurrence during rotary ultrasonic drilling **335**

Mikhail **Nikabadze**, Tamar **Moseshvili**, Armine **Ulukhanian**,
Ketevan **Tskhakaia**, Nodar **Mardaleishvili**
Formulation of initial boundary value problems in the theory of multilayer thermoelastic thin bodies in moments (part I) **345**

Mikhail **Nikabadze**, Tamar **Moseshvili**, Armine **Ulukhanian**,
Ketevan **Tskhakaia**, Nodar **Mardaleishvili**
Formulation of initial boundary value problems in the theory of multilayer thermoelastic thin bodies in moments (part II) **357**

Mikhail **Nikabadze**, Tamar **Moseshvili**, Armine **Ulukhanian**,
Ketevan **Tskhakaia**, Nodar **Mardaleishvili**
Formulation of initial boundary value problems in the theory of multilayer thermoelastic thin bodies in moments (part III) **369**

Gerard **Olivar Tost**, Luis Eduardo **López Montenegro**, Aníbal **Muñoz Loaiza**
A piecewise-smooth control of dengue **381**

Akinwale **Olutimo**
On the stability and ultimate boundedness of solutions for certain third order non-autonomous delay differential equations **389**

Marcin **Pękal**, Janusz **Frączek**, Marek **Wojtyra**
Nullspace method for the uniqueness analysis of reaction and driving forces in rigid multibody systems with redundant nonholonomic constraints **401**

Arnold **Pérez**, Guillermo **Muñoz**, Fabiola **Angulo**
Enhancing the stability of the boost converter using the saltation matrix..... **413**

Katarina Y. **Plaksiy,** Yuri **Mikhlin**
Resonance behaviour of dissipative spring-pendulum systems..... **423**

Arion **Pons**, Stefanie **Gutschmidt**
Aeroelastic stability analysis via multiparameter eigenvalue problems **435**

Jacek **Przybylski**, Grzegorz **Gąsiorski**
Theoretical and experimental investigations of nonlinear vibrations of a beam with piezoelectric actuators **447**

Stanisław **Radkowski,** Maciej **Słomczyński**
Model of a quarter car suspension with a silencer containing magnetorheological fluid and with damaged parts controlled by backstepping method control **461**

Dennis **Roeser**, Samuel **Jackson**, Thomas **Sattel**, Stefanie **Gutschmidt**
Nonlinear mode veering for enhanced resonant sensing **475**

Philipp **Schorr**, Susanne **Sumi**, Valter **Böhm**, Klaus **Zimmermann**
Dynamical investigation of a vibration driven locomotion system based on a multistable tensegrity structure **485**

Yury **Selyutskiy**
Equilibria and global dynamics of a 2 DoF aeroelastic system **497**

Martin **Svoboda**, Václav **Schmid**, Josef **Soukup,** Milan **Sapieta**
Influence of the spring system in vehicle vibrafon **505**

Piotr **Szmidt**
A compensation for positioning of the remote control artillery-missile set in external disturbance conditions **513**

Utz **von Wagner**, Lukas **Lentz**
On artifacts in nonlinear dynamics **525**

Jerzy **Warmiński**, Jarosław **Latalski**, Zofia **Szmit**
Vibration modes of rotating thin-walled composite blades **537**

Krzysztof **Witkowski**, Grzegorz **Kudra**, Grzegorz **Wasilewski**, Fryderyk **Wiądzkowicz**, Jan **Awrejcewicz**
Experimental and numerical investigations of one-degree-of-freedom impacting oscillator **549**

Mateusz **Wojna**, Grzegorz **Wasilewski**, Jan **Awrejcewicz**, Adam **Wijata**
Dynamics of a double physical pendulum with magnetic interaction **559**

Alena A. **Zakharova**, Jan **Awrejcewicz**, Tatyana V. **Yakovleva**, Vadim S. **Kruzhilin**, Anton V. **Krysko**
Contact interaction of a nano-plate, reinforced by a local set of nano-beams located in a stationary temperature field **571**

Jaroslav **Zapoměl**, Jan **Kozánek,** Petr **Ferfecki**
The mathematical modelling of nonlinear vibration of rotors influenced by magnetic and electric effects **579**

Paweł **Zdziebko**, Adam **Martowicz**, Tadeusz **Uhl**
Contact force control for a high speed pantograph using co-simulations **587**

Ambrus **Zelei**, Bernd **Krauskopf**, Tamás **Insperger**
Control optimization for a three-segmented hopping leg model of human locomotion **599**

Experimental observations on rotor-to-stator contact

Oliver Alber, Ulrich Ehehalt, Richard Markert, Georg Wegener

Abstract: If a flexible rotor contacts its stator, the nonlinearities induced by contact may result in a great variety of vibration phenomena. This article presents experimental results gained at test rigs. Fundamental phenomena are analyzed and discussed. First, a modular kit for rotordynamic experiments is described. The kit allows customizing the properties of rotor and stator that are relevant for the dynamic behavior. The system allows to specify target values for natural frequencies, modal damping, clearance width, contact friction and others. Basic configurations based on this kit were used to study the influence of mass, stiffness and damping of both rotor and stator, contact friction and misalignment of the stator on the vibration of the rotor-stator system. Extensions of the kit allowed the experimental investigation of systems with a multitude of natural frequencies, highly flexible stators and even drop down and overload incidents of rotors supported by active magnetic bearings. The article also analyzes and explains the various vibration phenomena resulting from contact. In particular, resonance diagrams from run-up and run-down processes, orbit plots and frequency spectra are utilized to discuss the dynamic characteristics. The motion types encountered include not only rotor synchronous motions, but also multi frequency motions (forward and backward whirl), sub- and super-harmonic motions, motions including sidebands as well as chaotic motions. Emphasis is put on sensitive system parameters and on existence and stability of the various types of motion.

1. Introduction

If a rotor contacts its stator, the rotor-stator system becomes nonlinear and, due to rubbing, a wide variety of different motion types are possible. Contact and rubbing between rotating and stationary parts of rotating machinery may lead to severe failures. However, not every rubbing event will necessarily lead to a destruction of the rotor system. Thus, a priori knowledge about the various types of rotor motion and their characteristics is necessary allowing early detection of contact from measured vibration signals and predicting the severity of the resulting rotor motion.

If the rotor contacts the stator, the following typical motion patterns may arise: purely synchronous, sub- and superharmonic vibrations, forward and backward whirl, motion with sidebands around the rotor speed and even chaotic motions [11]. These types of motion may exist parallel and independent from each other. They may occur depending on the rotor and stator parameters, but also on the rotor speed and the initial conditions of the rotor-stator motion [5].

A first insight into the manifold dynamics of a rotor contacting its stator can already be gained with the simple JEFFCOTT rotor model of Figure 1 extended by a stator taking into account the friction between rotor and stator.

Run-up experiments of a test rotor similar to the JEFFCOTT rotor shown in Figure 1 may generate for instance amplitude curves as shown in Figure 2. The curves in Figure 2 show the amplitude $|\widehat{r}_R|$ of the rotor deflection of an unbalanced rotor during a slow run-up. The measured curves are compared to the characteristic steady state synchronous unbalance response, which may develop if the contact friction μ_F is low.

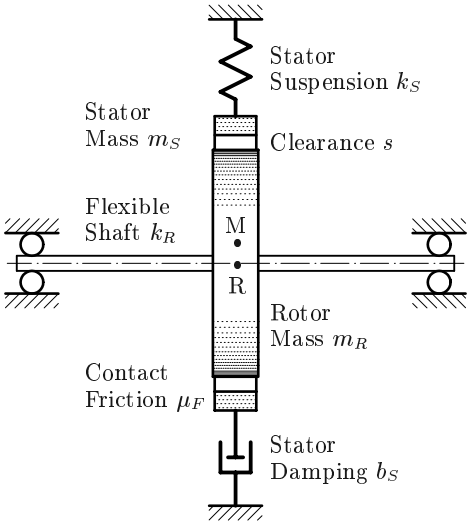

Figure 1. JEFFCOTT rotor with a simple model of a flexible stator

Just after the rotor deflection $|\widehat{r}_R|$ exceeds the clearance s, the rotor contacts the stator and due to the high contact friction the synchronous unbalance response (a) becomes unstable. The synchronous motion changes to a non-synchronous quasi-periodic forward whirl (b). If the rotor speed increases further, the forward whirl may disappear. However, as can be seen on the right hand side of Figure 2, the forward whirl can turn into a much more dangerous motion. In this case the rotor amplitude jumps very quickly to large values. Backward whirl (c) is established where the rotor center orbits opposite to the direction of the rotor rotation.

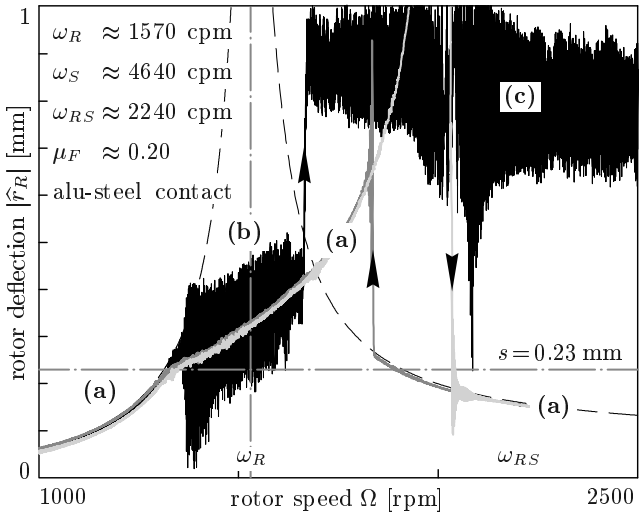

Figure 2. Measured rotor deflection during run-up

It can also be observed that backward whirl may occur in the speed range where the synchronous unbalance response is stable. Under certain conditions the backward whirl becomes

unstable and the motion turns back to synchronous whirl and follows the steady state unbalance response curve with small amplitudes. Figure 2 shows only three of a plurality of possible motion types which may arise if the rotor contacts the stator [4]. Extensive theoretical investigations as well as experimental results for many more motion patterns and phenomena are presented in the theses [2, 10, 18].

This article presents a selection of experimental results which have been obtained with experimental setups of a modular rotor kit. First, the modular rotor kit used for conducting principle rotor dynamic investigations is described. Subsequently, various measured motion types are analyzed and discussed. Finally, some phenomena are discussed which were observed experimentally on rotor and stator systems with several eigenfrequencies within the speed range of the rotor.

2. Modular TUD kit for rotordynamic experiments

General description of the TUD kit: Most studies on rotor-stator contact are theoretical using either analytical or numerical approaches. The results depend very much on the modeling. Contradictions may arise with different model approaches. Therefore, it is essential to verify experimentally the calculated dynamic phenomena and the underlying model assumption.

For demonstration and experimental verification of various rotordynamic effects, a flexible rotordynamic kit as sketched in Figure 3 was designed in 1981 and has been continuously expanded and improved at the TUD (Technische Universität Darmstadt). The modular kit allows to quickly assemble test rigs for examining various rotordynamic phenomena by combining individual components. The core of this modular kit is a high-strength, 8 mm thick shaft, on which disks, ball bearings, bushes of journal and magnetic bearings, external dampers and many other accessories may be clamped at any desired axial position. The additional components are fixed to the shaft by special cone-type clamping sleeves generating high contact force. High contact force suppresses micro slip and avoids destabilization by internal rotor damping. For safety reasons, the rotor deflections are limited directly at the

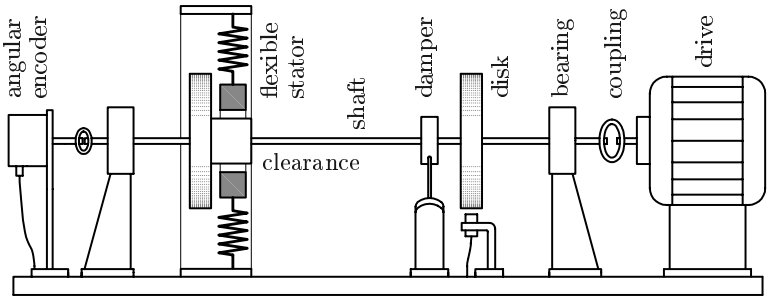

Figure 3. Principle of the modular kit for basic rotordynamic experiments

disks by retainer bearings. The rotor is driven by a speed-controlled electric motor connected to the rotor by a flexible coupling. The radial displacements of disks and stators are measured in two orthogonal directions by contactless eddy current sensors. An incremental angular encoder attached to the rotor generates sine and cosine signals of the current angle of rotation. The measured displacements and the rotational signals are filtered and subsequently recorded and analyzed by a measuring PC.

Additional components are, for example, elastic bearings, journal bearings [8], active magnetic bearings [20], external actuators on the bearing or on the shaft, viscous dampers, controllable ERF dampers [7], as well as various disks for demonstrating gyroscopic effects [15, 17]. A similar but less comprehensive modular system is offered by Bentley Nevada [9].

First experimental results in [14] address non-stationary balancing methods on the test rig shown in Figure 4. Subsequently, passive and active measures for passing the resonance including retainer bearings were investigated experimentally [1, 19].

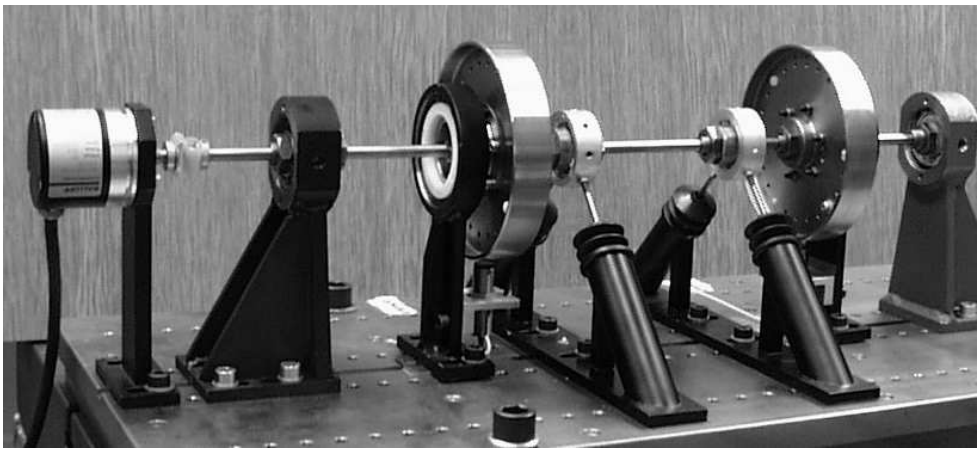

Figure 4. Test rig for non-stationary balancing [16]

With the modular TUD kit, various rotor-stator configurations were assembled to investigate the influences of various system parameters on motion patterns and phenomena caused by contact and rubbing between rotor and stator.

Test rig for SDOF rotor-stator systems: To verify the theoretical results for rotor-stator systems with a single disk and a single stator ring (SDOF) experimentally, the rotor-stator test rig shown in Figure 5 (left) was built. It consists of a simple rotor and a flexible stator. The shaft is supported by ball bearings at both ends and carries a disk in the middle. A cylindrical bush at the front side of the rotor disk contacts the stator if the rotor deflection exceeds the clearance. The SDOF stator body (a) is flexibly suspended within the rigid housing (b) by four stator springs (c). The stator mass can be changed by adding mass

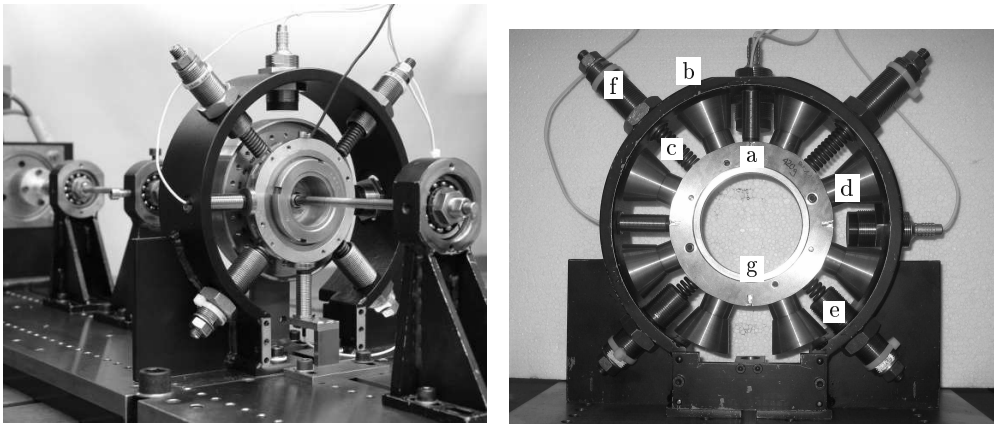

Figure 5. Test rig for SDOF systems; left: assembled test rig; right: stator assembly [10]

elements (d). The lower spring housings (e) can be filled with oil to adjust the stator damping. The stator can be centered to the rotor or a desired misalignment can be set up by shifting the suspensions (f) of the stator springs. The stator body can accommodate different contact rings (g). Thus, different clearances s and different friction coefficients μ_F between rotor and stator can be realized by simply changing the contact rings. For the experiments discussed in this paper, the radial clearance between rotor and stator was mostly set to $s = 0.23$ mm.

The rotor deflection $r_R(t) = w_R(t) + i\, v_R(t)$ was measured in vertical and horizontal direction. The measured rotor deflection components $w_R(t)$ and $v_R(t)$ are post-processed to illustrate the orbits and to calculate the spectra by transforming into the frequency domain, $W_R(\widetilde{\Omega})$ and $V_R(\widetilde{\Omega})$. The forward component (positive frequency range $\widetilde{\Omega} > 0$) is simply calculated by summing up the complex spectra of the two orthogonal displacement components. The backward component (negative frequency range $\widetilde{\Omega} < 0$) however is calculated by summing up the conjugate complex spectra of the two orthogonal displacement components given in the positive frequency range,

$$\begin{aligned} R(\widetilde{\Omega}) &= W(\widetilde{\Omega}) + iV(\widetilde{\Omega}) \qquad \text{for} \quad \widetilde{\Omega} > 0 \\ R(\widetilde{\Omega}) &= W^*(-\widetilde{\Omega}) + iV^*(-\widetilde{\Omega}) \qquad \text{for} \quad \widetilde{\Omega} < 0. \end{aligned} \tag{1}$$

Test rig for MDOF rotor-stator systems: The setup of the test rig for conducting the experimental investigation on rotor and stator systems with several eigenfrequencies within the speed range of the rotor (MDOF) is similar to the one for SDOF systems described in the previous paragraph [3]. Drive, instrumentation and signal processing are identical. The shaft is supported by ball bearings and carries two disks and an external damper as presented in Figure 6 (left). A contact ring is mounted on the left disk a to provide the contact to the

stator if the rotor deflection exceeds the clearance. The two lowest resonance frequencies of the rotor are below 50 Hz and located within the speed range of the rotor.

The stator with two (complex) degrees of freedom consists of an inner ring (mass m_{S1}) and an outer ring (mass m_{S2}). The two stator rings are connected to each other and to the stator cage by springs. To illustrate the operation principle, a functional design sketch of the MDOF stator is shown in Figure 6 (right). Contact rings of different sizes and materials can be inserted to adjust the friction coefficient and the gap size at the contact position. Tilting of the stator rings is avoided by guiding each ring with thin flexible beams. The lowest two natural frequencies of the stator system are also located within the speed range of the rotor.

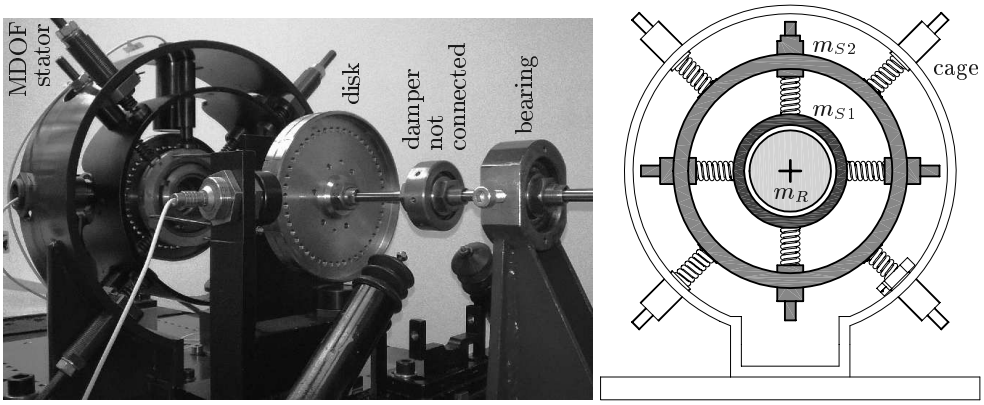

Figure 6. Test rig for MDOF systems; left: assembled test rig; right: sketch of the stator [2]

3. Measured Motion Types of SDOF Rotor-Stator Systems

Synchronous Motion: For isotropic rotors, the synchronous motion excited by unbalance occurs always whenever the rotor is not in contact with the stator. Furthermore, synchronous motion can also occur when rotor and stator contact each other, if rotor and stator are isotropic and concentric, even though the total restoring force F_{tot} of the rotor contacting the stator is nonlinear. As illustrated in Figure 7, for synchronous motion the absolute value of the rotor deflection r_R remains constant per revolution and thus the same holds for the total restoring force as well.

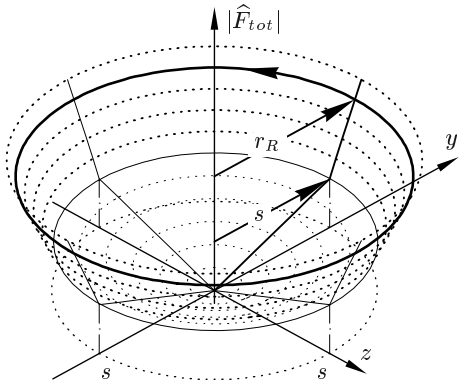

Figure 7. Total restoring force of a rotor-stator system with clearance s

Depending on the natural frequencies ω_R and ω_S of rotor and stator, the unbalance response curves may have significantly different shapes, [12]. Figure 8 (left) shows the measured rotor deflection during run-up (black curve) and run-down (grey curve) for a system with a stator classified as very light ($\omega_S \gg \omega_R$). As soon as the rotor contacts the stator the unbalance response curve is bent and hangs over towards higher speeds. This leads to the well known jump phenomenon typical for non-linear systems. If the synchronous unbalance response under contact is stable the motion is purely synchronous even though the entire system under contact is nonlinear. This is illustrated by the orbit at $\Omega = 1600$ rpm and the corresponding spectrum shown in Figure 8 right.

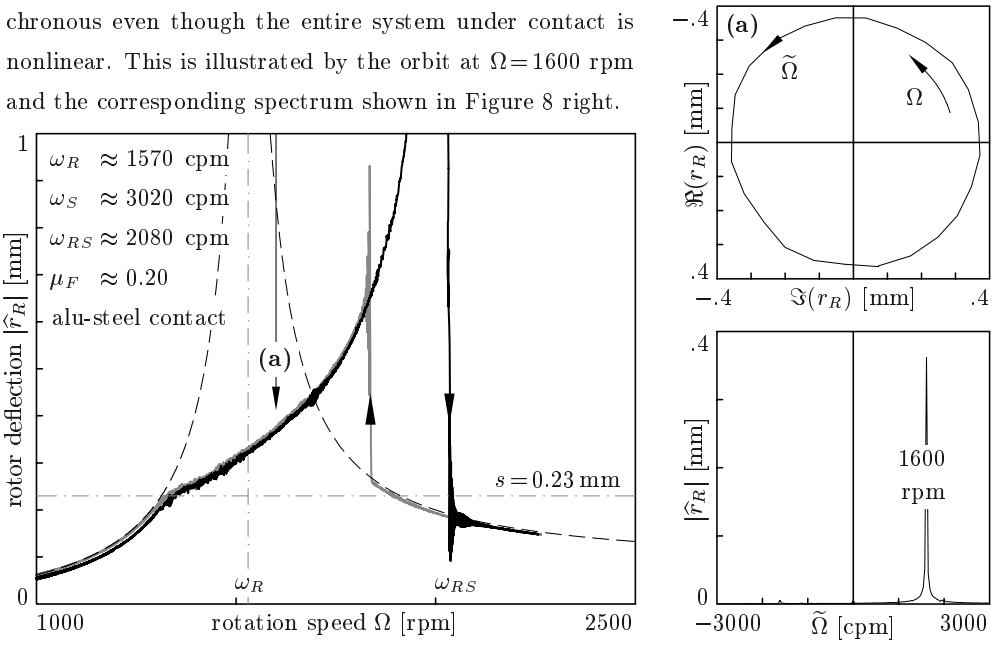

Figure 8. Measured unbalance response; left: rotor deflection of synchronous motion during slow run-up and slow run-down; right: rotor orbit and spectrum at $\Omega = 1600$ rpm

For a rotor-stator system with a heavy stator ($\omega_S < \omega_R$), the main branch of the unbalance response does not exceed the clearance during normal run-up and run-down. For such systems however, an additional isolated synchronous branch (island) can occur at subcritical rotor speed, marked by (b) in Figure 9 (left). This isolated branch will not be reached during normal operation as illustrated by the grey curve depicting a run-down. To enter into the isolated branch, the rotor was forced into contact with the stator at $\Omega \approx 1300$ rpm. The subsequent run-up (black curve) first follows the isolated branch. At the upper speed limit of the isolated branch, the rotor amplitude drops down to small values and the rotor stays in contact with the stator during the subsequent run-up. Rotor and stator do not separate in the shown speed range even though the rotor amplitude is smaller than the clearance. The unbalance response on the isolated branch at $\Omega = 1160$ rpm (b) and also at the normal area

at 1800 rpm (c) is stable and the motion under contact is synchronous as demonstrated by the orbits and the spectra in Figure 9 (right).

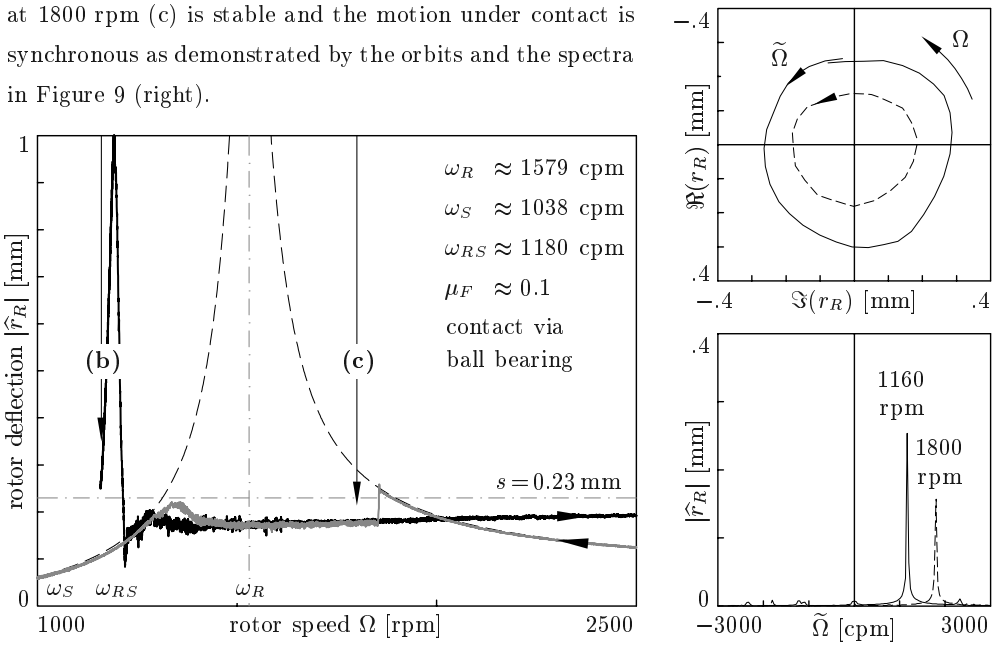

Figure 9. Measured unbalance response; left: rotor deflection of synchronous motion during slow run-up and slow run-down; right: rotor orbits and spectra at two rotor speeds

The synchronous motion under contact may become unstable in a certain speed range and then another vibration pattern emerges. Depending on the parameters, the unstable speed range occurs in the subcritical speed range (right after rotor and stator get into contact during run-up), or in the supercritical speed range, [10].

Forward Whirl: Forward whirl can emerge when the synchronous unbalance response becomes unstable. An even lighter stator compared to the one of Figure 8 results for example in an unbalance response curve shown in Figure 10 (left). The synchronous motion becomes unstable in the speed range between $\Omega \approx 1300$ rpm and 1640 rpm and non-synchronous quasi-periodic forward whirl emerges. Forward whirl is characterized by an additional component with a negative non-synchronous frequency leading to a non-constant amplitude. The previously smooth line becomes an area.

The orbit in Figure 10 (right) is not closed, it takes about five revolutions to traverse the shown segment at $\Omega = 1470$ rpm. The frequency spectrum in Figure 10 (right) shows the forward (positive) rotor speed $\Omega = 1470$ rpm and a smaller component with the negative frequency $\widetilde{\Omega} = -1180$ cpm whirling backwards. As the forward whirling component dominates, the orbit is in overall traversed in direction of rotor rotation.

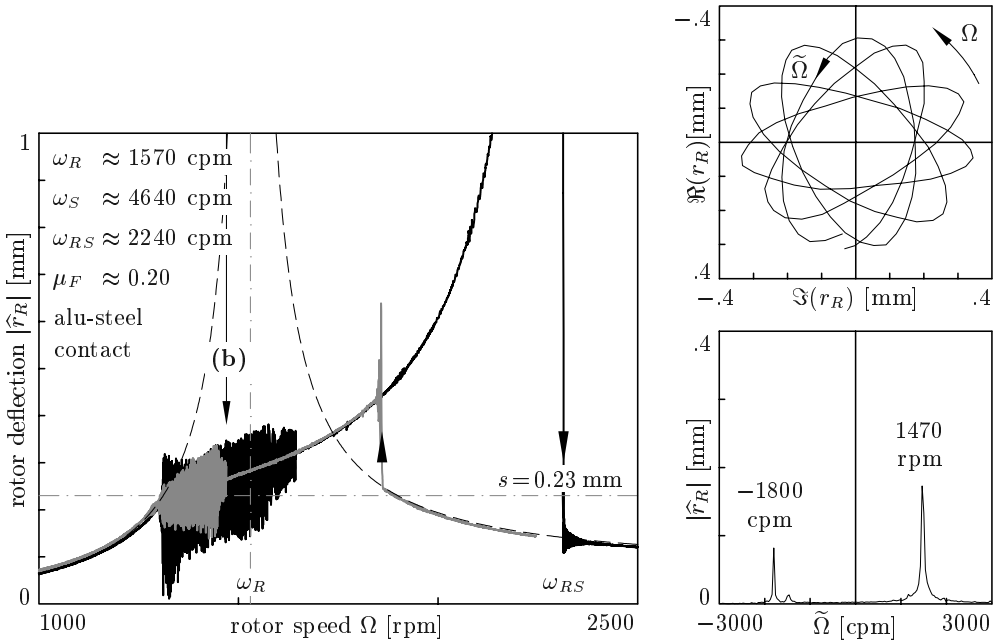

Figure 10. Measured unbalance response; left: rotor deflection of forward whirl during slow run-up and slow run-down; right: rotor orbit and spectrum at $\Omega = 1470$ rpm

Backward Whirl: Backward whirl can emerge in cases when the synchronous unbalance response becomes unstable. In addition, backward whirl is also possible in speed ranges where the synchronous motion with or without contact is stable or stable forward whirl exists. This is demonstrated by Figure 11 with the same parameters as in Figure 10. During the shown run-up (black line) the rotor was forced from non-contacting state into permanent contact already at very low speed. Subsequently, backward whirl emerges throughout a wide speed range characterized by high vibration amplitudes and large contact forces. As illustrated, backward whirl can co-exist with all other stable motion patterns.

Backward whirl is characterized by a dominating component with non-synchronous negative frequency leading to a non-constant amplitude as shown in Figure 11. The shape of the orbit in Figure 11 (right) is similar to the one of the forward whirl. However, the backward whirling component dominates over the synchronous component and hence the orbit traverses against the rotating direction. The backward whirling frequency is typically higher than the rotational frequency and the backward whirl causes high reverse bending stresses.

The waterfall diagram of the run-up shown in Figure 11 demonstrates that frequency and amplitude of the backward whirling component are nearly independent from the running speed, confirming theoretical results given in [10, 13].

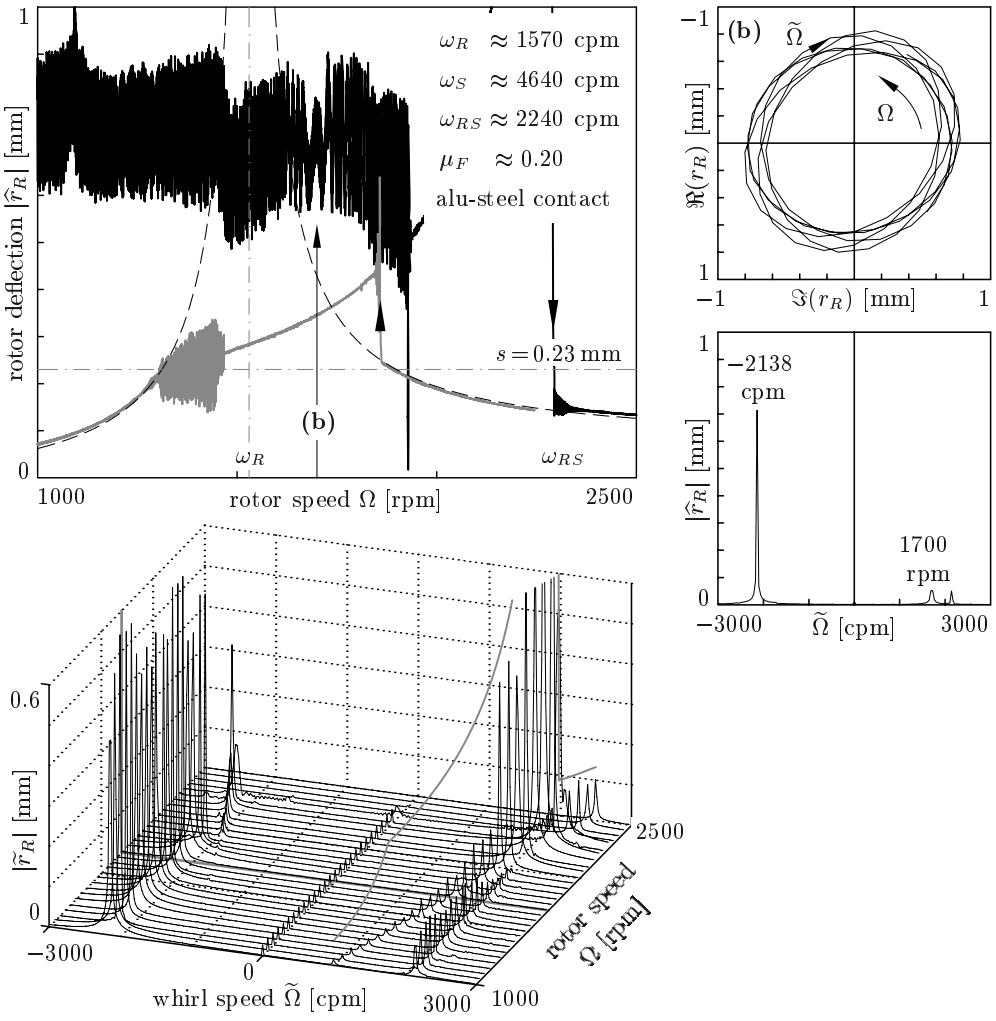

Figure 11. Measured unbalance response; left: rotor deflection of backward whirl during slow run-up triggered by artificial disturbance at low rotor speed; right: rotor orbit and spectrum for backward whirl at $\Omega = 1700$ rpm; bottom: waterfall diagram of run-up

While the existence of backward whirl strongly depends on the relation between friction coefficient and rotor damping, its whirling frequency is not significantly influence by the two parameters. The measured frequency and amplitude of the backward component are shown by the circles in Figure 12 verifying the analytical results. Unless the frequency, the amplitude of the backward component strongly increases with increasing friction μ_F and decreases with increasing rotor damping D_R.

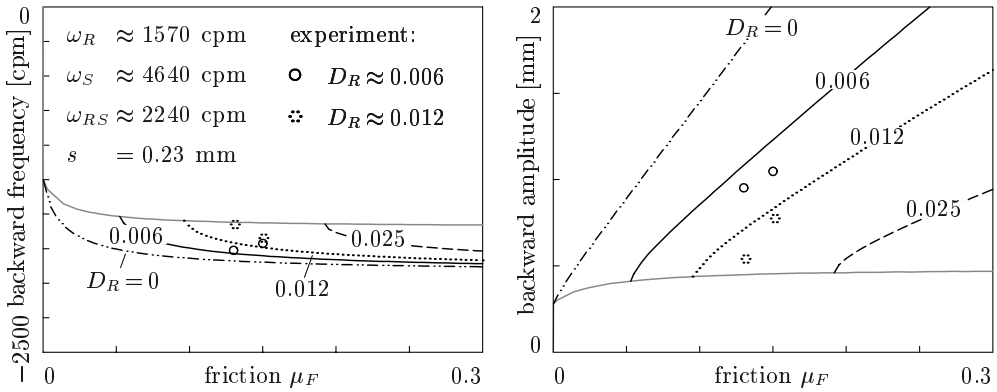

Figure 12. Frequency and amplitude of the asynchronous backward component of a system with a light stator depending on rotor damping D_R and friction coefficients μ_F

Subharmonic Vibrations: Subharmonic vibrations occur if stator and rotor are not concentrically aligned. Figure 13 shows the unbalance response of a rotor with a stator misalignment of approximately 80% of the clearance. Due to the misalignment, contact is established during run-up already before the rotor deflection exceeds the nominal clearance. With increasing rotor amplitudes full annular contact is established and the amplitude follows on average the synchronous unbalance response (grey line) of the corresponding aligned system. Due to the high misalignment rotor and stator do not separate in the super-

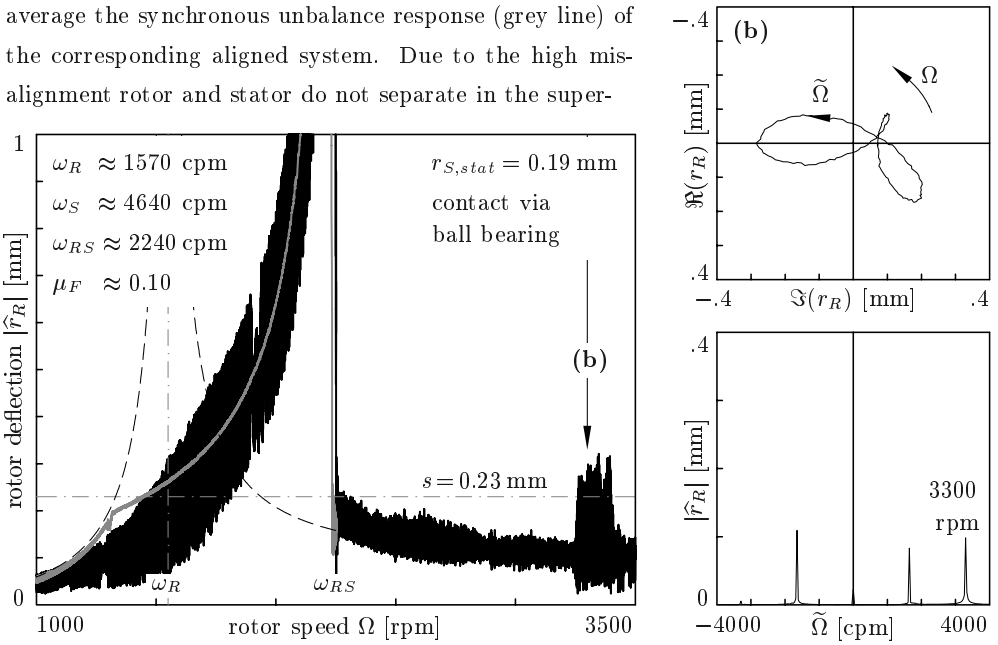

Figure 13. Measured unbalance response for misaligned stator; left: rotor amplitudes during run-up and run-down; right: orbit and spectrum of the subharmonic motion at Ω = 3300 rpm

critical speed range. Around $\Omega \approx 3300$ rpm a subharmonic resonance occurs. It takes two rotor revolutions to fully traverse the orbit shown in Figure 13 (right). The subharmonic orbit contains only the frequencies $\widetilde{\Omega}/\Omega = -1\,, -0.5\,, \ldots\,, 1$ and is hence closed after two revolutions.

Vibrations with Side Bands: For a system with light stator, the unbalance response curve is not bent. For such a system the synchronous unbalance response can become unstable in the supercritical speed range, [10]. In Figure 14 (left) a slow run-up for such a system is shown. The synchronous unbalance response becomes unstable in the speed range from $\Omega \approx 1710$ rpm to $\Omega \approx 1810$ rpm. The spectrum shown in Figure 14 (right) shows that in this speed range the synchronous component is still dominant, but several minor components appear with a frequency spacing of $\Delta\widetilde{\Omega} \approx 30$ cpm. Due to the multitude of vibration components the orbit amplitude varies.

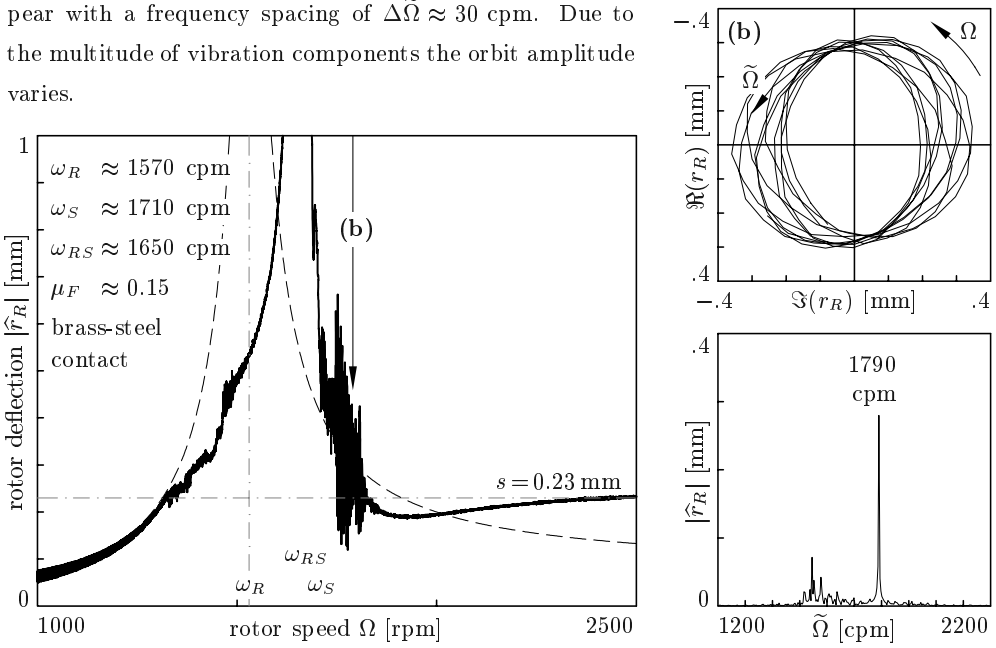

Figure 14. Measured unbalance response; left: rotor amplitudes during slow run-up; right: orbit and spectrum for motion with sidebands at $\Omega = 1790$ rpm

4. Measured Motion Types at MDOF Rotor-Stator Systems

Interaction of individual modes of MDOF rotor-stator systems: In speed ranges where only one rotor and one stator mode are interacting during contact, the same phenomena were measured with MDOF systems as described in the previous section for SDOF systems. This presumes rotor and stator systems with quite separated natural frequencies. Amplitude curves, orbits and spectra show the same typical shapes which occur in SDOF rotor-stator systems.

Coexistence of several backward whirl characteristics: Figure 15 (left) shows the measured rotor deflection at the disk contacting the stator. The rotor has a very low damping. During run-up, immediately after the rotor has passed the first resonance range, backward whirl occurs. It is noteworthy that in the subsequent run-up different backward characteristics are observed. As the spectrum in Figure 15 (right) proves, these backward whirls have different frequencies and amplitudes. Within the speed ranges A and C, the frequency of the backward component is lower than that within range B. Frequency and rotor amplitude change when the motion changes from one backward characteristic to the other. The experiments confirm the theory [2,6] that backward whirl motions with different whirl frequencies may coexist.

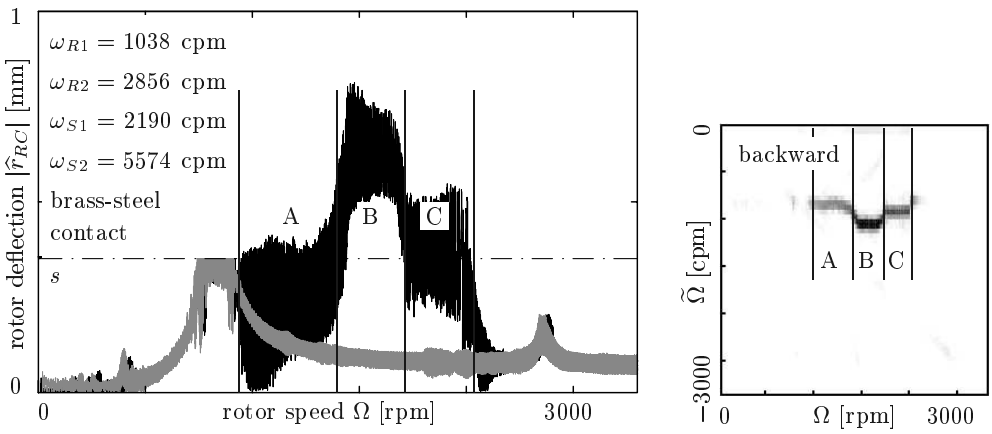

Figure 15. Measured unbalance response; left: rotor deflection of contacting disk during slow run-up and slow run-down; right: short time fast Fourier transformation (STFFT)

MDOF rotor-stator systems with interacting modes: For certain parameter constellations, the dynamics of MDOF systems can not be described adequately by simple SDOF treatment. This is particularly the case if more than one rotor and one stator mode determine the dynamics in the relevant speed range. Figure 16 shows the measurements at a test setup, in which the first two stator natural frequencies are located close to the first rotor natural

frequency; one below and one above the first rotor resonance. During run-up, just after the rotor is contacting the stator at the rotor's first eigenfrequency, motions with sidebands and partial contact are observed. After passing the first resonance, the rotor separates from the stator and continues running up without contact. When the rotor speed reaches the second natural frequency of the rotor, the rotor contacts the stator again and partial contact occurs. Again, the motion includes synchronous and sideband components.

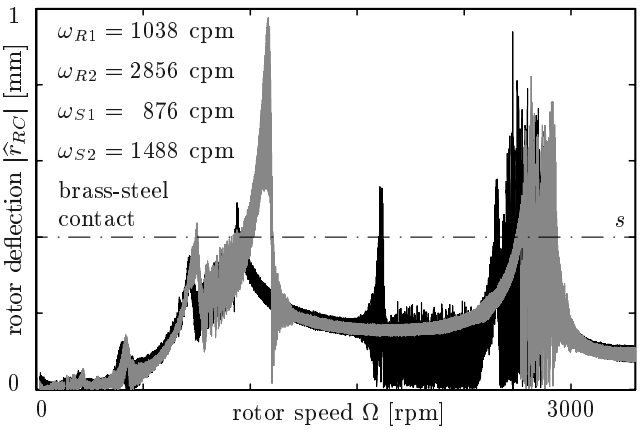

In summary, characteristics of SDOF rotor-stator systems with a lower natural frequency of the stator than the rotor eigenfrequency and another with a higher natural frequency are present at the same time. Thus, both stator modes influence the system dynamics significantly.

Figure 16. Measured unbalance response; rotor deflection of contacting disk during slow run-up and slow run-down containing several different motion patterns

The run-down (black curve) shows another phenomenon: An isolated branch with synchronous motion under contact exists in the speed range from 2000 rpm to 2500 rpm, that is between the two rotor eigenfrequencies. During run-down the vibration within the second rotor resonance triggers the system to jump to the isolated branch. The motion pattern at this island is synchronous. This motion with contact occurs even though a non-contact motion of the rotor with small amplitudes would be possible in parallel. Although the rotor speed is far away from the resonance zones of the subsystems and the motion is synchronous, quite large rotor deflections can occur. The synchronous motion on the isolated branch will continue until the branch ends or until the motion on the branch becomes unstable. Thereafter, the rotor returns to the non-contact motion with small synchronous deflection. This motion remains during subsequent run-down until the rotor speed approaches the first rotor resonance. During run-up the isolated branch will not be reached due to the small rotor deflection unless there is an external disturbance.

5. Conclusion

The presented modular kit for rotordynamic experiments allows precise experimental observations on rotor-stator contact, which have been used for the validation of theoretical models. The experimental results verify impressively most simulation results found in literature and the theoretical hypothesis that the friction coefficient is a major determining parameter for asynchronous motion. All motion patterns measured at SDOF rotor-stator systems can also be observed at MDOF systems, if the rotor and stator resonances are clearly separated. However, at MDOF systems modal interaction leads to new phenomena like coexisting backward whirl motions or modification of the resonance curves.

References

[1] Abraham, D., Markert, R., and Witfeld, H. Experimentelle Untersuchungen zu aktiven und passiven Resonanzdurchlaufhilfen für extrem elastische Rotoren (Experimental investigations on active and passive measures for passing resonance of flexible rotors). *VDI-Berichte 695* (1988), 145–169.

[2] Alber, O. *Anstreifen mit vielen Schwingungsmoden (Rubbing with many vibration modes)*. Shaker, Aachen, 2015.

[3] Alber, O. Experimental analysis of rotor-stator contact with many degrees of freedom. *9th IFToMM Conf. on Rotor Dynamics* (2015), 1935–1944.

[4] Alber, O., and Markert, R. Bifurcation of contact between rotor and stator. *Int. Conf. on Structural Nonlinear Dynamics and Diagnosis (CSNDD12)* (2012), 1–5.

[5] Alber, O., and Markert, R. Rotor-stator contact – overview of current research. *MATEC Web of Conferences 16*, 03001 (2014), 1–5.

[6] Alber, O., Norrick, N., and Siegl, B. Multimode backward whirl motion in rotor-stator contact. *11th ICOVP, Lissabon* (2013), 1–10.

[7] Bauer, J. Smart fluid damper for rotor systems. *ICSV19, Vilnius* (2012), 1–8.

[8] Baumann, K., Dohnal, F., and Markert, R. Magnetic bearings as actuators and sensors in journal bearing measurements. *12th ISMB, Wuhan* (2010), 686–693.

[9] Bently Nevada. *RK 4 Rotor Kit (Part Number 141592-01) Manual*, 07 2016.

[10] Ehehalt, U. *Bewegungsformen elastischer Rotoren bei Statorkontakt (Motion patterns of elastic rotors at stator contact)*. VDI Fortschritt-Berichte 11-336, VDI-Verlag, Düsseldorf, 2008.

[11] Ehehalt, U., Hahn, E., and Markert, R. Motion patterns at rotor stator contact. *IDETC/CIE, ASME Int. Design Eng. Technical Conf.*, DETC2005-84440 (2005), 1–12.

[12] Ehehalt, U., Hahn, E., and Markert, R. Experimental validation of various motion patterns at rotor-stator-contact. *ISROMAC-11*, Paper No. 37 (2006).

[13] Ehehalt, U., Hochlenert, D., and Markert, R. An analytical description of backward whirl caused by rotor-stator-contact. *ISROMAC-10*, Paper No. 152 (2004).

[14] Markert, R. System- und Unwuchtidentifikation von elastischen Rotoren aus Anfahrmessungen (System and unbalance identification of flexible rotors using run-up measurements). *VDI-Berichte 536* (1984), 121–139.

[15] Norrick, N., Siegl, B., and Alber, O. Backward whirl during rotor-stator contact of gyroscopic rotors. *11th ICOVP, Lissabon* (2013), 1–10.

[16] Seidler, M., and Markert, R. Non-stationary balancing of flexible rotors. *ZAMM 81*, 2 (2001), 429–430.

[17] Siegl, B., and Markert, R. Model-based non-stationary unbalance identification. *ISROMAC-16* (2016).

[18] Wegener, G. *Elastische Fanglager zur Amplitudenbegrenzung elastischer Rotoren (Elastic retainer bearings for amplitude reduction of elastic rotors).* VDI Fortschritt-Berichte 11-290, VDI-Verlag, Düsseldorf, 2000.

[19] Wegener, G., and Markert, R. Influence of contact and impact on the dynamics of an elastic rotor with an elastic retainer bearing. *In V. I. Babitsky: Dynamics of Vibro-Impact Systems, Springer, Berlin, Heidelberg* (1999).

[20] Zhang, X., and Markert, R. Adaptive control methods to minimize the unbalance response of magnetically suspended elastic rotors during run-up and run-down. *6th Int. Symp. on Magnetic Suspension Technology, Turin* (2001), 13–18.

Oliver Alber, Dr.-Ing.: MTU, 80995 München, Dachauer Str. 665, Germany (*oliver.alber@gmx.de*).

Ulrich Ehehalt, Dr.-Ing.: Siemens AG, 45479 Mülheim, Rheinstr. 100, Germany (*u.ehehalt@gmx.de*).

Richard Markert, Prof. Dr.-Ing.: Technische Universität Darmstadt, Otto-Berndt-Str. 2, 64287 Darmstadt, Germany (*markert@ad.tu-darmstadt.de*).
The author presented this contribution at the conference in the special session: "Dedicated to Professor Peter Hagedorn on the occasion of granting him the honor of doctor honoris causa of the Lodz University of Technology" organized by J. Awrejcewicz.

Georg Wegener, Prof. Dr.-Ing.: Hochschule Aschaffenburg – University of Applied Sciences, Würzburger Str. 45, 63743 Aschaffenburg, Germany (*georg.wegener@h-ab.de*).

Torsional vibration energy harvesting through transverse vibrations of a passively tuned beam

Panagiotis Alevras, Stephanos Theodossiades, Homer Rahnejat, Tim Saunders

Abstract: The paper highlights the potential of harvesting vibration energy from mechanical systems in the form of electrical power to activate remote electronic devices. The principal idea is based upon the resonant response of a lightweight oscillator subjected to applied external excitation, coupled with an electrodynamic transducer (e.g. piezoelectric material, inductive coils). As far as the mechanical system is concerned, the aim is to maximize the harvested energy when an attachment vibrates with relatively high amplitudes. This means that the system natural frequency should be close to the expected dominant frequency of the applied (host) vibrations. However, in practice the dominant vibration frequency varies either within a limited range due to system uncertainties or across a large band due to the fundamental operation of the host structure, such as in rotational power transmission systems with speed variations. Recently, the introduction of nonlinearities has been proposed in order to compensate for small-scale frequency shifts. Nevertheless, in most cases one cannot fully bypass the necessary tuning effects, attributed to linear stiffness components in system dynamics. In this paper, a rotational vibration energy harvester is outlined, based upon a beam attachment, coupled with an electromagnetic transducer. The stiffening effect due to centrifugal action is utilized in order to passively tune the attachment to the dominant frequency of the rotational host structure. A reduced order model of the harvester is presented and its power extraction potential is assessed.

1. Introduction

Vibration energy harvesting is an emerging field, converting the environmental vibration energy of a host structure or machine for usable electric output [1]. This energy can then potentially be used to power low consumption electronic devices, such as wireless sensors. Common energy harvesters initially comprised linear oscillators, coupled with an electrodynamic element, such as piezoelectric patches or permanent oscillatory magnets in the proximity of a coil of thin wire. The main drawback of this technique is the limited frequency response of such oscillators [2]. Briefly, these harvesters need to be tuned to a certain frequency in order to resonate with the host's vibrations. However, mechanical systems often operate across a wide range of frequencies leading to mistuning of the harvesting devices. Consequently, their efficiency in terms of power output dramatically reduces when frequency variations occur.

In recent years, the introduction of non-linearity has broadened the frequency band response of mechanical oscillators [3-4]. Many researchers have employed the transverse vibrations of a beam, attached to a host structure to exploit its nonlinear response. A recent review is provided by Wei and Jing [5]. Erturk and Inman studied a distributed beam model for piezoelectric energy harvesting [6]. They also studied experimentally a bimorph cantilever beam for enhanced harvesting capabilities [7]. Recently, significant progress has been made with bi-stable energy harvesters, a vast majority of which concern transverse vibrations of buckled beams [8].

An overwhelming majority of reported studies have considered the translational vibration problems in this regard, largely neglecting the opportunities with torsional systems that abound in powertrains and rotor dynamic applications. One can conceive the design of a piezo-generator, based on torsional stressing of its active elements [9-10]. Furthermore, the piezoelectric cantilever design has been used for either torsional vibratory modes with piezoelectric attachments, or in bending modes, extending radially from a shaft subjected to torsional oscillations [11].

In this paper, a vibration energy harvester based on transverse beam vibrations is proposed for rotational systems. Torsional vibrations in rotor systems often experience large scale frequency shifts attributed to changing operating speed. The proposed concept aims to passively tune the beam element of the harvester to the speed-dependent torsional vibrations. This is accomplished through induced centrifugal action acting upon an attached beam as an agent for passive tuning. The design strategy is presented and the harvested power is predicted numerically.

2. System modelling

A disc (D) is assumed to rotate with angular speed $\omega = 2\pi n/60$, as shown in Fig. 1. A thin beam of length L, width a and thickness b is attached to the disc with one end connected to its rotational axis via the support S1. The other end is connected at an eccentric location on the disc via the support S2, such that the beam extends radially from the disc centre. These supports can be one of clamped, pinned or roll independent from each other. The beam has modulus of elasticity E, density ρ and it is positioned with its width b perpendicular to the plane of the disc, such that it can experience transverse vibrations along the disc's plane. The distance of a point P on the beam from the axis of rotation is denoted by x, whereas the beam deflection in the transverse direction is denoted by $w(x)$. A magnet is fixed at an arbitrary point P on the beam via a massless, rigid link. A coil of thin wire is also fixed onto the disc, at a position such that the magnet lies within the coil. Torsional vibrations of the disc D cause transverse beam vibrations with respect to its rotating plane. The vibratory response of the beam entails relative motion between the magnet and the coil, thus inducing a coil voltage due to electromagnetic coupling, k_c. Then, an electric load with an electric resistance equal to the coil's, $R_l = R_c$, is connected at the

coil ends, completing the circuit. The harvested energy is usually taken as the energy that the load consumes. This also holds for the harvested power as well. The described system corresponds to an elemental vibration energy harvester for the purpose of demonstrating the utility of the proposed concept.

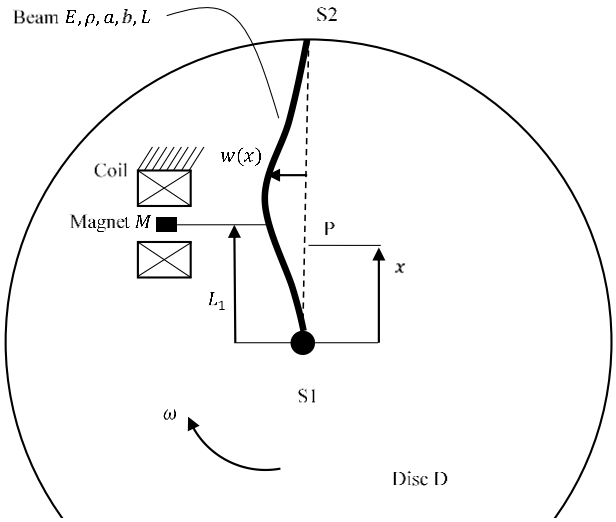

Figure 1. Sketch of the proposed torsional vibration energy harvester.

It is assumed that the beam is sufficiently thin to follow the Euler-Bernoulli beam theory. Therefore, considering an axial load $P(x)$, the transverse vibrations of the beam are described by the following spatio-temporal differential equation:

$$m_1(x)\ddot{w} + c_1\dot{w} + \frac{\partial}{\partial x}[P(x)w'] + EIw'''' - \frac{EA}{2L}w'' \int_0^L (w')^2 dx = -m_1(x)\ddot{z}, \tag{1}$$

where $m_1(x) = [\rho A + M\delta(x - L_1)]$, $A = ab$ is the beam cross-sectional area, c_1 is the viscous damping coefficient, I is the second area moment of inertia of the beam cross-section and z denotes the disc's vibration response. Using a single mode approximation such that $w(x,t) = q(t)\varphi(x)$, where $\varphi(x)$ is the first mode shape, one arrives at:

$$m\ddot{q} + c\dot{q} + kq + k_3q^3 = -f_m\ddot{z}, \tag{2}$$

where

$$m = \int_0^L \rho A\varphi^2 \, dx + M\varphi^2(L_1), \tag{3}$$

$$c = \int_0^L c_1\varphi^2 \, dx, \tag{4}$$

$$k = EI\int_0^L(\varphi'')^2\,dx + \int_0^L P(x)\,(\varphi')^2\,dx, \tag{5}$$

$$k_3 = -\frac{EA}{2L}\int_0^L \varphi''\varphi\,dx\int_0^L(\varphi')^2\,dx, \tag{6}$$

$$f_m = \int_0^L \rho A\varphi\,dx + M\varphi(L_1), \tag{7}$$

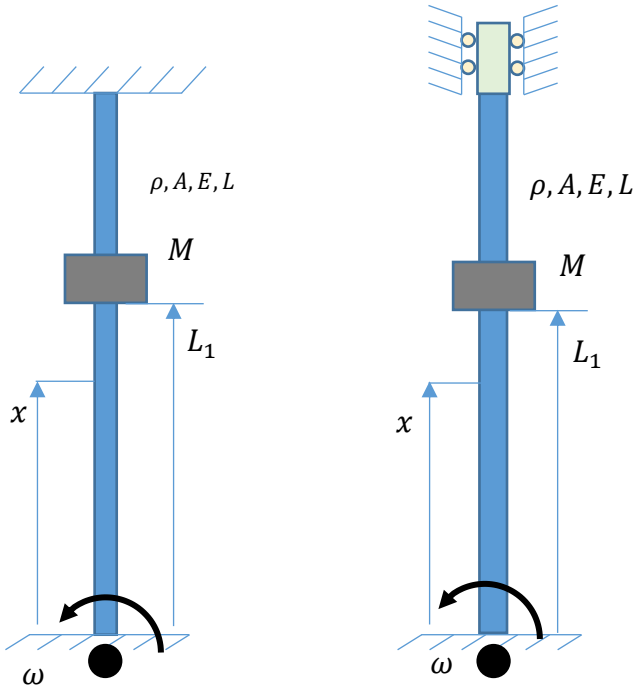

Figure 2. Two cases of boundary conditions: (a) clamped-clamped; (b) clamped-roll.

3. Passive tuning of the beam

The axial load in the proposed concept is as a result of the centrifugal action on the beam and the lumped mass, M. This is heavily dependent on the boundary conditions. In this paper, two cases of beam support are considered: (i)- clamped-clamped (C-C) and (ii)- clamped-roll (C-R), as shown in Fig. (2). The axial load depends on the position of the lumped mass, L_1, representing the magnet and its fixture, and on the disc's rotational speed. Fig. (3) shows the axial load across the span of the beam with respect to the position of the mass, L_1 and the rotation speed, n. Note that for C-C boundaries the load is tensile when $x < L_1$ and compressive elsewhere, whereas for the C-R supports the load is always tensile. This is caused by the axial reaction of the outer clamp, contrary to the inability of the roll support to contribute in the axial direction.

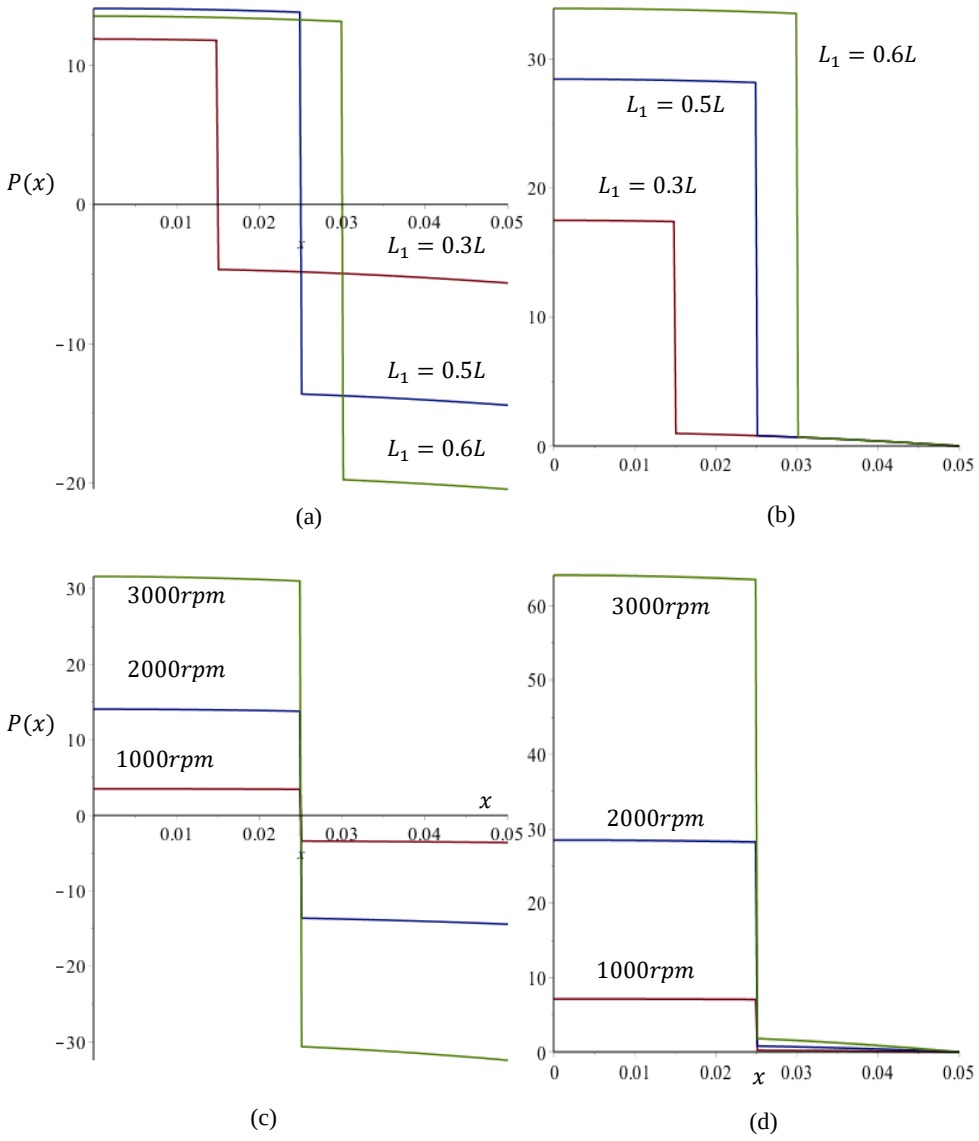

Figure 3. Axial load acting on the beam along its length. The left column corresponds to C-C support and the right column to C-R. The top figures depict the influence of the position L_1 at 2000 rpm and the bottom figures show the influence of the rotation speed n for $L_1 = 0.5L$.

The axial load variation induces the beam modal frequencies to vary accordingly. Following the reduced model in Eq. (2)-(7), the natural frequency can be calculated as:

$$f_n = \frac{1}{2\pi}\sqrt{\frac{k}{m}}, \tag{8}$$

As an example we consider a beam with the following characteristics: $E = 200\ GPa, L = 50mm, b = 5mm, t = 0.5mm, \rho = 7810\ kg/m^3, M = 0.100\ kg$. Fig. (4) shows the variation of the beam's first modal frequency with respect to the rotational speed of the disc, n. As the torsional vibrations in most rotational systems directly correspond to the system rotational speed, one can potentially passively tune the beam to the frequency of the speed-dependent vibrations, subjected to proper design provisions and *a priori* knowledge of the expected system response. Therefore, resonant conditions may be maintained in a wide-band of frequencies, promoting efficient vibration energy harvesting.

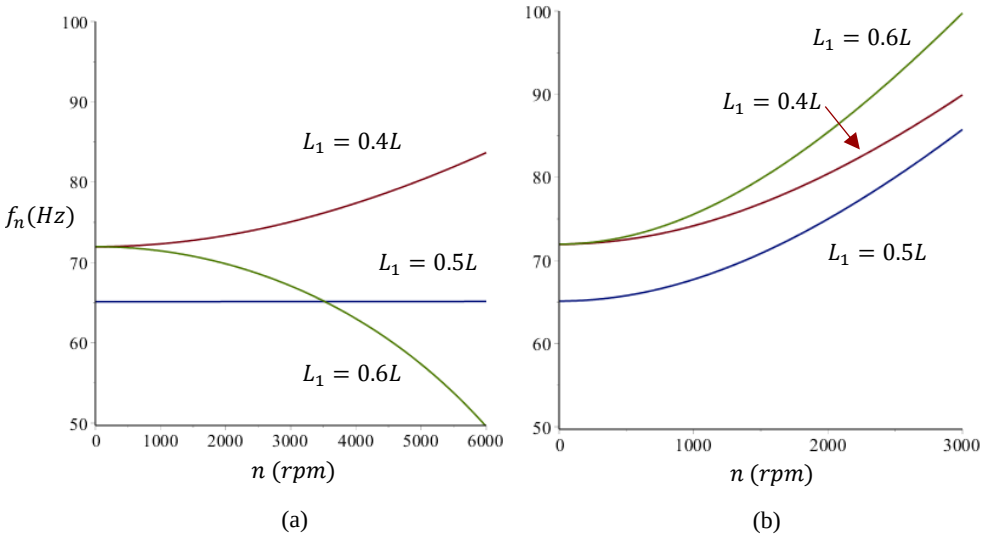

Figure 4. Dependence of the model's modal frequency for varying speed and different positions of the mass M; (a) C-C boundaries; (b) C-R boundaries.

Fig. (4) shows the frequency variations for the two considered boundary condition options. Depending on the desired variation of the system's natural frequency, one can choose the proper boundary conditions to passively tune the beam to higher or lower frequencies. Note that with the C-C supports, if the mass is positioned at the middle of the beam no tuning would be achieved. This is

consistent with Fig. (3c), which shows that the tensile load is opposing symmetrically the compressive load.

As a second example, consider the case of torsional vibrations in automotive powertrains. In such systems, vibrations unfold with a frequency directly linked to the system's rotational speed; specifically to the engine's firing frequency. In order to achieve efficient vibration energy harvesting, resonant conditions must be satisfied across a wide operating frequency range, which is nearly impossible with typical linear harvesters. The design proposed herein requires the modal frequency to closely match the expected vibration frequency. Consider then the following beam: $E = 200\,GPa, L = 80\,mm, b = 15\,mm, t = 0.2\,mm$, $\rho = 7810\,kg/m^3$, $M = 0.100\,kg$, which is clamped at one side and supported by a roller at the other. Fig. (5) shows the variation of the beam's first modal frequency with the system's rotational speed. The magnet is fixed at $L_1 = 0.575L$ in order to ensure good coincidence with the excitation frequency. It is observed that the modal frequency is tuned such that it remains close to the excitation frequency. In this manner, the harvester's response is expected to reside close to the resonant region.

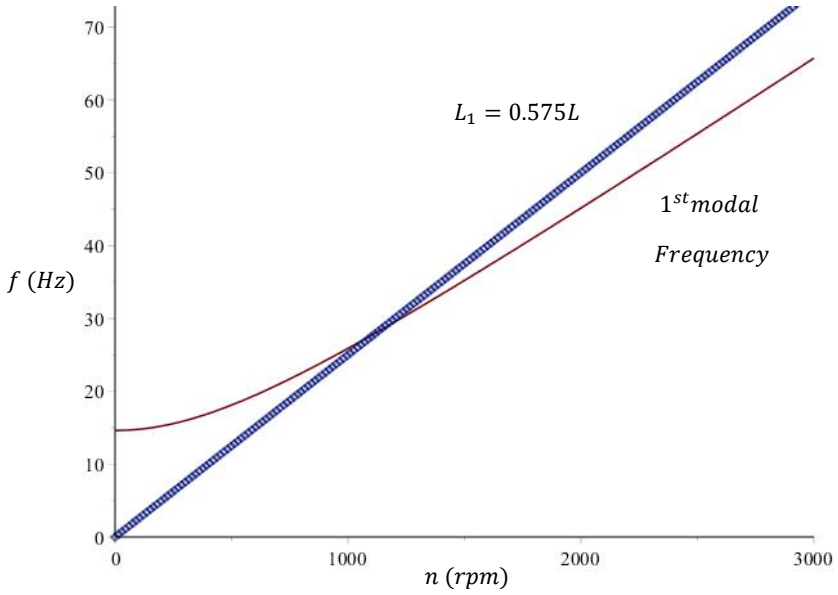

Figure 5. Variation of the C-R beam's first modal frequency across a wide range of frequencies (solid line), plotted with the expected dominant frequency of the host's torsional vibrations (circles).

4. Harvested power

Including the electric circuit in the equations of motion introduces an additional damping term which dissipates energy from the beam and so, $c_1 = c_m + c_e$, where $c_e = k_c^2/2R_l$. Furthermore, the harvested power is given by:

$$P_l = \frac{k_c^2}{2R_l}\dot{w}^2(L_1), \tag{8}$$

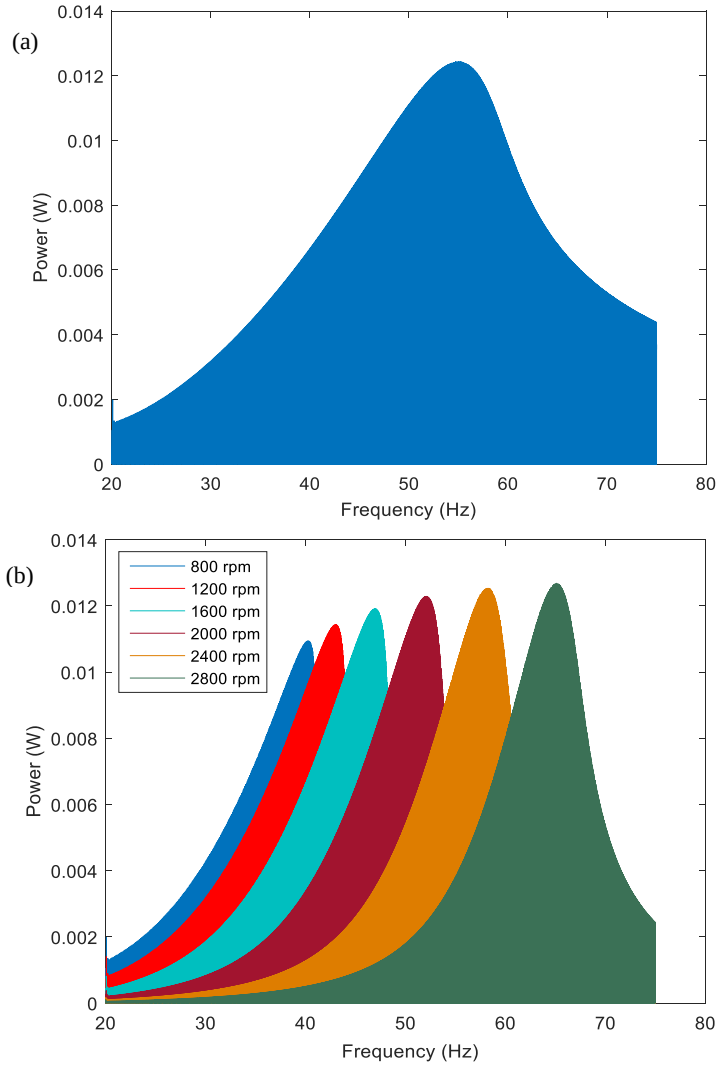

Figure 6. Comparison of the power output; (a) harvester tuned by centrifugal effect; (b) harvesters tuned at different shaft speeds.

Adopting these formulae for the assumed beam in Fig. (5), selected for the purpose of demonstration $k_c = 11\,Tm, R_l = 50\,\Omega$, then the harvested power with the proposed passively tuned concept – Fig. (6a) – is compared with several non-tunable harvesters with set frequencies in the range of interest in Fig. (6b). One can readily observe that the passively tuned harvester demonstrates a far wider frequency response as opposed to its narrow-band counterparts tuned at specific frequencies.

5. Conclusions

In this paper, a concept for harvesting vibration energy from rotating systems is presented. The concept utilizes the dependence of a thin beam's natural frequency on externally applied axial loads. A means of passively tuning the harvester to the host's torsional vibrations through the utilization of the centrifugal action is proposed. It is shown that the proposed device can target a wide frequency range offering resonant vibration energy harvesting over a large range of operating conditions of the host structure.

Acknowledgments

The authors wish to express their gratitude to the Engineering and Physical Sciences Research Council (EPSRC) for the financial support extended to the "**Targeted energy transfer in powertrains to reduce vibration-induced energy losses**" Grant (EP/L019426/1), under which this research was carried out.

References

[1] Stephen, N.G. On energy harvesting from ambient vibration. *J. Sound and Vibration* 293,1 (2006), 409-425.

[2] Priya, S. and Inman, D.J. *Energy harvesting technologies*, Springer, New York, NY, 2009.

[3] Mann, B. P. and Sims, N. D. Energy harvesting from the nonlinear oscillations of magnetic levitation. *J. Sound and Vibration* 329, 9 (2009), 515-530.

[4] Cottone, F., Vocca, H., and Gammaitoni, L. Nonlinear energy harvesting. *Phys. Rev. Lett.* 102 (2009), 080601.

[5] Wei, C. and Jing, X. A comprehensive review on vibration energy harvesting: Modelling and realization. *Renewable and Sustainable Energy Reviews* 74 (2017), 1-18.

[6] Erturk, A., and Inman, D., A Distributed Parameter Electromechanical Model for Cantilevered Piezoelectric Energy Harvesters. *Journal of Vibration and Acoustics* 30, 4 (2009), 025009 (18pp).

[7] Erturk, A., and Inman, D., An experimentally validated bimorph cantilever model for piezoelectric energy harvesting from base excitations. *Smart materials and structures* 18, 2 (2008), 041002 (15pp).

[8] Harne, R.L. and Wang, K.W. Harnessing Bistable Structural Dynamics: For Vibration Control, Energy Harvesting and Sensing. Wiley, Chichester, UK, 2017.

[9] Chen, Z.-G., Hu, Y.T. and Yang, J.-S. Piezoelectric generator based on torsional modes for power harvesting from angular vibrations. *Applied Mathematics and Mechanics*, 28, 6 (2007), 779-784.

[10] Musgrave, P., Wanlu Z., and Lei, Z., Piezoelectric Energy Harvesting From Torsional Vibration. *Proc. ASME 2015 International Design Engineering Technical Conferences and Computers and Information in Engineering Conference*, Volume 8: 27th Conference on Mechanical Vibration and Noise Boston, Massachusetts, USA, August 2–5, 2008, Paper No. DETC2015-47574.

[11] Kim, G.W. Piezoelectric energy harvesting from torsional vibration in internal combustion engines. *Int. J. Automotive Technology* 16, 4 (2015), 645-651.

Panagiotis Alevras, Ph.D. (Research Associate): Wolfson School of Mechanical, Electrical and Manufacturing Engineering, Loughborough University, Wolfson Building, Epinal Way, Loughborough, Leicestershire, LE11 3TU, United Kingdom (*p.alevras@lboro.ac.uk*). The author gave a presentation of this paper during one of the conference sessions.

Stephanos Theodossiades, Professor: Wolfson School of Mechanical, Electrical and Manufacturing Engineering, Loughborough University, Wolfson Building, Epinal Way, Loughborough, Leicestershire, LE11 3TU, United Kingdom (*s.theodossiades@lboro.ac.uk*).

Homer Rahnejat, Professor.: Wolfson School of Mechanical, Electrical and Manufacturing Engineering, Loughborough University, Wolfson Building, Epinal Way, Loughborough, Leicestershire, LE11 3TU, United Kingdom (*h.rahnejat@lboro.ac.uk*).

Tim Saunders, Ph.D.: Ford Motor Company Ltd, Dunton Technical Centre, Laindon, Basildon, Essex, SS15 6GB, United Kingdom (*tsaunde2@ford.com*).

Natural oscillations of rectangular plates with holes: using Reissner's approach

Igor V. Andrianov, Jan Awrejcewicz, Alexander A. Diskovsky

Abstract: The problem regarding the influence of holes on natural oscillations of rectangular plates has not been completely solved yet. Analytical solutions based on the traditional Rayleigh-Ritz and Bubnov-Galerkin approaches are associated with difficulties due to the approximate choice of the approximating functions for the plate deflections which should satisfy the boundary conditions. In this work, in order to study the influence of an arbitrary hole on the frequencies of a rectangular plate with an arbitrary hole, Reissner's variational principle is employed. In order to validate the proposed algorithm, a test problem is solved aimed defining the fundamental frequency of the continuous simply supported square plate. The proposed algorithm of the estimation of fundamental frequency of vibrations of the rectangular plates with a free hole possesses numerous advantages in comparison to the methods used in earlier published works. Namely, it does not introduce any limits on the dimension form and location of the hole and can be extended to study a few holes and other boundary conditions for both the plate and the hole. However, the obtained frequencies can be either larger or smaller than the exact values, and there is no any way to estimate the sign of this deviation.

The problem regarding influence of holes on the natural oscillations of rectangular plates is not completely solved yet. Analytical solutions based on the traditional Rayleigh-Ritz and Bubnov-Galerkin approaches are associated with difficulties due to the approximate choice of the approximating functions for the plate deflections which should satisfy the boundary conditions [1].

This is why the many investigations have been aimed on carrying out either experimental [2] or theoretical-experimental studies [3]. The mentioned and my other papers have been focused on study of the square plates with clamping edges, since the latter boundary conditions are easily realized experimentally. Free vibrations of simply supported square plates with centrally located circle holes have been also investigated in reference [4].

However, the results obtained there have been limited to the relatively small holes: $2r / a \le 0.3$ (a – length of the plate side; r – hole radius).

In this work, in order to study influence of an arbitrary hole on the frequencies of rectangular plate with arbitrary hole (Fig.1) the Reissner's variational principle is employed [5]. This principle has been successfully used in reference [6] to the problems of deflections of a cantilever plate. It seems that a

similar like approach can be used effectively also in the case of our problems because the fundamental difficulties of investigation of the free vibrations of the cantilever and multi-coupled plates (different boundary conditions should be satisfied on different parts of a contour) coincide.

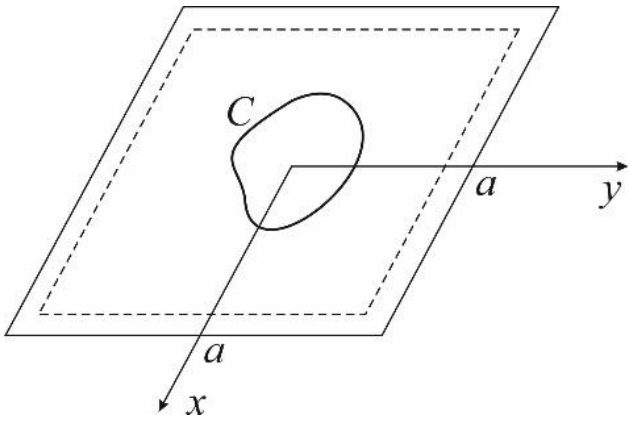

Figure 1. Investigated plate with a hole

In the case of the natural oscillations of thin plates the Reissner's variation principle takes the following form

$$\delta\left\{\iint_A\left[-M_x\frac{\partial^2 w}{\partial x^2}-M_y\frac{\partial^2 w}{\partial y^2}+2M_{xy}\frac{\partial^2 w}{\partial x\partial y}-\frac{1}{2D(1-\nu^2)}(M_x^2+M_y^2+\right.\right.$$
$$\left.\left.+2(1+\nu)M_{xy}^2)-\frac{\Omega^2\rho}{2}w^2\right]dxdy-\int_C\left[-M_n\frac{\partial w}{\partial \mathbf{n}}+\left(\frac{\partial M_n}{\partial \mathbf{n}}+2\frac{\partial M_{nt}}{\partial s}\right)w\right]ds\right\}=0, \tag{1}$$

where: w – oscillation form; $D=\frac{Eh^3}{12(1-\nu^2)}$; E – Young modulus; ν - Poisson's coefficient; Ω - circular frequency; ρ - mass density per unit plate surface; $\mathbf{n}$ – normal vector to the hole contour, A – area of plate, $-a\le x,y\le a$; s – coordinate along hole contour.

The variational equation (1) is equivalent to a differential equation of plate equilibrium state, physical relations of elasticity and static boundary conditions on the hole contour C (see Fig. 1).

Equation (1) is used for the approximate determination of the eigenfrequency of plate vibration in the following way. Deflection and moments are approximated independently through the function with a few (not defined yet) parameters in order to satisfy boundary conditions on the plate edges. Substituting those expressions into the variational equation (1) and carrying out the variational procedure the algebraic system of linear homogeneous equations with respect to the parameters is

obtained. Comparing the determinant of the system of equations to zero, we find the equation for the eigenfrequency.

A success of the so far described method depends on how accurately the assumed functions for deflection and moments approximate the real/true functions while appropriately choosing the undefined parameters. Therefore, in order to improve convergence of the computational process it is reasonable to require satisfaction of the approximating the boundary conditions functions on the hole contour. Note, that in the latter case the curvilinear integral in formula (1) vanishes, and the input system of equations is essentially simplified.

The boundary conditions for the simply supported square plate with free hole (Fig.1) are taken

$$\text{for } \xi^2 = 1, \quad \omega = 0, \quad M_\xi = 0 \quad \text{and for } \eta^2 = 1, \quad \omega = 0, \quad M_\eta = 0, \tag{2}$$

whereas on the contour *C* they have the following forms

$$\begin{aligned} M_n &= M_\xi \cos^2\varphi + M_\eta \sin^2\varphi - 2M_{\xi\eta}\cos\varphi\sin\varphi = 0, \\ M_{nt} &= M_{\xi\eta}(\cos^2\varphi - \sin^2\varphi) + (M_\xi - M_\eta)\cos\varphi\sin\varphi = 0, \\ Q_n &= \left(\frac{\partial M_{\xi\eta}}{\partial\eta} + \frac{\partial M_\xi}{\partial\xi}\right)\cos\varphi + \left(\frac{\partial M_\eta}{\partial\eta} - \frac{\partial M_{\xi\eta}}{\partial\xi}\right)\sin\varphi = 0, \end{aligned} \tag{3}$$

where: $\xi = \frac{2x}{a}$; $\eta = \frac{2y}{a}$; φ - angle between the axis *x* and a normal to the hole contour *C*.

Here we have employed boundary conditions on contour *C* (3) in the form proposed by Poisson. This differs from the Kirchhoff's boundary conditions, since the taken ones can be solved only with respect to M_ξ, M_η, $M_{\xi\eta}$. In result, on the hole boundary we obtain

$$M_\xi = M_\eta = M_{\xi\eta} = 0. \tag{4}$$

Deflection and moments can be described by the following relations satisfying the boundary conditions

$$\begin{aligned} w &= \omega_1 \sum_{n=1}^{k} c_{1n}\varphi_{1n}, \qquad M_\xi = \omega_2 \sum_{n=1}^{k} c_{2n}\varphi_{2n}, \\ M_\eta &= \omega_3 \sum_{n=1}^{k} c_{3n}\varphi_{3n}, \qquad M_{\xi\eta} = \omega_4 \sum_{n=1}^{k} c_{4n}\varphi_{4n}. \end{aligned} \tag{5}$$

Here $\omega_i = 0$ on those parts of the boundary which require satisfactions of the boundary conditions (2), (3); φ_{in} - certain a priori chosen approximating functions; c_{in} - arbitrary constants. Now, employing the R - function method [7-9] to construct ω_i, it is not difficult to satisfy boundary conditions of the plate with a hole of an arbitrary form.

The described algorithm has been realized numerically to study influence of the free central circle hole localized in a square plate on its fundamental frequency of vibration. For simplicity, we have used only one approximating functions in the series (5), i.e.

$$w = c_1 \cos\frac{\pi\xi}{2}\cos\frac{\pi\eta}{2}, \qquad M_\xi = c_2(\xi^2 - \eta^2 - R^2)\cos\frac{\pi\xi}{2}\cos\frac{\pi\eta}{2},$$
$$M_\eta = c_3(\xi^2 + \eta^2 - R^2)\cos\frac{\pi\xi}{2}\cos\frac{\pi\eta}{2}, \qquad M_{\xi\eta} = c_4(\xi^2 + \eta^2 - R^2)\sin\frac{\pi\xi}{2}\sin\frac{\pi\eta}{2}, \tag{6}$$

where: $R = 2r / a.$ Our results have been compared with those obtained by Hegarty [4] (Fig. 2). The largest error on amount of 16% occurs for small holes; increase of the hole dimension it decrease up to 10%.

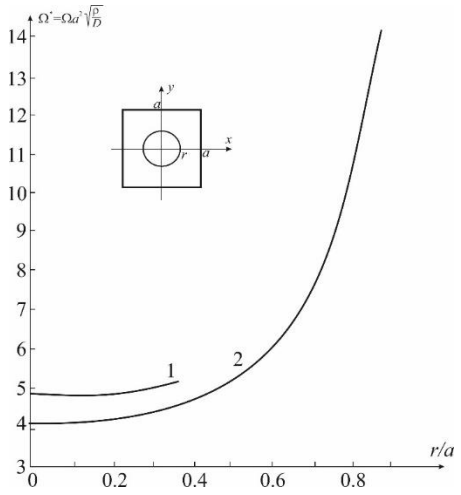

Figure 2. The fundamental frequency of the plate versus hole radius
(1 – results reported in [4]; 2 – our results)

This error has its motivation in a lack of a guarantee of the limiting transition to the continuous plate by the taken approximation of the moments (6). However, Hegarty obtained only upper estimation of the fundamental frequency, and hence the real error is lower.

In order to validate the proposed algorithm, a taste problem is solved in order to define the fundamental frequency of the continuous simply supported square plate. Its deflection and moments are approximated by the following formulas:

$$\varpi = c_1 \cos\frac{N\pi\xi}{2}\cos\frac{N\pi\eta}{2}, \qquad M_\xi = c_2 \cos\frac{N\pi\xi}{2}\cos\frac{N\pi\eta}{2},$$
$$M_\eta = c_3 \cos\frac{N\pi\xi}{2}\cos\frac{N\pi\eta}{2}, \qquad M_{\xi\eta} = c_4 \sin\frac{N\pi\xi}{2}\sin\frac{N\pi\eta}{2}. \tag{7}$$

Note that in this case a difference comparing with the exact result achieved only 2%.

It should be emphasized that the proposed algorithms of the estimation of fundamental frequency of vibrations of the rectangular plates with free hole possesses numerous advantages in comparison to the methods used in works [1,4]. Namely, it does not introduce any limits on the dimension form and location of a hole, and can be extended to study a few of holes and other boundary conditions for the plate and hole.

There is, however, one drawback while applying the Reissner's principle to the problems of vibrations. In contrary to the Rayleigh-Ritz method, which allows to estimate frequencies located over their exact values, the Reissner's method cannot guarantee this rule [5]. In words, the obtained frequencies can be either larger or smaller than the exact values, and there is no any way to estimate a sign of this deviation.

References

[1] Kristiansen, U., Soedel, W., Fundamental of cutout square plates with clamped edges, J. Eng. Ind. 93(1) (1971) 343-345.

[2] Weaver Jr., W., Timoshenko, S.P., Young, D.H., Vibration Problems in Engineering, John Wiley & Sons, 1990.

[3] Konoplev, Yu.G., Shishkin, A.G., Free vibrations of plates and shells with holes or on point supports, in: Studies on Theory of Plates and Shells 14 (1979) Kazan, pp. 82-99 (in Russian).

[4] Hegarty, R.F., Elasto-dynamic analysis of rectangular plates with circular holes, Int. J. Solid Struc. 11(7-8) (1975) 895-906.

[5] Slivker, V., Mechanics of Structural Elements. Theory and Applications, Springer, Berlin, 2007.

[6] Plass, H.J., Gains, J.H., Newsom, C.D., Application of the Reissner's variational principle to cantilever plate deflection and vibration problems, Applied Mechanics 29(1) (1962) 127-135.

[7] Rvachev, V.L., Methods of Logic Algebra in Mathematical Physics, Kiev, Naukova Dumka, 1974 (in Russian).

[8] Shapiro, V., Semi-analytic geometry with R-Functions, Acta Numerica 16 (2007) 239-303.

[9] Kurpa, L.V., Natural vibrations of plates with holes, Soviet Applied Mechanics 15(2) (1979) 173-175.

Igor V. Andrianov: Institut für Allgemeine Mechanik, RWTH Aachen University, Templergraben 64, D-52056, Aachen, Germany (igor_andrianov@hotmail.com)

Jan Awrejcewicz: Department of Automation, Biomechanics and Mechatronics, Lodz University of Technology, 1/15 Stefanowski St., 90-924, Lodz, Poland (awrejcew@p.lodz.pl)

Alexander A. Diskovsky: National Metallurgical Academy of Ukraine, Department of Higher Mathematics, 23 Gagarina Str., UA-49005, Dnepr, Ukraine (alex_diskovskiy@ukr.net)

The pendulum dynamic analysis with DC motors and generators for sea waves energy harvest

Rafael Avanço, Angelo Tusset, Marcelo Suetake, Helio Navarro, José Balthazar, Airton Nabarrete

Abstract: The present analysis is based on ideal and nonideal excitation of a pendulum. The models studied considered 4 different pendulous mechanisms and comparisons among them. The first mechanism is a pendulum ideally excited on its pivot by a crank-shaft-slider mechanism above it and the second a nonideal excitation of the same mechanism powered by a DC motor. The third considers also a nonideal excitation, however the crank and the DC motor are on the left side of the pendulum, so horizontally displacing its support. Finally, the last considers a DC generator above the pendulum collecting energy from its motion. The pendulum is suspended on a boat by its pivot and sea waves shakes the set. Hence, the generator is spun by the pendulum pivot co-axially linked to the axis of the motor or linked by the crank-shaft-slider, where this crank is co-axially coupled to the generator. The first mechanism exhibits different types of motion including chaos, rotations, oscillations and fixed points for the main resonance frequency and subhamonic frequencies. The second and third, due to the nonideal source of energy, more commonly demonstrates results with synchronization. The last, where the DC generator is coupled to the pendulum, is the novelty brought by this paper. The types of motion observed in the pendulum coupled to the DC generator include both rotations and oscillations.

1. Introduction

This article provide analyses of 4 different models and comparisons among them. The first mechanism consists of a pendulum parametrically excited by a crank-shaft-slider mechanism. The vertical displacement on the pivot of the pendulum approaches to the harmonic motion when the crank radius is smaller enough when compared to the shaft length. The second mechanism is a DC motor executing the motion on the pivot of the pendulum in the vertical direction using the same crank-shaft-slider mechanism. The third mechanism is also a pendulum coupled to a crank-shaft-slider powered by a DC motor, but the crank is on the left side of the pendulum, so moving horizontally the support of the pendulum. The fourth mechanism studied is the novelty. The model include a DC generator coupled to a pendulum. This pendulum is harmonically vibrated on its pivot and the motion of the pendulum provokes the rotation of the generator shaft.

2. Dynamical models

2.1. Ideal excitation with a crank-shaft-slider mechanism

This model was developed and firstly analyzed in Avanço et al [1-2]. The crank rotates with constant speed moving the support of the pendulum in the vertical direction. In comparison with the classical parametric pendulum studied in Leven and Koch [3], the mechanism analyzed in this section, and represented in Fig.1, exhibits more complexity. The same mechanism of [3] was well studied in Xu et al [4], where the focus was the rotating orbits.

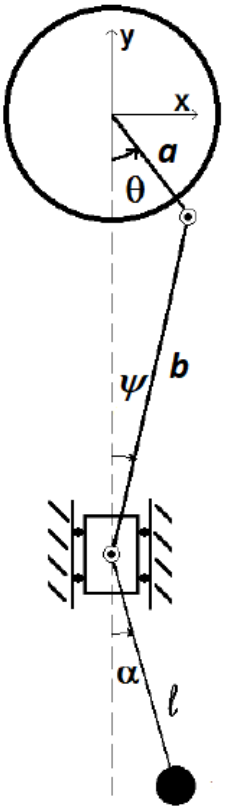

Figure 1. The crank-shaft-slider mechanism

Considering the center of the crank as the zero level of potential energy, the equations of kinetic energy and potential energy are written in Eq.2 and Eq.3, respectively. The Cartesian coordinates are represented in terms of the angles θ and α in Eq.1:

$$\begin{aligned} x &= l\sin\alpha \\ y &= -a\cos\theta - b\cos\psi - l\cos\alpha \end{aligned} \tag{1}$$

The kinetic energy is given by *T* and the potential energy by *V*:

$$T = \frac{1}{2}m(\dot{x}^2 + \dot{y}^2) \quad (2)$$

$$V = -mgy \quad (3)$$

The length of the pendulum is given by l, the bob in the tip of the pendulum has mass m, the crank length is represented by a, the shaft length is the letter b, all of them according to the Fig.1.

A function F is defined duo to the intrinsic trigonometric relation between the angles θ and ψ. The value of the angle ψ is written in terms of the values of θ and the lengths a and b.

$$F = \sin\theta + \frac{a}{b} \cdot \frac{\sin\theta\cos\theta}{(1-\frac{a^2}{b^2}\sin^2\theta)^{0.5}} \quad (4)$$

The Lagrangian function is written in terms of the coordinates α and θ, determined by the subtraction T-V:

$$L = \frac{1}{2}m(l^2\dot{\alpha}^2\cos^2\alpha + [a\dot{\theta}F + l\dot{\alpha}\sin\alpha]^2) + mgl\cos\alpha + mgb(1 - \frac{a^2}{b^2}\sin^2\theta)^{1/2} + mga\cos\theta \quad (5)$$

Applying the derivatives related to α and $\dot{\alpha}$ we obtain the Langrange equation related to the coordinate α:

$$\frac{d}{dt}\frac{\partial L}{\partial \dot{\alpha}} - \frac{\partial L}{\partial \alpha} = G_{\alpha}^{nc} \quad (6)$$

The result is the Eq. 7, where the dots mean the derivatives related to the physical time t. The nonconservative force in the right-hand side of Eq.7 is given by the dissipation in the joint. The term c is the coefficient of the viscous friction.

$$ml^2\ddot{\alpha} + mal\dot{\theta}\dot{F}\sin\alpha + mgl\sin\alpha = -cl^2\dot{\alpha} \quad (7)$$

Inserting the dimensionless time τwe obtain derivatives related to it. The physical time t multiplied by the natural frequency of the pendulum ω_0 results in the dimensionless term. The derivatives are found through the chain rule and are present in Eq.8.

$$\tau = \omega_0 t\alpha' = \frac{d\alpha}{d\tau} = \frac{1}{\omega_0}\frac{d\alpha}{dt}\alpha'' = \frac{d^2\alpha}{d\tau^2} = \frac{1}{\omega_0^2}\frac{d^2\alpha}{dt^2}\omega = \frac{d\theta}{d\tau} = \frac{1}{\omega_0}\frac{d\theta}{dt}F' = \frac{dF}{d\tau} = \frac{1}{\omega_0}\frac{dF}{dt} \quad (8)$$

The other dimensionless terms are demonstrated in Eq.9 and our final differential equation is the Eq.10.

$$\omega = \frac{\dot{\theta}}{\omega_0}p = \frac{a}{l}\frac{\dot{\theta}^2}{\omega_0^2}\varepsilon = \frac{a}{b}\gamma = \frac{c}{m\omega_0} \quad (9)$$

The final differential equation is given in dimensionless terms:

$$\alpha'' + \gamma\alpha' + \sin\alpha(1 + p\cos(\omega\tau) + \frac{\varepsilon p\cos(2\omega\tau)}{[1-\varepsilon^2\sin^2(\omega\tau)]^{1/2}} + \frac{\varepsilon^3 p\sin^2(2\omega\tau)}{[1-\varepsilon^2\sin^2(\omega\tau)]^{3/2}}) = 0 \quad (10)$$

In Fig.2 the Poincaré section is plotted which demonstrates chaotic appearance. As it was verified in Avanço et al [1] and Xu et al [4] , after a cascade of doubling period the chaotic motion may rises.

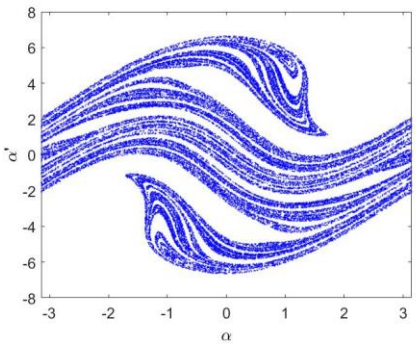

Figure 2. The Poincaré section shows the chaotic attractor with the parameters p=2.8, ω=1.8 and ε=0.9

The other types of motion include rotational motion, oscillations and fixed point. The Fig.3 demonstrates time history and Poincaré section with 2-period rotation.

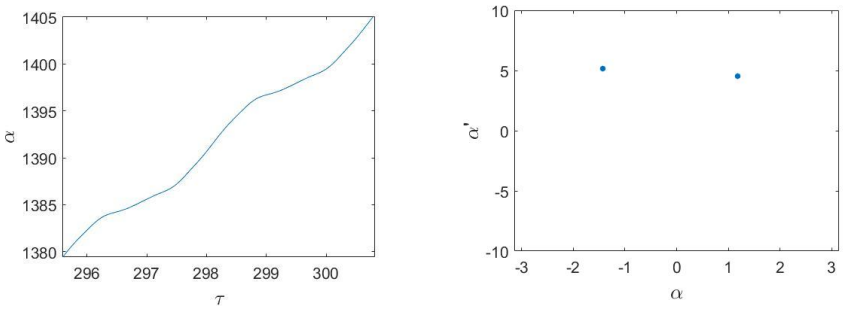

Figure 3. Time history and Poincaré section for ideal excitation with p =11.6, γ = 0.102, ω = 4.9 and ε=0.4

2.2. Nonideal vertical excitation with a crank-shaft-slider mechanism

In this model the pendulum is excited by a crank powered with a DC motor. The consequence is the pendulum interfere in the motion of the crank, while in the ideal model in the section 2.1 the crank speed is not affected by the pendulum dynamics.

The kinetic energy of the whole system includes the inertia of the rotor in the motor and the disc considered above the pendulum. The sum of the moment of inertia of the disc and the rotor is J. Therefore, the Lagrangian function in this case consists in:

$$L = \frac{1}{2}J\dot{\theta}^2 + \frac{1}{2}m(l^2\dot{\alpha}^2\cos^2\alpha + [a\dot{\theta}F + l\dot{\alpha}\sin\alpha]^2) + mgl\cos\alpha + mgb(1 - \frac{a^2}{b^2}\sin^2\theta)^{1/2} + mga\cos\theta \quad (11)$$

The dynamical system is represented in Fig.4, where the unique difference is the presence of the inertia of the disc in the crank.

In this case, two degrees of freedom demand two coordinates and consequently two Lagrange equations:

$$\frac{d}{dt}\frac{\partial L}{\partial \dot{\alpha}} - \frac{\partial L}{\partial \alpha} = G_{\alpha}^{nc}$$
$$\frac{d}{dt}\frac{\partial L}{\partial \dot{\theta}} - \frac{\partial L}{\partial \theta} = G_{\theta}^{NC} \quad (12)$$

The Lagrangian equations are found with the derivatives considering the 2 degrees of freedom. The Eq.13 was found by the coordinate θ and the Eq.14 by the coordinate α.

$$J\ddot{\theta} + ma^2F^2\ddot{\theta} + ma^2F\dot{F}\dot{\theta} + maFl\cos(\alpha)\dot{\alpha}^2 + maFl\sin(\alpha)\ddot{\alpha} + mgaF = M_{motor} - c_m\dot{\theta} \quad (13)$$

$$ml^2\ddot{\alpha} + mal\sin(\alpha)F\ddot{\theta} + mal\sin\alpha\dot{F}\dot{\theta} + mgl\sin\alpha = -cl^2\dot{\alpha} \quad (14)$$

The torque supplied by the motor is given by the Eq.(15). The terms K_T and K_E represent the constant of torque and speed constant equals 127.10^{-3} Nm/A. The voltage set is given by U.

$$M_{motor} = \frac{K_T U}{R} - \frac{K_E K_T \dot{\theta}}{R} \quad (15)$$

Using dimensionless time derivatives, the Eq 13, Eq.14 and Eq.15 lead to the Eq.16, Eq.17 and Eq.18:

$$J\omega_0^2\theta'' + ma^2F^2\omega_0^2\theta'' + ma^2FF'\theta'\omega_0^2 + maFl\cos(\alpha)\omega_0^2\alpha'^2 + maFl\sin(\alpha)\omega_0^2\alpha'' + mgaF = M_{motor} - c_m\theta'\omega_0 \quad (16)$$

$$\alpha'' + \gamma\alpha' + \frac{a\sin(\alpha)F\theta''}{l} + \frac{a}{l}\sin(\alpha)F'\theta' + \sin(\alpha) = 0 \quad (17)$$

$$M_{motor} = \frac{K_T U}{R} - \frac{K_E K_T}{R}\omega_0\theta' \quad (18)$$

Where the derivative of function F:

$$F' = \theta'\cos\theta + \varepsilon\frac{\theta\prime\cos(2\theta)}{(1-\varepsilon^2\sin^2\theta)^{1/2}} + \varepsilon^3\frac{\theta\prime\sin^2(2\theta)}{4(1-\varepsilon^2\sin^2\theta)^{3/2}} \quad (19)$$

The results obtained in Fig.5 are the time history and dimensionless angular speed of the pendulum. In the Fig.6 the dimensionless angular speed of the crank is plotted. The term ω in the vertical axis is the same of θ□ in Eq.17 and Eq.18. The voltage set is 4.5 Volt.

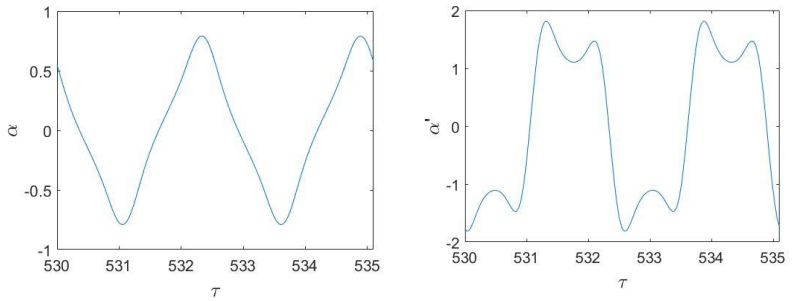

Figure 4. Time history and dimensionless angular speed of the pendulum for V=4.5 Volt

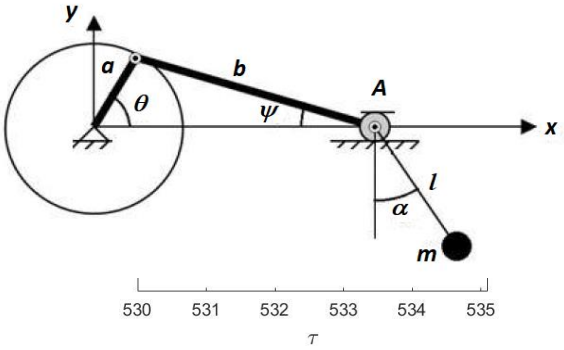

Figure 5. Dimensionless angular speed of the crank

Someone may observe that when the pendulum performed two cycles the crank performed four cycles in the interval between 530 and 535 forτ.A visible occurrence is a synchronization of the pendulum and crank speed.

The situation in Fig.3 did not have its parameters chosen by chance. They are worked out by the results seen in the simulation of Fig.5 and Fig.6 , when the voltage is 4.5 Volt. The mean value of the crank speed in Fig.6 was used in the ideal model of 2.1 section where the crank has a constant speed approached to 4.9 for the parameter ω.

The ideal model from section 2.1 demonstrated a rotational motion for the pendulum and the nonideal model from 2.2 section demonstrated an oscillatory solution. Hence there is a good reason to not approach a nonidel model to an ideal model. In some conditions it may be observed high discrepancies.

2.3. Nonideal horizontal excitation with a crank-shaft-slider mechanisms

This nonideal mechanism was analyzed in Belato et al [5], in the PhD Thesis [6] and in Krasnopolskaya and Shvets[7]. A DC motor powered the crank which moves horizontally the support of the pendulum. The reference for the potential energy is the center of the crank. The Eq.20 brings the position of the pendulum in terms of the angles and the length of the links.

Figure 6. Pendulum nonideally excited in the horizontal direction

$$x_p = a\cos\theta + b\cos\phi + l\sin\alpha$$
$$y_p = -l\cos\alpha \tag{20}$$

The kinetic energy considers the inertia of the rotor and the pendulum:

$$T = \frac{1}{2}m[\dot{x_p}^2 + \dot{y_p}^2] + \frac{1}{2}J\dot{\theta}^2$$
$$V = -mgl\cos\alpha \tag{21}$$

In this case we have two degrees of freedom related to the coordinates α and θ. The right hand side of the Eq.22 are the nonconservative generalized forces.

$$\begin{aligned} ml^2\ddot{\alpha} - malF\dot{\theta}\dot{\theta}\cos\alpha - malF\ddot{\theta}\cos\alpha + mgl\sin\alpha &= Q_{\alpha}^{NC} \\ J\ddot{\theta} + ma^2F\frac{dF}{d\theta}\dot{\theta}^2 + ma^2F^2\ddot{\theta} - maFl\ddot{\alpha}\cos\alpha + maFl\dot{\alpha}^2\sin\alpha &= Q_{\theta}^{NC} \end{aligned} \tag{22}$$

The nonconservative generalized forces for the two coordinates are the external torques acting in the directions α and θ:

$$\begin{aligned} Q_{\alpha}^{NC} &= -c_{\alpha}l^2\dot{\alpha} \\ Q_{\theta}^{NC} &= -c_Aa^2F^2\dot{\theta} + M_{motor} \end{aligned} \tag{23}$$

The Eq.24 and Eq.25 are the differential equations governing the system and in Eq.26 there are the dimensionless terms:

$$\begin{aligned} (J\omega_0^2 + ma^2F^2\omega_0^2)\theta'' = -ma^2F\frac{\partial F}{\partial\theta}\omega_0^2\theta'^2 + maFl\cos\alpha\omega_0^2\alpha'' - maFl\sin\alpha\omega_0^2\alpha'^2 \\ -c_Aa^2F^2\omega_0\theta' + M_{motor} - c_m\theta'\omega_0 \end{aligned} \tag{24}$$

$$\alpha'' = \frac{a}{l}\frac{\partial F}{\partial\theta}(\cos\alpha)\theta'^2 + \frac{a}{l}F(\cos\alpha)\theta'' - \sin\alpha - \frac{c_{\alpha}\alpha'}{m\omega_0} \tag{25}$$

Below it is represented the dimensionless terms and in Eq.27 these dimensionless terms are inserted:

$$\begin{aligned} C_1 = \frac{ma^2}{J}\ C_2 = \frac{mal}{J}\ C_3 = \frac{c_Aa^2}{J\omega_0}\ C_4 = \frac{K_TV}{RJ\omega_0^2} \\ C_5 = \frac{K_EK_T}{RJ\omega_0}\ C_6 = \frac{a}{l}\ C_7 = \frac{c_{\alpha}}{m\omega_0}\ \varepsilon = \frac{a}{b} \end{aligned} \tag{26}$$

$$\begin{aligned} \theta'' = -\frac{C_1F}{1+C_1F^2}\frac{\partial F}{\partial\theta}\theta'^2 + \frac{C_2F\cos\alpha}{1+C_1F^2}\alpha'' - \frac{C_2F\sin\alpha}{1+C_1F^2}\alpha'^2 - C_3F^2\theta' + C_4 - C_5\theta' \\ \alpha'' = C_6\frac{\partial F}{\partial\theta}(\cos\alpha)\theta'^2 + C_6F\cos\alpha\theta'' - \sin\alpha - C_7\alpha' \end{aligned} \tag{27}$$

In this section, the results from nonideal excitation are not compared with the respective ideal excitation as executed for the vertical nonideal excitation. The intention of this section is to demonstrated the diferent types of motion observed for small changes in the parameter control. The term C_4 is the parameter control and stand for the voltage set.

The graphics in Fig.8 represent the phase portraits of the pendulum for C_4 equals 12.9 in Fig.8(a), C_4 equals 13.02 in Fig.8(b), C_4 equals 13.125 in Fig.8(c) and C_4 equals 22.5 in Fig.8(d). As the control parameter C_4 increases, more periods appears in the phase portraits when you compare Fig.8(a), (b) and (c). Finally, about the Fig.8(d) a quasiperiodic motion occurs. It has 2 peaks of frequency (0.1465 Hz and 0.2411 Hz), which means according to Parker and Chua [8] a quasiperiodic attractor takes place, because the spikes of the spectrum are not spaced at integer multiples of one particular frequency.

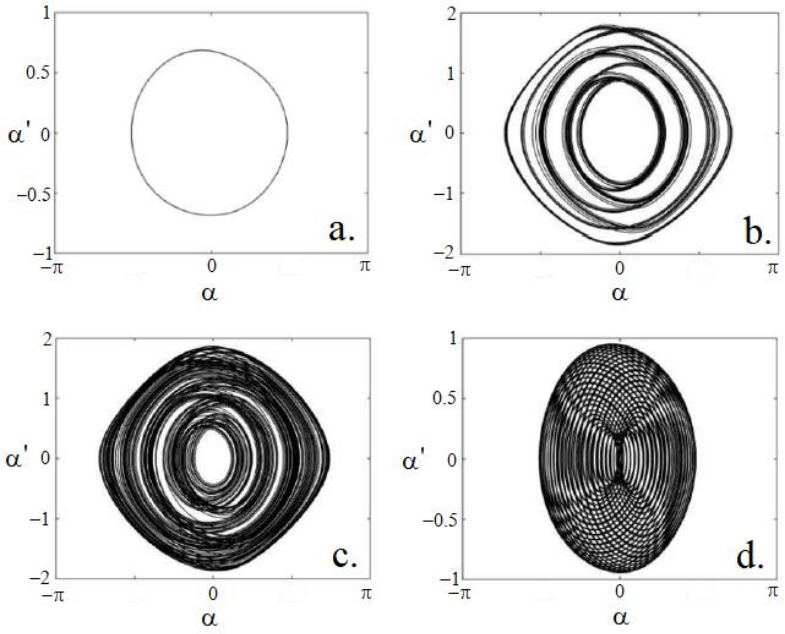

Figure 7. Phase portraits for the pendulum under nonideal excitation in horizontal direction

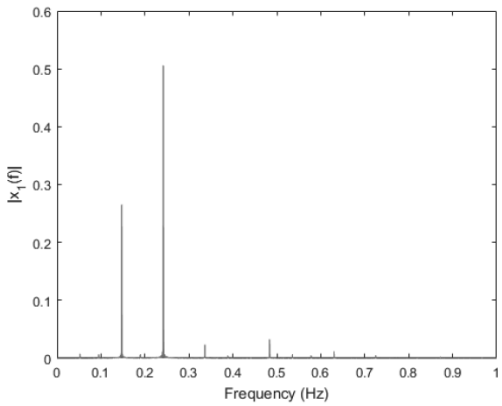

Figure 8. The power spectral density (FFT) for the angle.

2.4. Parametric pendulum coupled to a DC generator

The intention with the modeling in this section is to obtain the pendulum motion and energy harvest from sea waves. The pendulum is suspended on a boat and its joint goes up and down. A DC generator has the shaft that spin with the same speed of the pendulum, because they are linked.

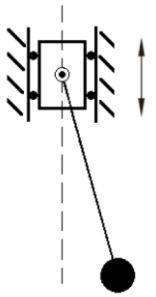

Figure 9. The pendulum under sinusoidal excitation

The pendulum moved by a crank-shaft-slider mechanism may have its excitation approached to a sinusoidal function when the parameter e approaches to zero. The term which represents the excitation by sea waves is the parameter p and the electric current in the generator causes an opposing torque to the spin of the pendulum. The Eq.(28) brings the differential equation of the pendulum motion under the influence of sea waves and the DC generator. The term Ω means the angular frequency of the excitation,$K_T$is the torque constant and i is the electric current.

$$ml^2\ddot{\alpha} + cl^2\dot{\alpha} + mgl\sin\alpha = -mal\Omega^2\cos(\Omega t)\sin\alpha - K_T i \quad (28)$$

The respective dimensionless equation is the Eq.29 where it was used the dimensionless terms present in Eq.30 and in Eq.9:

$$\alpha'' = -\gamma\alpha' - \sin\alpha[1 + p\cos(\omega\tau)] - \beta I \quad (29)$$

The term I is considered a dimensionless current where Q is an arbitrary value for electric charge and. The term β considers the torque constant K_T and λconsiders the speed constant K_E.

$$\beta = \frac{K_T Q}{ml^2\omega_0} I = \frac{i}{Q\omega_0}\lambda = \frac{K_E}{Q\omega_0 L}\zeta = \frac{(R_a+R_L)}{\omega_0 L} \quad (30)$$

The electric equation of the DC generator is present below in Eq.31, where the R_a is an additional resistor for test and R_L is the internal resistance of the armature.

$$L\frac{di}{dt} = -(R_a + R_L)i + K_E\dot{\alpha} \quad (31)$$

The dimensionless version of the electric equation of the generator is written in Eq.(32)

$$\frac{dI}{d\tau} = -\zeta I + \lambda\alpha' \quad (32)$$

The dimensionless parameters for the results found and plotted in Fig.10 are p=5, γ =0.1, ω = 1.8, λ = 1 and ζ = 1. The result of the pendulum motion was a 1-period rotation. The Fig.10 shows the time history of the pendulum and the phase portrait on the right side.

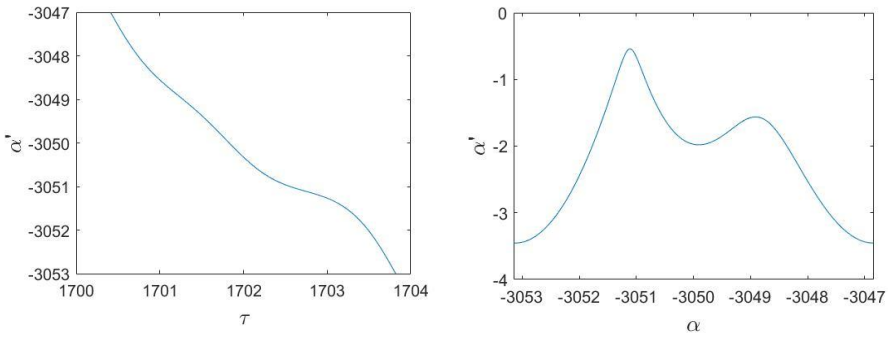

Figure 10. Time history and phase portraits for rotational solution of the pendulum

Afterwards, the parameter*p*which stands for the amplitude of excitation was decreased to the value 2.2. The result obtained was a 2-period oscillation. The time history and the phase portrait are in Fig.11.

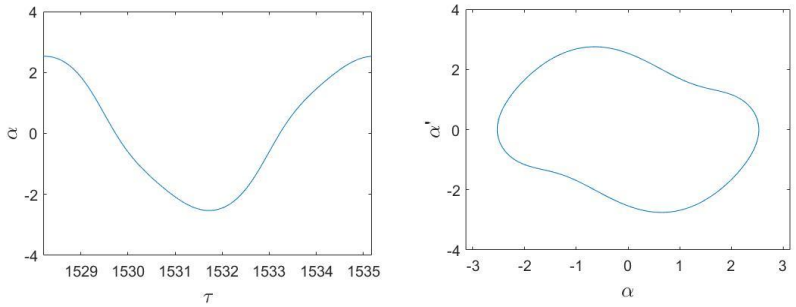

Figure 11. Time history and phase portrait for two-period oscillation with p=2.2

As expected, the pendulum coupled to a DC generator could performed both oscillations and rotations. Considering that the DC generator works as a damper that opposes to the pendulum motion, other results as fixed point and tumbling chaos may probably be obtained. It is just an issue of variate the parameters of amplitude and frequency of the excitation.

Probably, if a more powerful generator is considered to be used, it will be necessary to increase the amplitude of excitation, the mass and length of the pendulum and the frequency will need to fit.

3. Acknowledgments

The first author is thankful to the agency CNPq for the Postdoctoral scholarship Proc.433816/2016-3. The fifth author thanks the funding provided by CAPES-PVS- SPArq (100445/2014). The last author gratefully acknowledges financial support from the Fundação de Amparo à Pesquisa do Estado de São Paulo (FAPESP), grant no. 2015/20363-6.

4. Conclusions

In this paper, 4 different mechanisms with pendulum were studied. The last of them was the generator coupled to the pendulum. The main practical motivation for the study of pendulums in mechanisms is the energy harvest from sea waves. The usage of DC motor in these mechanism is justified by the fact that it is the DC generator with a inverted function. In this paper the objective reached was the demonstration of the different types of motion present both in DC motor or generator. Another important reflection is about the divergence between the ideal and nonideal models. Under the same conditions of amplitude and frequencies the type of motion may be completely different.

References

[1] Avanço, R.H., Navarro, H.A., Brasil, R.M.L.R.F., Balthazar, J.M., Bueno, A.M., Tusset, A.M., Statements on nonlinear dynamics behavior of a pendulum, excited by a crank-shaft-slider mechanism, Meccanica 51, 2016, 1301-1320.

[2] Avanço, R.H., Navarro, H.A., Brasil, R.M.L.R.F., Balthazar, J.M. Nonlinear Dynamics of a Pendulum excited by a crank-shaft-slider mechanism. ASME International Mechanical Engineering Congress and Exposition, *Volume 4B: Dynamics, Vibration, and Control* (): V04BT04A025. doi:10.1115/IMECE2014-36643.

[3] Leven, R.W., Koch, B.P. Chaotic Behavior of a Parametrically-Excited Pendulum, *Physics Letters A*, vol.86, 1981.

[4] Xu, X.; WIERCOGROCH, M.; CARTMELL, M.P. Rotating Orbits of a Parametrically-excited pendulum, *Chaos Solitons and Fractals*, v.23, 2005, pp.1537-1548.

[5] BELATO, D.; WEBER, H.I.; BALTHAZAR, J.M.; MOOK, D.T. Chaotic Vibrations of a nonideal eletro-mechanical system, *International Journal of Solids and Structures*, Vol.38, 2001, pp. 1699-1706.

[6] Belato, D. Nonlinear analysis of non ideals holonomic Dynamical Systems. PhD Thesis. State University of Campinas, 2002, Supervisor Hans Ingo Weber.

[7] KRASNOPOLSKAYA, T.S. and SHVETS, A.Y. Chaos in vibrating systems with a limited power-supply, *Chaos*, Vol.3, n.3, American Institute of Physics, 1993.

[8] Parker, T.S. and Chua, L.O. "Practical Numerical Algorithms for Chaotic Systems." by Springer-Verlag New York. 1989.

Rafael Henrique Avanço, PhD, Postdoctoral fellow: Aeronautics Technological Insittute, Mechanical Aeronautics Division, Praça Marechal Eduardo Gomes, 50, Vila das Acacias, CEP 12228-900,São José dos Campos, Brazil (avancorafael*@gmail.com*). The author gave a presentation of this paper during one of the conference sessions.

Angelo Marcelo Tusset, PhD, Professor: Technological University of Paraná, Avenida Monteiro Lobato, 84016-210, Ponta Grossa, Paraná, Brazil. (tusset@utfpr.edu.br)

Marcelo Suetake, PhD, Professor: Federal University of São Carlos, Rodovia Washington Luís, s/n, São Carlos, SP, CEP13565-905, Brazil. (mclsuetake@gmail.com)

Helio Aparecido Navarro, PhD, Professor: University of São Paulo, Avenidade Trabalhador São-carlense Av. Trab. São-Carlense, 400 - Parque Arnold Schimidt, São Carlos - SP,CEP 13566-590 , Brazil.(han@sc.usp.br)

José Manoel Balthazar, PhD, Professor: Aeronautics Technological Insittute, Mechanical Aeronautics Division, Praça Marechal Eduardo Gomes, 50, Vila das Acacias, CEP 12228-900,São José dos Campos, Brazil (jmbaltha@gmail.com)

Airton Nabarrete, PhD, Professor: Aeronautics Technological Insittute, Mechanical Aeronautics Division, Praça Marechal Eduardo Gomes, 50, Vila das Acacias, CEP 12228-900,São José dos Campos, Brazil (nabarret@ita.br)

Dissipative dynamics of a geometrically nonlinear Bernoulli-Euler beam under the action of a transverse load and color noises

Jan Awrejcewicz, Nikolay P. Erofeev, Vitalyi Dobriyan, Vadim A. Krysko

Abstract. In this paper a theoretical background of nonlinear dynamics for Euler-Bernoulli flexible beams under the transverse alternating load influence with account of color noises is proposed. It is shown that the concept of a phase transition admits a further generalization. For such systems the medium properties are time impermanent, as usually assumed in the study of nonequilibrium phenomena, but are subject to random time variations known as external noise. The random nature of the medium induces a more complicated system behavior. This new type of nonequilibrium transitions in [1] is called noise induced transitions. In this paper we investigate the effect of color noises on a system with an infinite number of degrees-of-freedom.

Keywords: geometric nonlinearity, Bernoulli-Euler beam, color noise, noise-induced transition.

1. Introduction

In deterministic systems several scenarios for the transition of a system from periodic to chaotic vibrations are known and well described. These are scenarios of Ruelle and Takens [2], where only three frequencies are used. The "noisy" scenario behavior has been found numerically after occurrence of a strange attractor implied three by three consecutive period doubling bifurcations. This means that simple deterministic systems are able to generate internal noise. The scenarios were found through the sequence of Andronov-Hopf bifurcations and through intermittence and noisy effects [3]. The random nature of the medium is capable of inducing a much richer variety of vibration modes than those described in the well-known scientific literature. Transitions from one structure to another in their properties are analogous to equilibrium phase transitions and transitions encountered in nonequilibrium systems under determinated external influences. It is possible to extend classical transitions to phenomena in which noise plays an important role. This makes it possible to study theoretically the transitions induced by noise through a numerical study (see references [4-10]). The present paper aims to generalize these studies to the case of noise-induced transitions.

The study of complex oscillations for distributed systems is an important issue, but the available results, in general, are obtained for mathematical models with one freedom degree. In the works of

Szemplinska-Stupnicka [11], Azrar [12] and Azrar et al. [13] the oscillations of distributed systems are replaced by a single-mode approximation in the Bubnov-Galerkin method. The results of the studies should be regarded rather as qualitative, since an increase in the number of modes often leads to substantially different modes of oscillation. In work [4], studies of global bifurcations and chaotic dynamics in nonlinear nonplanar oscillations of a cantilever beam under the influence of axial harmonic excitations and transverse excitations at the free end of a beam are presented. Analysis of the chaotic phenomena in the problems of vibrations of plates and shells with geometric nonlinearity are carried out in references [5-10]. In this paper we study oscillations of a geometrically nonlinear Bernoulli-Euler beam as a system with many freedom degrees when adding an external component in the form of colored noises. For example, white noise is a generalized stationary random process X(t) with a constant spectral density. The term "white" was assigned by analogy with white light, which in the visible part of the spectrum has the whole set of frequencies. The correlation (generalized) function of the white noise process has the form: $B(t) = \sigma^2 \delta(t)$, where σ^2 is a positive constant, and $\delta(t)$ is the delta function. An essentially nonlinear character of the behavior of plates and shells under loading by sound pressure has been found in a number of works. Gaussian white noise as a model is well suited for the mathematical description of many natural processes. The concept of color noise is introduced by analogy with the term white noise: the distribution of the color noise spectrum corresponds to the distribution of the visible part of the light spectrum of the corresponding color.

2. Problem statement

The investigation object is a single-layer isotropic elastic beam (Fig. 1), which is a two-dimensional zone of space R^2 with a Cartesian coordinate system introduced as follows: in the beam body a reduction line is fixed, being called further the midline $z = 0$. The *OX* axis is directed from the left to the right along the median line, whereas the *OZ* axis goes downwards, and it is perpendicular to *OX*. In this coordinate system, the beam as a 2D domain Ω, is defined as follows: $\Omega = \{x \in [0, a]; -h \le z \le h\}$, $0 \le t \le \infty$. Here and in the following we will use the notation: $2h$ - height, a — length of the beam.

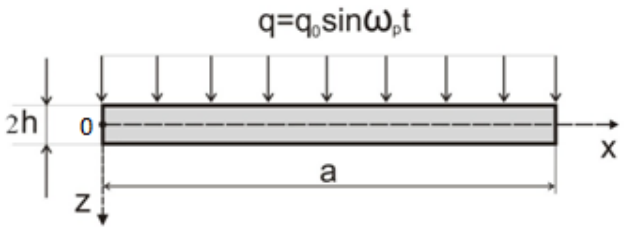

Figure 1. Scheme of the investigated beam.

3. Mathematical model

The mathematical model is constructed on the basis of the Bernoulli-Euler hypothesis and taking into account the nonlinear dependence between deformations and displacements in the form of Kármán. A system of differential equations in displacements, describing the motion of a beam with energy dissipation is obtained from the system of equations for a nonlinear plate [14] in the case of one spatial coordinate, and it has the following form

$$\begin{aligned} &E2h\left\{\frac{\partial^2 u}{\partial x^2}+L_3(w,w)\right\}-2h\frac{\gamma}{g}\frac{\partial^2 u}{\partial t^2}=0,\\ &E2h\left\{L_1(u,w)+L_2(w,w)-(2h)^2\left(\frac{1}{12}\right)\frac{\partial^4 w}{\partial x^4}\right\}+q+\dot{q}-2h\frac{\gamma}{g}\frac{\partial^2 w}{\partial t^2}-2h\varepsilon\frac{\gamma}{g}\frac{\partial w}{\partial t}=0, \end{aligned} \tag{1}$$

$$L_1(u,w)=\frac{\partial^2 u}{\partial x^2}\frac{\partial w}{\partial x}+\frac{\partial u}{\partial x}\frac{\partial^2 w}{\partial x^2},\quad L_2(w,w)=\frac{3}{2}\frac{\partial^2 w}{\partial x^2}\left(\frac{\partial w}{\partial x}\right)^2,\quad L_3(w,w)=\frac{\partial^2 w}{\partial x^2}\frac{\partial w}{\partial x},$$

where: $w(x,t)$ - beam deflection, $u(x,t)$ - beam movement along the *OX* axis, ε - dissipation coefficient, $q=q(x,t)$ - transverse load, $\dot{q}(t)$ - color noise (obtained from MATLAB), E - Young's modulus, γ - specific weight, g - gravity acceleration. Dimensionless variables are introduced as follows:

$$\bar{w}=\frac{w}{2h},\ \bar{u}=\frac{ua}{(2h)^2},\ \bar{x}=\frac{x}{a},\ \lambda=\frac{a}{2h},\ \bar{q}=q\frac{a^4}{(2h)^4E},\ \bar{t}=\frac{t}{\tau},\ \tau=\frac{a}{c},\ c=\sqrt{\frac{Eg}{\gamma}},\ \bar{\varepsilon}=\varepsilon\frac{a}{c}. \tag{2}$$

Taking into account (2) the system (1) is written in the following form:

$$\begin{aligned} &\frac{\partial^2 u}{\partial x^2}+L_3(w,w)-\frac{\partial^2 u}{\partial t^2}=0,\\ &\frac{1}{\lambda^2}\left\{L_2(w,w)+L_1(u,w)-\left(\frac{1}{12}\right)\frac{\partial^4 w}{\partial x^4}\right\}-\frac{\partial^2 w}{\partial t^2}-\varepsilon\frac{\partial w}{\partial t}+q+\dot{q}=0, \end{aligned} \tag{3}$$

where bars over the dimensionless parameters are omitted for simplicity.

The following boundary conditions are introduced

$$w(0,t)=w(a,t)=u(0,t)=u(a,t)=\partial^2 w(0,t)/\partial x^2=\partial^2 w(a,t)/\partial x^2=0, \tag{4}$$

and the following initial conditions are taken into account

$$w(x,t)\big|_{t=0}=\left.\frac{\partial w(x,t)}{\partial t}\right|_{t=0}=u(x,t)\big|_{t=0}=\left.\frac{\partial u(x,t)}{\partial t}\right|_{t=0}=0. \tag{5}$$

4. Method of solution

We replace the differential operators with respect to the spatial variable *x* by the difference operators for the functions $w(x,t), u(x,t)$ with the help of finite difference method (FDM) with approximation $O\left(h^2\right)$. System (3) reduces to an ordinary differential equations system of the following form:

$$\ddot{w}_i + \varepsilon_1 \dot{w}_i = L_{1,h}(w_i, u_i),\ \ddot{u}_i + \varepsilon_2 \dot{u}_i = L_{2,h}(w_i, u_i), \quad i = 0,...,n, \tag{6}$$

where n stands for the number of partitions with respect to spatial coordinates, and the difference operators $L_{1,h}$, $L_{2,h}$ have the standard form. Boundary and initial conditions are added to the system (6) in a difference form. The differential problem is solved by the Runge-Kutta method of the fourth accuracy regarding time. The increase in order of the method did not lead to significant changes in the results and only the running time increased of the employed numerical programs.

5. Determining Lyapunov exponents

Wolf et al. [15] proposed an algorithm that allows us to estimate non-negative Lyapunov exponents on the basis of time series. They have shown that the Lyapunov exponents are related to the exponentially fast divergence or convergence of neighboring orbits in the phase space. Conceptually, the method relies on a previously developed technique. There is a tracking of the long-term growth rates of small volume elements in the attractor. The method calculates the largest Lyapunov exponent from a single coordinate sample and is used when the evolution equations of the system are unknown and all of their phase coordinates cannot be measured. The methods of Kantz [16] and Rosenstein [17] are based on the construction of time functions, taking into account the divergence in the phase space of the nearest neighboring points through a certain time period. Next, it is proposed to find the most straightforward section of such functions (that is not always possible) and the tangent of the slope angle of this section will be approximately equal to the largest Lyapunov exponent.

6. Analysis of the obtained results

In order to study the behavior of nonlinear beams under the action of the harmonic transverse load $q = q_0 \sin(\omega_p t)$ with the addition of color noise with amplitude C_n, a software package has been developed that allows to build maps of the oscillations type depending on the control parameters $\{q_0, \omega_p, C_n\}$ (Table 1), for which the power spectra and Lyapunov exponents (LEs) are constructed and analyzed for each set of values $\{q_0, \omega_p, C_n\}$. The algorithm makes it possible to identify on the maps the areas of periodic oscillations, the period doubling bifurcation areas, the beam vibration zones with independent frequencies (quasi-periodicity) and the chaotic zones (Tables 1, 2).

The beam vibrations have been examined over a time interval $t \in [0; 2024]$, the number of partitions in FDM $n = \{80;160\}$, the beam length to thickness ratio $\lambda = 50$, and the results are obtained for the central point of the beam middle plane. In order to get a map of the vibration type, the range of the external load amplitudes $q_0 \in [100; 60000]$ has been divided into 600 parts, the frequency interval

of the external load $\omega_p \in [0.0003;12]$ to 350 parts. In other words the 2.1×10^5 different combinations of control parameters have been considered during the numerical simulations. The identification of the vibrations type for each of the combinations has been based on the signal analysis, the Fourier power spectrum, the Morlet wavelet spectrum, the phase and modal portraits, the autocorrelation function, and the Lyapunov exponent for every noise type.

During the study, a frequency was chosen for which the noise action with a small amplitude did not change the system state. In connection with this, studies were made for the system state when the noise was added with an amplitude $C_n = 50000$ comparable to the amplitude of the periodic load.

Table 1. Different kinds of vibrations on the plane $\{q_0, \omega_p\}$

$C_n = 0$, n=40 (point 1 means studied point)	
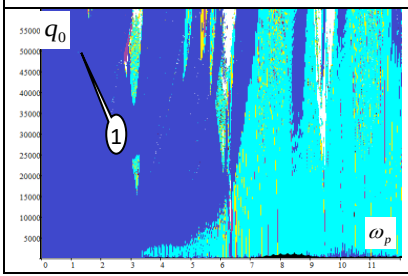	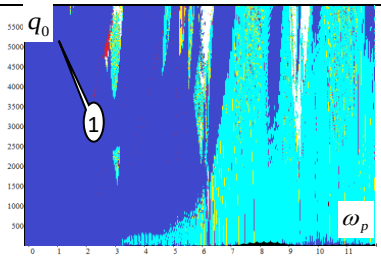

Table 2. Color notation

- periodic vibrations - chaotic vibrations - bifurcation vibrations	- 2 independent frequencies - damped vibrations - undefined vibrations	- asymmetric vibrations

Table 3. Largest Lyapunov exponents

Kantz	Rosenstein	Wolf
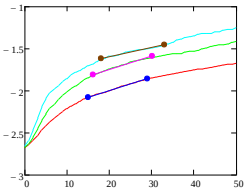	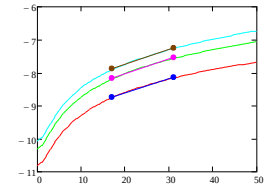	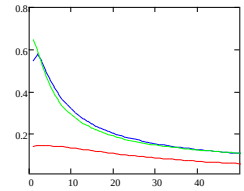

The spectral density of the used color noises is approximately proportional to the law $1/f^{\alpha}$, where f is the frequency of the spectrum, and α has the following values: $\alpha = -2$ – violet noise; $\alpha = -1$ – blue noise; $\alpha = 0$ – white noise; $\alpha = 1$ – pink (flicker) noise; $\alpha = 2$ – brownian noise.

The values of all time series for color noises are located on the interval [-1; 1] and the coefficients C_n are added to the harmonic load. Tables 4 and 5 present the Morlet wavelet transform, Fourier

spectra, signal waveforms, the Poincaré maps, 2D and 3D phase portraits for beam partitions n={80;160} for C_n =50000.

Table 4. Vibration characteristics computed for fixed ω_0 =1.0853, q_0 =50000

	Morlet	Gaus32	FFT	W(t)	Phase 2D	Phase 3D	Poincare
n=40, C_n=0	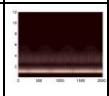	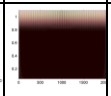	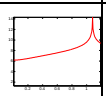	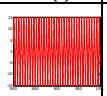	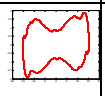	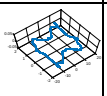	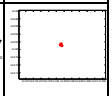
n=80, C_n=0	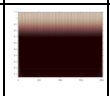	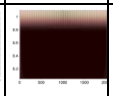	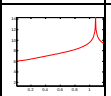	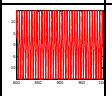	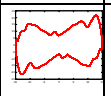	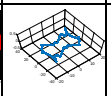	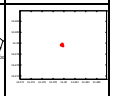
n=160, C_n=0	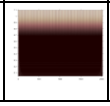	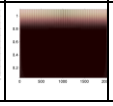	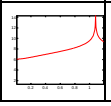	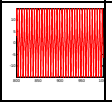	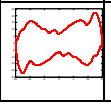	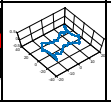	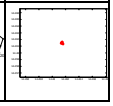

Table 5. Vibration characteristics computed for fixed n=160, C_n=50000, ω_0 =1.0853, q_0 =50000

	Morlet	Gaus32	FFT	W(t)	Phase 2D	Phase 3D	Poincaré maps
$\alpha=-2$	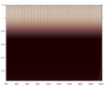	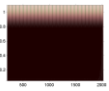	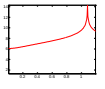	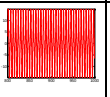	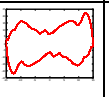	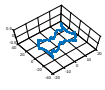	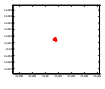
$\alpha=-1$	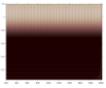	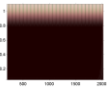	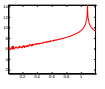	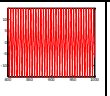	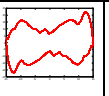	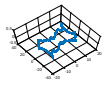	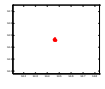
$\alpha=0$	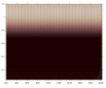	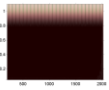	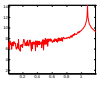	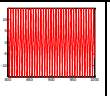	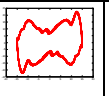	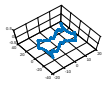	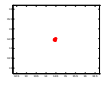
$\alpha=1$	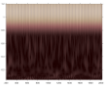	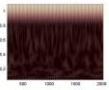	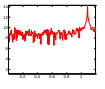	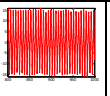	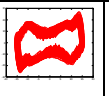	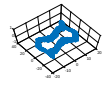	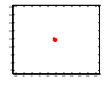
$\alpha=2$	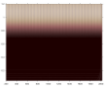	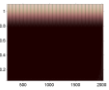	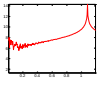	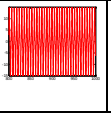	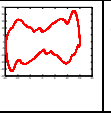	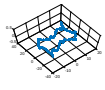	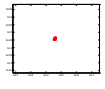

In order to estimate the largest Lyapunov exponent by the methods of Kantz and Rosenstein, it is necessary to find the tangent of the slope angle of the most straightforward graph section for the corresponding method functions of t (Table 3). For this purpose, an algorithm was constructed for fitting the curve by the method of least squares with the specification of the least length of the approximating segment along time axis as a percentage of the total number of points. In this case all possible points of the graph are taken for a given minimum time length in percent and the segment

with the least sum of squares of the deviations for the original data from this segment has been selected.

Table 6. Largest Lyapunov exponents for studied solutions

$\alpha = -2$	$\alpha = -1$	$\alpha = 0$	$\alpha = 1$	$\alpha = 2$
W: 0.00011	W: 0.00011	W: 0.00010	W: 0.00011	W: 0.00012
K: 0.00765	K: 0.03276	K: 0.03276	K: 0.05128	K: 0.03360
0.00222	0.00391	0.00391	0.01530	0.01922
R: 0.00065	R: 0.00065	R: 0.00065	R: 0.09901	R: 0.06540
0.00033	0.00033	0.00033	0.06858	0.04201

7. Conclusions

As can be seen in Table 4, the increase in the number of partitions within $n \in [40;160]$ practically does not affect the results of the studies, and therefore the option was chosen with the maximum n=160. Table 6 shows the values of the largest Lyapunov exponents estimated using the Wolf calculation (W), Kantz (K) and Rosenstein (R) (the last 2 in two ways) methods. It can be seen that the calculation results can produce values that differ by several orders of magnitude for the same noise, whereas they correlate well between different types of noise (a chaotic state is measured by positive values of the Lyapunov exponents).

From the obtained dependencies (Table 5) one may conclude that the least noticeable effect on the system is associated with addition of violet noise where vibrations of the system remain periodic. The maximum effect takes place in the case of pink noise, and other noises generate chaotic vibrations of the system. The employed Morlet and Gauss wavelet transforms demonstrated uneven frequencies distribution in time for chaotic vibrations in a quite predictable way, but the Morlet wavelet more clearly revealed the system response at low frequencies. For the studied signals the largest Lyapunov exponents are positive, which indicates chaotic state of the system, whereas the heuristic spectrum analyzer used in the program did not always detect this state. All this once again confirms a need to use several methods for analyzing dynamic processes in the studied system.

Acknowledgements

This work has been supported by the grants the Russian Science Foundation, RSF 16-19-10290

References

[1] Horsthemke, W., Lefever, R., Noise-Induced Transitions. Theory and Applications in Physics, Chemistry, and Biology, Springer-Verlag, Berlin, 1984.

[2] Ruelle, D., Takens, F. On the nature of turbulence, Comm. Math Phys. 20 (1971) 167.

[3] Berge, P., Dubois, M., Manneville, P., Pomeau, Y., Intermittency in Rayleigh-Benard convection, J. Phys. Paris Lett. 41 (1980) L341.

[4] Zhang, W., Wang, F., Yao, M., Global bifurcations and chaotic dynamics in nonlinear nonplanar oscillations of a parametrically excited cantilever beam, Nonlinear Dynamics 3(40) (2005) 251-279.

[5] Awrejcewicz, J., Krysko, V.A., Vakakis, A.F., Nonlinear Dynamics of Continuous Elastic System, Springer, Berlin, 2004.
[6] Krysko, V.A., Zhigalov, M.V., Saltykova, O.A., About taking into account an influence of the transverse shifts on complex nonlinear oscillations of elastic beams, Journal of Applied Mechanics and Technical Physics 5(52) (2011) 186-193 (in Russian).
[7] Krysko, V.A., Papkova, I.V., Soldatov, V.V., Analysis of nonlinear chaotic vibrations of shallow shells of revolution by using the wavelet transform, Mechanics of Solids 45(1) (2010). (in Russian).
[8] Awrejcewicz, J., Krysko, V.A., Papkova, I.V., Routes to chaos in continuous mechanical systems. Part 1, Mathematical models and solution methods Chaos, Solitons & Fractals. Nonlinear Science, and Nonequilibrium and Complex Phenomena 45 (2012).
[9] Awrejcewicz, J., Krylova, E.Y., Papkova, I.V., Krysko, V.A., Wavelet-based analysis of the regular and chaotic dynamics of rectangular flexible plates subjected to shear-harmonic loading, Shock and vibration 19 (2012) 979-994.
[10] Krylova, E.Y., Papkova, I.V., Krysko, V.A., On scenarios of the transition for plate oscillations into chaotic ones on the basis of Fourier analysis, Nonlinear World 12(10) 2012 903-912 (in Russian).
[11] Szemplinska-Stupnicka, W., Nonlinear normal modes and the generalized Ritz method in the problems of vibrations of non-linear elastic continuous systems, International Journal of Nonlinear Mechanics 18(2) (1983) 149–165.
[12] Azrar, L., Semi-Analytic and Asymptotic-Numerical Methods for Non-Linear Vibrations. Applications to Large Amplitude Vibrations of Beams and Plates, PhD Thesis, Ecole Mohammadia d'Ingenieurs, Rabat, Morocco, 1999.
[13] Azrar, L., Benamar, R., White, R.G., A semi-analytical approach to non-linear dynamic response problem of s-s and c-c beams at large vibration amplitudes. Part I: General theory and application to the single mode approach to free and forced vibration analysis. Journal of Sound and Vibration 224 (1999) 183–207.
[14] Volmir, A.S., Nonlinear Dynamics of Plates and Shells, Nauka, Moscow, 1972.
[15] Wolf, A., Swift, J.B., Swinney, H.L., Vastano, J.A., Determining Lyapunov exponents from a time series, Physica D 16 (1985) 285-317.
[16] Kantz, H., A robust method to estimate the maximum Lyapunov exponent of a time series, Phys. Lett. A 185 (1994) 77-87.
[17] Rosenstein, M.T., Collins, J.J., De Luca, C.J., A practical method for calculating largest Lyapunov exponents from small data sets, Neuro Muscular Research Center and Department of Biomedical Engineering, Boston University, 1992.

_____

Jan Awrejcewicz, Professor: Lodz University of Technology, Faculty of Mechanical Engineering, Department of Automation, Biomechanics and Mechatronics, 1/15 Stefanowskego Str., 90-924 Lodz, POLAND (jan.awrejcewicz@p.lodz.pl), the author presented this contribution at the conference.

Nikolay P. Erofeev, Professor: Department of Mathematics and Modeling, Saratov State Technical University, Politehnicheskaya 77, 410054 Saratov, RUSSIAN FEDERATION (erofeevnp@mail.ru).

Vitalyi Dobriyan, M.Sc. (Ph.D. student): Department of Mathematics and Modeling, Saratov State Technical University, Politehnicheskaya 77, 410054 Saratov, RUSSIAN FEDERATION (dobriy88@yandex.ru).

Vadim A. Krysko, Professor: Department of Mathematics and Modeling, Saratov State Technical University, Politehnicheskaya 77, 410054 Saratov, RUSSIAN FEDERATION (tak@san.ru).

Gyroscopic forces and asymptotic stability for mechanical systems with partial energy dissipation

Jan Awrejcewicz, Nataliya Losyeva, Volodymyr Puzyrov

Abstract: We study the stability problem for autonomous non - conservative mechanical system in presence of potential, gyroscopic, and dissipative forces. The matrix of dissipative forces is semi-positive, so Kelvin - Chetaev theorems cannot be applied. The significance of gyroscopic forces (GF) and their contribution to the overall phenomenon is discussed. The fact that energy dissipation is incomplete is essential, because the influence of gyroscopic terms in this case may be significantly different from the full dissipation case. It is shown that this influence may be both positive and negative (there are some sets in space of parameters where the asymptotic stability of the motion is broken). As an example, the problem of passive stabilization of permanent rotations of Lagrange gyroscope is considered. It is proved that adding a dashpot to gyro with stretched inertia ellipsoid stabilizes its permanent rotations with the exception of some "critical" values. The last may be found analytically from special conditions.

1. Introduction

In 1879 W. Thomson and P. Tait [1] put their attention on the fact that equations of motion of the system, in which the gyroscopes are present, contain terms linear with respect to velocities with a skew-symmetric coefficient matrix. When these terms are treated as forces, then their work on the actual displacement of the system will be zero $\sum_{i=1}^{n} \Gamma_i \, dq_i = 0$. This property was accepted by Thomson and Tait for the general definition of gyroscopic forces and, using it, they proved several theorems on the stability of the motion of gyroscopic systems. Gyroscopic forces can be found not only in systems containing gyroscopes, but also in various mechanical, electrical and other systems in which gyroscopes are absent. Therefore, for the systems of the most diverse physical nature, one can draw far-reaching analogies that can be used in various constructions. Non-conservative systems with both dissipative and gyroscopic force are widely presented in numerous publications from physical viewpoint [2 - 6], as well as for application purposes [7, 8].

Let the equilibrium position of the conservative mechanical system be unstable. Is it possible to stabilize it by adding dissipative forces, i.e. to select the force in such a way that the equilibrium position which is unstable in the presence of potential forces only becomes

stable or asymptotically stable? The answer to this question is negative. Also it is known that such an equilibrium position can be stabilized by a certain combination of dissipative and circulation forces, but can this goal be achieved in the absence of the latter? In the case when the dissipation is complete (the matrix D is positive) the answer to this question is given by classical Kelvin-Chetaev [1, 9, 10] theorems:

Theorem 1. If the equilibrium of the mechanical system is stable under the action of potential forces only, it becomes asymptotically stable while adding dissipative forces with full dissipation.

Theorem 2. If the isolated equilibrium is unstable under the action of potential forces only, it cannot be stabilized by adding arbitrary dissipative forces with full dissipation.

Theorem 3. If the isolated equilibrium is unstable under the action of potential forces only, it remains unstable while adding arbitrary gyroscopic forces and dissipative forces with full dissipation.

At the same time, concerning Theorem 1, as noted in a number of works (see, for instance [11 - 13]), the requirement that the matrix characterizing dissipative forces should be positive is in some cases superfluous. In particular, a semi-positive matrix as a rule (with the exception of a set of measure zero) makes the stable equilibrium position of the conservative system asymptotically stable. However, how important is the influence of the gyroscopic forces in this case? Does the statement of the theorems 2, 3 extend to the case of partial energy dissipation?

In this paper, we would like to draw attention to two points: 1) In contradiction to Theorem 3, partial dissipative forces can make the gyroscopically stabilized motion of the system asymptotically stable; 2) Gyroscopic forces can "spoil" the asymptotic stability of the system. Namely, a motion that is asymptotically stable with potential forces and partial dissipative forces can become marginally stable when the gyroscopic forces are added.

2. Main results

We consider the motion of a holonomic mechanical system subject to stationary, ideal constraints. The position of this system is specified by n positional and m cyclic generalized coordinates. If such a system has stationary motion, then stability problem may be solved by consideration the linearized system which may be presented in the following form

$$\boldsymbol{M}\ddot{\boldsymbol{\xi}} + \boldsymbol{B}\dot{\boldsymbol{\xi}} + \boldsymbol{K}\boldsymbol{\xi} = \boldsymbol{0}, \tag{1}$$

where $\boldsymbol{M}, \boldsymbol{K}, \boldsymbol{B}$ are square real matrices (two first of them are symmetric and positive), $\boldsymbol{B}$ is semi-positive and always may be separated on symmetric (dissipative) and skew-symmetric (gyroscopic) components $\boldsymbol{B} = \boldsymbol{D} + \boldsymbol{G}$, $\boldsymbol{\xi} \in \mathbb{R}^n$.

Below we use the block notation for square matrix $\boldsymbol{P}$ of $s+l$ order in the form

$$\boldsymbol{P} = \begin{pmatrix} \boldsymbol{P}_{11} & \boldsymbol{P}_{12} \\ \boldsymbol{P}_{21} & \boldsymbol{P}_{22} \end{pmatrix},$$

where $\boldsymbol{P}_{11}, \boldsymbol{P}_{22}$ are square matrices of s and l orders respectively, and $\boldsymbol{P}_{12}$, $\boldsymbol{P}_{21}$ stand for the corresponding rectangle matrices. Also we split the vector $\boldsymbol{\xi}$ on sub-vectors

$$\boldsymbol{\xi} = col(\boldsymbol{x}, \boldsymbol{y}), \quad \boldsymbol{x} \in \mathbb{R}^s, \quad \boldsymbol{y} \in \mathbb{R}^l.$$

We suppose that matrix $\boldsymbol{D} = \boldsymbol{0}_s \bigoplus diag(d_1, d_2, \cdots, d_l)$. In other words the right lower block $\boldsymbol{D}_{22}$ is diagonalized, and three other blocks are zero matrices. Matrix $\boldsymbol{D}_{22}$ is positive. Similarly, we denote differential operators

$$L = \boldsymbol{M}\frac{d^2}{dt^2} + \boldsymbol{B}\frac{d}{dt} + \boldsymbol{K}, \quad L_{11} = \boldsymbol{M}_{11}\frac{d^2}{dt^2} + \boldsymbol{G}_{11}\frac{d}{dt} + \boldsymbol{K}_{11},$$

and the corresponding lambda-matrices (matrix polynomials)

$$\boldsymbol{\Lambda}(\lambda) = \boldsymbol{M}\lambda^2 + \boldsymbol{B}\lambda + \boldsymbol{K}, \quad \boldsymbol{\Lambda}_{11}(\lambda) = \boldsymbol{M}_{11}\lambda^2 + \boldsymbol{G}_{11}\lambda + \boldsymbol{K}_{11}. \tag{2}$$

Let λ_0 be some eigenvalue of $\boldsymbol{L}_{11}$, and $\boldsymbol{\beta}_{10}-$ the corresponding eigenvector, i.e.

$$\boldsymbol{\Lambda}_{11}(\lambda_0)\boldsymbol{\beta}_{10} = \boldsymbol{0}_s.$$

Here $\boldsymbol{0}_s$ means the matrix-column with s zero elements. Introduce the equality

$$\boldsymbol{\Lambda}_{21}(\lambda_0)\boldsymbol{\beta}_{10} = \boldsymbol{0}_l. \tag{3}$$

For our purposes we shall use the following theorem [14]:

Theorem 4. Let us consider a mechanical system which motion equations are described by (1) and suppose that none of the eigenvectors of operator $\boldsymbol{L}_{11}$ satisfies condition (3). Then adding to system an arbitrary dissipative force, which provides full dissipation on $\dot{\boldsymbol{y}}$ leads to the following results:

I) If all eigenvalues of matrix $\boldsymbol{K}$ are positive, then equilibrium of (1) becomes asymptotically stable. Stability is exponential and uniform.

II) If matrix $\boldsymbol{K}$ has some negative eigenvalues – then equilibrium is unstable, even if it was stabilized before by gyroscopic forces. Among particular solutions of the system at least one has negative Lyapunov characteristic number.

Comparing with the statements of theorems 1 - 3, in case of incomplete dissipation results of Kelvin - Chetaev theorems mostly persist, excluding some special relations between quantitative values that characterize the forces (some surfaces in space of mechanical

parameters). A way of finding these relations is proposed by formulas (3). The key difference, we believe, is that case of full dissipation allows to solve the problem in qualitative manner – by analysis only potential (or potential and gyroscopic) forces, and conclusion does not depend on quantitative nature of them. In other words, only signs of matrix eigenvalues are important, not their exact values or connections between them. When dissipation is partial, this feature is lost, as it follows from (3). In particular, if matrix D is positive and system (1) is asymptotically stable or unstable, varying the GF cannot change this. The case of partial energy dissipation is somewhat opposed to this circumstance. More precisely, this property is inherent only with respect to "pure dissipative" component $\boldsymbol{y}$ of state vector, and variation of the other gyroscopic terms related to $\boldsymbol{x}-$ component can change the result.

2.1. Example 1

Let system (1) is given with matrices

$$\boldsymbol{M} = \begin{pmatrix} 5 & 0 & 2 & 0 \\ 0 & 1 & 0 & 0 \\ 2 & 0 & 2 & 0 \\ 0 & 0 & 0 & 1 \end{pmatrix}, \quad \boldsymbol{G} = \begin{pmatrix} 0 & g_1 & 0 & g_2 \\ -g_1 & 0 & 0 & 0 \\ 0 & 0 & 0 & g_3 \\ -g_2 & 0 & -g_3 & 0 \end{pmatrix}, \quad \boldsymbol{K} = \begin{pmatrix} 4 & 0 & 2 & 0 \\ 0 & 1 & 0 & 0 \\ 2 & 0 & 2 & 0 \\ 0 & 0 & 0 & 3 \end{pmatrix},$$

$$\boldsymbol{D} = h \ \mathrm{diag}(1, 1, 0, 0), \tag{4}$$

and g_1, g_2, g_3 are unknown parameters.

Suppose that there exist λ_0 and $\boldsymbol{\beta}_0$ which satisfy (3). This means that all minors of second order of the matrix

$$\boldsymbol{\Lambda}^\star = \begin{pmatrix} 2\lambda^2 + 2 & 0 & 2\lambda^2 + 2 & -g_3\lambda \\ g_2\lambda & 0 & g_3\lambda & \lambda^2 + 3 \end{pmatrix}^T$$

are equal to zero. In fact, otherwise the rank of $\boldsymbol{\Lambda}^\star$ is maximal, and (3) cannot take place.

The rank of matrix $\boldsymbol{\Lambda}^\star$ is less then 2 if and only if all minors of second order are equal to zero. This fact leads to restrictions

$$g_2 = g_3, \tag{5}$$

and

$$f(\lambda) = 2(\lambda^2 + 1)(\lambda^2 + 3) + g_3^2\lambda^2 = 0. \tag{6}$$

For any value of g_3 the polynomial $f(\lambda)$ has purely imaginary roots only, hence if $g_2 \neq g_3$, then $rank\ \boldsymbol{\Lambda} = 2$, and, according to theorem, system $MDGK$ is asymptotically

stable. However, if (5) holds, then system (1), (4) is marginally stable. Its characteristic polynomial

$$det(\boldsymbol{M}\lambda^2 + (\boldsymbol{D}+\boldsymbol{G})\lambda + \boldsymbol{K}) = \begin{vmatrix} 3\lambda^2 + h\lambda + 2 & g_1\lambda \\ -g_1\lambda & \lambda^2 + h\lambda + 1 \end{vmatrix} \begin{vmatrix} 2\lambda^2 + 2 & g_3\lambda \\ -g_3\lambda & \lambda^2 + 3 \end{vmatrix}$$

has two pairs of purely imaginary roots and four roots with negative real part. The last correspond to variables $x_1, x_2, \dot{x}_1, \dot{x}_2$ – the "direct dissipative part" of state vector, and this does not depend from magnitude of g_1.

Over against, the borderline between marginal stability and asymptotic stability of the system is tied with restriction (5), which determines a set in subspace of system parameters, associated with $\boldsymbol{x}$ being a component of state vector, where asymptotic stability is lost.

3. Passive stabilization of Lagrange's gyroscope permanent rotations

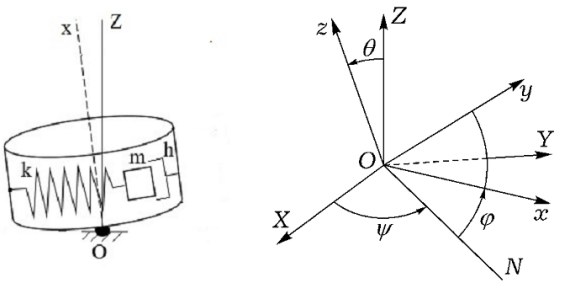

Figure 1. Rigid body with dashpot.

Consider a rigid body with a fixed point O, and introduce it into consideration two coordinate systems: the fixed one $OXYZ$ and system $Oxyz$ which is connected with the body. It is assumed that the body is dynamically symmetric, and the center of mass C of the body belongs to the axis Oz. As generalized coordinates that determine the position

of the coordinate system $Oxyz$ with respect to the fixed one, we choose the Euler angles θ, φ, ψ which are introduced in a common way (Fig.1). Inside the body a dashpot is situated which is considered as mass m that can oscillate along the line which is orthogonal to axis of symmetry Ox and intersects it in point O_1. It is connected with carrier by viscoelastic spring with stiffness $\varkappa$ and coefficient of damping $\hbar$. Since the body is dynamically symmetric, we can assume that dashpot axis is collinear to the principal axis of inertia of the body (for example, the second). The corresponding radius vector in the coordinate system connected with the body can be written as

$$\boldsymbol{r}_1 = l_1\ \boldsymbol{e}_X + \eta\ \boldsymbol{e}_Y = (l_1, \eta, 0),$$

where η is the distance from point O_1.

Taking into account the formula $\boldsymbol{v}_1 = \acute{\boldsymbol{r}}_1 + \boldsymbol{\omega} \times \boldsymbol{r}_1$, where $\acute{\boldsymbol{r}}_1$ is the relative derivative on time (relative velocity) and $\boldsymbol{\omega}$ is the angular velocity of the rigid body, the following expression for kinetic energy of dashpot holds

$$\mathcal{K}_1 = \frac{1}{2} m[\dot{\eta}^2 + 2\ l_N \dot{\eta}\omega_3 + \eta^2(\omega_1^2 + \omega_3^2) - 2\ l_N\ \eta\omega_1\omega_2 + l_N^2\ (\omega_2^2 + \omega_3^2)].$$

Components of angular velocity vector are given by the kinematic Euler relations

$$\omega_1 = \dot{\theta}\cos\varphi + \dot{\psi}\sin\theta\sin\varphi,\ \omega_2 = -\dot{\theta}\sin\varphi + \dot{\psi}\sin\theta\cos\varphi,\ \omega_3 = \dot{\varphi} + \dot{\psi}\cos\theta. \tag{7}$$

The generalized inertia tensor of the system may be written as

$$\widetilde{\boldsymbol{I}} = \begin{pmatrix} I_1 + m\eta^2 & -ml_1\ \eta & 0 \\ -ml_1\ \eta & I_2 + ml_1^2 & 0 \\ 0 & 0 & I_3 + m(\eta^2 + l_1^2) \end{pmatrix}. \tag{8}$$

The potential forces are presented by gravitational force and elasticity of the spring. Hence, the potential energy of the system is given by the following formula

$$\Pi = g\sin\theta\ [(Ml + ml_1)\sin\varphi + m\eta\ cos\varphi] + \frac{1}{2}\varkappa\eta^2,$$

where M is the mass of the rigid body, $l = |OC|,\ l_1 = |OO_1|$.

The kinetic energy of the system is as follows

$$\mathcal{K} = \mathcal{K}_0 + \mathcal{K}_1 = \frac{1}{2}\langle\boldsymbol{\omega}, \tilde{\boldsymbol{I}}\boldsymbol{\omega}\rangle + m\langle\boldsymbol{\omega}, \boldsymbol{r}_1 \times \acute{\boldsymbol{r}}_1\rangle + m\acute{\boldsymbol{r}}_1^2 = \frac{1}{2}\sum_{j,s=1}^{4} a_{js}\ \dot{\xi}_j\ \dot{\xi}_s.$$

Here $\boldsymbol{\xi} = (\theta, \varphi, \eta, \psi)^T$, generalized coordinate ψ is cyclic, and

$$a_{11} = I_1 cos^2\varphi + \widetilde{I}_2 sin^2\varphi + 2ml_N\eta sin\varphi\ cos\varphi,\ a_{12} = 0,\ a_{13} = 0,$$

$$a_{14} = sin\varphi\ [(I_1 - \widetilde{I}_2)sin\varphi\ cos\varphi + ml_N\eta(sin^2\varphi - cos^2\varphi)],\ a_{22} = \widetilde{I}_2 + m\eta^2,\ a_{23} = ml_N,$$

$$a_{24} = cos\theta(\widetilde{I}_2 + m\eta^2),\ a_{33} = m,\ a_{34} = ml_N cos\theta,$$

$$a_{44} = I_1 sin^2\theta\ sin^2\varphi + \widetilde{I}_2(sin^2\theta\ cos^2\varphi + cos^2\theta) + m\eta^2 cos^2\theta - 2ml_N\eta sin^2\theta\ sin\varphi\ cos\varphi.$$

Excluding the cyclic velocity

$$\dot{\psi} = \frac{1}{a_{44}}(\beta_\psi - a_{14}\dot{\theta} - a_{24}\dot{\varphi} - a_{34}\dot{\xi}),$$

where β_ψ represents cyclic constant, we can write the following Routh kinetic potential

$$L_R = \frac{1}{2a_{44}}\sum_{j,s=1}^{3}(a_{js}a_{44} - a_{j4}a_{s4})\ \dot{\xi}_j\ \dot{\xi}_s + \frac{\beta_\psi}{a_{44}}\sum_{j=1}^{3}a_{j4}\ \dot{\xi}_j - W, \quad W = \frac{\beta_\psi^2}{2a_{44}^2} + \Pi.$$

Then equations of the motion of mechanical system under study are

$$\frac{d}{dt}\frac{\partial L_R}{\partial \dot{q}_j} - \frac{\partial L_R}{\partial q_j} = Q_j,\ Q = (0, 0, -\hbar\dot{\eta})^T,\ (j = \overline{1,3}). \tag{9}$$

Stationary motions of mechanical system are governed by equality $grad\ W = \mathbf{0}$ or

$$g\cos\theta\ [(Ml + ml_N)\sin\varphi + m\eta\ cos\varphi] - \frac{\beta_\psi^2}{a_{44}^2}\frac{\partial a_{44}}{\partial\theta} = 0,$$

$$g\sin\theta\ [(Ml + ml_N)\cos\varphi - m\eta\ sin\varphi] - \frac{\beta_\psi^2}{a_{44}^2}\frac{\partial a_{44}}{\partial\varphi} = 0,$$

$$gm\eta\sin\theta\ cos\varphi - m\frac{\beta_\psi^2}{a_{44}^2}(\eta\ cos^2\theta - l_N sin^2\theta\ sin\varphi\ cos\varphi) + \varkappa\eta = 0.$$

It is easy to see that the last system has a solution $(\pi/2, \pi/2, 0)$ and equations (9) has equilibrium

$$\theta^0 = \frac{\pi}{2},\ \varphi^0 = \frac{\pi}{2},\ \eta^0 = 0,\ \dot{\theta}^0 = 0,\ \dot{\varphi}^0 = 0,\ \dot{\eta}^0 = 0, \tag{10}$$

which describes permanent rotations of the body with angular velocity β_ψ/I_1 and with "frozen" mass m. To investigate the stability of solution (9) let us introduce the following perturbations

$$\theta = \widetilde{\xi}_1 + \frac{\pi}{2},\ \varphi = \widetilde{\xi}_2 + \frac{\pi}{2}.$$

For our purpose it is sufficient to get linear approximation of (9), i.e. terms of second order from L_R :

$$L_R^{(2)} = \frac{1}{2}[\widetilde{I}_2(\dot{\xi}_1^2 + \dot{\xi}_2^2) + m\dot{\eta}^2] + ml_1\xi_2\eta + \frac{\beta_\psi}{I_1}\{\dot{\xi}_1[(\widetilde{I}_2 - I_1)\widetilde{\xi}_2 + ml_1\eta] - \widetilde{I}_2\dot{\xi}_2\widetilde{\xi}_1 - ml_1\dot{\eta}\xi_1\} +$$

$$+\frac{\beta_\psi^2}{2I_1^2}[(\widetilde{I}_2 - I_1)(\widetilde{\xi}_1^2 + \widetilde{\xi}_2^2) - 2ml_1\widetilde{\xi}_2\eta] + \frac{g}{2}(Ml + ml_1)(\widetilde{\xi}_1^2 + \widetilde{\xi}_2^2) + mg\widetilde{\xi}_2\eta - \frac{1}{2}\varkappa\eta^2.$$

Introducing the dimensionless parameters

$$\xi_3 = \frac{\eta}{l_1},\ \tau = \frac{\beta_\psi}{I_1}t,\ a = \frac{I_2 + ml_1^2}{I_1},\quad p = \frac{ml_1^2}{I_1},\quad \mu = \frac{MglI_1}{\beta_\psi^2},$$

$$\mu_1 = \frac{mgl_1I_1}{\beta_\psi^2},\ h = \frac{\hbar}{\beta_\psi},\ \kappa = \frac{\varkappa I_1}{\beta_\psi^2}, \tag{11}$$

we finally arrive to system (1) with the matrices

$$\boldsymbol{M} = \begin{pmatrix} a & 0 & 0 \\ 0 & a & p \\ 0 & p & p \end{pmatrix},\ \boldsymbol{D} = \mathrm{diag}(0, 0, h),\quad \boldsymbol{G} = \begin{pmatrix} 0 & 2a-1 & 2p \\ -2a+1 & 0 & 0 \\ -2p & 0 & 0 \end{pmatrix},$$

$$\boldsymbol{K} = \begin{pmatrix} a-1-\mu-\mu_1 & 0 & 0 \\ 0 & a-1-\mu-\mu_1 & -1-\mu_1 \\ 0 & -1-\mu_1 & \kappa \end{pmatrix}.$$

To satisfy the requirements of paragraph 1 of theorem 4, matrix $\boldsymbol{K}$ must be positive, and hence the following restrictions are yielded:

$$a - 1 - \mu - \mu_1 > 0,\quad \kappa > \frac{p^2(1+\mu_1)^2}{a-1-\mu-\mu_1}. \tag{12}$$

If a gyro is upstanding (the case of top), parameters μ, μ_1 are positive, and the first inequality (12) requires $a > 1$ ($I_2 + ml_1^2 > I_1$), i.e. the generalized inertia ellipsoid is stretched (rotations around major axis). Also the angular velocity of rotation must be high enough. Then the second inequality (12) gives the lower limit value for stiffness of the spring $\varkappa$.

In order to make sure that stabilization is in effect – solution (10) is asymptotically stable – we have to consider the following matrix

$$\boldsymbol{\Lambda}^\star = \begin{pmatrix} a\lambda^2 + a - 1 - \mu - \mu_1 & -(2a-1)\lambda & -2p\lambda \\ (2a-1)\lambda & a\lambda^2 + a - 1 - \mu - \mu_1 & p(\lambda^2 - 1 - \mu_1) \end{pmatrix}^T.$$

If its rank is equal to 2, the motion is asymptotically stable, if not – it is marginally stable. The last case means that columns of matrix $\boldsymbol{\Lambda}^\star$ are proportional, and therefore

$$2(a\lambda^2 + a - 1 - \mu - \mu_1) = (2a-1)(\lambda^2 - 1 - \mu_1), \tag{13}$$

$$(a\lambda^2 + a - 1 - \mu - \mu_1)^2 + (2a-1)^2\lambda^2 = 0. \tag{14}$$

Expressing λ^2 from (13) and substituting into (14) we have

$$(2a-1)^2[(\mu_1^2+4\mu_1+4)a^2-2(\mu\mu_1+2\mu+2\mu_1+4)a+\mu^2+4\mu+\mu_1+4]=$$

$$=(2a-1)^2\{[(\mu_1+2)a-\mu-2]^2+\mu_1\}.$$

Triangle inequalities for moments of inertia $I_1 < 2I_2$ imply $a > 1/2$, and the system (13) - (14) is inconsistent. Consequently, $rank\ \mathbf{\Lambda}^\star = 2$, and the motion is asymptotically stable. It happens because energy transfer between "pure dissipative" variable ξ_3 and two others occurs, and this transfer with respect to ξ_1 is implemented by GF influence only for any values of gyroscopic terms (without exceptions).

The last feature surprisingly changes when gyroscope is pendent (hanging down). To analyze this case we can add a sign "-" before g in formulas (11), now μ, μ_1 are negative. With this change, if

$$a=\frac{2+\mu\pm\sqrt{-\mu_1}}{2+\mu_1}, \tag{15}$$

then $rank\ \mathbf{\Lambda}^\star = 1$, and the motion is marginally stable. This inference can be easily verified, because there are purely imaginary eigenvalues $\pm\ i\ (1+\sqrt{-\mu_1})$. Equality (15) determines two critical values for angular velocity value ω. Notice that mass, stiffness and viscosity of dashpot don't affect condition (15) – only position of point O_1 (parameter l_1) is essential.

Remark. We proved that inequalities (12) are the sufficient conditions of asymptotic stability of the motion studying. At the same time they give the necessary conditions of asymptotic stability. In fact, if at least one of these inequalities takes the opposite sign, then the matrix $\boldsymbol{K}$ has positive eigenvalue, and according to paragraph 2 of theorem 4 (as $rank\ \mathbf{\Lambda}^\star = 2$) the solution (10) is unstable.

4. Discussion and concluding remarks

In this paper we turned our attention to the role played by gyroscopic forces in stability issues for systems with incomplete energy dissipation. Influence of these forces can seriously differ from the case of full energy dissipation. In particular, some stabilizing effect are possible which are not available in common frames of the Kelvin-Chetaev theorems. As an example the stabilization of symmetrical rigid body rotations is considered. It is shown that energy dissipation in dashpot is conveying to the whole body due to presence of GF, and without it this stabilization is not possible.

References

[1] W. Thomson, P.G. Tait, Treatise on Natural Philosophy, vol. I, part I, New Edition, Cambridge University Press, Cambridge (1879).

[2] S.H. Crandall, The effect of damping on the stability of gyroscopic pendulums, ZAMP Z. angew. Math. Phys. 46, 761-780 (1995).

[3] R. Hryniv, P. Lancaster, Stabilization of gyroscopic systems, ZAMM Z. angew. Math. Mech. 81, 675-681 (2001).

[4] S.A. Agafonov, Stability and motion stabilization of nonconservative mechanical systems, J. Math. Sci. 112, 4419-4497 (2002).

[5] O. Kirillov, Nonconservative stability problems of modern physics, De Gruyter Studies in Mathematical Physics, Berlin (2013).

[6] N.I. Zhinzher, Effect of dissipative forces with incomplete dissipation on the stability of elastic systems, Izv. Ross. Akad. Nauk. MTT 1, 149-155 (1994).

[7] Skliba J., Problem of the gyroscopic stabilizer damping, Applied and Computational Mechanics, 3 (2009), 205212. Puzyryov V., Awrejcewicz J., Asymptotical stability of the motion of mechanical systems with partial energy dissipation, Nonlinear Dynamics, to appear. E.J. Routh, Treatise on the Stability of a Given State of Motion, Particularly, Steady Motion, MacMillan, London, (1877).

[8] Hao Dong, Jing Zeng, Liang Wu, and Huanyun Dai, Analysis of the Gyroscopic Stability of the Wheelset, Shock and Vibration, Volume 2014, Article ID 151625.

[9] N.G. Chetaev, Stability of Motion, Pergamon Press, 1961.

[10] D.R. Merkin, Introduction to the Theory of Stability, Springer, Berlin (1997).

[11] E.E. Zajac, Kelvin - Tait - Chetaev theorem and extensions, Journal of the Astronautical Sciences, 11, 46-49 (1964).

[12] R.E. Robertson, Notes on the Thomson-Tait-Chetaev stability theorem, Journal of the Astronautical Sciences, 15, 319-324 (1968).

[13] T.J. Moran, A simple alternative to the RouthHurwitz criterion for symmetric systems, ASME Journal of Applied Mechanics, 37 (1970), 11681170.

[14] Puzyrov V., Awrejcewicz J., Asymptotical stability of the motion of mechanical systems with partial energy dissipation, Nonlinear Dynamics (to appear).

Jan Awrejcewicz, Professor: Department of Automation,Biomechanics and Mechatronics, Faculty of Mechanical Engineering of Lodz University of Technology, 1/15 Stefanowski Str., 90-924 Lodz, Poland (*jan.awrejcewicz@p.lodz.pl*).

Nataliya Losyeva, Professor: Vasyl Stus Donetsk National University, Faculty of Mathematics and Information Technology, Department of Applied Mechanics and Computing, 600-richya, 21, Vinnytsia, 21021,Ukraine (*n.losieva@donnu.edu.ua*).

Volodymyr Puzyrov, Professor: Vasyl Stus Donetsk National University, Faculty of Mathematics and Information Technology, Department of Applied Mechanics and Computing, 600-richya, 21, Vinnytsia, 21021,Ukraine (*v.puzyryov@donnu.edu.ua*).

Control of vibrations of multistory buildings with use of passive dampers

Ersin Aydin, Baki Öztürk, Maciej Dutkiewicz

Abstract: The purpose of the paper is application of additional dampers which will absorb the part of energy supplied to the building. The cost function is defined as the sum of damping coefficients of the dampers. Minimizing the sum of the damping coefficients of the added dampers is the criteria for analysis. After the optimal designs and the minimum costs and their variation with respect to fundamental period and target added damping are found, the optimal designs are tested using the spectral analysis. Numerical example for six storey building is presented to prove the validity of the proposed method. The numerical results show that the proposed damper optimization method is efficient to find optimal damper distribution for a target damping ratio.

1. Introduction

Application of supplemental dampers has transitioned from protection related structures to commercial applications on building structures and bridges exposed to seismic or wind loads. Fluid damping technology has been proven to be thoroughly reliable and robust for implementation to structures. A fluid viscous damper is one of the commonly known passive dampers.

The results of reducing the seismic response of multi-storey shear buildings with first storey damping were presented by an optimization study [1]. In this study, authors remarked that flexibility of structure actually affected the optimal damping of system; and suitable objective functions were proposed for both short and high buildings. Ashour and Hanson [2] conducted an interesting study on the optimal placement of visco-elastic dampers in relation to seismic excitation. An evaluation of the effect of added visco-elastic dampers on reducing the earthquake response of multi-storey steel frame structures was presented by Zhang et al [3]. The seismic responses of simple building structures were examined in a study carried out by Hahn and Sathiavageeswaran [4] to assess the effects of different distributions and magnitudes of damping derived from added visco-elastic dampers. A simple optimal design procedure was proposed by which dimension and number of visco-elastic dampers could be determined and the results of the proposed method were also supported by experimental measurements [5]. Cao and Mlejnek [6] developed a finite element perturbation method, which provided a simple tool for the prediction of damping in a wide frequency range without the need for repeated analyses. An algorithm was introduced to find the optimum sets of storey stiffness

coefficients and damping coefficients of the dampers of an elastic planar shear building with viscous dampers [7].

For planar building frames, a new objective function considering base shear force transfer function was defined; and the optimal damper's both location and size were determined [8]. Cimellaro [9] defined top absolute acceleration as an objective function to find. A gradient based evolutionary optimization procedure was proposed for determining the optimal allocation of added visco-elastic dampers and their supporting members to minimize the transfer function of the sum of interstorey drifts [10]. A new optimal damper placement method using penalty function and first order optimization theory in long span suspension bridges was presented by Wang [11]. A gradient-based evolutionary optimization methodology is presented for finding the optimal design of viscous dampers to minimize an objective function defined for a linear multi-storey structure [12]. An optimal damper method was investigated to find optimal seismic design of added viscous dampers in yielding plane frames and the total added damping is minimized for allowable values of local performance indices under the excitation of a set of ground motions in both regular and irregular structures [13].Applications for the seismic design of building structures equipped with viscous damperswere carried out [14].Some basic methodologies were also compared with respect to some structural response and usability measures in practice [15]. A new objective function for finding optimal size and location of the added viscous dampers was proposed based on the elastic base moment in planar steel building frames [16].

In the present study, a cost function that is the sum of damping coefficients of the added dampers is minimized to find optimal damping coefficients of the added dampers under a specified added damping ratio and both lower and upper bounds of each damping coefficient of the added dampers. Differential Evolution, Nelder Mead and Simulated Annealing are used to solve the simple optimization problem.

2. Theoretical formulation

In the paper an n-storey shear building model such as linear manufactured viscous dampers that are added to each story shown in Fig. 1 is considered.

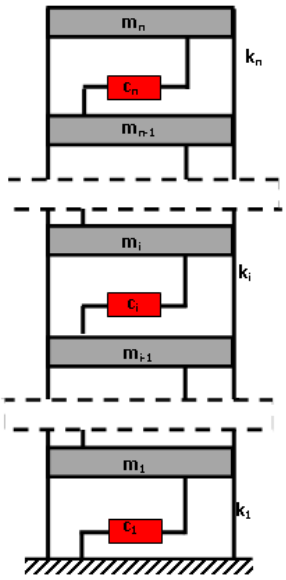

Figure 1. n-Storey shear building model with supplemental dampers

Two ends of the viscous dampers have different velocity since one end is attached to one building storey and the other end to a different storey. These devices produce damping forces in proportion to relative velocity between each one of the ends. These elements achieve the energy dissipation during an external vibration such as a wind and an earthquake excitation. The damping force of a linear viscous damper is given as

$$F_{ad} = c_{ad}.\dot{u} \tag{1}$$

where c_{ad}, $\dot{u}$ denote the damping coefficient of manufactured viscous damper and relative velocity between each one of the ends of damper, respectively. This type of manufactured damper is considered to add to each one of storeys in a shear building shown in Fig.1. After the dampers are inserted to the structure subjected to earthquake vibration, the equation of motion can be written as

$$\boldsymbol{M}\ddot{\boldsymbol{u}}(t) + (\boldsymbol{C} + \boldsymbol{C_{ad}})\dot{\boldsymbol{u}}(t) + \boldsymbol{K}\boldsymbol{u}(t) = -\boldsymbol{M}\boldsymbol{r}\ddot{u}_g(t) \tag{2}$$

where $\boldsymbol{M}$, $\boldsymbol{C}$ and $\boldsymbol{K}$ present mass, structural damping and stiffness matrices, respectively,$\ddot{\boldsymbol{u}}(t)$, $\dot{\boldsymbol{u}}(t)$and$\boldsymbol{u}(t)$ are acceleration, velocity and displacement vectors, respectively. The $\boldsymbol{r}$ denotes influence vector that all elements is equal to one, $\ddot{u}_g(t)$is defined as ground acceleration. $\boldsymbol{C_{ad}}$ is the non-proportional damping matrix that should be designed optimally to minimize an objective. The matrix,$\boldsymbol{C_{ad}}$ can be decomposed into corresponding added viscous dampers and is written as

$$\boldsymbol{C_{ad}} = c_1\boldsymbol{C_1} + c_2\boldsymbol{C_2} + \cdots + c_n\boldsymbol{C_n} \tag{3}$$

wherec_i $(i = 1, \dots, n)$correspondsto the damping coefficient of i[th] added damper; and $\boldsymbol{C}_i$ $(i = 1, \dots, n)$ denotes the location matrix of the i[th] added damper. Moreover, the location matrix is also equal to the partial differential of $\boldsymbol{C_{ad}}$ with respect to i[th] added damping coefficient of dampers as

$$\boldsymbol{C}_i = \frac{\partial \boldsymbol{C}_{ad}}{\partial c_i} \tag{4}$$

As an example; for values of$i = 1$ and 2

$$\boldsymbol{C}_1 = \begin{bmatrix} 1 & 0 & \dots & 0 & 0 & \dots & 0 & 0 \\ 0 & 0 & \dots & 0 & 0 & \dots & 0 & 0 \\ \vdots & \vdots & \vdots & \vdots & \vdots & \vdots & \vdots & \vdots \\ 0 & 0 & \dots & 0 & 0 & \dots & 0 & 0 \\ 0 & 0 & \dots & 0 & 0 & \dots & 0 & 0 \\ \vdots & \vdots & \vdots & \vdots & \vdots & \vdots & \vdots & \vdots \\ 0 & 0 & \dots & 0 & 0 & \dots & 0 & 0 \\ 0 & 0 & \dots & 0 & 0 & \dots & 0 & 0 \end{bmatrix}_{nxn} \quad \boldsymbol{C}_2 = \begin{bmatrix} 1 & -1 & \dots & 0 & 0 & \dots & 0 & 0 \\ -1 & 1 & \dots & 0 & 0 & \dots & 0 & 0 \\ \vdots & \vdots & \vdots & \vdots & \vdots & \vdots & \vdots & \vdots \\ 0 & 0 & \dots & 0 & 0 & \dots & 0 & 0 \\ 0 & 0 & \dots & 0 & 0 & \dots & 0 & 0 \\ \vdots & \vdots & \vdots & \vdots & \vdots & \vdots & \vdots & \vdots \\ 0 & 0 & \dots & 0 & 0 & \dots & 0 & 0 \\ 0 & 0 & \dots & 0 & 0 & \dots & 0 & 0 \end{bmatrix}_{nxn} \tag{5}$$

In the fundamental mode,the damping ratio is calculated as follows

$$2\zeta_1\omega_1 = \frac{\boldsymbol{\phi_1^T(C+C_{ad})\phi_1}}{\boldsymbol{\phi_1^T M\phi_1}} = \frac{\boldsymbol{\phi_1^T C\phi_1}}{\boldsymbol{\phi_1^T M\phi_1}} + \frac{\boldsymbol{\phi_1^T C_{ad}\phi_1}}{\boldsymbol{\phi_1^T M\phi_1}} \tag{6}$$

whereζ_1 denotes damping ratio after dampers are inserted to the structure,$\boldsymbol{\phi_1}$is the normalized fundamental mode vector and ω_1 is the undamped natural circular frequency of the model structure. The first term on the right side of Eq. (6) covers proportional damping matrix, and therefore there are no couplings between first mode and any of the other modes. This situation is expressed as

$$\frac{\boldsymbol{\phi_1^T C\phi_i}}{\boldsymbol{\phi_1^T M\phi_i}} = \begin{cases} 2\zeta_s\omega_1 & i = 1 \\ 0 & i \neq 1 \end{cases} \tag{7}$$

whereζ_s denotes structural damping ratio for the fundamental mode. The second term on the right side of Eq. (6) include non-proportional damping matrix. However, only for purposes of a simplified design it is convenient to assume that

$$\frac{\boldsymbol{\phi_1^T C_{ad}\phi_i}}{\boldsymbol{\phi_1^T M\phi_i}} = \begin{cases} 2\zeta_{ad}\omega_1 & i = 1 \\ 0 & i \neq 1 \end{cases} \tag{8}$$

whereζ_{ad} denotes added damping ratio for the fundamental mode. The Eq. (6) can be rewritten as follows

$$2\zeta_1\omega_1 = 2(\zeta_s + \zeta_{ad})\omega_1 \tag{9}$$

and; therefore

$$\zeta_1 = \zeta_s + \zeta_{ad} \tag{10}$$

Structural damping ratio ζ_s is generally assumed to be constant as 0.02 in steel structures or 0.05 in RC structures. The parameter ζ_1 denotes the desired value of the damping ratio when the dampers are inserted to the structure. The parameter ζ_{ad}, which occurs due to the effects of the added dampers, is the added damping ratio.The desired ζ_{ad} is determined from Eq.(10), if the structural damping ratio and the desired total damping ratio are known. Therefore, the desired added damping ratio is calculated as

$$\zeta_{ad} = \zeta_1 - \zeta_s \tag{11}$$

The Eq.(6) can be rewritten for only added damping ratio as

$$2\zeta_{ad}\omega_1 = \frac{\boldsymbol{\phi_1^T C_{ad} \phi_1}}{\boldsymbol{\phi_1^T M \phi_1}} = c_1 \frac{\boldsymbol{\phi_1^T C_1 \phi_1}}{\boldsymbol{\phi_1^T M \phi_1}} + c_2 \frac{\boldsymbol{\phi_1^T C_2 \phi_1}}{\boldsymbol{\phi_1^T M \phi_1}} + \cdots + c_n \frac{\boldsymbol{\phi_1^T C_n \phi_1}}{\boldsymbol{\phi_1^T M \phi_1}} \tag{12}$$

where the coefficients (μ_i) of the c_i can be written as follows

$$\mu_i = \frac{\boldsymbol{\phi_1^T C_i \phi_1}}{\boldsymbol{\phi_1^T M \phi_1}} \tag{13}$$

The formula of the desired added damping ratio for fundamental mode is writtenas below using eqs. (12)- (13)

$$\zeta_{ad} = \frac{1}{2\omega_1}(\mu_1 c_1 + \mu_2 c_2 + \cdots + \mu_n c_n) = \frac{1}{2\omega_1}\sum_{i=1}^{n} \mu_i c_i \tag{14}$$

3. Definition of optimal damper problem for shear buildings

The aim of an optimal design is to minimize or maximize an objective or multiple objectives. Some objective functions appeared such as top displacements, maximum interstorey drifts, sum of interstorey drifts, base shears, top absolute accelerations, overturning moments, a defined damage index, and combinations of some structural performance functions in the previously mentioned literature. Various objective functions can be used in order to solve optimal damper problem and the importance of various cost functions can increase for different types of structures. While the decrease in displacements or inter-storey drifts is important for a displacement-based design, some internal forces and accelerations can be important for a forced-based design. In other words, a defined structural damage index and an energy index may be important for various structures.

In this study,design variables are considered as the damping coefficients of the added dampers. Optimal damper problem is based on minimization of total cost of the dampers that is expressed as the sum of damping coefficients of the added dampers which is given as

$$\text{Min.} f = \sum_{i=1}^{n} c_i \tag{15}$$

The cost function to be minimizedin Eq.(15)indicatesthe total damping coefficient of the added dampers. Eq.(14) can be rewritten as an equality constraint in terms of the added damping ratio

$$\zeta_{ad} = \frac{1}{2\omega_1}(\mu_1 c_1 + \mu_2 c_2 + \cdots + \mu_n c_n) = \frac{1}{2\omega_1}\sum_{i=1}^{n} \mu_i c_i \tag{16}$$

where ζ_{ad} is a fixed damping ratio that can be given as a desired damping ratio. The fundamental natural circular frequency and the parameter μ_i are known parameters from the vibration characteristics of the structure. Both objective function and equality constraint are the linear function of the design parameters.

Taking into account the inequality constraints on the upper and lower bounds of the damping coefficients of each added damper gives the following

$$0 \le c_i \le \bar{c}_i \text{ (i=1,2,…,n)} \tag{17}$$

where$\bar{c}_i$is the upper bound of damping coefficient of the damper in ith story. In practical applications, a damper capacity and size which corresponds to the upper bound of the added damper should be restricted because of commercial and manufacturing limitations.

The three various numerical minimization methodssuch as Differential Evolution, Nelder Mead and Simulated Annealing, which are well known in the optimization literature, are used to solve the optimization problem. These methods present the good agreement between them according to the numerical results in this problem.

4. Numerical Examples

Six-storey shear buildings, as shown in Fig. 2 is considered as numerical example.

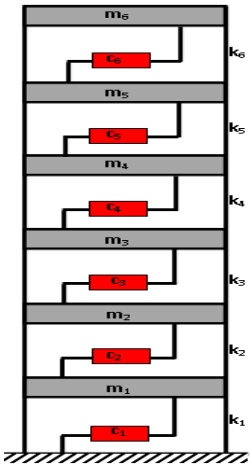

Figure 2. 6-Storey buildings with supplemental dampers

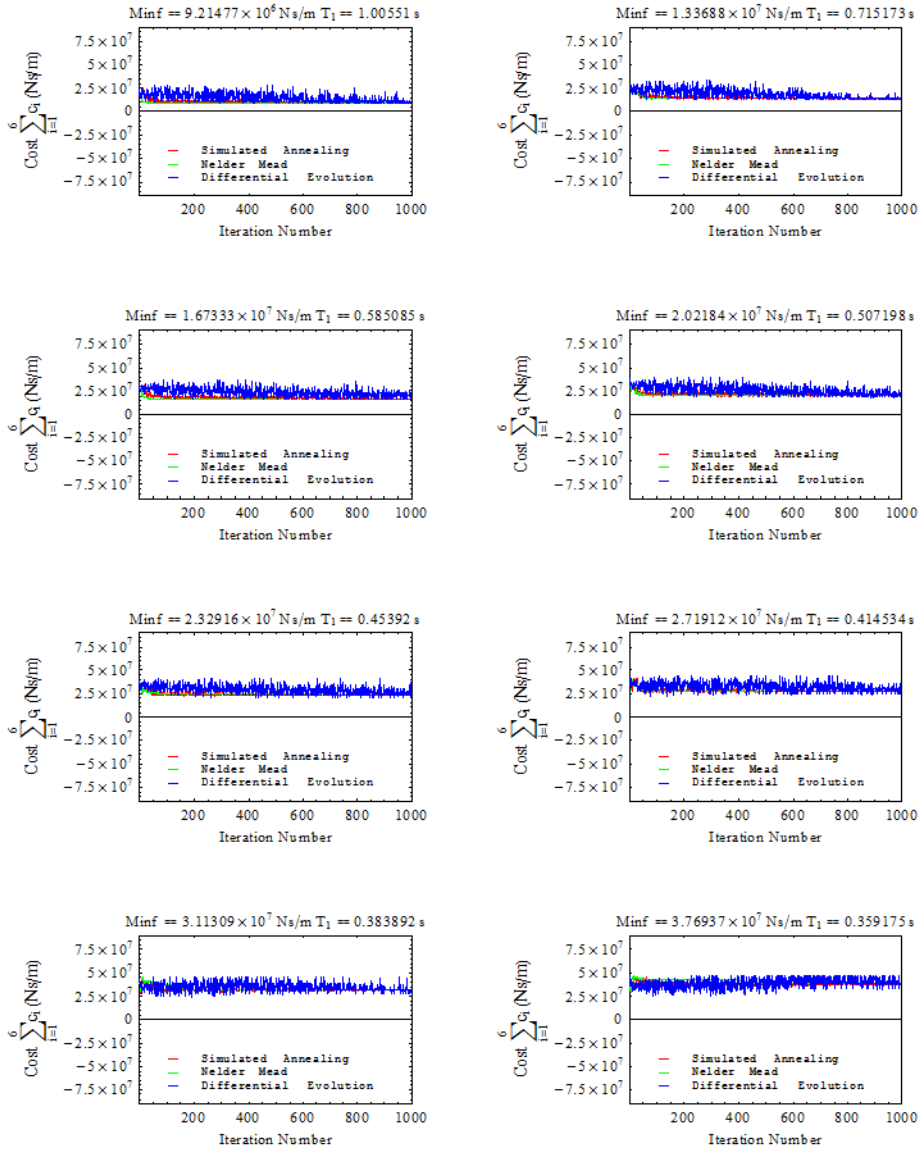

Figure 3. The variation of the cost function according to iteration number for ζ_{ad} =0.40

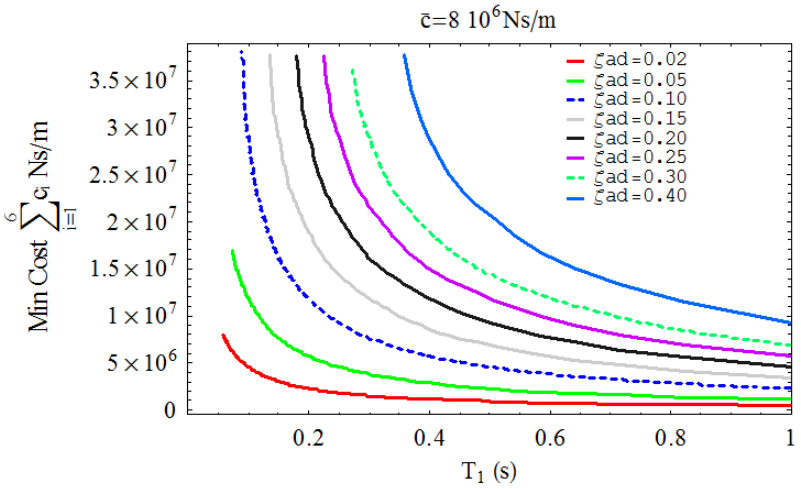

Figure 4. The variation of minimum values of cost function according to period of the structure for different added damping ratios

Each one of story mass is equal to 3.2 10^4 kg. Structural damping in the fundamental mode is assumed as 0.02 and itis proportional to mass. The upper value of a damping coefficient isassumed to be 8 10^6 Ns/m. Storey stiffness is uniformly distributed to storeys. Stiffness is changed in a certain range to attain to a certain period. Design variables (c_1, c_2, c_3, c_4, c_5 and c_6) are taken as the damping coefficient of added dampers for each storey. The sum of the design variables is minimized under a target added damping ratio and both upper and lower bound of the added damping coefficients. Optimization is done for different values of added damping ratio and different structural period. Optimal damping coefficients of the added dampers and the minimum value of the total damping coefficient are calculated at the optimization stage under an equality constrained (ζ_{ad}) and inequality constraints of the upper and lower bounds (0, $\bar{c}_i$) of each added damping coefficients. Figure3 illustrates the variation of the cost function with respect to iteration number for different structural period cases, while the added damping ratio is fixed to 0.40. It can be seen from Figure 3 that the decrease of structural period brings along the increase of the minimum cost function. Figure 4 illustrates the variation of the minimum cost function with respect to fundamental period for each target added damping ratio. When the added damping ratio is low, the optimal solutions appear in a wide period range. The increase of ζ_{ad} bring on moving of the optimal solutions to the upper period regions. Figure 5 shows the variation of the optimal values of design variables with respect to the fundamental period. The increase of the target damping ratio means that the dampers should be distributed to more storeys.

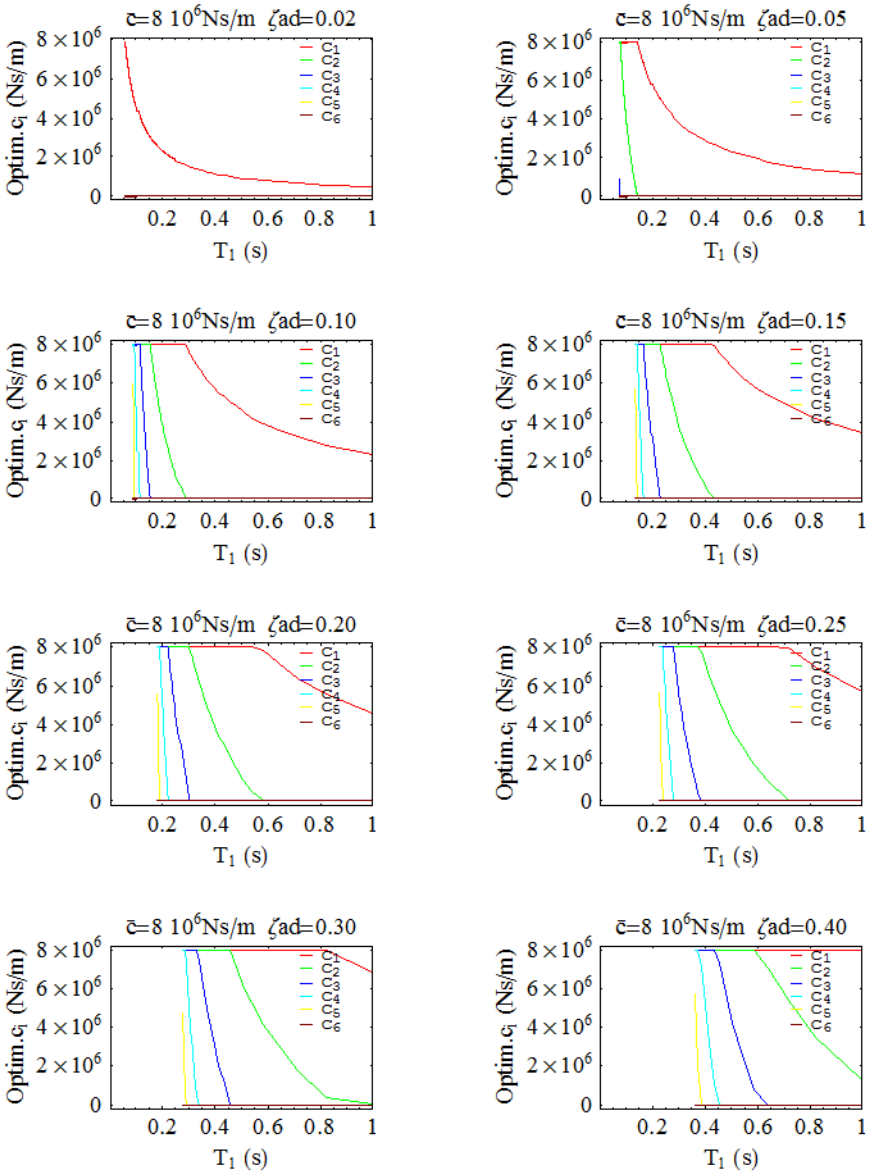

Figure 5. The variation of optimal values of design variables according to period of the structure for different target damping ratios

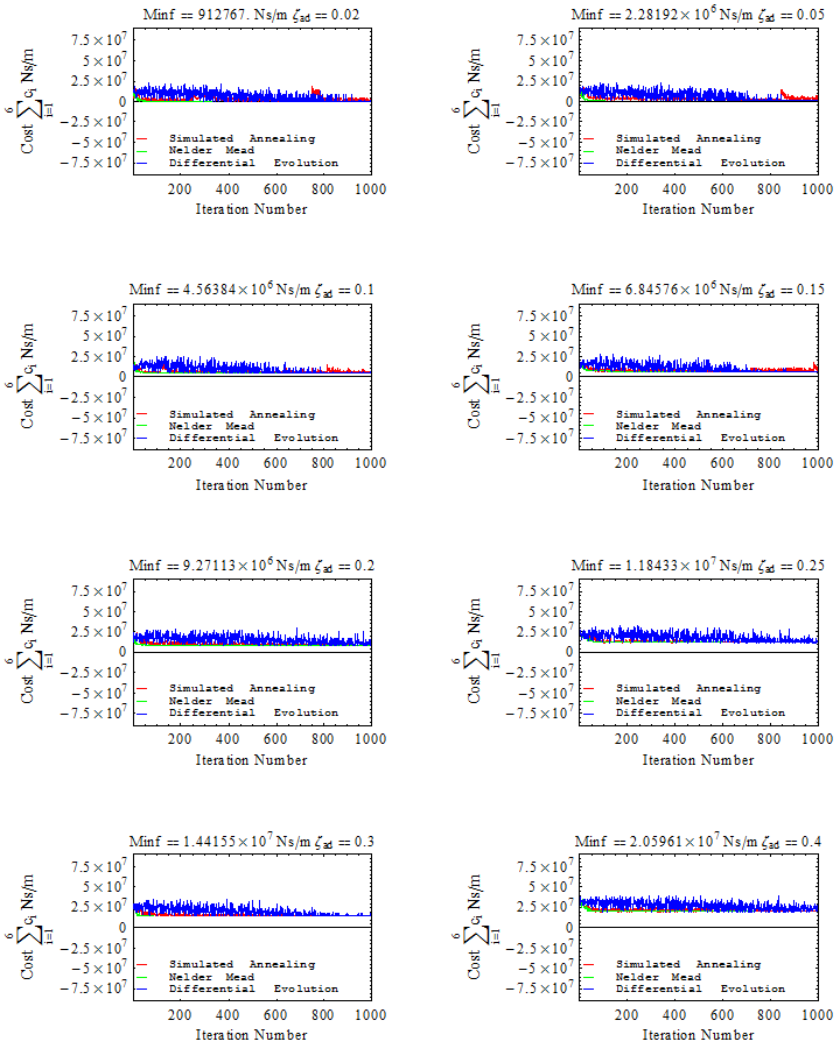

Figure 6. The variation of the cost function according to iteration number for T_1 =0.5s

In the next case, the optimal solutions are calculated for different target damping ratios by fixing the fundamental period. Figure 6 shows the variation of the cost function with respect to iteration number for different ζ_{ad} in case of T_1= 0.5s. The minimum values of the cost function are given in this figure. The increase of added damping ratio results in the increase of the minimum value of cost function.

5. Conclusions

The optimization problem is constructed based on minimizing the sum of the damping coefficients of the added dampers under a target added damping ratio in the first mode and both upper and lower bounds of the added dampers. Both the cost function and the constraint functions are linear function of the design variables. Three different numerical minimization methods are used for justification in this study. The results obtained from minimization methods match with each other. The effects of variation of the fundamental period and the target added damping ratio above the optimal designs are also investigated. The numerical results reveal that the increase of the fundamental period results in the decrease of cost function value for a fixed upper bound of added damping coefficient and a specified target added damping ratio. The more added damping ratio is needed, the more the cost function value occurs. In the numerical examples, the upper bound of the added damping coefficients is taken as a fixed value.

References

[1] Constantinou, M.C. and Tadjbakhsh, I.G., (1983), "Optimum design of a first storey damping", *Computer & Structures*, **17**(2), 305-310.

[2] Agrawal, A.K. and Yang, J.N. (2000), "Design passive energy dissipation systems based on LQR methods", *J. of Intell Mater Syst and Struct*, **10**(20), 933-944.

[3] Zhang, R.H., Soong, T.T. and Mahmoodi, P. (1989), "Seismic response of steel frame structures with added viscoelastic dampers", *Earthquake Engineering & Structural Dynamics*,**18**, 389-396.

[4] Hahn, G.D. and Sathiavageeswara, K.R.(1992), "Effects of added-damper distribution on the seismic response of building", *Computer & Structures*, **43**(5), 941-950.

[5] Zhang, R.H. and Soong, T.T. (1992), "Seismic design of visco–elastic dampers for structural applications", *StructEng ASCE*, **118**(5):1375-1392.

[6] Cao, X. and Mlejnek, H.P. (1995), "Computational prediction and redesign for visco-elastically damped structures", *Comput Methods ApplMechEngng*, **125**, 1-16.

[7] Tsuji, M. and Nakamura, T. (1996), "Optimum viscous dampers for stiffness design of shear buildings", *The Structural Design of Tall Buildings*, **5**, 217-234.

[8] Aydin, E., Boduroglu, M.H. and Guney, D. (2007), "Optimal damper distribution for seismic rehabilitation of planar building structures", *EngStruct*, **29**, 176-185.

[9] Cimellaro, G.P. (2007), "Simultaneous stiffness-damping optimization of structures with respect to acceleration displacement and base shear", *EngStruct*, **29**, 2853-2870.

[10] Fujita, K., Moustafa, A. and Takewaki, I. (2010), "Optimal placement of visco-elastic dampers and supporting members under variable critical excitations", *Earthq and Struc*,**1**, 43-67

[11] Wang, H., Li, A.Q., Jiao, C.K. and Spencer, B.F. (2010), "Damper placement for seismic control of super-long-span suspension bridges based on the first-order optimization method", *Science China Technological Sciences*, **53**(7), 2008-2014.

[12] Fujita, K., Yamamoto, K., Takewaki, I. (2010), "An evolutionary algorithm for optimal damper placement to minimize interstorey-drift transfer function in shear building", *Earthquakes and Structures*, **1**(3):289-306.

[13] Lavan, O. and Levy, R. (2010), "Performance based optimal seismic retrofitting of yielding plane frames using added viscous damping", *Earthquakes and Structures*, **1**(3), 307-326.

[14] Silvestri, S. and Trombetti, T. (2007), ''Physical and numerical approaches for the optimal insertion of seismic viscous dampers in shear-type structures'', J. Earthq. Eng. 11(5), 787-828.

[15] Whittle, J.K., Williams, M.S., Karavasilis, T.L. and Blakeborough, A. (2012), "A comparison of viscous damper placement methods for improving seismic building design", *J of Earthquake Engineering*, **16**, 540-560.

[16] Aydın, E. (2012), "Optimal Damper Placement Based on Base Moment in Steel Building Frames", *Journal of Constructional Steel Research*, **79**, 216-225.

Ersin Aydin, Professor, Faculty of Engineering, Department of Civil Engineering,ÖmerHalisdemir University, Nigde, Turkey, eaydin@ohu.edu.tr,

Baki Öztürk, Professor, Faculty of Engineering, Department of Civil Engineering, Hacettepe University, Ankara, Turkey, bakiozturk@hacettepe.edu.tr,

Maciej Dutkiewicz, Ph.D.: UTP University of Science and Technology in Bydgoszcz, Faculty of Civil, Architecture and Environmental Engineering, Department of Building Construction, Al. Prof. S. Kaliskiego 7, 85-796 Bydgoszcz, Poland, e-mail address: macdut@utp.edu.pl.

Stokes flow through a tube with wavy wall

Włodzimierz Bielski, Ryszard Wojnar

Abstract: We propose a study of the flow in a tube with wavy wall adopting Malevich - Mityushev - Adler's method, and find a correction to Hagen-Poiseuille's solution. The problem is to be solved by expanding the velocity and pressure fields in Fourier series involving an infinite set of unknown coefficients. The boundary surface is expanded in Taylor's series. A perturbation expansion in terms of the powers of the small parameter ε of the full set of Stokes' equations yields a cascade of boundary value problems which are solved at each step in closed form. Even in the first order approximation $O(\varepsilon)$, new results are obtained.

1. Introduction

The problem of flow through a tube with a wavy wall appears in different applications. It is important in hemorheology and hemodynamics, both fields of physiology, [1, 2]. It is well known that the two leading causes of death, myocardial infarction (heart attack), and stroke, may each directly result from an arterial system that has been slowly and progressively compromised by years of deterioration. An artery wall thickens as a result of invasion and accumulation of white blood cells and proliferation of intimal-smooth-muscle cell creating an atheromatous (fibro-fatty) plaque. This limits dynamic blood flow and in the consequence the oxygen flow within the brain.

The task is related also to problem of stream flow past the rough bottom and walls, in peculiarity in a channel with obstacles on the bottom, studied in geophysics and civil engineering, [3, 4]. And so, M. Lessen and P.-S. Huang investigated Hagen-Poiseuille's flow in a pipe with axially symmetric wavy walls, and studied the effect of small amplitude wall waviness on a steady flow. They assumed that the steady motion is composed of a spatially averaged mean flow and a periodic disturbance due to the wall wave, [4].

We adopt the method introduced in Malevich - Mityushev - Adler's papers, [5, 6]. The application of an analytical algorithm yields efficient formulae for the velocities and discharge. We consider a Stokesian pressure driven flow in pipe with a wavy wall, see Fig.1. The problem is axially-symmetric, and in cylindrical co-ordinates r, φ, z it does not depend on φ. The radius R of the pipe cross-section is a periodic function of the z-axis. In our example the waviness is described by a cosinus function $R = R_0 + \varepsilon a \cos Kz$, with $K = 2\pi/\lambda$, where λ denotes the length of the wall wave. When the small parameter ε increases, Hagen - Poiseuille's flow ($\varepsilon = 0$) is disturbed and eddies can arise above a critical value.

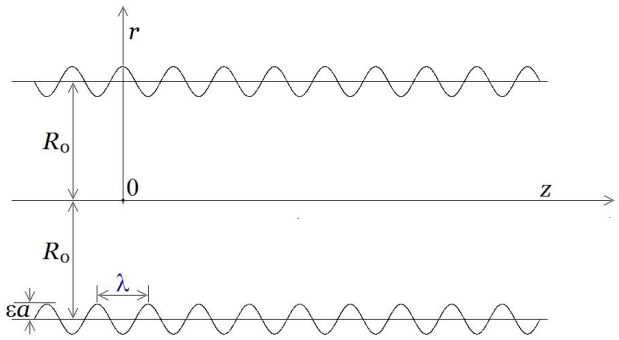

Figure 1. Cross-section of the considered axially-symmetric tube. Here R_0 is the mean value of the pipe radius, ε is a dimensionless smallness parameter, a is the amplititude of the wall waveness, and λ denotes the length of the wall waveness.

We apply an overall external gradient pressure $\overline{\nabla p} \equiv -G$ along the z-direction. It can be described by a constant jump along the z-axis of the periodic cell $p(z+\lambda, r) - p(z, r) = -\lambda G$.

A. E. Malevich, V. V. Mityushev and P. M. Adler, [5, 6], have shown how to apply the asymptotic analysis to reduce the problem of flow in channels with curvilinear walls to the problem of flow with the plane ones.

We consider flow through an axially symmetric pipe with a curvilinear (wavy) wall. Its radius is, however, constant in the mean. In the cylindrical coordinates the z-axis is simply the axis of rotational symmetry of the tube, and the r-axis is perpendicular to the z-axis. In an example, we will accept the wall surface $S(x)$ described by the sinusoid, cf. Fig. 1

$$r = S(z) = R_0 + \varepsilon\, a\, \cos Kz$$

where $S(z)$ is a smooth periodic function and ε is a small parameter. The mean value of the $S(z)$ is R_0. The coefficient a renders the amplitude of the wavy shape of the wall, and $K = 2\pi/\lambda$, where λ denotes the length of the wall wave.

For the infinitely differentiable function $S(z)$ a cascade of boundary value problems is deduced. The boundary conditions are substituted by Maclaurin's expansions, and the solution (the velocity and pressure fields) is calculated in the form of both, ε expansions and Fourier's series. The case $\varepsilon = 0$ corresponds to the zero-th approximation problem.

We express the velocity and the pressure as the expansions in powers of ε.

$$p(r, z) = \sum_{m=0}^{\infty} p_m \varepsilon^m \quad \text{and} \quad \boldsymbol{v}(r, z) = \sum_{m=0}^{\infty} \boldsymbol{v}_m \varepsilon^m$$

2. Geometrical description

Further the steady flow will be considered only. Moreover, the gravity components will be assumed to be zero, and the fluid will be assumed to be incompressible, it is $\rho =$ constant. The axisymmetric flow will be considered with the assumption of no tangential velocity ($v_\varphi = 0$), and the remaining quantities are being independent of the angle φ. The problem becomes two-dimensional. We simplify notation by substitution

$$v_r \equiv u \quad \text{and} \quad v_z \equiv v$$

The continuity equation for the steady flow reads

$$\frac{1}{r}\frac{\partial}{\partial r}(ru) + \frac{\partial v}{\partial z} = 0. \tag{1}$$

Navier-Stokes' equations are

$$\begin{aligned} \rho\left(u\frac{\partial u}{\partial r} + v\frac{\partial u}{\partial z}\right) &= -\frac{\partial p}{\partial r} + \eta\left\{\frac{1}{r}\frac{\partial}{\partial r}\left(r\frac{\partial u}{\partial r}\right) + \frac{\partial^2 u}{\partial z^2} - \frac{u}{r^2}\right\} \\ \rho\left(u\frac{\partial v}{\partial r} + v\frac{\partial v}{\partial z}\right) &= -\frac{\partial p}{\partial z} + \eta\left\{\frac{1}{r}\frac{\partial}{\partial r}\left(r\frac{\partial v}{\partial r}\right) + \frac{\partial^2 v}{\partial z^2}\right\} \end{aligned} \tag{2}$$

In the case of Hagen-Poiseuille's flow in a tube with constant radius equal to R_0, it is $a = 0$. Because the problem is axially-symmetric, we deal with only one velocity component v, directed parallely to the z-axis of the cylindrical co-ordinates. Two equations are identically satisfied and the third equation reads

$$\frac{1}{r}\frac{\partial}{\partial r}\left(r\frac{\partial v}{\partial r}\right) = -\frac{1}{\eta}\frac{\partial p}{\partial z} \tag{3}$$

Integrating Eq.(3) with $\partial p/\partial z =$ constant, and with the boundary condition $v = 0$ at $r = R_0$ results in, [7],

$$v = \frac{G}{4\eta}(R_0^2 - r^2) \tag{4}$$

Here G denotes the constant pressure gradient $G \equiv -\,\mathrm{d}p/\mathrm{d}z =$ constant. We write also

$$v = G\frac{R_0^2}{4\eta}\left(1 - \frac{r^2}{R_0^2}\right) \tag{5}$$

This is Hagen-Poiseuille's law describing the velocity distribution in the steady flow in tube.

3. Axially symmetric steady Stokesian flow

We neglect the inertial terms (at left hand side) in Navier-Stokes equations, and introduce notation $u(r,z) \equiv v_r(r,z)$ and $v(r,z) \equiv v_z(r,z)$.

Let $\boldsymbol{v} = (u, v)$ be an unknown two dimensional velocity field, and p be an unknown field of the pressure. We have $u = u(r, z), v = v(r, z)$ and $p = p(r, z)$. These fields satisfy:
the equation of incompressibility

$$\frac{1}{r}\,\frac{\partial(ru)}{\partial r} + \frac{\partial v}{\partial z} = 0 \tag{6}$$

and Stokes' equations

$$\begin{aligned} -\frac{\partial p}{\partial r} + \eta\left\{\frac{1}{r}\frac{\partial}{\partial r}\left(r\frac{\partial u}{\partial r}\right) + \frac{\partial^2 u}{\partial z^2} - \frac{u}{r^2}\right\} &= 0 \\ -\frac{\partial p}{\partial z} + \eta\left\{\frac{1}{r}\frac{\partial}{\partial r}\left(r\frac{\partial v}{\partial r}\right) + \frac{\partial^2 v}{\partial z^2}\right\} &= 0 \end{aligned} \tag{7}$$

The equations are subject to the boundary conditions

$$u = 0 \quad \text{and} \quad v = 0 \quad \text{at} \quad S(z) \tag{8}$$

3.1. Natural units

For convenience, new units are introduced, and new variables indicated by primes are given

$$r = R_0\, r' \quad \text{and} \quad z = R_0\, z' \tag{9}$$

Moreover,

$$u = \breve{v}\, u', \quad v = \breve{v}\, v' \quad \text{and} \quad p = \breve{p}\, p' \tag{10}$$

Here R_0 is the mean radius of the pipe cross-section, $\breve{v}$ is equal to four times the maximum velocity in Hagen-Poiseuille's problem, cf. Eq.(5), $\breve{v} = (G/\eta)\, R_0^2$ and $\breve{p} = G\, R_0$. The following equality holds $(R_0/\eta)\,(\breve{p}/\breve{v}) = 1$. In these units our equations are:
equation of incompressibility

$$\frac{1}{r'}\,\frac{\partial(r'u')}{\partial r'} + \frac{\partial v'}{\partial z'} = 0$$

and Stokes' equations

$$\begin{aligned} -\frac{\partial p'}{\partial r'} + \frac{1}{r'}\frac{\partial}{\partial r'}\left(r'\frac{\partial u'}{\partial r'}\right) + \frac{\partial^2 u'}{\partial (z')^2} - \frac{u'}{(r')^2} &= 0 \\ -\frac{\partial p'}{\partial z'} + \frac{1}{r'}\frac{\partial}{\partial r'}\left(r'\frac{\partial v'}{\partial r'}\right) + \frac{\partial^2 v'}{\partial (z')^2} &= 0 \end{aligned}$$

with the boundary conditions $u' = 0$ and $v' = 0$ at $S(z')$. For brevity, the primes for new variables are suppressed in the rest of this paper.

3.2. Zero-th approximation

We regard Hagen-Poiseuille's solution as the zero-th approximation of a solution we are looking for. We consider the following set of equations treated a zero-th approximation

$$\frac{\partial p_0}{\partial r} = 0 \quad \text{and} \quad \frac{1}{r}\frac{\partial}{\partial r}\left(r\frac{\partial v_0}{\partial r}\right) = 1 \tag{11}$$

which are subject to the boundary conditions

$$v_0 = 0 \quad \text{at} \quad r = R_0 \tag{12}$$

Moreover, we have

$$u_0 = 0 \quad \text{and} \quad \frac{\partial p_0}{\partial z} = -1 \quad \text{for} \quad 0 \le r \le R_0 \quad \text{and} \quad -\infty < z < \infty \tag{13}$$

In this approximation the velocity vector has only one not vanishing component $v_0 = v_0(r)$, cf. [7]. Hagen-Poiseuille's solution in the natural units reads

$$u_0 = 0, \quad v_0 = \frac{1}{4}\left(1 - r^2\right) \quad \text{and} \quad \frac{\partial p_0}{\partial z} = -1 \tag{14}$$

4. General solution

The unknown fields u, v and p satisfy the following set composed of the equation of incompressibility and Stokes' equations

$$\begin{aligned} &\frac{1}{r}\frac{\partial (ru)}{\partial r} + \frac{\partial v}{\partial z} = 0 \\ &\left\{\frac{1}{r}\frac{\partial}{\partial r}\left(r\frac{\partial u}{\partial r}\right) + \frac{\partial^2 u}{\partial z^2} - \frac{u}{r^2}\right\} - \frac{\partial p}{\partial r} = 0 \\ &\left\{\frac{1}{r}\frac{\partial}{\partial r}\left(r\frac{\partial v}{\partial r}\right) + \frac{\partial^2 v}{\partial z^2}\right\} - \frac{\partial p}{\partial z} = 0 \end{aligned} \tag{15}$$

The equations are subject to the boundary conditions

$$u = 0 \quad \text{and} \quad v = 0 \quad \text{at } S(z) \tag{16}$$

In the accepted frame of reference, see Fig.1,

$$r = S(x) = 1 + \varepsilon a \cos Kz \tag{17}$$

4.1. Expansion in ε series

The unknown velocity components and pressure functions are expanded in the ε series

$$u(r,z) = \sum_{m=0}^{\infty} u_m(r,z)\,\varepsilon^m, \quad v(r,z) = \sum_{m=0}^{\infty} v_m(r,z)\,\varepsilon^m, \quad p(r,z) = \sum_{m=0}^{\infty} p_m(r,z)\,\varepsilon^m \tag{18}$$

At the wall, it is at $r = 1 + \varepsilon a \cos z$ a Taylor's series of a function, say $g = g(r,z)$, is

$$g(1+\varepsilon a\cos z, z) = \sum_{m=0}^{\infty} \varepsilon^m \frac{(\varepsilon a \cos z)^m}{m!} \cdot \left.\frac{\partial^m g}{\partial r^m}\right|_{r=1}$$

and the wall boundary conditions for the functions (18) are represented by series

$$\begin{aligned}
u(1+\varepsilon a\cos z, z) &= \sum_{m=0}^{\infty} \varepsilon^m \sum_{k=0}^{m} \frac{a^k}{k!} \cos^k z \cdot \left.\frac{\partial^k u_{m-k}}{\partial r^k}\right|_{r=1} \\
v(1+\varepsilon a\cos z, z) &= \sum_{m=0}^{\infty} \varepsilon^m \sum_{k=0}^{m} \frac{a^k}{k!} \cos^k z \cdot \left.\frac{\partial^k v_{m-k}}{\partial r^k}\right|_{r=1} \\
p(1+\varepsilon a\cos z, z) &= \sum_{m=0}^{\infty} \varepsilon^m \sum_{k=0}^{m} \frac{a^k}{k!} \cos^k z \cdot \left.\frac{\partial^k p_{m-k}}{\partial r^k}\right|_{r=1}
\end{aligned} \tag{19}$$

In this manner the search for solution of the set of equations (15) with the boundary conditions (16) is substituted by solving these equations with the conditions (19).

4.2. Reduced problem

Solving the problem subject to the boundary conditions given at the waved boundary $r = 1 + \varepsilon a \cos z$ was reduced to the problem with the boundary being a cylindrical surface $r = 1$ without waves, but with modified values of boundary conditions. This means that at each step m the set (15) must be solved with the modified boundary conditions (19).

Substituting expansions (18) into Eqs. (15) leads to the equations

$$\begin{aligned}
&\frac{1}{r}\frac{\partial (r u_m)}{\partial r} + \frac{\partial v_m}{\partial z} = 0 \\
&\left\{\frac{1}{r}\frac{\partial}{\partial r}\left(r\frac{\partial u_m}{\partial r}\right) + \frac{\partial^2 u_m}{\partial z^2} - \frac{u_m}{r^2}\right\} - \frac{\partial p_m}{\partial r} = 0 \\
&\left\{\frac{1}{r}\frac{\partial}{\partial r}\left(r\frac{\partial v_m}{\partial r}\right) + \frac{\partial^2 v_m}{\partial z^2}\right\} - \frac{\partial p_m}{\partial z} = 0
\end{aligned} \tag{20}$$

The solution u_m, v_m and p_m is looked for in the form of Fourier's series

$$\begin{aligned} u_m(r,z) &= \sum_{s=1}^{\infty} \alpha_s^{(m)}(r)\,(A^{(m)}\,\sin sz\,+\,B^{(m)}\,\cos sz) \\ v_m(r,z) &= \sum_{s=1}^{\infty} \beta_s^{(m)}(r)\,\frac{\partial}{\partial z}\,(A^{(m)}\,\sin sz\,+\,B^{(m)}\,\cos sz) \\ p_m(r,z) &= \sum_{s=1}^{\infty} \gamma_s^{(m)}(r)\,(A^{(m)}\,\sin sz\,+\,B^{(m)}\,\cos sz) \end{aligned} \tag{21}$$

with r-functions $\alpha_s^{(m)},\ \beta_s^{(m)}$ and $\gamma_s^{(m)}$, as well the constants $A^{(m)}$ and $B^{(m)}$ must be found. Substituting the expansions (21) into Eqs.(20) we obtain for the incompressibility equation and for Stokes' equations, respectively,

$$\frac{1}{r}\,\frac{\mathrm{d}}{\mathrm{d}r}\left(r\alpha_s^{(m)}(r)\right)\,-\,\beta_s^{(m)}(r)s^2\,=\,0 \tag{22}$$

$$\frac{1}{r}\frac{\mathrm{d}}{\mathrm{d}r}\left(r\frac{\mathrm{d}}{\mathrm{d}r}\alpha_s^{(m)}(r)\right)-\left(s^2+\frac{1}{r^2}\right)\alpha_s^{(m)}(r)-\frac{\mathrm{d}}{\mathrm{d}r}\left(\gamma_s^{(m)}(r)\right)\,=\,0 \tag{23}$$

$$\frac{1}{r}\,\frac{\mathrm{d}}{\mathrm{d}r}\left(r\frac{\mathrm{d}}{\mathrm{d}r}\beta_s^{(m)}(r)\right)-s^2\beta_s^{(m)}(r)-\gamma_s^{(m)}(r)\,=\,0 \tag{24}$$

4.3. Solution of the system

To solve the system (22)–(24) we differentiate Eq.(24). To eliminate $\gamma_s^{(m)}(r)$ we subtract (23) from the result and get the equation, in which we substitute $\beta_s^{(m)}(r)$ using Eq.(22)

$$\beta_s^{(m)}(r)\,=\,\frac{1}{s^2}\,\frac{1}{r}\,\frac{\mathrm{d}}{\mathrm{d}r}\,\left(r\alpha_s^{(m)}(r)\right) \tag{25}$$

After an arrangement we have

$$\begin{aligned} \frac{\mathrm{d}^4\alpha_s^{(m)}}{\mathrm{d}r^4}+\frac{2}{r}\frac{\mathrm{d}^3\alpha_s^{(m)}}{\mathrm{d}r^3}-\left(\frac{3}{r^2}+2s^2\right)\frac{\mathrm{d}^2\alpha_s^{(m)}}{\mathrm{d}r^2}+\left(\frac{3}{r^3}-\frac{2s^2}{r}\right)\frac{\mathrm{d}\alpha_s^{(m)}}{\mathrm{d}r}+ \\ +\left(s^4+\frac{2s^2}{r^2}-\frac{3}{r^4}\right)\alpha_s^{(m)}=0 \end{aligned} \tag{26}$$

A comment: Equation (26) for large r reads

$$\frac{\mathrm{d}^4\alpha_s^{(m)}}{\mathrm{d}r^4}-2s^2\frac{\mathrm{d}^2\alpha_s^{(m)}}{\mathrm{d}r^2}+s^4\alpha_s^{(m)}=0$$

Such an equation is discussed in [5]. Its general solution reads

$$\alpha_s^{(m)}(r)\,=\,(C_1^{(sm)}r+C_2^{(sm)})\,\mathrm{e}^{sr}\,+\,(C_3^{(sm)}r+C_4^{(sm)})\,\mathrm{e}^{-sr}$$

But this is not our case, as we need the range of $0 \le r \le 1$ (the interior of the tube). □

The solution of the Eq. (26) reads

$$\begin{aligned}\alpha_s^{(m)}(r) \;=\; & C_1\, r\, I_0(sr) + \; C_2\, x\, K_0(sr) + \\ & + C_3[2\cdot K_1(sr) + K_0(sr)\, sr]\cdot x\cdot [I_0(sr)\cdot K_1(sr) + K_0(sr)\cdot I_1(sr)] + \\ & + C_4\left(4x^2 I_0^2(sr)\cdot K_1(sr)\cdot s^2 - 8r\cdot I_o(sr)\cdot K_1(sr)\cdot I_1(sr)\cdot s + \right) \\ & + C_4\left(4r^2 I_0(sr)\cdot K_0(sr)\cdot I_1(sr)\cdot s^2 - 8r\cdot I_o^2(sr)\cdot K_0(sr)\cdot s + \right) \\ & + C_4\left(16 I_0(sr)\cdot K_0(sr)\cdot I_1(sr) - s^3 r^3 F(\frac{3}{2}, 3, 3, s^2 r^2)\cdot K_0(sr)\right)\end{aligned} \tag{27}$$

where $I_0(sr), I_1(sr)$ and $K_0(sr), K_1(sr)$ are modified Bessel functions of the first and the second kind, respectively. Unlike the ordinary Bessel functions, which are oscillating as functions of a real argument, I_n and K_n are exponentially growing and decaying functions, respectively. Like the ordinary Bessel function J_n, the function I_n goes to zero at $r = 0$ for $n > 0$ and is finite (equal 1) at $r = 0$ for $n = 0$. Analogously, as Bessel functions of the second kind, the modified function K_n diverges at $x = 0$ with the singularity being of logarithmic type, [9].

For small arguments $r \leq n$, both $I_n(r)$ and $K_n(r)$ become, asymptotically, simple powers of their argument

$$I_n(r) \approx \frac{1}{n!}\left(\frac{r}{2}\right)^n \quad n \geq 0, \quad K_0(r) \approx -\ln r, \quad K_n(r) \approx \frac{(n-1)!}{2}\left(\frac{r}{2}\right)^{-n} \quad n > 0 \tag{28}$$

The confluent function is defined as

$$F(a; b; c, r) = \sum_{n=0}^{\infty} \frac{(a)_n\,(b)_n}{(c)_n\, n!}\, r^n \tag{29}$$

where, for example, $(a)_n \equiv a\cdot(a+1)\cdot(a+2)\cdot\cdots\cdot(a+n-1)$.

Finding $\alpha_s^{(m)}$ by Eq.(27), the expressions (25) and (24) give $\beta_s^{(m)}$ and $\gamma_s^{(m)}$, respectively.

5. An example

In this example we consider the waviness of the tube wall described by the relation

$$R = 1 + \varepsilon\cos z \tag{30}$$

it is we take $a = 1$ and $K = 1$. Moreover, in this example all terms with coefficients ε in powers greater than 2 are omitted. In peculiar, the small parameter expansions (18) read

$$\begin{aligned} u(r,z) \;&=\; u_0(r,z) \;+\; \varepsilon\, u_1(r,z) + \varepsilon^2\, u_2(r,z) \\ v(r,z) \;&=\; v_0(r,z) \;+\; \varepsilon\, v_1(r,z) + \varepsilon^2\, v_2(r,z) \\ p(r,z) \;&=\; p_0(r,z) \;+\; \varepsilon\, p_1(r,z) + \varepsilon^2\, p_2(r,z) \end{aligned} \tag{31}$$

In calculations of the functions $\alpha_s^{(m)}$, $\beta_s^{(m)}$ and $\gamma_s^{(m)}$ we use approximations of the type (28),

$$\begin{aligned} &I_0(r) = 1, \quad I_1(r) = \frac{r}{2} \\ &K_0(r) \approx -\ln r, \quad K_1(r) \approx \frac{1}{r}, \quad F(\frac{3}{2}, 3, 3, s^2 r^2) = 1, \quad s = 0, 1, 2 \end{aligned} \tag{32}$$

We get

$$\alpha_s^{(m)}(r) = C_1 \cdot r - C_2 \cdot r \cdot \ln(sr) + C_3 \left(\frac{2}{sr} - r \cdot \ln(sr) - \frac{sr}{2} \ln(sr) \right) - C_4 \cdot s^3 r^3 \cdot \ln(sr) \tag{33}$$

and consequently, by Eq.(25)

$$\begin{aligned} \beta_s^{(m)}(r) \;=\; & \frac{1}{s^2} \frac{1}{r} \frac{\mathrm{d}}{\mathrm{d}r} \left(r \alpha_s^{(m)}(r) \right) = \frac{1}{s^2} \left\{ 2C_1 - C_2[1 + 2\ln(sr)] \right\} \\ & - C_3 \frac{1}{s^2} \left\{ \frac{5}{2} + (2+s) \cdot \ln(sr) \right\} - C_4 \cdot sr^2 \cdot [1 + 4 \cdot \ln(sr)] \end{aligned} \tag{34}$$

By Eqs.(24) and (34) we obtain

$$\begin{aligned} \gamma_s^{(m)}(r) \;=\; & - \left\{ 2C_1 - C_2[1 + 2\ln(sr)] \right\} + C_3 \left\{ \frac{5}{2} + (2+s) \cdot \ln(sr) \right\} + \\ & + C_4 \left\{ 4 \cdot s \cdot \left(1 + \frac{1}{r} - 4\ln(sr) \right) + s^3 r^2 \cdot [1 + 4 \cdot \ln(sr)] \right\} \end{aligned} \tag{35}$$

Above, $u_0(1, z)$ and $v_0(1, z)$ are known and equal to zero, while $p_0(1, z) = -z + C$ is a linear function of z, with C being an arbitrary constant.

5.1. Elaboration of the example

By Eq.(21) for $m = 1$ we have

$$\begin{aligned} u_1(r, z) &= \alpha_1(r)(A \sin z + B \cos z) \\ v_1(r, z) &= \beta_1(r)(A \cos z - B \sin z) \\ p_1(r, z) &= \gamma_1(r)(A \sin z + B \cos z) \end{aligned} \tag{36}$$

where $\alpha_1(r), \beta_1(r)$ and $\gamma_1(r)$ are given by Eqs.(33), (34) and (35) with $s = 1$, it is We get

$$\begin{aligned}
\alpha_1(r) &= C_1 \cdot r - C_2 \cdot r \cdot \ln r + C_3 \left(\frac{2}{r} - r \cdot \ln r - \frac{r}{2} \ln r \right) - C_4 \cdot r^3 \cdot \ln r \\
\beta_1(r) &= 2C_1 - C_2[1 + 2\ln(sr)] - C_3 \left(\frac{5}{2} + 3 \cdot \ln r \right) - C_4 \cdot r^2 \cdot (1 + 4 \cdot \ln r) \\
\gamma_1(r) &= -[2C_1 - C_2(1 + 2\ln r) + C_3 \left(\frac{5}{2} + 3 \cdot \ln r \right) + \\
&\qquad + C_4 \left\{ 4 \cdot \left(1 + \frac{1}{r} - 4 \ln r \right) + r^2 \cdot (1 + 4 \cdot \ln r) \right\}
\end{aligned} \tag{37}$$

To avoid the singularity at $r = 0$ in expressions for $v_1(r)$ and $p_1(r)$ in the set (36) we put

$$C_2 = 0, \quad C_3 = 0 \quad \text{and} \quad C_4 = 0 \tag{38}$$

Then

$$\alpha_1(r) = C_1 \cdot r, \quad \beta_1(r) = 2C_1 \quad \text{and} \quad \gamma_1(r) = -2C_1 \tag{39}$$

and Eqs.(36) become

$$\begin{aligned}
u_1(r, z) &= C_1 \cdot r \cdot (A \sin z + B \cos z) \\
v_1(r, z) &= 2C_1 \cdot (A \cos z - B \sin z) \\
p_1(r, z) &= -2C_1 \cdot (A \sin z + B \cos z)
\end{aligned} \tag{40}$$

If the expansions (18) are limited up to $\mathrm{O}(\varepsilon^2)$, only the terms with $m = 0, 1$ must be left, and the boundary conditions (19) reduce to the following ones

$$\begin{aligned}
u(1 + \varepsilon a \cos z, z) &\doteq u_0(1, z) + \varepsilon \left(u_1(1, z) + \cos z \cdot \left. \frac{\partial u_0(r, z)}{\partial r} \right|_{r=1} \right) \\
v(1 + \varepsilon a \cos z, z) &\doteq v_0(1, z) + \varepsilon \left(v_1(1, z) + \cos z \cdot \left. \frac{\partial v_0(r, z)}{\partial r} \right|_{r=1} \right) \\
p(1 + \varepsilon a \cos z, z) &\doteq p_0(1, z) + \varepsilon \left(p_1(1, z) + \cos z \cdot \left. \frac{\partial p_0(r, z)}{\partial r} \right|_{r=1} \right)
\end{aligned} \tag{41}$$

where $\doteq$ means the asymptotic equality with the accuracy $O(\varepsilon^2)$. By solution (14)

$$u_0(1, z) = 0, \quad v_0(1, z) = 0$$

and p_0 is a linear function of z only. Moreover

$$\left.\frac{\partial u_0(r,z)}{\partial r}\right|_{r=1} = 0, \quad \left.\frac{\partial v_0(r,z)}{\partial r}\right|_{r=1} = -\frac{1}{2} \quad \text{and} \quad \left.\frac{\partial p_0(r,z)}{\partial r}\right|_{r=1} = 0$$

Hence

$$\begin{aligned} u(1+\varepsilon a\cos\, z, z) &\doteq u_0(1,z) + \varepsilon\, u_1(1,z) \\ v(1+\varepsilon a\cos\, z, z) &\doteq v_0(1,z) + \varepsilon \left(v_1(1,z) - \frac{1}{2}\cos\, z \right) \\ p(1+\varepsilon a\cos\, z, z) &\doteq p_0(1,z) + \varepsilon\, p_1(1,z) \end{aligned} \tag{42}$$

Next, we submit Fourier's series (21) into Taylor's expansions (19) taken at the wall boundary up to $O(\varepsilon^2)$ approximation, and after exploiting relations (39) we received

$$\begin{aligned} u(1+\varepsilon a\cos\, z, z) &\doteq u_0(1,z) + \varepsilon \cdot C_1 \left(A\sin z + B\cos z \right) \\ v(1+\varepsilon a\cos\, z, z) &\doteq v_0(1,z) + \varepsilon \cdot \left(2C_1 \left(A\cos z - B\sin z \right) - \frac{1}{2}\cos\, z \right) \\ p(1+\varepsilon a\cos\, z, z) &\doteq p_0(1,z) - \varepsilon \cdot 2C_1 \left(A\sin z + B\cos z \right) \end{aligned} \tag{43}$$

The subscripts and coefficients at z are put $s = 1$. Above, $u_0(1,z)$ and $v_0(1,z)$ are known and equal to zero, cf. Eqs.(14).

The boundary conditions should be satisfied separately at each power of ε. Thus we find

$$2C_1 A = \frac{1}{2} \quad \text{and} \quad B = 0 \tag{44}$$

Finally, we get

$$\begin{aligned} u(r,z) &= u_0(r,z) + \varepsilon u_1(r,z) = \frac{1}{2}\,\varepsilon\, \sin z \\ v(r,z) &= v_0(r,z) + \varepsilon v_1(r,z) = \frac{1}{4}\left(1 - r^2\right) + \varepsilon\, \cos z \\ p(r,z) &= p_0(r,z) + \varepsilon p_1(r,z) = -z - \frac{1}{2}\,\varepsilon\, \sin z + C \end{aligned} \tag{45}$$

where C is an arbitrary constant (only gradient of pressure are important in the flow).

6. Conclusions

We have presented a study of an axisymmetrical (it is two-dimensional) flow in the tube with wavy wall in the first order approximation of the parameter ε, which denotes the amplitude of the wall waviness. The wall waviness results in appearance of transversal velocity and variations of pressure. These two phenomena are periodic functions of the longitudinal variable z.

Acknowledgments

This work was partially supported within statutory activities No 3841/E-41/S/2017 of the Ministry of Science and Higher Education of Poland.

References

[1] ROSS R., The pathogenesis of atherosclerosis: a perspective for the 1990s, *Nature* **362** (6423) 801–809 (1993).

[2] SINGH R. B., MENGI S. A., XU Y.-J., ARNEJA A. S., DHALLA N. S., Pathogenesis of atherosclerosis: a multifactorial process. *Experimental & Clinical Cardiology* **7**(1) 40–53 (2002).

[3] MUNSON B. R., Experimental results for oscillating flow in a curved pipe, *The Physics of Fluids* **19**(7) (1975)

[4] LESSEN M. AND HUANG P.-S., Poiseuille flow in a pipe with axially symmetric wavy walls, *Physics of Fluids* **19** (7) 945–950 (1976).

[5] MALEVICH A. E., MITYUSHEV V. V., AND ADLER P. M., Stokes flow through a channel with wavy walls, *Acta Mechanica* **182** (3-4) 151–182 (2006).

[6] MALEVICH A. E., MITYUSHEV V. V., AND ADLER P. M., Couette flow in channels with wavy walls, *Acta Mechanica* **197** (3) 247–283 (2008).

[7] LANDAU L. D., AND LIFSHITZ E. M., *F*luid mechanics, Volume 6 of Course of Theoretical Physics, transl. from the Russian by J. B. Sykes and W. H. Reid, Second edition, Pergamon Press, Oxford - New York 1987.

[8] JAHNKE E. AND EMDE F., *Funktionentafeln mit Formeln und Kurven*, (*Tables of functions with formulae and graphs*), second edition, B. G. Teubner, Leipzig and Berlin 1933.

[9] ABRAMOWITZ M., AND STEGUN I.A., eds., *Handbook of mathematical functions with formulas, graphs, and mathematical tables*, Chapter 9, Applied Mathematics Series. 55, National Bureau of Standards, Washington D.C., New York 1972.

Włodzimierz Bielski, Prof.: Institute of Geophysics, Polish Academy of Sciences, 01-452 Warszawa, ul. Księcia Janusza 64 (*wbielski@igf.edu.pl*).

Ryszard Wojnar, Ph.D.: Institute of Fundamental Technological Research, PAS, 02-106 Warszawa, ul. Pawińskiego 5B (*rwojnar@ippt.pan.pl*).

Analysis of the propagation of the vibration of the rail vehicle while driving with and without locomotive wheel slip

Rafał Burdzik, Łukasz Konieczny, Bogusław Nowak, Jakub Młyńczak, Jacek Rozmus

*Abstract:*Wheel-rail contact properties determine safety of rail vehicle, thus there are very wide scope of papers on this scientific problem. The number of papers focused on aspect of influence of wheel-rail contact on vibration is much less numerous. Thus the paper deals with vibration occurred by the wheel-rail contact while rail vehicle is passing by. The major source of railway rolling noise is the structural vibration of the wheel and rail which is generated by the combination of small-scale undulations on the wheel and rail contact surfaces. The profile irregularity of a railway line is one of the essential vibration sources for vehicles and track. The experiments were conducted on the test track. The track used was composed of two rails lying on wood sleepers joined by railpads. The scope of research contained measurement of axial vibration for the regular drive of train simulator (without locomotive wheel slip) and for the mixed drive process (including locomotive wheel slip). Such the situations can be considered as vibration generated by friction rolling and sliding.

1.Introduction

Wheel-rail contact properties determine safety of rail vehicle, thus there are very wide scope of papers on this scientific problem.The number of papers focused on aspect of influence of wheel-rail contact on vibration is much less numerous. Thus the paper deals with vibration occurred by the wheel-rail contact while rail vehicle is passing by. The major source of railway rolling noise is the structural vibration of the wheel and rail which is generated by the combination of small-scale undulations on the wheel and rail contact surfaces. The profile irregularity of a railway line is one of the essential vibration sources for vehicles and track.When wheelsets suffer variational traction/braking torque or a stick/slip vibration,the dominant vibration frequency is the longitudinal frequency of contact patch.As the frequency of contact patch is a specific value, it produces theperiodicimpact to the wheels as well as to the wear ofwheel rim, this may lead the polygonization of wheels. It is well known that in the contact zone between railway wheel and rail the surfaces must be strong enough to resist the normal (vertical) forces introduced by heavy loads and the dynamic response induced by track and wheel irregularities.The dynamic phenomena accompanying the wheel rolling over a road (rail, track), with lateral slip effects occur in rolling of a wheel and wheelset on a straight track in the case of lateral load and especially on curves. Different curvature radii and rotary oscillations of wheelsets result

in skew rolling and, in turn, in lateral slip oscillation in the contact zone between the wheel and rail. It significantly increases noise, vibrations and wear [1,2,9,10,13,15,16,18].

2. Research object

The research was conducted on experimental rail track at Faculty of Transport (Katowice) Silesian University of Technology. The experimental rail track is composed of two rails lying on wood sleepers joined by rail pads. On the experimental rail track was moving the test truck. The view of the experimental rail track is shown in the figure 1.

Fig.1. Experimental rail truck in Faculty of Transport (Katowice)

The scope of research contained measurement of axial vibration for the regular drive of test truck simulator (without wheel slip) and for the mixed drive process (including wheel slip). Such the situations can be considered as vibration generated by friction rolling and sliding.

3.Measuremnt system

The signals were recorded in digital form with 5kHz sampling frequency. The scheme of measurement system has been depicted in fig. 2. The acceleration of vibration were measured by VIS-311A .sensors. The accelerations were recorded with the use of specially mounting kitfor accelerometers (fig.3). For the data acquisition the analog-digital cardNi 9233was used.. The main technical parameters of the cardNi 9233 are 24 bit resolution, max 25 kHz sampling.

Fig. 2. Scheme of measurement system

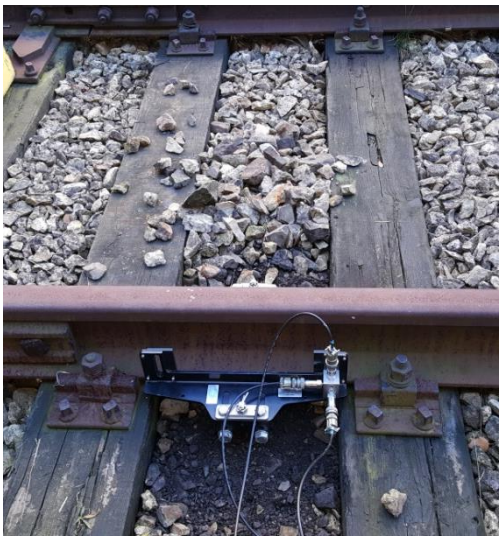

Fig.3. Specially mounting kit for accelerometers

4. Method of analysis

As the result of the research the vibration signals were collected.The digital signals were analysed with MatLab software. The signals are non-stationary thus processing should be conducted simultaneously in the time and frequency domain. The STFT is a simple and effective method widely used in machine diagnostics [3-8,11,12,14,17]. The result of STFT are 3-dimensional spectrum presenting the behavior of signal amplitude in time and frequency domain.

The Short Time Fourier Transform equation:

$$S(b, f) = \int_{-\infty}^{+\infty} x(t) \cdot e^{-j2\pi ft} \cdot w(t-b)dt$$

where: (t-b)- window width

The STFT algorithm is as follows. Frequency analysis is made by Fast Fourier Transformation (FFT) for the following fragment of signal multiply by window function with constant width *w(t-b)=const*. The following fragments are analysed independently. The main disadvantage of this method is constant width of window. For example when using narrow window in time domain we can get good time resolution but in the resolution in frequency domain will be worst. For rectangle window the jump function changes at the beginning and at the end of windows are the source of leak in spectrum. For minimalizing of this kind of effects other windows are often used (for example triangle, Hanning, Hamming) [15,16].

Thus the windows width is treated as a compromise between resolution in time and frequency domain.

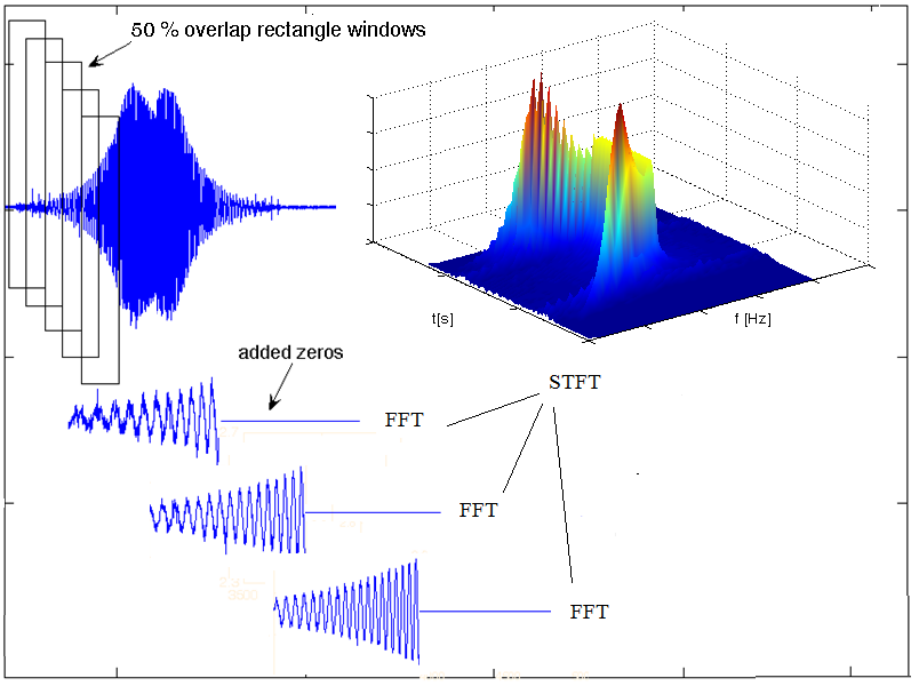

Fig.4. STFT procedure with overlap and with added zeros

To improve the resolution in frequency domain it can be used zero-complementing method. This method is based on adding samples with zero value of amplitude to the original signal to multiple the number of samples of the signal.

The next method of improving the selectivity of STFT method is superposition of windows (each sample is used several times for single FFT process).

The paper presents some result of acceleration of vibration. For the signal processing the STFT with the Hamming window were used. Each window of the signal was 100% elongated by using complement zero method and analysed with FFT process. The windows were superpositioned in 50 % - fig.4.

It can be noticed that using overlappingwindowsand addingzerosincreases theprecision of thedeterminationof individualspectralcomponents ofthe spectrogramSTFT. Zero-paddingdirectly affects thefrequency resolutionspectraof individualcomponents. In contrast,the overlappingwindowsallows to overcome theclear limitspassbetween thesespectra. In the end,appliedoperationsallowed to determinethe smoothedspectrographSTFTespeciallyfor further analysisof a particularfrequency band selection.

5. Results of STFT analysis

The results of STFT procedure for acceleration signals (in three direction x,y,z) measured without wheel slip are presented in figures 5,7,9 and measured without wheel slip are presented in figures 6,8,10.

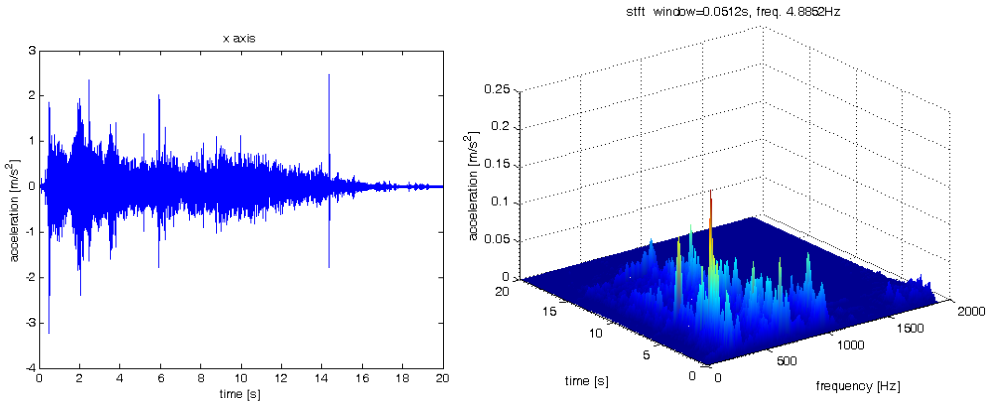

Fig.5. Time realization and STFT result without wheel slip (x - axis)

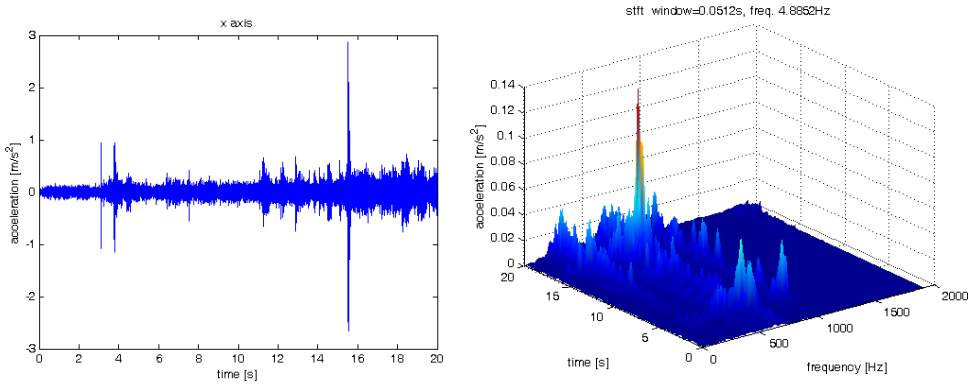

Fig.6. Time realization and STFT result with wheel slip (x - axis)

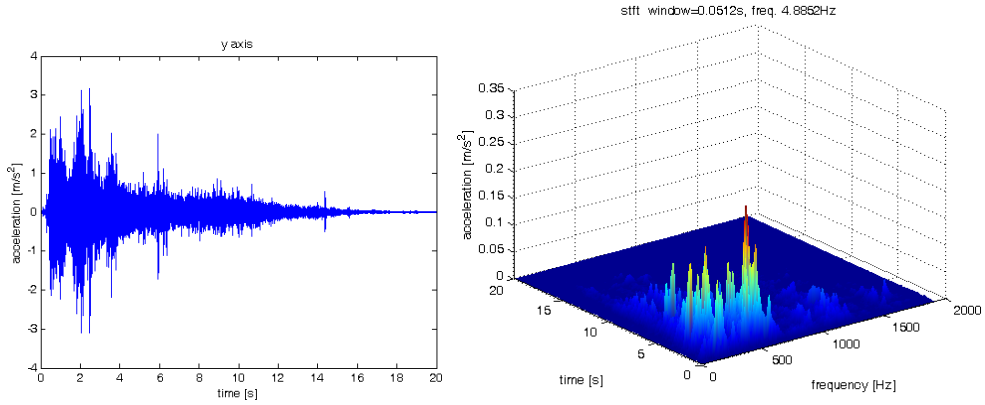

Fig.7. Time realization and STFT result without wheel slip (y - axis)

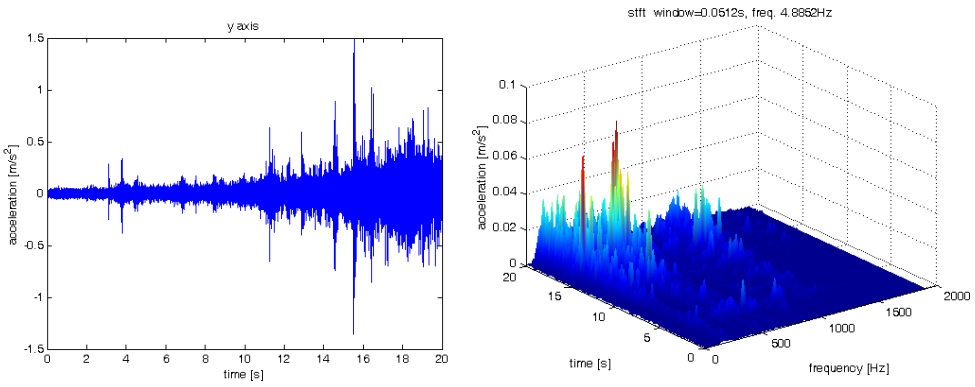

Fig.8. Time realization and STFT result with wheel slip (y - axis)

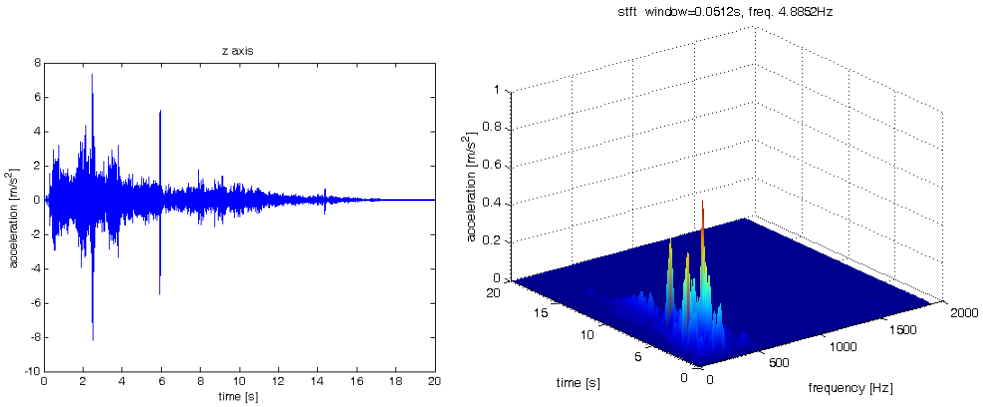

Fig.9. Time realization and STFT result without wheel slip (z - axis)

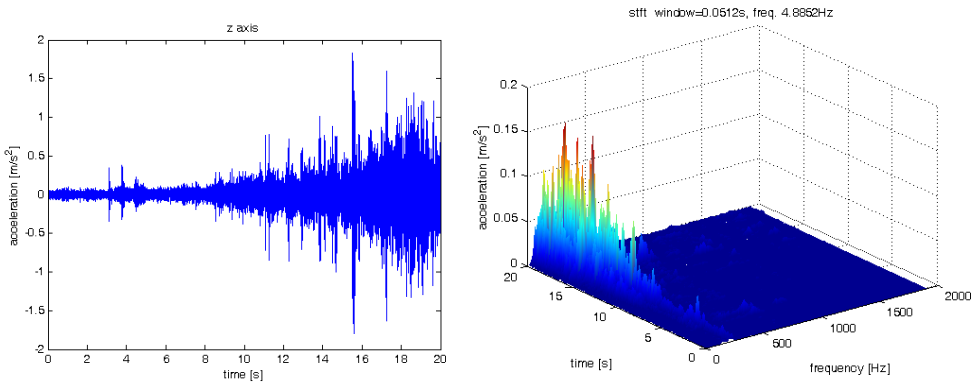

Fig.10. Time realization and STFT result withwheel slip (z - axis)

6. Conclusion

Designated spectra STFT allow simultaneous observation of signal structure in the frequency and time domain. Both for with and without wheel slipcases, there are a broadband impulse in signal and that is associated with the quality of co-operation in the rail wheel contact. In the case of x and y direction, the frequency components dominate in the range up to about 1 kHz while the z direction in the range up to 0.5 kHz. It is difficult to distinguish the state of cooperation on the basis of the evaluation of vibration signals or spectra alone. Further research will focus on proposing estimators (based, for example, on analyzes in selected frequency bands), to classify and distinguish the nature of cooperation in the rail wheel contact.

References

[1] Baek KS, Kyogoku K, Nakahara T. An experimental investigation of transient traction characteristics in rolling–sliding wheel/rail contacts under dry wet conditions. Wear 2007;263 (1):169-179

[2] Bezin Y. , Iwnicki S. D. , Cavallett M., "The Effect of Dynamic Rail Roll on the Wheel-Rail Contact Conditions," Vehicle System Dynamics, Vol. 46, No. 1, 2008, pp. 107-117.

[3] Burdzik, R. Monitoring system of vibration propagation in vehicles and method of analysing vibration modes. J. Mikulski (ed.): TST 2012, CCIS 329, Springer, Heidelberg, 2012, pp. 406-413

[4] Burdzik R., Konieczny Ł. Diagnosing of shock absorbers of car vehicles at changeable pressure in tires. Diagnostyka, Vol. 3, Issue 51, 2009, p. 27-32.

[5] Burdzik R., Folęga P., Konieczny Ł., Młyńczak J.. Concept of engine vibration monitoring system. Solid State Phenomena ; vol. 236 1662-9779)

[6] Burdzik R., Konieczny Ł., Warczek J., Cioch. W. Adapted linear decimation procedures for TFR analysis of non-stationary vibration signals of vehicle suspensions. Mech. Res. Commun. 2017 vol. 82, s. 29-35,

[7] Doleček R., Novak J., Cerny O. Research of conductive currents in traction drive with PMSM. Cybernetic Letters, Vol. 1.1, 2012.

[8] Dąbrowski D., Cioch W.: Neural classifiers of vibroacoustic signals in implementation on programmable devices (FPGA) – comparison, ActaPhysicaPolonica. A, 2011, vol. 119 no. 6–A, s. 946–949.

[9] Iwnicki S. , Handbook of Railway Vehicle Dynamics, Taylor & Francis, Boca Raton, 2006.

[10] Johansson A, Andersson C. Out-of-round railway wheels-a study of wheel polygonalization through simulation of three-dimensional wheel–rail interaction and wear. Vehicle System Dynamics 2005;43(8): 539-559.

[11] Konieczny Ł., Burdzik R., Młyńczak J., Obuchowski J., Kruczek P., Laskowski D. Vibration signal processing for identification of relation between liquid volume and damping properties in hydraulic dampers.Applied Condition Monitoring, vol. 6 2363-698X, Springer International Publishing, 2016, p. 213-228,.

[12] Konieczny Ł., Burdzik R., Warczek J., Czech P., Wojnar G., Młyńczak J.. Determination of the effect of tire stiffness on wheel accelerations by the forced vibration test method. –Journal of Vibroengenering 2015 vol. 17 no. 8, s. 4469-4477

[13] Konowrocki R., Bajer C., Friction rolling with lateral slip in rail vehicles. Journal of theoretical and applied mechanics 47, 2, pp. 275-293, Warsaw 2009

[14] Ragulskis K., Kanapeckas K., Jonušas R., Juzėnas K. Applications of torsional vibrations for vibro-driling operations. Mechanika, Vol.17, Issue 5, 2011, p. 498-502

[15] Soedel W. Vibrations of Shells and Plates. Second Edition, Marcel Dekker Inc., New York, 1993.

[16] Wagner U. , Nonlinear Dynamic Behavior of a Railway Wheelset, Vehicle, System, Dynamics Vol. 47, No. 5, 2009, pp. 627-640.

[17] Warczek J., Burdzik R. ,Peruń G.: The method for identification of damping coefficient of the trucks suspension , Key Engineering Materials Vol. 588 (2014) p 281-289.

[18] Ziqiang X, Shihuib L., Xiaoqing D., Weihua M. Study on longitudinal vibration of wheel/rail contact and its implications for wheel polygnization. Journal of Advances in Vehicle Engineering 3(1)(2017) p.22-28

Rafał Burdzik, Professor: Silesian University of Technology,Faculty of Transport, Department of Automotive Vehicle Construction, Krasinskiego Street 8, 40-019Katowice, Poland (*rafal.burdzik@polsl.pl).*

Łukasz Konieczny, DSc: Silesian University of Technology,Faculty of Transport, Department of Automotive Vehicle Construction, Krasinskiego Street 8, 40-019Katowice, Poland (*lukasz.konieczny@polsl.pl).*

Bogusław Nowak, M. Sc.: DR-TECH Sp. z. o.o., Ks. Ignacego Rembowskiego 11, Imielin 41-407, Poland (*boguslaw@drtech.pl).*

Jakub Młyńczak, PhD: Silesian University of Technology,Faculty of Transport, Krasinskiego Street 8, 40-019Katowice, Poland (*jakub.mlynczak@polsl.pl).*

Jacek Rozmus, M. Sc.: DR-TECH Sp. z. o.o., Ks. Ignacego Rembowskiego 11, Imielin 41-407, Poland (*jacek@drtech.pl).*

Modeling, simulation and control of a pipe inspection mobile robot with an active adaptation system

Michał Ciszewski, Tomasz Buratowski, Mariusz Giergiel

Abstract: In this paper, a tracked inspection mobile robot with an active adaptation system is presented. It can be used for visual inspection of various pipelines. Mathematical modeling of pedipulator mechanisms that allow adaptation of the robot to different shapes and sizes of pipes is described with focus on forward and inverse kinematics methods, implemented in MATLAB software. Application of a custom trajectory planning algorithm for the pedipulators is shown with numerical and graphical validation. Co-simulations of the robot motion, prepared in V-REP and MATLAB software are performed for rough surfaces, horizontal pipes with connections and straight vertical pipes. A prototype of the robot with a model-based control system is tested and laboratory experiments are compared to the simulation results. Different motion scenarios of the robot are shown with focus on adaptation capabilities of the motion unit to work environment.

1. Introduction

Inspection of pipelines has several objectives. After building a new pipeline, it is required by regulations that the pipe must be inspected by a device, equipped with a camera. In addition, inclination of the pipe has to be precisely measured. With the initial inspection, engineering errors can be found and eliminated before exploitation of an industrial facility. Other uses of inspection techniques include periodical checks of pipe condition or documentation of old pipes.

Due to the fact that pipelines are not accessible by operators for direct visual assessment, robotic inspection systems are applied for search of leakages, discontinuities, corrosion, blockages and other defects. The robots have to be designed to move in changeable environment because wide variety of pipelines exist in industry. Horizontal pipelines are relatively easy to inspect, but inclined or vertical pipe segments with junctions can be challenging for designers of robot motion units and control system engineers.

At present, there exist many constructions of pipe inspection robots. The most popular ones are wheeled platforms intended for visual monitoring of horizontal pipelines, equipped with Pan-Tilt-Zoom cameras such as ABE Group products [1]. Tracked motion units are also used in the robots. A manually adjustable chassis for motion in different types of pipelines is present in Inuktun Versatrax 300, which can move in horizontal pipe segments of rectangular or circular cross-section, beyond Ø300 mm [2].

Several robots that operate in vertical pipes are also present in the market. The Inuktun Versatrax Vertical tracked robot features pantograph adjustment mechanism and can be used in vertical pipes with diameters in range Ø200÷300 mm [2]. Another solution is provided by Neovision company that offers a tracked robot, Jetty, intended for inspection and cleaning of vertical ducts [3]. It features six track drive modules, mounted on pantograph mechanisms and provides inspection of circular and rectangular ducts with diameters from Ø400 mm to Ø1300 mm in extended arm version.

In this paper, a tracked inspection robot with an active adaptation mechanism is presented with focus on modeling, simulations and control system that can serve as a versatile inspection device. The robot is able to move in pipes and ducts with round and rectangular cross-section that are horizontal or vertical, with bends and interconnections.

2. Mechanical structure of the robot

The design of the robot adaptable driving mechanism is based on two pedipulators that control the pose of track drive modules. Virtual mechanical model of the robot is shown in Fig. 1. Each pedipulator is a subsystem, attached to the body (2) that consists of two actuated rings (3, 4), front and rear arm (5, 6) and a track drive module (1). The rings, with an axis of rotation in the center of the robot body are driven by servomotors, from which torque is transferred by sprockets of internal meshing gear transmissions. Front and rear arms are mounted to the rings by revolute joints. Other sides of the arms are attached to the track drive module by rotary joints. The rear arm is equipped with an additional servomotor that sets orientation of the track module with respect to the arm.

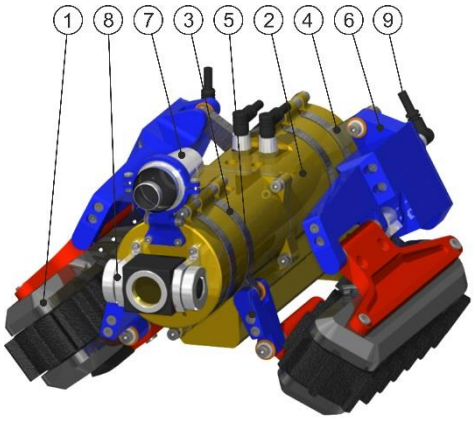

Figure 1. Robot model: 1 – track drive module; 2 – robot body; 3 – front rotating ring; 4 – rear rotating ring; 5 – front arm; 6 – rear arm; 7 – camera; 8 – light; 9 – waterproof connector

By assembling two pedipulator modules, motion unit of the robot can adapt to different types of pipes and thus realize dexterous manipulations, resembling capabilities of human legs. The robot is

equipped with eight drives in total, from which six servomotors are responsible for setting position and orientation of two independently motorized track drive modules.

The robot model was created in Autodesk Inventor software. In the CAD 3D model creation process, optimization of construction, drive selection and initial validation of operational capabilities were conducted with the assumptions of maximum versatility, compactness and watertightness.

3. Mathematical modeling of the robot

Mathematical modeling of the robot was divided into three main sections: kinematic motion model for even surfaces and parallelly oriented tracks, described in [4], dynamic model of the robot motion in water that was shown in [5] and kinematic modeling of pedipulator motion necessary for adaptation of the robot chassis to changeable work environment. The last modeling task, presented in this paper, involves unconventional modeling approach focused on control of robot servomotors to attain desired poses of two track drive modules. Inverse kinematics solution is implemented iteratively in an original algorithm for calculation of pedipulators transformation trajectories.

The pedipulator mechanism can be treated as planar, due to the fact that the rotational joints axes are parallel. One pedipulator consists of six rotary joints of which three are actuated (see Fig. 2). The mechanism was divided into two planar manipulators with two and three degrees of freedom that represent front and rear parts of the pedipulator to facilitate modeling tasks.

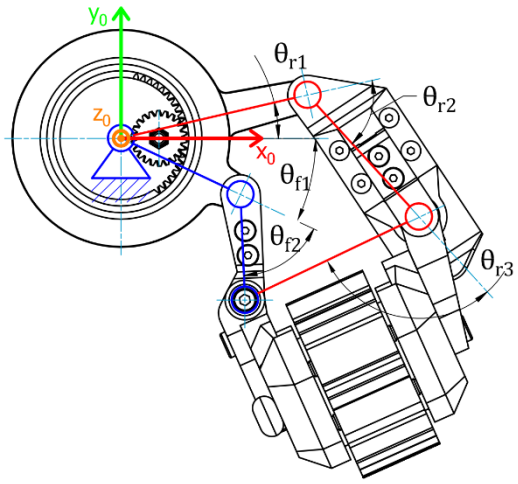

Figure 2. Kinematic model of pedipulator: θ_{r1}-rear ring (5) rotation angle; θ_{f1}-front ring (2) rotation angle; θ_{r3} - rear arm rotation angle with respect to track drive module (1); θ_{r2}, θ_{f2} – unactuated joints rotation angles.

Forward kinematic equations for the pedipulators were formulated for 2-DOF (front) and 3-DOF (rear) manipulators extracted from the structure with usage of Denavit-Hartenberg notation. Additionally, it was assumed that the manipulators have to move their end-effectors concurrently to fulfil constraints of the closed kinematic chain. It is realized by equating *x* and *y* positions of both D-H transformation matrices [6].

Inverse kinematics task is the most important calculation procedure for control of the pedipulators. Analytical methods cannot be simply used for the tasks due to complex mechanical structure, existence of redundancies and kinematic constraints that arise in these closed kinematic chains. Numerical differential kinematics with usage of manipulator Jacobian is an effective approach for calculation of inverse kinematics, but for the closed structure, additional conditions had to be applied.

Calculation of manipulator Jacobian matrices was done on the basis of D-H transformation matrices, with use of a method shown in [7]. Next, a numerical algorithm was used that on the basis of Virtual Work principle, iteratively minimizes error between initial and goal poses of the end-effector. This method, whilst valid for dynamic modeling is useful in general inverse kinematics [8]. In Fig. 3, a scheme of the 3-DOF (rear) manipulator, extracted from the pedipulator structure is presented.

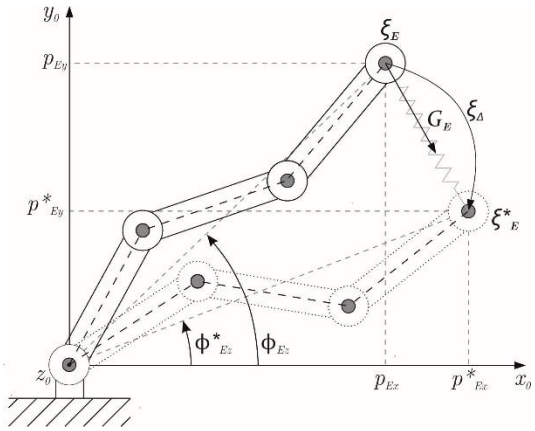

Figure 3. Scheme of the 3-DOF manipulator inverse kinematics – numerical solution.
ξ_Δ- end-effector pose difference, $\xi_E(p_{Ex}, p_{Ey}, \phi_{Ez})$ – end-effector current pose
ξ^*_E $(p^*_{Ex}, p^*_{Ey}, \phi^*_{Ez})$ - end-effector desired pose.

Principle of this method relies on a so called "special spring" between current and desired pose. This spring is a set of generalized external forces G_E that are able to change position and orientation of the end-effector towards the desired pose. It is proportional to the difference between poses, where proportionality is denoted by a constant γ_P as stated in Eq. 1. Current pose at a given calculation step

$\xi_E\langle k\rangle$, is computed with forward kinematics (Eq. 2), where $q\langle k\rangle$ represents current estimate of inverse kinematics solution and $T_{E,0}$ is a transformation matrix from end-effector to base coordinate system.

$$G_E \propto \Delta(\xi_E, \xi_E^*) \rightarrow G_E = \gamma_P \cdot \Delta(\xi_E, \xi_E^*), \quad (1)$$

$$\xi_E\langle k\rangle = T_{E,0}(q\langle k\rangle), \quad (2)$$

External forces Q that act on the end-effector can be mapped to joint forces and torques for each calculation step *k* with usage of Eq. 3 by application of manipulator Jacobian transpose $J(q\langle k\rangle)^T$. The mapping is never singular as it can be in the case of velocity kinematics using Jacobian approach, therefore it can be efficiently used for numerical solution of complex inverse kinematics problems [8].

$$Q\langle k\rangle = J(q\langle k\rangle)^T \cdot G_E\langle k\rangle \quad (3)$$

By assumption that the virtual robot does not have joint motors, but only viscous dampers that impose proportionality of applied forces to joint velocity, it is possible to express generalized joint velocity by Eq. 4 and for a discrete time-update of joint coordinates by Eq. 5, where B is a joint damping coefficient and α_C is a gain selected according to desired calculation convergence speed.

$$\dot{q}\langle k\rangle = Q\langle k\rangle / B, \quad (4)$$

$$q\langle k+1\rangle = \alpha_C \cdot \dot{q}\langle k\rangle + q\langle k\rangle, \quad (5)$$

The calculations are performed iteratively until the magnitudes of generalized external forces G_E that actuate the manipulator to desired pose are sufficiently small. With usage of this method, numerical determination of inverse kinematics can be executed. The analyzed robot has less than 6-DOF, therefore a mask vector M has to be applied that specifies controllable degrees of freedom. In this case it is used to select $p_{Ex}, p_{Ey}, \phi_{Ez}$ coordinates on a planar.

$$Q\langle k\rangle = J(q\langle k\rangle)^T \cdot diag(M) \cdot G_E\langle k\rangle. \quad (6)$$

Finally, after substitution of Eq. 4, 5, 6, discrete update of joint coordinates for an under-actuated robot is given by Eq. 7.

$$q\langle k+1\rangle = \alpha_C \cdot \frac{J(q\langle k\rangle)^T \cdot diag(M) \cdot G_E\langle k\rangle}{B} + q\langle k\rangle. \quad (7)$$

The method specified above is used for numerical inverse kinematics calculations of the 3-DOF and also 2-DOF manipulators, subdivided from the robot pedipulator structure. It is integrated as a part of the calculation procedure, described in the trajectory calculation algorithm and plays an important role in control system of the robot.

4. Trajectory calculation algorithm for pedipulators transformation

For trajectory planning, a dedicated algorithm was developed that is composed of different methods utilized iteratively, numerical inverse kinematics based on Jacobian transpose and pseudo-inverse, analytical inverse kinematics, forward kinematics, sets of geometric conditions and custom rules.

Pedipulator poses dedicated for particular pipe sizes were determined from the 3D CAD model of the robot. With usage of this data, all angular positions of pedipulators joints were saved and used as initial and final poses for trajectory generation. The second step was to generate 5^{th} order polynomial interpolated joint space trajectories for the front manipulator between initial and final poses. Next, inverse kinematics problem was solved with usage of Jacobian transpose for the rear manipulator to match its position with end-effector of the front manipulator. In case of this pipe inspection robot, calculation of the pedipulator analytical inverse kinematics problem gives 8 solutions for the entire structure. Therefore, additional conditions were used for the planar manipulators with limitation of joint rotation angles. The final step was to eliminate oscillations of the manipulator, caused by transition through singular positions. Finally, joint trajectories of both 2-DOF and 3-DOF planar manipulators were merged and only actuated joints were selected to perform reconfiguration of the pedipulators. The calculations were performed in MATLAB software with addition of the Robotics Toolbox [8]. As a result, smooth trajectories for transformation of both robot pedipulators were obtained. Due to the fact that each pedipulator mechanism is a closed kinematics chain of specific structure, it is sufficient to use three motors to set particular pose of one track drive module.

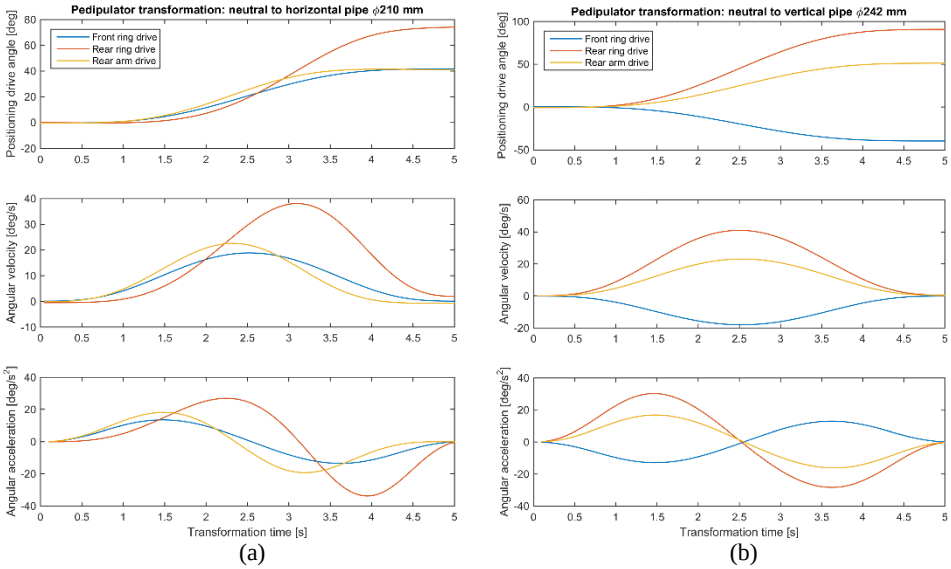

Figure 4. Pedipulator transformations from the neutral pose – drives positions, velocities and accelerations: (a) to a Ø210 mm horizontal pipe; (b) to a Ø242 mm vertical pipe.

On the basis of the previously presented mathematical models, implemented in the original algorithm, joint trajectories for different transformations were obtained. Transformation time was assumed to be 5 seconds for all cases to ensure easier comparison of the results. The results for transformation from neutral pose to horizontal pipes with diameter Ø210 mm and vertical pipe with diameter Ø242 mm is shown in Fig. 4. It can be noted that results of the transformations are smooth due to utilization of 5^{th} order polynomial interpolation and application of custom rules for trajectory generation task. The presented approach is effective for solving inverse kinematics task for the closed kinematics chain of the robot.

Graphical validation of the trajectories on a pedipulator model is shown in Fig. 6. All characteristic points were marked with cylinders. Traces of trajectories of all joints and track contact points are visualized in range from initial to final pose. The visualization was prepared in MATLAB software.

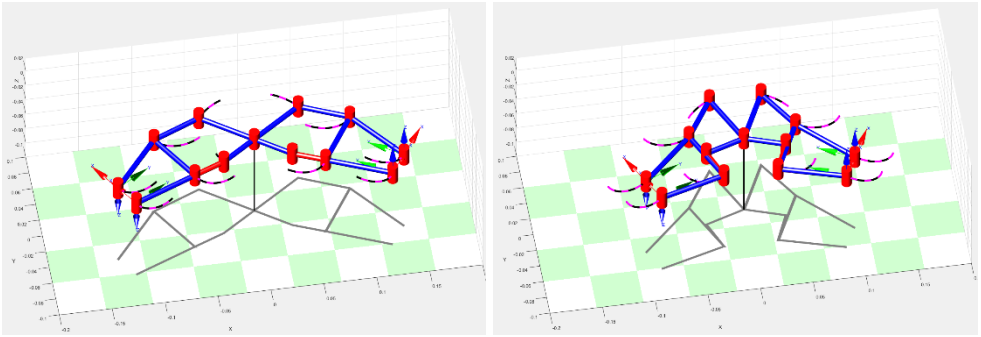

(a) (b)

Figure 5. Pedipulators transformation trajectory from the neutral pose to a Ø210 mm horizontal pipe: (a) initial pose; (b) final pose.

5. Co-simulation is MATLAB and V-REP software

Co-simulations of the robot control in V-REP and MATLAB environments were prepared to analyze and verify mathematical models of the robot, especially trajectory calculation for adaptation of pedipulators to different work environments. V-REP is a multi purpose robotic simulation software that allows integration of control algorithms or connection with external applications to run the models. Robot model creation process was described in [6]. The co-simulation of robot model required creation of a MATLAB/Simulik schematic diagram that allowed integration of the previously described trajectory planning algorithm with hardware support of a physical joystick used for control of the robot model, as well as synchronous communication with the V-REP simulator.

The simulations involved tests in horizontal pipes with different diameters and obstructions such as bends and reducers. In Fig. 6a, the robot after negotiation of a bend is shown. Reconfiguration of the pedipulators is controlled with usage of the control algorithm developed in MATLAB, whereas, track

drives velocities are adjusted in real time by the operator by the hardware joystick. In Fig. 6b, the robot is depicted in a vertical pipe run. In this case, the simulation shows ability of the pedipulators to extend the track drives and exert clamp force, sufficient to move vertically. Several attempts to negotiate a pipe segment with smooth diameter change was made, but due to limitations of the robot model in rubber track contact with the pipe, it was not always possible to safely guide the robot through. To check whether the prototype would be capable of driving on rough surfaces, a special simulation environment was prepared. The simulation was stable for motion on a randomly generated rough terrain, as depicted in Fig. 7a.

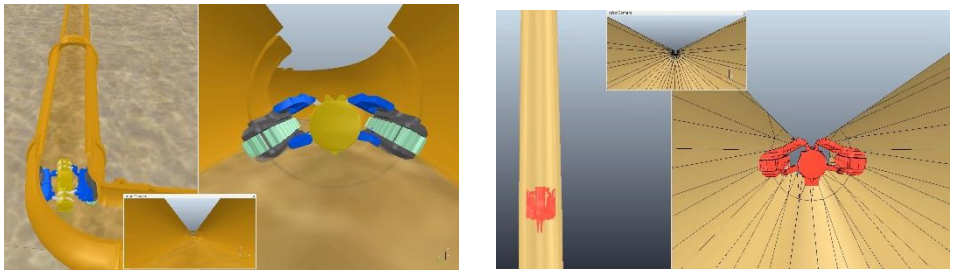

(a) (b)

Figure 6. Simulation of the robot motion: (a) horizontal a Ø315 mm pipe; (b) vertical Ø242 mm pipe.

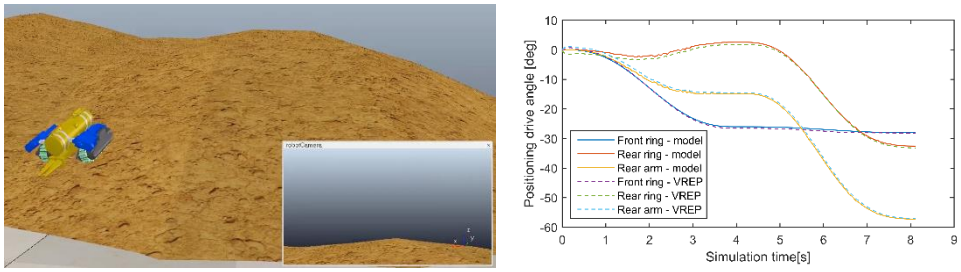

(a) (b)

Figure 7. Simulation of the robot motion on rough terrain: (a) simulation environment; (b) drive position comparison during pedipulators transformation.

Operation of the robot model in the V-REP environment was compared to the theoretical pedipulators trajectory planning results obtained in MATLAB. In Fig. 7b, comparison of drive positions for pedipulator transformation phase is shown. The absolute position error between those two models do not exceed 1.5 degrees. It should be noted that the theoretical results obtained in MATLAB do not take into consideration gravitational dependencies and elasticity of joints. However, in the V-REP model, the Bullet simulation engine, used for the simulations, adds some elasticity and damping to revolute joints. Nevertheless, the results can be viewed as valid, since very precise positioning is not crucial for proper operation of the prototype.

6. Prototype of the pipe inspection robot

A prototype of the tracked mobile robot for pipeline inspection is shown in Fig. 8. The robot subsystems were integrated with a control system, designed for compatibility with the trajectory planning algorithm, remote operation by a joystick control and transmission of video signal to operator by a tether cable. Prototype tests were conducted in different environments. The robot in a horizontal pipe is shown in Fig. 8a. Transformation of pedipulators was successfully verified in a pipe reducer, based on trajectory obtained from the trajectory planning algorithm.

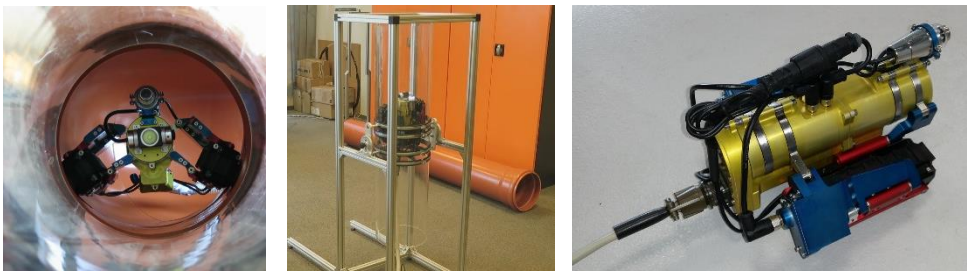

(a) (b) (c)

Figure 8. Prototype of the robot: (a) transformation in a horizontal Ø315 to Ø242 mm pipe; (b) vertical Ø242 mm pipe; (c) horizontal surface.

Operation of the prototype in a vertical pipe segment is depicted in Fig. 8b. The tests proved that the robot can operate in dry and wet vertical pipes. Operation of the prototype on horizontal surfaces with tracks oriented parallelly was also checked (see Fig. 8c) along with motion on inclined surfaces and negotiation of obstacles.

7. Conclusions

Application of mathematical tools and computer simulations proved to be effective and provided initial testing platform of control system designed for the robot's pedipulators. The modeling approach with use of differential kinematics and iterative solution of inverse kinematics problem was integrated in a trajectory planning algorithm that enables to smoothly transform of the robot's motion unit for operation in different types of pipelines. The simulations performed in V-REP and MATLAB provided valuable resources for control system of the robot prototype with tuning and optimization of the original pedipulator trajectory calculation algorithm. A prototype of the pipe inspection robot was checked and previously simulated functionalities were verified during laboratory experiments.

The future works would include elaboration of an active adaptation system with regulation of extension forces, based on measurements from current drain sensors for the servomotors and the tracks. This system would provide improved safety during motion in vertical pipelines with sediments, obstructions and other disturbances of pipe geometry by automatic adjustment of clamp force.

References

[1] ABE Group. Kamery do inspekcji rurociągów i kanalizacji. 2017. [Online]. Available: http://abe-group.eu/kamery-inspekcyjne/. [Accessed: 26-Sep-2017]

[2] Inuktun, Inuktun | The Multi-Mission Modular Robotics Company, 2017. [Online]. Available: http://inuktun.com/en/products/. [Accessed: 26-Sep-2017]

[3] NEOVISION s.r.o. Jetty, Cleaning and inspectional robot for air-induction ducting. [Online]. Available: http://www.neovision.cz/sols/jetty.html. [Accessed: 31-Mar-2016]

[4] Ciszewski, M., Buratowski, T., Giergiel, M., Kurc, K., Malka. P. Mobile inspection robot. *Applied Mechanics and Materials*, 319 (2013), 385–392.

[5] Ciszewski, M., Buratowski, T., Giergiel, M., Malka, P., Kurc, K., Virtual Prototyping, Design and Analysis of an in-Pipe Inspection Mobile Robot. *Journal of Theoretical and Applied Mechanics 52*, 2 (2014), 417–429.

[6] Ciszewski, M., Mitka, Ł., Buratowski, T., Giergiel, M. Modeling and simulation of a tracked mobile inspection robot in MATLAB and V-REP software. *Postępy robotyki*, vol. 1, 195 (2016), Prace Naukowe Politechniki Warszawskiej. Elektronika, Warszawa, 135–144.

[7] Wu C. H., Young, K. Y., An efficient solution of a differential inverse kinematics problem for wrist-partitioned robots. *IEEE Transactions on Robotics and Automation* 6, 1 (1990), 117–123.

[8] Corke, P. *Robotics, Vision and Control: Fundamental Algorithms in MATLAB*. Springer Science & Business Media, 2011

Michał Ciszewski, (Ph.D. student): AGH University of Science and Technology, Faculty of Mechanical Engineering and Robotics, Department of Robotics and Mechatronics, Al. Mickiewicza 30, 30-059 Kraków, Poland (*mcisz@agh.edu.pl*).

Tomasz Buratowski, (DSc): AGH University of Science and Technology, Faculty of Mechanical Engineering and Robotics, Department of Robotics and Mechatronics, Al. Mickiewicza 30, 30-059 Kraków, Poland (*tburatow@agh.edu.pl*).

Mariusz Giergiel, (Professor): AGH University of Science and Technology, Faculty of Mechanical Engineering and Robotics, Department of Robotics and Mechatronics, Al. Mickiewicza 30, 30-059 Kraków, Poland (*giergiel@agh.edu.pl*). "The author gave a presentation of this paper during one of the conference sessions."

Effect of anisotropy on surface wave attenuation through fluid medium: a comparison between Rayleigh and Love type waves

Nathan Paul Craig, Harriet Grigg

Abstract: Surface wave propagation in anisotropic materials is common for biosensor based applications, in which contact between the device and a fluid layer is required. The attenuation of the propagating wave due to the fluid layer is different depending on the choice of the wave, due to the generation of pressure waves by out of plane displacements. In the isotropic cases, the Rayleigh wave type experiences greater attenuation than the multi-layer Love wave type which only has a transverse displacement. In the case of an anisotropic wave the displacement axis no longer lines up with the direction of propagation. A generalised anisotropic Love wave propagating in a multi-layered structure comprised of anisotropic materials will no longer have a zero valued out of plane displacement. The effect of this anisotropy on Love waves is investigated by numerical analysis and compared to the Rayleigh wave type. The results show an increase in attenuation in generalised Love wave solutions for cases of interest to the application mentioned, for which wave displacements are presented.

1. Introduction

Surface acoustic wave (SAW) propagation through anisotropic structures is of interest for applications such as biosensors, in which contact between the devices and a fluid layer is a requirement [1]. The fluid layer can cause leakage of energy out of the system by the generation of pressure waves, by out of plane displacements, leading to leaky type wave existence. Understanding the effect of anisotropy on the waveforms is necessary for the mitigation of the effects of fluid loss in the design.

A number of different SAW types exist in a multi-layered structure, this paper compares the effect of the Rayleigh and Love wave types on a fluid, in which the Love wave has the most appealing properties. In the isotropic case the Rayleigh wave may exists in a half space; traveling along the surface as a combination of displacements in the propagation and out of plane directions in an elliptical motion which decays into the bulk of the material. Many generalised Rayleigh wave types exist in anisotropic half spaces [2], they also may exist in multi-layered mediums [3] and at material interfaces [4]. In addition another type of wave that may exist in a half space is the leaky wave [5], the fluid-elastic waves which will be studied are a type of leaky wave. The Love wave is a wave type which only existences in a multi-layered medium. It is allowed to exist when the velocity is greater than the shear bulk velocity

of the layer but less than the shear bulk of the substrate [6]. In the isotropic case the Love wave travels along the surface with only a transverse displacement and decays into the bulk of the substrate.

Traditionally, Love waves are perceived to be more suitable to the application of biosensors than Rayleigh waves, which leak energy through fluid coupling. A majority of the materials of interest for biosensors cannot be assumed as isotropic and so the anisotropic effects of materials must also be considered; for these cases the quasi Love waves which now exists, will no longer be purely transverse. The purpose of this study is to investigate the effect of material anisotropy on Love waves in contact with a fluid medium and compare to the Rayleigh wave type. The contributions of the anisotropy of the layer and substrate to the overall waveform will be considered, which are dependent on the material properties and cut rotation. These inputs effect the propagation direction, decay depth and out of plane displacements which can contribute to the energy leakage by fluid or various acoustic sinks.

The anisotropy causes rotational variation of solutions around a crystal cut which is of interest in circular geometry biosensors which take advantage of degenerate modes [7]. Quartz on silicon configuration leads to a material combination which is compatible for propagating non-leaky Love waves, due to the velocity condition and exists even in the non-fluid case. Though these waves can exist in a pure mechanical case for high symmetry directions, does not imply that these waves have the desired properties of the isotropic Love wave. Quartz in the cut of interest has a six fold rotation axis whereas silicon has a four fold rotation axis in the highly symmetric directions taken as common cuts. Hexagonal crystals are assumed to have an isotropic transverse plane due to the hexagonal shape, this is similar to quartz but without the additional stiffness coefficients that deforms this plane. Therefore, if a cut exists that has low rotational variation in a cubic crystal it will most likely be in the form of a deformed hexagonal plane, not only will this cut have desirable properties for circular based biosensors but may also have a six fold rotation axis similar to quartz. In this study the waveforms in these anisotropic low variation cuts will be compared to the highly symmetric cases.

2. Mathematical formulation

The Stroh formulation [8] is capable of solving, through the use of numerical methods, wave propagating in anisotropic half spaces. Making some extensions to this formulation will allow the study of leaky waveforms in a multi-layered medium. Starting with the 3-dimensional linear homogenous wave equation below:

$$C_{ijkl}\frac{\partial^2 u_l}{\partial x_j \partial x_k} = \rho\frac{\partial^2 u_i}{\partial t^2}. \tag{1}$$

The solution using the Stroh formulation with attenuation is assumed in the following form:

$$u_i = A_i e^{(\alpha - ik)\left[(m_j - pn_j)x_j - vt\right]}, \tag{2}$$

where summation is assumed over repeating indices i, j, k, l = 1 to 3 and with wave propagation set in the $-km_jx_j$ direction. Substituting the solution and rearranging results into the eigenvalue problem:

$$\left[C_{ijkl}\left(m_j + pn_j\right)\left(m_k + pn_k\right) - \rho v^2 \delta_{il}\right]A_l = 0. \tag{3}$$

As a result of the definition of velocity (v) as:

$$v = \frac{\omega}{(k - i\alpha)}, \tag{4}$$

the problem is a function of velocity alone instead of attenuation (α), wave number (k) and frequency (ω) reducing the numerical computation when searching over lines of constant velocity.

The solutions to the eigenvalue problem are the partial waves which are found through the multiplier p in which the summation forms the wave solutions for each layer shown below:

$$u_i = \sum_{r=1}^{6} B_r A_i^{(r)} \, e^{(\alpha i - k)\left[\left(m_j - p^{(r)} n_j\right)x_j - vt\right]}. \tag{5}$$

For half spaces only three partial waves are required in the summation for the boundary conditions; therefore the three which are discarded are the solutions that yield exponential increase into the bulk of the material, which is not a characteristic of surface waves. The solutions can now be used to form a boundary condition determinant where numerically zero values are waves which may exist. The boundary conditions used in this investigation are the continuity of tractions (t) in the following form:

$$t_i = C_{ijkl} \frac{\partial u_l}{\partial x_k} n_j, \tag{6}$$

and displacements at material boundaries. For all the cases presented in this paper the fluid interface is fixed at $n_j x_j = 0$ and the elastic interface is fixed at $n_j x_j = 1$.

2.1. Linearised fluid wave equation

Assuming a small signal approximation on equations of state [9] the mass continuity equation and 3-dimensional linearised fluid equation of motion can be written in the following form:

$$\frac{1}{{v_0}^2} \frac{\partial P}{\partial t} + \rho_0 \frac{\partial^2 u_i}{\partial x_i \partial t} = 0, \tag{7}$$

$$-\frac{\partial P}{\partial x_i} + \mu_{ijkl} \frac{\partial^3 u_l}{\partial x_j \partial x_k \partial t} = \rho_0 \frac{\partial^2 u_i}{\partial t^2}. \tag{8}$$

Assuming a solution for both the pressure (P) and displacement (u_i) in the form (2) a coupled eigenvalue problem can be formulated. The 1-dimensional pressure amplitude can be arranged out to get the 3-dimensional eigenvalue problem for the displacement amplitudes as follows:

$$\left[(\alpha - ik)v \cdot \mu_{ijkl}\left(m_j + pn_j\right)\left(m_k + pn_k\right) + \left(m_i + pn_i\right)^2 \rho_0 {v_0}^2 \delta_{il} - \rho_0 v^2 \delta_{il}\right]A_l = 0. \tag{9}$$

The form of the eigenvalue problem imposes a pressure wave that couples to the out of plane displacements through the partial solutions. The wavelength and propagation direction of this pressure wave is dependent on k and α. The boundary conditions along the interface of the elastic surface and fluid half space may be formed using the displacements and fluid tractions given by the following:

$$t_i = -P\delta_{ij}n_j + \mu_{ijkl}\frac{\partial^2 u_l}{\partial x_k \partial t}n_j. \tag{10}$$

2.2. Numerical methods

Numerical methods are required to obtain a solution to both the individual eigenvalue problems of each material and the boundary condition determinant. A complex phase tracking algorithm is developed for fast tracking over lines of constant complex phase (see fig. 1) by making use of ridge tracking methods [10]. Using this method, a close approximation for all complex minimums can be made within a set boundary, to be followed by a secondary search using any preferred numerical method. The number of partial wave solutions is given by the characteristic equation of (3), whereas the boundary condition determinant may allow infinite solutions depending on the geometry.

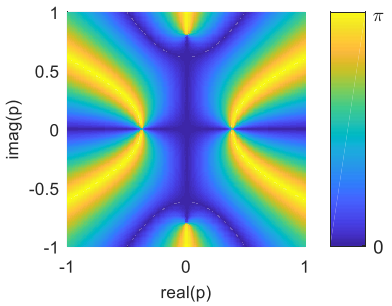

Figure 1. The partial wave determinant of an isotropic material, color map denotes absolute value of the complex phase of the determinant.

3. Results and discussion

Two cases of interest are studied in this paper, the first is detailed in section 3.2, the isotropic and cubic combinations in which the anisotropy can be scaled using a factor. The second, discussed in section 3.3, is the study of the particular case of trigonal quartz on cubic silicon in which the effect of conflicting anisotropies is of interest, for material properties see [11]. The fluid used for all the cases presented is water [12] at a constant temperature of 25°C. For both cases the cut of low variation of cubic materials is used, which is discussed in the following section.

3.1. Rotational variation of silicon

A low variation cut can be found by inspecting the longitudinal bulk wave variation around all cuts of a crystal, in this case silicon (see fig. 2). The rotations are preformed around the Stroh vectors $\boldsymbol{m}$ and $\boldsymbol{n}$ and the third direction at the tangent to this plane denoted as $\boldsymbol{p}$; the angles are given in this order [$\boldsymbol{m}$ $\boldsymbol{p}$ $\boldsymbol{n}$] angles are denoted [φ θ ψ]. The cut which will be averaged over is in the $\boldsymbol{m}$-$\boldsymbol{p}$ plane, to ensure that the low variation cut is suitable for Love waves which are only a transverse displacement. Great circle rotations can be applied directly to the stiffness tensors [13] to allow independent rotations between layers or to the Stroh vectors which rotates the whole geometry.

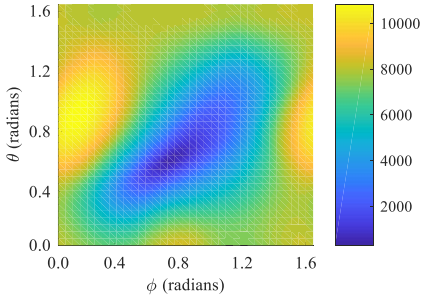

Figure 2. Presented is the surface of rotation variation of silicon bulk waves in the $\boldsymbol{m}$-$\boldsymbol{p}$ plane. Colour map denotes cut variation.

The low variation cut is given by the minimum of fig. 2 which is the cut [0.763 0.628 ψ]. The bulk waves are compared to the original [0 0 ψ] symmetric cut of silicon (see fig. 3), which corresponds to the crystal cut in miller indices [001]. It is clear that six peaks are now present in the new cut and can be rotated in line with the Quartz six fold rotation. The combination between these materials is still compatible for Love wave propagation in this new cut.

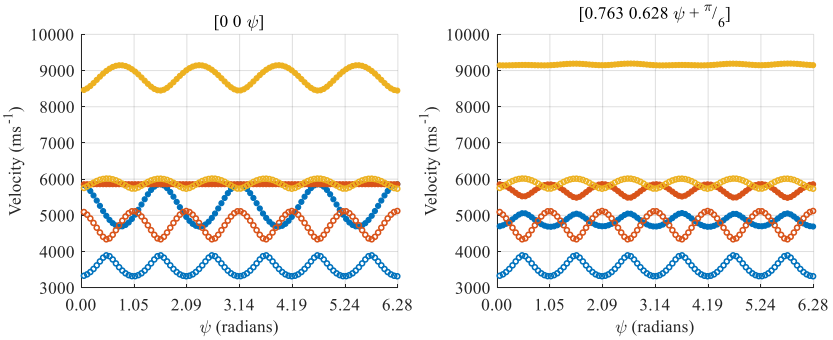

Figure 3. Bulk waves of quartz and silicon in the $\boldsymbol{m}$-$\boldsymbol{p}$ plane for the silicon cuts [0 0 ψ] and [0.763 0.628 $\psi + \frac{\pi}{6}$] (solid points), both compared to quartz cut [0 0 ψ] (unfilled points).

Additionally, a second compatible region for cuts above the second quartz bulk wave, between the first and second bulk waves of silicon, is now possible using the low variation cut. The supersonic Rayleigh and Love types in this region, will have additional bulk wave contributions leading to leaky wave types into the bulk of the substrate. The leakage is not desirable and so the investigation is restricted to the first compatible region between the first bulk waves of quartz and silicon.

3.2. Effect of anisotropic contributions between layer and substrate

The effect of the anisotropies of each layer on the overall structure of the Love wave and the coupling to the fluid is studied, making use of the low variation cut from the previous section. The materials under investigation are cubic copper [14] on cubic silicon, due to the high compatibility for Love wave propagation under transformations of the anisotropic factor [11].

Setting the anisotropic factors of both layers to $A = 1$ reduces the problem to a layered isotropic case, for which both Love waves and Rayleigh type waves exist (see fig. 4). The fluid layer shows greater coupling to the Rayleigh wave due to the non-zero out of plane displacement (in the $\boldsymbol{n} \cdot \boldsymbol{x}$ given by x_3). Note the numerically zero displacements in the x_1 and x_3 directions for the Love wave.

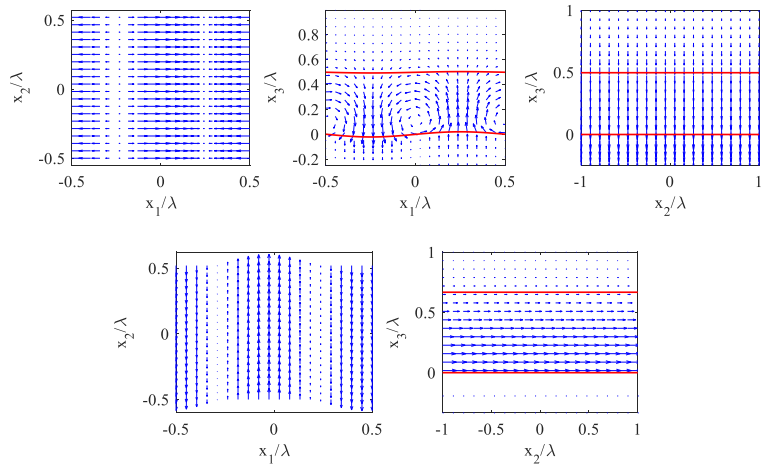

Figure 4. For the isotropic case, on the top Rayleigh type wave displacements ($k = 3.12$ and $\alpha = -0.068$) and on the bottom are the Love wave displacements ($k = 4.19$ and $\alpha = 0$) all normalised to the wave length, red lines are displacements along the boundaries.

The anisotropic factor of the substrate is increased to $A_{sub} = 1.5$, and rotational data for the first Rayleigh mode (see fig. 5) and Love mode (see fig. 6) is computed for the substrate cuts [0 0 ψ] and low variation cut [0.763 0.628 ψ].

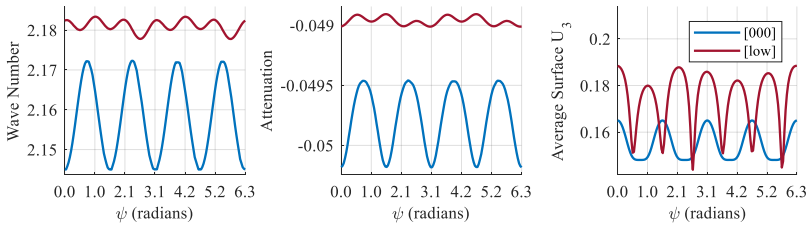

Figure 5. Isotropic on cubic case, the Rayleigh wave solutions for substrate cut [00 ψ] and [0.763 0.628 ψ]. From left to right are the wave number, attenuation and average surface u_3 displacement plots at a velocity of 2000ms^{-1}.

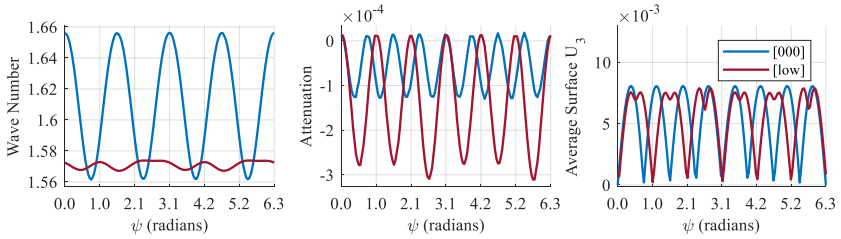

Figure 6. Isotropic on cubic case, the Love wave solutions for substrate cut [00 ψ] and [0.763 0.628 ψ]. From left to right are the wave number, attenuation and average surface u_3 displacement plots at a velocity of 2000ms^{-1}.

The wave number takes on the structure of the substrate for both types of wave indicating that a significant portion of the wave exists in the substrate. The attenuation value is a combination of the leakiness due to anisotropy and the fluid coupling. The Love wave attenuation for the low variation cut is slightly larger than the high symmetry cut, with similar out of plane displacements.

The effect of an anisotropic layer on rotational variation will be considered in the next section but first the displacements are presented for the case of both materials with an anisotropic factor of $A = 1.5$. For the layer cut [0.763 0.628 ψ] the first Rayleigh type and Love modes are presented for substrate cut [0 0 ψ] in fig. 7 and substrate cut [0.763 0.628 ψ] in fig. 8.

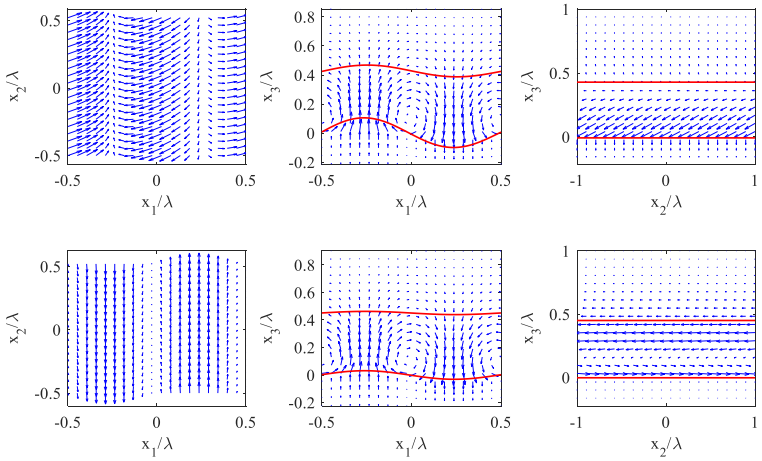

Figure 7. For layer cut $[0.763\ 0.628\ \psi]$ on substrate cut $[0\ 0\ \psi]$ the displacements. On the top the Rayleigh mode ($k = 2.68, \alpha = -0.057$) and on the bottom the Love mode ($k = 2.83, \alpha = -0.001$) at a velocity of $2000ms^{-1}$. Red lines trace boundary displacements.

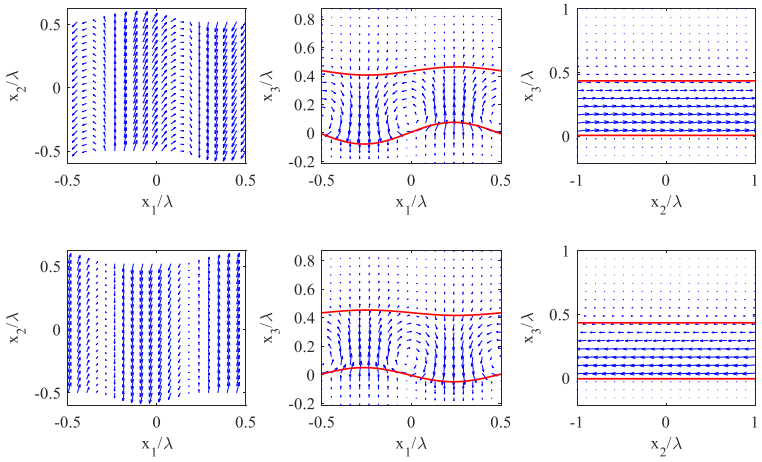

Figure 8. For layer cut $[0.763\ 0.628\ \psi]$ on substrate cut $[0.763\ 0.628\ \psi]$ the displacements. On the top the Rayleigh mode ($k = 2.74, \alpha = -0.037$) and on the bottom the Love mode ($k = 2.72, \alpha = -0.021$) at a velocity of $2000ms^{-1}$. Red lines trace boundary displacements.

By setting the layer cut to $[0.763\ 0.628\ \psi]$, which has off axis anisotropic displacements, the line between Love and Rayleigh waves becomes burred unlike the distinctive waves presented in the isotropic case. For the high symmetry cut of the substrate $[0\ 0\ \psi]$ the waveforms share contributions of the other wave type. When the substrate also has the low variation cut $[0.763\ 0.628\ \psi]$, for the first

mode only, the wave number and attenuation are almost the same value and have an almost indistinguishable displacement pattern.

3.3. Effect of quartz and silicon cut anisotropy on Love waves

Comparisons will be made between the SAWs that exist in the low variation cut and high symmetry cut of cubic crystal, with a quartz layer that has a six fold rotation axis. For both cuts the wave number, attenuation and surface displacement are presented for the generalised multi-layer Rayleigh (see fig. 9) and Love (see fig. 10) type waves. The velocity is fixed at $4000ms^{-1}$ which is above the first shear wave velocity of quartz and below the bulk velocities of silicon.

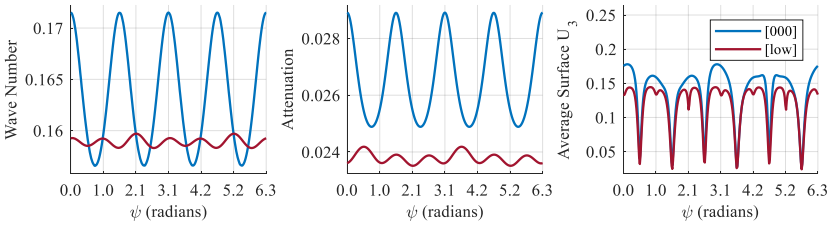

Figure 9. From left to right are the wave number, attenuation and average surface u_3 displacement plots for Rayleigh type waves for substrate cuts $[0\ 0\ \psi + \frac{\pi}{6}]$ and $[0.763\ 0.628\ \psi + \frac{\pi}{6}]$ at fixed velocity of $4000ms^{-1}$.

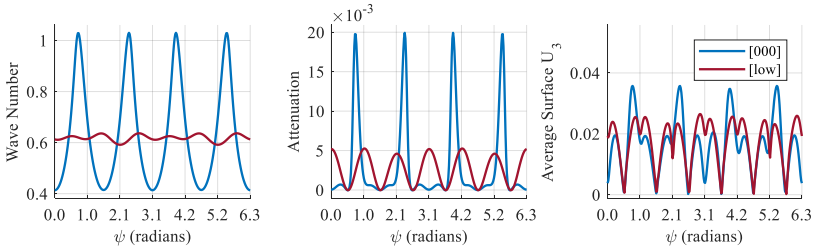

Figure 10. From left to right are the wave number, attenuation and average surface u_3 displacement plots for Love type waves for substrate cuts $[0\ 0\ \psi + \frac{\pi}{6}]$ and $[0.763\ 0.628\ \psi + \frac{\pi}{6}]$ at fixed velocity of $4000ms^{-1}$.

It is clear that the cut $[0.763\ 0.628\ \psi + \frac{\pi}{6}]$ for both wave types no longer has any cubic behavior opposite to the $[0\ 0\ \psi + \frac{\pi}{6}]$ cut which shows a dominated cubic behavior imposed by the substrate. Focusing on the attenuation of the Love wave, the $[0\ 0\ \psi + \frac{\pi}{6}]$ cut not only has the largest variation but severally different behaviors in the displacements. This is due to the changing Rayleigh type displacement between the two layers and can be shown by the comparison between the maximum peaks,

observed at $\frac{\pi}{4}$, and at the minimums, observed at $\frac{\pi}{6}$. Presented is the comparison of u_3 displacement surface with projections (see fig. 11) and displacement vectors (see fig. 12) between both points mention for high symmetry cut.

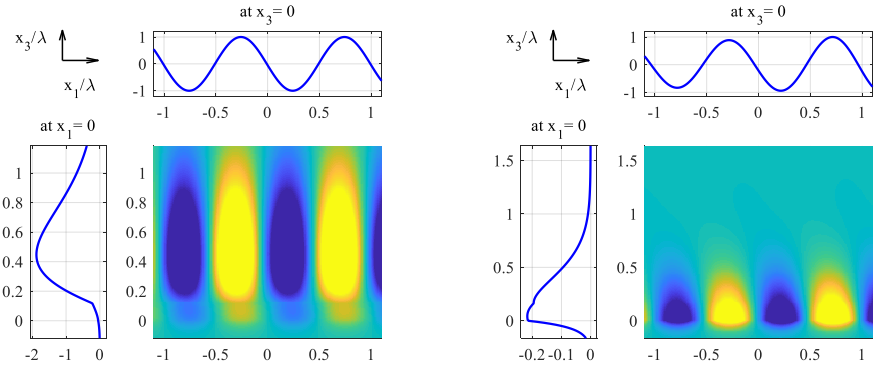

Figure 11. Presented are the u_3 displacement surfaces and projections for the Love wave solution of the $[0\ 0\ \psi + \frac{\pi}{6}]$ cut for, on the left, point $\frac{\pi}{6}$ and on the right point $\frac{\pi}{4}$. Displacements normalised to maximum surface displacement.

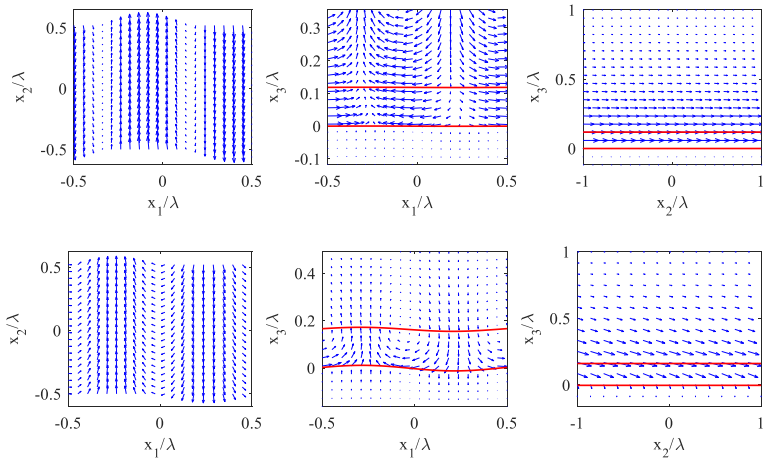

Figure 12. Presented are the displacements for the Love wave solution of the $[0\ 0\ \psi + \frac{\pi}{6}]$ cut for, on the top, point $\frac{\pi}{6}$ and on the bottom point $\frac{\pi}{4}$. Red lines trace boundary displacements.

At the point $\frac{\pi}{6}$ the maximum u_3 displacement and Rayleigh type displacement pattern is at the interface of the two crystals and so the displacement pattern at the fluid interface is of a shear type in the x_1-x_3

and x_2-x_3 planes. At the point of $\frac{\pi}{4}$ the displacement is confined mostly to the layer with the Rayleigh pattern at the surface increasing out of plane displacements seen in the x_1-x_3 and x_2-x_3 planes. The out of plane displacements leads to fluid coupling and increases the decay length of the displacement into the bulk of the fluid. In comparison the displacement pattern remains consistent throughout the $[0.763\ 0.628\ \psi + \frac{\pi}{6}]$ cut with variation in attenuation due to changing Rayleigh displacements in the x_1-x_3 plane (see in fig. 13).

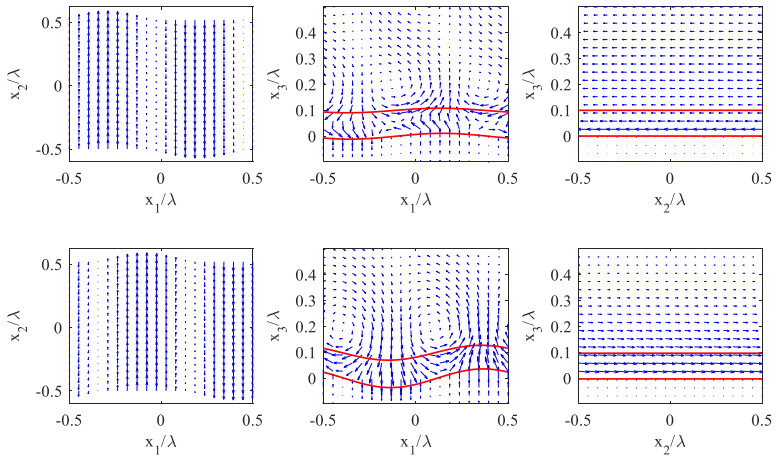

Figure 13. Presented are the displacements for the Love wave solution of the $[0.763\ 0.628\ \psi + \frac{\pi}{6}]$ cut for, on the top, point $\frac{\pi}{6}$ and on the bottom point $\frac{\pi}{4}$. Red lines trace boundary displacements.

4. Conclusion

A cause of leaky behavior of the anisotropic Love wave is by Rayleigh wave type displacements inducing out of plane displacement components at the fluid interface. For this reason, in the cases shown, the Love wave attenuation by fluid coupling can never be greater than the multi-layer Rayleigh waveform. But it has been shown that the wave number and attenuation of these waves can become numerically close resulting in similar displacement patterns. It follows that for anisotropic combinations these Rayleigh type displacements can have a significant effect on the attenuation of multi-layered Love waves.

The concept of anisotropic compatibility for multi-layered waves has been presented in which the wave variation around a crystal cut may be reduced by selection of the anisotropies. For the case of a trigonal layer on cubic substrate the changing Rayleigh contributions to the Love wave is the cause of wave number and attenuation variation around a cut. In this paper it has been shown that a low variation cut for cubic crystals, intrinsic to the cubic shape, exists which takes a similar form to crystals with six

fold rotation symmetry. For Love wave propagation in this cut, a lower variation in wave number and attenuation has been seen with increased consistently in the displacement form.

References

[1] Länge, K., Rapp, B. E., and Rapp, M. Surface acoustic wave biosensors: a review. *Anal Bioanal Chem* 391, 5 (2008), pp. 1509-1519.

[2] Favretto-Crustini, N., et al. Elastic surface waves in crystals. Part 1: Review of the physics, *Ultrasonics* 51, 6 (2011), pp. 653-660.

[3] Potel, C., et al. Experimental verification of the theory of multilayered Rayleigh waves. *Journal of Applied Physics 86, 2* (1999), pp. 1128-1135.

[4] Stoneley, R. Elastic waves at the Surface of Separation of Two Solids, *Proceedings of the Royal Society of London* 106, 738 (1924), pp. 416-428.

[5] Schröder, C. T., and Waymond, R. S. On the complex conjugate roots of the Rayleigh equation: The leaky surface wave. *J. Acoust* 11, 6 (2001), pp. 2867-2877.

[6] Graff, K. F. *Wave Motion in Elastic Solids*. Dover, New York, 1991.

[7] Grigg, H. T. D, Hanley, T. H, and Gallacher, B. J. Degeneracy Breaking, Modal Symmetry and MEMS Biosensor. *Proceedings of COMSOl Conference*, Rotterdam, (2013).

[8] Tanuma, K. Stroh Formulation and Rayleigh Waves. *Journal of Elasticity* 89, 1-3 (2007), pp. 5-154.

[9] Blackstock, D. T. *Fundamentals of Physical Acoustics.* John Wily & Sons, New York, 2000.

[10] Musuvathy, S., et al. Principal curvature ridges and geometrically salient regions of parametric B-spline surfaces. *Computer-Aided Design* 43, 7 (2011), pp. 756-770.

[11] Royer, D., and Dieulesaint, E. *Elastic Waves in Solids I: Free and Guided Propagation*. Springer-Verlag, Berlin, 2000.

[12] Holmes, M. J., Parker, N. G., and Povey M. J. W. Temperature dependence of bulk viscosity in water using acoustic spectroscopy. *J. Phys.: Conf. Ser.* **269** 012011, (2011).

[13] Fahmy, A. H., and Adler, E. L. Computer-program description. Transformation of tensor constants of anisotropic materials due to rotations of the co-ordinate axes. *Proceedings of the Institution of Electrical Engineers* 122, 5 (1975), pp. 591-592.

[14] Birch, F., Schairer, J. F., and Spicer, H. C. *Handbook of Physical Constants*. Geological Society of America, New York, 1950.

Nathan Craig, M.Sc. (Ph.D. student): Newcastle University, School of Mechanical and System Engineering, Stephenson Building, Claremont Road, Newcastle upon Tyne, NE1 7RU, UK (n.p.craig@newcastle.ac.uk). The author gave a presentation of this paper during one of the conference sessions.

Harriet Grigg, Ph.D.: Newcastle University, School of Mechanical and System Engineering, Stephenson Building, Claremont Road, Newcastle upon Tyne, NE1 7RU, UK (harriet.grigg@newcastle.ac.uk).

Irreversibility of mechanical and hydrodynamic instabilities

Carlos D. Díaz-Marín, Alejandro Jenkins

Abstract: The literature on dynamical systems has, for the most part, considered self-oscillators (i.e., systems capable of generating and maintaining a periodic motion at the expense of an external energy source with no corresponding periodicity) either as applications of the concepts of limit cycle and Hopf bifurcation in the theory of differential equations, or else as instability problems in feedback control systems. Here we outline a complementary approach, based on physical considerations of work extraction and thermodynamic irreversibility. We illustrate the power of this method with two concrete examples: the mechanical instability of rotors that spin at super-critical speeds, and the hydrodynamic Kelvin-Helmholtz instability of the interface between fluid layers with different tangential velocities. Our treatment clarifies the necessary role of frictional or viscous dissipation (and therefore of irreversibility), while revealing an underlying unity to the physics of many irreversible processes that generate mechanical work and an autonomous temporal structure (periodic, quasi-periodic, or chaotic) in the presence of an out-of-equilibrium background.

1. Introduction

A self-oscillator is a physical system that excites and maintains a periodic variation at the expense of a source of energy lacking any corresponding periodicity. This definition is due to mathematical physicist A. A. Andronov (1901–1952) and his school, but the same class of phenomena are referred to by many other names and its scientific study dates back to the work of mechanical engineer Robert Willis (1800–1875) and mathematical astronomer Sir George Airy (1801–1892) on the operation of the vocal cords; see [8] and references therein. Self-oscillators are described by homogeneous equations of motion, distinguishing them from forced and parametric resonators. The treatment of self-oscillators in the scientific and engineering literatures has been largely based on the concepts of limit cycles and Hopf bifurcations in the theory of differential equations, or of instability in the theory of feedback control systems.

This work is part of an effort to develop and promote a more physical perspective on self-oscillators, based on considerations of energy, work, and efficiency. This effort is inspired by the observation made long ago by applied physicist Philippe Le Corbeiller (1891–1980) that cyclical motors are self-oscillators, so that the study of self-oscillators may benefit from

the thermodynamic perspective and vice-versa [15, 16]. Unfortunately, Le Corbeiller did not develop this idea very far and it was not taken up by others.

We begin in Sec. 2 by reviewing and generalizing an analysis, due to Shen and Mote [22], of how a rotating dashpot can transfer some of its mechanical energy into the oscillation of the elastic disk over which it moves, thus causing the disk to self-oscillate transversely when the dashpot's speed of rotation exceeds the oscillation's phase velocity. This analysis is instructive because it reveals how the process depends on dissipation within the dashpot. We point out that a similar analysis applies to a large class of instabilities in mechanical rotors, including the well known problem of "shaft whirling" in mechanical engineering.

In Sec. 3 we consider the hydrodynamical Kelvin-Helmholtz (KH) instability, by which, e.g., the action of a steady wind makes waves on the surface of a body of water. We point out the close analogy between this instability and the mechanical ones considered previously. We then review the simple argument used by theoretical physicist Y. B. Zel'dovich (1914 – 1987) to deduce, from the same considerations that account for the KH instability, that a spinning black hole should radiate [1, 2, 26, 27]. This illustrates the power of thermodynamic reasoning to abstract and generalize across diverse physical phenomena.

In Sec. 4 we discuss how these various phenomena illuminate the physics of what applied mathematician Jerry Marsden (1942 – 2010) and collaborators called "dissipation-induced instabilities"; see [13] and references thererin. We shall see that, far from being a paradoxical curiosity, the fact that dissipative forces may destabilize an equilibrium reflects the elementary facts that cyclical engines can be powered only by non-conservative forces and that, according to the second law of thermodynamics, any non-conservative force must be accompanied by the generation of entropy (i.e., by dissipation). Thus, the ubiquity of self-oscillators (from turbines to neurons) reflects the *thermodynamic irreversibility* of macroscopic physical interactions. We conclude by connecting this to the observation, stressed in the recent literature on "finite-time thermodynamics", that a cyclical engine capable of delivering non-zero power must operate irreversibly (see [20] and references therein).

2. Rotors

In [22], Shen and Mote studied the possible mechanisms of instability of an elastic disk under a rotating spring-mass-dashpot system, and found that a viscous dashpot destabilizes the disk when the dashpot moves faster than the phase velocity of a transverse wave on the free disk. Here we review their result, considering a general dissipative force of the dashpot on the disk and then underlining how this analysis can be generalized to other systems.

2.1. Action of rotating dashpot on elastic disk

Let $w(t, r, \theta)$ be the transverse displacement at time t of a mass element of the disk corresponding to polar coordinates (r, θ) on the disk's equilibrium plane. We work in a frame of reference in which the disk does not rotate and write $w_t \equiv \partial w/\partial t$, $w_\theta \equiv \partial w/\partial\theta$. The dashpot moves with angular velocity $\dot\theta \equiv d\theta/dt$ and $r = r_0 = \text{const}$. The transverse velocity of the disk element in contact with the dashpot is $\dot w \equiv dw/dt = w_t + \dot\theta w_\theta$. The dashpot exerts a dissipative force that resists this transverse displacement:

$$F_{\rm dis} = -\,\mathrm{sgn}\,(\dot w) f_{\rm pos} \tag{1}$$

where $f_{\rm pos}$ is arbitrary but strictly non-negative (Shen and Mote take $f_{\rm pos} = c|\dot w|$ for a constant $c > 0$, corresponding to linear damping).

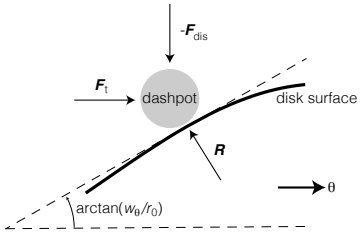

Figure 1. Free-body diagram for a dashpot in contact with the surface of the elastic disk.

Taking the dashpot to be massless (or, equivalently, requiring that its kinetic energy remain constant) and neglecting the friction between the disk and the dashpot, the tangential force $F_{\rm t}$ required to keep the dashpot in uniform circular motion with $\dot\theta = \Omega = \text{const.}$ is

$$F_{\rm t} = -\left[\frac{F_{\rm dis}\cdot w_\theta}{r_0}\right]_{\theta=\Omega t,\, r=r_0} = \left[\frac{\mathrm{sgn}\,(\dot w) f_{\rm pos} w_\theta}{r_0}\right]_{\theta=\Omega t,\, r=r_0} \tag{2}$$

(see Fig. 1). The work done by this force over a period τ is

$$W_{\rm t} = \int_0^\tau F_{\rm t} r_0 \Omega dt = \Omega \int_0^\tau \left[\,\mathrm{sgn}\,(\dot w) f_{\rm pos} w_\theta\right]_{\theta=\Omega t,\, r=r_0} dt \tag{3}$$

and the energy dissipated in the dashpot is

$$W_{\rm d} = -\int_0^\tau \left[F_{\rm dis}\dot w\right]_{\theta=\Omega t,\, r=r_0} dt = \int_0^\tau \left[\,\mathrm{sgn}\,(\dot w) f_{\rm pos}\dot w\right]_{\theta=\Omega t,\, r=r_0} dt \geq 0. \tag{4}$$

The energy absorbed by the oscillation is therefore

$$\begin{aligned}\Delta E = W_{\rm t} - W_{\rm d} &= \int_0^\tau \left[(\Omega w_\theta - \dot w)\ \mathrm{sgn}\,(\dot w) f_{\rm pos}\right]_{\theta=\Omega t,\, r=r_0} dt \\ &= -\int_0^\tau \left[w_t\,\mathrm{sgn}\,(\dot w) f_{\rm pos}\right]_{\theta=\Omega t,\, r=r_0} dt = \int_0^\tau \left[w_t F_{\rm dis}\right]_{\theta=\Omega t,\, r=r_0} dt.\end{aligned} \tag{5}$$

If we consider a traveling wave of the form $w = A(r)\sin(m\theta - \omega t)$ for $\omega \geq 0$ and define a parameter $\sigma \equiv m\Omega - \omega$ this becomes

$$\begin{aligned}\Delta E &= \int_0^\tau \left[\omega A(r)\cos(m\theta - \omega t)\ \mathrm{sgn}(\dot{w}) f_{\mathrm{pos}}\right]_{\theta=\Omega t,\, r=r_0} dt \\ &= \omega A(r_0)\int_0^\tau \cos(\sigma t)\,\mathrm{sgn}\left[A(r_0)\sigma\cos(\sigma t)\right]\ f_{\mathrm{pos}}|_{\theta=\Omega t,\, r=r_0}\, dt \\ &= \mathrm{sgn}(\sigma)\cdot\omega|A(r_0)|\int_0^\tau |\cos(\sigma t)|\ f_{\mathrm{pos}}|_{\theta=\Omega t,\, r=r_0}\, dt.\end{aligned} \tag{6}$$

The last integral in Eq. (6) is strictly non-negative. If $f_{\mathrm{pos}} \neq 0$, then $\mathrm{sgn}(\Delta E) = \mathrm{sgn}(\sigma)$. This means that if the dashpot moves with Ω less than the phase velocity ω/m, then $\Delta E < 0$, indicating that the dashpot damps the transverse oscillation of the disk. We call this the sub-critical regime. On the other hand, when the dashpot moves with Ω greater than the wave's phase velocity, $\Delta E > 0$, which means that the transverse oscillation is powered by the dashpot's motion. We call this the super-critical regime.

One way of understanding the change of sign of ΔE is to note that, according to Eq. (5), the power delivered to the oscillation is $w_t F_{\mathrm{dis}}$, where w_t is measured with respect to the static disk's equilibrium position. When $\Omega < \omega/m$, the force F_{dis} *lags* behind the oscillation, because of dissipation in the dashpot. The corresponding work done on the oscillation is therefore negative. When $\Omega > \omega/m$ the oscillation travels backwards with respect the dashpot, so that F_{dis} *leads* the oscillation, making the work on it positive. [3, 22]

This analysis is more generalizable than it might seem at first. For starters, rather than a massless dashpot maintained at constant angular velocity by an external force F_{t}, one could take W_{t} as coming out of a massive dashpot's kinetic energy, causing it to decelerate. If the dashpot were initially moving super-critically ($\sigma > 0$), this would power the self-oscillation until the dashpot's velocity fell below the critical $\Omega = \omega/m$. This is also equivalent to considering the dashpot to be at rest and endowing the spinning disk with kinetic energy. A similar result is obtained for the stability of a circular saw subject to an in-plane edge load, as in a sawmill: see [18] and references therein.

2.2. Shaft whirling

The theoretical analysis of shaft whirling dates back to the work of Kimball in 1920s, in which he argued that the whirling of a super-critically spinning shaft is an instability induced by the shaft's internal friction [10, 11]. In Kimball's model, the stretching or compression of the material fibers in the shaft is opposed by a dissipative force. When the shaft turns faster than the natural frequency of the whirling, the force on the fibers *injects* energy into the whirling. This destabilizes the system, much like the disk of Sec. 2.1 is destabilized by the super-critically spinning dashpot.

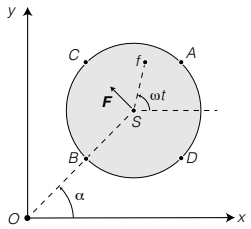

Figure 2. Cross-section of a shaft turning at rate ω and whirling at rate $\dot{\alpha}$. The direction of the non-conservative force $\boldsymbol{F}$ shown corresponds to the super-critical case $\omega > \dot{\alpha}$.

Consider a cross section of a shaft, centered at S. A given material fiber that runs along the shaft's length passes through this cross section at a point f, which turns around S with angular velocity ω (see Fig. 2). If the shaft is initially perturbed, displacing S away from the position O that it would occupy if the shaft were straight, then the shaft whirls with rate $\dot{\alpha}$ and amplitude OS. The whirling rate $\dot{\alpha}$ is given by the elastic force on the shaft, which points from S to O. Being conservative, this restoring force does no net work over a complete period of the shaft's motion. This may also be seen from the fact that the force always points at right angles to the whirl component of S's velocity.

Following Kimball, we consider an internal friction that opposes the time rate of change of each fiber's length. Just like the restoring force acting on S points from the longer to the shorter elastic fibers, this internal friction gives rise to a force that points from the fibers being stretched to those being compressed. This force can have a tangential component and thus do net work on the whirling shaft. If $\omega = \dot{\alpha}$ then individual material fibers maintain fixed lengths, with the fiber at B being shortest and the fiber at A longest. In this case the shaft experiences no internal friction and only the elastic force along OS acts on the shaft. But if $\omega \neq \dot{\alpha}$, then a fiber moving from A to B is being shortened, while a fiber moving from B to A is being stretched.

If the shaft turns sub-critically ($\omega < \dot{\alpha}$) for positive $\dot{\alpha}$ and ω, then the fiber at C is under frictional tension and the fiber at D under frictional compression, and the resulting force $\boldsymbol{F}$ points against the whirl, damping its amplitude OS. If the sign of $\dot{\alpha}$ is flipped then so is the sign of $\boldsymbol{F}$, so that whirling in either direction is damped. On the other hand, if the shaft turns super-critically ($\omega > \dot{\alpha}$) the fiber at C is under frictional compression and the fiber at D is under frictional tension, regardless of the sign of $\dot{\alpha}$. The force $\boldsymbol{F}$ will therefore inject energy into a whirl with $\dot{\alpha} > 0$, destabilizing the rotating shaft's straight configuration.

2.3. Non-conservative positional force

In the super-critical case, the equations of motion for the rectangular coordinates (x, y) of the shaft's center of mass at S take the form

$$\begin{cases} m\ddot{x} + kx + py = 0 \\ m\ddot{y} + ky - px = 0 \end{cases} \tag{7}$$

where k is the elastic constant for the bending of the fibers and p is equal to the magnitude of the tangential force F divided by the radius OS. The terms with p in Eq. (7) correspond, in the language of [13], to a "non-conservative positional force" (NPF). As a vector $\boldsymbol{F} = (-py, px, 0)$ has non-zero circulation $\boldsymbol{\nabla} \times \boldsymbol{F} = (0, 0, 2p)$ and is therefore not expressible as $-\boldsymbol{\nabla} V$ for any potential V.

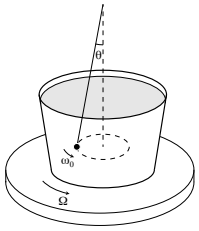

Figure 3. Conical pendulum moving with amplitude θ and angular velocity ω_0 in a bucket of water that spins at rate Ω. Image adapted from [3].

A simple analogy, originally due to physicist Sir Brian Pippard (1920–2008), helps clarify the origin of the NPF: Consider the conical pendulum swinging inside a rotating bucket filled with water, shown in Fig. 3. If the water rotates more slowly than the free pendulum, then the water's viscosity damps the pendulum's motion, causing it to sink towards the vertical ($\theta \to 0$). If the water rotates faster than the free pendulum, the water drags the pendulum forwards, causing the amplitude θ to increase [3, 21]. Only in the latter case can the water's effect on the pendulum be described by an NPF. Note that a model in which the NPF is obtained without reference to the elastic force that determines the critical speed is therefore inconsistent; cf. [4, 17].

3. Hydrodynamic instabilities

The interface between two layers of fluid with different tangential velocities is unstable against a traveling transverse perturbation when the difference in the velocities of the layers exceeds the phase velocity of the perturbation with respect to the fluid. This is known as the Kelvin-Helmholtz (KH) instability (see, e.g., [25]) and it is the fundamental mechanism by

which a steady wind makes waves on the surface of a body of water, as illustrated in Fig. 4. Since the wind has no periodicity corresponding to the water wave, this is a self-oscillation.

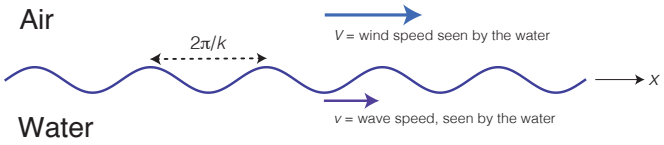

Figure 4. Illustration of the hydrodynamic KH instability by which wind can generate waves on the surface of a body of water. Image adapted from [24].

Neglecting the viscosity of the water, in the linear regime a wave that propagates in the x direction along the surface of the water and that has wave number k can be expressed as the real part of

$$\xi_0 = A \cdot e^{i(kx-\omega t)}, \text{ for } \omega = kv. \tag{8}$$

If we take into account the air's viscosity, then when the bulk of the air is a rest ($V = 0$ in Fig. 4) the water wave ξ is described by an equation of motion that includes a linear damping term of the form $c \cdot \partial\xi/\partial t$. If the air blows with constant velocity $V > 0$, we can go to the air's rest frame by a Galilean coordinate transformation. The damping term acting on the free wave $\xi = \xi_0$ transforms as

$$\frac{\partial \xi_0}{\partial t} \to \frac{\partial \xi_0}{\partial t} + V\frac{\partial \xi_0}{\partial x} = -i\omega\xi_0 + V \cdot ik\xi_0 = -i\omega\xi_0\left(1 - \frac{V}{v}\right). \tag{9}$$

The sign of Eq. (9) flips when V passes the critical value $V = v$. The wind therefore anti-damps a water wave with phase velocity v less than the wind speed V.

Much like in the analysis of Sec. 2.1, this reflects that fact that when $V < v$ the oscillation of the air pressure induced by the wave lags behind the wave, because of the air's viscosity, but when $V > v$ the wave travels backwards with respect the air, so that the oscillation of the air pressure leads the wave. Without dissipation, the phase between the air pressure and the wave must be either 0 or π, preventing the air from doing any work at all on a full period of the wave. It is therefore clear that the KH instability requires non-zero dissipation in the air, just like we saw in Sec. 2 that some energy had to be dissipated in the dashpot for the self-oscillation of the elastic disk to be excited, and that Kimball's explanation of shaft whirling depended on internal friction.

Aeronautical engineer Erik Mollo-Christensen (1923 – 2009) stressed that the KH instability depends on non-vanishing viscosity in [19], but many leading textbooks do not make this quite so clear. For instance, Landau and Lifshitz derive an instability for inviscid flow

because they work in a limit in which the power injected into the wave is vanishing [14]. The same is true of Rayleigh's inviscid instability argument for rotating Couette flow [25]. Indeed, a simplified account of Rayleigh's argument (see, e.g., [6]) could lead a novice to conclude that the fluid circulation in a Taylor cell is driven by centrifugal force, which is impossible because the centrifugal force is conservative.

The simple argument of Eq. (9) led Zel'dovich to conclude that any body that, when stationary, damps an incident wave must also, if its surface moves faster than the wave's phase velocity, amplify the wave at the expense of the body's kinetic energy [1, 26, 27]. Moreover, some of the kinetic energy lost must heat the body, making the process thermodynamically irreversible. In this way, Zel'dovich argued in 1971 that a spinning black hole should radiate, a result that motivated the rise of black-hole thermodynamics as an active field of research in theoretical physics (for an entertaining historical account of Zel'dovich's argument and its impact, see ch. 12 in [23]). The process predicted by Zel'dovich is now called "superradiance"; see [2] and references therein.

4. Dissipation-induced instabilities

Following Krechetnikov and Marsden [13] we may classify the possible terms in the linearized, homogeneous equation of motion for an n-dimensional system with an equilibrium at $\boldsymbol{q} = 0$ as:

$$\underset{\text{inertia}}{\mathsf{M}\ddot{\boldsymbol{q}}} + \underset{\text{dissip.}}{\mathsf{C}\dot{\boldsymbol{q}}} + \underset{\text{gyroscopic}}{\mathsf{G}\dot{\boldsymbol{q}}} + \underset{\text{potential}}{\mathsf{K}\boldsymbol{q}} + \underset{\text{non-cons.}}{\mathsf{N}\boldsymbol{q}} = 0 \tag{10}$$

where M, C, and K are $n \times n$ symmetric matrices, while G and N are anti-symmetric. The system is trivially unstable when K has negative eigenvalues, which corresponds to perturbing about a configuration that is not a local minimum of potential energy. Such a system may be stabilized by G, a phenomenon familiar from the sleeping top. Any non-zero, positive dissipation, no matter how small, will destabilize it again: a top which is initially sleeping will always end up falling if it dissipates mechanical energy. This is therefore a "dissipation-induced instability".

Self-oscillation is seen either as a negative eigenvalue of C or as $\mathsf{N} \neq 0$. In a physically realistic description, negative damping results from a positive feedback involving a non-conservative dynamic not explicitly included in Eq. (10); see [8]. Similarly, we have seen here that $\mathsf{N} = 0$ requires super-critical motion in a dissipative medium. The laws of thermodynamics thus reveal something that cannot be deduced from the mathematics of Eq. (10): that self-oscillation is always irreversible.

Mechanical engineer Hans Ziegler (1910–1985) discovered in 1952 that some configurations of a double pendulum with a follower load could be destabilized by arbitrarily small

friction at the joints. This "Ziegler paradox" launched a research program on the mathematical characterization of dissipation-induced instabilities; see [12] and references therein. Ziegler's result is not so paradoxical in light of the physical approach that we advocate here: damping is always potentially destabilizing when, as Pippard put it, a moving part "carries its dissipative mechanisms around with it" [21]; see also [4]. For instance, in Fig. 4 the energy that excites the waves comes from the wind's motion. Instability therefore depends on the air's non-zero viscosity. The water's viscosity, on the other hand, always damps the waves and therefore can only be stabilizing.

4.1. Tidal acceleration and other analogs

This approach reveals interesting analogies. For instance in Fig. 2 the shaft could be replaced by the Earth and O by the position of the Moon. The viscous damping of the motion of the Earth's tidal bulge acts as internal friction. Since

$$\omega = \frac{2\pi}{1 \text{ day}} > \dot{\alpha} = \frac{2\pi}{1 \text{ month}}, \tag{11}$$

the Earth spins super-critically. The net gravitational force exerted by the Moon on the tidally deformed Earth therefore has a tangential component along the Earth's orbital velocity, explaining why the semi-major axis of the Earth-Moon orbit is currently increasing by about 4 cm/yr, a phenomenon known as "tidal acceleration". [2, 7]

All of the processes that we have discussed depend on dissipation within the medium whose kinetic energy powers the self-oscillation. The non-conservative force that drives the self-oscillation is usually exerted by that same energetic medium. But in tidal acceleration the energy comes from the Earth's rotation, while the non-conservative force comes from the Moon's gravitational field. This is possible because the Moon's gravity acts on a spinning Earth that is being periodically deformed by the combination of tidal and viscous forces. This gives rise to a tangential component of the Moon's tidal force, acting with respect to the Earth's center of mass as a NPF [7]. Something similar is seen when a child enjoys a playground swing: the force that drives the swinging is the tension of the chain that holds up the swing. The child provides the energy by periodically deforming her body in a way that causes the chain's tension to have a component along the velocity of the child's center of mass. That deformation results from (very complex!) irreversible processes within the child.

Other dissipation-induced instabilities include sonic booms, Kelvin wakes, and Čerenkov radiation. One of us has recently argued that the Earth's Chandler wobble should also be understood in these terms: as a destabilization of the Earth's axis of rotation, powered by the circulation of geophysical fluids and associated with viscous dissipation within them. [9]

4.2. Towards a physical theory of engines

Thermodynamic theory allows for reversible engines, such as the cycle described by military engineer Sadi Carnot (1796–1832). Carnot realized that reversibility required the heat flow between the working substance and the external reservoirs to occur isothermally, making it infinitely slow. The phenomenological thermodynamics that Clausius, Kelvin and others built upon Carnot's work never considers the time dependence of the state variables, giving it a qualitatively different character to that of a mechanical description. More recent work on "finite-time thermodynamics" has established that obtaining non-zero power necessarily reduces the limit efficiency of a heat engine, compared to the zero-power Carnot cycle running between the same reservoirs. [20]

Conventional thermodynamics says that all of the instabilities that we have considered can have efficiencies arbitrarily close to 1, since their energy source is mechanical rather than thermal. We have seen, however, that these processes are *necessarily* irreversible, since they must be accompanied by non-zero dissipation in the body that cedes energy. A realistic, physical description of engines capable of delivering non-zero power should take into account this distinction between necessary and avoidable dissipation.

These considerations apply not just to self-oscillators with regular limit cycles, but also to any autonomous mechanical system (i.e., one describable by homogenous differential equations) that generates a temporal structure —whether periodic, quasi-periodic, or chaotic— as the result of non-conservative forces. The laws of thermodynamics imply that such systems must generate entropy; see [5] and references therein.

5. Conclusions

Krechetnikov's and Marsden's observation that "ubiquitous dissipation is one of the paramount mechanisms by which instabilities develop in nature" [13] seems to us both broader and deeper than the authors may have realized: almost all of what makes our everyday experience of the physical world interesting depends on irreversibility. We have illustrated this by considering several mechanical and hydrodynamic instabilities from a different perspective than the one commonly adopted in the dynamical systems literature. This approach clarifies the role of dissipation, without entering into the details of the processes behind it. In the case of the KH instability, for instance, all that we needed was the fact that when the bulk of the air is at rest above the water the air tends to damp out the waves on the water's surface, as one may easily verify experimentally. From this and from some very general symmetry principles, Zel'dovich arrived at a result that applies to ocean waves just as much as to quantum fields incident on spinning black holes.

Acknowledgments

This work was supported by the Vice-rectorate for Research (project no. 112-B6-509) and the Vice-rectorate for Student Life of the University of Costa Rica. AJ thanks Robert Alicki, Stan Hutton, John McGreevy, Huajiang Ouyang, Juan Sabuco, and Miguel Sanjuán for stimulating discussions, and Bob Jaffe for help procuring copies of Refs. [10, 16].

References

[1] Bekenstein, J. D., and Schiffer, M. The many faces of superradiance. *Physical Review D 48*, 6 (1998), 064014.

[2] Brito, R., Cardoso, V., and Pani, P. *Superradiance*, vol. 906 of *Lecture Notes in Physics*. Springer, Cham, 2015.

[3] Crandall, S. H. Physical explanation of the destabilizing effect of damping in rotating parts. In *Rotordynamic Instability Problems in High-Performance Turbomachinery* (1980), vol. 2133, NASA Conference Publications, pp. 369–382.

[4] Crandall, S. H. Heuristic explanation of journal bearing instability. In *Rotordynamic Instability Problems in High-Performance Turbomachinery* (1982), vol. 2250, NASA Conference Publications, pp. 274–283.

[5] Cross, M., and Greenside, H. *Pattern Formation and Dynamics in Nonequilibrium Systems*. Cambridge U. P., Cambridge, 2009.

[6] Feynman, R. P. The flow of wet water. In *Feynman Lectures on Physics* (2010 [1964]), vol. II, Basic Books, pp. 41.1–41.12.

[7] Hut, P. Tidal evolution in close binary systems. *Astronomy and Astrophysics 99*, 1 (1981), 126–140.

[8] Jenkins, A. Self-oscillation. *Physics Reports 525*, 2 (2013), 167–222.

[9] Jenkins, A. Chandler wobble: Stochastic and deterministic dynamics. In *Dynamical Systems: Theoretical and Experimental Analysis* (2016), vol. 182, Springer Proceedings in Mathematics & Statistics, pp. 177–186.

[10] Kimball, A. L. Internal friction theory of shaft whirling. *General Electric Review 27*, 4 (1924), 244–251.

[11] Kimball, A. L. Internal friction as a cause of shaft whirling. *Philosophical Magazine, ser. 6 49*, 292 (1925), 724–727.

[12] Kirillov, O. N., and Verhulst, F. Paradoxes of dissipation-induced destabilization or who opened Whitney's umbrella? *Zeitschrift für Angewandte Mathematik und Mechanik 90*, 6 (2010), 462–488.

[13] Krechetnikov, R., and Marsden, J. E. Dissipation-induced instabilities in finite dimensions. *Reviews of Modern Physics 79*, 2 (2007), 519–553.

[14] Landau, L. D., and Lifshitz, E. M. *Fluid Mechanics*, 2nd ed. Elsevier, Oxford, 1987.

[15] Le Corbeiller, P. E. The non-linear theory of the maintenance of oscillations. *Journal of the Institution of Electrical Engineers 79*, 477 (1936), 361–378.

[16] Le Corbeiller, P. E. Theory of prime movers. In *Non-Linear Mechanics* (1943), Brown U. Advanced Instruction and Research in Mechanics, pp. 2.1–2.18.

[17] Merkin, D. R. *Introduction to the Theory of Stability*. Springer-Verlag, New York, 1997.

[18] Mohammadpanah, A., and Hutton, S. G. Dynamics behavior of a guided spline spinning disk, subjected to conservative in-plane edge loads, analytical and experimental investigations. *Journal of Vibration and Acoustics 138*, 4 (2016), 041005.

[19] Mollo-Christensen, E. L. Flow instabilities. In *Illustrated Experiments in Fluid Mechanics* (1972), National Committee for Fluid Mechanics Films, pp. 113–120.

[20] Ouerdane, H., Apertet, Y., Goupil, C., and Lecoeur, P. Continuity and boundary conditions in thermodynamics: From Carnot's efficiency to efficiencies at maximum power. *European Physical Journal Special Topics 224*, 5 (2015), 839–854.

[21] Pippard, A. B. *The physics of vibration*, omnibus ed. Cambridge U. P., Cambridge, 1989 [1979].

[22] Shen, I. Y., and Mote, C. D. On the mechanisms of instability of a circular plate under a rotating spring-mass-dashpot system. *Journal of Sound and Vibration 148*, 2 (1991), 307–318.

[23] Thorne, K. S. *Black Holes and Time Warps*. W. W. Norton, New York, 1994.

[24] Thorne, K. S. Physics bets and conversations with John. Talk delivered at the Conference in Honor of John Preskill's 60th Birthday, 2013.

[25] Tritton, D. J. *Physical Fluid Dynamics*, 2nd ed. Oxford U. P., Oxford, 1988.

[26] Zel'dovich, Y. B. Generation of waves by a rotating body. *JETP Letters 14*, 4 (1971), 180–181.

[27] Zel'dovich, Y. B. Amplification of cylindrical electromagnetic waves reflected from a rotating body. *Soviet Physics JETP 35*, 6 (1972), 1085–1087.

Carlos D. Díaz-Marín, B.A.: University of Costa Rica, School of Mechanical Engineering, 36-2060, COSTA RICA (*cdiaz95@hotmail.es*).

Alejandro Jenkins, Professor: University of Costa Rica, School of Physics, 11501-2060, COSTA RICA (*alejandro.jenkins@ucr.ac.cr*). The author gave a presentation of this paper during one of the conference sessions.

Nonlinear dynamics and control applied to an aircraft in a longitudinal flight considering gusts of wind in flight

Guilherme Pacheco dos Santos, Jose Manoel Balthazar, Frederic Conrad Jansen, Rodrigo Tumolin Rocha, Airton Nabarrete, Angelo Marcelo Tusset

Abstract: Modern high-performance aircrafts operate regularly in-flight regimes where system's nonlinearities influence directly into their dynamic response. This paper considers the study of a fighter aircraft which operates in high angles of attack of the wing. The mathematical modelling and numerical simulations were developed, becoming at a system of nonlinear differential equations that represent the dynamics of an aircraft in longitudinal flight, considering the effect of wind speed variation due to atmospheric turbulence in the dynamic response of the aircraft. The dynamic system consists in a two-degrees-of-freedom coordinate for the aircraft and a single-degree-of-freedom for the variation of wind gusts. To understand the system we performed the 0-1 test to determine if the system is chaotic or periodic, performed in relation to the speed and angle of attack of the aircraft F-8 "Crusader". The control is proposed having as control parameter the tail deflection angle and designed using the control method of State Dependent Riccati Equations (SDRE) with the purpose of stabilizing oscillations of angle of attack of the wing, considering critical regions of aircraft behaviour. Numerical simulations demonstrated the effectiveness of the proposed control strategy, where controller was able to respond quickly to retrieve the aircraft

1. Introduction

The analysis of dynamics in aircraft models has been of great relevance due to technological and scientific development in recent years. New approaches are proposed in different ways for the dynamics, control and stability of aircrafts. As an example, the fighter aircraft which is submitted to operate in great angles of attack and at high speeds, which may affect the dynamic response during the flight. In these situations, the response can be improved designing a controller based on the use of mathematical model that represents the aircraft motion and its dynamic nonlinearities. Therefore, this paper aims to analyze the control of the nonlinear dynamics of an aircraft in longitudinal flight at high angles of attack (above the stall condition), considering wind gusts as a source of excitation. As a study object, it is proposed the analysis of the dynamic behavior of the F-8 "Crusader" considering the tail deflection angle as a control parameter and controlled by the technique of nonlinear feedback of State Dependent Riccati Equations (SDRE control).

2. Mathematical modeling

2.1. Nonlinear dynamic model of the F-8 "Crusader" aircraft

The considered forces and the coordinate system used to represent the aircraft motion are presented in Fig. 1. The drag force is disregarded in relation to the other parameters and the moment of inertia is taken to be proportional to the mass of the aircraft.

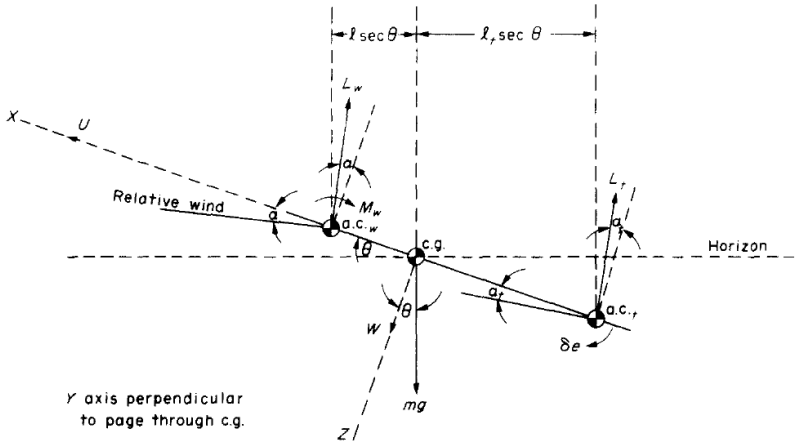

Figure 1. Dynamic aircraft model [4].

The lift force is separated into two components, wing and tail. The equations of motion are written in terms of four variables ($x = (u, \alpha, \theta, q)$), where u is the longitudinal flight speed, the angle of attack is represented by α, the pitch angle is θ, the aircraft pitch rate is given by q and V is the variation of wind speed (virtual wind tunnel) over time. The basic equations of longitudinal motion are represented in the system of equations (1) [4].

$$\begin{aligned} m(\dot{u} + w\dot{\theta}) &= -mg\sin\theta + L_w \sin\alpha + L_t \sin\alpha_t \\ m(\dot{w} - u\dot{\theta}) &= mg\cos\theta + L_w \cos\alpha + L_t \cos\alpha_t \\ I_y\ddot{\theta} &= M_w + lL_w \cos\alpha - lL_t \cos\alpha_t - c\dot{\theta} \end{aligned} \tag{1}$$

Where: m= mass of aircraft, u= velocity of aircraft in X direction, w= velocity of aircraft in direction, θ= angular displacement about Y axis, measured clockwise from the horizon as shown in Fig. 1, I_r= moment of inertia of aircraft about Y axis, L_w= wing lift, L_t= tail lift, α= wing angle of attack, α_t= tail angle of attack, M_w = wing moment, l= distance between wing aerodynamic center and aircraft center of gravity, l_t= distance between tail aerodynamic center and aircraft center of gravity, $c\dot{\theta}$= damping moment, C_L= coefficient of wing lift, C_{L_t}= coefficient of tail lift, $\bar{q}$= dynamic pressure, S= wing area and S_t= horizontal tail area.

The lift forces of the tail and wing are given by $L_w = C_{L_w}\bar{q}S$ and $L_t = C_{L_t}\bar{q}S_t$, respectively. In addition, the wing moment M_w is a function of α, and the angle of attack of the tail α_t is a function of α and δ_e. Figure 2 shows the velocity components u, v and w along the axes X, Y and Z [10].

$$u = V\cos\beta\cos\alpha$$
$$v = V\sin\beta$$
$$w = V\cos\beta\sin\alpha$$
$$V = (u^2 + v^2 + w^2)^{\frac{1}{2}}$$

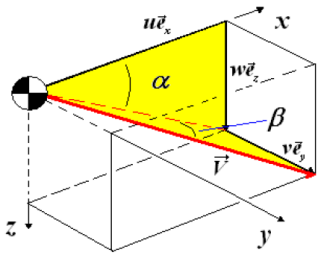

Figure 2. Models of speed components [10].

Where:

$$w = u\tan\alpha$$
$$\dot{w} = \dot{u}\tan\alpha + u\dot{\alpha}\sec^2\alpha \tag{2}$$

Thus, rewriting Eq. (1) [10], it has Eq. (3)

$$\dot{u} = -u\dot{\theta}\tan\alpha - g\sin\theta + (L_w/m)\sin\alpha + (L_t/m)\sin\alpha_t$$
$$\dot{\alpha} = \dot{\theta}\cos^2\alpha + \left(\frac{g}{u}\right)\cos^2\alpha\cos\theta - (L_w/um)\cos^3\alpha - (L_t/um)\cos^2\alpha\cos^2\alpha_t - \tag{3}$$
$$-(\dot{u}/u)\sin\alpha\cos\alpha$$
$$\ddot{\theta} = M_w/I_y + (lL_w/I_y)\cos\alpha - (lL_t/I_y)\cos\alpha_t - (c/I_y)\dot{\theta}$$

Replacing $\dot{u} = -u\dot{\theta}\tan\alpha - g\sin\theta + (L_w/m)\sin\alpha + (L_t/m)\sin\alpha_t$ in Eq. (3), It has Eq. (4) [10].

$$\dot{u} = -u\dot{\theta}\tan\alpha - g\sin\theta + (L_w/m)\sin\alpha + (L_t/m)\sin\alpha_t$$
$$\dot{\alpha} = \dot{\theta}\sin^2\alpha + \left(\frac{g}{u}\right)\sin\theta\sin\alpha\cos\alpha - (L_w/um)\,sin^2\alpha\cos\alpha - (\tfrac{L_t}{um})\sin\alpha\cos\alpha\,sin\alpha_t + \tag{4}$$
$$+\dot{\theta}\cos^2\alpha + \left(\frac{g}{u}\right)\cos^2\alpha\cos\theta - (L_w/um)\cos^3\alpha - (L_t/um)\cos^2\alpha\cos^2\alpha_t$$
$$\ddot{\theta} = M_w/I_y + (lL_w/I_y)\cos\alpha - (lL_t/I_y)\cos\alpha_t - (c/I_y)\dot{\theta}$$

Equation (4) represents a model of fourth-order longitudinal flight dynamics, in which the states are $(u, \alpha, \theta, \dot{\theta})$. As previously described, the lift force of wing L_w is a function of α, and the lift of tail L_t is a function of α and δ_e. Two cubic polynomial functions were proposed by [4] to approximate the coefficient of lift of the wing and the tail. These functions are given by [4]:

$$L_w = C_{L_w}\bar{q}S = \bar{q}S(C_{L_w}{}^0 + C_{L_w}{}^1\alpha - C_{L_w}{}^2\alpha^3) \tag{5}$$

$$L_t = C_{L_t}\bar{q}S_t = \bar{q}S_t({C_{L_t}}^0 + {C_{L_t}}^1\alpha_t - {C_{L_t}}^0{\alpha_t}^3 + a_e\delta_e) \tag{6}$$

where ${C_{L_w}}^0$, ${C_{L_w}}^1$, ${C_{L_w}}^2$, ${C_{L_t}}^0$, ${C_{L_t}}^1$ and ${C_{L_t}}^2$ are constants and depend individually on the aircraft, δ_e represents the deflection angle of the horizontal tail measured to the right of the X axis and a_e is the linear approximation of the effect of δ_e on C_{L_t}.

Since the horizontal tail of the F-8 "Crusader" is within the wing wake, the downwash angle $\in$ (defined as the angle formed between the direction of the air flow entering the wing and the direction of the air flow as it exits the wing) was included in the determination of the angle of attack of the tail. Considering a linear approximation of $\in = a_\in\alpha$, the tail angle of attack is given by [10]:

$$\alpha_t = \alpha - \in + \delta_e = (1 - a_\in)\alpha + \delta_e \tag{7}$$

Considering $a_\in = 0.75$, it has $\alpha_t = 0.25\alpha + \delta_e$. As presented by [7], the approximation of the wing lift coefficient proposed by [1] is more realistic in stall regions and larger regions of stall than in Eq. (5), in this way, the wing lift coefficient is given by [10]:

$$\begin{aligned} L_w &= \bar{q}S({C_{L_w}}^0 + {C_{L_w}}^1\alpha - {C_{L_w}}^2\alpha^3)W \\ W &= \left\{\frac{1}{[1 + (\alpha/0.41)^{60}]}\right\} \end{aligned} \tag{8}$$

Substituting Eqs. (6), (7) and (8) into Eq. (4), the longitudinal motion of the aircraft is represented by [10]:

$$\begin{aligned} \dot{u} &= -uq\tan\alpha - g\sin\theta + \frac{\bar{q}}{m}\{SW\sin\alpha\left({C_{L_w}}^0 + {C_{L_w}}^1\alpha - {C_{L_w}}^2\alpha^3\right) + S_t\sin(0.25\alpha + \\ &\quad +\delta_e)\left[{C_{L_t}}^0 + {C_{L_t}}^1(0.25\alpha + \delta_e) - {C_{L_t}}^2(0.25\alpha + \delta_e)^3 + a_e\delta_e\right]\} \\ \dot{\alpha} &= q + \left(\frac{g}{u}\right)\cos\alpha\cos(\alpha - \theta) - \frac{\bar{q}}{mu}\cos\alpha\{SW\left({C_{L_w}}^0 + {C_{L_w}}^1\alpha - {C_{L_w}}^2\alpha^3\right) - \\ &\quad -S_t\cos(0.75\alpha + \delta_e)\left[{C_{L_t}}^0 + {C_{L_t}}^1(0.25\alpha + \delta_e) - {C_{L_t}}^2(0.25\alpha + \delta_e)^3 + a_e\delta_e\right]\} \\ \dot{\theta} &= q \\ \dot{q} &= M_w/I_y - (c/I_y)q + (\bar{q}/I_y)\{lS\cos\alpha\left({C_{L_w}}^0 + {C_{L_w}}^1\alpha - {C_{L_w}}^2\alpha^3\right)W - \\ &\quad -l_t\,S_t\cos(0.25\alpha + \delta_e)[{C_{L_t}}^0 + {C_{L_t}}^1(0.25\alpha + \delta_e) - {C_{L_t}}^2(0.25\alpha + \delta_e)^3 + a_e\delta_e]\} \end{aligned} \tag{9}$$

where

$$M_w = l_t mg\cos\theta - (l - l_t)(\bar{q}S\left({C_{L_w}}^0 + {C_{L_w}}^1\alpha - {C_{L_w}}^2\alpha^3\right)W)\cos\alpha \tag{10}$$

$$\bar{q} = \frac{1}{2}\rho V^2 \tag{11}$$

where ρ = atmospheric density. The data of the F-8 "Crusader" aircraft, considered for further numerical simulations, is presented in Table 1 [4].

Table 1. Data of the F-8 "Crusader" [4]

${C_{L_w}}^0 = {C_{L_t}}^0$	0
${C_{L_w}}^1 = {C_{L_t}}^1$	4.0
${C_{L_w}}^2 = {C_{L_t}}^2$	12
a_e	0.1
S	33.75 m^2
S_t	8.41 m^2
$C_{m_{a.c}}$	0
$\bar{c}$	3.53 m
I_y	127512 Kgm^2
l	0.06 m
l_t	5.01m

Substituting Eq. (10) and considering the data of Table 1 in the system of Eqs. (9), the final form of the equations of motion of the aircraft's longitudinal motion is given by Eqs. (12) [10].

$$\begin{aligned}
\dot{u} &= -uq\tan\alpha - 10\sin\theta + \frac{\bar{q}}{m}\{33.75W\sin\alpha\,(4\alpha - 12\alpha^3) + 8.41\sin(0.25\alpha + \\
&\quad +\delta_e)[4(0.25\alpha + \delta_e) - 12(0.25\alpha + \delta_e)^3 + 0.1\delta_e]\} \\
\dot{\alpha} &= q + \left(\frac{10}{u}\right)\cos\alpha\cos(\alpha - \theta) - \frac{\bar{q}}{mu}\cos\alpha\,\{33.75W(4\alpha - 12\alpha^3) - 8.41\cos(0.75\alpha + \\
&\quad +\delta_e)\,[4(0.25\alpha + \delta_e) - 12(0.25\alpha + \delta_e)^3 + 0.1\delta_e]\} \\
\dot{\theta} &= q \\
\dot{q} &= \frac{50.1}{127512}m\cos\theta - \frac{171.1125(4\alpha - 12\alpha^3)}{127512}\bar{q}W\cos\alpha - \frac{50494.752}{127512}q + \frac{\bar{q}}{127512}\{2.025(4\alpha - \\
&\quad -12\alpha^3)W\cos\alpha - 42.1341\cos(0.25\alpha + \delta_e)[4(0.25\alpha + \delta_e) - 12(0.25\alpha + \delta_e)^3 + \\
&\quad +0.1\delta_e]\}
\end{aligned} \tag{12}$$

2.2. Wind gusts model

To simulate the wind action in a given direction, it is divided into two parts, a floating parcel and an average parcel. According to the proposed method, the average parcel is applied statically to the body exposed to the wind and the floating portion is divided into series of harmonic components with random phase angles.

The study is based on the Wind Speed Power Spectral Density [6-12]. For the floating part, it was used n harmonic components, where it is proposed the excitation of the random part as a superposition of n harmonic components, according to Eq. (13).

$$Sg = \frac{1}{n}\sum_{k=1}^{n} C_k \cos(2\pi f_k t) \tag{13}$$

Being that $n = 6$ and the amplitude C and frequency f of each of the components are given through Table 2 [11].

Table 2. Data of the wind [11]

$C\ (m)$	$f\ (Hz)$
10.0	0.25
14.0	0.40
18.0	0.60
22.0	0.80
26.0	1.00
30.0	1.19

The velocity considering the two parts, fixed and floating, is given by Eq. (14) and the dynamic pressure in which is directly induced into the system of Eqs. (12) is given by Eq. (15).

$$\mathrm{V(t)} = V_0 + Sg \tag{14}$$

$$\bar{q} = \frac{1}{2}\rho V(t)^2 \tag{15}$$

2.3. Numerical Simulations

The numerical simulations of the nonlinear dynamics of the aircraft considers the model of wind gusts as the excitation of the system. The system of Eq. (12) with Eqs. (14) and (15) will be integrated by using the 4th order Runge-Kutta method. The parameters to be considered, besides Tabs. 1 and 2, are considered $V_0 = 277.7\ m/s$, the initial mass of the aircraft given by $m = 9773\ Kg$ and atmospheric density to 9144 meters of altitude $\rho = 0.4938$. The initial conditions are $u = 257.7\ m/s$, $\alpha = 0.24\ rad$, $\theta = 0.23\ rad$, $q = 0\ rad/s$ and $\delta_e = -0.1\ rad$ [10].

Figures 3 show the time histories of all coordinates of the system that are the velocity of the aircraft in Fig. 3a, angle of attack in Fig. 3b, pitch angle in Fig. 3c and rate of pitch in Fig. 3d.

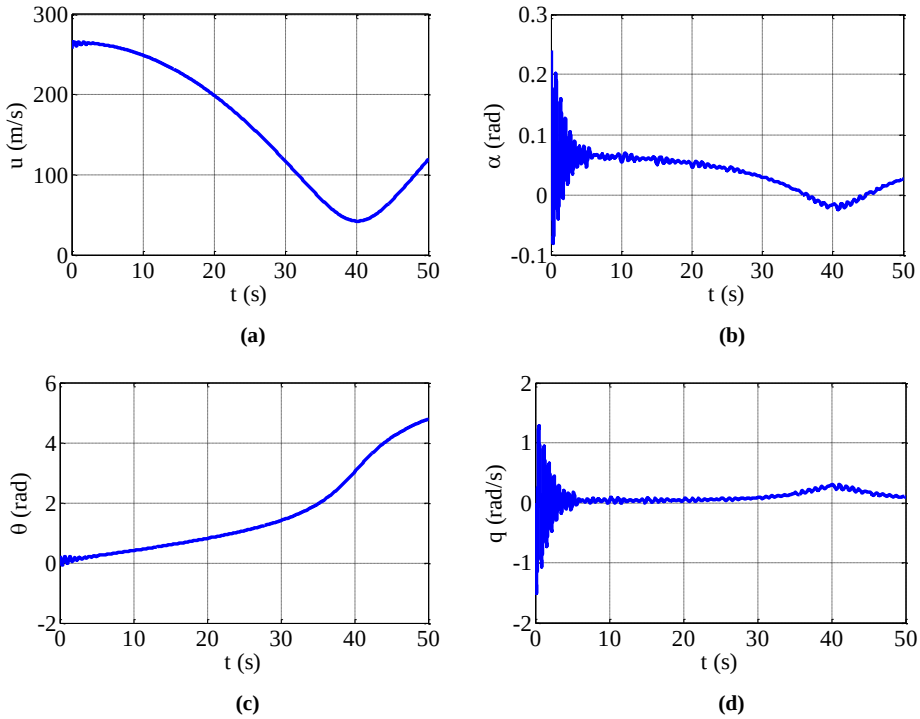

Figure 3. Time histories of **(a)** aircraft's speed, **(b)** angle of attack of the aircraft, **(c)** aircraft's pitch angle, **(d)** aircraft's rate of pitch.

In order to analyse the behaviour of the system, the 0-1 test was performed to determine if the system is chaotic or periodic. The 0-1 test for chaos takes as input a time series of measurements and returns a single scalar value of either 0 for periodic attractors or 1 for chaotic attractors [3-14]. According to the methodology presented in [5], the 0-1 test was applied for the coordinates u and α, resulting the values of 0.85 and 0.83 for each variable, respectively, demonstrating that the studied system is characterized as chaotic. As chaos is undesired to the aircraft for it may difficult the flight or even damage the aircraft, a control design is proposed and discussed in the next section.

3. Proposed control

The dynamic system defined by Eq. (12) with a control signal (U) can be parameterized in first order equations and written in the state dependent coefficient (SDC) form [8]:

$$\dot{x} = A(x)x + BU \tag{16}$$

A state feedback rather than output feedback is adopted to enhance the control performance. The non-quadratic cost function for the regulator problem is given by [13]:

$$J = \frac{1}{2}\int_{t_0}^{\infty} [x^T Q(x)x + U^T R(x)U]dt \tag{17}$$

where $Q(x)$ is semi-positive-definite matrix and $R(x)$ positive definite. There are weighting matrices on the outputs and control inputs, respectively. For a pointwise linear fashion, the matrices are assumed as constant control coefficients. Assuming full state feedback, the control law is given by [9]:

$$U = -R^{-1}(x)B^T(x)P(x)x \tag{18}$$

The state dependent Riccati equation (SDRE control) to obtain $P(x)$, is given by [13]:

$$A^T(x)P(x) + P(x)A(x) - P(x)B(x)R^{-1}(x)B^T(x)P(x) + Q(x) = 0 \tag{19}$$

Equation (16) is controllable if the rank of the matrix M is n, as follows [13]:

$$M = \lfloor B \;\; A_{nxn}B \;\; \ldots \;\; A_{nxn}^{n}B \rfloor \tag{20}$$

The SDRE technique to obtain a suboptimal solution for dynamic control problem has the following procedure [13]:

Step 1. Define the state-space model with the state dependent coefficient form as in Eq.(16).

Step 2. Define $x(0) = x_0$, so that the rank of M is n and choose the coefficients of weight matrices Q and R.

Step 3. Solve the Riccati Eq. (19) for the state $x(t)$.

Step 4. Calculate the input signal from Eq. (18).

Step 5. Integer the Eq. (16) and update the state of the system $x(t)$ with this results.

Step 6. Calculate the rank of Eq. (20), if $rank = n$ go to step 4. If $rank < n$, using the last matrix A controllable obtained, and go step 4.

3.1. Deflection angle of the horizontal tail as control parameter

The deflection angle of the horizontal tail is used as a control actuator to mitigate and recover the airplane from different flight situations and maneuvers that request a wing angle of attack higher than its stall angle. From the flight dynamics described in Eq. (12), some mathematical manipulations were carried out to obtain the state matrices of control, where it was consider:

$$\begin{aligned} &\tan\alpha \cong \alpha + \frac{\alpha^3}{3} \\ &\sin\alpha \cong \alpha - \frac{\alpha^3}{6}\ ,\ \sin\theta \cong \theta - \frac{\theta^3}{6} \text{ and } \sin\delta_e \cong \delta_e - \frac{{\delta_e}^3}{6} \\ &\cos\alpha \cong 1 - \frac{\alpha^2}{2}\ ,\ \cos\theta \cong 1 - \frac{\theta^2}{2} \text{ and } \cos\delta_e \cong 1 - \frac{{\delta_e}^2}{2} \end{aligned} \tag{21}$$

where the terms $\alpha^n, \theta^n, {\delta_e}^n$ with $n = 2,3,4, \ldots$ and ${\alpha^n \delta_e}^m$ with $n, m = 1,2,3,4, \ldots$ are eliminated, since these terms are small and they can be adopted by this simplification. In this way, it has:

$$\begin{aligned}
\dot{u} &= uq\alpha - 10\theta \\
\dot{\alpha} &= q + \left(\frac{10}{u}\right)\alpha\theta + 8.41\frac{\bar{q}}{mu}\alpha + 34.481\frac{\bar{q}}{mu}\delta_e \\
\dot{\theta} &= q \\
\dot{q} &= \frac{50.1}{127512}m - \frac{50494.752}{127512}q - \frac{42.1341}{127512}\bar{q}\alpha - \frac{172.7498}{127512}\bar{q}\delta_e
\end{aligned} \tag{22}$$

where $u = x_1, \alpha = x_2, \theta = x_3$ and $q = x_4$, and for the control signal we have $\delta_e = U$. From Eq. (16) and considering Eq. (22) the state matrices of control are given by

$$A(x) = \begin{bmatrix} 0 & x_1 x_4 & -10 & 0 \\ 10/{x_1}^2 & \frac{8.41\bar{q}}{mx_1} & \frac{10x_2}{x_1} & 1 \\ 0 & 0 & 0 & 1 \\ 0 & -0.000331\bar{q} & 0 & -0.396 \end{bmatrix}; B = \begin{bmatrix} 0 \\ 34.481 \\ 0 \\ -0.001354\bar{q} \end{bmatrix} \tag{23}$$

Defining:

$$x^* = \begin{bmatrix} x_1 \\ 0.04 \\ x_3 \\ x_4 \end{bmatrix}; Q = 0.1\begin{bmatrix} 1 & 10 & 0 & 0 \\ 10 & 100 & 0 & 0 \\ 0 & 0 & 1 & 0 \\ 0 & 0 & 0 & 1 \end{bmatrix} \text{ and } R = [1000] \tag{24}$$

where x^* represents the desired states, Q and R are the matrices of Eq. (17), used in the calculation of the matrix of Riccati Eq. (19).

4. Results and discussion

As previously proposed, the angle of attack will be varied with values above the stall angle to verify the efficiency of the controller applied in recovering and stabilizing the aircraft during the flight. In this way, some parameters are fixed for the simulations, being: $V_0 = 277.7\ m/s$, the initial mass of the aircraft given by $m = 9773\ Kg$, atmospheric density to 9144 meters of altitude $\rho = 0.4938$ and the stall situation occurs in the F-8 "crusader" with an angle of attack of $0.41\ rad$ $(23{,}5°\ deg)$. For a first case, the following initial conditions were considered for the system of Eq. (12) that are $u = 257.7\ m/s,\ \alpha = 0.54\ rad,\ \theta = 0.53\ rad,\ q = 0\ rad/s$, and for the case without control $\delta_e = -0.1\ rad$ and $\delta_e = U$ for the case with control. Figures 4 and 5 show the time histories of velocity, angle of attack, pitch angle and rate of pitch with control (With C. in red) and without the influence of the control (Without C. in blue).

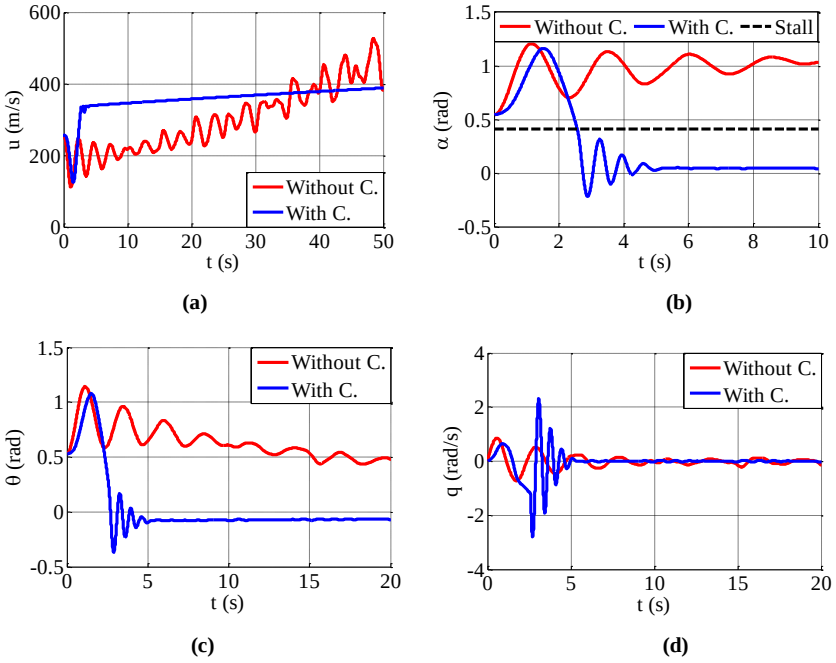

Figure 4. Time histories with control (in blue) and without control (in red) of **(a)** aircraft's speed, **(b)** angle of attack of the aircraft, **(c)** aircraft's pitch angle, **(d)** aircraft's rate of pitch.

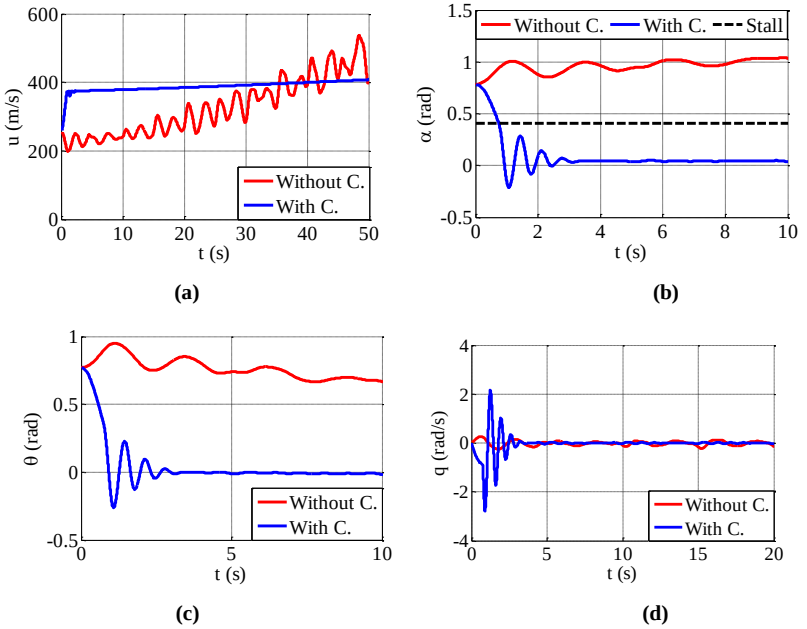

Figure 5. Time histories with control (in blue) and without control (in red) of **(a)** aircraft's speed, **(b)** angle of attack of the aircraft, **(c)** aircraft's pitch angle, **(d)** aircraft's rate of pitch

In Figure 4b is observed the efficiency of the control in recovering the aircraft of an angle of attack of $\alpha = 0.54\,rad$ $(30{,}1°\,deg)$, above the angle of stall of the aircraft, which is $0.41\,rad$ $(23{,}5°\,deg)$, in a time less than 4 seconds, making possible for the aircraft to resume lift and maintain flight balance as can be observed in the Figs. 4a, 4c and 4d. For the second case, the aircraft is considered under an even more adverse environment for the flight, thus, it is considered the following initial conditions for the system of Eq. (12), $u = 257.7\,m/s$, $\alpha = 0.78\,rad$, $\theta = 0.77\,rad$, $q = 0\,rad/s$, for the case without control $\delta_e = -0.1\,rad$ and $\delta_e = U$ for the case with control.In Figure 5b is observed the efficiency of the control in recovering the aircraft of an angle of attack of $\alpha = 0.78\,rad$ $(44{,}7°\,deg)$, higher than the angle of stall of the aircraft of $0.41\,rad$ $(23{,}5°\,deg)$, in a time less than 4 seconds, making possible for the aircraft to resume lift and maintain flight balance as can be seen in Figs. 5a, 5c and 5d. These values of angle of attack were the maximum parameters that the controller was effective, values above of those presented in this second case were not effective in controlling the system.

5. Conclusions

The results presented in this paper indicated that the designed control can lead to significant improvements in aircraft performance. When placed in flight conditions with angle of attack above the stall situation and influenced by the model of wind gusts, is was shown that the control was able to soften and maintain the flight conditions in equilibrium for an angle of attack up to 90% above the stall angle.

For future a work, there is the objective of modeling and coupling the transversal dynamical equations of the aircraft, using as an excitation a wind gust model with two-degrees-of-freedom, and thus design the control for the new considered system.

Acknowledgments

The authors acknowledge support by CNPq (GRANT:306525/2015-1) and (GRANT:447539/2014-0), CAPES and FAPESP (GRANT 2015/20363-6) both Brazilian research funding agencies.

References

[1] Abed, E. H., Lee, H. C. Nonlinear Stabilization of High Angle-of-Attack Flight Dynamics Using Bifurcation Control. Proceedings of the 1990 American Control Conference, IEEE Publications, Piscataway, NJ, 1990, pp.2235 – 2238.

[2] Etkin, B., "Dynamics of Atmospheric Flight". John Wiley, New York, 1972.

[3] Felix, J. L. P., Silva, E. L., Balthazar, J. M., Tusset, A. M., Bueno, A. M., and Brasil, R. M. L. R. F. Onnonlinear dynamics and control of a robotic arm with chaos. MATEC Web of Conferences (05002), 2014, pp.1-16.

[4] Garrard, W.L., Jordan, J.M. Design of Nonlinear Automatic Flight Control Systems. Automatica, v.13, nº 5. Pergamon Press, 1977, pp. 497–505.

[5] Gopal, R., Venkatesan, A., and Lakshmanan, M. Applicability of 0-1 test for strange nonchaotic attractors, Chaos 23 (023123), 2013, pp. 1-15.

[6] Kanai, K. Semi-empirical formula for the seismic characteristic of the ground. Bulletin of Earthquake Research Institute, Tokyo, v. 35, 1957, pp.309-325.

[7] Liaw, D. C., Song, C. C. Analysis of Longitudinal Flight Dynamics: A Bifurcation-Theoretic Approach. Journal of Guidance, Control and Dynamics. Vol. 24, nº 1, 2001, pp. 109 – 116.

[8] Molter, A., Silveira, O. A. A., Fonseca, Jun S. O., Bottega, V. Simultaneous Piezoelectric Actuator and Sensor Placement Optimization and Control Design of Manipulators with Flexible Links Using SDRE Method. Mathematical Problems in Engineering, 2010, pp.1-23.

[9] Nozaki, R., Balthazar, J. M., Tusset, A. M., Pontes, B. R., Bueno, A. M. Nonlinear Control System Applied to Atomic Force Microscope Including Parametric Errors. Journal of Control, Automation and Electrical Systems, v. 24, 2013, pp. 223-231.

[10] Pereira, D. C. Non linear dynamics and control of an aircraft in longitudinal flight. Doctoral. thesis, University of Campinas, 2007. José Manoel Balthazar.

[11] Smith, M. S. Analysis of wind tunnel oscillatory data of the X-31A aircraft. NASA. The George Washington University. Institute for Advancement of Flight Sciences Langley Research Center, Hampton, Virginia, 1999, pp.1-111.

[12] Tajimi, H. A statistical method of determining the maximum response of a building structure during an earthquake. In: World Conference on Earthquake Engineering, 2, Japan: WCEE, 1960, pp. 781-797.

[13] Tusset, A. M. et al. Slewing control of flexible space structures: on state dependent ricatti equations approach. XXXIV Iberian Latin-American Congress on Computational Methods in Engineering, CILAMCE, 2013, pp. 1-16.

[14] Tusset, A. M., Piccirillo, V., Balthazar, J. M., and Brasil R. M. R. F. On Suppression of chaotic motions of a portal frame structure under non-ideal loading using a magneto-rheological damper. Journal of Theoretical and Applied Mechanics,53 (3), 2015, pp. 653-664.

Guilherme Pacheco dos Santos, B.A.: Federal University of Technology - Paraná (UTFPR), Ponta Grossa, PR, BRAZIL (guipacheco37@gmail.com).

Jose Manoel Balthazar, Professor: Aeronautics Technological Institute (ITA), São José dos Campos, SP, BRAZIL (jmbaltha@gmail.com). The author gave a presentation of this paper during one of the conference sessions.

Frederic Conrad Janzen, Assistant Professor: Federal University of Technology - Paraná (UTFPR), Ponta Grossa, PR, BRAZIL (fcjanzen@utfpr.edu.br).

Rodrigo Tumolin Rocha, Ph.D.: Federal University of Technology - Paraná (UTFPR), Ponta Grossa, PR, BRAZIL (digao.rocha@gmail.com).

Airton Nabarrete, Assistent Professor: Aeronautics Technological Institute (ITA), São José dos Campos, SP, BRAZIL (profnabarrete@gmail.com).

Angelo Marcelo Tusset, Assistant Professor: Federal University of Technology - Paraná (UTFPR), Ponta Grossa, PR, BRAZIL (tusset@utfpr.edu.br).

Transient dynamics of impacting beams with lost connection

Larysa Dzyubak, Atul Bhaskar

Abstract: The study of transient dynamics of impacting beams with lost connections is associated with problems of chaotic vibrations and noise generation in bolted and riveted structures with loose fastening. Analytical solutions, describing the transient dynamics of two cantilever beams under harmonic excitation with tips separated by clearance, are obtained. They are presented as a superposition of particular solutions that satisfy inhomogeneous boundary conditions, and the eigenfunctions series with time dependent coefficients and homogeneous boundary conditions. The switch conditions between impact and out-of-contact phases are based on expressions for shear forces and relative position of beam tips. The system of the impacting beams reveals complex dynamics, including chaotic behaviour. Transient dynamics surfaces, time histories of beams deflections, impact forces, coefficients of restitution, and phase planes are presented. Intensive impacts of beam tips are observed in both cases at zero and non-zero clearance.

1. Introduction

Problems related to vibro-impact dynamics of structures are of great interest in mechanical or mechatronic engineering [1, 2]. The dynamics of two impacting beams with clearance nonlinearity can be associated with the study of vibrating bolted and riveted structures with loose fastening, noise generation and chaotic vibrations due to lose connections between structural elements as well as it can be applied to design of impact dampers employing attached flexible beam/beams. In numerous cases non-linear effects caused by clearance may lead to many undesirable effects, in particular to premature failure of structures.

2. Mathematical model

The transient dynamics of two impacting cantilever Euler-Bernoulli beams with tips separated by clearance Δ is depicted schematically in Fig. 1. The tips of the beams impact when beam 1 is harmonically excited by a force $F(t)$. l_1 and l_2 are lengths of the beams, and δ_1, δ_2 are the initial uplifts at the free ends. The two beams are not allowed to cross each other at their tips, that is $y_1(l_1,t) \geq y_2(l_2,t)-\Delta$ always. After the impact-induced phase, they must separate in opposite directions. This interaction of the two beams is governed by the partial differential equations

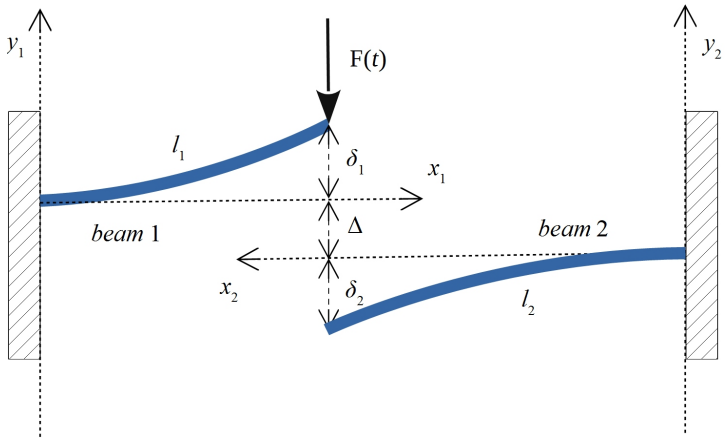

Figure 1. Impacting beams under harmonic excitation.

$$a_1^2\frac{\partial^4 y_1(x_1,t)}{\partial x_1^4}+\frac{\partial^2 y_1(x_1,t)}{\partial t^2}=0\ ,\ \ a_2^2\frac{\partial^4 y_2(x_2,t)}{\partial x_2^4}+\frac{\partial^2 y_2(x_2,t)}{\partial t^2}=0 \tag{1}$$

with different set of boundary conditions for the impact phase and for the out-of-contact phase. For the impact phase the boundary conditions are

$$y_1(0,t)=0\ ,\ \ y_2(0,t)=0\ ,\ \ \frac{\partial y_1(0,t)}{\partial x_1}=0\ ,\ \ \frac{\partial y_2(0,t)}{\partial x_2}=0\ , \tag{2}$$

$$M_1(l_1,t)=E_1I_1\frac{\partial^2 y_1(l_1,t)}{\partial x_1^2}=0\ ,\ \ M_2(l_2,t)=E_2I_2\frac{\partial^2 y_2(l_2,t)}{\partial x_2^2}=0\ , \tag{3}$$

$$Q_1(l_1,t)=E_1I_1\frac{\partial^3 y_1(l_1,t)}{\partial x_1^3}=Q_2(l_2,t)+F(t)=E_2I_2\frac{\partial^3 y_2(l_2,t)}{\partial x_2^3}+F(t)\ , \tag{4}$$

$$y_1(l_1,t)=y_2(l_2,t)-\Delta\ . \tag{5}$$

Here E_i,I_i,ρ_i,A_i are the Young modulus, area moment of inertia, mass density and cross-section of i-th beam, $a_i=\sqrt{E_iI_i/\rho_iA_i}$, i=1,2. Boundary conditions (2), (3) are identical for the impact and out-of-contact phases. Conditions (2) correspond to fixed both the position and slope of the cantilever beams at points x_1=0 and x_2=0. Since no external bending moments are applied at the beam tips $x_1=l_1$ and $x_2=l_2$, the bending moments $M_1(x_1,t)$ and $M_2(x_2,t)$ at that locations are zero (conditions (3)). The shearing force $Q_1(x_1,t)$ at the tip $x_1=l_1$ is equal to the sum of the applied force $F(t)$ and the reaction force $Q_2(x_2,t)$ at the tip $x_2=l_2$ (condition (4)). Condition (5) is the necessary and sufficient condition for beam tips to be in contact. In the out-of-contact case boundary conditions (4) and (5) are replaced by boundary conditions

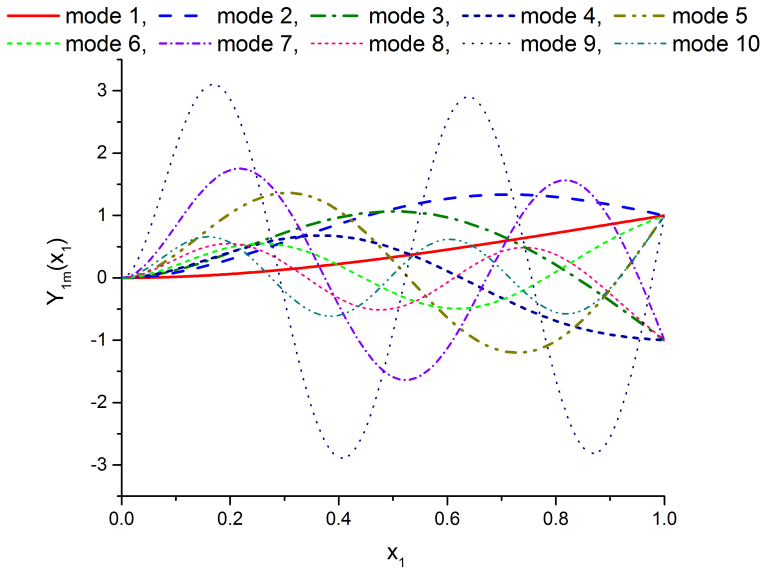

(a)

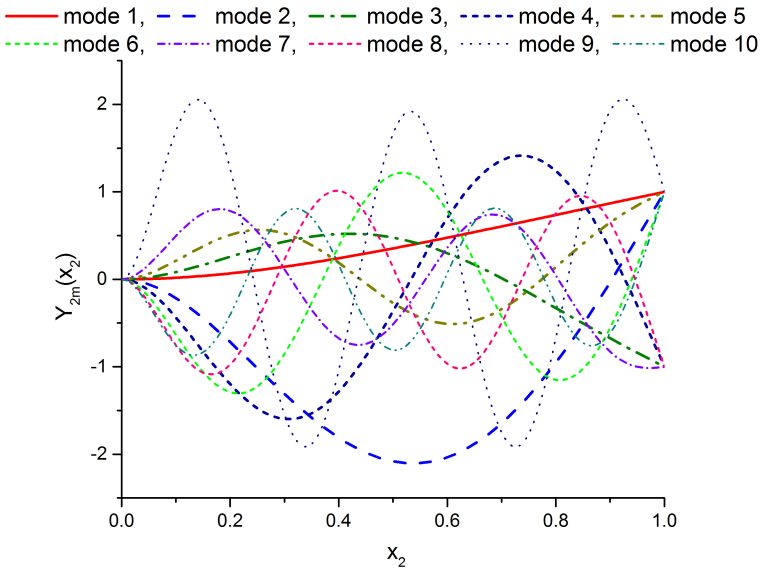

(b)

Figure 2. Normalized in-contact mode shapes (a) Y_{1m} of the 1st vibrating cantilever beam, (b) Y_{2m} of the 2nd vibrating cantilever beam.

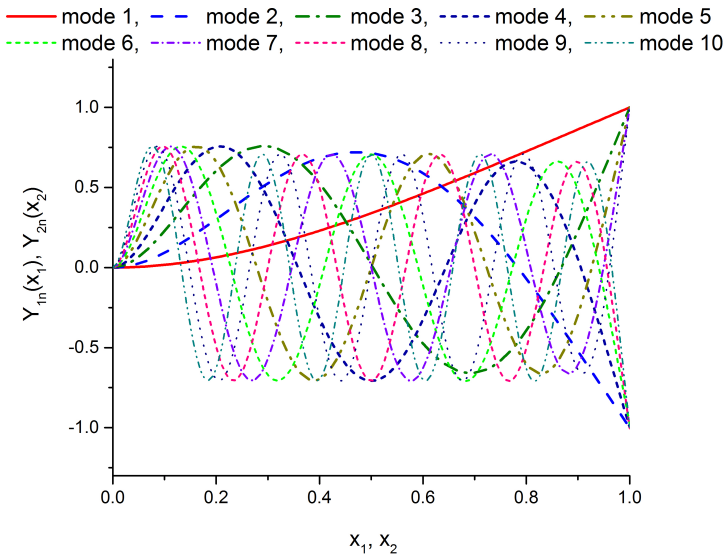

Figure 3. Normalized out-of-contact mode shapes Y_{1n}, Y_{2n} of the vibrating cantilever beams.

$$Q_1(l_1,t)=E_1I_1\frac{\partial^3 y_1(l_1,t)}{\partial x_1^3}=F(t),\quad Q_2(l_2,t)=E_2I_2\frac{\partial^3 y_2(l_2,t)}{\partial x_2^3}=0. \tag{6}$$

The discretization of the system is based on the eigenvalue problem that gives infinite number of beam natural frequencies, as well as mode shapes for the cases of impact phase and out-of-contact phase.

2.1. Impact phase

Expressions of transient dynamics (functions $y_1(x_1,t)$ and $y_2(x_2,t)$) are presented as a superposition of particular solutions $y_{1s}(x_1,t)$ and $y_{2s}(x_2,t)$ that satisfy to inhomogeneous boundary conditions, and eigenfunctions series with time dependent coefficients and homogeneous boundary conditions:

$$y_1(x_1,t)=y_{1s}(x_1,t)+\sum_{m=1}^{\infty}Y_{1m}(x_1)q_m(t)\ ,\ \ y_2(x_2,t)=y_{2s}(x_2,t)+\sum_{m=1}^{\infty}Y_{2m}(x_2)q_m(t) \tag{7}$$

Expressions for the particular solutions are obtained in the form:

$$y_{1s}(x_1,t)=\frac{1}{6}\frac{3E_2I_2\Delta-l_2^3F(t)}{E_2I_2l_1^3-E_1I_1l_2^3}\left(x_1^3-3l_1x_1^2\right)\ ,\ \ y_{2s}(x_2,t)=\frac{1}{6}\frac{3E_1I_1\Delta-l_1^3F(t)}{E_2I_2l_1^3-E_1I_1l_2^3}\left(x_2^3-3l_2x_2^2\right)\ . \tag{8}$$

The corresponding natural frequencies of vibration $\omega_{1m}=\omega_{2m}$, $\omega_{1m}=a_1k_{1m}^2$, $\omega_{2m}=a_2k_{2m}^2$ are defined from the equation that follows by conditions for the existence of non-trivial solutions

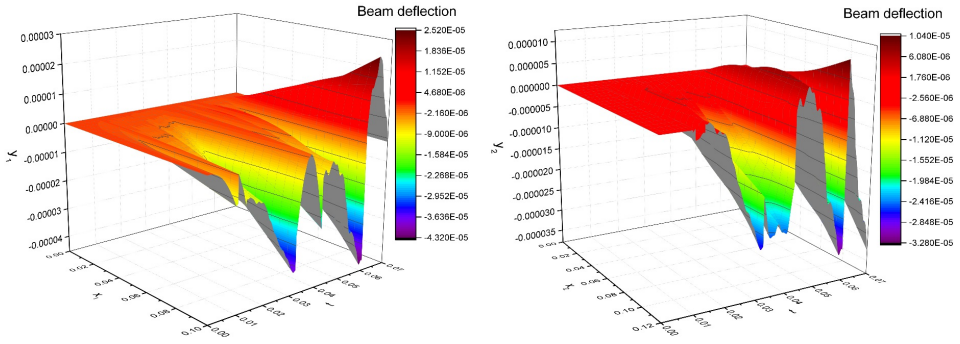

(a) (b)

Figure 4. Beam deflections surfaces depending on time and the lengths: (a) $y_1(x_1,t)$ for the first beam; (b) $y_2(x_2,t)$ for the second beam at A=0.0005, w=40, l_1=0.1, l_2=0.12, δ_1= δ_2=0.0, Δ=0.000011, Δt=0.0001, 0<t<0.07.

$$E_1 I_1 k_{1m}^3 \left(1+\cos k_{1m} l_1 \cosh k_{1m} l_1\right)\left(\cosh k_{2m} l_2 \sin k_{2m} l_2 - \cos k_{2m} l_2 \sinh k_{2m} l_2\right) +$$
$$E_2 I_2 k_{2m}^3 \left(1+\cos k_{2m} l_2 \cosh k_{2m} l_2\right)\left(\cosh k_{1m} l_1 \sin k_{1m} l_1 - \cos k_{1m} l_1 \sinh k_{1m} l_1\right)=0. \quad (9)$$

So, as it follows by the eigenvalue problem, the mode shapes in the impact phase are represented by the expressions:

$$Y_{1m}=A_m\left[\sin k_{1m} x_1 - \sinh k_{1m} x_1 + \frac{\sin k_{1m} l_1 + \sinh k_{1m} l_1}{\cos k_{1m} l_1 + \cosh k_{1m} l_1}\left(\cosh k_{1m} x_1 - \cos k_{1m} x_1\right)\right],$$
$$Y_{2m}=A_m \frac{E_1 I_1 k_{1m}^3 \left(1+\cos k_{1m} l_1 \cosh k_{1m} l_1\right)}{E_2 I_2 k_{2m}^3 \left(\cos k_{1m} l_1 + \cosh k_{1m} l_1\right)\left(1+\cos k_{2m} l_2 \cosh k_{2m} l_2\right)} \times$$
$$\left[\left(\cos k_{2m} l_2 + \cosh k_{2m} l_2\right)\left(\sin k_{2m} x_2 - \sinh k_{2m} x_2\right) + \left(\sin k_{2m} l_2 + \sinh k_{2m} l_2\right)\left(\cosh k_{2m} x_2 - \cos k_{2m} x_2\right)\right]. \quad (10)$$

The time dependent coefficients are defined as follows

$$q_m(t)=q_m(0)\cos \omega_m t + \frac{1}{\omega_m}\dot{q}_m(0)\sin \omega_m t + \frac{1}{\omega_m}\int_0^t \ddot{\psi}_m(\tau)\sin(t-\tau)\,d\tau\ . \quad (11)$$

In Fig. 2 the normalized in-contact mode shapes Y_{1m} , Y_{2m} of the first and the second vibrating cantilever beams are depicted.

2.2. Out-of-contact phase

In this case the motions of the beams don't depend on each other. Natural frequencies $\omega_{1n}=a_1 k_{1n}^2$,

$\omega_{2n}=a_2 k_{2n}^2$ are defined for both beams from equations: $\cos(k_{in} l_i)\cosh(k_{in} l_i)+1=0$, i=1,2.

Expressions for functions $y_1(x_1,t)$ and $y_2(x_2,t)$ are presented as a superposition of particular solutions $y_{1s}(x_1,t)= -F(t)\left(3 l_1 x_1^2 - x_1^3\right)/6 E_1 I_1$ and $y_{2s}(x_2,t)=0$ that satisfy to inhomogeneous boundary conditions, and eigenfunctions series with time dependent coefficients and homogeneous boundary conditions:

$$y_1(x_1,t)=y_{1s}(x_1,t)+\sum_{n=1}^{\infty} Y_{1n}(x_1) q_{1n}(t)\ ,\ \ y_2(x_2,t)=\sum_{m=1}^{\infty} Y_{2n}(x_2) q_{2n}(t)\ , \tag{12}$$

the mode shapes in the out-of-contact phase are represented by the expressions:

$$Y_{1i}=A_{1i}\left[\sin k_{in} x_1-\sinh k_{in} x_1+\frac{\sin k_{in} l_1+\sinh k_{in} l_1}{\cos k_{in} l_1+\cosh k_{in} l_1}\left(\cosh k_{in} x_1-\cos k_{in} x_1\right)\right]\ , \ i=1,2. \tag{13}$$

The time dependent coefficients are defined as follows

$$q_{1n}(t)=q_{1n}(0)\cos\omega_{1n} t+\frac{1}{\omega_{1n}}\dot{q}_{1n}(0)\sin\omega_{1n} t+\frac{1}{\omega_{1n}}\int_0^t \ddot{\psi}_{1n}(\tau)\sin(t-\tau)\,d\tau\ ,\ +$$

$$q_{2n}(t)=q_{2n}(0)\cos\omega_{2n} t+\frac{1}{\omega_{2n}}\dot{q}_{2n}(0)\sin\omega_{2n} t\ . \tag{14}$$

In Fig. 3 the normalized out-of-contact mode shapes Y_{1n}, Y_{2n} of the first and the second vibrating cantilever beams are depicted.

2.3. Switching between phases

The transition from impact phase to out-of-contact phase and vice versa is implemented using conditions that switch, involving construction of expressions for shear forces and relative position of beam tips.

out-of-contact phase → impact phase transition:

$$y_2(l_2,t)-y_1(l_1,t)=\Delta\ ,\ \frac{d}{dt}\left(y_2(l_2,t)-y_1(l_1,t)\right)\geqslant 0 \tag{15}$$

impact phase → out-of-contact phase transition:

$$P(t)=0,\ \ \frac{dP(t)}{dt}\leqslant 0,\ \text{where}\ \ P(t)=E_1 I_1\frac{\partial^3 y_1(l_1,t)}{\partial x_1^{\,3}}-F(t)\ . \tag{16}$$

After each transition from one phase to another, the functions describing the time dependent coefficients in the eigenfunctions series are updated. This update involves the solution of ordinary differential equations with initial conditions corresponding to the end of the previous phase.

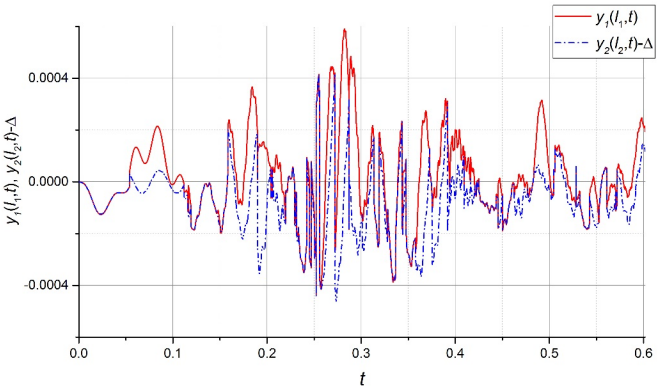

(a)

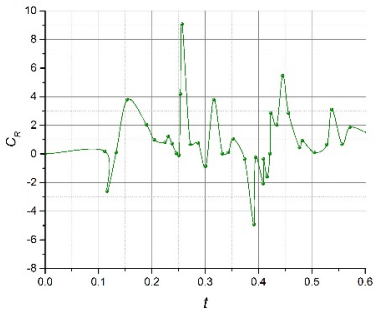

(b)

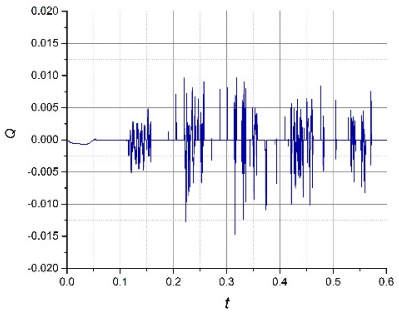

(c)

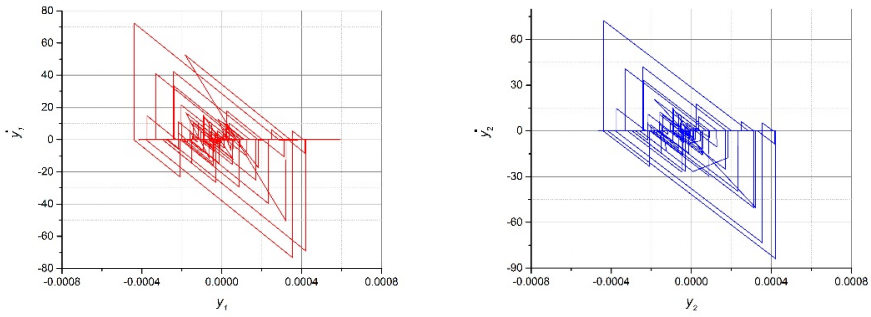

(d)

Figure 5. Clearance between beams is equal to zero: (a) Beams deflections $y_1(l_1,t)$, $y_2(l_2,t)$-Δ; (b)Coefficient of restitution C_R of impacting beams; (c) Impact-induced force Q; (d) phase planes at A=0.002, ω=60, l_1=0.1, l_2=0.12, δ_1= δ_2=0.0, Δ=0.0, Δt=0.00001, 0<t<0.6.

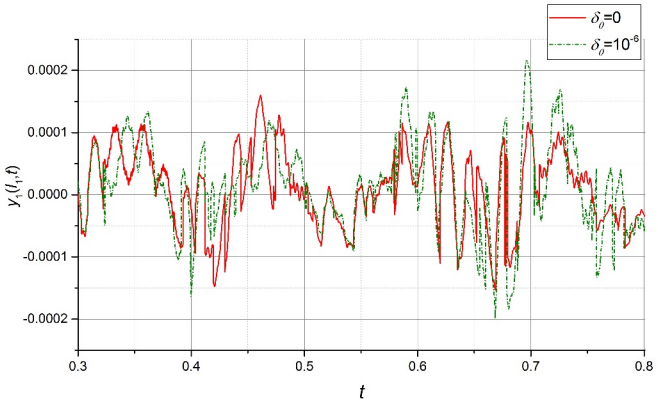

(a)

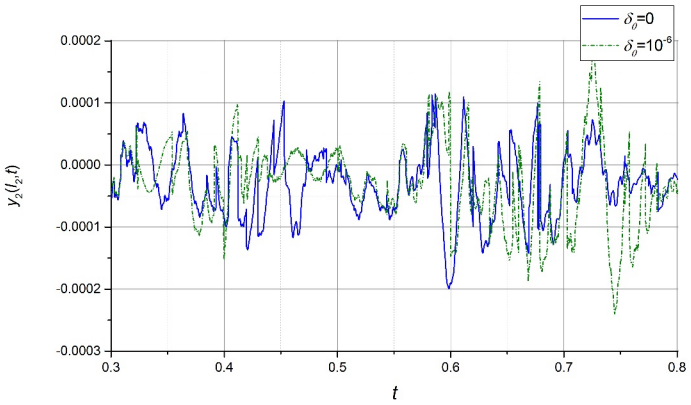

(b)

Figure 6. Chaotic motion (a) of the 1st and (b) of the 2nd impacting beam; Nearby trajectories $y_1(l_1,t)$ and $y_2(l_2,t)$ diverge exponentially; δ_0 is the initial uplift at the free end; A=0.001, ω=50, l_1=0.1, l_2=0.12, δ_1=0 and δ_1=10^{-6}, δ_2=0.0, Δ=0.000011, Δt=0.00001, 0<t<0.8.

3. Graphical representation of the analytical solutions obtained

The solutions obtained were tested on numerous examples with various set of parameters. Convergence of eigenfunction series as well as convergence of the solutions in time were investigated. Terms of eigenfunction series with time dependent coefficients evaluated at the tips in the case of out-of-contact phase $y_{1s}(l_1,t)$, $Y_{1n}(l_1)q_{1n}(t)$, $Y_{2n}(l_2)q_{2n}(t)$ (n=1,2,3,4,5) and in the case of impact phase $y_{1s}(l_1,t)$, $Y_{1m}(l_1)q_{1m}(t)$, $y_{2s}(l_2,t)$, $Y_{2m}(l_2)q_{2m}(t)$ (m=1,2,3,4,5) were seen to be fast decreasing.

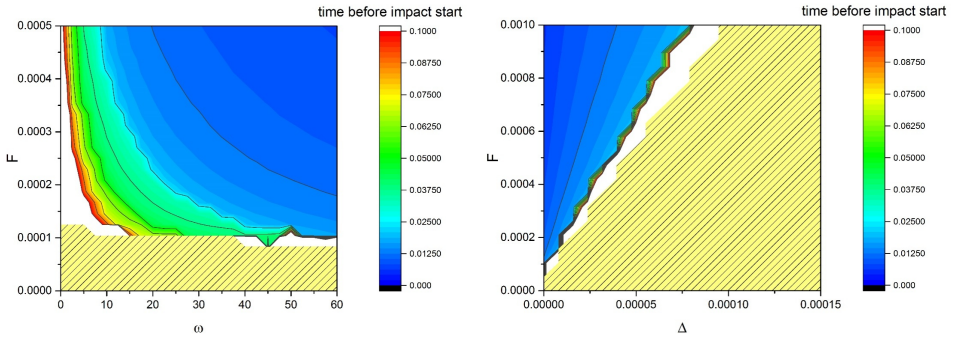

Figure 7. Timebefore impact start as function of (a) frequency and amplitude of external excitation (ω, F); (b) clearance and amplitude of external excitation (Δ, F).

The solutions with truncated eigenfunction series at n=4, m=4 and at n=5, m=5 are almost identical. A necessary convergence of the solutions in time was reached by an appropriate choice of time steps. So, the time step is chosen correctly if the solutions obtained with this time step and with the doubled time step are identical.

Several examples were considered for various set of parameters. Intensive impacts of beam tips are observed in both cases at zero and non-zero clearance. In Fig. 4 the beam deflections surfaces vs time and length for the first beam and for the second beam are shown. Fig. 5 represents beams deflections $y_1(l_1,t)$, $y_2(l_2,t)$-Δ, coefficient of restitution of impacting beams and the impact-induced force at amplitude and frequency of external harmonic excitation A=0.002 and ω=60, initial uplifts δ_1=δ_2=0.0, zero clearance Δ=0.0, a_1=0.7, a_2=0.7, time instant is $0\le t\le 0.6$. Such time instant is chosen for convenience to observe the dynamics of the beams. During numerical experiment long term solutions were constructed for $0\le t\le 30$ and more. Fig. 6 shows exponential divergence of (a) nearby trajectories $y_1(l_1,t)$, (b) nearby trajectories $y_2(l_2,t)$ with very close initial uplifts δ_1=δ_2=0.0 and $\delta_1=10^{-6}$, δ_2=0.0. It is sure sign of chaotic vibrations of the beams. In Fig. 7 contours describing time before impact start are plotted in control parameter planes (ω, F) and (Δ, F). Areas with hatch fill correspond to vibrations without any impact. initial uplifts δ_1=δ_2=0.0, clearance Δ=0.000011, a_1=0.7, a_2=0.7, time instant is $0\le t\le 0.6$. Such time instant is chosen for convenience to observe the dynamics of the beams.

4. Conclusions

The analytical solutions, describing the transient dynamics of two impacting beams with clearance nonlinearity, were obtained in the form of eigenfunctions series with time dependent coefficients. Several examples were considered for various set of parameters. Intensive impacts of beam tips are

observed in both cases at zero and non-zero clearance. Transient dynamics surfaces, time histories of beams deflections, impact forces, coefficients of restitution as well as phase planes and Poincare sections were presented. Chaotic behavior of the beams was ascertained on the base of sensitive dependence of the trajectories of motion on the initial conditions using procedure that similar to one presented in [3]. Time before impact start level contours were obtained in various control parameter planes (ω, F), (Δ, F) and (ω, Δ). Solutions obtained allow to construct long term vibrations of the impacting beams.

Acknowledgments

The authors acknowledge the use of the IRIDIS High Performance Computing Facility, and associated support services at the University of Southampton. This research received funding from the post doctorate exchange project in the field of Applied Mechanics at the Academic Unit of Aeronautics, Astronautics & Computational Engineering, Faculty of Engineering and the Environment, University of Southampton within the framework of the Erasmus Mundus Action 2 ACTIVE program.

References

[1] Yin, X.C., Qin, Y., Zou, H. Transient responses of repeated impact of a beam against a stop. *International Journal of Solids and Structures* 44, 2007, 7323–7339.

[2] Chen, L.A., Semercigil, S.E. A beam-like damper for attenuating transient vibrations of light structures. *Journal of Sound and Vibration* 164(1), 1993, 53-65.

[3] Awrejcewicz, J., Dzyubak, L.P. Chaos caused by hysteresis and saturation phenomenon in 2-dof vibrations of the rotor supported by the magneto-hydrodynamic bearing, *International Journal of Bifurcation and Chaos* 15(6), 2011, 2041-2055.

Larysa Dzyubak, Associate Professor: Department of Applied Mathematics, National Technical University, 2 Kyrpychova Str., 61002 Kharkiv, Ukraine (*dzyubak.larissa@interdiscipline.org*). The author gave a presentation of this paper during one of the conference sessions.

Atul Bhaskar, Professor: Faculty of Engineering and Environment, University of Southampton, Southampton SO16 7QF, United Kingdom (*a.bhaskar@soton.ac.uk*).

Vibrations of a cantilevered viscoelastic beam of a fractional derivative type with a tip mass and subjected to the base motion

Jan Freundlich

Abstract: The objective of the present study is vibration of the Bernoulli-Euler cantilevered beam carrying a tip mass subjected to a base motion. The tip mass centre of gravity coincide with the point of attachment. The viscolestic properties of the beam material are expressed in terms of a fractional Kelvin-Voigt model. The Riemann –Liouville fractional derivative of order $0 < \alpha < 1$ is used. Exact relationships for natural frequencies and mode shapes of the beam are derived. The forced-vibration solution of the beam is derived using the mode superposition method. Steady-state and transient vibrations analysis are presented. Transient movement of the base is expressed by a oscillating function with linearly time-varying frequency. A convolution integral of the fractional Green's function and forcing function is used to achieve the beam response. The Green's function is formulated by two terms. The first term describes damped vibrations around the drifting equilibrium position, while the second term describes the drift of the equilibrium position. The dynamic responses are numerically calculated. A comparison between results obtained using the fractional and integer viscoelastic material models is presented. In the analyzed system, the influence the term describing the drift of the equilibrium position on the beam deflection is relatively low and may be neglected in some cases. Achieved results show that an increase in the derivative order causes a decrease in vibration amplitudes of the beam.

1. Introduction

Cantilever beams with tip mass appear frequently in engineering practice and it can be used as simplified models of more complex structures [3, 8, 22, 23]. These elements during their operation are often subjected to oscillating load that can lead to undesirable their vibration. Moreover, machines often work above their first or subsequent resonance and therefore they must pass through one or more critical speeds during starting or stopping them. Therefore, the problem of determining the maximum amplitudes and stresses in the system due to the forced vibrations during operating in the steady and transient state is very important [7, 21]. This problem has many applications in engineering analysis; some of these applications are vibrations that occur in moving cranes, masts or high buildings [8, 11, 17, 22, 23]. This issue was studied by many authors for various configurations of the analyzed system. However, in many studies, some important topics such as the effect of damping on the system dynamics have been omitted. It is well know that the viscoelastic properties of

material could have significant effect on dynamic behaviour of the analysed system. For this reason, an appropriate viscoelastic material model ought to be used in dynamic analysis. A large number of engineering materials exhibit a weak frequency dependence of their damping properties within a broad frequency range [1, 5, 7]. This property is difficult to describe using classical viscoelastic models which are based on integer order rate laws [6, 15]. In the recent years, fractional derivatives have been increasingly used in modelling viscoelastic material properties [12, 15, 20]. Application of fractional-order derivatives allows for more accurate modeling viscoelastic material properties within a broad frequency range [2, 6].

2. Problem formulation

A cantilever beam carrying an element of mass m_p and moment of inertia I_B at the tip is analysed. The mass centre of the tip element is coincident with the beam end (Fig. 1). The uniform cross-section and mass density of the beam are assumed. The equation of motion of the analysed beam is derived using Bernoulli-Euler theory, i.e. neglecting rotary inertia and shear deformation. Beam motion is assumed to be in the xz plane and the gravitational force is perpendicular to the xz plane, therefore does not affect on the motion. The base motion is assumed only along z axis (Fig.1). Moreover, viscoelastic properties of a beam are described by the fractional Kelvin-Voigt model. This model is defined as follows [2, 15]

$$\sigma = E\varepsilon(t) + E'_\gamma \frac{d^\gamma \varepsilon(t)}{dt^\gamma} = E\left(\varepsilon + \mu_\gamma \frac{d^\gamma \varepsilon(t)}{dt^\gamma}\right), \tag{1}$$

where , $\mu_\gamma = \frac{E'_\gamma}{E}$, E is Young modulus of the beam material , E'_γ is damping coefficient, $\frac{d^\gamma}{dt^\gamma}$ is the Riemann-Liouville fractional derivative of order γ [18]

$$\frac{d^\gamma}{dt^\gamma} f(t) \equiv {}_0D_t^\gamma f(t) \equiv \frac{1}{\Gamma(m-\gamma)} \frac{d^m}{dt^m} \int_0^t \frac{f(\tau)d\tau}{(t-\tau)^{\gamma+1-m}}, \quad m-1 < \gamma \le m \tag{2}$$

where $\Gamma(m\text{-}\gamma)$ is Euler gamma function and $t \ge 0$

For many real materials , the fractional derivative order is commonly assumed to be in the range $0 < \gamma \le 1$ [2, 6]

Using assumptions above, the equation of forced transverse motion of the analysed beam is formulated as below

$$EJ\left(\frac{\partial^4 w(x,t)}{\partial x^4} + \mu_\gamma \frac{d^\gamma}{dt^\gamma}\left(\frac{\partial^4 w(x,t)}{\partial x^4}\right)\right) + A\rho \frac{\partial^2 w(x,t)}{\partial t^2} = q(x,t) \tag{3}$$

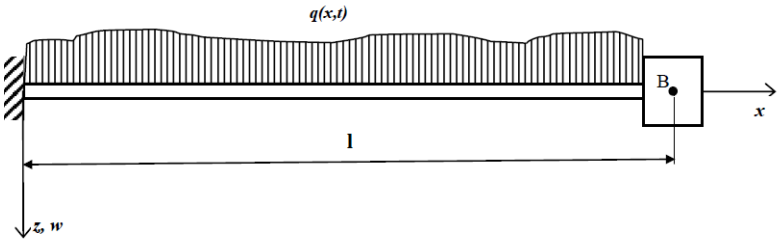

Figure 1. Schema of the analysed beam.

where A is a cross-section area of the beam, J is a moment of inertia of the beam cross-section respect the neutral axis, ρ is material mass density of the beam, $q(x,t)$ is external load acting on the beam, $w(x,t)$ is transversal displacement of the neutral beam axis (Fig. 1), t is time, x is a longitudinal coordinate

The following boundary conditions for the cantilever beam are defined: the deflection and slope (angle of deflection) at the clamped end equals zero, thus these boundary conditions at x = 0 can be expressed as

$$w(0,t)=0 \quad \text{and} \quad \frac{\partial w(0,t)}{\partial x}=0 \tag{4}$$

The boundary conditions at the end of the beam carrying the mass element are derived with the help of principles of change of momentum and angular momentum respect point B (Fig. 1) [8, 13]. Thus

$$m_p \frac{\partial^2 w_B(t)}{\partial t^2} = -Q \quad \text{and} \quad I_B \cdot \frac{\partial^2 \phi(l,t)}{\partial t^2} = M_b(l,t) \tag{5}$$

where Q and M_b are the shear force and bending moment respectively.

The bending moment can be calculated as bellow (e.g. [10])

$$M_b = \int_A \sigma \cdot y dy = -\left(\int_A E \frac{\partial^2 w(x,t)}{\partial x^2} y^2 dy + \int_A E'_\gamma \frac{d^\gamma}{dt^\gamma} \frac{\partial^2 w(x,t)}{\partial x^2} y^2 dy \right) = \\ - EJ \left(\frac{\partial^2 w(x,t)}{\partial x^2} + \mu_\gamma \frac{d^\gamma}{dt^\gamma} \frac{\partial^2 w(x,t)}{\partial x^2} \right) \tag{6}$$

Using relationships above, the boundary conditions at x = l are formulated as follows

$$m_p \frac{\partial^2 w(l,t)}{\partial t^2} = EJ \left(\frac{\partial^3 w(l,t)}{\partial x^3} + \mu_\gamma \frac{d^\gamma}{dt^\gamma} \frac{\partial^3 w(l,t)}{\partial x^3} \right) \tag{7}$$

$$I_B \cdot \frac{\partial^3 w(l,t)}{\partial x \partial t^2} = -EJ\left(\frac{\partial^2 w(l,t)}{\partial x^2} + \mu_\gamma \frac{d^\gamma}{dt^\gamma} \frac{\partial^2 w(l,t)}{\partial x^2} \right) \tag{8}$$

where *w(l,t)* is transversal displacement of the neutral beam axis at the right beam end (Fig. 1)

In the case of the base motion, the transverse displacement of the beam can be expressed as a sum of the rigid body and relative displacement [21]. In the case of a displacement of a cantilever beam [21]

$$w(x,t) = w_{st}(t) + w_{rl}(x,t) \tag{9}$$

where $w_{st}(t)$ is a base displacement and $w_{rel}(x,t)$ is displacement of the neutral beam axis relative the clamped end of the beam.

Thus calculating appropriate derivatives of the expression Eq. (9), the equation of motion of the beam is expressed as

$$EJ\left(\frac{\partial^4 w_{rl}(x,t)}{\partial x^4} + \mu_\gamma \frac{d^\gamma}{dt^\gamma} \left(\frac{\partial^4 w_{rl}(x,t)}{\partial x^4} \right) \right) + A\rho \frac{\partial^2 w_{rl}(x,t)}{\partial t^2} = q(x,t) - A\rho \frac{d^2 w_{st}(t)}{dt^2} \tag{10}$$

with transformed boundary conditions

$$m_p \frac{\partial^2 w_{rl}(l,t)}{\partial t^2} - EJ\left(\frac{\partial^3 w_{rl}(l,t)}{\partial x^3} + \mu_\gamma \frac{d^\gamma}{dt^\gamma} \frac{\partial^3 w_{rl}(l,t)}{\partial x^3} \right) = -m_p \frac{d^2 w_{st}(t)}{dt^2} \tag{11}$$

$$I_B \frac{\partial^3 w_{rl}(l,t)}{\partial x \partial t^2} + EJ\left(\frac{\partial^2 w_{rl}(l,t)}{\partial x^2} + \mu_\gamma \frac{d^\gamma}{dt^\gamma} \frac{\partial^2 w_{rl}(l,t)}{\partial x^2} \right) = 0 \tag{12}$$

The solution of equations Eq. (10-12) is sought in the form of its eigenfunction series expansion [16] i.e.

$$w_{rl}(x,t) = \sum_{n=1}^{\infty} S_n(t) W_n(x) \tag{13}$$

where $S_n(t)$ are time-dependent generalized coordinates, $W_n(x)$ are the eigenfunctions of the system [16].

Eigenfunctions are obtained solving Eq. (11) with its right hand side equals 0 (homogenous equation) and homogenous boundary conditions. The solution is derived using separation of variables method i.e.

$$w_{rl}(x,t) = \sum_{n=1}^{\infty} \xi_n(t) W_n(x) \tag{14}$$

thus

$$\frac{\partial^4 w_{rl}(x,t)}{\partial x^4} = W^{IV}(x)\xi(t), \quad \frac{d^\gamma}{dt^\gamma}\left(\frac{\partial^4 w_{rl}(x,t)}{\partial x^4}\right) = W^{IV}(x)\xi^{(\gamma)}(t), \quad \frac{\partial^2 w_{rl}(x,t)}{\partial t^2} = W(x)\ddot{\xi}(t) \tag{15}$$

Using well-know mathematical transformations (e.g. [7, 16, 21]) the following equations are derived

$$W^{IV}(x) - k^4 W(x) = 0 \tag{16}$$

$$\ddot{\xi}(t) + \mu_\gamma \omega^2 \dot{\xi}^{(\gamma)}(t) + \omega^2 \xi(t) = 0 \tag{17}$$

where $\omega = k^2 \sqrt{\frac{EJ}{\rho A}}$

The solution of Eq. (16) has a form [16, 21]

$$W(x) = A\sin(kx) + B\cos(kx) + Csh(kx) + Dch(kx) \tag{18}$$

Using boundary conditions for the clamped end of the beam, it is derived that A = -C and B = -D. Employing this results and utilizing the boundary conditions for the beam at the end carrying the mass element, the system of equations for constant A and B is obtained

$$\begin{cases} \{z^3 \cdot \beta \cdot [\cos(z) - ch(z)] + [\sin(z) + sh(z)]\}A + \{-z^3 \cdot \beta \cdot [\sin(z) + sh(z)] + [\cos(z) + ch(z)]\}B = 0 \\ \{\alpha \cdot z \cdot [\sin(z) - sh(z)] - [\cos(z) + ch(z)]\}A + \{\alpha \cdot z \cdot [\cos(z) - ch(z)] + [\sin(z) - sh(z)]\}B = 0 \end{cases} \tag{19}$$

where $\alpha = \frac{m_p}{\rho A l}$ *and* $\beta = \frac{I_B}{\rho A l^3}$, $z = k \cdot l$

Above system of equations for constants A and B could be fulfil if the determinant of coefficients matrix of Eq. (19) equals zero. Equating the determinant of Eq (19) to zero, after lengthy and tedious arithmetical transformations, the characteristic equation of the considered system is derived

$$\begin{aligned} &- z^4 \alpha \cdot \beta \cdot [1 - \cos(z)ch(z)] + z^3 \beta \cdot [\cos(z)sh(z) + ch(z)\sin(z)] + \\ &+ z \cdot \alpha \cdot [\sin(z)ch(z) - sh(z)\cos(z)] - 1 - \cos(z)ch(z) = 0 \end{aligned} \tag{20}$$

Roots of the equation above correspond to sequent eigenvalues of the beam. Therefore, the eigenfunction can be expressed as

$$W_n(x) = A_n\{[\sin(k_n x) - sh(k_n x)] - \lambda_n[\cos(k_n x) - ch(k_n x)]\} \tag{21}$$

where $\lambda_n = \frac{\{z_n \cdot \alpha \cdot [\sin(z_n) - sh(z_n)] - [\cos(z_n) + ch(z_n)]\}}{\{z_n \cdot \alpha \cdot [\cos(z_n) - ch(z_n)] + [\sin(z_n) - sh(z_n)]\}}$ and $k_n = \frac{z_n}{l}$

Therefore the n-th natural frequency of the analyzed beam ω_n is calculated as in Eq. (17)

Indeterminate coefficients A_n can be calculated with the help of the orthogonality condition..The orthogonallity condition is obtained using standard procedure [13][16]. Thus using well-know arithmetical transformations of Eq.(16), this condition can be expressed as

$$\int_0^l W_n(x) m_l W_m(x) dx + m_p \cdot W_n(l) W_m(l) + I_B \cdot W_n^I(l) W_m^I(l) = \delta_{nm} \tag{22}$$

or the companion orthogonality condition expressed as

$$\int_0^l W_n^{IV}(x) \cdot EJ \cdot W_m(x) dx - EI \cdot W_n^{III}(l) W_m(l) + EI \cdot W_n^{II}(l) W_m^I(l) = \omega_n^2 \delta_{nm} \tag{23}$$

where δ_{mn} is the Kronecker delta.

Calculated eigenvalues (Eq. (20)) and eigenfunction (Eq. (21)) enables us to derive the forced vibration solution. Substituting Eq. (13) into Eq. (10) gives the following expression

$$EJ\left(\sum_{n=1}^{\infty} W_n^{IV}(x) S_n(t) + \mu_\gamma \sum_{n=1}^{\infty} W_n^{IV}(x) \dot{S}_n^{(\gamma)}(t)\right) + m_l \sum_{n=1}^{\infty} W_n(x) \ddot{S}_n(t) = F(t) \tag{24}$$

where $m_l = A \cdot \rho$, F(t) is the right hand side of Eq. (10)

Multiplying both sides of Eq (24) by the mass-normalized eigenfunction $W_s(x)$ and integrating over the length of the beam, the relationship below is obtained

$$\begin{aligned} &EJ\left(\sum_{n=1}^{\infty}[S_n(t)\int_0^l W_s(x) W_n^{IV}(x) dx] + \mu_\gamma \sum_{n=1}^{\infty}[\dot{S}_n^{(\gamma)}(t)\int_0^l W_s(x) W_n^{IV}(x) dx]\right) + \\ &+ \sum_{n=1}^{\infty}[\ddot{S}_n(t)\int_0^l W_s(x) m_l W_n(x) dx] = \int_0^l W_s(x) F(t) dx \end{aligned} \tag{25}$$

Arranging and grouping appropriate terms of Eq. (25) and using the orthogonality conditions Eqs. (22-23), after some arithmetical transformations, the following expressions is derived

$$\begin{aligned} &\ddot{S}_n(t) + \omega_n^2 \cdot [S_n(t) + \mu_\gamma \dot{S}_n^{(\gamma)}(t)] - m_p \cdot \sum_{n=1}^{\infty} \ddot{S} \cdot W_n(l) + \sum_{n=1}^{\infty} EI \cdot W_n^{III}(l) \cdot [S_n(t) + \mu_\gamma \dot{S}_n^{(\gamma)}(t)] \cdot W_s(l) + \\ &- EI \cdot \sum_{n=1}^{\infty} [S_n(t) + \mu_\gamma S_n^{(\gamma)}(t)] W_n^{II}(l) - I_B \sum \ddot{S}_n \cdot W_n^I(l) \cdot W_s^I(l) = \int_0^l W_s(x) F(t) dx \end{aligned} \tag{26}$$

Substituting the sought solution (Eq. (13)) into boundary conditions Eqs. (11-12) and multiplying both sides of the equations by normalized eigenfunction $W_s(x)$, the expressions for boundary condition are as below

$$\begin{cases} I_B \cdot \sum_{n=1}^{\infty} W_n^I(l)\ddot{S}_n(t) \cdot W_s^I + EJ \sum_{n=1}^{\infty} \left(W_n^{II}(l) S_n(t) + \mu_\gamma W_n^{II}{}_n(l) \ddot{S}_n{}^{(\gamma)}(t) \right) \cdot W_s^I = 0 \\ m_p \cdot \sum_{n=1}^{\infty} W_n(l)\ddot{S}_n(t) \cdot W_s^I - EJ \sum_{n=1}^{\infty} \left(W_n^{III}(l) S_n(t) + \mu_\gamma W_n^{III}(l) \ddot{S}_n{}^{(\gamma)}(t) \right) \cdot W_s^I = -m_p \frac{d^2 w_{st}}{dt^2} \end{cases} \quad (27)$$

Since the expressions under the sign of the sum in the Eq. (26) are the same as left sides of the transformed expression for boundary conditions Eq. (27), finally the expression Eq. (26) has the form

$$\ddot{S}_n(t) + \omega_n^2 \cdot [S_n(t) + \mu_\gamma \ddot{S}_n^{(\gamma)}(t)] = \int_0^l W_n(x) F(t) dx - m_p \frac{d^2 w_{st}(t)}{dt^2} \cdot W_n(l) \quad (28)$$

Assuming zero initial conditions and q(x,t) = 0 each generalized coordinate $S_n(t)$ can be calculated as [18]

$$S_n(t) = -m_p \int_0^t G_n(t-\tau) \cdot \frac{d^2 w_{st}(t)}{dt^2} \cdot W_n(l) d\tau \quad (29)$$

where $G_n(t)$ is the fractional Green's function corresponding to Eq. (28). This Green's function comprises two terms, namely [14, 20]

$$G_n(t) = K_{1n}(t) + K_{2n}(t) \quad (30)$$

The first term in expression above, K_{1n} (Eq. 30) represents damped vibrations around the drifting equilibrium position, whereas the second term K_{2n} describes the drift of the equilibrium position [14], [19]. The term K_{1n} could be calculated from formula given by Beyer and Kempfle [4][14],

$$K_{1n}(t) = \alpha_n e^{-\sigma_n t} \sin(\Omega_n t + \phi_n) \quad (31)$$

where

$$\alpha_n = \frac{2}{\sqrt{\mu_k^2 + \nu^2}}, \quad \phi_n = \arctan\left(\frac{\mu_k}{\nu} \right) \quad \mu_k = \mathrm{Re}(W'(s_{1,2})), \ \nu = \mathrm{Im}(W'_{(s,1,2)}),$$

$W(s) = s^2 + \mu_\gamma \omega_n^2 s^\gamma + \omega_n^2$ — is the characteristic polynomial of Eq. (28),

$W'(s) = 2s + \gamma \mu_\gamma \omega_n^2 s^{\gamma-1}$ — is a derivative of the characteristic polynomial with respect *s*,

$s_{1,2} = -\sigma_n \pm i\Omega_n$ — are conjugate complex roots of the characteristic polynomial *W(s)*.

The term K_{2n} could be calculated using formula [4, 10]

$$K_{2n}(t) = \frac{\mu_\gamma \omega_n^2 \sin(\pi\gamma)}{\pi} \int_0^\infty \frac{r^\gamma e^{-rt} dr}{\left[r^2 + \mu_\gamma \omega_n^2 r^\gamma \cos(\pi\gamma) + \omega_n^2 \right]^2 + \left[\mu_\gamma \omega_n^2 r^\gamma \sin(\pi\gamma) \right]^2} \quad (32)$$

In some systems and time regions, values K_{2n} are considerably small in comparison with the values of K_{1n} [9, 14, 19], therefore can be omitted.

For the of viscoelastic integer order Kelvin-Voigt material model the governing equation of the considered beam is described by equation [7,13, 21]

$$EJ\left(\frac{\partial^4 w_{rl}(x,t)}{\partial x^4}+\mu\frac{\partial^5 w_{rl}(x,t)}{\partial x^4\partial t}\right)+A\rho\frac{\partial^2 w_{rl}(x,t)}{\partial t^2}=q(x,t)-A\rho\frac{d^2 w_{st}(t)}{dt^2} \tag{33}$$

The solution of the equation Eq. (33) can be derived in similar manner as in the case of the equation with the fractional derivative. For each nth eigenvalue, the response could be calculated using Duhamel integral [7] [13]

$$\begin{aligned} S_n(t)&=\frac{f_0}{\omega_{hn}}\int_0^t e^{-h_n(t-\tau)}\sin(\omega_{hn}(t-\tau))q_w(\tau)d\tau \quad \text{for } h_n<\omega_n \\ S_n(t)&=\frac{f_0}{\tilde{\omega}_{hn}}\int_0^t e^{-h_n(t-\tau)}sh(\tilde{\omega}_{hn}(t-\tau))q_w(\tau)d\tau \quad \text{for } h>\omega_n \end{aligned} \tag{34}$$

where $h_n=\frac{1}{2}\mu\omega_n^2$, $\omega_{hn}=\sqrt{\omega_n^2-h_n^2}$, $\tilde{\omega}_{hn}=\sqrt{h_n^2-\omega_n^2}$

3. Exemplary calculations and discussion

The derived formulae above are used to examine effect of order of fractional derivative γ on dynamics of the analysed system. Moreover, responses of the systems with fractional and integer order damping to support motion of the beam with tip element are compared. The obtained expressions Eqs (28-32) are used to compute responses of the system with the fractional derivative, whereas the responses of the system with the integer derivative are computed using Eqs (33-34). The computations are performed with the help of the "Mathematica" package. It is assumed that the beam is not subjected to any distributed load (q(x,t) = 0, Fig. 1) and the motion of the beam support is described by equation

$$w_{st}(t)=w_0\sin(\varepsilon t^2/2) \tag{35}$$

where w_0, is a displacement amplitude, ε is an angular acceleration

The dimensionless dynamic deflection of the beam w/w_0 versus the dimensionless time parameter τ is computed for the point located at the beam end carrying the mass element (Fig. 1). The dimensionless time is defined as $\tau=\varepsilon\cdot t/\omega_1$, where ω_1 is the first natural frequency of the analysed beam Eq. (17). The calculations are performed for several values of the order of fractional derivative γ and coefficient μ_γ, angular acceleration ε = 10 and 20 1/s^2. Calculations are performed for the beam of length 0.8 m, mass density 1190 kg/m^3, cross-section area $5\cdot10^{-4}$ m^2, cross-section moment of inertia

$1.667 \cdot 10^{-8}$ m^4, Young's modulus $3.2 \cdot 10^3$ MPa, mass of a tip body 0.4 kg, moment of inertia of a tip body 0.0002 kg·m^2.

The calculated maximum amplitudes of the beam responses for several values of the order of the fractional derivative γ and coefficient μ_γ are presented in Tables 1 and 2. The amplitude value shown in the tables is calculated for the first and second resonance regions.

The obtained results have shown that when the order of the fractional derivative is increased, vibration amplitudes decrease (Tabs 1-2, Figs 1-2). Moreover, in the case of fractional derivative order γ=0.25, the computed vibration amplitudes are greater for the second mode of vibration than for the first mode (Figs 1). In the case γ=0.5 and μ_γ = 0.001[s$^\gamma$], the maximum amplitude values are similar in the first and second region of resonance (Tab. 1 and 2). In the case γ = 0.75 and 1.0 vibration amplitudes not reveal increase in a value in the region corresponding to the second resonance (Fig. 2).

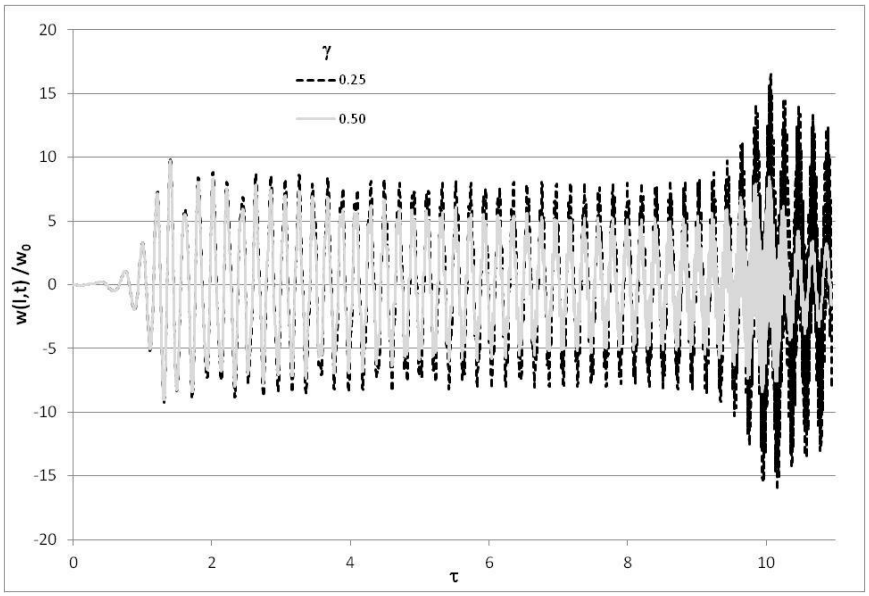

Figure 2. Beam response for ε = 20 [1/s^2], μ_γ = 0.2 [s$^\gamma$].

Table 1. Maximal vibration amplitudes ε = 10 [1/s^2]

γ	First mode			Second mode		
	μ_γ = 0.1 [s$^\gamma$]	μ_γ = 0.2 [s$^\gamma$]	μ_γ = 0.4 [s$^\gamma$]	μ_γ = 0.1 [s$^\gamma$]	μ_γ = 0.2 [s$^\gamma$]	μ_γ = 0.4 [s$^\gamma$]
0.25	13.661	13.587	13.454	24.022	20.650	16.335
0.50	13.501	13.167	12.661	13.386	7.958	4.131
0.75	12.902	12.171	10.867	3.879	2.113	1.539
1.00	11.795	10.220	7.846	1.287	1.138	1.136

Table 2. Maximal vibration amplitudes $\varepsilon = 20\ [1/s^2]$

γ	First mode			Second mode		
	$\mu_\gamma = 0.1\ [s^\gamma]$	$\mu_\gamma = 0.2\ [s^\gamma]$	$\mu_\gamma = 0.4\ [s^\gamma]$	$\mu_\gamma = 0.1\ [s^\gamma]$	$\mu_\gamma = 0.2\ [s^\gamma]$	$\mu_\gamma = 0.4\ [s^\gamma]$
0.25	9.983	9.956	9.917	17.994	16.501	13.972
0.50	9.752	9.751	9.508	8.448	8.103	4.815
0.75	9.584	9.197	8.471	4.434	2.181	1.516
1.00	8.930	8.010	6.537	1.355	1.142	1.136

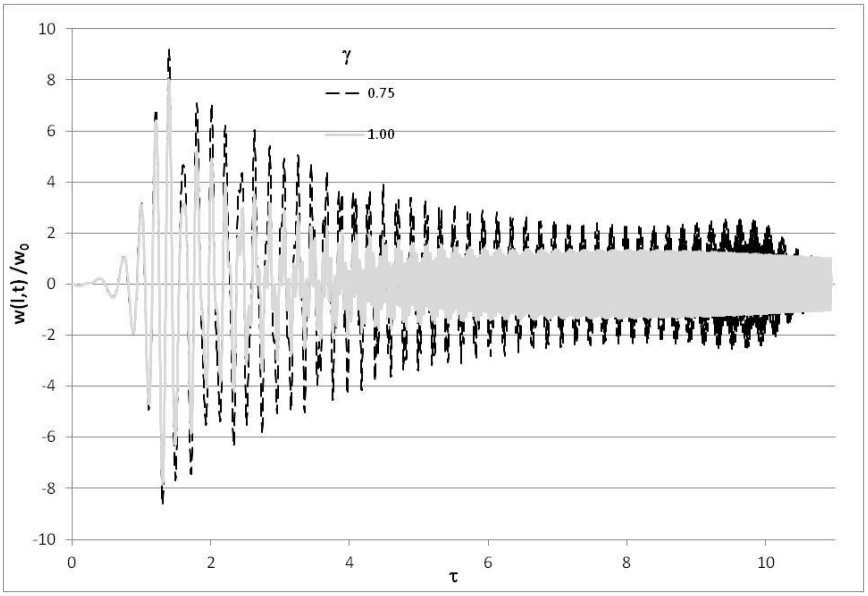

Figure 3. Beam response for $\varepsilon = 20\ [1/s^2]$, $\mu_\gamma = 0.2\ [s^\gamma]$.

4. Conclusions

In this work, the transient vibration of a viscoelastic cantilever beam made of a material described by the fractional derivative Kelvin-Voigt model and carrying a tip mass element for the case of base motion excitation is presented. The characteristic equation, modal frequencies, eigenfunction and orthogonality condition are achieved. Additionally, the solution for the case of the base motion excitation is derived. The solution is employed to calculate the transient beam responses to harmonic excitation by movement of the beam base. A linearly time-varying increasing function is assumed as the excitation frequency. The achieved results show that a decrease in the derivative order causes an increase in vibration amplitudes of the beam. For some values of the order of the fractional derivative γ and coefficient μ_γ the amplitudes appeared in the region near the second resonance are

greater than for those obtained for the region of the first resonance. Analogous results were obtained for a simply supported beam analyzed in paper [9]. Actual parameters of the fractional Kelvin-Voigt model corresponding to the system analysis can be determined by conducting appropriate experimental researches.

References

[1] Bagley R.L., Torvik P.J., Fractional Calculus – A Different Approach to the Analysis of Viscoelastically Damped structures, *AIAA Journal*, 21**,** 5 (1983), 741-748

[2] Bagley R.L., Torvik P.J., A Theoretical Basis for the Application of Fractional Calculus to Viscoelasticity, *Journal of Rheology*, 27**,** 3 (1983), 201-210

[3] Bath R.B., Wagner H., Natural Frequencies of a Uniform Cantilever With a Tip Mass Slender in the Axial Direction, *Journal of Sound and Vibration*, 45, 2 (1976), 304-307

[4] Beyer H, Kempfle S.,: Definition of Physically Consistent Damping Laws with Fractional Derivatives *ZAMM***,** 75, 8 (1995), 623-635

[5] Caputo M., Linear Models of Dissipation whose Q is almost Frequency Independent-II, *Geophysical Journal of the Royal Astronomical Society*, 13, 5 (1967), 529-539

[6] Caputo M., Mainardi F., A new Dissipation Model Based on Memory Mechanism, *Pure and Applied Geophysics*, 91**,** 8 (1971), 134-147

[7] Clough R. W., Penzien J., *Dynamics of Structures*, MacGraw-Hill, New York, 1993

[8] Erturk A. Imman D.J., Piezoelectric energy harvesting, John Wiley and Sons, The Atrium, Southern Gate, Chichester, West Sussex, 2011

[9] Freundlich J., Transient vibrations of a simply supported viscoelastic beam of a fractional derivative type under the transient motion of the supports, Dynamical Systems: Theoretical and Experimental Analysis. Łódź, Poland, December 7–10, 2015, *Springer Proceedings in Mathematics & Statistics*, vol. 182, 2016, 113-124

[10] Freundlich J., Dynamic Response of a Simply Supported Viscoelastic Beam of a Fractional Derivative Type to a Moving Force Load, *Journal of Theoretical and Applied Mechanics*, Vol 54 , No 4 (2016), 1433-1445

[11] M. Gurgoze, A note on the vibrations of a restrained cantilever beam carrying a heavy tip body, *Journal of Sound and Vibration*, 106, 3 (1986), 533-536

[12] Hedrih (Stevanović), The Transversal Creeping Vibrations of a Fractional Derivative Order Constitutive Relation of Nonhomogeneous Beam, *Mathematical Problems in Engineering*, 2006, 2006, 1-18

[13] Kaliski S. (Ed.), *Vibrations and waves in solids* (in Polish, title: *Drgania i fale w ciałach stałych)*, Państwowe Wydawnictwo Naukowe, Warszawa, 1966

[14] Kempfle S, Schäfer I., Beyer H,:, Fractional Calculus via Functional Calculus: Theory and application, *Nonlinear Dynamics*, 29 (2002), 99-127

[15] Mainardi F., *Fractional Calculus and Waves in Linear Viscoelastisity: an Introduction to Mathematical Models*, Imperial College Press, London, 2009

[16] Meirovitch L., *Analytical methods in vibrations*, Macmillan, New York, 1967

[17] Mousavi Lajimi S.A, Heppler G.R., Comments on ‘‘Natural frequencies of a uniform cantilever with a tip mass slender in the axial direction’’, *Journal of Sound and Vibration* 331 (2012) 2964–2968

[18] Podlubny I., *Fractional Differential Equations*, Academic Press, San Diego,1999

[19] Rossikhin Y. A., Shitikova M. V.; Application of fractional derivatives to the analysis of damped vibrations of viscoelastic single mass systems, Acta Mechanica 120, 109-125 (1997)

[20] Rossikhin Y. A., Shitikova M. V., 2010, Application of Fractional Calculus for dynamic Problems of Solid Mechanics: Novel Trends and Recent Results, *Applied Mechanics Reviews*, 63, (2010), 010801-1- 010801-51

[21] Timoshenko S., Young D. H., Weaver W., *Vibration Problems in Engineering*, John Willey & Sons, New York, 1974

[22] To C. W. S., Vibration of a Cantilever Beam With a Base Excitation and Tip Mass, *Journal of Sound and Vibration*, 83, 4 (1982), 445-460

[23] Zhou D., The Vibrations of a Cantilever Beam Carrying a Heavy Tip Mass With Elastic Supports, *Journal of Sound and Vibration*, 206, 2 (1997), 275-279

Jan Freundlich, Ph.D.: Warsaw University of Technology, Faculty of Automotive and Construction Machinery Engineering, 02-254 Warszawa, ul. Narbutta 84, POLAND (*jfr@simr.pw.edu.pl*). The author gave a presentation of this paper during one of the conference sessions.

Sensitivity investigations of the lane change maneuver with an automatic control system

Mirosław Gidlewski, Leszek Jemioł, Dariusz Żardecki

Abstract: The authors' model of a conceptual control system was presented at several papers. The aim of extensive simulation studies was: testing of the controller operations, and evaluation of its sensitivity to changes of the vehicle and road parameters. This paper presents unpublished results of the studies. In simulation based sensitivity investigations special sensitivity indexes computed with using error signals support this analysis. Simulation-based sensitivity analysis provides more reliable conclusions on the controller's performance and show us: what parameters should be identified on-line, and what accuracy of measured signals is sufficient. The paper presents information on the models, the method used, as well as example results of studies. The presented method of automatic control and the method of it's investigations can be an attractive proposition for designers and researchers of active steering systems which enhance active safety of vehicles.

1. Introduction

Numerous research centres are working on autonomous vehicles. Such automated cars require special sophisticated controllers interacting with steering mechanisms and brakes. Note, that mechatronic systems directly related to steering mechanisms are very limited, as yet. They apply mainly to support the driver's effort (servo-type systems), and to stabilize the vehicle's lateral motion (Lane Assist Systems). The fully automatic steering of the vehicle's trajectory concerns rather low speeds (e.g. Park Assist Systems), when the vehicle's dynamics can be neglected. A synthesis of automatic control systems for high-speed maneuvering appears to be a difficult scientific and technological challenge. In high-speed conditions the car must be treated as a dynamical system functioning with variable operating conditions (because of variations of the tire-road friction characteristics, because of variations of the vehicle speed, because of variations of the vehicle loading, etc)).

The lane change automatic control of is a key to automate more complex vehicle maneuvers (e.g. avoiding, overtaking etc.). The subject of automation of the lane change was undertaken by many researchers (eg. [2], [4], [12], [13], [14]). The scientific papers report problems of reference vehicle trajectory calculations, problems of synthesis control algorithms, problems of optimization of steering process, etc. In all such papers theoretical studies are supported by simulation investigations. The problems of automation of lane change processes are present in several authors' papers (eg. [6], [7],

[8], [9], [10]) too. These papers focus on the lane change control process of the car which is driven in difficult operation conditions and scenarios (high speed, sleep road, suddenly appearing obstacle).

The authors' model of the conceptual control system (described in p.2) is based on a simple reference model of the lane change process. The controller algorithm is tested in extensive simulation studies with using, as a virtual object, a very detailed model of the motion dynamics of a medium truck. This paper presents unpublished results of the studies which can be treated as sensitivity investigations (described in p.3).

2. Theoretical background

The car driving on the straight road have to change the lane because of the sudden appearance of an obstacle. The lane change process refers to two variables – the displacement Y of the centre of mass and the angular position ψ of the car body in relation to the trajectory of the centre of mass. According to experiences as well as the control theory of time-optimal systems, the steering wheel angle signal δ_H should have the "bang-bang" form and the control process can be divided into two phases - transposition and stabilization (fig.1).

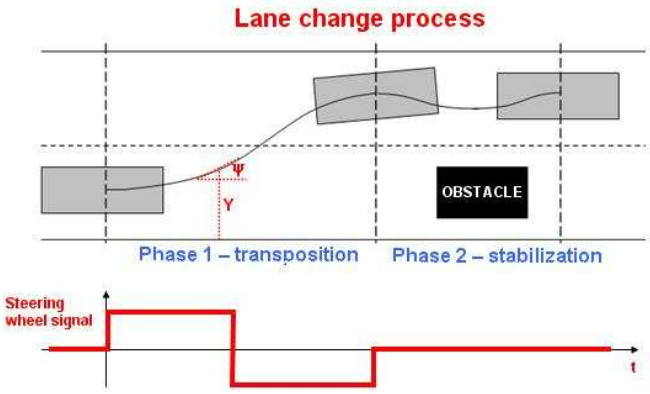

Figure 1. The concept of "bang-bang" type steering and time decomposition of lane change control.

The lane change controller is composed by a reference signal generator and two regulators acting in a switchable structure (fig.2). The generator provides three reference signals $\delta_{HR}(t)$ (bang-bang type waveform signal of the steering system angle), $Y_R(t)$ and $\psi_R(t)$ (waveform signals of the linear and angular vehicle positions computed for $\delta_{HR}(t)$ signal) which describe the lane change maneuver according to a simple reference model of the vehicle motion. The signals $Y_R(t)$, $\psi_R(t)$ are set-point signals for two Kalman - type regulators which correct the real steering angle signal $\delta_H(t)$ to minimize errors between measured and desired waveforms of the variables. In the first phase of the control

process, the transposition system is ON (activated) and the angular stabilization system is OFF (deactivated); in the second phase, these connections are reversed. The switching over takes place when the centre of vehicle mass reaches the position where the obstacle avoidance is ensured.

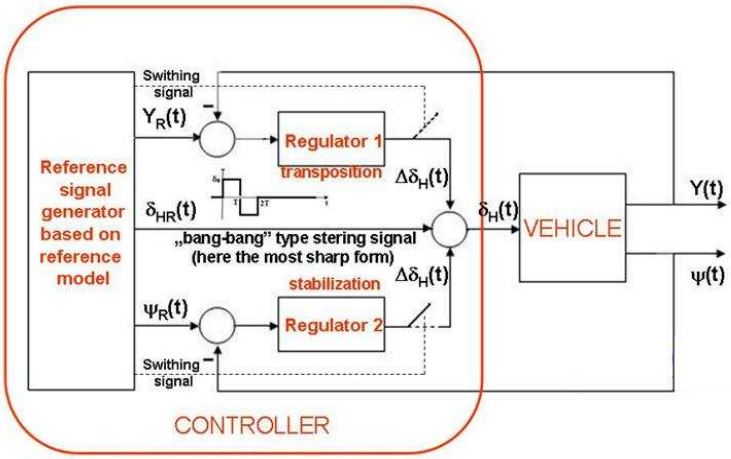

Figure 2. Block diagram of the automatic control system.

The generated signals, and regulators' algorithms are based on a simple reference model. This model is linearized and reduced form of the well known "bicycle model" transformed from the local coordinate system (connected with the car body) to the global coordinate system describing the vehicle trajectory and its angular position. This is presented with details in authors' papers [6], [9].

Note, that such simplified controller has to steer a real object having more complicated dynamic properties than the bicycle model. Therefore very extensive investigations are necessary to confirm controller's algorithms. Such investigations can be done with using a lot of simulation tests when the simple controller model steers a very detail model of the virtual car for various model parameters. Variation of the parameters enables checking of the controller action also in difficult car - road interactions. Simulation-based sensitivity studies provide more reliable conclusions on the controller's performance and show what parameters should be identified on-line, and what accuracies of measured signals are sufficient.

For supporting such simulation based sensitivity analysis of the controller, comparative investigations can be supplemented by calculation of special sensitivity indexes [15] (fig. 3).

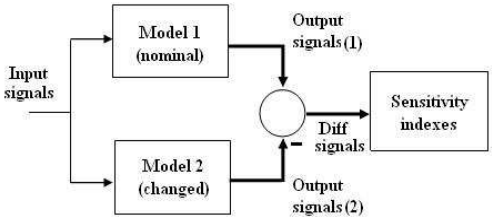

Figure 3. Schematic diagram of sensitivity analysis. Example index: $Wx = 100 \frac{\int_0^\tau (x_1(t) - x_2(t))^2 dt}{\int_0^\tau (x_1(t))^2 dt}$

The sensitivity index can express robustness of the controller for variation of a selected parameter. When the analysis concerns multiple parameters, the aggregation (by superposition) of the indexes is desirable and possible in many cases (hypothesis). This property can be explained for regular models without non-smooth nonlinearities. In such case the well known sensitivity model (based on sensitivity variables ξ [3]) is useful.

When errors between nominal and changed models result from deviation ε between nominal and changed values of a some parameter, the sensitivity index W_X can be expressed (using Taylor series) by an approximation formula, setting $(x_1(t)-x_2(t))^2 \approx \varepsilon^2\xi(t)^2$. For multiple deviations of parameters ε_1, ε_2, …, the sensitivity index W_X can be computed as a sum of subtotals for ε_i, where i = 1, 2,… .

Note, the proposed method of aggregation seems to be attractive also for analysis of the sensitivity index W_X when the model is strongly non-linear (even non-smooth) but regular (without non-stability and any another peculiar effects like bifurcations and chaos) and its calculation must be based on the simulation.

This sensitivity analysis method is presented on selected representative examples in the paper. We look for an answer to the question: if the controller algorithm is robust enough due to disturbances (noise and offset) of the measured signals Y(t) and ψ(t) as well as due to errors of the reference model parameters.

3. Simulation investigations

Repeated simulation tests of the lane change controller have been carried out with using, as a virtual object, a very detail model of motion of a modified (by typical mechatronic elements and systems) medium truck STAR 1142 treated as 3D multi-body non-linear dynamic system [5] (fig.4).

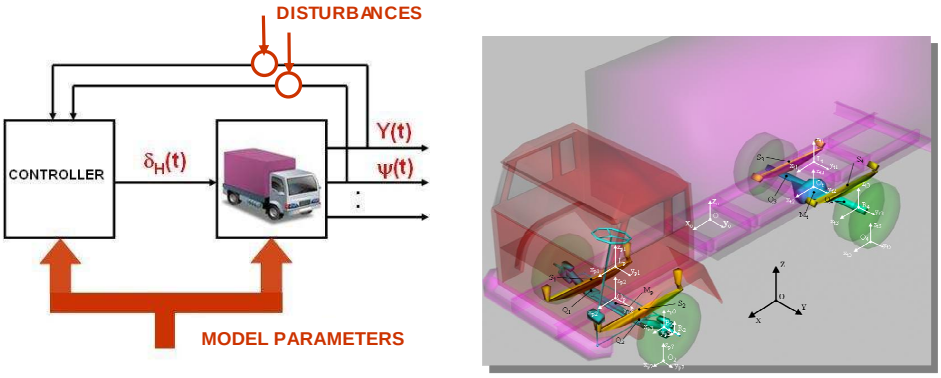

Figure 4. Block diagram visualizing simulation tests of the control system.
δ_H - angle of steering system, Y - lateral transposition, ψ - yaw angle.

The physical model of the vehicle contains 7 masses (car body, 2 axles, 4 wheels) joined by nonlinear spring/damper elements. The model has 20 degrees of freedom (6 DOF for the car body, 2x4=8 DOF for two axles, 2x2=4 DOF for front wheels, 2x1=2 DOF for rear wheels). Wheel-road interactions are desribed by Dugoff formulas which ensure description of the vehicle motion for many different surfaces (also with a full wheel slip) [1]. The vehicle is going on a straight even road.

The steering system model takes into consideration geometrical, kinetic as well as dynamical properties. In our studies the system has an additional equipment – an electrical servomechanism with planetary gears, regulators etc. Its digital controller basing on the simple reference model and signals delivered from sensors has to ensure an automatic control for lane-change maneuvers.

Nonlinear equations of motion have been derived with using Boltzmann-Hamel method of modeling non-holonomic systems [11]. They are complemented by algebraic equations of constrains. These ODE/ADE equations are resolved in a simulation program written in FORTRAN. Based on the main program, a package of computational programs has been prepared. This software is useful for sensitivity studies. The programs can handle not only problems with various parameter inaccuracies, but also problems with disturbances applied to the measured signals.

The model requires about 200 parameters (note, that the reference model in the controller demands only 7 parameters). Values of parameters were identified on the base of many experiments with the real object in static as well as dynamic conditions. Investigations of tires were done on a special drum stand and a dynamometer trailer. For identification of unknown parameters the simulation program were executed as an virtual object. Note, that in these investigations, a method of tuning of the parameters is compatible to the method used for the sensitivity analysis. Thank to many investigations the model of the STAR 1142 lorry were verified with success.

Simulation tests have been repeated for various inequalities between the nominal and changed models. In this paper we present only example results of such investigations. They concerns two groups of inaccuracies:

 Errors in the measurements of the variables (noise plus offset signals) that represent the current vehicle's position on the road . Thus, the signals $Y_D(t)$, $\psi_D(t)$ sent to the controller are

$Y_D(t) = Y(t) + Y_{NOISE}\, NOISE(t) + Y_{OFFSET}$, $\psi_D(t) = \psi(t) + \psi_{NOISE}\, NOISE(t) + \psi_{OFFSET}$, where:

Y_{NOISE} , ψ_{NOISE} – amplitudes of the noise signals (here Y_{NOISE} = 0.2 m, ψ_{NOISE} = 3 deg),

Noise(t) – standard white noise signal (selected amplitude = 1),

Y_{OFFSET} , ψ_{OFFSET} – constant values (here Y_{OFFSET}= ± 0.1 m , ψ_{OFFSET} = 0.5 deg).

Example graphical interpretation of the measurements of disturbed signals is shown in Fig.5.

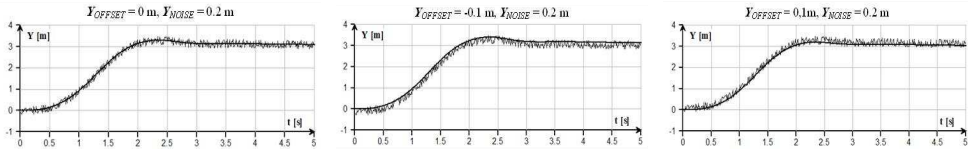

Figure 5. Interpretation of errors in disturbed signals (here for $Y_D(t)$.

In the nominal model, no measurement errors is assumed, while they occur in the modified model.

 Errors in estimations of parameters, like masses, wheel-road friction coefficients, speed, etc. In the presented studies only two parameters were changed (total mass of the car M and speed of the car V)

$M = M_0 + \Delta M$, $V = V_0 + \Delta V$, where:

M_0 , V_0 – nominal values of parameters (here: M_0 = 11300 kg , V_0 = 19.4 m/s (~70 km/h)),

$\Delta M = a_M M_0$, $\Delta V = a_V V_0$ – errors of parameters (in modified model). Here: $a_M = \pm 0.05$, $a_V = \pm 0.05$.

Example results of investigations are presented below (fig.6, 7, 8). In all these simulations the set point steering signal was the same. In all these simulations operation conditions have been rather difficult for the car (speed about 70 km/h, wet asphalt road).

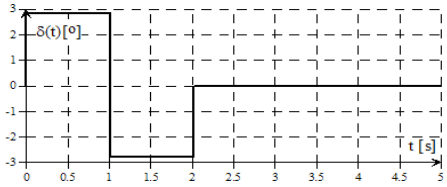

Figure 6. Set point signal (bang-bang type) of the front wheels turning angle.

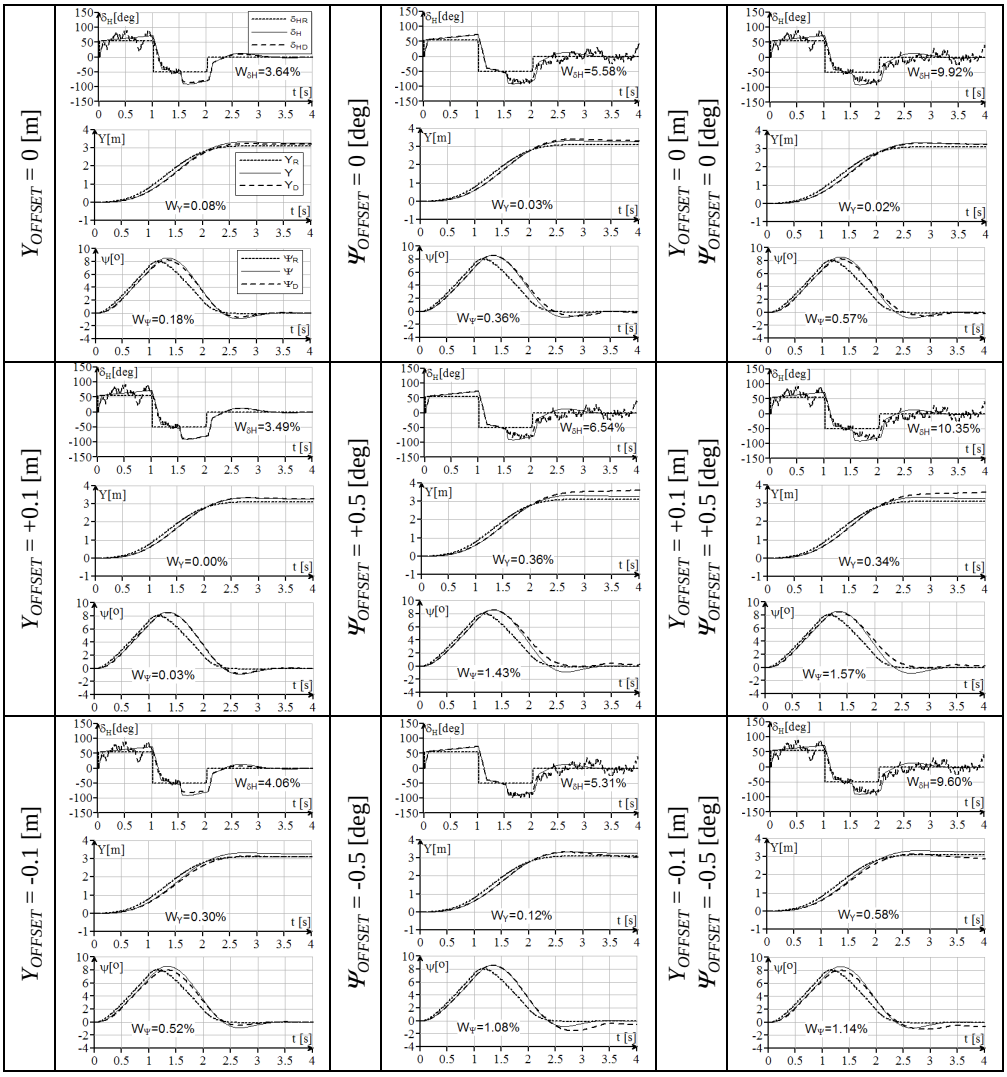

Figure 7. Results of simulations when measured signals have disturbances (noise and offset). Here all model parameters have no errors.

Notation: Dotted lines for signals from the reference signal generator,
Solid lines for nominal model (output signals without errors),
Dashed lines for changed model (output signals with errors).

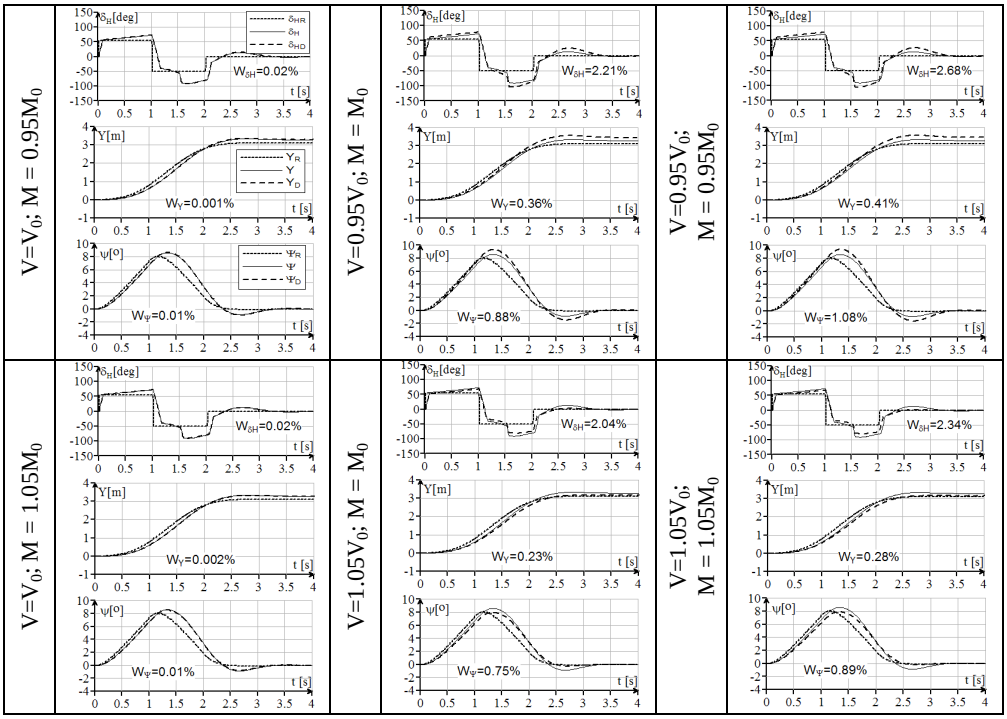

Figure 8. Results of simulations when parameters M and V have errors (±5%). Here measured signals have no disturbances.

Notation: Dotted lines for signals from the reference signal generator,

Solid lines for nominal model,

Dashed lines for changed model.

5. Conclusion

The paper has delivered information on sensitivity simulation based investigations of an automatic vehicle steering system which realizes the lane change maneuver. This simple system has been tested with using very complicated model of the track treated as a virtual object of the control.

The presented simulation results show that the lane change maneuver has been successfully carried out, in spite of the measurement disturbances (noise and offset) of the vehicle position signals Y(t) (lateral displacement) and Ψ(t) (yaw angle). The results of simulations performed with an assumed error level in estimation of the model parameters M (total mass) and V (vehicle speed) also led to the similar conclusion. Satisfactory results have been observed when the controller parameters

were properly chosen for given nominal values of operating conditions in the reference model, and the signals' offset and noise were not too large. After increasing the measurement offset to a higher level (greater then +/- 1 deg) and the noise to a higher amplitude (greater then 3 deg.) one observed for selected operating conditions (lightly loaded lorry and very wet road), that the vehicle was losing directional stability. At the small offset and the low noise levels in the measurement signals, despite wide range changes of operating conditions of the vehicle, automatically operated vehicle was able to change lane without losing directional stability. The same conclusion could be formulated due to errors of model parameters estimation.

Values of the sensitivity indexes show that in these investigations their aggregation by superposition is possible. Unfortunately this remark concern only selected combinations of disturbances and errors.

Finally, it can be stated that the proposed control system have proven to be enough robust to the measurement errors and varying operating conditions when the differences between nominal and changed model are not too large. Determination of these areas requires next extensive simulation tests for many operating conditions.

References

[1] Andrzejewski, R.; Awrejcewicz, J.: *Nonlinear Dynamics of Wheeled Vehicle.* Springer New York, 2003.

[2] Bevan, G. P.; Gollee, H.; O'Reilly, J: *Trajectory generation for road vehicle obstacle avoidance using convex optimization*. Proceedings of the Institute of Mechanical Engineers Part D – Journal of Automobile Engineering, Vol. 224 (4), 2010.

[3] Frank, P. M.: *Introduction to system sensitivity theory*. Academic Press, 1978.

[4] Gao, Y.; Lin, T.; Borrelli, F.; Tseng, E.; Hrovat, D.: *Predictive control of autonomous ground vehicles with obstacle avoidance on slippery roads.* Dynamic Systems and Control Conference, 2010.

[5] Gidlewski, M.: *Model of a dual axis heavy truck for handling studies in complex road situations*. 11th European Automotive Congress, Budapest 2007.

[6] Gidlewski, M.; Żardecki, D.: *Automatic Control of Steering System During Lane Change.* Proceedings of ESV'2015 Conference in Gothenburg, Sweden, available on the Internet.

[7] Gidlewski, M.; Jemioł, L.; Żardecki, D.: *Simulation investigation of the dynamics of the process of sudden obstacle avoiding by a motor vehicle*. The Archives of Automotive Engineering, 73 (3), 2016.

[8] Gidlewski, M.; Żardecki, D.: *Investigation of vehicle motion control process due to the linearization of the lateral dynamics reference model used in the controller*. Mechanics Research Communications, 82, 2017.

[9] Gidlewski, M.; Jankowski, K.; Muszyński, A.; Żardecki, D.: *Vehicle Lane Change Automation with Active Steering – Theoretical Studies and Numerical Investigations.* SAE Paper 2017-01-1555, 2017.

[10] Gidlewski, M.; Żardecki, D.: *Simulation investigations of lane change process with automatic steering system.* Proceedings of 25th ESV'2017 Conference in Detroit, USA, available on the Internet.

[11] Jarzębowska, E.: *Analytic Mechanics*. Oficyna Wydawnicza. Politechniki Warszawskiej (Publishing House of the Warsaw University of Technology), Warszawa 2003 (in Polish).

[12] Moshchuk, N.; Shih-Ken Chen; Zagorski, C.; Chatterjee A.: *Path planning for collision avoidance maneuver.* Proceedings of the ASME 2013 International Mechanical Engineering Congress and Exposition IMECE2013, San Diego, California, 2013.

[13] Park, J. M.; Kim, D. W.; Yoon, Y. S.; Kim, H. J.; Yi, K. S: *Obstacle avoidance of autonomous vehicles based on model predictive control.* Proceedings of the Institute of Mechanical Engineers Part D – Journal of Automobile Engineering, Vol. 223, 2009.

[14] Shiller, Z.; Sundar, S.: *Optimal Emergency Maneuvers Of Automated Vehicles*. Research Reports California Partners for Advanced Transit and Highways (PATH) – UC Berkeley, 1996.

[15] Żardecki, D.: *The λ-sensitivity analysis and its application in simulation studies of dynamical systems*. Archiwum Automatyki i Telemechaniki: 1980, XXV (3), 335–354 (in Polish).

Mirosław Gidlewski, PhD. Eng.: Automotive Industry Institute (PIMOT), Jagiellonska Street 55, 03-301 Warsaw, University of Technology and Humanities in Radom, Malczewski Street 29, 26-600 Radom, Poland (*m.gidlewski@pimot.eu*, *miroslaw.gidlewski@uthrad.pl*).

Leszek Jemioł, MSc. Eng.: University of Technology and Humanities in Radom, Malczewski Street 29, 26-600 Radom, Poland (*leszek.jemiol@uthrad.pl*).

Dariusz Żardecki, Prof.: Military University of Technology (WAT), Kaliski Street 2, 00-908 Warsaw, Automotive Industry Institute (PIMOT), Jagiellonska Street 55, 03-301 Warsaw, Poland (*d.zardecki4@upcpoczta.pl*, *dariusz.zardecki@wat.edu.pl*).

Stability of a rectangular plate under dynamic load generated by unhomogeneous magnetic field

Piotr Kędzia, Krzysztof Magnucki, Mikołaj Smyczyński, Iwona Wstawska

Abstract: The subject of the theoretical study is a rectangular plate under dynamic in-plane load generated by magnetic field. The plate is made of polyethylene (PE) and on the two opposite edges of the plate there are pockets filled with ferrofluid. Both pockets are the same fixed width and are placed inside the magnetic field coils systems. These systems are build of Helmholtz and Golay coils and generate nonhomogeneous magnetic field. Homogeneity and strength of magnetic field depends on the radii of the coils. Magnetic field acts on ferrofluid in the pockets and induce load on the two opposite edges of the plate. If the magnetic field is more homogeneous, the compression load is induced. In other cases tensile local load occurs (compression load dominates). The analytical model of the plate with consideration of nonlinear geometrical relations is formulated, inclusive of the kinetic energy, elastic strain energy and the work of the load. The equation of motion is derived based on the Hamilton's principle. The critical load of the plate is described for the static load and the equation of motion for dynamical problem is numerically solved. The equilibrium paths for the example plate are determined for different configurations of the coils systems.

1. Introduction

Plates are flat structures whose thickness h is small compared to the other in–plane dimensions. They have many applications in engineering fields. Composite materials have gained many advantages over their metal counterparts in engineering applications, in particular aerospace engineering. On the other hand, plates are quite often subjected to in–plane external loads which may cause buckling. Such loadings may occur at different times under in–service conditions, necessitating a design approach which is capable of taking into account these various loading conditions [1]. The determination of the minimal value of critical load corresponding to the certain mode of plate buckling requires the conduct of the general solution, without the limitation to only axisymmetric mode of buckling [2].

The behaviour of plates under compressive loads has been studied for many years. Lateral pressure causes out–of–plane displacements in a mode that is one half wave in both directions. These types of deflections will decrease the strength of the plate whenever they coincide with the main buckling mode. However, when this is not the case the presence of lateral pressure can in fact increase the ultimate strength of the plate [3].

Stability problem of rectangular plates was presented by various amount of researchers. Chen et al. [4] described stability of parametric vibrations of laminated composite plate subjected to arbitrary periodic loads. The in–plane load were supposed to be a combination of periodic biaxial and bending stress. Dynamic buckling of isotropic simply supported plates subjected to in–plane load was investigated by Petry and Fahlbusch [5]. The dynamic behaviour of the plate was essentially influenced by the loading function, the duration of impact and the geometric imperfections. Dynamic stability of composite plates subjected to periodic in–plane load was studied by Dey and Singha [6]. The formulation included the effects of transverse shear deformation, in–plane and rotary inertia. Dynamic instability of composite plates subjected to non–uniform in–plane loads was presented by Ramachandra et al. [7]. The static and the dynamic component of the applied periodic in–plane loading were assumed to vary according to either parabolic or linear distributions. The analysis of nonlinear vibration of an initially stressed laminated plate was conducted by Chen et al. [8]. The nonlinear governing equations were derived using a higher–order theory approach. Chen et al. [9] also discussed numerical solutions to hybrid laminate plates in a general state of non–uniform initial stress based on various plate theories. The governing equations were used to investigate the natural frequencies and buckling loads of hybrid plates subjected to initial stresses. The effects of various parameters on the vibration frequency and buckling coefficient were examined. Numerical analysis of dynamic buckling of rectangular plates subjected to intermediate–velocity impact was carried out by Cui et al. [10]. Dynamic buckling and a dynamic yielding critical condition were formulated, and the corresponding values of critical dynamic loads were estimated. Dynamic analysis of stability of metal foam rectangular plate was performed by Dębowski et al. [11]. Mechanical properties of the foam varied continuously through plate of the thickness. Nonlinear hypothesis of deformation of plane cross section was formulated. Dynamic buckling of thin–walled composite plates with varying widthwise material properties was described by Kubiak [12]. The plate was subjected to in–plane pulse loading. The plate was made of orthotropic (fibre composite) material in which the principal directions of orthotropy was assumed to be parallel to the plate edges. Wang and Lee [13] investigated dynamic stability of ferromagnetic plate under transverse magnetic field and in–plane periodic compression. The effects of magnetic damping and excitation frequency of the in–plane periodic compression on the regions of stability were studied. Global and local buckling of sandwich circular and beam–rectangular plates with metal foam core was studied by Jasion et al. [14]. Mathematical model of displacements, which included a shear effect, was presented. Static and dynamic stability of an axially compressed five-layer sandwich beam was presented by Smyczyński and Magnucka–Blandzi [15]. The mechanical properties were various through the thickness of the beam and depended on the material of each layer. The analysis of buckling of functional graded polymeric sandwich panel was conducted by Uysal and Güven [16]. Buckling problem in polymer sandwich structures subjected in–plane shear force, in–plane normal

compression force, and out–of–plane distributed load according to the two different boundary conditions were considered. Homogeneity of magnetic field influence on buckling of three–layer polyethylene plate was discussed by Kędzia and Smyczyński [17].

The paper is devoted to a rectangular plate under in–plane compression load generated by magnetic field (Fig. 1). The dimensions of the plate are *a* (length) and *b* (width).

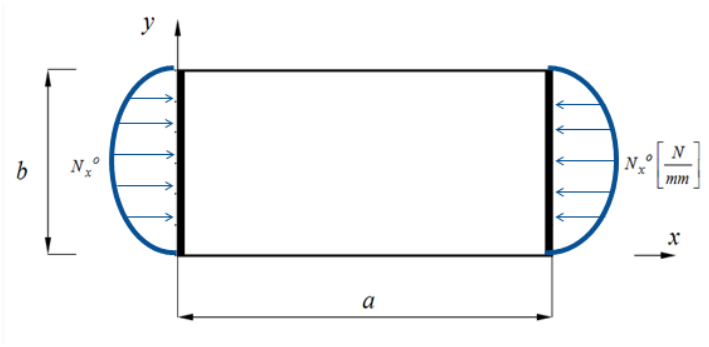

Fig. 1. The scheme of the plate and compression load.

There are two pockets on each of the two opposite edges of the plate, for $x = 0$ and $x = a$. These pockets with porous structure are filled with ferrofluid. Cells in the pockets avoid to flow the ferrofluid along the edge. Magnetic field coils are placed near the ferrofluid. The coil system consists of two magnetic field coil subsystems. The first one (MC–main coil) generates homogeneous magnetic field in the volume of the pockets. The second one is a gradient coil (GC) that generates nonhomogeneous magnetic field. This coil is also called Golay coil. These systems are build of Helmholtz and Golay coils and they both generate nonhomogeneous magnetic field. Coils are presented schematically as loops in Fig. 2a and Golay coil is shown in Fig. 2b.

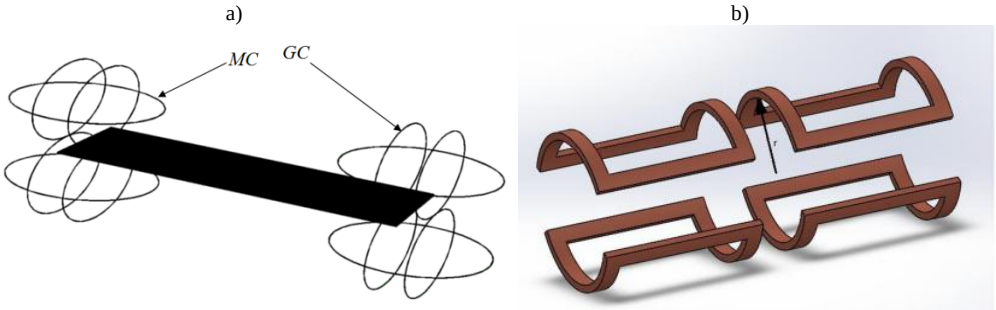

Fig. 2. (a) Arrangement of coils with respect to plate, (b) Golay coil with arc radius *r*.

Intensity N_x^0 of load is expressed by Kelvin force applied per unit volume of ferrofluid:

$$N_x{}^o = t_s{}^2 \cdot \mathbf{f}_x{}^m = t_s{}^2 \cdot \frac{1}{2}\mu_0\chi(1+\chi)\left(\nabla H^2\right)_x \tag{1}$$

where $\mathbf{H} = \left[h_{x,z}{}^1 \cdot z, 0, h_z{}^0 + h_{z,x}{}^1 \cdot x\right]$, $h_z{}^0 = const.$, $h_{z,x}{}^1 = h_{x,z}{}^1$, $\mu_0\chi$ - magnetic permeability, $\mu_0\chi$ - magnetic susceptibility.

Top indexes indicate that the component of the magnetic field vector (1) is derived from MC–main coil (index 0) and from GC coil (index 1).

2. Analytical model

The analytical model of the plate was formulated with the use of classical Kirchoff–Love hypothesis. Displacements in the *x* and *y* directions were formulated:

$$u(x,y,z) = -z\frac{\partial w}{\partial x},\ v(x,y,z) = -z\frac{\partial w}{\partial y}, \tag{2}$$

where $w(x,y)$ is the deflection of the plate.

Deformations – nonlinear geometric connections are as follows:

$$\varepsilon_x = \frac{\partial u}{\partial x} + \frac{1}{2}\left(\frac{\partial w}{\partial x}\right)^2 = -z\frac{\partial^2 w}{\partial x^2} + \frac{1}{2}\left(\frac{\partial w}{\partial x}\right)^2, \tag{3}$$

$$\varepsilon_y = \frac{\partial v}{\partial y} + \frac{1}{2}\left(\frac{\partial w}{\partial y}\right)^2 = -z\frac{\partial^2 w}{\partial y^2} + \frac{1}{2}\left(\frac{\partial w}{\partial y}\right)^2, \tag{4}$$

$$\gamma_{xy} = \frac{\partial u}{\partial y} + \frac{\partial v}{\partial x} + \frac{\partial w}{\partial x}\frac{\partial w}{\partial y} = -2z\frac{\partial^2 w}{\partial x \partial y} + \frac{\partial w}{\partial x}\frac{\partial w}{\partial y}. \tag{5}$$

Elastic strain energy, with taking into account linear physical relation – the Hooke's law, as well as nonlinear geometric relations takes the form:

$$U_\varepsilon = \frac{Et_s^3}{24\left(1-\nu^2\right)}\int_0^a\int_0^b\left[\Phi_1(w) + \frac{3}{t_s^2}\Phi_2(w)\right]dxdy, \tag{6}$$

where: E, ν - material constants, t_s - thickness of the plate,

$$\Phi_1(w) = \left(\frac{\partial^2 w}{\partial x^2}\right)^2 + 2\nu\frac{\partial^2 w}{\partial x^2}\frac{\partial^2 w}{\partial y^2} + \left(\frac{\partial^2 w}{\partial x^2}\right)^2 + 2(1-\nu)\left(\frac{\partial^2 w}{\partial x \partial y}\right)^2,$$

$$\Phi_2(w)=\left(\frac{\partial w}{\partial x}\right)^4+2\left(\frac{\partial w}{\partial x}\right)^2\left(\frac{\partial w}{\partial y}\right)^2+\left(\frac{\partial w}{\partial x}\right)^4 .$$

Kinetic energy of the plate is as follows:

$$T_k=\frac{1}{2}\rho_s t_s\int_0^a\int_0^b\left(\frac{\partial w}{\partial t}\right)^2 dxdy \ , \tag{7}$$

where ρ_s – density of the material, t – time.

Work of load:

$$W=\frac{1}{2}N_x^o(y)\int_0^a\int_0^b\left(\frac{\partial w}{\partial x}\right)^2 dxdy \ , \tag{8}$$

where N_x^o is the intensity of load.

Equations of motion are based on the Hamilton's principle:

$$\delta\int_{t_1}^{t_2}\left[T_k-\left(U_\varepsilon-W\right)\right]dt=0 \ . \tag{9}$$

The equation of motion is in the following form:

$$\rho_s t_s\frac{\partial^2 w}{\partial t^2}+D\nabla^4 w-\frac{Et_s}{2\left(1-\nu^2\right)}\Phi_3(w)+N_x^o(y)\frac{\partial^2 w}{\partial x^2}=0 \ , \tag{10}$$

where $D=\frac{Et_s^3}{12\left(1-\nu^2\right)}$ is flexural rigidity of the plate,

$$\Phi_3(w)=\Phi_{31}(w)+\Phi_{32}(w)+\Phi_{33}(w),$$

$$\Phi_{31}(w)=\left[3\left(\frac{\partial w}{\partial x}\right)^2+\left(\frac{\partial w}{\partial y}\right)^2\right]\frac{\partial^2 w}{\partial x^2}, \quad \Phi_{32}(w)=4\frac{\partial w}{\partial x}\frac{\partial w}{\partial y}\frac{\partial^2 w}{\partial x\partial y}, \quad \Phi_{33}(w)=\left[\left(\frac{\partial w}{\partial x}\right)^2+3\left(\frac{\partial w}{\partial y}\right)^2\right]\frac{\partial^2 w}{\partial y^2}.$$

The intensity of load N_x^o depends on the radius of Golay coil arcs. The higher values of the radius of GC, the more homogeneous gradient of magnetic field appears in the same volume (if the radius of GC strives to infinity, we can assume the presence of homogeneous magnetic field in the pockets). The change of the radius of saddle coils also influences on the strength of the gradient of the magnetic

field (the higher radius of coils, the weaker magnetic field appears in the volume). The shape of the gradient magnetic field along *y*–axis is presented in Fig. 3.

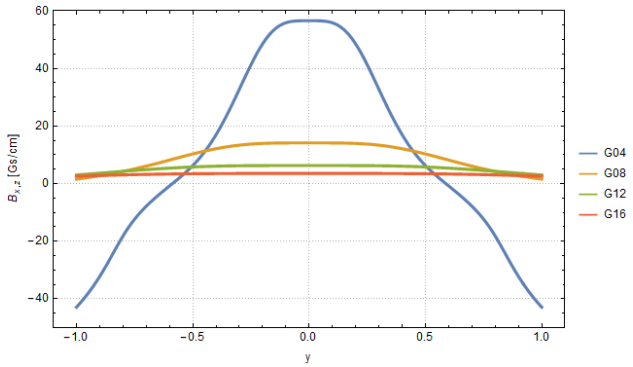

Fig. 3. The load intensity distribution.

Letter G with a number indicates the radius of GC. The base is G10 with the radius of the coil equals *b/2*. G04, G08, G12 and G16 correspond to the radius of 40%, 80%, 120% and 160% of initial radius of G10 respectively.

3. Static and dynamic loads

Equation of equilibrium of the plate is:

$$D\nabla^4 w - \frac{Et_s}{2\left(1-\nu^2\right)}\Phi_3(w) + N_x^o(y)\frac{\partial^2 w}{\partial x^2} = 0 \ . \tag{11}$$

We assume a following function:

$$w(x,y) = w_a \sin\frac{\pi x}{a_1}\sin\frac{\pi y}{b_1} \ , \tag{12}$$

where $a_1 = \frac{a}{m}$, $b_1 = \frac{b}{n}$, m, n – natural numbers.

Substituting (12) into equation (11), with the use of the Galerkin method, allows to calculate the values of critical forces:

$$N_{x,CR}^0 = k_{cr\_coef}\frac{\pi^2 E}{3\left(1-\nu^2\right)}\frac{t_s^3}{b^2} \ . \tag{13}$$

Coefficient k_{cr_coef} depends on the GC radius and is presented in Fig. 4.

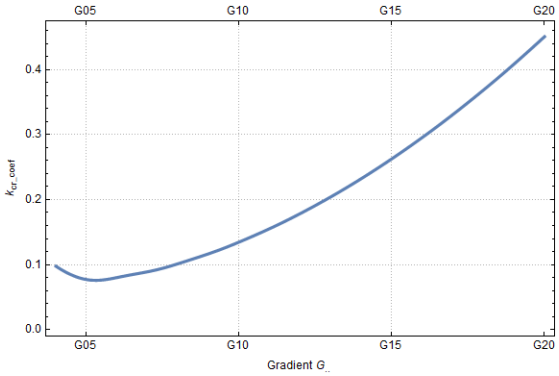

Fig. 4. Coefficient of critical force.

Equation of motion is obtained by substituting function (12) into equation (10) and by using the Galerkin method.

$$\frac{d^2\tilde{w}_a}{dt^2} + k_N\left\{\left[1-\tilde{N}_x^o(t)\right]\tilde{w}_a(t) + \frac{15}{8}\tilde{w}_a^3(t)\right\} = 0 \ , \tag{14}$$

where $\tilde{w}_a(t) = \frac{w_a(t)}{t_s}$ –dimensionless deflection, $\tilde{N}_x^o(t) = \frac{N_x^o(t)}{N_{x,CR}^o}$ – dimensionless intensity of load,

$k_N = \frac{\pi^2 N_{x,CR}^o}{\rho_s t_s a_1^{\ 2}}$ – parameter of equation.

Equation (14) is solved with the use of the Runge–Kutta method with automatic step control for the following data:

- polyethylene plate

$$a = 3b,\ b = 300mm,\ t_s = 4mm,\ E = 1.07\cdot 10^3\,\frac{N}{mm^2},\ \nu = 0.41,\ \rho_s = 952\,\frac{kg}{m^3},$$

- ferrofluid and magnetic field (data for gradient G10)

$$\mu_0 = 4\pi\cdot 10^{-7}\,\frac{V\cdot s}{A\cdot m},\ \chi = 6\cdot 10^{-2},\ h_z = 80000\,\frac{A}{m},\ h_{z,x} = 800\,\frac{A}{m^2}.$$

For varying load $N_1(t) = N_x^{\ o}\cdot t$, dynamic equilibrium paths obtained from the calculations, are presented in Fig. 5.

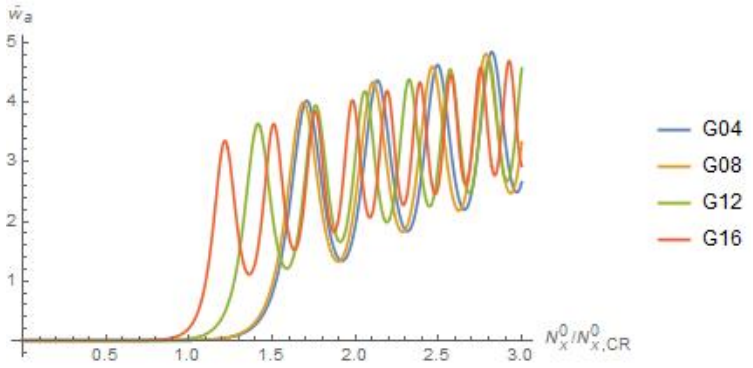

Fig. 5. Dynamic equilibrium paths.

In case of low values of the GC radius (G04 and G 08), the equilibrium paths, with similar values of critical forces, are similar to each other. However, the shape of the load is different. It is affected by the presence of partially occurring tensile load for G04.

Conclusions

In this paper, the analytical model of rectangular plate with nonlinear geometrical relations is presented. On the opposite edges there are pockets filled with ferrofluid placed in magnetic field generated by the system of Helmholtz and Golay coils. Magnetic fields affects the ferrofluid by inducing the compression force (and locally–tensile load) which is various along pockets.

- Critical forces are calculated for the corresponding values of load. In general, the smaller Golay coils the lower value of critical load appears, with the exception of the beginning of the calculations, when tensile load locally increases the values of critical load.
- Dynamic equilibrium paths are determined for different values of the radius of Golay coils.
- The values of critical force increases rapidly for coils with the radius higher than half of the width of the plate. For smaller radius of the GC, changes with the values of critical force are lower as well.
- Vibrations in dynamic equilibrium paths starts earlier for higher radius of GC, for lower radius paths are overlapping. For gradient coil which generates more homogeneous gradient magnetic field, the vibrations has almost the same amplitude. For coils with worse homogeneity (Golay coils with lower value of radius) the vibrations are unstable.

Acknowledgement

Presented research results, carried out by the statutory activities DSPB, were founded by grants for education by the Ministry of Science and Higher Education.

References

[1] Topal, U. Multiobjective optimum design of laminated composite annular sector plates. *Steel and Composite Structures* 14(2), 2013, 121-132.

[2] Pawlus, D. Solution to the problem of axisymmetric and asymmetric dynamic instability of three-layered annular plates. *Thin-Walled Structures* 49, 2011, 660–668.

[3] Teixeira, AP., Guedes Soares, C. Strength of compressed rectangular plates subjected to lateral pressure. *Journal of Constructional Steel Research* 57, 2001, 491–516.

[4] Chen, WR., Chen, CS., Shyu, JH. Stability of parametric vibrations of laminated composite plates. *Applied Mathematics and Computation* 223, 2013, 127–138.

[5] Petry, D., Fahlbusch, G. Dynamic buckling of thin isotropic plates subjected to in–plane impact. *Thin-Walled Structures* 38, 2000, 267–283.

[6] Dey, P., Singha, MK. Dynamic stability analysis of composite skew plates subjected to periodic in–plane load. *Thin-Walled Structures* 44, 2006, 937–942.

[7] Ramachandra, LS., Kumar Panda, S. Dynamic instability of composite plates subjected to non–uniform in–plane loads. *Journal of Sound and Vibrations* 331, 2012, 53–65.

[8] Chen, CS., Fung, CP., Chien RD. Nonlinear vibration of an initially stressed laminated plate according to a higher–order theory. *Composite Structures* 77, 2007, 521–532.

[9] Chen, CS. The nonlinear vibration of an initially stressed laminated plate. *Composites Part B: Engineering* 38(4), 2007, 437–447.

[10] Cui, S., Hao, H., Cheong HK. Numerical analysis of dynamic buckling of rectangular plates subjected to intermediate–velocity impact. *International Journal of Impact Engineering* 25, 2001, 147–167.

[11] Dębowski, D., Magnucki, K., Malinowski M. Dynamic stability of a metal foam rectangular plate. *Steel and Composite Structures* 10(2), 2010, 151–168.

[12] Kubiak, T. Dynamic buckling of thin-walled composite plates with varying widthwise material properties. *International Journal of Solids and Structures* 42, 2005, 5555–5567.

[13] Wang, X., Lee, JS. Dynamic stability of ferromagnetic plate under transverse magnetic field and in-plane periodic compression. *International Journal of Mechanical Sciences* 48, 2006, 889–898.

[14] Jasion, P., Magnucka-Blandzi, E., Szyc W., Magnucki K. Global and local buckling of sandwich circular and beam-rectangular plates with metal foam core. *Thin-Walled Structures* 61, 2012, 154-161.

[15] Smyczyński, M., Magnucka-Blandzi, E. Static and dynamic stability of an axially compressed five-layer sandwich beam. *Thin-Walled Structures* 90, 2015, 23-30.

[16] Uysal, MU., Güven U. Buckling of functional graded polymeric sandwich panel under different load cases. *Composite Structures* 121, 2015, 182–196.

[17] Kędzia, P., Smyczyński, M. Homogeneity of magnetic field influence on buckling of three layer polyethylene plate. Composite Structures, 2017, , http://dx.doi.org/10.1016/j.compstruct.2017.03.079.

Piotr Kędzia, Ph.D.: Poznan University of Technology, Faculty of Mechanical Engineering and Management, Piotrowo St. 3, 60-965 Poznan, POLAND (piotr.kedzia@put.poznan.pl), the author presented this work at the conference.

Krzysztof Magnucki, Professor: Institute of Rail Vehicles, TABOR, Warszawska Street 181, 61-055 Poznan, POLAND (krzysztof.magnucki@put.poznan.p.).

Mikołaj Smyczyński, Ph.D.: Poznan University of Technology, Faculty of Mechanical Engineering and Management, Piotrowo St. 3, 60-965 Poznan, POLAND (mikolaj.smyczynski@put.poznan.pl).

Iwona Wstawska, M.Sc. (Ph.D. student): Poznan University of Technology, Faculty of Mechanical Engineering and Management, Piotrowo St. 3, 60-965 Poznan, POLAND (iwona.wstawska@put.poznan.pl).

Application of numerical simulation in thermal cycle acquisition errors identification

Tomasz Kik, Bernard Wyględacz

Abstract: In acquisition of highly variable thermal cycles present in welding processes errors caused by plethora of physical phenomena impact drastically measured data, especially when heat cycles must be measured not on material surface. This mistakes cause analysis of recorded thermal cycles often lead to false conclusions. Modern non-linear FEM software like SYSWELD, enables accurate thermos-metallurgical calculations of highly variable thermal cycles. Aim of this paper is identification of errors caused factors like: hole drilled to place thermocouple on set depth, wrong contact point and plane of thermocouple, limited contact patch between material and condenser welded thermocouple. Additionally, solutions for systematic error correction in FEM model will be proposed that could enable comparison between measured and calculated thermal cycles.

1. Introduction

Weldability is important term in metallic material science. By definition it is: "Metallic material is considered to be susceptible to welding to an established extent with given processes and for given purposes when welding provides metal integrity by a corresponding technological process for welded parts to meet technical requirements as to their own qualities as well as to their influence on a structure they form [1]. Thermal cycle acquisition, calculation and analysis is one of most important aspects of understanding welding process and underlying problems causing poor weldability [2].

1.1. Thermal cycle acquisition and errors

Most widespread method of thermal cycle recording is use of thermocouples and digital acquisition methods. To gather most valuable data often surface measurements are not sufficient. To perform thermal cycle measurement from quasi-inside of material small hole is drilled and thermocouple is placed on the bottom of said hole and secured in place by condenser welding. The physical measurement to digital data result path enables us to divide errors during acquisition into 2 main categories:

- errors on physical property-voltage signal transformation – there are mostly connected to faulty placement or fabrication of thermocouples, to small contact patch between spherical thermocouple and metal surface, changes in sample properties caused by drilled hole.

- digital acquisition errors – there are wildly known and caused by discretization in time and value, and non-ideal characteristic of digital measurement circuits.

Based on prior work of authors much more impacting and much harder to eliminate are errors of the first group [2-7].

1.2. Welding numerical simulation

On the present market there is a lot of software solution, which are more or less suitable for numerical simulations of welding processes. In the presented works SYSWELD – product of ESI Group was used. SYSWELD covers now the complete area of non-linear Finite Element Method (FEM) analyses such as non-linear heat conduction, non-linear geometry of large distortions, isotropic and kinematic material hardening or metallurgical transformations. Connection of many different phenomena present during welding process results in very high precision of simulations results and their coherence with real welding results. It is possible to simulate welding with or without filler material using heat sources with physical contact (friction stir welding, resistance welding) and without contact (electric arc, laser and electron beam). Similarly wide is a range of possible analyses of heat treatment. It is possible to analyse for example: tempering, hardening, carburizing, nitriding. Input data for calculations are the same as data in the Welding Procedure Specification prepared and also based on the typical knowledge and experience of welding engineers and moderate from the FEM area. Important is fact, that results of these analyses are not only the temperature distribution fields but also metallurgical phases, distortions, stresses and hardness distribution [4,8].

To ensure high level of results accuracy and real results compatibility, very important are well prepared material databases. In SYSWELD mechanical properties are defined as dependent on the temperature and metallurgical phases mixture. Outside of the thermo-mechanical data such as heat transfer coefficient, specific heat/enthalpy, density, Young modulus, Poisson's ratio, Yield strength or strengthening important are also metallurgical properties. SYSWELD takes into consideration metallurgical phase changes, austenite transformation kinetic during heating (TTA diagram) and ferrite, bainite and martensite transformation during cooling (CCT, TTT diagrams) [3,4].

Except the well prepared material database, also very important is a proper definition of heat source model. From FEM analysis point of view, a heat source is modelled in SYSWELD by a volume density of energy applied to elements Q(x,y,z), which move along the welding trajectory. All process parameters are included in definition of heat source: energy, efficiency coefficient, torch shape, etc. FORTRAN type function used for description heat source depends on current location of and time. It consists on the mathematical description of the energy distribution and the welding trajectory.

"Volumetric density of energy" defined by this FORTRAN function on the current point depends on the distribution of density around the centre of the source and trajectory. In SYWELD except our own heat source definition, we have three predefined sources shapes: 2D Gauss, double ellipsoid (also called Goldak's heat source) and 3D cone [4,8].

A volume heat source defined by a double ellipsoid is advised to simulate welding processes as a MIG and TIG. But thanks to thermal load area shaping it is also possible to model other methods. As a standard, this model consists of two different single ellipsoids. Both ellipsoids are described by geometrical parameters as: a_f, a_r, a, b and c as it was shown at figure 1.

By changing these parameters we have the advantages in the greater flexibility in modelling of a heat source shape. SYSWELD enable the capability to introduce density energy Q_R [w/mm^3] which is divided on O_f and Q_r values. First of them is a heat energy density in the front half of the ellipsoid (maximum source frontal intensity) and second is the rear part (maximum source rear intensity), figure 2. Values of the power density energy function $Q_R(x,y,z,t)$ is described by equations:

$$Q_R = Q_f \cdot e^{-\frac{x^2}{a_f^2}} \cdot e^{-\frac{y^2}{b^2}} \cdot e^{-\frac{z^2}{c^2}} \quad \text{for the front half of the heat source model,} \tag{1}$$

$$Q_R = Q_r \cdot e^{-\frac{x^2}{a_r^2}} \cdot e^{-\frac{y^2}{b^2}} \cdot e^{-\frac{z^2}{c^2}} \quad \text{for the rear half of the the heat source model.} \tag{2}$$

Finally, the total power of this source model is:

$$P = \int_{structure} Q_R \tag{3}$$

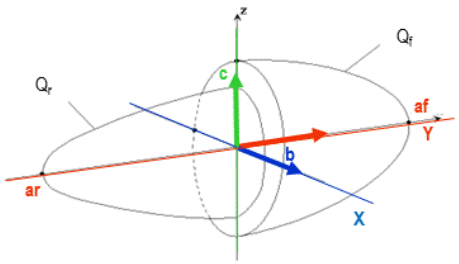

Figure 1. Definition of a double ellipsoid heat source model in SYSWELD [4]

Due to the specific of High Power Diode Lasers (HPDL), which have mainly rectangular or square beam spot shape, it is not possible to use 3D cone model as usually for lasers is used. Thanks to the some possibilities which give us SYSWELD and combined available models with definition of places where the heat source model affects the 3D model, we can configure our own method of

putting heat into the structure which is very similar to the rectangular beam spot of HDPL lasers, Fig. 2 [2].

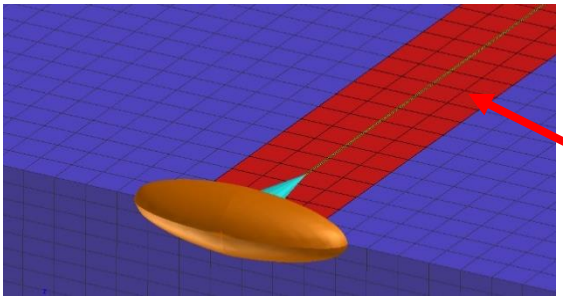

Figure 2. View of heat source –heat application area combination for HDPL heat source

2. Experimental

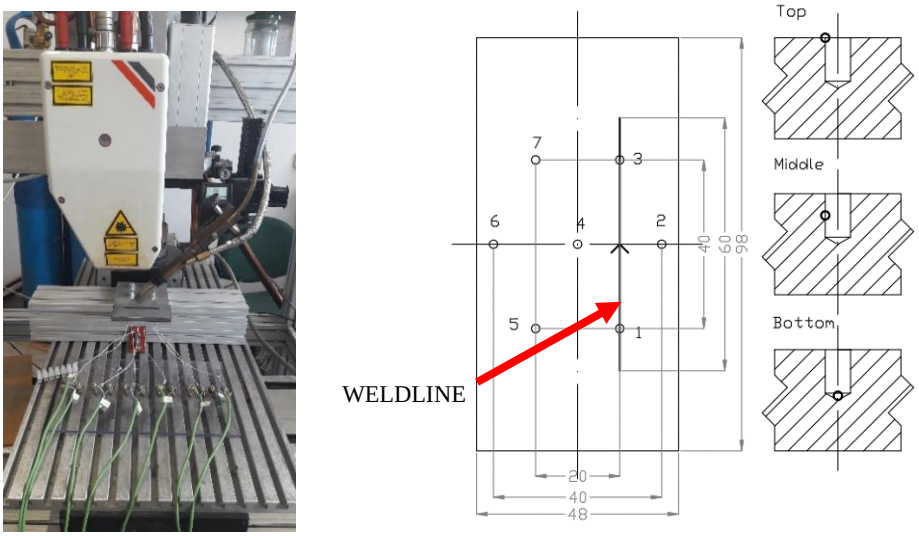

Figure 3. View of experimental stand (on the left side) and thermocouple placement on samples and 3 types of thermocouple welding to circular channel (on the right)

For thermal cycle acquisition several rectangular samples were prepared. Samples were cut from S355 8 mm thick steel plate. Steel surface was grinded smooth to ensure stable and uniform absorption coefficient across all the samples. Heat source used in all tests was high power diode laser (HPDL) Rofin DL020, figure 3. Laser welding is characterized by high parameter stability if worked surface is uniform. Three beam power levels were used 1200 W, 1600 W and 2000 W. Welding speed was 0,5 m/min. Shielding gas was argon 5.0 in purity with flow rate of 18 l/min. All temperature

measurements were performed by K type thermocouples (NiCr-NiAl). Thermocouples were placed in 7 spots around welding path in circular cross section channels 2 mm in diameter 4 mm in depth. 2 types of faulty placements were tested: welding thermocouple on the edge of the channel, welding thermocouple to the side of circular channel in the middle of its depth, as well as, correct placement of thermocouple on the bottom of drilled channel. Placement of thermocouples on sample and on channels cross-sections, as well as, sample dimensions are presented in figure 3. Voltage data from thermocouples was capture by Agilent 34970A capture card. Sampling rate with all 7 channels active was 5.8 Hz, and with one channel active sampling rate was 55 Hz. Lower sampling rate was sufficient to omit any loss of information.

FEM model consisting of 56448 3D elements and 63315 nodes was prepared. Specific heat source of HDPL was modeled by modified Goldak's heat source (double ellipsoidal heat source). As a result of heat source fitting 3 heat source functions corresponding to 3 welding parameter sets were achieved. Surface and cross section distribution of heat sources are visible in figure 4. From several calculation methods of SYSWELD software 3D transient thermos-metallurgical calculations, as it enables simulation of temperature field in welded workpiece volume during welding. Node collectors were placed in ideal thermocouple region point.

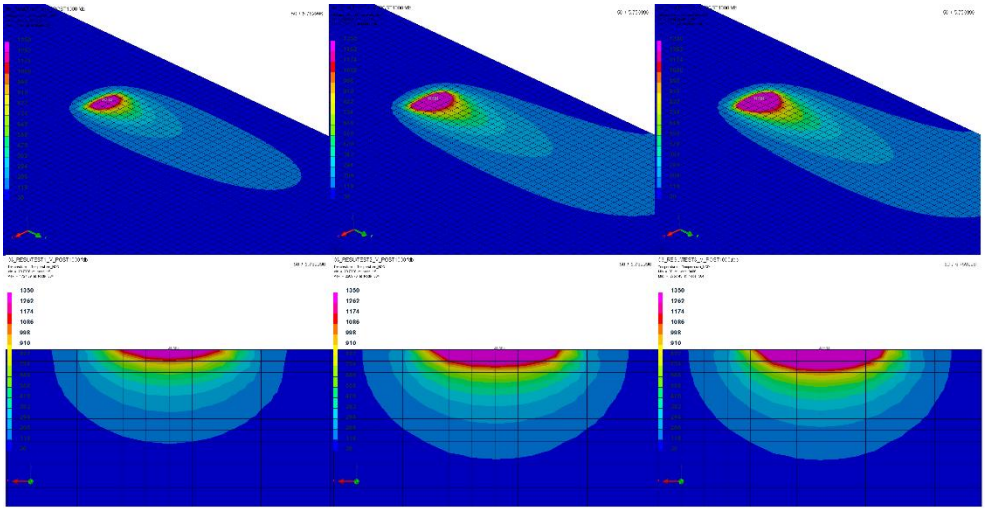

Figure 4. Fitted heat sources on surface and cross-section for (from left) power 1200 W, 1600 W, 2000 W

3. Result and analysis

Heat cycle results from 7 thermocouples in all placements were recorded and extracted as tables. Heat cycles from simulation solution were extracted from points corresponding to ideal thermocouple placement. Numeric values were plotted and timing of acquired data was adjusted to simplify data analysis. Sample plot of simulation results against data from correctly placed thermocouples from sample welded with HDPL power 1600 is shown in figure 5. Simulated heat cycles show much higher maximal values as well as higher heating and cooling speeds. It is general tendency across all dataset and from authors experience is connected to limited contact area of globular thermocouple and its heat inertia. These two properties make thermocouple to act as first order inertial element, which is further proved by small delay in peak value timepoint.

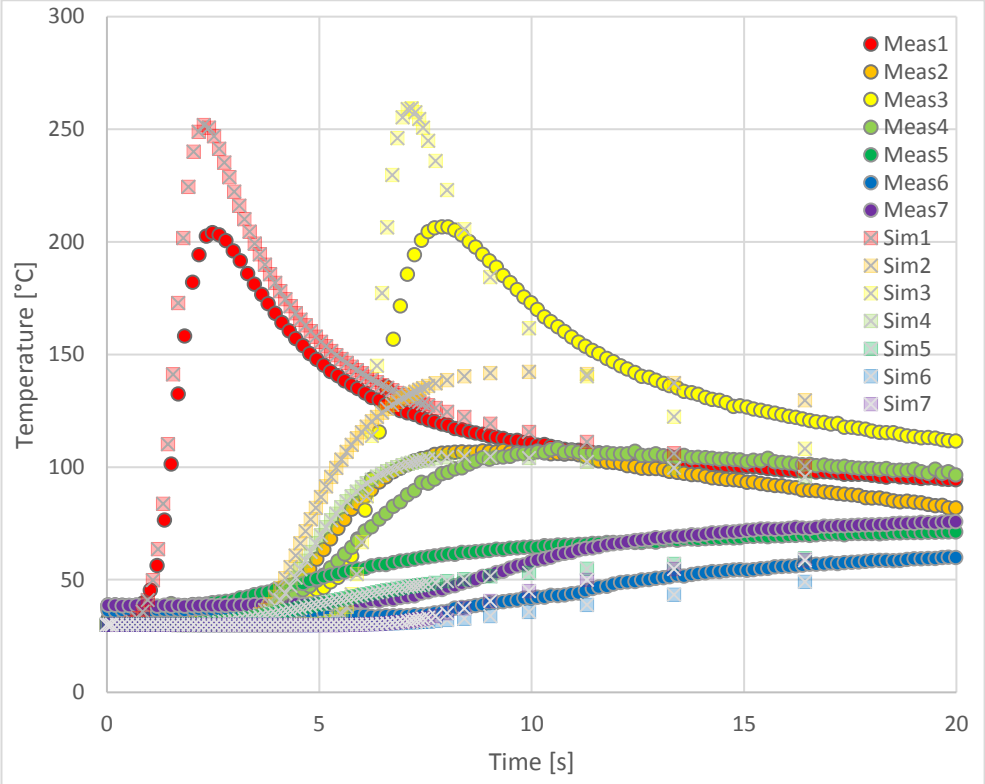

Figure 5. Measured and simulated heat cycles. Data from Simulation and correctly placed thermocouples from sample welded with laser power of 1600 W

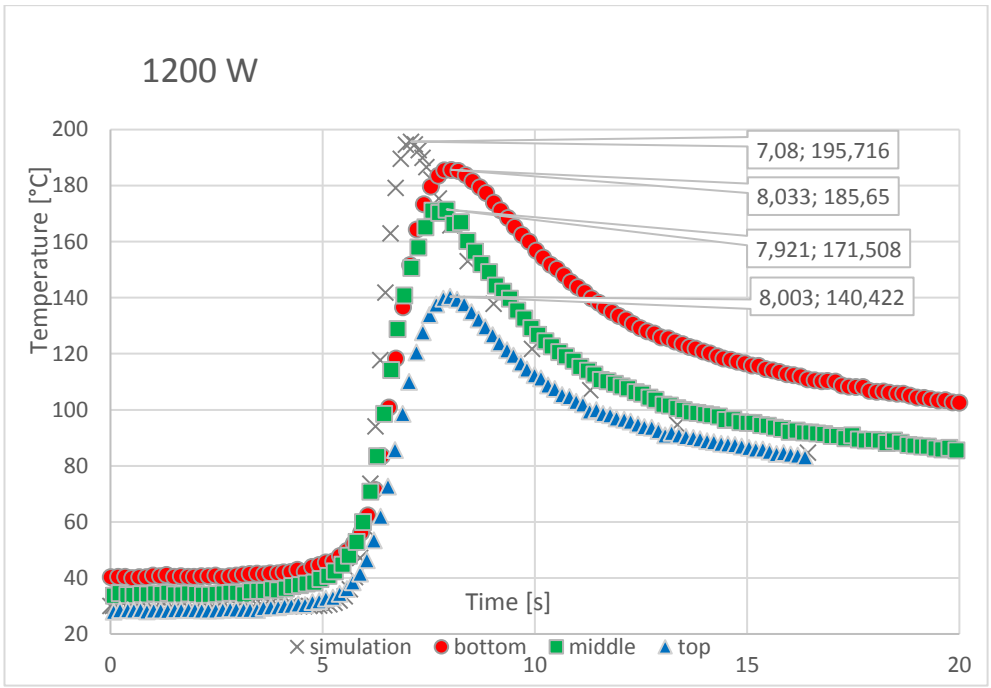
1200 W
Temperature [°C]
200
180
160
140
120
100
80
60
40
20
0
5
10
15
20
Time [s]
7,08; 195,716
8,033; 185,65
7,921; 171,508
8,003; 140,422
simulation
bottom
middle
top

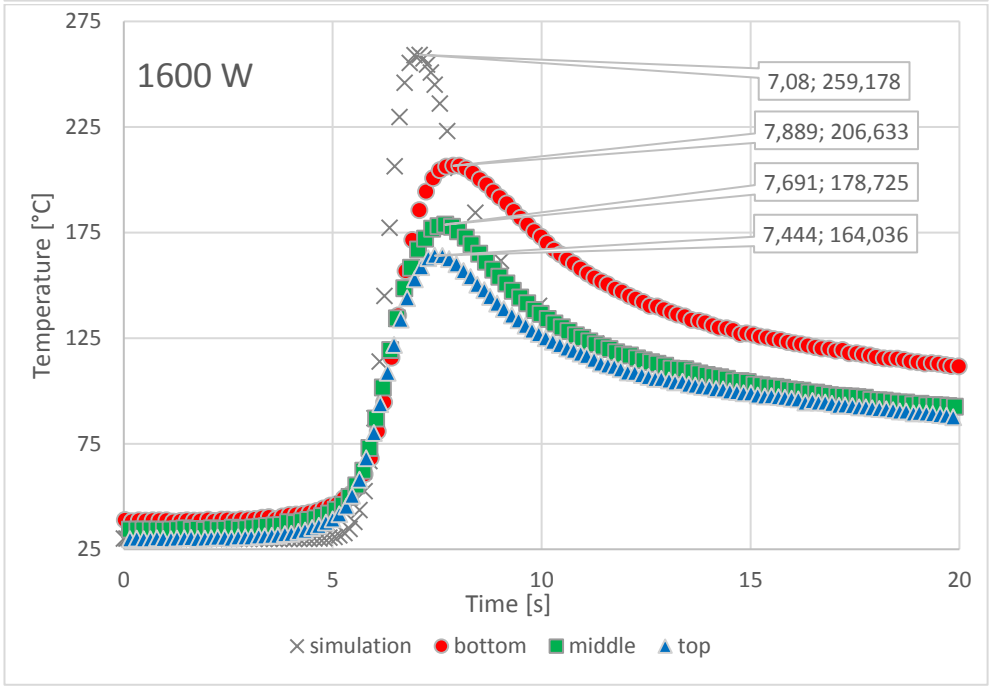
1600 W
Temperature [°C]
275
225
175
125
75
25
0
5
10
15
20
Time [s]
7,08; 259,178
7,889; 206,633
7,691; 178,725
7,444; 164,036
simulation
bottom
middle
top

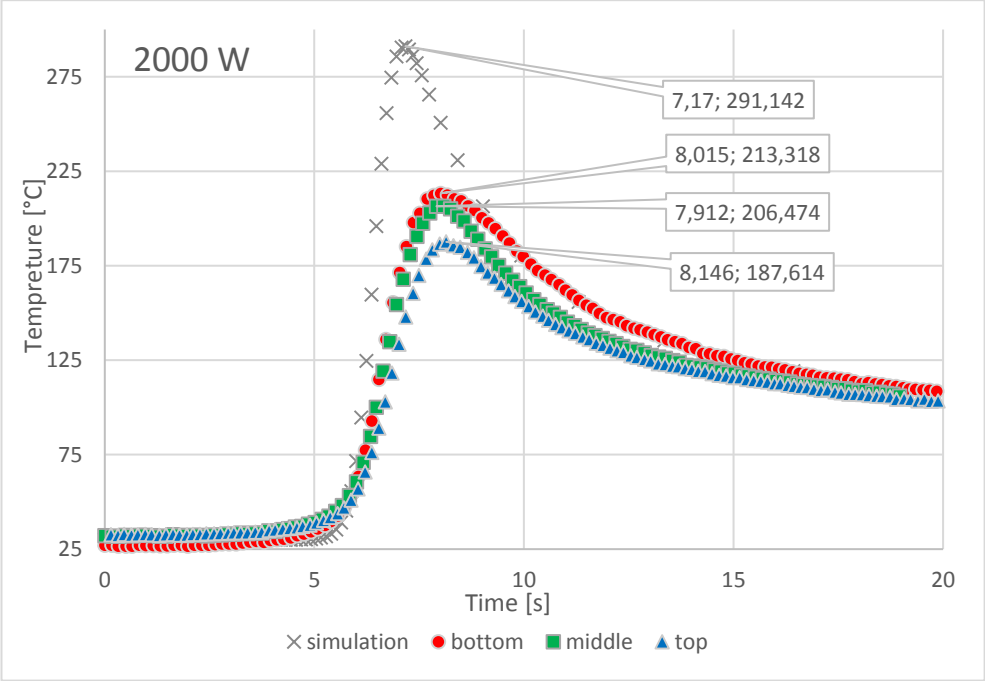

Figure 6. Thermocouple No. 3 simulated and measured heat cycles across all parameter and variation placement

Additionally, plots from one of the thermocouple placements for all variation of faulty placements across 3 parameters sets are shown in figure 6. Thermocouple No. 3 (see figure 4) was chosen as one of the closest to welding path, resulting in most distinctive heat cycle. As predicted most accurate are results from thermocouples placed correctly. However, with increasing laser power, which with constant welding speed increases welding linear energy, the measured temperatures are increasingly lower compared to calculated values. This is result of inertial behavior of measuring method. This makes heat cycle measured close to welding with this method high error rate. This is problematic as heat cycles nearest the path are most important when analyzing welding and working out causes of reduced weldability. Incorrect placement of thermocouple in drilled channel results in increasing difference between ideal heat cycle and measured one. Proposed resolution for reducing this difference is change of measured temperature node placement to actual placement of thermocouple. This would be possible after determining real thermocouple placement after destructive testing made post heat cycle acquisition. This method can be used when measured data is used to scale, correct and verify simulation.

After recalculation of simulation with corrected plotted node placement, results were compared to measured results. Most accurate were results from thermocouple condenser welded to edge of drilled hole. This results present very high convergence with simulation and surprisingly sharply reducing inertia of thermocouple (decreased difference between highest temperature and heating and cooling speeds. This could be caused by increase of energy concentration and resistance during condenser welding of thermocouple to sample resulting in increased contact area. Sample results plots of corrected model and measured values is shown in Fig. 7.

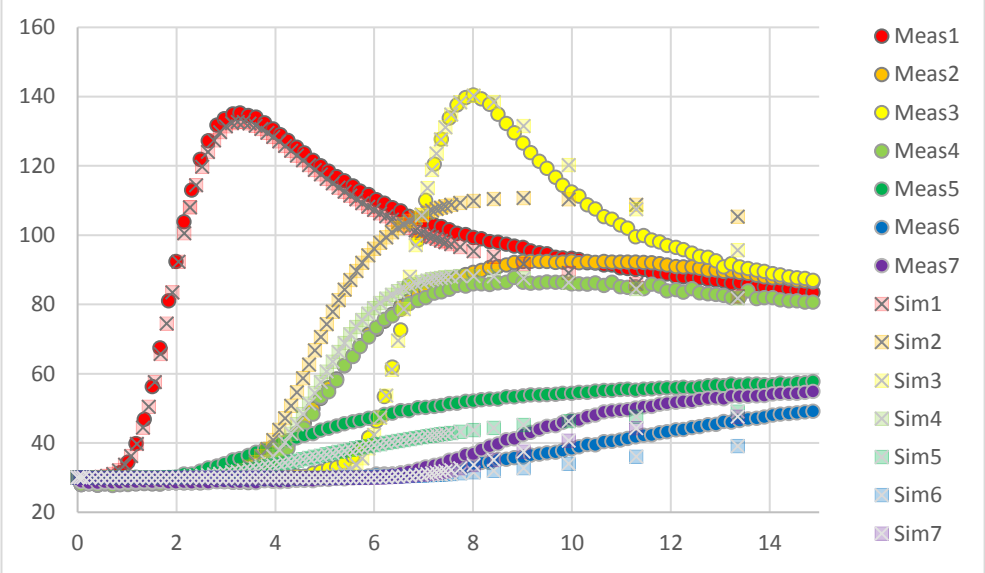

Figure 7. Heat cycle from HPDL power 1200 W and top placement of thermocouples and corrected placement of nodes in simulated model

4. Conclusions

Presented study proves high impact of faulty measuring element placement on measured heat cycles. This is valid problem as non-destructive verification of measuring element placement is not possible when drilled hole placement is used.

Proposed solution increased convergence of simulation results in case of data collection node location correction when faulty connected thermocouples where used during heat cycle acquisition. This enables use of collected data for scaling, correction and verification of simulation when faulty placement of measuring element is detected after measurements were taken in lieu of retaking measurements which can be costly and time consuming.

Another defined high error cause is inertial behavior of measuring element, probably caused by to small contact patch between element and sample or to big diameter of spherical thermocouple.

Due to described problems, useful and free of these faults are well prepared numerical simulations. They give us the possibilities to avoid some technical disturbances and offer very high repeatability in analyses, especially when we take into consideration lots of variants. As presented results shown, compared to the real measurement tests, FEM analyses offer also high level of coherence between calculated and real values.

References

[1] ISO standard 581-2005*: Weldability -- Metallic materials -- General principles.*

[2] Wyględacz, B., Kik, T., Janicki, D. Numerical simulation and heat cycle examination of WCL steel laser hardening. *Przegląd Spawalnictwa* 89, 5 (2017), 91-95.

[3] Kik, T., Burda, M. Numerical simulation in laboratory research of welding processes as a tool for study CNT stability in molten metal. *The First International Conference on Modern Manufacturing Technologies in Industrial Engineering. ModTech 2013, Sinaia, Romania, June 27-29, 2013. Book of abstracts.* Modtech Publishing House,(2013), 2286-4369.

[4] *Welding simulation user guide 2016*, Sysweld manual ESI Group.

[5] Pathak, C. S., Navale, L. G., Sahasrabudhe, A. D., and Rathod, M. J. Analysis of Thermal Cycle during Multipass Arc Welding, *Welding Journal* 91, 5 (2012), 149-154.

[6] Wu, CS., Wang, HG., Zhang, YM. A new heat source model for keyhole plasma arc welding in FEM analysis of the temperature profile. *Welding Journal* 85, 12 (2006), 284-291.

[7] Yanhong, T., Chunqing, W., Danyang, Z., Zhouc, Y. Finite element modeling of electron beam welding of a large complex Al alloy structure by parallel computations. *Journal of materials Processing Technology* 199 (2008), 41–48.

[8] Bradáč, J. Calibration of heat source model in numerical simulations of fusion welding, 11 (2013), 9-12.

Tomasz Kik, Ph.D.: Silesian University of Technology – Department of Welding, Konarskiego 18A, 44-100 Gliwice, Poland (*tomasz.kik@posl.pl*).

Bernard Wyględacz, M.Sc. (Ph.D. student): Silesian University of Technology – Department of Welding, Konarskiego 18A, 44-100 Gliwice, Poland (*bernard.wygledacz@polsl.pl*)

The control of the artillery-rocket set in conditions of random interferences

Zbigniew Koruba

Abstract: On the contemporary battlefield, there is a need for continuous improvement of combat capabilities, including speed, target detection, target identification and firing capabilities by short range artillery-rocket sets. The challenge is to be able to successfully fire such sets in conditions of interference not only from the cannon side but also from the moving platform on which the cannon and self-propelling missiles are mounted. In addition, the set is a system with variable mass because in a short time from a few to dozens to even hundreds of missiles can be fired - so we are dealing with a strongly nonlinear system with variable parameters (non-stationary). The paper presents a method of controlling such a set under kinematic conditions of the mobile base on which the set is mounted and during shooting to the captured air target. Some results of numerical simulation tests are presented in graphical form.

1. Introduction

In modern Artillery-Rocket Sets (ARSs), it is aimed to capture low-flying, manoeuvring air targets not only in all weather conditions, but also during movement of the carrier on the unevenness of the surface on which such a set is mounted – both on land and water surface [3, 4, 8].

An example of the set discussed in this paper is the Pilica system. It is a very short-range anti-aircraft system dedicated to the defence of important military and civilian objects, both fixed and mobile, from air attacks from up to 5 km. It has an integrated computerized system for detecting, identifying and managing targets, which ensures high efficiency with high mobility and low cost of exploitation.

The set is equipped with a stabilized optoelectronic day-night head, which can work independently from armament in the scope of observation, detection and target identification. It is not only an element of the guidance system, but also a source of information for the entire system, since the data on detected and observed objects are exchanged throughout the chain of command. Each set is also equipped with a laser radiation warning system.

The paper analyses the issue of selection of such a stabilization and control system with this type of set, so that the search and tracking process can reliably take place at the disadvantageous conditions mentioned in the introduction. It is necessary to develop an adequate mathematical model of the set in question, because in the systems of automatic self-propelled rocket control PD or PID controllers are most commonly used, that fail in cases where a change in the structure or parameters of the set occurs (e.g. during ammunition storage firing or damage in combat conditions) [4, 5]. In addition, inevitably during the operation of the set, there are both process and measurement noises, so it is necessary to

restore condition variables and filter the measurement data. Therefore, the extended Kalman filter was used to control the set, along with a modified Jacobian LQR regulator instead of a state matrix [1, 7]. As a result of this synthesis, a modified LQG regulator was used.

2. Mathematical model of the set movement

The linearized ARS motion equations are represented in the following form [2, 7]:

$$\Delta\dot{\mathbf{x}}_{ARS} = \mathbf{J}_{ARS}\Delta\mathbf{x}_{ARS} + \mathbf{B}_{ARS}\mathbf{u}_{ARS} \tag{1}$$

where: $\Delta\mathbf{x}_{ARS} = \mathbf{x}_{ARS} - x^*_{ARS} = \begin{bmatrix} x_1 \\ x_2 \\ x_3 \\ x_4 \end{bmatrix} - \begin{bmatrix} x_1^* \\ x_2^* \\ x_3^* \\ x_4^* \end{bmatrix}$; $\mathbf{B}_{ARS} = \begin{bmatrix} 0 & 0 \\ \dfrac{1}{ax_3^3 + bx_3^2 + cx_3 + \tilde{I}_1} & 0 \\ 0 & 0 \\ 0 & \dfrac{1}{I_2} \end{bmatrix}$; $\mathbf{u}_{ARS} = \begin{bmatrix} M_{c1} \\ M_{c2} \end{bmatrix}$

while $\Delta\mathbf{x}_{ARS}$ – vector of state variables deviation from desired values; $\mathbf{x}_{ARS} = [x_1; x_2; x_3; x_4]$ – vector of real variables of ARS state; $x^*_{SAR} = [x_1^*, x_2^*, x_3^*, x_4^*]$ – vector of ARS state variables at work point, i.e. the vector of the desired values of state variables.

The present in the equation (1) $\mathbf{J}_{ARS}$ matrix is a Jacobian of the following form:

$$J_{ARS} = \begin{bmatrix} \left.\frac{\partial g_1}{\partial x_1}\right|_{x_1^*} & \left.\frac{\partial g_1}{\partial x_2}\right|_{x_2^*} & \left.\frac{\partial g_1}{\partial x_3}\right|_{x_3^*} & \left.\frac{\partial g_1}{\partial x_4}\right|_{x_4^*} \\ \left.\frac{\partial g_2}{\partial x_1}\right|_{x_1^*} & \left.\frac{\partial g_2}{\partial x_2}\right|_{x_2^*} & \left.\frac{\partial g_2}{\partial x_3}\right|_{x_3^*} & \left.\frac{\partial g_2}{\partial x_4}\right|_{x_4^*} \\ \left.\frac{\partial g_3}{\partial x_1}\right|_{x_1^*} & \left.\frac{\partial g_3}{\partial x_2}\right|_{x_2^*} & \left.\frac{\partial g_3}{\partial x_3}\right|_{x_3^*} & \left.\frac{\partial g_3}{\partial x_4}\right|_{x_4^*} \\ \left.\frac{\partial g_4}{\partial x_1}\right|_{x_1^*} & \left.\frac{\partial g_4}{\partial x_2}\right|_{x_2^*} & \left.\frac{\partial g_4}{\partial x_3}\right|_{x_3^*} & \left.\frac{\partial g_4}{\partial x_4}\right|_{x_4^*} \end{bmatrix} \tag{2}$$

where: $\left.\frac{\partial g_1}{\partial x_1}\right|_{x_1^*} = 0;\ \left.\frac{\partial g_1}{\partial x_2}\right|_{x_2^*} = 1;\ \left.\frac{\partial g_1}{\partial x_3}\right|_{x_3^*} = 0;\ \left.\frac{\partial g_1}{\partial x_4}\right|_{x_4^*} = 0;\ \left.\frac{\partial g_2}{\partial x_1}\right|_{x_1^*} = 0;$

$$\left.\frac{\partial g_2}{\partial x_2}\right|_{x_2^*} = -\frac{3a\left(x_3^*\right)^2 + 2bx_3^* + c}{ax\left(x_3^*\right)^3 + b\left(x_3^*\right)^2 + cx_3^* + \tilde{I}_1} x_4^*;$$

$$\left.\frac{\partial g_2}{\partial x_3}\right|_{x_3^*} = -\frac{\left[a\left(x_3^*\right)^3 + b\left(x_3^*\right)^2 + cx_3^* + \bar{I}_1\right]\left(6a\left(x_3^*\right)^2 + 2b\left(x_3^*\right)^2 + c\right) + \left[3a\left(x_3^*\right)^3 + b\left(x_3^*\right)^2 + c\right]^2}{\left[a\left(x_3^*\right)^3 + b\left(x_3^*\right)^2 + cx_3^* + \bar{I}_1\right]^2};$$

$$\left.\frac{\partial g_2}{\partial x_4}\right|_{x_4^*} = -\frac{3a\left(x_3^*\right)^2 + 2bx_3^* + c}{ax\left(x_3^*\right)^3 + b\left(x_3^*\right)^2 + cx_3^* + \bar{I}_1}x_2^*;\ \left.\frac{\partial g_3}{\partial x_1}\right|_{x_1^*} = 0;\ \left.\frac{\partial g_3}{\partial x_2}\right|_{x_2^*} = 0;\ \left.\frac{\partial g_3}{\partial x_3}\right|_{x_3^*} = 0;\ \left.\frac{\partial g_3}{\partial x_4}\right|_{x_4^*} = 1;$$

$$\left.\frac{\partial g_4}{\partial x_1}\right|_{x_1^*} = 0;\ \left.\frac{\partial g_4}{\partial x_2}\right|_{x_2^*} = -\frac{3a\left(x_3^*\right)^2 + 2bx_3^* + c}{I_2}x_2^*;\ \left.\frac{\partial g_4}{\partial x_3}\right|_{x_3^*} = -\frac{3a\left(x_3^*\right)^2 + b\left(x_2^*\right)^2 + \frac{mgr}{I_2}\sin\left(x_3^* + \gamma\right)}{I_2};\ \left.\frac{\partial g_4}{\partial x_4}\right|_{x_4^*} = 0,$$

On the other hand, g_1, g_2, g_3, g_4 functions in the above relationships are the right-hand sides of the non-linear state equations describing the ARS dynamics model [4]:

$$\frac{dx_1}{dt} = x_2 = g_1 \tag{3}$$

$$\frac{dx_2}{dt} = -\frac{3ax_3^2 + 2bx_3 + c}{ax_3^3 + bx_3^2 + cx_3 + \bar{I}_1}x_2x_4 + \frac{\eta_1\dot{x}_2 + M_{z1} + M_{c1}}{ax_3^3 + bx_3^2 + cx_3 + \bar{I}_1} = g_2 \tag{4}$$

$$\frac{dx_3}{dt} = x_4 = g_3 \tag{5}$$

$$\frac{dx_4}{dt} = -\frac{0.5\left(3ax_3^2 + 2bx_3 + c\right)}{I_2}x_2^2 - \frac{mgr}{I_2}\cos\left(x_3 + \gamma\right) + \frac{\eta_1\dot{x}_2 + M_{z1} + M_{c1}M_2}{I_2} = g_4 \tag{6}$$

where: $x_1 = \Theta_1$ – ARS azimuth angle; $x_2 = \dot{\Theta}_1$ – ARS azimuth angle speed; $x_3 = \Theta_2$ – ARS elevation angle; $x_4 = \dot{\Theta}_2$ – ARS elevation angle speed; η_1, η_2 – coefficients of moments of friction forces acting in ARS azimuth and elevation, respectively; $\bar{I}_1 = I_1 pn + q + d$ – variable mass moment of inertia of the set with respect to the azimuth axis, depending on the number of cartridges in cases *n*; I_1 – constant mass moment of inertia of the set with respect to azimuth axis; I_2 – constant mass moment of inertia of the set with respect to bearing axis; *m* – mass of 2 member; *g* – gravitational acceleration; *a*, *b*, *c*, *d*, *q*, *r*, γ – parameters of the set described in detail in the paper [4]; M_{z1}, M_{z1} – moments of external disturbances in azimuth and elevation, respectively; M_{c1} – moment controlling the deviation of the set in azimuth; M_{c2} – moment controlling the set tilt in elevation.

3. ARS control algorithm with modified LQG method

Control law $\mathbf{u}_{ARS}$ for ARS will be defined by means of linear-square optimization method [2] with the function in the following form:

$$I_{ARS} = \int_0^{\infty} \left(\mathbf{x}_{ARS}^T \mathbf{Q}_{ARS} \mathbf{x}_{ARS} + \mathbf{u}_{ARS}^T \mathbf{R}_{ARS} \mathbf{u}_{ARS} \right) dt \tag{7}$$

Let's present this law using a formula

$$\mathbf{u}_{ARS} = -\mathbf{K}_{ARS} \cdot \left(\mathbf{x}_{ARS} - \mathbf{x}_{ARS}^* \right) \tag{8}$$

Where $\mathbf{x}_{ARS}^* = \left[\sigma \quad \dot{\sigma} \quad \varepsilon \quad \dot{\varepsilon} \right]$ – the set (desired) condition variables that determine the location of the Line Of Sight (LOS) are determined from the following equations [2]:

$$\frac{dR_{LOS}}{dt} = -V_c \left[\cos\chi_c \cos\sigma \left(\varepsilon - \gamma_c \right) + \sin\chi_c \sin\sigma \right] = f_1 \tag{9a}$$

$$\frac{d\varepsilon}{dt} = -\frac{V_c \cos\chi_c \sin\left(\varepsilon - \gamma_c \right)}{R_{LOS} \cos\sigma} = f_2 \tag{9b}$$

$$\frac{d\sigma}{dt} = -\frac{V_c \left[\cos\chi_c \sin\sigma \cos\left(\varepsilon - \gamma_c \right) - \sin\chi_c \cos\sigma \right]}{R_{LOS}} = f_3 \tag{9c}$$

where: ε, σ – pitch and yaw angles of the line of sight, respectively; R_{LOS} – distance between the ARS and the aerial target; V_c – velocities of the target; χ_c, γ_c – pitch and yaw angles of the target velocity vector, respectively.

Convergence matrix $\mathbf{K}_{ARS}$ occurring in equation (8) is derived from the following relationship

$$\mathbf{K}_{ARS} = \mathbf{R}_{ARS}^{-1} \cdot \mathbf{B}_{ARS}^T \cdot \mathbf{P}_{ARS} \tag{10}$$

Matrix $\mathbf{P}_{ARS}$ is a solution to the Riccati algebraic equation

$$J_{ARS}^T \mathbf{P}_{ARS} + \mathbf{P}_{ARS} J_{ARS} - 2\mathbf{P}_{ARS} \mathbf{B}_{ARS} \mathbf{R}_{ARS}^{-1} \mathbf{B}_{ARS}^T \mathbf{P}_{ARS} + \mathbf{Q}_{ARS} = \mathbf{0} \tag{11}$$

The occurring in equations (10) and (11) $\mathbf{R}_{ARS}$ i $\mathbf{Q}_{ARS}$ weight matrixes reduced to a diagonal form are selected experimentally, while the search is starting with values equal to [2]:

$$q_{ii} = \frac{1}{2x_{i\max}}, \quad r_{jj} = \frac{1}{2u_{j\max}}, \quad \left(i = 1,2,..4 \right), \quad \left(j = 1,2 \right) \tag{12}$$

where: $x_{i\max}$ – maximum scope of changes of *i*- value of the status variable; $u_{j\max}$ – maximum scope of changes of *j*- control variable value.

In the case of ARS interference in the form of process noise and measurement noise, we will use the extended Kalman filter, which we write in the form of the following differential equations:

$$\mathbf{x}_{ARS\_k} = \mathbf{J}_{ARS}\mathbf{x}_{ARS\_k-1} + \mathbf{B}_{ARS}\mathbf{u}_{ARS\_k-1} + \mathbf{w}_{ARS\_k-1} \tag{13}$$

$$\mathbf{z}_{ARS\_k} = \mathbf{H}_{ARS}\mathbf{x}_{ARS\_k} + \mathbf{v}_{ARS\_k} \tag{14}$$

where: $\mathbf{z}_{ARS}$ – vector containing measurement of the output of state variables ARS; $\mathbf{H}_{SAR}$ – measurement matrix; **w** – process noise vector of zero expected value and known covariance matrix $\mathbf{Q}_{ARS}^{FK}$; **v** – measurement noise vector of zero expected value and known covariance Prediction of ARS state in k moment on the basis of the estimate of state and control from the previous moment:

$$\hat{\mathbf{x}}_{ARS\_k|k-1} = \mathbf{J}_{ARS\_k-1}\hat{\mathbf{x}}_{ARS\_k-1|k-1} + \mathbf{B}_{ARS}\mathbf{u}_{ARS\_k-1} \tag{15}$$

$$\mathbf{P}_{ARS\_k|k-1}^{FK} = \mathbf{A}_{ARS\_k-1}\mathbf{P}_{ARS\_k-1|k-1}^{FK}\mathbf{A}_{ARS\_k-1}^{T} + \mathbf{Q}_{ARS}^{FK} \tag{16}$$

where: $\hat{\mathbf{x}}_{ARS\_k-1|k-1}$ – assessment of ARS variables a priori (before measurement); $\hat{\mathbf{x}}_{SAR\_k|k-1}$ – assessment of ARS variables a posteriori (after measurement); $\mathbf{A}_{ARS\_k-1} = \mathbf{I} - \mathbf{J}_{ARS\_k-1} \cdot \Delta t$ – ARS state matrix in *k*-1 in discrete form; Δt – discretization step (integration); I – unit matrix; $\mathbf{P}_{ARS\_k-1|k-1}^{FK}$ – covariance matrix of predictive error before measurement for ARS; $\mathbf{P}_{ARS\_k|k-1}^{FK}$ – covariance matrix of predictive error after measurement for ARS; $\mathbf{Q}_{ARS}^{FK} = E\left[\mathbf{w}_{ARS\_k-1}\left(\mathbf{w}_{ARS\_k-1}\right)^{T}\right]$ – covariance matrix of process noise for ARS.

Update (i.e. correction) of state estimate and covariance error matrix based on input measurement at present:

$$\mathbf{K}_{ARS\_k}^{FK} = \mathbf{P}_{ARS\_k|k-1}^{FK}\mathbf{H}_{ARS}^{T}\left(\mathbf{H}_{ARS}\mathbf{P}_{ARS\_k|k-1}^{FK}\mathbf{H}_{ARS}^{T} + \mathbf{R}_{ARS}^{FK}\right)^{-1} \tag{17}$$

$$\hat{\mathbf{x}}_{ARS\_k|k} = \hat{\mathbf{x}}_{ARS\_k|k-1} + \mathbf{K}_{ARS\_k}\left(\mathbf{z}_{ARS\_k} - \mathbf{H}_{ARS}^{FK}\hat{\mathbf{x}}_{k|k-1}\right) \tag{18}$$

$$\mathbf{P}_{ARS\_k|k}^{FK} = \left(\mathbf{I} - \mathbf{K}_{ARS\_k}^{FK}\mathbf{H}_{ARS}^{FK}\right)\mathbf{P}_{ARS\_k|k-1}^{FK} \tag{19}$$

where: $\mathbf{K}_{ARS}^{FK}$ – Kalman filter gain matrix for ARS; $\mathbf{R}_{ARS}^{FK} = E\left[\mathbf{v}_{ARS\_k-1}\cdot\left(\mathbf{v}_{ARS\_k-1}\right)^T\right]$ – covariance matrix of measurement noise for ARS; $\mathbf{P}_{ARS\_k|k}^{FK}$ – covariance matrix of filtration error for ARS.

As a result of the control synthesis we get an LQG regulator in the form of

$$\mathbf{u}_{ARS} = -\mathbf{K}_{ARS}\cdot\left(\hat{\mathbf{x}}_{ARS} - \mathbf{x}_{ARS}^{*}\right) \tag{20}$$

In the case of random interactions on the target tracking system, Jacoban should be created for the LOS movement model described by equations (9). It will be as follows:

$$\mathbf{J}_{LOS} = \begin{bmatrix} \frac{\partial f_1}{\partial r} & \frac{\partial f_1}{\partial \varepsilon} & \frac{\partial f_1}{\partial \sigma} \\ \frac{\partial f_2}{\partial r} & \frac{\partial f_2}{\partial \varepsilon} & \frac{\partial f_2}{\partial \sigma} \\ \frac{\partial f_3}{\partial r} & \frac{\partial f_3}{\partial \varepsilon} & \frac{\partial f_3}{\partial \sigma} \end{bmatrix} \tag{21}$$

where: $\frac{\partial f_1}{\partial r} = 0$; $\frac{\partial f_1}{\partial \varepsilon} = V_c\cos\chi_c\cos\sigma\sin\left(\varepsilon-\gamma_c\right)$; $\frac{\partial f_1}{\partial \sigma} = V_c\left[\sin\chi_c\sin\sigma - \cos\chi_c\sin\sigma\cos\left(\varepsilon-\gamma_c\right)\right]$;

$\frac{\partial f_2}{\partial r} = \frac{V_c\cos\chi_c\sin\left(\varepsilon-\gamma_c\right)}{r^2\cos\sigma}$; $\frac{\partial f_2}{\partial \varepsilon} = -\frac{V_c\cos\chi_c\cos\left(\varepsilon-\gamma_c\right)}{r\cos\sigma}$;

$\frac{\partial f_2}{\partial \sigma} = -\frac{V_c\cos\chi_c\sin\sigma\sin\left(\varepsilon-\gamma_c\right)}{r\cos^2\sigma}$; $\frac{\partial f_3}{\partial r} = \frac{V_c\left[\cos\chi_c\sin\sigma\sin\left(\varepsilon-\gamma_c\right) - \sin\chi_c\cos\sigma\right]}{r^2}$;

$\frac{\partial f_3}{\partial \varepsilon} = \frac{V_c\cos\chi_c\sin\sigma\sin\left(\varepsilon-\gamma_c\right)}{r}$; $\frac{\partial f_3}{\partial \sigma} = -\frac{V_c\left[\cos\chi_c\cos\sigma\cos\left(\varepsilon-\gamma_c\right) + \sin\chi_c\sin\sigma\right]}{r}$.

The formulas for the extended Kalman filter for LOS will then be written as:

$$\mathbf{x}_{LOS\_k} = \mathbf{A}_{LOS}\mathbf{x}_{LOS\_k-1} + \mathbf{w}_{LOS\_k-1} \tag{22}$$

$$\mathbf{z}_{LOS\_k} = \mathbf{H}_{LOS}\mathbf{x}_{LOS\_k} + \mathbf{v}_{LOS\_k} \tag{23}$$

$$\hat{\mathbf{x}}_{LOS\_k|k-1} = \mathbf{A}_{LOS\_k-1}\hat{\mathbf{x}}_{LOS\_k-1|k-1} \tag{24}$$

$$\mathbf{P}_{LOS\_k|k-1}^{FK} = \mathbf{A}_{LOS\_k-1}\mathbf{P}_{LOS\_k-1|k-1}^{FK}\mathbf{A}_{LOS\_k-1}^{T} + \mathbf{Q}_{LOS}^{FK} \tag{25}$$

$$\mathbf{K}_{LOS\_k}^{FK} = \mathbf{P}_{LOS\_k|k-1}^{FK}\mathbf{H}_{LOS}^{T}\left(\mathbf{H}_{LOS}\mathbf{P}_{LOS\_k|k-1}^{FK}\mathbf{H}_{LOS}^{T} + \mathbf{R}_{LOS}^{FK}\right)^{-1} \tag{26}$$

$$\hat{\mathbf{x}}_{LOS\_k|k} = \hat{\mathbf{x}}_{LOS\_k|k-1} + \mathbf{K}_{LOS\_k}\left(\mathbf{z}_{LOS\_k} - \mathbf{H}_{LOS}^{FK}\hat{\mathbf{x}}_{k|k-1}\right) \tag{27}$$

$$\mathbf{P}_{LOS\_k|k}^{FK} = \left(\mathbf{I} - \mathbf{K}_{LOS\_k}^{FK}\mathbf{H}_{LOS}^{FK}\right)\mathbf{P}_{LOS\_k|k-1}^{FK} \tag{28}$$

where: $\hat{\mathbf{x}}_{LOS\_k-1|k-1}$ – assessment of LOS state variables a priori (before measurement); $\hat{\mathbf{x}}_{LOS\_k|k-1}$ – assessment of LOS state variables a posteriori (after measurement); $\mathbf{A}_{LOS\_k-1} = \mathbf{I} - \mathbf{J}_{LOS\_k-1} \cdot \Delta t$ – LOS state matrix at *k*-1 in discrete form; $\mathbf{P}_{LOS\_k-1|k-1}^{FK}$ – covariance matrix of predictive error before measurement for LOS; $\mathbf{P}_{LOS\_k|k-1}^{FK}$ – covariance matrix of predictive error after measurement for ARS; $\mathbf{Q}_{LOS}^{FK} = E\left[\mathbf{w}_{LOS\_k-1}\left(\mathbf{w}_{LOS\_k-1}\right)^T\right]$ – covariance matrix of process noise for LOS; $\mathbf{R}_{LOS}^{FK} = E\left[\mathbf{v}_{LOS\_k-1} \cdot \left(\mathbf{v}_{LOS\_k-1}\right)^T\right]$ – covariance matrix of measurement noise for LOS;.

Taking into account the Kalman filtering of target sight lines, the LQG regulator for control of the artillery-rocket set in terms of random interferences influence will be as follows:

$$\mathbf{u}_{ARS} = -\mathbf{K}_{ARS} \cdot \left(\hat{\mathbf{x}}_{ARS} - \hat{\mathbf{x}}_{ARS}^{*}\right) \tag{29}$$

where $\hat{\mathbf{x}}_{ARS}^{*} = \left[\hat{\sigma} \quad \dot{\hat{\sigma}} \quad \hat{\varepsilon} \quad \dot{\hat{\varepsilon}}\right]$.

Therefore, the optimal control moments that we will use to control the ARS while tracking and shooting to the manoeuvring air target, will take the form of

$$M_{c1} = \mathbf{u}_{ARS}(1) \tag{30a}$$

$$M_{c2} = \mathbf{u}_{ARS}(2) \tag{30b}$$

(30a) and (30b) include the following limitations:

$$\left|M_{c1}\right| \le M_{c1\max};\ \left|M_{c2}\right| \le M_{c2\max} \tag{31}$$

where: $M_{c1\max}$ – maximum allowable control moment in azimuth; $M_{c2\max}$ – maximum allowable control moment in elevation.

4. Numerical example and results

Let's consider a hypothetical artillery-rocket set that detects and tracks the maneuvering low-flying target. The basic parameters of the considered set are taken from [4]. Numerical simulations were performed in MATLAB environment with integration step *dt*= 0.001 [s]. The following initial conditions for ARS status variables and their evaluations were adopted: $\mathbf{x}_{ARS0} = \left[0 \quad 1.5 \quad 0 \quad 2.5\right]$,

$\hat{\mathbf{x}}_{ARS0} = [0 \quad 0 \quad 0 \quad 0]$. Weight matrixes for optimal controls LQR:

$$\mathbf{Q}_{ARS} = \begin{bmatrix} 40000 & 0 & 0 & 0 \\ 0 & 0.1 & 0 & 0 \\ 0 & 0 & 40000 & 0 \\ 0 & 0 & 0 & 0.1 \end{bmatrix}; \ \mathbf{R}_{ARS} = \begin{bmatrix} 0.0001 & 0 \\ 0 & 0.0001 \end{bmatrix}.$$

he effectiveness of the modified LQR and LQG regulators has been examined by comparing the optimum settings of the PID controller described in the paper [4].

It was assumed that the ARS state variables measurement matrix is as follows: $H_{ARS} = \begin{bmatrix} 1 & 0 & 0 & 0 \\ 0 & 1 & 0 & 0 \\ 0 & 0 & 1 & 0 \\ 0 & 0 & 0 & 1 \end{bmatrix}$. The covariance matrix of the ARS process noise– $\mathbf{Q}_{ARS}^{FK} = \alpha_{proc}^2 \mathbf{H}_{ARS} \mathbf{H}_{ARS}^T$,

where $\alpha_{proc} = 0.1$ – amplitude of process noise; Covariance matrix of ARS measurement noise – $R_{ARS}^{FK} = \alpha_{mes}^2 \mathbf{H}_{ARS} \mathbf{H}_{ARS}^T$, where $\alpha_{mes} = 0.1$ – measurement noise amplitude; covariance matrix of initial conditions; Initial covariance matrix of error of estimation of ARS state variables – $\mathbf{P}_{ARS} = \mathbf{Q}_{ARS}^{FK}$. On the other hand, air targets data have the following values:

Location of the target relative to the ARS when detected by the observing-tracking head $x_{co} = 1000[\text{m}]$; $y_{co} = 500[\text{m}]$; $z_{co} = 1000[\text{m}]$; speed of the moving targer – $V_c = 100[m/s] = const$; target observation initial conditions: – $R_{LOS0} = \sqrt{x_{co}^2 + y_{co}^2 + z_{co}^2}$; $\varepsilon_o = arctg \dfrac{y_{co}}{x_{co}}$; $\sigma_o = \arcsin \dfrac{z_{co}}{R_{LOS0}}$; $\gamma_{co} = 0$; $\chi_{co} = 0$; $\omega_{co} = 0.75[\text{rd/s}]$ – angular velocity of the target maneuver. It has been assumed that the angles of a target flight change according to the law (target maneuver): $\gamma_c = \omega_{co} t$; $\chi_c = \omega_{co} t$.

Taking into consideration the fact that the distance R_{LOS} is measured with a laser distance meter, it is assumed that the target observation system measurement matrix has the form of: $H_{LOS} = \begin{bmatrix} 1 & 0 & 0 \\ 0 & 1 & 0 \\ 0 & 0 & 1 \end{bmatrix}$. The initial conditions for the individual state vectors are as follows:

$$\mathbf{x}_{LOS0} = [R_{LOS0} \quad \varepsilon_o \quad \sigma_o], \ \hat{\mathbf{x}}_{LOS0} = [0.8R_{LOS0} \quad 0.9\varepsilon_o \quad 0.9\sigma_o], \ \hat{\mathbf{x}}_{ASR0}^* = [0 \quad 0 \quad 0 \quad 0].$$

The covariance matrix of the LOS process noise – $\mathbf{Q}_{SLOS}^{FK} = \alpha_{proc}^2 \mathbf{H}_{LOS} \mathbf{H}_{LOS}^T$; the covariance matrix of the LOS measurement noise $R_{LOS}^{FK} = \alpha_{mes}^2 \mathbf{H}_{LOS} \mathbf{H}_{LOS}^T$; initial covariance matrix of LOS state variables estimation error – $\mathbf{P}_{LOS} = \mathbf{Q}_{LOS}^{FK}$.

Interferences were introduced in form of three shots simulated as rectangular pulses in the form of: $M_{s1} = \Pi(t_{z11}, t_{z12})M_{01} + \Pi(t_{z21}, t_{z22})M_{01} + \Pi(t_{z31}, t_{z32})M_{01}$,

$M_{s2} = \Pi(t_{z11}, t_{z12})M_{02} + \Pi(t_{z21}, t_{z22})M_{02} + \Pi(t_{z31}, t_{z32})M_{02}$,

where $t_{z11} = 3[s]$, $t_{z12} = 3.02[s]$, $t_{z21} = 3.22[s]$, $t_{z22} = 3.24[s]$, $t_{z31} = 3.44[s]$, $t_{z32} = 3.46[s]$ – moments of firing individual shots; $M_{01} = 1000[\text{Nm}]$, $M_{02} = 12000[\text{Nm}]$ – moments of forces acting from the shot in azimuth and elevation, respectively; $\Pi(...)$ – rectangular stroke function in the time interval $[t_{zi1}; t_{zi2}]$, $i = 1,2,3$.

It was assumed that the base on which the set is mounted is affected by both azimuth and elevation in the form of the following moments:

$M_{b1} = 0.8 \cdot [(\sin(0.9t - \pi/2) + 1)]$, $M_{b2} = 1.5 \cdot [(\sin(0.5t - \pi/2) + 1)]$.

Fig. 1–14 present the results of the conducted simulation tests. Trajectories during the interference moments from the base and the three shot fired are shown in fig. 1 and 2. Figures 3-10 compare the performance of the modified LQR controller (right-hand graphs) with respect to the regulator with optimally selected PID settings (left-hand graphs). Figures 11-14 illustrate the effectiveness of the modified LQG regulator with simultaneous interference from the base, interference during firing three shots and noises in ARS and LOS, both process and measurement. The results clearly demonstrate that the modified LQR regulators work better with respect to the optimal PID controller in case of interference. This is particularly evident in Figures 5 and 6. On the other hand, in the case of random effects, the LQR regulator is also insufficient to ensure the accuracy of LOS tracking (see Fig. 8 and 10). In this case, the most effective in action is the modified LQG regulator. This is shown in fig.11-14.

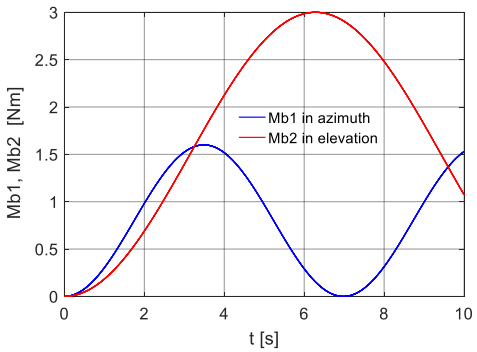

Figure 1. Moments interfering as a function of time affecting on ARS from the base side

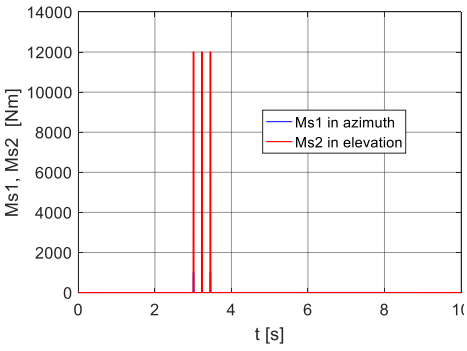

Figure 2. Moments interfering as a function of time when firing 3 shots affecting on ARS

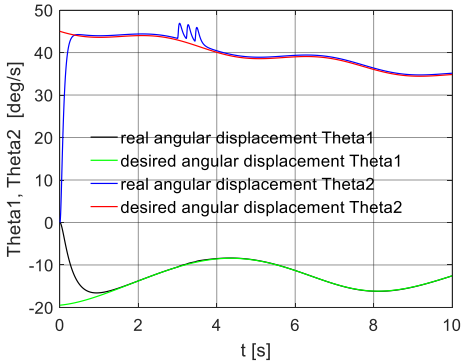

Figure 3. Angular displacements real and desired in azimuth and elevation with interference – PID control

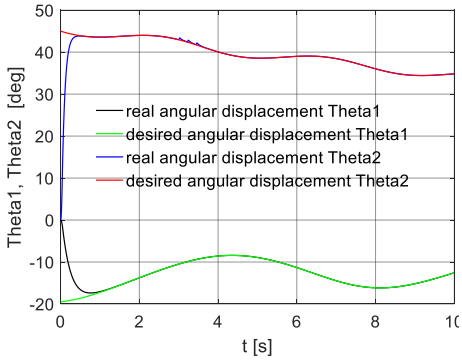

Figure 4. Angular displacements real and desired in azimuth and elevation with interference – LQR control

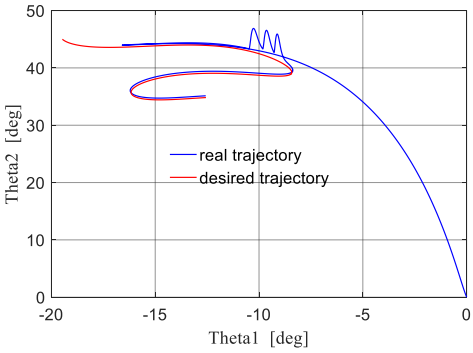

Figure 5. Trajectory real and desired of ARS with interference – PID control

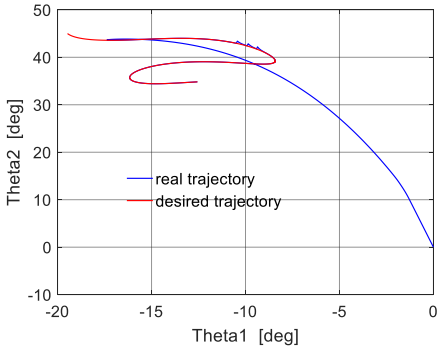

Figure 6. Trajectory real and desired of ARS with interference – LQR control

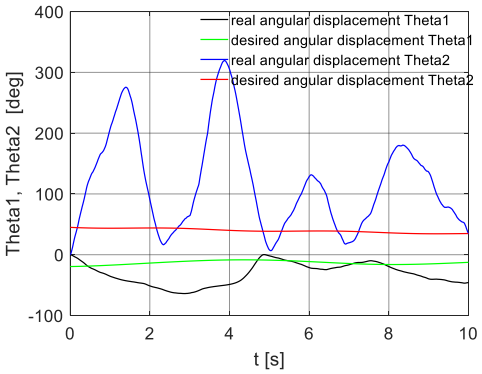

Figure 7. Angular displacements real and desired in azimuth and elevation with random interference – PID control

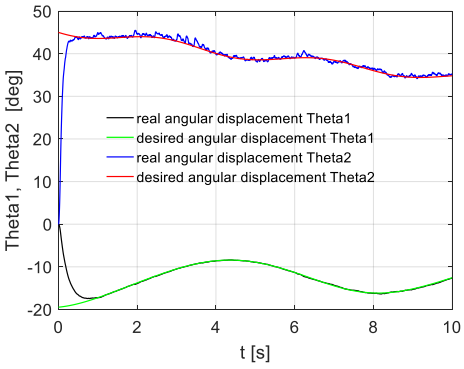

Figure 8. Angular displacements real and desired in azimuth and elevation with random interference – LQR control

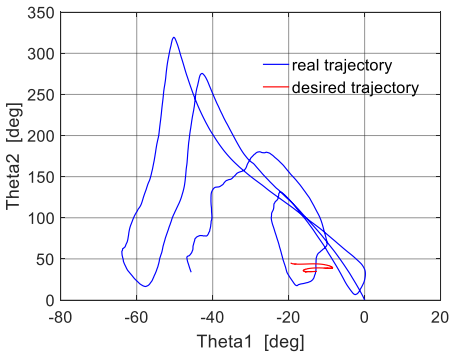

Figure 9. Trajectory real and desired ARS with random interference – PID control

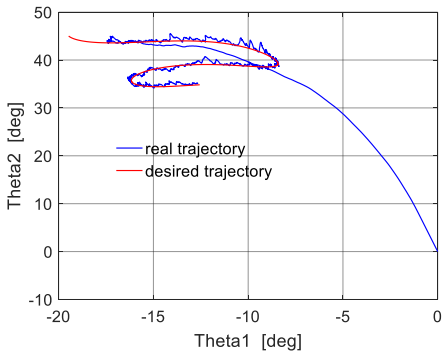

Figure 10. Trajectory real and desired ARS with random interference – LQR control

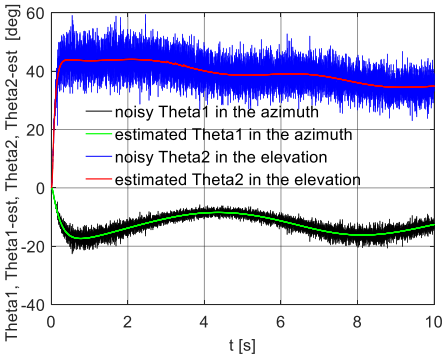

Figure 11. Angular displacements noised and estimated in azimuth and elevation – LQG control

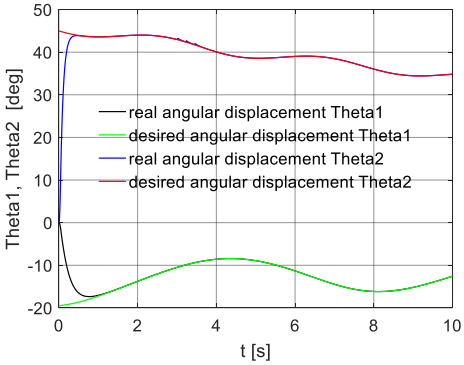

Figure 12. Angular displacements noised and estimated in azimuth and elevation – LQG control

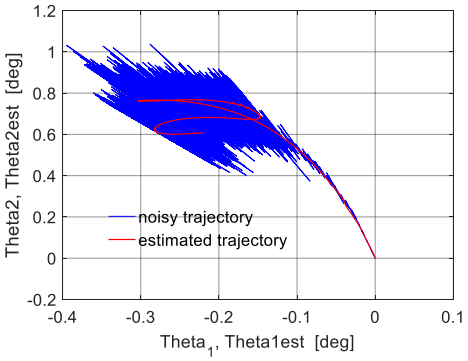

Figure 13. Noised and estimated trajectories ARS – LQG control

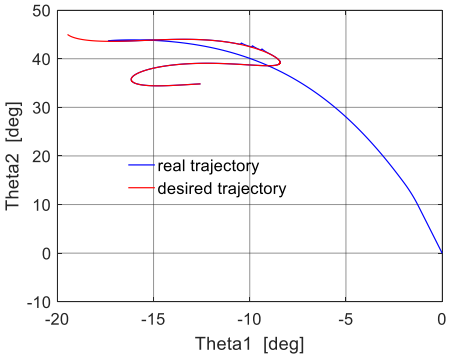

Figure 14. Noised and estimated trajectories ARS – LQG control

5. Conclusions

The algorithm presented in this paper allows for precise control of ARS system in case of interference. The example shown in this article shows that ARS tracking of the manoeuvring air target using the Jacobian in closed control loop is more effective than using classical PID or LQR control. As the preliminary results show, improving the precision of the ARS control by around 10% can be crucial in reaching the target in such artillery-rocket systems.

As a result, the algorithm allows for such control of the set so that it is possible to minimize the impact of kinematic effects on the side of moving carrier (off-road vehicle or ship) and random external interferences. This increases its effectiveness and mobility and allows it to attack air targets during movement of the base on uneven surfaces. In the case of a land vehicle, the shooting can take place without the necessity to stop it.

Theoretical considerations and simulation studies have shown that, in conditions of ARS interference, it is preferable to use Jacobins in both extended Kalman filtering and optimum LQR control. In this way, the effectiveness of the modified LQG regulator has been demonstrated. In further research, the effectiveness of this regulator should be tested in field conditions when firing an artillery-rocket set to a low-flying maneuvering air target.

References

[1] Ashish T. *Modern control design with Matlab and Simulink*. John Wiley & Sons, New York 2002.

[2] Awrejcewicz J., Koruba Z. *Classical Mechanics. Applied Mechanics and Mechatronics. Advances in Mechanics and Mathematics*, v. 30, Monograph, Springer, 2013.

[3] Gacek J., Gwardecki J., Kobierski J., Leciejewski Z., Łuszczak S., Milewski S., Świętek T., Woźniak R., Wójcik Z. Structure and innovative Technologies In the new Polish 35 mm naval weapon system. *Conference materials of 11th International Armament Conference on Scientific Aspects of Armament & Safety Technology*, 2016, pp. 246-247.

[4] Koruba Z., Gapiński D., Szmidt P. The analysys of optimal PID controllers parameters selection for missile-artillery system. *Engineering Mechanics* 2017, pp. 970-973.

[5] Koruba Z., Krzysztofik I., Zbigniew Dziopa: An analysis of the gyroscope dynamics of an anti-aircraft missile launched from a mobile platform. *Bulletin of the Polish Academy of Sciences – Technical Sciences*, 2010, pp. 645-650.

[6] Paul Zarchan: *Tactical and strategic missile Guidance*. MIT Lincoln Laboratory Lexington, Messachuetts, 2012..

[7] Phil Kim, *Kalman Filter for Beginners with MATLAB Examples*, A-JIN Publishing, 2010.

[8] Shneyder N.A.: *Missile Guidance and Pursuit: Kinematics, Dynamics and Control*. Horwood Publishing Chichester, 1998.

Zbigniew Koruba, Professor: Kielce University of technology, Department of Computer Technology and Armaments, 7 Aleje Tysiąclecia PP St., 25-314 Kielce, Poland (ksmzko@tu.kielce.pl).

Non-linear dynamics of flexibly suspended spring pendulum embedded in gravity and electric fields

Angelika Kosińska, Dariusz Grzelczyk, Jan Awrejcewicz

Abstract: In this paper we study non-linear behavior of vertically and flexibly suspended spring pendulum embedded in both gravity and electric fields. Due to strong non-linearity of the analyzed three-degree-of-freedom mechanical system, some interesting non-linear behaviors are observed and discussed. The motion of the system for different parameters is considered by employing standard numerical methods dedicated for non-linear systems, including both qualitative and quantitative methods as well as own original animations of the system dynamics, created in Mathematica software. The investigated energy transition between fixed points and other non-linear behaviors of the considered system can be potentially applied to other similar systems such as, for instance, real electro-mechanical systems.

1. Introduction

Dynamics of a nonlinear dynamical systems belongs to the important area of an interest of numerous investigators. In those systems the steady-state motion is often observed and therefore this regime of motion is usually investigated. On the other hand, in dynamical systems with stable and unstable fixed points it may happen that the unsteady or transient behavior should also be taken into account. In many situations, in the non-steady vibrations intensive energy exchange between the coupled elements of the analyzed system and either external source, or environment, can be detected. In systems with many degrees of freedom also energy exchange between parts of the structure or between modes may often occur. For instance, the aforementioned phenomena are widely illustrated and discussed in references [1-4].

Motivated by above cited and other references, in this paper the dynamics of vertically and flexibly suspended spring pendulum embedded in both gravity and electric fields is studied. On the contrary to the previous papers, in this article, the influence of the presence of additional electric/electromagnetic forces acting on the spring pendulum is analyzed. The proposed mechanical system serves as a very good example of a study of non-linear phenomena. The motion analysis for different cases is carried out by employing standard numerical methods dedicated for nonlinear systems, including both qualitative and quantitative methods, as well as original animations of the system dynamics created in Mathematica. Main goal of this paper is calculation all stable and unstable fixed points of the system and investigations of its dynamics. To detect some interesting

results (periodic, quasi-periodic and chaotic orbits, or different scenarios of transition from regular to chaotic motion, etc.), in the future the behavior of the analyzed system will be monitored via bifurcation diagrams, Lyapunov exponents as well as power spectra densities.

2. Model of the considered system

Figure 1 shows the model of the considered planar system embedded in the gravity field of Earth with coefficient $g = 9.81\,\mathrm{m/s}^2$. The system is characterized by the following parameters: masses M and m, stiffness coefficients k and k_1, damping coefficients c and c_1, as well as lengths l_0 and L_0. The mass M is additionally excited by harmonic excitation $F_0 \cos \omega t$. Moreover, the influence of the presence of additional electric/electromagnetic force $\mathbf{Q}(t)$ acting on the spring pendulum is taken into account. The motion of considered 3-degree-of-freedom system is governed by the angle $\varphi(t)$ and linear displacements $y(t)$ and $\Delta r(t)$. Equations of motion of the system have been obtained by the Newton-Euler method, and Free Body Diagrams of the system are shown in Fig. 2.

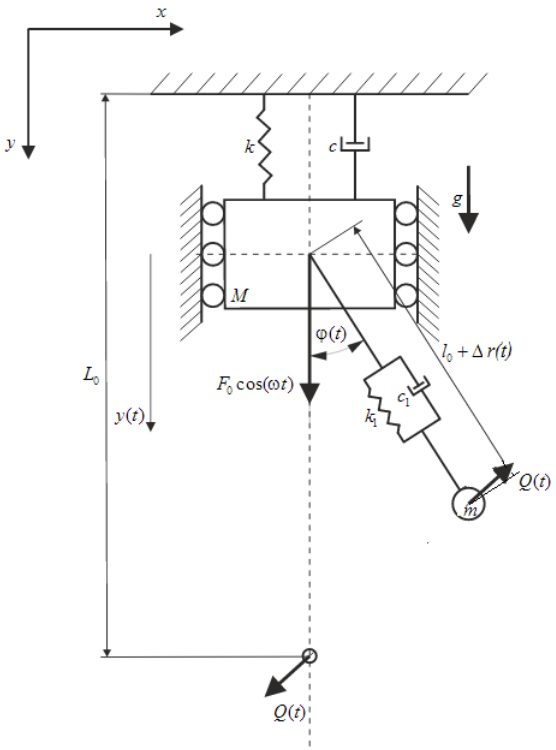

Figure 1. Model of vertically and flexibly suspended spring pendulum embedded in both gravity and electric fields.

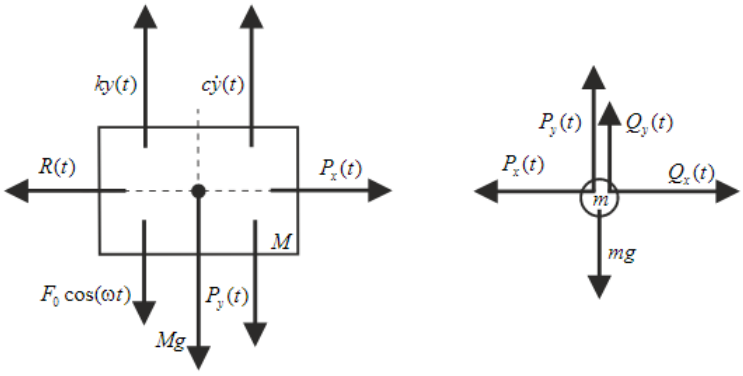

Figure 2. Free Body Diagrams of the considered mechanical planar system.

Equations of motion of the considered system have the following form:

$$M\ddot{x}(t) = P_x(t) - R(t) = 0, \tag{1}$$

$$M\ddot{y}(t) = Mg + P_y(t) - ky(t) - c\dot{y}(t) + F_0 \cos \omega t, \tag{2}$$

$$m\ddot{x}_1(t) = Q_x(t) - P_x(t), \tag{3}$$

$$m\ddot{y}_1(t) = mg - P_y(t) - Q_y(t), \tag{4}$$

where:

$x_1(t) = (l_0 + \Delta r(t)) \sin \varphi(t)$, $y_1(t) = y(t) + (l_0 + \Delta r(t)) \cos \varphi(t)$, $P_x(t) = (k_1 \Delta r(t) + c_1 \Delta \dot{r}(t)) \sin \varphi(t)$, $P_y(t) = (k_1 \Delta r(t) + c_1 \Delta \dot{r}(t)) \cos \varphi(t)$, $R(t)$ is reaction force, and $Q_x(t)$, $Q_y(t)$ are components of force $\mathbf{Q}(t)$. Additional interaction $\mathbf{Q}(t)$ acting on the point mass m in the following form:

$$\mathbf{Q}(t) = \frac{\kappa}{r^2} \frac{\mathbf{r}}{|\mathbf{r}|}, \tag{5}$$

with proportionality coefficient κ and distance r. The proposed force $\mathbf{Q}(t)$ can have both electrostatic or electromagnetic nature. After transformation this force can be estimated in the following way:

$$\mathbf{Q}(t) = \left[Q_x(t), Q_y(t)\right]^T = \left[\frac{\kappa r_x(t)}{(r_x^2(t) + r_y^2(t))^{1.5}}, \frac{\kappa r_y(t)}{(r_x^2(t) + r_y^2(t))^{1.5}} \right]^T, \tag{6}$$

where $r_x(t) = x_1(t)$ and $r_y(t) = L_0 - y_1(t)$.

3. Computational Methods

Equations of motion of the considered system written in the dimensional form have been solved numerically by the Runge-Kutta method implemented in Mathematica. Moreover, to illustrate and understand the obtained results the appropriate animation of the analyzed system has been carried out, also in Mathematica (see Fig. 3). In numerical simulations, the following initial parameters are fixed: $M = 1\,\text{kg}$, $m = 0.2\,\text{kg}$, $k = 100\,\text{N/m}$, $c = 10\,\text{N}\cdot\text{s/m}$, $k_1 = 10\,\text{N/m}$, $c_1 = 0.1\,\text{N}\cdot\text{s/m}$, $l_0 = 0.2\,\text{m}$, $L_0 = 1.0\,\text{m}$, $\kappa = 1.1\,\text{N}\cdot\text{m}^2$, and zero initial conditions are used. The obtained numerical solutions of the equations of motion presented in the dimensional form are directly applied for animation created in Mathematica. However, in our further global numerical analysis the non-dimensional equations will be used. Moreover, our future investigations (not reported here) will be aimed on getting an approximate asymptotic solution of the non-steady state motion of the considered system using the multiple time scale method [1,3].

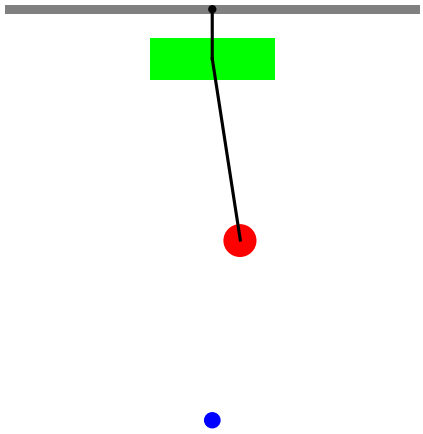

Figure 3. Frame of animation of the analyzed mechanical system presented with help of Mathematica software (the lines represent spring-damper elements).

4. Numerical results

In our numerical investigations, first all stable and unstable fixed points of the considered system (without harmonic excitation) were calculated. For $\kappa = 0$ the system possesses the following two fixed points:

(1): $y = \dfrac{(M+m)g}{k}$, $\Delta r = \dfrac{mg}{k_1}$, $\varphi = 0$,

(2): $y = \dfrac{(M+m)g}{k}$, $\Delta r = -\dfrac{mg}{k_1}$, $\varphi = \pi$.

For initial values presented in Section 3, the system has six fixed points, which, in general, can be obtained numerically. Configurations of the system for the mentioned fixed points (for initial parameters presented in Section 3 are depicted in Figs. 4 and 5.

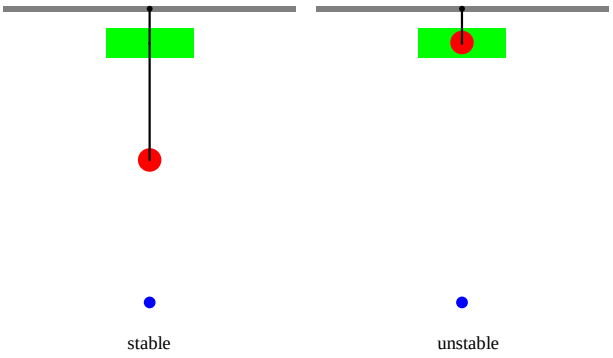

Figure 4. System configurations and fixed points for $\kappa = 0$.

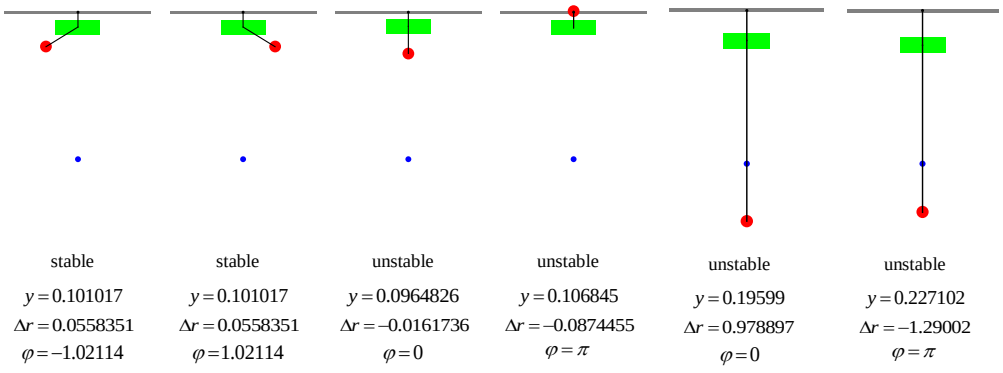

Figure 5. System configurations and fixed points for $\kappa = 1.1\,\mathrm{N}\cdot\mathrm{m}^2$.

In the first case (Fig. 4) we have classical simple and inverted gravity pendulum (a stable equilibrium position for the simple pendulum and unstable equilibrium position for the inverted pendulum). In the cases of configurations of the system presented in Fig. 5, both simple or inverted pendulum in vertical position are located in unstable positions. Between these unstable fixed points there are also fixed stable points.

In our numerical analysis we obtained some chosen time histories of angles $\varphi(t)$ and trajectories of the point mass m . We detected different scenarios of transition of the system from initial conditions to stable fixed points. For instance, point mass m moves from initial conditions to a near first unstable point (simple hanging pendulums placed in vertical positions), and finally reaching the

first or the second stable position. In other cases, spring pendulum moves from initial conditions, and oscillate near all stable and unstable fixed points, being finally attracted by one of the stable position. The considered system is sensitive on the parameter κ responsible for additional force acting on the spring pendulum. Even a small change of these parameters push the considered pendulum to move from the initial conditions to the different fixed points.

Movements of the considered spring pendulum can be regular or irregular, depending on the system parameters. Therefore, the periodic and non-periodic solutions of the considered system have been globally detected using bifurcation diagrams. For instance, in Figs. 6-8 we presented bifurcation diagrams with frequency ω of harmonic excitation as a control parameter.

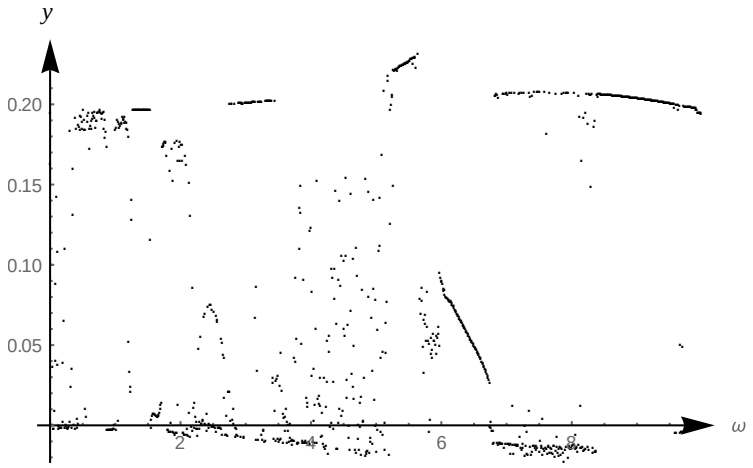

Figure 6. Bifurcation diagram of the system: y vs. frequency ω as the control parameter.

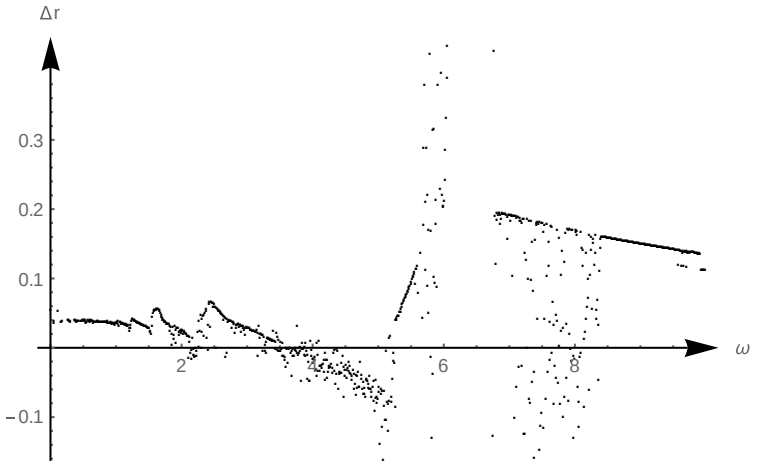

Figure 7. Bifurcation diagram of the system: Δr vs. frequency ω as the control parameter.

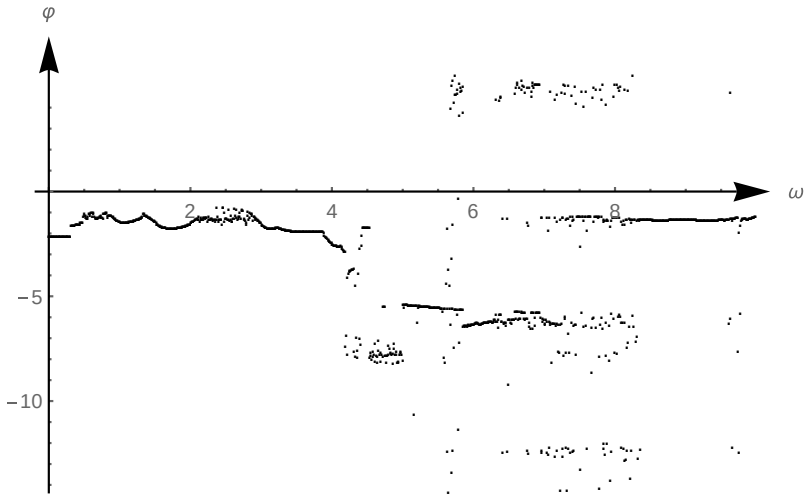

Figure 8. Bifurcation diagram of the system: φ vs. frequency ω as the control parameter.

5. Conclusions

In this paper dynamics of flexibly suspended spring pendulum embedded in gravity and electric fields is investigated. First, stable and unstable fixed points of the system are calculated analytically and numerically. Next, dynamical behaviors near fixed points are presented and discussed. Due to mathematical complexity the considered system is investigated numerically with a help of the Mathematical software. Numerical calculations are performed for certain set of parameters and initial conditions. Therefore, a few nonlinear phenomena occurring for a narrow range of the parameters may be not detected. In should be emphasized that analytical approach allows to obtain the solution as a function of some chosen parameters which gives the opportunity to discuss the results for full spectrum of the system parameters. Our further research will be focused on analytical and/or numerical analysis of the considered system in the non-dimensional form, including resonance and synchronization effects, different scenarios of transition from regular to chaotic motion, bifurcation diagrams, Lyapunov exponents, power spectra densities, etc.

References

[1] Awrejcewicz, J., Starosta, R., Sypniewska-Kamińska, G. Asymptotic analysis and limiting phase trajectories in the dynamics of spring pendulum. In: *Applied Non-Linear Dynamical Systems, Springer Proceedings in Mathematics & Statistics* 93, (2014), 161-173.

[2] Grzelczyk, D., Awrejcewicz, J. Resonances and synchronization in two coupled oscillators with stick-slip vibrations and spring pendulums. *Proceedings of the 5th International Conference on Nonlinear Dynamics*, Kharkov, Ukraine, September 27-30, 2016, 100-107.

[3] Manevitch, L.I., Musienko, A.I. Limiting phase trajectories and energy exchange between anharmonic oscillator and external force. *Nonlinear Dynamics* 58, (2009), 633-642.

[4] Starosvetsky, Y., Gendelman, O.V. Dynamics of a strongly nonlinear vibration absorber coupled to a harmonically excited two-degree-of-freedom system. *Journal of Sound and Vibration* 312, (2008), 234-256.

Angelika Kosińska, M.Sc. (Ph.D. student): Lodz University of Technology, Department of Automation, Biomechanics and Mechatronics, 1/15 Stefanowski Str., 90-924 Lodz, Poland (*angelika.kosinska@dokt.p.lodz.pl*). The author gave a presentation of this paper during one of the conference sessions.

Dariusz Grzelczyk, Ph.D.: Lodz University of Technology, Department of Automation, Biomechanics and Mechatronics, 1/15 Stefanowski Str., 90-924 Lodz, Poland (*dariusz.grzelczyk@ p.lodz.pl*).

Jan Awrejcewicz, Professor: Lodz University of Technology, Department of Automation, Biomechanics and Mechatronics, 1/15 Stefanowski Str., 90-924 Lodz, Poland (*jan.awrejcewicz@p.lodz.pl*).

Sliding control of a gyroscopic scanning and tracking system mounted on a moveable base

Izabela Krzysztofik

Abstract: The basic tasks of the self-propelled anti-aircraft missile set are performed by the weapon module. An important element of the weapon module equipment is the system for searching and tracking the target. Its purpose is to determine the location of the line of sight (LOS). Target detecting and tracking systems are subject to disturbances caused by vehicle movements on uneven ground. In this paper, the LOS stabiliser and controller is a gyroscopic system and high precision of operation is required of it. Therefore, the control system and parameters of the controller itself must be carefully selected. A sliding controller has been designed and implemented in a gyroscopic scanning and tracking system mounted on a combat vehicle. Simulations of dynamics of a controlled gyroscopic system were performed in Matlab/Simulink environment. The selected research results are presented in graphical form.

1. Introduction

Contemporary battlefields make increased demands on anti-aircraft defense systems. There is a need to increase effectiveness and mobility of missile sets. Hence, military equipment used by the army includes self-propelled missile sets, i.e. combat vehicles with remote-controlled weapons modules mounted on the chassis. Self-propelled missile sets provide the automation of searching and tracking of air targets and reliability in all weather conditions. They allow for changing the current position very quickly. The compact size of the set allows air transport and discharge into the target area. The basic tasks of a self-propelled anti-aircraft missile set are performed by the weapon module. An important element of the weapon module equipment is the system for searching and tracking the target. This system has a stabilised base, independent of the ground angular movements, on which a television camera and / or an infrared camera and a coordinating device for finding and tracking the target are mounted. Greater precision in operation of observation and tracking systems allows for effective combat operations [1,2].

This paper presents a scanning-tracking system in which the control and stabilisation element of the line of sight is the gyroscopic system described in detail in the study [3]. The principle of operation of a gyroscopic system mounted on a combat vehicle is as follows: during target searching, the axis of the system scans the airspace over the preset track where the target is likely to stay so as to capture the infrared radiation emitted by the target. When the target is detected, the gyroscopic system

starts automatically target tracking. Then the axis of the system covers with the line of sight. The use of the gyroscopic system increases the efficiency and mobility of a self -propelled missile set.

It has been assumed that the centre of the mass of the gyroscopic system covers with the centre of gravity and the inertia of the frames is omitted.

The mathematical model of the motion of the gyroscopic system is as follows:

$$J_{gk}\ddot{\vartheta} + J_k\omega_{Cy_1} + J_{go}n_g\omega_{Bz_2} - J_{gk}\omega_{Bx_2}\omega_{Bz_2} + \eta_b\dot{\vartheta} = U_b \tag{1}$$

$$\begin{aligned} &J_{gk}\dot{\omega}_{Cz_1}\cos^2\vartheta - \frac{1}{2}J_{gk}\left(\omega_{Cz_1}\dot{\vartheta} - \omega_{Cx_1}\right)\sin 2\vartheta + J_{gk}\omega_{Cx_1}\dot{\vartheta}\cos^2\vartheta + \\ &- J_{gk}\omega_{Bz_2}\omega_{By_2}\sin\vartheta - J_{go}n_g\omega_{By_2}\cos\vartheta + J_{gk}\omega_{By_2}\omega_{Bx_1} + \eta_c\dot{\psi} = U_c \end{aligned} \tag{2}$$

where:

ϑ,ψ – tilt and yaw angles of the axis of the gyroscopic system in space;

$\omega_{Cx_1} = p_n\cos\psi + q_n\sin\psi$;

$\omega_{Cy_1} = -p_n\sin\psi + q_n\cos\psi$;

$\omega_{Cz_1} = \dot{\psi} + r_n$;

$\omega_{Bx_2} = \omega_{Cx1}\cos\vartheta - \omega_{Cz1}\sin\vartheta$;

$\omega_{By_2} = \omega_{Cy1} + \dot{\vartheta}$;

$\omega_{Bz_2} = \omega_{Cx1}\sin\vartheta + \omega_{Cz1}\cos\vartheta$;

$\omega_{Cx1} = p_n\cos\psi + q_n\sin\psi + \dot{\psi}\omega_{Cy_1}$;

$\omega_{Cy1} = -p_n\sin\psi + q_n\cos\psi - \dot{\psi}\omega_{Cx_1}$;

$\omega_{Cz_1} = \dot{\psi} + r_n$;

p_n, q_n, r_n – components of angular velocity of the combat vehicle (carrier);

J_{go}, J_{gk} – adequately longitudinal and transverse moment of inertia of the gyroscopic system;

n_g – speed of rotations of the gyroscopic system;

η_b, η_c – coefficients of friction in the suspension bearings;

U_b, U_c – moments of control forces impacting on the frames of the gyroscopic system.

2. Sliding control of a gyroscopic scanning and tracking system

The gyroscopic system is affected by interferences from the combat vehicle board. An important task is optimal suppression of transient processes that occur when the vehicle hits a ground obstacle. When searching for a target, the gyroscopic system axis should make programmed movements and, upon

detection of the target, tracking movements. It is recommended to carefully select the control system and the parameters of the controller itself [4,5].

We determine the control moments from the dependence:

$$U_{b,c} = \begin{cases} U_{b,c}^{p}(t) \text{ for } t_o < t < t_w \\ U_{b,c}^{s}(t) \text{ for } t_s < t < t_k \end{cases} \tag{3}$$

where:

U_b^p ,U_c^p – programmed control moments;

U_b^s ,U_b^s – tracking control moments;

t_o – moment of starting space scanning;

t_w – moment the target is detected;

t_s – moment of starting the target tracking;

t_k – moment of a self-guidance process completion.

A sliding mode controller is designed to control the gyroscopic system both during scanning and tracking [6-8].

We define the following sliding surfaces:

$$s_b = \left(\vartheta - \vartheta_z\right) + \lambda_b\left(\vartheta - \vartheta_z\right) \tag{4}$$

$$s_c = \left(\psi - \psi_z\right) + \lambda_c\left(\psi - \psi_z\right) \tag{5}$$

where:

λ_b, λ_c – positive constants.

In order to reduce the *chattering* phenomenon, the sliding control was proposed in the form of [9]

$$U_b = -\gamma_b \frac{s_b}{|s_b| + \delta_b} + U_{beq} \tag{6}$$

$$U_c = -\gamma_c \frac{s_c}{|s_c| + \delta_c} + U_{ceq} \tag{7}$$

where:

U_{beq}, U_{ceq} – equivalent controls;

γ_b, γ_c – sliding gains.

We determine the equivalent controls from the dependence:

$$s_b = 0 \text{ and } s_c = 0 \tag{8}$$

While scanning the space, the axis of the gyroscopic system marks in the space strictly defined lines, while during target tracking, the preset angles of the axis position are determined from the LOS motion equations.

The general diagram of sliding mode controller is shown in Figure 1.

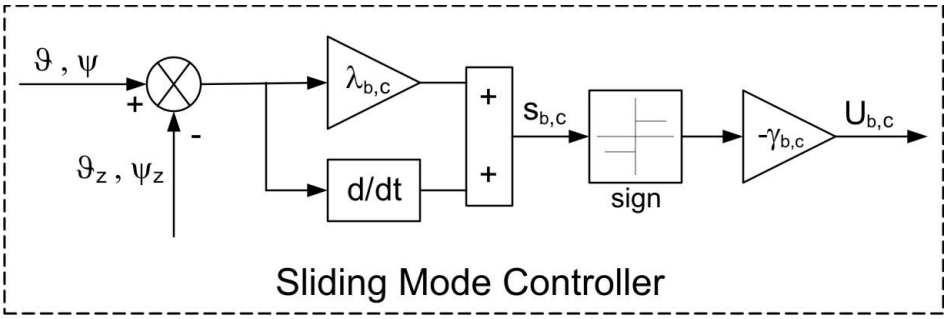

Figure 1. A schematic diagram of SMC

3. Results of numerical research

Simulation studies were conducted in Matlab / Simulink with an integration step: $dt = 0.00001$ [10]. The results of the research are shown in Figures 2-13. The following parameters of the gyroscopic system were adopted:

$J_{go} = 5 \cdot 10^{-4}\,\text{kgm}^2$; $J_{gk} = 2.5 \cdot 10^{-4}\,\text{kgm}^2$; $n_g = 500\,\text{rad/s}$; $\eta_b = \eta_c = 0.01\,\text{Nms}$.

The kinematic inputs affecting gyroscopic system on the vehicle side were taken in harmonic form:

$$p_n = p_{no}\sin(\nu_n t),\ q_n = q_{no}\cos(\nu_n t);\ r_n = r_{no}\sin(\nu_n t)$$

where:

$p_{no} = q_{no} = r_{no} = 2.5\,\text{rad/s}$, $\nu_n = 10\,\text{rad/s}$.

Figures 2-5 show the results of the simulation when gyroscopic system axis makes programmed movements in a n-leaf rosette, according to the following:

$$\vartheta_z(t) = \alpha \cdot \sin(\omega_2 \cdot t) \cdot \cos(\omega_1 \cdot t) \tag{9}$$

$$\psi_z(t) = \alpha \cdot \sin(\omega_2 \cdot t) \cdot \sin(\omega_1 \cdot t) \tag{10}$$

where:

$\alpha = 0.75\,\text{rad}$, $\omega_1 = 1.25\,\text{rad/s}$, $\omega_2 = 29\,\text{rad/s}$.

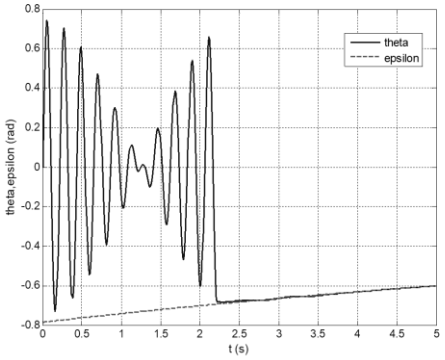

Figure 2. Tilt angle of gyroscopic system axis and LOS

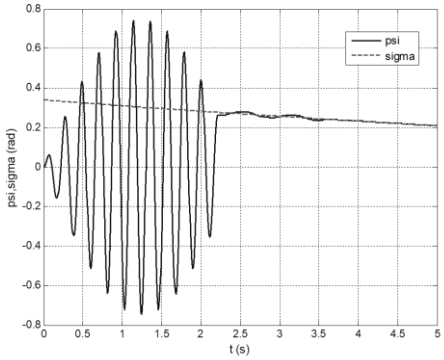

Figure 3. Yaw angle of gyroscopic system axis and LOS

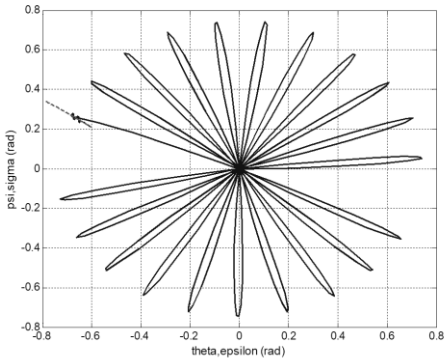

Figure 4. Tracks of gyroscopic system axis and LOS

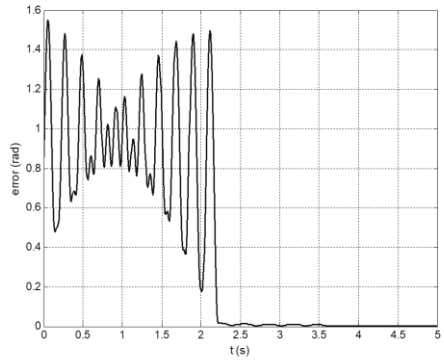

Figure 5. Control error

Figures 6-9 show the results of the simulation when gyroscopic system axis performs programmed movements in the developing Archimedean spiral, according to the following:

$$\vartheta_z(t) = b \cdot t \cdot \sin(\omega \cdot t) \tag{11}$$

$$\psi_z(t) = b \cdot t \cdot \cos(\omega \cdot t) \tag{12}$$

where:

$b = 0.1\text{rad}$, $\omega = 25\text{rad/s}$.

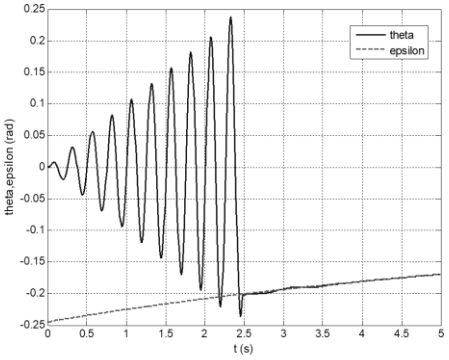

Figure 6. Tilt angle of gyroscopic system axis and LOS

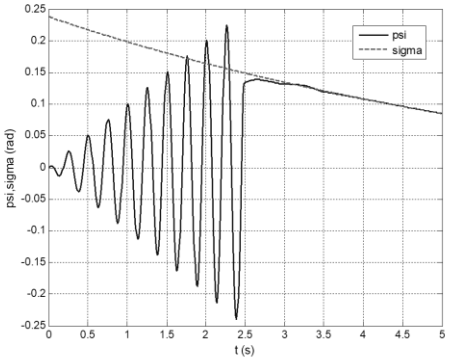

Figure 7. Yaw angle of gyroscopic system axis and LOS

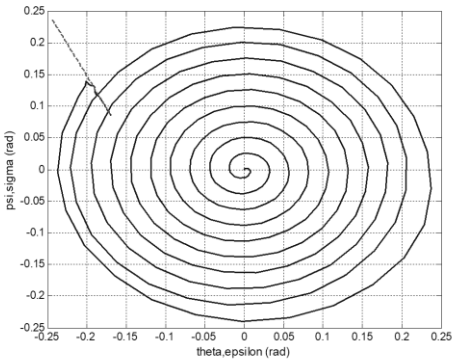

Figure 8. Tracks of gyroscopic system axis and LOS

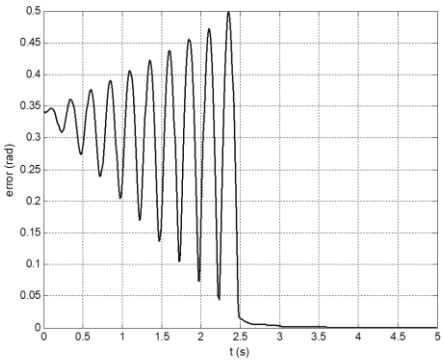

Figure 9. Control error

Figures 10-13 show the results of the simulation when gyroscopic system axis performs programmed movements in a modified n-leaf rosette, according to the following:

$$\vartheta_z(t) = a\left[\sin(\omega_2 \cdot t) + 0.2\sin(3\omega_2 \cdot t) + 0.04\sin(5\omega_2 \cdot t)\right] \cdot \cos(\omega_1 \cdot t) \tag{13}$$

$$\psi_z(t) = a\left[\sin(\omega_2 \cdot t) + 0.2\sin(3\omega_2 \cdot t) + 0.04\sin(5\omega_2 \cdot t)\right] \cdot \sin(\omega_1 \cdot t) \tag{14}$$

where:

$a = 0.1\text{rad}$, $\omega_1 = 15\text{rad/s}$, $\omega_2 = 50\text{rad/s}$.

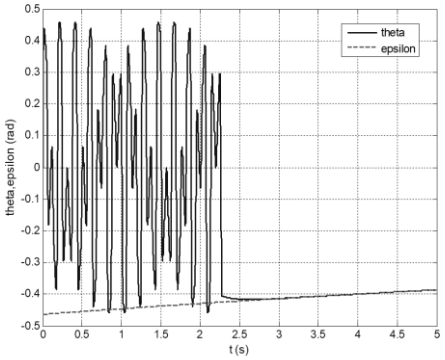

Figure 10. Tilt angle of gyroscopic system axis and LOS

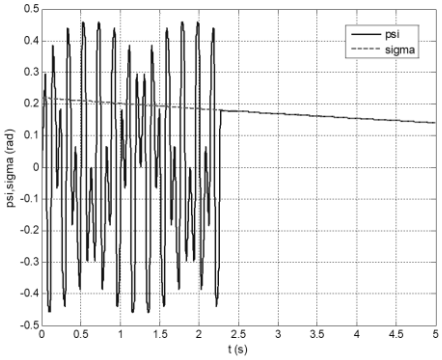

Figure 11. Yaw angle of gyroscopic system axis and LOS

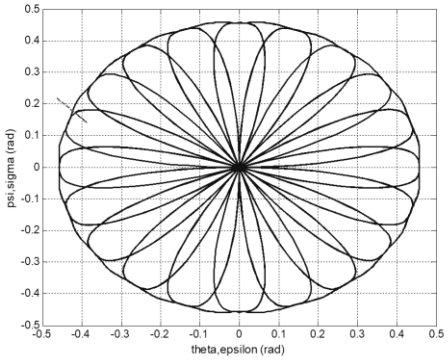

Figure 12. Tracks of gyroscopic system axis and LOS

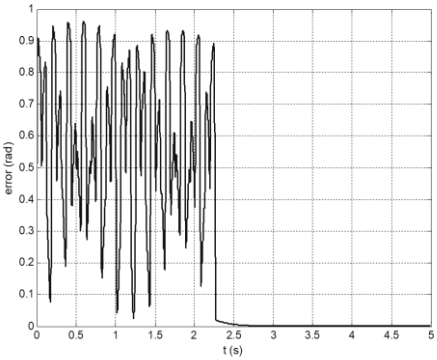

Figure 13. Control error

4. Conclusions

The study presents the analysis of the dynamics of the gyroscopic scanning and tracking system during vehicle motions. The results confirm that the designed sliding controller works correctly. It allows for quick target tracking in space. The target detection time is from 2.21 s when the gyroscopic system axis makes programmed movements in a rosette and up to 2.27 s in case when the gyroscopic system axis makes programmed movements in a spiral.

The sliding controller also ensures stable keeping the detected target in the field of view of the optical system. Deviations of the gyroscopic system axis from a predetermined position during the impact of kinematic inputs from the combat vehicle are minimal. The proposed control system allows for detecting and tracking a moving air target during missile set motions.

Moreover, the sliding controller is characterized by simple structure and can be used for strongly nonlinear systems such as gyroscopic system.

References

[1] Krzysztofik, I., and Koruba, Z. Mathematical Model of Movement of the Observation and Tracking Head of an Unmanned Aerial Vehicle Performing Ground Target Search and Tracking. *Journal of Applied Mathematics*, 2014, (2014), 11 pages, Article ID 934250.

[2] Krzysztofik, I., and Koruba, Z. Model of Dynamics and Control of Tracking-Searching Head, Placed on a Moving Object. *Journal of Automation and Information Sciences*, 44, (2012), 38-47.

[3] Krzysztofik, I., Takosoglu, J., and Koruba, Z. Selected methods of control of the scanning and tracking gyroscope system mounted on a combat vehicle. *Annual Reviews in C*ontrol. http://dx.doi.org/10.1016/j.arcontrol.2016.10.003.

[4] Szymak, P. Course Control of Unmanned Surface Vehicle. *Solid State Phenomena*, 196, (2013), 117-123.

[5] Olejnik, P., and Awrejcewicz, J. Low-Speed Voltage-Input Tracking Control of a DC-Motor Numerically Modelled by a Dynamical System With Stick-Slip Friction. *Differential Equations and Dynamical System*, 21, (2013), 3-13.

[6] Utkin, V. I. Sliding Mode Control: Mathematical Tools, Design and Applications in *Nonlinear and Optimal Control Theory*, Springer-Verlag, Heidelberg, 2008.

[7] Tomera, M. Sterowanie ślizgowe w układzie połączonych zbiorników. *Zeszyty Naukowe Wydziału Elektrotechniki i Automatyki PG*, 40/2014, (2014), 111-118.

[8] Utkin, V., Guldner, J., and Shi, J. *Sliding Mode Control in Electro-Mechanical Systems*. CRC Press, Boca Raton, 2009.

[9] Wang, C.-C., and Yau, H.-T. Nonlinear dynamic analysis and sliding mode control for a gyroscope system. *Nonlinear Dynamics* 66, (2011), 53-65.

[10] Baranowski, L. Effect of the mathematical model and integration step on the accuracy of the results of computation of artillery projectile flight parameters. *Bulletin of the Polish Academy of Sciences: Technical Sciences* 61, (2013), 475-484.

Izabela Krzysztofik, Dr habil. Eng: Department of Applied Computer Science and Armament Engineering, Kielce University of Technology, Al. Tysiąclecia PP 7, 25-314 Kielce, Poland (*pssik@tu.kielce.pl*). The author gave a presentation of this paper during one of the conference sessions.

Modelling of rigid body dynamics with spatial frictional contacts

Grzegorz Kudra, Michał Szewc, Michał Ludwicki, Krzysztof Witkowski, Jan Awrejcewicz

Abstract: The work focuses on a special class of reduced models of resultant friction forces coupled with rolling resistance for finite size of contact area and their applications in modelling and effective numerical simulations of spatial rigid body dynamics. The contact models are based on the integral expressions assuming fully developed sliding and Coulomb's friction law at each element of a finite contact zone. The integral models are then approximated by special functions, more effective in numerical simulations. The contact models are applied in different configurations of a spatial pendulum with Cardan joints, equipped with a special movable obstacle situated below the pendulum and limiting the space of admissible positions of the system. The models are tested numerically during investigations of bifurcation dynamics of the pendulum as well as a special experimental rig is prepared for their experimental validation.

1. Introduction

In many fields of science like mechanical engineering, mechatronics, robotics or control theory there are systems which consists of pendulums or multi-pendulums. They often play a significant role in system dynamics and may lead to interesting bifurcation phenomena. Analyzing the systems with pendulums, one can encounter models with spatial pendulums with a leading example, which is a single spherical pendulum and its different configurations [1,2]. The other more complex system, which is a spatial multi-dimensional pendulum is much less frequent object of interest and scientific analysis concerning pure non-linear dynamics [3]. The reason for the lack of works in this area may be the complexity of the system and its analysis.

Another important part of the analysis of a mechanical system is the friction and impact investigation. Both above mentioned components of the system play a significant role in changing bifurcation dynamics. Therefore, their investigation and developing new methods of analysis should be one of the most important steps in mechanical system study. On the other hand, new developed methods should lead to fast and reliable numerical simulations of the analyzed mechanical system. For this reason it is necessary to validate the numerical results with the real object measurements. In this case, not only the friction forces distribution is important, but modelling of impact in 3D space as well.

However, the analysis of full contact problem may result in high computational cost and a need to use such methods as finite element method. Therefore, the simplified or reduced models may be introduced.

An example of such approach is presented in the paper of Contensou [4], where one can find an integral model of friction force for fully developed sliding on a circular contact area. Another example may be found in the work of group of researches, who developed special group of approximations of the integral model friction [5], which allows to avoid integration over the contact area. Special approximations were presented for different shapes of the contact, not only the circular one [6]. An exemplary usage of the introduce approximations was presented in the numerical simulations of wobblestone, billiard ball and full ellipsoid of revolution [7-9].

This paper presents the mechanical system consisting of the double spatial pendulum with a spherical end of the second pendulum's limb, which can be in contact with a movable obstacle. This work is the collection of elements of the previous works [3, 6-10] with the continuation by new experimental rig development and further analysis of the system of double spatial pendulum with obstacle. The friction force is modelled in the similar way as presented in works [6-9], while Hertz stiffness with special model of damping [11] is used for normal force modelling.

Section 2 of this paper presents the model of the pendulum and the special laboratory stand for the results verification. In section 3 the numerical analysis of the system is presented. The summary and conclusions are drawn in section 4.

2. Mathematical model

The analyzed mechanical system is the double spatial pendulum with a solid ball at the end of second limb. The ball can be in contact with a rotating obstacle. The physical model and its application in an experimental rig is presented in Fig. 1. The center O_1 of the global coordinate system O_1xyz is situated at the geometric center of the first massless Cardan-Hook joint. The joint connects the first element (body 1 of mass m_1) of the pendulum with the body 0. The body 0 is connected to the DC motor, which generates the rotational motion of the body 0, with angular position represented by angle ψ_1. Since the next coordinate system $O_1x_1y_1z_1$ is fixed with respect to the body 1, the angular position of the first limb of pendulum may be represented by the following sequence of rotations: by angle ψ_1 about axis z_1, by angle θ_1 about axis x_1 and by angle φ_1 about axis y_1. It is assumed that for each rotation angle equal to zero, the two coordinate systems $O_1x_1y_1z_1$ and O_1xyz overlap each other.

The second element (limb 2 with mass m_2) of the pendulum is connected to the first one by the identical massless Cardan-Hook joint. The centre O_2 of the joint lies on the axis O_1z_1 and its position is defined by the parameter $L_1 = O_1O_2$. The similar sequence of rotations is used to describe angular position of the second limb: by angle θ_2 about axis y_2 and by angle φ_2 about axis z_2 of the body 2 – fixed coordinate system $O_2x_2y_2z_2$, with the centre at the point O_2. It is assumed that the coordinate system

$O_2x_2y_2z_2$ has the parallel axes to the corresponding ones of the coordinate system $O_1x_1y_1z_1$ for θ_2 and φ_2 equal to 0.

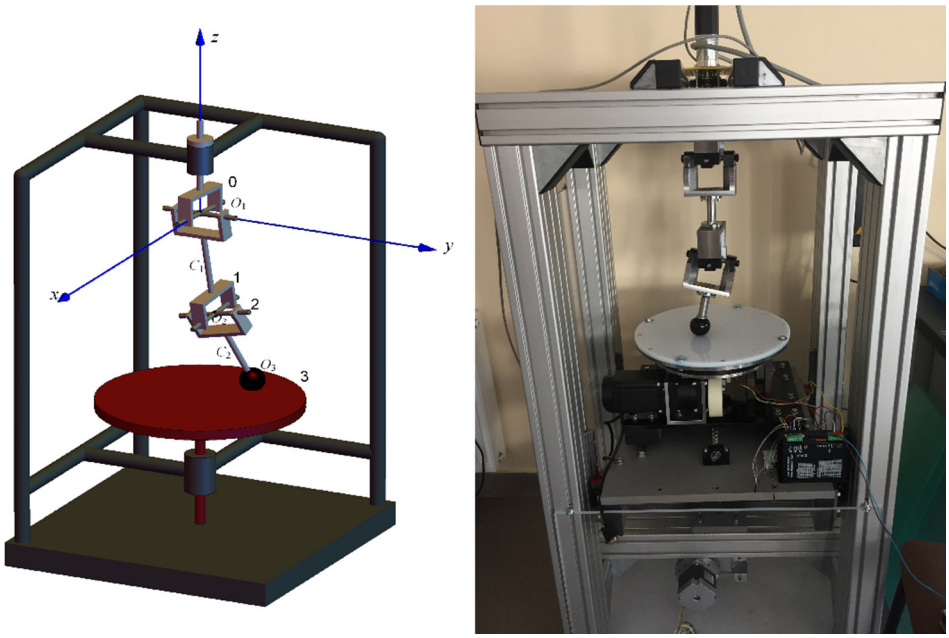

Figure 1. The double spatial pendulum with movable obstacle – model and experimental rig.

The ball at the end of second limb of pendulum, which can contact the movable obstacle 3, has a radius R_b and is centered at the point O_3 lying on the axis O_2z_2. The position of the center of the ball is described by the parameter $L_2 = O_2O_3$. The assumption has been made, that the mass centres of both links of pendulum (C_1 and C_2) lie on the corresponding axes O_1z_1 or O_2z_2. Parameters $e_1 = O_1C_1$ and $e_2 = O_2C_2$ define positions of the mass centres. Additionally, the coordinate systems $O_1x_1y_1z_1$ and $O_2x_2y_2z_2$ are the principal axes of inertia of the corresponding bodies. Finally their mass distribution are defined by six parameters I_{xi}, I_{yi} and I_{zi} (i=1,2), which describes the principal central moments of inertia of the corresponding bodies with respect to the axes parallel to the corresponding axes O_ix_i, O_iy_i or O_iz_i. The last body in the mechanical system analysed is the rotating disk 3. Its rotation about the axis z of the global coordinate system is defined by the velocity ω_d. Moreover, the disk can change its horizontal position, which is described by the parameter z_0 - the coordinate of any point of the disk's surface along the axis z.

Based on the physical model described above, the experimental rig was made, which is presented in Fig. 1. It consists of exactly the same elements as presented in the physical model - body 0, limbs 1 and 2 and movable obstacle 3. To provide the rotational movement of the body 0 the highly dynamic

DC servo drive with integrated 4Q servo controller is used. It is equipped with incremental encoder with a resolution of 1024 pulses per revolution. To measure the movement of the pendulum limbs, there are two separate internal measurement units, which combine a 3-axis gyroscope and a 3-axis accelerometer on each board. Sensors are communicating with the processor by I2C bus and all wirings are made through the slip ring. The transmission between its stator and rotor takes place via sliding contacts, which allows the data to be transferred to the processor.

Mathematical model of the system is based on the work [10] and is expressed using the Lagrange's formalism

$$\frac{d}{dt}\left(\frac{\partial T}{\partial \dot{\theta}_i}\right)-\frac{\partial T}{\partial \theta_i}+\frac{\partial V}{\partial \theta_i}=Q_{\theta_i}, \quad \frac{d}{dt}\left(\frac{\partial T}{\partial \dot{\varphi}_i}\right)-\frac{\partial T}{\partial \varphi_i}+\frac{\partial V}{\partial \varphi_i}=Q_{\varphi_i}, \quad i=1,2 \tag{1}$$

where angles θ_i and φ_i $(i=1,2)$ are chosen as generalized co-ordinates and T denotes kinetic energy, V – is potential energy of gravity forces, Q_{θ_i} and Q_{φ_i} $(i=1,2)$ – the corresponding generalized forces. It is assumed that the pendulum is driven by the angular velocity of the body 0 defined by the following function of time

$$\omega(t)=\omega_0+q\cos(\Omega t). \tag{2}$$

The generalized forces are divided into the parts $Q_{\xi_{ic}}$ $(\xi=\theta,\varphi;\ i=1,2)$ representing the contact forces and $Q_{\xi_{ib}}$ representing damping in the joints:

$$Q_{\xi i}=Q_{\xi ic}-Q_{\xi ib}. \tag{3}$$

Resistance in the joints is modelled in the following way

$$Q_{\xi_i b}=M_b\frac{\dot{\xi}_i}{\sqrt{\dot{\xi}_i^2+\varepsilon_b^2}}, \quad \xi=\theta,\varphi, \quad i=1,2 \tag{4}$$

where M_b is magnitude of the resistance torque common for all the joints and ε_b is parameter, which initially was assumed to be small and played a role of regularization of non-smooth sign function. But during different experiments performed by the authors, it occurred that the function (4) with higher values of ε_b can lead to better modelling of resistance in rolling bearings working in similar dynamical systems.

The generalized contact forces $Q_{\xi_i c}$ are related to the reaction $\mathbf{F}_c=\mathbf{N}+\mathbf{T}$ of the obstacle acting on the ball in following way

$$Q_{\xi_i c} = \left(\mathbf{N} + \mathbf{T}\right) \cdot \frac{\partial \mathbf{r}_{A_2}}{\partial \xi_i}, \quad \xi = \theta, \varphi, \quad i = 1,2 \tag{5}$$

where vector $\mathbf{r}_{A_2}$ indicates the position in the co-ordinate system O_1xyz of the point A_2 being the body's 2 fixed point taking temporarily the position of the circular contact zone center, while **N** and **T** are normal and tangent components of the reaction, respectively.

Normal component of the impact force is modelled based on the Hertzian contact stiffness and damping [11]

$$\mathbf{N} = N\mathbf{n} \tag{6}$$

where

$$N = \begin{cases} |h|^{3/2} k\left(1 - b\dot{h}\right) & \text{for } \mathrm{h} \le 0 \text{ and } 1 - b\dot{h} \ge 0 \\ 0 & \text{for } \mathrm{h} > 0 \text{ or } 1 - b\dot{h} < 0 \end{cases} \tag{7}$$

where **n** is unit vector normal to the obstacle, h is distance between the ball and the surface of the disk, k is stiffness and b is damping coefficient of the contact.

For the contact of a ball of radius R_b with an elastic semi-space one gets based on the Hertz's theory

$$k = \frac{4\sqrt{R_b}}{3\left(\frac{1-\nu_1}{E_1} + \frac{1-\nu_2}{E_2}\right)}, \tag{8}$$

where ν_1 and ν_2 are Poisson's coefficients, while E_1 and E_2 are Young's modulus of the materials of the contacting bodies.

Friction force **T** is modelled based on assumption of fully developed sliding and Coulomb friction model valid at each point of the circular contact area with circularly symmetric contact pressure distribution. The corresponding integral model is approximated using special function of the following form [6-9]

$$\mathbf{T} = -\mu N \frac{\mathbf{v}_s}{\sqrt{\mathbf{v}_s^2 + b_T^2 a_r^2 \boldsymbol{\omega}_s^2 + \varepsilon^2}}, \tag{9}$$

where μ is friction coefficient, $\mathbf{v}_s$ and $\boldsymbol{\omega}_s$ are translational and angular sliding relative velocities at the center of the contact, a_r – radius of the contact calculated based on the Hertz theory and depending on the current normal loading of the contact, b_T – parameter depending on the contact stress distribution and ε – the parameter introduced in order to regularize function (9) and avoid singularity for vanishing relative motion of the contacting bodies.

3. Numerical simulations

The following values of the parameters were obtained based on materials and geometric shapes of the corresponding parts of the real pendulum being under preparation: m_1=4.59 kg, m_2 = 2.41 kg, $I_{x1} = I_{y1}$ = 0.0315 kg·m^2, I_{z1} = 0.0078 kg·m^2, I_{x2} = 0.0084 kg·m^2, I_{y2} = 0.0055 kg·m^2, I_{z2} = 0.0038 kg·m^2, L_1 = 0.228 m, L_2 = 0.175 m, e_1 = 0.122 m, e_2 = 0.0586 m, R_b = 0.025 m. Additionally the following set of parameters is assumed to be constant during the subsequent numerical simulations as well: g = 9.81 m/s^2, M_b = 0.04 N·m, ε_b = 0.4, $\nu_1 = \nu_2$= 0.3, $E_1 = 2 \cdot 10^9$ N/m^2, $E_2 = 0.1 \cdot 10^9$ N/m^2, b = 0.5 m^{-1}s, z_0 = –425mm , μ = 0.2, $\omega_d = 0$ rad/s , $\omega_0 = 0$ rad/s , $q = 5$ rad/s , $\Omega = 5$ rad/s and $\varepsilon = 10^{-3}$ m/s (except the cases where one of them is chosen as bifurcation parameter).

Figure 2 presents bifurcation diagrams with angular frequency of the obstacle ω_d playing a role of control parameter. Bifurcation diagrams are made for two cases: with the parameter $b_T = 0.681$ (a) corresponding to circular contact with Hertzian stress distribution and with $b_T = 0$ (b), i.e. for the case of a point contact and no relation between friction force and rotational relative motion of the contacting surfaces.

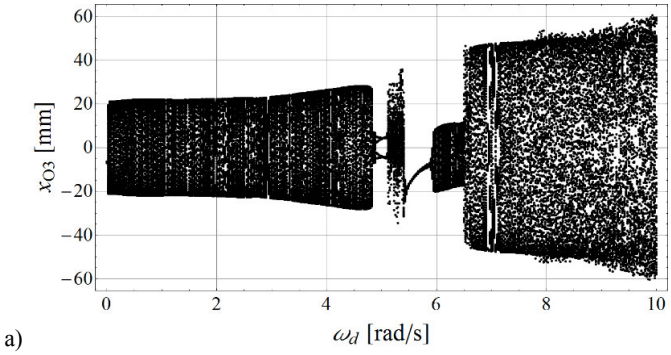

a)

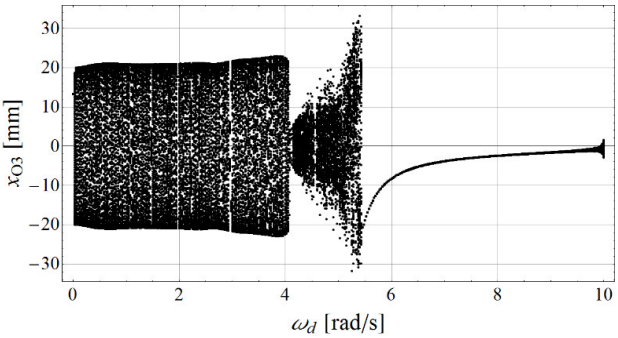

b)

Figure 2. Bifurcation diagrams of the system with angular frequency of the obstacle ω_d as a control parameter, for $b_T = 0.681$ (a) and $b_T = 0$ (b)

Results of further analysis of the influence of the model (9) on the system dynamics is presented in Fig. 3, on bifurcation diagram, where as a control parameter is chosen coefficient b_T. One can observe a significant role in bifurcation dynamics of the pendulum played by the contact pressure distribution. Next pair of bifurcation diagrams is exhibited in Fig. 4, where the friction coefficient μ is chosen as a bifurcation parameter. Fig. 5 and Fig. 6 exhibits bifurcation diagrams with position of the obstacle z_0 varying quasi-statically from -428 mm to -417 mm. Note that for $z_0 \le z_0^* = -L_1 - L_2 - R_b = -427\,\text{mm}$ the obstacle is below the range of the pendulum and for the assumed parameters the system tends to the stable fixed point with $\theta_1=\varphi_1=\theta_2=\varphi_2=0$. For $z_0 = z_0^*$ one observe collision of this equilibrium position with the limiter of motion. Further increase of height of the obstacle leads to complex bifurcation dynamics. Fig. 5 is the bifurcation diagram for $b_T = 0.681$ and Fig. 6 is the bifurcation diagram for $b_T = 0$.

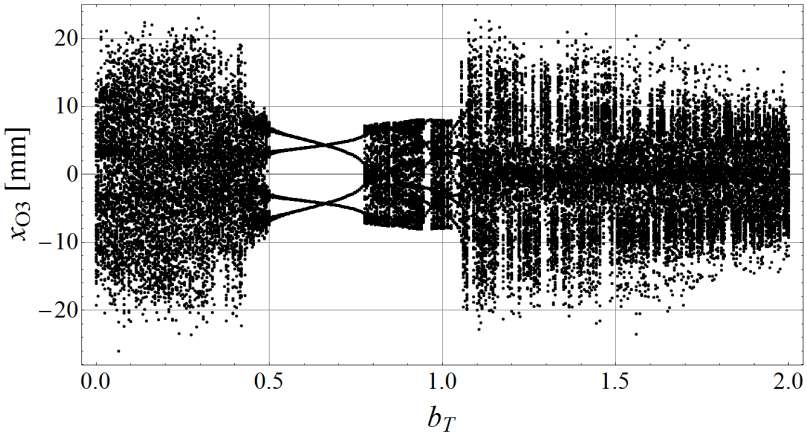

Figure 3. Bifurcation diagram of the system with the coefficient b_T of the contact model as a control parameter

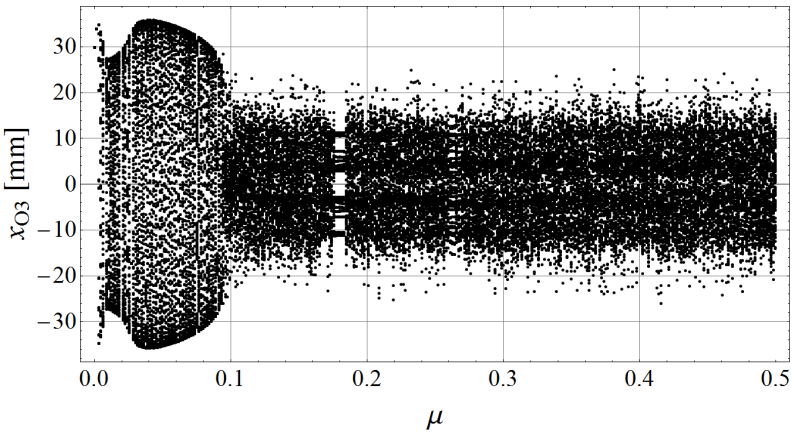

a)

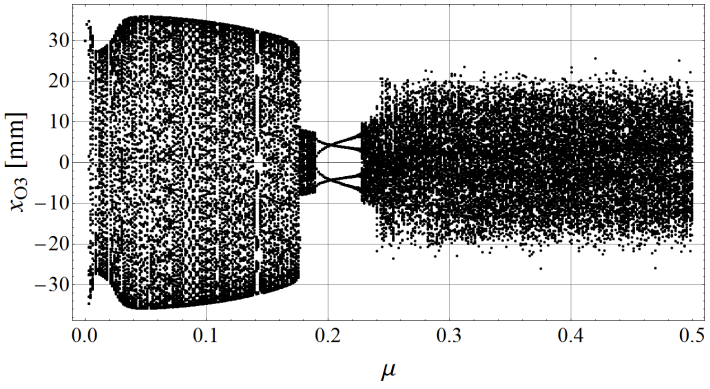

b)

Figure 4. Bifurcation diagrams of the system with friction coefficient μ as a control parameter, for $b_T = 0.681$ (a) and $b_T = 0$ (b)

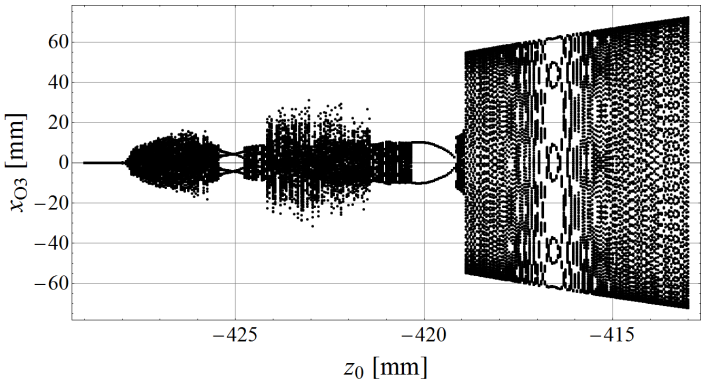

Figure 5. Bifurcation diagram of the system with obstacle position z_0 as a control parameter, for $b_T = 0.681$.

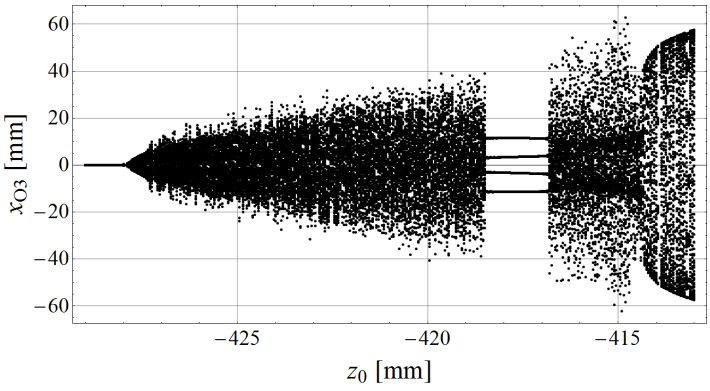

a)

Figure 6. Bifurcation diagram of the system with obstacle position z_0 as a control parameter, for $b_T = 0$

4. Conclusions

In this paper, the dynamic analysis of the double spatial pendulum is presented. It consists of two limbs connected with the Cardan-Hook joints. At the end of the second limb there is a spherical end, which comes in contact with the moveable obstacle. The friction force between contacting bodies is modelled based on the previous works and experience of the authors and uses the special approximation model. The bifurcation dynamics analysis, presented in this paper, shows the differences in model's behavior, while using the special model developed by the authors and in the case of point contact and no relation between friction force and rotational relative motion of contacting bodies.

The bifurcation diagrams analysis shows that the contact pressure distribution has a significant influence on the bifurcation dynamics of the system, which proves the necessity of developing advanced models of contact forces. On the other hand, this paper presents the experimental rig, which is made to verify the results obtained by the authors during the dynamics analysis. The results found out to be promising and convincing enough to make the experimental verification, which is currently being developed by the authors.

References

[1] Shen, J., Sanyal, A.K., Chaturvedi, N.A., Bernstein, D., McClamroch, H. ,"Dynamics and control of a 3D pendulum" 43rd IEEE Conference on Decision and Control, Georgia, USA, December 2004, pp. 323–328.

[2] Chaturvedi, N.A., McClamroch, N.H. , "Asymptotic stabilization of the hanging equilibrium manifold of the 3D pendulum" International Journal of Robust and Nonlinear Control, 17(16), 2007, pp. 1435–1454.

[3] Ludwicki, M., Awrejcewicz, J., Kudra, G., „Spatial double physical pendulum with axial excitation: computer simulation and experimental set-up" International Journal of Dynamics and Control, *3*(1), 2015, 1–8. http://doi.org/10.1007/s40435-014-0073-x.

[4] Contensou, P., 1963, "Couplage entre frottement de glissement et de pivotement dans la téorie de la toupe", In: Ziegler H. (Ed.), Kreiselprobleme Gyrodynamic, IUTAM Symposium Celerina, Springer-Verlag, Berlin, 1962, pp. 201-216.

[5] Zhuravlev V. P., Kireenkov A.A., "Padé expansions in the two-dimensional model of Coulomb friction", Mechanics of Solids 40(2), 2005 1-10.

[6] Kudra, G., Awrejcewicz, J.,"Approximate modelling of resulting dry friction forces and rolling resistance for elliptic contact shape", European Journal of Mechanics And Solids, 42, 2013

[7] Kudra, G., Awrejcewicz, J., "Application and experimental validation of new computational models of friction forces and rolling resistance", Acta Mechanica, 226(9) (2015), 2831-2848.

[8] Kudra, G., Szewc, M., Wojtunik, I., Awrejcewicz, J., „Shaping the trajectory of the billiard ball with approximations of the resultant contact forces", Mechatronics, 37, 2016, pp. 54–62. http://doi.org/10.1016/j.mechatronics.2016.01.002.

[9] Kudra, G., Szewc, M., Wojtunik, I., Awrejcewicz, J., "On some approximations of the resultant contact forces and their application in rigid body dynamics", Mechanical Systems and Signal Processing, 79, 2016, pp. 182–191.

[10] Awrejcewicz, J., and Kudra, G. Modelling and simulation of bifurcation dynamics of spatial double pendulum with rigid limiter of motion. Proceedings of the International Conference on Structural Engineering Dynamics (ICEDYN 2017), Ericeria, Portugal, July 3-5 (2017), 10 pages.

[11] Gilardi, G., Sharf, I., "Literature survey of contact dynamics modelling. Mechanism and Machine Theory", 37(10), 2012, pp.1213–1239. http://doi.org/10.1016/S0094-114X(02)00045-9.

Kudra Grzegorz, Associate Professor: Lodz University of Technology, Department of Automation, Biomechanics and Mechatronics, Stefanowskiego 1/15, 90-924 Lodz, Poland (*grzegorz.kudra@p.lodz.pl*).

Szewc Michał, Ph.D. Student: Lodz University of Technology, Department of Automation, Biomechanics and Mechatronics, Stefanowskiego 1/15, 90-924 Lodz, Poland (*michal.szewc@dokt.p.lodz.pl*), the author presented this contribution at the conference.

Ludwicki Michał, Ph.D.: Lodz University of Technology, Department of Automation, Biomechanics and Mechatronics, Stefanowskiego 1/15, 90-924 Lodz, Poland (*michal.ludwicki@p.lodz.pl*).

Witkowski Krzysztof, Ph.D. Student: Lodz University of Technology, Department of Automation, Biomechanics and Mechatronics, Stefanowskiego 1/15, 90-924 Lodz, Poland (*Krzysztof.witkowski@dokt.p.lodz.pl*).

Awrejcewicz Jan, Professor.: Lodz University of Technology, Department of Automation, Biomechanics and Mechatronics, Stefanowskiego 1/15, 90-924 Lodz, Poland (*jan.awrejcewicz@p.lodz.pl*).

Remote synchronization and multistability in a star-like network of oscillators

Juliana Lacerda, Celso Freitas, Elbert Macau

Abstract: In the phenomenon of remote synchronization, oscillators that are not directly connected synchronize. In this work, we investigate this phenomenon for a system of Stuart-Landau oscillators interconnected in a network with a star-like structure in which all oscillators have different natural frequencies, being that the peripheral nodes have close frequencies and the central nodes frequency is detuned against them. We numerically find a regime of remote synchronization, where the peripheral nodes synchronize and the hub continues at its own dynamics. In this regime, the nodes exhibit a quasi-periodic motion in their phase space. By changing the initial conditions of the system, we were able to find that the peripheral nodes lose their synchronization with each other for some of these conditions, causing remote synchronization to disappear, which characterize a multistability behavior. The behavior of the system is studied extensively for initial conditions that give and do not give rise to remote synchronization for a fixed value of the coupling strength.

1. Introduction

Synchronization between a system's unities is an universal behavior that appears in many natural and artificial systems [3]. One of the most iconic examples of this area are the rare species of fireflies that are capable of synchronizing their light emission [5, 23]. Similar phenomena of multi-agent systems can also be found in areas such as biology [1, 13, 26, 27], physics [7, 18] and social systems [16, 21].

Synchronization can be defined as the "adjustment between rhythms of objects that oscillate due to the presence of weak interaction between them" [20]. Formally, one can say that synchronization is a process in which a certain number of dynamical subsystems, not necessarily identical, are coupled or are conducted by a common force and manage to coordinate some dynamic property. The most adopted mathematical models employed in the literature in this context are: coupled periodic oscillators [24] and networks of coupled chaotic oscillators [4].

In this work, our focus is on the phenomenon of *remote synchronization*, which occurs when two or more subsystems, that are not directly coupled, synchronize while the ones between them do not. This type of synchronization has already been observed in networks

of non-linear electronic oscillators [2] and has been taken into consideration in the study of climate [6, 14, 15] and the brain [17]. We will perform this study by using the Stuart-Landau oscillator [19] model in star like networks which are the main building blocks of several communication systems [2,8]. Remote synchronization in star-like networks where the oscillators are modeled by the Stuart-Landau equation was studied by [2], where the influence between the difference of the natural frequency of the hub and of the peripheral nodes was analyzed. This phenomenon was also studied by [9, 10], which studies the emergence of remote synchronization in complex networks.

We investigate the role of the initial conditions in the system's remote synchronization, which leads us to the phenomena of multistability. The paper is organized as follows: Section 2 presents the Stuart-Landau equations that are used to model our system, in Section 3 the regime of remote synchronization for fixed values of initial conditions is studied and then we show how the initial conditions influence the synchronization of the system. Conclusions are presented in Section 4.

2. Model

In our study of remote synchronization, the dynamics of each active element of the network is given by the Stuart-Landau equation, that allows oscillators to experience amplitude variations, which has been shown to play an important role in the emergence of remote synchronization [2, 9]. The Stuart-Landau equation, for a single oscillator is given by

$$\dot{u} = (\alpha + i\omega - |u|^2)u, \tag{1}$$

where u represents the position of an oscillator on the complex plane, ω is the natural frequency of the oscillator and α the Hopf bifurcation parameter [12]. Considering a network of N non-identical oscillators with a common coupling parameter through all communication channels are the same of all nodes, the dynamics of the system will be described by

$$\dot{u}_n = (\alpha + i\omega_n - |u_n|^2)u_n + \frac{k}{d_n}\sum_{m=0}^{N-1} g_{nm}(u_m - u_n), \tag{2}$$

where $n = 0, \ldots, N-1$, k is the coupling constant, ω_n is the natural frequency and d_n is the degree of node n, (g_{nm}) is the adjacency matrix of the coupling graph, that is, g_{nm} will have value 1 if nodes n and m are connected and 0 otherwise. The coupling graphs considered in this work are simple and connected. The phase of the oscillators $\theta_n(t)$ is given by the argument of the complex number u_n. The real equivalent of Eq. (2), with $u = x + iy$, is given by

$$\dot{x}_n = x_n(\alpha - {x_n}^2 - {y_n}^2) - w_n y_n + \frac{k}{d_n}\sum_{m=0}^{N-1} g_{nm}(x_m - x_n) \tag{3}$$

$$\dot{y}_n = y_n(\alpha - {x_n}^2 - {y_n}^2) - w_n x_n + \frac{k}{d_n}\sum_{m=0}^{N-1} g_{nm}(y_m - y_n) \tag{4}$$

In this paper, Eqs. 3 and 4 will always be used to analyze the system. We will say that a pair of oscillators is synchronized when the difference between their phases converges to a constant value and therefore, they move as a "single phase oscillator". This regime is known in the literature as *phase locking* [20]. In order to measure the emergence of this kind of synchronization, we will make use of the *partial synchronization index* $r \in [0, 1]$ [11]:

$$r_{nm} = \left| \lim_{\Delta t \to \infty} \frac{1}{\Delta t} \int_{t_r}^{t_r + \Delta t} e^{i[\theta_n(t) - \theta_m(t)]} \right|, \tag{5}$$

where n and m are the index of oscillators n and m, t is time, $\theta_{\{n,m\}}(t)$ is the phase of oscillator n and m and t_r is a time of reference after the transient. The equation above can also be written as:

$$r_{nm} = | < e^{i[\theta_n(t) - \theta_m(t)]} >_t |, \tag{6}$$

where $< . >_t$ denotes the average over time. This index is close to one when oscillators n and m are synchronized, i.e., are in phase locking. In order to characterize remote synchronization in star networks, we will make use of the indices defined by Ref. [2], r^{direct} and $r^{indirect}$.

To quantify the coherence of the hub with the rest of the network we use the index called $r^{direct} \in [0, 1]$ and to measure the coherence of the peripheral nodes we use $r^{indirect} \in [0, 1]$, which are defined as follows:

$$r^{direct} = \frac{1}{N-1}\sum_{n=1}^{N-1} r_{0n}, \tag{7}$$

$$r^{indirect} = \frac{2}{(N-1)(N-2)}\sum_{n=1, m>n}^{N-1} r_{nm}, \tag{8}$$

where r_{nm} is the partial synchronization index, Eq. 6, and N is the number of nodes. Here the hub is represented by the number 0. When r^{direct} has a value close to 1, the hub and the peripheral nodes are moving as a rigid body and they are said to be synchronized. If this value is low, the hub is not synchronized with the rest of the network. When $r^{indirect}$ has a value close to one, the peripheral nodes are said to be synchronized. If both r^{direct} and $r^{indirect}$ are close to 1, there is global synchronization. In this paper, *we will characterize remote synchronization when* $r^{indirect} > 0.97$ *and* $r_{indirect} < 0.6$.

3. Remote Synchronization in Star Networks

The focus of this work will be on star networks like the one in Fig.1. We will fix a set of initial conditions and natural frequencies to show the emergence of remote synchronization, then the initial conditions will be varied to see how they affect the synchronization of the system and how this leads to the phenomenon of multistability.

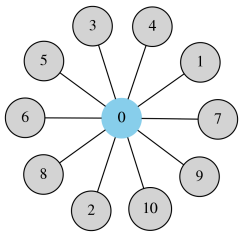

Figure 1. Star network composed of $N = 11$ nodes. The hub is blue and the peripheral nodes are gray.

3.1. Fixed values of initial conditions and natural frequencies

Considering first a network composed of $N = 11$ nodes, the initial conditions will be fixed as

$$\begin{aligned}(x_0, \ldots, x_{(N-1)}) = (&-0.03672411, 0.38024460, 0.27386404, 0.23925263,\\ &0.05347882, -0.22111217, 0.46526363, -0.47368003, 0.17426283,\\ &-0.31198457, 0.27797903),\\ (y_0, \ldots, y_{(N-1)}) = (&-0.38243125, -0.31546865, 0.48294293, -0.29909983,\\ &0.39475024, -0.38066357, 0.32721335, 0.37426591, -0.48784350,\\ &-0.37711057, 0.24857760),\end{aligned} \tag{9}$$

where $N = 11$, x_0 and y_0 are the hub's initial conditions. The natural frequencies of the nodes will be fixed as

$$\begin{aligned}(\omega_0, \ldots, \omega_{(N-1)}) = (&2.5000, 1.0158, 1.0060, 1.0170, 1.0065, 1.0067, 1.0323,\\ &1.0185, 1.0390, 1.0076, 1.0186),\end{aligned} \tag{10}$$

where $\omega_0 = 2.5$ is the hub's natural frequency and $N = 11$. Let us define $\Delta\omega = \omega_0 - < \omega_n >$ as the difference between the natural frequency of the hub and the mean frequency of the peripheral nodes. By choosing those natural frequencies we have $\Delta\omega \cong 1.5$ and for this value of $\Delta\omega$ there is remote synchronization for a relatively large interval of coupling values [2].

We then perform numerical integration of Eqs. 3 and 4 for different values of the coupling constant $k \in [0, 1]$. The results can be seen in Fig. 2(a), where the indices r^{direct} and $r^{indirect}$ are functions of the coupling k. Note that $r^{indirect}$ reaches its maximum value before r^{direct} does. So, in the region $0.425 \lesssim k \lesssim 0.75$ there is remote synchronization. For $k \gtrsim 0.75$, r^{direct} reaches one, meaning that global synchronization has been achieved by the system.

3.2. Influence of initial conditions on the synchronization of the system

Now, the initial conditions of the system will be varied, keeping the natural frequencies of the nodes fixed and still given by Eq. 10 to see how this affects synchronization. The initial conditions will be generated randomly following a uniform distribution over (-0.5,0.5). For each value of the coupling, 20 initial conditions are generated and the mean and the standard deviation (which is close to zero for most values of k) of r^{direct} and $r^{indirect}$ are calculated. This result is presented in Fig. 2(b). One can note that the system reaches remote synchronization at $k \cong 0.425$, just like when the initial conditions were fixed, and that at $0.55 \lesssim k \lesssim 0.65$ the system loses this synchronization for some values of the initial conditions, retaking remote synchronization for all sets of initial conditions when $k \gtrsim 0.65$.

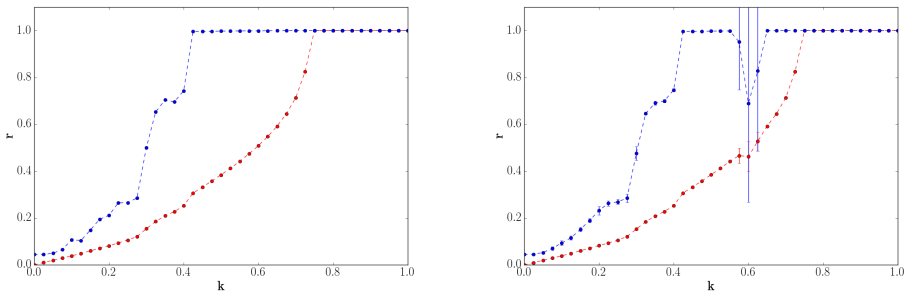

(a) Fixed initial conditions (b) Random sets of initial conditions

Figure 2. r^{direct} (red) and $r^{indirect}$ (blue) as a function of the coupling k for a fixed set of natural frequencies, Eq. 10, applied to the star network of Fig. 1, and (a) a fixed set of initial conditions given by Eq. 9, (b) random initial conditions. For each value of k, 20 sets of random initial conditions were generated.

In order to better visualize the set of initial conditions that give and do not give rise to remote synchronization, the number of nodes will be reduced to three. Fixing the natural frequencies as $(\omega_0, \omega_1, \omega_2) = (2.5000, 1.0158, 1.0060)$ (note that $\Delta\omega$ is kept very close to 1.5), like before, the system given by Eqs. 3 and 4 is integrated for 20 different initial conditions,

resulting in Fig. 3(a). We can still see that around $k = 0.6$, the peripheral nodes lose their synchronization, just like our 11 node star.

Now, fixing $k = 0.6$, the system given by Eqs. 3 and 4 will be integrated several times with random initial conditions with uniform distribution between (-0.5,0.5) and analise the mean values of r^{direct} and $r^{indirect}$. After this procedure, we are left with two groups of initial conditions for each of the three oscillators, one group has all the initial conditions (x^i, y^i) that gives rise to remote synchronization and one that gives not. To better visualize it, the initial phase of these oscillators will be plotted and marked as red if the set (x^i, y^i) leads to remote synchronization and as blue if it does not. The outcome can be seen in Fig. 3(b), where the multistability is clearly shown since there are some initial conditions yielding remote synchronization (red) or others not (blue).

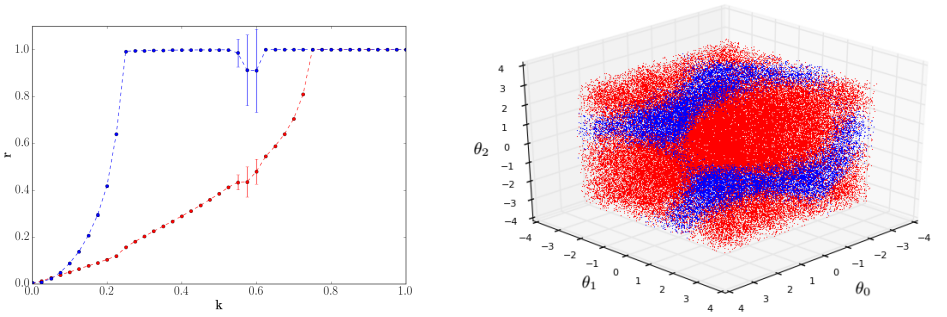

(a) Random sets of initial conditions (b) Initial phase of each oscilator

Figure 3. (a) r^{direct} (red) and $r^{indirect}$ (blue) as a function of the coupling k, for fixed natural frequencies and random initial conditions in star network of 3 nodes. (b) Initial phase of each oscillator, given by $\theta_n = \tan^{-}1\frac{x_n}{y_n}$, calculated using the set of initial conditions that give (red) and do not give (blue) rise to remote synchronization at $k = 0.6$.

3.2.1. Two different sets of initial conditions

In order to better understand the behavior of the system for coupling values close to $k = 0.6$, the natural frequencies will be kept fixed (given by Eq. 10). Returning to the star network of $N = 11$ nodes, two sets of initial conditions will be fixed, one that gives rise to remote synchronization, given by Eq. 9, which will be called System 1, and one set that gives not,

which will be called System 2 and will be given by

$$\begin{aligned}(x_0, \ldots, x_{(N-1)}) = (&0.18310904, -0.38851311, 0.23313545, -0.25566342,\\ &0.41649033, 0.16081773, -0.41299378, 0.22859424, -0.27097222,\\ &0.36025168, 0.39478912),\\ (y_0, \ldots, y_{(N-1)}) = (&-0.02144717, 0.21144214, 0.36246123, 0.46202932,\\ &-0.47923800, -0.01556482, 0.25587219, 0.12446036, -0.42247640,\\ &-0.16294013, 0.18085761),\end{aligned} \tag{11}$$

where $N = 11$, x_0 and y_0 are the hub's initial conditions.

As seen in Fig. 2(a), we already showed that System 1 presents remote synchronization at $k = 0.6$ Fig. 4 reveals that System 2 reaches remote synchronization at $k \cong 0.425$, just like System 1, but this regime is lost when $0.575 \lesssim k \lesssim 0.65$, and regained when $k \gtrsim 0.65$, reaching global synchronization, like System 1, at $k \cong 0.75$. One can note that the single fact that the system starts oscillating with different initial conditions seems to be enough for the system to lose the state of remote synchronization for intermediate values of k. When we pass this region where multistability takes place, the peripheral nodes synchronize again for all sets of initial conditions.

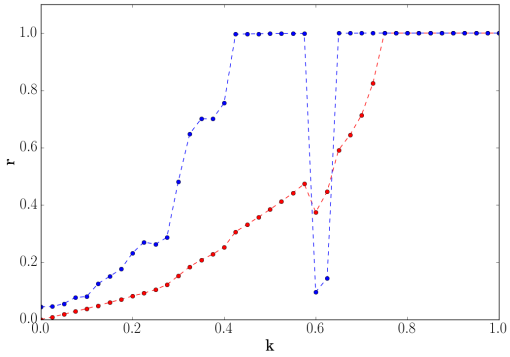

Figure 4. r^{direct} (red) and $r^{indirect}$ (blue) as a function of the coupling k for a fixed set of initial conditions (Eq. 11) and natural frequencies (Eq. 10).

In order to better understand the difference in the behavior of both systems, lets consider some new synchronization quantifiers. In Fig. 5(a) and 5(b) we have the instantaneous frequencies $\dot{\theta}$ of Systems 1 and 2 respectively as a function of time for a coupling fixed at $k = 0.6$. The data regarding the hub is plotted in red and the one regarding the peripheral

nodes is plotted in blue. One can clearly notice the difference in the behavior of both systems. For System 1, the instantaneous frequency of the peripheral nodes are very similar to each other, on the other hand, for System 2 , each oscillator has a different behavior.

In Figs. 5(c) and 5(d) there are the phase space of the hub (in red) and of two peripheral nodes (all pheriperal nodes behave in the same way, the ones labeled as $n = 1, 2$ were chosen) and their respective Poincaré sections, also at $k = 0.6$. The Poincaré section was built from the local maxima of the x coordinate of each hub cycle, that is, every time the hub reaches its local maxima x^{hub}, we plot (x^{hub}, y^{hub}),(x^{p_1}, y^{p_1}) and (x^{p_2}, y^{p_2}), where p_1 and p_2 represent the first two peripheral nodes respectively. Both the phase spaces and the Poincaré sections were plotted using 200 unities of time. Observing the phase spaces in Figs. 5(c) and 5(d), there is numerical evidence of dense trajectories that seem to move through the surface of a torus, indicating that those oscillators are moving in a quasi-periodic trajectory [25]. To be sure there is such dynamical behavior, we need to analyze their Poincaré sections. If an oscillator exhibits a periodic movement, it is expected that its Poincaré section will be composed of a single point, for if we plot its x and y coordinates every time its coordinate x reaches a local maxima, this pair of coordinates will always be the same, result in only one point. If, on the other hand, an oscillators presents a quasi-periodic motion, the values of the x local maxima vary and never repeat, so the points that form its Poincaré section spread through their phase space [22].

It can be clearly seen in Figs. 5(c) and 5(d) that, for both systems, the peripheral nodes present a dense Poincaré section, indicating that they are in fact in a quasi-periodic motion and that in System 1, all oscillators present this quasi-periodic behavior, including the hub. As for System 2, the hub has a periodic movement, for its trajectory in the phase space is a limit cycle and its Poincaré section is composed of a single point. So, when the system is in the regime of remote synchronization, all nodes move in a quasi-periodic trajectory and when this synchronization is lost due to the initial conditions, the hub starts oscillating in a periodic motion while the peripheral nodes remain in the quasi-periodic movement.

4. Conclusions

In this paper, the phenomenon of remote synchronization in a star-like network composed of Stuart-Landau oscillators was studied. In the regime of remote synchronization, only the peripheral nodes are synchronized and it was shown that in this regime, all the oscillators exhibit a quasi-periodic behavior. When different sets of initial conditions were used, we could notice that the peripheral nodes lose their synchronization for some of these sets of initial conditions, indicating that this system presents a multistability behavior.

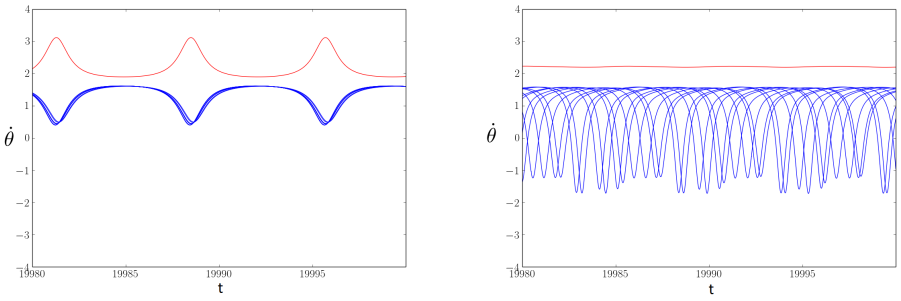

(a) System 1 (b) System 2

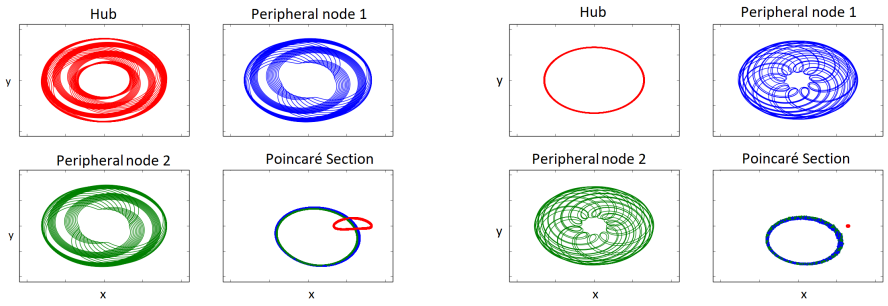

(c) System 1 (d) System 2

Figure 5. (a)-(b) Instantaneous frequency $\dot{\theta}$ of Systems 1 and 2 respectively (hub in red and peripheral nodes in blue) and their (c)-(d) phase spaces and Poincaré sections at $k = 0.6$ for 200 unities of time.

Acknowledgments

JCL would like to thank the Conselho Nacional de Desenvolvimento Científico e Tecnológico - CNPq for the financial support. This research is also supported by grant 2015/50122-0 of São Paulo Research Foundation (FAPESP) and DFG-IRTG 1740/2.

References

[1] Avoli, M., and de Curtis, M. Gabaergic synchronization in the limbic system and its role in the generation of epileptiform activity. *Progress in neurobiology 95*, 2 (2011), 104–132.

[2] Bergner, A., Frasca, M., Sciuto, G., Buscarino, A., Ngamga, E., Fortuna, L., and Kurths, J. Remote synchronization in star networks. *Physical Review E 85*, 2 (2012), 026208.

[3] Boccaletti, S. The synchronized dynamics of complex systems. *Monograph series on nonlinear science and complexity 6* (2008), 1–239.

[4] Boccaletti, S., Kurths, J., Osipov, G., Valladares, D., and Zhou, C. The synchronization of chaotic systems. *Physics reports 366*, 1 (2002), 1–101.

[5] Buck, J. Synchronous rhythmic flashing of fireflies. ii. *Quarterly review of biology* (1988), 265–289.

[6] Donges, J. F., Zou, Y., Marwan, N., and Kurths, J. The backbone of the climate network. *EPL (Europhysics Letters) 87*, 4 (2009), 48007.

[7] Fortuna, L., and Frasca, M. Experimental synchronization of single-transistor-based chaotic circuits. *Chaos: an interdisciplinary journal of nonlinear science 17*, 4 (2007), 043118.

[8] Frasca, M., Bergner, A., Kurths, J., and Fortuna, L. Bifurcations in a star-like network of stuart–landau oscillators. *International Journal of Bifurcation and Chaos 22*, 07 (2012), 1250173.

[9] Gambuzza, L. V., Cardillo, A., Fiasconaro, A., Fortuna, L., Gómez-Gardenes, J., and Frasca, M. Analysis of remote synchronization in complex networks. *Chaos: an interdisciplinary journal of nonlinear science 23*, 4 (2013), 043103.

[10] Gambuzza, L. V., Gómez-Gardeñes, J., and Frasca, M. Amplitude dynamics favors synchronization in complex networks. *Scientific reports 6* (2016).

[11] Gómez-Gardenes, J., Moreno, Y., and Arenas, A. Paths to synchronization on complex networks. *Physical review letters 98*, 3 (2007), 034101.

[12] Guckenheimer, J., and Holmes, P. J. *Nonlinear oscillations, dynamical systems, and bifurcations of vector fields*, vol. 42. Springer Science & Business Media, New York, 2013.

[13] Loppini, A., Capolupo, A., Cherubini, C., Gizzi, A., Bertolaso, M., Filippi, S., and Vitiello, G. On the coherent behavior of pancreatic beta cell clusters. *Physics Letters A 378*, 44 (2014), 3210–3217.

[14] Maraun, D., and Kurths, J. Epochs of phase coherence between el nino/southern oscillation and indian monsoon. *Geophysical Research Letters 32*, 15 (2005).

[15] Mokhov, I. I., Smirnov, D. A., Nakonechny, P. I., Kozlenko, S. S., Seleznev, E. P., and Kurths, J. Alternating mutual influence of el-niño/southern oscillation and indian monsoon. *Geophysical Research Letters 38*, 8 (2011).

[16] Néda, Z., Ravasz, E., Brechet, Y., Vicsek, T., and Barabási, A.-L. Self-organizing processes: the sound of many hands clapping. *Nature 403*, 6772 (2000), 849–850.

[17] Nicosia, V., Valencia, M., Chavez, M., Díaz-Guilera, A., and Latora, V. Remote synchronization reveals network symmetries and functional modules. *Physical review letters 110*, 17 (2013), 174102.

[18] Pantaleone, J. Synchronization of metronomes. *American Journal of Physics 70*, 10 (2002), 992–1000.

[19] Panteley, E., Loria, A., and El Ati, A. On the stability and robustness of stuart-landau oscillators. *IFAC-PapersOnLine 48*, 11 (2015), 645–650.

[20] Pikovsky, A., Rosenblum, M., and Kurths, J. *Synchronization*, vol. 12. Cambridge university press, Cambridge, 2003.

[21] Pluchino, A., Latora, V., and Rapisarda, A. Changing opinions in a changing world: a new perspective in sociophysics. *International Journal of Modern Physics C 16*, 04 (2005), 515–531.

[22] Premalatha, K., Chandrasekar, V., Senthilvelan, M., and Lakshmanan, M. Imperfectly synchronized states and chimera states in two interacting populations of nonlocally coupled stuart-landau oscillators. *Physical Review E 94*, 1 (2016), 012311.

[23] Strogatz, S. *Sync*. Hyperion, New York, 2003.

[24] Strogatz, S. H. From kuramoto to crawford: exploring the onset of synchronization in populations of coupled oscillators. *Physica D: nonlinear phenomena 143*, 1 (2000), 1–20.

[25] Strogatz, S. H. *Nonlinear dynamics and chaos*. Westview press, Boulder, 2014.

[26] Van Leeuwen, P., Geue, D., Thiel, M., Cysarz, D., Lange, S., Romano, M., Wessel, N., Kurths, J., and Grönemeyer, D. Influence of paced maternal breathing on fetal–maternal heart rate coordination. *Proceedings of the National Academy of Sciences 106*, 33 (2009), 13661–13666.

[27] Varela, F., Lachaux, J.-P., Rodriguez, E., and Martinerie, J. The brainweb: phase synchronization and large-scale integration. *Nature reviews neuroscience 2*, 4 (2001), 229–239.

Lacerda Juliana, M.Sc.(Ph.D. student): National Institute for Space Research - INPE, 12243-010, Brazil (*juliana.lacerda@inpe.br*). The author presented this contribution at the conference in the special session: "New trends in dynamics and control of nonlinear naval and aerospace systems" organized by J.M. Balthazar and E. Jarzbowska.

Freitas Celso, Ph.D.: National Institute for Space Research - INPE, 12243-010, Brazil (*cbnfreitas@gmail.com*).

Macau Elbert, Ph.D. (Professor): National Institute for Space Research - INPE, 12243-010, Brazil (*elbert.macau@inpe.br*).

Geometrically exact beam equations in the adaptive DCA-framework

Jeremy Laflin, Kurt Anderson

Abstract: This work examines the suitability of two popular methods of modeling bodies that undergo large deformation for use in the adaptive DCA framework where the system contains a mixed set of other bodies that are modeled using different model types, such as rigid-bodies that use a Newton-Euler formulation or flexible-bodies that use a Floating Frame of Reference (FFR). This work shows that the ANCF is not immediately suitable for this purpose and that the GEBF will be suitable after some modest manipulations. Then the geometrically exact equations-of-motion are derived for beam-type bodies that can be used in the DCA-framework, using the Geometrically Exact Beam Formulation (GEBF) to describe the deformations of a beam-type body.

1. Introduction

Simulation of the full nonlinear dynamic response of articulated multibody systems is an important instrument used by scientists and engineers to gain understanding about the behavior of complex systems which may be reasonably modeled as a collection of interconnected bodies. The information provided by these simulations can be used to make better informed decisions about design, control, or other aspects of such systems, provided the simulation can predict the system's behavior and internal state to a sufficient level of accuracy in a timely fashion. Providing accurate information in a timely manner is essential in cases where the system-of-interest's behavior cannot be studied directly. For traditional mechanical systems, this may be due to a high cost of building, instrumenting, or testing a prototype.

Simulating complex dynamic systems consists of three main tasks: (1) Determination of the external forces acting on the system; (2) Formation of the equations-of-motion and their subsequent solution for the state variable derivatives; and (3) Temporal integration of the state variable derivatives. For articulated multibody systems, there has been a great deal of research that has produced a variety of efficient methods to perform the formation and solution of the equations-of-motion. Of these, the Divide-and-Conquer Algorithm (DCA), first used by Featherstone in a multibody context [6,7], provides several of advantages for use in large-scale nonlinear coupled multibody dynamic systems. In addition to computational efficiency, these advantages include: a straight-forward coarse-grain parallel implementation,

easy accommodation of changes in the number of degrees-of-freedom of the system, and a structure that allows any method to be used to generate the equations-of-motion for a particular body or sub-domain.

There has been significant progress associated with modeling and simulating dynamic systems in an adaptive manner [5,12,15,21–23,25], which ideally considers only those degrees-of-freedom that are deemed important, there are still opportunities for further computational savings. Ideally, an adaptive simulation of complex systems should self-identify and utilize different model types which are best suited to the nature of the local behavior of each subdomain. As such, a complex system may ultimately be comprised of rigid-bodies (no deformation), flexible-bodies (small deformation), and highly-flexible bodies (large deformations). A decrease in computation labor may be achieved by adjusting the definition of the computational model to best match the needs of the associated subdomain, which results in fewer degrees-of-freedom without appreciable loss in the accuracy of predicting the system's behavior.

In some cases flexible-bodies may accurately reproduce the aggregate behavior of many rigid-bodies with significantly fewer degrees-of-freedom. Similarly, highly-flexible bodies can be constructed from a number of flexible-bodies which all undergo small displacements, resulting in still fewer degrees-of-freedom. With intelligent internal metrics guiding adaptive adjustments in local model resolution and type, such adjustments could be located anywhere in the system. Therefore, an automatic method to form and solve the equations-of-motion for a system comprised of a mixture of these body/model types must seamlessly perform these operations with bodies (subdomain models) of any type. Then, aggregating various bodies into a psuedo-body (subdomain) of a new type is a matter of monitoring various degrees-of-freedom, making a determination of which degrees-of-freedom to add or remove, and changing the resolution of the model to reflect the desired change. The decision to add or remove various degrees-of-freedom may be based on a variety of indicators including, but not limited to, statistics collected from the degrees-of-freedom, physics-based metrics, or knowledge-based metrics. A statistical-based approach that removes "lazy" degrees-of-freedom that have a low standard deviation from their average position has already been shown to more accurately predict the overall motion of the system than traditional model reduction methods used in molecular dynamics simulations with a comparable amount of computational effort by Poursina et al. [21].

This notion of changes in the number, location of, or type of degrees-of-freedom when using the DCA is the essence of the "adaptive-DCA-framework". Due to the advantages of this framework for both electro-mechanical and biological systems, it is a promising platform on which to make improvements. Before examining the modifications needed to extend

the capabilities of this framework to include changes in model definition the basic DCA is presented.

There have been a number of modifications to the original DCA method [13, 14, 17–20] since it was first applied to multibody systems. The basic method is briefly summarized herein using the notation of Mukherjee and Anderson [16]. The DCA consists of two recursive processes (kernels): assembly and disassembly which are diagrammed in Fig. 1.

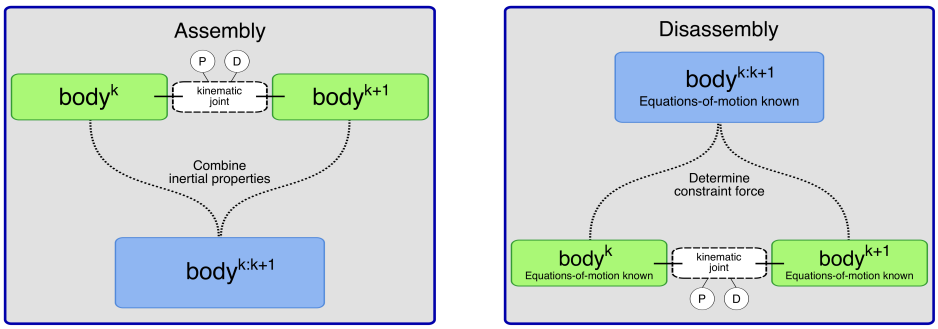

Figure 1. The two key DCA kernel operations

These kernels both require that the motion allowed by the kinematic joint is mapped into a matrix containing the unit vectors of allowed motion ($\boldsymbol{P}$), and a matrix containing the unit vectors of restricted motion ($\boldsymbol{D}$). The assembly process is performed first and assumes that the equations-of-motion for all points coincident with the connecting kinematic joints for all bodies are able to be expressed in a specific form, which will be discussed later, and that the kinematics have been determined. This algorithm can work for any number of kinematic connections to any body but is easily explained using a chain topography where each body has two connections to other bodies. These points are commonly referred to as "handles" and for a chain-type system, there are two for each body.

The assembly process uses the four equations-of-motion written at each of the two "handles" for a pair connected by a joint (parent bodies) to write two equations-of-motion for the outboard "handles" of the pair of bodies being assembled. These equations are not functions of the constraint forces and accelerations acting at the connecting joint. They are only functions of the constraint forces and accelerations at the outboard joints and the combined inverse inertial properties of the two bodies. Now the two parent bodies may be effectively treated as a single (child) body at the next level of recursion.

This approach is possible because the relative motion between the parent bodies can be captured by an equation that describes the modes of motion [24] permitted by the joint, which are known. This process is then repeated recursively until there are only two equations-of-

motion for the entire system, as shown in Fig. 2, which are only a function of the constraint

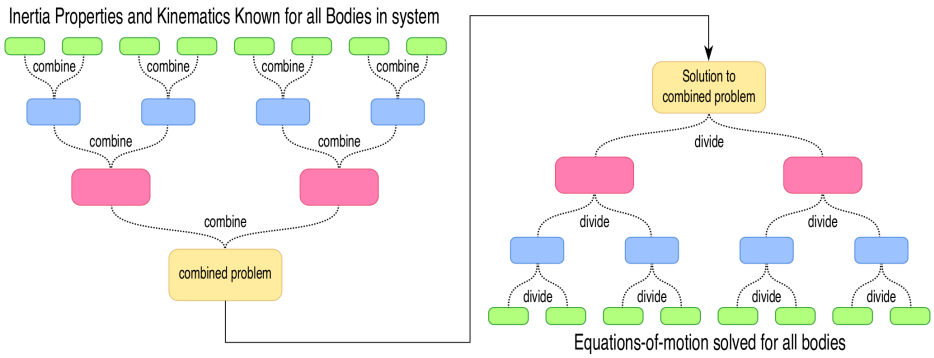

Figure 2. Divide-and-Conquer Algorithm (DCA) for multibody dynamics

forces and accelerations acting at the boundary joints, the combined inverse inertial properties of the entire system, and any applied or body forces. The assembly kernel is applied recursively to pairs of adjacent bodies until there is only one assembly left in the system. At this stage the equations-of-motion can be solved since all constraint forces have been eliminated from the equations-of-motion of the final assembly (combined problem), except the constraint forces acting at the boundary joints, which are effectively known. The disassembly kernel is then applied recursively re-introducing and determining the constraint force acting between these pairs and the acceleration of the "handles". The constraint force and the acceleration of the points on the bodies coincident with the joint are determined as a function of the constraint forces and accelerations determined at the previous level of recursion. Solving the equations-of-motion for the final assembly is possible knowing the conditions of these boundary joints.

In the disassembly phase, the assemblies are split back into their constituent bodies, which for all levels of recursion except the last one are other assemblies. This process basically propagates information from the solution of the two equations-of-motion of an assembly (child) to the four equations-of-motion of the constituent (parent) bodies. The accelerations and constraint forces determined for the assembly are the solution to the outboard equations-of-motion for each constituent body. Therefore, all that needs to be determined is the constraint force acting at, and the acceleration of, the connecting joint. Both of these quantities are able to be determined from the known information. This process occurs recursively until all constraint forces and accelerations are known for all bodies in the system. Both of these recursive processes are most efficiently implemented in a hierarchical tree structure.

For this recursive process to work, every body of the system including those fictitious bodies resulting from assembly, it must be possible to write the equations-of-motion as

$$\vec{A}_1^k = \boldsymbol{\zeta}_{11}^k \vec{F}_{1c}^k + \boldsymbol{\zeta}_{12}^k \vec{F}_{2c}^k + \boldsymbol{\zeta}_{13}^k \ , \tag{1}$$

$$\vec{A}_2^k = \boldsymbol{\zeta}_{21}^k \vec{F}_{1c}^k + \boldsymbol{\zeta}_{22}^k \vec{F}_{2c}^k + \boldsymbol{\zeta}_{23}^k \ , \tag{2}$$

and

$$\vec{A}_1^{k+1} = \boldsymbol{\zeta}_{11}^{k+1} \vec{F}_{1c}^{k+1} + \boldsymbol{\zeta}_{12}^{k+1} \vec{F}_{2c}^{k+1} + \boldsymbol{\zeta}_{13}^{k+1} \ , \tag{3}$$

$$\vec{A}_2^{k+1} = \boldsymbol{\zeta}_{21}^{k+1} \vec{F}_{1c}^{k+1} + \boldsymbol{\zeta}_{22}^{k+1} \vec{F}_{2c}^{k+1} + \boldsymbol{\zeta}_{23}^{k+1} \ . \tag{4}$$

$\vec{A}_i^k$, and $\vec{F}_i^k$, are the spatial acceleration of, and force on, handle i respectively and are defined as

$$\vec{A}_i^k = \begin{bmatrix} \vec{\alpha}^k \\ \vec{a}_i^k \end{bmatrix} \tag{5}$$

and

$$\vec{F}_{ic}^k = \begin{bmatrix} \vec{\tau}_i^k \\ \vec{f}_i^k \end{bmatrix} \ . \tag{6}$$

The rotational acceleration of $Body^k$ is $\vec{\alpha}^k$, $\vec{a}_i^k$ is the translational acceleration of the reference point H_i^k, and $\vec{\tau}_i^k$ and $\vec{f}_i^k$ are the constraint torques and forces acting at H_i^k, respectively. The $\boldsymbol{\zeta}_{ij}^k$ $(i, j = 1, 2)$ terms are the spatial matrix representations of the inverse inertial properties at the handles, while $\boldsymbol{\zeta}_{i3}^k$ $(i = 1, 2)$ contains applied forces acting on the body and other velocity dependent terms.

The bodies, $Body^k$ and $Body^{k+1}$, are connected by a kinematic joint j and therefore are subject to the kinematic constraint

$$\boldsymbol{P}^j \dot{\vec{u}} = \ \vec{A}_1^{k+1} - \vec{A}_2^k - \dot{\boldsymbol{P}}^j \vec{u}. \tag{7}$$

Here, $\vec{u}$ is the vector of generalized speeds and the $\boldsymbol{P}$ matrix is a property of the kinematic joint whose columns define the unit vectors that are aligned with the directions of motion permitted by the kinematic joint. Similarly, the $\boldsymbol{D}$ matrix is that whose columns define the directions of motion that are restricted by the joint. For example, if the number of degrees-of-freedom allowed by the joint is m and the number of degrees-of-freedom restricted by the joint is m, then the $(6 \times m)$ matrix $\boldsymbol{P}$ and the $(6 \times m)$ matrix $\boldsymbol{D}$ for a revolute (pin) joint are

$$\boldsymbol{P} = \begin{bmatrix} 1 & 0 & 0 & 0 & 0 & 0 \end{bmatrix}^T \tag{8}$$

and

$$\boldsymbol{D} = \begin{bmatrix} 0 & 0 & 0 & 0 & 0 \\ 1 & 0 & 0 & 0 & 0 \\ 0 & 1 & 0 & 0 & 0 \\ 0 & 0 & 1 & 0 & 0 \\ 0 & 0 & 0 & 1 & 0 \\ 0 & 0 & 0 & 0 & 1 \end{bmatrix} . \tag{9}$$

The set of equations for two connected bodies, Eqs. (1 - 4), are redundant since the translational acceleration of the connecting point is included in the equations-of-motion for each body. This redundancy can be eliminated by exploiting the fact that the constraint forces are equal and opposite, i.e, $\vec{F}^{k}_{2c} = -\vec{F}^{k+1}_{1c}$, and that the kinematics of the connecting joint are specified. Specifically, Eq. (7) describes the relative acceleration between connecting bodies using the generalized acceleration $\dot{\vec{u}}$ along known directions defined by the connecting joint partial velocity (mode of motion) $\boldsymbol{P}^{j}$. The equations-of-motion for the assembled fictitious pseudo-body $Body^{k:k+1}$, at H^{k}_{1} and H^{k+1}_{2} can be expressed as

$$\vec{A}^{k}_{1} = \boldsymbol{\zeta}^{k:k+1}_{11}\vec{F}^{k}_{1c} + \boldsymbol{\zeta}^{k:k+1}_{12}\vec{F}^{k+1}_{2c} + \boldsymbol{\zeta}^{k:k+1}_{13} \tag{10}$$

and

$$\vec{A}^{k+1}_{2} = \boldsymbol{\zeta}^{k:k+1}_{21}\vec{F}^{k}_{1c} + \boldsymbol{\zeta}^{k:k+1}_{22}\vec{F}^{k+1}_{2c} + \boldsymbol{\zeta}^{k:k+1}_{23} \tag{11}$$

by algebraically eliminating the constraint forces at the connecting joint from Eq. (1) and Eq. (4). The resulting equations, Eq. (10) and Eq. (11), are of the same form as the equations-of-motion for the handles of any generic body.

In the above equations, $\boldsymbol{\zeta}^{k:k+1}_{ij}$ represents the inertial quantities of the fictitious pseudo-body resulting from the assembly of $Body^{k}$ and $Body^{k+1}$. For the derivation of the inverse inertial terms and the details of the assembly process, the reader is referred to the work of Featherstone [6] or Mukherjee and Anderson [16]. This assembly process is then repeated recursively, until only a single assembled pseudo-body remains (root body), as shown in Fig. 2. This is possible because the form of the equations-of-motion for the handles of an assembled-body is indistinguishable in form from the form of the equations-of-motion for the handles of a generic body. The assembly process yields the equations-of-motion associated with the two boundary handles

$$\vec{A}^{1}_{1} = \boldsymbol{\zeta}^{1:n}_{11}\vec{F}^{1:n}_{1c} + \boldsymbol{\zeta}^{1:n}_{12}\vec{F}^{1:n}_{2c} + \boldsymbol{\zeta}^{1:n}_{13} \tag{12}$$

and

$$\vec{A}^{n}_{2} = \boldsymbol{\zeta}^{1:n}_{21}\vec{F}^{1:n}_{1c} + \boldsymbol{\zeta}^{1:n}_{22}\vec{F}^{1:n}_{2c} + \boldsymbol{\zeta}^{1:n}_{23} \ , \tag{13}$$

which are written in terms of only the spatial inverse inertial quantities of all bodies in the system and the constraint forces acting at the two handles of the root body (boundary handles).

The spatial accelerations of, and constraint forces acting at, H_1^1 and H_2^n can now be determined using the known boundary conditions. After determining these quantities, the disassembly process begins, in which all unknown spatial accelerations of the handles and constraint forces acting at all connecting joints are determined. This recursive process determines the constraint forces acting at a joint in terms of the constraint forces acting at the handles of the assembly, and the inertial properties of the assembled body, as

$$\vec{F}_{1c}^{k+1} = \boldsymbol{W}\boldsymbol{\zeta}_{21}^{k}\vec{F}_{1c}^{k} - \boldsymbol{W}\boldsymbol{\zeta}_{12}^{k+1}\vec{F}_{2c}^{k+1} + \boldsymbol{Y} \ . \tag{14}$$

The terms $\boldsymbol{W}$ and $\boldsymbol{Y}$ are terms containing inverse inertial properties from the assembly of the two bodies, see Featherstone [6], or Mukherjee and Anderson [16] for derivation of these terms. Once this constraint force acting at a joint is determined, the spatial accelerations of the handles that are connected by this joint can be determined using Eq. (10) and Eq. (11). This allows the computation of the generalized acceleration ($\dot{\vec{u}}$) at the joint using Eq. (7).

2. Kinematic requirements for adaptive changes in body-definition

If the DCA is to be used to seamlessly form and solve the equations-of-motion for a mixed system, it is crucial that the equations-of-motion of an assembled-body are indistinguishable from those of a "leaf" or component-body from the perspective of executing the recursive kernels, which depend on the form and makeup of Eqs. (1 - 4). This poses a challenge for allowing adaptive changes in model definition due to the variety of generalized coordinates used in various models of flexiblity. If the generalized coordinates are not compatible, Eq. (7) cannot be satisfied and the assembly kernel cannot be executed because the inverse inertial matrices $\boldsymbol{\zeta}_{ij}^{k}$ $(i,j = 1,2)$ and $\boldsymbol{\zeta}_{i3}^{k}$ $(i = 1,2)$ of bodies of different type will have different meaning. Therefore, the algebraic operations constituent to the assembly kernel that produce Eq. (10) and Eq. (11) from Eqs. (1 - 4) are not longer valid.

A variety of methods already meet these requirements, such as the FFR formulation using modal coordinates and associated admissible shape functions, which has been cast for use in the DCA framework by Mukherjee and Anderson [17], or the FFR formulation using interpolating splines, which has been formulated in the DCA framework by Khan et al. [11]. This is because for these small deformation formulations use the method of superposition which allow the generalized coordinates associated with modeling the deformation to be decoupled from the rigid-body generalized coordinates. However, if the body undergoes large deformations, these methods require an undesirably large amount of sub-structuring. There-

fore, two popular methods of modeling bodies undergoing large deformations are examined for use in the adaptive DCA framework with systems who's constituent bodies are modeled with different formulations.

3. Suitability of GEBF for use in an adaptive DCA-based framework

The method introduced by Simo [27–29], which is referred to as the Geometrically Exact Beam Formulation (GEBF) when implemented for beam elements, is another option to model large deformations of bodies in multibody systems. This method defines the position vector of a point on the deformed-body as the sum of a reference line displacement vector and the rotation of a vector defining the point in the rigid cross-section, as shown in Fig. 3. Therefore, this method does incorporate rotational coordinates into the equations-of-motion of the cross-section, which is promising for use in DCA with bodies of other definition.

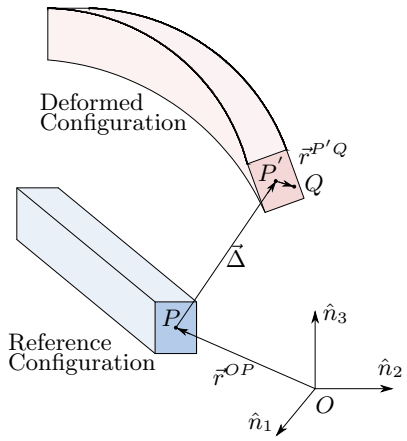

Figure 3. Geometric Description of the Deformation

Another advantage of the method that Bauchau et al. [4] demonstrates is that the GEBF more accurately predicts the behavior of beam elements than the ANCF in predicting various displacements, rotations, and strains. This is attributed to the kinematic description of the beam element by ANCF, which uses a second derivative of displacement to give the curvature, instead of a first derivate which is used by GEBF. The error introduced by using higher order derivatives in the displacement-strain relationship is well documented in texts detailing the fundamentals of finite element analysis [8]. Furthermore, Bauchau et al. [2] predict that modeling the behavior of two-dimensional and three-dimensional objects using plate and shell elements, respectively, based on the ANCF, will suffer the same loss of accuracy because they will also use a second derivative of displacement to determine the curvature.

With these advantages, geometrically-exact methods are an attractive means of modeling the large deformation of highly-flexible bodies. Therefore, the equations-of-motion are examined for use in the adaptive DCA framework. The equations-of-motion of a beam-element are given by Bauchau [1] as

$$\dot{\vec{g}} = -\tilde{\vec{u}}\ \vec{h} + \left(\tilde{\vec{x}}_0{}' + \tilde{\vec{u}}\ '\right)\vec{n} + \vec{m}\ ' + \vec{\tau} \tag{15}$$

and

$$\dot{\vec{h}} = \vec{n}\ ' + \vec{f}\,. \tag{16}$$

These equations give the temporal rate of change of rotational ($\dot{\vec{g}}$) and translational ($\dot{\vec{h}}$) momentum, respectively. The rate of change of momentum quantities are functions of the body forces ($\vec{n}$) and moments ($\vec{m}$), applied forces ($\vec{f}$) and moments ($\vec{\tau}$). The displacements are ($\vec{u}$) and the ($\vec{x}_0$) is the vector that locates the nodes in the reference configuration. The prime symbol ($'$) denotes a derivative with respect to the coordinate along the beam's axis. The tilde accent ($\tilde{}$) indicates that the quantity is a skew symmetric matrix of the vector quantities that performs the cross product operation. In this form, the equations-of-motion for a body are not compatible with the DCA for use in the assembly or disassembly sweep. However, it is reasonable that Eq. (15) and (16) can be modified or re-derived to produce a set of equations that can be used in the key operations of the DCA because the generalized coordinates required for use in the adaptive DCA framework are time-derivatives of those used in this formulation.

4. Deriving the GEBF equations-of-motion for use in the adaptive DCA

Although the equations-of-motion for a GEBF-element are widely available in the literature, they are cast in terms of momentum. Since the DCA requires a kinematic relationship for acceleration to be formed between for adjacent bodies at the kinematic joint, this section derives the kinematics and kinetics of the element. Then the equations-of-motion are algebraically manipulated into the form of Eq. (1) and Eq. (2) for use in the DCA.

4.1. Kinematics

Figure 3 shows a generic point located in the deformed configuration of a GEBF beam element with respect to the reference configuration. In this derivation, the cross-section remains rigid and therefore the point does not move relative to the centroid of the cross-section. The large-deformation of a flexible body is decomposed into the deformation of the neutral axis of the body and the rotation of the cross-section of the beam at any point along the neutral axis. The motion of the centroid in the reference configuration (P) to its

location in the deformed configuration ($P^{'}$) defines the deformation vector of the node at the coordinate along the beam's centerline corresponding with the cross-section.

If the warp of the beam's cross-section is neglected, the position of any point ($\vec{r}^{\,Q}$) on a flexible beam may be described by the sum of the vectors locating the centroid of a rigid cross-section ($\vec{r}^{\,OP}$) in the undeformed configuration, the deformation vector of the centroid ($\vec{r}^{\,PP'} = \vec{\Delta}$), and the location of the point in the cross-section ($\vec{r}^{\,P'Q}$). The resulting vector is expressed in the Newtonian frame as

$$\left\{\vec{r}^{\,Q}\right\}_N = \left\{\vec{r}^{\,OP}\right\}_N + \underbrace{\left\{\vec{r}^{\,PP'}\right\}_N}_{\vec{\Delta}} + {}^N\underline{\underline{C}}^B \left\{\vec{r}^{\,P'Q}\right\}_B \ . \tag{17}$$

The subscript on the vector ({}) indicates the basis with which the vector is expressed. Since the position vector locating the point in the rigid cross-section is easily expressed in the reference frame of the rigid cross-section, the rotation tensor (${}^N\underline{\underline{C}}^B$) transforms the vector from the cross-section basis (B) to the Newtonian basis (N). It is through this term that the rotational coordinates enter the equations-of-motion.

Taking the derivative of $\vec{r}^{\,Q}$ gives the velocity of the generic point as

$$\left\{{}^N\vec{v}^{\,Q}\right\}_N = \underbrace{\frac{d}{dt}\left\{\vec{r}^{\,OP}\right\}_N}_{\vec{0}} + \underbrace{\frac{d}{dt}\left\{\vec{r}^{\,PP'}\right\}_N}_{\dot{\vec{\Delta}}} + \frac{d}{dt}\left({}^N\underline{\underline{C}}^B\right)\left\{\vec{r}^{\,P'Q}\right\}_B + \underbrace{{}^N\underline{\underline{C}}^B \frac{d}{dt}\left\{\vec{r}^{\,P'Q}\right\}_B}_{\vec{0}} \ . \tag{18}$$

The velocity expression can be simplified since some of the derivatives with respect to time are zero, such as the location of the centroid of the cross-section in the reference frame with respect to the origin. Also, because the point is not moving in the cross-section, the derivative of that vector with respect to time is zero. The remaining quantities are the velocity of the deformation ($\dot{\vec{\Delta}}$) and the time rate of change of the rotation tensor (${}^N\dot{\underline{\underline{C}}}^B$). Thus, the velocity of an arbitrary point 'Q' of the beam in 'N' is

$$\left\{{}^N\vec{v}^{\,Q}\right\}_N = \left\{\dot{\vec{\Delta}}\right\}_N + {}^N\dot{\underline{\underline{C}}}^B \left\{\vec{r}^{\,P'Q}\right\}_B \ . \tag{19}$$

The rotation (direction cosine) tensor temporal derivative (${}^N\dot{\underline{\underline{C}}}^B$) can be converted into the skew-symmetric matrix that defines the angular velocity ($\tilde{\omega}$) of the reference frame corresponding to the beam cross-section. This matrix performs the cross-product operation with the following vector ($\tilde{\omega}\,\vec{r} = \vec{\omega} \times \vec{r}$). This is done by post multiplying the rotation tensor's

time derivative by the identity matrix ($\underline{\underline{U}}$) as,

$$\left\{ {}^N\vec{v}^Q \right\}_N = \frac{d}{dt}\left\{ \vec{r}^Q \right\}_N \tag{20}$$

$$= \left\{ \dot{\vec{\Delta}} \right\}_N + {}^N\dot{\underline{\underline{C}}}^B \, \underline{\underline{U}} \, \left\{ \vec{r}^{P'Q} \right\}_B \tag{21}$$

$$= \left\{ \dot{\vec{\Delta}} \right\}_N + \underbrace{{}^N\dot{\underline{\underline{C}}}^B \left({}^N\underline{\underline{C}}^B \right)^T}_{{}^N\tilde{\omega}^B} \underbrace{{}^N\underline{\underline{C}}^B \left\{ \vec{r}^{P'Q} \right\}_B}_{\left\{ \vec{r}^{P'Q} \right\}_N}, \tag{22}$$

yielding

$$\left\{ {}^N\vec{v}^Q \right\}_N = \left\{ \dot{\vec{\Delta}} \right\}_N + {}^N\tilde{\omega}^B \left\{ \vec{r}^{P'Q} \right\}_N . \tag{23}$$

The acceleration of a generic point is obtained by differentiating the expression for velocity as

$$\left\{ {}^N\vec{a}^Q \right\}_N = \frac{d}{dt}\left\{ \dot{\vec{\Delta}} \right\}_N + \frac{d}{dt}\left({}^N\tilde{\omega}^B \right)\left\{ \vec{r}^{P'Q} \right\}_N + {}^N\tilde{\omega}^B \underbrace{\frac{d}{dt}\left\{ \vec{r}^{P'Q} \right\}_N}_{{}^N\tilde{\omega}^B \left\{ \vec{r}^{P'Q} \right\}_N} . \tag{24}$$

The kinematic derivative is used to differentiate the vector locating the point in the cross-section because it is now expressed in the Newtonian basis. The acceleration of the generic point expressed with respect to the origin expressed in the Newtonian basis is now

$$\left\{ {}^N\vec{a}^Q \right\}_N = \left\{ \ddot{\vec{\Delta}} \right\}_N + {}^N\tilde{\alpha}^B \left\{ \vec{r}^{P'Q} \right\}_N + {}^N\tilde{\omega}^B \, {}^N\tilde{\omega}^B \left\{ \vec{r}^{P'Q} \right\}_N . \tag{25}$$

To develop the equations-of-motion for the GEBF-element the kinematics are needed for a generic point at any cross-section along the beam's length. To produce the kinematics as a function of the coordinate along the beam's length (s) the deformation of the beam's axis at any point is interpolated from the deformations of the axis at the nodes. Additionally, the rotation of the cross-section at any point along the beam's axis is interpolated from the rotation of the cross-section at the nodes. Therefore, the velocity and acceleration of any point on a cross-section at any location along the beam's axis are

$$\left\{ {}^N\vec{v}^Q(s) \right\}_N = \dot{\vec{\Delta}}(s) + {}^N\tilde{\omega}^X(s) \left\{ \vec{r}^{P'Q}(s) \right\}_N \tag{26}$$

and

$$\left\{ {}^N\vec{a}^Q(s) \right\}_N = \ddot{\vec{\Delta}}(s) + {}^N\tilde{\alpha}^X(s) \left\{ \vec{r}^{P'Q}(s) \right\}_N + {}^N\tilde{\omega}^X(s) \, {}^N\tilde{\omega}^X(s) \left\{ \vec{r}^{P'Q}(s) \right\}_N . \tag{27}$$

Note that

$$\left\{ \vec{r}^{P'Q}(s) \right\}_N = {}^N\underline{\underline{C}}^X(s) \left\{ \vec{r}^{P'Q} \right\}_B , \tag{28}$$

where ${}^N\underline{\underline{C}}^X$ is the interpolated rotation matrix as a function of the beam's axis coordinate. Interpolation of the angular quantities is not straight-forward, as discussed previously, and a variety of techniques can be used to determine the interpolated rotational quantities. These methods are presented in detail by Bauchau [1–3].

4.2. Kinetics of a two-node beam-element

Instead of attempting to manipulate Eq. (15) and Eq. (16) into a form in terms of rotational and translational acceleration, the equations-of-motion for each node of a two-node GEBF-element are developed using a generalized version of Jourdain's principle [9], which has been popularized by Kane [10] and Schiehlen [26]. The equations-of-motion for the r^{th} degree-of-freedom can be written as

$$\vec{F}_r^* = \vec{F}_r \ , \tag{29}$$

modifying slightly the equations-of-motion given in Kane and Levinson [10]. These equations are not derived herein, but can be expanded to a form that is more useful. For a system of N particles using r generalized coordinates ($q_{i=1\ldots r}$) the equations-of-motion for the r^{th} degree-of-freedom is expanded as

$$\sum_{i=1}^{N} \vec{v}_r^i \cdot m\vec{a}^i = \sum_{i=1}^{N} \vec{v}_r^i \cdot \vec{R}_i \tag{30}$$

and

$$\sum_{i=1}^{N} \frac{\partial \vec{v}^i}{\partial u_r} \cdot m\vec{a}^i = \sum_{i=1}^{N} \vec{v}_r^i \cdot \vec{R}_i \ , \tag{31}$$

where $\vec{R}_i$ is the resultant force vector acting on particle i. The generalized speeds (u_r) can be any invertible combination of the time derivatives of the generalized coordinates ($\dot{q}_r$), but are commonly chosen to be $u_r = \dot{q}_r$. The "partial velocities" ($\vec{v}_r^i$) of particle i [10] form the modes of motion [24] for the particle. Effectively these form the basis vectors for the velocity space of the i^{th} particle.

To develop the equations-of-motion for a GEBF-element, the equations-of-motion for a generic point as a function of the coordinate along the beam's neutral axis are written using the above method, then the equations are integrated over the volume of the element as

$$\rho \int_V \frac{\partial \vec{v}^Q(s)}{\partial u_r} \cdot \vec{a}^Q(s)\, dV = \rho \int_V \frac{\partial \vec{v}^Q(s)}{\partial u_r} \cdot \vec{f}(s)\, dV + \frac{\partial \vec{v}^i}{\partial u_r} \cdot \vec{R}_i \ . \tag{32}$$

In this version of the equations-of-motion, $\vec{f}$ is the body force vector and $\vec{R}$ is the resultant of the point load force vectors acting at handle i and $\frac{\partial \vec{v}^i}{\partial u_r}$ are the partial velocities at the handle i. The equations-of-motion for a finite number of degrees-of-freedom can be represented in matrix notation, after discretization of the beam and Eq. (32), as

$$\boldsymbol{M} \left\{ \dot{\vec{u}} \right\} = \left\{ R\vec{H}S \right\} \ . \tag{33}$$

Careful selection of the generalized speeds will produce a matrix equation that can be partitioned to produce the equations-of-motion of the handles, which are chosen to coincide with the nodes of the element. This produces the equations of the element as,

$$\begin{bmatrix} \boldsymbol{M}_{11} & \boldsymbol{M}_{12} \\ \boldsymbol{M}_{21} & \boldsymbol{M}_{22} \end{bmatrix} \begin{bmatrix} \begin{Bmatrix} {}^N\vec{\alpha}^1 \\ \vec{a}^1 \end{Bmatrix}_1 \\ \begin{Bmatrix} {}^N\vec{\alpha}^2 \\ \vec{a}^2 \end{Bmatrix}_2 \end{bmatrix} = \begin{bmatrix} \boldsymbol{M}_{11} & \boldsymbol{M}_{12} \\ \boldsymbol{M}_{21} & \boldsymbol{M}_{22} \end{bmatrix} \begin{bmatrix} A_1 \\ A_2 \end{bmatrix} = \begin{bmatrix} \boldsymbol{\gamma}_{11} \\ \boldsymbol{\gamma}_{12} \end{bmatrix} \vec{F}_{1c} + \begin{bmatrix} \boldsymbol{\gamma}_{21} \\ \boldsymbol{\gamma}_{22} \end{bmatrix} \vec{F}_{2c} + \begin{bmatrix} \vec{\gamma}_{13} \\ \vec{\gamma}_{23} \end{bmatrix} , \tag{34}$$

where the M_{ij} terms are mass-matrix sub-matrices resulting from the shown partitioning (6x6 in the full $3D$ case). Equation (34) can be algebraically decomposed into an equation-of-motion for each boundary node in the element in terms of only the constraint forces at the boundaries as

$$A_1 = \boldsymbol{\zeta}_{11}\vec{F}_{1c} + \boldsymbol{\zeta}_{12}\vec{F}_{2c} + \vec{\zeta}_{13} \tag{35}$$

and

$$A_2 = \boldsymbol{\zeta}_{21}\vec{F}_{1c} + \boldsymbol{\zeta}_{22}\vec{F}_{2c} + \vec{\zeta}_{23}. \tag{36}$$

Now the equations-of-motion for a GEBF-element given by Eq. (35) and Eq. (36), are in a form which facilitates use with the DCA. The $\boldsymbol{\zeta}_{ij}$ terms are the inverse inertial properties and result from the algebraic manipulations required to produce Eq. (35) and Eq. (36).

Due to the choice of generalized speeds, the kinematic relationship of a rigid-body (k) and a GEBF-body or element ($k+1$) connected at a kinematic joint is expressed as

$$A_2^{rigid} = \begin{bmatrix} \vec{\alpha}^k \\ \vec{a}_2^k \end{bmatrix} = A_1^{GEBF} = \begin{bmatrix} \vec{\alpha}^{k+1} \\ \vec{a}_2^{k+1} \end{bmatrix} + \dot{\boldsymbol{P}}^j\vec{u} + \boldsymbol{P}^j\dot{\vec{u}} \, , \tag{37}$$

where $\boldsymbol{P}^j$ is the space of admissible motions permitted by the connecting joint. From this equation, it can be seen that the coordinates used for rigid-body and the highly-flexible body are compatible. This is because, as can be seen in the preceding derivation, the rotational coordinates used for a GEBF-element cross-section are fundamentally the same as the rotational coordinates associated with the rigid-bodies. This allows the assembly and disassembly operations to be used without differentiation of the body type.

5. Conclusions

This work presents a method of modeling large deformation of beam-type bodies that is now compatible with the adaptive DCA framework. Additionally, this method can and will be

repeated to model other types of bodies that may be better represented as plates or shells. Automatic changes in body-type are now possible across all possible degrees of flexibility. This will allow adaptive simulations to further reduce the number of degrees-of-freedom while maintaining adequate accuracy predicting the overall motion of the system. These adaptive techniques are particularly attractive to the application of molecular dynamics where predicting the model type of much of the system is impossible a priori, when a fully atomistic simulation is impractical. For mechanical systems, the nature of the body is typically known. However, these adaptive capabilities can be used to simulate the mechanism through failure because the time and mode of failure is often not anticipated. Furthermore, the work developed herein allow a seamless coexistence of bodies of all degrees of flexibility (modeled with the appropriate formulation) in a multibody simulation.

Acknowledgments

This work was completed under grant 1161872 from the National Science Foundation and the authors are grateful for this support.

References

[1] Bauchau, O. a. *Flexible Multibody Dynamics*, vol. 176 of *Solid Mechanics and Its Applications*. Springer Netherlands, Dordrecht, 2011.

[2] Bauchau, O. A., Epple, A., Heo, S., and Guggenheim, D. Interpolation of Finite Rotations in Flexible Multibody Dynamics Simulations. *Proceedings of the Institution of Mechanical Engineers, Part K: Journal of Multi-body Dynamics, 222(K4) 222*, 4 (dec 2008), 353–366.

[3] Bauchau, O. A., and Han, S. Interpolation of rotation and motion. *Multibody System Dynamics 31*, 3 (mar 2014), 339–370.

[4] Bauchau, O. A., Han, S., Mikkola, A., and Matikainen, M. K. Comparison of the absolute nodal coordinate and geometrically exact formulations for beams. *Multibody System Dynamics 32*, 1 (jun 2014), 67–85.

[5] Bosson, M., Grudinin, S., and Redon, S. Block-adaptive quantum mechanics: An adaptive divide-and-conquer approach to interactive quantum chemistry. *Journal of Computational Chemistry 34*, 6 (mar 2013), 492–504.

[6] Featherstone, R. A Divide-and-Conquer Articulated-Body Algorithm for Parallel O(log(n)) Calculation of Rigid-Body Dynamics. Part 1: Basic Algorithm. *The International Journal of Robotics Research 18*, 9 (sep 1999), 876–892.

[7] Featherstone, R. A Divide-and Conquer Articulated-Body Algorithm for Parallel O(log(n)) Calculation of Rigid-Body Dynamics. Part 2: Part 2: Trees, Loops, and Accuracy. *International Journal of Robotics Research 18*, 9 (sep 1999), 876–892.

[8] Hughes, T. J. R. *The Finite Element Method: Linear Static and Dynamic Finite Element Analysis*, vol. 65 of *Dover Civil and Mechanical Engineering Series*. Dover Publications, Mineola, NY, 2000.

[9] Jourdain, P. E. B. Note on an analogue of Gauss principle of least constraint. *Quarterly Journal of Pure Applied Mathmatics 40*, 1909 (1909), 153–157.

[10] Kane, T. R., and Levinson, D. a. *Dynamics Theory and Applications*. McGraw-Hill, New York, NY, 2005.

[11] Khan, I. M., Ahn, W., Anderson, K. S., and De, S. A logarithmic complexity floating frame of reference formulation with interpolating splines for articulated multi-flexible-body dynamics. *International Journal of Non-Linear Mechanics 57* (dec 2013), 146–153.

[12] Laflin, J. J., Anderson, K. S., Khan, I. M., and Poursina, M. New and Extended Applications of the Divide-and-Conquer Algorithm for Multibody Dynamics. *Journal of Computational and Nonlinear Dynamics 9*, 4 (jul 2014), 41004.

[13] Malczyk, P., Fraczek, J. C., and Cuadrado, J. Parallel index-3 formulation for real-time multibody dynamics simulations. In *... Conference on Multibody System Dynamics, ...* (Lappeenranta, Finland, 2010).

[14] Malczyk, P., and Fraqczek, J. A divide and conquer algorithm for constrained multibody system dynamics based on augmented Lagrangian method with projections-based error correction. *Nonlinear Dynamics 70*, 1 (oct 2012), 871–889.

[15] Morin, S., and Redon, S. A force-feedback algorithm for adaptive articulated-body dynamics simulation. In *Proceedings - IEEE International Conference on Robotics and Automation* (Roma, Italy, apr 2007), IEEE, pp. 3245–3250.

[16] Mukherjee, R. M., and Anderson, K. S. An Orthogonal Complement-Based Divide-and-Conquer Algorithm for Constrained Multibody Systems. *Nonlinear Dynamics 48*, 1-2 (nov 2006), 199–215.

[17] Mukherjee, R. M., and Anderson, K. S. A Logarithmic Complexity Divide-and-Conquer Algorithm for Multi-flexible Articulated Body Dynamics. *Journal of Computational and Nonlinear Dynamics 2*, 1 (2007), 10–21.

[18] Mukherjee, R. M., Bhalerao, K. D., and Anderson, K. S. A divide-and-conquer direct differentiation approach for multibody system sensitivity analysis. *Structural and Multidisciplinary Optimization 35*, 5 (may 2008), 413–429.

[19] Poursina, M., and Anderson, K. S. An extended divide-and-conquer algorithm for a generalized class of multibody constraints. *Multibody System Dynamics 29*, 3 (mar 2013), 235–254.

[20] Poursina, M., and Anderson, K. S. Canonical ensemble simulation of biopolymers using a coarse-grained articulated generalized divide-And-conquer scheme. *Computer Physics Communications 184*, 3 (mar 2013), 652–660.

[21] Poursina, M., Bhalerao, K. D., Flores, S. C., Anderson, K. S., and Laederach, A. Strategies for articulated multibody-based adaptive coarse grain simulation of RNA. In *Methods in Enzymology*, M. L. Johnson and L. Brand, Eds., vol. 487 of *Methods in Enzymology*. Academic Press, Cambridge, MA, jan 2011, pp. 73–98.

[22] Praprotnik, M., Delle Site, L., and Kremer, K. Adaptive resolution molecular-dynamics simulation: Changing the degrees of freedom on the fly. *Journal of Chemical Physics 123*, 22 (feb 2005).

[23] Redon, S., Galoppo, N., and Lin, M. C. Adaptive dynamics of articulated bodies. *ACM Transactions on Graphics 24*, 212 (jul 2005), 936.

[24] Roberson, R. E., Roberson, R. E., Schwertassek, R., and Schwertassek, R. *Dynamics of Multibody Systems*. Springer - Verlag, Berlin, Heidelberg, 1988.

[25] Rossi, R., Isorce, M., Morin, S., Flocard, J., Arumugam, K., Crouzy, S., Vivaudou, M., and Redon, S. Adaptive torsion-angle quasi-statics: A general simulation method with applications to protein structure analysis and design. *Bioinformatics 23*, 13 (jul 2007), i408–i417.

[26] Schiehlen, W. O., and Kreuzer, E. J. Symbolic Computerized Derivation of Equations of Motion. In *Dynamics of Multibody Systems SE - 24*, K. Magnus, Ed., International Union of Theoretical and Applied Mechanics. Springer Berlin Heidelberg, Berlin, Heidelberg, 1978, pp. 290–305.

[27] Simo, J. C. A finite strain beam formulation. The three-dimensional dynamic problem. Part I. *Computer Methods in Applied Mechanics and Engineering 49*, 1 (may 1985), 55–70.

[28] Simo, J. C., and Vu-Quoc, L. A three-dimensional finite-strain rod model. part II: Computational aspects. *Computer Methods in Applied Mechanics and Engineering 58*, 1 (oct 1986), 79–116.

[29] Simo, J. C., and Vu-Quoc, L. A Geometrically-exact rod model incorporating shear and torsion-warping deformation. *International Journal of Solids and Structures 27*, 3 (jan 1991), 371–393.

Jeremy Laflin, Ph.D.: Lecturer Department of Mechanical, Aerospace, and Nuclear Engineering, Rensselaer Polytechnic Institute, 110 8th Street, Troy NY 12180 (*laflij2@rpi.edu*).

Kurt S. Anderson, Ph.D.: Professor Department of Mechanical, Aerospace, and Nuclear Engineering, Rensselaer Polytechnic Institute, 110 8th Street, Troy NY 12180 (*anderk5@rpi.edu*).
The author gave a presentation of this paper during one of the conference sessions.

Passive control of a linear structure via nonlinear oscillators in series

Claude-Henri Lamarque, Alireza Ture Savadkoohi, Simon Charlemagne

Abstract: A multi-degree-of-freedom system consisting of a linear main structure coupled to a chain of light nonlinear oscillators is investigated. We aim to develop tools to study mitigation of the vibratory energy of the main system, which is subjected to narrow-band harmonic solicitation, thanks to the nonlinear chain. A continuum approximation for the chain combined with a multiple time scales method is used to apprehend the complex dynamics of the overall system. At fast time scale, the discrete system of equations is transformed into a partial differential equation in time and space with boundary conditions. Fixed points solutions of this equation define the Slow Invariant Manifold (SIM), which gathers all possible asymptotic behaviors of the system. At slow time scale, equilibrium and singular points are detected around the SIM. The former describe periodic regimes and the latter are hints of strongly modulated responses, during which the system faces singularities and repeated bifurcations. Finally, these predictions are confronted with numerical simulations in order to validate this analytical approach. A good agreement is found.

1. Introduction

The use of additional nonlinear devices has shown its efficiency in terms of passive control of primary structures [8]. Indeed, essential nonlinearity enable secondary systems like Nonlinear Energy Sinks [2–4] to enter in resonance with any frequency, allowing a broadband control. Some works have also considered three degree-of-freedom (dof) vibration absorbers, showing their capacity to perform a multi-modal control of impulse-loaded systems [7, 10, 11].

In this paper, we aim to detail an analytical methodology for studying nonlinear chains of light oscillators coupled to a primary structure under harmonic excitation, in which the chain is to be examined with a continuous approximation. The paper is organized as follows: studied model along with analytical tools used to treat system equations are presented in Sect. 2. Multi-time scales behaviors of the system are then investigated in Sect. 3 while Sect. 4 confronts analytical predictions with numerical results. Conclusions are given in Sect. 5.

2. Presentation of the model

The system considered is described in Fig. 1. It consists of a linear oscillator (LO) with the mass M, stiffness K and damping C, subjected to external solicitation $F(t)$. A chain of nonlinear oscillators of equal mass for each particle as $m = \epsilon M$ is coupled to the LO. Linear connection in the chain is performed through springs of stiffness $\tilde{B}$ and viscous damping Γ while local nonlinearities $\tilde{V}$ are present.

We rescale the parameters as follows: $\frac{K}{M} = \omega_0^2$, $\frac{\tilde{B}}{M} = \epsilon B$, $\frac{\tilde{V}(z)}{M} = \epsilon D z^3$, $\frac{C}{M} = \epsilon c$, $\frac{\Gamma}{M} = \epsilon\gamma$,

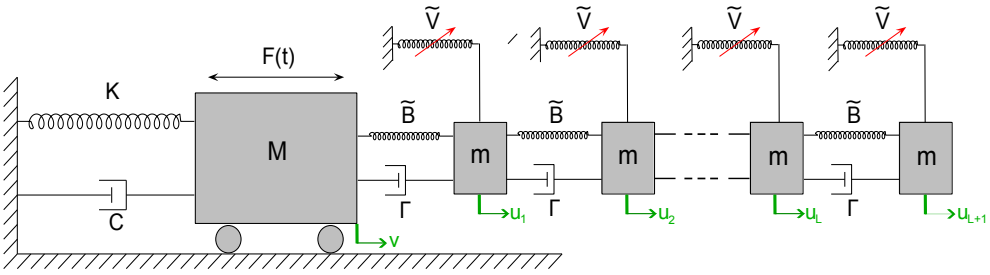

Figure 1. $(L+2)$ dof system consisting of a forced linear structure coupled to $(L+1)$ light nonlinear oscillators $(m = \epsilon M,\ 0 < \epsilon \ll 1)$.

$\frac{F(t)}{M} = \epsilon f \sin(\omega t)$ and $\omega^2 = \omega_0^2(1 + \sigma\epsilon)$. Hence, governing equations read:

$$\begin{cases} \ddot{v} + \epsilon c\dot{v} + \omega_0^2 v + \epsilon\gamma(\dot{v} - \dot{u}_1) + \epsilon B(v - u_1) = \epsilon f \sin(\omega t) \\ \ddot{u}_1 + \gamma(-\dot{v} + 2\dot{u}_1 - \dot{u}_2) + B(-v + 2u_1 - u_2) + Du_1^3 = 0 \\ \qquad\qquad \vdots \\ \ddot{u}_j + \gamma(-\dot{u}_{j-1} + 2\dot{u}_j - \dot{u}_{j+1}) + B(-u_{j-1} + 2u_j - u_{j+1}) + Du_j^3 = 0\ , \quad j = 2, \ldots, L \\ \qquad\qquad \vdots \\ \ddot{u}_{L+1} + \gamma(\dot{u}_{L+1} - \dot{u}_L) + B(u_{L+1} - u_L) + Du_{L+1}^3 = 0 \end{cases} \tag{1}$$

where v and u_j, $j \in [|0, L+1|]$, stand for the displacements of the LO and the oscillators of the chain, respectively.

While the chain is long enough, i.e. $L \gg 1$, we can consider the chain as a continuum medium and replace the discrete variables u_j by a continuous function of a space variable x measured in number of oscillators:

$$\begin{aligned} &u_j(t) = u(x = j - 1, t), \qquad j = 1, \ldots, L+1 \\ &x \in [0, L] \end{aligned} \tag{2}$$

L describes now the length of the chain. Introduction of this space variable enables to make Taylor expansions as follows:

$$u_{j\pm1} \approx u(j,t) \pm \frac{\partial u}{\partial x}(j,t) + \frac{1}{2!}\frac{\partial^2 u}{\partial x^2}(j,t) + \ldots \pm \frac{1}{n!}\frac{\partial^n u}{\partial x^n}(j,t) \tag{3}$$

Complex variables of Manevitch [5] are introduced ($i = \sqrt{-1}$):

$$\begin{cases} \psi(t)e^{i\omega t} = \dfrac{\partial v(t)}{\partial t} + i\omega v(t) \\ \\ \varphi(x,t)e^{i\omega t} = \dfrac{\partial u(x,t)}{\partial t} + i\omega u(x,t) \end{cases} \tag{4}$$

The mass ratio ϵ is used to derive a multiple time scale method introducing fast ($\tau_0 = t$) and slow ($\tau_k = \epsilon^k t \quad k = 1, 2, \ldots$) time scales [6].
Finally, we use a Galerkin technique via keeping only the first harmonic, by imposing:

$$S = \frac{\omega}{2\pi}\int_0^{\frac{2\pi}{\omega}} s(\tau_1, \tau_2, \ldots)e^{-i\omega\tau_0}d\tau_0 \tag{5}$$

In further developments, ψ and φ are assumed to be independent of τ_0. This will be either confirmed during the multiple scale developments or assumed through consideration of an asymptotic state when $\tau_0 \to \infty$.

3. Multiple time scale behaviors

3.1. Fast time scale τ_0

To investigate the system behavior at fast time scale, we derive system equations at the order ϵ^0. The first equation relative to the LO gives $\dfrac{\partial \psi}{\partial \tau_0} = 0$. Thus, ψ does not depend on the fast time scale. Searching for fixed points of the remaining equations, i.e. ϕ such as $\lim\limits_{\tau_0 \to +\infty} \dfrac{\partial \phi(x)}{\partial \tau_0} = 0$, we obtain (dependence on time is omitted):

$$\begin{cases} \dfrac{i\omega_0}{2}\phi(0) + \dfrac{1}{2}\left(\gamma - \dfrac{iB}{\omega_0}\right)\left(-\psi + \phi(0) - \dfrac{\partial \phi}{\partial x}(0)\right) - i\mathcal{D}|\phi(0)|^2\phi(0) = 0 \\ \\ \dfrac{i\omega_0}{2}\phi(x) - \dfrac{1}{2}\left(\gamma - \dfrac{iB}{\omega_0}\right)\dfrac{\partial^2 \phi}{\partial x^2}(x) - i\mathcal{D}|\phi(x)|^2\phi(x) = 0 \qquad x \in]0, L[\\ \\ \dfrac{i\omega_0}{2}\phi(L) + \dfrac{1}{2}\left(\gamma - \dfrac{iB}{\omega_0}\right)\dfrac{\partial \phi}{\partial x}(L) - i\mathcal{D}|\phi(L)|^2\phi(L) = 0 \end{cases} \tag{6}$$

where $\mathcal{D} = \dfrac{3D}{8\omega_0^3}$. This defines the Slow Invariant Manifold (SIM) which shelters all asymptotic behaviors of the system. It takes the form of a boundary value problem where the first

and third equations are the left and right boundary conditions of the chain. System (6) is now to be solved by searching solutions of the form $\psi = N_1 e^{i\delta_1}$ and $\phi(x) = N(x)e^{i\delta(x)}$. Let us point out that, although $N(x)$ should be a real positive function, calculations can lead to negative solutions. Hence, absolute value of the obtained expression of $N(x)$ has to be considered, which forces us to add π to the phase $\delta(x)$ at points where $N(x)$ is negative.
Setting $\gamma = 0$ or, equivalently, considering that the damping is of order ϵ^2, the ordinary differential equation can be split in real and imaginary parts and integrated into the following system:

$$\begin{cases} \left(\dfrac{\partial N}{\partial x}(x)\right)^2 = -\dfrac{\Theta}{N(x)^2} - \dfrac{\omega_0^2}{B}N(x)^2 + \dfrac{\mathcal{D}\omega_0}{B}N(x)^4 + C_1 \\ \\ \dfrac{\partial \delta}{\partial x}(x) = \dfrac{\Theta}{N(x)^2} \end{cases} \tag{7}$$

where C_1 and Θ are constants of integration. The second equation of Eq. (7) shows that δ should face a sudden jump each time N changes its sign, which is consistent with the previous remark. Injecting Eq. (7) into the right boundary condition, one is first able to derive a polynomial expression in $N(L)$ that can be solved into closed-form expressions of $N(L)$ as function of C_1. Moreover, we obtain that $\Theta = 0$. Therefore, $\delta(x)$ is piece-wise constant.
First equation of Eq. (7) can now be rewritten:

$$dx = \pm \frac{dN}{\sqrt{-\dfrac{\omega_0^2}{B}N^2 + \dfrac{\mathcal{D}\omega_0}{B}N^4 + C_1}} \tag{8}$$

For given values of C_1 and $N(x)$, Eq. (8) can be integrated analytically (for other cases, numerical integration is required):

$$\begin{aligned} &N(x) = \sqrt{X_1}\,\mathrm{sn}\left(\sqrt{\frac{C_1}{X_1}}(x - C_2), \frac{X_1}{X_2}\right) \\ &\text{with } C_2 = L - \sqrt{\frac{X_1}{C_1}}\,\mathrm{F}\left(\arcsin\left(\frac{N(L)}{\sqrt{X_1}}\right), \frac{X_1}{X_2}\right) \end{aligned} \tag{9}$$

where $\mathrm{sn}(X, k^2)$ is a Jacobian elliptic function and $\mathrm{F}(X, k^2)$ is the incomplete elliptic integral of the first kind. It should be reminded that $N(L)$ is determined through the right boundary condition. We are now able to inject this expression of $N(x)$ into the left boundary condition to determine ψ. This procedure enables to plot a projection of the SIM in the $N_1 - N(L)$ plane as shown in Fig. 2 where the solid line denotes branches obtained from analytical integration of Eq. (8) and the dashed line branches obtained from numerical integration.

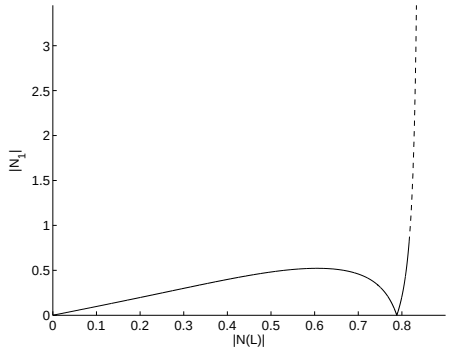

Figure 2. $L = 35$, $\omega_0 = 1$, $B = 120$ and $D = 2$ - Example of SIM: solid line denotes branches obtained from analytical integration of Eq. (8) and the dashed line branches obtained from numerical integration

3.2. Slow time scale τ_1

In this section, equilibrium and singular points are detected around the SIM. They predict periodic regimes and Strongly Modulated Responses [9], respectively.

The equation relative to the LO around the SIM derived at the ϵ^1 order reads:

$$\frac{\partial \psi}{\partial \tau_1} + \frac{1}{2}\left(c\psi + i\sigma\omega_0 - \frac{iB}{\omega_0}\right)\psi + \frac{iB}{\omega_0}\phi(0) = \frac{f}{2i} \tag{10}$$

Left boundary condition of the SIM gives:

$$\begin{aligned} &\psi = F_l(N_0)e^{i\delta_0} \\ &F_l(N_0) = -N_x(0) + \left(1 - \frac{\omega_0^2}{B} + 2\tilde{\mathcal{D}}N_0^2\right)N_0 \end{aligned} \tag{11}$$

Injecting Eq. (11) into Eq. (10), we obtain:

$$\begin{cases} \dfrac{\partial N_0}{\partial \tau_1} = \dfrac{f_1(N_0, \delta_0)}{g(N_0)} \\ \dfrac{\partial \delta_0}{\partial \tau_1} = \dfrac{f_2(N_0, \delta_0)}{g(N_0)} \end{cases} \tag{12}$$

where

$$\begin{cases} f_1(N_0, \delta_0) = -\dfrac{F_l(N_0)}{2}\left[cF_l(N_0) + f\sin(\delta_0)\right] \\ f_2(N_0, \delta_0) = \dfrac{1}{2}\dfrac{\partial F_l(N_0)}{\partial N_0}\left[\left(\dfrac{B}{\omega_0} - \sigma\omega_0\right)F_l(N_0) - \dfrac{B}{\omega_0}N_0 - f\cos(\delta_0)\right] \\ g(N_0) = F_l(N_0)\dfrac{\partial F_l(N_0)}{\partial N_0} \end{cases} \tag{13}$$

Equilibrium points verify $f_1 = f_2 = 0$ and $g \neq 0$ while singular points verify $f_1 = f_2 = g = 0$.

4. Numerical results

Analytical predictions obtained from the method described in Sects. 2 and 3 are compared in this section to numerical results. A Runge-Kutta scheme (*ode45* function of Matlab) is used to solve system (1), with following options: time step is 0.1 and relative and absolute error tolerance set to 10^{-12}. We will suppose that all oscillators are at rest initially. Moreover, in order to compare analytical and numerical results, we compute the discrete numerical equivalent of $\varphi(x,t)$ as follows:

$$\varphi_{j+1}(t) = (\dot{u}_j(t) + i\omega u_j(t))\, e^{-i\omega t} = N_{j+1}(t) e^{i\delta_{j+1}(t)} \quad j = 0, \ldots, L+1 \tag{14}$$

As a first example, let us consider the system described by $L = 45$, $\epsilon = 0.001$, $\omega_0 = 1$, $B = 200$, $D = 2$, $c = 0.5$, $f = 0.4$ and $\sigma = 0$. In numerical simulations, damping has been set to $\gamma = 2$. The system has one stable equilibrium point and one singular point (see Fig. 3). As a consequence, its behavior should be quickly attracted by the SIM and stabilize around the equilibrium point or face SMR. Figs. 4(a)-(b) show that the system reaches a periodic regime. However, despite a good qualitative agreement between analytical predictions and numerical results, Figs. 4(b)-(c) exhibit a quantitative difference, which is due to the continuous approximation. Indeed, predictions made by an analytical discrete approach using the exact same hypotheses [1] fit numerical simulations (see Fig. 4(c)).

In the second example, we use following new parameters: $L = 35$, $\epsilon = 0.001$, $\omega_0 = 1$,

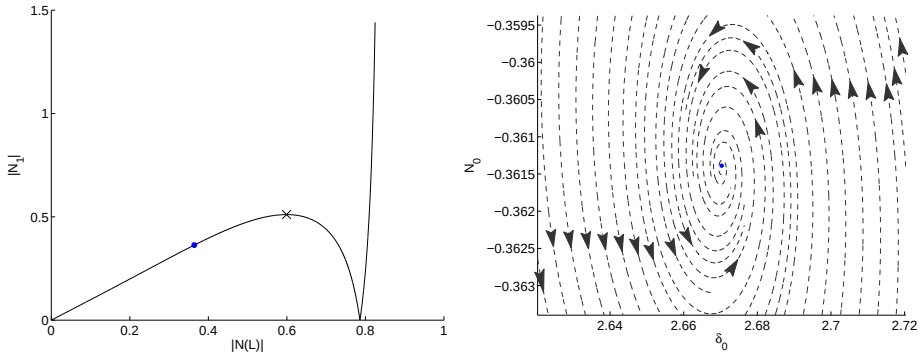

(a) (b)

Figure 3. $L = 45$, $\epsilon = 0.001$, $\omega_0 = 1$, $B = 200$, $D = 2$, $c = 0.5$, $f = 0.4$ and $\sigma = 0$ - (a) SIM of the system (black line) with equilibrium and singular points (blue point and black cross, respectively) (b) Phase portrait around the equilibrium point.

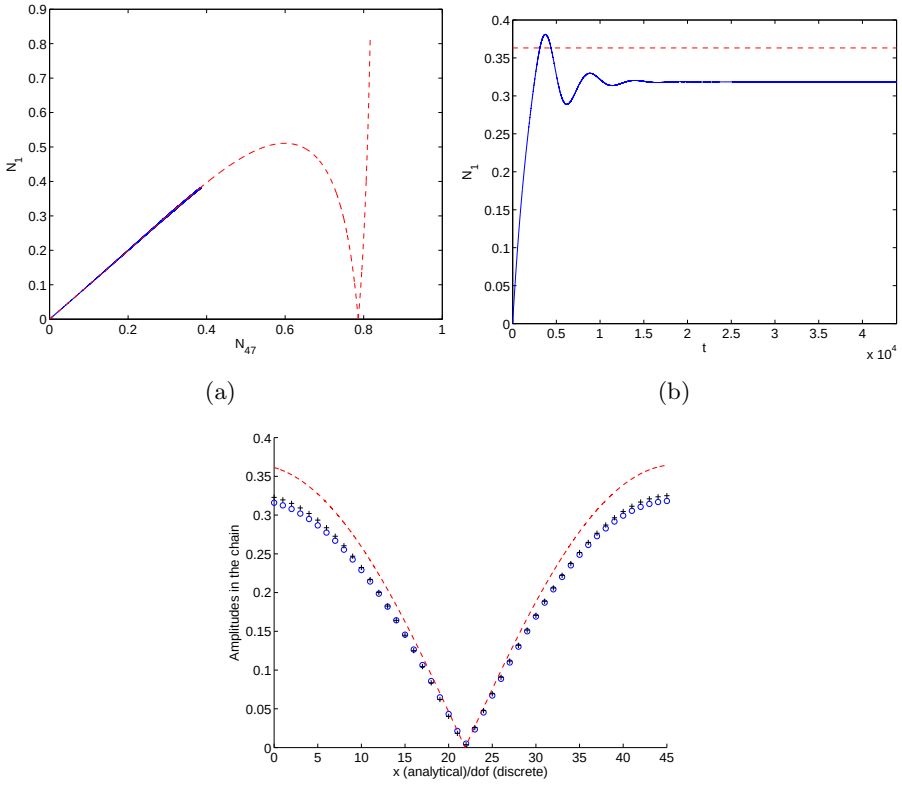

Figure 4. $L = 45$, $\epsilon = 0.001$, $\omega_0 = 1$, $B = 200$, $D = 2$, $c = 0.5$, $f = 0.4$ and $\sigma = 0$ - (a) SIM of the system (dashed red line) with corresponding numerical results (blue line) (b) N_1 versus time obtained from numerical results (blue line) and amplitude predicted on the equilibrium point (red dotted line) (c) Comparison of amplitudes predicted by analytical results on the equilibrium point from continuous (red dotted line) and discrete approach (black crosses) and numerical results during the steady-state regime (blue circles).

$B = 120$, $D = 2$, $c = 0.5$, $f = 3.5$ and $\sigma = 7$. Damping has been set to $\gamma = 10$. As shown in Fig. 5, the system has three equilibrium points. Points no. 1 and 2 are unstable while point no. 3 is stable (see phase portraits in Figs. 5(b)-(d)). Figure 6 shows that the system faces SMR, making repeated cycles around the SIM and showing properties of intense energy exchange between the LO and the chain.

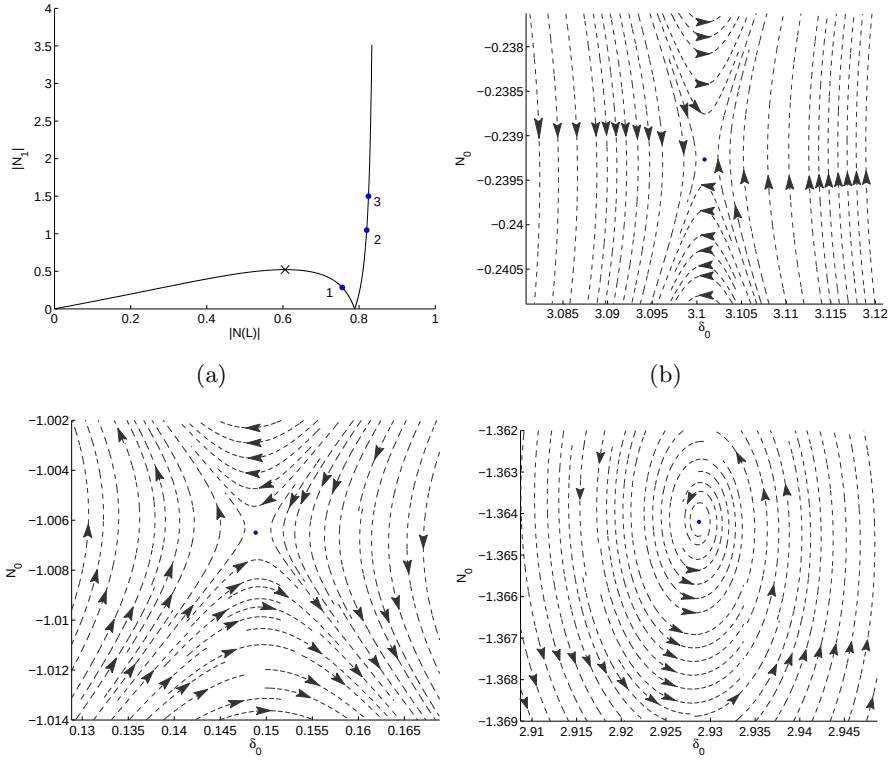

Figure 5. $L = 35$, $\epsilon = 0.001$, $\omega_0 = 1$, $B = 120$, $D = 2$, $c = 0.5$, $f = 3.5$ and $\sigma = 7$ - (a) SIM of the system (black line) with equilibrium and singular points (blue points and black cross, respectively) (b)-(d) Phase portraits around equilibrium points no. 1, 2 and 3, respectively.

5. Conclusions

A system consisting of a linear system coupled to a chain of oscillators with on-site nonlinear potentials is studied. A continuous approximation is used to describe the dynamics of the chain. At fast time scale, the slow invariant manifold of the system, taking the form of a boundary value problem, is computed. Equilibrium and singular points are detected around this manifold at slow time scale. They predict periodic regimes and strongly modulated responses of the system, respectively. A good accordance between numerical simulations and analytical results is found. Thus, the method described in this work appears as a strong tool to design nonlinear chains for purposes of passive control.

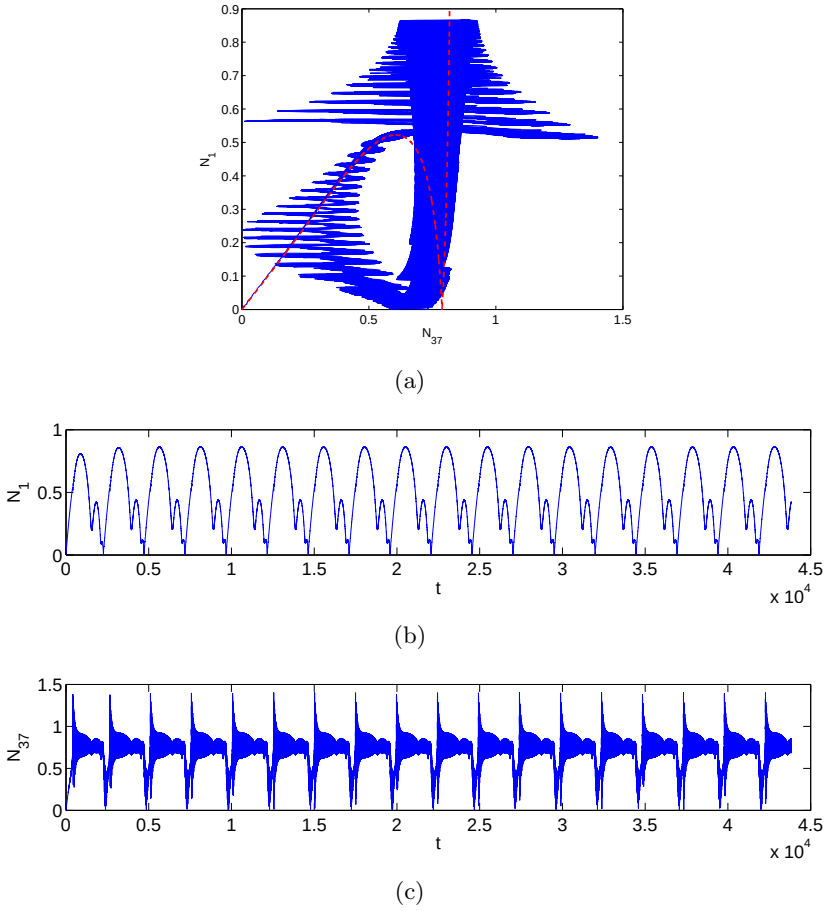

Figure 6. $L = 35$, $\epsilon = 0.001$, $\omega_0 = 1$, $B = 120$, $D = 2$, $c = 0.5$, $f = 3.5$ and $\sigma = 7$ - (a) SIM of the system (dashed red line) with corresponding numerical results (blue line) (b) N_1 versus time obtained from numerical results (c) N_{37} versus time obtained from numerical results.

Acknowledgments

The authors would like to thank following organizations for supporting this research: i) The "Ministère de la Transition Écologique et Solidaire" ii) LABEX CELYA (ANR-10-LABX-0060) of the "Université de Lyon" within the program "Investissement d'Avenir" (ANR-11-IDEX-0007) operated by the French National Research Agency (ANR).

References

[1] Charlemagne, S., Lamarque, C.-H., and Ture Savadkoohi, A. Vibratory control of a linear system by addition of a chain of nonlinear oscillators. *Acta Mechanica 228*, 9 (2017), 3111–3133.

[2] Gendelman, O. V. Targeted energy transfer in systems with external and self-excitation. *Proceedings of the Institution of Mechanical Engineers, Part C: Journal of Mechanical Engineering Science 225*, 9 (2011), 2007–2043.

[3] Gendelman, O. V., and Alloni, A. Dynamics of forced system with vibro-impact energy sink. *Journal of Sound and Vibration 358* (2015), 301–314.

[4] Luongo, A., and Zulli, D. Aeroelastic instability analysis of nes-controlled systems via a mixed multiple scale/harmonic balance method. *Journal of Vibration and Control 20* (2014), 1985–1998.

[5] Manevitch, L. I. The description of localized normal modes in a chain of nonlinear coupled oscillators using complex variables. *Nonlinear Dynamics 25* (2001), 95–109.

[6] Nayfeh, A., and Mook, D. *Nonlinear Oscillations*. John Wiley and Sons, 1979.

[7] Panagopoulos, P. N., Vakakis, A. F., and Tsakirtzis, S. Transient resonant interactions of finite linear chains with essentially nonlinear end attachments leading to passive energy pumping. *International Journal of Solids and Structures 41*, 2223 (2004), 6505 – 6528.

[8] Roberson, R. E. Synthesis of a nonlinear dynamic vibration absorber. *Journal of the Franklin Institute 254*, 3 (1952), 205 – 220.

[9] Starosvetsky, Y., and Gendelman, O. V. Strongly modulated response in forced 2dof oscillatory system with essential mass and potential asymmetry. *Physica D 237* (2008), 1719–1733.

[10] Tsakirtzis, S., Kerschen, G., Panagopoulos, P. N., and Vakakis, A. F. Multi-frequency nonlinear energy transfer from linear oscillators to mdof essentially nonlinear attachments. *Journal of Sound and Vibration 285*, 12 (2005), 483 – 490.

[11] Tsakirtzis, S., Panagopoulos, P. N., Kerschen, G., Gendelman, O., Vakakis, A. F., and Bergman, L. A. Complex dynamics and targeted energy transfer in linear oscillators coupled to multi-degree-of-freedom essentially nonlinear attachments. *Nonlinear Dynamics 48*, 3 (2007), 285–318.

Claude-Henri Lamarque, Pr.: University of Lyon, École Nationale des Travaux Publics de l'État, LTDS (UMR CNRS 5513), Rue Maurice Audin 69518, Vaulx-en-Velin Cedex (*claude.lamarque@entpe.fr*). The author gave a presentation of this paper during one of the conference sessions.

Alireza Ture Savadkoohi, Ph.D.: University of Lyon, École Nationale des Travaux Publics de l'État, LTDS (UMR CNRS 5513), Rue Maurice Audin 69518, Vaulx-en-Velin Cedex (*alireza.turesavadkoohi@entpe.fr*).

Simon Charlemagne, M.Sc. (Ph.D. student): University of Lyon, École Nationale des Travaux Publics de l'État, LTDS (UMR CNRS 5513), Rue Maurice Audin 69518, Vaulx-en-Velin Cedex (*simon.charlemagne@entpe.fr*).

The influence of anti-roll bar in the dynamics of a full-car control

Wagner Barth Lenz, Angelo Marcelo Tusset, Rodrigo Tumolin Rocha, Frederic Conrad Janzen, Adriano Kossoski, Jose Manoel Balthazar, Airton Nabarrete

Abstract: This paper presents the control strategy of a nonlinear full-car model using magnetorheological (MR) damper. The control strategy is used in two-step design. First, the LQR control is design and formulated in order to control the nonlinear suspension. The nonlinear suspension is composed by the anti-roll bar, nonlinear springs and dampers. The second one is defined by Lugre model which calculates the value of the voltage to have the same force as the control requested. To study the impact of the anti-roll bar, numerical simulations were carried out with and without the anti-roll bar. The results showed that the efficiency of the control did not decreased by the addition of the anti-roll bar, however the control need less interaction with the suspension, then less power was used to control the motion.

1. Introduction

Nowadays, the improvement of ride quality and comfort of passengers in a car have been strongly studied due to vibrations of a vehicle body may harm the passengers due to high amplitude and frequency induced into passengers' body. Therefore, such vibrations should be reduced.

In recent years, many researchers have kept their attention to design control techniques of vehicle suspension systems aiming to reduce the vibrations [1-3]. There are three types of vibration control methods proposed and implemented successfully in the literature, which are passive, active and semi-active control methods aiming to control suspension systems [4]. However, the most common mathematical models that represent such vehicle systems are usually based on models that do not consider the anti-roll bar related to the vehicle vertical dynamics. On the other hand, the main studies of these anti-roll bars are linked to fatigue and vehicle dynamics in curves.

The anti-roll bar was introduced to reduce the motion on bending. Such motion is not particularly problematic, however in sinuous road and in constant excitation the roll moment can make the vehicle overturn. In addition, in big trucks and vehicles with elevate CM (center of mass), this kind of motion can be more problematic. Introducing the anti-roll bar to the dynamics of a car soften the springs, with that, the load can be shared with the bar. Consequently, the ride comfort is improved due to the impact on the lower sprung mass.

Therefore, this work proposes the analysis of the introduction of an anti-roll bar in a full-car model with nonlinear suspension and with a semi-active control by a MR damper which will be controlled by a signal obtained by the LQR control. The analysis of the influence of the addition of the anti-roll bar, the torsional rigidity and semi-active control in the vehicle dynamics is carried out with the goal to increase comfort and safety of passengers.

MR dampers are widely used in the modern industry and are capable to generate a force enough for a fast response in many applications [5,6]. The magnetic properties allow its use as a damper controlled by an electric current [7]. Moreover, these devices offer highly reliable operations and their performance is relatively insensible to temperature fluctuations or impurities in the fluid [8].

The MR damper can be used in the suppression of undesired oscillations, which can be controlled through the electrical current or voltage, which changes the viscosity of the fluid's internal damper. The damping force will depend on the speed of the piston of the damper and the density of internal fluid.

The feedback of state variables can provide information about the behavior of the controlled system over time by means of sensors, and the optimal intensity of force being applied by the MR damper. In this work, a mathematical model proposed by [9] to transform the values of control force into electric current signal will be considered.

2. Mathematical Model

In this section, a full-car model will be discussed and the modelling of its equations of motion will be developed considering the anti-roll bar to transfer energy between the roll and wheels.

The nonlinear full-car model, illustrated in Fig. 1, is of a seven-degrees-of-freedom rigid body with mass m. The heave, pitch and roll motions of the sprung mass are considered. The four unsprung masses (front-left, front-right, rear-left and rear-right) are connected to each corner of the rigid body and by an anti-roll bar, whose bar is modelled as a torsional spring. The suspensions between the sprung mass and unsprung masses are modelled as nonlinear springs and nonlinear dampers elements, while the tires are modelled as linear springs.

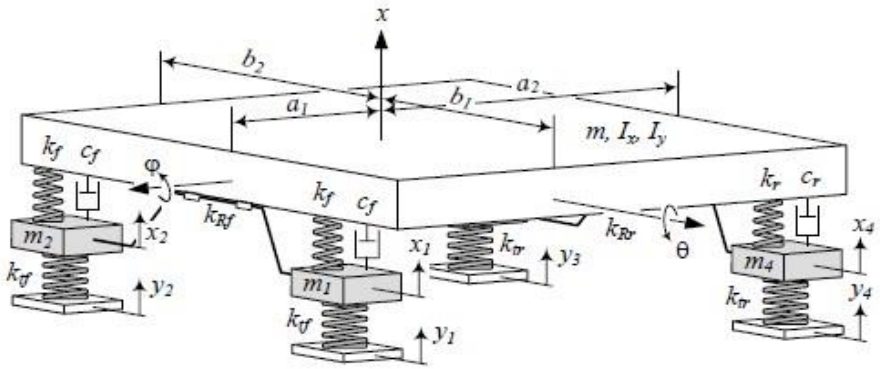

Figure 1. Nonlinear full-car model considering an anti-roll bar and MR dampers

The road, in generic terms

$$X_{road} = amp * sing(\sin(2\pi ft)) \quad (1)$$

For each road if time is less than 10 seconds

$$X_{fr} = amp * sing(\sin(2\pi ft)) \quad (2)$$

$$X_{fl} = amp * sing(\sin(2\pi ft + \beta)) \quad (3)$$

$$X_{rr} = amp * sing(\sin(2\pi ft + \alpha)) \quad (4)$$

$$X_{rl} = amp * sing(\sin(2\pi ft + \beta + \alpha)) \quad (5)$$

The tire was modelled as a linear spring:

$$F_{tire} = K_{pn}(X_{UN} - X_{road}) \quad (6)$$

where, X_{un} is the mass of the unsprung mass and X_{road} is the matching road profile. The spring of the suspension was modelled as [10]:

$$F_{sfl} = K_{fl}(\Delta X_{fl}) + K_{fnl}(\Delta X_{fl})^3 \quad (7)$$

$$F_{sfr} = K_{fr}(\Delta X_{fr}) + K_{fnl}(\Delta X_{fr})^3 \quad (8)$$

$$F_{srl} = K_{rl}(\Delta X_{rl}) + K_{rnl}(\Delta X_{rl})^3 \quad (9)$$

$$F_{srr} = K_{rr}(\Delta X_{rr}) + K_{rnl}(\Delta X_{rr})^3 \quad (10)$$

The damper was modelled according to the following equations [10]:

$$F_{dfl} = c_1(\Delta\dot{X}_{fl}) - c_2|\Delta\dot{X}_{fl}| + c_3 * sign(\Delta\dot{X}_{fl})\sqrt[2]{|\Delta\dot{X}_{fl}|} \quad (11)$$

$$F_{dfr} = c_1(\Delta\dot{X}_{fr}) - c_2|\Delta\dot{X}_{fr}| + c_3 * sign(\Delta\dot{X}_{fr})\sqrt[2]{|\Delta\dot{X}_{fr}|} \quad (12)$$

$$F_{drl} = c_1(\Delta\dot{X}_{rl}) - c_2|\Delta\dot{X}_{rl}| + c_3 * sign(\Delta\dot{X}_{rl})\sqrt[2]{|\Delta\dot{X}_{rl}|} \quad (13)$$

$$F_{drr} = c_1(\Delta\dot{X}_{rr}) - c_2|\Delta\dot{X}_{rr}| + c_3 * sign(\Delta\dot{X}_{rr})\sqrt[2]{|\Delta\dot{X}_{rr}|} \quad (14)$$

where the relative speeds and relative displacements can be calculated by using the following equations, where roll α, pitch β.

$$\Delta X_{fl} = \frac{s}{2}\sin(X_\propto) - a\sin(X_\beta) + X_{cg} - X_{fl} \quad (15)$$

$$\Delta X_{fr} = -\frac{s}{2}\sin(X_\propto) - a\sin(X_\beta) + X_{cg} - X_{fr} \quad (16)$$

$$\Delta X_{rl} = \frac{s}{2}\sin(X_\propto) + b\sin(X_\beta) + X_{cg} - X_{rl} \quad (17)$$

$$\Delta X_{rr} = -\frac{s}{2}\sin(X_\propto) + b\sin(X_\beta) + X_{cg} - X_{rr} \quad (18)$$

$$\Delta\dot{X}_{fl} = \frac{s}{2}\dot{X}_\propto\cos(X_\propto) - \dot{X}_\beta a\cos(X_\beta) + \dot{X}_{cg} - \dot{X}_{fl} \quad (19)$$

$$\Delta\dot{X}_{fr} = -\frac{s}{2}\dot{X}_\propto\cos(X_\propto) - \dot{X}_\beta a\cos(X_\beta) + \dot{X}_{cg} - \dot{X}_{fr} \quad (20)$$

$$\Delta\dot{X}_{rl} = \frac{s}{2}\dot{X}_\propto\cos(X_\propto) + \dot{X}_\beta b\cos(X_\beta) + \dot{X}_{cg} - \dot{X}_{rl} \quad (21)$$

$$\Delta\dot{X}_{rr} = -\frac{s}{2}\dot{X}_\propto\cos(X_\propto) + \dot{X}_\beta b\cos(X_\beta) + \dot{X}_{cg} - \dot{X}_{rr} \quad (22)$$

The anti-roll bar is modelled as

$$M_{ar} = k_t(X_{cg} - \left(\frac{X_{fr}-X_{fl}}{s}\right)) \quad (23)$$

However, to better express the stiffness of the anti-roll bar, it will be compared to the stiffness of the spring, as denote by Eq. (26).

$$\sigma = \frac{k_t}{sK_{fl}} \quad (26)$$

In consequence, the anti-roll bar can be modelled as:

$$M_{ar} = \sigma sK_{fl}(X_{cg} - \left(\frac{X_{fr}-X_{fl}}{s}\right)) \quad (25)$$

Applying the newton's second law in all the bodies, the dynamics of the car can be described as:

$$m_{xg}\ddot{X}_{xg} = -(F_{dfl} + F_{dfr} + F_{drl} + F_{drr} + F_{sfl} + F_{sfr} + F_{srl} + F_{srr}) \quad (26)$$

$$I_{\propto}\ddot{X}_{\propto} = (\frac{scos(X_{\propto})}{2})(-F_{dfl} + F_{dfr} - F_{drl} + F_{drr} - F_{sfl} + F_{sfr} - F_{srl} + F_{srr}) + M_{ar} \quad (27)$$

$$I_{\beta}\ddot{X}_{\beta} = (\frac{acos(X_{\beta})}{2})\left(F_{dfl} + F_{dfr} + F_{sfl} + F_{sfr}\right) - (\frac{bcos(X_{\beta})}{2})(+F_{srl} + F_{srr} + F_{drl} + F_{drr}) \quad (28)$$

$$m_{fl}\ddot{X}_{fl} = +\left(F_{dfl} + F_{sfl} - F_{tfl}\right) + \frac{M_{ar}}{s} \quad (29)$$

$$m_{fr}\ddot{X}_{fr} = +\left(F_{dfr} + F_{sfr} - F_{tfr}\right) - \frac{M_{ar}}{s} \quad (30)$$

$$m_{rl}\ddot{X}_{rl} = +(F_{drl} + F_{srl} - F_{trl}) \quad (31)$$

$$m_{rr}\ddot{X}_{rr} = +(F_{drr} + F_{srr} - F_{trr}) \quad (32)$$

3. Numerical Simulations and Control Design

The numerical simulations were performed using the fourth order Runge-Kutta method considering the parameters of the following Tab. 1, that were adapted from [10-12].

Table 1. Parameters' value

Variable	Value	Variable	Value	Variable	Value
c_1	700	m_r	59kg	I_β	2160kgm^2
c_2	200	m_f	59kg	s	3m
c_3	400	$I_\propto$	460kgm^2	a	1.4m
amp	0.08m	sK_{fl}	245000N	b	1.7m
f	9.69Hz	m_s	1500kg	K_{fl}	23500
K_{pn}	190000N/m	K_{rl}	23800	K_{fnl}	2350000
$\propto$	180	K_{rnl}	2380000	β	180

For the controller, the whole dynamics was rewrite according with the following system

$$\dot{X} = Ax + A_{nl} + Bu \quad (33)$$

where *A* is the linear part of the car, A_{nl} is the nonlinear matrix, B is a matrix of the control force using MR dampers, and u is the conversion of the force required to the MR dampers to achieve such result at such instant. Matrix B is given by Eq. (34), and matrices *A* and A_{nl} will not be showed due to space.

$$B = \begin{bmatrix} 0 & 0 & 0 & 0 \\ -1/m_{cg} & -1/m_{cg} & -1/m_{cg} & -1/m_{cg} \\ 0 & 0 & 0 & 0 \\ -s\frac{cos(x_3)}{2I_\alpha} & s\frac{cos(x_3)}{2I_\alpha} & -s\frac{cos(x_3)}{2I_\alpha} & s\frac{cos(x_3)}{2I_\alpha} \\ 0 & 0 & 0 & 0 \\ a\frac{cos(x_5)}{I_\beta} & a\frac{cos(x_5)}{I_\beta} & -b\frac{cos(x_5)}{I_\beta} & -b\frac{cos(x_5)}{I_\beta} \\ 0 & 0 & 0 & 0 \\ \frac{1}{m_f} & 0 & 0 & 0 \\ 0 & 0 & 0 & 0 \\ 0 & \frac{1}{m_f} & 0 & 0 \\ 0 & 0 & 0 & 0 \\ 0 & 0 & \frac{1}{m_r} & 0 \\ 0 & 0 & 0 & 0 \\ 0 & 0 & 0 & \frac{1}{m_r} \end{bmatrix} \quad (34)$$

Due to dependency of the magnetization of the fluid, which is the damper nonlinearity that is temporal, and the speed. The predicted force can be determined by

$$F_{predicted} = -KX \quad (35)$$

The damping force control can be obtained through the LQR control, given by:

$$\mathrm{u} = -R^{-1}B^{T}PX \quad (36)$$

where Q and R are positive definite matrices, the matrix P is obtained solving the Riccati equation given by:

$$\mathrm{PA} + A^{T}P - PBR^{-1}B^{T}P + Q = 0 \quad (37)$$

so that the feedback of the force output (36) is able to minimize the performance index J as following:

$$J = \frac{1}{2}\int_{t_0}^{\infty}(X^{T}QX + u^{T}Qu)\,dt \quad (38)$$

Therefore, the minimization of the functional (38) implies the minimization of the states X, and the force (u) applied by the MR damper. The control signal u is determined using the matrices A and B, and the positives definite matrices Q and R are defined as follows: Q_{14X14} and R_{4X4}, diagonal matrices with ($q_{1,1} = 0.1$; $q_{2,2} = 10^8$; $q_{3,3} = 0.1$; $q_{4,4} = 10^8$; $q_{5,5} = 0.1$; $q_{6,6} = 0.1$; $q_{7,7} = 0.1$; $q_{8,8} = 0.1$; $q_{9,9} = 0.1$; $q_{10,10} = 0.1$; $q_{11,11} = 0.1$; $q_{12,12} = 0.1$; $q_{13,13} = 0.1$; $q_{14,14} = 0.1$), and ($r_{1,1} = 0.1$; $r_{2,2} = 0.1$; $r_{3,3} = 0.1$; $r_{4,4} = 0.1$).

Using the current status of the MR damper and setting the parameters for maximum speed velocity and voltage, it is possible to establish the desired next voltage to be applied by an interactive process.

Considering the predicted force on a regression model for the MR damper, it is possible to know the electric current needed to have the required force of the controller on each MR damper. This mechanism is needed because of the controller may demand a force that the damper cannot dissipate due to physical limitations, such as high speeds or force on the opposite direction of the MR damper so that it can provide resistance.

A nonlinear friction mechanism of the MR damper causes a hysteretic effect and many researches have been devoted to consider this nonlinear behavior in the mathematical model. An alternative is the LuGre friction model [13] which was originally developed to describe the nonlinear friction phenomena [14].

The friction mechanism is a phenomenon in which two surfaces make contact at a number of asperities at microscopic level. In the modified LuGre friction model [14] this mechanism is expressed by the average behavior of the bristles. In [13,15], another MR damper model based on the LuGre model is described as:

$$F = \sigma_a Z + \sigma_0 ZU - \sigma_0 \sigma_1 A_0 \left|\dot{X}\right| Z + (\sigma_1 + \sigma_2)\dot{X} + \sigma_b \dot{X} U \tag{39}$$

$$\dot{Z} = \dot{X} - \sigma_0 A_0 \left|\dot{X}\right| Z \tag{40}$$

Table 2. Parameters of LuGre model to Eqs. (39) and (40) [13]

σ_0	$6x10^5$N/(m.V)	σ_1	$1.8x10^3$ N.s/m
σ_b	$9.0x10^2$N.s/(m.V)	A_0	$2.5x10^{-3}$V/N
σ_2	0 N.s/m	σ_a	$5.5x10^5$N/m

The voltage *V* required to the force of the MR damper can be numerically determined to coincide with the desired control force *u* obtained from the control strategy [16].

Figures 2 show the behavior of the vehicle for the system without semi-active control and without anti-roll bar, with anti-roll bar with σ = 50% and without semi-active, and with anti-roll bar with σ = 50% and semi-active control of the MR damper.

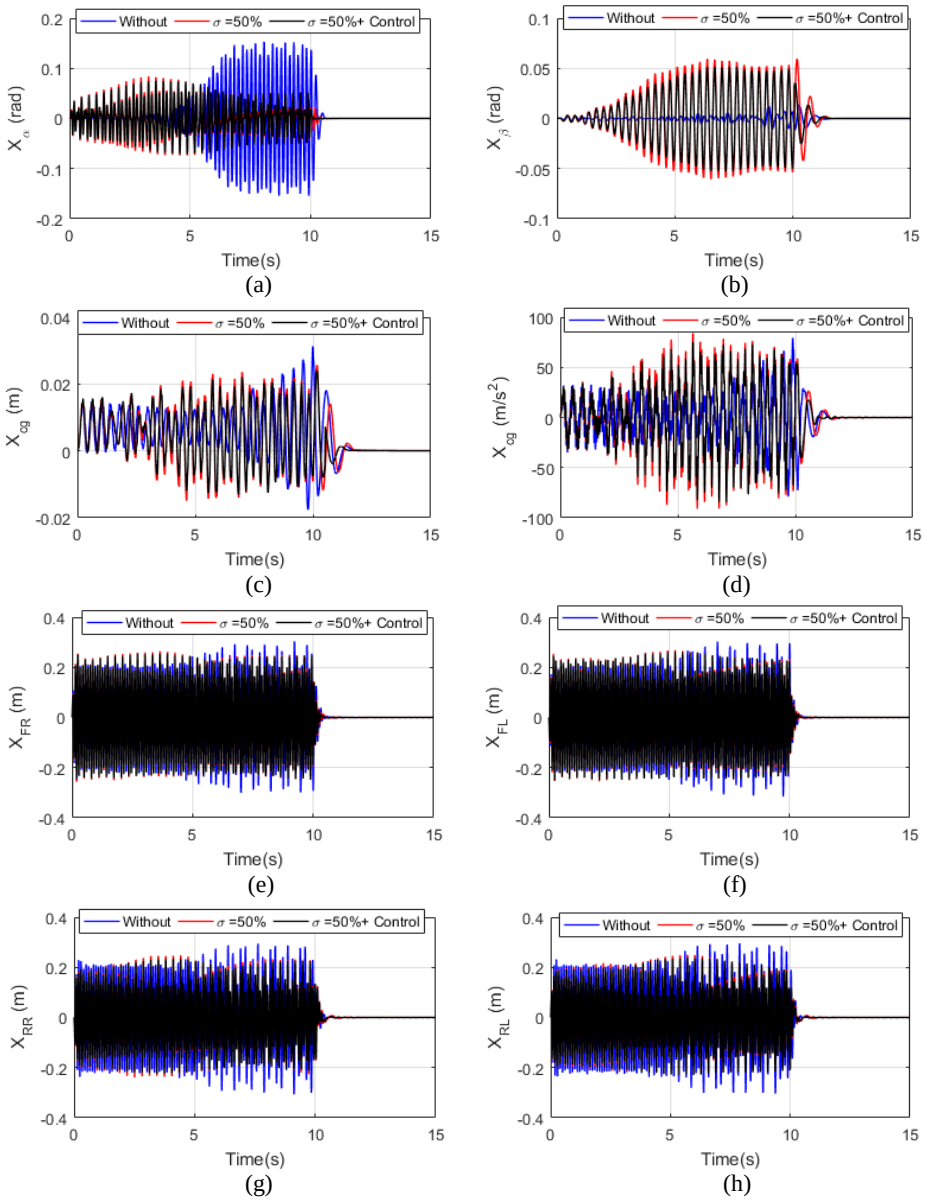

Figure 2. Vehicle system with anti-roll bar and semi-active control, with σ = 50%: (a) Roll α , (b) pitch β (c) displacement of the center of mass (X_{xg}), (d) acceleration of the center of mass ($\ddot{X}_{xg}$), (e) wheel axis displacement (front-right), (f) wheel axis displacement (front-left), (g) wheel axis displacement (rear-right), (h) wheel axis displacement (rear-left)

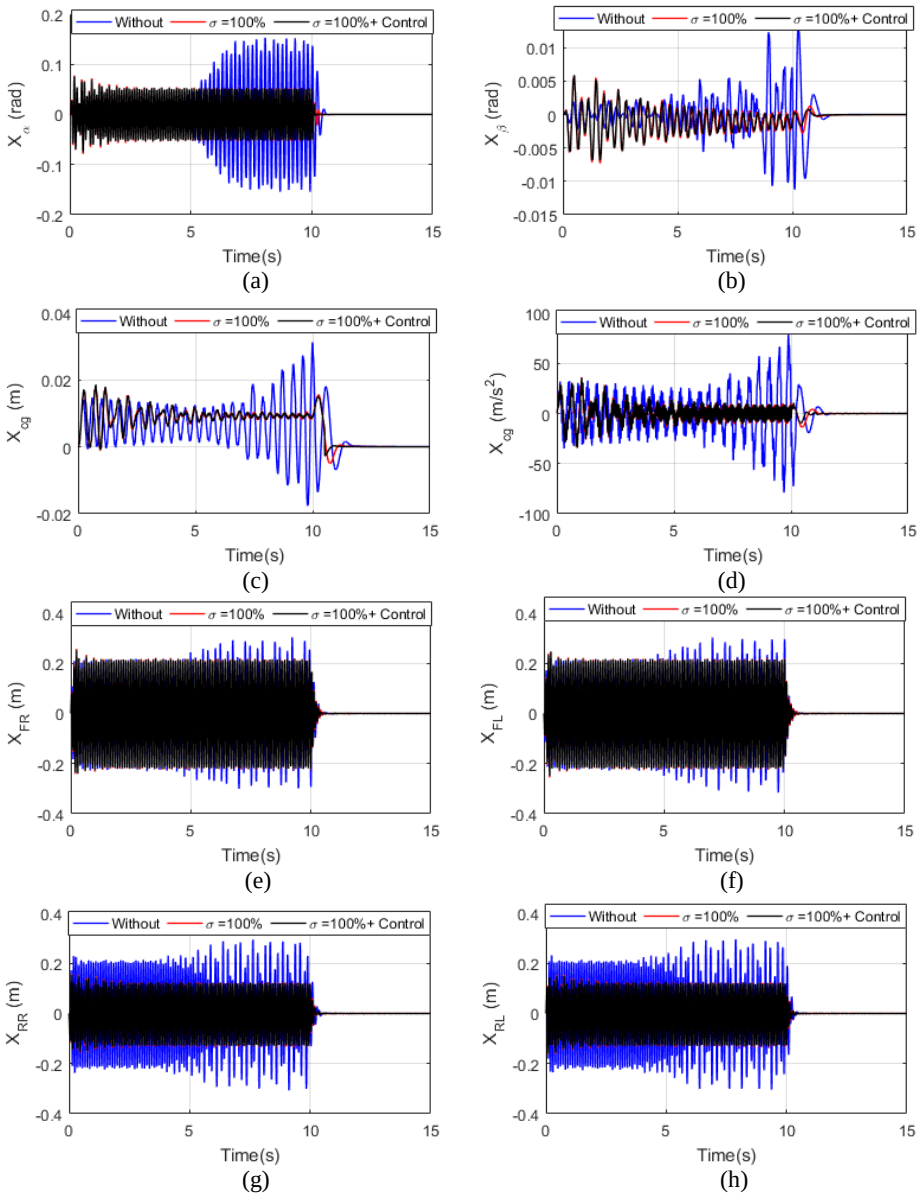

Figure 3. Vehicle system with antiroll bar and semi-active control, with σ = 100%: (a) Roll α , (b) pitch β (c) displacement of the center of mass (X_{xg}), (d) acceleration of the center of mass ($\ddot{X}_{xg}$), (e) wheel axis displacement (front-right), (f) wheel axis displacement (front-left), (g) wheel axis displacement (rear-right), (h) wheel axis displacement (rear-left)

Figures 3 show the behavior of the vehicle for the system without semi-active control and without anti-roll bar, with anti-roll bar with σ = 100% and without semi-active, and with anti-roll bar with σ = 100% and semi-active control of the MR damper.

The preliminary results showed that the anti-roll bar has relevance and good results in averaging the motion. However, to amplify the displacement it is needed that β be near 180º. In this kind of motions, the control is required to support establish the motion σ = 50%. Table 3 shows the RMS variation for the cases presented in Figs. 2 and 3.

Table 3. Acceleration of the center of mass ($\ddot{X}_{xg}$) in RMS

Simulation	RMS
No control, σ = 0%	22.41
No control, σ = 50%	36.93
No control, σ = 100%	9.56
Control, σ = 0%	6.80
Control, σ = 50%	33.47
Control, σ = 100%	9.47

Table 3 shows that the addition of the anti-roll bar provided a significant reduction in the acceleration levels of the vehicle ($\ddot{X}_{xg}$), contributing to more comfort to the passengers. In addition, the semi-active control acts more effectively at low levels of stiffness of the anti-roll bar (σ = 50% or σ = 0%) and that its contribution reduces the stiffness of the anti-roll bar (σ = 100%).

4. Conclusions

As predicted, the comfort performance is better with σ = 100% than with σ = 50% or σ = 0%. The use of control makes the comfort improve, although the time for the displacement of the CG, roll and pitch settle quickly with the controller.

The use of the anti-roll bar supports the system to avoid the resonance area, and provide a displacement of the tire more stable and reliable. In addition, the use of controller in all simulations showed a reduction on time and an improvement on comfort level, however, with the anti-roll bar, the comfort levels became worse near σ = 50%.

Acknowledgments

The authors acknowledge support by CNPq (GRANT:306525/2015-1) and (GRANT:447539/2014-0), CAPES and FAPESP (GRANT 2015/20363-6) both Brazilian research funding agencies.

References

[1] Liu, H., Nonami, K. and Hagiwara, T.. “Active following fuzzy output feedback sliding mode control of real-vehicle semi-active suspensions”. *Journal of Sound and Vibration*, Vol. 314, p. 39-52, 2008.

[2] Silva, R. N. E., Lenz, W. B., Balthazar, J. M., Bueno, A. M. and Tusset, A. M.. “Fuzzy control strategy of a nonlinear full-car model using a magnethorheological (MR) damper”. *In: COBEM 2013, 2013, Ribeirão Preto. 22nd International Congress of Mechanical Engineering, 2013*. p. 2068-2079, 2013.

[3] Tusset, A. M., Piccirillo, V., Janzen, F. C., Lenz, W. B., Lima, J. J., Balthazar, J. M. and Brasil, M. R. L. F.. “Suppression of vibrations in a nonlinear half-car model using a magneto-rheological damper”. *Mathematics in Engineering, Science and Aerospace: the transdisciplinary international journal*, v. 5, p. 427-443, 2014.

[4] Sun, T., Huang, Z. and Chen, D.. “Signal frequency-based semi-active fuzzy control for two-stage vibration isolation system”. *Journal of Sound and Vibration*, Vol. 280, p. 965-981, 2005.

[5] Truong, D. Q., Ahn, K. K. ‘Nonlinear black-box models and force-sensorless damping control for damping systems using magneto-rheological fluid dampers’, Sensors and Actuators A, Vol. 167, pp. 556–573, 2011.

[6] Spelta, C., Previdi, F., Savaresi, S. M., Fraternale, G. and Gaudiano, N. (2009) ‘Control of magnetorheological dampers for vibration reduction in a washing machine’, Mechatronics, Vol. 19, pp. 410–421, 2009.

[7] Tusset, A,M,, Rafikov, M. and Balthazar, J.M.. ‘An Intelligent controller design for magnetorheological damper based on quarter-car model’, Journal of Vibration and Control, Vol. 15, pp. 1907-1920.

[8] Carlson, J. D. and Weiss, K. D. ‘A growing attraction to magnetic fluids’, Journal Machine Design, Vol. 66, pp. 61–64, 1994.

[9] Tusset, A.M., Balthazar, J.M., Chavarette, F.R. and Felix, J.L.P. 'On energy transfer phenomena, in a nonlinear ideal and nonideal essential vibrating systems, coupled to a (MR) magneto-rheological damper', Nonlinear Dynamics, Vol. 69, pp. 1859-1880, 2012.

[10] Gaspar, P., Sazaszi, I., and Bokor, J.. “Active suspension design using linear parameter varying control”. *International Journal of Vehicle Autonomous Systems*, Vol. 1, No. 2, p. 206-221, 2003.

[11] Szászi, I., Gáspár, P. and Bokor, J.. “Nonlinear active suspension modeling using linear parameter vary-ing approach”. *In Proceedings of the 10th IEEE Mediterranean Conference on Control and Automation*. Lisbon, Portugal, 2002.

[12] Zhu, Q. and Ishitobi, M.. “Chaotic vibration of a nonlinear full-vehicle model”. *International Journal of Solids and Structures*, Vol. 43, p. 747-759, 2006.

[13] Sakai, C., Ohmori, H., and Sano, A. Modeling of MR damper with hysteresis for adaptive vibration control. In Decision and Control, 2003. Proceedings. 42nd IEEE Conference on (Vol. 4, pp. 3840-3845). IEEE.

[14] Jimenez R., Alvarez L., Real time identification of structures with magnetorheological dampers, Proceedings of the 41st IEEE Conference on Decision and Control, 1017-1022, 2002.

[15] Piccirillo, V., Tusset, A. M., Nalthazar, J. M.. Dynamical jump attenuation in a non-ideal system through magneto rheological damper. Journal of Theoretical and Applied Mechanics (Warsaw), v. 53, p. 595-604, 2014.

[16] Tusset A. M., Balthazar J. M., Felix J. L. P.. On elimination of chaotic behavior in a non-ideal portal frame structural system, using both passive and active controls, Journal of Vibration and Control, 19, 803-813, 2013.

Wagner Barth Lenz, B.A. (M.Sc. Student): Federal University of Technology - Paraná (UTFPR), Ponta Grossa, PR, BRAZIL (*guipacheco37@gmail.com*).

Angelo Marcelo Tusset, Assistant Professor: Federal University of Technology - Paraná (UTFPR), Ponta Grossa, PR, BRAZIL (*tusset@utfpr.edu.br*).

Rodrigo Tumolin Rocha, Ph.D.: Federal University of Technology - Paraná (UTFPR), Ponta Grossa, PR, BRAZIL (*digao.rocha@gmail.com*).

Frederic Conrad Janzen, Assistant Professor: Federal University of Technology - Paraná (UTFPR), Ponta Grossa, PR, BRAZIL (*fcjanzen@utfpr.edu.br*).

Adriano Kossoski, B.A. (M.Sc. Student): Federal University of Technology - Paraná (UTFPR), Ponta Grossa, PR, BRAZIL (*adrianoutf@gmail.com*).

Jose Manoel Balthazar, Professor: Aeronautics Technological Institute (ITA), São José dos Campos, SP, BRAZIL (*jmbaltha@gmail.com*). The author gave a presentation of this paper during one of the conference sessions.

Airton Nabarrete, Assistent Professor: Aeronautics Technological Institute (ITA), São José dos Campos, SP, BRAZIL (*nabarret@gmail.com*).

Dynamical response of a bistable system with clearance

Grzegorz Litak, Piotr Wolszczak, Krystian Łygas

Abstract: We study the dynamics of an elastic inverted pendulum with an horizontal excitation and imperfect clamping. Complex nonlinear responses of the system appear due to the existence of double potential wells and impacts. The simulation results are analysed by means of phase portraits and Fourier spectra. The results show clearly that increasing the distance between the amplitude limiters can lead to increase in bending amplitude up to the bifurcation point. Beyond this point the large pendulum amplitude response is destabilized. We claim that an inverted pendulum with imperfect clamping of mechanical resonator can be used in frequency broadband energy harvesting.

1. Introduction

Energy harvesting from ambient mechanical vibration is a concept to apply ambient sources to power small devices [7, 10, 11, 16]. For example, sensors, monitoring system, or small size electronic devices can be designed to work directly on harvested energy, or indirectly powered by designed batteries with an option for energy charging from energy harvesting [10]. Early results were obtained by using a simple cantilever beams with piezoelectric, electrostatic, or electromagnetic couplings [2] working in a linear limit.

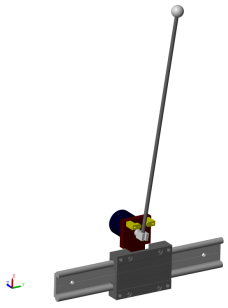

Figure 1. Schema of the multibody system arrangements including the moving harmonically frame, planar inverted pendulum and amplitude limiters. The pendulum has a hollow cylindrical shape which ends with a tip mass. Its geometrical and material properties are given in Tab. 1.

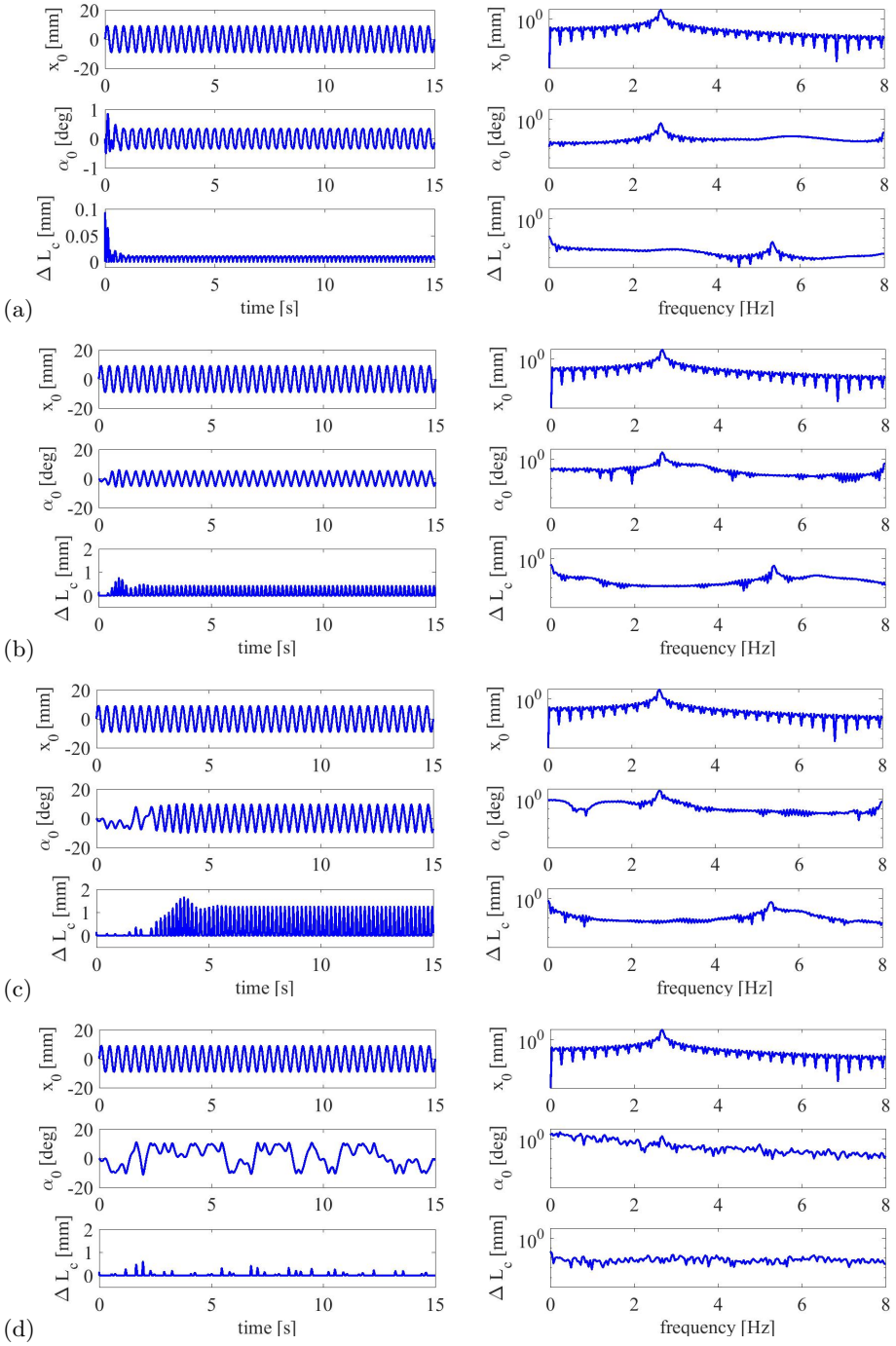

Figure 2. Imposed harmonic motion of the frame x_0 and calculated results of the angular pendulum position α_0 and the deflection of the elastic pendulum shape by the chord reduction ΔL_c, respectively, for the assumed excitation frequency f =2.76Hz and for various distance between amplitude limiters: (a) - 10mm, (b) - 12mm, (c) - 14mm, (d) - 16mm. The initial condition were fixed in the same way for all calculations. The beam starting position was on one of the limiters with zero relative velocity with respect to the frame.

In such simplified linear cases, the mono frequency excitation is engaged leading to resonance-based energy harvesting [2, 8]. Consequently, the energy harvesting device must be adjusted to the ambient energy sources and frequency available.

Recently, to obtain a broad frequency response, application of nonlinear phenomena were suggested [4]. Our model is following this direction proposing a nonlinear mechanical resonator which can be coupled to a piezoelectric transducer.

2. Multibody model and simulation results

Our model (Fig. 1) is based on a vertical flexible beam with a tip mas excited horizontally (see [6]). However, instead of the usual clamping we consider the hinged connection with additional clearance. Such a system posses two potential wells useful for a frequency broadband response [4]. Additional nonlinear effects are related to impacts into the amplitude limiters. Flexible nonlinear beam systems have been already discussed in the collection of papers [12, 15, 17]. Among them, Tang and Ren [15] and Xu and Yu [17] invented a control algorithm to stabilize the pendulum in the upright position. In the other report by Semenov et al. [12] the authors discussed of a concept of elastic inverted pendulum with the vertical excitation. In their treatment pendulum was also exposed on backlash in the hysteretic switching coupling. Continuing this subject, Semenov at al. [13,14] considered the horizontal excitation with a similar hysteretic coupling between the excitation frame and the inverted pendulum. It is worth to note that their model is close to our concept. However we implemented the clearance between amplitude limiters as well as the contact between amplitude limiters and the pendulum in different ways. The purpose of our analysis is to study capability of the system with a double well potential and impacts to convert energy.

$$T = \sum_{i=1}^{N} \frac{\Delta m_i (\mathbf{v}_i + \mathbf{v}_{i-1})^2}{8} + \sum_{i=1} \frac{\Delta I_i \dot{\alpha_i}^2}{2} + \frac{M \mathbf{v}_N^2}{2}, \tag{1}$$

$$V = \sum_{i=1}^{N} \Delta m_i g \frac{(y_i + y_{i-1})}{2} + \sum_{i=1}^{N} \frac{k(\alpha_i - \alpha_{i-1})^2}{2} + M g y_N, \tag{2}$$

where $g = 9.81\mathrm{m/s}^2$ is the gravity acceleration, M is a tip mass attached to the end node of beam element No. N, $\mathbf{v}_i = [x_i, y_i]$ are vectors denoting local connecting node velocities, α are angles between the neighbour short beam elements. All the elements have the same shape and sizes. Note that α_0 is the bearing angle and the assumed $v_0 = \dot{x}_0$ of harmonic motion in the horizontal direction:

$$x_0 = A \sin(\omega t), \qquad y_0 = 0, \tag{3}$$

where A is the amplitude while ω is the corresponding frequency of kinematic excitation. Furthermore, $\Delta m_i = \Delta m$ is mass of a short beam element while $\Delta I_i = \Delta I$ is the moment of inertia for defined elements. Finally, k is the local spring coefficient.

The Lagrangian of the beam without further constraints (limiters) has the following form:

$$L(q_1, ..., q_i, ..., q_N, \dot{q}_1, ..., \dot{q}_i, ..., \dot{q}_N, t) = T(q_1, ..., q_i, ..., q_N, \dot{q}_1, ..., \dot{q}_i, ..., \dot{q}_N, t)$$
$$-V(q_1, ..., q_i, ..., q_N, \dot{q}_1, ..., \dot{q}_i, ..., \dot{q}_N, t), \tag{4}$$

where the generalized coordinates this multistage inverted pendulum $q_i \in \{\alpha_1, ..., \alpha_n\}$ and their corresponding velocities $\dot{q}_i \in \{\dot{\alpha}_1, ..., \dot{\alpha}_n\}$. Consequently, the general equation of motions for such a kinetically forced inverted pendulum can be written as:

$$\frac{d}{dt}\left(\frac{\partial L}{\partial \dot{q}_j}\right) - \frac{\partial L}{\partial q_j} = Q_j + Q_n^{imp}. \tag{5}$$

The generalized forces Q_j appearing in the above equation are defined

$$Q_j = -\beta(\dot{\alpha}_j - \dot{\alpha}_{j-1}) - \beta(\dot{\alpha}_j - \dot{\alpha}_{j+1}), \tag{6}$$

while the additional generalized force Q_n^{imp} is caused by an inelastic contact to one of amplitude limiters with local contact elasticity and damping properties (see Tab. 1 for parameter values and Figs. 1 and 2a for view). They are attached to the beam elements and cause the whole beam to bounce on the amplitude limiters.

The calculations of the dynamical response of the introduced pendulum-impact model were performed by using *Maltab-Simulink* and *Simscape Multibody* with *Flexible Beam* and *Contact Forces* libraries. The results of simulations for chosen three values of the frequency (f =2.67Hz) are presented in Figs. 2-3. In Fig. 2 We show the displacements of frame, holder angle, and the deflection of the elastic pendulum, together with their short time Fourier spectra. Note that increasing the distance between the pendulum amplitude limiters lead to the larger angular amplitude oscillations of the pendulum and consequently to larger bending. The fist simulation (Fig. 2a) was done for the limiters' distance of $\delta_0 l$ =10mm. Note that the beam has D =6mm width and Therefore the clearance was very small. In such situation we obtained periodic solution including small variation of the rotation angle α and consequently a small influence of impacts in the beam length reduction (caused by its bending). For larger limiters' distance the range of rotation angle, α_0, variations and also the level of bending increased. This trend is valid for the distance of 12mm and 14mm (see

Table 1. Material and geometrical properties of beam structure.

length of the beam	L =375mm
material density	ρ =7850 kg/m^3
modulus of elasticity	2×10^{11} Pa
shear modulus	77 GPa
damping constant	0.35
diameters of beam correction	d =3.5mm, and
(hollow cylinder shape)	D = 6mm
tip mas	11.95g
beam mas	55.25g
contact stiffness	10^4 N/m
contact damping	10^2 N/m
stopper height with respect to the	
pendulum rotation axis	18mm

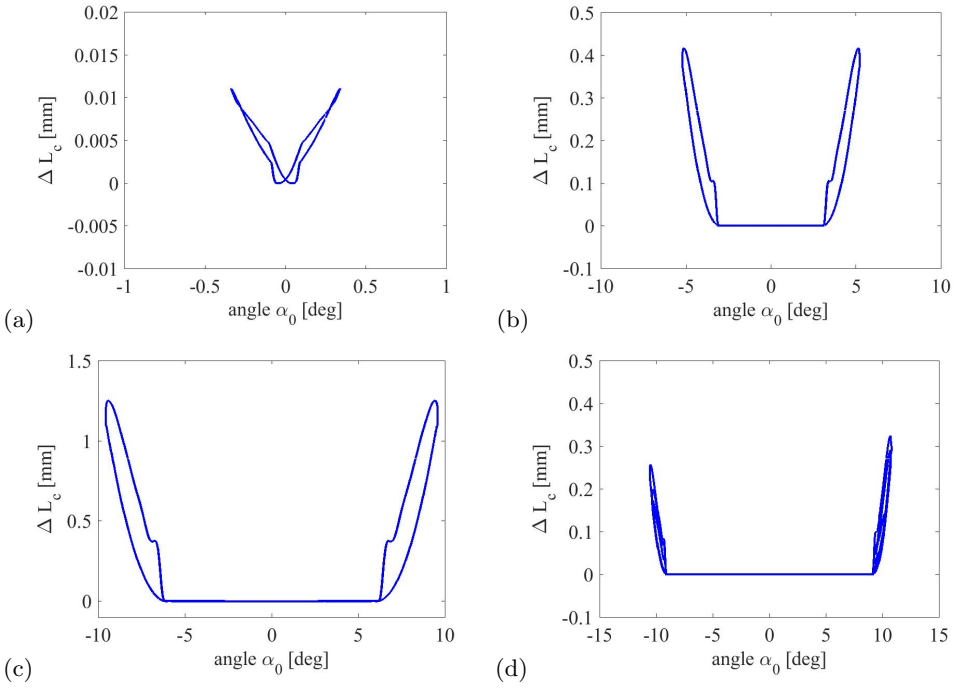

Figure 3. Phase plane results: the chord reduction ΔL_c versus angular displacement of pendulum for various distance between amplitude limiters. (a) - 10mm, (b) - 12mm, (c) - 14mm, (d) - 16mm

Table 2. Variance of angular rotation α_0 and bending parameter ΔL_c for various distance between the amplitude δl limiters.

δl [mm]	var(ΔL_c) [mm^2]	var(α_0) [deg^2]
10	0.00001	0.0684
12	0.0240	11.9377
14	0.2122	40.4633
16	0.0033	47.5054

Fig. 2b,c). Then the solution of larger amplitude is destabilized. Instead of periodic solutions (Fig. 2a-c), the chaotic solutions (fig. 2d) appears. This is confirmed by the corresponding Fourier transform where in place of singular peaks (see Fig. 2a-c on the right side) of the flat and continues distribution of frequencies are visible. Unfortunately, these figures are not very clear because of only short time series were available in the calculations. Note also that in our model the main sources of deflection are impacts. This is better visible in Fig. 3 where we ploted the phase portraits angular rotation versus bending. Here also one can easily distinguish the periodic solutions (Fig. 2a-c) represented by the closed lines on the phase portrait and the non-periodic solution where the multiple passes with different paths are visible. Finally, we summarize the results in a quantitative way Tab. 2. Here, we show the variations of the pudendum angular displacement var(α) and the bending parameter var(ΔL_c).

3. Conclusions

The obtained results show that the system of elastic inverted pendulum with amplitude limiters has a nonlinear features of double well oscillator with impacts. In particular we observed the evolution of the system response with the change of the distance between amplitude bumpers. For the fixed excitation frequency and the corresponding amplitude, enlarging the limiters distance lead initially to better performance in the angular rotation and pendulum bending on the bumpers. However this trend was stopped by the disappearance of the regular large amplitude solution. In other words the larger distance between the limiters produces the higher potential barrier between the minima which were defined at the pendulum positions at the limiters. By reaching this condition the large amplitude solution related to the passing potential barrier was destabilized. Instead a non-periodic (presumably chaotic solution appeared as a nonlinear mixture of the and larger amplitude double well and single potential well oscillations [3,5,9]. Finally, we advocate the application of the proposed mechanical system as a resonator in a frequency broadband energy harvester. Here, the

beam deflection response is formed in a sequence of peaks depending on impacts in the chosen system geometry and dynamical conditions. Such peaks will produce an electrical impulses [1] on the system once it is adapted to energy harvesting.

Literatura

[1] Adhikari, S., Friswell, M. I., Litak, G., and Khodaparast, H. H. Design and analysis of vibration energy harvesters based on peak response statistics. *Smart Materials and Structures 25* (2016), 065009.

[2] Beeby, S., Tudor, M., and White, N. Energy harvesting vibration sources for microsystems applications. *Measurement Science and Technology 17* (2006), R175–R195.

[3] Cottone, F., Vocca, H., and Gammaitoni, L. Nonlinear energy harvesting. *Phys. Rev. Lett. 102* (2009), 080601.

[4] Daqaq, M. F., Masana, R., Erturk, A., and Quinn, D. D. On the role of nonlinearities in vibratory energy harvesting: a critical review and discussion. *Applied Mechanics Reviews 66* (2014), 040801.

[5] Erturk, A., Hoffmann, J., and Inman, D. A piezomagnetoelastic structure for broadband vibration energy harvesting. *Appl. Phys. Lett. 94* (2009), 254102.

[6] Friswell, M. I., Ali, S. F., Adhikari, S., Lees, A. W., Bilgen, O., and Litak, G. Nonlinear piezoelectric vibration energy harvesting from a vertical cantilever beam with tip mass. *Intell. Mater. Syst. Struct. 23* (2012), 1505–1521.

[7] Harne, R. L., and Wang, K. W. A review of the recent research on vibration energy harvesting via bistable systems. *J. Intell. Mater. Syst. Struct. 24* (2013), 1303–1312.

[8] Koszewnik, A., Grzes, P., and Walendziuk, W. Mechanical and electrical impedance matching in a piezoelectric beam for energy harvesting. *European Phys. J-Spec. Topics 224* (2015), 2719–2731.

[9] Litak, G., Friswell, M. I., and Adhikari, S. Regular and chaotic vibration in a piezoelectric energy harvester. *Meccanica 51* (2016), 1017–1025.

[10] Mitcheson, P. D., Yeatman, E. M., Rao, G. K., Holmes, A. S., and Green, T. C. Energy harvesting from human and machine motion for wireless electronic devices. *Proceedings of the IEEE 96* (2008), 1457–1486.

[11] Pellegrini, S. P., Tolou, N., Schenk, M., and Herder, J. L. Bistable vibration energy harvesters: A review. *Intell. Mater. Syst. Struct. 24* (2013), 1303–1312.

[12] Semenov, M. E., Meleshenko, P. A., Solovyov, A. M., and Semenov, A. M. *Hysteretic Nonlinearity in Inverted Pendulum Problem.* Springer, Cham, 2012, pp. 463–506.

[13] Semenov, M. E., and Solovyev, A. M. Stabilization of elastic pendulum with hysteresis. In *International Conference Information Technology and Nanotechnology* (Samara, 2016), CEUR Workshop Proceedings DOI: 10.18287/1613-0073-2016-1638-650-657, pp. 650–657.

[14] Semenov, M. E., Solovyov, A. M., and Meleshenko, P. A. Elastic inverted pendulum with hysteretic nonlinearity in suspension: stabilization problem. *Nonlinear Dynamics 82* (2015), 677–688.

[15] Tang, J., and Ren, G. Modeling and simulation of a flexible inverted pendulum system. *Tsinghua Science and Technology 14* (2009), 22–26.

[16] Twiefel, J., and Westermann, H. Survey on broadband techniques for vibration energy harvesting. *Intell. Mater. Syst. Struct. 24* (2013), 1291–1302.

[17] Xu, C., and Yu, X. Mathematical modeling of elastic inverted pendulum control system. *Journal of Control Theory and Application 3* (2014), 281–282.

Grzegorz Litak, Prof.: Department of Automation, Lublin University of Technology, Nadbystrzycka 36, PL-20-618 Lublin, Poland (*g.litak@pollub.pl*). The author gave a presentation of this paper during one of the conference sessions.

Grzegorz Litak, Prof.: Department of Process Control, AGH University of Science and Technology, Mickiewicza 30, PL-30-059 Krakow, Poland (*g.litak@pollub.pl*).

Piotr Wolszczak, Ph.D.: Department of Automation, Lublin University of Technology, Nadbystrzycka 36, PL-20-618 Lublin, Poland (*p.wolszczak@pollub.pl*).

Krystian Łygas, M.Sc.: Department of Automation, Lublin University of Technology, Nadbystrzycka 36, PL-20-618 Lublin, Poland (*k.lygas@pollub.pl*).

Thermal buckling of triangular plates

Olga Mazur, Atul Bhaskar

Abstract: Buckling and dynamics of plates of simple geometries have been widely investigated in the past. For complex geometrical shapes, mathematical formulation is complicated and an analytical treatment frequently infeasible. One has to resort to the use of numerical methods, which are often time-consuming and computationally expensive. Here we propose a scaling to estimate the critical temperature in the thermal buckling problems of isotropic triangular plates within a uniform temperature field. Ritz-method in conjunction with R-function theory is used for calculations that are performed for plates of fixed area but changing shape. The plate is assumed to be simply supported, clamped, or to satisfy mixed boundary conditions. The influence of shape on buckling is studied to explore optimal design of triangular plates with the buckling temperature as the objective function. Critical buckling temperature for triangular plates of varying shape is obtained. Results show that the most unstable triangular plate for thermal loading, is one with equal sides. Clamping of the boundary increases critical buckling temperature, making plate less susceptible to buckling upon temperature rise.

1. Introduction

Plates are widely used within modern engineering constructions They are often subjected to elevated temperature environment, influence of which can lead to structural instability even without the application of any mechanical load. The instability of plates due to temperature rise has been previously studied by many researchers [6,13]. Extensive reviews of the results obtained for thermal buckling are presented in the works of Thornton [21] and Tauchert [20]. In Murphy [13], results of theoretical as well as experimental research for clamped isotropic plates are presented. Xiao and Chen [22] studied thermal buckling of elastic-plastic plates. In [4, 14], circular isotropic and orthotropic plates under special heating are investigated. It should be noted that practically all recent studies are focused on the research of multilayer plates, functionally graded material plates, thermo-mechanical loading plates or another features [7, 19]. However, in the literature, results for plates with complex shape (not rectangular or circular) are sparse. In [1], thermal bucking of circular and rectangular orthotropic plates with rounded angles is analyzed. In publication [15], the optimization under thermal buckling of skew plates is considered. Thermal buckling of plates with holes

is considered in [3]. In [5] analytical solution for equilateral triangular plates on elastic foundations is presented.

From the literature review, it is observed, that thermal buckling of plates with arbitrary triangular shape is not considered previously. Of particular interest is the question of the rule of shape design to achieve maximum critical temperatures. It should be noted that the use of numerical methods, which are mostly applied for plates with complex shape, is time-consuming and computationally expensive. Here we present a general methodology to obtain the critical buckling temperature of triangular plate. We also propose a special scaling procedure relating the shape and the critical temperature which can be useful for evaluating this parameter at engineering designing. Results are obtained using the *R-function method* (RFM) [16]. The main idea of this method is analytical description of geometrical information of the plate planform. Taking geometrical data into account in an analytical way allows us to construct basis functions for variational methods which satisfy boundary conditions. The method has been previously applied for many plate and shell problems [8–11, 16]. Related to considered task buckling of loaded in plane plates are investigated in publications Rvachev and Kurpa [9, 17]. In [17] it is presented results of buckling load for equilateral triangular shape plate. Influence of temperature on objects with nonclassical form is investigated with RFM in [18]. The thermoelasticity problem for objects with complex form such as aircraft engine blade is studied.

2. Method of solution

Let us consider isotropic triangular plate with constant thickness h. The plate has one edge aligned to y-axis, the other two inclined at angles β and γ to y-axis as shown on Fig. 1 Suppose that the plate is in a uniform temperature field with constant difference T.The plate

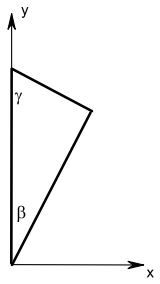

Figure 1. Triangular shape of the plate.

bending mechanics is described in the framework of Kirchhoff-Love hypothesis. Strains in

the plate have the following form

$$\varepsilon_x = \frac{\partial u}{\partial x}, \varepsilon_y = \frac{\partial v}{\partial y}, \gamma_{xy} = \frac{\partial u}{\partial y} + \frac{\partial v}{\partial x}, \tag{1}$$

where u, v and w represent the in-plane and out of plane displacements in the plate respectively. Stresses including temperature effect given by

$$\begin{aligned} \sigma_x &= \frac{E}{1-\nu^2}\left[\varepsilon_x + \nu\varepsilon_y - (1+\nu)\alpha T\right], \\ \sigma_y &= \frac{E}{1-\nu^2}\left[\varepsilon_y + \nu\varepsilon_x - (1+\nu)\alpha T\right], \\ \tau_{xy} &= G\gamma_{xy}. \end{aligned} \tag{2}$$

Here E is the Young modules, ν is the Poissons ratio, G is the shear modulus, α is the coefficient of thermal expansion.

The governing equation for buckling problem is given by

$$D\nabla^4 w = \frac{\partial^2 w}{\partial x^2} N_x + 2\frac{\partial^2 w}{\partial x \partial y} N_{xy} + \frac{\partial^2 w}{\partial y^2} N_y. \tag{3}$$

In (3) N_x, N_y, N_{xy} are internal in-plane forces per unit edge length of the plate

$$\begin{aligned} N_x &= \frac{Eh}{1-\nu^2}\left[\frac{\partial u}{\partial x} + \nu\frac{\partial v}{\partial y} - (1+\nu)\alpha T\right], \\ N_y &= \frac{Eh}{1-\nu^2}\left[\frac{\partial v}{\partial y} + \nu\frac{\partial u}{\partial x} - (1+\nu)\alpha T\right], \\ N_{xy} &= \frac{1}{2}\frac{Eh}{1+\nu}\left(\frac{\partial u}{\partial y} + \frac{\partial v}{\partial x}\right), \end{aligned} \tag{4}$$

where $D = Eh^3/12(1-\nu^2)$ is bending stiffness.

The boundary conditions for deflection w are considered of four types:

simply supported $w = 0, M_n = 0.$;

clamped $w = 0, \frac{\partial w}{\partial n} = 0$;

mixed boundary conditions (MBC1): two sides of triangular are clamped $\partial\Omega_1$ one side is simply supported $\partial\Omega_2$

$$\begin{aligned} &w = 0, M_n = 0.(x,y) \in \partial\Omega_1 \\ &w = 0, M_n = 0.(x,y) \in \partial\Omega_2; \end{aligned} \tag{5}$$

mixed boundary conditions (MBC2): one side of triangular is clamped $\partial\Omega_1$ two side are simply supported $\partial\Omega_2$

$$\begin{aligned} &w = 0, M_n = 0.(x,y) \in \partial\Omega_1 \\ &w = 0, M_n = 0.(x,y) \in \partial\Omega_2. \end{aligned} \tag{6}$$

As it is shown in [2] , in-plane internal forces should satisfy

$$N_T = N_x = N_y = -\frac{EhT\alpha}{1-\nu}, N_{xy} = 0 \tag{7}$$

The bending energy of the plate is given by

$$I_1 = \frac{D}{2}\int\int\left[\left(\frac{\partial^2 w}{\partial x^2}+\frac{\partial^2 w}{\partial y^2}\right)^2 - 2(1-\nu)\frac{\partial^2 w}{\partial x^2}\frac{\partial^2 w}{\partial y^2} - \left(\frac{\partial^2 w}{\partial x \partial y}\right)^2\right] d\Omega. \tag{8}$$

The potential energy of plate under action of temperature field is negative of the work done by external forces when edges move inwards

$$I_2 = -\frac{N_T}{2}\int\int\left[\left(\frac{\partial w}{\partial x}\right)^2 + \left(\frac{\partial w}{\partial y}\right)^2\right] d\Omega. \tag{9}$$

The variational statement of problem considered is reduced to minimization of the functional [12]

$$\begin{aligned} I = \frac{D}{2}\int\int\left[\left(\frac{\partial^2 w}{\partial x^2}+\frac{\partial^2 w}{\partial y^2}\right)^2 - 2(1-\nu)\frac{\partial^2 w}{\partial x^2}\frac{\partial^2 w}{\partial y^2} - \left(\frac{\partial^2 w}{\partial x \partial y}\right)^2\right] d\Omega + \\ \frac{N_T}{2}\int\int\left[\left(\frac{\partial w}{\partial x}\right)^2 + \left(\frac{\partial w}{\partial y}\right)^2\right] d\Omega. \end{aligned} \tag{10}$$

which is carried out on system of basis functions which satisfy boundary conditions in domain considered.

3. R-functions method.

The novelty of proposed method lies in the use of *R-function theory* for construction of basis functions for this class of problems. The main idea of applying of RFM is describing of geometrical information analytically. The first step is to construct of the logical predicate of considered domain. For triangular shapes, we have

$$\Omega = \Omega_1 \wedge \Omega_2 \wedge \Omega_3. \tag{11}$$

Here $\wedge$ is logical conjunction, $\Omega_1, \Omega_2, \Omega_3$ are predicates of subdomains:

$$\Omega_1 = \{\omega_1 = x \geq 0\} \tag{12}$$

is semi-plane right-hand straight line $x = 0$;

$$\Omega_2 = \{\omega_2 = -\cos(\beta)x + \sin(\beta)y \geq 0\} \tag{13}$$

is semi-plane above straight line $y = \cot(\beta)x$

$$\Omega_3 = \{\omega_3 = -\cos(\gamma)x - \sin(\gamma)y + \sin(\gamma)a \geq 0\} \tag{14}$$

is semi-plane under straight line $y = -\cot(\gamma)x + a$.

According to RFM, we need to replace logical operation by corresponded *R-functions* [16], [17] to obtain the equation of the boundary:

$$\omega = \omega_1 \wedge_0 \omega_2 \wedge_0 \omega_3. \tag{15}$$

In Eq. (15) $\wedge_0$ means function of the system of *R-functions*:

$$x \vee_0 y = x + y + \sqrt{x^2 + y^2}, x \wedge_0 y = x + y - \sqrt{x^2 + y^2}, \bar{x} = -x. \tag{16}$$

For boundary conditions considered we use following structures of solutions. If the plate is simply supported :

$$w = \omega P, \tag{17}$$

if the plate is clamped we have,

$$w = \omega^2 P, \tag{18}$$

and for mixed boundary conditions Eq. (5),(6), we get

$$w = \omega\omega_1 P, \tag{19}$$

where ω_1 is analytical expression of the clamped part. In formulas Eq. (17)-(19) P is undetermined component, which is expressed as decomposition of complete system functions $\{\varphi_i\}$ as

$$P = \sum_{i=1}^{n} c_i \varphi_i. \tag{20}$$

For complete system functions $\{\varphi_i\}$, power polynomials, trigonometrical polynomials, Chebychev polynomials or splines can be used . We use the following system of power polynomials:

$$1, x, y, x^2, xy, y^2, ... \tag{21}$$

It should be noted that structure of solution Eq. (17),(19) satisfy just geometric boundary conditions. One can find the structure of solutions that satisfy all boundary conditions

in [9, 16, 17], but they have complex form. For the considered problem the used structure are adequate.

For simply supported plate, using the structure of solution Eq. (17) system of basis functions has the form

$$w_1 = \omega, w_2 = \omega x, w_3 = \omega y, w_4 = \omega x^2, w_5 = \omega xy, w_6 = \omega y^2, ... \tag{22}$$

After substituting the above into the functional Eq. (10), we carry out the minimization of the functional in Eq. (10) as per the Ritz method which leads to an algebraic eigenvalue problem. Elements of the matrices within the generalized eigenvalue problem involving two matrices are integrals over the domain. For clamped plate, basis functions

$$w_1 = \omega^2, w_2 = \omega^2 x, w_3 = \omega^2 y, w_4 = \omega^2 x^2, w_5 = \omega^2 xy, w_6 = \omega^2 y^2, ... \tag{23}$$

are used.

4. Results and discussion

The formulation presented above was computationally implemented. Illustrative examples, the role of plate shape and a related optimization problem are presented next.

4.1. Triangular plate with various boundary conditions

We assume that plate has unit area. For triangular shape we use RFM as described in section 2 Mechanical and properties are taken as follows:

$$E = 73 \times 10^9 \text{ Pa}, \nu = 0.3, b/a = 1, h/a = 0.01. \tag{24}$$

Coefficient of thermal expansion is $\alpha = 2 \times 10^{-6}/^{\circ}\text{C}$. Calculations are performed for thickness ratio $h/a = 0.01$.

First we present results obtained for right and equilateral triangle, Fig. 2. The shape

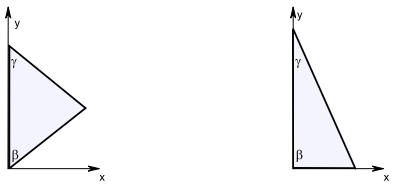

Figure 2. Right and equilateral triangular shapes

of the triangular plate, in general, is not symmetrical, so we use complete system of power

polynomials Eq. (21). Integration is performed over whole domain. Results are presented for 21 basic functions, which corresponds to 7th power of polynomials.

Table 1. Critical buckling temperature(in °C) for isotropic equilateral and right triangular plate

Shape	equilateral	right	
Simply supported	72.204		85.899
Clamped	206.003		250.659
MBC1	103.916	[1]	127.767
		[2]	108.040
		[3]	136.121
MBC2	145.83	[4]	159.863
		[5]	197.232
		[6]	173.246

[1] greater side, [2] smaller side, [3]hypotenuse [4] two sides, [5] greater side and hypotenuse, [6]smaller side and hypotenuse are clamped

Results presented, it can be concluded that clamping of the part of the domain increases buckling temperature, thus the more stable to temperature action is clamped over all domain plate. Also it should be noted that buckling temperature for equilateral triangular plate with all types of boundary conditions is less. Thereby the right triangular is more stable to temperature action.

4.2. The effect of plate shape on buckling temperature

In the following section let us consider influence of shape o the triangular plate on buckling temperature. We change angles β and γ in interval 10° to 160° to study the effect of the plate shape on T_{cr}. In Fig. 3 The critical buckling temperature T_{cr} for various values of angles are shown for two types of boundary conditions simply supported and clamped plate. In both cases, we obtain surface of the same type with only minimum at the point, corresponding to $\beta = \gamma = 60^\circ$ which corresponds to equilateral triangular shape. This is also demonstrated by the figure Fig. 4 and 5. Level curves of buckling temperature depending on angles β and γ in interval $10^\circ..160^\circ$ are presented in equilateral triangle with unit side using barycentric coordinates, Fig. 4. This figure shows maximum at the center, what means that equilateral triangular has lowest critical temperature. On Fig. 5 buckling temperature for changing angle β with fixed angle $\gamma = 30^\circ, 60^\circ, 90^\circ$ for simply supported and clamped plate (cross-section of surface on Fig. 5) are presented.

It is clear that the minimum of the buckling temperature occurs for equilateral triangles.

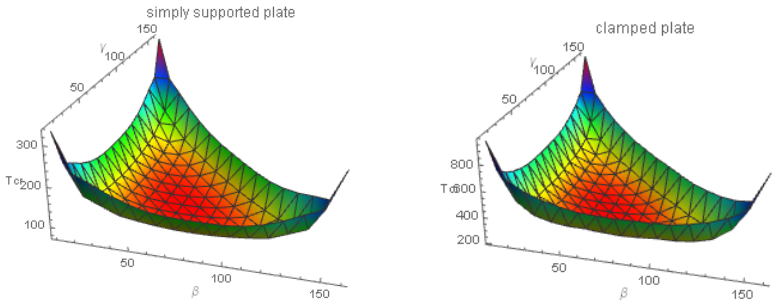

Figure 3. Influence of shape of the plate on buckling temperature (in °C) for simply supported and clamped triangular plate

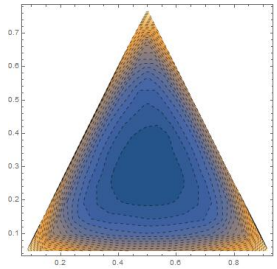

Figure 4. Level curves of buckling temperature for simply supported triangular plate in barycentric coordinates

For fixed $\gamma = 30^\circ$ minimum achieves for triangle with angles $30^\circ, 75^\circ, 75^\circ$, for fixed $\gamma = 90^\circ$ minimum is for triangle with angles $90^\circ, 45^\circ, 45^\circ$.

4.3. Scaling of buckling temperature

The results presented in section 4.2 are obtained using the variational-structural method RFM require complex mathematical calculations, that obviously consumes a lot of computer resources. At the same time, the finite element method which is often used for this type of research also consumes a lot of computational time. Complexity arises if it is necessary to vary the shape as it is done in considered problem of finding optimal shape of triangular plate with a fixed area from the point of view of the influence of the temperature field.

In the following, we propose a simple approach to find the scaled value of the critical temperature, which will easily allow to predict its approximate value.

Let us introduce a scale for the deflection of the plate as

$$w \sim A. \tag{25}$$

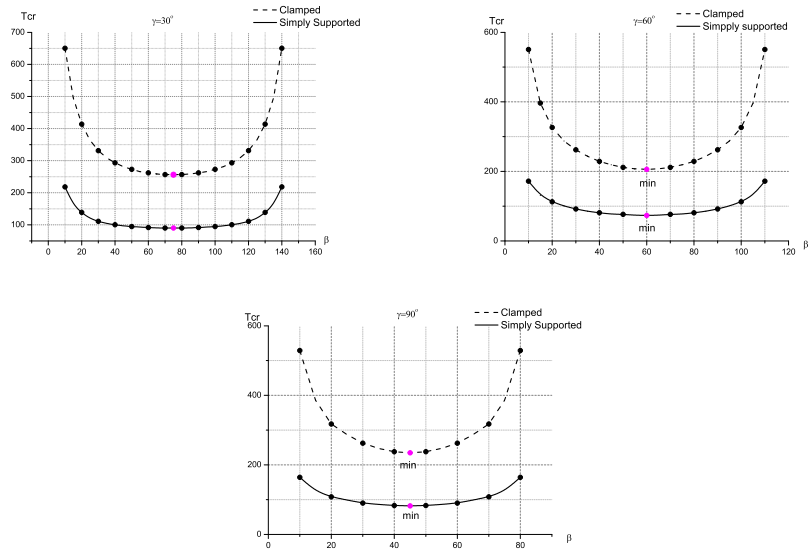

Figure 5. Influence of shape of the plate on buckling temperature (in °C) for two types of boundary conditions

The differential operators scale according to

$$\frac{\partial}{\partial x} \sim \frac{1}{L_1}, \frac{\partial}{\partial y} \sim \frac{1}{L_2}, \frac{\partial^2}{\partial x^2} \sim \frac{1}{L_1^2}, \frac{\partial^2}{\partial y^2} \sim \frac{1}{L_2^2}. \tag{26}$$

Then we introduce L_1 and L_2 as characteristic lengths

$$L_1 = (I_1)^{\frac{1}{4}}, L_2 = (I_2)^{\frac{1}{4}}, \tag{27}$$

where I_1, I_2 denoted principal second moments of area of the triangular plate. Thus critical temperature can be scaled as

$$T_{cr} \sim \frac{\frac{Eh^3}{12(1-\nu^2)} \int\int \left[\left(\frac{\partial^2 w}{\partial x^2} + \frac{\partial^2 w}{\partial y^2} \right)^2 \right] d\Omega}{\frac{Eh\alpha}{1-\nu} \int\int \left[\left(\frac{\partial w}{\partial x} \right)^2 + \left(\frac{\partial w}{\partial y} \right)^2 \right] d\Omega} \sim \frac{h^2(1+\nu)}{\alpha} \left(\frac{1}{L_1^2} + \frac{1}{L_2^2} \right). \tag{28}$$

The expression on the right side of equation Eq. (28) enables us with a scaling argument:

$$\frac{h^2(1+\nu)}{\alpha} \left(\frac{1}{L_1^2} + \frac{1}{L_2^2} \right). \tag{29}$$

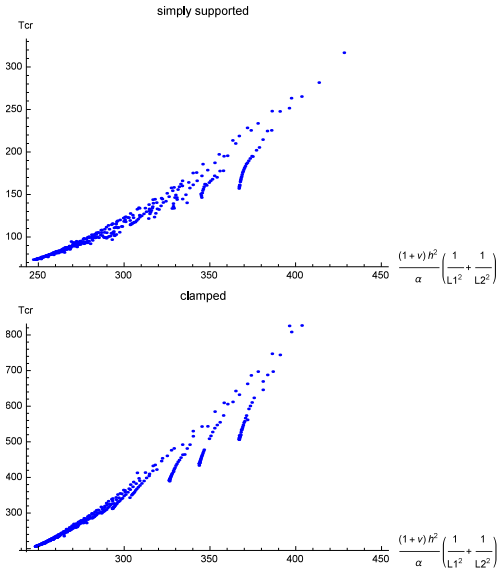

Figure 6. Dependence between critical buckling temperature (in °C) and scaling expression

In Fig. 6, values of this expression is plotted against the numerically calculated values of the critical temperature for triangular plates of various shapes. Results are obtained for plate parameters Eq. (24), $h/a = 0.01$ and unit area.

There is approximate linear correlation between suggested scaling expression and numerically calculated critical bucking temperature for both conditions. The inclination for the clamped plate is steeper as accepted.

5. Conclusions

In this paper, a method to predict the thermal buckling behavior of the triangular plates is presented. A scaling argument proposed here provides an estimate of the critical buckling temperature approximately, avoiding detailed calculations for triangular plates of all shapes. This may be useful at early stages of design search and optimization where approximate calculations are often adequate. Also the use R-function method is novel for the class of problems considered here. The application of RFM allows analytical description of the boundaries of the domain exactly, followed by a variational minimization, to determine the critical buckling temperature. Parametric studies, enabled by R-functions method combined with a variational approach, are carried out. The study also demonstrates that the smallest value of critical temperature corresponds to equilateral triangles with simply supported edges.

References

[1] Biswas, P. Thermal buckling of orthotropic plates. *J. Appl. Mech. 2*, 43 (1976), 361–363.

[2] Boley, B., and Weiner, J. *Theory of Thermal Stresses*. Wiley, New York, 1960.

[3] Chang, J., and Shiao, F. Thermal buckling analysis of isotropic and composite plates with a hole. *Journal of Thermal Stresses*, 13 (1990), 315–320.

[4] Cotterell, B., and Parkes, E. W. Thermal buckling of orthotropic plates. *R. M.*, 3245 (1960).

[5] Datta, S. Thermal buckling of some heated plates on elastic foundation. *Defence Science Journal 26*, 3 (1974), 119–122.

[6] Gossard, M. L., Seide, P., and Parkes, E. W. . *Thermal Buckling of Plates*. NASA, 1952.

[7] Javaheri, R., and Eslami, M. Thermal buckling of functionally graded plates. *AIAA JOURNAL 40*, 1 (2002), 16–169.

[8] Kurpa, L. *R-functions Method for Solving Linear Problems of Bending and Vibrations of Shallow Shells*. Kharkiv NTU Press, Kharkiv, 2009.

[9] Kurpa, L., and Mazur, O. Parametric vibrations of orthotropic plates with complex shape. *Int. App. Mechanics 46*, 4 (2010), 438–449.

[10] Kurpa, L., and Mazur, O. Parametric vibrations of multilayer plates of complex shape. *J. of Mathematical Sciences 174*, 2 (2014), 438–449.

[11] Kurpa, L., Shmatko, T., and Timchenko, G. Free vibration analysis of laminated shallow shells with complex shape using the r-functions method. *Composite Structures 39*, 1 (2010), 225–233.

[12] Mikhlin, S. *Variational Methods in Mathematical Physics*. Nauka, Moscow, 1970.

[13] Murphy, K., and Ferreira, D. Thermal buckling of rectangular plates. *Int. J. of Solids and Structures 38*, 22-23 (2001), 3979–3994.

[14] Najafizadeh, M., and Eslami, M. Thermoelastic stability of orthotropic circular plates. *Journal of Thermal Stresses 25*, 10 (2002), 985–1005.

[15] Prakash, T., Singha, M., and Ganapathi, M. Thermal postbuckling analysis of fgm skew plates. *Engineering Structures 30*, 1 (2008), 22–32.

[16] Rvachev, V. *Theory of R-functions and Some of Its Applications*. Naukova Dumka, Kiev, 1960.

[17] Rvachev, V., and Kurpa, L. *The R-functions in Problems of Plates Theory.* Naukova Dumka, Kiev, 1987.

[18] Rvachev, V., Shevchenko, A., and Sizova, N. R-function analysis of the thermally stressed state of an aircraft engine blade. *Int. App. Mechanics 32*, 2 (1996), 117–121.

[19] Singha, M., Ramachandra, L. S., and Bandyopadhyay, J. N. Optimum design of laminated composite plates for maximum thermal buckling loads. *Journal of Composite Materials* (2000).

[20] Tauchert, T. Thermally induced flexure, buckling, and vibrations of plates. *Appl. Mechanics Review 44*, 8 (1991), 374–360.

[21] Thornton, E. Thermal buckling of plates shells. *Appl. Mechanics Reviews 46*, 10 (1993), 485–506.

[22] Xiao, S., and Chen, B. Dynamic and buckling analysis of a thin elastic-plastic square plate in a uniform temperature field. *Acta Mechanica Sinica* (2005).

Olga Mazur, Ph.D.: National Technical University "KhPI"/Department of applied mathematics, Kyrpychova str. 2,61002, Kharkiv, Ukraine (*mazuroly@gmail.com*). The author gave a presentation of this paper during one of the conference sessions.

Atul Bhaskar, Professor: University of Southampton /Faculty of Engineering and the Environment, SO16 7QF, UK (*A.Bhaskar@soton.ac.uk*).

Off-road 4-wheel drive vehicle dynamics and control

Tomasz Mirosław, Jan Szlagowski, Adam Zawadzki, Zbigniew Żebrowski

Abstract: In this paper the dynamic model of 4 wheel drive off-road autonomous vehicle or wheeled mobile robots is presented. This model was developed from tractor dynamic model which was verified in real field tests. The way of building universal model is proposed and used for simulation of various electric drive configurations as: 2 axles-1 motor, 2 axles -2 motors and 4 wheels 4 motor. The simulation results are discussed. The various properties of vehicle driven in various ways are presented and explained based on this model rules. The model was built in Matlab/Simulink software. The simulation results are compared with real tests of physical model behavior. In the conclusion the comparison of various drive properties and skills are presented, and recommendations are suggested.

1. Introduction

Off road vehicle is one of the most important domains in human economy similarly to hard road transport. Currently the off-road riding became the sport and significant part of automotive business. Some clients are looking for off-road looking vehicle for normal use. Of course some of users living in the suburbs with unpaved roads really need the off-road vehicle. But we also have to remember about great part of economy like agriculture, foresting etc. In this domain the off-road vehicles are the platform for machineries or they are the transport mean for workers or emergency services [1, 2, 3, 4].

The most common solution 4x4 drive vehicle with ICE hasn't exhausted the possibilities of development but a new concept of hybrid or electric vehicles appeared.

When we are thinking about hybrid solution we should underline that the off-road vehicles are dominated by ICE-Hydraulic hybrids. Many solution of construction machinery have individual hydraulic motors "in wheels" which are supplied with oil pumped by pump propelled by ICE [5].

But this solution isn't popular in small machinery or off-road cars.

Going together with hard road automotive solution SUV class we are looking for universal solution. Other branch which is currently developed very spectacularly are the full electric vehicles. Currently the average range of electric vehicles is about 100km – it is enough for everyday use e.g. journey to work, to school with children, for shopping etc. If we would like to take into account the off-road travel the expected range decreases. The terrain obstacles like hills, sand etc. cause that ICE vehicles are lower efficient than on the road. Coming down the hill ICE cannot harvest energy, if it slips on the sand it can't distribute the energy in optimised way to wheels [6, 7]. Working on electric 4 wheel drive with separate driven front and rear axles Authors noticed unusual skill of this solution.

When we use 4x4 drive vehicle with one engine the drive for two axes is delivered only up to speed of about 40km/h or even less. For higher speeds this solution can cause some danger. But on the over hand the 4x4 wheel drive has the best traction on the bends. The rear axle drive is over-steered; with front – under-steered, but the both axle driven vehicle is just -steered. In traditional solution we can't do it. The traditional solution 4x4 is less efficient during acceleration or braking. We can improve some skills by blocking differentials mechanisms but we lose the possibilities of direction control. The energy flows between wheels via ground with one engine generate some interesting but danger phenomena of circulating power as well.

Figure 1. The concept of SUV project IEVS & PoLevs companies. Result of Free Moby Eu Project.

Electric drive especially with electric torque motors which can be built-in the wheel gives new possibilities. We can control energy flow to each wheel and adjust its rotation speed to its load, surface under is to optimize the efficiency and direction control.

Separately driven wheels are truly 4x4 driven vehicles without limit of speed, with fully electrically controlled speed, traction, acceleration and braking. All functions like ABS and ESP can be provided by electronic controlled electric motors.

The only disadvantages of this solution are the price and weight and inertia of direct driven wheels. From technical point of view, we can produce "high-speed" electric motor with the same power much smaller and lighter than the same power low-speed/torque motor. So the amount of materials (specially rare-earth) are lower and motors are cheaper. The rate weight to power is not the linear function, that

means that for producing motor of 50KW we need much less materials that to produce 2 motors of 25KW. The possibilities of energy sharing is the great advantages which cannot be available for truly 4x4 driven car even the fantastic skill of torque overload electric motors (3-5 time for short time).

Based on those thesis the concept of two axle drive 4x4 off road vehicle Mini SUV (presented in figure 1) was tested and designed. This vehicle is dedicated for famers, vets, etc. In this paper some piece of analyses is presented.

2. The concept of 4-wheel SUV

The concept of a vehicle based on 2 identical driving axles for front and rear with identical electric powertrain, suspension and separated supplying batteries was analysed. The difference concerns only the steering of wheel while making a turn. The turn of rear wheels can be blocked for road and off road riding, but for better maneuverability the turn can be switch on, and rear wheel would turn in opposite direction to the front wheel. The structure of vehicle is presented in fig. 2.

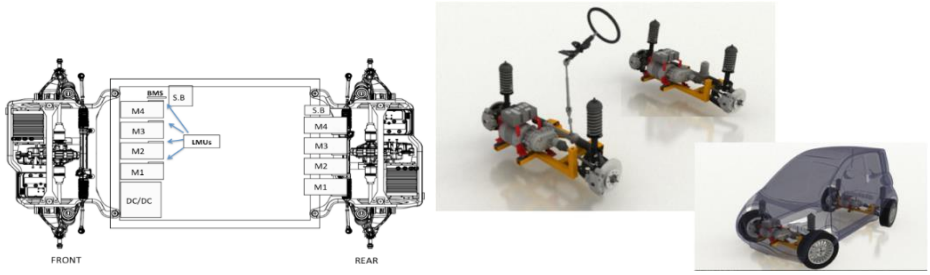

Figure 2. The 4-wheel drive concept according to Free Moby project

This driving system consists of batteries with electronic battery management systems, motor controller, motor, two speed gear box and axle with lockable differential and axles with wheels. Both motor controllers are driven by central processing unit which monitors rotation speed and torques of both axles and angle of steering wheel and acceleration and brake pedals.

The vehicle has the suspension with adjustable length and stiffness. To evaluate the traction feature the computer model was built.

3. The principia and analyses for vehicle modelling

In vehicle modelling the following assumptions were made [20, 21, 22, 23, 24, 26]:

- The body (cage) of the vehicle can be treated as a rigid body suspended on four springs with dampers on the wheels.
- The vehicle body rotates around 3 axels changing the loads of the wheels
- The dynamic radius of wheels is constant

– The propelling forces are produced by friction of tires on the road and gravity (the till of road is taken account)
– The steering forces are produced by changing of motor supplying voltage and front wheel turning.
– The resistance of wheel rolling depends on ground which change its feature and characteristics under wheel load.
– The wheel can slip, rotate, or stick to the surface.
– The tire and ground are modelled in a simplified way as general phenomena is isometric. The construction specific features of tire are omitted.

4. The concept of 4x4 drive vehicle –ground model

The model consists of 3 main parts, the vehicle body, tire and ground.

The vehicle can be treated as a rigid body. The forces generated under the tire act on the centre causing vehicle acceleration in two dimensions. Each "wheel force" can be split out into force laying on the line connecting tire with mass centre Fr and orthogonal Fn. The Fn forces generate rotation torque around vertical axes of vehicle (figure 3). But if we have four wheels and each generate Fr some torques coming from those forces can compensate each other. The compensated torques give the forces back to the system and they should be summed geometrically like forces Fr and act on mass centre.[21]

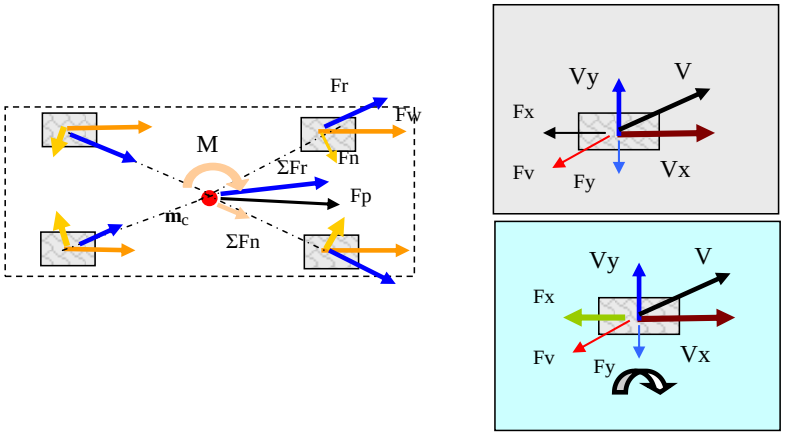

Figure 3. Forces acting for the vehicle

We can see that the sum of forces depends on a wheel dislocation and forces under wheel. When dislocation is symmetric and forces are equal the resultant force acts forward, in other cases can act in various directions.

According to this analyses, sharing the propelling force among axles we can affect the vehicle's movement direction.

A pneumatic tire is the crucial element in the cooperation of a vehicle with a road. Most of commonly used models are based on empirical experiments and observations, often without theoretical rules. The simplest model of propelling force generation is occurring between a tire and a pavement described with eq.1 and this force depends on slip *s [8,9,10,11,12,13,14,15,16]*.

$$F(s) = N \bullet \mu(s) \tag{1}$$

where: ***F*** – propelling force,

N – load (weight of a vehicle),

μ(s) – friction coefficient depending on slip

Slip does not have any physical representation – it is not possible to measure it and is defined as a result of a mathematical operation:

$$s = 1 - \frac{V}{V_t} \tag{2}$$

where: ***V*** – real velocity of a vehicle,

V_t – theoretical velocity (peripheral speed of wheel)

Thus range of the slip for the wheel changes, as said earlier, in the ranges $-\infty < s < 0$ for braking and

$0 < s < 1$ for propelling.

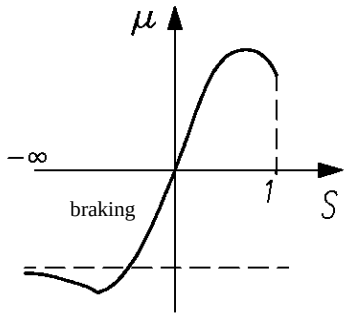

Figure 4. Diagram of the wheel's slip as a function of the propelling force coefficient *[25]*

One of the most common wheel models was developed by Hanse. This model is called “the magic formula”. It is written in form:

$$F(s) = d \bullet sin\{c \bullet arctan[b \bullet (1-e) \bullet k + e \bullet arctan(b \bullet k)]\}. \quad (3)$$

Where***:*** ***F(s)*** is the propelling force that depends on s (slip),

b, c, d and ***e*** that represent fitting parameters.

In the paper Miroslaw T Zebrowski Z “The Vehicle Tire Model Based on Energy Flow [27] the multi-layer model of wheel cooperation with ground were presented. The vehicle propelling force is a result of tyre friction on the road surface. This friction force can be modelled with Columbus model. This force is flowing to the vehicle through deformed by this force tyre. The Colobus model is applied for forces lower than critical – attrition force, which above the force is approximately constant.

So, one of the main part of this model is road surface. When we are talking about off road vehicles we have to consider such surfaces like: sand, mud which are movable, deformable and compactable [17, 18, 19].

For cooperation of wheel with ground the cellular model was developed.

The ground was divided into cubes (figure 5). These cubes of constant mass are replaced, deformed and compacted under pressure of wheel. The wheel acts on cube with vertical load and horizontal force of friction of rotating wheel. The deformed or moved cube reacts with others neighbouring cubes deforming them or by friction forces (figure 5).

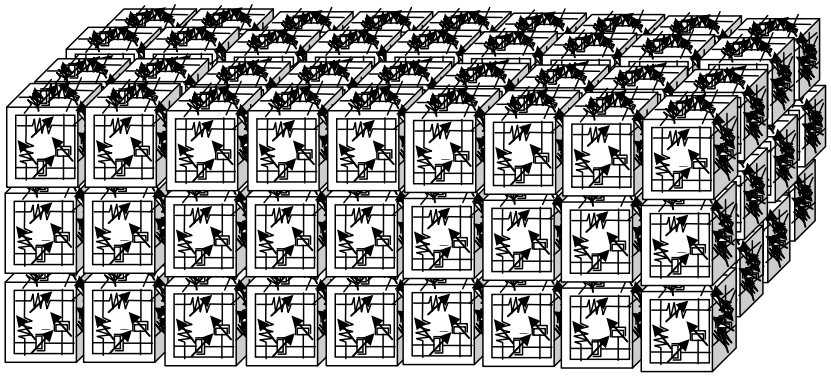

Figure 5. Concept of cellular ground model

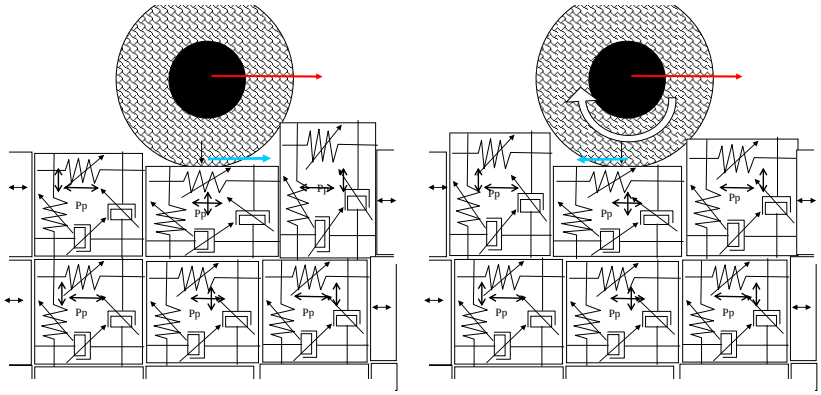

Figure 6. Ground reaction model for wheel load and movement.

According to this analyses, sharing the propelling force among axles we can affect the vehicle's movement direction.

Based on above assumption computer model was built in MATLAB/SIMULIK software.

5. Model description

The general model is presented in figure 7. It consists of a wheel – ground model (green blocks), electric motors (cyan blocks) control unit (yellow block), vehicle kinetics (blue block) external forces (orange block) responsible for gravity, wind and air speed resistance.

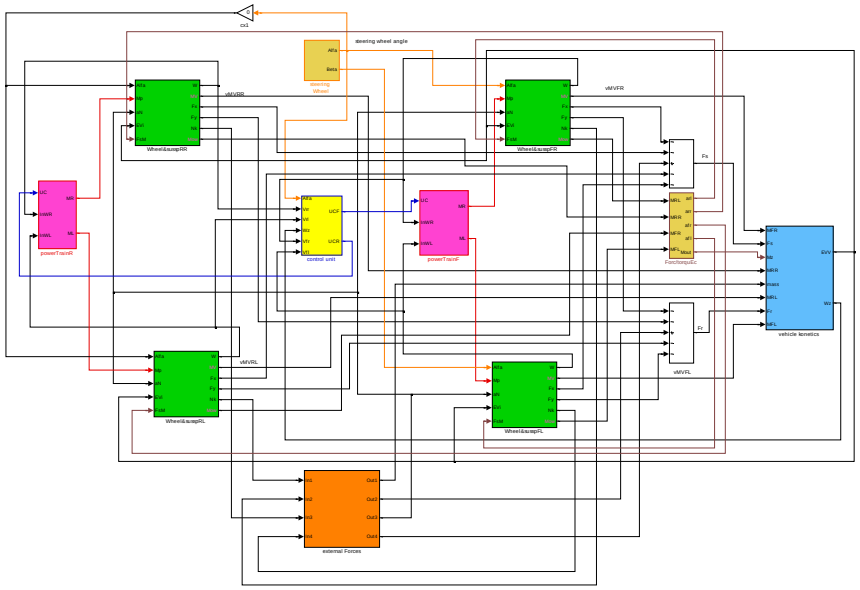

Figure 7. General view of vehicle model in Matlab/Simulink

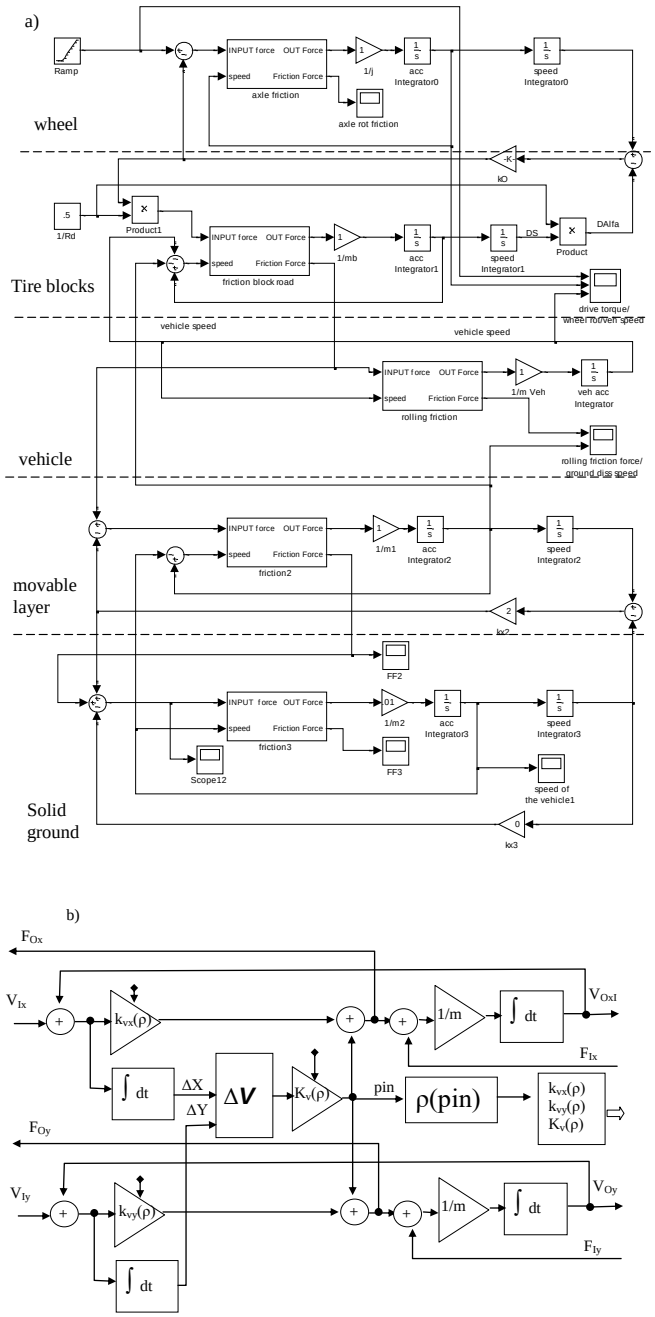

Figure 8. The schema of model a) multi-layer model of wheel ground system b) model of cell (cubic) of ground.

The most interesting part of the model is the wheel –ground. It is presented in figure 8 and 9.

In “wheel and suspension” model we have the block of wheel parameters and dimensions where it's dimension, location in reference to mass centre and friction parameter are declared.

Block of force and torque calculation where force and torques values presented in global reference system are recalculated to the reference system joined with vehicle and wheels. It is necessary because the direction of speed and force can be different especially when car rotates.

The crucial block is the wheel-ground block presented in figure 8a. In this model system of power transmission from wheel to ground is presented as the layers which the forces are passing through. The layer of ground is modelled with cellular model. The displacement caused by wheel load or pressure of neighbouring cell effects in cell displacement, or increasing internal pressure which acts in all direction. The pressure together with external forces causes the cell deformation. When this pressure is too high (overcome the critical value) the ground is transformed to next stage (is compacted) and change its properties represented by coefficients or flexibility and internal damping.

The model was tested for several combinations of drive structures and control algorithms. It was tested as the one axle front and rear drive, two axle drives with different rotation speed depending on the ground. The vehicle was moving on sandy surface and climbing top and down the hill of sand.

Tested scenarios are presented in figure 9.

6. The result discussion

For terrain the more effective one axle dive is the front wheel drive especially on soft surface, because the front wheel works as the compactor of ground. IF front wheels are pushed, they can lift up the ground barrier and the resistance of vehicle movement is bigger. In the worst case it can cause the digging in the front axle.

For tow axle drive we can change the movement resistance by differing the wheel rotation speeds. For very soft ground the higher speed of front wheel improve the traction, but in some cases it can destroy the ground and work in opposite way.

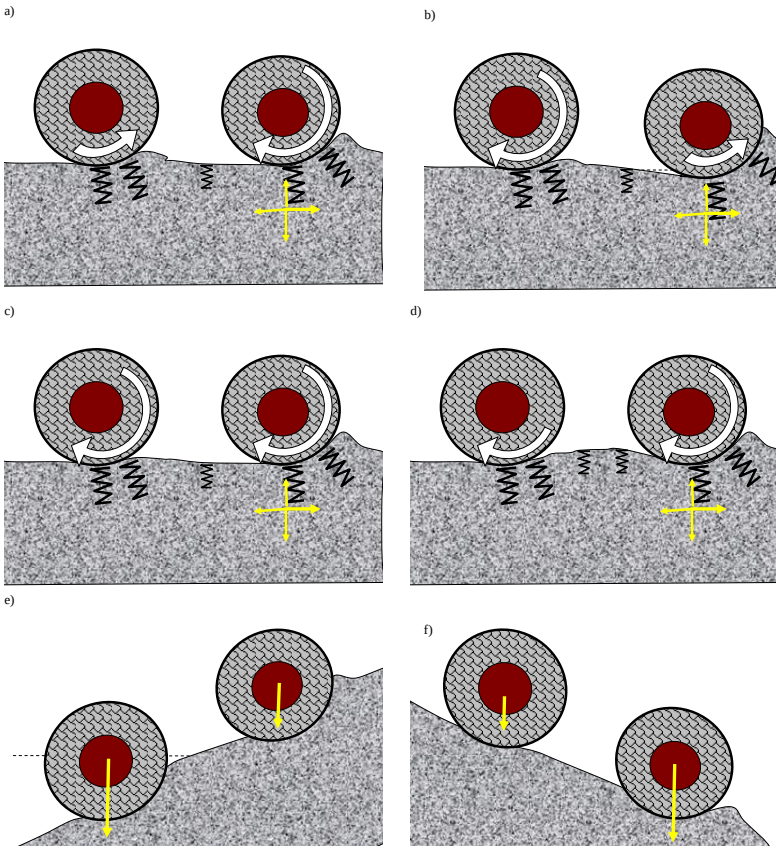

Figure 9. e visualization tested scenarios a) front wheel drive b) rear wheels drive, c) tow axle drive with the same speed d) two axle drive with different speed. e) ride up the sandy hill, the schema of model f) ride down the sandy hill.

7. Conclusion

The presented concept of 4-wheel drive electric SUV developed under Plus MOBY EU project proposed FEVS and POLEVS seems to be quite attractive solution for off road transport.

The separate driving system gives new possibilities of traction control of various surfaces.

The separated drive make easier realization of ABS and ESP functions.

The disadvantage of proposed modeling is the computational time. Presented model of a whole vehicle can't work in real time on a car-embedded computer.

After additional tests the model will be optimized for real time application. Probably the real measurement data coming from real vehicle (not calculated in model) will allow to speed up regulator calculation.

References

[1] Roth, Hans (March 2011). Das erste vierrädrige Elektroauto der Welt [The first four-wheeled electric car in the world] (in German). pp. 2–3.

[2] Jump up to: a b Guarnieri, M. (2012). "Looking back to electric cars". Proc.

[3] HISTELCON 2012 - 3rd Region-8 IEEE HISTory of Electro - Technology CONference: The Origins of Electrotechnologies: #6487583. doi:10.1109/HISTELCON.2012.6487583.

[4] Chronologia wydarzeń w upowszechnianiu samochodu elektrycznego. W: Grażyna Jastrzębska: Odnawialne źródła energii i pojazdy proekologiczne. Warszawa: Wydawnictwa Naukowo-Techniczne, 2007, s. 155. ISBN 978-83-204-3250-3

[5] History of Hybrid Vehicles, hybridcars.com, 14 June 2011

[6] Pacejka H. B.: Tyre and vehicle dynamics (2nd ed.). SAE International. (2006).

[7] Pieniążek W.: Obiektywne i subiektywne badania eksperymentalne samochodu osobowego podczas podwójnej zmiany pasa ruchu. Zeszyty instytutu Pojazdów. 2(20)/96

[8] Pokorski J., Szwabik B.: Zmienność współczynnika przyczepności w przekroju poprzecznym i podłużnym drogi. Zeszyty Naukowe Instytutu Pojazdów, 1(40)2001

[9] Bekker M., 1969.: Introduction to terrain-vehicle systems. Michigan Press, An Arbor, USA

[10] Bakker, E. ; Nyborg, L. ; Hans B. Pacejka H. B.: Tyre modelling for use in vehicle dynamics studies 1987 Jan. Society of Automotive Engineers, Warrendale, PA.

[11] Goriaczkin B.P.: "Theory of Wheel", Moscow 1937.

[12] Grečenko A.: Einflüsse auf die Kraftübertragung von Ackerschlepperreifen. Agrartechnische Kolloquium, Hohenheim, 1989.

[13] Gurkan Erdogan, Tire modelling Lateral and longitudinal Tire Forces Aprill 27, 2009.

[14] Jakliński L., 1999. „Models of pneumatic wheel effecting on the soil" the scientific work Warsaw University of Technology Mechanics edition 175.

[15] Kutzbach D., 1982. Ein Beitrag zur Fahrmechanik der Ackerschleppers-Reifenschlupf, Schleppermasse und Flächenleistung. Grundladen Landtechnik Bd. 32(2).

[16] Mirosław T., Żebrowski Z.: „The steering of front drive switching for wheeled Tractors" Mechanical Review 1'01.

[17] Mirosław T., Żebrowski Z.: "Modelling and Simulation of Tractor Differential Mechanism.; „Mechanical Review" 6'2013.

[18] Pacejka H. B.: The wheel shimmy phenomenon: A theoretical and experimental investigation with particular reference to the nonlinear problem (Analysis of shimmy in pneumatic tires due to lateral flexibility for stationary and no-stationary conditions), Ph.D. Thesis, Delft University of Technology, Delft, 1966.

[19] Pacejka H. B.: Tire and Vehicle Dynamics, Butterworth-Heinemann, Oxford, 2002.

[20] Pacejka H., 2004.: Tyre and Vehicle Dynamics. Elsevier Press

[21] Prochowski L., 2004. "Mechanics of movement" Care Vehicles edition, WKiŁ Warsaw

[22] Pytka J. "Theoretical experimental Study of drive on flexible surface" Lublin Universi-ty of Technology Edition. Lublin 2011

[23] Renius K.T.: Traktoren: Technik und ihre Anwendung. Aufb. – München: BLV Verlagsgesellschaft. Frankfurt (Mein)1987.

[24] Schreiber M., Kutzbach H.D., 2007. Comparison of different zero-slip definitions and a proposal to standardize tire traction performance. J. Terramechanics 44.

[25] Zebrowski Z.: The Methodology of wheeled tractor work automation. Scientific Works of Warsaw University of Technology. Mechanics Edition 256 Warsaw 2013

[26] Reimpell J, Betzler J.: Podwozia samochodów. Podstawy konstrukcji. WNT

[27] Miroslaw T Zebrowski Z "The Vehicle Tire Model Based on Energy Flow" Springer Proceedings in Mathematics & Statistics 184 Volumes from 2012 – 2017

Tomasz Miroslaw Ph.D. (Assistant Professor) Warsaw University of Technology Faculty of Automotive and construction Machinery. Institute of construction Machinery Engineering. 84 Narbutta str. 02-524 Warsaw POLAND (tmiroslaw@simr.pw.edu.pl)

Jan Szlagowski Prof. (Professor) Warsaw University of Technology Faculty of Automotive and construction Machinery. Institute of construction Machinery Engineering. 84 Narbutta str. 02-524 Warsaw POLAND (jan.szlagowski@simr.pw.edu.pl)

Adam Zawadzki MSc Eng. (Teaching Assistant) Warsaw University of Technology Faculty of Automotive and construction Machinery. Institute of construction Machinery Engineering. 84 Narbutta str. 02-524 Warsaw POLAND (azawadzki@simr.pw.edu.pl)

Zbigniew Żebrowski Ph.D.. (Professor) Warsaw University of Technology Faculty of Automotive and construction Machinery. Institute of construction Machinery Engineering. 84 Narbutta str. 02-524 Warsaw POLAND (zbigniew.zebrowski@simr.pw.edu.pl)

Nonlinear analysis of rotors with rigid coupling misalignment

Airton Nabarrete, Vinicius Yoshida de Melo, José Manoel Balthazar, Angelo Marcelo Tusset

Abstract: Most rotating machinery consists of a driver coupled to a driven system through mechanical couplings. In these, angular and parallel misalignments of shafts are common with more or less degree due to system assembly or maintenance proceedings. Several mechanical couplings can be present in a long shaft-line and the misalignment between connected shafts causes vibration to the holy assembly. In the literature, theoretical and experimental analyses were published in order to demonstrate the stability and misalignment effects on a rotor system. In this work, the misalignment of a rigid coupling is analyzed and highlighted to give the diagnostic information. The bifurcation analysis of the problem considers the nonlinear damping and stiffness of the journal bearings. The finite element model of the shaft-line considers the Timoshenko beam theory. The nonlinear behavior of the journal bearings is analyzed as function of the periodical change of the bearing load after adding a significant level of coupling misalignment. Nonlinear oil-film forces and their Jacobians are calculated simultaneously. The analysis of the unstable periodic orbit and the period-doubling orbit is performed for the center of the rotor at the bearing station.

1. Introduction

Misalignment is a common disturbance source of vibrations in rotor systems. The misalignment of the machinery shafts generates reaction forces and moments that affect the behavior of the journal bearings. A total modeling of the motor and the driver shaft, flexible coupling and the rotor was performed by Xu & Marangoni [1] using the method of component mode synthesis. Two rotor segments with angular misalignment were considered by Al-Hussain [2], where a flexible coupling was used to connect both rotor segments having each one mounted on two hydrodynamic bearings. Sekhar & Prabhu considered standard parallel and angular misalignments at the coupling locations [3] and a higher order finite element model was introduced to evaluate the force and moment due to misalignment. They showed the presence of the second order harmonic in response by performing a linear finite element analysis. Penacchi et al. studied the ratios between higher order harmonic components and synchronous vibrations and observed that superharmonic components are the most remarkable nonlinear effects caused by coupling misalignment in rotors [4].

Many literatures reported the typical nonlinear vibration phenomena caused by oil-film instability, such as the occurrence of rotor lateral self-excited vibrations like whirl, whip and instability that arises from the presence of nonlinear fluid and contribute to unstable operation of the system, high-level vibration and potential damage of the rotating machinery [5]. Adiletta et al. studied the nonlinear behavior with the chaotic motions of a rigid rotor in short journal bearings [6]. Jing et al. considered the nonlinear model proposed by Capone to analyze the nonlinear dynamic behavior of bearings, taking into account the oil-whip phenomenon [7]. Wang et al. analyzed the bifurcation behavior of a flexible rotor supported by two fluid-film journal bearing [8]. De Castro et al. studied whirl and whip instabilities in rotor-bearing system considering a nonlinear force model [9].

The nonlinearity of the bearing-rigid rotor system arises from the oil film forces acting on the bearing. Although nonlinear oil film forces act locally, at any single point, on the rotor, their effects are global due to the general coupling of all system. Nonlinear dynamic behaviors of a large flexible rotor system can be obtained by implicit or explicit numerical methods, as well as, the stability and bifurcation type of periodic responses of the system. In this paper, the model of a continuous rotor system which incorporates a misaligned coupling element is presented. It is assumed that both the angular and parallel misalignments are present in the coupling location.

2. Modeling of the rotor-bearing system

2.1. The finite element model of the rotor with coupling

In rotor systems, the shafts can be modeled as a continuous beam with distributed mass, stiffness and damping. In this work, the shaft is considered to turn in different rotational speeds and lateral vibrations can appear. The Timoshenko beam theory is used to formulate the finite element model of the shaft. It includes the effect of inertia for the beam section rotation and the shear deformation.

The rotor-bearing system is composed by two or more rotor segments connected by a rigid coupling and is supported by oil-lubricated bearings. In order to study the rotor-bearing-coupling system, the FE model of the rotor is formulated considering only the flexural deformations. Therefore, axial and torsional deformations are neglected.

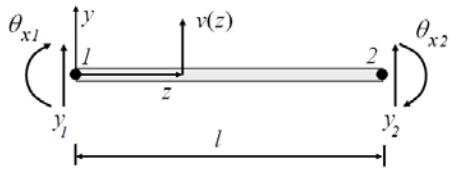

Figure 1. Timoshenko finite element description for the orthogonal plane *y*-*z*.

In the FE model, each node has four degrees of freedom, or two degrees of freedom for each orthogonal plane, as depicted in the Fig. 1. The general displacement vector $\mathbf{q}^e$ is then expressed as

$$\mathbf{q}^e = \begin{bmatrix} x_1 & \theta_{y1} & y_1 & \theta_{x1} & x_2 & \theta_{y2} & y_2 & \theta_{x2} \end{bmatrix} \tag{1}$$

where the superscript e stands for element number.

The coupling connecting two shaft segments is modeled as a lumped mass element which is superimposed upon the corresponding shaft node. Both, mass and polar moments of inertia of the coupling are considered. In this work it was considered the addition of the effect of the gyroscopic moment to the FE model. Also the nonlinear oil-film forces, the forces and bending moments caused by the rigid coupling misalignment and the rotor weight are considered in the FE model. Then, dynamic equations of the rotor-bearing-coupling system are written as

$$\mathbf{M}\ddot{\mathbf{q}} + \left(\dot{\varphi}\mathbf{G} + \mathbf{C}\right)\dot{\mathbf{q}} + \mathbf{K}\mathbf{q} = \mathbf{F}_b + \mathbf{F}_{coupl} + \mathbf{W} \tag{2}$$

where $\mathbf{M}, \mathbf{K}, \mathbf{C}$ and $\mathbf{G}$ are the mass, stiffness, damping and gyroscopic finite element matrices, considering the Timoshenko beam elements and couplings. $\mathbf{q}$ denotes the global displacement vector. $\dot{\varphi}$ represents the operational speed of the rotor. $\mathbf{F}_b$, $\mathbf{F}_{coupl}$ and $\mathbf{W}$ are respectively, the nonlinear oil-film force vector, the excitation force vector due to misalignment of the rigid coupling, and the vector related to the shaft weight in *y* direction.

2.2. Nonlinear forces of hydrodynamic bearing

The required nonlinear oil-film forces shall be calculated as an iterative process when the nonlinear dynamic responses of the system are solved. The accuracy of nonlinear oil-film forces and their derivatives affects not only the convergence of the dynamic numerical solutions, but also the analysis of stability and bifurcation.

A short journal-bearing scheme is considered. The calculation of the nonlinear hydrodynamic forces of the cylindrical journal bearing is performed by solving the simplified Reynolds equation described as

$$\left(\frac{R}{L}\right)^2 \frac{\partial}{\partial z}\left(h^3 \frac{\partial p}{\partial z}\right) = \frac{\partial h}{\partial \varphi} + 2\frac{\partial h}{\partial \tau} \tag{3}$$

where p is the oil film pressure, h is the oil film thickness, φ is the circumferential angle, z is the axial coordinate of calculation, $\tau = \dot{\varphi} t$ is the dimensionless time. The necessary bearing parameters are radial clearance C, bearing length L, bearing radius R and oil viscosity μ.

Considering the finite element method to solve Eq. 3, the distribution of pressures of the oil-film field around the journal of the bearing is calculated. It is necessary to consider the imposed variational inequalities for nonlinear problems like elastic contact, fluid lubrication, etc. For fluid lubrication of the finite length journal bearing with the Reynolds boundary, the solution must satisfy certain restricted requirements in the solution domain. In this work, if negative values are calculated for the pressure distribution of the oil film (cavitation) in the iterative process, a restriction of null values (no cavitation) is applied.

The circumferential surface is meshed by finite elements and for each node the pressure p_k is calculated. Considering the n interpolation functions L_k, the pressure p of the oil-film is

$$p = \sum_{k=1}^{n} p_k L_k \tag{4}$$

The vector of nonlinear bearing forces $\mathbf{F}_b$ has two orthogonal components, considering the plane x-y of the journal section, as follows

$$\mathbf{F}_b = \begin{pmatrix} F_{bx} \\ F_{by} \end{pmatrix} = \begin{pmatrix} f_x\left(x, y, \dot{x}, \dot{y}\right) \\ f_y\left(x, y, \dot{x}, \dot{y}\right) \end{pmatrix} = -\begin{pmatrix} \iint_\Omega p\left(x, y, \dot{x}, \dot{y}\right)\sin(\varphi) d\Omega \\ \iint_\Omega p\left(x, y, \dot{x}, \dot{y}\right)\cos(\varphi) d\Omega \end{pmatrix} = \begin{pmatrix} \sum_{k=1}^{n} p_k u_k \\ \sum_{k=1}^{n} p_k v_k \end{pmatrix} = \begin{pmatrix} \mathbf{U}^{\mathrm{T}}\mathbf{p} \\ \mathbf{V}^{\mathrm{T}}\mathbf{p} \end{pmatrix} \tag{5}$$

where, considering $\mathbf{L}$ as the vector of n interpolation functions,

$$\mathbf{U} = -\iint_\Omega \mathbf{L}\sin(\varphi) d\Omega \ , \quad \mathbf{V} = -\iint_\Omega \mathbf{L}\cos(\varphi) d\Omega \tag{6}$$

The Jacobians of oil film forces $f_x\left(x, y, \dot{x}, \dot{y}\right)$ and $f_y\left(x, y, \dot{x}, \dot{y}\right)$ with respect to the journal displacements x, y and velocities $\dot{x}$, $\dot{y}$ are calculated firstly, and the computational cost spent on the Jacobians is much less than those spent on the oil film forces themselves. The vector of the nonlinear bearing forces $\mathbf{F}_b$ of the journal located at the respective i^{th} rotor node is evaluated as

$$\begin{pmatrix} f_x\left(x_i, y_i, \dot{x}_i, \dot{y}_i\right) \\ f_y\left(x_i, y_i, \dot{x}_i, \dot{y}_i\right) \end{pmatrix} = \begin{bmatrix} \mathbf{U}^{\mathrm{T}}\frac{\partial \mathbf{p}}{\partial x} & \mathbf{0} & \mathbf{U}^{\mathrm{T}}\frac{\partial \mathbf{p}}{\partial y} & \mathbf{0} \\ \mathbf{V}^{\mathrm{T}}\frac{\partial \mathbf{p}}{\partial x} & \mathbf{0} & \mathbf{V}^{\mathrm{T}}\frac{\partial \mathbf{p}}{\partial y} & \mathbf{0} \end{bmatrix} \begin{Bmatrix} x_i \\ \theta_{yi} \\ y_i \\ \theta_{xi} \end{Bmatrix} + \begin{bmatrix} \mathbf{U}^{\mathrm{T}}\frac{\partial \mathbf{p}}{\partial \dot{x}} & \mathbf{0} & \mathbf{U}^{\mathrm{T}}\frac{\partial \mathbf{p}}{\partial \dot{y}} & \mathbf{0} \\ \mathbf{V}^{\mathrm{T}}\frac{\partial \mathbf{p}}{\partial \dot{x}} & \mathbf{0} & \mathbf{V}^{\mathrm{T}}\frac{\partial \mathbf{p}}{\partial \dot{y}} & \mathbf{0} \end{bmatrix} \begin{Bmatrix} \dot{x}_i \\ \dot{\theta}_{yi} \\ \dot{y}_i \\ \dot{\theta}_{xi} \end{Bmatrix} \tag{7}$$

3. Modeling of rigid coupling misalignment

The term angular misalignment is easily understood in the literature, although the term offset is not always clear and correct as used [4]. Related to the misalignment concept, offset does not represent the distance between two parallel shafts not coaxial, which could be understood as fixed in the space. Offset occurs when there is a wrong static alignment between the two rotors to be coupled, many times due to the flanges that are wrongly machined and have wrong distributed bolt holes. In this case, when both flanges are mounted a radial rotating misalignment is imposed. As a consequence, it is necessary to take into account the effect of rigid coupling misalignment on the static centerline and consider that the reaction forces of the bearing are changing owing to the rotation of the shaft, or in other words, to the orientation of the misalignment with respect to the phase reference.

In the finite element model of the connected shafts, the mounted coupling flanges are represented in the connection node between both shaft segments. Looking for imperfections in this coupling one possible representation of an imperfect machining causing angular and radial misalignments is drafted schematically in Fig. 2(a) and a wrong mounting of the coupling flanges in Fig. 2(b).

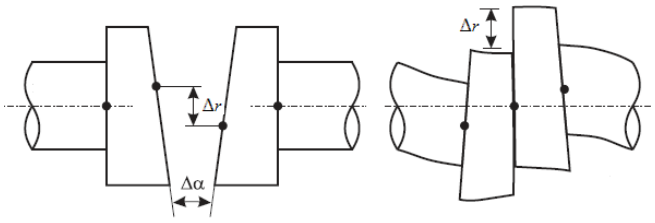

(a) (b)

Figure 2. (a) Draft with angular and radial measurements of the flange faces considering the same plane of reference; (b) Correspondent wrong mounting for the coupling.

The front draft views represented in Fig. 2(a) and Fig.2(b) are too much simplified and cannot give the idea of all possibilities for the imperfect machining or the wrong mounting of the flanges. The machining of one flange of the coupling is not necessarily executed together with the other one. Then it is possible to have bolt holes machined in any axial angle when comparing one flange to the other. Therefore, not only the magnitudes of these misalignments have to be considered, but also the possibility of a relative angle between the maximum radial misalignment direction and the direction of maximum $\Delta\alpha$. Considering the fact that the shaft is rotating with a rotational speed, a relative phase with respect to the phase reference is recommended for the formulation of each misalignment.

Then radial and angular misalignments are conveniently formulated to impose the generalized displacements $\Delta\mathbf{q}_{coupl}$, which are function of the angular position $\theta = \dot{\varphi} t$ of the shaft as follows

$$\Delta\mathbf{q}_{coupl}(\theta) = \Delta\mathbf{q}_{coupl}(\dot{\varphi}\, t) = \begin{bmatrix} 1 & 0 \\ 0 & i \\ i & 0 \\ 0 & 1 \end{bmatrix} \begin{Bmatrix} \Delta r e^{i\phi_r} \\ \Delta\alpha e^{i\phi_\alpha} \end{Bmatrix} e^{i\dot{\varphi} t} \tag{8}$$

The imposed generalized displacements cause static reactions $\mathbf{R}(\theta)$ on the bearings that can be calculated by the static equilibrium of the free-body composed by shaft segments and coupling as

$$\mathbf{R}(\theta) = \mathbf{K}\left(\mathbf{q} + \Delta\mathbf{q}_{coupl}(\theta)\right) + \mathbf{W} = \mathbf{K}\,\mathbf{q} + \mathbf{F}_{coupl}(\theta) + \mathbf{W} \tag{9}$$

where $\mathbf{F}_{coupl}(\theta)$ is the equivalent force vector due to the coupling misalignment. For the free-body shaft-coupling, the weight force is

$$\mathbf{W} = \mathbf{M}\{-g \quad 0 \quad 0 \quad 0 \quad \ldots \quad -g \quad 0 \quad 0 \quad 0\}^{\mathrm{T}} \tag{10}$$

The static reactions are then calculated considering the partitioning of the stiffness matrix and re-ordering the degrees of freedoms of the nodes and grouping the free and the constrained ones as

$$\begin{Bmatrix} \mathbf{0} \\ \mathbf{R}(\theta) \end{Bmatrix} = \begin{bmatrix} \mathbf{K}_{ff} & \mathbf{K}_{fc} \\ \mathbf{K}_{cf} & \mathbf{K}_{cc} \end{bmatrix} \begin{Bmatrix} \mathbf{q}_f \\ \mathbf{q}_c \end{Bmatrix} + \begin{Bmatrix} \mathbf{W}_f \\ \mathbf{W}_c \end{Bmatrix} + \begin{Bmatrix} \mathbf{F}_{coupl_f}(\theta) \\ \mathbf{0} \end{Bmatrix} \tag{11}$$

where $\mathbf{F}_{coupl_c}(\theta) = \mathbf{0}$, because the coupling is not in the same position of bearings.

Firstly by Eq. 11 the static free displacements of the rotor shall be solved as function of its angular position θ. Then the reactions on the bearings are calculated. Due to the presence of the coupling misalignment, these bearing reactions have generally both *x* and *y* components which are *1*x periodical.

4. Dynamical behavior of the rotor-bearing-coupling system

The dynamic model of the rotor-bearing-coupling system at the operating speed is performed including the dynamic characteristics of the rotor shaft, the nonlinear hydrodynamic forces acting on the journals at the bearing positions $\mathbf{F}_b$, the static weight of the system $\mathbf{W}$ and the equivalent forces due to the coupling misalignments $\mathbf{F}_{coupl}$. Finally the equations of motion are rewritten as

$$\mathbf{M}\ddot{\mathbf{q}} + \left(\dot{\varphi}\mathbf{G} + \mathbf{C}\right)\dot{\mathbf{q}} + \mathbf{K}\mathbf{q} - \mathbf{F}_b(\mathbf{q}, \dot{\mathbf{q}}) = \mathbf{F}_{ext} = \mathbf{F}_{coupl} + \mathbf{W} \tag{12}$$

The dynamic response is calculated considering the nonlinear equations of motion. At any time t the accelerations may be solved in terms of the displacements, velocities, and the applied forces. Given values for accelerations, velocities, displacements and applied forces at time t_i, if it is possible to extrapolate the velocities and displacements forward in time by a time step Δt to time $t_{i+1} = t_i + \Delta t$, then the acceleration $\ddot{\mathbf{q}}$ for the time t_{i+1} can be computed by manipulating Eq. 12.

Typically, responses of the highest vibration modes of a numerical model are physically meaningless, insignificantly small, but potentially lightly damped. However, the shortest natural period governs the stability of numerical integration methods. The explicit numerical integration methods can artificially add numerical damping to suppress instabilities with the higher vibration mode responses while the implicit numerical methods can be unconditionally stable.

The Newmark method is used in this work for solving the nonlinear equations numerically. This implicit method is quite popular for the numerical integration of linear equations of motion in structural dynamics [10]. However the nonlinear behavior of the system brings some known difficulties for implicit methods. Note that since differentiation amplifies high frequencies of the dynamic model, changes in $\mathbf{q}$ and $\dot{\mathbf{q}}$ from t_i to t_{i+1} will be much smoother than the corresponding changes in $\ddot{\mathbf{q}}$. It is not sufficient to consider the equilibrium for each time step of calculation, but the differential equilibrium of the system in the form

$$\mathbf{M}\,\Delta\ddot{\mathbf{q}}^i + \left(\dot{\phi}\mathbf{G} + \mathbf{C}\right)\Delta\dot{\mathbf{q}}^i + \mathbf{K}\,\Delta\mathbf{q}^i - \Delta\mathbf{f}_{nl}^i = \Delta\mathbf{F}_{ext}^i \tag{13}$$

where the finite difference relationships are

$$\begin{aligned}
\Delta\mathbf{f}_{nl}^i &= \mathbf{F}_b\left(\mathbf{q}^{i+1}, \dot{\mathbf{q}}^{i+1}\right) - \mathbf{F}_b\left(\mathbf{q}^i, \dot{\mathbf{q}}^i\right) = \mathbf{F}_b\left(\mathbf{q}^i + \Delta\mathbf{q}^i, \dot{\mathbf{q}}^i + \Delta\dot{\mathbf{q}}^i\right) - \mathbf{F}_b\left(\mathbf{q}^i, \dot{\mathbf{q}}^i\right) \\
\Delta\ddot{\mathbf{q}}^i &= \ddot{\mathbf{q}}^{i+1} - \ddot{\mathbf{q}}^i \\
\Delta\dot{\mathbf{q}}^i &= \dot{\mathbf{q}}^{i+1} - \dot{\mathbf{q}}^i \\
\Delta\mathbf{q}^i &= \mathbf{q}^{i+1} - \mathbf{q}^i
\end{aligned} \tag{14}$$

Also, the incremental acceleration and velocity are evaluated as

$$\begin{aligned}
\Delta\ddot{\mathbf{q}}^i &= \frac{1}{\beta\,\Delta t^2}\Delta\mathbf{q}^i - \frac{1}{\beta\,\Delta t}\dot{\mathbf{q}}^i - \frac{1}{2\beta}\ddot{\mathbf{q}}^i \\
\Delta\dot{\mathbf{q}}^i &= \frac{\gamma}{\beta\,\Delta t}\Delta\mathbf{q}^i - \frac{\gamma}{\beta}\dot{\mathbf{q}}^i + \Delta t\left(1 - \frac{\gamma}{2\beta}\right)\ddot{\mathbf{q}}^i
\end{aligned} \tag{15}$$

The substitution of Eq. 15 into Eq. 13, then re-grouping terms and solving for the increment in displacements, it follows

$$\left[\frac{1}{\beta\,\Delta t^2}\mathbf{M}+\frac{\gamma}{\beta\,\Delta t}\left(\dot{\varphi}\mathbf{G}+\mathbf{C}\right)+\mathbf{K}\right]\Delta\mathbf{q}^i=\left[\frac{1}{\beta\,\Delta t}\mathbf{M}+\frac{\gamma}{\beta}\left(\dot{\varphi}\mathbf{G}+\mathbf{C}\right)\right]\dot{\mathbf{q}}^i$$
$$+\left[\frac{1}{2\beta}\mathbf{M}-\Delta t\left(1-\frac{\gamma}{2\beta}\right)\left(\dot{\varphi}\mathbf{G}+\mathbf{C}\right)\right]\ddot{\mathbf{q}}^i+\Delta\mathbf{f}_{nl}^i+\Delta\mathbf{f}_{ext}^i \tag{16}$$

The incremental displacement $\Delta\mathbf{q}^i$ is then obtained from Eq. 16 as follows

$$\Delta\mathbf{q}^i=\hat{\mathbf{K}}^{-1}\left(\hat{\mathbf{C}}\,\dot{\mathbf{q}}^i+\hat{\mathbf{M}}\,\ddot{\mathbf{q}}^i+\Delta\mathbf{f}_{nl}^i+\Delta\mathbf{f}_{ext}^i\right)=\hat{\mathbf{K}}^{-1}\,\hat{\mathbf{f}}^i \tag{17}$$

where

$$\hat{\mathbf{K}}=\left[\frac{1}{\beta\,\Delta t^2}\mathbf{M}+\frac{\gamma}{\beta\,\Delta t}\left(\dot{\varphi}\mathbf{G}+\mathbf{C}\right)+\mathbf{K}\right]$$
$$\hat{\mathbf{C}}=\left[\frac{1}{\beta\,\Delta t}\mathbf{M}+\frac{\gamma}{\beta}\left(\dot{\varphi}\mathbf{G}+\mathbf{C}\right)\right] \tag{18}$$
$$\hat{\mathbf{M}}=\left[\frac{1}{2\beta}\mathbf{M}-\Delta t\left(1-\frac{\gamma}{2\beta}\right)\left(\dot{\varphi}\mathbf{G}+\mathbf{C}\right)\right]$$

The dynamic system described in Eq. 2 has a local nonlinearity due to the not negligible nonlinear bearing force increment $\Delta\mathbf{f}_{nl}^i$. This fact is observed by the dependence of $\hat{\mathbf{f}}^i$ on the incremental displacement $\Delta\mathbf{q}^i$ and the incremental velocity $\Delta\dot{\mathbf{q}}^i$, as described in Eq. 14. The common Newmark method cannot obtain the response of the system at time t_{i+1} directly, but is possible to improve it. The prediction value for the next step can be taken as the initial value and then a correcting process is done by the Newton–Raphson method. Here, the Newton-Raphson algorithm is an efficient method to solve the Eq. 17, calculating the incremental displacement. The iterative algorithm proceeds as follows

1. The initial value for $\Delta\mathbf{q}^i$ is denoted $\Delta\mathbf{q}_0^i$ and is arbitrarily set to zero. The corresponding value for $\hat{\mathbf{f}}^i$ is

$$\hat{\mathbf{f}}^i\left(\Delta\mathbf{q}^i{}_0\right)=\Delta\mathbf{f}_{ext}^i+\hat{\mathbf{C}}\,\dot{\mathbf{q}}^i+\hat{\mathbf{M}}\,\ddot{\mathbf{q}}^i \tag{19}$$

2. The Newton-Raphson recurrence relation is simply

$$\Delta\mathbf{q}^i{}_{n+1}=\hat{\mathbf{K}}^{-1}\,\hat{\mathbf{f}}^i\left(\Delta\mathbf{q}^i{}_n\right) \tag{20}$$

where

$$\hat{\mathbf{f}}^{i}\left(\Delta\mathbf{q}^{i}{}_{n}\right)=\hat{\mathbf{f}}^{i}\left(\Delta\mathbf{q}^{i}{}_{0}\right)+\mathbf{F}_{b}\left(\mathbf{q}^{i}+\Delta\mathbf{q}^{i}{}_{n},\dot{\mathbf{q}}^{i}+\Delta\dot{\mathbf{q}}^{i}_{n}\right)-\mathbf{F}_{b}\left(\mathbf{q}^{i},\dot{\mathbf{q}}^{i}\right) \tag{21}$$

and

$$\Delta\dot{\mathbf{q}}^{i}_{n}=\frac{\gamma}{\beta\,\Delta t}\Delta\mathbf{q}^{i}{}_{n}-\frac{\gamma}{\beta}\dot{\mathbf{q}}^{i}+\Delta t\left(1-\frac{\gamma}{2\beta}\right)\ddot{\mathbf{q}}^{i} \tag{22}$$

3. Eq. 20 is iterated upon until the incremental displacement $\Delta\mathbf{q}^{i}$ converges, or $\left\|\Delta\mathbf{q}^{i}{}_{n+1}-\Delta\mathbf{q}^{i}{}_{n}\right\|<\varepsilon$, with ε representing the tolerance for the convergence.

The convergence of this form of the Newton-Raphson method depends on the local smoothness of $\mathbf{F}_{b}\left(\mathbf{q}^{i},\dot{\mathbf{q}}^{i}\right)$. Convergence can be improved, for a particular time step, by making Δt smaller.

After obtaining the solution for $\Delta\mathbf{q}^{i}$, the displacements and velocities are updated with

$$\begin{aligned}\mathbf{q}^{i+1}&=\mathbf{q}^{i}+\Delta\mathbf{q}^{i}\\ \dot{\mathbf{q}}^{i+1}&=\left(1-\frac{\gamma}{\beta}\right)\dot{\mathbf{q}}^{i}+\Delta t\left(1-\frac{\gamma}{2\beta}\right)\ddot{\mathbf{q}}^{i}+\frac{\gamma}{\beta\,\Delta t}\Delta\mathbf{q}^{i}\end{aligned} \tag{23}$$

The accelerations are updated with the Eq. 2 as

$$\ddot{\mathbf{q}}^{i+1}=\mathbf{M}^{-1}\left[\mathbf{F}_{b}\left(\mathbf{q}^{i+1},\dot{\mathbf{q}}^{i+1}\right)+\mathbf{F}_{ext}^{i+1}-\left(\dot{\phi}\mathbf{G}+\mathbf{C}\right)\dot{\mathbf{q}}^{i+1}-\mathbf{K}\mathbf{q}^{i+1}\right] \tag{24}$$

It is important to note that $\hat{\mathbf{K}}$ is positive definite and does not depend on $\Delta\mathbf{q}^{i}$. The matrices $\hat{\mathbf{K}}$ and $\mathbf{M}$ shall be inverted or factorized only once at the beginning of the simulation. The equilibrium of the nonlinear system is obtained by iteration with the Newton–Raphson method where the prediction value of the next step is taken as the initial values, and then the correcting process is implemented. The proposed method can improve the iteration convergence. The parameters β and γ of this improved Newmark method were considered in accordance to the linear acceleration method $\left(\beta=1/6,\gamma=1/2\right)$. With these Newmark parameters the numerical solution is unconditionally stable, as described by Chopra [11].

5. Numerical results

Nonlinear dynamic behaviors of the bearing-rotor system are analyzed by using the above methods. The rotor showed in Fig. 3 is composed by a flexible shaft, for which the density of mass is 7800 kg/m^3, the Young's elastic modulus is 206.7 GPa, the Poisson ratio is 0.3, the proportional damping to stiffness value is $25\text{x}10^{-5}$, the shaft length is 1.16 m and the shaft diameter is 0.02 m.

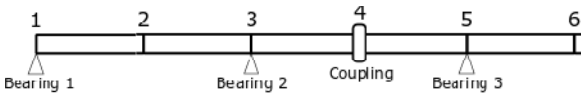

Figure 3. Two segments of rotors with a rigid coupling.

All the four cylindrical bearings have the same dimensions. The width is 14 mm and the internal diameter is 23 mm. In each one it is included a 360° pad. The clearance between journal and bearing is 6×10^{-4} m. The dynamic viscosity of oil film is 55×10^{-3} Pa.s.

5.1. Effect of radial and angular misalignment

Different combinations of radial and angular misalignment conditions of the rigid coupling have been analyzed. One simulation of the dynamic response of the rotor-bearing-coupling system is performed at the operating speed of 955 rpm, as depicted in Fig. 4. Fig. 4(a) and Fig. 4(b), represent the orbits of the journal near the first bearing, considering radial and angular misalignments, respectively.

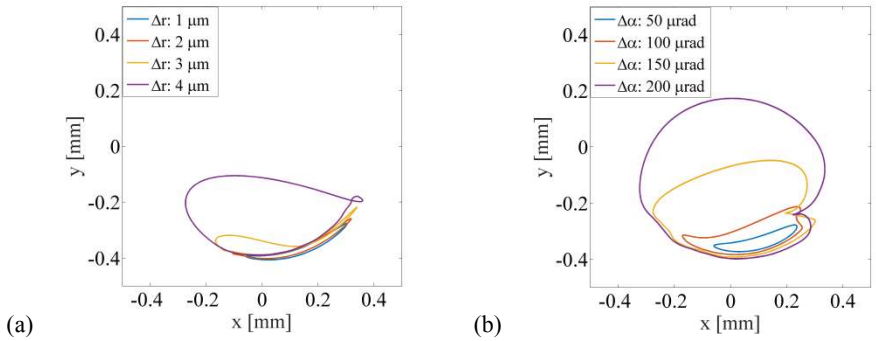

Figure 4. Radial (a) and angular (b) misalignment in bearing #1 with phase 0º, for $\dot{\varphi}$ = 100 rad/s.

5.2. Nonlinear analysis of the radial misalignment

The nonlinear behavior is better demonstrated with a bifurcation analysis as depicted in Fig. 5. The bifurcation diagram was obtained with the variation of the intensity of the radial misalignment considering the operating speed of 4775 rpm. In this diagram, one can observe different steady-state orbits for the shaft region near the first bearing. From the bifurcation analysis it is possible to see that an unstable periodic orbit of the centre of the shaft happens with $\Delta r = 3\ \mu m$, as demonstrated in Fig. 6(a). With $\Delta r = 4\ \mu m$ a period-doubling orbit is formed as depicted in Fig. 6(b). The quasi-periodic orbit of the centre of the rotor at the bearing station is depicted in Fig. 6(c), considering the radial

misalignment as $\Delta r = 10\ \mu m$. By increasing the radial misalignment with $\Delta r \geq 12\ \mu m$, the bifurcation occurs again, i.e. the quasi-periodic solution turns to periodic solution.

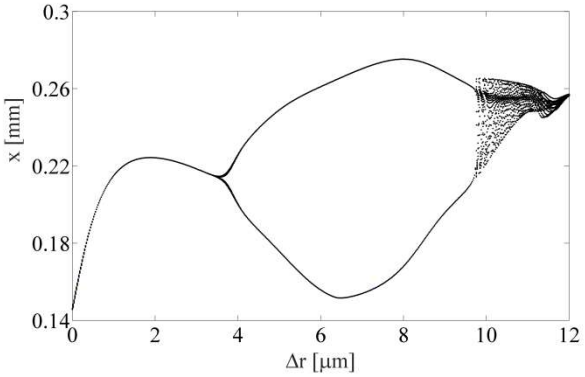

Figure 5. Bifurcation diagram for radial misalignment considering $\dot{\varphi}$ = 500 rad/s.

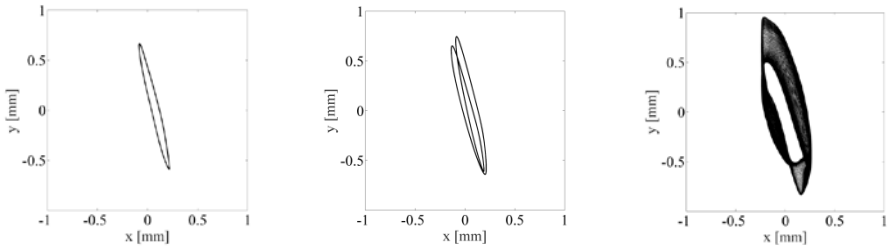

Figure 6. Phase diagrams for $\dot{\varphi}$ = 500 rad/s: (a) $\Delta r = 3\ \mu m$; (b) $\Delta r = 4\ \mu m$; (c) $\Delta r = 10\ \mu m$.

6. Conclusions

It is necessary to take into account the effect of rigid coupling misalignment on the reaction forces of the bearings, considering that these forces are changing owing to the rotation of the shaft, i.e. to the orientation of the misalignment with respect to the phase reference. In this work, the nonlinear responses of a rotor system due to the radial and angular misalignments in the rigid coupling were performed by an improved Newmark method, with a local iteration using the Newton–Raphson method. The proposed method is considered as unconditionally stable and had the iteration executed only on the degrees of freedom related to the nonlinear forces acting on the bearings. The nonlinear steady-state shaft orbits were obtained for different intensities of radial and angular misalignments and the bifurcation analysis was used to identify the complex nonlinear behaviors such as periodic, period-doubling and quasi-periodic.

Acknowledgments

The first author is grateful to the Fundação de Amparo à Pesquisa do Estado de São Paulo (FAPESP) for funding this research, grant no. 2015/20363-6.

References

[1] Xu, M. and Marangoni, R.D. 1994. Vibration analysis of a motor-flexible coupling-rotor system subject to misalignment and unbalance, Part I: Theoretical model and analysis. *Journal of Sound and Vibration* 176, 5 (1994), 663-679.

[2] Al-Hussain, K.M. Dynamic stability of two rigid rotors connected by a flexible coupling with angular misalignment. *Journal of Sound and Vibration* 266 (2003), 217-234.

[3] Sekhar, A. S. and Prabhu, B. S. Effects of coupling misalignment on vibrations of rotating machinery. *Journal of Sound and Vibration* 185, 4 (1995), 655-671.

[4] Pennacchi, P, Vania, A., Chatterton, S. Nonlinear effects caused by coupling misalignment in rotors equipped with journal bearings. *Mechanical Systems and Signal Processing* 30 (2012), 306-322.

[5] Muszynska, A. *Rotordynamics*. Taylor & Francis, Boca Raton, FL, 2005.

[6] Adiletta, G., Guido, A.R., Rossi, C. Chaotic motions of a rigid rotor in short journal bearings. Nonlinear Dynamics 10 (1996), 251-269.

[7] Jing, J., Meng, G., Sun, Y., Xia, S. On the non-linear dynamic of a rotor-bearing system. *Journal of Sound and Vibration* 274 (2004) 1031–1044.

[8] Wang, J.K., Khonsari, M.M. Bifurcation analysis of a flexible rotor supported by two fluid-film journal bearing. *Journal of Tribology* 128 (2006) 594–603.

[9] De Castro, H.F., Cavalca, K.L., Nordmann, R. Whirl and whip instabilities in rotor-bearing system considering a nonlinear force model. *Journal of Sound and Vibration* 317 (2008) 273–293.

[10] Bathe, K.-J. *Finite element procedures in engineering analysis.* Prentice-Hall, New Jersey, 1996.

[11] Chopra, A.K. Dynamics of Structures: Theory and applications to earthquake engineering. Prentice-Hall, New Jersey, 1995.

Airton Nabarrete, Professor: Aeronautics Technological Institute, Aerospace Engineering Division, Praça Marechal Eduardo Gomes 50, 12228-900 São José dos Campos, SP, Brazil (*nabarret@ita.br*). The author presents this paper during one of the conference sessions.

Vinicius Yoshida de Melo, Engineer (M.Sc. student): Aeronautics Technological Institute, Aerospace Engineering Division, Praça Marechal Eduardo Gomes 50, 12228-900 São José dos Campos, SP, Brazil (*yoshida190@gmail.com*).

José Manoel Balthazar, Professor: Aeronautics Technological Institute, Mechanical Engineering Division, Praça Marechal Eduardo Gomes 50, 12228-900 São José dos Campos, SP, Brazil (*josebaltha@gmail.com*).

Angelo Marcelo Tusset, PhD, Professor: Technological University of Paraná, Avenida Monteiro Lobato, 84016-210, Ponta Grossa, Paraná, PR, Brazil. (*tusset@utfpr.edu.br*)

Analysis of vibration effects on edge-chipping occurrence during rotary ultrasonics drilling

Milan Naď, Lenka Kolíková, Ladislav Rolník, Rastislav Ďuriš

Abstract: Rotary ultrasonic drilling (RUD) is considered as a hybrid process combining grinding process using diamond tool that simultaneously performs axial vibrations with frequency at the ultrasound level. The application of this method hole drilling is mainly in machining of high-strength or brittle materials - alloys, composites and ceramics in industrial and medical applications. During the hole drilling, the hole bottom thickness is changing and consequently as a plate structure is subjected to transition through the resonance states. This resonant state can be considered as one of the important effects that leads to occure the "edgechipping" phenomenon. Although intensive research in this application area is still ongoing, the impact of ultrasonic vibrations as well as the influence of the shape of the contact surface of drilling tool on this phenomenon is still insufficiently analyzed. The effects different contact surfaces of drilling tools on the stress-strain states and prediction of "edge-chipping" phenomenon occuring during RUD are analyzed in this paper.

1. Introduction

Advanced materials such as ceramics, composites and other materials with supetior properties are increasingly used in industries such as aerospace, automotive, electronics but they are also used in medical applications. Mechanical properties of such materials are characterized by specific properties such as high hardness, excellent wear resistance and brittleness. However, these properties usually cause difficulties and complications in machining and obtaining the desired shapes and dimensions of the products from these materials. As mentioned, these materials are hardly machinable by conventional machining processes. For these reasons, it is very important to develop efficient machining processes that will ensure the quality of the machining process and the energy and cost efficiency of machining.

One of the advanced processes used for drilling holes into the above mentioned materials is rotary ultrasonic drilling (RUD). The RUD process is characterized by sufficiently high removal rate while cutting pressures remain low with relatively low surface damage and strength degradation [1]. Process of rotary ultrasonic drilling is shown in Fig. 1. Rotating drilling tool has metal-bonded diamond abrasives on active surface. During drilling proces, tool is ultrasonically vibrating in axial

direction and fed towards the workpieceat the constant feedrate or a constant force. The coolant is pumped through the core of drilling tool into the cutting zone and chips are washed away.

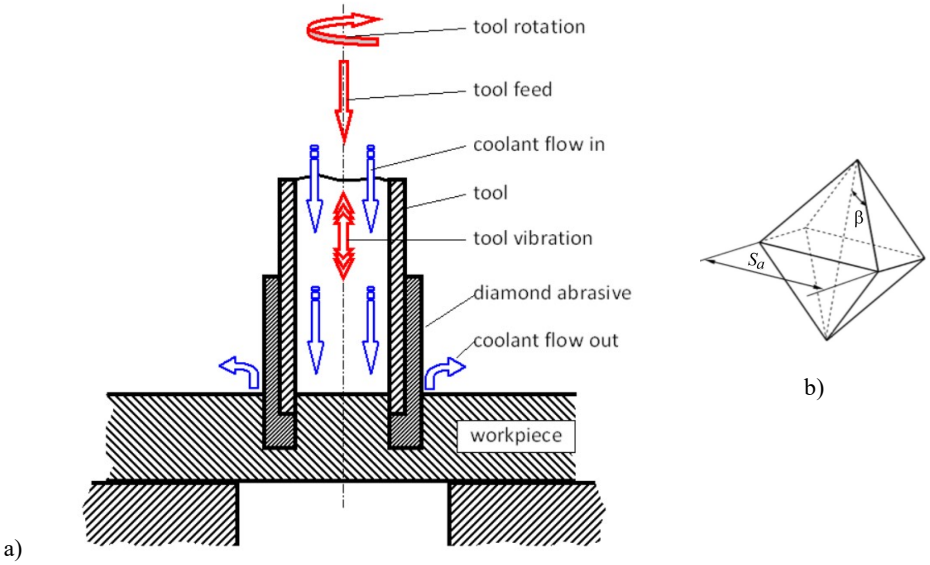

Figure 1. RUD process (a - principle, b - diamond particle).

Significant attention is paid to the processess and problems arising in the rotary ultrasonic machining from both the theoretical and experimental points of view. One of the important problem that has to be solved in the RUD process is the formation of undesirable phenomenon called edge-chipping. When the drilling tool is finishing the hole drilling, the bottom edge of the hole is degraded by breaking the edge (see Fig. 2).

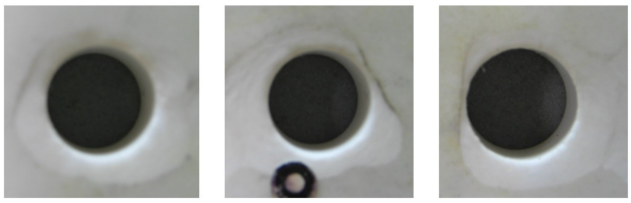

Figure 2. Typical cases of edge-chipping formation [4].

In this paper the finite-element model for the final-element analysis of the RUD process is developed to investigate the impact of ultrasonic vibration and shape parameters of the drilling tools on the edge-chipping phenomenon formation. The maximum equivalent von Mises stresses are analyzed in critical zones of the drilled hole. The dependence of equivalent stresses on the edge radii of drilling tool and on the change in the bottom thickness of drilling hole is investigated.

2. Formulation of the cutting force for RUD process

Rotary ultrasonic drilling might be considered as a combination of ultrasonic machining process and grinding process. It is a complex proces with a large number of input variables. The basic input parameters influencing the rotary ultrasonic drilling process, i.e., the input parameters for creating a model describing the RUD process are divided into different categories (see Fig. 3).

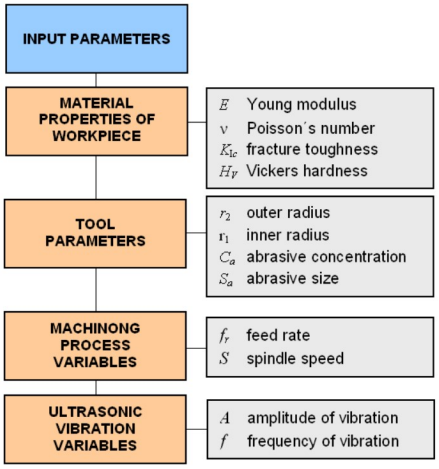

Figure 3. Input parameters of RUD process [3].

When analyzing the RUD process, the value of cutting force is important to determine. As can be seen from the RUD input data (see Fig. 3), the cutting force depends on a large number of parameters. To determine the value of cutting force, the significant attention is paid [2], [3] from a theoretical and experimental point of view. The general equation [3] for determining the dependence between cutting force and input parameters has the following form:

$$F = \left\{ 2\tan\beta\sqrt{\tan^2\beta + 2}\left[\frac{1}{2} - \frac{1}{\pi}\arcsin\left(1 - \frac{w}{A}\right)\right] H_v N_a \right\} w^2 , \tag{1}$$

where w is the maximum penetration depth, N_a is the number of abrasive particles on abrasive surface, β is the semi-angle between two oposite edges of abrasive diamond particle (see Fig. 1b) and H_v if the Vicker´s hardness.

It is assumed that abrasive particles are uniformly distributed on abrasive surface of the drilling tool. The number of active abrasive particles on the face of drilling tool can be determined by:

$$N_a = \sqrt[3]{A_0\left(\frac{0{,}88.10^{-3}}{\rho\frac{\sqrt{2}}{3}S_a^3}\frac{C_a}{100}\right)^2} , \tag{2}$$

where $A_0 = \pi(r_2^2 - r_1^2)$ is the area of contact sufrace of drilling tool face, C_a is concentration of abrasive and S_a is size of abrasive (see Fig. 1b)

3. Assumption for edge-chipping initiation

There is assumed, that the edge-chipping phenomenon will be initiated in a brittle fracture mode when the maximum stress will be satisfy the failure criterion. The equivalent stress of von Mises failure criterion can be used to determination of initiation process edge-chipping phenomenon. With the von Mises stress criterion, tge edge-chipping is assumed to initiate when the von Mises equivalent stresses reach the tensile strength of the workpiece material. The generally, the von Mises equivalent stress is defined by the folowing equation:

$$\sigma_{eq,Mise} = \sqrt{\frac{(\sigma_1 - \sigma_2)^2 + (\sigma_2 - \sigma_3)^2 + (\sigma_1 - \sigma_3)^2}{2}}, \tag{3}$$

where σ_1, σ_2 and σ_3 are the stresses in principle directions.

4. Finite element model of RUD process

The finite element analysis of RUD process is used to the prediction of edge-chipping phenomenon. The numerical simulation of drilling proces using the RUD process was realized on finite element model (see Fig. 4). Pre tvorbu finite element model were used 3D finite elements.

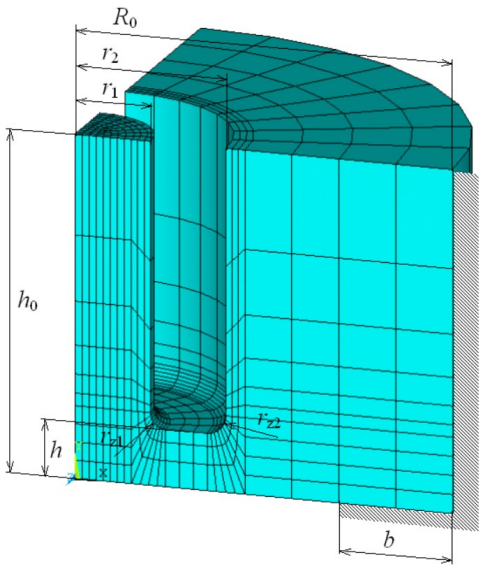

Figure 4. FE model of RUD process simulation (quarter of the model).

The boundary conditions were specified so that the bottom of the workpiece is supported on the area determined by dimension b (see Fig. 4), where all degrees of freedom were removed. The workpiece was also fixed on the workpiece's cylindrical surface, where all degrees of freedom were also removed. The drilling load in the RUD simulation process is determined as a pressure load on the bottom of the drilled hole. The magnitude of the excitation pressure amplitude is determined based on the results obtained from theoretical knowledge and experimental measurements [2], [3] and it is considered to be 15.0 MPa.

Table 1. Parameters of RUD process

Parameter			Value
radius of workpiece	R_0	[mm]	8.0
thickness of workpiece	h_0	[mm]	9.0
inner radius of drilled hole	r_1	[mm]	3.5
outer radius of drilled hole	r_2	[mm]	4.0
bottom thickness	h	[mm]	0.0 ÷ 9.0
radius on inner edge of drilling tool	r_{z1}	[mm]	0.05
radius on outer edge of drilling tool	r_{z2}	[mm]	0.05 ÷ 0.15
width of the support of workpiece	b	[mm]	3.0
Young modulus of workpiece material	E	[GPa]	300.0
Poisson number of workpiece material	ν	[-]	0.21
density of workpiece material	ρ	[kg.m^{-3}]	3720.0
pressure on bottom of drilled hole	p	[MPa]	15.0

5. Numerical analysis and results

During the RUD process, the changes in the workpiece structure occurs. These changes cause a modification mass and stiffness distribution in workpiece. As a result of this process, the changes in the workpiece modal properties occur, i.e. natural frequency and mode shapes are changing. When increasing the depth of drilled hole, the vibration of workpiece has a significant shape as shown in Fig. 5a. From the results obtained, it is evident that with the increasing depth of drilling (decreasing the bottom thickness of drilled hole), the influence of the support width of b on natural frequency of workpiece decreases (see Fig. 5b) and becomes insignificant. For bottom thickness h = 0.5 mm, the change of natural frequency is very small in the relation to changing the support width. Dependency of natural frequency on various values of edge radii r_{z1} and r_{z2} is also insignificant (see Fig. 6).

From the point of view of edge-chipping phenomenon formation, it is important to analyze the stress-strain state, which is created in the workpiece during the RUD process. This state is caused by an ultrasound excitation with 20 kHz excitation frequency. The concentration of extreme stresses during the RUD process occurs at those locations of workpiece where the edges of drilling tool are in contact with workpiece. Some results for demonstrating the distribution of stress fields during the

drilling process are shown in Fig. 6. With a decrease in the thickness of the bottom of drilled hole there is a significant growth in the value of equivalent von Mises stresses.

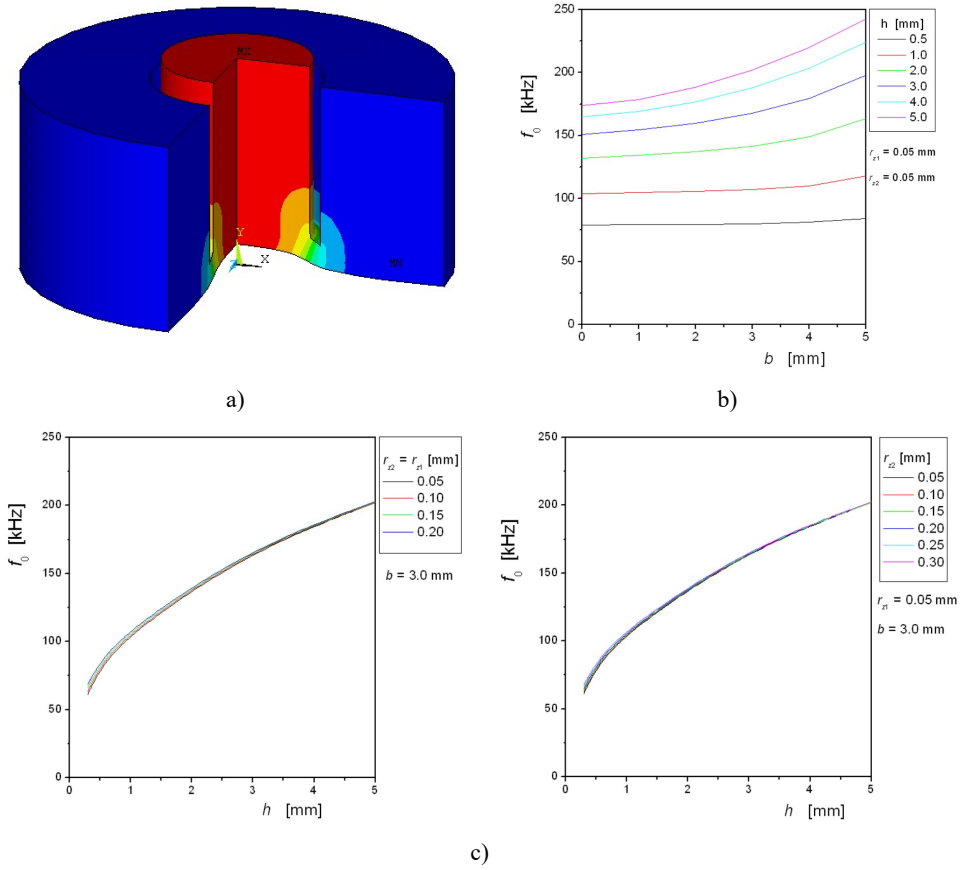

Figure 5. The changes in modal properties of workpiece during the RUD process. a) significant mode shape; b) dependency of significant mode shape frequency on parameter *b* for various thickness of drilled hole bottom *h*; c) dependencies of natural frequency on various values of edge radii r_{z1} and r_{z2}

In a further process of analysis RUD process the effect of edge radii of drilling tool on the values and distribution of equivalent stress has been studied. To illustrate the distribution of equivalent stresses on the edge arcs of a drilled hole (arcs between the bottom and the cylindrical surface), the structure of node configuration of the finite element model (see Fig. 7) is used. For performing stress-strain analyzes, it was assumed that the radius on the inner arc to the bottom of drilled hole is r_{z1} = 0.05 mm and this will not change. The radius on the outer arc to the bottom of the drilled hole will vary from 0.05 to 0.3 mm..

a)

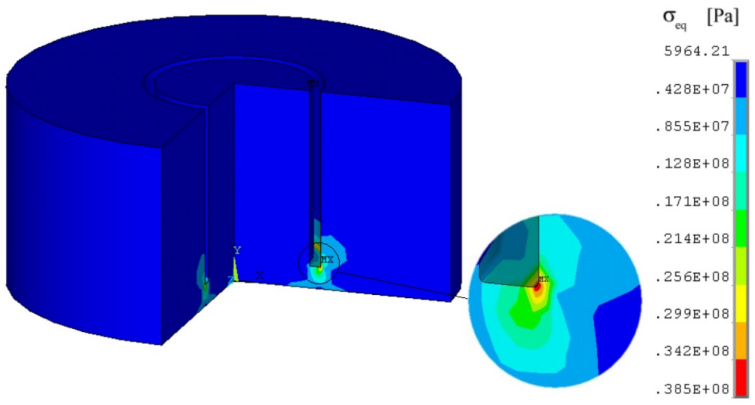

h = 1.0 mm

b)

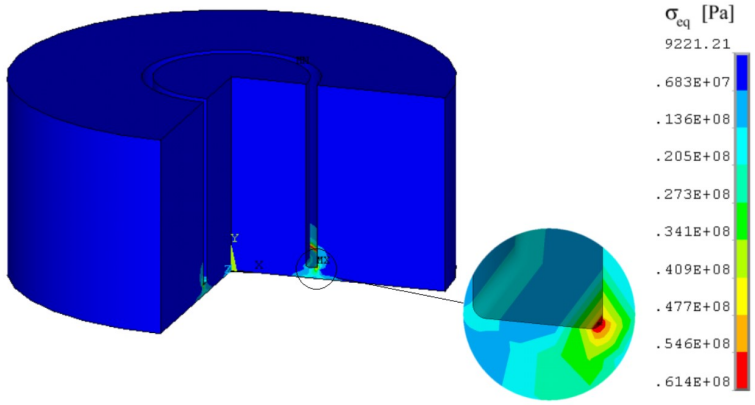

h = 0.5 mm

c)

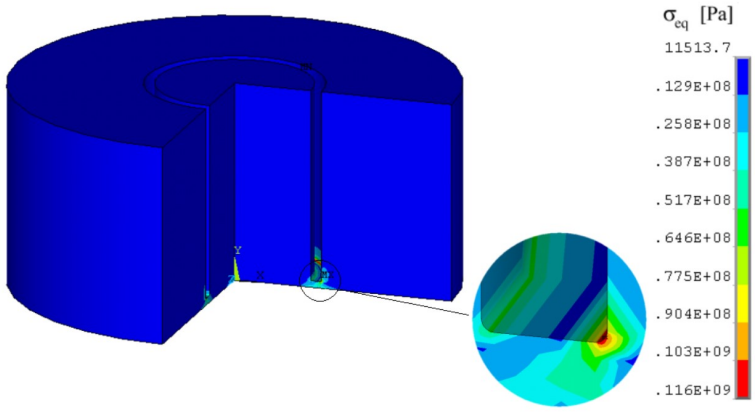

h = 0.3 mm

Figure 6. Ekvivalent stress distribution for $r_{z1} = r_{z2} = 0.05$ mm for various bottom thickness h.

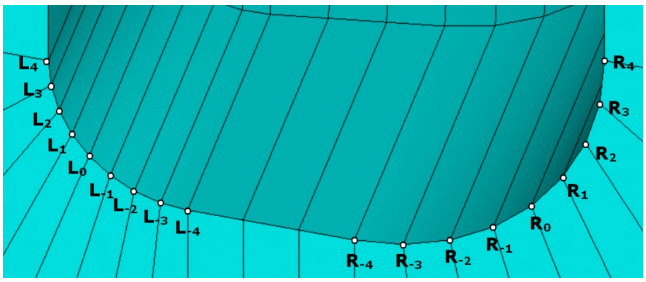

Figure 7. Configuration of nodes on the workpiece finite element model.

The distribution of equivalent stresses along the length of the inner arc is shown in Fig. 8. From these dependencies it is obvious that the change of radius on the outer arc affects the value and distribution of stresses on the inner arc. The increasing the radius of the outer arc causes the reduction in the value of the ekvivalent stresses on the inner arc. A similar situation arises also on the outside arc (see Fig. 9). Enlarging the value of the outer radius of curvature a significant decline in the value of equivalent stress along thelength of the outer arc occurs.

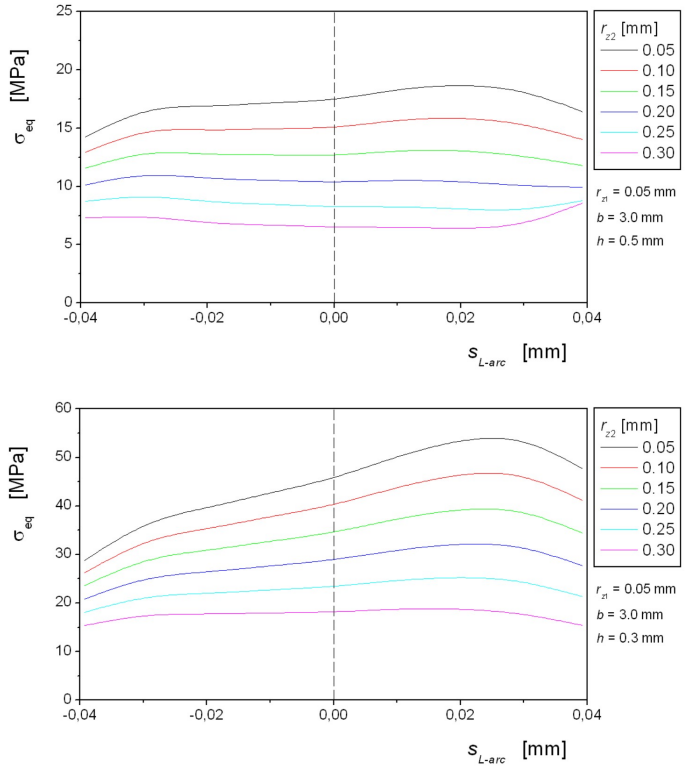

Figure 8. Distribution of equivalent stresses on inner arc (radius r_{z1}).

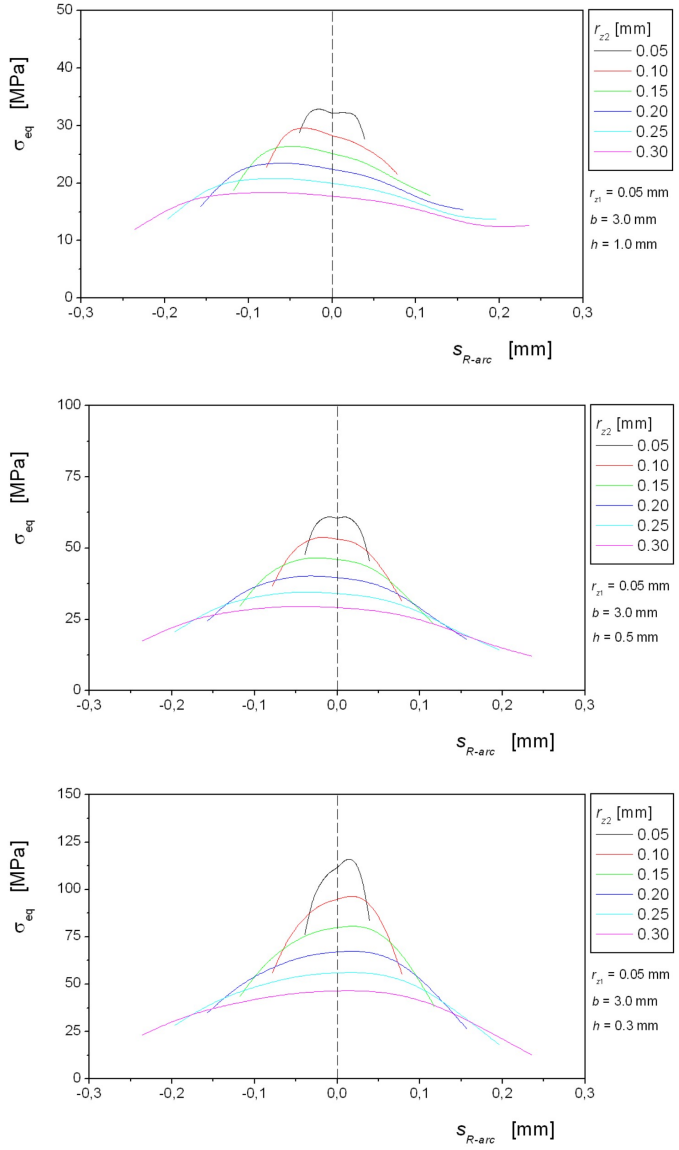

Figure 9. Distribution of equivalent stresses on outer arc (radius r_{z2}).

6. Conclusions

The investigation and analysis of the influence of RUD process parameters on the occurrence of edge-chipping phenomenon are presented in this paper. A possible solutions for the geometrical treatments of the active surfaces of drilling tool leading to the reduction of the peak stresses in workpiece result from the analysis results.

The main knowledge and conclusions are:

- As the drilled depth increases, the maximum values of equivalent von Mises stress are growing.
- The critical zones in which stress peaks appear are located in the zone between the bottom surface and the cylindrical surfaces of the drilled hole. The largest voltage peaks are in the outer radius zone. This fact confirms the assumption based on the practical findings that the initiation of cracks leading to edge-chipping begins at these locations.
- With the increasing radius r_{z2} of the outer curvature between the bottom surface and the surface of drilled hole, the stress peaks in this zone are significantly decreasing. When changing the radius of curvature from 0.05 mm to 0.3 mm, they drop by almost 50%.

The results which follow from this study have indicate a practical way leading to reduction stress peaks and elimination of the formation of edge-chipping phenomenon in rotary ultrasonic drilling.

Acknowledgments

This work was supported by the poject VEGA 1/1010/16 and project IP MTF 1603/2017.

References

[1] Khoo C. Y., Hamzah E., Sudin I. A review on the rotary ultrasonic machining of advanced ceramics. *Jurnal Mekanikal*, No. 25, pp 9-23.

[2] Li Z.C, Liang-Wu Cai, Pei Z.J., Treadwell C. Edge-chipping reduction in rotary ulrasonic machining of ceramics: Finite lelement analysis and experimental verification, *Int. Journal of Machine Tools and Manufacture*, 46, (2006), pp 1469-1477.

[3] Liu De Fu, Cong W. L., Pei Z. J., Tang Yong Jun A cutting force model for rotary ultrasonic machining brittle materials. Int. Joiurnal of Machine Tools & Manufacture, 52, (2012), pp 77-84.

[4] Zvončan, M. *Research of edge-chipping in rotary ultrasonic machining*. PhD Thesis, Slovak University of Technology, Faculty of Materials Science and Technology in Trnava, 2012, 108 pages, (Supervisor: Jozef Peterka).

Milan Naď, Associated Professor: Slovak University of Technology, Faculty of Materials Science and Technology, Instutute of Informatics, Automation and Mechatronics, Department of Applied Mechanics and Mechatronics, J. Bottu 25, 917 24 Trnava, Slovakia (*milan.nad@stuba.sk*). "The author gave a presentation of this paper during one of the conference sessions."

Lenka Kolíková, Ph.D.: Slovak University of Technology, Faculty of Materials Science and Technology, Instutute of Informatics, Automation and Mechatronics, Department of Applied Mechanics and Mechatronics, J. Bottu 25, 917 24 Trnava, Slovakia (*lenka.kolikova@stuba.sk*).

Ladislav Rolník, Ph.D.: Slovak University of Technology, Faculty of Materials Science and Technology, Instutute of Informatics, Automation and Mechatronics, Department of Applied Mechanics and Mechatronics, J. Bottu 25, 917 24 Trnava, Slovakia (*ladislav.rolnik@stuba.sk*).

Rastislav Ďuriš, Ph.D.: Slovak University of Technology, Faculty of Materials Science and Technology, Instutute of Informatics, Automation and Mechatronics, Department of Applied Mechanics and Mechatronics, J. Bottu 25, 917 24 Trnava, Slovakia (*rastislav.duris@stuba.sk*).

Formulation of the initial boundery velue problems in the theory of multilayer thermoelastic thin bodies in moments (part I)

Mikhail U. Nikabadze, Tamar Moseshvili, Armine R. Ulukhanian, Ketevan Tskhakaia, Nodar Mardaleishvili

Abstract: In the paper the new parametrization of a multilayer thin domain is applied. In contrast with classic approaches, several base surfaces and an analytic method with application of orthogonal polynomial systems are used. Geometric characteristics typical for the proposed parametrizations are considered. The new parametrization in the case of a one-layered thin body is described in detail in [5–10]. Various representations of the equations of motion, the heat influx, the constitutive relations of physical and heat content are given for the new body domain parametrization. The definition of the kth order moment of a certain quantity with respect to an orthonormal polynomial systems is given. The expressions of moments of first- and second-order partial derivatives of a certain tensor field are obtained and this is also done for some important expressions required for constructing different variants of the theory of thin body. Various variants of the equations of motion in moments with respect to orthogonal polynomial systems are also obtained. The interlayer conditions are written down under various connections of adjacent layers of a multilayer body. Formulation of the initial boundery velue problems in the theory of multilayer thermoelastic thin bodies in moments are given.

1. Parametrization of a multilayer thin domain of the three-dimensional Euclidean space with several base surfaces

Consider a multilayer thin domain of the Euclidean space consisting of not more than countably many layers. We perform the parametrization of this domain in the same way as in [1,2]. Let the layers be enumerated in the ascending order, i.e., for example, if $\alpha \geq 2$ is the serial number of a certain layer, then the serial number of the previous layer is $\alpha - 1$ and the serial number of the next layer is $\alpha + 1$. Each layer has two frontal surfaces. The frontal surface of the layer α, which lies to the side of the previous layer $\alpha - 1$, is called the interior base surface and denoted by $\overset{(-)}{\underset{\alpha}{\mathrm{S}}}$, whereas the frontal surface of the layer α, which lies to the side of the next layer $\alpha + 1$, is called the exterior base surface and denoted by $\overset{(+)}{\underset{\alpha}{\mathrm{S}}}$.

If the multilayer structure consists of K layers, then $\overset{(-)}{\underset{1}{\mathrm{S}}}$ ($\overset{(+)}{\underset{1}{\mathrm{S}}}$) and $\overset{(-)}{\underset{K}{\mathrm{S}}}$ ($\overset{(+)}{\underset{K}{\mathrm{S}}}$) are the interior and exterior surfaces of the first and last layers, respectively. In this case, $\overset{(-)}{\underset{1}{\mathrm{S}}}$ and $\overset{(+)}{\underset{K}{\mathrm{S}}}$ are also called the interior and exterior surfaces of the multilayer structure.

We assume that the frontal surfaces of each layer are regular surfaces and its lateral surface is a ruled surface in the case where the layer is bounded and unclosed.

Note that the analytic method with the use of the Legendre polynomial system in constructing the one-layer thin body theory [11–39] and multilayer thin body theory [40–49] was also applied by other authors. In this direction the author had published the papers [1–8, 50–59] and others with the application of Legendre and Chebyshev polynomial systems. These expansions can be successfully used in constructing any thin body theory. Despite this, the classic theories constructed by this method are far to be complete, and the more so, the micropolar theories and theories of other rheology are.

1.1. Vector parametric equation of the layer α and the system of vector parametric equations of a multilayer thin domain

The radius-vector of an arbitrary point $\underset{\alpha}{\mathrm{M}}$ of the layer α has the form

$$\underset{\alpha}{\mathbf{r}}(x^1,x^2,x^3)=\overset{(-)}{\underset{\alpha}{\mathbf{r}}}(x^1,x^2)+x^3\underset{\alpha}{\mathbf{h}}(x^1,x^2)=(1-x^3)\overset{(-)}{\underset{\alpha}{\mathbf{r}}}(x^1,x^2)+x^3\overset{(+)}{\underset{\alpha}{\mathbf{r}}}(x^1,x^2) \tag{1}$$

for all $\alpha\in\mathbb{N}$ and $\forall\, x^3\in[0,1]$, where the vector relations

$$\overset{(-)}{\underset{\alpha}{\mathbf{r}}}=\overset{(-)}{\underset{\alpha}{\mathbf{r}}}(x^1,x^2),\quad \overset{(+)}{\underset{\alpha}{\mathbf{r}}}=\overset{(+)}{\underset{\alpha}{\mathbf{r}}}(x^1,x^2),\quad \alpha\in\mathbb{N}, \tag{2}$$

are the vector equations of the base surfaces $\overset{(-)}{\underset{\alpha}{\mathrm{S}}}$ and $\overset{(+)}{\underset{\alpha}{\mathrm{S}}}$, respectively, x^1, x^2 are curvilinear (or Gaussian) coordinates on the interior base surface $\overset{(-)}{\underset{\alpha}{\mathrm{S}}}$, and $\mathbb{N}$ is the set of natural numbers. The vector $\underset{\alpha}{\mathbf{h}}(x^1,x^2)=\overset{(+)}{\underset{\alpha}{\mathbf{r}}}(x^1,x^2)-\overset{(-)}{\underset{\alpha}{\mathbf{r}}}(x^1,x^2)$, which topologically maps the interior base surface $\overset{(-)}{\underset{\alpha}{\mathrm{S}}}$ onto the exterior base surface $\overset{(+)}{\underset{\alpha}{\mathrm{S}}}$, in general, is not orthogonal to the base surfaces, and, moreover, the endpoint of each $\underset{\alpha}{\mathbf{h}}(x^1,x^2)$ is the initial point of $\underset{\alpha+1}{\mathbf{h}}(x^1,x^2)$, $\forall\alpha$, i.e., the following relation holds:

$$\begin{aligned}&\overset{(+)}{\underset{\alpha+\delta}{\mathbf{r}}}(x^1,x^2)=\overset{(-)}{\underset{\alpha}{\mathbf{r}}}(x^1,x^2)+\sum_{\nu=\alpha}^{\alpha+\delta}\underset{\nu}{\mathbf{h}}=\overset{(+)}{\underset{\alpha}{\mathbf{r}}}(x^1,x^2)+\sum_{\nu=\alpha+1}^{\alpha+\delta}\underset{\nu}{\mathbf{h}}=\overset{(-)}{\underset{\alpha}{\mathbf{r}}}(x^1,x^2)\\&+\sum_{\nu=\alpha}^{\alpha+\delta}\Big[\overset{(+)}{\underset{\nu}{\mathbf{r}}}(x^1,x^2)-\overset{(-)}{\underset{\nu}{\mathbf{r}}}(x^1,x^2)\Big]=\overset{(+)}{\underset{\alpha}{\mathbf{r}}}(x^1,x^2)+\sum_{\nu=\alpha+1}^{\alpha+\delta}\Big[\overset{(+)}{\underset{\nu}{\mathbf{r}}}(x^1,x^2)-\overset{(-)}{\underset{\nu}{\mathbf{r}}}(x^1,x^2)\Big],\ \ \forall\alpha,\delta.\end{aligned} \tag{3}$$

Let a multilayer domain[1] consist of K layers. Then introducing the notation

[1]We use the usual rules of tensor calculus [9, 10, 60–63]. We mainly preserve the notation and conventions of the previous works. Under symbols, we write indices denoting the serial numbers of layers . The Greek indices under symbols assume their values according to circumstances, and capital and small Latin indices assume the values 1, 2 and 1, 2, 3, respectively. A record of the form (I: 24) means a reference to formula (24) from the first part of the paper, and (II: 26) means a reference to formula (26) from the second part of the work.

$$\mathbf{h} = \sum_{\nu=1}^{K} \underset{\nu}{\mathbf{h}} = \sum_{\nu=1}^{K} \left[\overset{(+)}{\underset{\nu}{\mathbf{r}}}(x^1, x^2) - \overset{(-)}{\underset{\nu}{\mathbf{r}}}(x^1, x^2) \right], \tag{4}$$

we have

$$\overset{(+)}{\underset{K}{\mathbf{r}}}(x^1, x^2) = \overset{(-)}{\underset{1}{\mathbf{r}}}(x^1, x^2) + \mathbf{h}(x^1, x^2) = \overset{(-)}{\underset{1}{\mathbf{r}}}(x^1, x^2) + \sum_{\nu=1}^{K} \left[\overset{(+)}{\underset{\nu}{\mathbf{r}}}(x^1, x^2) - \overset{(-)}{\underset{\nu}{\mathbf{r}}}(x^1, x^2) \right]. \tag{5}$$

Note that Eq. (1) is the vector parametric equation of the layer α for a fixed α, and when α varies in the corresponding range and conditions (3) hold, the system of vector parametric equations of the multilayer thin domain considered. It is easy to see that (1) for any x^1, x^2 and $x^3 = 0$ defines the interior base surface $\overset{(-)}{\underset{\alpha}{\mathrm{S}}}$, and for any x^1, x^2 and $x^3 = 1$, it defines the exterior lateral surface $\overset{\alpha}{\overset{(+)}{\mathrm{S}}}$, whereas for any x^1, x^2 and $x^3 = \text{const}$,where $x^3 \in (0, 1)$, it defines the equidistance surface for the base surfaces $\overset{(-)}{\underset{\alpha}{\mathrm{S}}}$ and $\overset{(+)}{\underset{\alpha}{\mathrm{S}}}$, which is denoted by $\underset{\alpha}{\mathrm{S}}$.

1.2. Two-dimensional families of bases and the families of parametrizations of the surface of the layer α generated by them

For the derivatives of relations (1) and (2) in x^P at the points $\overset{(\star)}{\underset{\alpha}{\mathrm{M}}} \in \overset{(\star)}{\underset{\alpha}{\mathrm{S}}}$, $\star \in \{-, \emptyset, +\}$ $\forall\alpha$, let us introduce the notation

$$\underset{\alpha}{\mathbf{r}}_P \equiv \partial_P \underset{\alpha}{\mathbf{r}} \equiv \partial_P \underset{\alpha}{\mathbf{r}} / \partial x^P, \quad \underset{\alpha}{\mathbf{r}}_{\star P} \equiv \partial_P \overset{(\star)}{\underset{\alpha}{\mathbf{r}}} \equiv \partial \overset{(\star)}{\underset{\alpha}{\mathbf{r}}} / \partial x^P, \quad \star \in \{-, +\}, \ \forall\alpha. \tag{6}$$

The pair of vectors $\underset{\alpha}{\mathbf{r}}_{\star 1}$ $\underset{\alpha}{\mathbf{r}}_{\star 2}$, $\star \in \{-, \emptyset, +\}$ $\forall\alpha$ defined at the points $\overset{(\star)}{\underset{\alpha}{\mathrm{M}}} \in \overset{(\star)}{\underset{\alpha}{S}}$, $\star \in \{-, \emptyset, +\}$, $\forall\alpha$ obviously compose two-dimensional covariant surface bases, and $\overset{(\star)}{\underset{\alpha}{\mathrm{M}}} \underset{\alpha}{\mathbf{r}}_{\star 1}$ $\underset{\alpha}{\mathbf{r}}_{\star 2}$, $\star \in \{-, \emptyset, +\}$ $\forall\alpha$ are two-dimensional covariant surface frames, which, in turn, generate the corresponding parametrizations of the surfaces considered. As is known [60–63] (see also [9,10]), according to these frames (bases), we can construct the corresponding contravariant frames $\overset{(\star)}{\underset{\alpha}{\mathrm{M}}}$ $\overset{\star}{\underset{\alpha}{\mathbf{r}}}{}^1$ $\overset{\star}{\underset{\alpha}{\mathbf{r}}}{}^2$ (bases $\overset{\star}{\underset{\alpha}{\mathbf{r}}}{}^1$ $\overset{\star}{\underset{\alpha}{\mathbf{r}}}{}^2$), $\star \in \{-, \emptyset, +\}$, $\forall\alpha$. Naturally, the covariant and contravariant bases generate the geometric characteristics inherit for them. Defining the frames (bases) at each point of the surfaces $\overset{(\star)}{\underset{\alpha}{\mathrm{S}}}$, $\star \in \{-, \emptyset, +\}$, $\forall\alpha$, we obtain the corresponding families of frames (bases), which, in turn, generate the corresponding parametrizations.

1.3. Three-dimensional families of bases and the families of parametrization of the domain of the layer α generated by them

Taking into account the expression of the radius-vector $\underset{\alpha}{\mathbf{r}}$ (1) in the first relation in (6) and introducing the notation $\underset{\alpha}{\mathbf{h}}_P \equiv \partial\mathbf{h}/\partial x^P \equiv \partial_P \underset{\alpha}{\mathbf{h}}$, we obtain

$$\underset{\alpha}{\mathbf{r}}_P = \underset{\alpha}{\mathbf{r}}_{-P} + x^3 \underset{\alpha}{\mathbf{h}}_P = (1 - x^3) \underset{\alpha}{\mathbf{r}}_{-P} + x^3 \underset{\alpha}{\mathbf{r}}_{+P}, \ \forall\alpha. \tag{7}$$

Now, differentiating (1) in x^3, we have

$$\underset{\alpha}{\mathbf{r}}_3 \equiv \partial_3 \underset{\alpha}{\mathbf{r}} \equiv \partial \underset{\alpha}{\mathbf{r}}/\partial x^3 = \underset{\alpha}{\mathbf{h}}(x^1, x^2), \quad \forall x^3 \in [0,1], \quad \forall \alpha. \tag{8}$$

According to (8), we assume that

$$\underset{\alpha}{\mathbf{r}}_{\overset{-}{3}} \equiv \underset{\alpha}{\mathbf{r}}_3 \equiv \underset{\alpha}{\mathbf{r}}_{\overset{+}{3}} \equiv \partial_3 \underset{\alpha}{\mathbf{r}} = \underset{\alpha}{\mathbf{h}}(x^1, x^2), \quad \forall x^3 \in [0,1], \quad \forall \alpha. \tag{9}$$

Relation (9) allows us to define the spatial covariant bases $\underset{\alpha}{\mathbf{r}}_{\overset{\star}{p}}$, $\star \in \{-, +\}$, $\forall \alpha$ at the points $\underset{\alpha}{\overset{(\star)}{M}} \in \underset{\alpha}{\overset{(\star)}{S}}$, $\star \in \{-, +\}$, $\forall \alpha$, respectively. Therefore, the third basis vector of the spatial covariant bases at the points $\underset{\alpha}{\overset{(\star)}{\mathrm{M}}} \in \underset{\alpha}{\overset{(\star)}{\mathrm{S}}}$, $\star \in \{-, \emptyset, +\}$, for each layer α is the same vector $\underset{\alpha}{\mathbf{h}}(x^1, x^2)$. In view of (9), we can join relations (7)and (8) and represent them as

$$\underset{\alpha}{\mathbf{r}}_p = \underset{\alpha}{\mathbf{r}}_{p}^{-} + x^3 \underset{\alpha}{\mathbf{h}}_p = (1 - x^3) \underset{\alpha}{\overset{(-)}{\mathbf{r}}}_{p}^{-} + x^3 \underset{\alpha}{\overset{(+)}{\mathbf{r}}}_{p}^{+}, \quad \forall \alpha. \tag{10}$$

The triples of vectors $\underset{\alpha}{\mathbf{r}}_{1}^{\star}\ \underset{\alpha}{\mathbf{r}}_{2}^{\star}\ \underset{\alpha}{\mathbf{r}}_{3}^{\star}$, $\star \in \{-, \emptyset, +\}$, $\forall \alpha$ defined at the points $\underset{\alpha}{\overset{(\star)}{\mathrm{M}}} \in \underset{\alpha}{\overset{(\star)}{S}}$, $\star \in \{-, \emptyset, +\}$, $\forall \alpha$ obviously compose three-dimensional covariant spatial bases, and $\underset{\alpha}{\overset{(\star)}{\mathrm{M}}}\ \underset{\alpha}{\mathbf{r}}_{1}^{\star}\ \underset{\alpha}{\mathbf{r}}_{2}^{\star}\ \underset{\alpha}{\mathbf{r}}_{3}^{\star}$, $\star \in \{-, \emptyset, +\}$, $\forall \alpha$ compose three-dimensional spatial covariant frames, which, in turn, generate the corresponding parametrizations. As is known [9, 10, 60–62], according to these frames(bases), we can construct the corresponding contravariant frames $\underset{\alpha}{\overset{(\star)}{\mathrm{M}}}\underset{\alpha}{\mathbf{r}}^{\overset{\star}{1}}\underset{\alpha}{\mathbf{r}}^{\overset{\star}{2}}\underset{\alpha}{\mathbf{r}}^{\overset{\star}{3}}$ (bases $\underset{\alpha}{\mathbf{r}}^{\overset{\star}{1}}\underset{\alpha}{\mathbf{r}}^{\overset{\star}{2}}\underset{\alpha}{\mathbf{r}}^{\overset{\star}{3}}$), $\star \in \{-, \emptyset, +\}$, $\forall \alpha$. Indeed, by their definition [9, 10, 60–62], we have

$$\underset{\alpha}{\mathbf{r}}^{\tilde{k}} = \frac{1}{2} \underset{\alpha}{\overset{(\sim)}{\mathrm{C}}}{}^{\tilde{k}\tilde{p}\tilde{q}} \underset{\alpha}{\mathbf{r}}_{\tilde{p}} \times \underset{\alpha}{\mathbf{r}}_{\tilde{q}}, \quad \sim \in \{-, \emptyset, +\}, \ \forall \alpha, \tag{11}$$

where $\underset{\alpha}{\overset{(\sim)}{\mathrm{C}}}{}^{\tilde{k}\tilde{p}\tilde{q}} = (\underset{\alpha}{\mathbf{r}}^{\tilde{k}} \times \underset{\alpha}{\mathbf{r}}^{\tilde{p}}) \cdot \underset{\alpha}{\mathbf{r}}^{\tilde{q}}$, $\sim \in \{-, \emptyset, +\}$, $\forall \alpha$, are contravariant components of the discriminant tensors [60] of the layer α at the points $\underset{\alpha}{\overset{(\star)}{\mathrm{M}}} \in \underset{\alpha}{\overset{(\star)}{\mathrm{S}}}$, $\star \in \{-, \emptyset, +\}$, $\forall \alpha$. It is easy to see that (10) is shortly represented in the form

$$\underset{\alpha}{\mathbf{r}}_p = \underset{\alpha}{g}_{p}^{\overset{\star}{q}} \underset{\alpha}{\mathbf{r}}_{\overset{\star}{q}} = \underset{\alpha}{g}_{p\overset{\star}{q}} \underset{\alpha}{\mathbf{r}}^{\overset{\star}{q}}, \ \star \in \{-, +\}, \ \forall \alpha, \tag{12}$$

where we have introduced the notation

$$\underset{\alpha}{g}_{\breve{p}\tilde{q}} = \underset{\alpha}{\mathbf{r}}_{\breve{p}} \cdot \underset{\alpha}{\mathbf{r}}_{\tilde{q}}, \quad \underset{\alpha}{g}_{\breve{p}}^{\tilde{q}} = \underset{\alpha}{\mathbf{r}}_{\breve{p}} \cdot \underset{\alpha}{\mathbf{r}}^{\tilde{q}}, \quad \breve{} \in \{-, \emptyset, +\}, \quad \sim \in \{-, +\}, \quad \forall \alpha. \tag{13}$$

in view of (10) and (13), for $\underset{\alpha}{g}_{p\tilde{q}}$ and $\underset{\alpha}{g}_{p}^{\tilde{q}}$, we have

$$\underset{\alpha}{g}_{p\breve{q}} = (1 - x^3) \underset{\alpha}{g}_{p\breve{q}}^{-} + x^3 \underset{\alpha}{g}_{p\breve{q}}^{+}, \quad \underset{\alpha}{g}_{p}^{\breve{q}} = (1 - x^3) \underset{\alpha}{g}_{p}^{\breve{q}-} + x^3 \underset{\alpha}{g}_{p}^{\breve{q}+}, \quad \breve{} \in \{-, +\}, \quad \forall \alpha. \tag{14}$$

Also, it is easy to obtain the expressions for $\underset{\alpha}{g}_{pq}$. Indeed, by (12) and (14), we have

$$\underset{\alpha}{g}_{pq} = \underset{\alpha}{\mathbf{r}}_p \cdot \underset{\alpha}{\mathbf{r}}_q = (1-x^3)^2 \underset{\alpha}{g}_{\overset{-}{p}\overset{-}{q}} + x^3(1-x^3)(\underset{\alpha}{g}_{\overset{-}{p}\overset{+}{q}} + \underset{\alpha}{g}_{\overset{+}{p}\overset{-}{q}}) + (x^3)^2 \underset{\alpha}{g}_{\overset{+}{p}\overset{+}{q}}, \quad \star \in \{-,+\}, \quad \forall \alpha. \tag{15}$$

Let us find the expressions for $\sqrt{\underset{\alpha}{g}} = (\underset{\alpha}{\mathbf{r}}_1 \times \underset{\alpha}{\mathbf{r}}_2) \cdot \underset{\alpha}{\mathbf{r}}_3$. By the first relation in (12), we obtain

$$\sqrt{\underset{\alpha}{g}} = \frac{1}{2}\epsilon^{IJ}(\underset{\alpha}{\mathbf{r}}_I \times \underset{\alpha}{\mathbf{r}}_J) \cdot \underset{\alpha}{\mathbf{r}}_3 = \sqrt{\overset{(\sim)}{\underset{\alpha}{g}}}\det(\underset{\alpha}{g}_p^{\tilde{q}}) = \sqrt{\overset{(\sim)}{\underset{\alpha}{g}}}\det(\underset{\alpha}{g}_P^{\tilde{Q}}), \quad \sim \in \{-,+\}, \quad \forall \alpha, \tag{16}$$

where ϵ^{IJ}, ϵ_{KL} are the Levi-Civita symbols and

$$\sqrt{\overset{(\sim)}{\underset{\alpha}{g}}} = (\underset{\alpha}{\mathbf{r}}_{\tilde{1}} \times \underset{\alpha}{\mathbf{r}}_{\tilde{2}}) \cdot \underset{\alpha}{\mathbf{r}}_{\tilde{3}}, \quad \sim \in \{-,+\}, \quad \sqrt{\overset{(-)}{\underset{\alpha}{g}}} = \sqrt{\underset{\alpha}{g}}\Big|_{x^3=0}, \quad \sqrt{\overset{(+)}{\underset{\alpha}{g}}} = \sqrt{\underset{\alpha}{g}}\Big|_{x^3=1}, \quad \forall \alpha.$$

In turn, from (16), we have

$$\overset{(\sim)}{\underset{\alpha}{\vartheta}} \equiv \sqrt{\underset{\alpha}{g}\,\overset{(\sim)^{-1}}{\underset{\alpha}{g}}} = \frac{1}{2}\,\epsilon^{IJ}\epsilon_{KL}\underset{\alpha}{g}_I^{\tilde{K}}\underset{\alpha}{g}_J^{\tilde{L}} = \det(\underset{\alpha}{g}_P^{\tilde{Q}}), \quad \sim \in \{-,+\}, \quad \forall \alpha. \tag{17}$$

Note that analogously to (16), in a more general case, we have

$$\sqrt{\overset{(\sim)}{\underset{\alpha}{g}}} = \frac{1}{2}\sqrt{\overset{(\smile)}{\underset{\alpha}{g}}}\epsilon^{IJ}\epsilon_{KL}\underset{\alpha}{g}_{\check{I}}^{\check{K}}\underset{\alpha}{g}_{\check{J}}^{\check{L}} = \sqrt{\overset{(\smile)}{\underset{\alpha}{g}}}\det(\underset{\alpha}{g}_{\check{P}}^{\check{Q}}), \quad \sim, \smile \in \{-,\emptyset,+\}, \quad \forall \alpha. \tag{18}$$

It is easy to see from this that

$$\overset{(\smile)}{\underset{\alpha}{\tilde{\vartheta}}} \equiv \sqrt{\underset{\alpha}{g}\,\overset{(\smile)^{-1}}{\underset{\alpha}{g}}} = \frac{1}{2}\epsilon^{IJ}\epsilon_{KL}\underset{\alpha}{g}_{\check{I}}^{\check{K}}\underset{\alpha}{g}_{\check{J}}^{\check{L}} = \det(\underset{\alpha}{g}_{\check{P}}^{\check{Q}}) = \det(\underset{\alpha}{g}_{\tilde{p}}^{\tilde{q}}), \quad \smile, \sim \in \{-,\emptyset,+\}, \quad \forall \alpha. \tag{19}$$

It is seen that for $\sim = \emptyset$, $\smile \in \{-,+\}$, from (18) we obtain (16), and from (19), we obtain (17). It is easy to verify that by (19), we have

$$\overset{(\smile)}{\underset{\alpha}{\tilde{\vartheta}}} = \overset{(\smile)}{\underset{\alpha}{\vartheta}}{}^{-1}, \quad \smile, \sim \in \{-,+\}, \quad \forall \alpha; \qquad \overset{(\approx)}{\underset{\alpha}{\vartheta}} = 1, \quad \sim \in \{-,+\}, \quad \forall \alpha. \tag{20}$$

Using (19), we can write relations (17) in the following more detailed form:

$$\begin{aligned}
&\overset{(-)}{\underset{\alpha}{\vartheta}} = \sqrt{\underset{\alpha}{g}\,\overset{(-)^{-1}}{\underset{\alpha}{g}}} = (1-x^3)^2\overset{(=)}{\underset{\alpha}{\vartheta}} + x^3(1-x^3)\underset{\alpha}{g}_{+}^{\bar{I}}{}_{\bar{I}} + (x^3)^2\overset{(\mp)}{\underset{\alpha}{\vartheta}},\\
&\overset{(+)}{\underset{\alpha}{\vartheta}} = \sqrt{\underset{\alpha}{g}\,\overset{(+)^{-1}}{\underset{\alpha}{g}}} = (1-x^3)^2\overset{(\pm)}{\underset{\alpha}{\vartheta}} + x^3(1-x^3)\underset{\alpha}{g}_{-}^{\overset{+}{I}}{}_{I} + (x^3)^2\overset{\binom{+}{}}{\underset{\alpha}{\vartheta}}, \quad \forall \alpha.
\end{aligned} \tag{21}$$

It is easy to express $\underset{\alpha}{\mathbf{r}}^k$, $\forall \alpha$, through the vectors $\underset{\alpha}{\mathbf{r}}_{\tilde{m}}$ or $\underset{\alpha}{\mathbf{r}}^{\tilde{m}}$, $\sim \in \{-,+\}$, $\forall\, \alpha$. Indeed, taking into account the first relation of (12) from (11) for $\sim = \emptyset$, we obtain

$$\underset{\alpha}{\mathbf{r}}{}^k = \frac{1}{2}\overset{(\sim)}{\underset{\alpha}{\vartheta}}{}^{-1}\epsilon^{kpq}\epsilon_{lmn}\underset{\alpha}{g}_p^{\tilde{m}}\underset{\alpha}{g}_q^{\tilde{n}}\underset{\alpha}{\mathbf{r}}^{\tilde{l}}, \quad \sim \in \{-,+\}, \quad \forall\, \alpha, \tag{22}$$

where ϵ^{kpq}, ϵ_{lmn} are the Levi-Civita symbols. By (22),we introduce the notation

$$\underset{\alpha}{g^{k}_{\tilde{l}}} = \frac{1}{2}\overset{(\sim)}{\underset{\alpha}{\vartheta}}{}^{-1}\epsilon^{kpq}\epsilon_{lmn}\underset{\alpha}{g^{\tilde{m}}_{p}}\underset{\alpha}{g^{\tilde{n}}_{q}}, \quad \underset{\alpha}{g^{k\tilde{l}}} = \frac{1}{2}\overset{(\sim)}{\underset{\alpha}{\vartheta}}{}^{-1}\epsilon^{kpq}\epsilon_{smn}\underset{\alpha}{g^{\tilde{m}}_{p}}\underset{\alpha}{g^{\tilde{n}}_{q}}\underset{\alpha}{g^{\tilde{s}\tilde{l}}}, \quad \sim \in \{-,+\}, \quad \forall\alpha. \tag{23}$$

Using this notation, we represent relation (22) in the desired form

$$\underset{\alpha}{\mathbf{r}^{p}} = \underset{\alpha^{\tilde{q}}\alpha}{g^{p}_{\tilde{q}}}\underset{\alpha}{\mathbf{r}^{\tilde{q}}} = \underset{\alpha}{g^{p\tilde{q}}}\underset{\alpha^{\tilde{q}}}{\mathbf{r}}, \quad \sim \in \{-,+\}, \quad \forall\alpha. \tag{24}$$

It is easy to see that from the first relation in (23), we have

$$\underset{\alpha^{\tilde{K}}}{g^{K}} = \overset{(\sim)}{\underset{\alpha}{\vartheta}}{}^{-1}\underset{\alpha}{g^{\tilde{I}}_{I}}, \quad \Rightarrow \quad \underset{\alpha^{\tilde{K}}}{g^{\check{K}}} = \overset{(\backsim)}{\underset{\alpha}{\vartheta}}{}^{-1}\underset{\alpha^{\check{I}}}{g^{\tilde{I}}} = \overset{(\backsim)}{\underset{\alpha}{\vartheta}}\underset{\alpha^{\check{I}}}{g^{\tilde{I}}}, \quad \sim \in \{-,+\}, \quad \forall\,\alpha. \tag{25}$$

Note that in writing the second relation in (25), (19) and (20) were taken into account. Also, let us consider the following objects (matrices):

$$\underset{\alpha\beta^{\check{p}}_{\cdot}}{g^{\cdot\,\tilde{q}}} = \underset{\alpha^{\check{p}}}{\mathbf{r}}\cdot\underset{\beta}{\mathbf{r}^{\tilde{q}}}, \quad \backsim, \sim \in \{-,\emptyset,+\}, \quad \forall\alpha,\beta, \tag{26}$$

and the objects obtained from (26) by alternating the indices. We calculate that the number of such objects is equal to 36. It is easy to see that for $\alpha = \beta$ (26) contains (13), (15) and (23). Indeed, from (26), we have

$$\underset{\alpha^{\check{p}}}{g^{\tilde{q}}} = \underset{\alpha\alpha^{\check{p}}_{\cdot}}{g^{\cdot\,\tilde{q}}} = \underset{\alpha^{\check{p}}}{\mathbf{r}}\cdot\underset{\alpha}{\mathbf{r}^{\tilde{q}}}, \quad \backsim, \sim \in \{-,\emptyset,+\}, \quad \forall\alpha, \tag{27}$$

and alternating the indices, we obviously obtain the objects considered above and also $\underset{\alpha}{g^{pq}} = \underset{\alpha}{\mathbf{r}^{p}}\cdot\underset{\alpha}{\mathbf{r}^{q}}$, $\forall\alpha$, i.e., in this case, the number of the introduced quantities is equal to 36. It is easy to see that by (26) and (27), the connections between the families of bases are represented in the form

$$\underset{\alpha^{\tilde{p}}}{\mathbf{r}} = \underset{\alpha^{\tilde{p}}}{g^{\check{n}}}\underset{\alpha^{\check{n}}}{\mathbf{r}} = \underset{\alpha\beta^{\tilde{p}}_{\cdot}}{g^{\cdot\,\check{n}}}\underset{\beta^{\check{n}}}{\mathbf{r}}, \quad \backsim, \sim \in \{-,\emptyset,+\}, \quad \forall\alpha,\beta, \tag{28}$$

which remains valid under index alternation. By (28), it we show that the relation holds

$$\underset{\alpha\beta^{\tilde{p}}_{\cdot}}{g^{\cdot\,\check{q}}} = \underset{\alpha\delta^{\tilde{p}}_{\cdot}}{g^{\cdot\,\overset{\star}{n}}}\underset{\beta\beta^{n}_{\cdot}}{g^{\overset{\star}{\cdot}\,\check{q}}}, \quad \backsim, \sim, \star \in \{-,\emptyset,+\}, \quad \forall\alpha,\beta,\delta. \tag{29}$$

Differentiating (3)–(5) in x^I and taking into account (28), we obtain

$$\begin{aligned}
&\underset{\alpha+\beta\,I}{\mathbf{r}^{+}} = \underset{\alpha\,I}{\mathbf{r}^{-}} + \sum_{\nu=\alpha}^{\alpha+\beta}\Big[\underset{\nu\,I}{g^{\bar{k}}_{+}} - \underset{\nu\,I}{g^{\bar{k}}_{-}}\Big]\underset{\nu\,k}{\mathbf{r}^{-}} = \underset{\alpha\,I}{\mathbf{r}^{+}} + \sum_{\nu=\alpha+1}^{\alpha+\beta}\Big[\underset{\nu\,I}{g^{\bar{k}}_{+}} - \underset{\nu\,I}{g^{\bar{k}}_{-}}\Big]\underset{\nu\,k}{\mathbf{r}^{-}},\\
&\partial_I\mathbf{h}(x^1,x^2) = \sum_{\nu=1}^{N}\partial_I\underset{\nu}{\mathbf{h}}(x^1,x^2) = \sum_{\nu=1}^{N}\Big[\underset{\nu\,I}{g^{\bar{k}}_{+}}(x^1,x^2) - \underset{\nu\,I}{g^{\bar{k}}_{-}}(x^1,x^2)\Big]\underset{\nu\,k}{\mathbf{r}^{-}}(x^1,x^2),\\
&\underset{N\,I}{\mathbf{r}^{+}}(x^1,x^2) = \underset{1\,I}{\mathbf{r}^{-}}(x^1,x^2) + \sum_{\nu=1}^{N}\Big[\underset{\nu\,I}{g^{\bar{k}}_{+}}(x^1,x^2) - \underset{\nu\,I}{g^{\bar{k}}_{-}}(x^1,x^2)\Big]\underset{\nu\,k}{\mathbf{r}^{-}}(x^1,x^2).
\end{aligned} \tag{30}$$

Naturally, all spatial covariant and contravariant bases constructed above have geometric characteristics specific for the parametrizations generated by them. Defining the spatial frames (bases) at each point of the surfaces $\overset{(\star)}{\underset{\alpha}{\mathrm{S}}}$, $\star \in \{-, \emptyset, +\}$, $\forall\, \alpha$, we obtain the corresponding families of spatial frames (bases), which, in turn generate the corresponding families of parametrizations. Once more, we note that the structure of $\overset{(\sim)}{\underset{\alpha}{\mathrm{S}}}$ $\underset{\alpha}{\overset{(\sim)}{g}}$-families frames (bases), $\sim \in \{-, \emptyset, +\}$, $\forall\, \alpha$, is such that the third basis vectors $\underset{\alpha\tilde{3}}{\mathbf{r}} = \underset{\alpha}{\mathbf{h}}(x^1, x^2)$, $\sim \in \{-, \emptyset, +\}$, $\forall\, \alpha$ are not perpendicular to the corresponding base surface $\overset{(\sim)}{\underset{\alpha}{\mathrm{S}}}$, $\sim \in \{-, \emptyset, +\}$, $\forall\, \alpha$ in general. However, in a particular case, they can be perpendicular, and in a more particular case, they can be unit normal vectors to the surfaces $\overset{(\sim)}{\underset{\alpha}{\mathrm{S}}}$, $\sim \in \{-, \emptyset, +\}$, $\forall\, \alpha$, which are denoted by $\overset{(\sim)}{\underset{\alpha}{n}}$, $\sim \in \{-, \emptyset, +\}$, $\forall\, \alpha$, respectively.

The corresponding relations for a one-layered thin body under a new parametrization, as well as for other parametrizations considered in the works, are valid for each layer.

It is seen from the material presented above that in the parametrization of a multilayer domain considered for each layer, and all the corresponding relations for a one-layered thin body under a new parametrization in [5–10], as well as for other parametrizations considered in [5–7, 11, 60], are hold under the condition that the root letters of quantities entering these relations must be equipped with the bottom index, which denote the number of the layer considered. In this connection, we do not consider the problems on the parametrization of a multilayer domain in detail. In what follows, if necessary, we write the necessary formulas from the corresponding relations of the works mentioned in this paragraph by the above method (equipping the root letters of quantities with the bottom index of the layer considered), and obtain some relations, which do not enter the above works.

1.4. Representation of the unit tensor of the second rank

It is easy to find this representation. Indeed, starting from the usual representation of this tensor [9, 10, 61, 62], by (28) and (29), we obtain the relation [1–5]

$$\underset{\sim}{\mathbf{E}} = \underset{\underset{\alpha}{\sim}}{\mathbf{E}} = \underset{\alpha}{\overset{\check{n}}{g}}_{\tilde{p}}\, \underset{\alpha}{\mathbf{r}}^{\tilde{p}}\, \underset{\alpha}{\mathbf{r}}_{\check{n}} = \underset{\underset{\beta}{\sim}}{\mathbf{E}} = \underset{\beta}{\overset{\check{n}}{g}}_{\tilde{p}}\, \underset{\beta}{\mathbf{r}}^{\tilde{p}}\, \underset{\beta}{\mathbf{r}}_{\check{n}} = \underset{\alpha\beta}{g}\, \overset{\cdot}{\tilde{p}}\, \overset{\check{n}}{\cdot}\, \underset{\alpha}{\mathbf{r}}^{\tilde{p}}\, \underset{\beta}{\mathbf{r}}_{\check{n}}, \quad \sim, \quad \smile \in \{-, \emptyset, +\}, \quad \forall \alpha, \beta, \tag{31}$$

which remains valid under index alternating. As is seen from (31), the quantities (26) and (27) introduced above represent the components of the unit tensor of the second rank (UTSR) for a multilayer thin domain of the three-dimensional Euclidean space. Now let us introduce the following definitions.

Definition 1.1 *The parametrization considered above, which is characterized by assigning the radius-vector of an arbitrary point of any layer α in the form* (1) *and by the fulfillment of relation* (3)*, is called the new parametrization of a multilayer thin domain.*

Definition 1.2 *The components* $g\limits_{\alpha\beta}{}^{\cdot\ \check{n}}_{\tilde{p}\ \cdot}$, *for* $\tilde{p} \in \{\bar{p}, p, \overset{+}{p}\}$, $\check{n} \in \{\bar{n}, n, \overset{+}{n}\}$, $\forall\,\alpha \neq \beta$, *and also the components* $g\limits_{\alpha}{}^{\cdot\ \check{n}}_{\tilde{p}\ \cdot}$, $\forall\,\alpha$, *for* $\sim \neq \smile$, *where* $\sim, \smile \in \{+, \emptyset, -\}$, *and the images obtained from them by index alternating are called the components of the unit second-rank tensor translation under the new parametrization of a multilayer thin domain.*

Definition 1.3 *The components* $g\limits_{\alpha\beta}{}^{\cdot\ \cdot}_{\tilde{p}\tilde{q}}$, $g\limits_{\alpha\beta}{}^{\cdot\ \tilde{q}}_{\tilde{p}\ \cdot}$, $g\limits_{\alpha\beta}{}^{\tilde{p}\tilde{q}}_{\cdot\ \cdot}$ *for* $\sim = -$ $(\sim = +)$, $\forall\,\alpha, \beta$, *and the components of the translation* $g\limits_{\alpha\beta}{}^{\cdot\ \cdot}_{\tilde{p}\check{q}}$, $g\limits_{\alpha\beta}{}^{\cdot\ \check{q}}_{\tilde{p}\ \cdot}$, *for* $\sim = +, \smile = -$ $(\sim = -, \smile = +)$, $\forall\,\alpha, \beta$, *are called the basic components of the second-rank unit tensor under the new parametrization of a multilayer thin domain if as as base surface, the inner (exterior) base surface of layers are taken.*

It is easy to find the expressions for $g\limits_{\alpha\beta}{}^{pq}$ via basic translation components. Indeed, by (14), (26) and (29), we have

$$g\limits_{\alpha\beta}{}^{pq} = g\limits_{\alpha}{}^{\check{m}}_{p}\, g\limits_{\beta}{}^{\check{n}}_{q}\, g\limits_{\alpha\beta}{}^{}_{\check{m}\check{n}} = (1-x^3)^2\, g\limits_{\alpha\beta}{}^{}_{\bar{p}\,\bar{q}} + x^3(1-x^3)\big(g\limits_{\alpha\beta}{}^{}_{\bar{p}\,\overset{+}{q}} + g\limits_{\alpha\beta}{}^{}_{\overset{+}{p}\,\bar{q}}\big) + (x^3)^2\, g\limits_{\alpha\beta}{}^{}_{\overset{+}{p}\,\overset{+}{q}}, \tag{32}$$

where $\sim, \smile \in \{-, +\}$, $\forall \alpha, \beta$. Whence, for $\alpha = \beta$, we obtain (15).

Acknowledgments

This work was supported by the Shota Rustaveli National Science Foundation (project no. DI-2016-41).

References

[1] Nikabadze, M.U. *Variants of mathematical theory of multilayer structures with several base surfaces.* Deposited in VINITI RAS, 21.08.2008. No. 721–B2008., (in Russian), Moscow, 2008, 127 p.

[2] Nikabadze, M.U. A variant of the theory of multilayer structures. *Mech. Solids.* 1 (2001), 143–158.

[3] Nikabadze, M.U. Mathematical modeling of multilayer thin body deformation. *J. Math. Sci.*, 187 (3) (2012), 300-336.

[4] Nikabadze, M.U. *The method of orthogonal polynomials in the classical and micropolar mechanics of elastic thin bodies.* II. Deposited in VINITI RAS, No. 136-B2014, (in Russian), Moscow, 2014, 218 p.

[5] Nikabadze, M.U. *Development of the method of orthogonal polynomials in the classical and micropolar mechanics of elastic thin bodies.* Moscow University, Moscow, 2014, 515 p.

[6] Nikabadze, M.U. *The method of orthogonal polynomials in the classical and micropolar mechanics of elastic thin bodies.* Diss. Doctor Phys.–Math. Sciences. (in Russian), Moscow, 2014, 384 p.

[7] Nikabadze, M.U. *The method of orthogonal polynomials in the classical and micropolar mechanics of elastic thin bodies.* I. Deposited in VINITI RAS, No. 135-V2014, 20.05.2014, (in Russian), Moscow, 2014, 278 p.

[8] Nikabadze, M.U. *The application of systems of Legendre and Chebyshev polynomials at modeling of elastic thin bodies with a small size.* Deposited in VINITI RAS, No. 720-V2008, 21.08.2008, (in Russian), Moscow, 2014, 287 p.

[9] Nikabadze, M.U. On several issues of tensor calculus with applications to mechanics. *Contemporary Math.*, 55 (2015), 3-194.

[10] Nikabadze, M.U. Topics on tensor calculus with applications to mechanics. *J. Math. Sci.*, 225(1) (2017), 194.

[11] Vekua I. N. Shell theory, general methods of construction. Pitman Adv. Pub. Program, 1985.

[12] Alekseev A.E. Construction of equations of a layer with variable thickness based on expansions over Legendre polynomials. *J. Appl. Mech. Techn. Phys.,* 35(4) (1994), 137–147.

[13] Alekseev A. E. Bend of a three-layer orthotropic beam. *J. Appl. Mech. Techn. Phys.,* 36(3) (1995), 158–166.

[14] Alekseev A. E. Iterative solution method for laminated structures deformation problems taking into account the slipping of layers. *Continuum Dynamics.* Inst. Hydrodynamics, Sib. Branch. RAS, Novosibirsk, 116 (2000), 170–174.

[15] Alekseev, A. E., Alekhin, V.V. and Annin, B. D. Plane elastic problem for an inhomogeneous layered body. *J. Appl. Mech. Techn. Phys.,* 42(6) (2001), 1038-1042.

[16] Alekseev, A. E. and Annin, B. D. Equations of deformation of an elastic inhomogeneous laminated body of revolution. *J. Appl. Mech. Techn. Phys.,* 44(3) (2003), 432-437.

[17] Alekseev, A. E. and Demeshkin, A. G. Detachment of a beam glued to a rigid plate. *J. Appl. Mech. Techn. Phys.,* 44(4) (2003), 151–158.

[18] Vekua I. N. A method of calculation of prismatic shells. *Proc. Tbilisi Math. Inst.*, Metsniereba, Tbilisi, 29(1955), 191–259.

[19] Vekua I. N. *The theory of thin and sloping shells of variable thickness.* Novosibirsk, 1964.

[20] Vekua I. N. The theory of thin sloping shells of variable thickness. *Proc. Tbilisi Math. Inst.*, Metsniereba, Tbilisi, 30(1965), 1–104.

[21] Vekua I. N. *Variational principles of shell theory construction.* Tbilisi Univ., Tbilisi, 1970.

[22] Vekua I. N. *One direction of shell theory construction. Mechanics of USSR in 50 years.* Vol. 3. Nauka, Moscow, 1972, 267–290.

[23] Volchkov, Yu. M. and Dergileva, L.A. Solution of elastic layer problems by approximate equations and comparison with solutions of the theory of elasticity *Continuum Dynamics.* Inst. Hydrodynamics, Sib. Branch Acad. Sci. USSR, Novosibirsk, 28(1977), 43–54.

[24] Volchkov, Yu. M., Dergileva, L.A. and Ivanov, G. V. Numerical simulation of stressed states in plane elasticity problems by the method of layers. *J. Appl. Mech. Techn. Phys.*, 35(6), (1994), 129–135.

[25] Volchkov, Yu. M. and Dergileva, L.A. Edge effects in the stress state of a thin elastic interlayer. *J. Appl. Mech. Techn. Phys.*, 40(2), (1999), 354-359.

[26] Volchkov, Yu. M. Finite elements with adjustment conditions on their faces. *Continuum Dynamics.* Vol. 116. Inst. Hydrodynamics, Sib. Branch. RAS, Novosibirsk, 2000, 175–180.

[27] Volchkov, Yu. M. and Dergileva, L.A. Equations of an elastic anisotropic layer. *J. Appl. Mech. Techn. Phys.*, 45(2) (2004), 301-309.

[28] Volchkov, Yu. M. and Dergileva, L.A. Reducing three-dimensional elasticity problems to two-dimensional problems by approximating stresses and displacements by Legendre polynomials. *J. Appl. Mech. Techn. Phys.*, 48(3) (2007), 450–459.

[29] Dergileva, L.A. Solution method for a plane contact problem for an elastic layer. *Continuum Dynamics.* Vol. 25. Inst. Hydrodynamics, Sib. Branch. Acad. Sci. USSR, Novosibirsk, 1976, 24–32.

[30] Ivanov, G. V. Solution of a plane mixed problems of the theory of elasticity in the form of series over Legendre polynomials. *J. Appl. Mech. Techn. Phys.*, 6 (1976), 126–137.

[31] Ivanov, G. V. Solutions of plane mixed problems for the Poisson equation in the form of series over Legendre polynomials. *Continuum Dynamics.* Vol. 28. Inst. Hydrodynamics, Sib. Branch. Acad. Sci. USSR, Novosibirsk, 1977, 43–54.

[32] Ivanov, G. V. Reduction of a three-dimensional problem for an inhomogeneous shell to a two-dimensional problem. *Dynamic Problems Continuum Mechanics.* V. 39. Novosibirsk, 1979.

[33] Ivanov, G. V. *Theory of plates and shells.* Novosibirsk Univ., Novosibirsk, 1980.

[34] Vajeva, D. V. and Volchkov,Yu. M. The equations for determination of stress-deformed state of multilayer shells. *Proc. 9th Russian–Korean Symp. Sci. and Technol.*, June 26 – July 2, 2005. Novosibirsk Univ., Novosibirsk, Russia, 547–550.

[35] Medick, M. A. One-dimensional theories of wave and oscillation propagation in elastic rods of rectangular cross-sections. Applied theory of symmetric oscillations of elastic rods of rectangular and square cross-sections. *Appl. Mech.*, 3 (1966), 11–19.

[36] Soler, A. Higher-order theories for structural analysis using Legendre polynomial expansions. *J. Appl. Mech.*, 36(4) (1969), 757–763.

[37] Fellers, J. and Soler, A. Approximate solution of the finite cylinder problem using Legendre polynomials. *AIAA J.*, 8(11) (1970).

[38] Hertelendy, P. *An approximate theory governing symmetric motions of elastic rods of rectangular or square cross section.* ASME, 1968.

[39] Mindlin, R. D. and Medick, M. A. Extensional vibrations of elastic plates. *J. Appl. Mech.*, 26(4) (1959), 561–569.

[40] Galimov, N.K. Application of Legendre polynomials to construction of an improved theory of trilaminar plates and shells. *Studies in the theory of plates and shells.* Vol. 10. Kazan State Univ., Kazan, 1973, pp. 371–385.

[41] Pelekh, B. L. and Sukhorolskii, M. A. Construction of the generalized theory of transversal-isotropic shells in application to contact problems. *Composites and new structures.* Naukova Dumka, Kiev, 1977, 27–39.

[42] Pelekh, B. L. and Sukhorolskii, M. A. *Contact problems of the theory of elastic anisotropic shells.* Naukova Dumka, Kiev, 1980.

[43] Pelekh, B. L., Maksimuk, A. V. and Korovaichuk, I. M. *Contact problems for laminated elements of constructions and bodies with coating.* Naukova Dumka, Kiev, 1988.

[44] Chepiga, V. E. To the improved theory of laminated shells *Appl. Mech.*, 12(11) (1976), 45–49.

[45] Chepiga, V. E. Construction of the theory of multilayer ani.sotropic shells with given conditional accuracy of order h^N *Mech. Solids.*, 4(1977), 111–120.

[46] Chepiga, V. E. Application of Legendre polynomials to construction of the theory of multilayer shells. *Mech. Solids.*, 5(1982), 190.

[47] Chepiga, V. E. *The study of stability of multilayer shells by an improved theory.* Deposited in VINITI, No. 289-, 14.01.1986, (in Russian), Moscow, 1986.

[48] Chepiga, V. E. *Numerical analysis of equations of the improved theory of laminated shells.* Deposited in VINITI, No. 290-, 14.01.1986, (in Russian), Moscow, 1986.

[49] Chepiga, V. E. Asymptotic error of some hypotheses in the theory of laminated shells. *Theory and calculation of elements of thin-walled structures.* Moscow, 1986, 118–125.

[50] Nikabadze, M.U. and Ulukhanyan, A. R. *Formulations of problems for a shell domain according to three-dimensional theories.* Deposited in VINITI RAS, No. 83–2005, 21.01.2005, (in Russian), Moscow, 2005, 7 p.

[51] Nikabadze, M.U. and Ulukhanyan, A. R. Statements of problems for a thin deformable three-dimensional body. *Vestn. Mosk. Univ., Matem. Mekhan.*, 5(2005), 43–49.

[52] Nikabadze, M.U. A variant of the system of equations of the theory of thin bodies. *Vestn. Mosk. Univ., Matem. Mekhan.*, 1(2006), 30–35.

[53] Nikabadze, M.U. *Application of classic orthogonal polynomials to the construction of the theory of thin bodies. Elasticity and non-elasticity.* LENAND, Moscow, 2006, 218–228.

[54] Nikabadze, M.U. Application of a system of Chebyshev polynomials to the theory of thin bodies. *Vestn. Mosk. Univ., Matem. Mekhan.*, 5(2007), 56–63.

[55] Nikabadze, M.U. Some issues concerning a version of the theory of thin solids based on expansions in a system of Chebyshev polynomials of the second kind. *Mech. Solids.*, 42(3) (2007), 391-421.

[56] Nikabadze, M.U. *Mathematical modeling of elastic thin bodies with two small dimensions with the use of systems of orthogonal polynomials.* Deposited in VINITI RAS, No. 722 – B2008, 21.08.2008,, (in Russian), Moscow, 2008, 107 p.

[57] Nikabadze, M.U. and Ulukhanyan, A. R. *Mathematical modeling of elastic thin bodies with one small dimension with the use of systems of orthogonal polynomials.* Deposited in VINITI RAS, No. 723 – B2008, 21.08.2008, (in Russian), Moscow, 2008, 64 p.

[58] Nikabadze, M.U. *Application of systems of orthogonal polynomials in the mathematical modeling of plane elastic thin bodies.* Deposited in VINITI RAS, No. 724 – B2008, 21.08.2008, (in Russian), Moscow, 2008, 44 p.

[59] Meunargiya, T.V. *Development of the method of I. N. Vekua for problems of the three-dimensional moment elasticity.* Tbilisi Univ., Tbilisi, 1987.

[60] Vekua, I. N. *Fundamentals of tensor analysis and covariant theory.* Nauka, Moscow, 1978.

[61] Lur'e, A. I. *Nonlinear elasticity.* Nauka, Moscow, 1980.

[62] Pobedrya, B. E. *Lectures in tensor analysis.* Moscow Univ., Moscow, 1986.

[63] Pobedrya, B. E. *Numerical methods in the theory of elasticity and plasticity.* 2nd ed. Moscow Univ., Moscow, 1995.

Mikhail Nikabadze, Prof.: Lomonosov Moscow State University, Department of Mechanics and Mathematics, Leninskie Gory, 1, Moscow 119992, Russia (*Bauman Moscow State Technical University, Baumanskaya 2-ya, str., 5, Moscow 105005, Russia*). nikabadze@mail.ru

The author gave a presentation of this paper during one of the conference sessions.

Tamar moseshvili, Ph.D.: Akaki Tsereteli Kutaisi State University, Design and Technology Department, Tamar Mephe street 59, Kutaisi 4600, Georgia (*tamarmoseshvili@yahoo.com*).
The author gave a presentation of this paper during one of the conference sessions.

Armine Ulukhanian, Ph.D.: Bauman Moscow State Technical University, Departament of Calculation Mathematics and Mathematical Physics, Baumanskaya 2-ya, str., 5, Moscow 105005, Russia (*armine_msu@mail.ru*). The author gave a presentation of this paper during one of the conference sessions.

Ketevan Tskhakaia, Ph.D.: Akaki Tsereteli Kutaisi State University, Energy and Telecommunications Department, Tamar Mephe street 59, Kutaisi 4600, Georgia (*spectri@gmail.com*).

Nodar Mardaleishvili, Ph.D.: Akaki Tsereteli Kutaisi State University, Mechanics and Mechanical Engineering Department, Tamar Mephe street 59, Kutaisi 4600, Georgia (*nodarmard3@mail.ru*).

Formulation of the initial boundery velue problems in the theory of multilayer thermoelastic thin bodies in moments (part II)

Mikhail U. Nikabadze, Tamar Moseshvili, Armine R. Ulukhanian, Ketevan Tskhakaia, Nodar Mardaleishvili

Abstract: Various representations of the equations of motion, the heat influx, the constitutive relations of physical and heat content are given for the new body domain parametrization. The definition of the kth order moment of a certain quantity with respect to an orthonormal polynomial systems is given. The expressions of moments of first- and second-order partial derivatives of a certain tensor field are obtained and this is also done for some important expressions required for constructing different variants of the thin body theory.

1. Representation of equations of motion and heat influx and constitutive relations of physical and heat contents of micropolar theory of multilayer elastic thin bodies with one small size

In what follows, for brevity, we present certain representations of equations of motion and constitutive relations in the case of a one-layer thin body, and then we show how one can obtain the desired relations using the rule presented above and write certain relations.

1.1. Representation of equations of motion and constitutive relations of physical and heat contents of the micropolar theory of one-layertic thin bodies with one small size

The new parametrization of a one-layer thin domain [1–6] is performed by the relation, which is obtained from (I: 1) under the absence of index α under the symbols. To obtain the representations of equations of motion and constitutive relations, we need the representations of the gradient and the divergence under the parametrization considered. Let us obtain the representations of these operators. Omitting the index α, from (I: 12) and (I: 24), we find

$$\mathbf{r}_p = g^{\bar{m}}_{p}\mathbf{r}_{\underset{m}{}} = g_{\underset{pm}{}}{}^{\underset{+}{}}\mathbf{r}^{\bar{m}}, \quad \mathbf{r}^p = g^{p}_{\underset{m}{}}\mathbf{r}^{\bar{m}} = g^{p}_{\underset{m}{+}}\mathbf{r}^{\bar{m}}, \tag{1}$$

and also from (I:1.23), we have

$$\begin{gathered} g^{P}_{\underset{M}{}} = \overset{(-)}{\vartheta}{}^{-1}A^{P}_{\underset{M}{}}, \quad \overset{(-)}{\vartheta} = \det(g^{\bar{J}}_{I}), \quad g^{3}_{\underset{M}{}} = -g^{\bar{3}}_{P}g^{P}_{\underset{M}{}}, \quad g^{\bar{3}}_{P} = x^3 g^{\bar{3}}_{\underset{P}{+}}, \\ g^{\bar{3}}_{\underset{P}{+}} = h^{-1}\partial_P h, \quad h = |\mathbf{h}|, \quad A^{P}_{\underset{M}{}} \equiv g^{\bar{P}}_{\underset{M}{}} + x^3 a^{P}_{\underset{M}{+}}, \quad a^{P}_{\underset{M}{+}} \equiv (g^{\bar{I}}_{\underset{I}{+}} - 1)g^{\bar{P}}_{\underset{M}{}} - g^{\bar{P}}_{\underset{M}{+}}. \end{gathered} \tag{2}$$

Moreover, note that the following relations hold [1–6]:

$$g^{P}_{\underset{M}{-}} = \sum_{s=0}^{\infty} A^{\bar{P}}_{\underset{(s)M}{+}}(x^3)^s, \quad A^{\bar{P}}_{\underset{(s)M}{+}} = (g^{\bar{P}}_{\underset{N_1}{-}} - g^{\bar{P}}_{\underset{N_1}{+}}) \cdot \ldots \cdot (g^{\bar{N}_{s-1}}_{\underset{M}{-}} - g^{\bar{N}_{s-1}}_{\underset{M}{+}}), \quad A^{\bar{P}}_{\underset{(0)M}{+}} = g^{\bar{P}}_{\underset{M}{-}}. \tag{3}$$

By the first and third relations in (2) and the second relation in (1), we find that

$$\mathbf{r}^P = g^{P}_{\underset{M}{-}}\mathbf{r}^{\bar{M}}, \quad \mathbf{r}^3 = g^{3}_{\underset{M}{-}}\mathbf{r}^{\bar{M}} + \mathbf{r}^{\bar{3}} = \mathbf{r}^{\bar{3}} - g^{\bar{3}}_{P}\mathbf{r}^P = \mathbf{r}^{\bar{3}} - g^{\bar{3}}_{P}g^{P}_{\underset{M}{-}}\mathbf{r}^{\bar{M}}. \tag{4}$$

The gradient operator can be applied to any tensor. Therefore, denoting a certain tensor quantity by $\mathbb{F}(x', x^3)$, by the definition of the gradient [7–9] and by (4), we have [1–4]

$$\mathrm{grad}\mathbb{F} = \nabla\mathbb{F} = \mathbf{r}^p\partial_p\mathbb{F} = \mathbf{r}^P\partial_P\mathbb{F} + \mathbf{r}^3\partial_3\mathbb{F} = \mathbf{r}^{\bar{M}}g^{P}_{\underset{M}{-}}(\partial_P - g^{\bar{3}}_{P}\partial_3)\mathbb{F} + \mathbf{r}^{\bar{3}}\partial_3\mathbb{F}.$$

Whence, introducing the differential operator

$$N_p = \partial_p - g^{\bar{3}}_{p}\partial_3, \quad \mathbf{N} = \mathbf{r}^pN_p = \mathbf{r}^PN_P = \mathbf{r}^{\bar{M}}g^{P}_{\underset{M}{-}}N_P, \quad N_3 = 0, \tag{5}$$

we obtain the desired representation of the gradient in the form

$$\mathrm{grad}\mathbb{F} = \nabla\mathbb{F} = \mathbf{N}\mathbb{F} + \mathbf{r}^{\bar{3}}\partial_3\mathbb{F} = \mathbf{r}^PN_P\mathbb{F} + \mathbf{r}^{\bar{3}}\partial_3\mathbb{F} = \mathbf{r}^{\bar{M}}g^{P}_{\underset{M}{-}}N_P\mathbb{F} + \mathbf{r}^{\bar{3}}\partial_3\mathbb{F}. \tag{6}$$

The divergence operator is applied to a tensor whose rank is no less than 1. Applying this operator, e.g. to a second-rank tensor $\underset{\sim}{\mathbf{P}}$, by the third relation in (2) and (5), we obtain

$$\mathrm{div}\,\underset{\sim}{\mathbf{P}} = \nabla\cdot\underset{\sim}{\mathbf{P}} = g^{P}_{\underset{M}{-}}N_P\mathbf{P}^{\bar{M}} + \partial_3\mathbf{P}^{\bar{3}} \quad (\mathbf{P}^{\bar{m}} = \mathbf{r}^{\bar{m}}\cdot\underset{\sim}{\mathbf{P}}). \tag{7}$$

Note that (7) can also be easily obtained from (6) if in this relation we replace the sign of tensor product, which is omitted, with the sign of inner product.

1.1.1. Representations of equations of motion

As is known [10–13], at very small displacements and rotations and gradients of displacements and rotations three-dimensional equations of motion of micropolar deformable rigid bodies are represented in the form

$$\nabla\cdot\underset{\sim}{\mathbf{P}} + \rho\mathbf{F} = \rho\partial_t^2\mathbf{u}, \quad \nabla\cdot\underset{\sim}{\boldsymbol{\mu}} + \underset{\approx}{\mathbf{C}}\overset{2}{\otimes}\underset{\sim}{\mathbf{P}} + \rho\mathbf{m} = \underset{\sim}{\mathbf{J}}\cdot\partial_t^2\boldsymbol{\varphi}. \tag{8}$$

Here $\underset{\sim}{\mathbf{P}}$ and $\underset{\sim}{\boldsymbol{\mu}}$ are tensors of stresses and couple stresses, $\underset{\approx}{\mathbf{C}}$ is the discriminant tensor (third-rank tensor) [7], $\mathbf{u}$ is the vector of displacements, $\boldsymbol{\varphi}$ is the vector of (inner) rotation, ρ is the material density, $\mathbf{F}$ is the mass force density, $\mathbf{m}$ is the mass moment density, and $\overset{2}{\otimes}$ is

the inner 2-product (for example, $\underset{\approx}{\mathbf{C}} \overset{2}{\otimes} \underset{\sim}{\mathbf{P}} = \mathbf{r}^i C_{ijk} P^{jk}$). The definition of inner r-product and the problems related to it are considered in [1–7, 14]. Proceeding analogously to [15], for the equations of the classical deformable rigid body mechanics (DRBM) under the classical parametrization of thin body domain, in the case considered, from (8), we find the following form of representation of equations of micropolar DRMB:

$$\begin{gathered}
\big(1/\sqrt{\overset{(-)}{g}}\big)\partial_P\big(\sqrt{\overset{(-)}{g}}\,\overset{(-)}{\vartheta}\,\mathbf{P}^P\big) + \partial_3\big(\overset{(-)}{\vartheta}\,\mathbf{P}^3\big) + \rho\,\overset{(-)}{\vartheta}\,\mathbf{F} = \rho\,\overset{(-)}{\vartheta}\,\partial_t^2\mathbf{u}, \\
\big(1/\sqrt{\overset{(-)}{g}}\big)\partial_P\big(\sqrt{\overset{(-)}{g}}\,\overset{(-)}{\vartheta}\,\boldsymbol{\mu}^P\big) + \partial_3\big(\overset{(-)}{\vartheta}\,\boldsymbol{\mu}^3\big) + \underset{\approx}{\mathbf{C}} \overset{2}{\otimes} \big(\overset{(-)}{\vartheta}\,\underset{\sim}{\mathbf{P}}\big) + \rho\,\overset{(-)}{\vartheta}\,\mathbf{m} = \overset{(-)}{\vartheta}\,\underset{\sim}{\mathbf{J}} \cdot \partial_t^2\boldsymbol{\varphi}, \\
\overset{(-)}{g} = \det(g_{\bar{m}\bar{n}}), \quad g_{\bar{m}\bar{n}} = \mathbf{r}_{\bar{m}} \cdot \mathbf{r}_{\bar{n}}.
\end{gathered} \tag{9}$$

It is easy to see that by (7), Eqs. (8) can be rewritten in the form

$$g^P_{\bar{M}} N_P \mathbf{P}^{\bar{M}} + \partial_3 \mathbf{P}^{\bar{3}} + \rho\mathbf{F} = \rho\partial_t^2\mathbf{u}, \quad g^P_{\bar{M}} N_P \boldsymbol{\mu}^{\bar{M}} + \partial_3 \boldsymbol{\mu}^{\bar{3}} + \underset{\approx}{\mathbf{C}} \overset{2}{\otimes} \underset{\sim}{\mathbf{P}} + \rho\mathbf{m} = \underset{\sim}{\mathbf{J}} \cdot \partial_t^2\boldsymbol{\varphi}. \tag{10}$$

Note that the following relations hold:

$$g^P_{\bar{M}} N_P \mathbf{P}^{\bar{M}} = g^P_{\bar{m}} N_P \mathbf{P}^{\bar{m}} = N_P(g^P_{\bar{m}} \mathbf{P}^{\bar{m}}) = N_P(g^P_{\bar{M}} \mathbf{P}^{\bar{M}}) = N_P \mathbf{P}^P;$$

using them, we can represent Eqs. (10) in the form

$$\begin{gathered}
N_P \mathbf{P}^P + \partial_3 \mathbf{P}^{\bar{3}} + \rho\mathbf{F} = \rho\partial_t^2\mathbf{u}, \quad N_P \boldsymbol{\mu}^P + \partial_3 \boldsymbol{\mu}^{\bar{3}} + \underset{\approx}{\mathbf{C}} \overset{2}{\otimes} \underset{\sim}{\mathbf{P}} + \rho\mathbf{m} = \underset{\sim}{\mathbf{J}} \cdot \partial_t^2\boldsymbol{\varphi}, \\
N_P(g^P_{\bar{M}} \mathbf{P}^{\bar{M}}) + \partial_3 \mathbf{P}^{\bar{3}} + \rho\mathbf{F} = \rho\partial_t^2\mathbf{u}, \quad N_P(g^P_{\bar{M}} \boldsymbol{\mu}^{\bar{M}}) + \partial_3 \boldsymbol{\mu}^{\bar{3}} + \underset{\approx}{\mathbf{C}} \overset{2}{\otimes} \underset{\sim}{\mathbf{P}} + \rho\mathbf{m} = \underset{\sim}{\mathbf{J}} \cdot \partial_t^2\boldsymbol{\varphi}.
\end{gathered} \tag{11}$$

Multiplying each relation in (10) by $\overset{(-)}{\vartheta}$, with the help of the first relation in (2), we have

$$\begin{gathered}
A^P_{\bar{M}} N_P \mathbf{P}^{\bar{M}} + \overset{(-)}{\vartheta}\,\partial_3 \mathbf{P}^{\bar{3}} + \rho\,\overset{(-)}{\vartheta}\,\mathbf{F} = \rho\,\overset{(-)}{\vartheta}\,\partial_t^2\mathbf{u}, \\
A^P_{\bar{M}} N_P \boldsymbol{\mu}^{\bar{M}} + \overset{(-)}{\vartheta}\,\partial_3 \boldsymbol{\mu}^{\bar{3}} + \underset{\approx}{\mathbf{C}} \overset{2}{\otimes} \big(\overset{(-)}{\vartheta}\,\underset{\sim}{\mathbf{P}}\big) + \rho\,\overset{(-)}{\vartheta}\,\mathbf{m} = \overset{(-)}{\vartheta}\,\underset{\sim}{\mathbf{J}} \cdot \partial_t^2\boldsymbol{\varphi}.
\end{gathered} \tag{12}$$

Note that (9) – (12) are different forms of representation of the equations of micropolar DRBM (8) for the parametrization of thin body domain considered. They are called the different forms of the equations of micropolar deformable rigid thin body mechanic (DRTBM) under the new parametrization of thin body domain. Taking into account the first relation in (3), we can write Eqs. (10) in the form

$$\begin{gathered}
\sum_{s=0}^{\infty} A^{\bar{P}}_{+\,\bar{M}} (x^3)^s N_P \mathbf{P}^{\bar{M}} + \partial_3 \mathbf{P}^{\bar{3}} + \rho\mathbf{F} = \rho\partial_t^2\mathbf{u}, \\
\sum_{s=0}^{\infty} A^{\bar{P}}_{+\,\bar{M}} (x^3)^s N_P \boldsymbol{\mu}^{\bar{M}} + \partial_3 \boldsymbol{\mu}^{\bar{3}} + \underset{\approx}{\mathbf{C}} \overset{2}{\otimes} \underset{\sim}{\mathbf{P}} + \rho\mathbf{m} = \underset{\sim}{\mathbf{J}} \cdot \partial_t^2\boldsymbol{\varphi}.
\end{gathered} \tag{13}$$

It is seen that Eqs. (13) contain infinitely many summands. Therefore, they cannot be used in practice. Naturally, we need to consider approximate equations with finitely many summands. In this connection, let us introduce the following definition.

Definition 1.1 *The equations, which are obtained from* (10) *if, in the expansion of* $g^{P}_{\underset{M}{-}}$ *(see the first formula in* (3)*), we preserve first* $s+1$ *terms, are called the equations of approximation of order* s*.*

Obviously, the equation of approximation of order s are represented in the form

$$g^{P}_{\underset{(s)M}{-}} N_P \mathbf{P}^{\bar{M}} + \partial_3 \mathbf{P}^{\bar{3}} + \rho\mathbf{F} = \rho\partial_t^2 \mathbf{u}, \quad g^{P}_{\underset{(s)M}{-}} N_P \boldsymbol{\mu}^{\bar{M}} + \partial_3 \boldsymbol{\mu}^{\bar{3}} + \underset{\sim}{\mathbf{C}} \overset{2}{\otimes} \underset{\sim}{\mathbf{P}} + \rho\mathbf{m} = \underset{\sim}{\mathbf{J}} \cdot \partial_t^2 \boldsymbol{\varphi}, \quad (14)$$

$$g^{P}_{\underset{(s)M}{-}} = \sum_{m=0}^{s} A^{\bar{P}}_{\underset{M}{+}} (x^3)^m. \quad (15)$$

From (14) for $s=0$, we obtain the equations of zero approximation, for $s=1$ the equations of first approximation, etc.

1.1.2. Representation of the equation of heat influx in micropolar DRTBM

In the general case, the heat influx equation in micropolar DRBM has the form [16]

$$-\nabla \cdot \mathbf{q} + \rho q - T\frac{d}{dt}(\underset{\sim}{\mathbf{a}} \overset{2}{\otimes} \underset{\sim}{\mathbf{P}} + \underset{\sim}{\mathbf{d}} \overset{2}{\otimes} \underset{\sim}{\boldsymbol{\mu}}) + W^* = \rho c_p \partial_t T, \quad (16)$$

where $\mathbf{q}$ is the vector of exterior heat influx, q is the mass heat influx, T is the temperature, $\underset{\sim}{\mathbf{a}}$, $\underset{\sim}{\mathbf{d}}$ are the tensors of heat extension, $\underset{\sim}{\mathbf{P}} \neq \underset{\sim}{\mathbf{P}}^T$ is the stress tensor, $\underset{\sim}{\boldsymbol{\mu}} \neq \underset{\sim}{\boldsymbol{\mu}}^T$ is the couple stress tensor, W^* is the scattering function, ρ is the medium density, and c_p is the heat capacity under a constant pressure. If we consider the physically linear medium, then the nonlinearity in (16) is in the third summand of the left-hand side. A similar situation holds in a particular variant of this equation, which is obtained from (16) for $\underset{\sim}{\mathbf{d}} = 0$ (see [17]). In the latter case, since both heat capacities c_p and c_v (the heat capacity under a constant volume) cannot be constant simultaneously (independent of the temperature), very often, one assumes that in this summand, the temperature T is replaced with the temperature $T_0 = \text{const}$. Taking into account this assumption, we see that the desired representation of the heat influx equation has the following form analogous to (10):

$$-g^{P}_{\underset{M}{-}} N_P q^{\bar{M}} - \partial_3 q^{\bar{3}} + \rho q - T_0 \frac{d}{dt}(\underset{\sim}{\mathbf{a}} \overset{2}{\otimes} \underset{\sim}{\mathbf{P}} + \underset{\sim}{\mathbf{d}} \overset{2}{\otimes} \underset{\sim}{\boldsymbol{\mu}}) + W^* = \rho c_p \partial_t T. \quad (17)$$

If necessary, it is easy to write the relations analogous to (9) and (12). Therefore, for brevity, we do not dwell on this. Note that by (17), analogously to (14), the heat influx equation of approximation of order s is represented in the form

$$-g^{P}_{\underset{(s)M}{-}} N_P q^{\bar{M}} - \partial_3 q^{\bar{3}} + \rho q - T_0 \frac{d}{dt}(\underset{\sim}{\mathbf{a}} \overset{2}{\otimes} \underset{\sim}{\mathbf{P}} + \underset{\sim}{\mathbf{d}} \overset{2}{\otimes} \underset{\sim}{\boldsymbol{\mu}}) + W^* = \rho c_p \partial_t T. \quad (18)$$

1.1.3. Representations of constitutive relations of physical and heat content

In linear micropolar elasticity theory, the constitutive relations of physical content under non-isothermal processes can be represented in the following form by the generalized Duhamel–Neumann principle [16, 17]:

$$\underset{\sim}{\mathbf{P}} = \underset{\approx}{\mathbf{A}} \overset{2}{\otimes} (\underset{\sim}{\boldsymbol{\gamma}} - \underset{\sim}{\mathbf{a}}\vartheta) + \underset{\approx}{\mathbf{B}} \overset{2}{\otimes} (\underset{\sim}{\boldsymbol{\varkappa}} - \underset{\sim}{\mathbf{d}}\vartheta), \quad \underset{\sim}{\boldsymbol{\mu}} = \underset{\approx}{\mathbf{C}} \overset{2}{\otimes} (\underset{\sim}{\boldsymbol{\gamma}} - \underset{\sim}{\mathbf{a}}\vartheta) + \underset{\approx}{\mathbf{D}} \overset{2}{\otimes} (\underset{\sim}{\boldsymbol{\varkappa}} - \underset{\sim}{\mathbf{d}}\vartheta), \tag{19}$$

where $\underset{\sim}{\boldsymbol{\gamma}} = \nabla\mathbf{u} - \underset{\simeq}{\mathbf{C}} \cdot \boldsymbol{\varphi}$ is the deformation tensor in micropolar theory (see [12]), $\underset{\sim}{\boldsymbol{\varkappa}} = \nabla\boldsymbol{\varphi}$ is the bend-torsion tensor, $\underset{\approx}{\mathbf{A}}$, $\underset{\approx}{\mathbf{B}}$, $\underset{\approx}{\mathbf{D}}$ ($\underset{\approx}{\mathbf{C}} = \underset{\approx}{\mathbf{B}}^T$) are material tensors of the fourth rank, and ϑ is the temperature overfall. By the expression for $\underset{\sim}{\boldsymbol{\gamma}}$, we can write (19) in the form

$$\underset{\sim}{\mathbf{P}} = \underset{\approx}{\mathbf{A}} \overset{2}{\otimes} \nabla\mathbf{u} + \underset{\approx}{\mathbf{B}} \overset{2}{\otimes} \nabla\boldsymbol{\varphi} - \underset{\approx}{\mathbf{A}} \overset{2}{\otimes} \underset{\simeq}{\mathbf{C}} \cdot \boldsymbol{\varphi} - \underset{\sim}{\mathbf{b}}\vartheta, \quad \underset{\sim}{\boldsymbol{\mu}} = \underset{\approx}{\mathbf{C}} \overset{2}{\otimes} \nabla\mathbf{u} + \underset{\approx}{\mathbf{D}} \overset{2}{\otimes} \nabla\boldsymbol{\varphi} - \underset{\approx}{\mathbf{C}} \overset{2}{\otimes} \underset{\simeq}{\mathbf{C}} \cdot \boldsymbol{\varphi} - \underset{\sim}{\boldsymbol{\beta}}\vartheta, \tag{20}$$

$$\underset{\sim}{\mathbf{b}} = \underset{\approx}{\mathbf{A}} \overset{2}{\otimes} \underset{\sim}{\mathbf{a}} + \underset{\approx}{\mathbf{B}} \overset{2}{\otimes} \underset{\sim}{\mathbf{d}}, \quad \underset{\sim}{\boldsymbol{\beta}} = \underset{\approx}{\mathbf{C}} \overset{2}{\otimes} \underset{\sim}{\mathbf{a}} + \underset{\approx}{\mathbf{D}} \overset{2}{\otimes} \underset{\sim}{\mathbf{d}},$$

which are called the tensors of thermomechanical properties. Note that a particular case of law (20) was considered in [12, 13], and more general relations were presented in [16, 18]. Now it is easy to find the desired representations of the Hooke law (20) under the new parametrization of thin body domain. Indeed, taking into account the representation of the gradient operator (6), after simple transformations, from (20), we have

$$\begin{aligned}
\underset{\sim}{\mathbf{P}} &= \underset{\approx}{\mathbf{A}} \overset{2}{\otimes} (\underset{M}{\overset{P}{g}} \mathbf{r}^{\bar{M}} N_P\mathbf{u} + \mathbf{r}^{\bar{3}}\partial_3\mathbf{u}) + \underset{\approx}{\mathbf{B}} \overset{2}{\otimes} (\underset{M}{\overset{P}{g}} \mathbf{r}^{\bar{M}} N_P\boldsymbol{\varphi} + \mathbf{r}^{\bar{3}}\partial_3\boldsymbol{\varphi}) - \underset{\approx}{\mathbf{A}} \overset{2}{\otimes} \underset{\simeq}{\mathbf{C}} \cdot \boldsymbol{\varphi} - \underset{\sim}{\mathbf{b}}\vartheta, \\
\underset{\sim}{\boldsymbol{\mu}} &= \underset{\approx}{\mathbf{C}} \overset{2}{\otimes} (\underset{M}{\overset{P}{g}} \mathbf{r}^{\bar{M}} N_P\mathbf{u} + \mathbf{r}^{\bar{3}}\partial_3\mathbf{u}) + \underset{\approx}{\mathbf{D}} \overset{2}{\otimes} (\underset{M}{\overset{P}{g}} \mathbf{r}^{\bar{M}} N_P\boldsymbol{\varphi} + \mathbf{r}^{\bar{3}}\partial_3\boldsymbol{\varphi}) - \underset{\approx}{\mathbf{C}} \overset{2}{\otimes} \underset{\simeq}{\mathbf{C}} \cdot \boldsymbol{\varphi} - \underset{\sim}{\boldsymbol{\beta}}\vartheta.
\end{aligned} \tag{21}$$

Taking into account the first relation in (3), it is easy to note that relations (21) contain infinitely many summands. Therefore, they cannot be used in such a form. In applications, one uses approximate constitutive relations (CR), i.e., the relations represented by finitely many summands. In this connection, we introduce the following definition.

Definition 1.2 *The relations obtained from* (21) *under the condition that in the expansion of* $\underset{M}{\overset{P}{g}}$ *(see the first formula in* (3)*), first* $s+1$ *are preserved are called the CR of approximation of order* s.

It is easy to see that analogously to Eqs. (14) and (18), CR of approximation of order s are represented in the form

$$\begin{aligned}
\underset{\sim}{\mathbf{P}}_{(s)} &= \underset{\approx}{\mathbf{A}} \overset{2}{\otimes} (\underset{(s)M}{\overset{P}{g}} \mathbf{r}^{\bar{M}} N_P\mathbf{u} + \mathbf{r}^{\bar{3}}\partial_3\mathbf{u}) + \underset{\approx}{\mathbf{B}} \overset{2}{\otimes} (\underset{(s)M}{\overset{P}{g}} \mathbf{r}^{\bar{M}} N_P\boldsymbol{\varphi} + \mathbf{r}^{\bar{3}}\partial_3\boldsymbol{\varphi}) - \underset{\approx}{\mathbf{A}} \overset{2}{\otimes} \underset{\simeq}{\mathbf{C}} \cdot \boldsymbol{\varphi} - \underset{\sim}{\mathbf{b}}\vartheta, \\
\underset{\sim}{\boldsymbol{\mu}}_{(s)} &= \underset{\approx}{\mathbf{C}} \overset{2}{\otimes} (\underset{(s)M}{\overset{P}{g}} \mathbf{r}^{\bar{M}} N_P\mathbf{u} + \mathbf{r}^{\bar{3}}\partial_3\mathbf{u}) + \underset{\approx}{\mathbf{D}} \overset{2}{\otimes} (\underset{(s)M}{\overset{P}{g}} \mathbf{r}^{\bar{M}} N_P\boldsymbol{\varphi} + \mathbf{r}^{\bar{3}}\partial_3\boldsymbol{\varphi}) - \underset{\approx}{\mathbf{C}} \overset{2}{\otimes} \underset{\simeq}{\mathbf{C}} \cdot \boldsymbol{\varphi} - \underset{\sim}{\boldsymbol{\beta}}\vartheta.
\end{aligned} \tag{22}$$

Definition 1.3 *The relations obtained from* (22) *for* $s = 0$ *are called CR of zero approximation, and for* $s = 1$*, they are called CR of the first approximation.*

It is easy to see that CR of zero approximation have the form

$$\underset{\approx}{\mathbf{P}}_{(0)} = \underset{\approx}{\mathbf{A}} \overset{2}{\otimes} (\mathbf{r}^{\bar{M}} N_P \mathbf{u} + \mathbf{r}^{\bar{3}} \partial_3 \mathbf{u}) + \underset{\approx}{\mathbf{B}} \overset{2}{\otimes} (\mathbf{r}^{\bar{M}} N_P \boldsymbol{\varphi} + \mathbf{r}^{\bar{3}} \partial_3 \boldsymbol{\varphi}) - \underset{\approx}{\mathbf{A}} \overset{2}{\otimes} \underset{\approx}{\mathbf{C}} \cdot \boldsymbol{\varphi} - \underset{\sim}{\mathbf{b}} \vartheta,$$
$$\underset{\sim}{\boldsymbol{\mu}}_{(0)} = \underset{\approx}{\mathbf{C}} \overset{2}{\otimes} (\mathbf{r}^{\bar{M}} N_P \mathbf{u} + \mathbf{r}^{\bar{3}} \partial_3 \mathbf{u}) + \underset{\approx}{\mathbf{D}} \overset{2}{\otimes} (\mathbf{r}^{\bar{M}} N_P \boldsymbol{\varphi} + \mathbf{r}^{\bar{3}} \partial_3 \boldsymbol{\varphi}) - \underset{\approx}{\mathbf{C}} \overset{2}{\otimes} \underset{\approx}{\mathbf{C}} \cdot \boldsymbol{\varphi} - \underset{\sim}{\boldsymbol{\beta}} \vartheta.$$

Note that if we consider a body without center of symmetry [12,13], then $\underset{\approx}{\mathbf{A}} = 0$, $\underset{\approx}{\mathbf{B}} = 0$, and in this case, the CR presented above simplify. Let us find the corresponding representation for the Fourier heat conduction law (which defines the relations of heat content) under the new parametrization of the thin body domain.Since the Fourier heat conduction law [13,17] has the form $\mathbf{q} = -\underset{\sim}{\Lambda} \cdot \nabla T$, where the second-rank positive-definite tensor $\underset{\sim}{\mathbf{\Lambda}}$ is called the heat conduction tensor, by (6), the Fourier heat conduction law of zero approximation and approximation of order s is represented in the form

$$\mathbf{q}_{(0)} = -\mathbf{\Lambda}^{\bar{M}} N_P T - \mathbf{\Lambda}^{\bar{3}} \partial_3 T, \quad \mathbf{q}_{(s)} = -\mathbf{\Lambda}^{\bar{M}} \underset{(s)\bar{M}}{g} \overset{P}{} N_P T - \mathbf{\Lambda}^{\bar{3}} \partial_3 T, \quad \mathbf{\Lambda}^{\bar{m}} = \underset{\sim}{\mathbf{\Lambda}} \cdot \mathbf{r}^{\bar{m}}. \tag{23}$$

2. To micropolar theory with respect to system of orthonormal Chebyshev polynomials of second kind

To construct the micropolar theory with respect to a certain system of orthogonal polynomials (Legendre, Chebyshev, etc.), we need recursive relations for these polynomials. For example, for the shifted Chebyshev polynomials, the main recursive relations on the orthogonality closed interval [0,1] are represented in the following form [1–4, 19, 20]:

$$\begin{aligned} &4tU_n^*(t) = U_{n-1}^*(t) + 2U_n^*(t) + U_{n+1}^*(t),\ 2tU_n^{*'}(t) = 2nU_n^*(t) + U_{n-1}^{*'}(t) + U_n^{*'}(t),\ n \geq 1, \\ &U_n^{*'}(t) = 4nU_{n-1}^*(t) + U_{n-2}^{*'}(t), \quad n \geq 2, \quad 0 \leq t \leq 1. \end{aligned} \tag{24}$$

Note that formulas (24) are obtained in the same way as analogous formulas for Legendre polynomials on the orthogonality closed interval [-1,1], e.g, in [21] (see also [22]). Using the main recursive relations (24), it is easy to obtain the following relations, which are necessary for constructing thin body theories [1–4, 19, 20]:

$$2^{2s} t^s U_n^*(t) = \sum_{p=0}^{2s} C_{2s}^p U_{n-s+p}^*(t), \quad s, n \in \mathbb{N}_0; \tag{25}$$

$$2^{2s} t^s U_m^*(t) U_n^*(t) = \sum_{p=0}^{m} \sum_{q=0}^{2s} C_{2s}^q U_{n-m-s+2p+q}^*(t), \quad n, m, s \in \mathbb{N}_0; \tag{26}$$

$$U_n^{*'}(t) = 4\sum_{k=0}^{[(n-1)/2]}(n-2k)U^*_{n-(2k+1)}(t) = 4\sum_{k=0}^{[(n-1)/2]}(2k+1+a)U^*_{2k+a}(t),\ n\geq 1; \quad (27)$$

$$2^{2s}t^sU_n^{*'}(t) = 4\sum_{k=0}^{[(n-1)/2]}(2k+1+a)U^*_{2k+a-s+p},\ \ n\geq 1,\ s\geq 0; \quad (28)$$

$$U_n^{*''}(t) == 2^2\sum_{k=0}^{[(n-2)/2]}(2k+2-a)[(n+1)^2-(2k+2-a)^2]U^*_{2k+1-a}(t), \quad n\geq 2; \quad (29)$$

$$\begin{aligned}2^{2s}t^sU_n^{*''}(t) &= 2^4\sum_{k=0}^{[(n-2)/2]}\sum_{p=0}^{2s}(k+1)(n-k)[n-(2k+1)]C^p_{2s}U^*_{n-(s+2k+2)+p}\\ &= 2^2\sum_{k=0}^{[(n-2)/2]}(2k+2-a)[(n+1)^2-(2k+2-a)^2]C^p_{2s}U^*_{2k+1-a-s+p},\ n\geq 2,\ s\geq 0.\end{aligned} \quad (30)$$

Here, $a = n-1-2\big[(n-1)/2\big]$, $[x]$ is the integral part of x, and C^n_m are the binomial coefficients. It should be noted that all relations (25) – (30),which also hold for the system of orthonormal Chebyshev polynomials of the second kind $\{\hat{U}^*_k\}_{k=0}^{\infty}$, except for (26), can be proved by induction. For a system of orthonormal polynomials (26) is presented in the form

$$2^{2s}t^s\hat{U}^*_m(t)\hat{U}^*_n(t) = \hat{U}^*_0\sum_{p=0}^{m}\sum_{q=0}^{2s}C^q_{2s}\hat{U}^*_{n-m-s+2p+q}(t), \quad n,m,s\in\mathbb{N}_0. \quad (31)$$

Note that extending the definition of system of Chebyshev polynomials of the second kind to the set of negative numbers, we obtain the relation $U^*_{-n} = -U^*_{n-2}$, $n\in\mathbb{N}_0$, under which (25) – (30) were obtained.

Let us consider a certain tensor field $\mathbb{F}(x^1,x^2,x^3)$, which depends on the coordinates x^1,x^2,x^3 of the thin body domain under its new parametrization. For brevity, instead of $\mathbb{F}(x^1,x^2,x^3)$, we write $\mathbb{F}(x',x^3)$, where $x' = (x^1,x^2)$, $x^3\in[0,1]$. Moreover, we assume that the tensor fields considered are sufficiently smooth. For example, $\mathbb{F}(x',x^3)\in C_m(V\cup\partial V)$, $m\geq 1$; V is the domain occupied by the thin body considered and ∂V is its boundary. Then the tensor field $\mathbb{F}(x',x^3)$ can be expanded in a series with respect to the system of shifted Chebyshev polynomials of the second kind $\{\hat{U}^*_k\}_{k=0}^{\infty}$ with respect to the coordinate $x^3\in[0,1]$ for each fixed point $x'\in\overset{(-)}{S}$ [21]. This expansion is represented in the form

$$\mathbb{F}(x',x^3) = \sum_{k=0}^{\infty}\overset{(k)}{\mathbb{F}}(x')\hat{U}^*_k(x^3), \quad x'\in\overset{(-)}{S}, \quad x^3\in[0,1], \quad (32)$$

where $\overset{(k)}{\mathbb{F}}(x')$ is called the coefficient with number k in the expansion of $\mathbb{F}(x',x^3)$ in the series with respect to the polynomial system $\{\hat{U}^*_k\}_{k=0}^{\infty}$.

Definition 2.1 *The moment of the kth order of a certain tensor field $\mathbb{F}(x',x^3)$ with respect to the polynomial system $\{\hat{U}^*_k\}_{k=0}^{\infty}$, which is denoted by $\overset{(k)}{\mathbb{M}}(\mathbb{F})$, is the integral*

$$\overset{(k)}{\mathbb{M}}(\mathbb{F}) = \int_0^1\mathbb{F}(x',x^3)\hat{U}^*_k(x^3)h^*(x^3)dx^3, \quad k\in\mathbb{N}_0. \quad (33)$$

It is easy to prove that the following assertions hold:

Assertion 2.1 *For any tensor fields $\mathbb{F}(x', x^3)$ and $\mathbb{G}(x', x^3)$ and any functions $\alpha(x')$ and $\beta(x')$, the following relation holds:*

$$\overset{(k)}{\mathbb{M}}[\alpha(x')\mathbb{F} + \beta(x')\mathbb{G}] = \alpha(x')\overset{(k)}{\mathbb{M}}(\mathbb{F}) + \beta(x')\overset{(k)}{\mathbb{M}}(\mathbb{G}), \quad k \in \mathbb{N}_0. \tag{34}$$

This implies that the moment operator is a linear operator.

Assertion 2.2 *The kth-order moment of a tensor field $\mathbb{F}(x', x^3)$ with respect to the polynomial system $\{\hat{U}_k^*\}_{k=0}^{\infty}$ is equal to the coefficient with number k in the expansion of $\mathbb{F}(x', x^3)$ with respect to x^3 in this polynomial system, i.e.,*

$$\overset{(k)}{\mathbb{M}}(\mathbb{F}) = \int_0^1 \mathbb{F}(x', x^3)\hat{U}_k^*(x^3)h^*(x^3)dx^3 = \overset{(k)}{\mathbb{F}}(x'), \quad k \in \mathbb{N}_0. \tag{35}$$

Assertion (34) follows from (33), whereas (35) is proved by using (32), (33) and the orthonormality of the system $\{\hat{U}_k^*\}_{k=0}^{\infty}$. It is easy to prove that the relations hold

$$\overset{(k)}{\mathbb{M}}(\partial_i\mathbb{F}) = \begin{cases} \partial_I \overset{(k)}{\mathbb{F}}(x'), & i = I, \\ \overset{(k)}{\mathbb{F}}{}'(x'), & i = 3, \end{cases} \qquad \overset{(k)}{\mathbb{M}}(\partial_i\partial_j\mathbb{F}) = \begin{cases} \partial_I\partial_J \overset{(k)}{\mathbb{F}}(x'), & i = I,\ j = J, \\ \partial_I \overset{(k)}{\mathbb{F}}{}'(x'), & i = I,\ j = 3, \\ \overset{(k)}{\mathbb{F}}{}''(x'), & i = j = 3, \end{cases} \tag{36}$$

where we have introduced the following notation:

$$\begin{aligned} \overset{(k)}{\mathbb{F}}{}'(x') &= 2(k+1)\left[\sum_{p=k}^{N}\left(1-(-1)^{k+p}\right)\overset{(p)}{\mathbb{F}}(x') + \overset{(+)}{\mathbb{F}}{}'(x') - (-1)^k\overset{(-)}{\mathbb{F}}{}'(x')\right], \\ \overset{(k)}{\mathbb{F}}{}''(x') &= 2(k+1)\left[\sum_{p=k}^{N}(p-k)(k+p+2)\left(1+(-1)^{k+p}\right)\overset{(p)}{\mathbb{F}}(x') + \overset{(+)}{\mathbb{F}}{}''+(-1)^k\overset{(-)}{\mathbb{F}}{}''\right], \end{aligned} \tag{37}$$

$$\begin{aligned} \overset{(+)}{\mathbb{F}}{}'(x') &= \sum_{p=N+1}^{\infty}\overset{(p)}{\mathbb{F}}(x'), \quad \overset{(+)}{\mathbb{F}}{}''(x') = \sum_{p=N+1}^{\infty}(p-k)(k+p+2)\overset{(p)}{\mathbb{F}}(x'), \\ \overset{(-)}{\mathbb{F}}{}'(x') &= \sum_{p=N+1}^{\infty}(-1)^p\overset{(p)}{\mathbb{F}}(x'), \quad \overset{(-)}{\mathbb{F}}{}''(x') = \sum_{p=N+1}^{\infty}(-1)^p(p-k)(k+p+2)\overset{(p)}{\mathbb{F}}(x'). \end{aligned} \tag{38}$$

Note that the first relation in (37) can be taken as the definition of the "prime" operator, and the second can be obtained by applying the "prime" operator to $\overset{(k)}{\mathbb{F}}$ two times. The following relations are generalizations of (36):

$$\overset{(k)}{\mathbb{M}}[P_N(x^3)\partial_i^p\partial_j^q\mathbb{F}] = \begin{cases} \partial_I^p\partial_J^q\overset{(k)}{\mathbb{M}}\big[P_N(x^3)\mathbb{F}\big], & i = I,\ j = J, \\ \partial_I\big\{\overset{(k)}{\mathbb{M}}\big[P_N(x^3)\mathbb{F}\big]\big\}^{(q)}, & i = I,\ j = 3, \\ \big\{\overset{(k)}{\mathbb{M}}\big[P_N(x^3)\mathbb{F}\big]\big\}^{(p+q)}, & i = j = 3. \end{cases} \tag{39}$$

where $P_N(x^3)$ is a polynomial of degree N, k, N, p, $q \in \mathbb{N}_0$, and $\big\{\overset{(k)}{\mathbb{M}}\big[P_N(x^3)\mathbb{F}\big]\big\}^{(m)}$, $m \in \mathbb{N}_0$, means that the "prime" operator is applied m times. To prove first lines of (36) and (39), we use Definition (33). The second and third lines of (36) are proved by using (27) and (29), respectively, and the second and third lines of (39) are proved by induction. Using (25) and the last relation in (39), we can prove the relations

$$\overset{(n)}{\mathbb{M}}\big[(x^3)^s\mathbb{F}\big]=\sum_{p=0}^{2s} 2^{-2s}C_{2s}^{p}\ \overset{(n-s+p)}{\mathbb{F}},\ \ \overset{(n)}{\mathbb{M}}\big[(x^3)^s\partial_3^m\mathbb{F}\big]=\sum_{p=0}^{2s} 2^{-2s}C_{2s}^{p}\ \overset{(n-s+p)}{\mathbb{F}}{}^{(m)},\ \ n,\ s,\ m\in\mathbb{N}_0. \tag{40}$$

It can be seen that the first relation (40) is obtaind from the second for $m = 0$. Let us represent (40) for $m = 1$ in another form. Using easy transformations, the first relation in (37) and first two relations in (38), from the second relation (40) for $m = 1$, we obtain

$$\begin{aligned}
&\overset{(k)}{\mathbb{M}}{}'\big[(x^3)^{s+1}\mathbb{F}\big] = \overset{(k)}{\mathbb{M}}\big[(x^3)^{s+1}\partial_3\mathbb{F}\big] = \sum_{p=0}^{2s+2} 2^{-2(s+1)}C_{2s+2}^{p}\ \overset{(p-v)}{\mathbb{F}}{}',\\
&= \sum_{p=0}^{2s+2}\sum_{q=l-1}^{N} l\,2^{-2(s+1)}C_{2s+2}^{p}\big[1-(-1)^{l+q}\big]\overset{(q)}{\mathbb{F}} + a_{(s,k)}\overset{(+)}{\mathbb{F}}{}',\\
&v = s+1-k,\ \ l = k-s+p,\ \ s\ge 0,\ \ k\ge 0.
\end{aligned} \tag{41}$$

where we have introduced the notation $a_{(s,k)} = 2^{-(2s+1)}\sum\limits_{p=0}^{2s+2}(k-s+p)C_{2s+2}^{p},\ s\ge 0,\ k\ge 0.$

Let us find the expression for $\overset{(k)}{\mathbb{M}}(\underset{(s)M}{g}{}^{P}_{-}\mathrm{N}_P\mathbb{F})$. By (5) and (34), we obtain

$$\overset{(k)}{\mathbb{M}}(\underset{(s)M}{g}{}^{P}_{-}\mathrm{N}_P\mathbb{F}) = \overset{(k)}{\mathbb{M}}(\underset{(s)M}{g}{}^{P}_{-}\partial_P\mathbb{F}) - \underset{P}{g}{}^{3}_{+}\overset{(k)}{\mathbb{M}}(x^3\underset{(s)M}{g}{}^{P}_{-}\partial_3\mathbb{F}). \tag{42}$$

Furthermore, by (15), (34), (39) and the first relation (40), we find that

$$\overset{(k)}{\mathbb{M}}(\underset{(s)M}{g}{}^{P}_{-}\partial_P\mathbb{F}) = \sum_{m=0}^{s}\sum_{n=0}^{2m} 2^{-2m}C_{2m}^{n}\underset{(m)M}{A}{}^{\bar{P}}_{+}\partial_P\ \overset{(k-m+n)}{\mathbb{F}},\ \ k,\ s\in\mathbb{N}_0 \tag{43}$$

Whence, for $s = 0$ and $s = 1$, we obtain

$$\overset{(k)}{\mathbb{M}}(\underset{(0)M}{g}{}^{P}_{-}\partial_P\mathbb{F})=\partial_M\overset{(k)}{\mathbb{F}},\ \ \overset{(k)}{\mathbb{M}}(\underset{(1)M}{g}{}^{P}_{-}\partial_P\mathbb{F})=\partial_P\overset{(k)}{\mathbb{F}}+\frac{1}{4}\underset{M}{A}{}^{\bar{P}}_{+}\partial_M\big(\overset{(k-1)}{\mathbb{F}}+2\overset{(k)}{\mathbb{F}}+\overset{(k+1)}{\mathbb{F}}\big),\ k\ge 0. \tag{44}$$

Here, we have introduced the notation $\underset{M}{A}{}^{\bar{P}}_{+} \equiv \underset{(1)M}{A}{}^{\bar{P}}_{+} = \underset{M}{g}{}^{\bar{P}}_{-} - \underset{M}{g}{}^{\bar{P}}_{+}$. Moreover, we assume that $\overset{(m)}{\mathbb{F}} = 0$ if $m < 0$. On what follows, we assume that this condition holds. Analogously, by (15), (34), (39) and (41), we have

$$\begin{aligned}
&\overset{(k)}{\mathbb{M}}(x^3\underset{(s)M}{g}{}^{P}_{-}\partial_3\mathbb{F}) = \sum_{m=0}^{s}\sum_{n=0}^{2m+2} 2^{-2(m+1)}C_{2m+2}^{n}\underset{(m)M}{A}{}^{\bar{P}}_{+}\ \overset{(n-v)}{\mathbb{F}}{}'(x')\\
&= \sum_{m=0}^{s}\sum_{n=0}^{2m+2}\sum_{q=l-1}^{N} 2^{-2(m+1)}C_{2m+2}^{n}l\,\underset{(m)M}{A}{}^{\bar{P}}_{+}\big[1+(-1)^{l+q}\big]\overset{(q)}{\mathbb{F}}(x')+\Big(\sum_{m=0}^{s} a_{(m,k)}\underset{(m)M}{A}{}^{\bar{P}}_{+}\Big)\overset{(+)}{\mathbb{F}}{}',\\
&v = m+1-k,\quad l\equiv k-m+n,\quad N\ge s+k+1,\quad k\ge 0,\quad s\ge 0.
\end{aligned} \tag{45}$$

Whence, for $s=0$ and $s=1$, we find that

$$\begin{aligned}
&\overset{(k)}{\mathbb{M}}(x^3\underset{(0)M}{\overset{P}{g}}\partial_3\mathbb{F})=\underset{M}{\overline{P}}\overset{(k)}{\mathbb{M}}{}'(x^3\mathbb{F})=\frac{1}{4}\underset{M}{\overline{P}}(\overset{(k-1)}{\mathbb{F}}{}'+2\overset{(k)}{\mathbb{F}}{}'+\overset{(k+1)}{\mathbb{F}}{}')\\
&=\underset{M}{\overline{P}}\big[k\overset{(k)}{\mathbb{F}}+2(k+1)\big(\sum_{p=k}^{N}\overset{(p)}{\mathbb{F}}-\overset{(k)}{\mathbb{F}}+\overset{(+)}{\mathbb{F}}{}'\big)\big],\quad k\geq 0,
\end{aligned}\tag{46}$$

$$\begin{aligned}
&\overset{(k)}{\mathbb{M}}(x^3\underset{(1)M}{\overset{P}{g}}\partial_3\mathbb{F})=\overset{(k)}{\mathbb{M}}\big[\big(\underset{M}{\overline{P}}x^3+\underset{M}{\overline{P}}(x^3)^2\big)\partial_3\mathbb{F}\big]=\underset{M}{\overline{P}}\overset{(k)}{\mathbb{M}}{}'(x^3\mathbb{F})+\underset{M}{\overline{P}}\overset{(k)}{\mathbb{M}}{}'[(x^3)^2\mathbb{F}]\\
&=\underset{M}{\overline{P}}\big[k\overset{(k)}{\mathbb{F}}+2(k+1)\big(\sum_{p=k}^{N}\overset{(p)}{\mathbb{F}}-\overset{(k)}{\mathbb{F}}+\overset{(+)}{\mathbb{F}}{}'\big)\big]+\frac{1}{4}\underset{M}{\overline{P}}\big[(k-1)\overset{(k-1)}{\mathbb{F}}\\
&-4(k+2)\overset{(k)}{\mathbb{F}}-(k+3)\overset{(k+1)}{\mathbb{F}}+8(k+1)\big(\sum_{p=k}^{N}\overset{(p)}{\mathbb{F}}+\overset{(+)}{\mathbb{F}}{}'\big)\big],\quad k\geq 0.
\end{aligned}\tag{47}$$

Taking into account (43) and (45), from (42) we obtain the desired relation in the form

$$\begin{aligned}
&\overset{(k)}{\mathbb{M}}(\underset{(r)M}{\overset{P}{g}}N_P\mathbb{F})=\sum_{s=0}^{r}\underset{(s)M}{\overset{P}{A}}\big\{\nabla_P\overset{(k)}{\mathbb{M}}[(x^3)^s\mathbb{F}]-\underset{P}{\overset{3}{g}}\overset{(k)}{\mathbb{M}}{}'[(x^3)^{s+1}\mathbb{F}]\big\}\\
&=\sum_{s=0}^{r}\sum_{p=0}^{2s}2^{-2s}\underset{(s)M}{\overline{A}}C_{2s}^{p}\nabla_P\overset{(p-u)}{\mathbb{F}}-\underset{P}{\overline{g}}\sum_{s=0}^{r}\sum_{p=0}^{2s+2}2^{-2(s+1)}\underset{(s)M}{\overline{A}}C_{2s+2}^{p}\overset{(p-v)}{\mathbb{F}}{}',\\
&u=s-k,\ v=u+1,
\end{aligned}\tag{48}$$

where the expression for $\overset{(p-v)}{\mathbb{F}}{}'$ is given by the first formula (37) for $k=p-v$.

From (48) for $s=0$ and $s=1$ by (44), (46) and (47) we find that

$$\overset{(k)}{\mathbb{M}}(\underset{(0)I}{\overset{J}{g}}N_J\mathbb{F})=\overset{(k)}{\mathbb{M}}(N_I\mathbb{F})=\nabla_I\overset{(k)}{\mathbb{F}}-\underset{I}{\overset{3}{g}}\big[k\overset{(k)}{\mathbb{F}}+2(k+1)\big(\sum_{p=k}^{N}\overset{(p)}{\mathbb{F}}-\overset{(k)}{\mathbb{F}}+\overset{(+)}{\mathbb{F}}{}'\big)\big],\ k\geq 0,\tag{49}$$

$$\begin{aligned}
&\overset{(k)}{\mathbb{M}}(\underset{(1)I}{\overset{J}{g}}N_J\mathbb{F})=\overset{(k)}{\mathbb{M}}[(\underset{I}{\overline{g}}+x^3\underset{I}{\overline{A}})N_J\mathbb{F}]=\nabla_I\overset{(k)}{\mathbb{F}}+\frac{1}{4}\underset{I}{\overline{A}}\nabla_J\big(\overset{(k-1)}{\mathbb{F}}+2\overset{(k)}{\mathbb{F}}+\overset{(k+1)}{\mathbb{F}}\big)\\
&-\underset{J}{\overset{3}{g}}\big\{\underset{I}{\overline{g}}\big[k\overset{(k)}{\mathbb{F}}+2(k+1)\big(\sum_{p=k}^{N}\overset{(p)}{\mathbb{F}}-\overset{(k)}{\mathbb{F}}+\overset{(+)}{\mathbb{F}}{}'\big)\big]+\frac{1}{4}\underset{I}{\overline{A}}\big[(k-1)\overset{(k-1)}{\mathbb{F}}-4(k+2)\overset{(k)}{\mathbb{F}}\\
&-(k+3)\overset{(k+1)}{\mathbb{F}}+8(k+1)\big(\sum_{p=k}^{N}\overset{(p)}{\mathbb{F}}+\overset{(+)}{\mathbb{F}}{}'\big)\big]\big\},\quad k\geq 0.
\end{aligned}\tag{50}$$

Therefore, we have deduced the main relation in the form (48); using this relation from the equations of motion (14), the heat influx equation (18), CR of physical content (22), and CR of heat content (23) (second formula) of approximation of order r, we obtain the corresponding relations in moments; in turn by using the above rule, from them, we obtain the corresponding relations for multilayer thin bodies. Analogously, we obtain the boundary conditions of physical and heat contents in moments. Formulas (49) and (50) are applied in deducing the above relations from the corresponding relations of zero and first approximations. Formulas analogous to (49) and (50) certainly hold for the Legendre polynomial system. The relation for Legendre polynomial system analogous to (48) is very cumbersome, and so we do not write it.

Acknowledgments

This work was supported by the Shota Rustaveli National Science Foundation (project no. DI-2016-41).

References

[1] Nikabadze, M.U. *Development of the method of orthogonal polynomials in the classical and micropolar mechanics of elastic thin bodies.* Moscow University, Moscow, 2014, 515 p.

[2] Nikabadze, M.U. *The method of orthogonal polynomials in the classical and micropolar mechanics of elastic thin bodies.* Diss. Doctor Phys.–Math. Sciences. (in Russian), Moscow, 2014, 384 p.

[3] Nikabadze, M.U. *The method of orthogonal polynomials in the classical and micropolar mechanics of elastic thin bodies.* I. Deposited in VINITI RAS, No. 135-V2014, 20.05.2014, (in Russian), Moscow, 2014, 278 p.

[4] Nikabadze, M.U. *The application of systems of Legendre and Chebyshev polynomials at modeling of elastic thin bodies with a small size.* Deposited in VINITI RAS, No. 720-V2008, 21.08.2008, (in Russian), Moscow, 2014, 287 p.

[5] Nikabadze, M.U. On several issues of tensor calculus with applications to mechanics. *Contemporary Math.*, 55 (2015), 3-194.

[6] Nikabadze, M.U. Topics on tensor calculus with applications to mechanics. *J. Math. Sci.*, 225(1) (2017), 194.

[7] Vekua, I. N. *Fundamentals of tensor analysis and covariant theory.* Nauka, Moscow, 1978.

[8] Lur'e, A. I. *Nonlinear elasticity.* Nauka, Moscow, 1980.

[9] Pobedrya, B. E. *Lectures in tensor analysis.* Moscow Univ., Moscow, 1986.

[10] Eringen, A. C. *Microcontinuum field theories. 1. Foundation and solids.* N.Y.: Springer-Verlag, 1999.

[11] Pal'mov, V. A. Basic equations of the theory of asymmetric elasticity. *Appl. Math. Mech.*, 28(3) (1964), 401–408.

[12] Kupradze, V. D., Gegelia, T. G.,Basheleishvili, M. O. and Burchuladze, T. V. *Three-dimensional problems of the mathematical theory of elasticity and thermoelasticity.* Nauka, Moscow, 1976.

[13] Novacky, V. *Theory of elasticity.* Mir, Moscow, 1975 (transl. in Russian).

[14] Nikabadze, M.U. On some Problems of Tensor Calculus. I. *J. Math. Sci.*, 161(5) (2009), 668-697.

[15] Vekua I. N. Shell theory, general methods of construction. Pitman Adv. Pub. Program, 1985.

[16] Pobedrya, B. E. *Theory of thermomechanical processes. Elasticity and nonelasticity.* LENAND, Moscow, 2006, 70–85.

[17] Pobedrya, B. E. *Numerical methods in the theory of elasticity and plasticity.* 2nd ed. Moscow Univ., Moscow, 1995.

[18] Pobedrya, B. E. The theory of determining relations in the mechanics of deformable solid body. *Problems of mechanics. Collected papers dedicated to 90th anniversary of A. Yu. Ishlinskii. Ed. by D. M. Klimov.*, Fizmatlit, Moscow, 2003, 635–657.

[19] Nikabadze, M.U. Some issues concerning a version of the theory of thin solids based on expansions in a system of Chebyshev polynomials of the second kind. *Mech. Solids.*, 42(3) (2007), 391-421.

[20] Nikabadze, M.U. *The method of orthogonal polynomials in the classical and micropolar mechanics of elastic thin bodies.* II. Deposited in VINITI RAS, No. 136-B2014, (in Russian), Moscow, 2014, 218 p.

[21] Suetin, P. K. *Classic orthogonal polynomials.* Nauka, Moscow, 1976.

[22] Nikabadze, M.U. A variant of the system of equations of the theory of thin bodies. *Vestn. Mosk. Univ., Matem. Mekhan.*, 1(2006), 30–35.

Mikhail Nikabadze, Prof.: Lomonosov Moscow State University, Department of Mechanics and Mathematics, Leninskie Gory, 1, Moscow 119992, Russia (*Bauman Moscow State Technical University, Baumanskaya 2-ya, str., 5, Moscow 105005, Russia*). nikabadze@mail.ru

The author gave a presentation of this paper during one of the conference sessions.

Tamar moseshvili, Ph.D.: Akaki Tsereteli Kutaisi State University, Design and Technology Department, Tamar Mephe street 59, Kutaisi 4600, Georgia (*tamarmoseshvili@yahoo.com*).
The author gave a presentation of this paper during one of the conference sessions.

Armine Ulukhanian, Ph.D.: Bauman Moscow State Technical University, Departament of Calculation Mathematics and Mathematical Physics, Baumanskaya 2-ya, str., 5, Moscow 105005, Russia (*armine_msu@mail.ru*). The author gave a presentation of this paper during one of the conference sessions.

Ketevan Tskhakaia, Ph.D.: Akaki Tsereteli Kutaisi State University, Energy and Telecommunications Department, Tamar Mephe street 59, Kutaisi 4600, Georgia (*spectri@gmail.com*).

Nodar Mardaleishvili, Ph.D.: Akaki Tsereteli Kutaisi State University, Mechanics and Mechanical Engineering Department, Tamar Mephe street 59, Kutaisi 4600, Georgia (*nodarmard3@mail.ru*).

Formulation of the initial boundery velue problems in the theory of multilayer thermoelastic thin bodies in moments (part III)

Mikhail U. Nikabadze, Tamar Moseshvili, Armine R. Ulukhanian, Ketevan Tskhakaia, Nodar Mardaleishvili

Abstract: Various variants of the equations of motion in moments with respect to orthogonal polynomial systems are obtained. The interlayer conditions are written down under various connections of adjacent layers of a multilayer body. Formulation of the initial boundary value problems in the theory of multilayer thermoelastic thin bodies in moments are given.

Note that the analytic method with the use of the Legendre polynomial system in constructing the one-layer thin body theory and multilayer thin body theory can be successfully used in constructing any thin body theory. Despite this, the classic theories constructed by this method are far to be complete, and the more so, the micropolar theories and theories of other rheology are.

1. Systems of equations of motion in moments for multilayer thin bodies with one small size

1.1. Systems of equations of motion in moments of contravariant components of stress tensors and couple stresses with respect with respect to Chebyshev polynomial systems for multilayer thin bodies with one small size

We restrict ourselves to obtaining the systems of equations of motion of approximations $(0,N)$ and $(1,N)$ in moments. Using the rule presented above, by analogous systems of equations from [1, 2], we represent the desired systems of equations in the form

$$\begin{aligned}
&\Big\{\nabla_I \overset{(k)}{\underset{\alpha}{\mathbf{P}}}{}^{\overline{I}} - g^{\overline{3}}_{+\,\alpha P}\Big[k\overset{(k)}{\underset{\alpha}{\mathbf{P}}}{}^{\overline{I}} + 2(k+1)\Big(\sum_{p=k}^{N}\overset{(p)}{\underset{\alpha}{\mathbf{P}}}{}^{\overline{I}} - \overset{(k)}{\underset{\alpha}{\mathbf{P}}}{}^{\overline{I}}\Big)\Big]\\
&+2(k+1)\sum_{p=k}^{N}\Big[1-(-1)^{k+p}\Big]\overset{(p)}{\underset{\alpha}{\mathbf{P}}}{}^{\overline{3}}\Big\} + \rho\overset{(k)}{\underset{\alpha}{\mathbf{F}}} = \rho\partial_t^2\overset{(k)}{\underset{\alpha}{\mathbf{u}}},\\
&\Big\{\mathbf{P}\Rightarrow\boldsymbol{\mu}\Big\} + \underset{\widetilde{\alpha}}{\mathbf{C}}\overset{2}{\otimes}\overset{(k)}{\underset{\widetilde{\alpha}}{\mathbf{P}}} + \rho\overset{(k)}{\underset{\alpha}{\mathbf{m}}} = \underset{\widetilde{\alpha}}{\mathbf{J}}\cdot\partial_t^2\overset{(k)}{\boldsymbol{\varphi}}, \quad k=\overline{0,N}, \quad \alpha=\overline{0,K};
\end{aligned} \tag{1}$$

$$\begin{aligned}
&\Big\{\nabla_I \overset{(k)}{\underset{\alpha}{\mathbf{P}}}{}^{\overline{I}} + \frac{1}{4}\Big(g^{\overline{J}}_{-\,\alpha I} - g^{\overline{J}}_{+\,\alpha I}\Big)\nabla\nabla_J\Big(\overset{(k-1)}{\underset{\alpha}{\mathbf{P}}}{}^{\overline{I}} + 2\overset{(k)}{\underset{\alpha}{\mathbf{P}}}{}^{\overline{I}} + \overset{(k+1)}{\underset{\alpha}{\mathbf{P}}}{}^{\overline{I}}\Big) - g^{\overline{3}}_{+\,\alpha I}\Big[g^{\overline{I}}_{-\,\alpha J}\Big[k\overset{(k)}{\underset{\alpha}{\mathbf{P}}}{}^{\overline{J}} + 2(k+1)\Big(\sum_{p=k}^{N}\overset{(p)}{\underset{\alpha}{\mathbf{P}}}{}^{\overline{J}} - \overset{(k)}{\underset{\alpha}{\mathbf{P}}}{}^{\overline{J}}\Big)\Big]\\
&+\frac{1}{4}\Big(g^{\overline{I}}_{-\,\alpha J} - g^{\overline{I}}_{+\,\alpha J}\Big)\Big[(k-1)\overset{(k-1)}{\underset{\alpha}{\mathbf{P}}}{}^{\overline{J}} - 4(k+2)\overset{(k)}{\underset{\alpha}{\mathbf{P}}}{}^{\overline{J}} - (k+3)\overset{(k+1)}{\underset{\alpha}{\mathbf{P}}}{}^{\overline{J}}\\
&+8(k+1)\Big(\sum_{p=k}^{N}\overset{(p)}{\underset{\alpha}{\mathbf{P}}}{}^{\overline{J}}\Big)\Big]\Big] + 2(k+1)\Big[\sum_{p=k}^{N}(1-(-1)^{k+p})\overset{(p)}{\underset{\alpha}{\mathbf{P}}}{}^{\overline{3}}\Big]\Big\} + \rho\overset{(k)}{\underset{\alpha}{\mathbf{F}}} = \rho\,\partial_t^2\overset{(k)}{\underset{\alpha}{\mathbf{u}}},
\end{aligned} \tag{2}$$

$$\Big\{\mathbf{P}\Rightarrow\boldsymbol{\mu}\Big\}+\underset{\widetilde{\alpha}}{\overset{\approx}{\mathbf{C}}}\overset{2}{\otimes}\overset{(k)}{\underset{\widetilde{\alpha}}{\mathbf{P}}}+\underset{\alpha}{\rho}\overset{(k)}{\underset{\alpha}{\mathbf{m}}}=\underset{\widetilde{\alpha}}{\mathbf{J}}\cdot\partial_t^2\overset{(k)}{\underset{\alpha}{\boldsymbol{\varphi}}},\quad k=\overline{0,N},\quad \alpha=\overline{0,K}.$$

Here the notation $\{\mathbf{P}\Rightarrow\boldsymbol{\mu}\}$ means that the expression in brackets is obtained from the expression in brackets of the previous relation if the letter $\mathbf{P}$ is replaced with $\boldsymbol{\mu}$; the notation is also used later. Note that Eqs. (1) and (2) are also obtained by using formulas (II: 25) and (II: 27).

1.2. Systems of equations of motion in moments of contravariant components of stress tensors and couple stresses with respect to Legendre polynomial systems for multilayer thin bodies with one small size

Let us write systems of equations of motion of approximations $(0,N)$ and $(1,N)$ in moments taking into account only boundary conditions of physical content on frontal surface, since the systems of equations without boundary conditions on frontal surfaces, which can be obtained by using the corresponding systems of equations from [1, 2], have the form analogous to (1) and (2). It is easy to prove that analogously to the system of equations for a one-layer classical elastic body [3], the desired systems of equations have the form (see also [1, 2])

$$\begin{aligned}
&\Bigg\{\nabla_I\overset{(k)}{\underset{\alpha}{\mathbf{P}}}{}^{\bar{I}}-\underset{\alpha I}{g}{}^{\bar{3}}_{+}\Big[k\overset{(k)}{\underset{\alpha}{\mathbf{P}}}{}^{\bar{I}}-(2k+1)\sum_{p=0}^{k}\overset{(p)}{\underset{\alpha}{\mathbf{P}}}{}^{\bar{I}}\Big]-(2k+1)\sum_{p=0}^{k}\big[1-(-1)^{k+p}\big]\overset{(p)}{\underset{\alpha}{\mathbf{P}}}{}^{\bar{3}}\\
&+(2k+1)\Bigg[\sqrt{\underset{\alpha}{g}{}^{++}_{33}}\overset{(+)}{\underset{\alpha}{\mathbf{P}}}+(-1)^k\sqrt{\underset{\alpha}{g}{}^{\bar{-}\bar{-}}_{3\,3}}\overset{(-)}{\underset{\alpha}{\mathbf{P}}}\Bigg]\Bigg\}+\underset{\alpha}{\rho}\overset{(k)}{\underset{\alpha}{\mathbf{F}}}=\underset{\alpha}{\rho}\partial_t^2\overset{(k)}{\underset{\alpha}{\mathbf{u}}},
\end{aligned}\tag{3}$$

$$\Big\{\mathbf{P}\Rightarrow\boldsymbol{\mu}\Big\}+\underset{\widetilde{\alpha}}{\overset{\approx}{\mathbf{C}}}\overset{2}{\otimes}\overset{(k)}{\underset{\widetilde{\alpha}}{\mathbf{P}}}+\underset{\alpha}{\rho}\overset{(k)}{\underset{\alpha}{\mathbf{m}}}=\underset{\widetilde{\alpha}}{\mathbf{J}}\cdot\partial_t^2\overset{(k)}{\underset{\alpha}{\boldsymbol{\varphi}}},\quad k=\overline{0,N},\quad \alpha=\overline{0,K};$$

$$\begin{aligned}
&\Bigg\{\nabla_I\overset{(k)}{\underset{\alpha}{\mathbf{P}}}{}^{\bar{I}}+\frac{1}{2}\Big(\underset{\alpha M}{g}{}^{\bar{P}}_{-}-\underset{\alpha M}{g}{}^{\bar{P}}_{+}\Big)\Big(\frac{k}{2k-1}\nabla_P\overset{(k)}{\underset{\alpha}{\mathbf{P}}}{}^{\bar{M}}+\nabla_P\overset{(k)}{\underset{\alpha}{\mathbf{P}}}{}^{\bar{M}}+\frac{k+1}{2k+3}\nabla_P\overset{(k+1)}{\underset{\alpha}{\mathbf{P}}}{}^{\bar{M}}\Big)\\
&-(2k+1)\sum_{p=0}^{k}\big[1-(-1)^{k+p}\big]\overset{(p)}{\underset{\alpha}{\mathbf{P}}}{}^{\bar{3}}-\underset{\alpha P}{g}{}^{\bar{3}}_{+}\Bigg[\underset{\alpha M}{g}{}^{\bar{P}}_{-}\Bigg[k\overset{(k)}{\underset{\alpha}{\mathbf{P}}}{}^{\bar{M}}-(2k+1)\sum_{p=0}^{k}\overset{(p)}{\underset{\alpha}{\mathbf{P}}}{}^{\bar{M}}\Bigg]\\
&+\Big(\underset{\alpha M}{g}{}^{\bar{P}}_{-}-\underset{\alpha M}{g}{}^{\bar{P}}_{+}\Big)\Bigg[\frac{(k-1)k}{2(2k-1)}\overset{(k-1)}{\underset{\alpha}{\mathbf{P}}}{}^{\bar{M}}+k\overset{(k)}{\underset{\alpha}{\mathbf{P}}}{}^{\bar{M}}-\frac{(k+1)(k+2)}{2(2k+3)}\overset{(k+1)}{\underset{\alpha}{\mathbf{P}}}{}^{\bar{M}}\\
&-(2k+1)\sum_{p=0}^{k}\overset{(p)}{\underset{\alpha}{\mathbf{P}}}{}^{\bar{M}}\Bigg]\Bigg]+(2k+1)\Bigg[\sqrt{\underset{\alpha}{g}{}^{++}_{33}}\overset{(+)}{\underset{\alpha}{\mathbf{P}}}+(-1)^k\sqrt{\underset{\alpha}{g}{}^{\bar{-}\bar{-}}_{3\,3}}\overset{(-)}{\underset{\alpha}{\mathbf{P}}}\Bigg]\Bigg\}+\underset{\alpha}{\rho}\overset{(k)}{\underset{\alpha}{\mathbf{F}}}=\underset{\alpha}{\rho}\partial_t^2\overset{(k)}{\underset{\alpha}{\mathbf{u}}},
\end{aligned}\tag{4}$$

$$\Big\{\mathbf{P}\Rightarrow\boldsymbol{\mu}\Big\}+\underset{\widetilde{\alpha}}{\overset{\approx}{\mathbf{C}}}\overset{2}{\otimes}\overset{(k)}{\underset{\widetilde{\alpha}}{\mathbf{P}}}+\underset{\alpha}{\rho}\overset{(k)}{\underset{\alpha}{\mathbf{m}}}=\underset{\widetilde{\alpha}}{\mathbf{J}}\cdot\partial_t^2\overset{(k)}{\underset{\alpha}{\boldsymbol{\varphi}}},\quad k=\overline{0,N},\quad \alpha=\overline{0,K}.$$

Note that Eqs. (3) and (4) are deduced by using formulas for Legendre polynomials that are analogous to (II: 25) and (II: 27). Also, note that $\overset{(+)}{\underset{\alpha}{\mathbf{P}}}$ ($\overset{(+)}{\underset{\alpha}{\boldsymbol{\mu}}}$) and $\overset{(-)}{\underset{\alpha+1}{\mathbf{P}}}$ ($\overset{(-)}{\underset{\alpha+1}{\boldsymbol{\mu}}}$) ($\alpha=\overline{1,K-1}$) are stress vectors (couple-stresses) of interaction between the layers α and $\alpha+1$, which act on the surfaces $\overset{(+)}{\underset{\alpha}{S}}$ and $\overset{(-)}{\underset{\alpha+1}{S}}$, respectively, and $\overset{(+)}{\underset{1}{\mathbf{P}}}$ ($\overset{(+)}{\underset{1}{\boldsymbol{\mu}}}$) and $\overset{(-)}{\underset{K}{\mathbf{P}}}$ ($\overset{(-)}{\underset{K}{\boldsymbol{\mu}}}$) are given stress vectors (couple-stresses) on the frontal surfaces $\overset{(+)}{\underset{1}{S}}$ and $\overset{(-)}{\underset{K}{S}}$, respectively. The systems of equations of

heat influx of approximations $(0,N)$ and $(1,N)$, and also CR of heat content for multilayer thin bodies are obtained in full analogy with (1)–(4). Therefore, for brevity, we do not dwell on them. To understand the article we refer [1, 2, 4], where for the theories of one-layer thin body with one small size and two small sizes, and also for theory of multilayer constructions with the use of the Legendre and Chebyshev polynomial systems, many analogous problems are presented in detail. In particular, using the deduced recursive relations for the Legendre and Chebyshev polynomial systems, these works obtained the moments of derivatives of the first and second order of a scalar function, tensors of the first and second ranks and their components, and also some differential operators of these quantities. These works obtained constitutive relations of physical and heat contents, equations of motion and heat influx, boundary conditions of various kind in moments with respect to the Legendre and Chebyshev polynomial systems, and also initial conditions of kinematic and heat contents. Moreover, the constitutive relations were obtained for an inhomogeneous material. These works presented the statements of related and non-related dynamical problems in moments of approximation (r,N) of micropolar thermomechanics of a deformable rigid thin body and also the statement of non-stationary temperature problem in moments of approximation (r,N), where r and N are arbitrary nonnegative integers. All relations for one-layer thin body presented in this paragraph are automatically transferred to the case of multilayer thin body theory by using the rule presented above.

1.3. Systems of equations in moments of the displacement vector with respect to Legendre and Chebyshev polynomial systems for multilayer thin bodies with one small size

Let us write systems of equations of zero and first approximation in moments for the displacement vector. The system of equations of zero approximation in moments with respect to Legendre and Chebyshev polynomials has the form

$$\begin{aligned}&\underset{\widetilde{\alpha}}{\mathbf{A}}^{\overline{I}\cdot\overline{J}\cdot}\cdot\nabla_I\nabla_J\overset{(k)}{\underset{\alpha}{\mathbf{u}}}+\Bigl(\underset{\widetilde{\alpha}}{\mathbf{A}}^{\overline{3}\cdot\overline{I}\cdot}+\underset{\widetilde{\alpha}}{\mathbf{A}}^{\overline{I}\cdot\overline{3}\cdot}\Bigr)\cdot\nabla_I\overset{(k)}{\underset{\alpha}{\mathbf{u}}}{}'+\underset{\widetilde{\alpha}}{\mathbf{A}}^{\overline{3}\cdot\overline{3}\cdot}\cdot\overset{(k)}{\underset{\alpha}{\mathbf{u}}}{}''\\&-\Bigl(\underset{\alpha}{\mathbf{b}}^{\overline{I}}\nabla_I\overset{(k)}{\underset{\alpha}{\vartheta}}+\underset{\alpha}{\mathbf{b}}^{\overline{3}}\overset{(k)}{\underset{\alpha}{\vartheta}}{}'\Bigr)+\rho\overset{(k)}{\underset{\alpha}{\mathbf{F}}}=\underset{\alpha}{\rho}\,\partial_t^2\overset{(k)}{\underset{\alpha}{\mathbf{u}}},\quad k\in\mathbb{N}_0,\quad\alpha=\overline{0,K}.\end{aligned}\tag{5}$$

Taking into account the formulas for moments of the kth order of first and second derivatives of a vector(vector components, a scalar function) with respect to these polynomial systems [1, 2], from (5), we obtain the desired systems of equations of zero approximation in moments. For brevity, we do not write them. Analogously to (5), the system of equations of the first approximation is represented in the form

$$\underset{\widetilde{\alpha}}{\mathbf{A}}^{\overline{M}\cdot\overline{N}\cdot}\cdot\left\{\underset{\alpha M}{g^{\overline{P}}}\underset{\alpha N}{g^{\overline{Q}}}\nabla_P\nabla_Q\overset{(k)}{\underset{\alpha}{\mathbf{u}}}+\left[\underset{(1\alpha)\,MN}{B^{\overline{P}\overline{Q}}_{++}}\nabla_P\nabla_Q\overset{(k)}{\mathbf{M}}(x^3\underset{\alpha}{\mathbf{u}})+\underset{(2\alpha)\,MN}{B^{\overline{P}\overline{Q}}_{++}}\nabla_P\nabla_Q\overset{(k)}{\mathbf{M}}\bigl((x^3)^2\underset{\alpha}{\mathbf{u}}\bigr)\right]\right\}$$

$$+\Big(\underset{\widetilde{\alpha}}{\mathbf{A}}^{\bar{3}\cdot\bar{M}\cdot}+\underset{\widetilde{\alpha}}{\mathbf{A}}^{\bar{M}\cdot\bar{3}\cdot}\Big)\cdot\Big[g^{\bar{P}}_{\underset{M}{-}}\nabla_P\overset{(k)}{\underset{\alpha}{\mathbf{u}}}{}'+(g^{\bar{P}}_{\underset{\alpha M}{-}}-g^{\bar{P}}_{\underset{\alpha M}{+}})\nabla_P\overset{(k)}{\mathbf{M}}{}'\Big(x^3\underset{\alpha}{\mathbf{u}}\Big)\Big]+\underset{\widetilde{\alpha}}{\mathbf{A}}^{\bar{3}\cdot\bar{3}\cdot}\cdot\overset{(k)}{\underset{\alpha}{\mathbf{u}}}{}'' \tag{6}$$

$$-\underset{\alpha}{\mathbf{b}}^{\bar{M}}\Big[g^{\bar{P}}_{\underset{\alpha M}{-}}\nabla_P\overset{(k)}{\underset{\alpha}{\vartheta}}+\Big(g^{\bar{P}}_{\underset{\alpha M}{-}}-g^{\bar{P}}_{\underset{\alpha M}{+}}\Big)\nabla_P\overset{(k)}{\mathbf{M}}\big(x^3\underset{\alpha}{\vartheta}\big)\Big]-\underset{\alpha}{\mathbf{b}}^{\bar{3}}\overset{(k)}{\underset{\alpha}{\vartheta}}{}')+\underset{\alpha}{\rho}\overset{(k)}{\underset{\alpha}{\mathbf{F}}}=\underset{\alpha}{\rho}\,\partial_t^2\overset{(k)}{\underset{\alpha}{\mathbf{u}}},\ k\in\mathbb{N}_0,\ \alpha=\overline{0,K},$$

where we have introduced the following notation:

$$B^{\bar{P}\bar{Q}}_{(1\alpha)\underset{M}{+}\underset{N}{+}}=\Big(g^{\bar{P}}_{\underset{\alpha M}{-}}-g^{\bar{P}}_{\underset{\alpha M}{+}}\Big)g^{\bar{Q}}_{\underset{\alpha N}{-}}+g^{\bar{P}}_{\underset{\alpha M}{-}}\Big(g^{\bar{Q}}_{\underset{\alpha N}{-}}-g^{\bar{Q}}_{\underset{\alpha N}{+}}\Big),\quad B^{\bar{P}\bar{Q}}_{(2\alpha)\underset{M}{+}\underset{N}{+}}=A^{\bar{P}}_{(2\alpha)\underset{M}{+}}g^{\bar{Q}}_{\underset{\alpha N}{-}}+A^{\bar{P}}_{(1\alpha)\underset{M}{+}}A^{\bar{Q}}_{(1\alpha)\underset{N}{+}}+g^{\bar{P}}_{\underset{\alpha M}{-}}A^{\bar{Q}}_{(2\alpha)\underset{N}{+}},$$

$$A^{\bar{P}}_{(1\alpha)\underset{M}{+}}=g^{\bar{P}}_{\underset{\alpha M}{-}}-g^{\bar{P}}_{\underset{\alpha M}{+}},\quad A^{\bar{P}}_{(2\alpha)\underset{M}{+}}=\Big(g^{\bar{P}}_{\underset{\alpha N}{-}}-g^{\bar{P}}_{\underset{\alpha N}{+}}\Big)\Big(g^{\bar{N}}_{\underset{\alpha M}{-}}-g^{\bar{N}}_{\underset{\alpha M}{+}}\Big).$$

Taking into account the expressions for the kth-order moments entering (6) and using the corresponding formulas for Legendre and Chebyshev polynomial systems [1, 2] from (6), we obtain various representations of the equations of of first approximation of the displacement vector in moments with respect to these polynomial systems. It is easy to deduce the equations of motion of first approximation in moments for the displacement vector with respect to the systems of Chebyshev polynomials of the first kind. For brevity, we do not write the equations in moments mentioned in this paragraph.

Note that to close systems (1)–(4), we need to add to them the system of equations of heat influx, CR, boundary and initial conditions of physical and heat contents in moments of the corresponding approximations, and also inter-layer contact conditions depending on the connections of neighboring surfaces. Hence to close systems (5) and (6), we need to add to them all relations of the previous proposition, except for CR in the case of first boundary-value problem where kinematic boundary conditions are given on the whole surface. Of course, it is easy to write all missed relations and formulate the statement of problems analogous to those presented in [1, 2, 4, 5, 6] (CR; see also above) for one-layer domains, except for inter-layer contact conditions, by using the rule presented above. Otherwise, we need to repeat almost all presented in [1, 2, 4] being applied to multilayer thin body theory. Owing to this, we do not dwell on them and consider inter-layer contact conditions below.

2. Inter-Layer Contact Conditions

In studying strained-deformed states of multilayer constructions and composite media, as a rule, one assumes that component layers (elements, phases) work jointly, without sliding. Obviously, such a model does not cover the variety of connection methods used in technology and does not take into account the existence of interphase defects, which manifest themselves in non-perfect connection of phases in contact. Defects of such a type often are undoubt because of peculiarities of technological character (see [7, 8, 9]). Therefore, the deformation of multilayer thin bodies can be without violation or with violation of complete layer contact

owing to their separation in normal or tangential direction. Between the layers, there can arise contact domain and contact-free domain. Moreover, the boundaries of these domains can vary in the deformation process, the layer can slide with respect to each other, the sliding can be with friction,etc. All these phenomena can essentially influence on the mechanical behavior of a thin body, its strained-deformed state. Of course, the account of these phenomena is necessary in studying strained-deformed state of multilayer bodies. In contrast to other parametrization, the use of frontal surfaces as base surfaces in parametrization of multilayer thin body domain allows one to easily take into account these phenomena. In consideration the phenomena occurring on frontal surfaces, the main problem is the problem of modelling the interface. In this direction,there exist two approaches. The first approach is physical, which take into account thin adhesion layers via generalized weld condition of elements being in contact. For the first time, such an approach was proposed for heat conduction problems in [10]. Later on, it was generalized to mechanical problems [11]. The second approach is phenological; it is based on the assumption that a priori, the exist discontinuity zones of displacements. To study these problems, we assume that a multilayer thin construction consists of K layers. Denote by $\overset{(+)}{S}_{\alpha}$ and $\overset{(-)}{S}_{\alpha}$ $(\alpha = \overline{1,K})$ the exterior and inner surfaces of the layer α $(\alpha = \overline{1,K})$, respectively and consider several cases of mutual relation of neighboring surfaces $\overset{(+)}{S}_{\alpha}$ $\overset{(-)}{S}_{\alpha+1}$ $(\alpha = \overline{1,K-1})$, which are important in practice.

2.1. Weld conditions (complete ideal contact conditions)

In this case the forces and moments of interaction between the layers α and $\alpha+1$ $(\alpha = \overline{1,K-1})$ are unknown. These forces and moments certainly are equal and have opposite directions. Therefore, there additionally arise six unknown functions. However, in the case considered, we have six additional conditions, which express the continuity of displacement vectors and the rotation of welded surface points. In other words, displacement vectors and rotation vectors of contacted surfaces are equal. Denoting the forces and moments of interaction of the contacted surfaces $\overset{(+)}{S}_{\alpha}$ and $\overset{(-)}{S}_{\alpha+1}$ $(\alpha = \overline{1,K-1})$ by $\overset{(+)}{\mathbf{P}}_{\alpha}$, $\overset{(+)}{\boldsymbol{\mu}}_{\alpha}$ and $\overset{(-)}{\mathbf{P}}_{\alpha+1}$, $\overset{(-)}{\boldsymbol{\mu}}_{\alpha+1}$ $(\alpha = \overline{1,K-1})$, respectively, and the displacement and rotation vectors of points of these surfaces by $\overset{(+)}{\mathbf{u}}_{\alpha}$, $\overset{(+)}{\boldsymbol{\varphi}}_{\alpha}$ and $\overset{(-)}{\mathbf{u}}_{\alpha+1}$, $\overset{(-)}{\boldsymbol{\varphi}}_{\alpha+1}$ $(\alpha = \overline{1,K-1})$, we can represent the complete contact conditions in micropolar theory of multilayer thin bodies in the form

$$\overset{(+)}{\mathbf{P}}_{\alpha} = -\overset{(-)}{\mathbf{P}}_{\alpha+1}, \quad \overset{(+)}{\boldsymbol{\mu}}_{\alpha} = -\overset{(-)}{\boldsymbol{\mu}}_{\alpha+1}, \quad \overset{(+)}{\mathbf{u}}_{\alpha} = \overset{(-)}{\mathbf{u}}_{\alpha+1}, \quad \overset{(+)}{\boldsymbol{\varphi}}_{\alpha} = \overset{(-)}{\boldsymbol{\varphi}}_{\alpha+1}, \quad \alpha = \overline{1,K-1}. \tag{7}$$

Neglecting the characteristics of micropolar theory (the second and fourth relations) in (7), we obtain the ideal contact conditions for the classical theory (the first and third relations).

2.2. Conditions under relative displacement of contacted layer surfaces

As above, in the process of deformation of a multilayer construction, relative displacements of points of the surfaces $\overset{(+)}{S}_{\alpha}$ and $\overset{(-)}{S}_{\alpha+1}$ withe the same Gaussian coordinates (x^1, x^2) are possible. Let us consider various variants. First, we note that there exist bounded limit intensities of coupling forces of the layers α and $\alpha+1$ ($\alpha = \overline{1, K-1}$) in normal and tangential direction. Denote the normal and tangent components of the limit force of action of the layer α on the layer $\alpha+1$ by

$$\overset{(-)}{\mathbf{P}}{}^{*}_{\alpha+1(n)} = \overset{(-)}{P}{}^{*}_{\alpha+1(n)}(x^1, x^2)\overset{(-)}{\mathbf{n}}_{\alpha+1}, \quad \overset{(-)}{\mathbf{P}}{}^{*}_{\alpha+1(s)} = \overset{(-)}{P}{}^{*}_{\alpha+1(s)}(x^1, x^2, \overset{(-)}{\mathbf{s}}_{\alpha+1})\overset{(-)}{\mathbf{s}}_{\alpha+1}, \quad \alpha = \overline{1, K-1},$$

respectively. Here, certainly, $\overset{(-)}{\mathbf{n}}_{\alpha+1}$ and $\overset{(-)}{\mathbf{s}}_{\alpha+1}$ are unit exterior normal and tangent vectors to the surface $\overset{(-)}{S}_{\alpha+1}$. Note that we take into account the possibility of dependence of the limit tangent force preventing the mutual sliding of layers of the direction in the tangent plane (anisotropy of the limit tangent force).

2.3. Conditions under relative displacement of points of ideal (smooth) contacted layer surfaces

In this case, a free slipping of layers with respect to each other can take place in the process of deformation of a multilayer thin body. The parametrization retains valid all the relations of the theory of thin bodies in the case considered here, only the required and given functions are changed. Obviously, if the layers are united, then the following equalities hold:

$$\begin{gathered}\overset{(+)}{\mathbf{r}}_{\alpha}(x^1, x^2) = \overset{(\circ)}{\mathbf{r}}_{\alpha}(x^1, x^2) + \overset{(+)}{\mathbf{u}}_{\alpha}(x^1, x^2), \quad \overset{(-)}{\mathbf{r}}_{\alpha}(x^1, x^2) = \overset{(\circ)}{\mathbf{r}}_{\alpha}(x^1, x^2) + \overset{(-)}{\mathbf{u}}_{\alpha}(x^1, x^2), \quad \alpha = \overline{1, K}, \\ \overset{(\circ)}{\mathbf{r}}_{\alpha}(x^1, x^2) = \overset{(\circ)}{\mathbf{r}}_{\alpha+1}(x^1, x^2), \quad \overset{(+)}{\mathbf{r}}_{\alpha}(x^1, x^2) = \overset{(-)}{\mathbf{r}}_{\alpha+1}(x^1, x^2), \quad (\overset{(+)}{\mathbf{u}}_{\alpha} = \overset{(-)}{\mathbf{u}}_{\alpha+1}), \quad \alpha = \overline{1, K-1}.\end{gathered} \tag{8}$$

where $\overset{(+)}{\mathbf{r}}_{\alpha}$ ($\overset{(\circ)}{\mathbf{r}}_{\alpha}$) and $\overset{(-)}{\mathbf{r}}_{\alpha}$ ($\overset{(\circ)}{\mathbf{r}}_{\alpha}$) are the radius-vectors of the surfaces $\overset{(+)}{S}_{\alpha}$ ($\overset{(\circ)}{S}_{\alpha}$) and $\overset{(-)}{S}_{\alpha}$ ($\overset{(\circ)}{S}_{\alpha}$), respectively, in the deformed (non-deformed) state of the multilayer thin body. It is not difficult to see that in this case (under a slipping of absolutely smooth contacted surfaces) we have the following relations instead of (8):

$$\begin{gathered}\overset{(+)}{\mathbf{r}}_{\alpha}(x^1, x^2) = \overset{(\circ)}{\mathbf{r}}_{\alpha}(x^1, x^2) + \overset{(+)}{\mathbf{u}}_{\alpha}(x^1, x^2), \quad \overset{(-)}{\mathbf{r}}_{\alpha}(x^1, x^2) = \overset{(\circ)}{\mathbf{r}}_{\alpha}(x^1, x^2) + \overset{(-)}{\mathbf{u}}_{\alpha}(x^1, x^2), \quad \alpha = \overline{1, K}, \\ \overset{(\circ)}{\mathbf{r}}_{\alpha}(x^1, x^2) = \overset{(\circ)}{\mathbf{r}}_{\alpha+1}(x^1, x^2), \quad \overset{(+)}{\mathbf{r}}_{\alpha}(x^1, x^2) \neq \overset{(-)}{\mathbf{r}}_{\alpha+1}(x^1, x^2), \quad \overset{(+)}{\mathbf{u}}_{\alpha}(x^1, x^2) \neq \overset{(-)}{\mathbf{u}}_{\alpha+1}(x^1, x^2), \\ \mathbf{v}_{\alpha}(x^1, x^2) = \overset{(-)}{\mathbf{u}}_{\alpha+1}(x^1, x^2) - \overset{(+)}{\mathbf{u}}_{\alpha}(x^1, x^2), \quad \alpha = \overline{1, K-1}.\end{gathered} \tag{9}$$

Obviously, $\underset{\alpha}{\mathbf{v}}(x^1, x^2)$ is the vector of the relative displacement of the corresponding points of the contacted surfaces $\overset{(+)}{\underset{\alpha}{S}}$ and $\overset{(-)}{\underset{\alpha}{S}}$ ($\alpha = \overline{1, K-1}$), being an unknown in the considered case. The absence of the friction between the layers allows us to write the additional relations

$$\begin{gathered}\overset{(-)}{\underset{\alpha+1}{u}}{}_{(n)} = \overset{(+)}{\underset{\alpha}{u}}{}_{(n)} \quad (\underset{\alpha}{v}_{(n)} = 0), \quad \overset{(+)}{\underset{\alpha}{\mathbf{P}}}{}_{(s)} = 0, \quad \overset{(-)}{\underset{\alpha+1}{\mathbf{P}}}{}_{(s)} = 0, \quad \overset{(+)}{\underset{\alpha}{\mathbf{P}}}{}_{(n)} = -\overset{(-)}{\underset{\alpha+1}{\mathbf{P}}}{}_{(n)}, \\ \alpha = \overline{1, K-1}, \quad x' \in \overset{(+)}{\underset{\alpha}{S}}{}^0 \subset \overset{(+)}{\underset{\alpha}{S}},\end{gathered} \tag{10}$$

where $\overset{(+)}{\underset{\alpha}{\mathbf{P}}}{}_{(s)}$ ($\overset{(-)}{\underset{\alpha+1}{\mathbf{P}}}{}_{(s)}$) and $\overset{(+)}{\underset{\alpha}{\mathbf{P}}}{}_{(n)}$ ($\overset{(-)}{\underset{\alpha+1}{\mathbf{P}}}{}_{(n)}$) are the tangent and normal components of the stress vector (the interaction force intensity) $\overset{(+)}{\underset{\alpha}{\mathbf{P}}}$ ($\overset{(-)}{\underset{\alpha+1}{\mathbf{P}}}$), i.e., $\overset{(+)}{\underset{\alpha}{\mathbf{P}}} = \overset{(+)}{\underset{\alpha}{\mathbf{P}}}{}_{(s)} + \overset{(+)}{\underset{\alpha}{\mathbf{P}}}{}_{(n)}$, $\overset{(-)}{\underset{\alpha+1}{\mathbf{P}}} = \overset{(-)}{\underset{\alpha+1}{\mathbf{P}}}{}_{(s)} + \overset{(-)}{\underset{\alpha+1}{\mathbf{P}}}{}_{(n)}$,, $\alpha = \overline{1, K-1}$. It is not difficult to see that (10) implies the relations

$$\begin{gathered}\overset{(-)}{\underset{\alpha+1}{u}}{}_{(n)} = \overset{(+)}{\underset{\alpha}{u}}{}_{(n)}, \ \underset{\alpha}{v}_{(n)} = 0), \ \overset{(-)}{\underset{\alpha+1}{\mathbf{n}}} \cdot \overset{(-)}{\underset{\widetilde{\alpha+1}}{\mathbf{P}}}(\underset{\alpha+1}{\mathbf{u}}, \underset{\alpha+1}{\vartheta}) \cdot \overset{(-)}{\underset{\alpha+1}{\mathbf{s}}} = 0, \ \overset{(+)}{\underset{\alpha}{\mathbf{n}}} \cdot \overset{(+)}{\underset{\widetilde{\alpha}}{\mathbf{P}}}(\underset{\alpha}{\mathbf{u}}, \underset{\alpha}{\vartheta}) \cdot \overset{(+)}{\underset{\alpha}{\mathbf{s}}} = 0, \\ \overset{(+)}{\underset{\alpha}{\mathbf{n}}} \cdot \overset{(+)}{\underset{\widetilde{\alpha}}{\mathbf{P}}}(\underset{\alpha}{\mathbf{u}}, \underset{\alpha}{\vartheta}) \cdot \overset{(+)}{\underset{\alpha}{\mathbf{n}}} = \overset{(+)}{\underset{\alpha}{\mathbf{n}}} \cdot \overset{(-)}{\underset{\widetilde{\alpha+1}}{\mathbf{P}}}(\underset{\alpha+1}{\mathbf{u}}, \underset{\alpha+1}{\vartheta}) \cdot \overset{(+)}{\underset{\alpha}{\mathbf{n}}}, \ \alpha = \overline{1, K-1}, \ x' \in \overset{(+)}{\underset{\alpha}{S}}{}^0 \subset \overset{(+)}{\underset{\alpha}{S}}.\end{gathered} \tag{11}$$

Here the notation $\overset{(\sim)}{\underset{\widetilde{\alpha}}{\mathbf{P}}}(\underset{\alpha}{\mathbf{u}}, \underset{\alpha}{\vartheta})$, $\sim \in \{-, +\}$ means the dependence of $\overset{(\sim)}{\underset{\widetilde{\alpha}}{\mathbf{P}}}$ on $\underset{\alpha}{\mathbf{u}}$ and $\underset{\alpha}{\vartheta}$, and $\overset{(-)}{\underset{\widetilde{\alpha}}{\mathbf{P}}} = \underset{\widetilde{\alpha}}{\mathbf{P}}|_{x^3=0}$, $\overset{(+)}{\underset{\widetilde{\alpha}}{\mathbf{P}}} = \underset{\widetilde{\alpha}}{\mathbf{P}}|_{x^3=1}$. The corresponding relations are obtained from the first equality of (II: 21) with $\underset{\widetilde{\widetilde{\alpha}}}{\mathbf{A}} = 0$, $\underset{\alpha}{\boldsymbol{\varphi}} = 0$. In the case considered here, relations (11) close the system of equations of the classic theory of multilayer thin bodies. In the case of the micropolar theory of multilayer thin bodies equalities (11) should be replaced by the following ones:

$$\begin{gathered}\overset{(-)}{\underset{\alpha+1}{u}}{}_{(n)} = \overset{(+)}{\underset{\alpha}{u}}{}_{(n)}, \quad \overset{(-)}{\underset{\alpha+1}{\varphi}}{}_{(n)} = \overset{(+)}{\underset{\alpha}{\varphi}}{}_{(n)}, \quad \overset{(-)}{\underset{\alpha+1}{\mathbf{n}}} \cdot \overset{(-)}{\underset{\widetilde{\alpha+1}}{\mathbf{P}}}(\underset{\alpha+1}{\mathbf{u}}, \underset{\alpha+1}{\boldsymbol{\varphi}}, \underset{\alpha+1}{\vartheta}) \cdot \overset{(-)}{\underset{\alpha+1}{\mathbf{s}}} = 0, \\ \overset{(+)}{\underset{\alpha}{\mathbf{n}}} \cdot \overset{(+)}{\underset{\widetilde{\alpha}}{\mathbf{P}}}(\underset{\alpha}{\mathbf{u}}, \underset{\alpha}{\boldsymbol{\varphi}}, \underset{\alpha}{\vartheta}) \cdot \overset{(+)}{\underset{\alpha}{\mathbf{s}}} = 0, \quad \overset{(+)}{\underset{\alpha}{\mathbf{n}}} \cdot \overset{(+)}{\underset{\widetilde{\alpha}}{\mathbf{P}}}(\underset{\alpha}{\mathbf{u}}, \underset{\alpha}{\boldsymbol{\varphi}}, \underset{\alpha}{\vartheta}) \cdot \overset{(+)}{\underset{\alpha}{\mathbf{n}}} = \overset{(+)}{\underset{\alpha}{\mathbf{n}}} \cdot \overset{(-)}{\underset{\widetilde{\alpha+1}}{\mathbf{P}}}(\underset{\alpha+1}{\mathbf{u}}, \underset{\alpha+1}{\boldsymbol{\varphi}}, \underset{\alpha}{\vartheta}) \cdot \overset{(+)}{\underset{\alpha}{\mathbf{n}}}, \\ \overset{(-)}{\underset{\alpha+1}{\mathbf{n}}} \cdot \overset{(-)}{\underset{\widetilde{\alpha+1}}{\boldsymbol{\mu}}}(\underset{\alpha+1}{\boldsymbol{\varphi}}) \cdot \overset{(-)}{\underset{\alpha+1}{\mathbf{n}}} = 0, \quad \overset{(+)}{\underset{\alpha}{\mathbf{n}}} \cdot \overset{(+)}{\underset{\widetilde{\alpha}}{\boldsymbol{\mu}}}(\underset{\alpha}{\boldsymbol{\varphi}}) \cdot \overset{(+)}{\underset{\alpha}{\mathbf{n}}} = 0, \\ \overset{(+)}{\underset{\alpha}{\mathbf{n}}} \cdot \overset{(+)}{\underset{\widetilde{\alpha}}{\boldsymbol{\mu}}}(\underset{\alpha}{\boldsymbol{\varphi}}) \cdot \overset{(+)}{\underset{\alpha}{\mathbf{s}}} = \overset{(+)}{\underset{\alpha}{\mathbf{n}}} \cdot \overset{(-)}{\underset{\widetilde{\alpha+1}}{\boldsymbol{\mu}}}(\underset{\alpha+1}{\boldsymbol{\varphi}}) \cdot \overset{(+)}{\underset{\alpha}{\mathbf{s}}}, \quad \alpha = \overline{1, K-1}, \quad x' \in \overset{(+)}{\underset{\alpha}{S}}{}^0 \subset \overset{(+)}{\underset{\alpha}{S}}.\end{gathered} \tag{12}$$

In this case, along with the vector of relative displacement, the vector of relative rotation $\underset{\alpha}{\boldsymbol{\psi}} = \overset{(-)}{\underset{\alpha+1}{\boldsymbol{\varphi}}} - \overset{(+)}{\underset{\alpha}{\boldsymbol{\varphi}}}$ of the corresponding points of the contacted surfaces is introduced into consideration; $\overset{(-)}{\underset{\alpha+1}{\varphi}}{}_{(n)}$ and $\overset{(+)}{\underset{\alpha}{\varphi}}{}_{(n)}$ are the normal components of the vectors $\overset{(-)}{\underset{\alpha+1}{\boldsymbol{\varphi}}}$ and $\overset{(+)}{\underset{\alpha}{\boldsymbol{\varphi}}}$, respectively. Note that relations (12) are written subject to the fact that each layer has a center of symmetry, i.e. the tensors $\underset{\widetilde{\alpha}}{\mathbf{A}} = 0$ and $\underset{\widetilde{\alpha}}{\mathbf{B}} = 0$ in (II: 21) for all α. If this is not the case, then these relations should be replaced by other ones depending on the considered

governing relations. For example, if relations (II: 21) are considered as governing ones for a material having no center of symmetry, then instead of (12) we have

$$\begin{array}{l}
\overset{(-)}{u}_{\alpha+1(n)} = \overset{(+)}{u}_{\alpha(n)}, \quad \overset{(-)}{\varphi}_{\alpha+1(n)} = \overset{(+)}{\varphi}_{\alpha(n)}, \quad \overset{(-)}{\mathbf{n}}_{\alpha+1} \cdot \overset{(-)}{\underset{\sim}{\mathbf{P}}}_{\alpha+1}(\overset{}{\mathbf{u}}_{\alpha+1}, \overset{}{\boldsymbol{\varphi}}_{\alpha+1}, \overset{}{\vartheta}_{\alpha+1}) \cdot \overset{(-)}{\mathbf{s}}_{\alpha+1} = 0, \\
\overset{(+)}{\mathbf{n}}_{\alpha} \cdot \overset{(+)}{\underset{\sim}{\mathbf{P}}}_{\alpha}(\mathbf{u}, \boldsymbol{\varphi}, \vartheta)_{\alpha} \cdot \overset{(+)}{\mathbf{s}}_{\alpha} = 0, \quad \overset{(+)}{\mathbf{n}}_{\alpha} \cdot \overset{(+)}{\underset{\sim}{\mathbf{P}}}_{\alpha}(\mathbf{u}, \boldsymbol{\varphi}, \vartheta)_{\alpha} \cdot \overset{(+)}{\mathbf{n}}_{\alpha} = \overset{(+)}{\mathbf{n}}_{\alpha} \cdot \overset{(-)}{\underset{\sim}{\mathbf{P}}}_{\alpha+1}(\overset{}{\mathbf{u}}_{\alpha+1}, \overset{}{\boldsymbol{\varphi}}_{\alpha+1}, \vartheta)_{\alpha} \cdot \overset{(+)}{\mathbf{n}}_{\alpha}, \\
\overset{(-)}{\mathbf{n}}_{\alpha+1} \cdot \overset{(-)}{\underset{\sim}{\boldsymbol{\mu}}}_{\alpha+1}(\overset{}{\boldsymbol{\varphi}}_{\alpha+1}, \overset{}{\mathbf{u}}_{\alpha+1}, \overset{}{\vartheta}_{\alpha+1}) \cdot \overset{(-)}{\mathbf{n}}_{\alpha+1} = 0, \quad \overset{(+)}{\mathbf{n}}_{\alpha} \cdot \overset{(+)}{\underset{\sim}{\boldsymbol{\mu}}}_{\alpha}(\boldsymbol{\varphi}, \mathbf{u}, \vartheta)_{\alpha} \cdot \overset{(+)}{\mathbf{n}}_{\alpha} = 0, \\
\overset{(+)}{\mathbf{n}}_{\alpha} \cdot \overset{(+)}{\underset{\sim}{\boldsymbol{\mu}}}_{\alpha}(\boldsymbol{\varphi}, \mathbf{u}, \vartheta)_{\alpha} \cdot \overset{(+)}{\mathbf{s}}_{\alpha} = \overset{(+)}{\mathbf{n}}_{\alpha} \cdot \overset{(-)}{\underset{\sim}{\boldsymbol{\mu}}}_{\alpha+1}(\overset{}{\boldsymbol{\varphi}}_{\alpha+1}, \overset{}{\mathbf{u}}_{\alpha+1}, \vartheta)_{\alpha} \cdot \overset{(+)}{\mathbf{s}}_{\alpha}, \quad \alpha = \overline{1, K-1}, \quad x' \in \overset{(+)}{S}{}^{0}_{\alpha} \subset \overset{(+)}{S}_{\alpha}.
\end{array} \tag{13}$$

Note also that the contact conditions should be supplied with the conditions of heat content on the contacted surfaces, which is not difficult. Therefore, in order to shorten the presentation, we do not consider them here.

2.4. Conditions under relative displacement of points of uneven contacted surfaces of layers

In the case considered here, the slipping with the friction of layers with respect to each other can take place in the process of deformation of the multilayer thin body. The relative slipping does not occur until the magnitude of the tangent component of the interaction force $\overset{(+)}{\mathbf{P}}_{\alpha(s)}$ ($\overset{(-)}{\mathbf{P}}_{\alpha+1(s)}$) (force of friction) between the contacted surfaces reaches its limit (maximal possible) value $\left|\overset{(+)}{\mathbf{P}}{}^{*}_{\alpha}\right|$ $\left(\left|\overset{(-)}{\mathbf{P}}{}^{*}_{\alpha+1}\right|\right)$, therefore, $\underset{\alpha}{\mathbf{v}}(x^1, x^2) = 0$, $\alpha = \overline{1, K-1}$. When the force of friction reaches its limit value, the slipping begins, and the relations presented above should be replaced by other ones. First of all, note that for the case of the classic theory of multilayer thin bodies instead of (11) we have

$$\begin{array}{l}
\overset{(-)}{u}_{\alpha+1(n)} = \overset{(+)}{u}_{\alpha(n)}, \quad \overset{(-)}{\mathbf{n}}_{\alpha+1} \cdot \overset{(-)}{\underset{\sim}{\mathbf{P}}}_{\alpha+1}(\overset{}{\mathbf{u}}_{\alpha+1}, \overset{}{\vartheta}_{\alpha+1}) \cdot \overset{(-)}{\mathbf{s}}_{\alpha+1} = \overset{(-)}{P}{}^{*}_{\alpha+1(s)}, \quad \overset{(+)}{\mathbf{n}}_{\alpha} \cdot \overset{(+)}{\underset{\sim}{\mathbf{P}}}_{\alpha}(\mathbf{u}, \vartheta)_{\alpha} \cdot \overset{(+)}{\mathbf{s}}_{\alpha} = \overset{(+)}{P}{}^{*}_{\alpha(s)}, \\
\overset{(+)}{\mathbf{n}}_{\alpha} \cdot \overset{(+)}{\underset{\sim}{\mathbf{P}}}_{\alpha}(\mathbf{u}, \vartheta)_{\alpha} \cdot \overset{(+)}{\mathbf{n}}_{\alpha} = \overset{(+)}{\mathbf{n}}_{\alpha} \cdot \overset{(-)}{\underset{\sim}{\mathbf{P}}}_{\alpha+1}(\overset{}{\mathbf{u}}_{\alpha+1}, \overset{}{\vartheta}_{\alpha+1}) \cdot \overset{(+)}{\mathbf{n}}_{\alpha}, \quad \alpha = \overline{1, K-1}, \quad x' \in \overset{(+)}{S}{}^{0}_{\alpha} \subset \overset{(+)}{S}_{\alpha},
\end{array} \tag{14}$$

and in the case of the micropolar theory of multilayer thin bodies whose layers do not have a center of symmetry, we assume the following relations instead of (13):

$$\begin{array}{l}
\overset{(-)}{u}_{\alpha+1(n)} = \overset{(+)}{u}_{\alpha(n)}, \quad \overset{(-)}{\varphi}_{\alpha+1(n)} = \overset{(+)}{\varphi}_{\alpha(n)}, \quad \overset{(-)}{\mathbf{n}}_{\alpha+1} \cdot \overset{(-)}{\underset{\sim}{\mathbf{P}}}_{\alpha+1}(\overset{}{\mathbf{u}}_{\alpha+1}, \overset{}{\boldsymbol{\varphi}}_{\alpha+1}, \overset{}{\vartheta}_{\alpha+1}) \cdot \overset{(-)}{\mathbf{s}}_{\alpha+1} = \overset{(-)}{P}{}^{*}_{\alpha+1(s)}, \\
\overset{(+)}{\mathbf{n}}_{\alpha} \cdot \overset{(+)}{\underset{\sim}{\mathbf{P}}}_{\alpha}(\mathbf{u}, \boldsymbol{\varphi}, \vartheta)_{\alpha} \cdot \overset{(+)}{\mathbf{s}}_{\alpha} = \overset{(+)}{P}{}^{*}_{\alpha(s)}, \quad \overset{(+)}{\mathbf{n}}_{\alpha} \cdot \overset{(+)}{\underset{\sim}{\mathbf{P}}}_{\alpha}(\mathbf{u}, \boldsymbol{\varphi}, \vartheta)_{\alpha} \cdot \overset{(+)}{\mathbf{n}}_{\alpha} = \overset{(+)}{\mathbf{n}}_{\alpha} \cdot \overset{(-)}{\underset{\sim}{\mathbf{P}}}_{\alpha+1}(\overset{}{\mathbf{u}}_{\alpha+1}, \overset{}{\boldsymbol{\varphi}}_{\alpha+1}, \overset{}{\vartheta}_{\alpha+1}) \cdot \overset{(+)}{\mathbf{n}}_{\alpha}, \\
\overset{(-)}{\mathbf{n}}_{\alpha+1} \cdot \overset{(-)}{\underset{\sim}{\boldsymbol{\mu}}}_{\alpha+1}(\overset{}{\boldsymbol{\varphi}}_{\alpha+1}, \overset{}{\mathbf{u}}_{\alpha+1}, \overset{}{\vartheta}_{\alpha+1}) \cdot \overset{(-)}{\mathbf{n}}_{\alpha+1} = \overset{(-)}{\mu}{}^{*}_{\alpha+1(n)}, \quad \overset{(+)}{\mathbf{n}}_{\alpha} \cdot \overset{(+)}{\underset{\sim}{\boldsymbol{\mu}}}_{\alpha}(\boldsymbol{\varphi}, \mathbf{u}, \vartheta)_{\alpha} \cdot \overset{(+)}{\mathbf{n}}_{\alpha} = \overset{(+)}{\mu}{}^{*}_{\alpha(n)}, \\
\overset{(+)}{\mathbf{n}}_{\alpha} \cdot \overset{(+)}{\underset{\sim}{\boldsymbol{\mu}}}_{\alpha}(\boldsymbol{\varphi}, \mathbf{u}, \vartheta)_{\alpha} \cdot \overset{(+)}{\mathbf{s}}_{\alpha} = \overset{(+)}{\mathbf{n}}_{\alpha} \cdot \overset{(-)}{\underset{\sim}{\boldsymbol{\mu}}}_{\alpha+1}(\overset{}{\boldsymbol{\varphi}}_{\alpha+1}, \mathbf{u}_{\alpha}, \vartheta_{\alpha+1}) \cdot \overset{(+)}{\mathbf{s}}_{\alpha}, \quad \alpha = \overline{1, K-1}, \quad x' \in \overset{(+)}{S}{}^{0}_{\alpha} \subset \overset{(+)}{S}_{\alpha}.
\end{array} \tag{15}$$

Here, naturally, $\overset{(+)}{\underset{\alpha}{\mu}}{}^{*}_{(n)} = \overset{(+)}{\underset{\alpha}{\boldsymbol{\mu}}}{}^{*} \cdot \overset{(+)}{\underset{\alpha}{\mathbf{n}}}$, $\overset{(-)}{\underset{\alpha+1}{\mu}}{}^{*}_{(n)} = \overset{(-)}{\underset{\alpha+1}{\boldsymbol{\mu}}}{}^{*} \cdot \overset{(+)}{\underset{\alpha+1}{\mathbf{n}}}$, where $\overset{(+)}{\underset{\alpha}{\boldsymbol{\mu}}}{}^{*}$ ($\overset{(-)}{\underset{\alpha+1}{\boldsymbol{\mu}}}{}^{*}$) is the intensity of the limit momentum. Therefore, $\overset{(+)}{\underset{\alpha}{P}}{}^{*}_{(s)}$, $\overset{(-)}{\underset{\alpha+1}{P}}{}^{*}_{(s)}$, $\overset{(+)}{\underset{\alpha}{\mu}}{}^{*}_{(n)}$ and $\overset{(-)}{\underset{\alpha+1}{\mu}}{}^{*}_{(n)}$ are unknown values in relations (14) and (15) determined from some a priori dependencies, conditions of slipping with friction, which, generally speaking, must depend on geometric and physical-mechanical properties of contacted bodies. In the classic case we may suppose the relations hold

$$\mathbf{L}(x^1, x^2, \mathbf{v}_s, \dot{\mathbf{v}}_s, [T], \mathbf{P}^{(l)*}, \dots) = 0, \tag{16}$$

where $\mathbf{v}_s$ and $\dot{\mathbf{v}}_s$ are the tangent components of the vectors of the relative displacement and relative velocity, $[T]$ is the temperature jump, $\mathbf{P}^{(l)*}$ is the limit stress vector on a plane element with the normal $\mathbf{l}$, the ellipsis denotes the dependence on some other parameters. Based on (16), we can accept that the generalized model of Coulomb friction is valid:

$$\mathbf{P}^{*}_{(s)} = \underset{\sim}{\mathbf{f}}(x^1, x^2, [T], \mathbf{P}^{*}_{(n)}) \cdot \dot{\mathbf{v}}_s, \tag{17}$$

which takes into account the anisotropy of the friction. Here $\mathbf{P}^{*}_{(s)}$ and $\mathbf{P}^{*}_{(n)}$ are the limit tangent and normal components of the stress vector $\mathbf{P}^{(l)*}$. The second rank tensor $\underset{\sim}{\mathbf{f}}(x^1, x^2, [T], \mathbf{P}^{*}_{(n)})$ is called the tensor of friction coefficients. Obviously, in the isotropic case we have $\underset{\sim}{\mathbf{f}} = f\underset{\sim}{\mathbf{E}}$, where $\underset{\sim}{\mathbf{E}}$ is the unit second rank tensor. Representing (17) for contacted surfaces of a multilayer thin body, we obtain the missing required relations. Based on similar arguments in the case of the micropolar theory, we can assert that the following a priori relations are valid:

$$\begin{aligned} &\mathbf{L}(x^1, x^2, \mathbf{v}_s, \dot{\mathbf{v}}_s, \boldsymbol{\psi}_n, \dot{\boldsymbol{\psi}}_n, [T], \mathbf{P}^{(l)*}, \dots) = 0, \\ &\mathbf{M}(x^1, x^2, \mathbf{v}_s, \dot{\mathbf{v}}_s, \boldsymbol{\psi}_n, \dot{\boldsymbol{\psi}}_n, [T], \boldsymbol{\mu}^{(l)*}, \dots) = 0, \end{aligned} \tag{18}$$

where $\boldsymbol{\psi}_n$ and $\dot{\boldsymbol{\psi}}_n$ are the normal components of the vectors of the relative internal rotation and relative internal rotation velocity of adjacent layers, $\boldsymbol{\mu}^{(l)*}$ is the limit vector of the couple stress on a plane element with the normal $\mathbf{l}$, the other parameters are the same as in (16). Based on (18) and similar to (17), for the micropolar theory we can assume that the following relations are valid:

$$\begin{aligned} \mathbf{P}^{*}_{(s)} &= \underset{\sim}{\mathbf{f}}(x^1, x^2, [T], \mathbf{P}^{*}_{(n)}) \cdot \dot{\mathbf{v}}_s + \underset{\sim}{\mathbf{h}}(x^1, x^2, [T], \mathbf{P}^{*}_{(n)}) \cdot \dot{\boldsymbol{\psi}}_n, \\ \boldsymbol{\mu}^{*}_{(n)} &= \underset{\sim}{\mathbf{g}}(x^1, x^2, [T], \boldsymbol{\mu}^{*}_{(s)}) \cdot \dot{\boldsymbol{\psi}}_n + \underset{\sim}{\mathbf{l}}(x^1, x^2, [T], \boldsymbol{\mu}^{*}_{(s)}) \cdot \dot{\mathbf{v}}_s, \end{aligned} \tag{19}$$

that take into account the anisotropy of the friction. Here $\underset{\sim}{\mathbf{f}}$, $\underset{\sim}{\mathbf{h}}$, $\underset{\sim}{\mathbf{g}}$ and $\underset{\sim}{\mathbf{l}}$ are the second rank tensors called the tensors of friction coefficients. Therefore, in the case of an isotropic friction we have $\underset{\sim}{\mathbf{f}} = f\underset{\sim}{\mathbf{E}}$, $\underset{\sim}{\mathbf{h}} = h\underset{\sim}{\mathbf{E}}$, $\underset{\sim}{\mathbf{g}} = g\underset{\sim}{\mathbf{E}}$ and $\underset{\sim}{\mathbf{l}} = l\underset{\sim}{\mathbf{E}}$, where $\underset{\sim}{\mathbf{E}}$ is the unit second rank tensor. It should be noted here that the coefficients of friction are determined by experiments and are

given in tables. The author knows little in this direction for the micropolar theory, but for the classic theory these coefficients can be obtained, e.g., from [12, 13, 14]. Representing (19) for the contacted surfaces of a multilayer thin body, we get the missing required relations in the case of the micropolar theory.

2.5. Conditions under a partial exfoliation of contacted surfaces of layers

For the classic theory of multilayer thin bodies in this case we have the conditions

$$\begin{gathered}\underset{\alpha}{\mathbf{v}}(x^1,x^2)=\overset{(-)}{\underset{\alpha+1}{\mathbf{u}}}(x^1,x^2)-\overset{(+)}{\underset{\alpha}{\mathbf{u}}}(x^1,x^2)\neq 0,\quad \overset{(+)}{\underset{\alpha}{\mathbf{P}}}(x^1,x^2)=0,\quad \overset{(-)}{\underset{\alpha+1}{\mathbf{P}}}(x^1,x^2)=0,\\ (x^1,x^2)\subset \overset{(+)}{\underset{\alpha}{S}}{}^0\subset \overset{(+)}{\underset{\alpha}{S}},\quad \alpha=\overline{1,K-1},\end{gathered}\tag{20}$$

and for the micropolar theory of multilayer thin bodies we get the conditions

$$\begin{gathered}\underset{\alpha}{\mathbf{v}}(x^1,x^2)=\overset{(-)}{\underset{\alpha+1}{\mathbf{u}}}(x^1,x^2)-\overset{(+)}{\underset{\alpha}{\mathbf{u}}}(x^1,x^2)\neq 0,\quad \overset{(+)}{\underset{\alpha}{\mathbf{P}}}(x^1,x^2)=0,\quad \overset{(-)}{\underset{\alpha+1}{\mathbf{P}}}(x^1,x^2)=0,\\ \underset{\alpha}{\boldsymbol{\psi}}(x^1,x^2)=\overset{(-)}{\underset{\alpha+1}{\boldsymbol{\varphi}}}(x^1,x^2)-\overset{(+)}{\underset{\alpha}{\boldsymbol{\varphi}}}(x^1,x^2)\neq 0,\quad \overset{(+)}{\underset{\alpha}{\boldsymbol{\mu}}}(x^1,x^2)=0,\quad \overset{(-)}{\underset{\alpha+1}{\boldsymbol{\mu}}}(x^1,x^2)=0,\\ (x^1,x^2)\subset \overset{(+)}{\underset{\alpha}{S}}{}^0\subset \overset{(+)}{\underset{\alpha}{S}},\quad \alpha=\overline{1,K-1}.\end{gathered}\tag{21}$$

Note that if $\overset{(+)}{\underset{\alpha}{S}}{}^0=\overset{(+)}{\underset{\alpha}{S}}$, then we have a complete exfoliation of contacted layers. Other conditions posed on deformed and force states of exterior surfaces of multilayer thin bodies are also possible: a contact with rigid or elastic bodies, a forced displacement of points, etc. Note also that based on [5, 15] and quite similarly to this paper, one can construct micropolar theories of multilayer thin bodies with two small sizes and those of plane domains with one small size, respectively (it remains to write down the corresponding relations). We do not pay attention to this in the present paper.

In conclusion we note that the other important direction is the study of eigenvalue problems for the tensor and tensor-block matrix of any even rank, since the constitutive relations for most classical and micropolar media of different rheology (here, of course, also include porous and multilayer textile media) are written using a tensor and tensor-block matrix of even rank, respectively. Several questions concerning these problems, as well as tensor calculus, have been studied in some detail in [16, 19, 18, 20, 17]. A very important direction is also the investigation of internal structures of differential tensors-operators and tensor-block matrix operators of even rank. This is due to the fact that such operators are operators of systems of equations of motion and static boundary conditions with respect to kinematic characteristics (displacement, rotation, velocity, angular velocity) for most classical and micropolar mediums. The study of these problems promotes the decomposition

of initial-boundary value problems in the case of linear theories. Some questions about the decomposition of initial-boundary value problems can be found in [1, 2, 21].

Acknowledgments

This work was supported by the Shota Rustaveli National Science Foundation (project no. DI-2016-41).

References

[1] Nikabadze, M. U. *Development of the method of orthogonal polynomials in the classical and micropolar mechanics of elastic thin bodies.* Moscow Univ. Press, Moscow, 2014, 515 p.

[2] Nikabadze, M. U. *The method of orthogonal polynomials in the classical and micropolar mechanics of elastic thin bodies.* Diss. Doctor Phys.–Math. Sci. (in Russian), Moscow, 2014, 384 p.

[3] Vekua, I. N. Shell theory, general methods of construction. Pitman Adv. Pub. Program, 1985.

[4] Nikabadze, M. U. Some issues concerning a version of the theory of thin solids based on expansions in a system of Chebyshev polynomials of the second kind *Mech. Solids*, 42(3) (2007), 391-421.

[5] Nikabadze, M. U. *Mathematical modeling of elastic thin bodies with two small dimensions with the use of systems of orthogonal polynomials.* Deposited in VINITI RAS, No. 722 – B2008, 21.08.2008, (in Russian), Moscow, 107 p.

[6] Nikabadze, M. U. and Ulukhanyan, A. R. *Mathematical modeling of elastic thin bodies with one small dimension with the use of systems of orthogonal polynomials.* Deposited in VINITI RAS, No. 723 – B2008, 21.08.2008, (in Russian), Moscow, 64 p.

[7] Bolotin, V. V. Influence of technological factors on mechanical reliability of composite structures *Mechanics of Polymers*, 3(1972), 529–540.

[8] Krasulin, Yu. L. and Shorshorov, M. Kh. Formation mechanism of joining heterogeneous materials in solid state *Phys.-Chem. Material Processing*, 1(1967), 89–94.

[9] Potapov, A. I. *Quality control and reliability prediction for constructions of composites.* Leningrad, 1980.

[10] Podstrigach, Ya. S. Conditions of heat contact of solid bodies *Dokl. Akad. Nauk URSR*, 7(1963), 872–874.

[11] Podstrigach, Ya. S. Jump conditions for stresses and displacements on a thin-walled elastic inclusion in a continuum *Dokl. Akad. Nauk URSR*, 12(1982), 30–32.

[12] Braun, E. D., Bushe, N. A., Buyanovskii, I. A. and et al., *Fundamentals of tribology (friction, wear, lubrication).* Ed. by A. V. Chichinadze. Nauka i Tekhnika, Moscow, 1995.

[13] Kragelskii, I. V. and Vinogradova, I. E. *Coefficients of friction.* Mashgiz, Moscow, 1962.

[14] Kragelskii, I. V. *Friction and wear.* Mashinostroenie, Moscow, 1969, 88 p.

[15] Nikabadze, M. U., Kantor, M. M. and Ulukhanian, A. R. *To mathematical modeling of elastic thin bodies and numerical realization of several problems on the band.* Deposited in VINITI RAS, No. 204 – B2011, 29.04.2011, (in Russian), Moscow, 207 p.

[16] Nikabadze, M. U. On some problems of tensor calculus. I. *J. Math. Sci.*, 161(5) (2009), 668-697.

[17] Nikabadze, M. U. Topics on tensor calculus with applications to mechanics. *J. Math. Sci.*, 225(1) (2017), 194.

[18] Nikabadze, M. U. On the construction of linearly independent tensors *Mech. Solids*, 44(1) (2009), 14-30.

[19] Nikabadze, M. U. On some problems of tensor calculus. II. *J. Math. Sci.*, 161(5) (2009), 698-733.

[20] Nikabadze, Mikhail U. Eigenvalue Problems of a Tensor and a Tensor-Block Matrix (TMB) of Any Even Rank with Some Applications in Mechanics. *H. Altenbach and S. Forest (eds.), Generalized Continua as Models for Classical and Advanced Materials, Advanced Structured Materials*, Springer International Publishing Switzerland, 42 (2016), 279-317.

[21] Nikabadze, Mikhail U. and Ulukhanyan, Armine R. Analytical Solutions in the Theory of Thin Bodies. *H. Altenbach and S. Forest (eds.), Generalized Continua as Models for Classical and Advanced Materials, Advanced Structured Materials*, Springer International Publishing Switzerland, 42 (2016), 319-361.

Mikhail Nikabadze, Prof.: Lomonosov Moscow State University, Department of Mechanics and Mathematics, Leninskie Gory, 1, Moscow 119992, Russia (*Bauman Moscow State Technical University, Baumanskaya 2-ya, str., 5, Moscow 105005, Russia*). nikabadze@mail.ru

The author gave a presentation of this paper during one of the conference sessions.

Tamar Moseshvili, Ph.D.: Akaki Tsereteli Kutaisi State University, Design and Technology Department, Tamar Mephe street 59, Kutaisi 4600, Georgia (*tamarmoseshvili@yahoo.com*).
The author gave a presentation of this paper during one of the conference sessions.

The author gave a presentation of this paper during one of the conference sessions.

Armine Ulukhanian, Ph.D.: Bauman Moscow State Technical University, Departament of Calculation Mathematics and Mathematical Physics, Baumanskaya 2-ya, str., 5, Moscow 105005, Russia (*armine_msu@mail.ru*).

Ketevan Tskhakaia, Ph.D.: Akaki Tsereteli Kutaisi State University, Energy and Telecommunications Department, Tamar Mephe street 59, Kutaisi 4600, Georgia (*spectri@gmail.com*).

Nodar Mardaleishvili, Ph.D.: Akaki Tsereteli Kutaisi State University, Mechanics and Mechanical Engineering Department, Tamar Mephe street 59, Kutaisi 4600, Georgia (*nodarmard3@mail.ru*).

A piecewise-smooth control of dengue

Gerard Olivar-Tost, Luis E. López, Anibal Muñoz

Abstract: The following research focuses on mathematical modeling of the transmission and control of Dengue fever using systems of nonlinear ordinary differential equations. Initially, a mathematical model is formulated to represent the transfer of the disease to the human population considering breeding grounds where mosquito proliferates, the phases of evolution of the mosquito, and the human population. The model comprises a nonlinear system of nine differential equations where each equation represents the variation of a single subpopulation. Based on the original model, a system of twelve differential equations is formulated representing the dynamic transmission and constant control of the disease. In this model, biological control is applied using the Wolbachia bacteria, which inhibits the transfer of the virus from an infected mosquito to humans. Finally, a new model with biological control is developed from the original two-dimensional model. We consider a constant control and derive a piecewise smooth dynamical system, in which a non-smooth local bifurcation of codimension-1 that determines the collision of equilibrium points on the discontinuity boundary. This bifurcation occurs when the parameter R_0, which represents the Basic Reproduction Number of Dengue fever, is varied.

1. Introduction

Dengue is a viral disease transmitted to humans through the mosquito bite of the Aedes family, especially the species *A. Aegypti*. The virus transmitted has five serotypes DEN1, DEN2, DEN3, DEN4, and DEN5 and so far no vaccine provides temporary or total immunity against all virus serotypes. Due to this situation, the only alternative to deal with the disease is the application of control to the transmitting mosquito [6].

Three types of controls are distinguished: mechanical control or preventive control, chemical control (larvicides and insecticides) and biological control. The latter one uses living beings as predators of the mosquito and helps to reduce the transmission of the virus. For the model, biological control is taken into account by the use of the Wolbachia bacterium, which infects the mosquito in the immature state (egg) and helps to decrease the probability of transmitting the virus to the human population [7, 14].

The proposed model arises from the two-dimensional model presented in [10], which is formulated from a system of ordinary nonlinear differential equations of dimension nine, which is divided into three decoupled subsystems. The first one represents the spatial growth

of the hatcheries. The second one represents the population growth of the Aedes aegypti mosquito taking into account its evolutionary phases, and the third one represents the transmission of the virus in the human population. This last system is normalized to obtain the two-dimensional system

$$\begin{cases} \dot{p} &= \mu(1-p) - R_0(\theta+\mu)pq \\ \dot{q} &= R_0(\theta+\mu)pq - (\theta+\mu)q \end{cases} \tag{1}$$

where p and q represent the proportion of healthy and infected individuals, respectively (variables), and R_0, θ, μ the model parameters. The model proposed in this article is a non-smooth system of dimension two, which is obtained from the system (1) by adding a constant control u that decreases the proportion of infected people. By varying the parameter R_0, keeping fixed μ and θ, we obtain a non-smooth local bifurcation of codimension 1.

2. The model

By incorporating a constant control $u \in [0,1]$ into the system (1), which represents the effectiveness to reduce the proportion of infected persons using the bacterium Wolbachia as a biological control, the control system is obtained.

$$\begin{cases} \dot{p} &= \mu(1-p) - R_0(\theta+\mu)pq \\ \dot{q} &= R_0(\theta+\mu)pq - (\theta+\mu)q - u \end{cases} \tag{2}$$

The system (2) is defined in the region of biological interaction

$$\Omega = \left\{ w = (p,q)^T : p \geq 0, q \geq 0, p+q \leq 1 \right\}$$

with initial conditions $w_0 = (p_0, q_0)^T$.

The equilibrium points of (2) are defined by the following equations:

$$\mu R_0 p^2 - (\mu + \mu R_0 - u R_0)\, p + \mu = 0 \quad \text{and} \quad q = \frac{\mu(1-p) - u}{\theta + \mu} \tag{3}$$

Thus the existence of equilibrium points is related to the following condition:

$$(\mu + \mu R_0 - u R_0)^2 \geq 4\mu^2 R_0$$

Thus, system (2) will have two equilibrium points at most,

$$(p_{11}, q_{11}) \quad \text{and} \quad (p_{12}, q_{12}) \tag{4}$$

which satisfy the equations defined in (3).

2.1. Non-smooth system

Now, we define the region $q = \zeta$ en Ω. We will consider a control u, such that:

$$\begin{cases} \text{If} \quad q > \zeta, \quad u \neq 0, \quad u \in (0, 1] \\ \text{If} \quad q < \zeta, \quad u = 0 \end{cases}$$

Thus, surface $q = \zeta$ divides the vector field (2) into two zones:

$$f^{(1)}(w) = \begin{pmatrix} \mu(1-p) - R_0(\theta+\mu)pq \\ R_0(\theta+\mu)pq - (\theta+\mu)q \end{pmatrix} \quad \text{with} \quad q < \zeta$$

and

$$f^{(2)}(w) = \begin{pmatrix} \mu(1-p) - R_0(\theta+\mu)pq \\ R_0(\theta+\mu)pq - (\theta+\mu)q - u \end{pmatrix} \quad \text{with} \quad q > \zeta$$

Now, let $\mathbf{H} : \mathbb{R}^2 \to \mathbb{R}$ be a continuously differentiable function defined as:

$$\mathbf{H}(w) = q - \zeta$$

which has a gradient $\mathbf{H}_w(w) = (0, 1)$ (non-zero). Then we define the following regions:

$$S_1 = \left\{ w \in \mathbb{R}^2 : \mathbf{H}(w) < 0 \right\} = \left\{ w \in \mathbb{R}^2 : q < \zeta \right\}$$

$$S_2 = \left\{ w \in \mathbb{R}^2 : \mathbf{H}(w) > 0 \right\} = \left\{ w \in \mathbb{R}^2 : q > \zeta \right\}$$

$$\Sigma = \left\{ w \in \mathbb{R}^2 : \mathbf{H}(w) = 0 \right\} = \left\{ w \in \mathbb{R}^2 : q = \zeta \right\}$$

Thus we have a *non-smooth* system which can be written as:

$$\dot{w} = \begin{cases} f^{(1)}(w), & w \in S_1 \\ f^{(2)}(w), & w \in S_2 \end{cases} \tag{5}$$

2.2. Standard and Sliding solutions

For $w \in \Sigma$, we define

$$\begin{aligned} \ell(w) &= \left\langle \mathbf{H}_w(w), f^{(1)}(w) \right\rangle \left\langle \mathbf{H}_w(w), f^{(1)}(w) \right\rangle \\ &= \left(R_0(\theta+\mu)p\zeta - (\theta+\mu)\zeta\right)\left(R_0(\theta+\mu)p\zeta - (\theta+\mu)\zeta - u\right) \end{aligned}$$

The set

$$\Sigma_c = \{ w \in \Sigma : \ell(w) > 0 \}$$

corresponds to the *crossing region* in Σ and the set

$$\Sigma_s = \{w \in \Sigma : \ell(w) \leq 0\}$$

corresponds to the *sliding zone*.

For system (5) in Σ_s, we define the following tangent points:

$$T_1 = \left(\frac{1}{R_0}, \zeta\right) \quad \text{and} \quad T_2 = \left(\frac{1}{R_0}\left(1 + \frac{u}{(\theta+\mu)\zeta}\right), \zeta\right)$$

and the pseudo-equilibrium:

$$S_E = \left(\frac{\mu}{\mu + R_0(\theta+\mu)\zeta}, \zeta\right)$$

Regions S_1 and S_2 show two equilibrium points each one. Region S_2 contains the equilibrium points:

$$(p_{11}, q_{11}) \quad \text{and} \quad (p_{12}, q_{12}),$$

which satisfy the conditions defined in (3).

Region S_1 contains the equilibrium points

$$E_1 = (0,0) \quad E_2 = \left(\frac{1}{R_0}, \frac{\mu(R_0-1)}{R_0(\mu+\theta)}\right)$$

which are obtained from (3) when $u = 0$.

2.3. Codimension-1 local bifurcation

When we vary parameter $R_0 > 1$ and we keep constant parameters μ and θ, the system shows a local non-smooth bifurcation of codimension 1, when

$$\alpha_{R_0}^{(1)} = \frac{\mu}{\mu - (\theta+\mu)\zeta} \quad \text{and} \quad \alpha_{R_0}^{(2)} = \frac{\mu\left(u + (\theta+\mu)\zeta\right)}{\left(\mu - u - (\theta+\mu)\zeta\right)(\theta+\mu)\zeta}$$

Such a bifurcation appears when the equilibrium points E_2, S_E, T_1 y T_2 of (5) collide on the switching surface $q = \zeta$ [1], [12]. Such bifurcation is shown in Figures 1 and 2.

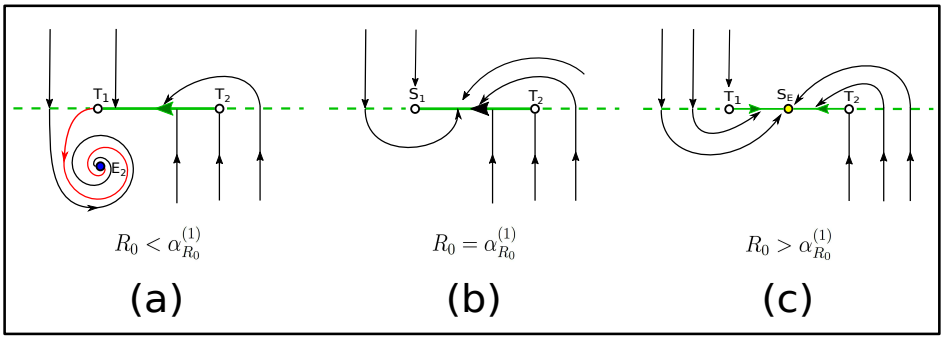

Figure 1. Bifurcation when $R_0 = \alpha_{R_0}^{(1)}$

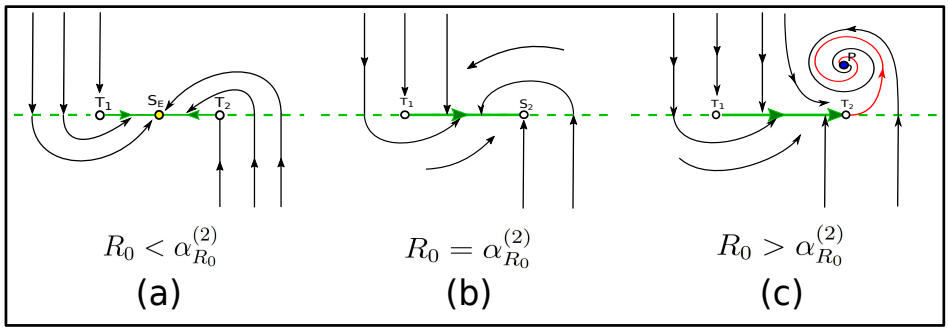

Figure 2. Bifurcation when $R_0 = \alpha_{R_0}^{(2)}$

If $1 < R_0 < \alpha_{R_0}^{(1)}$, the solutions in Ω of system (5) are attracted to the equilibrium E_2 (see Figure 1**(a)**). When R_0 reaches the bifurcaction value $\alpha_{R_0}^{(1)}$ the equilibrium point E_2 collides with the tangent point T_1 at the bifurcation point S_1 (see Figure 1**(b)**). When $R_0 > \alpha_{R_0}^{(1)}$, there is a change in system (5) and equilibrium E_2 changes stability. Also, an asymptotically stable pseudo-equilibrium S_E appears (see Figure 1**(c)**).

In a similar way, we obtain another bifurcation when $R_0 = \alpha_{R_0}^{(2)}$. If $\alpha_{R_0}^{(1)} < R_0 < \alpha_{R_0}^{(2)}$, the vector field in (5) is as in Figure 1**(c)**. When R_0 reaches the bifurcation value $\alpha_{R_0}^{(2)}$, pseudo-equilibrium S_E collides with the tangent point T_2 at S_2 (see Figure 2**(b)**). When $R_0 > \alpha_{R_0}^{(2)}$, point S_E disappears and a new equilibrium point $P = (p_{11}, q_{11})$ appears, which is asymptotically stable (See 4 and Figure 2**(c)**).

2.4. Numerical results

Figure 3 shows the numerical results for the solutions of system (5) for $\mu = 0.1$, $\theta = 0.1$, $u = 0.01$, $\zeta = 0.3$ and R_0 varying in the interval $[2, 5.26]$. In this case, we observe that if $R_0 < \alpha_{R_0}^{(1)} = 2.5$, equilibrium E_2 is asymptotically stable. If $R_0 = \alpha_{R_0}^{(1)} = 2.5$, E_2 collides with T_1 in S_1 (first bifurcation point). When $\alpha_{R_0}^{(1)} = 2.5 < R_0 < \alpha_{R_0}^{(2)} = 3.88$, pseudo-equilibrium S_E lies on Σ_S and it is an asymptotically stable point. If $R_0 = \alpha_{R_0}^{(2)} = 3.88$, S_E collides with T_2 at S_2 (second bifurcation point). Finally, if $R_0 > \alpha_{R_0}^{(2)} = 3.88$, the equilibrium point $P = (p_{11}, q_{11})$ appears, which was defined in (4), and it is asymptotically stable.

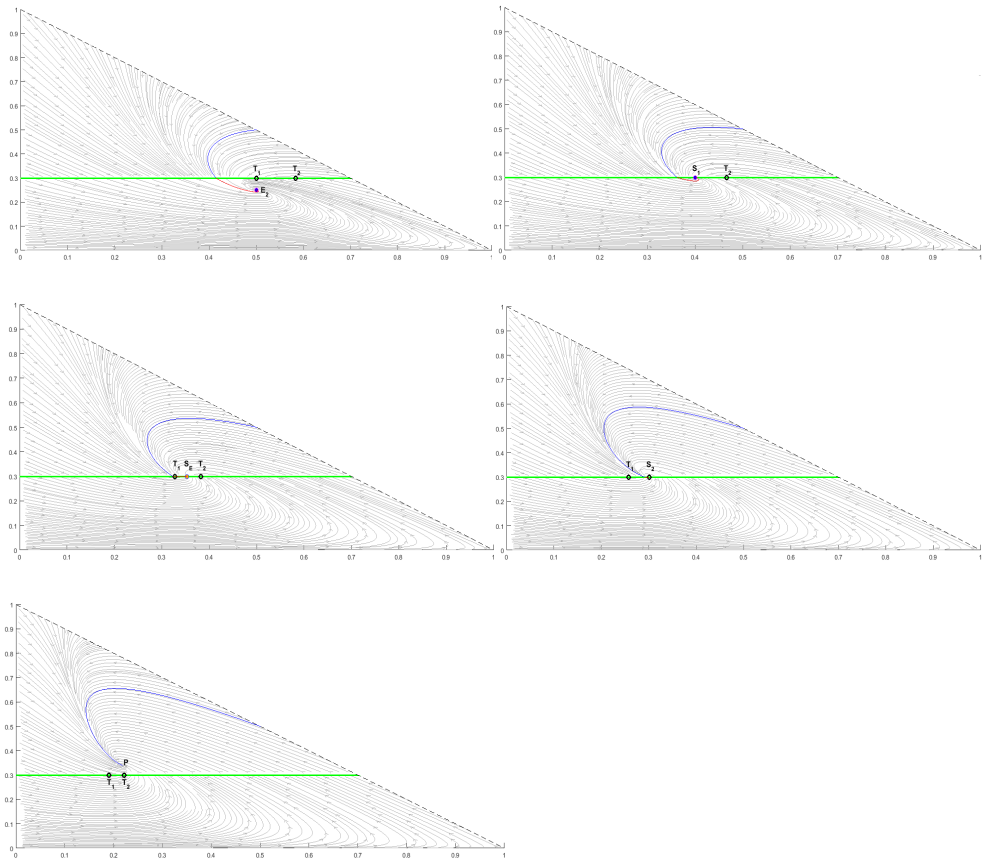

Figure 3. Bifurcations when $R_0 = \alpha_{R_0}^{(1)}$ and $R_0 = \alpha_{R_0}^{(2)}$

3. Conclusions

A mathematical model representing the dynamics of transmission and control of dengue virus in the human population was presented through the use of the bacterium Wolbachia, in a non-smooth system. In each zone $f^{(i)}(w), i = 1, 2$, two equilibrium points were found and three equilibria on the switching surface: two tangent points T_1 and T_2 , and a pseudo-equilibrium S_E.

According to the theory in [2], in the system (5) we can verify that if $R_0 \leq 1$, the equilibrium E_1 of (1) is asymptotically stable and E_2 is unstable. This means that the disease disappears from the environment. In addition, it can be concluded that:

- If $1 < R_0 < \alpha_{R_0}^{(1)}$, E_2 from $f^{(1)}$ is asymptotically stable.
- If $R_0 = \alpha_{R_0}^{(1)}$, equilibrium E_2 colides with T_1 at S_1 and system (5) has a local codimension-1 bifurcation.
- If $\alpha_{R_0}^{(1)} < R_0 < \alpha_{R_0}^{(2)}$, pseudo-equilibrium S_E is asymptotically stable.
- If $R_0 = \alpha_{R_0}^{(2)}$, equilibrium S_E colides with T_2 in S_2 and system (5) also has a bifurcation as in the previous case.
- If $R_0 > \alpha_{R_0}^{(2)}$, equilibrium $P = (p_{11}, q_{11})$ from $f^{(2)}$ is asymptotically stable.

The proposed scheme is an alternative to control the disease. It is based on the fact that if the fraction of infected persons exceeds the threshold θ, the biological control ($u \neq 0$). Otherwise, we must leave the disease to continue uncontrolled ($u = 0$). In this case, control u is considered constant. This strategy will not eliminate the disease from the environment, but will only stabilize the proportion of infected people under the desired threshold, provided that the basic number R_0 does not increase.

References

[1] Bernardo, M., Budd, C., Champneys, A. R., and Kowalczyk, P. *Piecewise-smooth dynamical systems: theory and applications*, vol. 163. Springer Science & Business Media, 2008.

[2] Brauer, F., and Castillo-Chavez, C. *Mathematical Models in Population Biology and Epidemiology*. Springer, 2012.

[3] Castillo-Chavez, C., and Horst, T. Asymptotically autonomous epidemic models. *Research Gate* (1994).

[4] Chen, H. Global bifurcation for a class of planar filippov systems with symmetry. *Qualitative Theory of Dynamical Systems 15*, 2 (2016), 349–365.

[5] Di Bernardo, M., Budd, C. J., Champneys, A. R., Kowalczyk, P., Nordmark, A. B., Tost, G. O., and Piiroinen, P. T. Bifurcations in nonsmooth dynamical systems. *SIAM review 50*, 4 (2008), 629–701.

[6] Götz, T., Altmeier, N., Bock, W., Rockenfeller, R., Wijaya, K. P., et al. Modeling dengue data from semarang, indonesia. *Ecological Complexity* (2016).

[7] Iturbe-Ormaetxe, I., Walker, T., and LO'Neill, S. Wolbachia and the biological control of mosquito-borne disease. *EMBO reports 12*, 6 (2011), 508–518.

[8] Kuznetsov, Y. *Elements of Applied Bifurcation Theory*. Springer, 1998.

[9] Kuznetsov, Y., Rinaldi, S., and Gragnani, A. One-parameter bifurcations in planar filippov systems. *International Journal of Bifurcation and Chaos* (2003).

[10] López, L. E., Muñoz, A., and Olivar, G. A mathematical model for transmission of dengue. *Applied Mathematical Sciences 10*, 7 (2016), 345–355.

[11] Ndii, M. Z., Hickson, R. I., Allingham, D., and Mercer, G. Modelling the transmission dynamics of dengue in the presence of wolbachia. *Mathematical biosciences 262* (2015), 157–166.

[12] Olejnik, P., and Awrejcewicz, J. Application of hénon method in numerical estimation of the stickslip transitions existing in filippov-type discontinuous dynamical systems with dry friction. *Nonlinear Dynamics, https://doi.org/10.1007/s11071-013-0826-7 73* (2013), 723.

[13] Tang, B., Xiao, Y., Sivaloganathan, S., and Wu, J. A piecewise model of virus-immune system with effector cell-guided therapy. *Applied Mathematical Modelling* (2017).

[14] Werren, J. Biology of wolbachia. *Rev. Entomol Vol. 42* (1997), 587 – 609.

Gerard Olivar-Tost, Ph.D.: Full Professor: Universidad Nacional de Colombia - Manizales, Campus La Nubia, Manizales, COLOMBIA (*golivart@unal.edu.co*). The author gave a presentation of this paper during one of the conference sessions.

Luis Eduardo López, M.Sc. (Ph.D. student): Universidad Nacional de Colombia - Manizales, Campus La Nubia, Manizales, COLOMBIA (*lelopezm@unal.edu.co*).

Anibal Muñoz Loaiza, Ph.D.: Professor: Universidad del Quindío, Facultad de Educación, Armenia, COLOMBIA (*anibalml@hotmail.com*).

On the stability and ultimate boundedness of solutions for certain third order non-autonomous delay differential equations

Akinwale Olutimo

Abstract: Sufficient conditions are established to ensure the uniform asymptotic stability and uniform ultimate boundedness of solutions of certain third order nonlinear non-autonomous delay differential equations. By using Lyapunov's second or direct method, we obtain new results on the subject which improve the well known results in the literature with particular cases of the equation considered for the ultimate boundedness and asymptotic behavior of solutions using complete Lyapunov functions. Our aim is to further extend and improve on the results to more general equation considered for which the forcing and nonlinear terms depend on certain variables and deviating arguments.

1. Introduction

This paper studies the uniform asymptotic stability and uniform ultimate boundedness of solutions of third order nonlinear non-autonomous delay differential equation

$$x'''(t)+\psi(t,x,\dot{x})x''(t)+a(t)\phi(x(t-r(t)),x'(t-r(t)))+b(t)h(x(t-r(t)),x'(t-r(t)))= p(t,x(t),x'(t),x(t-r(t)),x'(t-r(t)),x''(t)) \quad (1)$$

which is equivalent to the system

$$\begin{aligned} x' &= y,\\ y' &= z,\\ z' = &- \psi(t,x,y)z-a(t)\phi(x,y)-b(t)h(x,y)+a(t)\int_{t-r(t)}^{t}\phi'_x(x(s),y(s))y(s)ds\\ &+ a(t)\int_{t-r(t)}^{t}\phi'_y(x(s),y(s))z(s)ds+b(t)\int_{t-r(t)}^{t}h'_x(x(s),y(s))y(s)ds\\ &+ b(t)\int_{t-r(t)}^{t}h'_y(x(s),y(s))z(s)ds+p(t,x,y,x(t-r(t)),y(t-r(t)),z), \end{aligned} \quad (2)$$

where $a(t),b(t)\in\mathcal{C}(\mathbb{R}^+,\mathbb{R})$, $\psi(t,x,y)\in\mathcal{C}(\mathbb{R}^+\times\mathbb{R}^2,\mathbb{R})$, $\phi(x,y),h(x,y)\in\mathcal{C}(\mathbb{R}^2,\mathbb{R})$ and $p(t,x,y,x(t-r(t)),y(t-r(t)),z)\in\mathcal{C}(\mathbb{R}^+\times\mathbb{R}^5,\mathbb{R})$, $t\in\mathbb{R}^+$, $\mathbb{R}=(-\infty,\infty)$ and $\mathbb{R}^+=[0,\infty)$; $a(t),b(t),\psi,\phi,h$ *and* p depend only on the arguments displaced explicitly and $\psi_t,\psi_x(t,x,y),\phi_x(x,y),a'(t),b'(t)$ exist and are continuous for all t,x *and* y with $\psi(0,0,0)=\phi(0,0)=h(0,0)=0$ and

$0 \leq r(t) \leq \gamma$, γ is a positive constant that will be determined later with $r'(t) \leq \beta$, $0 < \beta < 1$. The functions $\psi(t,x,y), \phi(x,x'(t-r(t))), h(x,x'(t-r(t))$ *and* $p(t,x,y,x(t-r(t)),y(t-r(t)),z)$ satisfy a Lipschitz condition in $x, y, x(t-r(t)), y(t-r(t))$ *and* z; hence, the solutions of (1.1) are unique. Throughout the paper $x(t), y(t)$ *and* $z(t)$ are respectively abbreviated as x, y *and* z.

Nonlinear delay differential equations are important tools in scientific modeling of some practical problems arisen in many fields of science and technology such as after-effect, nonlinear oscillations, coupled oscillations and equations with deviating arguments (see [1]). Stability and boundedness of solutions of non-autonomous delay differential equations are quite complicated. It is even more complicated for ultimate boundedness of solutions of non-autonomous delay differential equations. It is known that ultimate boundedness is a very important problem in the theory and applications of differential equations. Equations of the form (1) in which $a(t) = b(t) = 1$ and ψ not explicitly depended on t have been studied by several authors, see for instance Sadek [2], Afuwape and Omeike [3], Ademola and Aramowo [4], Yao and Meng [5] to mention a few. They obtained the stability and boundedness of solutions. For the equations in which $a(t) \neq 1$, $b(t) \neq 1$ and ψ explicitly depending on t, some authors have obtained conditions for the stability and boundedness of solutions, see for example, Omeike [6], Tunc [7], Remili and Oudjedi [8] and Olutimo and Adams [9]. The Lyapunov function used in [6, 7, 8, 9] is not complete (see [10]). Particularly, the boundedness result considered in [6, 7, 8, 9] is of the type in which the bounding constant depends on the solution in question.

Our motivation comes from the above mentioned papers. With respect to our observation in the literature, till now, no author has discussed the ultimate boundedness of solutions for the more general non-autonomous equation (1). Thus, the investigation on the subject for (1) is worthwhile. Our result extends and improves the results obtained by [6, 7, 8, 9]. It may be useful to researchers as it plays an important role in characterizing the behavior of solutions of sufficiently complicated nonlinear delay differential equations.

1.1. Preliminary results

Now, we will state the stability criteria for the general non-autonomous delay differential system. We consider:

$$\dot{x} = f(t,x), x_t = x(t+\theta) \quad -r \leq \theta \leq 0, t \geq 0, \tag{3}$$

where $f : \mathbf{I} \times C_H \longrightarrow \mathbb{R}^n$ is a continuous mapping,

$$f(t,0) = 0, C_H := \{\varphi \in (C[-r,0], \mathbb{R}^n) : \|\varphi\| \leq H\}$$

and for $H_1 \leq H$, there exists $L(H_1) > 0$, with

$$|f(\varphi)| \leq L(H_1) \quad when \quad \|\varphi\| \leq H_1.$$

Lemma 1 *([2,3]) An element $\varphi \in C_H$ is such that the solution $x_t(\varphi)$ of (3) with $x_o(\varphi) = \varphi$ is defined on $[0, \infty)$ and $\|x_t(\varphi)\| \leq H_1 < H$ for $t \in [0, \infty)$, then $\Omega(\varphi)$ is a non-empty, compact, invariant set and*

$$dist(x_t(\varphi), \Omega(\varphi)) \to 0 \quad as \quad t \to \infty.$$

Lemma 2 *([2,3]) Let $V(t, \varphi) : I \times C_H \longrightarrow \mathbb{R}$ be a continuous functional satisfying a local Lipschitz condition. $V(t, \varphi) = 0$, and such that:*

(i) $W_1|\varphi(0)| \leq V(t, \varphi) \leq W_2\|\varphi\|$ *where $W_1(r)$, $W_2(r)$ are wedges*

(ii) $\dot{V}_{(3)}(t, \varphi) \leq 0$ *for $\varphi \leq C_H$.*

Then the zero solution of (3) is uniformly stable. If we define $Z = \{\varphi \in C_H : V_{(3)}(t, \varphi) = 0\}$, then the zero solution of (3) is asymptotically stable provided that the largest invariant set in Z is $Q = \{0\}$.

2. Statement of results

Theorem 1 *In addition to the basic assumptions imposed on the functions $a(t), b(t), \psi(t, x, y), \phi(x, y), h(x, y)$ and p. Suppose further that there are positive constants, $a, a_1, b, b_1, m, c, \nu_o, L_1, L_2, M_1, M_1, \delta_o, \delta_1$ such that the following conditions are satisfied:*

(i) $a \leq \psi(t, x, y) \leq a_1$, $b \leq \frac{\phi(x,y)}{y} \leq b_1$, $h_x(x, 0) \leq c$, $\frac{h(x,y)}{x} \geq m$, $ab - c > 0$;

(ii) $h_y(x, \theta_1 y) \leq 0$, $h_z(x, \theta_2 y) \leq 0$, $\psi_t(t, x, y) \leq 0$, *for all* t, x, y, z, $0 \leq \theta_1 \leq 1$, $0 \leq \theta_2 \leq 1$;

(iii) $a(t) \geq b(t) \geq \nu_o > 0$, $b'(t) \geq a'(t) \geq -\nu_o \leq 0$ *for all* $t \geq 0$;

(iv) $\int_0^y \sigma\psi_x(t, x, \sigma)d\sigma \leq 0$ *and* $\int_0^y \phi_x(x, \sigma)d\sigma \leq 0$ *for all t, x, y;*

(v) $|\phi'_x(x, y)| \leq L_1$, $|\phi'_y(x, y)| \leq L_2$, $|h'_x(x, y)| \leq M_1$, $|h'_y(x, y)| \leq M_2$, *for all x, y;*

Then, the zero solution of system (1.2) is asymptotically stable, provided that

$$\frac{1}{a} < \mu_1 < \frac{b}{c}, \tag{4}$$

$$\mu_2 < min\left\{ \frac{\nu_o(ab - c)}{\left(a + \nu_o^{-1}m(\frac{a(t)\phi(x,y)}{y} - b\right)^2}; \frac{\nu_o m(\mu_1 a - 1)}{(\psi(t, x, y) - a)^2}; \frac{\mu_1 a - 1}{\mu_1}; b \right\} \tag{5}$$

and

$$\gamma < min\Bigg\{ \frac{m\mu_2}{\big[\mu_2(L_1+L_2)+\mu_2(M_1+M_2)\big]};$$
$$\frac{2(b-\mu_1 c)(1-\beta)}{\big[(1+a)(L_1+L_2)+(1+a)(M_1+M_2)+(L_1+M_1)(\mu_1+\mu_2+a+1)\big]};$$
$$\frac{2a(1-\beta)}{\nu_o\big[(1+\mu_1)(L_1+L_2)+(1+\mu_1)(M_1+M_2)+(L_2+M_2)(\mu_1+\mu_2+a+1)\big]}\Bigg\}. \tag{6}$$

Theorem 2 *We assume that all the assumptions of Theorem 1 are satisfied and*

(i) $|p(t,x,y,x(t-r(t)),y(t-r(t)),z)| \leq \big[\delta_o + \delta_1(|x|+|y|+|z|)\big]$

uniformly for all $x,y,z \in \mathbb{R}$ where $\delta_o > 0$, $\delta_1 > 0$ are constants and δ_1 sufficiently small. Then, there exists a constant $\delta > 0$ such that any solution $(x(t),y(t),z(t)))$ of the system (2) uniformly satisfies

$$|x(t)| \leq \delta, \quad |y(t)| \leq \delta, \quad |z(t)| \leq \delta \quad for \;\; t \in \mathbb{R}^+,$$

where the magnitude of δ depend only on $\delta_o, \delta_1, a, b, c, m, \nu_o$ and p.

3. The function V

Our main tool is the following Lyapunov functional $V = V(x_t, y_t, z_t)$ defined as

$$\begin{aligned} 2V &= 2b(t)(1+a)\int_0^x h(\xi,0)d\xi + 2(1+a)\int_0^y \sigma\psi(t,x,\sigma)d\sigma \\ &+ 2a(t)(1+\mu_1)\int_0^y \phi(x,\sigma)d\sigma + 2b(t)(1+\mu_1)yh(x,0) \\ &+ (1+\mu_1)z^2 + \mu_2 bx^2 + 2a\mu_2 xy + 2(1+a)yz + 2\mu_2 xz - \mu_2 y^2 \\ &+ 2\lambda_1\int_{-r(t)}^0\int_{t+s}^t y^2(\theta)d\theta ds + 2\lambda_2\int_{-r(t)}^0\int_{t+s}^t z^2(\theta)d\theta ds, \end{aligned} \tag{7}$$

where μ_1, μ_2 satisfies (4) and (5) respectively and λ_1, λ_2 are positive constants which will be determined later.

We also assume that

$$lim_{t\to\infty} c(t) = c_o, \;\; lim_{t\to\infty} b(t) = b_o \;\; and \;\; lim_{t\to\infty} a(t) = a_o,$$

where $0 < \nu_o \leq c_o \leq b_o \leq a_o$.

Lemma 3 *Suppose conditions (i) - (iv) of Theorem 1 hold, then there exists positive constants δ_2, δ_3 such that*

$$\delta_2(x^2+y^2+z^2) \leq V \leq \delta_3(x^2+y^2+z^2) \tag{8}$$

Proof:

Then (7) can be recast in the form $2V = V_1 + V_2$,

where

$$\begin{aligned} V_1 &= 2b(t)\int_0^x h(\xi,0)d\xi + 2\int_0^y \sigma\psi(t,x,\sigma)d\sigma \\ &+ 2a(t)\mu_1\int_0^y \phi(x,\sigma)d\sigma + 2b(t)\mu_1 y h(x,0) \\ &+ \mu_1 z^2 + 2yz - \mu_2 y^2 \end{aligned}$$

and

$$\begin{aligned} V_2 &= \mu_2 b x^2 + 2ab(t)\int_0^x h(\xi,0)d\xi + 2a\int_0^y \sigma\psi(t,x,\sigma)d\sigma \\ &+ 2a(t)\int_0^y \phi(x,\sigma)d\sigma + 2b(t)yh(x,0) \\ &+ z^2 + 2a\mu_2 xy + 2ayz + 2\mu_2 xz \\ &+ 2\lambda_1\int_{-r(t)}^0\int_{t+s}^t y^2(\theta)d\theta ds + 2\lambda_2\int_{-r(t)}^0\int_{t+s}^t z^2(\theta)d\theta ds. \end{aligned}$$

V_1 re-arranged as

$$\begin{aligned} V_1 &= b(t)\left[2\int_0^x h(\xi,0)d\xi - \frac{\mu_1}{b}h^2(x,0)\right] + b(t)\mu_1 b\left[y + \frac{h(x,0)}{b}\right]^2 \\ &+ \left[2\int_0^y \sigma\psi(t,x,\sigma)d\sigma - \mu_1^{-1}y^2 - \mu_2 y^2\right] + \mu_1[z + \mu_1^{-1}y]^2 \\ &+ \mu_1\left[2a(t)\int_0^y \phi(x,\sigma)d\sigma - b(t)by^2\right]. \end{aligned}$$

The term

$$b(t)2\int_0^x h(\xi,0)d\xi - \frac{\mu_1}{b}h^2(x,0),$$

$$\begin{aligned} &= b(t)\left[2\int_0^x h(\xi,0)d\xi - 2\frac{\mu_1}{b}\int_0^x h(\xi,0)\frac{dh(\xi,0)}{d\xi} - \frac{\mu_1}{b}h^2(0,0)\right] \\ &= b(t)\left[2\int_0^x (1 - \frac{\mu_1}{b}h_\xi(\xi,0))\right]h(\xi,0)d\xi \\ &\geq b_o(1 - \frac{\mu_1}{b}c)mx^2 \\ &\geq \nu_o m(1 - \frac{\mu_1}{b}c)x^2. \end{aligned}$$

The term

$$2\int_0^y \sigma\psi(t,x,\sigma)d\sigma - \mu_1^{-1}y^2 - \mu_2 y^2,$$

by the hypotheses (i) of Theorem 1, we have

$$(a - \mu_1^{-1} - \mu_2)y^2 \geq 0.$$

The term,

$$\mu_1\left[2a(t)\int_0^y \phi(x,\sigma)d\sigma - b(t)by^2\right]$$

$$\begin{aligned}
&= \mu_1\left[2a(t)\frac{\phi(x,\sigma)}{y}\int_0^y \sigma d\sigma - b(t)by^2\right] \\
&= \mu_1(a(t)b - b(t)b)y^2 \\
&\geq \mu_1 b(a_o - b_o)y^2 \\
&\geq 0
\end{aligned}$$

and

$$b(t)b\mu_1\left[y + \frac{h(x,0)}{b}\right]^2 \geq 0.$$

Thus,

$$V_1 \geq \nu_o m(1 - \frac{\mu_1}{b}c)x^2 + (a - \mu_1^{-1} - \mu_2)y^2 + \mu_1[z + \mu_1^{-1}y]^2.$$

Similarly, V_2 after re-arrangement gives;

$$\begin{aligned}
V_2 &= \mu_2(b-\mu_2)x^2 + \left[2ab(t)\int_0^x h(\xi,0)d\xi - \frac{1}{b}h^2(x,0)\right] \\
&+ bb(t)\left[y + \frac{h(x,0)}{b}\right]^2 + \left[2a(t)\int_0^y \phi(x,\sigma)d\sigma - bb(t)y^2\right] \\
&+ a\left[2\int_0^y \sigma\psi(t,x,\sigma)d\sigma - ay^2\right] + [\mu_2 x + ay + z]^2 \\
&+ 2\lambda_1\int_{-r(t)}^0\int_{t+s}^t y^2(\theta)d\theta ds + 2\lambda_2\int_{-r(t)}^0\int_{t+s}^t z^2(\theta)d\theta ds,
\end{aligned}$$

where

$$2ab(t)\int_0^x h(\xi,0)d\xi - \frac{1}{b}h^2(x,0)$$

$$\begin{aligned}
&= b(t)\left[2\int_0^x (a - \frac{1}{b}h_\xi(\xi,0))h_\xi(\xi,0)\right]\frac{h(\xi,0)}{\xi}\xi d\xi \\
&= 2b(t)(a - \frac{1}{b}.c)\frac{h(x,0)}{x}\int_0^x \xi d\xi - \frac{1}{b}h^2(0,0) \\
&\geq b_o m(a - \frac{c}{b})x^2 \\
&\geq \nu_o m(a - \frac{c}{b})x^2.
\end{aligned}$$

Using (iii) of Theorem 1, we have that

$$2a(t)\int_0^y \phi(x,\sigma)d\sigma - bb(t)y^2$$

$$
\begin{aligned}
&= 2a(t)\frac{\phi(x,\sigma)}{y}\int_0^y \sigma d\sigma - bb(t)y^2 \\
&\geq b(a_o - b_o)y^2 \\
&\geq 0
\end{aligned}
$$

and by (i) of Theorem 1,

$$a\left[2\int_0^y \sigma\psi(t,x,\sigma)d\sigma - ay^2\right] \geq 0.$$

Thus,

$$
\begin{aligned}
V_2 &\geq \left[\mu_2(b-\mu_2) + b_o m(a - \frac{c}{b})\right]x^2 + b(a_o - b_o)y^2 \\
&+ (\mu_2 x + ay + z)^2.
\end{aligned}
$$

Combining the results, we have

$$2V = V_1 + V_2,$$

that is,

$$
\begin{aligned}
V &\geq \left\{\nu_o m(1 - \frac{\mu_1 c}{b}) + \mu_2(b-\mu_2) + \nu_o m(a - \frac{c}{b})\right\}x^2 \\
&+ \left\{(a - \frac{1}{\mu_1} - \mu_2) + \mu_1 b(\nu_o - \nu_o) + b(\nu_o - \nu_o)\right\}y^2 \\
&+ \mu_1(z + \mu_1^{-1}y)^2 + (\mu_2 x + ay + z)^2
\end{aligned}
$$

and integrals $2\lambda_1 \int_{-r(t)}^0 \int_{t+s}^t y^2(\theta)d\theta ds$ and $2\lambda_2 \int_{-r(t)}^0 \int_{t+s}^t z^2(\theta)d\theta ds$ are non-negative.
$1 - \frac{\mu_1 c}{b}$, $b - \mu_2$, $ab - c$, $a - \frac{1}{\mu_1} - \mu_2$, $a_o - b_o$ are either positive or zero, then there exist a positive constant δ_4 such that

$$V \geq \delta_4(x^2 + y^2 + z^2) \ \ for\ all\ x, y, z \ \ and \ \ t \geq 0. \tag{9}$$

To prove the right side of inequality (8), the hypothesis (i)-(iv) of Theorem 1 and using inequality

$$2|x||y| \leq x^2 + y^2$$

yields for

$$V \leq \delta_5(x^2 + y^2 + z^2). \tag{10}$$

From (9) and (10), (8) of Lemma 3 is established, where

$$\delta_4 = min\left\{\nu_o m(1 - \frac{\mu_1 c}{b}); (b - \mu_2); \nu_o m(a - \frac{c}{b}); (a - \frac{1}{\mu_1} - \mu_2)\right\}$$

and

$$\begin{aligned}\delta_5 &= max\Big\{(\nu_o c+\mu_2 b+a\nu_o c+a\mu_2+\mu_2);(a_1+\nu_o\mu_1 b+\nu_o\mu_1 c+1-\mu_2)+(aa_1+\nu_o b+\nu_o b_1\\ &+ a\mu_2+a+\nu_o c);(1+a+\mu_2)+(1+a+\mu_2)\Big\}.\end{aligned}$$

Now, differentiating (7) along the system (2), we have

$$\dot{V}=-W_1+W_2+W_3,$$

where

$$\begin{aligned}W_1 = &- (a+1)y\int_0^y \sigma\psi_x(t,x,\sigma)d\sigma-(\mu_1+1)a(t)y\int_0^y \phi_x(x,\sigma)d\sigma\\ &- (\mu_1+1)b(t)y^2h_x(x,0)+(a+1)a(t)y\phi(x,y)+(a+1)b(t)y^2h_y(x,\theta_1 y)\\ &+ [\psi(t,x,y)-a]z^2+[\mu_1\psi(t,x,y)-1]z^2-a\mu_2y^2\\ &+ \mu_2[a(t)\frac{\phi(x,y)}{y}-b]xy+\mu_2[\psi(t,x,y)-a]xz\\ &+ az^2+b(t)\mu_2x^2\frac{h(x,y)}{x}+ab(t)h_z(x,\theta_2 y)yz\\ &+ b(t)\mu_1z^2h_z(x,\theta_2 y)+b(t)\mu_1h_y(x,\theta_1 y)yz.\end{aligned}$$

By the conditions of Theorem 1 and the fact that

$$\mu_2[a(t)\frac{\phi(x,y)}{y}-b]xy$$

$$\begin{aligned}&= \frac{1}{4}\mu_2b_om\Big\{x+2b_o^{-1}m^{-1}\Big(\frac{a(t)\phi(x,y)}{y}-b\Big)y\Big\}^2\\ &+ \frac{1}{4}\mu_2b_omx^2+\frac{\mu_2}{b_om}\Big(\frac{a(t)\phi(x,y)}{y}-b\Big)^2y^2.\end{aligned}$$

and

$$\mu_2[\psi(t,x,y)-a]xz$$

$$\begin{aligned}&= \frac{1}{4}\mu_2b_om\Big\{x+2b_o^{-1}m^{-1}(\psi(t,x,y)-a)z\Big\}^2\\ &+ \frac{1}{4}\mu_2b_omx^2+\frac{\mu_2}{b_om}(\psi(t,x,y)-a)^2z^2.\end{aligned}$$

It follows that

$$\begin{aligned}W_1 &= \frac{1}{2}b_om\mu_2x^2+\Big[aa_ob-b_oc-\mu_2(a+b_o^{-1}m\big(\frac{a(t)\phi(x,y)}{y}-b\big)^2)\Big]y^2\\ &+ (a_ob-\mu_1b_oc)y^2+\Big[\mu_1a-1-\mu_2b_o^{-1}m^{-1}\big(\psi(t,x,y)-a\big)^2\Big]z^2\\ &+ az^2+\frac{1}{4}\mu_2b_om\Big[x+2b_o^{-1}m^{-1}\big(\frac{a(t)\phi(x,y)}{y}-b\big)y\Big]^2\\ &+ \frac{1}{4}\mu_2b_om\Big[x+2b_o^{-1}m^{-1}\big(\psi(t,x,y)-a\big)z\Big]^2.\end{aligned}$$

If μ_2 satisfy (5) and the last two addends are certainly negative,
it follows that

$$W_1 = \frac{1}{2}b_o m\mu_2 x^2 + (a_o b - \mu_1 b_o c)y^2 + az^2.$$

Since $a_o \geq b_o \geq c_o \geq \nu_o > 0$, we have that

$$W_1 = \frac{1}{2}\nu_o m\mu_2 x^2 + \nu_o(b - \mu_1 c)y^2 + az^2.$$

$$\begin{aligned} W_2 &= (\mu_1 z + y) + (z + ay + \mu_2 x)\Big[a(t)\int_{t-r(t)}^{t} \phi_x'(x(s), y(s))y(s)ds + a(t)\int_{t-r(t)}^{t} \phi_y'(x(s), y(s))z(s)ds \\ &+ b(t)\int_{t-r(t)}^{t} h_x'(x(s), y(s))y(s)ds + b(t)\int_{t-r(t)}^{t} h_y'(x(s), y(s))z(s)ds\Big] \\ &+ \lambda_1 r(t)y^2 + \lambda_2 r(t)z^2 - \lambda_1(1 - r'(t))\int_{t-r(t)}^{t} y^2(s)ds - \lambda_2(1 - r'(t))\int_{t-r(t)}^{t} z^2(s)ds. \end{aligned}$$

Following the argument used in [9], we can easily verify the following for W_2 after choosing

$$\lambda_1 = \frac{\nu_o L_1(\mu_1 + \mu_2 + a + 2) + \nu_o M_1(\mu_1 + \mu_2 + a + 2)}{4(1 - \beta)} > 0,$$

$$\lambda_2 = \frac{\nu_o L_2(\mu_1 + \mu_2 + a + 2) + \nu_o M_2(\mu_1 + \mu_2 + a + 2)}{4(1 - \beta)} > 0$$

and using $r(t)$ and $r'(t)$ yields

$$\begin{aligned} W_2 &\leq \frac{1}{2}\gamma\nu_o\Big\{\mu_2(L_1 + L_2) + \mu_2(M_1 + M_2)\Big\}x^2 \\ &+ \frac{1}{2}\gamma\nu_o\Big\{(1 + a)(L_1 + L_2) + (1 + a)(M_1 + M_2) + \frac{\nu_o L_1(\mu_1 + \mu_2 + a + 2) + \nu_o M_1(\mu_1 + \mu_2 + a + 2)}{2(1 - \beta)}\Big\}y^2 \\ &+ \frac{1}{2}\gamma\nu_o\Big\{(\mu_1 + 1)(L_1 + L_2) + (\mu_1 + 1)(M_1 + M_2) + \frac{\nu_o L_2(\mu_1 + \mu_2 + a + 2) + \nu_o M_2(\mu_1 + \mu_2 + a + 2)}{2(1 - \beta)}\Big\}z^2. \end{aligned}$$

And By (ii) and (vi) of Theorem 1,

$$\begin{aligned} W_3 &= (a + 1)b'(t)\int_0^x h(\xi, 0)d\xi + (\mu_1 + 1)a'(t)\int_0^y \phi(x, \sigma)d\sigma \\ &+ (\mu_1 +)b'(t)yh(x, 0) + (a + 1)y\int_0^y \sigma\psi_t(t, x, \sigma)d\sigma \\ &\leq 0. \end{aligned}$$

Thus, combining the estimates W_1, W_2 and W_3 for $\dot{V}$, we have

$$\begin{aligned}\dot{V} &\leq -\frac{1}{2}\nu_o\Big\{m\mu_2 - \gamma[\mu_2(L_1+L_2)+\mu_2(M_1+M_2)]\Big\}x^2 \\ &- \frac{1}{2}\nu_o\Big\{(b-\mu_1 c) - \gamma[(1+a)(L_1+L_2)+(1+a)(M_1+M_2) \\ &+ \frac{\nu_o L_1(\mu_1+\mu_2+a+2)+\nu_o M_1(\mu_1+\mu_2+a+2)]}{2(1-\beta)}\Big\}y^2 \\ &- \frac{1}{2}\Big\{a - \gamma\nu_o[(\mu_1+1)(L_1+L_2)+(\mu_1+1)(M_1+M_2) \\ &+ \frac{\nu_o L_2(\mu_1+\mu_2+a+2)+\nu_o M_2(\mu_1+\mu_2+a+2)]}{2(1-\beta)}\Big\}z^2.\end{aligned}$$

If γ satisfy (6), we get

$$\dot{V}(x_t, y_t, z_t) \leq -\delta_6(x^2+y^2+z^2), \tag{11}$$

for some $\delta_6 > 0$.

Proof of Theorem 1

It is obvious that the largest invariant set in Z is $Q = \{0\}$, where $Z = \{\varphi \in C_H : \dot{V}(t,\varphi) = 0\}$. It follows that $\dot{V}(x_t, y_t, z_t) = 0$ if and only if $x_t = y_t = z_t = 0$, $\dot{V}(\varphi) < 0$ for $\varphi \in C_H$ and for $V \geq U(|\varphi|) \geq 0$. Thus, by (8), (11) and the last statement agreed with lemmas 1 and 2 respectively. This shows that the trivial solution of (1) is uniformly asymptotically stable. Hence, the proof of Theorem 1 is complete.

Proof of Theorem 2

Let $x(t), y(t), z(t)$ be any solution of (2). By (8) and (11), it follows that $V(x_t, y_t, z_t) = 0$ iff $x^2+y^2+z^2 = 0$, $V(x_t, y_t, z_t) > 0$ iff $x^2+y^2+z^2 \neq 0$, $V(x_t, y_t, z_t) \to \infty$ iff $x^2+y^2+z^2 \to \infty$. In view of $\dot{V}_{(2)}$ at $p = 0$, according to (11), we have

$$\dot{V}_{(2)}(x_t, y_t, z_t) \leq -\delta_6(x^2+y^2+z^2).$$

For $p \neq 0$ in (1), along any solution (x_t, y_t, z_t) of (2), we obtain

$$\dot{V}_{(2)}(x_t, y_t, z_t) \leq -\delta_6(x^2+y^2+z^2) + (\mu_2|x| + (a+1)|y| + (\mu_1+1)|z|)|p(t,x,y,x(t-r(t)),y(t-r(t)),z)|$$

By condition (i) of Theorem 2, we have

$$\dot{V}_{(2)}(x_t, y_t, z_t) \leq -\delta_6(x^2+y^2+z^2) + \delta_7(|x|+|y|+|z|)[\delta_o + \delta_1(|x|+|y|+|z|)],$$

where $\delta_7 = max\{\mu_2, (a+1), (\mu_1+1)\}$.

Thus,

$$\dot{V}_{(2)}(x_t, y_t, z_t) \leq -(\delta_6 - 3\delta_1\delta_7)(x^2+y^2+z^2) + 3^{\frac{1}{2}}\delta_o\delta_7(x^2+y^2+z^2)^{\frac{1}{2}},$$

It follows that

$$\dot{V}(t) \quad \leq \quad -\delta_8(x^2+y^2+z^2)+\delta_9(x^2+y^2+z^2)^{\frac{1}{2}}, \tag{12}$$

where $\delta_8 = (\delta_6 - 3\delta_1\delta_7)$, $\delta_1 < 3^{-1}\delta_6^{-1}\delta_7^{-1}$ and $\delta_9 = 3^{\frac{1}{2}}\delta_o\delta_7$.
If we choose

$$(x^2+y^2+z^2)^{\frac{1}{2}} \geq \delta_{10} = \delta_9\delta_8^{-1}.$$

Inequality (12) implies that

$$\dot{V}(t) \quad \leq \quad -\delta_8(x^2+y^2+z^2).$$

Then, there exists a δ_{11} such that

$$\dot{V}(t) \quad \leq \quad -\delta_{11}, \ \textit{provided} \ x^2+y^2+z^2 \geq \delta_{11}\delta_8^{-1}.$$

The remainder of the proof of Theorem 2 may now be obtained by the use of the estimates (8) and (11) an obvious adaptation of the Yoshizawa type reasoning in [11].

4. Conclusions

Analysis of nonlinear non-autonomous systems with delay literarily shows that Lyapunov's theory in ultimate boundedness of solutions is rarely scarce due to the difficulty in constructing a complete Lyapunov function. The second Lyapunov's method allows us to predict the asymptotic and boundedness behavior of solutions of sufficiently complicated nonlinear physical system. The solutions of third-order non-autonomous delay differential equation (1) are asymptotically stable and uniformly ultimately bounded according to Lyapunov's theory if (4), (5) and (6) hold as $t \to \infty$.

.

References

[1] AFUWAPE, A.U. OMARI, P. AND ZANALIN, F. *Nonlinear pertubations of differential operators with nontrivial kernel and applications to third-order periodic boundary problems*, J. Math. Anal. Appl., 143, (1989) 35-36.

[2] SADEK, A.I. *On the stability of solutions of some non-autonomous delay differntial equations of third order*, Asymptotic Analysis, 43, (2005) 1-7.

[3] AFUWAPE, A.U. AND OMEIKE M.O. *On the stability and boundedness of solutions of a kind of third order delay differential equations*, Appl. Math. Comput., 200, (2008) 444-451.

[4] ADEMOLA, A.T. AND ARAMOWO, A.T. *Uniform stability and boundedness of solutions of non-linear delay differential equations of third order*, Math.J.Okayama Univ., 55, (2013) 157-166.

[5] YAO, H. AND MENG, W. *On the stability of solutions of certain non-linear third order delay differential equations*, International Journal of non-linear science, 6, (2008) 230-237.

[6] OMEIKE, M.O. *Stability and boundedness of solutions of some non-autonomous delay differential equation of the third order*, An. Stint. Univ. "AL.I. CUZA" Iasi. Mat.(N.S), 55, (2009) 49-58.

[7] TUNC, C. *Boundedness in third order nonlinear differential equations with bounded delay*, Bol.Mat., 16, (2009) 1-10.

[8] REMILI, M. AND OUDJEJI L.D. *Stability and boundedness of solutions of non-autonomous third-order differential equations with delay*, Acta Univ. Palacki. Olomuc. Fac.rer.nat., mathematica 53, (2014), 139-147.

[9] OLUTIMO, A.L. AND ADAMS D.O. *On the stability and bounddedness of solutions of certain non-autonomous delay differential equation of third order*, Applied Mathematics, 7, (2016) 457-467.

[10] CHUKWU, E.N. *On the boundedness of solutions of third order differential equations*, Ann. Mat. Pura Appl. 155, (1975) 123-149.

[11] YOSHIZAWA, T. *Stability theory by Liapunov's second method*, Math. Soc. Japan. (1966).

Akinwale Olutimo, Ph.D.: Lagos State University, Nigeria, Department of Mathematics, Badagary Expressway, Ojo, Lagos. Nigeria. (*aolutimo@yahoo.com*). The author gave a presentation of this paper during one of the conference sessions.

Nullspace method for the uniqueness analysis of reaction and driving forces in rigid multibody systems with redundant nonholonomic constraints

Marcin Pękal, Janusz Frączek, Marek Wojtyra

Abstract: Redundantly constrained mechanisms are common. When modelled as rigid multibody systems (MBS), they have—in general—non-unique reactions. However, some of the reactions may be uniquely determined. Analogous problem of indeterminacy is also present in overactuated MBS. In this paper, constraint matrix-based nullspace method for the uniqueness analysis of reactions and driving forces for nonholonomic MBS is developed and discussed. The method may be used for planar and spatial systems described by absolute or natural coordinates. The approach may be used for MBS with linear nonholonomic constraints. To illustrate the proposed approach, an exemplary planar system with knife-edge Pfaffian nonholonomic constraints and with three actuation cases—i.e. non-actuated, fully-actuated and overactuated—is considered.

1. Introduction

Rigid multibody approach is very popular in designing and simulation. Unfortunately, despite its advantages over flexible approach associated with shorter computation time, it has some limitations which occur for redundant multibody systems (MBS) and may be, in general, divided into two groups: numerical and indeterminacy problems. Redundant MBS are commonly used, e.g. due to strength reasons [31] or their ability to avoid singular positions [3]. Hence the problems cannot be ignored.

The first group of problems worsens computational efficiency or accuracy of numerical algorithms [17]. Fortunately, in sequential computations, appropriate methods for redundant systems are available (see, e.g. [14,15,22,23]). However, the redundant MBS are cumbersome in parallel computations. Hence it is very common to analyze only non-redundant systems (see, e.g. [1]) or serial systems (see, e.g. [2]).

The second group of problems concerns a global indeterminacy of reactions of redundant rigid multibody systems (see, e.g. [4, 7, 10, 11, 31, 32, 35]). This is the result of the structure of the system, hence it does not depend on the coordinates used to describe the system [7, 31, 32, 35–37]. Awareness of this phenomenon is crucial when the resulting reactions are used in simulations, e.g. in design process (e.g. for bearings selection) or when friction is considered. In such cases, the reactions are indeterminate (arbitrary), and the mentioned

analyses may lead to erroneous outcomes. Note that in the case of friction (see, e.g. [33,34]), not only the joint reactions but also the simulated motion may be non-physical (non-unique) [7]. As the paper is solely devoted to joint reactions uniqueness, friction is neglected.

For many redundant rigid MBS, despite the general non-uniqueness, some of the reactions (e.g. total joint reactions) may be unique [7, 31, 32, 35–37]. The methods allowing to check the uniqueness of the reactions are available and they are still under development. The approaches are based on the analysis of the Jacobian matrix of constraints (see, e.g. [10, 32, 35]) or kinetostatics (see, e.g. [21, 24, 26]). These methods may use one of two approaches originated from linear algebra—direct sum or nullspace method. Direct sum approach resulted in three alternative numerical methods of uniqueness checking, i.e. rank comparison method, QR method and SVD method (of course, just one of them should be used in order to check the reaction uniqueness).

The similar problem of indeterminacy may occur also for driving forces. Non-unique drives are introduced into MBS for several reasons, e.g. in order to reduce torques in joints of the system [8], to eliminate gear backlash and clearances [29] or to improve the performance of the MBS [38]. Fortunately, the uniqueness analysis of driving forces may be performed using the same methods as reaction uniqueness test. It is useful to point out that driving forces should be considered together with reactions, because they may change the uniqueness of the reactions (in the case of overactuated systems) [13].

The aim of this paper is to broaden the range of applicability of the Jacobian-based method which use nullspace approach. The method was previously studied in [13,25]. In [13] the novel nullspace formulation was proposed and applied to reaction and driving forces uniqueness analysis based on the study of Jacobian matrix of constraints (for holonomic systems only). In [25] the nullspace method was applied to reaction uniqueness analysis of linear nonholonomic systems. Note that previous papers about nullspace method allowed us to study the uniqueness of single reactions components only [5, 10]. This is not enough in many cases, e.g. unique joint reaction may have non-unique components (see, e.g. [31]). Hence, the novel nullspace formulation is used in this paper. The aim of this paper is to show that the method may be used to both reaction and driving forces uniqueness analysis of linear nonholonomic systems. The presented approach may be used for planar and spatial rigid MBS described by means of absolute or natural coordinates. This is because, for such coordinates, constraint matrix includes information about all joints, i.e. it contains the structure of the considered MBS [13]. In this paper absolute coordinates are used.

In order to illustrate the method, linear nonholonomic planar MBS is studied. The nonholonomic constraints are introduced in the form of knife-edge Pfaffian constraints. Moreover, to show that driving forces may influence reaction uniqueness, three actuation cases

are considered: non-actuated, fully-actuated and overactuated.

2. Governing equations

In this paper the absolute coordinates are used. For the systems described by such coordinates, the appropriate vector of constraints, has to be defined. Vector of holonomic constraints at the position level has, in general, the following form [9, 12]:

$$\mathbf{\Phi} = \mathbf{\Phi}(\mathbf{q}, t) = \mathbf{0}, \tag{1}$$

where $\mathbf{q}$ is a vector of absolute coordinates and t is time. Constraints contained in Eq. (1) can be divided into two groups: kinematic constraints that describe kinematic pairs ($\mathbf{\Phi}^K = \mathbf{\Phi}^K(\mathbf{q})$) and driving constraints that describe the imposed motion ($\mathbf{\Phi}^D = \mathbf{\Phi}^D(\mathbf{q}, t)$). Subsequently, Eq. (1) may be differentiated with respect to time, which gives [12]:

$$\dot{\mathbf{\Phi}} = \mathbf{\Phi}_\mathbf{q}\dot{\mathbf{q}} + \mathbf{\Phi}_t = \mathbf{0}, \tag{2}$$

where $\mathbf{\Phi}_\mathbf{q}$ is a Jacobian matrix of holonomic constraints.

Eqs. (1) and (2) determine only holonomic constraints. For linear nonholonomic constraints the equation of kinematic constraints is formulated at the velocity level as [37]:

$$\mathbf{\Psi}^K\dot{\mathbf{q}} = \mathbf{0}, \tag{3}$$

where $\mathbf{\Psi}^K$ is a constraint matrix of linear nonholonomic constraints.

There may exist nonholonomic driving constraints, which can be written as:

$$\mathbf{\Psi}^D\dot{\mathbf{q}} - \mathbf{f}(t) = \mathbf{0}, \tag{4}$$

where $\mathbf{f}(t)$ is a function determining the imposed motion of the system.

At the velocity level holonomic and nonholonomic constraints may be combined as:

$$\left[(\mathbf{\Phi}^K_\mathbf{q})^T \quad (\mathbf{\Psi}^K)^T \quad (\mathbf{\Psi}^D)^T \quad (\mathbf{\Phi}^D_\mathbf{q})^T\right]^T\dot{\mathbf{q}} = \mathbf{J}^T\dot{\mathbf{q}} = \left[\mathbf{0} \quad \mathbf{0} \quad (\mathbf{f}(t))^T \quad -(\mathbf{\Phi}_t)^T\right]^T, \tag{5}$$

where coefficient matrix is called a constraint matrix. Transposition of this matrix (denoted by $\mathbf{J}$) may be used to perform the uniqueness test. We assume the ordering of constraints according to Eq. (5). Naturally, the order of the coordinates may be arbitrary. Moreover, some of the elements of matrix $\mathbf{J}$ may be empty (depending on the considered case).

The usage of matrix $\mathbf{J}$ for constraint reactions analysis can be explained when equations of motion are considered. Lagrange equations of the first kind may be written as [20]:

$$\mathbf{M}\ddot{\mathbf{q}} - \mathbf{J}\lambda = \mathbf{Q}, \tag{6}$$

where $\mathbf{M}$ is a matrix with inertia terms, λ is a Lagrange multipliers vector, $\mathbf{Q}$ is a vector containing the other generalized forces and velocity dependent inertial components. Note that $\mathbf{J}\lambda$ contains generalized reactions (i.e. reaction and driving forces). Hence, the reaction and driving forces uniqueness may be studied by using transposed constraint matrix $\mathbf{J}$.

3. Nullspace method

Calculation of matrix $\mathbf{J}_{n\times m}$ (of rank r), defined by Eq. (5), allows us to perform the uniqueness test. In the case of nullspace method, the following steps have to be followed. First, the nullspace matrix $\mathbf{N}_{m\times(m-r)}$ of matrix $\mathbf{J}$ has to be calculated. This matrix fulfills the following equation [28]:

$$\mathbf{JN} = \mathbf{0}. \tag{7}$$

Note that in the case of existence of redundant constraints, matrix $\mathbf{J}$ is rank-deficient thus matrix $\mathbf{N}$ is non-empty. Hence, generalized reactions $\mathbf{J}\lambda = \mathbf{W}$ may be expressed as [27, 28]:

$$\mathbf{W} = \mathbf{J}\boldsymbol{\lambda} = \mathbf{J}(\boldsymbol{\lambda}_p + \boldsymbol{\lambda}_n) = \underbrace{\mathbf{J}\boldsymbol{\lambda}_p}_{\mathbf{W}} + \underbrace{\mathbf{J}\boldsymbol{\lambda}_n}_{\mathbf{0}}, \tag{8}$$

where $\boldsymbol{\lambda}_p$ is a particular solution and $\boldsymbol{\lambda}_n$ is a nullspace solution of reactions. Vector $\boldsymbol{\lambda}_n$ may be written in the form of a linear combination (see Eq. (7)) [27, 28]:

$$\boldsymbol{\lambda}_n = \mathbf{Nc}, \tag{9}$$

where $\mathbf{c}_{(m-r)\times 1}$ is a vector of arbitrary coefficients.

The next step is to select a studied element (denoted by U). It may be, e.g. total joint reaction or driving force. Generalized reaction $\mathbf{W}$ may be decomposed into the sum [32, 37]:

$$\mathbf{W} = \mathbf{W}_U + \mathbf{W}_V, \tag{10}$$

where $\mathbf{W}_U$ is a vector of generalized reaction of the element U and $\mathbf{W}_V$ contains the remaining reactions. This decomposition may be unique or not. If it is unique, then $\mathbf{W}_U$ and $\mathbf{W}_V$ are both unique. We will check when $\mathbf{W}_U$ is unique. Let the element U be described by $w \leq m$ columns of matrix $\mathbf{J}$ with indices $u = \{u_1, \ldots, u_w\}$. Using Eq. (8) yields:

$$\begin{aligned}\mathbf{W}_U = \mathbf{J}_{u_1}\lambda_{u_1} + \cdots + \mathbf{J}_{u_w}\lambda_{u_w} = \mathbf{J}_{u_1}(\lambda_{p_{u_1}} + \lambda_{n_{u_1}}) + \cdots + \mathbf{J}_{u_w}(\lambda_{p_{u_w}} + \lambda_{n_{u_w}}) = \\ = (\mathbf{J}_{u_1}\lambda_{p_{u_1}} + \cdots + \mathbf{J}_{u_w}\lambda_{p_{u_w}}) + (\mathbf{J}_{u_1}\lambda_{n_{u_1}} + \cdots + \mathbf{J}_{u_w}\lambda_{n_{u_w}}),\end{aligned} \tag{11}$$

where $\mathbf{J}_u$ is a column of matrix $\mathbf{J}$ of number u and λ_u is the u-th element of vector $\boldsymbol{\lambda}$.

Using Eq. (9), the following formula is obtained:

$$\begin{aligned}\mathbf{W}_U = \mathbf{J}_{u_1}\lambda_{p_{u_1}} + \cdots + \mathbf{J}_{u_w}\lambda_{p_{u_w}} + \mathbf{J}_{u_1}(c_1 n_{u_1 1} + \cdots + c_{(m-r)} n_{u_1(m-r)}) + \cdots + \\ + \mathbf{J}_{u_w}(c_1 n_{u_w 1} + \cdots + c_{(m-r)} n_{u_w(m-r)}) = \mathbf{J}_{u_1}\lambda_{p_{u_1}} + \cdots + \mathbf{J}_{u_w}\lambda_{p_{u_w}} + \\ + c_1\underbrace{(\mathbf{J}_{u_1} n_{u_1 1} + \cdots + \mathbf{J}_{u_w} n_{u_w 1})}_{\mathbf{a}_1} + \cdots + c_{(m-r)}\underbrace{(\mathbf{J}_{u_1} n_{u_1(m-r)} + \cdots + \mathbf{J}_{u_w} n_{u_w(m-r)})}_{\mathbf{a}_{(m-r)}},\end{aligned} \tag{12}$$

where c_i is the i-th element of vector $\mathbf{c}$ and n_{ij} is an element which represents the element at the i-th row and j-th column of matrix $\mathbf{N}$. Note that terms $c_i\mathbf{a}_i$ are responsible for non-uniqueness of $\mathbf{W}_U$ (because all c_i are arbitrary). Hence, the reaction corresponding to the studied element U is unique when all elements $\mathbf{a}_i$ are zero. This occurs when:

$$[\mathbf{J}_{u_1} \ \ldots \ \mathbf{J}_{u_w}]\begin{bmatrix} n_{u_1 1} & n_{u_1 2} & \ldots & n_{u_1(m-r)} \\ & \vdots & & \\ n_{u_w 1} & n_{u_w 2} & \ldots & n_{u_w(m-r)} \end{bmatrix} = [\mathbf{J}_{u_1} \ \ldots \ \mathbf{J}_{u_w}]\begin{bmatrix} \mathbf{n}_{u_1} \\ \vdots \\ \mathbf{n}_{u_w} \end{bmatrix} = \mathbf{0}, \tag{13}$$

where $\mathbf{n}_i$ is the i-th row of matrix $\mathbf{N}$. This equation may be converted into the form:

$$\mathbf{J}_U\mathbf{N}_U = \mathbf{0}, \tag{14}$$

where $\mathbf{J}_U$ is created from the columns of matrix $\mathbf{J}$, which describe the studied element U, and $\mathbf{N}_U$ is built (analogously to $\mathbf{J}_U$) from the rows of matrix $\mathbf{N}$. This formula is a uniqueness condition—generalized reaction of the element U is unique when Eq. (14) is fulfilled.

4. Example

In order to present the method, a planar MBS with nonholonomic constraints is considered. The system is presented in Fig. 1. This is a four-wheel mobile platform with multi-link steering mechanism; its concept was inspired by 4RRR Parallel-Kinematics Machine proposed in [30] (and considered in [16,18,19]). The system is described by absolute coordinates $\mathbf{q}_{30\times 1} = \left[\mathbf{q}_1^T \ \mathbf{q}_2^T \ \ldots \ \mathbf{q}_{10}^T\right]^T$, where $\mathbf{q}_i = [x_i \quad y_i \quad \varphi_i]^T$ is a vector of coordinates of body i. The system has 10 rigid bodies connected by 12 revolute joints (denoted by: Br, Cr, Dr, Fr, Gr, Hr, Jr, Kr, Lr, Nr, Pr and Qr) and 1 doubled revolute joint Ar created from 2 revolute joints $Ar1$ and $Ar2$. Doubled revolute joint is shown in details in the right-hand side of Fig. 1. The nonholonomic constraints are introduced by 4 wheels (Ew, Iw, Mw, Rw) modelled, for simplicity, in the form of knife-edge constraints. The system has 2 degrees of freedom (DoFs). The main dimension of the system is $h = 0.25\ m$ (see Fig. 1). Three actuation cases are considered: non-actuated, fully-actuated and overactuated mechanism. The uniqueness analyses are performed in non-singular position of the system, and the joint friction is neglected. Note that in the next subsections all the actuation cases are described first, and the obtained results are shown in the last subsection of the example, i.e. Sec. 4.4.

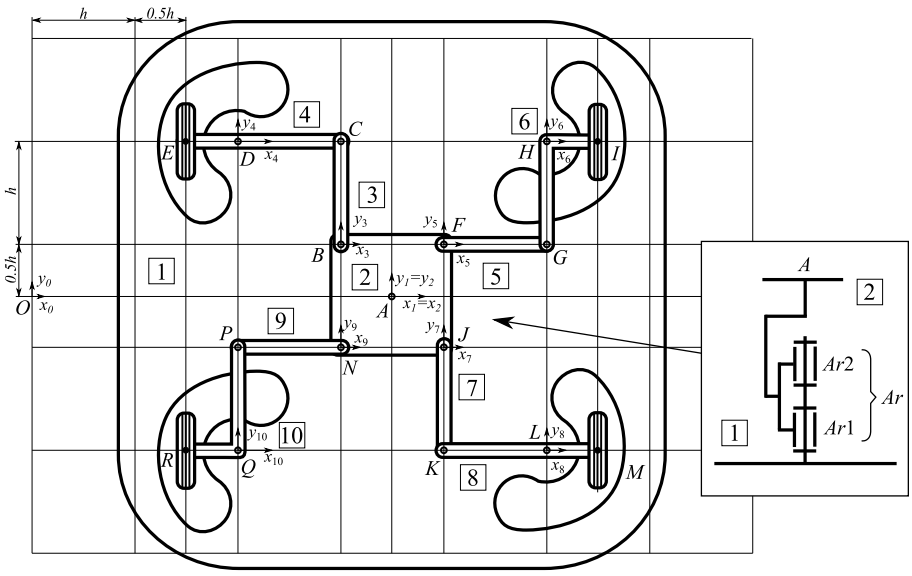

Figure 1. Nonholonomic mechanism

4.1. Non-actuated case

In the non-actuated case only matrix $\mathbf{\Psi}^K$ of linear nonholonomic constraints and Jacobian matrix $\mathbf{\Phi}^K_{\mathbf{q}}$ have to be specified. Linear nonholonomic constraints in the form of knife-edge Pfaffian constraints are introduced. For one knife-edge constraint describing the wheel Xw, the perpendicularity condition of the pair velocity and its edge is formulated (in global reference frame 0) as [37]:

$$(\mathbf{n}^0_X)^T\mathbf{v}^0_X=(\mathbf{R}_i\mathbf{n}^i_X)^T(\dot{\mathbf{p}}_i+\mathbf{\Omega}\mathbf{R}_i\mathbf{r}^i_X\varphi_i)=\begin{bmatrix}(\mathbf{R}_i\mathbf{n}^i_X)^T & (\mathbf{n}^i_X)^T\mathbf{\Omega}\mathbf{r}^i_X\end{bmatrix}\begin{bmatrix}\dot{\mathbf{p}}_i\\ \varphi_i\end{bmatrix}=\mathbf{b}_{Xi}\dot{\mathbf{q}}_i=\mathbf{0}, \quad (15)$$

where $\mathbf{v}^0_X$ is a velocity vector, $\mathbf{n}^k_X$ is a vector perpendicular to the allowed direction of motion of the wheel Xw resolved in reference frame k, $\dot{\mathbf{p}}_i$ is a time derivative of $\mathbf{p}_i=[x_i \quad y_i]^T$ which determines the position of body i, $\mathbf{r}^i_X$ is a vector from the reference frame of i-th body to joint Xr. This vector is resolved in local reference frame of body i. $\mathbf{R}_i=\begin{bmatrix}cos(\varphi_i) & -sin(\varphi_i)\\ sin(\varphi_i) & cos(\varphi_i)\end{bmatrix}$ is a rotation matrix and $\mathbf{\Omega}=\begin{bmatrix}0 & -1\\ 1 & 0\end{bmatrix}$ is an auxiliary matrix [6].

Therefore, matrix $\mathbf{\Psi}^K_{4\times30}$ (of rank $r_{\mathbf{\Psi}^K}=4$) has the following form (the wheels are described in the following order: Ew, Iw, Mw, Rw):

$$\mathbf{\Psi}^K=\begin{bmatrix}\mathbf{0}_{1\times9} & \mathbf{b}_{E4} & \mathbf{0}_{1\times3} & \mathbf{0}_{1\times3} & \mathbf{0}_{1\times3} & \mathbf{0}_{1\times3} & \mathbf{0}_{1\times3} & \mathbf{0}_{1\times3}\\ \mathbf{0}_{1\times9} & \mathbf{0}_{1\times3} & \mathbf{0}_{1\times3} & \mathbf{b}_{I6} & \mathbf{0}_{1\times3} & \mathbf{0}_{1\times3} & \mathbf{0}_{1\times3} & \mathbf{0}_{1\times3}\\ \mathbf{0}_{1\times9} & \mathbf{0}_{1\times3} & \mathbf{0}_{1\times3} & \mathbf{0}_{1\times3} & \mathbf{0}_{1\times3} & \mathbf{b}_{M8} & \mathbf{0}_{1\times3} & \mathbf{0}_{1\times3}\\ \mathbf{0}_{1\times9} & \mathbf{0}_{1\times3} & \mathbf{0}_{1\times3} & \mathbf{0}_{1\times3} & \mathbf{0}_{1\times3} & \mathbf{0}_{1\times3} & \mathbf{0}_{1\times3} & \mathbf{b}_{R10}\end{bmatrix}, \quad (16)$$

where $\mathbf{0}_{i\times j}$ is an $i \times j$ zero matrix.

To formulate $\mathbf{\Phi}^K_{\mathbf{q}}$, the vector of kinematic constraints $\mathbf{\Phi}^K$ (see Eq. (1)) has to be formed. This vector contains only constraints of revolute joints. Note that the constraints of an exemplary revolute joint Xr, built of bodies a and b, has the form:

$$\mathbf{\Phi}^{K(Xr)} \equiv \left[\mathbf{p}_a + \mathbf{R}_a\mathbf{r}^a_X - (\mathbf{p}_b + \mathbf{R}_b\mathbf{r}^b_X)\right] = \mathbf{0}. \tag{17}$$

It is assumed that constraints of revolute joints in vector $\mathbf{\Phi}^K$ are placed in the following order: Ar (built of $Ar1$ and $Ar2$), Br, Cr, Dr, Fr, Gr, Hr, Jr, Kr, Lr, Nr, Pr and Qr.

To obtain Jacobian matrix, vector $\mathbf{\Phi}^K_{28\times 1}$ is differentiated with respect to coordinates, yielding matrix $\mathbf{\Phi}^K_{\mathbf{q}\ 28\times 30}$ of rank $r_{\mathbf{\Phi}^K_{\mathbf{q}}} = 26$. This matrix has the following form:

$$\mathbf{\Phi}^K_{\mathbf{q}} = \begin{bmatrix}
\mathbf{a}_{A1} & -\mathbf{a}_{A2} & \mathbf{0}_{2\times3} & \mathbf{0}_{2\times3} & \mathbf{0}_{2\times3} & \mathbf{0}_{2\times3} & \mathbf{0}_{2\times3} & \mathbf{0}_{2\times3} & \mathbf{0}_{2\times3} & \mathbf{0}_{2\times3} \\
\mathbf{a}_{A1} & -\mathbf{a}_{A2} & \mathbf{0}_{2\times3} & \mathbf{0}_{2\times3} & \mathbf{0}_{2\times3} & \mathbf{0}_{2\times3} & \mathbf{0}_{2\times3} & \mathbf{0}_{2\times3} & \mathbf{0}_{2\times3} & \mathbf{0}_{2\times3} \\
\mathbf{0}_{2\times3} & \mathbf{a}_{B2} & -\mathbf{a}_{B3} & \mathbf{0}_{2\times3} & \mathbf{0}_{2\times3} & \mathbf{0}_{2\times3} & \mathbf{0}_{2\times3} & \mathbf{0}_{2\times3} & \mathbf{0}_{2\times3} & \mathbf{0}_{2\times3} \\
\mathbf{0}_{2\times3} & \mathbf{0}_{2\times3} & \mathbf{a}_{C3} & -\mathbf{a}_{C4} & \mathbf{0}_{2\times3} & \mathbf{0}_{2\times3} & \mathbf{0}_{2\times3} & \mathbf{0}_{2\times3} & \mathbf{0}_{2\times3} & \mathbf{0}_{2\times3} \\
\mathbf{a}_{D1} & \mathbf{0}_{2\times3} & \mathbf{0}_{2\times3} & -\mathbf{a}_{D4} & \mathbf{0}_{2\times3} & \mathbf{0}_{2\times3} & \mathbf{0}_{2\times3} & \mathbf{0}_{2\times3} & \mathbf{0}_{2\times3} & \mathbf{0}_{2\times3} \\
\mathbf{0}_{2\times3} & \mathbf{a}_{F2} & \mathbf{0}_{2\times3} & \mathbf{0}_{2\times3} & -\mathbf{a}_{F5} & \mathbf{0}_{2\times3} & \mathbf{0}_{2\times3} & \mathbf{0}_{2\times3} & \mathbf{0}_{2\times3} & \mathbf{0}_{2\times3} \\
\mathbf{0}_{2\times3} & \mathbf{0}_{2\times3} & \mathbf{0}_{2\times3} & \mathbf{0}_{2\times3} & \mathbf{a}_{G5} & -\mathbf{a}_{G6} & \mathbf{0}_{2\times3} & \mathbf{0}_{2\times3} & \mathbf{0}_{2\times3} & \mathbf{0}_{2\times3} \\
\mathbf{a}_{H1} & \mathbf{0}_{2\times3} & \mathbf{0}_{2\times3} & \mathbf{0}_{2\times3} & \mathbf{0}_{2\times3} & -\mathbf{a}_{H6} & \mathbf{0}_{2\times3} & \mathbf{0}_{2\times3} & \mathbf{0}_{2\times3} & \mathbf{0}_{2\times3} \\
\mathbf{0}_{2\times3} & \mathbf{a}_{J2} & \mathbf{0}_{2\times3} & \mathbf{0}_{2\times3} & \mathbf{0}_{2\times3} & \mathbf{0}_{2\times3} & -\mathbf{a}_{J7} & \mathbf{0}_{2\times3} & \mathbf{0}_{2\times3} & \mathbf{0}_{2\times3} \\
\mathbf{0}_{2\times3} & \mathbf{0}_{2\times3} & \mathbf{0}_{2\times3} & \mathbf{0}_{2\times3} & \mathbf{0}_{2\times3} & \mathbf{0}_{2\times3} & \mathbf{a}_{K7} & -\mathbf{a}_{K8} & \mathbf{0}_{2\times3} & \mathbf{0}_{2\times3} \\
\mathbf{a}_{L1} & \mathbf{0}_{2\times3} & \mathbf{0}_{2\times3} & \mathbf{0}_{2\times3} & \mathbf{0}_{2\times3} & \mathbf{0}_{2\times3} & \mathbf{0}_{2\times3} & -\mathbf{a}_{L8} & \mathbf{0}_{2\times3} & \mathbf{0}_{2\times3} \\
\mathbf{0}_{2\times3} & \mathbf{a}_{N2} & \mathbf{0}_{2\times3} & \mathbf{0}_{2\times3} & \mathbf{0}_{2\times3} & \mathbf{0}_{2\times3} & \mathbf{0}_{2\times3} & \mathbf{0}_{2\times3} & -\mathbf{a}_{N9} & \mathbf{0}_{2\times3} \\
\mathbf{0}_{2\times3} & \mathbf{0}_{2\times3} & \mathbf{0}_{2\times3} & \mathbf{0}_{2\times3} & \mathbf{0}_{2\times3} & \mathbf{0}_{2\times3} & \mathbf{0}_{2\times3} & \mathbf{0}_{2\times3} & \mathbf{a}_{P9} & -\mathbf{a}_{P10} \\
\mathbf{a}_{Q1} & \mathbf{0}_{2\times3} & \mathbf{0}_{2\times3} & \mathbf{0}_{2\times3} & \mathbf{0}_{2\times3} & \mathbf{0}_{2\times3} & \mathbf{0}_{2\times3} & \mathbf{0}_{2\times3} & \mathbf{0}_{2\times3} & -\mathbf{a}_{Q10}
\end{bmatrix}, \tag{18}$$

where $\mathbf{a}_{Xi} = \begin{bmatrix}\mathbf{I}_{2\times2} & \mathbf{\Omega}\mathbf{R}_i\mathbf{r}^i_X\end{bmatrix}_{2\times3}$ and $\mathbf{I}_{i\times j}$ is an identity matrix of dimensions $i \times j$.

In this case, transposed constraint matrix $\mathbf{J}_{30\times32} = \begin{bmatrix}(\mathbf{\Phi}^K_{\mathbf{q}})^T & (\mathbf{\Psi}^K)^T\end{bmatrix}$ and it has rank $r_{\mathbf{J}} = 28$. Subsequently, its nullspace matrix $\mathbf{N}_{32\times4}$ may be computed as:

$$\mathbf{N} = \begin{bmatrix}\mathbf{N}_{1\,(4\times4)} & \mathbf{0}_{4\times4} & \mathbf{N}_{2\,(4\times1)} & \mathbf{0}_{4\times5} & \mathbf{N}_{3\,(4\times1)} & \mathbf{0}_{4\times5} & \mathbf{N}_{4\,(4\times1)} & \mathbf{0}_{4\times5} & \mathbf{N}_{5\,(4\times1)} & \mathbf{0}_{4\times1} & \mathbf{N}_{6\,(4\times4)}\end{bmatrix}^T, \tag{19}$$

where submatrices $\mathbf{N}_i$ contain nonzero elements. The exact values of these elements are not presented here, because they depend on the algorithm applied for calculation of matrix $\mathbf{N}$.

Now, the uniqueness analysis of reactions may be performed using the algorithm described in Sec. 3. The results of the procedure are shown in Sec. 4.4.

4.2. Fully-actuated case

The considered system has 2 DoFs. Hence, to make it fully-actuated, two independent drives have to be introduced. In this case, joints Ew and $Ar1$ are actuated. Driving constraint for the wheel represented by a knife-edge constraint has the form:

$$\left[(\mathbf{R}_4\mathbf{m}^4_E)^T \quad (\mathbf{m}^4_E)^T\mathbf{\Omega}\mathbf{r}^4_E\right]\dot{\mathbf{q}}_4 = \mathbf{d}_{E4}\dot{\mathbf{q}}_4 = f(t), \tag{20}$$

where $\mathbf{m}_E^4$ is a vector parallel to the allowed direction of motion of the wheel Ew resolved in reference frame 4 and $f(t)$ a time function of the driving constraint.

Hence, matrix $\mathbf{\Psi}^D_{1\times 30}$ (of rank $r_{\mathbf{\Psi}^D} = 1$) may be written as:

$$\mathbf{\Psi}^D = \begin{bmatrix} \mathbf{0}_{1\times 9} & \mathbf{d}_{E4} & \mathbf{0}_{1\times 18} \end{bmatrix}. \tag{21}$$

For joint $Ar1$, vector of driving constraints $\mathbf{\Phi}^{DF}$ (where F means fully-actuated case) has the following form (note that it is scalar in this case):

$$\mathbf{\Phi}^{DF} = \mathbf{\Phi}^{D(Ar1)} \equiv \varphi_1 - \varphi_2 - \theta_{21}(t) = 0, \tag{22}$$

where $\theta_{21}(t)$ is a time function of the driving constraint. This vector, after differentiation with respect to coordinates, results in Jacobian matrix of driving constraints $\mathbf{\Phi}^{DF}_{\mathbf{q}(1\times 30)}$ of rank $r_{\mathbf{\Phi}^{DF}_{\mathbf{q}}} = 1$, which may be written as:

$$\mathbf{\Phi}^{DF}_{\mathbf{q}} = [\mathbf{0}_{1\times 2} \quad 1 \quad \mathbf{0}_{1\times 2} \quad -1 \quad \mathbf{0}_{1\times 24}]. \tag{23}$$

Note that scalar functions $f(t)$ and $\theta_{21}(t)$ do not depend on the vector of coordinates $\mathbf{q}$. Hence, they are not present in constraint matrix used in the uniqueness test and, therefore, they are not specified.

Moreover, the structure of the system is the same as in non-actuated case (matrices $\mathbf{\Phi}^K_{\mathbf{q}}$ and $\mathbf{\Psi}^K$ remains unchanged). Subsequently, transposed constraint matrix may be computed. In this case, $\mathbf{J}_{30\times 34}$ is a matrix of rank $r_{\mathbf{J}} = 30$ and has the general form as in Eq. (5). For this matrix, nullspace matrix $\mathbf{N}_{34\times 4}$ may be computed as:

$$\mathbf{N} = \begin{bmatrix} \mathbf{N}_{1\,(4\times 4)} & \mathbf{0}_{4\times 4} & \mathbf{N}_{2\,(4\times 1)} & \mathbf{0}_{4\times 5} & \mathbf{N}_{3\,(4\times 1)} & \mathbf{0}_{4\times 5} & \mathbf{N}_{4\,(4\times 1)} & \mathbf{0}_{4\times 5} & \mathbf{N}_{5\,(4\times 1)} & \mathbf{0}_{4\times 1} & \mathbf{N}_{6\,(4\times 4)} & \mathbf{0}_{4\times 2} \end{bmatrix}^T. \tag{24}$$

After this steps, the uniqueness of reaction and driving forces may be checked. The results of the procedure are presented in Sec. 4.4.

4.3. Overactuated case

In this case joints: Ew, $Ar1$ and Br are driven. Hence, two of three driving constraints are the same as in the previous case (see Eqs. (21) and (22)). Driving constraint of joint Br is analogous to the driving constraint of $Ar1$ (see Eq. (22)): $\mathbf{\Phi}^{(DBr)} \equiv \varphi_2 - \varphi_3 - \theta_{32}(t) = 0$. Hence, the row of Jacobian matrix ($\mathbf{\Phi}^{D(Br)}_{\mathbf{q}(1\times 30)}$) corresponding to $\mathbf{\Phi}^{(DBr)}$ may be written as:

$$\mathbf{\Phi}^{D(Br)}_{\mathbf{q}} = [\mathbf{0}_{1\times 5} \quad 1 \quad \mathbf{0}_{1\times 2} \quad -1 \quad \mathbf{0}_{1\times 21}]. \tag{25}$$

The total Jacobian matrix of driving constraints $\mathbf{\Phi}^{DO}_{\mathbf{q}(2\times 30)}$ (O means overactuated case) of rank $r_{\mathbf{\Phi}^{DO}_{\mathbf{q}}} = 2$ has the form:

$$\mathbf{\Phi}^{DO}_{\mathbf{q}} = \begin{bmatrix} (\mathbf{\Phi}^{DF}_{\mathbf{q}})^T & (\mathbf{\Phi}^{D(Br)}_{\mathbf{q}})^T \end{bmatrix}^T = \begin{bmatrix} (\mathbf{\Phi}^{D(Ar1)}_{\mathbf{q}})^T & (\mathbf{\Phi}^{D(Br)}_{\mathbf{q}})^T \end{bmatrix}^T. \tag{26}$$

Matrices $\mathbf{\Phi}_{\mathbf{q}}^{K}$, $\mathbf{\Psi}^{K}$ and $\mathbf{\Psi}^{D}$ are the same (as previously). Hence, matrix $\mathbf{J}_{30\times 35}$ of rank $r_{\mathbf{J}} = 30$ has the form of Eq. (5). Subsequently, matrix $\mathbf{N}_{35\times 5}$ may be written as:

$$\mathbf{N}=\left[\mathbf{N}_{1(5\times 5)}\mathbf{0}_{5\times 1}\mathbf{N}_{2(5\times 1)}\mathbf{0}_{5\times 1}\mathbf{N}_{3(5\times 1)}\mathbf{0}_{5\times 5}\mathbf{N}_{4(5\times 1)}\mathbf{0}_{5\times 5}\mathbf{N}_{5(5\times 1)}\mathbf{0}_{5\times 5}\mathbf{N}_{6(5\times 1)}\mathbf{0}_{5\times 1}\mathbf{N}_{7(5\times 4)}\mathbf{0}_{5\times 1}\mathbf{N}_{8(5\times 2)}\right]^{T}. \quad (27)$$

The uniqueness test may be performed now. Its results are discussed in Sec. 4.4.

4.4. Results

The results of reaction uniqueness are the same in the non-actuated and fully-actuated cases. Reactions in joints: Ar, Br, Cr, Fr, Gr, Jr, Kr, Nr and Pr are unique. The remaining reactions are non-unique. Result for double joint Ar, confirm the fact that unique reaction may have non-unique components (in this example $Ar1$ and $Ar2$). Reactions in the wheels are non-unique, which is consistent with intuition. Moreover, reactions in wheels' pivots, i.e. joints Dr, Hr, Lr and Qr, are non-unique. In fully-actuated case, both drives are unique.

In overactuated case, the reaction uniqueness test gives different results. In this case, drives in $Ar1$ and Br are non-unique. Moreover, overactuation introduced by drive in joint Br causes that unique double joint Ar became indeterminable, and all reactions in chain $B - C - D - E$ are non-unique. It is worth pointing out that different overactuation cases may not change uniqueness of the reactions or may influence other reactions.

5. Conclusions

The paper presents nullspace method for reactions and driving forces uniqueness analysis which may be used to MBS with linear nonholonomic constraints. In this paper knife-edge Pfaffian constraints are studied. The method can be used to planar and spatial systems described by absolute or natural coordinates. This paper shows that overactuation may affect the reaction uniqueness. Hence, the reaction and driving uniqueness should be performed together, especially for redundantly actuated systems.

Acknowledgments

This work was supported by the Faculty of Power and Aeronautical Engineering Dean's Grant 2017.

References

[1] Chadaj, K., Malczyk, P., and Frączek, J. A parallel Hamiltonian formulation for forward dynamics of closed-loop multibody systems. *Multibody Syst. Dyn. 39*, 1-2 (2017), 51–77.

[2] Chadaj, K., Malczyk, P., and Frączek, J. A Parallel Recursive Hamiltonian

Algorithm for Forward Dynamics of Serial Kinematic Chains. *IEEE T. Robot. 33*, 3 (2017), 647–660.

[3] Chiaverini, S., Oriolo, G., and Walker, I. D. Kinematically Redundant Manipulators. In *Springer Handbook of Robotics*, B. Siciliano and O. Khatib, Eds. Springer-Verlag Berlin Heidelberg, 2008.

[4] Featherstone, R. *Rigid Body Dynamics Algorithms*. Springer US, 2008.

[5] Featherstone, R., and Orin, D. E. Dynamics. In *Springer Handbook of Robotics*, B. Siciliano and O. Khatib, Eds. Springer-Verlag Berlin Heidelberg, 2008.

[6] Frączek, J., and Wojtyra, M. *Kinematyka układów wieloczłonowych. Metody obliczeniowe*. Wydawnictwa Naukowo-Techniczne, Warszawa, 2008.

[7] Frączek, J., and Wojtyra, M. On the unique solvability of a direct dynamics problem for mechanisms with redundant constraints and Coulomb friction in joints. *Mech. Mach. Theory 46*, 3 (2011), 312–334.

[8] Ganovski, L., Fisette, P., and Samin, J. C. Piecewise Overactuation of Parallel Mechanisms Following Singular Trajectories: Modeling, Simulation and Control. *Multibody Syst. Dyn. 12*, 4 (2004), 317–343.

[9] García de Jalón, J., and Bayo, E. *Kinematic and Dynamic Simulation of Multibody Systems, The Real-Time Challenge*. Springer-Verlag, New-York, 1994.

[10] García de Jalón, J., and Gutiérrez-López, M. D. Multibody dynamics with redundant constraints and singular mass matrix: existence, uniqueness, and determination of solutions for accelerations and constraint forces. *Multibody Syst. Dyn. 30*, 3 (2013), 311–341.

[11] González, F., and Kövecses, J. Use of penalty formulations in dynamic simulation and analysis of redundantly constrained multibody systems. *Multibody Syst. Dyn. 29*, 1 (2013), 57–76.

[12] Haug, E. J. *Computer aided kinematics and dynamics of mechanical systems, Volume I: Basic methods*. Allyn and Bacon, 1989.

[13] Marcin Pękal, Frączek, J., and Wojtyra, M. Nullspace Method for the Analysis of Uniqueness of Reactions and Driving Forces in Redundantly Constrained Multibody Systems. In *8^{th} ECCOMAS Thematic Conference on MULTIBODY DYNAMICS* (Prague, June 19–22 2017).

[14] Mariti, L., Belfiore, N. P., Pennestrì, E., and Valentini, P. P. Comparison of solution strategies for multibody dynamics equations. *Int. J. Numer. Meth. Eng. 88*, 7 (2011), 637–656.

[15] Mariti, L., Pennestrì, E., Valentini, P. P., and Belfiore, N. P. Review and Comparison of Solution Strategies for Multibody Dynamics Equations. In *The 1st Joint International Conference on Multibody System Dynamics* (Lappeenranta, Finland, May 25–27 2010).

[16] Müller, A. Consequences of Geometric Imperfections for the Control of Redundantly Actuated Parallel Manipulators. *IEEE T. Robot. 26*, 1 (2010), 21–31.

[17] Müller, A. Implementation of A Geometric Constraint Regularization For Multibody System Models. *Archive of Mechanical Engineering 61*, 2 (2014), 367–383.

[18] Müller, A., and Alalem, H. Goal-Oriented Resolution of the Actuator Redundancy in Parallel Manipulators. In *The 8th IEEE Africon Conference (Africon 2007)* (Windhoek, Namibia, September 26–28 2007), pp. 1–7.

[19] Müller, A., and Maisser, P. Generation and application of prestress in redundantly full-actuated parallel manipulators. *Multibody Syst. Dyn. 18*, 2 (2007), 259–275.

[20] Nikravesh, P. E. *Computer-Aided Analysis of Mechanical Systems.* Prentice Hall, 1988.

[21] Pękal, M., and Frączek, J. Badanie jednoznaczności reakcji i napędów w robotyce metodą kinetostatyki. In *Postępy robotyki. Tom 1*, K. Tchoń and C. Zieliński, Eds., Prace Naukowe Politechniki Warszawskiej. Elektronika. z. 195. Oficyna Wydawnicza Politechniki Warszawskiej, Warszawa, 2016. In *14. Krajowa Konferencja Robotyki* (Polanica Zdrój, September 14-18 2016).

[22] Pękal, M., and Frączek, J. Comparison of natural complement formulations for multibody dynamics. *Journal Theor. App. Mech.-Pol. 54*, 4 (2016), 1391–1404.

[23] Pękal, M., and Frączek, J. Comparison of selected formulations for multibody system dynamics with redundant constraints. *Archive of Mechanical Engineering 63*, 1 (2016), 93–112.

[24] Pękal, M., and Frączek, J. A Kinetostatics-Based Study of Uniqueness of Reactions and Drives in Robotics. *Journal of Automation, Mobile Robotics and Intelligent Systems 11*, 2 (2017), 21–30.

[25] Pękal, M., and Frączek, J. Nullspace Method for the Reaction Forces Uniqueness Analysis in Rigid Multibody Systems with Redundant Nonholonomic Constraints. In *International Interdisciplinary PhD Workshop 2017* (Łódź, September 9–11 2017).

[26] Pękal, M., Frączek, J., and Tomulik, P. Solvability of reactions and inverse dynamics problem for complex kinematic chains. In *The 21st International Conference on Methods and Models in Automation and Robotics* (Międzyzdroje, August 29–September 1 2016).

[27] Strang, G. *Introduction to Linear Algebra, Fourth Edition.* Wellesley-Cambridge Press, 2009.

[28] Strang, G., and Borre, K. *Linear Algebra, Geodesy, and GPS*. Wellesley-Cambridge Press, 1997.

[29] Tsai, L.-W. *Robot Analysis: The Mechanics of Serial and Parallel Manipulators*. Wiley-Interscience, 1999.

[30] Valášek, M., Bauma, V., Šika, Z., and Vampola, T. Redundantly actuated parallel structures-principle, examples, advantages. In *3rd Parallel Kinematics Seminar Chemnitz* (2002), pp. 993–1009.

[31] Wojtyra, M. Joint Reaction Forces in Multibody Systems with Redundant Constraints. *Multibody Syst. Dyn. 14*, 1 (2005), 23–46.

[32] Wojtyra, M. Joint reactions in rigid body mechanisms with dependent constraints. *Mech. Mach. Theory 44*, 12 (2009), 2265–2278.

[33] Wojtyra, M. On Some Problems With Modeling of Coulomb Friction in Self-Locking Mechanisms. *J Comput. Nonlin. Dyn. 11*, 1 (2016), 011008 (10 pages).

[34] Wojtyra, M. Modeling of static friction in closed-loop kinematic chainsUniqueness and parametric sensitivity problems. *Multibody Syst. Dyn. 39*, 4 (2017), 337–361.

[35] Wojtyra, M., and Frączek, J. Joint reactions in rigid or flexible body mechanisms with redundant constraints. *Bull. Pol. Ac.: Tech. 60*, 3 (2012), 617–626.

[36] Wojtyra, M., and Frączek, J. Comparison of Selected Methods of Handling Redundant Constraints in Multibody Systems Simulations. *J. Comput. Nonlin. Dyn. 8*, 2 (2013), 021007 (1–9).

[37] Wojtyra, M., and Frączek, J. Solvability of reactions in rigid multibody systems with redundant nonholonomic constraints. *Multibody Syst. Dyn. 30*, 2 (2013), 153–171.

[38] Wu, J., Wang, J., Li, T., and Wang, L. Performance Analysis and Application of a Redundantly Actuated Parallel Manipulator for Milling. *J. Intell. Robot. Syst. 50*, 2 (2007), 163–180.

Marcin Pękal, M.Sc. (Ph.D. student): Institute of Aeronautics and Applied Mechanics, Warsaw University of Technology, Nowowiejska 24, 00-665 Warsaw (*mpekal@meil.pw.edu.pl*). The author gave a presentation of this paper during one of the conference sessions.

Janusz Frączek, Professor: Institute of Aeronautics and Applied Mechanics, Warsaw University of Technology, Nowowiejska 24, 00-665 Warsaw (*jfraczek@meil.pw.edu.pl*).

Marek Wojtyra, Associate Professor: Institute of Aeronautics and Applied Mechanics, Warsaw University of Technology, Nowowiejska 24, 00-665 Warsaw (*mwojtyra@meil.pw.edu.pl*).

Enhancing the stability of the boost converter using the saltation matrix

Arnold Pérez, Guillermo Muñoz, Fabiola Angulo

Abstract: It is well known that using current mode control, the boost power converter requires a compensation ramp when the voltage gain is greater than twice the input voltage. However, as the slope of the compensation ramp increases overcompensation occurs, and the system response is slower when changes are applied, mainly if the converter feeds light loads. In this work, a new method to tune the parameters of the compensator in a peak-current mode-controlled converter is derived using information of the saltation matrix, particularly its induced norm. At the beginning, the tuning parameters obtained from a classical method are considered, including the slope of the compensation ramp, and after, analyzing the norm of the saltation matrix we obtain a new set of parameters which provides a very wide range to guarantee stability of the period-1 orbit. The method is validated by mean of numerical and analytical solutions.

1. Introduction

Power converters are devices intended to receive an energy signal and convert or adapt it according to the required applications. Among converter types, we can find DC-DC, AC-DC (Rectifiers), DC-AC (Inverters) and AC-AC (Transformers) converters [14]. With the advancement of electronics it has been possible to improve these devices to the point that quality and efficiency of energy delivered by the converters has become a topic widely researched [10, 16]. Even more, given the importance that renewable energy sources have, power converters play a key role to adapt these sources to the electrical grid [7,11,15]. Boost converters allow to step up the input voltage twice [12]. This converter can be used in different applications such as Fuel Cells [13] and Photovoltaic sources [4]. Boost converter is a very simple and used topology, it has been studied with different controllers, as peak current mode control which uses two different loops: an outer voltage loop and an inner current loop [3].

The peak current control [9] is the control mode used in this paper; its main disadvantage is that the period-1 orbit loses the stability when the voltage gain is greather than two [2]. This problem can be solved adding an adequate compensation ramp. However, to increase the range of stability the solpe compensation must be widened causing overcompensation

and affecting the proper performance of the converter [17]. For this reason other methods must be explored.

Peak current mode control has a mathematical expression to compute the slope compensantion in a boost converter [5, 9]. In [6], a new method to found the parameters of the controller based on Filippovs theory [1] is explored and the boundaries of stability by mean of Floquet exponents were found. The disadavantage of this method is the computational cost because it is necessary to recalculate the compensation until the eigenvalues are inside the unit circle. In this paper, we propose to use the information of the saltation matrix, in particular the induced norm, and modify it such that the stability of the whole system enhances. To achieve that, the induced norm of the commutation surface is modified computing a new set of parameters for the outer and inner control loops.

The main contribution of this paper is the application of the concept of the induced norm of a matrix with the aim of widenning the range of stability. The rest of the paper is organized as follows, in Section 2, the boost power converter is presented and analyzed. In Section 3, the satbility of the period-1 orbit is analyzed using the monodromy matrix. In Section 4, the method to tune the control parameters is presented and, finally, in Section 5, results and conclusions are shown.

2. Boost power converter

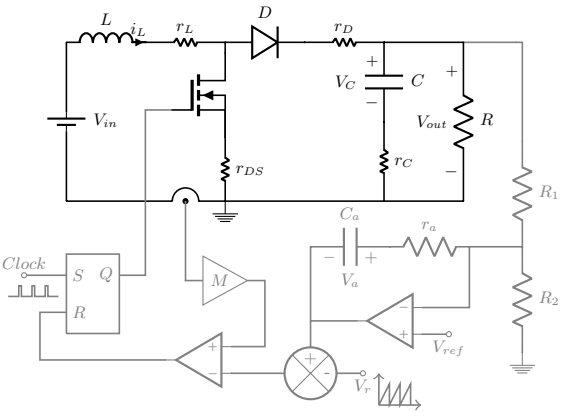

Figure 1. Peak current mode control

The boost power converter analyzed in this paper is presented in figure **1**. In the circuit

diagram, V_{in} is the input voltage and V_{ref} is a scaled reference voltage (or scaled desired output voltage). L is the inductor, C is the capacitor, and R is the load resistance. D and S resemble the diode and the MOSFET. r_L, r_s, r_D and r_C are the internal resistances of the inductor, MOSFET, diode and capacitor, respectively. R_1 and R_2 are the voltage divider. r_a and C_a with the operational amplifier conform the PI controller. A compensation ramp is added to the output of PI controller to obtain i_{ref}. Finally, the inductor current multiplied by M that is compared with i_{ref} and the flip-flop is handled by this signal, and it controls the MOSFET.

The converter is peak current mode controlled as in [9]. This controller includes current and voltage control loops. The current loop senses the current flowing through the inductor and multiplies it by a gain factor M, and the voltage one uses the output voltage V_{out} and the PI controller to provide a current reference i_{ref}.

The system has three state variables which are $X(t) = \begin{bmatrix} i_L & V_c & V_a \end{bmatrix}^T$ where i_L is the inductor current, V_C is the voltage in capacitor C and V_a is the voltage in capacitor C_a. the system can operate in three topologies depending on the switch and diode positions. In a compact form, the dynamical equations are written as:

$$\dot{X} = \begin{cases} A_1 X(t) + B_1 V_{in} & S = 1, \ D = 0 \\ A_2 X(t) + B_2 V_{in} & S = 0, \ D = 1 \\ A_3 X(t) + B_3 V_{in} & S = 0, \ D = 0 \end{cases} \tag{1}$$

The matrices A_1, A_2 and A_3 as well as vectors $B_1 = B_2$ and B_3 are defined as follows:

$$A_1 = \begin{bmatrix} -\frac{r_L + r_S}{L} & 0 & 0 \\ 0 & -\frac{1}{T_m(1+k_C)} & 0 \\ 0 & \frac{g}{T_a(1+k_C)} & 0 \end{bmatrix}, \qquad B_1 = \begin{bmatrix} \frac{V_{in}}{L} \\ 0 \\ -\frac{gk_D V_{ref}}{T_a V_{in}} \end{bmatrix} \tag{2}$$

$$A_2 = \begin{bmatrix} -\frac{r_L + r_D}{L} - \frac{r_C}{L(1+k_C)} & -\frac{1}{L(1+k_C)} & 0 \\ \frac{1}{C(1+k_C)} & -\frac{1}{T_m(1+k_C)} & 0 \\ \frac{g r_C}{T_a(1+k_C)} & \frac{g}{T_a(1+k_C)} & 0 \end{bmatrix}, \quad B_2 = \begin{bmatrix} \frac{V_{in}}{L} \\ 0 \\ -\frac{gk_D V_{ref}}{T_a V_{in}} \end{bmatrix} \tag{3}$$

$$A_3 = \begin{bmatrix} 0 & 0 & 0 \\ 0 & -\frac{1}{T_m(1+k_C)} & 0 \\ 0 & \frac{g}{T_a(1+k_C)} & 0 \end{bmatrix}, \qquad B_3 = \begin{bmatrix} 0 \\ 0 \\ -\frac{gk_D V_{ref}}{T_a V_{in}} \end{bmatrix} \tag{4}$$

With $g = r_a/R_1$, $T_m = RC$, $T_a = r_aC_a$ $k_c = r_c/R$, $k_D = (R_1 + R_2)/R_2$. The output of the voltage loop is V_k, which is given by:

$$\mathrm{V}_k(t) = V_{ref}(1 + gk_D) - \left(\tfrac{g}{1+k_C}\right) V_C(t) - V_a(t)$$

Where V_{ref} is the reference voltage. With the voltage V_k and the compensation ramp V_r, the reference current i_{ref} is generated as:

$$i_{ref} = \mathrm{V}_k(t) - V_r$$
$$V_r = m_a \bmod \left(\tfrac{t}{T}\right)$$

Where m_a is the slope of the compensation ramp. The current loop provides a current i_M which is defined as Mi_L, where M is a constant gain factor. i_M and i_{ref} are compared to obtain the control signal that drives the flip-flop. The PWM signal and the value of current i_L define the topology in which the system is at every moment. The value of the parameters are $L = 165\mu$H, $C = 150\mu$F, $r_L = 0.04\Omega$, $r_C = 0.03\Omega$, $r_D = 0.01\Omega$, $r_S = 0.055\Omega$, $T = 60\mu$s, $V_{ref} = 2.5$V, $R_1 = 47k\Omega$, $R_2 = 6.8k\Omega$, $r_a = 4.7k\Omega$, $C_a = 2000$nF, $M = 0.3$, $m_a = 0.445$.

Figure 2 shows a bifurcation diagram when the input voltage V_{in} varies. There, it can be observed the dynamical behavior of the inductor current i_L. When $V_{in} < 5.84V$ the period-1 orbit is unstable and for $V_{in} \in (5.84V\ 10V)$ is stable.

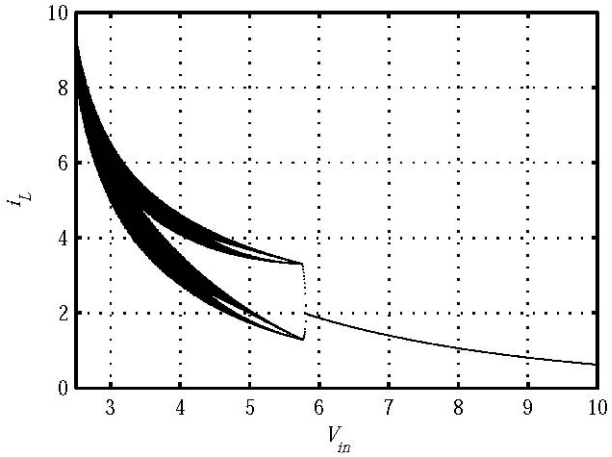

Figure 2. i_L (A) vs V_{in} (V)

3. Stability analysis of the period-1 orbit

The boost power converter can be analyzed as a piece-wise linear system (PWL). This means that the system changes between two linear systems when some events occur. One of the most important mathematical tools to analyze the stability of periodic orbits in PWL is the monodromy matrix. A complete explanation about the construction of the monodromy matrix can be found in [8]. Figure 3 shows schematically the evolution of the system in one period T. The system starts in $t = 0$ and evolves in the subspace V_- according to to flux ϕ_1. When the event occurs at $t = t_p$ the system changes the topology and evolves with flux ϕ_2 in the subspace V_+ until $t = T$. At this moment the topology changes again and the cycle is repeated. The condition to topology changes is given in a general form as $h(x(t)) = 0$ and it is represented as the hipersurface Σ. The name of the vector fields before and after the commutation are f_- and f_+, respectively.

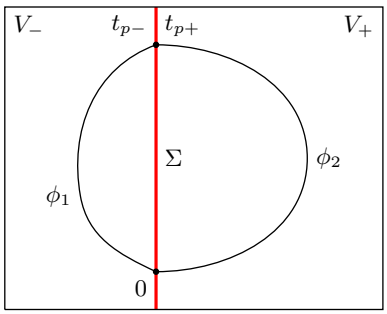

Figure 3. Periodic orbit with switching surface

The monodromy matrix M_m is the solution matrix of the system in a full clock cycle and it contains the evolution of the systems using the fluxes and the saltation matrix S. The monodromy matrix is given by

$$M_m\left(T, x_0, 0\right) = \phi_2\, S\, \phi_1 \tag{5}$$

and S can be expressed as [8]:

$$S = I + \frac{\left(f_+(x(t_p), t_p) - f_-(x(t_p), t_p)\right) n^T}{n^T f_-(x(t_p), t_p) + \frac{\partial h(x(t_p), t_p)}{\partial t}} \tag{6}$$

where I is the identity matrix and n is the normal vector to the switching surface. With the monodromy matrix and the Floquet theory it is possible to study the stability of periodic orbits in a PWL, such as the boost converter [6]. Applying this technique to the boost power converter, we find the same limit value of stability as the one already reported in the literature and equally found in the previous section.

Figure 4 shows the largest absolute value (MVP) of the eigenvalues of the monodromy matrix for the boost converter as V_{in} varies. It can be seen that the point where the MVP is greather than one agrees with the result presented in figure 2.

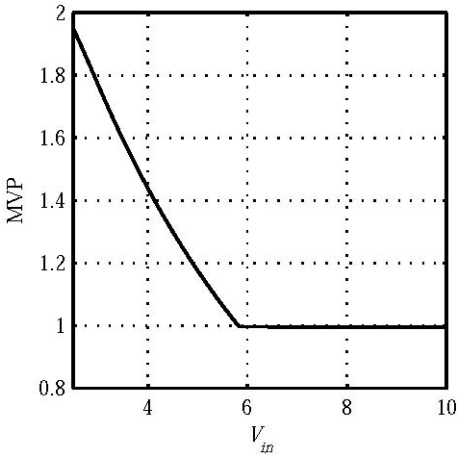

Figure 4. Maximum modulus of the eigenvalues (MVP) vs V_{in} (V)

4. A new method to enhance the stability of the period-1 orbit

We propose to change the norm of the saltation matrix to widen the range of stability of the period-1 orbit. In particular, retuning the parameters of the controller based on their original values (parameters of current and voltage loops). For a boost converter the switching function $h(x(t))$ is given by:

$$h\left(x(t)\right) = k_0 - Mi_L - \tfrac{g}{1+k_c}V_c - V_a - m_a\, mod\left(\tfrac{t}{T}\right)$$

Note that $h(x(t))$ affects the saltation matrix with its time derivative and its normal vector n. The normal vector n is obtained as follow

$$n = \left[\frac{\partial h}{\partial i_L} \;\; \frac{\partial h}{\partial V_C} \;\; \frac{\partial h}{\partial V_a}\right]^T = \left[-M \;\; -\frac{g}{1+k_c} \;\; -1\right]^T \tag{7}$$

Then we proposed to add a general term depending on the states such that the new normal vector n is given by:

$$n = \left[-M+\alpha \;\; -\frac{g}{1+k_c}+\beta \;\; -1+\gamma\right]^T \tag{8}$$

The constants α, β and γ must be tuning using information of the matrix norm. Recall that the matrix norm-2 is defined as $||M||_2 = \sqrt{\rho(M^T M)}$, where $\rho(M^T M)$ is the spectral radius of the $M^T M$ matrix, i.e. the maximum eigenvalue. The norm of the monodromy matrix for the boost converter as V_{in} varies is depicted in Figure 5(a). Close to the point where the system loses the stability the value of the monodromy matrix norm is 7.3 approximately. On the other hand, it can be seen that the value of the norm of the saltation matrix is very close to the the monodromy matrix one (fig. 5(b)), the difference between them is no greater than 0.08. Even more, as the proposed compensation only affects the normal vector of the switching surface, we will study the relation between the norm of this vector ($||n||$) and the saltation matrix one ($||S||$).

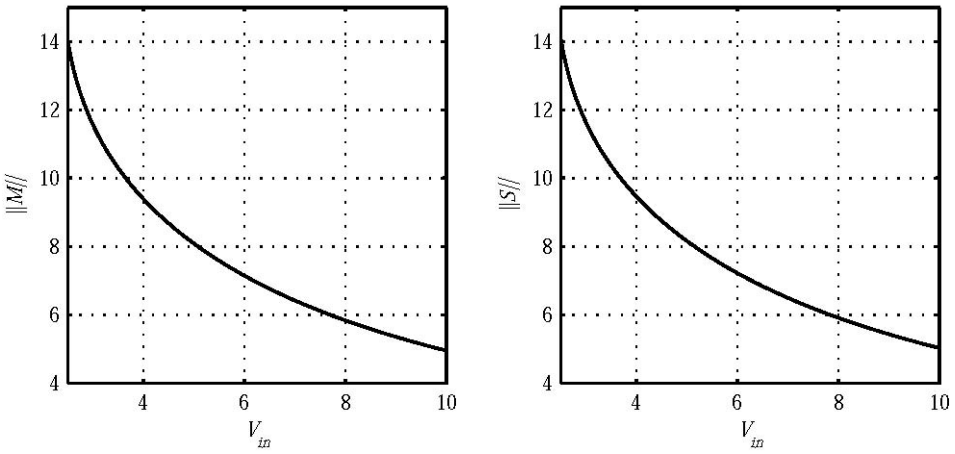

(a) $\|M\|$ vs V_{in} (V). (b) $\|S\|$ vs V_{in} (V).

Figure 5. Induced norm of monodromy matrix and saltation matrix.

The norm of the normal vector n in terms of the parameters of the paper is 1.0041, and the saltation matrix norm close to the value where the sytem loses the stability is 7.3. Note that the norm of normal vector does not depend on the input voltage V_{in}. At the follows, we decide to stabilize the period-1 orbit starting at least from $V_{in} = 3$V; for doing that we note that the norm of the saltation matrix is 12 approximately and propose to use an optimization algoritm such that the norm of the normal vector given by:

$$\|n\| = \left((-M + \alpha)^2 + \left(\frac{-g}{1 + k_c} + \beta \right)^2 + (-1 + \gamma)^2 \right)^{1/2}$$

is equal to 1.0041/2. $M = 0.3$ and $g/(1 + k_c) = 0.099$. The **sqp** minimization method

was implemented using the **fmincon** function provided by Matlab and we obtained $\alpha = 0.1570,\ \beta = 0.0523,\ \gamma = 0.5233$.

5. Results and conclusions

The proposed method to tuning the controller parameters for widennig the range of stability of the period-1 orbit is obtained, as can be seen in Figure 6. Figure 6(a) shows the evolution of the maximum absolut value of the eigenvalues of the monodromy matrix, and figure 6(b) displays the bifurcation diagram using V_{in} as bifurcation parameter. Note that the period-1 orbit is stable for a full range of input voltage V_{in} without increasing the slope compensation.

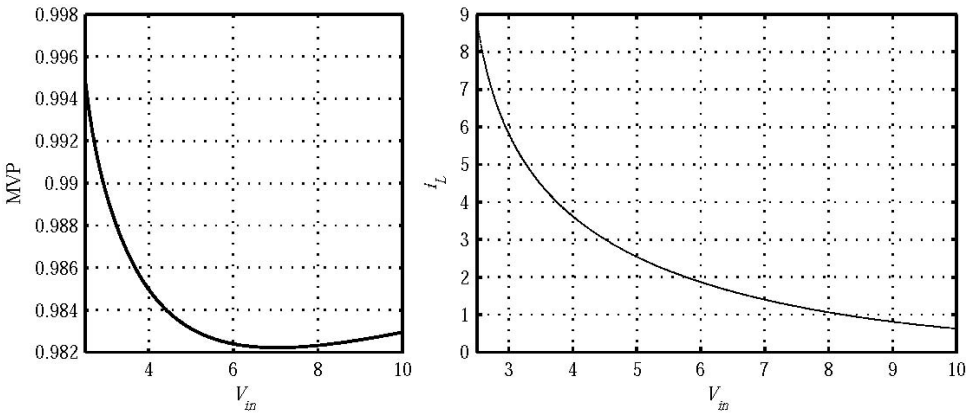

(a) MVP vs V_{in} (V)

(b) i_L (A) vs V_{in} (V)

Figure 6.

Control techniques starting from the study of the saltation matrix S have emerged in the last times. We apply this approach to develop a new strategy for widening the stability of the period-1 orbit, without changing the firstly defined compensation ramp value.

Converters need to be robust so that they are able to remain stable, even when variations in external parameters such as input voltage and load resistance are present. To achieve this, an adequate control technique considering those scenarios must be applied. The method proposed in this paper guarantees good behavior in both cases.

Acknowledgments

This work was supported by Universidad Nacional de Colombia, Manizales, Projects 27950 from Vicerrectoría de Investigación, DIMA, COLCIENCIAS under Contract FP44842-052-2016, COLCIENCIAS program Doctorados Nacionales 6172-2013, and COLCIENCIAS young researchers program.

References

[1] *Differential Equations with Discontinuous Righthand Sides*. American Mathematical Society Translations, 1978.

[2] Ahmed, K. Z., Bari, S. M. K., Hafiz, M., and Islam, D. Design and implementation of semi-quadratic slope compensation circuit for pwm peak current mode boost regulator. In *Electrical and Computer Engineering, 2008. ICECE 2008. International Conference on* (2008), IEEE, pp. 512–515.

[3] Amir, S., van der Zee, R., and Nauta, B. An improved modeling and analysis technique for peak current-mode control-based boost converters. *IEEE Transactions on Power Electronics 30*, 9 (Sept 2015), 5309–5317.

[4] Chen, S. M., Wang, C. Y., and Liang, T. J. A novel sinusoidal boost-flyback ccm/dcm dc-dc converter. In *2014 IEEE Applied Power Electronics Conference and Exposition - APEC 2014* (March 2014), pp. 3512–3516.

[5] Erickson, R. W., and Maksimovic, D. *Fundamentals of Power Electronics*. Springer, 2001.

[6] Giaouris, D., Maity, S., Banerjee, S., Pickert, V., and Zahawi, B. Application of filippov method for the analysis of subharmonic instability in dcdc converters. *International Journal of Circuit Theory and Applications 37*, 8 (2009).

[7] Hua, C., and Shen, C. Study of maximum power tracking techniques and control of dc/dc converters for photovoltaic power system. In *Power Electronics Specialists Conference, 1998. PESC 98 Record. 29th Annual IEEE* (1998), vol. 1, IEEE, pp. 86–93.

[8] Leine, R., Van Campen, D., and Van de Vrande, B. Bifurcations in nonlinear discontinuous systems. *Nonlinear dynamics 23*, 2 (2000), 105–164.

[9] Li, Y., Vannorsdel, K. R., Zirger, A. J., Norris, M., and Maksimovic, D. Current mode control for boost converters with constant power loads. *Circuits and Systems I: Regular Papers, IEEE Transactions on 59*, 1 (2012), 198–206.

[10] Singh, B., Singh, B. N., Chandra, A., Al-Haddad, K., Pandey, A., and Kothari, D. P. A review of three-phase improved power quality ac-dc converters. *Industrial Electronics, IEEE Transactions on 51*, 3 (2004), 641–660.

[11] Song, S.-H., Kang, S.-i., and Hahm, N.-K. Implementation and control of grid connected ac-dc-ac power converter for variable speed wind energy conversion system. In *Applied Power Electronics Conference and Exposition, 2003. APEC'03. Eighteenth Annual IEEE* (2003), vol. 1, IEEE, pp. 154–158.

[12] Tseng, K., and Liang, T. Novel high-efficiency step-up converter. *Electric Power Applications, IEE Proceedings - 151*, 2 (Mar 2004), 182–190.

[13] Tseng, K. C., Lin, J. T., and Cheng, C. A. An integrated derived boost-flyback converter for fuel cell hybrid electric vehicles. In *2013 1st International Future Energy Electronics Conference (IFEEC)* (Nov 2013), pp. 283–287.

[14] Undeland, T. M., Robbins, W. P., and Mohan, N. Power electronics: converters, applications, and design, 2003.

[15] Walker, G. R., and Sernia, P. C. Cascaded dc-dc converter connection of photovoltaic modules. *Power Electronics, IEEE Transactions on 19*, 4 (2004), 1130–1139.

[16] Wu, G., Ruan, X., and Ye, Z. Nonisolated high step-up dc–dc converters adopting switched-capacitor cell. *Industrial Electronics, IEEE Transactions on 62*, 1 (2015), 383–393.

[17] Yang, C.-C., Wang, C.-Y., and Kuo, T.-H. Current-mode converters with adjustable-slope compensating ramp. In *Circuits and Systems, 2006. APCCAS 2006. IEEE Asia Pacific Conference on* (2006), IEEE, pp. 654–657.

Arnold Pérez, M.Sc. student: Universidad Nacional de Colombia Sede Manizales, Facultad de Ingeniería y Arquitectura, Departamento de Ingeniería Eléctrica, Electrónica y Computación, Campus La Nubia, 170003 Manizales, Colombia (*aperezco@unal.edu.co*).

Guillermo Muñoz, M.Sc. (Ph.D. student): Universidad Nacional de Colombia Sede Manizales, Facultad de Ingeniería y Arquitectura, Departamento de Ingeniería Eléctrica, Electrónica y Computación, Campus La Nubia, 170003 Manizales, Colombia (*jgmunozc@unal.edu.co*).

Fabiola Angulo, Ph.D.: Universidad Nacional de Colombia Sede Manizales, Facultad de Ingeniería y Arquitectura, Departamento de Ingeniería Eléctrica, Electrónica y Computación, Campus La Nubia, 170003 Manizales, Colombia (*fangulog@unal.edu.co*). The author gave a presentation of this paper during one of the conference sessions.

Resonance behavior of dissipative spring-pendulum systems

Katarina Plaksiy, Yuri Mikhlin

Abstract: Some nonlinear dissipative system under external and internal resonance conditions is considered. In dissipative systems all important characteristics of dynamical process depend on time. Besides, nonlinear vibration modes (NNMs) here are not the classical nonlinear normal vibration modes because the vibration amplitude decreases here. The *reduced systems* which are written with respect to variables determining the system energy, the arctangent of the amplitudes ratio and the difference of phases, are used. Interaction of NNMs and appearance of the so-called *transient nonlinear normal modes* (TNNMs), which exist only for some levels of energy, are analyzed. The system motions approach TNNMs when the system energy is close to these specific levels. Then the energy decreases and motions tend to other stable vibration modes. All obtained results fully correspond to direct simulation of the basic system.

1. Introduction

Presence of external and internal resonances leads to complex behavior of nonlinear systems. In particular, few vibration modes can exist simultaneously; some vibration modes can lose their stability, and new vibration modes can appear as a result of bifurcations; the energy transfer from some vibration mode to another one can be observed etc. The resonance dynamics is analyzed in numerous publications, in particular, in books [1-3]. The vibration energy transfer and the energy localization under resonance conditions is discussed in various publications, in particular, in [4-7]. In particular, a process of energy transfer to a nonlinear absorber, where the energy is localized and dissipated, is described in different publications.

Nonlinear normal modes (NNMs) are the important part of nonlinear systems behavior. The Kauderer-Rosenberg concept of NNMs, first proposed in [8,9] for conservative systems, is based on determination of trajectories in the nonlinear system configuration space. Theory of NNMs for conservative and non-conservative systems and different applications of this theory are presented in numerous publications, in particular, in [2,10-12]. In nonlinear dissipative systems the classical NNMs by Kauderer-Rosenberg cannot appear due to exponential decrease of vibration amplitudes, but some similar vibration regimes exist.

Use of the so-called reduced system, which was utilized earlier for nonlinear non-dissipative systems [13,14], permits to describe the resonance behavior of nonlinear dissipative systems too. The

reduced system is written with respect to variables which characterize the system energy, the arctangent of the ratio of amplitudes and the difference of phases. The most important characteristics of the resonance behavior in nonlinear systems can be analyzed by such systems. They were successfully used in analysis of the resonance behavior of some nonlinear dissipative systems in [15,16]. Besides, the *transient nonlinear normal modes* (TNNMs) existing only for some specific values of the system energy, were first described in these publications. Although TNNMs disappear when the energy level decreases, they are temporarily attractive for other motions of the dissipative system, when the system energy is close to these specific energy values.

This paper is organized as follows. Model of the forced resonance vibrations of a spring-pendulum system (the rotator on the spring) is considered in Section 2. Note that the small mass pendulum can be considered as a vibration absorber. A case of external resonance on the frequency of spring vibrations is considered in Section 3. A case of simultaneous external and internal resonances is analyzed in Section 4. A case of external resonance on the frequency of pendulum vibrations is considered in Section 5. An investigation of the vibration modes stability and bifurcation is performed in these resonance cases. The energy transfer from the unstable mode to another stable one is considered. The transient nonlinear normal modes are determined and their influence on the system behavior is showed. The localization of energy is discussed and obtained results are compared with numerical simulations.

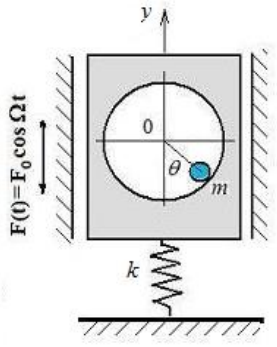

Figure 1. Rotator on the spring (spring-pendulum system)

2. Forced resonance vibrations of dissipative rotator on the spring

The model of the system under consideration is presented in Fig. 1.

Equations of motion of the system with small dissipation are the following:

$$\begin{cases} \ddot{u} + \omega_u^2 u + \varepsilon\eta_u \dot{u} - \mu(\ddot{\theta}\sin\theta + \dot{\theta}^2\cos\theta) = \varepsilon^2 f\cos\tau \\ \ddot{\theta} + \varepsilon\eta_\theta\dot{\theta} + p^2\sin\theta - \ddot{u}\sin\theta = 0, \end{cases} \tag{1}$$

where $u = \frac{y}{R}$, $\tau = \Omega t$, $\omega = \sqrt{k/(M+m)}$, $p^2 = g/(R\Omega)$, $\mu = m/(m+M)$, $\omega_u^2 = 1/\Omega^2$, $f = F_0/((M+m)R\omega^2\Omega^2)$, $\eta_u = \beta_u/((M+m)\Omega)$, $\eta_\theta = \beta_\theta/(m\Omega)$, β_x and β_θ are coefficients of dissipation; ε is the small parameter.

There are two NNMS by Kauderer-Rosenberg in the system (9) without dissipation and external excitation, namely, the localized $u-$mode of vertical vibrations ($u = u(\tau)$, $\theta = 0$) and the non-localized $\theta-$mode (or pendulum mode), when vibration amplitudes for vertical and angle coordinates are of the same order. When dissipation exists, such modes are not the NNMs by Kauderer-Rosenberg, because they are not periodic.

3. Case of external resonance on the frequency of spring vibrations

Using the multiple time scales method and introducing the transformations $u \to \varepsilon u$, $\theta \to \varepsilon\theta$ for small vibrations, we present coordinates in the form of the following asymptotic series:

$$\begin{cases} u = u_0 + \varepsilon^1 u_1 + \ldots \\ \theta = \theta_0 + \varepsilon^1 \theta_1 + \ldots \end{cases} \tag{2}$$

Here u_i and θ_i are functions of the independent time scales $T_n = \varepsilon^n \tau$ (n=0,1,2,…). To analyze the system (9) dynamics in the vicinity of the external resonance on the fundamental frequency ω_u, the detuning parameter Δ is introduced by the relation $\omega_u^2 = 1 + \varepsilon\Delta$. Using standard procedure of the multiple scales method [17], and expansions in power series for $\sin\theta$ and $\cos\theta$, one has as the intermediate result the following solution of the zero approximation by the small parameter:

$$\begin{cases} u_0 = C_u(T_1)e^{iT_0} + \overline{C}_u(T_1)e^{-iT_0}, \\ \theta_0 = C_\theta(T_1)e^{piT_0} + \overline{C}_\theta(T_1)e^{-piT_0}. \end{cases} \tag{3}$$

Then the solution (3) must be substituted to the system of the second approximation by ε, and secular terms are eliminated. The following condition of the secular terms elimination is received:

$$\begin{cases} 2i\dfrac{\partial C_u}{\partial T_1} + C_u\Delta + i\eta_u C_u - f/2 = 0, \\ 2\dfrac{\partial C_\theta}{\partial T_1} + \eta_\theta C_\theta = 0. \end{cases} \tag{4}$$

The change of variables $C_u = a_u e^{i\beta_u}$, $C_\theta = a_\theta e^{i\beta_\theta}$ leads the system (4) to the system of equations with respect to amplitudes a_u, a_θ and phases β_u, β_θ of the solution (3). The next change of variables, $a_u = 0.5\sqrt{\mu}\, K\cos\psi$, $a_\theta = K\sin\psi$ permits to make transformation to the *reduced system*, written with respect to the energy characteristic parameter *K*, the arctangent of the ratio of amplitudes ψ and the phases β_u, β_θ:

$$\begin{cases} K' = -0.5K(\eta_u \cos^2\psi + \eta_\theta \sin^2\psi) - 0.25 f \sin\beta_u \cos\psi, \\ \psi' = \sin\psi(0.5(\eta_u - \eta_\theta)\cos\psi + 0.25(f/K)\sin\beta_u), \\ \beta_u' = 0.5\Delta - 0.25(f/(K\cos\psi))\cos\beta_u, \\ \beta_\theta' = 0. \end{cases} \tag{5}$$

Equilibrium positions of the second and third equations of the system (5) are analyzed. These equilibrium positions, describing "vibrations in unison", correspond to NNMs of the original system (1). The additional analysis for the first equation of the system (5) is done for each vibration mode.

Relation $\sin\psi = 0$ corresponds to localized vibrations on the elastic spring. This vibration mode exists for all values of the parameter K. It is characterized by the straight line $\psi = 0$ in the space (ψ, φ). In this case it is necessary to analyze trajectories in the space (ψ, φ) to make some conclusion about stability of the mode localized vibrations.

The condition $\cos\psi = 0$. It corresponds to the straight line $\psi = \pi/2$ in the plane (ψ, φ). One has from the second equation of the system (5) that this equilibrium position exists if $\beta_u = 0 + \pi n$. The energy equation for the mode is the following: $K' = -\frac{\eta_\theta}{2} K$. We can see that the energy decreases, so, localized on pendulum vibrations are unstable, and this hypothetical vibration mode cannot be realized.

If both $\cos\psi \neq 0$ and $\sin\psi \neq 0$, the mode of coupled vibrations of the system (1) can appear. Condition of the mode existence is obtained from the second equation of the reduced system (5) in the form: $\cos\psi = \pm \frac{f}{2K\sqrt{(\eta_u - \eta_\theta)^2 + \Delta^2}}$, $tg\beta_u = \frac{\eta_\theta - \eta_u}{\Delta}$.

Then the reduced system (5) is integrated by the Runge-Kutta method of the 4-th order with step $h = 0.01$, when $0 \le \psi(0) \le \frac{\pi}{2}$ for the following parameters: $K(0) = 0.5$, $\Delta = 0.2$, $\eta_u = 0.4$, $\eta_\theta = 0.4$ and $f = 0.2$. Trajectories in the space (ψ, φ) are presented in Fig. 2.

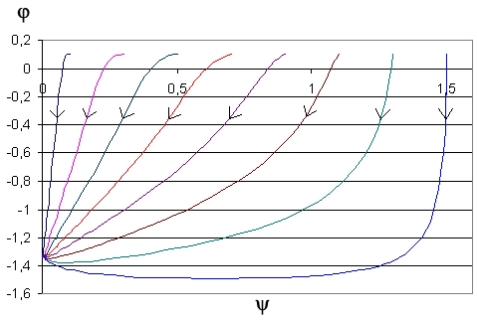

Figure 2. External resonance on the frequency of spring vibrations. Trajectories in the place (ψ,φ).

All trajectories in Fig. 2 approach the line $\psi = 0$ which corresponds to the stable vibration mode with localization on the spring. Stable modes of coupled vibrations do not appear.

Note that direct numerical simulation of the original system (1) by the method of Runge-Kutta of the 4-th order fully confirms the preceding analysis of the reduced system.

4. Case of simultaneous external and internal resonances

To consider motions of the system under consideration in the vicinity of both external and internal resonances one introduces to equations of motion (1) two detuning parameters Δ_1 and Δ_2 by relations: $\omega_u^2 = 1 + \varepsilon\Delta_1$, which corresponds to the vicinity of external resonance, and $p^2 = \frac{1}{4} + \varepsilon\Delta_2$, which corresponds to the vicinity of the main parametrical resonance of the system (1).

The solution of the first approximation by the multiple scales method can be written in the form (3) for $p = 1/2$. This solution is substituted to the equations of the second approximation by the small parameter, then secular terms are eliminated. Change of variables, $C_u = a_u e^{i\beta_u}$, $C_\theta = a_\theta e^{i\beta_\theta}$, gives the system of modulation equations written with respect to amplitudes a_u, a_θ and phases β_u, β_θ, which are not presented here. Next change of variables, $a_u = \frac{\sqrt{\mu}}{2} K\cos\psi$, $a_\theta = K\sin\psi$, leads to the *reduced system* (6), written with respect to the energy characteristic parameter *K*, the arctangent of the amplitudes ratio ψ and the phases β_u, β_θ. The equation (7) with respect to the phase difference $\varphi = \beta_u - 2\beta_\theta$ is written too.

$$\begin{cases} K' = -0.5K(\eta_u \cos^2\psi + \eta_\theta \sin^2\psi) - (f/\sqrt{\mu})\sin\beta_u \cos\psi, \\ \psi' = 0.5\sin\psi(\sqrt{\mu}K\sin(2\beta_\theta - \beta_u) + (\eta_u - \eta_\theta)\cos\psi + (f/(\sqrt{\mu}K))\sin\beta_u), \\ \beta_u' = 0.5(\Delta_1 + (\sqrt{\mu}K\sin^2\psi/\cos\psi)\cos(2\beta_\theta - \beta_u) - (f/(\sqrt{\mu}K\cos\psi))\cos\beta_u), \\ \beta_\theta' = \Delta_2 + 0.5\sqrt{\mu}K\cos\psi\cos(2\beta_\theta - \beta_u). \end{cases} \quad (6)$$

$$\varphi' = 0.5(\Delta_1 - 4\Delta_2 + \sqrt{\mu}K((\sin^2\psi/\cos\psi) - \cos\psi)\cos(2\beta_\theta - \beta_u) - (f/(\sqrt{\mu}K\cos\psi))\cos\beta_u). \quad (7)$$

Equilibrium positions for the second equation of the system (6) and equation (7) are considered. Condition $\sin\psi \equiv 0$ corresponds to the localized mode of spring vibrations. This mode exists for all values of the energy parameter K; it is described by straight line $\psi = 0$ in the plane (ψ, φ). If both $\cos\psi \neq 0$, and $\sin\psi \neq 0$, it is possible to observe the mode of coupled vibrations. Condition of the mode existence which can be obtained from the second equation of the reduced system (6) is the following: $\cos\psi = \sqrt{\mu}/(\eta_\theta - \eta_u)K\sin(2\beta_\theta - \beta_u) + f/(2\sqrt{\mu}K(\eta_\theta - \eta_u))\sin\beta_u$. This condition corresponds to two modes of coupled vibrations. The further analysis shows that one of them is stable mode of coupled vibrations and another one is the transient mode of coupled vibrations, which is a result of bifurcation.

To construct trajectories in the space (ψ, φ) the reduced system (6) is integrated by the Runge-Kutta method of 4th order, when the initial value of arctangent of the amplitudes ratio changes on the interval $0 \le \psi(0) \le \frac{\pi}{2}$, $K(0) = 0.5$ and system parameters are the following: $\eta_u = 0.3$, $\eta_\theta = 0.2$, $\mu = 0.4$, $\Delta_1 = 0.2$, $\Delta_2 = 0.1$, $f = 0.35$. Trajectories in the space (ψ, φ) are shown in Fig.3.

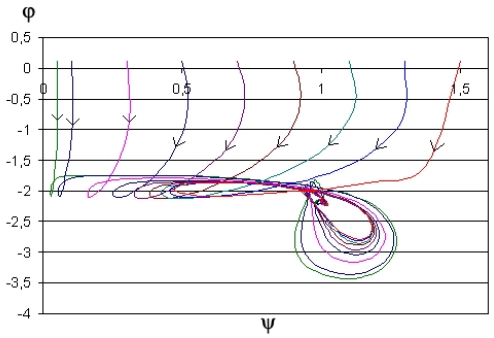

Figure 3. Simultaneous external and internal resonances. Trajectories in the space (ψ, φ)

Each trajectory has a loop near some quasi-equilibrium state of the reduced system. This state moves in the space (ψ,φ) and corresponds to the *transient nonlinear normal mode* (TNNM) which exists only for specific value of the system energy; so, the TNNM exists in some moments of time corresponding to this energy level. It is important, that this transient mode is attractive and other motions of a system are close to the TNNM near the mentioned moment of time. We can see in the Fig. 3, that later, when the transient mode disappears, trajectories in the plane (ψ,φ) tend to the equilibrium position which corresponds to the stable nonlinear normal mode of coupled vibrations. Note that this equilibrium position is closer to the straight line $\psi = \pi/2$, which corresponds to localized on pendulum vibrations, than to the straight line $\psi = 0$, which corresponds to localized vibrations of spring. So, the mode of the localized vibrations of spring is not stable here.

To illustrate behavior of the spring-pendulum system in vicinity of the resonances, the system (1) is integrated numerically by the Runge-Kutta method on the interval $\tau \in [0,1000]$ for the following initial values corresponding to localized vibrations of the spring, $u(0) = 0.0995004$, $\theta(0) = 0.00196013$, $\dot{u}(0) = -0.0115758$, $\dot{\theta}(0) = -0.000212261$, and for the system parameters $\eta_u = 0.3$, $\eta_\theta = 0.2$, $f = 0.35$, $\mu = 0.2$, $\Delta_1 = 0.2$, $\Delta_2 = 0.1$, $\varepsilon = 0.1$, $p^2 = 0.26$, $\omega_u^2 = 1.01$. Trajectories in the system configuration plane are shown in Fig.4 for the following intervals of time: $\tau \in [0,250]$ (Fig.4a), $\tau \in [400,500]$ (Fig.4b) and $\tau \in [0,1000]$ (Fig.4c).

So, one has the following conclusion about dynamics of the dissipative system (1) in the vicinity of simultaneous external and internal resonances: at first, the transient nonlinear normal mode of coupled vibrations appears. At the beginning of the process localized mode of spring vibrations loses stability and motions of the system become close to this TNNM which is determined by trajectories, which are close to parabola with branches down (Fig. 4a). Then, due to instability of this mode, motions of the system tend to the mode of coupled vibrations which is stable here. Trajectory of this stable mode is observed in Fig. 4b where vibrations for great values of time are shown. This stable mode is close to the localized mode of the pendulum vibrations, and it can be used in the problem of vibration absorption. Namely, it is possible to guarantee transfer of the energy from vibrations of spring to the pendulum vibrations, where the vibration energy can be dissipated. So, the numerical simulation fully confirms results obtained above by analysis of the reduced system.

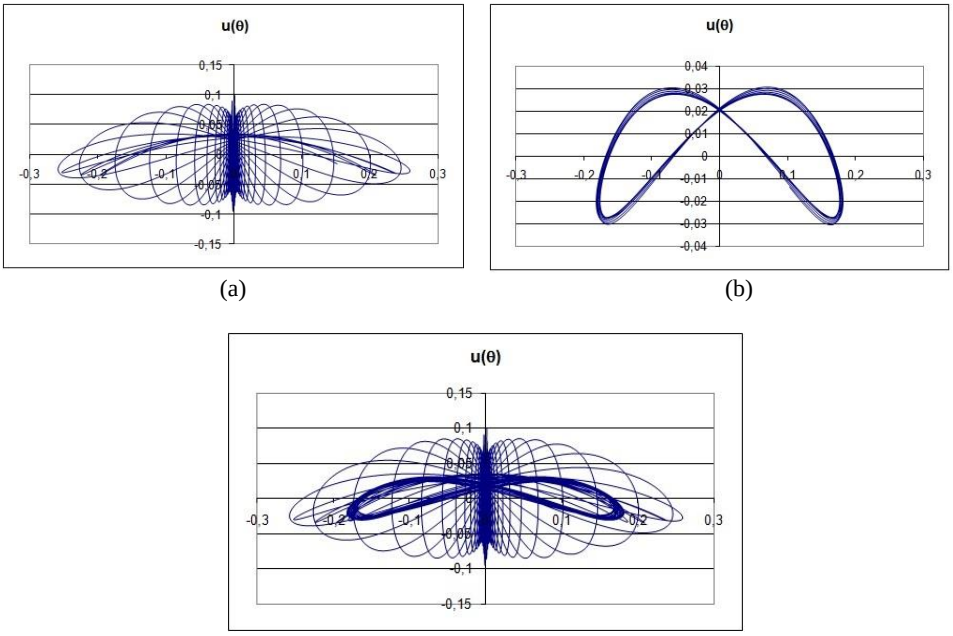

Figure 4. Trajectories $u(\theta)$ in configuration space for $\tau \in [0,250]$ (a); $\tau \in [400,500]$ (b); $\tau \in [0,1000]$ (c)

5. Case of external resonance on the frequency of pendulum vibrations

Similar approach permits to analyze the case of the external resonance on the natural frequency of pendulum vibrations. The detuning parameter is introduced by the relation $p^2 = \frac{1}{4} + \varepsilon\Delta_2$.

Using the same approach which was described above, one obtains the reduced system in the form

$$\begin{cases} K' = -0.5K(\eta_u \cos^2\psi + \eta_\theta \sin^2\psi) + 0.5(f/(\omega_u^2 - 1))\sin^2\psi \sin 2\beta_\theta, \\ \psi' = 0.5\sin\psi\cos\psi(\eta_u - \eta_\theta + (f/(\omega_u^2 - 1))\sin 2\beta_\theta), \\ \beta_u' = 0, \\ \beta_\theta' = 0.5(f/(\omega_u^2 - 1))\cos 2\beta_\theta + \Delta \end{cases} \tag{8}$$

The equation concerning phase difference can be written in the form:

$$\varphi' = -(f/(\omega_u^2 - 1))\cos 2\beta_\theta - 2\Delta \qquad (9)$$

Simultaneous analysis of the second equation of the reduced system (8) and equation (9) permits obtain two equilibrium states for this case. Namely, the equality $\sin\psi \equiv 0$ corresponds to localized vibrations of the spring, and $\cos\psi \equiv 0$ the equality corresponds to coupled vibrations of the pendulum and spring. In the last vibration mode amplitudes of pendulum vibrations increase due to external resonance and are essentially larger than amplitudes of the spring vibrations. It means that localization of the system energy on the pendulum is possible in this case.

For the case of localized spring vibrations, $\sin\psi \equiv 0$, there is no need in additional condition for phase difference. On the contrary, if $\cos\psi \equiv 0$, one has the condition for equilibrium state of the equation (9) as $\cos 2\beta_\theta = -2\Delta(\omega_u^2 - 1)/f$. This state exists in the region of parameters, $\left|-2\Delta(\omega_u^2 - 1)/f\right| \le 1$; so, its existence depends on value of amplitude of external excitation f: for small values of f this equilibrium state does not exist.

To construct trajectories in the space (ψ, φ) the reduced system (8) is integrated by the Runge-Kutta method of 4th order for two values of amplitude of external excitation, $f = 0.35$ and $f = 0.15$, when $0 \le \psi(0) \le \pi/2$, $K(0) = 0.5$ and the system parameters are the following $\omega_u = 0.2$, $\eta_u = 0.3$, $\eta_\theta = 0.2$, $\mu = 0.4$, $\Delta = 0.1$. Trajectories for two considered cases are presented in Figs. 5 a,b respectively.

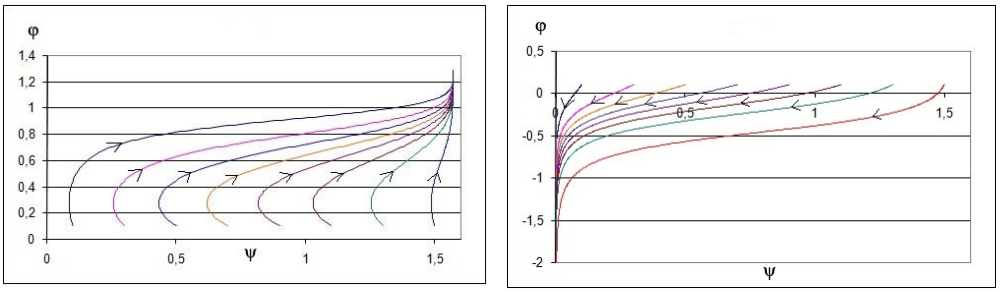

(a) (b)

Figure 5. Trajectories in the space (ψ, φ): (a) $f = 0.35$; (b) $f = 0.15$.

Trajectories in Fig.5a approach the straight line $\psi = \frac{\pi}{2}$, which corresponds to the mode with large amplitudes of pendulum vibrations. In this region of the system parameters localized vibrations of the spring lose stability and the mode of pendulum vibrations with large amplitudes is attractive. In

Fig.5b trajectories tend to the straight line $\psi = 0$, corresponding to localization on the spring. Here localized vibrations of the spring are stable and large amplitudes for the pendulum are not observed.

To illustrate behavior of the spring-pendulum system (1) for the case, when large vibrations of the pendulum appear, the system (1) is integrated by the Runge-Kutta method on the intervals $\tau \in [0,500]$ and $\tau \in [0,300]$ for the initial values $u(0) = 0.0630421$, $\theta(0) = 0.0019999$, $\dot{u}(0) = -0.00348917$, $\dot{\theta}(0) = -3.05634e-005$ and $u(0) = 0.0344584$, $\theta(0) = 0.0995004$, $\dot{u}(0) = -3.39984e-005$, $\dot{\theta}(0) = -0.0062685$ of localized and coupled vibrations respectively, and for the parameters $\omega_u = 0.2$, $\eta_u = 0.3$, $\eta_\theta = 0.2$, $f = 0.35$, $\mu = 0.4$, $p^2 = 0.26$, $\Delta = 0.1$, $\varepsilon = 0.1$. Trajectories in the system configuration space are presented in Figs. 6 a,b. Transfer to the stable mode of large vibrations of the pendulum is shown. It corresponds to Fig.5 a,b in the space $\varphi(\psi)$.

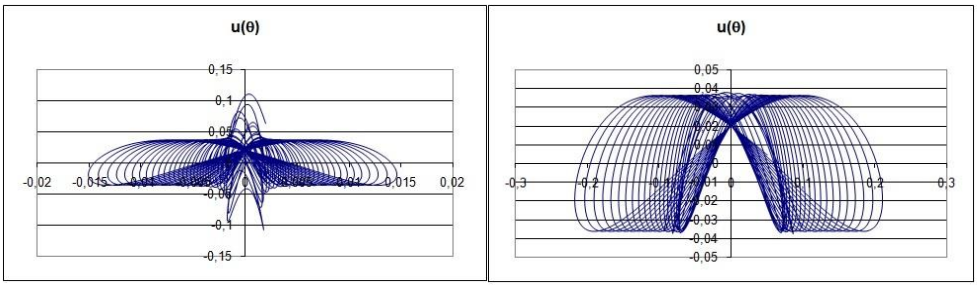

a) b)

Figure 6. Dependence $u(\theta)$. a) Transfer from localization on the spring to localization on the pendulum; b) Transfer from coupled vibrations to localization on the pendulum.

To illustrate behavior of the spring-pendulum system (1) in the vicinity of resonance, when large vibrations of the pendulum are absent, we consider coupled vibrations of the system for not large amplitude of external excitation. The system (1) is integrated by the Runge-Kutta method of the 4-th order on the intervals $\tau \in [0,500]$ and $\tau \in [0,300]$ for the initial values $u(0) = 0.015425$, $\theta(0) = 0.0099995$, $\dot{u}(0) = -3.04e-006$, $\dot{\theta}(0) = -0.000151775$, and for system parameters $\omega_u = 0.2$, $\eta_u = 0.3$, $\eta_\theta = 0.2$, $f = 0.15$, $p^2 = 0.26$, $\mu = 0.4$, $\Delta = 0.1$ $\varepsilon = 0.1$. Trajectories in the configuration space are shown in Fig.7. Here coupled vibrations in this region of the system parameters are unstable and trajectories tend to the stable mode if localized vibrations of the spring. This situation corresponds to Fig.5b in the place $\varphi(\psi)$. So, numerical simulations fully confirm results obtained by the reduced system approach.

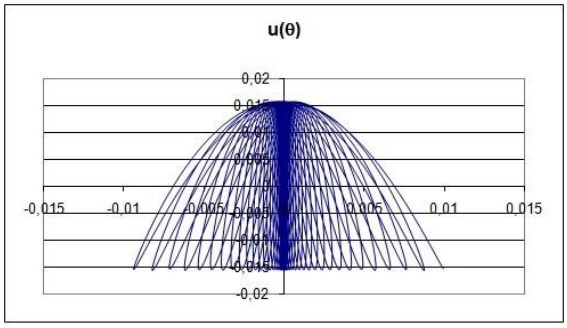

Figure 7. Dependence $u(\theta)$ Localization on the spring.

6. Conclusions

Dynamics of the dissipative spring-pendulum system (1) under the periodic external excitation is analyzed in the vicinity of external resonances and in the vicinity of simultaneous external and internal resonances. Analysis of the resonance dynamics in this system is made by using the concept of nonlinear normal modes by Kauderer-Rosenberg, which was generalized to dissipative systems. Transfer to the *reduced system*, written with respect to the system energy, the arctangent of amplitudes ratio and the difference of phases, is used in this analysis. We can note that earlier new results in dynamics of nonlinear non-dissipative systems were obtained by use of similar coordinates. It means an analysis of so-called «limiting phase trajectories» (LPT) [18] and of energetic interaction between nonlinear normal modes [14].

Here a transient from the unstable NNMs to the stable ones in vicinity of resonance is described in the dissipative spring-pendulum system. Besides, in the vicinity of the resonance the *transient nonlinear normal modes*, which exist only for some levels of the system energy, appear. Although each TNNM exists only for some moment of time, it attracts other motions of the system near this time value. When this mode disappears, motions of the system attract the stable nonlinear normal mode. For the case of the external resonance on the fundamental frequency of pendulum vibrations two variants are possible: if the value of amplitude of external excitation is large enough, then localization of the system energy on pendulum is observed and localized spring vibrations lose their stability; else the localized spring vibrations remain stable. Reliability of obtained analytical results is verified by numerical simulation. So, we can conclude, that the analysis of the reduced system is effective for nonlinear dissipative systems.

References

[1] Nayfeh, A.H., Mook, D.T. *Nonlinear Oscillations*. Wiley Inerscience, New York, 1979.

[2] Avramov, K.V., Mikhlin, Yu.V. *Nonlinear Dynamics of Elastic Systems.V.1. Models, Methods, Phenomena (Second Edition)*. IKI, Moscow-Izhevsk, 2015 (in Russian).

[3] Manevich A.I., Manevitch, L.I. *The Mechanics of Nonlinear Systems with Internal Resonances*. Imperial College Press, London, 2005.

[4] Mercer, C.A., Rees, P.L., Fahy V.J. Energy flow between two weakly coupled oscillators subject to transient excitation. *Journal of Sound and Vibration.* 15, 3 (1971), 373-379.

[5] Nayfeh, S.A., Nayfeh, A.H. Energy transfer from high to low-frequency modes in a flexible structure via modulation. *ASME J. Vibration and Acoustics* 116 (1994), 203-207.

[6] Gendelman, O.V. Transition of energy to nonlinear localized mode in highly asymmetric system of nonlinear oscillators. *Nonlinear Dynamics* 25 (2001), 237-253.

[7] Vakakis, A.F., Gendelman, O.V., Bergman, L.A., McFarland, D.M., Kerschen, G., Lee, Y.S. *Nonlinear Targeted Energy Transfer in Mechanical and Structural Systems*, Springer Science, 2008.

[8] Kauderer, H. *Nichtlineare Mechanik*. Springer-Verlag, Berlin, 1958.

[9] Rosenberg, R. Nonlinear vibrations of systems with many degrees of freedom. *Advances of Applied Mechanics* 9 (1966), 156–243.

[10] Vakakis, A., Manevitch, L., Mikhlin,Yu., Pilipchuk, V., Zevin, A. *Normal Modes and Localization in Nonlinear Systems*, Wiley Interscience, New York, 1996.

[11] Mikhlin, Yu.V., Avramov, K.V. Nonlinear normal modes for vibrating mechanical systems. Review of theoretical developments. *Applied Mechanics Review* 63 (2010), 4-20.

[12] Avramov, K.V., Mikhlin, Yu.V. Review of applications of nonlinear normal modes for vibrating mechanical systems. *Applied Mechanics Review* 65, 2 (2013), (20 pages).

[13] Wang, F., Bajaj, A., Kamiya, K. *Nonlinear Normal Modes and Their Bifurcations for an Inertially-Coupled Nonlinear Conservative System*. Purdue University, 2005.

[14] Pilipchuk, V.N. *Nonlinear Dynamics: Between Linear and Impact Limits*. Springer-Verlag, Berlin, 2010.

[15] Plaksiy, K.Y., Mikhlin, Yu.V. Dynamics of nonlinear dissipative systems in the vicinity of resonance. *J. of Sound and Vibration* 334 (2015), 319-337.

[16] Plaksiy, K.Y., Mikhlin, Yu.V. Resonance behavior of the limited power-supply system coupled with the nonlinear absorber. *Mathematics in Engineering, Science and Aerospace* 6, 3 (2015), 475-495.

[17] Nayfeh, A.H. *Perturbation Methods*. Wiley, New York, 1973.

[18] Manevitch, L.I., Gendelman, O.V.. *Tractable Models of Solid Mechanics*. Springer-Verlag, Berlin, 2011.

Katarina Plaksiy, PhD: National Technical University “Kharkov Polytechnic Institute”, Dept. of Applied Mathematics, Kyrpychev str, 2, 61002 Kharkov, Ukraine (*plaksiyya@rambler.ru*).

Yuri Mikhlin, Professor: National Technical University “Kharkov Polytechnic Institute”, Dept. of Applied Mathematics, Kyrpychev str, 2, 61002 Kharkov, Ukraine (*Yuri_Mikhlin@mail.ru*).

Aeroelastic stability analysis via multiparameter eigenvalue problems

Arion Pons, Stefanie Gutschmidt

Abstract: This paper presents a new method of identifying and analysing stability boundaries in parametric systems using multiparameter spectral theory. Considering our driving application, the analysis of aeroelastic flutter instability, we identify methods by which the location of the stability boundary be expressed as a multiparameter eigenvalue problem and thus solved. This approach yields far-reaching results, including direct solvers for arbitrarily large polynomial problems, iterative and approximate direct solvers for systems that are strongly nonlinear in the frequency domain, and a novel method of system visualisation. These solvers and methods are tested on two aeroelastic section models and the Goland wing benchmark model, and their advantages and limitations are explored.

1. Introduction

The understanding and prediction of aeroelastic instability is a primary concern in the discipline of aeroelasticity. Aeroelastic instability, often termed *flutter* when occurring dynamically, be observed in a wide variety of systems – not only wings and aerofoils, but wall plates [1], hosepipes [2] and more. In a linear system, or the linearisation of a nonlinear system, the onset of flutter can be described by the modal stability criterion:

$$\mathrm{Im}(\chi) > 0 \text{ for stability,} \tag{1}$$

where χ are the time-eigenvalues of the system, transformed according to $q(t) = \hat{q}e^{\imath\chi t}$ for the system coordinate q [3]. Note that other transforms and nondimensional eigenvalue definitions are possible. A flutter point then be described as a tuple of the modal frequency of instability, $\chi_\mathrm{f} \in \mathbb{R}$, and any relevant system parameters (in particular, a local airspeed). As flutter is often associated with structural failure, only the first few flutter points are usually of industrial relevance.

However, even in a linear or linearised system, Eq. 1 is not the only stability criterion available; it corresponds to what is known as the p-method [4]; and a variety of other aeroelastic 'methods' are available: A major strain of variants includes the k-method and p-k method, which utilize a structural damping term to describe stability. They are detailed and discussed in a number of reference works [3–5]. In recent years several authors have refined these methods [6–8] and devised new methods. The μ-type methods, including the μ-method by Lind and Brenner [9] and the μ-k method by Borglund [10,11], facilitate the propagation of uncertainty distributions through the system. Irani and

Sazesh [12] characterized flutter instability using stochastic methods, and Afolabi [13,14] applied eigenvector orthogonality conditions from catastrophe theory.

All of these approaches, however, are based on the single-parameter approach of computing a stability metric ($\mathrm{Im}(\chi)$, μ or whatever else) across a range of system parameter values and identifying relevant stability boundaries. We propose an entirely different method of analysis. We show that the solution of an aeroelastic system for its flutter points – or the analysis of any other frequency-domain stability problem – is nothing other than a multiparameter eigenvalue problem. We will demonstrate how this approach leads to a number of improved solvers for a wide range of parametric stability problems drawn from the field of aeroelasticity. Our methods are equally applicable in other fields.

2. Multiparameter analysis

Consider a linear finite-dimensional system with eigenvector $\mathbf{x} \in \mathbb{C}^n$, continuously dependent on both an eigenvalue parameter $\chi \in \mathbb{C}$, and another structural or environmental parameter $p \in \mathbb{R}$:

$$\mathrm{A}(\chi, p)\mathbf{x} = \mathbf{0}, \tag{2}$$

where $\mathrm{A} \in \mathbb{C}^{n\times n}$. Any complex-valued structural parameter can be split into two real parameters. We then note that the condition for the stability boundary, $\mathrm{Im}(\chi) = 0$, is equivalent to defining the problem with $\chi \in \mathbb{R}$. However, under $\chi \in \mathbb{R}$ a solution to Eq. 2 only exists on the stability boundary, and nowhere else. To define some form of solution in the subcritical and supercritical areas (above and below the stability boundary, respectively), following [15], we take the complex conjugate of Eq. 2 as another equation:

$$\mathrm{A}(\chi, p)\mathbf{x} = \mathbf{0}, \tag{3}$$

$$\overline{\mathrm{A}}(\chi, p)\bar{\mathbf{x}} = \mathbf{0}. \tag{4}$$

As $p \in \mathbb{R}$ and $\chi \in \mathbb{R}$ are unaffected by conjugation, this operation enforces these conditions. This procedure has been utilized before in the analysis of delay differential equations [15], and (in a limited form) in the context of Hopf bifurcation prediction [16], though in the latter its significance appears not to have been recognised. Equation 3 a multiparameter eigenvalue problem (MEP): an eigenvalue problem in which the eigenvalue point is not simply defined by a scalar and an eigenvector, but by an n-tuple and an eigenvector. A number of methods of analysis have been developed for such problems, and in this paper we will explore some of these.

3. Linear and polynomial problems

3.1. Direct solution

Consider a linear instability problem:

$$(\mathrm{A} + \mathrm{B}\chi + \mathrm{C}p)\mathbf{x} = \mathbf{0}, \tag{5}$$

$$(\overline{\mathrm{A}} + \overline{\mathrm{B}}\chi + \overline{\mathrm{C}}p)\bar{\mathbf{x}} = \mathbf{0}. \tag{6}$$

Post-multiplying Eq. 5 by $\overline{\mathrm{C}}\mathbf{y}$ and premultiplying Eq. 6 by $\mathrm{C}\mathbf{x}$, we obtain

$$(\mathrm{A} + \mathrm{B}\chi + \mathrm{C}p)\mathbf{x} \otimes (\overline{\mathrm{C}}\mathbf{y}) = 0, \tag{7}$$

$$(\mathrm{C}\mathbf{x}) \otimes (\overline{\mathrm{A}} + \overline{\mathrm{B}}\chi + \overline{\mathrm{C}}p)\mathbf{y} = 0. \tag{8}$$

Equations 7 and 8 are equal to zero and so we equate them. After cancelling the terms in p, the result becomes:

$$\Delta_1\mathbf{z} = \chi\Delta_0\mathbf{z}, \tag{9}$$

with an enlarged eigenvector $\mathbf{z} = \mathbf{x} \otimes \mathbf{y}$ and the operator determinants

$$\Delta_0 = \mathrm{B} \otimes \overline{\mathrm{C}} - \mathrm{C} \otimes \overline{\mathrm{B}}, \tag{10}$$

$$\Delta_1 = \mathrm{C} \otimes \overline{\mathrm{A}} - \mathrm{A} \otimes \overline{\mathrm{C}}, \tag{11}$$

$$\Delta_2 = \mathrm{A} \otimes \overline{\mathrm{B}} - \mathrm{B} \otimes \overline{\mathrm{A}}, \tag{12}$$

which are of size n^2 relative to system coefficients of size n. Equation 9 is a generalized eigenvalue problem (GEP), in the single parameter χ. GEP solvers are very widely available.

The operator determinants also define a GEP in p. Multiplying by $\overline{\mathrm{B}}\mathbf{y}$ and $\mathrm{B}\mathbf{x}$, we have:

$$\Delta_2\mathbf{z} = p\Delta_0\mathbf{z}. \tag{13}$$

However, only one of Eq. 9 or Eq. 13 need be solved: the solutions of one can be substituted back into the original system, which yields smaller GEP for the other parameter. Alternatively, Rayleigh quotients be used. The problem's stability boundary has thus been computed directly. This solution method is known as the operator determinant method. Its computational complexity is $\mathcal{O}(n^6)$ [17–19]; solving the GEP via the QZ algorithm (an $\mathcal{O}(n^3)$ process) [20], with operator determinants of size n^2. The operator determinant method has not previously been used in aeroelasticity, and has only rarely seen engineering application in the study of dynamic model updating [21]. We note that a variety of other iterative methods are also available for the solution of linear MEPs, including the Jacobi-Davidson [22], Implicitly Restarted Arnoldi [23] and Harmonic Rayleigh-Ritz [24] methods.

3.2. Linearisation of polynomials

Any polynomial MEP can be linearised [18,25]; a process which resembles the well-known linearisation of single-parameter problems. For example, a quadratic problem $(\mathrm{A} + \mathrm{B}\chi + \mathrm{C}\tau + \mathrm{D}\chi p + \mathrm{E}\chi^2 + \mathrm{F}p^2)\mathbf{x} = \mathbf{0}$ be linearised with the eigenvector definition $\mathbf{q} = [\mathbf{x};\ \chi\mathbf{x};\ p\mathbf{x}]$.

$$\left(\begin{bmatrix} \mathrm{A} & \mathrm{B} & \mathrm{C} \\ 0 & -I_n & 0 \\ 0 & 0 & -I_n \end{bmatrix} + \begin{bmatrix} 0 & \mathrm{D} & \mathrm{E} \\ I_n & 0 & 0 \\ 0 & 0 & 0 \end{bmatrix}\chi + \begin{bmatrix} 0 & 0 & \mathrm{F} \\ 0 & 0 & 0 \\ I_n & 0 & 0 \end{bmatrix}p\right)\begin{bmatrix} \mathbf{x} \\ \chi\mathbf{x} \\ p\mathbf{x} \end{bmatrix} = \mathbf{0}. \tag{14}$$

Quadratic problems are particularly relevant in aeroelasticity given the near-quadratic dependence of most systems on airspeed and modal frequency. There is also an alternate method of linearisation, known as quasilinearisation [18], which increases the number of eigenvalue parameters instead of the coefficient size. In this brief work however we focus on standard linearisation.

3.3. Singularity

A linear MEP be singular; as governed by the singularity of Δ_0. When this occurs the operator determinant method as described breaks down [18,26]. A number of problems that arise in the study of aeroelasticity are singular, because the linearization of polynomial problems tends to generate singular linear problems, even if all the coefficients of the original problem are at full rank (cf. Eq. 14). Recently, an extension to the operator determinant method was proposed that allows it to cope with this singularity. Muhič and Plestenjak [25] proved that the eigenvalues of a polynomial system are equivalent to the finite regular eigenvalues of the pair of singular operator determinant GEPs constructed via linearization. The finite regular eigenvalues of Eq. 5 and 6 are the pairs (χ, p) such that [26]:

$$\mathrm{rank}(\mathrm{A} + \mathrm{B}\chi + \mathrm{C}p) < \max_{(s,t)\in\mathbb{C}^2} \mathrm{rank}(\mathrm{A} + \mathrm{B}s + \mathrm{C}t), \tag{15}$$

that is, they are the points that cause the singular problem to have its maximum rank. On the basis of this proof, Muhič and Plestenjak [25] devised a set of algorithms which would extract the common regular part of the singular matrix pencils $\Delta_1 - \chi\Delta_0$ and $\Delta_2 - p\Delta_0$. This common regular part is represented by two smaller nonsingular matrix pencils ($\Delta_{1\mathrm{ns}} - \chi\Delta_{0\mathrm{ns}}$ and $\Delta_{2\mathrm{ns}} - p\Delta_{0\mathrm{ns}}$), which be solved by GEP solvers as per normal. The algorithms involved in the extraction of the common regular part are presented in [25] and published also in code [27]. Only one of the additional iterative algorithms mentioned in Section 3.1 are capable of solving singular systems with this extension; this is the Jacobi-Davidson method [22]. A comparison of this method with the operator determinant method for singular systems indicated that the latter is more computationally efficient [28].

4. Nonlinear problems

4.1. Direct methods

A variety of nonlinear eigenvalue problems arise in aeroelasticity, and take a variety of forms. Note that such problems are not equivalent to nonlinear stability problems; being already in the frequency domain. One particularly common class are polynomial problems containing a nonlinear scalar function – in aeroelasticity often Theodorsen's function [4]. Such problems be transformed into approximate polynomial problems (and thus solved) with the choice of an appropriate approximation for the nonlinear function. Polynomial, rational or rational fractional-order approximations are all admissible. We give a specific example of this method in Section 5.

4.2. Iterative methods

Another more general approach to nonlinear MEPs is the use of iterative algorithms that assume nothing about the problem's internal structure. Ruhe [29] proposed a method of successive linear problems for one-parameter eigenvalue problems; and generalizations to this method for MEPs were published independently by Pons [30] and Plestenjak [31]. For the system of Eq. 2-3 taking first-order Taylor series in the eigenvalue variables, we obtain an implicit fixed-point iteration via a linear MEP:

$$(\mathrm{A}_k + \Delta\chi_k \mathrm{X}_k + \Delta p_k \mathrm{P}_k)\mathbf{x} = 0, \tag{16}$$

$$(\overline{\mathrm{A}}_k + \Delta\chi_k \overline{\mathrm{X}}_k + \Delta p_k \overline{\mathrm{P}}_k)\bar{\mathbf{x}} = 0, \tag{17}$$

where $\mathrm{A}_k = \mathrm{A}(\chi_k, p_k)$, $\mathrm{P}_k = \partial_p \mathrm{A}(\chi_k, p_k)$, $\mathrm{X}_k = \partial_\chi \mathrm{A}(\chi_k, p_k)$ and $\Delta\chi_k = \chi_{k+1} - \chi_k$, etc. This linear problem be solved at each step with the operator determinant method. This however comes at the cost of $\mathcal{O}(n^6)$ computational complexity [31].

Alternatively, a more computationally efficient method of solving nonlinear MEPs be devised by applying Newton's method to the determinant of the nonlinear matrix coefficient. Defining a state vector $\mathbf{v} = [\chi, p]^T$ and the complex-valued scalar determinant function $z = \det(\mathrm{A}(\mathbf{v}))$, we obtain the Newton iteration

$$\mathbf{v}_{k+1} = \mathbf{v}_k - \mathrm{J}(\mathbf{v}_k)^{-1}\mathbf{F}(\mathbf{v}_k), \tag{18}$$

with a real-valued residual function

$$\mathbf{F}(\mathbf{v}) = \begin{bmatrix} \mathrm{Re}(z(\mathbf{v})) \\ \mathrm{Im}(z(\mathbf{v})) \end{bmatrix} = \mathbf{0}, \tag{19}$$

and where J is the Jacobian matrix of **F** with respect to **v**. We term this method the iterated contour plot (ICP) as it can be related to an iterative formulation of the contour plot [30]. It has been applied

(in basic form) to two-parameter linear MEPs by Podlevskii [32,33] and to nonlinear MEPs independently by Pons [30] and Plestenjak [31]. This method has computational complexity $\mathcal{O}(n^3)$, for LU-based determinant evaluation [34].

4.3. The contour plot

Modal damping or root locus plots are traditional methods of visualising the stability behaviour of an aeroelastic system. However, neither is suitable for visualising our multiparameter formulations, as we have $\chi \in \mathbb{R}$ always. To this purpose we introduce the contour plot, as per Pons and Gutschmidt [30,35]. This involves plotting contours of $\mathrm{Re}(z)$ and $\mathrm{Im}(z)$, where $z = \det\big(A(\chi, p)\big)$ for Eq. 2; i.e. the real and imaginary parts of the matrix function determinant, as a function of its parameters. These contours be plotted by evaluating z over a grid of χ and p; their intersection represents a point $z = 0$, i.e. a stability boundary. This process is particularly useful for strongly nonlinear matrix functions, including nondifferentiable ones. A variety of contour plots are presented in Section 5.

5. Numerical experiments

5.1. Section model

As an initial test system we consider an aerofoil with two degrees of freedom (plunge h and twist θ). Figure 1 shows a schematic of such a system, with dimensionless parameters as per Table 1 and the airspeed parameter Υ; the airspeed per semichord. A frequency domain analysis of this system, under Theodorsen's unsteady aerodynamic theory yields a problem of the form:

$$\left(\left(\mathrm{G}_0 + \mathrm{G}_1\frac{1}{\kappa} + \mathrm{G}_2\frac{C(\kappa)}{\kappa} + \mathrm{G}_3\frac{C(\kappa)}{\kappa^2}\right)\chi^2 - \mathrm{D}_0\chi - \mathrm{K}_0\right)\mathbf{x} = \mathbf{0}, \tag{20}$$

where $\mathbf{x} = [h; \theta]$, $\kappa = \Upsilon/\chi$ is the reduced frequency, and $C(\kappa)$ is Theodorsen's function, composed of a number of Bessel functions [4]. The matrix coefficients in Eq. 20 are:

$$\mathrm{G}_0 = \frac{1}{\mu}\begin{bmatrix} 2 & -a - r_\theta \\ -a - r_\theta & \frac{1}{8} + a^2 + r^2 \end{bmatrix}, \mathrm{G}_1 = \frac{1}{\mu}\begin{bmatrix} 0 & -1 \\ 0 & -\frac{1}{2} + a \end{bmatrix}, \mathrm{G}_2 = \frac{\iota}{\mu}\begin{bmatrix} -2 & -1 + 2a \\ 1 + 2a & \frac{1}{2} - 2a^2 \end{bmatrix} \tag{21}$$

$$\mathrm{G}_3 = \frac{1}{\mu}\begin{bmatrix} 0 & -2 \\ 0 & 1 + 2a \end{bmatrix}, \mathrm{D}_0 = 2\iota\begin{bmatrix} \zeta_h\omega_h & 0 \\ 0 & r^2\zeta_\theta\omega_\theta \end{bmatrix}, \mathrm{K}_0 = \begin{bmatrix} \omega_h^2 & 0 \\ 0 & r^2\omega_\theta^2 \end{bmatrix} \tag{22}$$

with parameters as per Table 1. See Pons and Gutschmidt [28] or Hodges and Pierce [4] for details. Taking $C(\kappa) = 1$ corresponds to the assumption of quasisteady aerodynamics, and with a change of variables produces a polynomial system:

$$(\mathrm{G}_0\chi^2 + \mathrm{G}_1\Upsilon\chi + \mathrm{G}_2\Upsilon^2 - \mathrm{D}_0\chi - \mathrm{K}_0)\mathbf{x} = \mathbf{0}, \tag{23}$$

where $\Upsilon = U/b$ is the local airspeed per semichord. This polynomial system be linearized and solved with the operator determinant method of Section 3.

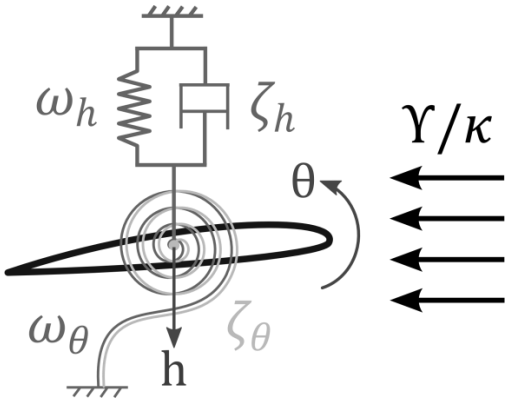

Figure 1. Schematic of section model

Table 1: Parameter values for the section model

Parameter	Value
mass ratio – μ	20
radius of gyration – r	0.4899
bending nat. freq. – ω_h	0.5642 rad/s
torsional nat. freq. – ω_θ	1.4105 rad/s
bending damping – ζ_h	1.4105 %
torsional damping – ζ_θ	2.3508 %
static imbalance – r_θ	-0.1
pivot point location – a	-0.2

The results of this process are shown in Figure 2(a), which includes a contour plot of the system. The flutter point is located at $\chi = 1.20$ rad/s and $\Upsilon = 1.98$ Hz ($\kappa = 0.606$). This agrees with nondimensional analytical results by Hodges and Pierce [4]. We can, however, go further than an analytical approach: we increase the matrix coefficient system size arbitrarily (and the polynomial system order) and still obtain exact solutions. A direct solver for polynomial flutter problems of arbitrary size and order has never before been presented.

We can also consider the case when $C(\kappa)$ is fully variable. The resulting MEP is nonlinear; however a variety of approximations for Theodorsen's function are available. We take a rational function given by Jones [36]:

$$C(\kappa) = \frac{\frac{1}{2}\kappa^2 + c_1\kappa + c_2}{\kappa^2 + c_3\kappa + c_2}, \tag{23}$$

with $c_1 = -0.2808\iota$, $c_2 = -0.01365$, $c_3 = -0.3455\iota$. Manipulating Eq. 20 we then obtain a polynomial problem of maximum order $\kappa^4\chi^2$, requiring a custom linearization of 10 blocks width. This be solved via the operator determinant method in under 0.2s on a laptop computer. The results are shown in Figure 2(b), also with a contour plot of the system. The fact that this solver is direct is a significant advantage over existing solvers for systems of this form.

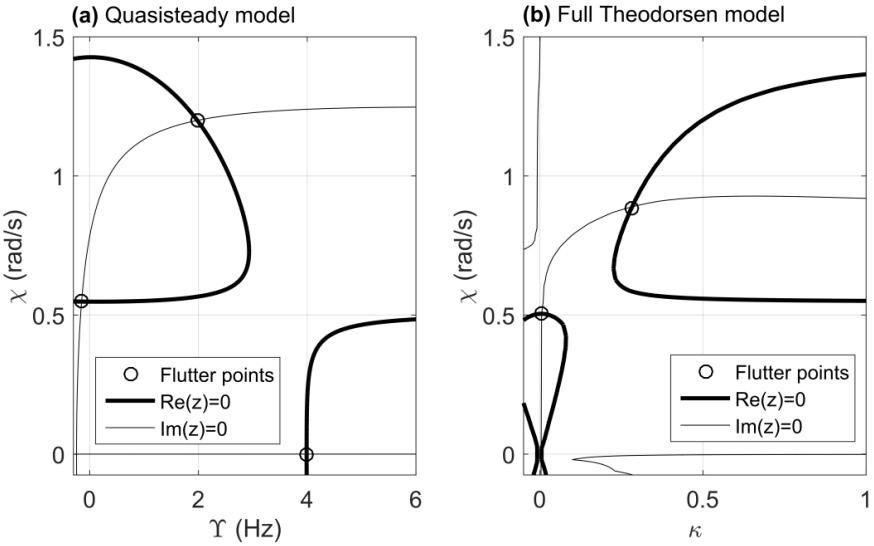

Figure 2. Flutter point results for the section model with two aerodynamic models.

5.2. Goland wing

As a benchmark test for our iterative algorithms, we analyse the well-known Goland Wing test case – representing a cantilever Euler-Bernoulli beam and Saint-Venant torsion model, with strip theory Theodorsen aerodynamics [37]. Originally a differential MEP (containing spatial derivatives as well as eigenvalue parameters), it is transformed by the Generalised Laplace Transform Method (GLTM) [35] into a nonlinear algebraic problem or fixed size (12×12). This transformation is without discretisation error, though it comes at the cost of obscuring the internal structure of the model – hence we treat the transformed problem as black-box nonlinear MEP. There is a small variation in parameter values for the Goland wing and so we take parameter values from Pons and Gutschmidt [35] and Wang [38]. For these parameters the Goland wing's first flutter point is located at airspeed $U_F = 138\,\mathrm{m/s}$ and modal frequency $\chi_F = 69.9\,\mathrm{rad/s}$. The first divergence point (static instability) is located nearby at $U_D = 253\,\mathrm{m/s}$. Figure 3 shows example SLP iteration paths converging to the flutter point, divergence point, and undamped modal frequencies at zero airspeed (also technically flutter points). All iterations are convergent, and agree with the results from the

literature. Figure 4 shows the convergence basins of the SLP and ICP algorithms to the flutter point, computed numerically. The SLP algorithm has the larger basin; though both are very satisfactory and the ICP is more computationally efficient.. The SLP algorithm is likely to be attractive for smaller systems with little a priori knowledge, whereas the ICP is effective for larger and more expensive systems, for which an initial flutter point estimate from an approximate model be available.

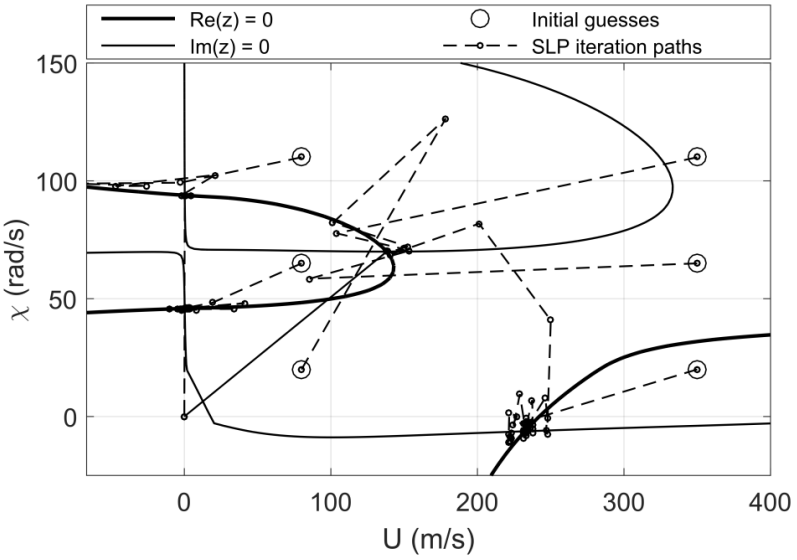

Figure 3. Six example iterations of the SLP algorithms applied to the Goland wing.

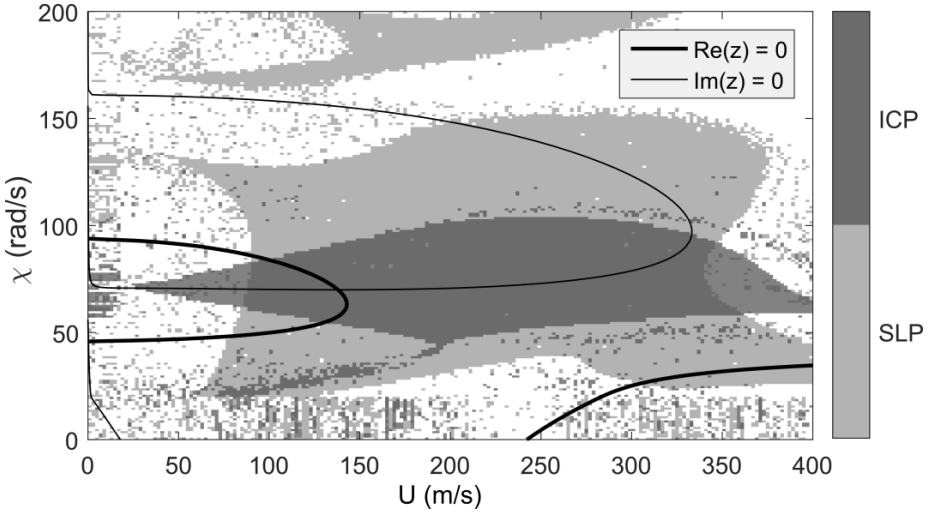

Figure 4. Convergence basins of the SLP and ICP algorithms to the Goland wing first flutter point.

6. Conclusions

In this paper we have demonstrated and discussed the use of multiparameter solution techniques for the solution of aeroelastic stability problems. We have introduced the link between multiparameter spectral theory and stability analysis, and we showed how this link can be used to reformulate stability problems with a complex-valued stability metric and a pertinent environmental parameter into a two-parameter eigenvalue problem. We demonstrated that this allows the direct solution of polynomial stability problems, as well as approximate direct and iterative solution methods for strongly nonlinear problems. The application of multiparameter methods – in aeroelasticity and in other disciplines – has the potential to provide a wide variety of new methods for stability analysis.

References

[1] Dowell, E. H., *Aeroelasticity of plates and shells*, Noordhoff International Publishing, Leyden, The Netherlands, 1975.

[2] Dowell, E. H., and Ilgamov, M., *Studies in Nonlinear Aeroelasticity*, Springer-Verlag, New York, 1988.

[3] Bisplinghoff, R. L., Ashley, H., and Halfman, R. L., *Aeroelasticity*, Addison-Wesley, Reading, MA, 1957.

[4] Hodges, D. H., and Pierce, G. A., *Introduction to Structural Dynamics and Aeroelasticity*, Cambridge University Press, New York, 2011.

[5] Hassig, H. J., "An approximate true damping solution of the flutter equation by determinant iteration.," *Journal of Aircraft*, 8, 11 (1971), pp. 885–889. DOI:10.2514/3.44311.

[6] Haddadpour, H., and Firouz-Abadi, R. D., "True damping and frequency prediction for aeroelastic systems: The PP method," *Journal of Fluids and Structures*, 25, 7 (2009), pp. 1177–1188. DOI:10.1016/j.jfluidstructs.2009.06.006.

[7] Namini, A., Albrecht, P., and Bosch, H., "Finite element-based flutter analysis of cable-suspended bridges," *Journal of Structural Engineering*, 118, 6 (1992), pp. 1509–1526. DOI:10.1061/(ASCE)0733-9445(1992)118:6(1509).

[8] Chen, P. C., "Damping perturbation method for flutter solution: the g-method," *AIAA Journal*, 38, 9 (2000), pp. 1519–1524. DOI:10.2514/2.1171.

[9] Lind, R., and Brenner, M., *Robust aeroservoelastic stability analysis*, Springer-Verlag, London, 1999.

[10] Borglund, D., "Robust aeroelastic stability analysis considering frequency-domain aerodynamic uncertainty," *Journal of Aircraft*, 40, 1 (2003), pp. 189–193. DOI:10.2514/2.3074.

[11] Borglund, D., "The mu-k method for robust flutter solutions," *Journal of Aircraft*, 41, 5 (2004), pp. 1209–1216. DOI:10.2514/1.3062.

[12] Irani, S., and Sazesh, S., "A new flutter speed analysis method using stochastic approach," *Journal of Fluids and Structures*, 40 (2013), pp. 105–114. DOI:10.1016/j.jfluidstructs.2013.03.018.

[13] Afolabi, D., "Flutter analysis using transversality theory," *Acta mechanica*, 103, 1–4 (1994), pp. 1–15. DOI:10.1007/BF01180214.

[14] Afolabi, D., Pidaparti, R. M. V., and Yang, H. T. Y., "Flutter Prediction Using an Eigenvector Orientation Approach," *AIAA Journal*, 36, 1 (1998), pp. 69–74. DOI:10.2514/2.353.

[15] Meerbergen, K., Schröder, C., and Voss, H., "A Jacobi-Davidson method for two-real-parameter nonlinear eigenvalue problems arising from delay-differential equations," *Numerical Linear Algebra with Applications*, 20, 5 (2013), pp. 852–868. DOI:10.1002/nla.1848.

[16] Meerbergen, K., and Spence, A., "Inverse Iteration for Purely Imaginary Eigenvalues with Application to the Detection of Hopf Bifurcations in Large-Scale Problems," *SIAM Journal on Matrix Analysis and Applications*, 31, 4 (2010), pp. 1982–1999. DOI:10.1137/080742890.

[17] Hochstenbach, M. E., and Plestenjak, B., "A Jacobi-Davidson Type Method for a Right Definite Two-Parameter Eigenvalue Problem," *SIAM Journal on Matrix Analysis and Applications*, 24, 2 (2002), pp. 392–410. DOI:10.1137/S0895479801395264.

[18] Hochstenbach, M. E., Muhič, A., and Plestenjak, B., "On linearizations of the quadratic two-parameter eigenvalue problem," *Linear Algebra and its Applications*, 436, 8 (2012), pp. 2725–2743. DOI:10.1016/j.laa.2011.07.026.

[19] Plestenjak, B., "A continuation method for a weakly elliptic two-parameter eigenvalue problem," *IMA Journal of Numerical Analysis*, 21, 1 (2001), pp. 199–216. DOI:10.1093/imanum/21.1.199.

[20] Quarteroni, A., Sacco, R., and Saleri, F., *Numerical mathematics*, Springer-Verlag Berlin, Berlin, Germany, 2007.

[21] Cottin, N., "Dynamic model updating – a multiparameter eigenvalue problem," *Mechanical Systems and Signal Processing*, 15, 4 (2001), pp. 649–665. DOI:10.1006/mssp.2000.1362.

[22] Hochstenbach, M. E., Muhič, A., and Plestenjak, B., "Jacobi–Davidson methods for polynomial two-parameter eigenvalue problems," *Journal of Computational and Applied Mathematics*, 288 (2015), pp. 251–263. DOI:10.1016/j.cam.2015.04.019.

[23] Meerbergen, K., and Plestenjak, B., "A Sylvester-Arnoldi type method for the generalized eigenvalue problem with two-by-two operator determinants," *Numerical Linear Algebra with Applications*, 22, 6 (2015), pp. 1131–1146. DOI:10.1002/nla.2005.

[24] Hochstenbach, M. E., and Plestenjak, B., "Harmonic Rayleigh–Ritz extraction for the multiparameter eigenvalue problem," *Electronic Transactions on Numerical Analysis*, 29 (2008), pp. 81–96.

[25] Muhič, A., and Plestenjak, B., "On the quadratic two-parameter eigenvalue problem and its linearization," *Linear Algebra and its Applications*, 432, 10 (2010), pp. 2529–2542. DOI:10.1016/j.laa.2009.12.022.

[26] Muhič, A., and Plestenjak, B., "On the singular two-parameter eigenvalue problem," *Electronic Journal of Linear Algebra*, 18 (2009), pp. 420–437.

[27] Plestenjak, B., and Muhič, A., *MultiParEig 1.0*, MATLAB File Exchange, Ljubljana, Slovenia, 2015.

[28] Pons, A., and Gutschmidt, S., "Multiparameter Solution Methods for Semi-structured Aeroelastic Flutter Problems," *AIAA Journal*, online article in advance (2017).

[29] Ruhe, A., “Algorithms for the Nonlinear Eigenvalue Problem,” *SIAM Journal on Numerical Analysis*, 10, 4 (1973), pp. 674–689. DOI:10.1137/0710059.

[30] Pons, A., “Aeroelastic flutter as a multiparameter eigenvalue problem,” Master’s Thesis, University of Canterbury, 2015, Gutschmidt, S.

[31] Plestenjak, B., “Numerical methods for nonlinear two-parameter eigenvalue problems,” *BIT Numerical Mathematics*, 56, 1 (2016), pp. 241–262. DOI:10.1007/s10543-015-0566-9.

[32] Podlevskyi, B. M., “Numerical solution of some two-parameter eigenvalue problems,” *Journal of Mathematical Sciences*, 165, 2 (2010), pp. 214–220. DOI:10.1007/s10958-010-9791-6.

[33] Podlevskii, B. M., “Newton’s method as a tool for finding the eigenvalues of certain two-parameter (multiparameter) spectral problems,” *Computational Mathematics and Mathematical Physics*, 48, 12 (2008), pp. 2140–2145. DOI:10.1134/S0965542508120038.

[34] Golub, G. H., and Van Loan, C. F., *Matrix computations*, The Johns Hopkins University Press, Baltimore, MA, 2013.

[35] Pons, A., and Gutschmidt, S., “Aeroelastic Flutter of Continuous Systems: A Generalized Laplace Transform Method,” *Journal of Applied Mechanics*, 83, 8, (2016), p. 081005. DOI:10.1115/1.4033597.

[36] Jones, R., *Operational treatment of the nonuniform-lift theory in airplane dynamics*, National Advisory Committee for Aeronautics, Washington D.C., 1938.

[37] Goland, M., “The Flutter of a Uniform Cantilever Wing,” *Journal of Applied Mechanics*, 12, 4 (1945), pp. A197–A208.

[38] Wang, I., “Component Modal Analysis of a Folding Wing,” Master’s Thesis, Duke University, 2011, Dowell, E.

Arion Pons, M.E. (Ph.D. student): Department of Engineering, University of Cambridge, Trumpington st., Cambridge CB2 1PZ, United Kingdom (*adp53@cam.ac.uk*). The author gave a presentation of this paper during one of the conference sessions.

Stefanie Gutschmidt, Senior Lecturer: Department of Mechanical Engineering, University of Canterbury, Private Bag 4800, Christchurch 8140, New Zealand (*stefanie.gutschmidt@canterbury.ac.nz*).

Theoretical and experimental investigations of nonlinear vibrations of a beam with piezoelectric actuators

Jacek Przybylski, Grzegorz Gąsiorski

Abstract: This paper presents theoretical and experimental investigations of the nonlinear flexural vibrations of a structure composed of a host beam with piezoelectric ceramic actuators symmetrically bonded to its top and bottom surfaces. The composite beam is supported at its ends to completely restrain axial displacements or to impose the displacement of one or both ends. Applying voltage to piezoelectric actuators one creates prestress which can stabilize the structure when the external compressive force appears. The analytical model for describing flexural vibration of a beam under both the external load and piezoelectric actuation is based on the Euler–Bernoulli model. The piezo material exhibits linear piezoelectricity with constitutive equations including electromechanical coupling. Due to the geometrical nonlinearity, the solution to the problem has been obtained by using the Lindstedt-Poincare method. The main results concern the effect of the residual piezo force on the non-linear vibration frequency of the structure. In the experimental part of the study two laboratory stands has been designed and built for three- and five segmented beams to find out and prove the effect of the electric field on the residual force and the natural frequency of both systems. A very good agreement between theoretical and experimental results has been observed.

1. Introduction

The problem of nonlinear vibration of beams with both ends restrained against axial displacement has been studied for many years on the basis of both the continuum approach [1-4] and the finite element method [5]. While most publications concerned classical Bernoulli-Euler beams, the effects of shear deformation and rotary inertia in the case of moderately thick and short beams are also reflected in the literature. Raju and Rao [3] used the admissible polynomial functions with multiple terms for evaluating the nonlinear (large amplitude) free-vibration behaviour of beams with axially immovable ends. The formulation based on the principle of conservation of the total energy of the vibrating system were applied to obtain the ratios of the nonlinear to linear frequencies for various maximum amplitude ratios. One- and two-term solutions were obtained for the uniform clamped–clamped beam and pinned–clamped beam. The two-term solutions showed a very good agreement with the accurate finite element solutions available in the literature. A general model based on Hamilton's principle was derived by Azrar et al. [4] who used spectral analysis, Lagrange's equations and the harmonic balance

method to describe non-linear free vibrations occurring at large displacement amplitudes of fully clamped and simply supported beams. It was shown that the numerical results obtained by the formulations presented in that work are very helpful when the higher order of accuracy is needed for very large amplitudes.

Piezoceramic smart materials are thoroughly applied for actuators and sensors applications because of their high electromechanical coupling coefficients. They are used, among others, for vibration control in civil engineering structures like beams, trusses, steel frames and cable-stayed bridges. These materials exhibit different types of nonlinearities under different combinations of electric and mechanical fields. A review of more than 90 papers including active, passive, semi-active and hybrid vibration control systems was presented by Song et al. [6]. Hagedorn and his colleagues provided an important contribution to the modeling and experimental testing of the nonlinear phenomena in piezoceramic actuators [7, 8] and piezo-beams systems [9]. It was observed in [7] that piezoceramics, when excited near resonance in the presence of weak electric fields, exhibit typical nonlinearities similar to a Duffing oscillator such as jump phenomena and presence of superharmonics in the response spectra. To model such nonlinearities, a nonlinear electric enthalpy density function (using quadratic and cubic terms) valid for a general 3-D piezoelectric continuum was proposed in that work. In order to optimize the existing applications and develop new applications based on the d_{15}-effect of piezoceramic actuators, the nonlinear effects such as softening behavior was modeled in [8] using higher-order cubic conservative and nonconservative terms in the constitutive equations. Using the approximate solution, nonlinear parameters were identified by comparing the theoretical and experimental results. One observed in [9] during experimental tests, typical non-linear effects in piezoceramics and in piezo–beam systems excited at resonance by weak electric fields, e.g., dependence of the resonance frequency on the amplitude, superharmonics in spectra and a non-linear relationship between excitation voltage and vibration amplitude. The equations of motion for the system consideration were derived via the Ritz method using Hamilton's principle. After determination the nonlinear' parameters, the numerical results were compared to those obtained experimentally.

The main idea of this paper is to find out how piezo actuators in the form of ceramic patches bounded symmetrically to a rectilinear beam might influence its static performance and nonlinear vibration. It is assumed that the beam from Fig. 1, being unloaded in its reference configuration, is subjected to a prescribed axial displacement of one of the supports, which leads to the initial stress. The same prestress can be achieved by the compressive axial force, which is related to the axial displacement according to Hook's law. The residual axial force, induced by piezoactuators applying the same in-phase voltage, may counteract the external load to prevent the structure becoming unstable. The effectiveness of inducing favourable in-plane stress by using piezoelectric elements to

enhance the mechanical performance of beams was investigated by Oguamanan et al. [10] and Faria [11]. In both works piezoelements were co-locally bonded to the top and bottom surfaces of a beam with a rectangular cross section and longitudinally restrained ends. It is necessary to add that only in the case when both ends of the beam are constrained against longitudinal displacement, the piezoelectric actuators may transfer the tensile forces to the substructure according to the applied voltage.

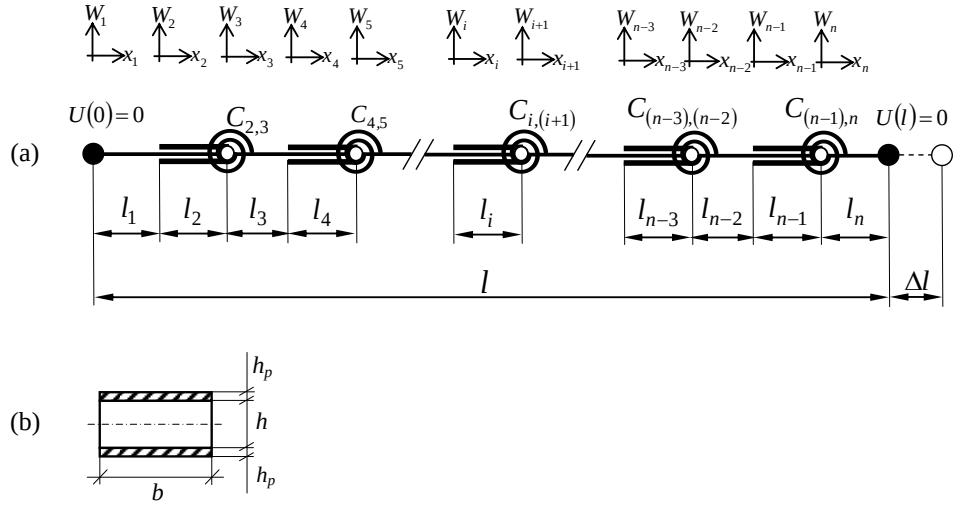

Figure 1. *N*-segmented beam with co-locally surface-bonded piezoactuators (a), cross-section of the piezo-segment (b).

The particular segments of the beam from Fig. 1 are connected to each other by frictionless pin joints with linear massless torsional springs. Modifying the stiffness of the sprigs from zero to infinity one may compare the system response adequate to its rigidity and, secondly, this type of articulation is often used as a crack model [12]. Free and forced vibrations of beams with cracks have been studied extensively for four decades due to its practical importance in order to e.g. control the dynamic response of structures to find a possible discrepancy between standard parameters and those demonstrating an unusual behaviour resulting from the presence of structure surface damage.

2. Formulation of the problem

The considered piezo-beam system shown in Fig. 1 represents *n*-segmented articulated rectilinear stepped beam which ends after application of an initial longitudinal displacement (Δl) are axially constrained. The change in the cross section area of the beam results from the application of $(n\text{-}1)/2$ pairs of collocated piezoceramic actuators bonded to the host structure. Przybylski derived in [13] that

such number of piezoactuators of the same cross-sectional area ($b \times h_p$), being supplied with an equal homogeneous electric field characterised by the voltage V, generate the residual piezo-force equal to:

$$F_r = F \sum_{i=1}^{\frac{1}{2}(n-1)} l_{2i} \left(\sum_{i=1}^{\frac{1}{2}(n-1)} l_{2i} + a_m \sum_{i=1}^{\frac{1}{2}(n+1)} l_{2i-1} \right)^{-1} \tag{1}$$

where: $a_m = (1 + E_p A_p)/EA$ denotes the axial stiffness ratio of the piezosegment to that of the beam, l_i is the length of the i-th segment, E_p, E are the Young's modulus of the piezoceramic and the beam, respectively, A_p, A are the cross section areas of the piezoactuators and the beam, respectively, and

$$F = -2be_{31}V \tag{2}$$

is the piezoelectric force resulting from the voltage V applied to one pair of actuators of width b made of the ceramic material characterised by piezoelectric strain constant e_{31}. In the derivation one assumed the linear electromechanical coupling and that for thin piezoceramic stripes d_{33}-effect could be omitted. It follows from the form of Eq. (1) that the residual force F_r being independent of piezosegments' location, depends not only on the piezoelectric force F, but also on the axial stiffness ratio a_m and the ratio between the length of all piezosegments to whole length of the beam.

Due to the large amplitude of the vibrations, the problem is formulated with the use of the von Karman nonlinear equations along with Bernoulli-Euler beam theory:

$$\varepsilon(x,t) = \frac{\partial U(x,t)}{\partial x} + \frac{1}{2}\left[\frac{\partial W(x,t)}{\partial x}\right]^2 \tag{3}$$

$$\kappa(x,t) = -\frac{\partial^2 W(x,t)}{\partial x^2} \tag{4}$$

where $\varepsilon(x,t)$ is the mid-plane strain, $\kappa(x,t)$ is the curvature, $U(x,t)$, $W(x,t)$ are the axial and transverse displacement, respectively.

2.1. Governing equations

To derive the governing equations which are given by the equations of motion one applies Hamilton's principle which for the conservative system takes the form:

$$\delta \int_{t_1}^{t_2} (T - V)dt = \int_{t_1}^{t_2} (\delta T - \delta V)dt = \int_{t_1}^{t_2} \delta T dt - \int_{t_1}^{t_2} \delta V dt = 0 \tag{5}$$

where T and V are the kinetic and potential energies, respectively.

The kinetic energy of the system from Fig. 1 is expressed as follows:

$$T = \frac{1}{2}\sum_{i=1}^{n} \int_0^{l_i} \rho_i A_i \left[\frac{\partial W_i(x_i,t)}{\partial t}\right]^2 dx_i \tag{6}$$

whereas the potential energy is equal to:

$$V = \frac{1}{2}\sum_{i=1}^{n}\left\{\int_0^{l_i} E_i J_i \left[\frac{\partial^2 W_i(x_i,t)}{\partial {x_i}^2}\right]^2 dx_i + \int_0^{l_i} E_i A_i \left[\frac{\partial U_i(x_i,t)}{\partial x_i} + \frac{1}{2}\left(\frac{\partial W_i(x_i,t)}{\partial x_i}\right)^2\right]^2 dx_i\right\} +$$
$$+ \frac{1}{2}\sum_{i=1}^{\frac{1}{2}(n-1)} C_{2i,2i+1}\left[\left.\frac{\partial W_{2i}(x_{2i},t)}{\partial x_{2i}}\right|_{x_{2i}=l_{2i}} - \left.\frac{\partial W_{2i+1}(x_{2i+1},t)}{\partial x_{2i+1}}\right|_{x_{2i+1}=0}\right]^2 - \frac{1}{2}R\sum_{i=1}^{n}\int_0^{l_i}\left[\frac{\partial W_i(x_i,t)}{\partial x_i}\right]^2 dx_i \tag{7}$$

where $C_{2i,2i+1}$ is the stiffness of the rotational spring located between two segments identified by the subscripts.

The piezosegments denoted in the expressions for energies (6, 7) by even indices have their bending and axial stiffnesses as well as masses per unit length equal to the respective sums of those for the host beam and piezoceramic layers. The axial force R has got two components:

$$R = F_r + P \tag{8}$$

- the residual force F_r and force P which results from an initial prescribed displacement of one or two supports. The value of the latter force may be determined from Hooke's law.

After inserting Eqs. (6) and (7) into Eq. (5), performing necessary integration and variational operations with assumptions that virtual displacements $\delta W_i(x_i,t)$ and $\delta U_i(x_i,t)$ are independent and arbitrary within each interval $0 < x_i < l_i$, one obtains the following system of $2n$ governing equations:

$$E_i J_i \frac{\partial^4 W_i(x_i,t)}{\partial x_i^4} - E_i A_i \frac{\partial}{\partial x_i}\left\{\left[\frac{\partial U_i(x_i,t)}{\partial x_i} + \frac{1}{2}\left(\frac{\partial W_i(x_i,t)}{\partial x_i}\right)^2\right]\frac{\partial W_i(x_i,t)}{\partial x_i}\right\} +$$
$$+ R\frac{\partial^2 W_i(x_i,t)}{\partial {x_i}^2} + \rho_i A_i \frac{\partial^2 W_i(x_i,t)}{\partial t^2} = 0, \tag{9}$$

$$\frac{\partial}{\partial x_i}\left[\frac{\partial U_i(x_i,t)}{\partial x_i} + \frac{1}{2}\left(\frac{\partial W_i(x_i,t)}{\partial x_i}\right)^2\right] = 0, \qquad i = 1, 2,..., n \tag{10}$$

Integration of Eq. (10) may be useful for defining an axial dynamic stretching force $S(t)$ which appears along each segment of the beam during transversal vibrations. Hence both Eqs. (9) and (10) may be transformed to the form:

$$E_i J_i \frac{\partial^4 W_i(x_i,t)}{\partial x_i^4} + [R - S(t)]\frac{\partial^2 W_i(x_i,t)}{\partial {x_i}^2} + \rho_i A_i \frac{\partial^2 W_i(x_i,t)}{\partial t^2} = 0 \tag{11}$$

$$S(t) = E_i A_i\left[\frac{\partial U_i(x_i,t)}{\partial x_i} + \frac{1}{2}\left(\frac{\partial W_i(x_i,t)}{\partial x_i}\right)^2\right] \qquad i = 1, 2,..., n \tag{12}$$

For the sake of providing more general analysis and discussion of results, the non-dimensional form of governing equations are introduced on the basis of the following introductions:

$$\xi_i = \frac{x_i}{l}, \quad d_i = \frac{l_i}{l}, \quad w_i(\xi_i,\tau) = \frac{W_i(x_i,t)}{l}, \quad u_i(\xi_i,\tau) = \frac{U_i(x_i,t)}{l}, \quad \tau = \Omega t,$$

$$f_r = \frac{F_r l^2}{EJ}, \quad f = \frac{Fl^2}{EJ}, \quad p = \frac{Pl^2}{EJ}, \quad r = \frac{Rl^2}{EJ}, \quad s(\tau) = \frac{S(t)l^2}{EJ}, \quad c_{i,i+1} = \frac{C_{i,i+1}l}{EJ} \tag{13}$$

$$\alpha_1 = \frac{E_p}{E}, \quad \alpha_2 = \frac{\rho_p}{\rho}, \quad r_m = \frac{E_p J_p}{EJ}, \quad \omega^2 = \Omega^2 l^4 \frac{\rho A}{EJ}, \quad \lambda = \frac{Al^2}{J}, \quad l = \sum_{i=1}^{n} l_i .$$

Hence the non-dimensional equation of motion of the *i*-th segment takes the form:

$$w_i^{IV}(\xi_i,\tau) + m_i[r - s(\tau)]w_i^{II}(\xi_i,\tau) + n_i\omega^2 \ddot{w}_i(\xi_i,\tau) = 0, \qquad i = 1, 2,..., n \tag{14}$$

where:

$$m_i = (1 + r_m)^{-\frac{1}{2}\left(j^{2i}+1\right)}, \qquad n_i = \left[\frac{\alpha_1 + (a_m - 1)\alpha_2}{\alpha_1(1 + r_m)}\right]^{\frac{1}{2}\left(j^{2i}+1\right)}, \qquad j = \sqrt{-1} \tag{15}$$

and Roman numerals denote the order of derivative with respect to the space variable and dots with respect to time.

Knowing that the axial displacement of supports are equal to zero ($u_1(0) = u_n(l_n) = 0$), dimensionless force $s(\tau)$ existing in Eq. (14) may be presented as:

$$s(\tau) = \frac{\lambda}{2}\left[\sum_{i=1}^{\frac{1}{2}(n+1)} d_{2i-1} + \frac{1}{a_m}\sum_{i=1}^{\frac{1}{2}(n-1)} d_{2i}\right]^{-1} \sum_{i=1}^{n}\int_0^{d_i}\left[\frac{\partial w_i(\xi_i,\tau)}{\partial \xi_i}\right]^2 d\xi_i \tag{16}$$

2.2. Boundary conditions

As the solution and analysis of the problem makes possible to cover all types of supports which provide axial restraint of the beam-ends, the boundary conditions are divided into two groups:

- the first group, being independent from the type of supports, describes the continuity of the piezo-beam system and the equality of the shearing forces and the bending moments at the piezo-segment boundaries (natural boundary conditions derived from Hamilton's principle):

$$w_i(\xi_i,\tau)\big|_{\xi_i = d_i} = w_{i+1}(\xi_{i+1},\tau)\big|_{\xi_{i+1}=0}, \qquad i = 1, 2,..., n\text{-}1 \tag{17}$$

$$w_i^I(\xi_i,\tau)\big|_{\xi_i = d_i} = w_{ii+1}^I(\xi_{i+1},\tau)\big|_{\xi_{i+1}=0}, \qquad i = 1, 3,..., n\text{-}2 \tag{18}$$

$$w_i^{II}(\xi_i,\tau)\Big|_{\xi_i=d_i} - (1+r_m)w_{i+1}^{II}(\xi_{i+1},\tau)\Big|_{\xi_{i+1}=0} = 0\,, \qquad i = 1, 3,..., n\text{-}2 \qquad (19)$$

$$(1+r_m)w_i^{II}(\xi_i,\tau)\Big|_{\xi_i=d_i} + c_{i,i+1}\left[w_i^{I}(\xi_i,\tau)\Big|_{\xi_i=d_i} - w_{i+1}^{I}(\xi_{i+1},\tau)\Big|_{\xi_{i+1}=0} \right] = 0\,, \qquad i = 2, 4,..., n\text{-}1 \qquad (20)$$

$$w_{i+1}^{II}(\xi_{i+1},\tau)\Big|_{\xi_{i+1}=0} + c_{i,i+1}\left[w_i^{I}(\xi_i,\tau)\Big|_{\xi_i=d_i} - w_{i+1}^{I}(\xi_{i+1},\tau)\Big|_{\xi_{i+1}=0} \right] = 0\,, \qquad i = 1, 3,..., n\text{-}2 \qquad (21)$$

$$w_i^{III}(\xi_i,\tau)\Big|_{\xi_i=d_i} - (1+r_m)w_{i+1}^{III}(\xi_{i+1},\tau)\Big|_{\xi_{i+1}=0} = 0\,, \qquad i = 1, 3,..., n\text{-}2 \qquad (22)$$

$$w_i^{III}(\xi_i,\tau)\Big|_{\xi_i=d_i} + [r - s(\tau)]w_i^{I}(\xi_i,\tau)\Big|_{\xi_i=d_i} - (1+r_m)w_{i+1}^{III}(\xi_{i+1},\tau)\Big|_{\xi_{i+1}=0} - [r - s(\tau)]w_{i+1}^{I}(\xi_{i+1},\tau)\Big|_{\xi_{i+1}=0} = 0 \qquad i = 2, 4,..., n\text{-}1 \qquad (23)$$

- the second group specifies the type of supports. For the pin-ended system the boundary conditions are:

$$w_1(\xi_1,\tau)\Big|_{\xi_1=0} = w_n(\xi_n,\tau)\Big|_{\xi_n=d_n} = w_1^{II}(\xi_1,\tau)\Big|_{\xi_1=0} = w_n^{II}(\xi_n,\tau)\Big|_{\xi_n=d_n} = 0\,, \qquad (24)$$

For a beam with clamped ends, both the displacement w and the slope w^I are equal to zero at those ends, whereas for a beam with both ends sliding the slope w^I and the shearing force - EIw^{III} vanish at the supporting points. When a mixed type of support is used, adequate boundary conditions need to be chosen from those described above.

2.3. Approximate solution

Lindstedt-Poincare method, which is a technique of uniformly approximating periodic solutions to ordinary differential equations, has been chosen to solve the stated non-linear boundary value problem. According to the method, the relevant quantities are expanded into exponential series with respect to the amplitude parameter ε ($\varepsilon << 1$).

$$w_i(\xi_i,\tau) = \sum_{n=1}^{N} \varepsilon^{2n-1} w_{i2n-1}(\xi_i,\tau) + \mathrm{O}\left(\varepsilon^{2N+1}\right), \qquad (25)$$

$$s(\tau) = \sum_{n=1}^{N} \varepsilon^{2n} s_{2n}(\tau) + \mathrm{O}\left(\varepsilon^{2(N+1)}\right) \qquad (26)$$

$$\omega^2 = \omega_0^2 + \sum_{n=1}^{N} \varepsilon^{2n}\, \omega_{2n}^2 + \mathrm{O}\left(\varepsilon^{2(N+1)}\right) \qquad (27)$$

where:

$$w_{ij}(\xi_i,\tau) \sum_{k=1}^{b} {}^{(2k-1)}w_{ij}(\xi_i)\cos(2k-1)\tau \qquad \text{for:} \quad b = \frac{j-1}{2} + 1 \qquad \text{and} \qquad j = 1,3,5,..., \qquad (28)$$

$$s_j(\tau)=\sum_{k=1}^{c} s_j^{(2k-2)}\cos 2(k-1)\tau \qquad \text{for:} \quad c=\frac{j}{2}+1 \qquad \text{and} \qquad j=2,4,6,... \tag{29}$$

By introducing Eqs. (25-27) into equations of motion (14) and axial force (16), then equating the terms of respective ε exponents to zero, one obtains an infinite set of equations, from which the first four equations are as follows:

$$\varepsilon^1: \qquad w_{i1}^{\ IV}(\xi_i,\tau)+m_i\, r\, w_{i1}^{\ II}(\xi_i,\tau)+n_i\,\omega_0^2\,\ddot{w}_{i1}(\xi_i,\tau)=0\,, \tag{30}$$

$$\varepsilon^2: \qquad s_2(\tau)=\frac{\lambda}{2}\left[\sum_{i=1}^{\frac{1}{2}(n+1)} d_{2i-1}+\frac{1}{a_m}\sum_{i=1}^{\frac{1}{2}(n-1)} d_{2i}\right]^{-1}\sum_{i=1}^{n}\int_0^{d_i}\left[\frac{\partial w_{i1}(\xi_i,\tau)}{\partial \xi_i}\right]^2 d\xi_i\,, \tag{31}$$

$$\varepsilon^3: \qquad w_{i3}^{\ IV}(\xi_i,\tau)+m_i\, r\, w_{i3}^{II}(\xi_i,\tau)+n_i\,\omega_0^2\,\ddot{w}_{i3}(\xi_i,\tau)=-m_i\, s_2(\tau) w_{i1}^{II}(\xi_i,\tau)-n_i\,\omega_2^2\,\ddot{w}_{i1}(\xi_i,\tau)\,, \tag{32}$$

$$\varepsilon^4: \qquad s_4(\tau)=\lambda\left[\sum_{i=1}^{\frac{1}{2}(n+1)} d_{2i-1}+\frac{1}{a_m}\sum_{i=1}^{\frac{1}{2}(n-1)} d_{2i}\right]^{-1}\sum_{i=1}^{n}\int_0^{d_i}\frac{\partial w_{i1}(\xi_i,\tau)}{\partial \xi_i}\frac{\partial w_{i3}(\xi_i,\tau)}{\partial \xi_i}d\xi_i \tag{33}$$

Boundary conditions for rising powers of ε, necessary for the solution procedure, are derived after introduction of Eqs. (25-26) into Eqs. (17-24). Having those sets of conditions, Eqs. (30-33) may be subjected to consecutive analytical solutions after separating time and space variables according to Eqs. (28-29). An analytical step-by-step process of the solution to these type of equations was given in [14]. The solution to Eq. (30) gives the relationship between load parameter *r*, which depends on both the nondimensional piezoelectric force *f* and force *p* resulting from the initial axial prestress, and the first term ω_0 of natural frequency ω. The second term of frequency ω_2 is established on the basis of the orthogonality condition applied to Eq. (32) to which the solution of Eqs. (30-31) has been previously introduced. Having computed ω_0 and ω_2 terms, the relationship between natural frequency ω and vibration amplitude parameter ε can be determined by using Eq. (27) with a customary restriction of up to the order of two terms. The procedure needs to apply the normalising condition in the form:

$$w_{max}=w_{i1}(\xi_A)=\varepsilon\sqrt{\lambda}\,, \tag{34}$$

where: ξ_A is the co-ordinate of maximal displacement determined by using derivative tests on the mode shape function, $\lambda=Al^2(J)^{-1}$ is the non-dimensional slenderness parameter of the host beam.

3. Exemplary numerical results

Knowing that the main object of the work is to find the effect of the residual piezoelectric force on the non-linear vibration of the system, the presented solution allows one to study the transversal

vibrations and stability of articulated stepped beams, i.e. the structures which are widely used in various engineering fields, such as robot arm and tall building, etc. Quasi-rigid connection between particular segments may be used for modelling a crack occurring in a structural element. Solution to Eq. (30) gives the opportunity to study the natural vibration frequency of an arbitrary mode as a function of the axial force. That has been done for three-segmented beam ($i = 3$) of three different support conditions and the following data: $a_m = 1.4242$, $\alpha_1 = 0.1484$, $\alpha_2 = 2.851$, $d_1 = d_3 = 0.2$, $d_2 = 0.6$. Fig. 2a shows the natural frequency of the first mode in dependency on the compressive and tensile force. The compressive axial force reduces the natural frequencies whereas the tensile force increases them independently from the way of supporting. The effect of compressive axial force is predominant over those of the corresponding tensile force on the natural frequency diminishing it to zero where the instability occurs. The tensile piezoelectric force increases the critical load whereas the compressive force diminishes it.

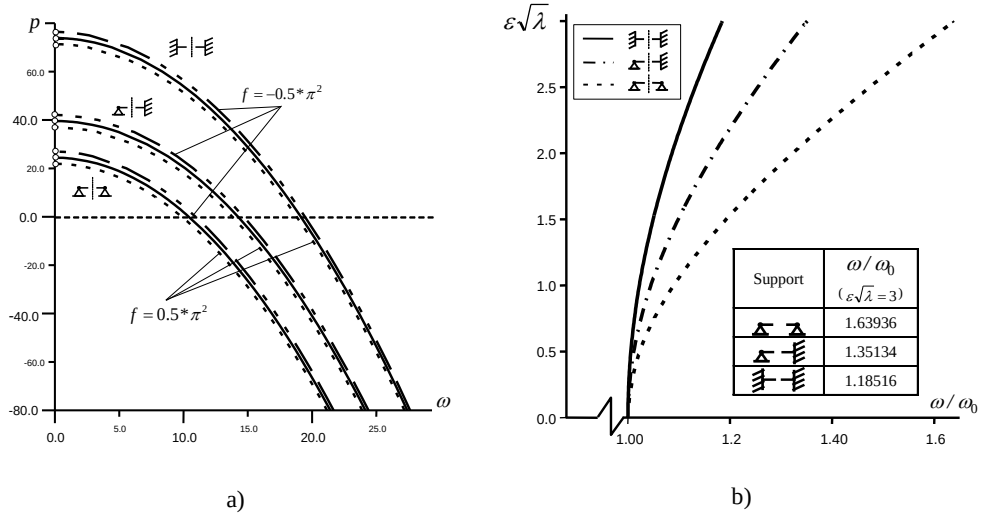

a) b)

Figure 2. Modification of the axial force-vibration frequency relationship by the piezoelectric force f for the three-segmented beam with different support conditions (a), Comparison of backbone curves for a fundamental mode of a homogeneous uniform beam with different supports (b)

The non-linear behaviour has been presented in the form of backbone curves in a dimensionless frequency-amplitude plane as in Fig. 2b for a homogeneous uniform beam with different support conditions. Such system has been chosen to validate the obtained results with those previously published. Both results are in a good agreement what is shown in Table 1.

Table 1. Comparison of the non-linear (ω) to linear natural frequency (ω_0) ratios for various support conditions for the uniform beam

ω/ω_0						
$\varepsilon\sqrt{\lambda}$						
	Authors	[4]	*Authors*	[3]	*Authors*	[4]
0	1	1	1	1	1	1
1	1.0222308	1.0222308	1.0448	1.0448	1.089724735	1.089724736
2	1.0861966	1.0861967	1.1692	1.1676	1.322875655	1.322875656
3	1.1851592	1.1851592	1.3513	1.3458	1.639359631	1.639359631

In Fig. 3a the amplitude-nonlinear frequency relationship is presented for a three-segmented beam with different spring stiffness c expressing local flexibility. As for the uniform beams, the shown curves characterise the nonlinearity of the hardening type. The greater the stiffness the lower the influence of the amplitude on the nonlinear frequency.

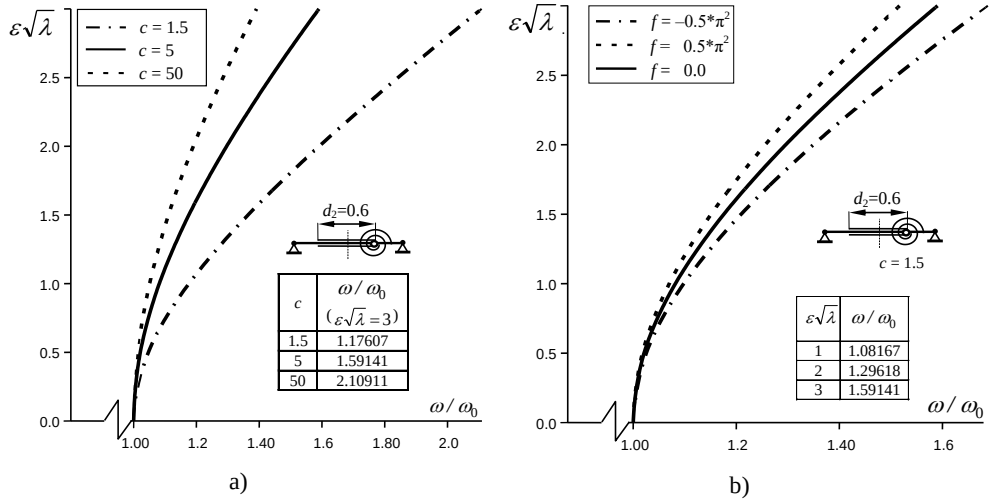

Figure 3. Comparison of backbone curves for a three-segmented beam with (a) different rotational spring stiffness, (b) different values of the piezoelectric force.

The effect of the piezoelectric force on the bone curves for the beam of the rotational spring stiffness c = 1.5 is sketched in Fig. 3b. The stretching of the beam realised by the piezoelectric force of the value $f = -0.5\pi^2$, where π^2 is the non-dimensional buckling critical force for the homogeneous uniform beam, decreases the nonlinear effect, whereas the compressing piezoelectric force $f = 0.5\pi^2$ increases this effect. The table settled in Fig. 3b contains ω/ω_0 values calculated for f = 0 and three values of the amplitude.

4. Experimental results

The test structure is a uniform aluminium beam with rectangular cross section and a pair of piezoelectric patches made of Soft PZT-PCM55 material (Noliac) which were symmetrically attached to either side of the beam - Fig. 4a. When both ends of the structure are clamped, the piezoelectric actuators under the electric field generate a residual axial force which can be calculated using Eq. (1)-(2) and measured by strain gauge transducers glued on both sides of the host beam and wired using Wheatstone bridge circuit. The strain gauge TFs-10/350 (Tenmex) had the base 10×15 [mm] of the thickness 60 [μm], resistance 350 [Ω] and accuracy ±0.2%. Details of the beam and piezoelectric patches are given in Table 2. The purpose of the first part of the experiment is to find the correspondence between theoretical and experimental results of the residual force when the voltage is gradually increased every 10 [V] from 0 to ±900 [V]. Before starting the force measurements using the experimental setup as in Fig. 4b, the bridge was calibrated by using an additional reference system loaded with known weights. The test was repeated fifty times at each level of the voltage and the average value of the measured residual force determined.

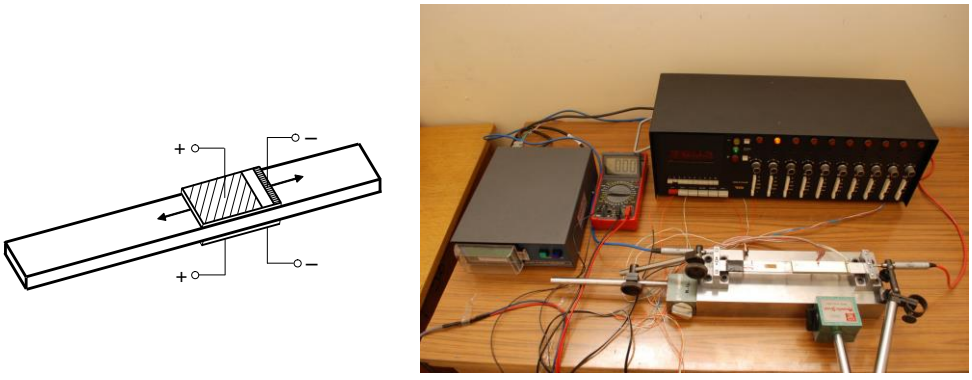

a) b)

Figure 4. Aluminium beam with co-locally surface-bonded piezoactuators (a), experimental setup for measuring residual forces (b).

The second part of the experiment concerned the natural frequency of the system as a function of the voltage applied to the piezoceramic patches. Two methods of measurements have been applied: the non-contact vibration measurement, which avoids mass loading or stiffness implications, by using Ometron VH-1000-D portable laser Doppler vibrometer of frequency range 0.5 [Hz] - 22 [kHz] and Brüel&Kjær accelerometer type 4508B, which was specifically designed to provide a combination of high sensitivity, low mass (4.8 [g]) and small physical dimensions. Both devices were connected to Brüel&Kjær 2515 vibration frequency spectrum analyzer.

Table 2. Parameters of the structure

Name	Beam	Piezoelectric patch
Length l [m]	0.23	0.09
Width b [m]	0.02	0.02
Thickness h [m]	0.002	0.002
Young's modulus E [GPa]	71.42	-
Poisson's ratio ν	0.3	0.3
Density ρ [kg/m^3]	3260.8	7930
Charge constant $-d_{31}$ [10^{-12} C/N]	-	325
Elastic compliance s_{11}^E [10^{-12} m^2/N]	-	15.8

During each test, after applying the voltage to the piezoceramic actuators, a smooth excitation by Brüel&Kjær 8202 impact hammer was imparted to the test structure over a broad frequency range. The output signal collected by laser Doppler vibrometer and accelerometer was processed by the analyzer (FFT) and presented in the form of vibration frequency spectrum on the computer linked to the analyzer.

Fig. 5a shows the correlation between the measured residual force as a function of the applied voltage and the computed voltage-residual force relationship. Both the stretching and compressing force has been determined and measured. Due to the linearity of the piezoceramic material model an adequate linear effect between the voltage and the force can be seen. The observed results indicate a small discrepancy in regard to the theoretical ones revealing a real nature of the phenomenon, but generally one can notice a very good correlation between both types of results.

Fig. 5b illustrates the relationship between the applied voltage and the natural vibration frequency obtained from both the theory and experimental tests. The maximum natural frequency equal to 135.4 [Hz] (an identical measured and calculated value) was obtained under -900 [V] voltage input generating the stretching force, whereas the minimum frequency: 118 [Hz] (measured) and 118.2 [Hz] (calculated) was observed for 900 [V] causing beam compressing. The frequency response for zero-voltage was equal to 127.7 [Hz] (theory) and 127.5 [Hz] (experiment). Simulation results were in very good agreement with experimental results.

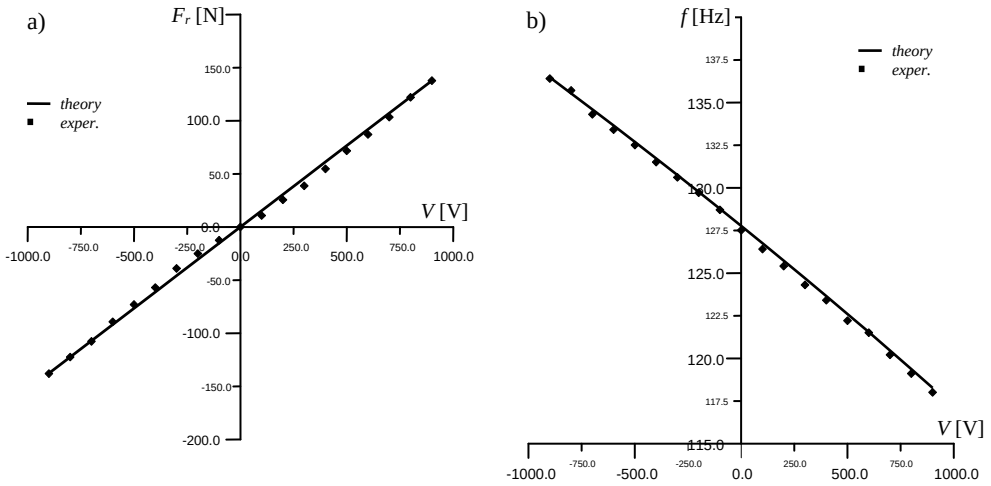

Figure 5. Response results of the (a) residual force and (b) vibration frequency at different voltage.

5. Conclusions

In this paper, non-linear vibration analysis of *n*-segmented articulated beams subjected to the prescribed end displacement was performed using a Bernoulli-Euler beam assumption and Lindstedt-Poincare method. The introductory results concerning an uniform beam provided good agreement with available results in the literature. The numerical results obtained for a three-segmented beam show that the amplitude–natural frequency relationship depends on the piezoelectric-induced in-plane stresses. Two opposing values of the piezoelectric force causing either stretching or compressing were taken for consideration. It was proved that the linear frequencies could be tuned by using the piezoelectric force. The tensile piezoforce increases the values of the linear natural frequency but decreases the non-linear effect, while the compressing force decreases the linear frequencies but increases the non-linear effect. The piezoelectric force may diminish or increase the critical buckling load dependently on the direction of the electric field vector.

Furthermore, an experimental setup for the measurement of residual forces and eigenfrequencies was introduced. The results of the experiment performed for a three segmented beam with two piezoceramic layers showed that the piezoelectric residual force increases with the increase of the applied voltage. The voltage affects also the natural vibration frequency of the system. All numerical results coincided well with the findings from numerical simulations.

References

[1] Wojnowsky-Krieger S. The effect of an axial force on the vibration of hinged beams. *Journal of Applied Mechanics* 17, (1950), 35-36.

[2] Evensen D.A. Nonlinear vibrations of beams with various boundary conditions. *AIAA Journal* 6, 2 (1968), 370-372.

[3] Raju K.K., Rao G.V. Towards improved evaluation of large amplitude free-vibration behaviour of uniform beams using multi-term admissible functions. *Journal of Sound and Vibration* 282, 3-5 (2005), 1238-1246.

[4] Azrar L., Benamar R., White R.G. Semi-analytical approach to the non-linear dynamic response problem of S–S and C–C beams at large vibration amplitudes Part I: General theory and application to the single mode approach to free and forced vibration analysis. *Journal of Sound and Vibration* 224, 2 (1999), 183-207.

[5] Sarma B.S., Varadan T.K. Ritz finite element approach to nonlinear vibrations of beams. *International Journal for Numerical Methods in Engineering* 20, 2 (1984), 353 – 367.

[6] Song G., Sethi V., Li, H.-N. Vibration control of civil structures using piezoceramic smart materials: A review. *Engineering Structures* 28, 11 (2006), 1513-1524.

[7] Samal M.K., Seshu P., Parashar S.K., von Wagner U., Hagedorn P., Dutta B.K., Kushawaha H. Nonlinear Behavior of Piezoceramics under Weak Electric Fields.Part I: Finite Element Formulation. *Int. J. of Solids and Structures* 43, 6 (2006), 1422–1436.

[8] Parashar S., von Wagner U., Hagedorn P. Nonlinear Shear-Induced Flexural Vibrations of Piezoceramic Actuators: Experiments and Modeling. *Journal of Sound and Vibration* 285, (2005), 989–1014.

[9] Von Wagner U., Hagedorn P. Piezo-Beam Systems Subjected to Weak Electric Field: Experiments and Modelling of Non-Linearities. *Journal of Sound and Vibration* 256, (2002), 861–872.

[10] Oguamanam D.C.D., Almeida S.F.M., Hansen J.S. Stress stiffening effects in laminated beams with piezoelectric actuators. *Journal of Intelligent Material Systems and Structures* 9, (1998) 137-145.

[11] Faria A.R. On buckling enhancement of laminated beams with piezoelectric actuators via stress stiffening. *Composite Structures* 65, 2, (2004) 187-192.

[12] Chondros, T.G. The continuous crack flexibility model for crack identification. *Fatigue & Fracture of Engineering Materials & Structures* 26, (2001), 643-650.

[13] Przybylski J. Stability of an articulated column with two collocated piezoelectric actuators. *Engineering Structures* 30, 12, (2008), 3739-375.

[14] Przybylski J. Non-linear vibrations of a beam with a pair of piezoceramic actuators. *Engineering Structures* 31, (2009), 2687–2695.

Jacek Przybylski, Professor: Institute of Mechanics and Machine Design Fundamentals, Częstochowa University of Technology, Dąbrowskiego 69, 42 201 Częstochowa, Poland, (*jacek.pr@imipkm.pcz.pl*). The author gave a presentation of this paper during one of the conference sessions.

Grzegorz Gąsiorski, Ph.D.: Institute of Mechanics and Machine Design Fundamentals, Częstochowa University of Technology, Dąbrowskiego 69, 42 201 Częstochowa, Poland

Model of a quarter car suspension with a silencer containing magnetorheological fluid and with damaged parts controlled by backstepping method control

Stanisław Radkowski, Maciej Słomczyński

*Abstract:*Work focuses on minimize deflection body from its equilibrium position after deflection by force applied to wheel which has a task to simulate obstacles encountered by the wheel. Model presents a quarter of the car's suspension with nonlinear spring and a silencer with magnetorheological fluid, by which modify the damping of the suspension. System was created in harmony with Lapunov stability. Model was designed in Matlab - Simulink.. Model was designed for testing many different damaged parts of suspension like for example, spring or silencer. Damaged part was represented by changing characteristic during the simulation. In further attempts model was tested for many damaged part and sequence of events was different. Model was tested for different characteristic of springs and dampers and variable method deflection wheel from its equilibrium position.

1. Introduction

The backstepping method was first formulated by Petar Kotovic in about 1990 as a method for stabilization of non-linear systems. It has been used to stabilize the position of vessels on the sea and as a control system for helicopters or mobile robots [1][3][4].

2. Backstepping

In order to start determining the backstepping, first it needs to be assumed that the parameter used to control the system is jest c_2 so that we can write:

$$u = c_2, \tag{1}$$

It is assumed that the first subsystem is the position of the body in axis perpendicular to the driving direction. Next, the derivative was calculated, which can be described with simple equations (9) and (10) and virtual control was introduced to the subsystem z_2 designated as $\propto (z_1)$:

$$z_1 = x_2, \tag{2}$$

$$z_2 = x_2 - \propto (z_1), \tag{3}$$

Then, based on the materials [2][3][7], the Lapunov function was determined (11) and the derivative (12) was calculated:

$$V_1(z_1) = \frac{1}{2} z_1^2, \tag{4}$$

$$\dot{V}_1(z_1) = z_1 \dot{z}_1, \tag{5}$$

The next step is to substitute the Lapunov function in the derivative $\dot{z}_1$:

$$\dot{V}_1(z_1) = z_1 \left[\frac{c_2}{m_2} x_1 - \frac{c_2}{m_2} x_2 + \frac{k_2 x_1 t}{m_2} - \frac{k_2 t (z_2 - \propto (z_1))}{m_2} \right], \tag{6}$$

If the system has a solution that belongs to the set of real numbers, it needs to satisfy the specific conditions:

$$V_1(z_1(0)) = 0, \tag{7}$$

$$V_1(z_1) > 0, dla\, z_1 \neq z_1(0), \tag{8}$$

$$\dot{V}_1(z_1) \leq 0, \tag{9}$$

based on [3][5][6].

When the above conditions are met, it can be found that subsystem z_1 is stabilized. The derivative of subsystem z_2 was calculated, which was described with this equation:

$$\dot{z}_2 = \dot{x}_2 - \dot{\propto} (z_1), \tag{10}$$

by $\propto (z_1)$ the first corrective constant was introduced K_1:

$$\propto (z_1) = -K_1 z_1 - z_1^2, \tag{11}$$

Then, the derivative $\propto (z_1)$ was calculated:

$$\dot{\propto} (z_1) = -K_1 \dot{z}_1 - 2 z_1 \dot{z}_1, \tag{12}$$

The next step is to substitute all equations to subsystem $\dot{z}_2$:

$$\dot{z}_2 = \frac{c_2}{m_2} x_1 - \frac{c_2}{m_2} x_2 + \frac{k_2 x_1 t}{m_2} - \frac{k_2 t (z_2 - \propto (z_1))}{m_2} - \dot{\propto} (z_1), \tag{13}$$

Assuming that $z_2 \to 0$ it was checked for which values $K_1 > 0$. This corresponds to the conditio:

$$V_1(z_1) = -K_1 z_1 \leq 0 \tag{14}$$

In order to stabilize the second subsystem, the Lapunov function for both equations should be determined and the function derivative needs to be calculated [5]:

$$V_2(z_1, z_2) = V_1(z_1) + \frac{1}{2} z_2^2, \tag{15}$$

$$\dot{V}_2(z_1, z_2) = z_1 \dot{z}_1 + z_2 \dot{z}_2, \tag{16}$$

$$\dot{V}_2(z_1, z_2) = z_1 \left[\frac{c_2}{m_2} x_1 - \frac{c_2}{m_2}\left(z_2 - \propto (z_1)\right) + \frac{k_2 x_1 t}{m_2} - \frac{k_2 t (z_2 - \propto (z_1))}{m_2}\right] + z_2(\dot{x}_2 - \dot{\propto}), \quad (17)$$

By introducing the second corrective parameter K_2 we should consider [4]:

$$z_1 - \dot{\propto} (z_1) - \frac{c_2}{m_2} - \frac{k_2 t}{m_2} = -K_2 z_2, \quad (18)$$

The second to last step is to check for which values of corrective constant $K_2 > 0$. The following equation is higher than 0 based on [6]:

$$\dot{V}_2(z_1, z_2) = -K_1 z_1^2 - K_2 z_2^2 \leq 0, \quad (19)$$

The final step is to determine the control parameter c_2 from equation (25). Corrective constants K1 and K2 were determined empirically based on Matlab simulations where the setpoints changed by 1. Ultimately, the best effects were achieved for setpoints of 999 and 1, respectively. The worst results were achieved for K1 and K2 of 100 and 1, which is shown by the time course marked in blue in Figure 1. The best results were achieved for K1 and K2 equal to 1 and 999. Moreover, a trend indicating improved stabilization time was determined when K2 increased and K1 dropped.

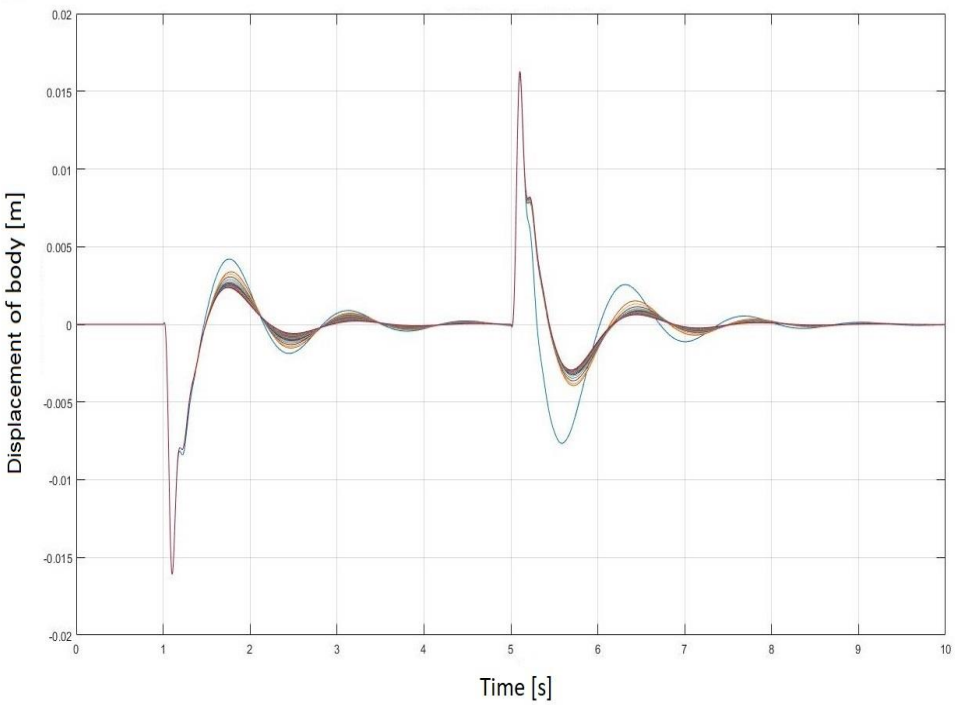

Figure 1. Selection of corrective constants K1 and K2 for controller.

3. Practical use – physical model

The model in which control with backstepping method is used is ¼ of a car, and precisely, it is the wheel system with suspension and the body. It is a classic system with two degrees of freedom and coercion. Its diagram with forces acting on individual elements is shown in Figure 2.

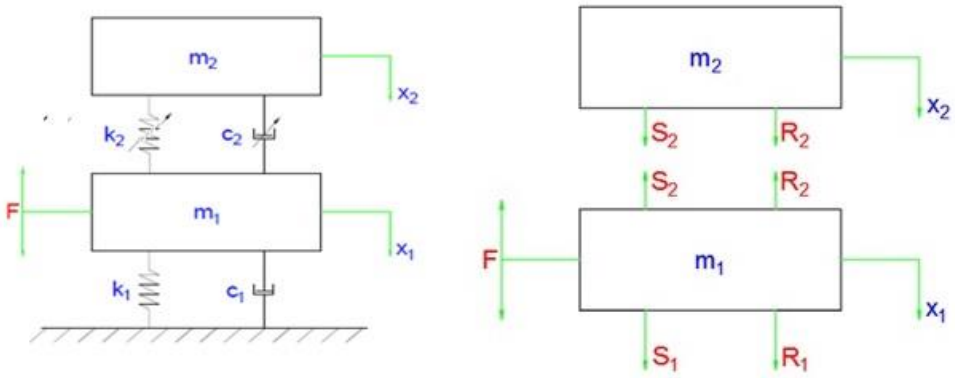

Figure 2. Diagram of analyzed system and release of force system diagram from constraints

The following motion equations are implied from Figure 3:

$$\begin{cases} m_1\ddot{x}_1 + S_1 - S_2 + R_1 - R_2 = F \\ m_2\ddot{x}_2 + S_2 + R_2 = 0 \end{cases}, \tag{20}$$

Where:

$$S_1 = k_1 x_1, \tag{21}$$

$$R_1 = c_1\dot{x}_1, \tag{22}$$

$$S_2 = k_2(x_2 - x_1), \tag{23}$$

$$R_2 = c_2(\dot{x}_2 - \dot{x}_1), \tag{24}$$

With substitution of formulas (2-5) to the system of equations (1), the equation system (6) was obtained:

$$\begin{cases} m_1\ddot{x}_1 + k_1x_1 - k_2(x_2 - x_1) + c_1\dot{x}_1 - c_2(\dot{x}_2 - \dot{x}_1) = 0 \\ m_2\ddot{x}_2 + k_2(x_2 - x_1) + c_2(\dot{x}_2 - \dot{x}_1) = 0 \end{cases} \tag{25}$$

where:

$m_1 = 90\ [kg]$ – non-sprung mass.

$m_2 = 500\ [kg]$ – mass of $\frac{1}{4}$ of a car

$k_1 = 200\ \left[\frac{kN}{m}\right]$ – tyre stiffness.

$c_1 = 40\ \left[\frac{N*s}{m}\right]$ – tyre damping coefficient.

$k_2\ \left[\frac{N}{m}\right]$ – suspension spring stiffness described with characteristics in Figure 3.

$c_2\ \left[\frac{N*s}{m}\right]$- damper damping coefficient. Assumes values during work from 1,100 to 2,500 $\left[\frac{N*s}{m}\right]$.

where:

$$x = x_2 - x_1, \tag{26}$$

Displacement x is the difference in positions of the body and the wheel. In the case in question it is important since the spring is described with a different equation when the displacement is higher than $0.1\ [m]$ which is shown in Figure 3.

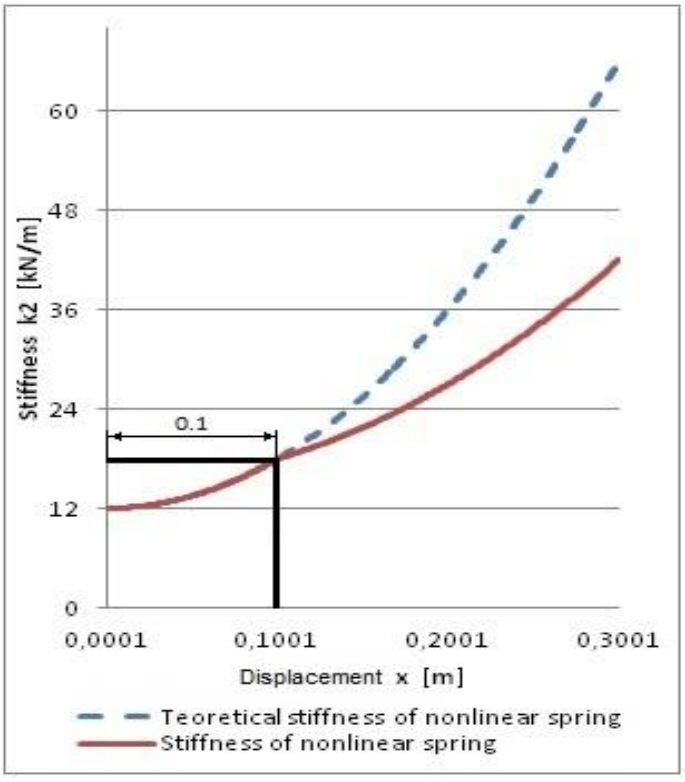

Figure 3. Spring k_2. characteristics

The system was modelled in Matlab – Simulink environment where the control parameter is the damper damping coefficient marked as c_2, in which the magnetorheological liquid is present. By using the technical documentation made available by LORD [8] the range in which the damping coefficient will vary was limited to 1,100 and $2{,}500\left[\frac{N*s}{m}\right]$,. These values were determined based on the dependence of damping force for the maximum and minimum current acting on the magnetorheological liquid. Additionally, non-linearity was introduced to the system by using a spring in the suspension with a varying characteristics (Figure 3). With the displacement coercion, the system was thrown out of equilibrium which under physical conditions means that the wheel encountered an obstacle. The goal is to determine the impact of individual damage on vibration damping and control. The following simplifications were introduced to the modelled system:

- Even vehicle mass distribution for each wheel.
- Force applied to the wheel is in the system symmetry axis.
- The model does not take into account any errors of calculated values.

Figure 4 shows the already mentioned spring with non-linear characteristics.

In order to model the damper as truly as possible, the signal delay was introduced based on the information in [9] of the change of damping parameter of 0.06 seconds. Thanks to this, the first coercion peak impacts the suspension when having a minimum damping. This causes the minimalization of vertical accelerations. In the next phase, that is after coercion of displacement, the damping coefficient in the damper increases causing the minimalization of displacement of the body and to a lesser extent, of the wheel and stabilization time of these components.

3 types of damage were modelled

- Damage by leakage of magnetorheological liquid
- Linear damage to the damper, such as damage to the coil or a bunch of conduits
- Pitch damage to the damper, such as delamination of magnetorheological liquid

In order to reduce the impact of damage made to the damper, it was put into the emergency mode which meant a change made to the damping of the system to the level corresponding to current 0.5 [A]. This solution enables further adjustment of damping maintaining the current adjustment range and also the highest damping increase related to the current variation was used.

Step damage – is the damage of fixed value and in case of this model it is $1{,}000\ \left[\frac{Nm}{s}\right]$, but no less than $200\ \left[\frac{Nm}{s}\right]$, due to the limited damping of the magnetorheological liquid.

Liner damage is described by the function:

$$f(t) = 200t + 120, \qquad (27)$$

This type of damage models the delamination of the magnetorheological liquid or a damage to the control system.

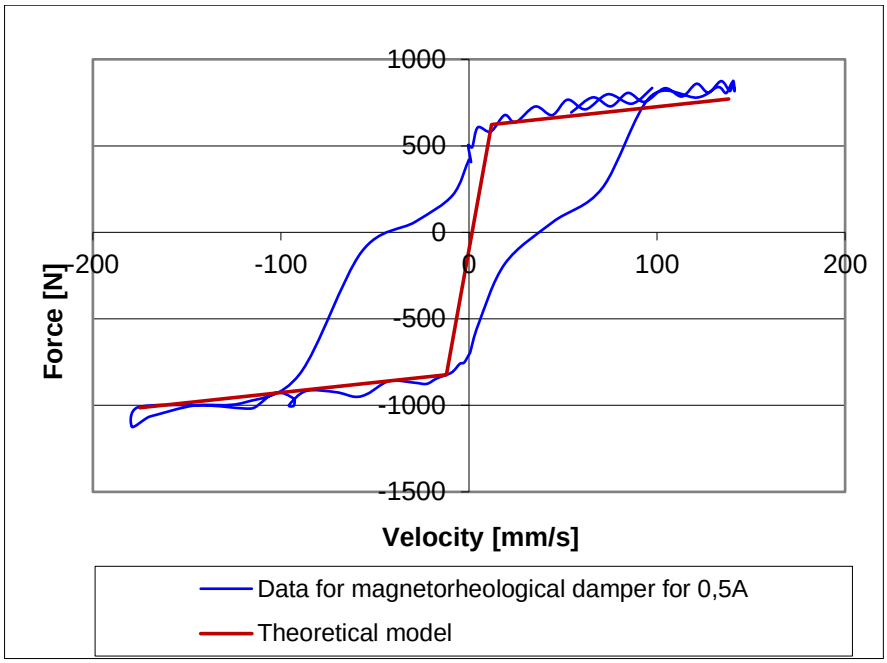

Figure 4. MR damper characteristics and theoretical model.

Leakage of the magnetorheological liquid is the worst analyzed case of damage since it prevents damping control of the damper and reduces its value to about 40 $\left[\frac{Nm}{s}\right]$. Damage of this type can be divided into two cases. The first one is when the piston rod moves only within the area of the magnetorheological liquid that remained in the cylinder and this case will be analyzed here. The function that describes the leakage is as follows:

$$f(t, x_1, x_2) = (x_{1_{max}} + 0.1[m])t - 0.011t * x_{2_{max}}, \tag{28}$$

The characteristics of variation of the damping value c_2 in the real system and in the model is shown in Figure 5. The theoretical model of the magnetorheological damper is described by the following system of equations:

$$\begin{cases} f(v) = 1.17 * v - 809 \; dla \; v \in \langle -175, -12) \\ f(v) = 60.25 * v - 100 \; dla \; v \in \langle -12,12 \rangle \\ f(v) = 1.17 * v + 609 \; dla \; v \in (12, 138\rangle \end{cases}, \tag{29}$$

4. Simulation results

As a simulation of operation of the suspension system, the wheel displacement in the first second of $0.1[m]$ with positive sense was assumed. In the 5th second, another displacement occurred with the opposite sense but the same value. This adjustment is to minimize the deviation of the body from the equilibrium position where the control parameter is damping of the damper with magnetorheological liquid marked as c_2. Further diagrams show the results of simulations of displacements and accelerations for the body and results of simulation for systems with damages to the magnetorheological liquid as well as systems with damages to the magnetorheological liquid under emergency mode as shown in Figure 5 – 10.

A. Damage caused by leakage of the magnetorheological liquid in the 5th second.

B. Linear damage of the damper since the 1st second.

C. Step damage of the damper since the 5th second.

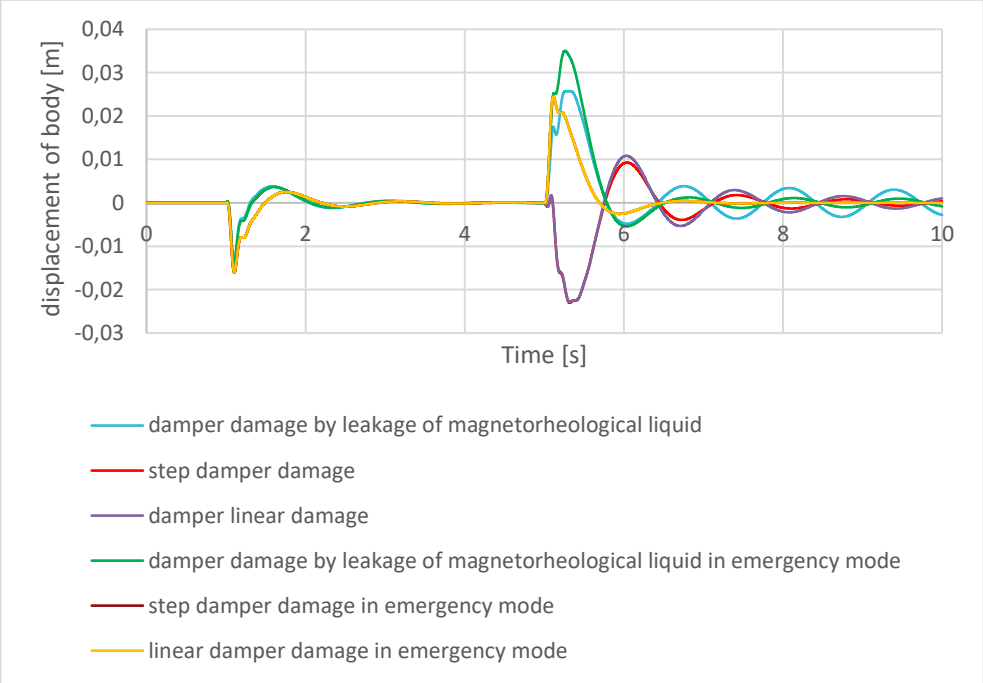

Figure 5. Body vertical displacement for damaged damper – comparison.

As shown in Figure 6, the linear damage of the damper affects the body inclination amplitude from balance position. With the increase of the damage, the system is not able to stabilize itself quickly (see also Table 1) and what is more, all damper damage results in a longer stabilization time. Re-

stabilization of body can be observed for 2 types of damage after the damper is put into the emergency mode.

Within seconds [0-5], the system operates correctly and has no damage except the linear one. The first damage comes after the 5th second and this is when the damper is affected. The linear and pitch damage of the damper changes the body displacement phase which is caused by the varying damping parameter. Also it can be seen that in case of simulation with a linear damage of the damper, it can be seen that the system falls into oscillations, which is also of concern and affects the driving comfort significantly and is destructive for the vehicle itself.

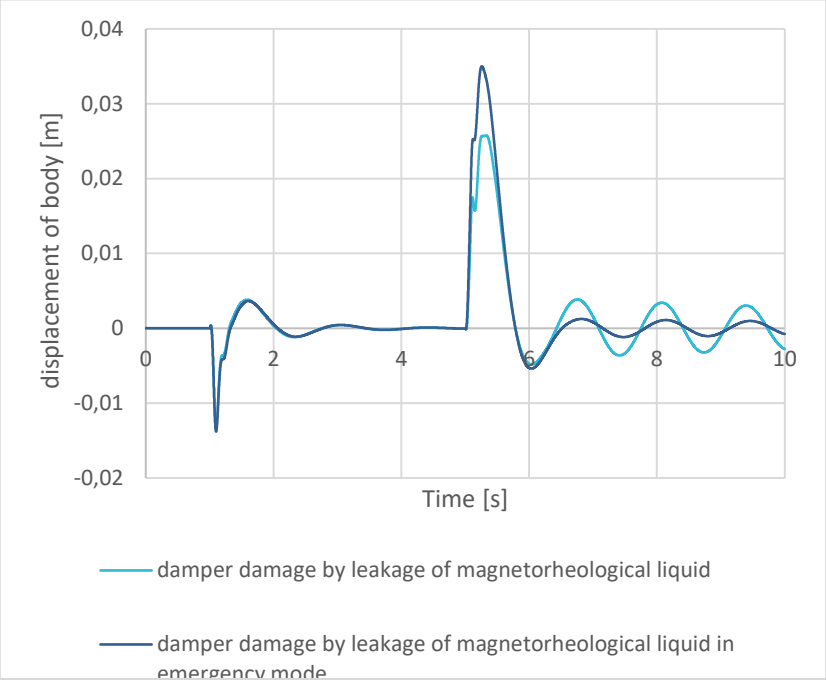

Figure 6. Body vertical displacement for damaged damper by magnetorheological liquid leakage with turning it into emergency mode.

The leakage of magnetorheological liquid is the worst case of damage due to the limited damping within wide ranges of displacement. With the increased duration of the damage, the range in which the system has the proper minimum damping is smaller and its further adjustment is possible. Because of this, the activated emergency mode initially increases the coercion amplitude for the body but for small amplitudes such a system will stabilize faster. The minimization of the damper displacements causes the work within the magnetorheological liquid making it possible to damp the displacements. Body displacements for the damper with a leakage and for the damper with a leakage in the emergency mode are virtually the same.

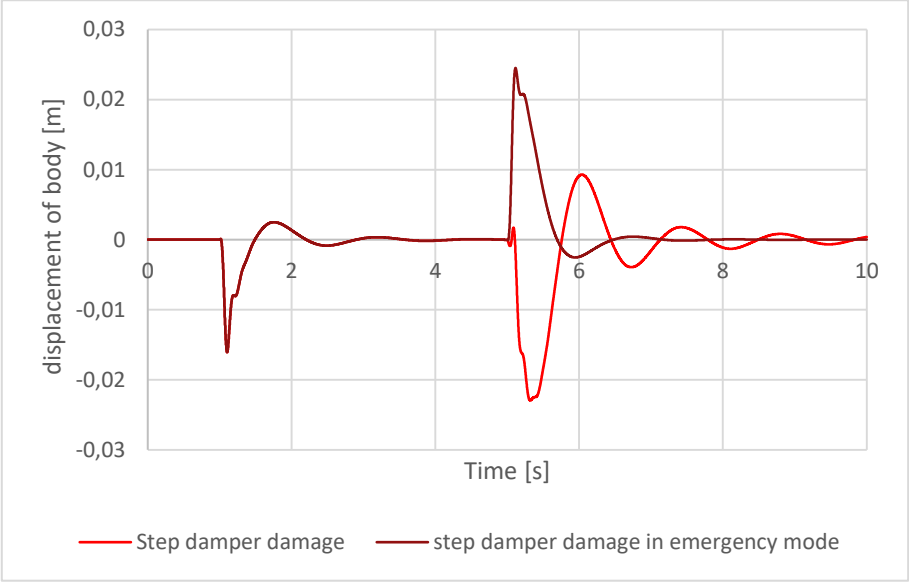

Figure 7. Body vertical displacement for step damaged damper with turning it into emergency mode.

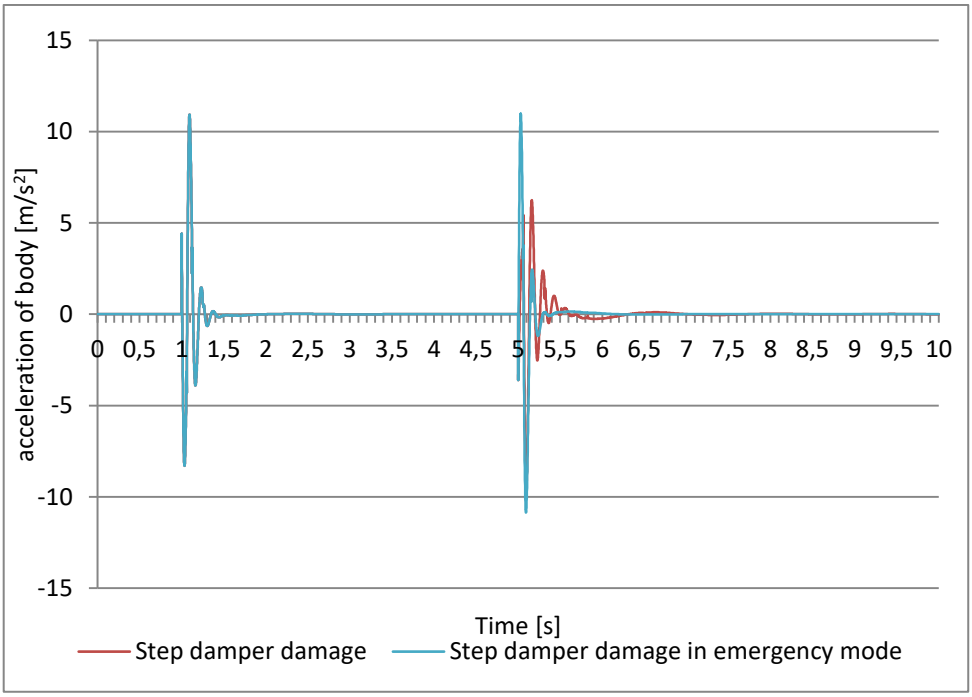

Figure 8. Body vertical accelerations for damaged magnetorheological damper with turning into emergency mode.

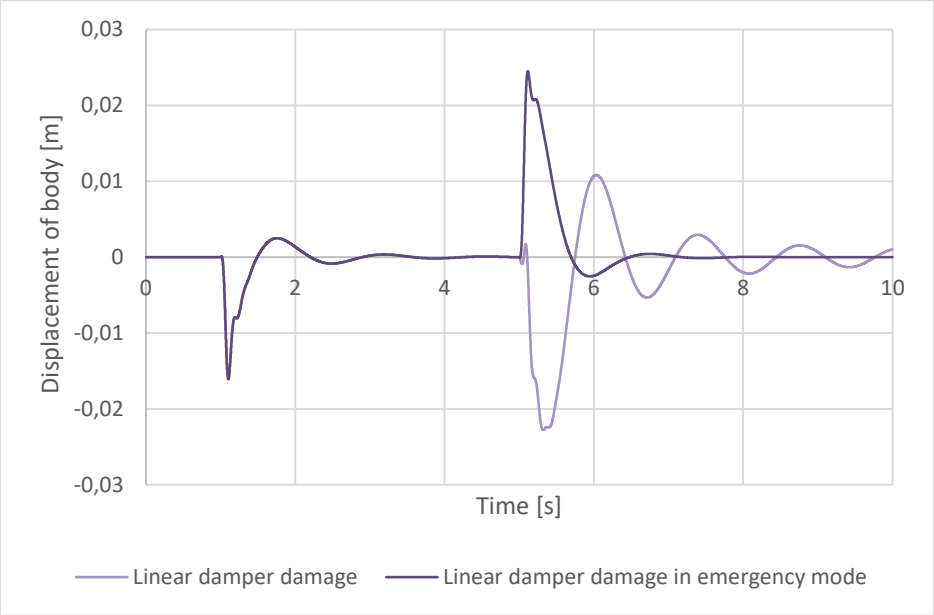

Figure 9. Body vertical displacement for linearly damaged damper with turning into emergency mode.

Putting the damper into emergency mode under step damage increased the body displacement amplitude because the vehicle with this configuration is fitted with a hard suspension and thanks to this solution, the system will re-stabilize within the time similar to a working system.

Body vertical accelerations after turning into the emergency mode are minimum and just after 5.25 seconds, while for the damper damage system, after 5.50 seconds, the passengers can feel the overloads.

Liner damage extends stabilization time and body displacement amplitude which affects the driving comfort. Putting the damper into emergency mode reinstates a satisfying stabilization time after about 2.5 seconds from coercion. Unfortunately, just as in other cases, this increases the body displacement amplitude.

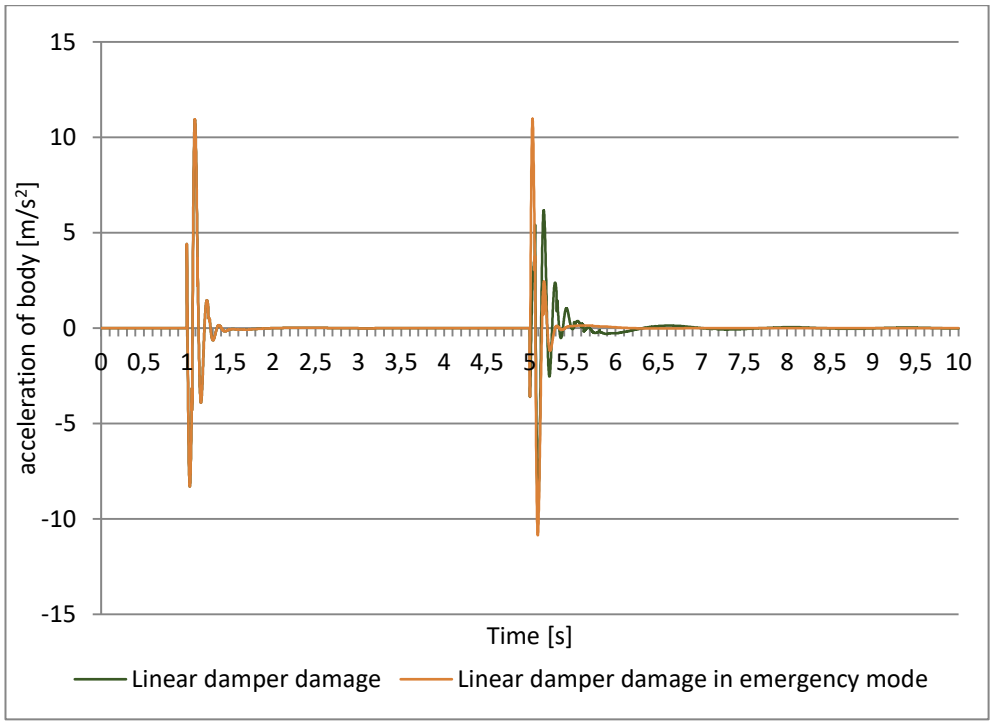

Figure 10. Body vertical accelerations for linearly damaged damper with turning into emergency mode.

The body accelerations under emergency mode increase, which causes a greater discomfort for the passengers and in exchange, the accelerations are minimized in respect of time and the amplitude of displacements in further periods after coercion is smaller.

Table 1. Table of results of extreme measurements.

BODY	Displacement $[m]$	Acceleration $\left[\frac{m}{s^2}\right]$	Stabilization time [s]
Leakage from magnetorheological damper	0.025	17,94	31
Damper linear damage	0.022	10.93	36
Damper step damage	0.022	10.93	40
Leakage from magnetorheological damper in emergency mode	0.037	19.44	8.75
Linear damage of damper in emergency mode	0.024	10.97	8.25
Step damage of damper in emergency mode	0.040	12.15	8.45

It was determined that the stabilization time corresponds to the decreased displacement amplitude below 2% of the displacement caused by coercion. Simulations where the damper with magnetorheological liquid was damaged showed that this damage considerably extends the stabilization time of the body. The system parameters after putting the damper into the emergency mode deteriorated considerably, however, the stabilization of the suspension system was achieved, which improved the vehicle's safety against the system with the damage itself.

5. Summary

Putting the damper into emergency mode resulted in improved parameters for all analyzed cases. During coercion, the displacement altitude and body acceleration altitude increased which is caused by a higher hardness of the suspension and has a negative effect on the driving comfort. In exchange, the efficiency of the suspension system was regained.

The assumed values of specific coefficients are as close as possible to the actual parameters of elements used. It was found that the use of the spring with a non-linear characteristics coupled with a controlled damper is a good alternative for conventional suspensions.

Further research in this respect will allow to introduce such a solution in a car and improve safety of the vehicle with such a suspension in a case of damage to the suspension system.

Tests of damage to the magnetorheological damper concluded successfully where the emergency mode allowed in two of three cases to regain the efficiency of the suspension system.

In further works, it is expected to test the second variant of leakage of the magnetorheological liquid and its impact on the passengers and the vehicle structure itself.

The goals assumed before starting the project were fulfilled.

Acknowledgments

This work was supported by Ph.D. Michał Makowski.

References

[1] Benaoumeur, Ibari; Laredj, Benchikh; Amar Reda, Hanifi Elhachimi; Zoubir, Ahmed-foitih. Backstepping Approach for Autonomous Mobile Robot Trajectory Tracking. *IJEECS* 2 3 (2016), s. 478. DOI: 10.11591/ijeecs.v2.i3.pp478-485.

[2] Chen, Cai-Xue; Xie, Yun-Xiang; Lan, Yong-Hong (2015): Backstepping control of speed sensorless permanent magnet synchronous motor based on slide model observer. w: *Int. J. Autom. Comput.* 12 (2), s. 149–155. DOI: 10.1007/s11633-015-0881-2.

[3] Fossen, Thor I.; Strand, Jan P., Tutorial on nonlinear backstepping. Applications to ship control., *MIC* 20 (2), (1999), s. 83–135. DOI: 10.4173/mic.1999.2.3.

[4] Herbert G. Tanner; Kostas J. Kyriakopoulos, Discontinuous Backstepping for Stabilization of Nonholonomic Mobile Robots. w: *IEEE* (May 2002).

[5] Jie Liu, Johan Eker, J¨orn W. Janneck, Xiaojun Liu, and Edward A. Lee Fellow Actor-Oriented Control System Design: A Responsible Framework Perspective., *IEEE*., (2003)

[6] Roger Skjetne, Thor I. *Fossen On Integral Control in Backstepping: Analysis of Different Techniques* (June 30 - July 2, 2004).

[7] Victor Santibanez, Rafael Kelly, Jesus Sandoval (2005): 44th IEEE Conference on Decision and Control, and European Control Conference ECC05. Proceedings ; CDC-ECC05, December 12 - 15, 2005, Seville, Spain. Piscataway, NJ: IEEE Operations Center.

[8] http://www.lordmrstore.com/lord-mr-products/rd-8040-1-mr-damper-short-stroke.

[9] Michał Makowski, Wiesław Grzesikiewicz, Lech Knap, IDENTYFIKACJA PARAMETRÓW STEROWANYCH TŁUMIKÓW MR I PZ., *ZESZYTY NAUKOWE INSTYTUTU POJAZDÓW* 3(89)/2012.

Stanisław Radkowski, Proffesor: Warsaw University of Technology Faculty of Automotive and Construction Machinery Engineering, Narbutta 84, 02-524 Warsaw, Poland (ras@simr.pw.edu.pl)

Maciej Słomczyński, B.A.: Warsaw University of Technology Faculty of Automotive and Construction Machinery Engineering, Narbutta 84, 02-524 Warsaw, Poland (Maciej.slomczynski@op.pl)

Nonlinear mode veering for enhanced resonant sensing

Dennis Roeser, Samuel Jackson, Thomas Sattel, Stefanie Gutschmidt

Abstract: A research trend in micro systems for resonant sensing is a sensitivity enhancement utilizing nonlinear and coupling effects, which is mainly applied to gas sensing and timing applications. In this article, we propose such an enhancement of the sensitivity for an atomic force microscopy probe. This scheme is based on a two beam array, where one beam is active and acting as probe, while the other beam is passive. Both beams of this array are designed to have an identical resonance frequency at a defined distance between the active beam and a surface, in the mechanically uncoupled case. The occurring mode localization close to this distance and the nonlinear interaction potential lead to an increased sensitivity in this region, with respect to frequency change and amplitude ratio. The proposed scheme is experimentally validated with a macro-scale test setup, mimicking a microscale system.

1. Introduction

Today, one challenge in micro-electro-mechanical systems (MEMS) for resonant sensing is to further increase their performance metrics. These performance metrics include increasing the sensitivity to measure changes of quantities and the time required to measure such changes. For instance, atomic force microscopy (AFM) in its dynamic operation modes is based on resonant sensing. Figure 1 a) shows the setup of an AFM, wherein a probe is excited at its resonance frequency and brought in close proximity to a sample surface. A positioning stage is moving the sample in a raster scan pattern to measure the topography of the sample. A change in tip-sample distance Δd_0 leads to a change in the probe's resonance frequency $\Delta\omega_0$, due to nonlinear interaction forces [7], as illustrated in Fig. 1 b). This change in resonance frequency, or the resulting amplitude or phase change, is the measured quantity, and its change with respect to the change in tip-sample distance is the corresponding sensitivity (e.g. $\Delta\omega_0/\Delta d_0$). For instance, in an AFM process the tip-sample distance d_0 is controlled to maintain a set resonance frequency ω_0 by adjusting the positioning stage's vertical $\bar{z}$-axis. Thus, the $\bar{z}$-axis motion of the positioning stage represents the topography of the sample relative to a reference point. Typical amplitudes of the probe and tip-sample distances are in the range of tens to a few hundreds of nanometers and are of the same order of magnitude [7].

Approaches to increase the performance metric of an AFM are mainly based on a linear methodology (e.g. focused on the probe's resonance frequency and damping) and have

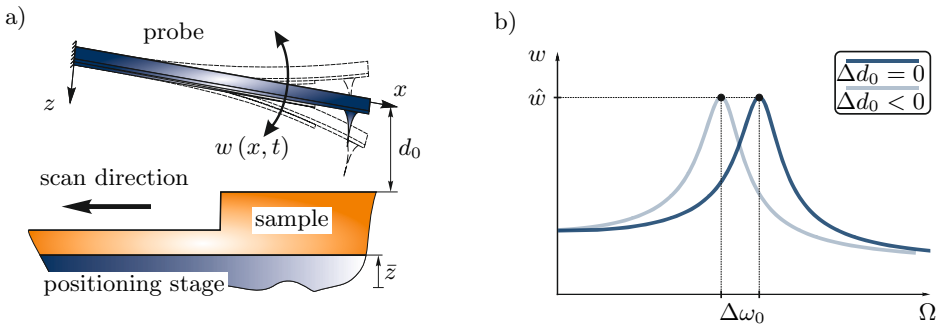

Figure 1. a) Basic AFM setup [13]. b) Shift of resonance frequency $\Delta\omega_0$ due to a change in tip-sample distance Δd_0.

reached their upper best. Recent approaches concentrate on utilizing nonlinear dynamic phenomena to significantly go beyond the performance of what can be achieved by linear methodology. Prakash et al. [11] utilized a parametric resonance, introduced by a control loop, to increase the sensitivity. The parametric resonance has a very high Q-factor and, thus, enhances the amplitude change per change in tip-sample distance $\Delta\hat{w}/\Delta d_0$. Jeong [8] used a special probe design in which an in-lay beam is integrated in a cantilever to realize an internal resonance, which is triggered by a change in tip-sample distance, also enhancing $\Delta\hat{w}/\Delta d_0$. However, approaches based on nonlinear dynamics applied to AFM are limited and require further investigation. Nonetheless, the potential of leveraging nonlinear dynamics in resonant sensing has been shown for MEMS in general. Among others, approaches aim to utilize parametric [12] and internal resonances [2, 13], modal interaction [16], frequency hardening [3, 15] as well as bifurcations [4] to increase sensitivity, reduce phase noise and achieve an increased detection speed.

Apart from the utilization of nonlinear dynamics, coupling effects in arrays of beams are a promising research area to achieve an increased sensitivity. This sensitivity increase is mainly based on mode-localization [14,17], which is a spatial confinement of energy within a system of coupled oscillators. In this case, a symmetry breaking perturbation (e.g. stiffness/mass change) can be measured with orders of magnitude increased sensitivity. However, utilizing nonlinearities or coupling effects is mainly applied to timing or mass detection applications.

In conclusion, recent research illustrates the potential of utilizing nonlinear dynamics and coupling effect to increase the performance metric of MEMS. However, consideration of those approaches to AFM are rare and a detailed study of these effects is missing.

In the scope of this article, a scheme is presented to use the *nonlinear interaction* between an AFM probe's tip and a surface together with a mechanical coupling effect between two

beams to achieve an increased sensitivity ($\Delta\omega_0/\Delta d_0$). The mechanical coupling between both cantilevers is caused by the clamp as their common base, seen in Fig. 2. One beam is active, i.e. is excited at its resonance frequency and the other is passive. The active beam undergoes the nonlinear interaction between tip and sample surface. For experimental validation of this approach, a macro-scale test setup has been build to emulating a micro scale AFM [5]. This setup allows for specific adjustments of the array's parameters (e.g. coupling, resonant frequencies, tip-sample distance). The following section begins with the model used for the analysis, followed by the macro-scale test setup, the analysis and experimental results. Finally, conclusions from the results and future work is presented.

2. Model

The considered system is an array of two cantilever beams, connected with a common base. Each beam has an integrated actuator and sensor and is subjected to a quadratic interaction force between probe tip and sample. Such interaction forces may be due to e.g. van der Waals or permanent magnet forces. Note that this type of sensor and actuator is especially for array technology in AFM, and differs from the commercially available AFM probes [10]. As illustrated for a single beam in Fig. 1, the displacement of the beam towards the sample surface is $w(x,t)$, which is also the coordinate the equations of motion are derived for. An extended Hamilton's principle is used to derive the partial differential equations (PDEs) describing the motion of the coupled two beam array, under Bernoulli assumptions. For the discretization of the system of PDEs, a Galerkin method (with $w_m(x,t) = \sum_n W_n(x) X_n(t)$) has been applied. The displacement of beam m is given by w_m, where W_m and X_m are the spatial mode shapes (i.e. comparison functions) and the time varying modal displacements of the m-th beam, respectively. A detailed derivation can be found in [5, 6]. Thus, the reduced order equations of motion including first intrinsic bending modes of both beams are given in matrix form by

$$\begin{bmatrix} \ddot{X}_1 \\ \ddot{X}_2 \end{bmatrix} + \begin{bmatrix} W_{\mathrm{c}11} & W_{\mathrm{c}12} \\ W_{\mathrm{c}21} & W_{\mathrm{c}22} \end{bmatrix} \begin{bmatrix} \dot{X}_1 \\ \dot{X}_2 \end{bmatrix} + \begin{bmatrix} W_{\mathrm{k}11} & W_{\mathrm{k}12} \\ W_{\mathrm{k}21} & W_{\mathrm{k}22} \end{bmatrix} \begin{bmatrix} X_1 \\ X_2 \end{bmatrix} - \begin{bmatrix} W_{\mathrm{F}11} & W_{\mathrm{F}12} \\ W_{\mathrm{F}21} & W_{\mathrm{F}22} \end{bmatrix} \begin{bmatrix} AC_1 F_{\mathrm{ext}} \\ AC_2 F_{\mathrm{ext}} \end{bmatrix} - \begin{bmatrix} W_{\mathrm{NL}11} & W_{\mathrm{NL}12} \\ W_{\mathrm{NL}21} & W_{\mathrm{NL}22} \end{bmatrix} \begin{bmatrix} \dfrac{\tau_m}{(\hat{d}_{01} - W_1 X_1)^2} \\ \dfrac{\tau_m}{(\hat{d}_{02} - W_2 X_2)^2} \end{bmatrix} = \begin{bmatrix} 0 \\ 0 \end{bmatrix}, \tag{1}$$

where $W_{\mathrm{c}mn}$ are the coupled damping terms, $W_{\mathrm{k}mn}$ are the coupled stiffness terms, $W_{\mathrm{F}mn}$ are the coefficients of the actuation term applied to each beam, $W_{\mathrm{NL}mn}$ are the coefficients of the nonlinear tip-sample interaction forces applied to each beam. These coefficients include

the integrals of the comparison functions used for the Galerkin approach [5, 6]. τ_m is the coefficient of the attractive force potential between tip and sample, and d_{0m} is the separation distance between the undeflected cantilever m and the sample surface (see Fig. 1). The forcing function F_{ext} is the nondimensional oscillatory component of the excitation signal, with the dimensional amplitude applied to beams 1 and 2 defined by AC_1 and AC_2, respectively. For frequency modulation AFM (FM-AFM), F_{ext} needs to be defined such that the excitation signal is sinusoidal with a phase lead of 90° over the measured output signal, which in this case will be the tip displacement $w_1(l,t)$ [1]. The resulting periodic response of the system as a function of tip-sample separation d_0 can be found by solving Eq. (1) in the time domain. The parameters used for the numerical analysis of Eq. (1) in the following sections can be found in [5].

3. Experimental setup

To simulate the operation of an AFM array, an equivalent macro-scale experiment is utilized. The experiment is scaled up 1000× in comparison to standard AFM cantilever dimensions (hundreds of micrometers in length). Using a macro-scale test rig allows key parameters of the system, including coupling strength and individual cantilever dimensions, to be easily varied for the purpose of studying their influence on system response. The macro-scale test rig is depicted in Fig. 2, and consists of a variable number of cantilevers clamped to a base structure. Each cantilever is equipped with a piezo-film actuator and strain gauge sensors. Permanent magnets at the tip of each cantilever are used to simulate attractive tip-sample interaction forces. The tip-sample separation distance is altered using a stepper motor assembly.

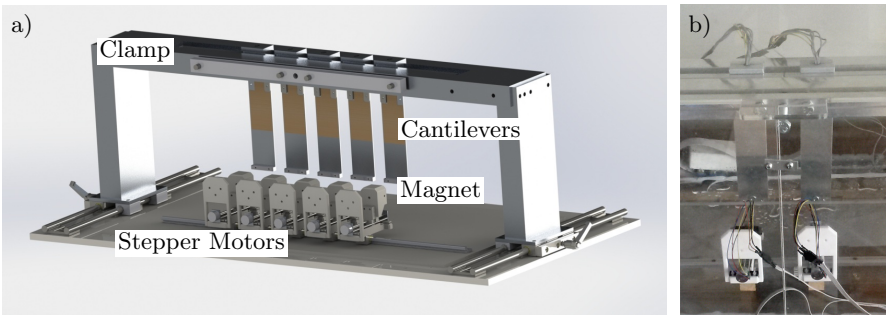

Figure 2. a) Rendering of the macro-scale test rig. b) Detail view of the real test rig.

To actuate the system at resonance for FM-AFM, a PID controller is employed to control a 90° phase angle between displacement the w_1 of beam 1 (measured by strain gauges) and

the excitation signal F_{ext}. The amplitude of the actuation signal is user controlled and constant in this case. The stepper motors are used to move permanent magnets relative to the cantilevers. This allows the tip-sample separation for each cantilever in the array to be altered independently. As with standard FM-AFM, the actuation frequency changes as a function of tip-sample separation, allowing actuation frequency to be used as a measurement variable. The macro-scale experiment was used as a proof of concept of the proposed method of sensitivity enhancement utilizing a two beam array instead of standard single cantilever techniques.

4. Results

The active beam is excited with an amplitude AC_1 at its resonance with FM control and is acting as a probe in close proximity to a surface. The passive beam is neither brought in close proximity nor excited. The effects utilized for the sensitivity increase are based on the nonlinear interaction potential between beam 1 and the surface, as well as the mode localization between the active and the passive beam. Thus, the nonlinear shift to lower resonance frequencies of beam 1 is used to trigger and break the symmetry of the array to achieve an increased frequency change per change in tip-sample distance. This general

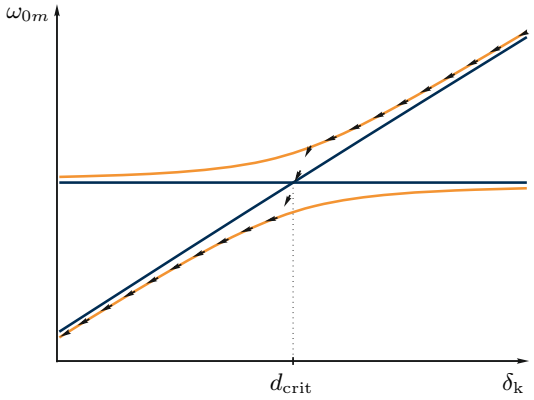

Figure 3. Mode veering for a two beam array, with eigenfrequencies ω_m, the stiffness detuning δ_{k} and the critical distance d_{crit}. Blue lines depict mechanically uncoupled modes (ω_{0m}), orange lines are out-of-phase (upper) and in-phase (lower) array mode, black arrows indicate path taken in FM-AFM.

concept is illustrated in Fig. 3, showing the eigenfrequencies ω_m over a stiffness detuning δ_{k} at beam 1. In the mechanically uncoupled case (blue lines) both frequencies (ω_{01} and ω_{02}) are identical at d_{crit}, at which $\delta_{\text{k}} = 0$. Changing δ_k leads to a change of ω_{01}, while ω_{02} remains

constant. In the coupled case (orange lines) the in-phase (lower frequencies) and out-of-phase (higher frequencies) mode have no intersection, but diverge from another with a varying δ_{k}. This effect is also known as eigenvalue veering [9], and is used in mode-localization sensing schemes. Thus, by controlling the phase between beam 1 and the excitation while decreasing δ_{k} from positive to negative leads to a sudden shift from the out-of-phase to the in-phase mode (arrows in Fig. 3), showing a steeper gradient $\Delta\omega_{\mathrm{a1}}\ \delta_k$ in the neighborhood of d_{crit}.

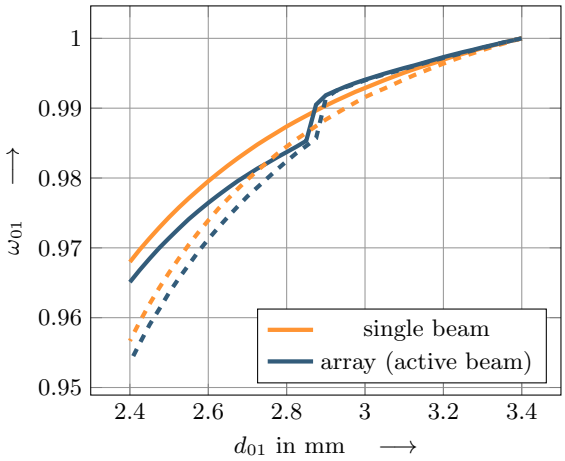

Figure 4. Change of normalized eigenfrequency of a two beam array while approaching a sample surface, damping ratio $\zeta = 0.007$. The amplitude of beam 1 is in the range of 0.5 to 1 mm. Line style represents the excitation amplitude; solid and dashed being $AC_1 = 0.001$ and $AC_1 = 0.002$, respectively.

Figure 4 shows a numerical simulation (model with FM-AFM) of the approach of the active beam to a fixed surface; depicted is its change of eigenfrequency (scaled) ω_{01} over the tip-sample distance d_{01}. The sharp change of eigenfrequency occurs at a critical distance $d_{\mathrm{crit}} \approx 2.875$ mm, which is not present in the approach curve of a single beam (orange line in Fig. 4). At d_{crit} the eigenfrequencies of the uncoupled beams are closest together. Every symmetry breaking detuning of parameters (e.g. stiffness of beam one in this case), leads to a divergence of the coupled eigenvalues of the array modes (i.e. in-phase and out-of-phase, c.f. Fig. 3). This mode veering, together with the nonlinear potential and the FM controller, leads to an increased sensitivity at this region about d_{crit}. As described earlier, the controller ensures a 90° phase angle between the excitation signal and w_1, leading to a change between out-of-phase and in-phase mode of the array, when crossing d_{crit}.

The conditions to define d_{crit} are determined by the uncoupled resonance frequencies of the two beams as well as the excitation amplitude AC_1. The influence of an increased

AC_1 can be observed as a shift of d_{crit} to higher values (Fig. 4). This shift is due to the amplitude dependent resonance frequency of the active probe (e.g. caused by the nonlinear potential). Thus, AC_1 influences the slope of the whole approach curve, also in case of the single beam. Additionally, the damping ratio ζ as well as the coupling between the beams influence the sensitivity. A decrease of ζ increases $\Delta\omega_{01}/\Delta d_{01}$ at d_{crit}, whereas a weaker coupling decreases it. A stronger coupling leads to an increased slope, until multiple coexisting solutions appear, connected by two saddle node bifurcations [5]. This behavior has also been shown experimentally. Figure 5 shows the frequency change of ω_{01} while approaching a permanent magnet with the array concept and a single beam with the macro-scale test setup. As can be seen, the characteristics reassemble those gained from numerical simulations (c.f. Fig. 4), resulting in an increased sensitivity in a region close to d_{crit} for the array configuration.

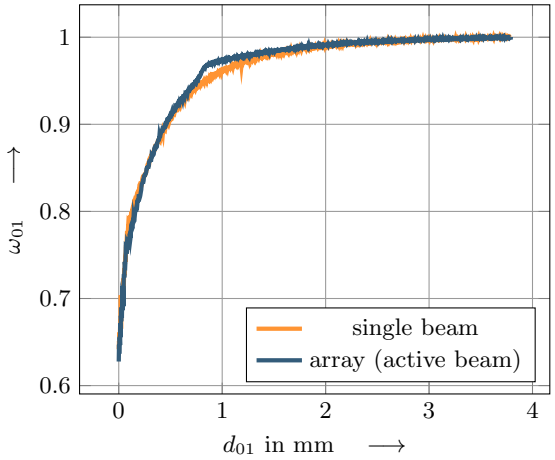

Figure 5. Experimental approach curves.

Another measure to increase the probe's sensitivity is the amplitude ratio between the two beams. As shown in Fig. 6, considering the system below d_{crit} (at which the amplitude ratio is equal to 1) leads to a strong increase of this ratio. In contrast to schemes used with classical mode localization sensing, the increase in this case is nonlinear, due to the interaction potential between tip and sample surface. The slope of this increase also depends on the excitation amplitude AC_1 as well as on the stiffness of the coupling between the beams. In this case, higher amplitudes result in an increased sensitivity. In contrast to the frequency slope shown in Fig. 4, the slope of the amplitude ratio increases in case of a decreased coupling. Thus, very low coupling results in a very high sensitivity, as also used in other schemes of localized mode sensing [17]. This strong increase for weakly coupled beams

is due to a strong change in eigenvectors of the array modes due to mode veering [9].

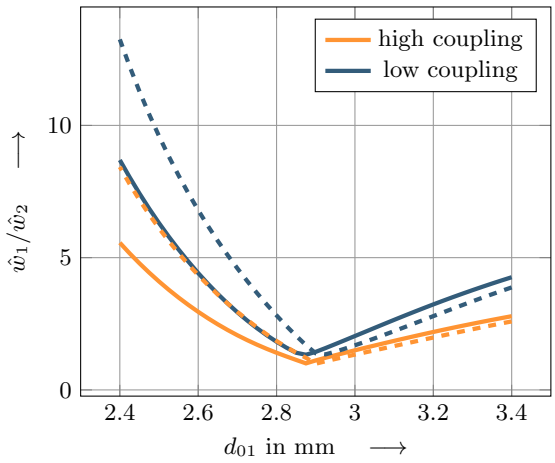

Figure 6. Amplitude ratio between the two beam's of an array while approaching a sample surface, damping ratio $\zeta = 0.007$. Line style represents the excitation amplitude; solid and dashed being $AC_1 = 0.001$ and $AC_1 = 0.002$, respectively.

5. Conclusion

The approach presented in this article to increase the sensitivity of an AFM probe is based on utilizing nonlinear and coupling effects with a two beam array. This array consists of an active beam sensing the actual topography changes and a passive beam for sensitivity enhancement. The occurring dynamic effect can be levered in two ways, first by using the increased frequency change over the tip-sample distance $\Delta\omega_{01}/\Delta d_{01}$ and, second, by utilizing the increased change of amplitude ratio between the two beams of an array $\hat{w}_1/\hat{w}_2$. Both effects show a higher increase in sensitivity for an increased amplitude. However, the frequency change increases for an increased coupling between the beams of the array, whereas the slope of the amplitude ratio decreases in this case. The sensitivity gain of both approaches can be increased by decreasing the damping coefficient ζ as well as by increasing the amplitude of excitation AC_1.

Using an increased $\Delta\omega_{01}/\Delta d_{01}$ has multiple benefits. When controlling the frequency in an AFM operation, the time to detect changes mainly depends on the control scheme used and is, thus, not limited by the decay coefficient of the individual beams. Additionally, the increased frequency change can be further magnified by using an amplitude detection scheme, or utilizing parametric resonance [11,12], which would combine an increased frequency change

with an increased amplitude change.

On the other hand, in combination with a very weak coupling, the amplitude ratio can be used to gain an orders of magnitude increased sensitivity compared to the frequency change. In this case, the probe is operated below the critical distance d_{crit} at a high slope. In contrast to most sensing schemes using mode localization, the probe in close proximity is driven at resonance using a phase locked loop (PLL) and both amplitudes are measured. Thus, there is no need for an observer base mode estimation, resulting in a faster control scheme. The influence of the nonlinear change of the amplitude on the image quality in an AFM process can be neglected, if the positioning stage is used in the PLL to maintain a phase shift of 90° between excitation and beam response.

Future work is devoted to an analytical solution for the dependency of d_{crit} on the systems's parameters (e.g. AC_1, ζ, coupling strength), the achievable sensitivity as well as the forces exerted onto a sample. Moreover, the implications gained are transferred to AFM array, in which all beams are actively probing the sample surface. In this case, higher modes of the array are considered in order to explain observed coupling phenomena while imaging a sample.

References

[1] Albrecht, T. R., Grtter, P., Horne, D., and Rugar, D. Frequency modulation detection using high-q cantilevers for enhanced force microscope sensitivity. *Journal of Applied Physics 69(2)* (1991), 668–672.

[2] Chen, C., Zanette, D. H., Czaplewski, D., Shaw, S., and López, D. Direct observation of coherent energy transfer in nonlinear micro-mechanical oscillators. *arXiv preprint arXiv:1612.00490* (2016).

[3] Cross, M., Kenig, E., and Allen, J.-M. A. Building better oscillators using nonlinear dynamics and pattern formation. *Pramana 84*, 3 (2015), 455–471.

[4] Harne, R., and Wang, K. Passive measurement of progressive mass change via bifurcation sensing with a multistable micromechanical system. *Journal of Intelligent Material Systems and Structures* (2014), 1045389X14546781.

[5] Jackson, S. *Modelling and control of coupled AFM arrays for parallel imaging verified through a macro scale experiment.* PhD thesis, University of Canterbury, 2017.

[6] Jackson, S., Gutschmidt, s., Roeser, D., and Sattel, T. Development of a mathematical model and analytical solution of a coupled two beam array with nonlinear tip forces for application to afm. *Nonlinear Dynamics 87*, 2 (2015), 775–787.

[7] Jalili, N., and Laxminarayana, K. A review of atomic force microscopy imaging systems: application to molecular metrology and biological sciences. *Mechatronics 14*, 8 (2004), 907–945.

[8] Jeong, B. *Constructive utilization of intentional nonlinearity in systems of coupled micro/nanomechanical resonators.* PhD thesis, University of Illinois at Urbana-Champaign, 2014.

[9] Manconi, E., and Mace, B. Veering and strong coupling effects in structural dynamics. *Journal of Vibration and Acoustics 139*, 2 (2017), 021009.

[10] Michels, T., and Rangelow, I. W. Review of scanning probe micromachining and its applications within nanoscience. *Microelectronic Engineering 126* (2014), 191–203.

[11] Prakash, G., Hu, S., Raman, A., and Reifenberger, R. Theoretical basis of parametric-resonance-based atomic force microscopy. *PHYSICAL REVIEW B 79*, 9 (MAR 2009).

[12] Rhoads, J. F., Guo, C., and Fedder, G. K. Parametrically excited micro- and nanosystems. *Resonant MEMS: Fundamentals, Implementation, and Application* (2015).

[13] Roeser, D., Gutschmidt, S., and Sattel, T. Considering nonlinearities to design micro systems vibrational sensitivity. *Proceedings in Applied Mathematics and Mechanics* (2017).

[14] Thiruvenkatanathan, P., and Seshia, A. Mode-localized displacement sensing. *Journal of Microelectromechanical Systems 21*, 5 (2012), 1016–1018.

[15] Villanueva, L., Karabalin, R., Matheny, M., Chi, D., Sader, J., and Roukes, M. Nonlinearity in nanomechanical cantilevers. *Physical Review B 87*, 2 (2013), 024304.

[16] Westra, H., Van der Zant, H., and Venstra, W. Modal interactions of flexural and torsional vibrations in a microcantilever. *Ultramicroscopy 120* (2012), 41–47.

[17] Zhao, C., Montaseri, M. H., Wood, G. S., Pu, S. H., Seshia, A. A., and Kraft, M. A review on coupled mems resonators for sensing applications utilizing mode localization. *Sensors and Actuators A: Physical 249* (2016), 93–111.

Dennis Roeser, Dipl.-Ing. (Ph.D. student): Technische Universität Ilmenau, Department of Mechanical Engineering, Mechatronics Group, Max-Planck-Ring 12, 98693 Ilmenau, Germany (*dennis.roeser@tu-ilmenau.de*).

Samuel Jackson, Ph.D.: University of Canterbury, Mechanical Engineering Department, Private Bag 4800,Christchurch, 8140, New Zealand (*samuel.jackson@pg.canterbury.ac.nz*).

Thomas Sattel, Professor: Technische Universität Ilmenau, Department of Mechanical Engineering, Mechatronics Group, Max-Planck-Ring 12, 98693 Ilmenau, Germany (*thomas.sattel@tu-ilmenau.de*). The author gave a presentation of this paper during one of the conference sessions.

Stefanie Gutschmidt, Senior Lecturer: University of Canterbury, Mechanical Engineering Department, Private Bag 4800,Christchurch, 8140, New Zealand (*stefanie.gutschmidt@canterbury.ac.nz*).

Dynamical investigation of a vibration driven locomotion system based on a multistable tensegrity structure

Philipp Schorr, Susanne Sumi, Valter Böhm, Klaus Zimmermann

Abstract: This paper discusses selected realization possibilities of vibration driven mobile robots based on compliant prestressed structures with multiple states of self-equilibrium. Therefore, a multistable tensegrity structure is considered exemplarily. The structure has two equilibrium configurations with different prestress states and corresponding dynamical properties. In the considered specific application, this discrete adjustable behavior of those structures is advantageous. The vibration modes of the structure and consequently the uniaxial locomotion of the system can be adapted according to the given environmental conditions. In order to study the dynamical behavior of the considered system, the nonlinear equations of motion are derived. Selected variants of periodic actuation are compared with the help of transient dynamical analyses, to show possible different vibration modes and the according locomotion. The movement efficiency of the system is evaluated depending on actuation and environmental parameters.

1. Introduction

Nowadays the increasing significance of mobile robotics requires a continuous optimization and miniaturization of the according sensors and actuators as well as the conception of innovative locomotion principles. In many application fields the working space is extremely limited that the use of conventional locomotion systems which base on wheels or legs is not possible anymore. Therefore the investigation of non-classical locomotion principles which enable an appropriate miniaturization is essential. Amongst others the application of tensegrity structures, known from the fields of architecture and modern arts, is a promising approach. Such prestressed structures contains of members which can be classified according to the resulting stress into compressed members and tensioned members. Corresponding to the tensegrity principle, compressed members are connected to each other via tensioned members. The mechanical behavior of robotic systems, based on these compliant structures, can be varied by modifying the prestress state. Beside this adaptability, the multifunctionality of those structures offers a huge potential for the application in mobile robotics. For example different types of motion like crawling, tilting, etc. can be realized using the pronounced shape change capability of tensegrity structures.

The locomotion of the most known tensegrity based mobile robots is generated by a shape change of the system induced by systematic modification of the length of selected members [5, 6, 9, 10, 12]. Another approach to create a movement of these robots bases on the shift of internal masses [7]. The use of compliant tensegrity structures in vibration driven locomotion systems offers several advantages, like simple system design and tunable motion behavior [2–4, 8, 11]. The dynamical properties of these systems can be influenced by varying the prestress state. In known systems this could be only realized by changing the mechanical parameters of selected members. The use of compliant mulistable tensegrity structures in robotic applications with more than one stable equilibrium state is a promising research topic. In contrast to the mentioned systems, based on tensegrity structures with only one equilibrium configuration, multistable tensegrity structures also allow to vary the prestress state by changing between their different stable equilibrium states. Variable movement performance can be realized by utilizing the different equilibrium configurations of these structures.

In this paper an uniaxial vibration driven locomotion system based on a multistable planar tensegrity structure, inspired by [1, 13] is investigated. The symmetric system is in contact with a plane horizontal underground and is excited by a single harmonic actuation. The according equations of motion are derived in section 2. The locomotion of the system with selected parameters for each member is simulated for different environmental and actuation conditions. The motion in the stationary state is evaluated in section 3 and essential locomotion characteristics are determined. With regard to the different stable equilibrium states used as initial configuration qualitative conclusions about the dynamical behavior of the locomotion system are given in order to show the advantageous properties of multistable tensegrity structures for the application in mobile robotics.

2. Mechanical description of the multistable tensegrity structures

2.1. Mechanical model

The investigated tensegrity structure is displayed in Fig. 1. The system consist of 9 members ($\mathrm{j} \in 1, 2, \ldots, 9$) which are connected by 5 pin-joints (nodes, $\mathrm{i} \in 1, 2, \ldots, 5$). The elements 1, 2, 3 are compressed members and the remaining elements are tensioned members. The tensegrity structure is considered as a planar system and is described in the cartesian coordinate system {x, y, z}. The current system configuration is given by the position vectors $\vec{\mathrm{x}}_\mathrm{i} = (\mathrm{x_i}, \mathrm{y_i}, \mathrm{z_i})^\mathrm{T}$ of the nodes i ($\mathrm{z_i} \equiv 0$). The locomotion system is in contact with a horizontal plane underground in the gravity field of the earth ($\vec{g} = -g\vec{e}_\mathrm{z}$). The nodes i are supposed to be the corresponding contact points. The resulting friction is modeled with Coulomb's Law of Friction.

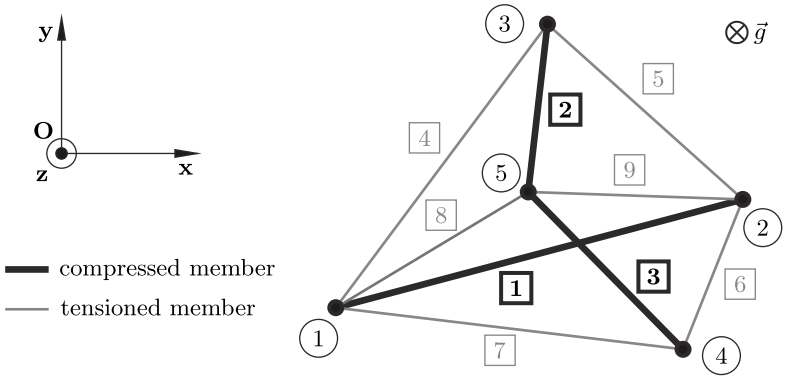

Figure 1. Multistable tensegrity structure in arbitrary state.

Each element j is defined by the nodes j_1 and j_2 and is modeled as linear elastic spring characterized by c_j as according spring rate and λ_{0j} as initial length. Furthermore material damping properties are taken into account by an additional linear damping element which is described by the damping coefficient k_j. The mass of each element j is given by m_j. The according mass distribution as well as the inertia of the elements are included by a linear link element known from the finite-element-method. The resulting element model is developed by an parallel arrangement of the mentioned components as shown in Fig. 2. Moreover the tensioned members are considered as massless.

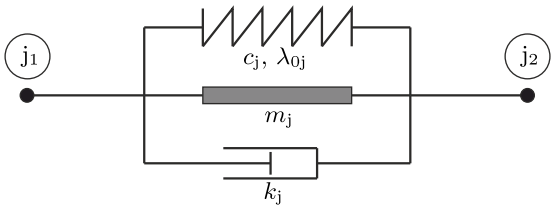

Figure 2. Model of the member j of the investigated tensegrity structure.

In this paper a one-dimensional locomotion is investigated. Therefore the given tensegrity structure is supposed to be symmetric with respect to the longitudinal axis of the compressed member 1 as axis of symmetry. Therefore, the elements 2 and 3, 4 and 7, 5 and 6 are supposed to be identical (see Tab. 1). The direction of motion is given by the orientation of the element 1. Without loss of generality it is assumed that the direction of motion equals the x-axis ($y_1 \equiv 0$, $y_2 \equiv 0$, $y_5 \equiv 0$, $x_4 = x_3$, $y_4 = -y_3$). Therefore the mechanical model of the structure can be simplified as shown in Fig. 3.

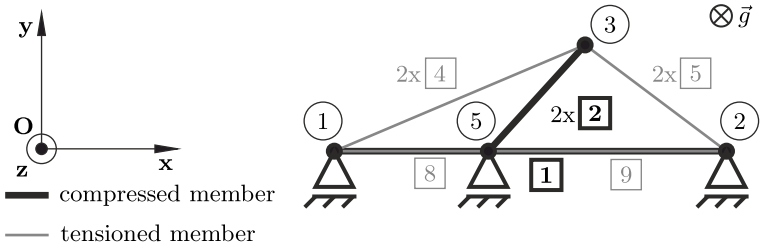

Figure 3. Uniaxial locomotion system based on multistable tensegrity structures.

Hence, the system can be considered as locomotion system with five degrees of freedom. As generalized coordinates the parameters $\vec{q} = (\mathrm{x}_1, \mathrm{x}_2, \mathrm{x}_3, \mathrm{y}_3, \mathrm{x}_5)^{\mathrm{T}}$ are chosen. The topology of the resulting structure and the chosen parameters are listed in Tab. 1.

Table 1. Structural topology and selected simulation parameters.

Element **j**	**Nodes** $\mathbf{j_1 - j_2}$	**Inital length** **[m]**	**Stiffness** **[N/m]**	**Damping** **[Ns/m]**	**Mass** **[kg]**
1	$1-2$	$\lambda_{01} = 0.2000$	$c_1 = 10^6$	$k_1 = 0.2$	$m_1 = 0.1$
2	$3-5$	$\lambda_{02} = 0.0800$	$c_2 = 10^6$	$k_2 = 0.2$	$m_2 = 0.05$
3	$4-5$	$\lambda_{03} = 0.0800$	$c_3 = 10^6$	$k_3 = 0.2$	$m_3 = 0.05$
4	$1-3$	$\lambda_{04} = 0.0644$	$c_4 = 43$	$k_4 = 0.2$	$m_4 = 0$
5	$2-3$	$\lambda_{05} = 0.0644$	$c_5 = 43$	$k_5 = 0.2$	$m_5 = 0$
6	$2-4$	$\lambda_{06} = 0.0644$	$c_6 = 43$	$k_6 = 0.2$	$m_6 = 0$
7	$1-4$	$\lambda_{07} = 0.0644$	$c_7 = 43$	$k_7 = 0.2$	$m_7 = 0$
8	$1-5$	$\lambda_{08} = 0.0299$	$c_8 = 84$	$k_8 = 0.2$	$m_8 = 0$
9	$2-5$	$\lambda_{09} = 0.0319$	$c_9 = 84$	$k_9 = 0.2$	$m_9 = 0$

2.2. Elastic deformation and self-equilibrium states

For the description of the dynamical behavior and the locomotion of the structure the equations of motions have to be derived. Therefore all acting forces have to be defined. Beside the actuation of the structure the elastic deformation of each member have to be taken into account. The according force $\vec{F}_{\mathrm{e,j}}$ of the element j is given by the equation formulated in (1).

$$\vec{F}_{\mathrm{e,j}} = \begin{pmatrix} F_{\mathrm{e,j,x}} \\ F_{\mathrm{e,j,y}} \end{pmatrix} = \left(-c_{\mathrm{j}} \left(|\vec{\mathrm{x}}_{\mathrm{j2}} - \vec{\mathrm{x}}_{\mathrm{j1}}| - \lambda_{0\mathrm{j}} \right) - k_{\mathrm{j}} \frac{(\dot{\vec{\mathrm{x}}}_{\mathrm{j2}} - \dot{\vec{\mathrm{x}}}_{\mathrm{j1}}) \cdot (\vec{\mathrm{x}}_{\mathrm{j2}} - \vec{\mathrm{x}}_{\mathrm{j1}})}{|\vec{\mathrm{x}}_{\mathrm{j2}} - \vec{\mathrm{x}}_{\mathrm{j1}}|} \right) \frac{\vec{\mathrm{x}}_{\mathrm{j2}} - \vec{\mathrm{x}}_{\mathrm{j1}}}{|\vec{\mathrm{x}}_{\mathrm{j2}} - \vec{\mathrm{x}}_{\mathrm{j1}}|} \tag{1}$$

The element forces can be combined to nodal force $\vec{F}_{\mathrm{n,i}} = (F_{\mathrm{n,i,x}}, F_{\mathrm{n,i,y}})^{\mathrm{T}}$. Regarding the chosen generalized coordinates $\vec{q}$ the relevant components of the nodal forces:

$$\begin{aligned}
F_{\mathrm{n,1,x}} &= -F_{\mathrm{e,1,x}} - 2F_{\mathrm{e,4,x}} - F_{\mathrm{e,8,x}} \\
F_{\mathrm{n,2,x}} &= F_{\mathrm{e,1,x}} - 2F_{\mathrm{e,5,x}} - F_{\mathrm{e,9,x}} \\
F_{\mathrm{n,3,x}} &= -2F_{\mathrm{e,2,x}} + 2F_{\mathrm{e,4,x}} + 2F_{\mathrm{e,5,x}} \\
F_{\mathrm{n,3,y}} &= -2F_{\mathrm{e,2,y}} + 2F_{\mathrm{e,4,y}} + 2F_{\mathrm{e,5,y}} \\
F_{\mathrm{n,5,x}} &= 2F_{\mathrm{e,2,x}} + F_{\mathrm{e,8,x}} + F_{\mathrm{e,9,x}}
\end{aligned} \tag{2}$$

Because of the given symmetry of the structure, the remaining components of the nodal forces are equal to zero. For the determination of the equilibrium states of the structure all of the in (2) listed components of the nodal forces have to be equal zero. This yields to a nonlinear system of equations which can be solved numerically. As consequence 5 symmetric equilibrium states were found for the given tensegrity structure with the parameters shown in Tab. 1. Further investigations regarding the according static stability show that there are 2 stable and 3 instable configurations. For the following analysis of the locomotion system only the 3 two dimensional equilibrium states (A, B, C) shown in Fig. 4 are relevant.

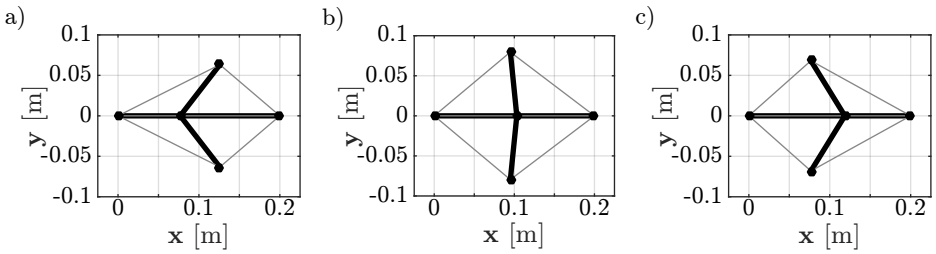

Figure 4. Two-dimensional symmetric equilibrium states of the investigated tensegrity-structure - a) stable state A, b) instable state B, c) stable state C.

2.3. Equations of motion

The actuation of the structure is realized as excitation of the massless member 8. The initial length of this element is varied by a harmonic function $s(t) = -a\sin(2\pi f t)$. In this paper the amplitude of the excitation function is restricted to $a = 0.01$ m. This yields to an actuation force $\vec{F}_{\mathrm{act}} = F_{\mathrm{act}}\vec{e}_{\mathrm{x}}$ which is formulated in (3).

$$\vec{F}_{\mathrm{act}} = (-c_8 \cdot s(t) - k_8 \cdot \dot{s}(t))\vec{e}_{\mathrm{x}} = -a(c_8 \sin(2\pi f t) + 2\pi f \cos(2\pi f t))\vec{e}_{\mathrm{x}} \tag{3}$$

Taken the illustrated actuation force into account the nodal forces have to be extended as shown in (4). To differentiate between these forces and the nodal forces for the static case they are defined as resulting forces $\vec{F}_{\mathrm{res,i}} = (F_{\mathrm{res,i,x}}, F_{\mathrm{res,i,y}})^{\mathrm{T}}$.

$$\begin{aligned} F_{\mathrm{res,1,x}} &= F_{\mathrm{n,1,x}} - F_{\mathrm{act}} \\ F_{\mathrm{res,2,x}} &= F_{\mathrm{n,2,x}} \\ F_{\mathrm{res,3,x}} &= F_{\mathrm{n,3,x}} \\ F_{\mathrm{res,3,y}} &= F_{\mathrm{n,3,y}} \\ F_{\mathrm{res,5,x}} &= F_{\mathrm{n,5,x}} + F_{\mathrm{act}} \end{aligned} \tag{4}$$

To model the friction forces $\vec{F}_{\mathrm{C,i}}$ between the nodes and the plane underground COULOMB's Law of Friction is used. In order to handle the zero velocity with the corresponding sticking effects despite of the numerical accuracy, an additional parameter δ is introduced. This method bases on an idea of KARNOPP. The resulting modified COULOMB's Law of Friction is formulated in (5). The parameter $\vec{F}_{\mathrm{N,i}}$ describes the according contact force.

$$\vec{F}_{\mathrm{C,i}} = \begin{cases} -\mu|\vec{F}_{\mathrm{N,i}}|\frac{\dot{\vec{x}}_{\mathrm{i}}}{|\dot{\vec{x}}_{\mathrm{i}}|} & \text{if } |\dot{\vec{x}}_{\mathrm{i}}| > \delta \\ -\mu|\vec{F}_{\mathrm{N,i}}|\frac{\vec{F}_{\mathrm{res,i}}}{|\vec{F}_{\mathrm{res,i}}|} & \text{if } |\dot{\vec{x}}_{\mathrm{i}}| \leq \delta \quad \text{and } |\vec{F}_{\mathrm{res,i}}| > \mu_0|\vec{F}_{\mathrm{N,i}}| \quad \text{with } \delta = 10^{-4}\,\dfrac{\mathrm{m}}{\mathrm{s}} \\ -\vec{F}_{\mathrm{res,i}} & \text{if } |\dot{\vec{x}}_{\mathrm{i}}| \leq \delta \quad \text{and } |\vec{F}_{\mathrm{res,i}}| \leq \mu_0|\vec{F}_{\mathrm{N,i}}| \end{cases} \tag{5}$$

As result the acting forces during the motion of the system $\vec{F}_{\mathrm{i}} = (F_{\mathrm{i,x}}, F_{\mathrm{i,y}})^{\mathrm{T}} = \vec{F}_{\mathrm{res,i}} + \vec{F}_{\mathrm{C,i}}$ can be formulated. Furthermore with regard to the generalized coordinates $\vec{q}$ an according force vector $\vec{F}_{\mathrm{q}}(\vec{q}, \dot{\vec{q}}, t)$ can be defined as shown in (6).

$$\vec{F}_{\mathrm{q}}(\vec{q}, \dot{\vec{q}}, t) = (F_{1,\mathrm{x}}, F_{2,\mathrm{x}}, F_{3,\mathrm{x}}, F_{3,\mathrm{y}}, F_{5,\mathrm{x}})^{\mathrm{T}} \tag{6}$$

Taken the given mass distribution of the structure into account the equations of motion can be derived as shown in (7). These are formulated as a nonlinear system of 2nd order differential equations.

$$\mathbf{M}\ddot{\vec{q}} = \vec{F}_{\mathrm{q}}(\vec{q}, \dot{\vec{q}}, t) \quad \Rightarrow \quad \begin{bmatrix} \frac{m_1}{3} & \frac{m_1}{6} & 0 & 0 & 0 \\ \frac{m_1}{6} & \frac{m_1}{3} & 0 & 0 & 0 \\ 0 & 0 & 2\frac{m_2}{3} & 0 & 2\frac{m_2}{6} \\ 0 & 0 & 0 & 2\frac{m_2}{3} & 0 \\ 0 & 0 & 2\frac{m_2}{6} & 0 & 2\frac{m_2}{3} \end{bmatrix} \begin{pmatrix} \ddot{\mathrm{x}}_1 \\ \ddot{\mathrm{x}}_2 \\ \ddot{\mathrm{x}}_3 \\ \ddot{\mathrm{y}}_3 \\ \ddot{\mathrm{x}}_5 \end{pmatrix} = \begin{pmatrix} F_{1,\mathrm{x}} \\ F_{2,\mathrm{x}} \\ F_{3,\mathrm{x}} \\ F_{3,\mathrm{y}} \\ F_{5,\mathrm{x}} \end{pmatrix} \tag{7}$$

3. Dynamical investigations of the multistable tensegrity structure

The equations of motion, derived in subsection 2.3, are solved numerically using Runge-Kutta-Method 4^{th} order and a suitable step size of 10^{-4} s. As initial configuration the stable equilibrium state A or C is chosen and the system is supposed to be at rest. The movement of the system is simulated for 1000 actuation periods (period duration of the actuation: $T = 1/f$, with f: actuation frequency). The steady state is assumed after 900 actuation periods. Evaluating the remaining time interval ($t \in (900T; 1000T]$), locomotion characteristics like the stationary locomotion velocity and the vibration mode are determined. In order to investigate the influence of environmental and actuation conditions, these studies are repeated for different friction properties and appropriate actuation frequencies.

Furthermore the eigenfrequencies of the multistable tensegrity structure are taken into account in order to illustrate relations to dynamical effects of the locomotion system. These frequencies are determined by a modal analysis. Therefore the structure was linearized with respect to the stable equilibrium states A and C and friction effects were neglected. Beside the rigid body motions, 7 eigenfrequencies result for each equilibrium state. Neglecting longitudinal oscillations of the compressed members as well as frequencies yielding to asymmetric eigenmodes, 2 eigenfrequencies remain ($f_{\text{A},1}$, $f_{\text{A},2}$ and $f_{\text{C},1}$, $f_{\text{C},2}$).

3.1. Chaotic behavior

Because of the non-linearity of the system chaotic motion behavior can appear. The resulting effects are critical to handle because the motion of the system cannot be predicted anymore. Especially with regard to a future technological application, those operating conditions have to be avoided to remain the controllability of the locomotion system. Hence, dynamical investigations considering the periodicity of the locomotion are necessary. Therefore, as criterion the relative motion of the node 5 along the x-axis ($\mathrm{x}_{5,\text{rel}} = \mathrm{x}_5 - \mathrm{x}_1$) is considered exemplarily and the corresponding Poincaré-Map is used to estimate the chaotic behavior of the system. In Fig. 5 the according bifurcation diagram is shown in dependence of the actuation frequency. In this figure different chaotic ranges of actuation frequencies can be identified. In general those depend among others of the friction and damping properties. An evaluation of typical locomotion characteristics is not possible for such cases. Therefore chaotic ranges are not taken into account for the further investigations.

Regarding the periodicity of the structural motion, a duplication or even a multiplication of the corresponding period duration can be observed for some non-chaotic actuation frequencies. This effect can also be reasoned with the non-linear behavior of the locomotion system. According to this phenomena the parameter $T_{\text{p}} = \mathrm{n}T$ ($\mathrm{n} \in \mathbb{N}$), which describes the period duration of the structural motion, is defined.

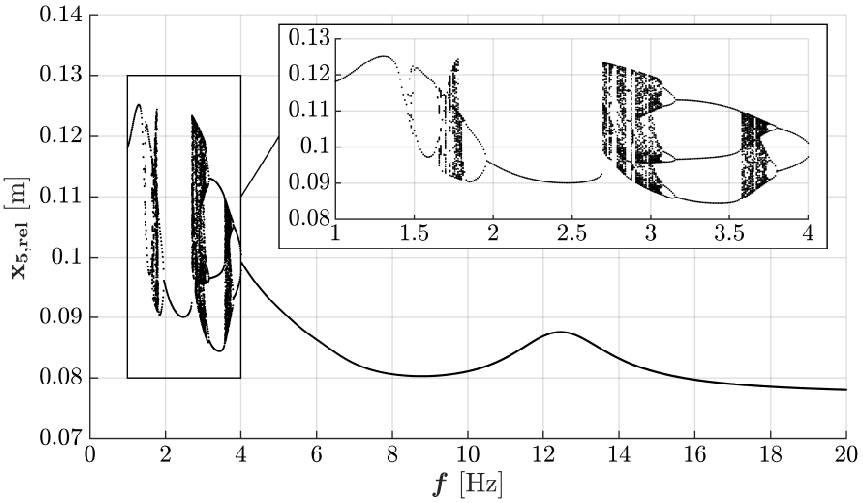

Figure 5. POINCARÉ-MAP of $x_{5,rel}$ of the locomotion system with $\mu = \mu_0 = 0.1$ and the stable equilibrium state A as inital configuration.

3.2. Vibration mode of the tensegrity structure

Evaluating the vibration mode of the structure in the stationary state, different types of vibration can be classified. The appearance of these different oscillation shapes depends on the actuation, the initial configuration and the friction properties. The mentioned vibrations modes are qualitatively displayed in Fig. 6. In contrast to systems with only one stable equilibrium states and therefore in general one vibration mode, multistable tensegrity structures enable several different types of oscillation. Beside small vibrations around each stable equilibrium state (see Fig 6 a, b), a continuous change between stable equilibrium configurations occurs for an appropriate actuation (see Fig 6 c).

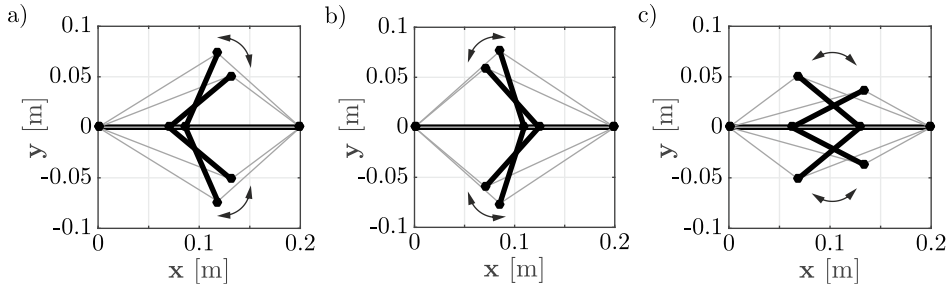

Figure 6. Vibration modes - a) vibration around state A, b) vibration around state C, c) continuous change between the states A and C.

Each type of oscillation leads to different locomotion characteristics. Therefore, depending on the given environmental conditions, the actuation properties as well as the equilibrium state as initial configuration can be chosen to effect a vibration mode with desired dynamical behavior. The appearance of these vibration modes are displayed exemplarily in Fig 7.

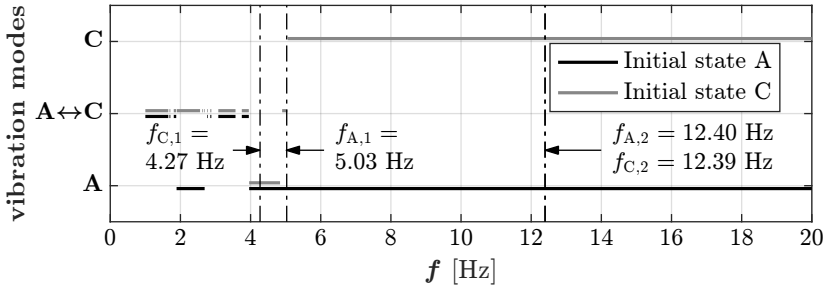

Figure 7. Simulation results regarding the vibration modes for $\mu = \mu_0 = 0.1$.

The resulting vibration mode can be influenced by the actuation frequencies and the initial configuration. However, the resulting vibration mode is not predetermined by the initial state. See for example the frequency range 4 - 5 Hz in Fig. 7. In this case the structure vibrates around the stable equilibrium state A although the equilibrium state C is chosen as initial configuration. However for frequencies above the first eigenfrequencies, a control of the vibration mode by the according equilibrium state which is chosen as initial condition is suitable (see Fig. 7: $f > \max[f_{A,1}, f_{C,1}]$).

3.3. Stationary locomotion velocity

The locomotion of the structure can be classified by its mean velocity in the stationary state and by its direction of motion. This values are given by the stationary locomotion velocity. The corresponding definition is given in (8). Hence, the time t_0 is an arbitrary moment in the stationary state.

$$\vec{\mathrm{v}}_{\mathrm{stat}} = \mathrm{v}_{\mathrm{stat}}\vec{\mathrm{e}}_{\mathrm{x}} = \frac{1}{T_{\mathrm{p}}}\int_{t_0}^{t_0+T_{\mathrm{p}}} \dot{\mathrm{x}}_{\mathrm{i}}\,\mathrm{d}t\;\vec{\mathrm{e}}_{\mathrm{x}} = \frac{\mathrm{x}_{\mathrm{i}}(t_0+T_{\mathrm{p}}) - \mathrm{x}_{\mathrm{i}}(t_0)}{T_{\mathrm{p}}}\vec{\mathrm{e}}_{\mathrm{x}} \qquad \mathrm{i} \in 1,2,3,5 \tag{8}$$

The resulting stationary velocity of the locomotion is displayed in Fig. 8 for different friction properties and initial configurations. As mentioned in subsection 3.1 chaotic effects can appear but are not taken into account (see e.g. Fig. 8 a: $f \approx 3$ Hz). Moreover, the motion of the system seems difficult to handle for frequencies near those chaotic ranges (see Fig. 8 a: $f < 4$ Hz).

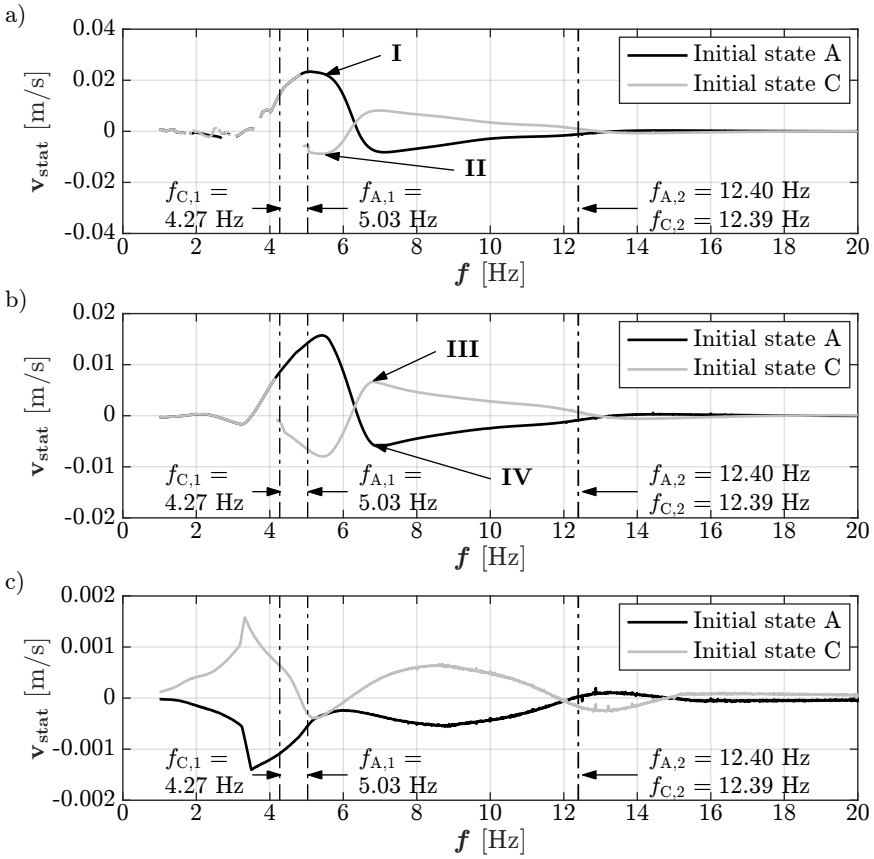

Figure 8. Evaluation of the stationary locomotion velocity - a) $\mu = \mu_0 = 0.1$, b) $\mu = \mu_0 = 0.2$, c) $\mu = \mu_0 = 0.5$.

Regarding the stationary locomotion velocity for the different equilibrium states as initial configuration, no useful locomotion results for actuation frequencies above the second eigenfrequency. This issue limits the working range of the actuation frequency. Nevertheless the stationary locomotion velocity and the according direction of motion can be controlled by varying the actuation frequency or switching the equilibrium state as initial configuration. Even for great friction coefficients a bidirectional locomotion with suitable velocity can still be realized by changing the equilibrium states (see Fig. 8 c). Comparing the absolute values of the stationary locomotion velocity for various initial configurations different locomotion characteristics result for actuation frequencies near the first eigenfrequency (see I and II). However for increasing actuation frequencies the influence of the initial configuration on the dynamical behavior of locomotion systems decreases (see III and IV). This phenomena can

be explained with the according eigenfrequencies. The second eigenfrequencies $f_{A,2}$ and $f_{C,2}$ are almost equal. Therefore a change of the equilibrium state effect no modification of the dynamical properties for actuation frequencies near $f_{A,2}$ and $f_{C,2}$. That means, the locomotion characteristics can be influenced by switching the equilibrium states only for actuation frequencies near the first eigenfrequencies.
According to the shown results, the simulations confirm, that indeed, it is possible to influence the dynamical behavior, especially the motion characteristics of the locomotion system, by changing the equilibrium state and the corresponding vibration mode.

4. Conclusion

This paper offers an approach to non-classical locomotion based on multistable tensegrity structures. A symmetric planar tensegrity structure with a single actuation is considered as uniaxial vibration driven locomotion system. The mechanical model is introduced and the equilibrium states of the structure are determined for selected parameters. The nonlinear equations of motion are derived and solved numerically. The locomotion of the system is simulated for different environmental and actuation conditions and the stationary state is evaluated. Chaotic motion behavior is shown and typical locomotion characteristics of the system are evaluated with regard to the different stable equilibrium states used as initial configuration. The simulation results confirm, that multistable tensegrity structures offers several vibration modes with different dynamical properties. Moreover, the dynamical behavior of the system can be influenced by changing the equilibrium state. Compared to systems with only one equilibrium state, multistable tensegrity structures enable additional opportunities to vary the prestress state and the corresponding motion characteristics of the locomotion system. Because of the controllable dynamical properties and great adaptability to variable environmental conditions, a vibration-driven locomotion system based on multistable tensegrity structures is advantageous for the application field of mobile robotics.

Acknowledgments

This work is supported by the Deutsche Forschungsgemeinschaft (DFG project BO4114/2-1).

References

[1] Böhm, V., Susanne, S., Kaufhold, T., et al. Compliant multistable tensegrity structures. *Mechanism and Machine Theory 115* (2017), 130–148.

[2] Böhm, V., Zeidis, I., and Zimmermann, K. Dynamic analysis of a simple planar tensegrity structure for the use in vibration driven locomotion systems. *12th Conference on Dynamical Systems - Theory and Applications 2* (2013), 341–352.

[3] Böhm, V., Zeidis, I., and Zimmermann, K. An approach to the dynamics and control of a planar tensegrity structure with application in locomotion systems. *Int. J. of Dynamics and Control 3*, 1 (2015), 41–49.

[4] Böhm, V., and Zimmermann, K. Vibration-driven mobile robots based on single actuated tensegrity structures. *IEEE ICRA* (2013), 5455–5460.

[5] Chen, L., Kim, K., Tangand, E., et al. Soft spherical tensegrity robot design using rod-centered actuation and control. *ASME Journal of Mechanisms and Robotics 9* (2017).

[6] Hustig-Schultz, D., SunSpiral, V., and Teodorescu, M. Morphological design for controlled tensegrity quadruped locomotion. *IEEE/RSJ IROS* (2016), 4714–4719.

[7] Kaufhold, T., Schale, F., Böhm, V., et al. Indoor locomotion experiments of a spherical mobile robot based on a tensegrity structure with curved compressed members. *IEEE AIM* (2017), 523–528.

[8] Khazanov, M., Jocque, J., and Rieffel, J. Evolution of locomotion on a physical tensegrity robot. *14th Int. Conf. on the Synthesis and Simulation of Living Systems* (2014), 232–238.

[9] Kim, K., Chen, L., Cera, B., et al. Hopping and rolling locomotion with spherical tensegrity robots. *IEEE/RSJ IROS* (2016), 4369–4376.

[10] Liu, H., Yu, Y., Sunand, P., et al. Motion analysis of the four-bar tensegrity robot. *IEEE International Conference on Mechatronics and Automation* (2016), 1483–1488.

[11] Rieffel, J., Valero-Cuevas, F., and Lipson, H. Morphological communication: exploiting coupled dynamics in a complex mechanical structure to achieve locomotion. *Journal of the Royal Society Interface 7* (2010), 613–621.

[12] Sabelhaus, A., Bruce, J., Caluwaerts, K., et al. System design and locomotion of superball,an untethered tensegrity robot. *IEEE ICRA* (2015), 2867–2873.

[13] Sumi, S., Böhm, V., and Zimmermann, K. A multistable tensegrity structure with a gripper application. *Mechanism and Machine Theory 114* (2017), 204–217.

Philipp Schorr, M.Sc. (Ph.D. student): Technische Universität Ilmenau, Technical Mechanics Group, Max-Planck-Ring 12, D-98693 Ilmenau, Germany (*Philipp.Schorr@tu-ilmenau.de*). The author gave a presentation of this paper during one of the conference sessions.

Susanne Sumi, M.Sc. (Ph.D. student): Technische Universität Ilmenau, Technical Mechanics Group, Max-Planck-Ring 12, D-98693 Ilmenau, Germany (*Susanne.Sumi@tu-ilmenau.de*).

Valter Böhm, Associate Professor: Technische Universität Ilmenau, Technical Mechanics Group, Max-Planck-Ring 12, D-98693 Ilmenau, Germany (*Valter.Boehm@tu-ilmenau.de*).

Klaus Zimmermann, Professor: Technische Universität Ilmenau, Technical Mechanics Group, Max-Planck-Ring 12, D-98693 Ilmenau, Germany (*Klaus.Zimmermann@tu-ilmenau.de*).

Equilibria and global dynamics of a 2 DoF aeroelastic system

Yury Selyutskiy

Abstract: Study of aerodynamic flutter has a long history. Interest to this problem is stimulated by applications: on the one hand, the flutter effect should be eliminated in order to ensure durability of structures; on the other hand, this phenomenon can be used to harvest energy from the flow. In the present work, an aeroelastic system with two degrees of freedom (translational and rotational) is considered. Aerodynamic load is simulated using the quasi-steady approach. Evolution of the set of equilibrium positions of the system (including both trivial and "oblique" ones) is studied depending on structural parameters. Stability criteria are obtained for these equilibria, and attraction domains are analyzed. Numerical simulation of the system behavior is performed for different values of parameters, including in the area of large angles of attack.

1. Introduction

Aeroelastic systems are mechanical systems, dynamics of which is determined by the interplay of elastic forces (e.g., in attachment of elements of these systems to some basement) and aerodynamic or hydrodynamic forces acting upon these systems. It is well known that the nominal" equilibrium of the system can become unstable for large enough flow speeds. A vast literature is dedicated to investigation of such systems, which is due to their importance from the point of view of applications (in aeronautics, civil engineering, etc.).

A large number of works are related with the classical flutter, when the flow remains practically laminar, and the amplitude of arising limit cycle oscillations is determined by structural nonlinearity. In these works, local analysis of the system behavior near the trivial equilibrium is performed: description of arising limit cycle oscillations, generation of control laws aimed at limiting the amplitudes of these cycles and/or prevention of their appearance, etc. (e.g., [1-2]). The so-called stall flutter related with separation of flow (amplitude of oscillations in this case is determined by non-linearity of the aerodynamic load) is also intensely studied. For instance, in [3], where experimental and analytical study of large-amplitude limit cycle oscillations of a flat plate is performed, and in [4], where limit cycle oscillations and bifurcations of an airfoil undergoing stall flutter are investigated. Influence of different types of nonlinearities (such as cubic or free-play) is discussed in [5]. Chaotic behavior of such system and various patterns of transition to chaos are investigated in [6].

In many applications, flutter effects are harmful, as they result in faster wear, increased fatigue, and destruction of structures. However, since recently, an interest appeared to using these effects to harvest the energy from the flow [7,8].

From this point of view, stability of equilibrium positions is undesired, and it is necessary to search for ranges of parameters where limit cycles with large enough amplitude and frequency exist. In such applications, it is not important for the wing to make a small angle with the flow. Hence, it is reasonable to investigate (analytically, numerically, as well as experimentally) behavior of the aeroelastic system in the entire range of angles of attack. However, currently there are practically no works of that kind.

In the present paper, questions of existence and stability of "oblique" equilibrium positions arising in the aeroelastic system are considered, and numerical simulation of the system dynamics under different values of parameters is performed.

2. Equations of motion

Consider an aeroelastic system consisting of a thin wing with symmetrical airfoil which is mounted on elastic support in such a way that it has two degrees of freedom (translational and rotational). The system is installed in the horizontal airflow, so that the axis OY of translation is perpendicular to the flow speed, and the axis of rotation (elastic axis) is vertical and can move along the axis OY (see Fig. 1). Choose the displacement y of the elastic axis and angle θ between the wing chord and the flow speed as the generalized coordinates. Suppose that the center of mass G of the wing coincides with the elastic axis.

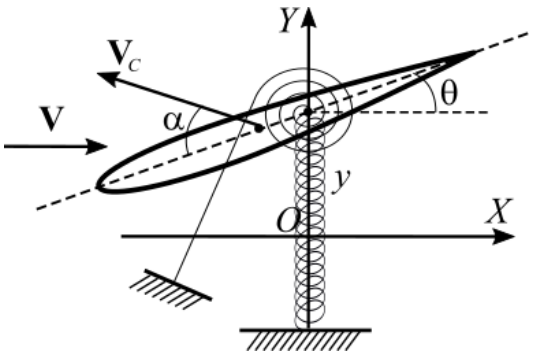

Figure 1. Aeroelastic system with translational and rotational degrees of freedom.

The pitch spring is unloaded when the wing makes a zero angle with the flow. Assume also that both plunge spring stiffness and pitch spring stiffness are linear.

In order to describe the aerodynamic load upon the wing, we use the quasi-steady approach. Under the conventional assumption that the flow about the wing is two-dimensional, the aerodynamic load can be represented as a force applied in the mid-chord point C of the wing, and the torque about this point. The aerodynamic force can be decomposed into two components: drag force D, which is directed against the airspeed V_C of the mid-chord point, and lift force L, which is perpendicular to V_C. Lift and drag forces, as well as the aerodynamic torque, are described by the following formulae:

$$L = \frac{\varrho S}{2} V_C^2 C_l(\alpha),\ D = \frac{\varrho S}{2} V_C^2 C_d(\alpha),\ M = \frac{\varrho S}{2} V_C^2 b C_m(\alpha). \tag{1}$$

Here ϱ is the air density; S is the wing area; b is the chord length; α is the efficient angle of attack; by which we will mean the angle between V_C and the wing chord; $C_l(\alpha)$, $C_d(\alpha)$, and $C_m(\alpha)$ are non-dimensional coefficients of the lift force, drag force, and torque, correspondingly. Dependencies of these coefficients upon the angle of attack can be taken from static experiments.

The angle of attack and the airspeed of the point C are given by the following kinematical relations:

$$\begin{aligned} V_C \cos\alpha &= V\cos\theta - \dot{y}\sin\theta, \\ V_C \sin\alpha &= V\sin\theta + \dot{y}\cos\theta - r\dot{\theta}, \end{aligned} \tag{2}$$

where r is the distance from the mid-chord point to the center of mass of the wing (positive towards the trailing edge of the wing).

Then equations of motion of the system can be represented as follows:

$$\begin{aligned} m\ddot{y} + ky &= L\cos(\alpha-\theta) + D\sin(\alpha-\theta), \\ J\ddot{\theta} + \kappa\theta &= M + Lr\cos\alpha + Dr\sin\alpha, \end{aligned} \tag{3}$$

where m is the mass of the wing, J is the moment of inertia of the wing with respect to the elastic axis, k is the plunge spring stiffness, κ is the pitch spring stiffness.

In order to simplify the notation, introduce the dimensionless time $\tau = \sqrt{b/V_0}$ (V_0 is a characteristic speed) and the following dimensionless variables and parameters: $\eta = y/b$, $\xi = r/b$, $u = V/V_0$, $u_C = V_C/V_0$.

Taking into account (1), equations (2) and (3) can be rewritten as follows (dot means derivative with respect to τ):

$$\begin{aligned} u_C \cos\alpha &= u\cos\theta - \dot{\eta}\sin\theta, \\ u_C \sin\alpha &= u\sin\theta + \dot{\eta}\cos\theta - \xi\dot{\theta}, \end{aligned} \tag{4}$$

$$
\begin{aligned}
&m\ddot{\eta} + k\eta = u_C^2\left(C_l(\alpha)\cos(\alpha-\theta) + C_d(\alpha)\sin(\alpha-\theta)\right),\\
&J\ddot{\theta} + \kappa\theta = u_C^2\left(C_m(\alpha) + C_l(\alpha)\xi\cos\alpha + C_d(\alpha)\xi\sin\alpha\right),
\end{aligned}
\tag{5}
$$

Relations (4)-(5) form a closed system of equations.

3. Equilibria and their stability

For symmetrical airfoils, lift coefficient and moment coefficient are equal to zero for $\alpha = 0$. Hence, (5) admits the trivial solution $\eta = 0$, $\theta = 0$. Usually, behavior of the aeroelastic system in the vicinity of this equilibrium is considered. However, this equilibrium, under certain conditions that we will discuss below, is not unique.

Write down equilibrium equations:

$$
\begin{aligned}
&k\eta_* = u^2 C_l(\theta_*),\\
&\kappa\theta_* = u^2\left(C_m(\theta_*) + C_l(\theta_*)\xi\cos\theta_* + C_d(\theta_*)\xi\sin\theta_*\right),
\end{aligned}
\tag{6}
$$

The second equation (6) contains only θ, so the first equation can be considered as equation on y. Functions $C_m(\alpha)$, $C_l(\alpha)$, and $C_d(\alpha)$ are 2π - periodic. Moreover, it is known from experiments that, for symmetric airfoils, $C_m(\alpha)$ and $C_l(\alpha)$ are uneven functions, and $C_d(\alpha)$ is even. Hence, the function in the right-hand side of the second equation (7) is uneven. This means that, for different values of κ, this equation can have multiple solutions, and their number tends to infinity as κ tends to zero. Consider the function $f(\alpha) = C_m(\alpha) + C_l(\alpha)\xi\cos\alpha + C_d(\alpha)\xi\sin\alpha$. Based on results of tests performed in wind tunnels, the following inequality can be established for relatively thin symmetrical airfoils:

$$
|\alpha f_{\alpha 0}| \geq |f(\alpha)|, \text{ where } f_{\alpha 0} = \left.\frac{df}{d\alpha}\right|_{\alpha=0}. \tag{7}
$$

From (7) it follows that if

$$
\kappa > u^2 f_{\alpha 0} \tag{8}
$$

then there exists only one equilibrium, namely, the trivial one. For smaller κ, there exist additional couples of equilibria (evidently, if (η_*, θ_*) is an equilibrium, then $(-\eta_*, -\theta_*)$ is also an equilibrium). Note that increase in the flow speed leads to violation of (8) and appearance of additional equilibria.

Stability conditions of equilibrium positions are rather cumbersome. However, one can readily find the condition of static instability:

$\kappa > u^2 f_{\alpha^*}$, where $f_{\alpha^*} = \left.\dfrac{df}{d\alpha}\right|_{\alpha=\theta_*}$. (9)

Comparing (8) and (9), we can conclude that "oblique" equilibria exist, when the trivial equilibrium becomes statically unstable.

Consider the situation when the wing is heavy:

$$J \gg 1,\ m \gg 1 \tag{10}$$

Taking into account (10), one can easily derive the following approximation formulae for roots of characteristic polynomial of the system linearized near the corresponding equilibrium:

$$\begin{aligned}
\lambda_{1,2} &= \pm i\sqrt{\frac{k}{m}} - \frac{1}{2}\frac{u\left(mu^2 f_{\alpha^*} C_{d^*} + \left(C_{d^*} + C_{l^*}^{\alpha}\right)\left(Jk - m\kappa\right)\right)}{m\left(mu^2 f_{\alpha^*} + Jk - m\kappa\right)} \\
\lambda_{3,4} &= \pm i\sqrt{\frac{\kappa - u^2 f_{\alpha^*}}{J}} - \frac{1}{2}\frac{ur\left(2f_* \sin\theta_* + f_{\alpha^*}\cos\theta_*\right)}{J} - \frac{1}{2}\frac{u^3 f_{\alpha^*} C_{l^*}^{\alpha}}{mu^2 f_{\alpha^*} + Jk - m\kappa}
\end{aligned} \tag{11}$$

Here $C_{d^*} = C_d(\theta_*)$, $C_{l^*}^{\alpha} = dC_l / d\alpha\big|_{\alpha=\theta_*}$.

Formulae (11) only hold for the situation when the value $mu^2 f_{\alpha^*} + Jk - m\kappa$ is not small.

Note that for small enough κ there exist equilibria, such that $\theta_{*_n} = \pi n + (-1)^n \varphi_n$, $\varphi_n \ll 1$, n are integers. For brevity, discuss only positive θ_* (for negative ones, the situation is similar). Static experiments show that f_* is practically linear in φ_n for such θ_*, and the following relations hold, if ξ is large enough: $C_{d^*} > 0$, $f_* > 0$, $C_{l^*}^{\alpha} > 0$; for even n $f_{\alpha^*} = f_{\alpha 0} > 0$, for odd n $f_{\alpha^*} = f_{\alpha}^{'}\big|_{\alpha=\pi} = f_{\alpha\pi} < 0$. Hence, from (11) it follows that for even n, when the wing is oriented almost "against" the flow, $\lambda_{3,4}$ are real (this follows from the fact that for small κ the inequality (8) is not satisfied), and have different signs, which means that the corresponding equilibria are unstable. For odd n (the wing is oriented practically along the flow), when the stiffness of the plunge spring is small enough, real parts of all λ are negative, and the equilibria are asymptotically stable. Evidently, the same holds for the case of large k. Real part of $\lambda_{3,4}$ becomes zero when

$$k = k_* = -\frac{mr\left(2f_* \sin\theta_* + f_{\alpha^*}\cos\theta_*\right)\left(u^2 f_{\alpha^*} - \kappa\right) + Ju^2 f_{\alpha^*} C_{l^*}^{\alpha}}{Jr\left(2f_* \sin\theta_* + f_{\alpha^*}\cos\theta_*\right)}$$

Note that $k_* > 0$ for odd n, which means that for each such equilibrium there exists an interval of values of the plunge spring stiffness where this equilibrium is unstable.

4. Global behavior

In order to study global behavior of the system, that is, its dynamics in the entire range of angles of attack, numerical simulation was performed with the following values of parameters: $J = 100$, $m = 100$, $\xi = 1$, $u = 1$. Hereinafter, aerodynamic characteristics of the standard NACA0015 airfoil provided in [9] are used.

Bifurcation diagrams for equilibrium positions are shown in Fig. 2 for different values of stiffness coefficients (a logarithmic scale for κ is used). Black points denote stable equilibrium positions, and grey points denote unstable ones. Note that "oblique" equilibria are mostly stable for high and low stiffness of plunge spring, while for $k \sim 1$ they are, as a rule, unstable.

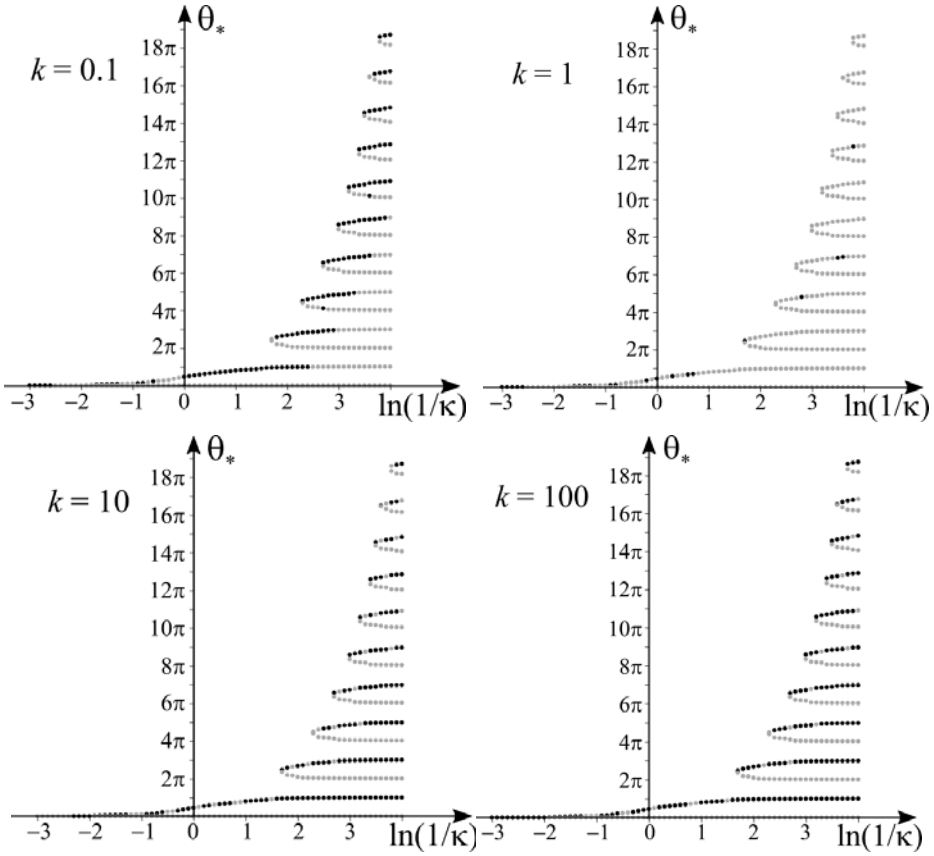

Figure 2. Bifurcation diagrams

In order to understand the influence of the plunge spring stiffness upon limit cycles, consider the case when the value of pitch spring $\kappa = 0.08$. Then there exist eleven equilibrium positions (one trivial and 10 "oblique" ones). Phase plane $(\theta, \dot{\theta})$ is shown in Fig. 3 for different values of *k* (circles

denote asymptotically stable positions, crosses denote saddle-type equilibria, and asterisks denote unstable equilibria, which are not saddles, black lines denote limit cycles, and grey lines denote phase trajectories).

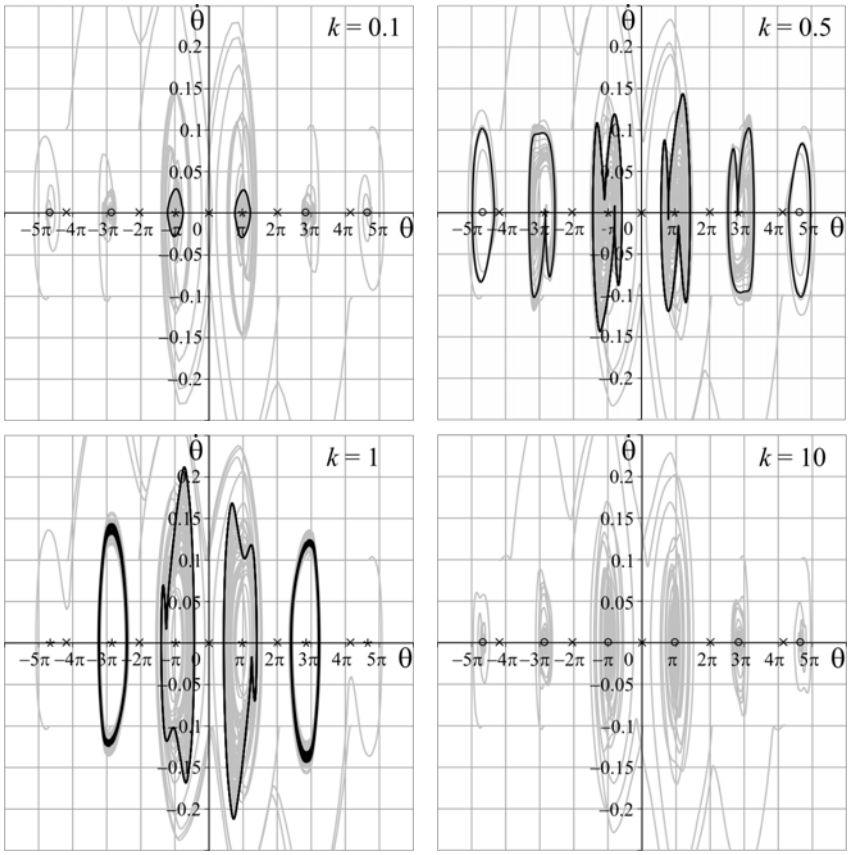

Figure 3. Limit cycles for different values of *k*.

Increase in *k* first leads to appearance of attracting limit cycles, growth in their amplitude, and increase of their number. Though there can exist asymptotically stable equilibria, their domains of attraction are small. However, as was mentioned before, larger *k* lead to "stabilization" of the system: domains of attraction of stable equilibria enlarge, and attracting limit cycles disappear.

Simulation shows that for larger values of *k* limit cycles disappear, and the only attractors are six asymptotically stable "oblique" equilibrium positions.

5. Conclusions

An aeroelastic system with two degrees of freedom (translational and rotational) is considered. Aerodynamic load is simulated using the quasi-steady approach. Evolution of the set of equilibrium

positions of the system (including both trivial and “oblique” ones) is studied depending on structural parameters.

Stability criteria are obtained for these equilibria, and attraction domains are analyzed. Numerical simulation of the system behavior is performed for different values of parameters, including in the area of large angles of attack.

Acknowledgments

This work was partially supported by RFBR (projects No. 17-08-01366, 15-01-06970).

References

[1] Ghommem, M., Nayfeh, A.H., Hajj, M.R. Control of Limit Cycle Oscillations of a Two-Dimensional Aeroelastic System. *Mathematical Problems in Engineering* 2010 (2010), 13 p.

[2] Strganac, T.W., Ko. J., Kurdila, A.J. Identification and Control of Limit Cycle Oscillations in Aeroelastic Systems. *J. of Guidance, Control, and Dynamics* 23, 6 (2000), pp. 1127-1133.

[3] Amandolese, X., Michelin, S., Choquel, M. Low speed flutter and limit cycle oscillations of a two-degree-of-freedom flat plate in a wind tunnel. *J. of Fluids and Structures* 43 (2013), pp. 244–255.

[4] Sun, Z., Haghighat, S., Liu, H.T., Bai, J. Time-domain modeling and control of a wing-section stall flutter. *J. of Sound and Vibration* 340 (2015), pp. 221–238.

[5] Lee, B.H.K., Price, S.J., Wong, Y.S. Nonlinear aeroelastic analysis of airfoils: bifurcation and chaos. *Progress in Aerospace Sciences* 35 (1999), pp. 205-334.

[6] Dai, H., Yue, X., Xie, D., Atluri, S.N. Chaos and chaotic transients in an aeroelastic system. *J. of Sound and Vibration* 333 (2014), pp. 7267–7285.

[7] Barrero-Gil, A., Pindado, S. Avila, S. Extracting energy from vortex-induced vibrations: a parametric study. *Appl. Math. Model.* 36, 7 (2012), pp. 3153–3160.

[8] Bryant, M., Garcia, E. Modeling and Testing of a Novel Aeroelastic Flutter Energy Harvester. *J. Vibration and Acoustics* 133(1), 011010 (11 p.).

[9] Sheldahl, R.E.; Klimas, P.C. Aerodynamic Characteristics of Seven Symmetrical Airfoil sections Through 180 Degree Angle of Attack for Use in Aerodynamic Analysis of Vertical Axis Wind Turbines. *Sandia National Laboratories: Albuquerque, NM, USA* (1981), 118 p.

Yury Selyutskiy, Ph.D.: Lomonosov Moscow State University, Institute of Mechanics, Michurinsky prosp. 1, 119192, Moscow, Russia (*seliutski@imec.msu.ru*). The author gave a presentation of this paper during one of the conference sessions.

Influence of the spring system in vehicle vibrafon

Martin Svoboda, Václav Schmid, Josef Soukup, Milan Sapieta

Abstract: The work deals with the adhesion of the wheels to the road and the resulting oscillation of the individual parts of the vehicle in dependence on its load, the inflation of the tires, the type of springing at different vehicle excitement. Wheel grip has been measured using EUSAMA chassis tester. Acceleration was measured by three-axis acceleration sensors deployed on the vehicle, both on the measuring station and in operation. The problems were evaluated from the point of view of individual technical solutions of damping systems. The work was carried out experimentally in the laboratory and under real conditions in operation.

1. Introduction

The issue of damping and determining the required properties of shock absorbers and springs in passenger cars is directly related to the efforts of motor vehicle designers to increase comfort and safety of the crew as well as road safety. The aim is also to reduce the negative impact of the vibration transfer on other parts of the vehicle, thus increasing wear and decreasing their lifetime.

When we overcome the unevenness of the vehicle, we need a fast damping system response and a change in the softness of the shock absorbers from a soft one - for the comfort of the crew to the hard - advantageous for quicker attenuation by suppressing the disadvantageous shape of the vibrations.

With the tire pressure monitoring car to meet for over 10 years, but nobody gives him with attention. In the Regulation of the European Union the system was the prerogative of special equipment and most importantly concerned primarily premium brands or models. According to the norms of the European Union EC 661/2009 and ECE-R 64 car manufacturers from 1. 11. 2014 obliged to equip all new cars for the European market monitoring system, tire pressure monitoring - TPMS (Tyre Pressure Monitoring System). The reason for this is to ensure optimum tire inflation, which affects the production of harmful gas emissions, road safety, vehicle operation economy and ride comfort [1, 2].

Theme of tire pressure monitoring is interesting in view of the technical solution of the system is supported by theoretical knowledge of mechanics and thermodynamics, also uses knowledge of electronics, automation and evaluation using computer technology.

The aim of the work was to assess the whole system of passenger car springs. The impact of tire inflation, tire types, springs and shock absorbers was assessed on the vehicle. The required data was obtained by measuring the acceleration of the various parts of the car (axle, steering wheel, driver's seat attachment, bodywork and acceleration to the driver). This was done by means of the acceleration and thrust sensors between the wheel and the road using test stands of shock absorbers operating under the EUSTAMA and CAP methodologies [3-4].

2. Methodology of measurement

Using acceleration sensors LIS331DL STMicroelectronics were measured and evaluated acceleration values of various operating conditions. The sensors were placed on the chassis, bodywork, in the interior of the vehicle were placed on the driver's seat and the steering wheel.

Measurements have been made:

- Tire adhesion to the road depending on the vehicle's driving mode with varying stiffness and acceleration on the chassis, bodywork, steering wheel and driver's seat.
- Tire-to-ground tire grip depending on load and acceleration on steering wheel and driver's seat.
- Tire adhesion to the road depending on tire inflation and acceleration on the driver's seat.
- Statistical measurement of damper condition.
- Acceleration on the seat mounts when crossing unevenness on the test track.

Measurement of tire acceleration and adhesion to the road (damping) was performed on the test bench of the silencers. At the same time pressure was measured using EUSAMA al. The EUSAMA methodology is the most commonly used way of assessing the chassis state, more precisely the adhesion of the wheels to the oscillating tester pad. The ratio of the dynamic dynamic force of the wheel to the static force was measured. The percentage of these forces was measured in the test. At the same time, the forces on the left and right sides of one axle were compared. The measurements were made on vehicles equipped with passive damping and damping adaptable. For vehicles with a controllable system, all dampers have been measured.

Tire-to-road adhesion measurements were measured and vibration transmitted to different parts of the vehicle, depending on the stiffness of the silencers for soft, medium and hard setting.

Securing a constant oscillation frequency can only be done by adjusting the damping unit to a vehicle height control device. This can provide either a constant height of the vehicle constant size and thus the spring travel of the spring or may purposefully vary this height, and thus achieve the desired frequency at different driving (driving on flat highways at higher speeds / crossing obstacles at slow speed).

Changing the stiffness of the damper changes the resistance of the system. This also changes the magnitude of the amplitude. The tougher the damping, the higher the resistance, the lower the amplitude and the faster the oscillation. This assumption was tested on a vehicle with a variable adjustable stiffness dampers. For some types of chassis, such as McPherson independent suspension, when crossing unevenness, a change in steering geometry is required.

Accelerometers sensed both the mechanical oscillation induced by the displacement of the test plate of the silencer tester as well as the non-periodic oscillation.

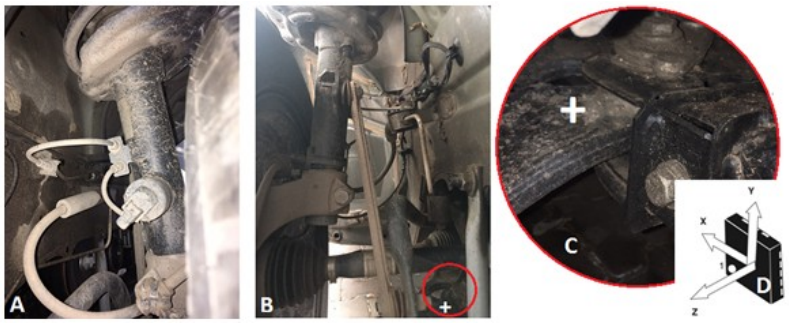

A- *shock absorber with variable efficiency,* B *and* C - *sensor location (marked with a cross),* D - *acceleration sensor measurement directions*

Figure 1. Scheme of system – asymmetrical arrangement of extra weights

Table 1. Variations of acceleration measurements made on the vehicle

	seat sensor	steering wheel sensor	sensor on the axle	sensor on the bodywork
0,5 A excitation	I	II	III	IV
0,8 A excitation	V	VI	VII	VIII
1,2 A excitation	IX	X	XI	XII
without excitation	XIII	XIV	XV	XVI

3. Measurement results

Before running the oscillating plates, the chassis tester measures the weight of the individual wheels on the test plates. This determines the static force F_{st} [N], the vehicles on individual wheels. This figure, together with the minimum force acting on the plate at oscillation F_s min [N], is required for the calculation of the wheel grip by the EUSAMA method.

$$EUS = \frac{F_s \min}{F_{st}} .100\,[\%] \tag{1}$$

After the shock absorber tester (left front and then right front wheel) was triggered, the force applied to the wheel was recorded. This force is determined by the adhesion of the tire to the road while measuring acceleration by three-axis acceleration sensors. The measurement results are shown in the following graph (Fig. 2).

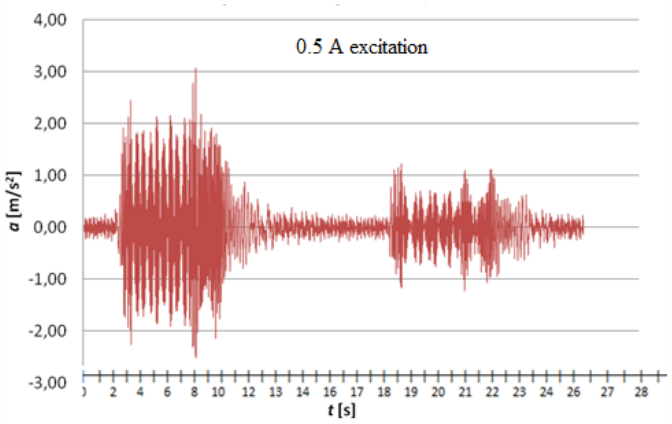

Figure 2. Measurement No: I. - Acceleration of the driver's seat in comfort mode.

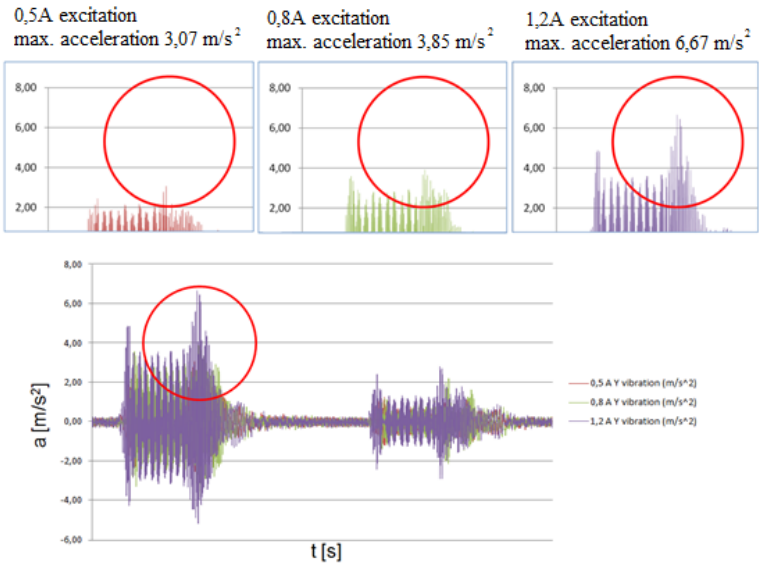

Figure 3. Acceleration of the driver's seat - Comparison of measurement No: I., V., IX.

For each measurement, the adhesion of the left (L) and right (P) front tire to the support was recorded (Fig. 4 - comfort mode).

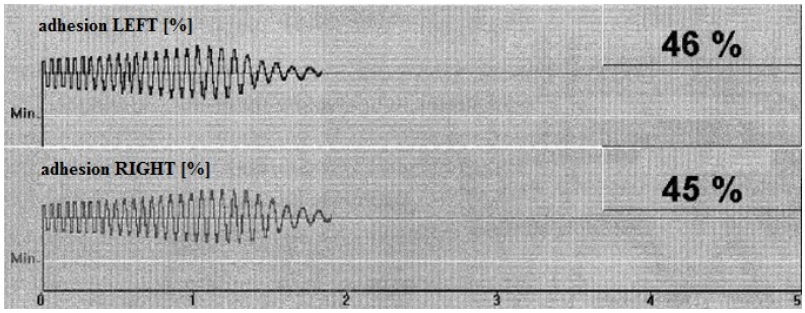

Figure 4. LINE 7000 chassis screen test - Comfort mode.

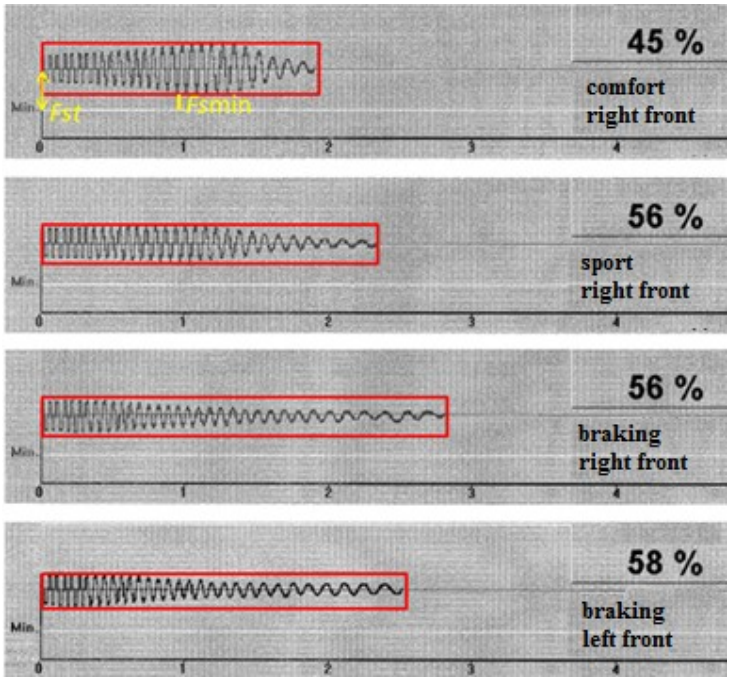

Figure 5. LINE 7000 chassis screen test - Comfort mode.

The compression force in comfort mode is noticeably smaller than in the sport mode. This corresponds to the theoretical assumption for passive silencers that the silencer is set to the compromise between safety and convenience. In the comfort mode, greater convenience is preferred, where the maximum acceleration measured on the driver seat mount is only 3,07 m /s^2, at a pressure of 45%.

The values of the force computation evaluation according to the EUSAMA methodology are [4]:

- over 60% excellent
- 41-60% good
- 21-40% compliant
- 1-20% unsatisfactory
- 0% inoperative.

Table 2 shows the results of the tire pressure measurement.

Table 2. Front wheel axle pressures with different stiffness of stiffeners

generation	adhesion - left front wheel	adhesion - right front wheel	difference
0,5 A	46,3 %	44,1 %	2,2%
0,8 A	55,8 %	55,7 %	0,1%
1,2 A	56,9 %	53,5 %	3,4%
without	57,2 %	57,3 %	0,1%

According to EUSTANA methodology, all damping state measurements were in the second area, with a grip of 41-60 %. This applies to areas marked as good shock absorbers.

The difference in pressure between the soft comfort mode and the hard mode of sport (in the front right wheel) is 17,6 %. The difference in the maximum acceleration at the driver's seat is 19,8 %. A more pronounced difference in acceleration is between the comfort mode and the excitement of the solenoid valve with a current of 1,2 A. In this comparison, the maximum acceleration on the driver's seat is 53,8 % larger and reaches 6,65 m/s^2, although adhesion is only 17,6% greater. The 1,2 A current excitation is not a normal driving mode but only a temporary state when the control unit evaluates the extreme load during braking, acceleration or tilting when cornering.

When comparing the measured values from individual acceleration sensors at 0,5 A (soft damping - comfort setting), it is clearly visible the difference in vibration on the individual parts of the vehicle. The vibration record shows that the vibration magnitude is significant for each side of the vehicle under test, that is, the wheel under which the test plate vibrates during the test.

When testing on the right side, there is no significant transverse vibration transmission on the driver's seat. At maximum, the acceleration is around 1 m/s^2, but most of the test runs below this value. For vibration transfer to the steering wheel, the maximum acceleration value is around 1 m/s^2, but the transmitted vibration is different from that of the seat.

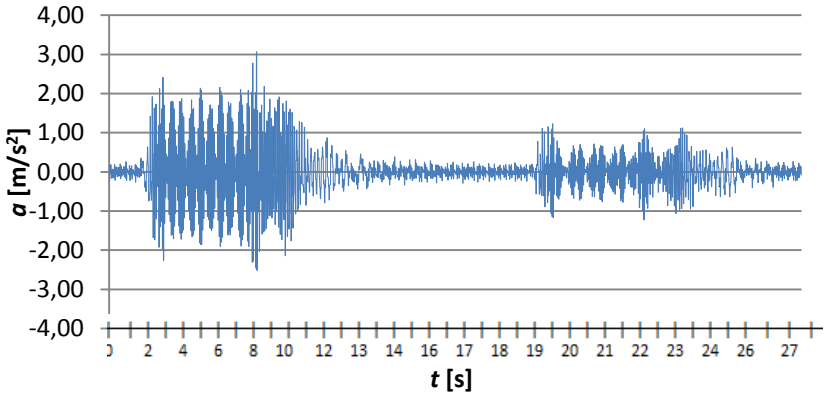

Figure 6. The course of acceleration acting on the handle of the seat in comfort mode

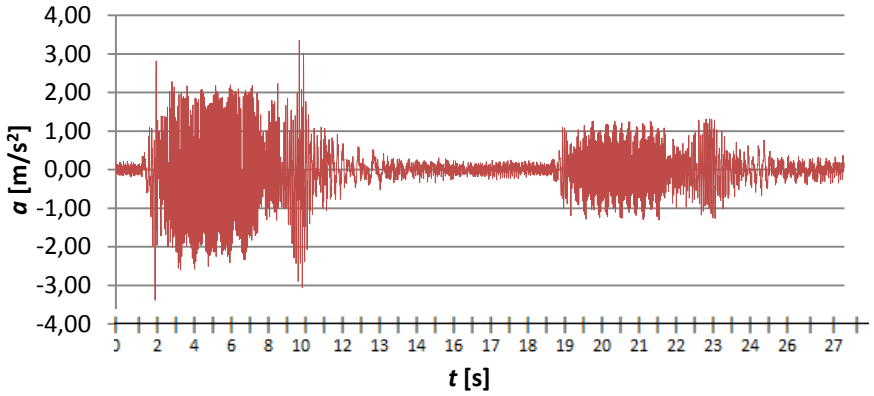

Figure 7. The course of accelerations on the steering wheel in comfort mode.

The vibration transfer to the sensor located on the right wheel axle when testing the wheel on the opposite (left) side is higher in the region of the resonant frequency. When testing the right front wheel vibration is significant. They reach an acceleration of up to 13 $m.s^{-2}$. The transmission of vibrations from the wheel to an undisturbed axle is crucial in terms of wear on the chassis components and the formation of clearance.

4. Conclusions

The aim of the measurement was to determine the response of the damping system to the different operating conditions of the tested passenger cars. All measurements made with the help of tester chassis and riding test were performed to reveal the possible impacts of operating conditions in particular on crew comfort and driving safety.

By measuring, it was found (verified theoretical assumption) that the magnitude of transmission of vibrations to different parts of the vehicle depends on the amount and type of connection between the wheel and the measured part of the vehicle. The type of connection that is disadvantageous to the vibration transfer is a fixed connection (most commonly spot welded) and glued. This is visible in the transmission of vibration to the post. Conversely, the advantageous connections for vibration transfer are flexible connections (seat cushion laid on a flexible metal structure, various types of joints of articulated, sliding, ridge gears, ie, classic gear transmission, pneumatic, hydraulic transmissions etc. Of course, the number of these elements At their distances from the source of vibration. With different tumbling stiffness, the tire's grip (tire pressure) was measured. By measuring it was found (also verified theoretical assumption) that manufacturers resolve damping as a compromise between pressure (safety) and comfort (acceleration on the crew). The soft damping has a 20% lower maximum acceleration value but also a 20% lower thrust than a hard mode. Even with one measurement, we are not outside the range of acceptable values. The difference in the pressure setting would be appreciated rather in extreme situations, ie in a fast ride on a low-quality surface in sports cars, regardless of the effect of higher vibrations on the crew. In conventional vehicles, the softer setting is more convenient, which is more comfortable for the crew and safer for cargoes when crossing unevenness. With the vehicle being measured, the most powerful auto-hard mode is the most meaningful, which is activated during braking, acceleration or quick cornering.

Acknowledgments

This work was supported by SGS University of Jan Evangelista in Ústí nad Labem.

References

[1] Laurin J., *New trends in construction and exploitation automobiles*, International scientific conference - Vehicles 2007, Nitra 2007

[2] Vlk, F.: *Dynamika motorových vozidel*, Brno 2003, ISBN 8023900242

[3] http://www.ecodrive.org/en/what_is_ecodriving-/additional_tips_and_tricks/ , cited: 14/02/2015

[4] internal material - surveillance des pressions de pneumatiques, Renault Academy TECHNIQUE, Renault S.A. 2015

Martin Svoboda, Ph.D.: Jan Evangelista Purkyně University in Ústí nad Labem / Faculty of Production Technology and Management / Department of Machines and Mechanics, Na Okraji 1001, Ústí nad Labem 400 01, Czech Republic (*svoboda@fvtm.ujep.cz*). The author gave a presentation of this paper during one of the conference sessions.

Josef Soukup, Assoc. Prof., Václav Schmid, Ing.: Jan Evangelista Purkyně University in Ústí nad Labem / Faculty of Production Technology and Management / Department of Machines and Mechanics, Na Okraji 1001, Ústí nad Labem 400 01, Czech Republic (*soukup@fvtm.ujep.cz*, *schmid@fvtm.ujep.cz*).

Milan Sapieta, Ph.D.: University of Žilina / Faculty of Mechanical Engineering / Department of Applied Mechanics, Univerzitná 8215/1, Žilina 010 26, Slovakia (*milan.sapieta@fstroj.uniza.sk*)

A compensation for positioning of the remote control artillery-missile set in external disturbance conditions

Piotr Szmidt

Abstract: An artillery-missile set mounted on a moveable object, such as a battleship, is subjected to movements that cause the line of sight to move relative to desired line of sight. This is a highly undesirable phenomenon during defense operations. The paper presents an attempt to compensate for these disturbances by using PID controllers and set's own driving systems. It has also been assumed that disruptive movements came from the ship motion on the sea wave, and that the object (e.g. a attack helicopter) hovers in place. Numerical simulations were performed in SciLab environment and the results was graphically presented.

1. Introduction

The paper is focused on controlling missile-artillery set during influence of external disturbances. Disturbances acting on the set can be in form of kinematic extortions coming from warship motion on which set is mounted and such case was considered in the paper. These kinematic extortions acting on the set make the line of sight changing its desired position. It results in inaccurate tracking of a target what is very undesired.

Precise manual control of the set under disturbance conditions is very difficult. Operator training is expensive and takes time [1] and additionally operator can be exposed to aggressor's fire. It is obvious that, for these reasons, it is preferable to replace human work with automatic control systems. In other research centre, this type of work is carried out [2,3], however, they involve 35 mm cannons. Here, attention will be paid to the popular and produced in Poland naval set ZU 23-2MR equipped with double-coupled 23 mm cannon and two GROM missiles [4].

2. Artillery-missile set model

In the Figure 1 there is presented scheme of artillery-missile set (AMS) model. It consist of two bodies and has two degrees of freedom which are responsible for position in azimuth deviation and elevation tilt. It was assumed that the generalized torque M_1 rotates the body 1 by an azimuth angle θ_1 about the axis z_1. Further, the generalized torque M_2 rotates the body 2 by the elevation angle θ_2 about the axis y_2 that moves along with the body 1. Also, some simplifications have been made to the impact of external disturbances. It was assumed that the linear acceleration and yawing of the ship is negligibly small, and the base of the set is subject only to rolling and pitching. However, they are sufficient to test the control system as they can cause large displacement of the aiming line.

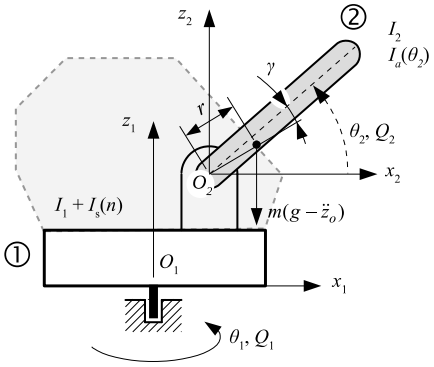

Figure 1. AMS mechanical model scheme

Designations presented in Fig. 1: θ_1– azimuth angle, θ_2– elevation angle, Q_i – generalised torque impacting on *i*-th body, I_1 – constant mass inertia moment of body 1 in relation to z_1 axis, $I_s(n)$ – variable mass inertia moment of body 1 in relation to z_1 axis depending on a number of cartridges n in boxes, I_2 – constant mass inertia moment of body 2 in relation to y_2 axis, $I_a(\theta_2)$ – variable mass inertia moment of body 2 in relation to z_1 axis depending on elevation angle θ_1, m – mass of body 2, g – gravitational acceleration, r – distance from the centre of gravity of body 2 in relation to y_2 rotation axis, γ – angular displacement of the centre of gravity of body 2 in relation to an axis of a gun barrel.

The non-linear equations of AMS dynamics are given by (1) and (2).

$$Q_1 = \left(3a\theta_2^2 + 2b\theta_2 + c\right)\dot{\theta}_1\dot{\theta}_2 + \left(I_1 + pn + q + a\theta_2^3 + b\theta_2^2 + c\theta_2 + d\right)\ddot{\theta}_1 \tag{1}$$

$$\begin{aligned} Q_2 = {} & I_2\left(\ddot{\theta}_2 + \ddot{\tau}_x \sin\theta_1 + \ddot{\tau}_y \cos\theta_1\right) - \frac{1}{2}\left(3a\theta_2^2 + 2b\theta_2 + c\right)\dot{\theta}_1^2 \ldots \\ & - mrg\cos\left(\theta_2 + \gamma + \tau_x \sin\theta_1 + \tau_y \cos\theta_1\right) \end{aligned} \tag{2}$$

Where: τ_x – roll angle, τ_y – pitch angle, $Q_i = M_i - T_i$ and M_i – driving torque acting on *i*-th body reduced by friction torque T_i; a, b, c, d, q, p – parameters of the set described in detail in the paper [5]. The nonlinear friction model for given parameters of set has been replaced with good accuracy by the 3rd degree polynomial. Coefficients were found by the least squares method and finally the friction has form (3) and (4).

$$T_1 = 86.15n_1^3 + 77{,}44n_1 \tag{3}$$

$$T_2 = 8.98n_2^3 - 8.04n_2 \tag{4}$$

3. Control loop structure

A control-loop structure along with additional devices is shown in Figure 2. The main additional element is the compensator, where target position signals α_T and ε_T from the scan-track head and the angular displacement of the base of the set τ_x and τ_y are received. The compensator allows for calculation of corrections and sends the resulting angular angles of the azimuth and elevation θ_1^d and θ_2^d respectively to the control system. In other words, the θ_1^d and θ_2^d are desired angles that will maintain the line of sight at target in spite of the effects of τ_x and τ_y extortion.

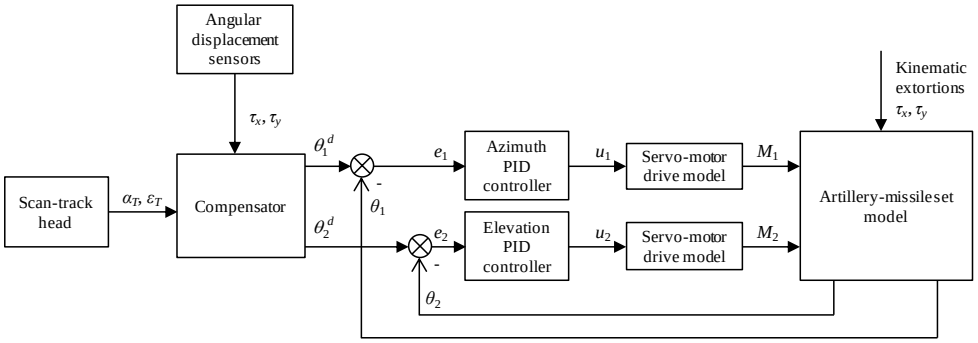

Figure 2. Control-loop structure for considered dynamical system

Next, the azimuth and elevation position errors e_1 and e_2 are calculated and are sent to PID controllers. The PID controllers have parallel structure and their parameters are $K_{P1} = 9.81$; $K_{I1} = 0$; $K_{D1} = 3.31$ and $K_{P2} = 9.23$; $K_{I2} = 4.16$; $K_{D2} = 1.3$. The controllers tuning was described in detail in [5], where optimal parameters were found by implementing Nelder-Mead optimization algorithm [6]. As result, the azimuth regulator is a PD regulator.

The controllers generate signals u_1 and u_2 (e.g. voltage) which corresponds to desired output torque in servo-motor drive models. Both for azimuth and elevation servo-motor drive models are based on SBL 4-0530 brushless motor [7] which has maximum output torque of 21 Nm. The drive models satisfy non-linear saturation of torque-speed curve shown in Figure 3. Also, the motors inertia are modelled by transfer function of 1st order system (5) [8]. Additionally, in drive models there are included reduction gear with ratios $i_1 = 53$ for azimuth and $i_2 = 38$ for elevation with $\eta = 95\%$ efficiency for both gears.

$$\frac{Y(s)}{X(s)} = \frac{1}{Ts+1} \tag{5}$$

Where: Y(s) – output torque, X(s) – desired torque, T – time constant [7].

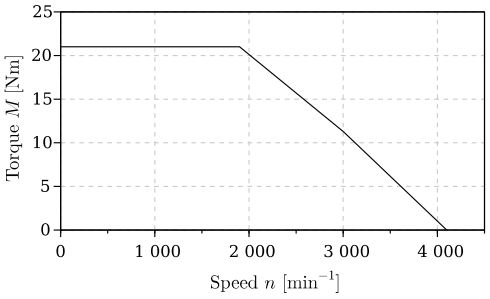

Figure 3. Peak torque-speed curve for the SBL 4-0530 servo-motor

4. Tracking a motionless target

As first example of maintaining target at line of sight let's consider a case of aiming to attack helicopter under influence of kinematic extortions. The scheme of the system is shown in the Figure 4. The *Oxyz* is fixed coordinate system and the *O'x'y'z'* is coordinate system related to AMS. The helicopter remains at place and scan-track head determined its location α_T = 15 deg, ε_T = 30 deg and distance r_T = 500 m. Assume also that these coordinates already include ballistic and weather corrections and head is internally stabilized. The task is to control the set in such a way to get azimuth angle $\theta_1(t) = \alpha_T$ = 15 deg and elevation angle $\theta_2(t) = \varepsilon_T$ = 30 deg.

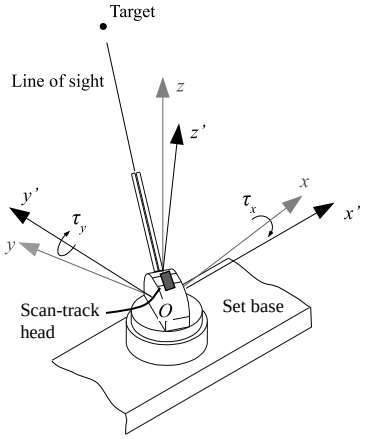

Figure 4. Scheme of rotations

However, kinematic extortions are acting on the basis of the set as roll τ_x and pitch τ_y angles relatively the longitudinal and transverse axes of the set base. Without compensation, line of sight will be moving in some way depending on current set configuration, i.e. θ_1 and θ_2 angles. The assumed kinematic extortions are presented in the Figure 5. The signals was obtained by inverse

Fourier transformation and linear amplitude scaling. Coefficients have been selected so that the graphs are similar in their character to irregular wave shown in the work [9].

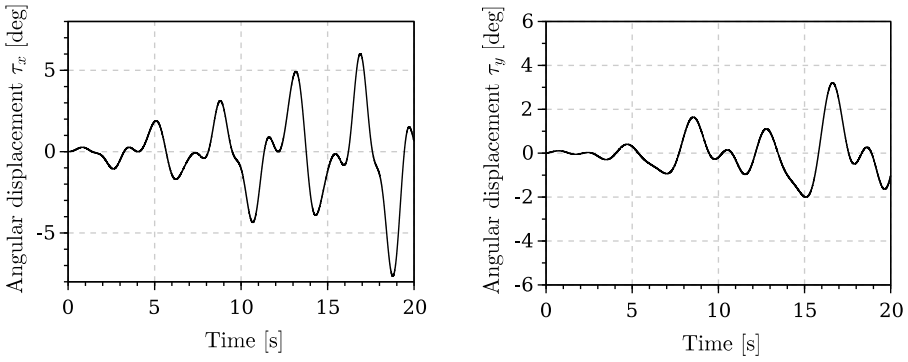

Figure 5. Assumed kinematic disturbances τ_x and τ_y

As a result of the simulation of the considered case, signals of desired and realized azimuth and elevation angles and driving torques both for azimuth and elevation were obtained and presented in the Figure 6. The initial set position was $\theta_1(0)$ = 20 deg and $\theta_2(0)$ = 25 deg.

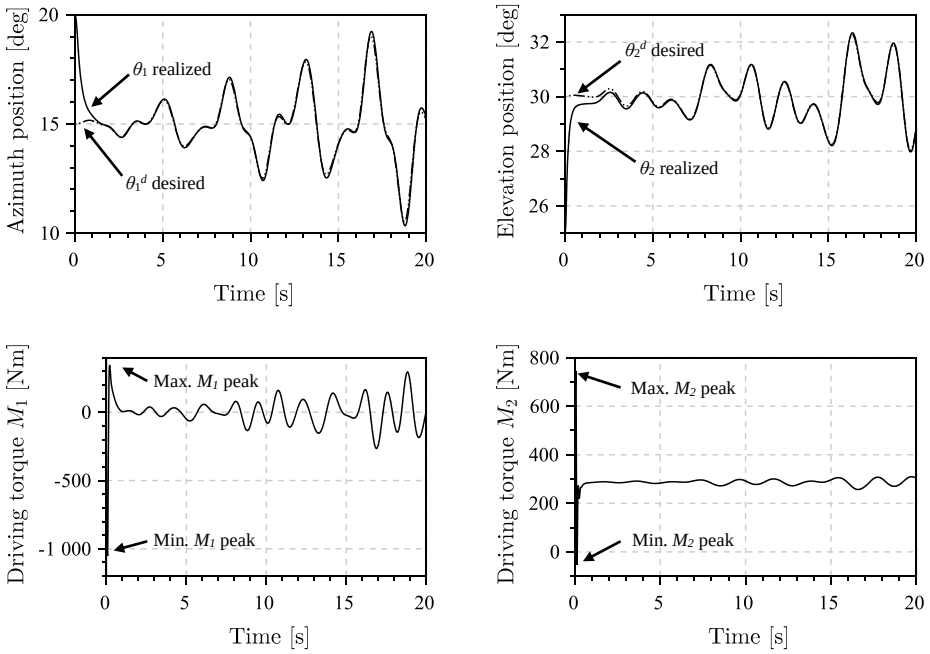

Figure 6. Realization of positioning and driving torques for azimuth and elevation

Figure 7 presents desired trajectory to maintain target at line of sight and trajectory that was realized. In the Figure 8 there are shown position errors for azimuth and elevation during the simulation.

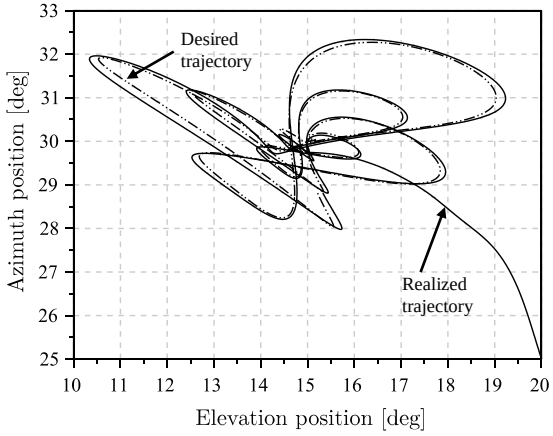

Figure 7. Desired and realized trajectory for still target

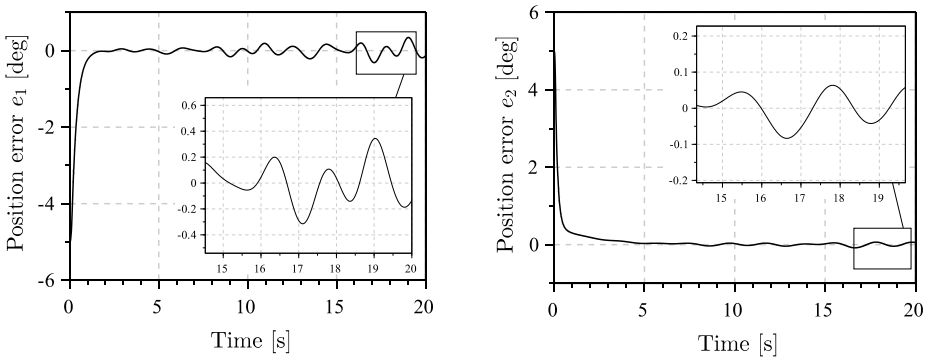

Figure 8. Azimuth and elevation position errors

5. Tracking a maneuvering target

In this part we examine tracking a maneuvering target during external disturbances. The target coordinates are also obtained from scanning-tracking head [10]. For this simulation it was supposed that the target (i.e. fighter) flies up almost perpendicular to the line of sight with speed 170 m/s and distance of 1000 m. Signals of target position α_T and ε_T are shown in the Figure 9.

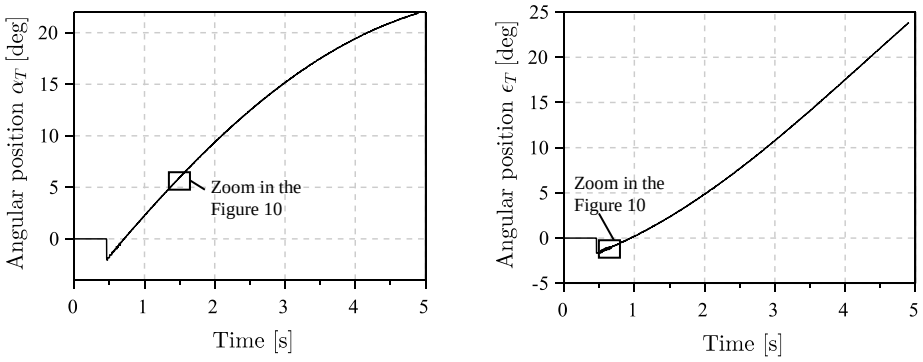

Figure 9. Waveforms obtained from the scan-track head

If we take a closer look to α_T and ε_T signals (Figure 10), they are a set of points actually. Thus, target position is known only at certain moments of time and, what is significant, the signals are noised. The linear interpolation between points will not give good results, so filtering approach was taken.

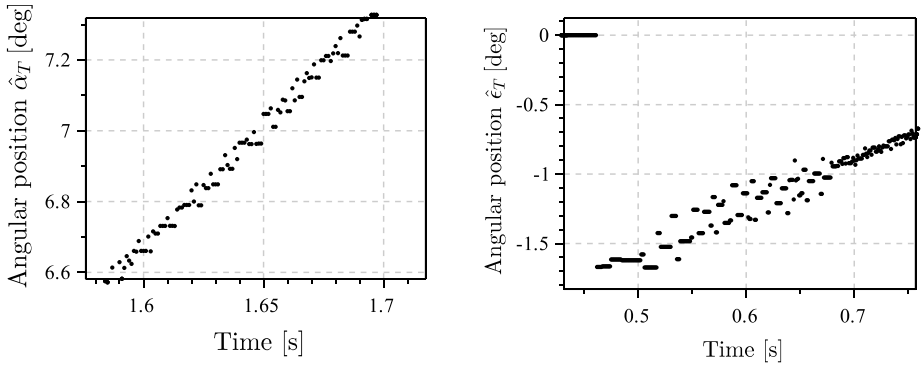

Figure 10. Close-up of fragments of signals directly from the head

6. Kalman filtering

To estimate real position of the target Kalman filtering [11] was implemented. Kalman filter was originally described in 1960s and since then has found application in many issues related to e.g. control, GPS positioning, DSP or even economics. For filtering process there was constructed the state-transition model **A** as constant acceleration motion (6).

$$\mathbf{A} = \begin{bmatrix} 1 & dt & \frac{dt^2}{2} \\ 0 & 1 & dt \\ 0 & 0 & 1 \end{bmatrix} \tag{6}$$

Where *dt* is simulation integration step. The estimated state vector $\hat{\mathbf{x}}$ will be thus given as (7).

$$\hat{\mathbf{v}} = \begin{bmatrix} \text{position} \\ \text{velocity} \\ \text{acceleration} \end{bmatrix} \tag{7}$$

The control input model **B** is zero matrix (8), since we have no influence on the signal run.

$$\mathbf{B} = \begin{bmatrix} 0 \\ 0 \\ 0 \end{bmatrix} \tag{8}$$

The observation model **H** is implemented as (9) because in such case we are interested only in target position.

$$\mathbf{H} = \begin{bmatrix} 1 & 0 & 0 \end{bmatrix} \tag{9}$$

The gain q = 0.5 of the covariance of the process noise **Q**, given by formula (10), and the covariance of the observation noise **R**, constant (11), have been experimentally selected to get satisfactory filtering performance.

$$\mathbf{Q} = \begin{bmatrix} \frac{1}{20}dt^5 & \frac{1}{8}dt^4 & \frac{1}{6}dt^3 \\ \frac{1}{8}dt^4 & \frac{1}{3}dt^3 & \frac{1}{2}dt^2 \\ \frac{1}{6}dt^3 & \frac{1}{2}dt^2 & dt \end{bmatrix} q \tag{10}$$

$$\mathbf{R} = 2 \tag{11}$$

Effects of filtering signals with Kalman filter and parameters presented above is shown in the Figure 11. As expected, the target position estimations appears to be accurate. The estimation graphs seems to cover theoretical average line drawn by measurement points with a very good results.

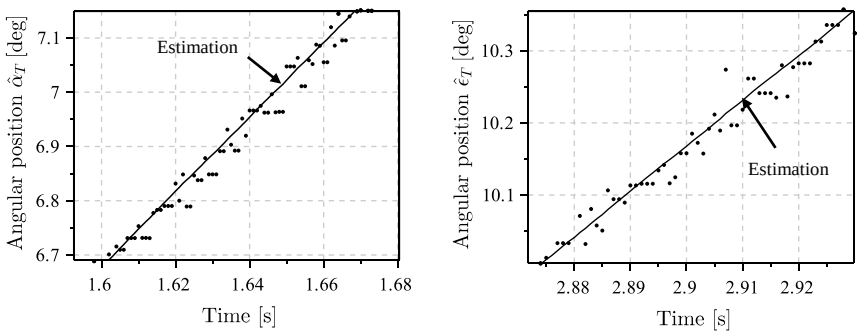

Figure 11. Effect of Kalman filter application

Assumed kinematic disturbances τ_x and τ_y for considered second case are shown in the Figure 12. These signals also was obtained by inverse Fourier transformation and linear amplitude scaling but the amplitude grows faster and reaches 9 deg for roll and 4.5 deg for pitch. In the Figure 13 there are shown positioning errors during simulation.

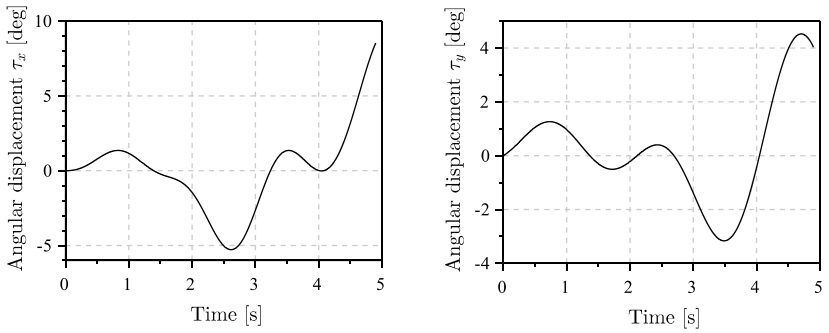

Figure 12. Assumed kinematic disturbances τ_x and τ_y

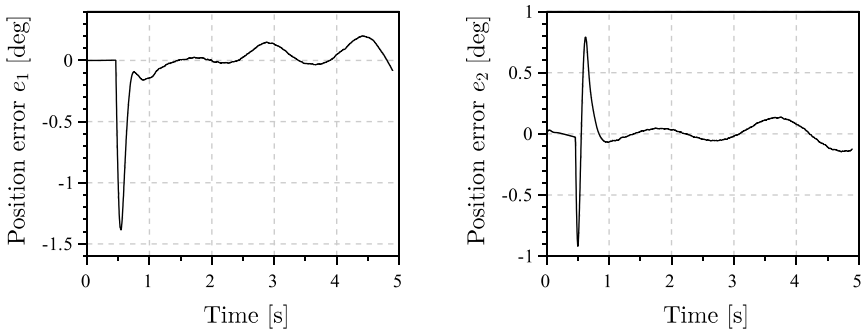

Figure 13. Azimuth and elevation errors during analyzed movement

As a result of the simulation of the second case, signals of desired and realized angles and driving torques both for azimuth and elevation were obtained and presented in the Figure 14. The initial set position was $\theta_1(0) = 0$ deg and $\theta_2(0) = 0$ deg. Desired and realized trajectory is presented in the Figure 15.

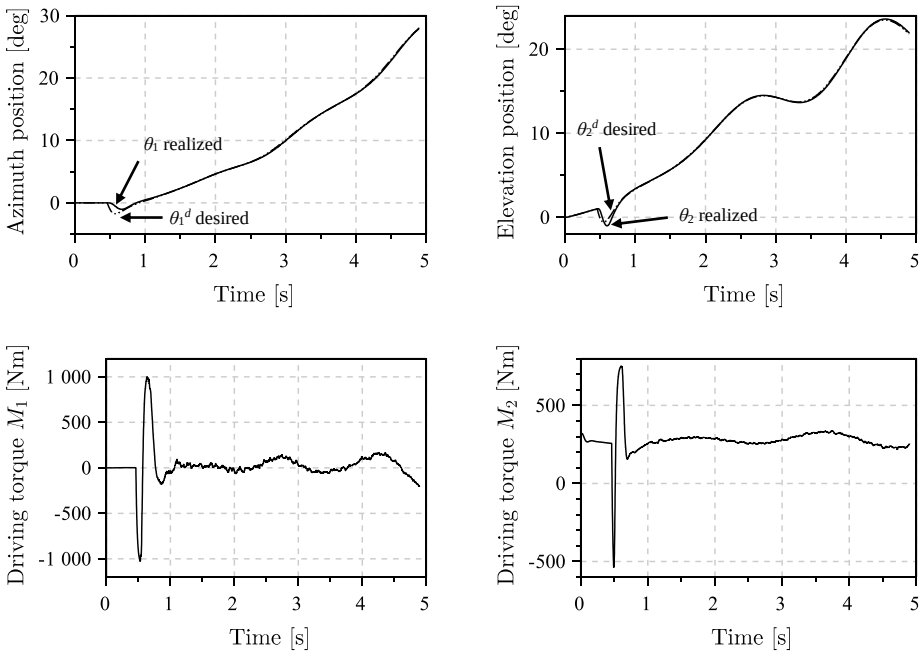

Figure 14. Realization of positioning and driving torques for azimuth and elevation

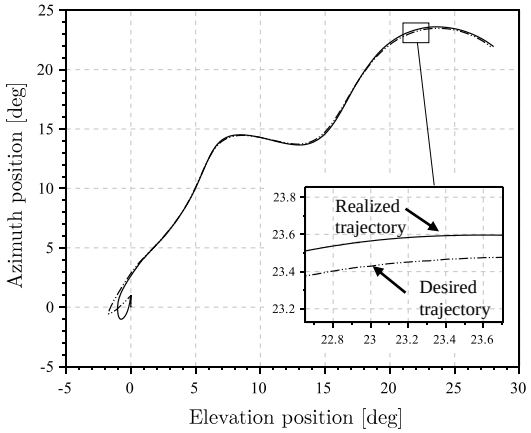

Figure 15. Desired and realised trajectory with zoom of maximal following error

7. Conclusions

In this paper there is presented mathematical model of ZU-23-2MR dynamics. Also, the control structure was proposed. It can be assumed with high probability that in relation to manual control improved tracking quality can be achieved through the use of PID based automatic control systems coupled with a scan-track head and displacement sensors.

As shown in simulations, PID regulators have provided quite good positioning of artillery-missile set quality under external disturbances. The control system remained stable and tried to keep up with the desired signals. As can be seen from the trajectory graphs, the maximum momentary of target position following error does not exceed 0.4 degrees for the first case and 0.25 degrees for the second one.

It has been shown that it is theoretically possible to compensate quite well for kinematic disturbances using PID based control system. However, by analyzing the driving torque waveforms, we can say that the motors still have some power reserves that can be used for more precise control, for example by using LQR or LQG controllers.

The results of these simulations will be used to compare the quality of regulation between different types of controllers. It is also worth mentioning of the internal disturbances, which will primarily be attributed to cannons firing. Undoubtedly, these disturbances will be a big challenge for the control system and they will be the subject of further research.

References

[1] Milewski, S. and Kobierski, J.W. *Training operators of shipboard reconnaissance and fire conduct systems using TR ZU-23-2MR training simulator* (in Polish). Mechanics in Aviation, Volume I, (2012), pp. 241-254.

[2] Gacek J., Gwardecki J., Kobierski J., Leciejewski Z., Łuszczak S., Milewski S., Świętek T., Woźniak R., Wójcik Z. *Structure and innovative Technologies In the new Polish 35 mm naval weapon system*. Conference materials of 11th International Armament Conference on Scientific Aspects of Armament & Safety Technology, (2016), pp. 246-247.

[3] Dura, M. *35mm Tytron Cannon for Kormoran* (in Polish), defence24.pl, http://www.defence24.pl/292995,fbm-armata-35-mm-tryton-dla-kormorana (02.09.2017).

[4] Zakłady Mechaniczne Tarnów, *23 mm Naval anti-aircraft gun and missile system ZU-23-2MR*. http://www.zmt.tarnow.pl/wordpress/item/23mm-przeciwlotniczy-morski-zestaw-artyleryjsko-rakietowy-zu-23-2mr/ (02.09.2017).

[5] Koruba, Z., Gapiński, D. and Szmidt P. *The analysis of optimal PID controllers parameters selection for missile-artillery system*. Engineering Mechanics (2017), pp. 970-973.

[6] Stachurski, A. *An introduction to optimization* (in Polish). Publishing House of Warsaw University of Technology, Warsaw, 2009.

[7] Motor Technology Ltd. SBL/K Motor Catalogue, http://docplayer.net/5976825-Sbl-k-motor-catalogue-2002.html (02.09.2017).

[8] Czemplik, A. *Models of dynamics of physical circuits for engineers*. WNT, Warsaw, 2008.

[9] Wełnicki, W., *Mechanics of ship movement (in Polish)*, script No. 598, Gdańsk University of Technology, 1989.

[10] Gapiński, D. *Modified optical scanning seeker for searching, identifying and tracking air targets (in Polish)*, Ph.D. thesis, Kielce University of Technology, 2016, Koruba, Z.

[11] Diniz, P. S. R.. *Adaptive Filtering: Algorithms and Practical Implementation*. MA: Springer US, Boston, 2013.

Piotr Szmidt, M.Sc. (Ph.D. student): Department of Applied Computer Science and Armament Engineering, Kielce University of Technology, Al. Tysiąclecia PP 7 St., 25-314 Kielce, POLAND (petersz@wp.pl). The author gave a presentation of this paper during one of the conference sessions.

On Artifacts in Nonlinear Dynamics

Utz von Wagner, Lukas Lentz

Abstract: Nonlinear oscillations are of permanent interest in the field of dynamics of mechanical and mechatronical systems. There exist several well-known semi-analytical methods like Harmonic Balance, perturbation analysis or multiple scales for such problems. We reconsider in our presentation the method of Harmonic Balance but add some additional steps in order to avoid artifacts and get information about the stability. The classical method of Harmonic Balance is therefore added by an error criterion, which considers the neglected terms. Looking on this error for increasing ansatz orders, it can be decided whether a solution exists or is an artifact of the method. For the low error solutions, a stability analysis is performed. As example, an extended Duffing oscillator with additional nonlinear damping and excitation is considered showing regions of separated island solutions. Also a nonlinear piezo-beam energy harvesting system is investigated. The described method enables to calculate solutions in a rapid manner with comparable low effort, to get an overview over regular responses of nonlinear systems.

1. Introduction

One of the most used academic examples for an oscillator in nonlinear dynamics is the so-called Duffing oscillator named after the German engineer Georg Duffing (1861-1944), who investigated in his original work 1918 an oscillator with quadratic and cubic stiffness and linear viscous damping performing free or forced harmonic vibrations [3]. Nowadays the term Duffing equation is used much broader and in general describes any nonlinear equation of motion including a cubic stiffness term. For solving such equations the method of Harmonic Balance was and is still very popular and described in many textbooks, e.g. by Hagedorn [2]. In the present paper an overview is given over some examples, where this method is extended by a corresponding error criterion introduced by Urabe et al. [7]. The examples are classical and extended Duffing oscillators added by an energy harvesting system.

2. Classical Duffing oscillator

Corresponding results for the classical softening Duffing oscillator are already described by the authors of the present paper in [9], where additionally to the Harmonic Balance an error criterion is applied which was also used much earlier by Urabe et al. [7]. This classical

softening Duffing oscillator is used in the present paper as well for introducing the method and showing some additional results compared to [9].

The Duffing oscillator is given by

$$m\ddot{x} + d\dot{x} + cx + \alpha x^3 = F_0 \cos \Omega t \tag{1}$$

with m being the oscillator mass, d the damping coefficient, c the linear stiffness, α the coefficient of the nonlinear stiffness, F_0 the excitation force amplitude and Ω the circular excitation frequency. In the case of the softening Duffing oscillator α is negative, while m, d, c and F_0 are positive. This equation is transformed with respect to dimensionless time derivatives by introducing the circular frequency of the undamped free linear vibrations $\omega_0^2 = c/m$, the damping ratio $D = d/(2\sqrt{cm})$ and the dimensionless time $\tau = \omega_0 t$ as

$$x''(\tau) + 2Dx'(\tau) + x(\tau) + \varepsilon x^3(\tau) = f \cos(\eta\tau) \tag{2}$$

with $()' = \mathrm{d}()/\mathrm{d}\tau$, $\varepsilon = \alpha/(m\omega_0^2)$, $f = F_0/(m\omega_0^2)$ and $\eta = \Omega/\omega_0$. Equation (2) is solved approximately by introducing the Harmonic Balance ansatz

$$x(\tau) = \sum_{k=1}^{n} \left(a_k \cos(k\eta\tau) + b_k \sin(k\eta\tau)\right). \tag{3}$$

Using the classical method of Harmonic Balance i.e. introducing (3) into (2) results in a system of nonlinear algebraic equations

$$\sum_{k=1}^{n} \left(\tilde{a}_k \cos(k\eta\tau) + \tilde{b}_k \sin(k\eta\tau)\right) = f \cos(\eta\tau) - \sum_{k=n+1}^{3n} \left(\tilde{a}_k \cos(k\eta\tau) + \tilde{b}_k \sin(k\eta\tau)\right). \tag{4}$$

Herein the coefficients $\tilde{a}_k,\ \tilde{b}_k$ are nonlinear functions of the original ansatz coefficients $a_k,\ b_k$. Following Harmonic Balance, the higher order frequency terms

$$\sum_{k=n+1}^{3n} \left(\tilde{a}_k \cos(k\eta\tau) + \tilde{b}_k \sin(k\eta\tau)\right) \tag{5}$$

in (4) are neglected. After this neglection the coefficients $a_k,\ b_k$ can be calculated from the modified equation (4).

For the visualization of the thereby determined approximate solution $x(\tau)$, $\hat{x}$ is defined as

$$\hat{x} = \max_{0 \le \tau \le \frac{2\pi}{\eta}} \left\{ \sum_{k=1}^{n} \left(a_k \cos(k\eta\tau) + b_k \sin(k\eta\tau)\right) \right\}. \tag{6}$$

Now as mentioned before an error criterion is introduced by considering the neglected terms in the Harmonic Balance method ([7], [9], [10]). The corresponding coefficients $\tilde{a}_k, \tilde{b}_k$ of the

neglected higher order terms can be calculated using the solution for a_k, b_k and the error $\hat{e}$ is defined from this by

$$\hat{e} = \max_{0 \le \tau \le \frac{2\pi}{\eta(n+1)}} \left\{ \sum_{k=n+1}^{3n} \left(\tilde{a}_k \cos(k\eta\tau) + \tilde{b}_k \sin(k\eta\tau) \right) \right\}. \tag{7}$$

For the decision, whether a solution is an artifact or not a relative error $\tilde{e}$ is introduced as

$$\tilde{e} = \frac{\hat{e}}{\hat{x}}. \tag{8}$$

With respect to the demonstration of some results, the same parameters as used in [9]

$$D = 0.06, \varepsilon = -0.1 \text{ and } f = 0.2 \tag{9}$$

are taken, but displayed by $\hat{x}$ (6) and by using a specific labeling. For this, the obtained solutions are first examined with respect for their relative error $\tilde{e}$ (8). Solutions with relative errors larger than 1% are marked by triangles. Solutions with relative error lower than 1% are investigated via Floquet theory for stability and corresponding results are marked with grey circles in the case of unstable and black circles in the case of asymptotically stable solutions. Corresponding results are shown in Figures 1-4 for increasing ansatz orders n.

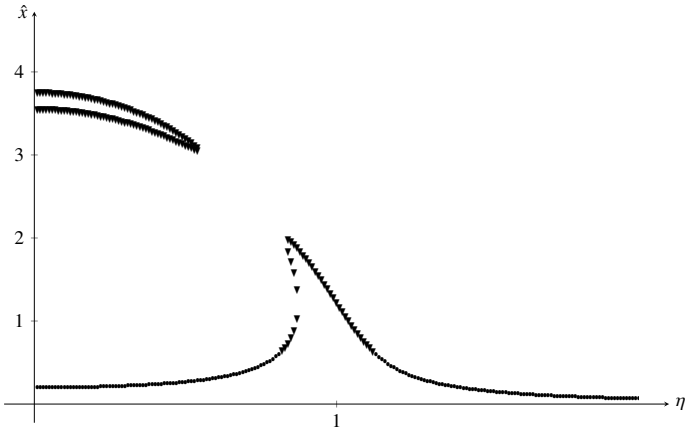

Figure 1. Solutions $\hat{x}$ according to (6) for the Duffing oscillator (2) with Harmonic Balance ansatz (3) in case of $n = 1$. Solutions with relative error $\tilde{e}$ according to (8) larger than 1% are marked by triangles. Solutions with relative error $\tilde{e}$ lower than 1% are marked by circles in grey color in the unstable case (not present in the actual figure) and circles in black color in the asymptotically stable case.

There are two areas of solutions. First the well-known resonance curve starting for small η

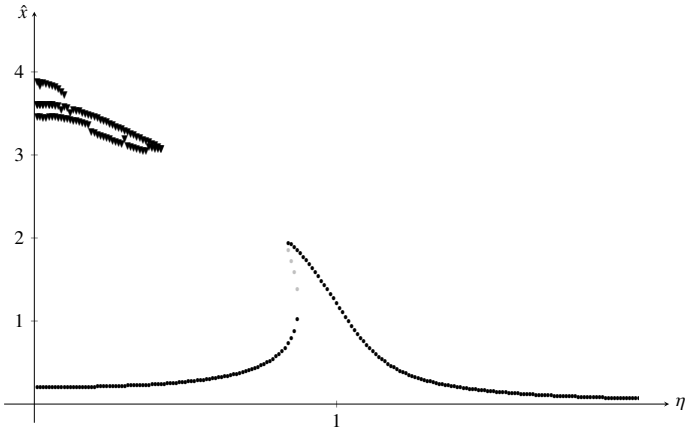

Figure 2. Solutions $\hat{x}$ according to (6) for the Duffing oscillator (2) with Harmonic Balance ansatz (3) in case of $n = 3$. Labeling of solutions as in Fig. 1

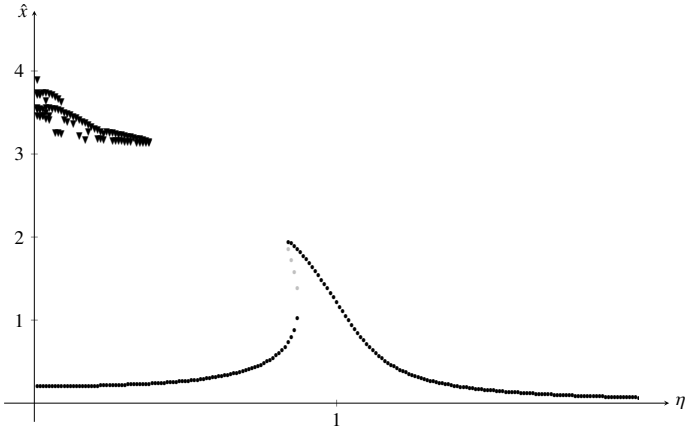

Figure 3. Solutions $\hat{x}$ according to (6) for the Duffing oscillator (2) with Harmonic Balance ansatz (3) in case of $n = 5$. Labeling of solutions as in Fig. 1.

with also small $\hat{x}$, having the resonance peak close to $\eta = 1$ and going to zero for $\eta \to \infty$. Due to the softening characteristic, the resonance peak is turning to the left. This solution preserves its basic shape for all ansatz orders. With the error analysis it can be seen, that this solution shows very small relative errors $\tilde{e}$ for higher ansatz orders and in case of three coexisting solutions for the same η the middle amplitude one is unstable (which is also well known).

The other solutions are the "nose-like" ones occuring for small η and large $\hat{x}$. For $n = 1$, this solution can be found sketched in many textbooks on nonlinear dynamics. They can also occur in case of using perturbation analysis [9]. Increasing the ansatz number, it changes its

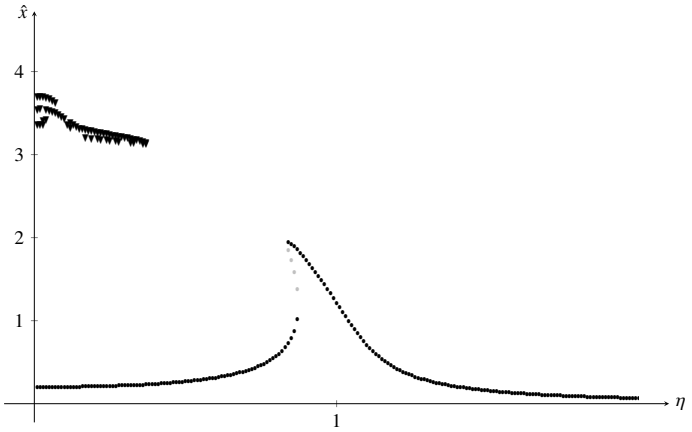

Figure 4. Solutions $\hat{x}$ according to (6) for the Duffing oscillator (2) with Harmonic Balance ansatz (3) in case $n = 7$. Labeling of solutions as in Fig. 1.

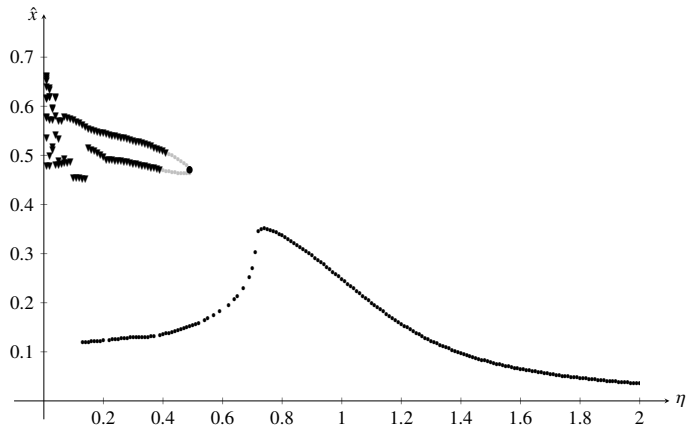

Figure 5. Solutions $\hat{x}$ according to (6) for the Duffing oscillator (2) with Harmonic Balance ansatz (3) in case of $n = 7$. Result from a parameter set investigated by van Dooren [8] with a small separated region with a stable solution. Labeling of solutions as in Fig. 1.

shape (without converging to a final one until $n = 7$) and the error remains large. Therefore we consider this solution to be an artifact solution. In general, solutions with large relative errors even for high ansatz orders are considered to be artifacts in the following. The change of solution shape is also characteristic for these artifacts due to our experience.

In [9] it was furthermore shown, that an additional unstable solution (not being an artifact) with non-zero mean value can be calculated also for small η. To get this solution

as a result of Harmonic Balance, the ansatz (3) has to be extended by a constant term a_0. Finally for this introductory chapter it should be mentioned, that not all parts of the nose-like solution are in any case an artifact. Van Dooren [8] investigated the Duffing oscillator with the parameter set

$$D = 0.2, \varepsilon = -4 \text{ and } f = 0.1105 \tag{10}$$

also using the error criterion by Urabe et al. [7] and focusing on the transition to chaos. Using for this parameter set the same analysis as before it can be seen in Figure 5 for $n = 7$ that small parts of the nose-like solution are not an artifact and that even a small part of this solution is asymptotically stable. This could also be confirmed by numerical integration.

3. Extended Duffing oscillator

In the following the focus will be, as in the last parameter set, on an example with "island" regions of separated solutions. Therefore we consider a modified Duffing oscillator

$$x'' + 2Dx' + x + \varepsilon_1 x^3 + \varepsilon_2 x^2 x' = f_1 \cos(\eta\tau) + f_2 x^2 \cos(\eta\tau) \tag{11}$$

with the methods introduced in section 2. Herein the same denominations are used as in (2) and the classic Duffing Oscillator where the cubic nonlinearity with parameter ε_1 is complemented by a cubic damping term x^2x' with parameter ε_2 and the harmonic excitation with intensity f_1 is combined with a nonlinear parameter excitation term with constant f_2. Such an equation can e.g. be obtained from piezoceramic continua by adding conservative and non-conservative terms in piezoelectric coupling and elasticity [6].

The parameters here are chosen arbitrarily to show certain nonlinear phenomena and do not necessarily represent a real piezoceramic. The same equation of motion is considered in [10] with other parameter sets. Here, the parameters are chosen as $\varepsilon_1 = -0.25$, $\varepsilon_2 = -0.3$, $D = 0.1$, $f_1 = 0.1$ and $f_2 = 0.1$. Using again the ansatz (4), $\hat{x}$ can be calculated according to equation (6) and the relative error $\tilde{e}$ corresponding to equation (8). Corresponding results are shown in Figures 6-9. The results show now three types of solutions for $n = 1$. Beside the well known resonance curve (which shows the well known behavior and converges for higher order n) there is again a nose-like solution for small η and additionally a new island of solutions for medium η i.e. $0 < \eta < 1$. These solutions show initially large errors and change their shape (both regions merge) for higher ansatz orders. Finally for $n = 7$ the right end of the solution island shows low-error but unstable solutions so that again main parts of the results obtained can be considered as artifacts especially the structure observed for $n = 1$.

From discussions of amplitude diagrams of such problems one might be used to, that stable

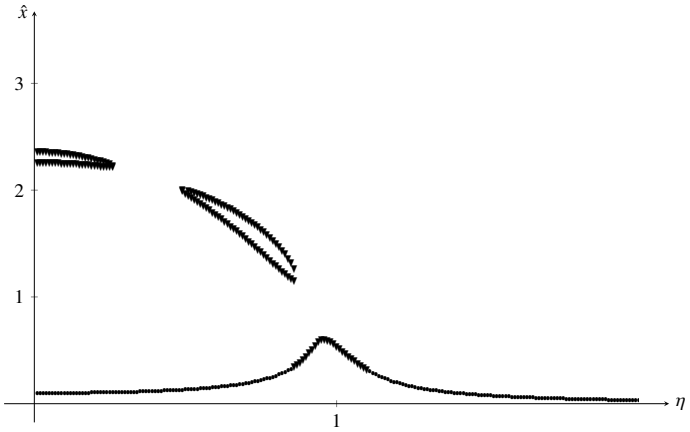

Figure 6. Solutions $\hat{x}$ according to (6) for the extended Duffing oscillator (11) with Harmonic Balance ansatz (3) in case of $n = 1$. Labeling of solutions as in Fig. 1.

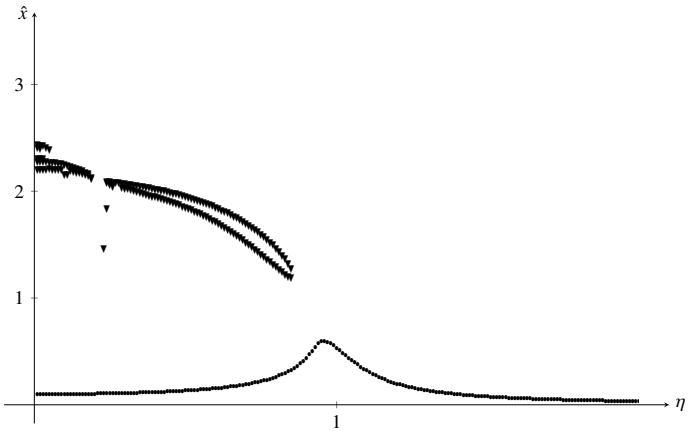

Figure 7. Solutions $\hat{x}$ according to (6) for the extended Duffing oscillator (11) with Harmonic Balance ansatz (3) in case of $n = 3$. Labeling of solutions as in Fig. 1.

and unstable solutions occur in an alternating manner. Therefore, the neighborhood of two unstable solutions might be surprising. In fact, these solutions are in an area of initial conditions showing a fractal character as can be seen in Figure 10 where the basins of attraction are displayed. Hereby, grey points denote initial conditions resulting in the stable solution on the resonance curve. Black points are initial conditions for solutions drifting away to $x \to -\infty$ and white points for $x \to +\infty$. In the immediate neighborhood of these solution, basins of attraction for all three types of solution can be found.

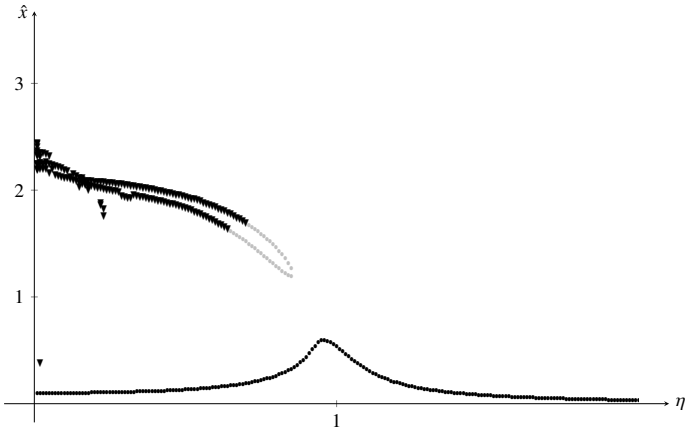

Figure 8. Solutions $\hat{x}$ according to (6) for the extended Duffing oscillator (11) with Harmonic Balance ansatz (3) in case of $n = 5$. Labeling of solutions as in Fig. 1.

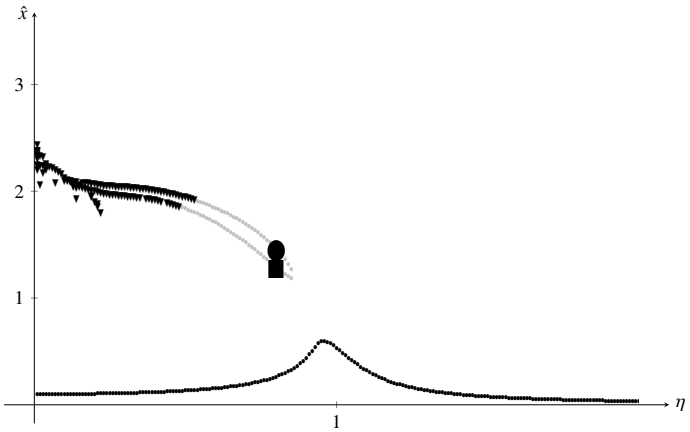

Figure 9. Solutions $\hat{x}$ according to (6) for the extended Duffing oscillator (11) with Harmonic Balance ansatz (3) in case of $n = 7$. Two unstable solutions in the "island" region are marked for $\eta = 0.8$. Labeling of solutions as in Fig. 1.

4. Energy Harvesting

Finally an example from an energy harvesting system shall be discussed in this section. This energy harvesting system consists of a cantilever beam with bonded piezoceramics on the surface close to the clamping. The excitation of the system is realized by a base excitation which may have a harmonic or a stochastic characteristic. In order to increase the energy output, nonlinearities are introduced by mounting two magnets on the frame

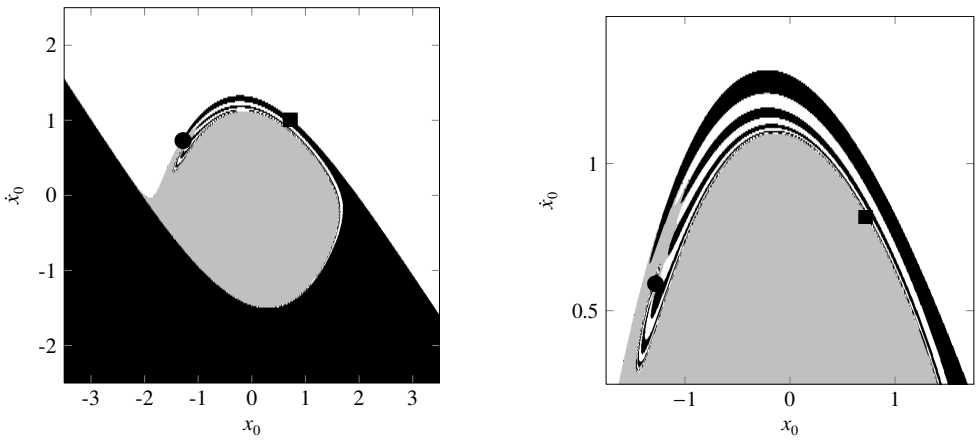

Figure 10. Basins of attraction for $\eta = 0.8$ (left) with detail (right). Grey points denote initial conditions resulting in the stable solution on the resonance curve. Black points are initial conditions for solutions drifting away to $x \to -\infty$ and white points for $x \to +\infty$. Circle and square are marking the initial conditions without transition for the solutions marked in same manner in Figure 9.

the cantilever beam is clamped in close to the tip of the beam. Depending on the magnet properties and positions, multiple stable equilibrium deflections of the beam can result. In our investigations, we are focusing on bistable systems. Corresponding results in case of stochastic excitation can be found e.g. in [5] where probability density functions are calculated. The system also shows a broad variety of solutions if excited harmonically. The simplest useful way of modeling such a system is to discretize the beam with a single mode and couple it with a model of the electric circuit [1], which consist in the present case beside the piezoceramics by a simple resistor. Performing a transformation to dimensionless time τ with circular frequency ω (this is not necessarily the circular eigenfrequency of the mode shape used for discretization) this results in two coupled ODEs namely

$$x''(\tau) + \xi x'(\tau) - \alpha x(\tau) + \beta x^3(\tau) - \chi v(\tau) = f\cos(\eta\tau), \tag{12a}$$

$$v'(\tau) + \lambda v(\tau) = -\kappa x'(\tau). \tag{12b}$$

Herein x is the dimensionless modal coordinate, v is the dimensionless voltage across the resistor, $(\cdot)'$ denotes the derivative with respect to τ and η is the ratio between the excitation frequency and ω. Modal damping is introduced with the coefficient ξ and α and β are the stiffness coefficients which are both strictly positive. χ and κ denote the electro-mechanical coupling coefficients, λ is reciprocal proportional to the product of the capacitance of the piezoce-

ramic layers and the resistance and f is the modal amplitude of the harmonic base excitation.
For the following calculations the parameter values $\xi = 0.0105,\ \alpha = \beta = 0.5,\ \chi = -0.1223,\ \lambda = 0.5396,$ $\kappa = -0.2331$ and $f = 0.1739$ are used.

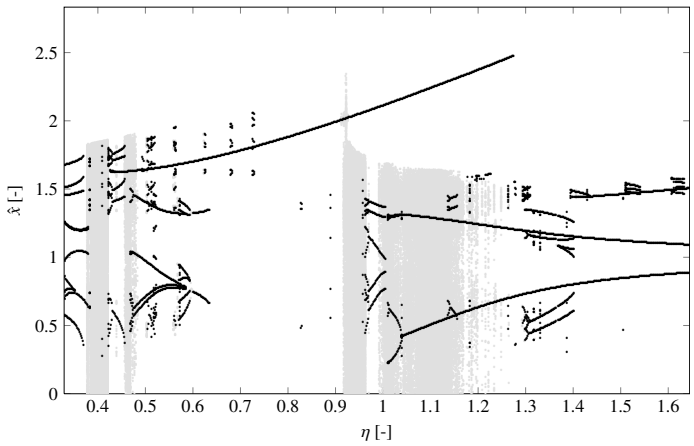

Figure 11. Solutions $\hat{x}$ (turning points of the displacement $x(\tau)$) for the energy harvester (12a), (12b) with numerical integration.

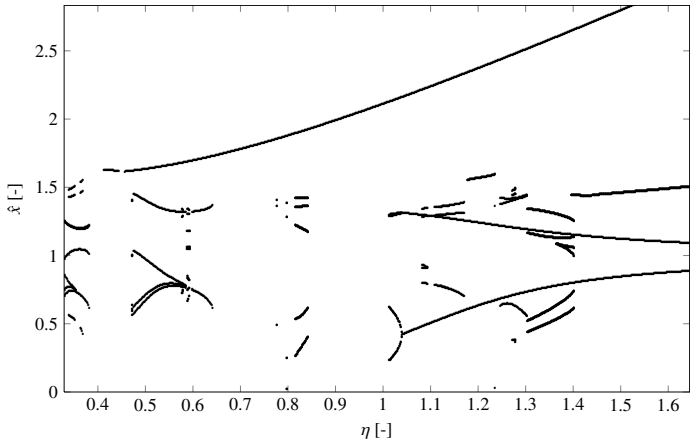

Figure 12. Solutions $\hat{x}$ (turning points of the displacement $x(\tau)$) for the energy harvester (12a), (12b) with Harmonic Balance ansatz (3). Only stable solutions with low relative errors are plotted.

Figure 11 shows results of a numerical integration. In comparison with the Harmonic Balance method of course only stable solutions (and not unstable solutions) can be identified;

but additionally also chaos can be detected. Performing the Harmonic Balance method with the error criterion and displaying only stable solutions, the results in Figure 12 are obtained. It should be mentioned, that the original Harmonic Balance results in numerous additional artifacts and unstable solutions which are neglected in this figure. Both results agree well but the effort for the Harmonic Balance is much lower. For special interest for increasing the energy output of the energy harvester is to obtain so-called interwell solutions, i.e. solutions with vibrations sweeping around both equilibrium positions. Compared to so-called intrawell solutions (vibrations around one equilibrium position) or chaotic solutions these interwell solutions are in general resulting in a higher energy output. In Figure 12 it can be seen, that there is around $\eta \approx 0.75$ an area, where just one interwell solution exists. Such interwell solutions can be identified by the procedure described in this paper in a comparably easy manner. A more detailed discussion of results related to applying the described method to the energy harvester can be found in [4].

5. Conclusions

The classical method of Harmonic Balance in an extended version using an error criterion was applied in the present paper to several nonlinear oscillators. In the error criterion the neglected terms in Harmonic Balance are considered and compared with the remaining terms of the approximate solution. Solutions showing large relative errors even for high ansatz orders are then considered to be artifacts. Solutions with low relative errors are examined for their stability using Floquet's theory. Very often, Harmonic Balance calculations are limited to the ansatz order $n = 1$. With the two examples of a classical and an extended Duffing oscillator it could be shown, that such results may be misleading and that parts of the results could be identified as artifacts. With the example of an energy harvesting system it can be demonstrated that the thereby extended Harmonic Balance is a powerful tool for the rapid identification of interwell solutions promising high energy output.

Acknowledgments

The work on energy harvesting at the Chair of Mechatronics and Machine Dynamics is supported by Deutsche Forschungsgemeinschaft DFG with grant WA 1427/23-1,2.

References

[1] Erturk A., H. J., and Inman, D. J. A piezomagnetoelastic structure for broadband vibration energy harvesting. *Applied Physics Letters*, 96 (2009), 11–14.

[2] Hagedorn, P. *Nichtlineare Schwingungen.* Akademische Verlagsgesellschaft, Wiesbaden, 1978.

[3] Kovacic, I., and Brennan, M. *The Duffing Equation: Nonlinear Oscillators and their Behaviour.* John Wiley & Sons, Ltd, 2011.

[4] Lentz, L., and von Wagner, U. Analysis of a nonlinear energy harvester by the high-order harmonic balance method. *Mechanical Systems and Signal Processing*, submitted (2017).

[5] Martens, W., von Wagner, U., and Litak, G. Stationary response of nonlinear magneto-piezoelectric energy harvester systems under stochastic excitation. *European Physical Journal Special Topics 7*, 222 (2013), 1665–1673.

[6] Parashar, S. K., von Wagner, U., and Hagedorn, P. Nonlinear shear-induced flexural vibrations of piezoceramic actuators: experiments and modeling. *Journal of Sound and Vibration*, 285 (2005), 989–1014.

[7] Urabe, M., and Reiter, A. Numerical computation of nonlinear forced oscillations by Galerkin's procedure. *Journal of Mathematical Analysis and Applications*, 14 (1966), 107–140.

[8] van Dooren R. On the transition form regular to chaotic behaviour in the Duffing oscillator. *Journal of Sound and Vibration 2*, 123 (1988), 327–339.

[9] von Wagner, U., and Lentz, L. On some aspects of the dynamic behavior of the softening Duffing oscillator under harmonic excitation. *Archive of Applied Mechanics 8*, 86 (2016), 1383–1390.

[10] von Wagner, U., and Lentz, L. On artifact solutions of semi-analytic methods in nonlinear dynamics. *Archive of Applied Mechanics*, submitted (2017).

Utz von Wagner, Univ.-Prof. Dr.-Ing.: Chair of Mechatronics and Machine Dynamics, Einsteinufer 5, 10587 Berlin, Germany (*utz.vonwagner@tu-berlin.de*). The author gave a presentation of this paper during one of the conference sessions.

Lukas Lentz, M.Sc.: Chair of Mechatronics and Machine Dynamics, Einsteinufer 5, 10587 Berlin, Germany (*lukas.lentz@tu-berlin.de*).

Vibration modes of rotating thin-walled composite blades

Jerzy Warminski, Jaroslaw Latalski, Zofia Szmit

Abstract: Dynamics of a rotating structure composed of a rigid hub with attached flexible blades is studied in this paper. The blades are represented by linear composite thin–walled beams with a rectangular box cross-section. A mathematical model of each single beam is based on classical laminate theory taking into account anisotropic properties of the composite material, full mechanical coupling between different components of the specimen deformation, linear constitutive laws and a specific reinforcing fibres placement. The reduced model of the whole hub-beam structure is, however, nonlinear due to nonconstant angular speed and non-linear coupling terms occur in the mathematical model. The modes of the rotor for selected configurations are determined analytically and then resonance zones for periodic torque supplied to the hub are presented.

1. Introduction

Rotating slender structures are of intensive scientific interest due to their applications in mechanical, aviation or aerospace engineering [9]. Modern helicopter blades, robot arms or aerospace rotating panels may serve as typical examples. With the development of new materials and control techniques, the importance of accurate modelling of these systems increases rapidly. A fundamental nonlinear model of a rotating helicopter blade has been presented by Crespo da Silva and Hodges [2, 4]. In the proposed formulation a nonlinear curvature and longitudinal deformation of the beam as well as coupling of flexural and torsional oscillations have been taken into account. A model of a nonlinear rotating beam carrying a tip mass has been also proposed in [9]. The considered nonlinear curvature and longitudinal deformation of the beam has been expanded up to the third perturbation order. The importance of the foreshortening effect for different models of the rotating beams has been studied in [7]. As reported, this phenomenon may be essential for the case of a rotating beam if its elongation caused by rotation is considered.

However, the mentioned above approaches have been essentially based on the assumption of isotropic properties of the specimen material. This is a serious drawback if referring to new designs based on composites having orthotropic, or even more general, nonsymmetric anisotropic properties [6]. Analysis of free vibrations of anisotropic thin-walled beams with a closed cross-section have been presented in paper [1]. Authors have shown that anisotropic

properties of the specimen may lead to different dynamics characteristics comparing to a similar structure made of an isotropic material. Moreover, it has been concluded that a properly designed configuration of reinforcing fibres orientation and placement may induce various intended deformation couplings.

A detailed mathematical model of the composite thin-walled beams with open or closed cross-sections has been presented by Song and Librescu in [8]. This formulation has been later extended to rotating structures [6]. The model of slender, flexible thin-walled beam attached to a rotating rigid hub has been also proposed in [3] and then updated in [5], where the importance of selected nonlinear terms in order to get proper results has been demonstrated. In this research the complex mathematical model represented by a set of seven partial differential equations has been derived. Next this model has been used for the analysis of the specific design case of Circumferentially Asymmetric Stiffness (CAS) beam. As demonstrated this configurations exhibits mutual coupling of flapwise bending and twisting deformations. The general analytical formulation of the problem enabled finding the maximum magnitude of the bending and twist coupling coefficient. In Fig. 1 we present the plot of this coefficient against the reinforcing fibres orientation angle for the typical rectangular box cross-section specimen [5]. This figure shows that the maximal coupling

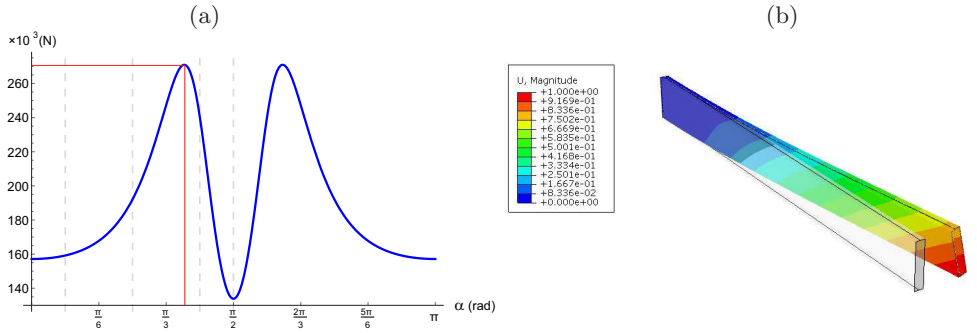

Figure 1. Bending-twisting coupling coefficient for CAS configuration with global maximum at approx. 72 deg. (a) and numerical FEM verification (b).

(indicated by red line) is observed for the fibres orientation $\alpha \approx 72^{\circ}$, where the angle is measured from the circumferential direction. The analytical model has been later confirmed by FEM and the excellent agreement between analytical and numerical models results has been obtained. The first complex bending-twisting natural mode is presented in Fig. 1 (b). This mode has been used for further analytical studies. In particullar, applying the Galerkin procedure, the partial differential equations of motion of the hub-beam structure have been reduced to ordinary differential ones as presented in paper [5]. The discussed complex

deformation mode could be of major interest in terms of possible structural control. The inherent bending-twisting coupling enables control of both coupled deformations just by a single actuator. Nonlinear control strategy applied for these complex flexural-torsional vibrations has been presented in [10].

The purpose of the present paper is to develop, on the basis of the previous authors research, the mathematical model of a three-blades rotor system. The new model has to represent the dynamics of the hub and complex flexural-torsional oscillations of the blades in CAS configuration. Moreover, the arbitrary orientation of reinforcing fibres is assumed to capture the possible detuning of the system.

2. Model of a rotating structure

The analysed rotating structure (a rotor) is composed of three flexible composite beams attached to a rigid hub (Fig. 2 a). The beams preset angle is fixed so that their flapwise bending occurs in the plane of system rotation (lead-lag bending). Moreover, we consider fibers in the opposite beam profile walls to be oriented according to the circumferentially asymmetric stiffness (CAS) lamination scheme. This layout leads to mutual bending-twisting coupling with the maximum value of coupling coefficient to be observed at about 72° – see Fig. 1 (a). Studying this plot one may notice that a small change above this value results in significant decrease of the coupling coefficient down to global minimum noted at $\pi/2$.

As already reported the CAS antisymmetric arrangement of reinforcing fibres decouples the full set of six beam equations of motion (six degrees of freedom) into two independent subsystems: one exhibiting flapwise bendingsheartwisting coupling and the second where axial stretching and chordwise bendingshear modes coexist. Following this observation, and bearing in mind that the stiffness of the blades in the orthogonal (lateral) direction is much larger (Fig. 1 a), so their out-of-plane deformation might be neglected in further analysis. Dynamics of the elastic thin-walled beam is described by a set of Partial Differential Equations (PDEs) originally derived in [5]. As it has been reported later in [10] also the hub inertia must be taken into account, since this parameter has significant impact on overall system characteristics.

The ordinary differential equations of motion of the rotor are based on paper [5] and if adopted for the three-blades rotor they take the form

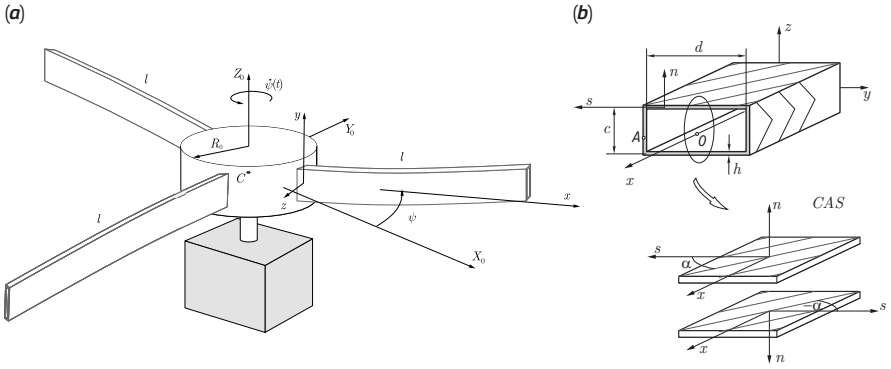

Figure 2. Model of a rotor (a) and CAS composite beam configuration (b).

$$\begin{aligned}
&\left(J_h + \sum_{i=1}^{3} J_{bi} + \sum_{i=1}^{3} \alpha_{hi2} q_i^2\right) \ddot{\psi} + \zeta_h \dot{\psi} + \sum_{i=1}^{3} \left(\alpha_{hi1} \ddot{q}_i + \alpha_{hi3} q_i \dot{q}_i \dot{\psi}\right) = \mu(t), \\
&\ddot{q}_1 + \zeta_1 \dot{q}_1 + \alpha_{12} \ddot{\psi} + \left(\alpha_{11} + \alpha_{13} \dot{\psi}^2\right) q_1 + \alpha_{14} q_1 \dot{q}_1 \dot{\psi} = 0, \\
&\ddot{q}_2 + \zeta_2 \dot{q}_2 + \alpha_{22} \ddot{\psi} + \left(\alpha_{21} + \alpha_{23} \dot{\psi}^2\right) q_2 + \alpha_{24} q_2 \dot{q}_2 \dot{\psi} = 0, \\
&\ddot{q}_3 + \zeta_3 \dot{q}_3 + \alpha_{32} \ddot{\psi} + \left(\alpha_{31} + \alpha_{33} \dot{\psi}^2\right) q_3 + \alpha_{34} q_3 \dot{q}_3 \dot{\psi} = 0,
\end{aligned} \tag{1}$$

where $i = 1, 2, 3$, and J_h, J_{bi} denote mass moment of inertia of the hub and beams, respectively, ζ_h, ζ_i, viscous damping coefficients, $\mu(t)$ represents an external torque imposed to the hub, $\alpha_{hi1}, \alpha_{hi2}, \alpha_{hi3}, \alpha_{i1}, \alpha_{i2}, \alpha_{i3}, \alpha_{i4}$ are coefficient obtained from the modal reduction procedure. One may observe, equations (1) are coupled due to inertia terms. If angular velocity of the hub is constant then all equations are uncoupled except the quadratic terms occurring in the first equation. These terms are of higher order and for small oscillations can be neglected too. However, if angular velocity is not constant then all equations are coupled and Coriolis forces and nonlinear quadratic term due to rotation are involved in the full structure dynamics.

3. Nonlinear normal modes - analytical solutions

Let us determine normal modes of the hub-beams rotor. Because the structure is nonlinear we may expect that the modes can be nonlinear too.

We seek nonlinear normal modes (NNM) of the rotor neglecting damping and external torque; so one presumes $\zeta_1 = 0$, $\zeta_2 = 0$, $\zeta_3 = 0$, $\zeta_h = 0$, $\mu(t) = 0$. Furthermore, we introduce a formal small parameter ε and express individual coordinates as

$$q_1 = \varepsilon \tilde{q}_1, \quad q_2 = \varepsilon \tilde{q}_2, \quad q_3 = \varepsilon \tilde{q}_3, \tag{2}$$

which, after substitution and rearrangement, yields

$$
\begin{aligned}
&\ddot{q}_1 \left[1 + J_{b2} + J_{b3} + J_h - \alpha_{h11}\alpha_{12} - \alpha_{h21}\alpha_{22} - \alpha_{h31}\alpha_{32}\right. \\
&\qquad \left. -\varepsilon^2\left(\alpha_{h12}q_1^2 + \alpha_{h22}q_2^2 + \alpha_{h32}q_3^2\right)\right] \\
&= \left(\alpha_{22}\alpha_{h21} + \alpha_{32}\alpha_{h31}\right)\left[\varepsilon q_1\left(\alpha_{11} + \alpha_{13}\dot{\psi}^2\right) + \varepsilon^2\alpha_{14}q_1\dot{q}_1\dot{\psi}\right] \\
&\qquad -\alpha_{12}\alpha_{h21}\left[\varepsilon q_2\left(\alpha_{21} + \alpha_{23}\dot{\psi}^2\right) + \varepsilon^2\alpha_{24}q_2\dot{q}_2\dot{\psi}\right] \\
&\qquad -\alpha_{12}\alpha_{h31}\left[\varepsilon q_3\left(\alpha_{31} + \alpha_{33}\dot{\psi}^2\right) + \varepsilon^2\alpha_{34}q_3\dot{q}_3\dot{\psi}\right] \\
&\qquad -\left[\varepsilon q_1\left(\alpha_{11} + \alpha_{13}\dot{\psi}\right) + \varepsilon^2\alpha_{14}q_1\dot{q}_1\dot{\psi}\right] \\
&\quad \times \left[1 + J_{b2} + J_{b3} + J_h + \varepsilon^2\left(\alpha_{h12}q_1^2 + \alpha_{h22}q_2^2 + \alpha_{h32}q_3^2\right)\right] \\
&\qquad +\varepsilon^2\alpha_{12}\left(\alpha_{h13}q_1\dot{q}_1 + \alpha_{h23}q_2\dot{q}_2 + \alpha_{h33}q_3\dot{q}_3\right)\dot{\psi},
\end{aligned}
\tag{3}
$$

$$
\begin{aligned}
&\ddot{q}_2 \left[1 + J_{b2} + J_{b3} + J_h - \alpha_{h11}\alpha_{12} - \alpha_{h21}\alpha_{22} - \alpha_{h31}\alpha_{32}\right. \\
&\qquad \left. -\varepsilon^2\left(\alpha_{h12}q_1^2 + \alpha_{h22}q_2^2 + \alpha_{h32}q_3^2\right)\right] \\
&= \left(\alpha_{12}\alpha_{h11} + \alpha_{32}\alpha_{h31}\right)\left[\varepsilon q_2\left(\alpha_{21} + \alpha_{23}\dot{\psi}^2\right) + \varepsilon^2\alpha_{24}q_2\dot{q}_2\dot{\psi}\right] \\
&\qquad -\alpha_{22}\alpha_{h11}\left[\varepsilon q_1\left(\alpha_{11} + \alpha_{13}\dot{\psi}^2\right) + \varepsilon^2\alpha_{14}q_1\dot{q}_1\dot{\psi}\right] \\
&\qquad -\alpha_{22}\alpha_{h31}\left[\varepsilon q_3\left(\alpha_{31} + \alpha_{33}\dot{\psi}^2\right) + \varepsilon^2\alpha_{34}q_3\dot{q}_3\dot{\psi}\right] \\
&\qquad -\left[\varepsilon q_2\left(\alpha_{21} + \alpha_{23}\dot{\psi}^2\right) + \varepsilon^2\alpha_{24}q_2\dot{q}_2\dot{\psi}\right] \\
&\quad \times \left[1 + J_{b2} + J_{b3} + J_h + \varepsilon^2\left(\alpha_{h12}q_1^2 + \alpha_{h22}q_2^2 + \alpha_{h32}q_3^2\right)\right] \\
&\qquad +\varepsilon^2\alpha_{22}\left(\alpha_{h13}q_1\dot{q}_1 + \alpha_{h23}q_2\dot{q}_2 + \alpha_{h33}q_3\dot{q}_3\right)\dot{\psi},
\end{aligned}
\tag{4}
$$

$$
\begin{aligned}
&\ddot{q}_3 \left[1 + J_{b2} + J_{b3} + J_h - \alpha_{h11}\alpha_{12} - \alpha_{h21}\alpha_{22} - \alpha_{h31}\alpha_{32}\right. \\
&\qquad \left. -\varepsilon^2\left(\alpha_{h12}q_1^2 + \alpha_{h22}q_2^2 + \alpha_{h32}q_3^2\right)\right] \\
&= \left(\alpha_{12}\alpha_{h11} + \alpha_{22}\alpha_{h21}\right)\left[\varepsilon q_3\left(\alpha_{31} + \alpha_{33}\dot{\psi}^2\right) + \varepsilon^2\alpha_{34}q_3\dot{q}_3\dot{\psi}\right] \\
&\qquad -\alpha_{32}\alpha_{h11}\left[\varepsilon q_1\left(\alpha_{11} + \alpha_{13}\dot{\psi}^2\right) + \varepsilon^2\alpha_{14}q_1\dot{q}_1\dot{\psi}\right] \\
&\qquad -\alpha_{32}\alpha_{h21}\left[\varepsilon q_2\left(\alpha_{21} + \alpha_{23}\dot{\psi}^2\right) + \varepsilon^2\alpha_{24}q_2\dot{q}_2\dot{\psi}\right] \\
&\qquad -\left[\varepsilon q_3\left(\alpha_{31} + \alpha_{33}\dot{\psi}^2\right) + \varepsilon^2\alpha_{34}q_3\dot{q}_3\dot{\psi}\right] \\
&\quad \times \left[1 + J_{b2} + J_{b3} + J_h + \varepsilon^2\left(\alpha_{h12}q_1^2 + \alpha_{h22}q_2^2 + \alpha_{h32}q_3^2\right)\right] \\
&\qquad +\varepsilon^2\alpha_{32}\left(\alpha_{h13}q_1\dot{q}_1 + \alpha_{h23}q_2\dot{q}_2 + \alpha_{h33}q_3\dot{q}_3\right)\dot{\psi},
\end{aligned}
\tag{5}
$$

$$
\begin{aligned}
\ddot{\psi}\left[1+J_{b2}+J_{b3}+J_h-\alpha_{h11}\alpha_{12}-\alpha_{h21}\alpha_{22}-\alpha_{h31}\alpha_{32}\right.&\\
\left.-\varepsilon^2\left(\alpha_{h12}q_1^2+\alpha_{h22}q_2^2+\alpha_{h32}q_3^2\right)\right]&\\
=\alpha_{h11}\left[\varepsilon q_1\left(\alpha_{11}+\alpha_{13}\dot{\psi}^2\right)+\varepsilon^2\alpha_{14}q_1\dot{q}_1\dot{\psi}\right]&\\
\alpha_{h21}\left[\varepsilon q_2\left(\alpha_{21}+\alpha_{23}\dot{\psi}^2\right)+\varepsilon^2\alpha_{24}q_2\dot{q}_2\dot{\psi}\right]&\\
\alpha_{h31}\left[\varepsilon q_3\left(\alpha_{31}+\alpha_{33}\dot{\psi}^2\right)+\varepsilon^2\alpha_{34}q_3\dot{q}_3\dot{\psi}\right]&\\
-\varepsilon^2\left(\alpha_{h13}q_1\dot{q}_1+\alpha_{h23}q_2\dot{q}_2+\alpha_{h33}q_3\dot{q}_3\right)\dot{\psi},&
\end{aligned}
\tag{6}
$$

Tilde has been dropped in the above notation for simplicity.

Solutions of Eqs. (3)-(6) are sought in the form

$$
\begin{aligned}
q_1&=A_1\sin\left(\omega_0 t+\phi\right), \quad q_2=A_2\sin\left(\omega_0 t+\phi\right),\\
q_3&=A_3\sin\left(\omega_0 t+\phi\right), \quad q_h=A_h\sin\left(\omega_0 t+\phi\right),
\end{aligned}
\tag{7}
$$

where A_1, A_2, A_3, A_h are unknown amplitudes, ϕ is a phase and ω_0 frequency of natural oscillations.

Substituting Eq. (7) into Eqs. (3)-(6), neglecting higher order terms and taking into account only the first harmonic we get

$$
\begin{aligned}
A_1\left[\left(\alpha_{11}-\omega_0^2+\tfrac{1}{4}A_h^2\alpha_{13}\right)\left(1+J_{b2}+J_{b3}+J_h-\alpha_{22}\alpha_{h21}-\alpha_{32}\alpha_{h31}\right)\right.&\\
\left.+\alpha_{12}\alpha_{h11}\omega_0^2\right]+A_2\alpha_{12}\alpha_{h21}\left(\alpha_{21}+\tfrac{1}{4}A_h^2\alpha_{23}\omega_0^2\right)&\\
+A_3\alpha_{12}\alpha_{h31}\left(\alpha_{31}+\tfrac{1}{4}\alpha_{33}\omega_0^2\right)=0,&\\
A_1\alpha_{22}\alpha_{h11}\left(\alpha_{11}+\tfrac{1}{4}A_h^2\alpha_{13}\omega_0^2\right)&\\
+A_2\left[\left(\alpha_{21}-\omega_0^2+\tfrac{1}{4}A_h^2\alpha_{23}\right)\left(1+J_{b2}+J_{b3}+J_h-\alpha_{12}\alpha_{h11}-\alpha_{32}\alpha_{h31}\right)\right.&\\
\left.+\alpha_{12}\alpha_{h11}\omega_0^2\right]+A_3\alpha_{22}\alpha_{h31}\left(\alpha_{31}+\tfrac{1}{4}\alpha_{33}\omega_0^2\right)=0,&\\
A_1\alpha_{32}\alpha_{h11}\left(\alpha_{11}+\tfrac{1}{4}A_h^2\alpha_{13}\omega_0^2\right)+A_2\alpha_{32}\alpha_{h21}\left(\alpha_{21}+\tfrac{1}{4}\alpha_{23}\omega_0^2\right)&\\
+A_3\left[\left(\alpha_{31}-\omega_0^2+\tfrac{1}{4}A_h^2\alpha_{33}\right)\left(1+J_{b2}+J_{b3}+J_h-\alpha_{12}\alpha_{h11}-\alpha_{32}\alpha_{h31}\right)\right.&\\
\left.+\alpha_{12}\alpha_{h11}\omega_0^2\right]=0,&\\
A_1\alpha_{h11}\left(\alpha_{11}-\tfrac{1}{4}A_h^2\alpha_{13}\omega_0^2\right)+A_2\alpha_{h12}\left(\alpha_{21}+\tfrac{1}{4}A_h^2\alpha_{23}\omega_0^2\right)&\\
+A_3\alpha_{h31}\left(\alpha_{31}+\tfrac{1}{4}A_h^2\alpha_{33}\omega_0^2\right)=0.&
\end{aligned}
\tag{8}
$$

A set of nonlinear algebraic equations (8) can be solved analytically and strict solutions for amplitudes can be determined as functions of unknown parameter ω_0. The trivial solution

$A_1 = 0$, $A_2 = 0$, $A_3 = 0$, $A_h = 0$ satisfies Eqs. (8). However, also nontrivial solutions $A_1 \neq 0$, $A_2 \neq 0$, $A_3 \neq 0$, $A_h \neq 0$ may exists for a certain domain of parameter ω_0. The analytical expressions for amplitudes are not prsented in this paper due to their complex form.

4. Numerical examples

Numerical calculations have been performed for data presented in [5, 8]. The following material constants are used $E_1 = 206.75 \cdot 10^9$ Pa, $E_2 = E_3 = 5.17 \cdot 10^9$ Pa, $G_{23} = 3.1 \cdot 10^9$ Pa, $G_{13} = G_{12} = 2.55 \cdot 10^9$ Pa, $\nu_{32} = 0.25$, $\nu_{21} = \nu_{31} = 0.00625$, $\rho = 1528.15$ kg/m^3. Dimensions of the beam are taken as $c = 0.00508$ m, $d = 0.0254$ m, $h = 0.001$ m, $l = 0.254$ m and hub radius $R_0 = 0.1 \times l$. After transformation to dimensionless form and the reduction procedure based on the first bending-twisting mode we get values of coefficients of Eqs. (1) computed for CAS layout and three different, arbitrary assumed, reinforcing fibres angles of 75, 80 and 60 degrees

$$
\begin{aligned}
&\text{beam } 1: 75 \text{ deg.} \\
&\alpha_{11} = 95.41318 \alpha_{12} = 2.9063 \alpha_{13} = 0.3527192 \alpha_{14} = -0.920491 \\
&\alpha_{h11} = 0.3201742 \alpha_{h12} = -0.146365 \alpha_{h13} = -0.29273 \\
&\text{beam } 2: 80 \text{ deg.} \\
&\alpha_{21} = 159.6166 \alpha_{22} = 3.765367 \alpha_{23} = 0.353319 \alpha_{24} = -0.69457 \\
&\alpha_{h21} = 0.244628 \alpha_{h22} = -0.085284 \alpha_{h23} = -0.170568 \\
&\text{beam } 3: 60 \text{ deg.} \\
&\alpha_{31} = 30.971 \alpha_{32} = 1.7747 \alpha_{33} = 0.3506 \alpha_{34} = -1.5447 \\
&\alpha_{h31} = 0.53051 \alpha_{h32} = -0.402182 \alpha_{h33} = -0.80436
\end{aligned}
\tag{9}
$$

We assume that all beams have the same geometry and mass moment of inertia $J_{b1} = J_{b2} = J_{b3} = 1$, but due to different orientation of the fibres the beams are de-tuned and thus coefficients in Eqs. (1) are different for each beam, as given in (9). Mass moment of inertia of the hub has been assumed as $J_h = 5$.

For these data three different vibration modes have been computed from Eqs. (8). In Fig. 3 amplitudes of the blades and hub are plotted versus natural frequency of the rotor. We can notice three different vibration modes with different amplitudes ratios. For all cases amplitudes vary nonlinearly against natural frequency, which results from nonlinearities of the system. If oscillations are very small then we obtain natural frequencies of the linear model, $\omega_{01} = 5.85$, $\omega_{02} = 10.35$, $\omega_{03} = 13.97$. As amplitudes increase natural frequency increases as well for all three vibration modes, the stiffening phenomenon is observed.

The motion of the beams and the hub is presented by time history plots in Fig. 4. The

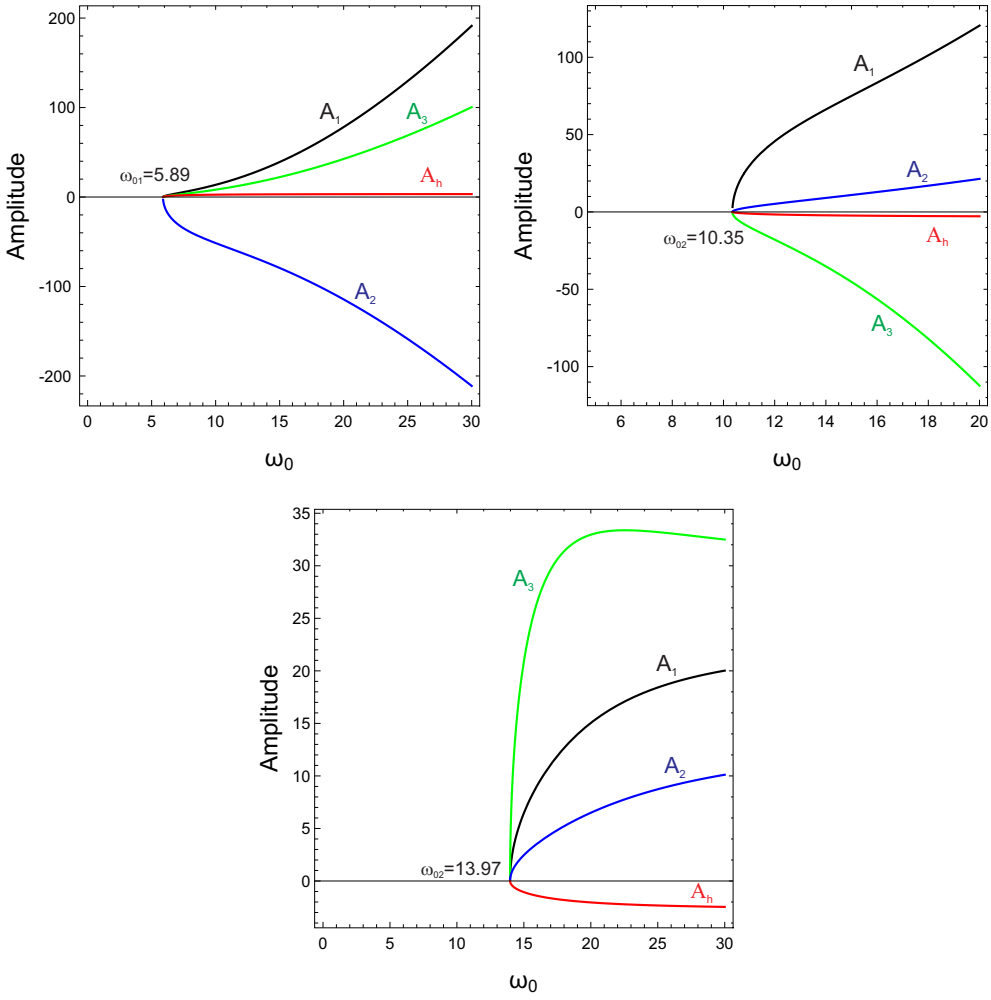

Figure 3. Natural frequency ω_0 versus amplitudes of the blades A_1, A_2, A_3 and the hub A_h.

time histories are obtained from direct numerical simulations of Eqs. (1). They are in a full agreement with analytical prediction. In Fig. 4 (a), (b) and (c) the first, the second and the third mode are activated by putting properly computed initial conditions for each coordinate. However, if the oscillations are very large then the numerical simulations shows different result then the analytical prediction. In Fig. 5 we demonstrate activation of the first mode by putting large initial conditions. As we may see in this case the response is not harmonic, due to large oscillations higher harmonics are involved in the motions.

In spite of the fact that in Fig. 3 stiffening phenomenon for all vibration modes has

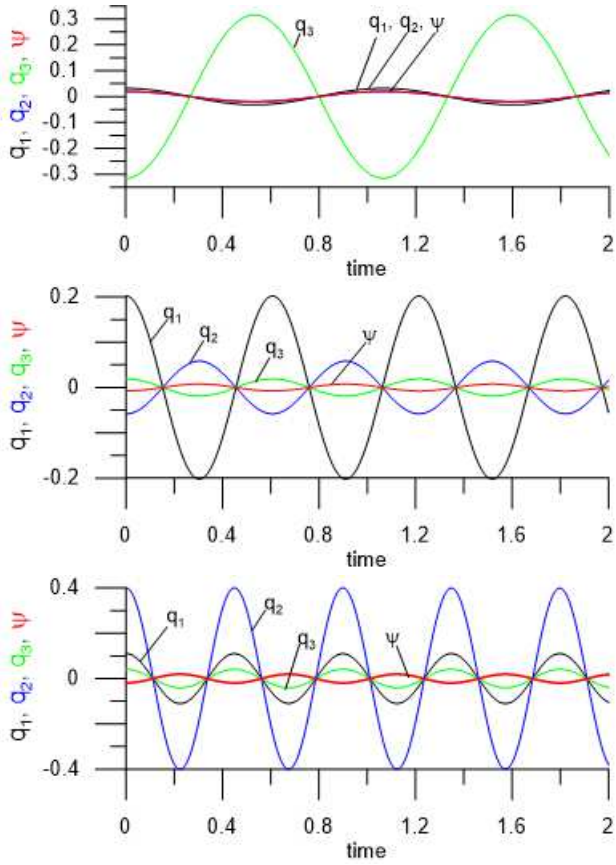

Figure 4. Time histories of blades and hub response q_1, q_2, q_3, ψ for the first, the second and the third mode activated; $J_h = 5$.

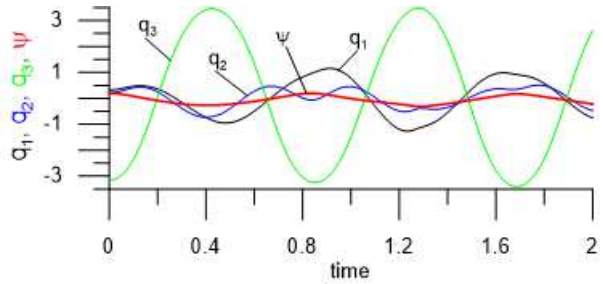

Figure 5. Time histories of blades and hub response q_1, q_2, q_3, ψ for the first mode activated; large oscillations; $J_h = 5$.

been observed if we plot modal lines (Rosenberg lines) we get linear dependencies between amplitudes (Fig. 6). Therefore the influence of nonlinear terms can be observed only for vary large values of amplitudes which are out of realistic examples (Fig. 7).

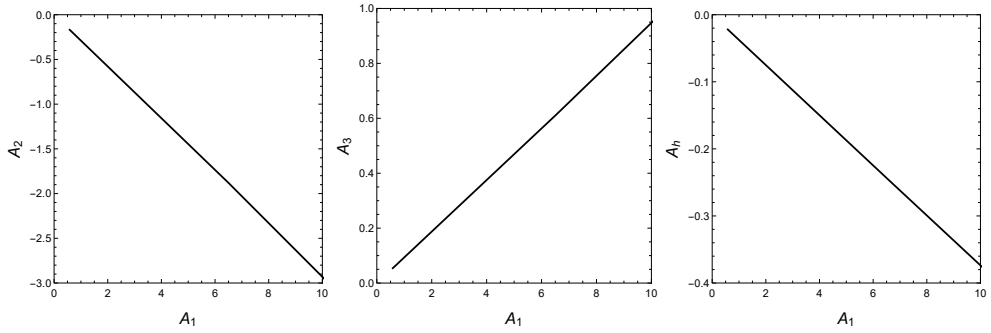

Figure 6. Modal lines $A_2 - A_1, A_3 - A_1, A_h - A_1$ for activated the first vibration mode, $J_h = 5$.

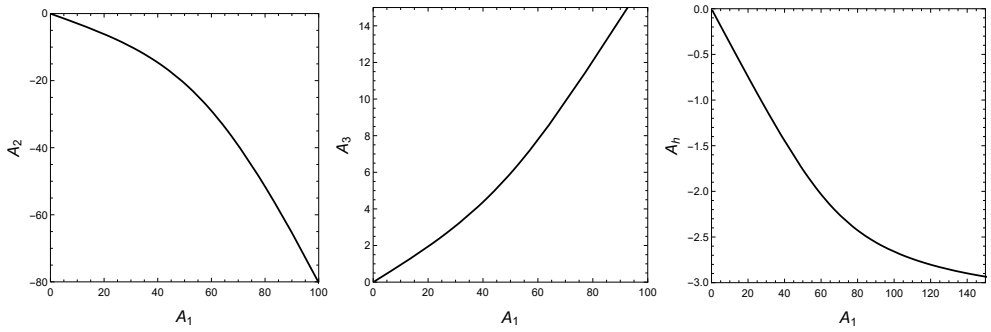

Figure 7. Modal lines $A_2 - A_1, A_3 - A_1, A_h - A_1$ for activated the first vibration mode, large amplitudes, $J_h = 5$.

The resonance curves presented in Fig. 8 computed for the harmonic external torque $\mu = \rho \sin \omega t$ have linear nature and they confirm the modal analysis results. It means that rotation shifts the natural frequency but modal lines and resonance characteristics does not exhibit nonlinear nature.

5. Conclusions

A reduced model of the three blades rotor has been analysed in this paper. It has been show that CAS composite layout leads to bending-twisting coupling of the thin-walled box beam. Due to nonconstant angular speed the equations of motion of individual beams and the hub

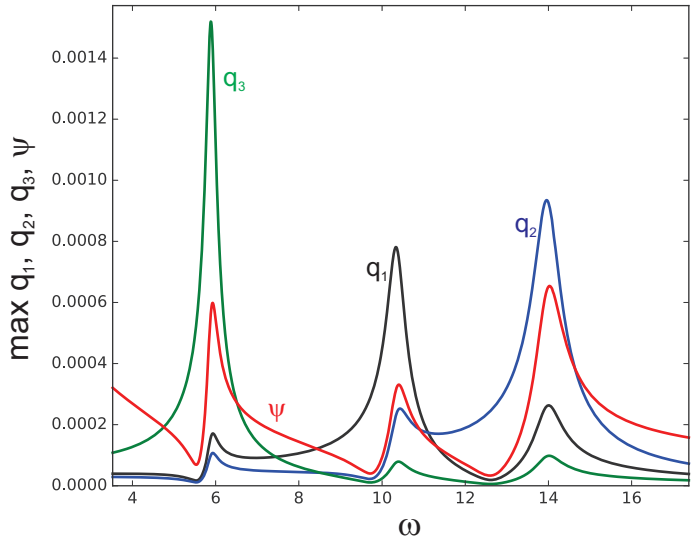

Figure 8. Amplitudes of blades q_1, q_2, q_3 and the hub ψ against excitation frequency ω; $\rho = 0.01,\ J_h = 5$.

equation are coupled by inertia terms. Analytically determined vibration modes show that natural frequencies depend on vibration amplitudes and stiffening phenomenon is observed as a right-shift of the characteristics on the amplitude frequency plot. In spite of this fact, however, modal lines remains linear. The nonlinearities occur only for very large amplitudes and then nonlinear normal modes occur. However, the resonance zones computed for real parameters do not demonstrate nonlinear behaviour.

Acknowledgments

The work is financially supported by grant 2016/23/B/ST8/01865 from the National Science Centre, Poland.

References

[1] Armanios, E. A., and Badir, A. M. Free vibration analysis of anisotropic thin-walled closed-section beams. *AIAA Journal 33*, 10 (1995), 1905–1910.

[2] Crespo da Silva, M., and Hodges, D. Nonlinear flexure and torsion of rotating beams with application to helicopter blade. *Vertica 10* (1986), 1225–1234.

[3] Georgiades, F., Latalski, J., and Warminski, J. Equations of motion of rotating composite beams with a nonconstant rotation speed and an arbitrary preset angle. *Meccanica 49*, 8 (2014), 1833–1858.

[4] Hodges, D. Proper definition of curvature in nonlinear beam kinematics. *AIAA Journal 22*, 12 (1984), 1825–1827.

[5] Latalski, J., Warminski, J., and Rega, G. Bending-twisting vibrations of a rotating hub–thin-walled composite beam system. *Mathematics and Mechanics of Solids 22*, 6 (2017), 1303–1325.

[6] Librescu, L., and Song, O. *Thin-Walled Composite Beams: Theory and Application*. Springer, Dordrecht and the Netherlands, 2006.

[7] Piedbœuf, J.-C., and Moore, B. On the foreshortening effects of a rotating flexible beam using different modeling methods. *Mechanics of Structures and Machines 30*, 1 (2002), 83–102.

[8] Song, O., and Librescu, L. Free vibration of anisotropic composite wthin-walled beams of closed cross-section contour. *Journal of Sound and Vibration 167*, 1 (1993), 129–147.

[9] Warminski, J., and Balthazar, J. Nonlinear vibrations of a beam with a tip mass attached to a rotating hub. *Proceedings of the ASME International Design Engineering Technical Conferences and Computers and Information in Engineering Conference 1*, Pts A-C (2005), 1619–1624.

[10] Warminski, J., and Latalski, J. Nonlinear control of flexural-torsional vibrations of a rotating thin-walled composite beam. *International Journal of Structural Stability and Dynamics 17*, 5 (2017), 1740003.

Jerzy Warminski, Prof. Ph.D. D.Sc. Eng.: Lublin University of Technology/Faculty of Mechanical Engineering/Department of Applied Mechanics, Nadbystrzycka 36, 20-560 Lublin, POLAND (*j.warminski@pollub.pl*). The author gave a presentation of this paper during one of the conference sessions.

Jaroslaw Latalski, Ph.D. Eng.: Lublin University of Technology/Faculty of Mechanical Engineering/Department of Applied Mechanics, Nadbystrzycka 36, 20-560 Lublin, POLAND (*j.latalski@pollub.pl*).

Zofia Szmit, M.Sc. Eng.: Lublin University of Technology/Faculty of Mechanical Engineering/Department of Applied Mechanics, Nadbystrzycka 36, 20-560 Lublin, POLAND (*z.szmit@pollub.pl*).

Experimental and numerical investigations of one-degree-of-freedom impacting oscillator

Krzysztof Witkowski, Grzegorz Kudra, Grzegorz Wasilewski, Fryderyk Wiądzkowicz, Jan Awrecjewicz

Abstract: The work concerns preliminary studies of dynamics of experimental setup consisting of cart mounted on a guide, connected with springs to the support and equipped with a rigid limiter of motion. The cart is excited by an unbalanced disk driven with step motor. Mathematical model of the system is developed with particular attention paid to modelling of impacts as well as resistance of linear ball bearing. The collisions are modelled as soft impacts with Hertzian contact stiffness. Model parameters are identified and good agreement between numerical simulations and experimental results is obtained. System dynamics is then analyzed using different numerical tools.

1. Introduction

Mechanical systems with impacts and friction are commonly encountered in physics and technology. This is a reason of interest of scientists and engineers in mathematical modelling and dynamical properties of mechanical oscillators with dry friction or rigid limiters of motion. Besides the practical and engineering aspects, mechanical systems with impacts and friction can often be modelled as discontinuous dynamical systems and therefore lead to special class of phenomena of nonlinear dynamics and con-classical bifurcation scenarios, being the branch of science undergoing rapid development in the last decades.

Analysis of impacting oscillators has a long history in scientific literature. For example in the work [1] there is presented a periodically forced one-degree-of-freedom oscillator, where for ideally plastic impacts the dynamics is modelled by discontinuous maps on the circle, which undergo period doubling bifurcations and other complex discontinuous transitions, leading to occurrence of arbitrary long super-stable periodic motions. Numerical evidence that discontinuous bifurcations occurring in impact oscillators are just the limits of classical bifurcations of smooth dynamical systems is given in [2]. Budd and Dux [3] use a piecewise linear forced oscillator with impacts to show numerically and analytically different non-linear dynamics bifurcation phenomena typical for systems with rigid stops. Among others there are presented special types of non-smooth bifurcations: chatter with infinitely many impacts in finite time and grazing, when a stable periodic orbit encounters an obstacle and disappears catastrophically. Hinrichs et al. [4] analyze two different types of non-smooth one-degree-of-freedom oscillators are analyzed: an impact system and self-excited friction oscillator. There are presented different types of motion and bifurcation phenomena, both experimentally and numerically. Lyapunov exponents are calculated based on the mathematical models using two different methods. One of them

uses linearization of the model and the corresponding jumps of the of perturbations at the instances of discontinuities. The second one is based on a discrete map and its Jacobian.

Impacts can be modelled as discontinuous instant phenomena or obstacle can treated as soft object. New bifurcation phenomena exhibited by oscillators with impacts, when stiffness of the limiter changes from zero to infinity, is presented in the work of Peterka [5]. Experimental investigations of one-degree-of-freedom forced oscillator with one-sided elastic stop is analyzed in [6], where different typical grazing scenarios are presented. A comprehensive review of contact dynamics modelling is presented by Gilardi and Sharf [7], as well as by Machado et al. [8], where special attention is paid to the compliant contact force models and Hertz contact theory. Earlier some aspects of restitution coefficient interpreted as damping during contact with compliant obstacle is investigated in the work [9].

In the present work there are reported preliminary results of experimental and numerical investigations of one-degree-of-freedom mechanical oscillator with one-sided stop. In Section 2 there is presented experimental rig of the system, while Section 3 exhibits mathematical model of the experimental stand. In Section 4 we present results of numerical simulations, including results of parameters' estimation and examples of bifurcation dynamics. Section 5 presents some concluding remarks.

2. Experimental stand

Fig. 1 exhibits the view of the built experimental rig. It is a part of the larger reconfigurable system allowing for investigations of multi-degree-of-freedom mechanical oscillations with multiple excitations and impacts. Presently the system plays a role of one-degree-of-freedom forced oscillator with one-sided stop.

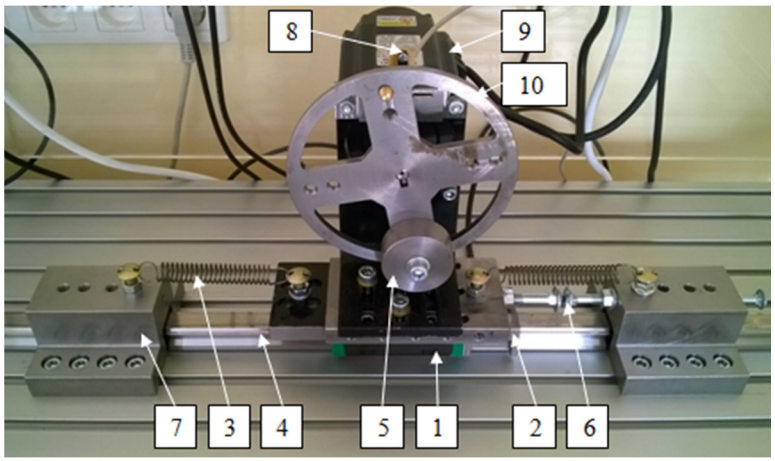

Figure 1. Real view of the experimental stand

The stand consists of linear trolley (1) integrated with Hall effect sensor (2). Trolley moves along the linear rail (4) and it is connected with the support (7) by springs (3). Harmonic excitation is performed by the use of the stepper motor (9) on the axis of which the disc (10) with unbalance (5) is mounted. Collisions are realized by the use of the stops (6) mounted in the support (7) and the trolley (1). In order to control absolute angular position of the stepper motor, the transoptor (8) is mounted behind the disc (10). Measurement data is collected by the Hall effect sensor and encoder integrated with the stepper motor and then registered by National Instrument data acquisition card and processed by the use of software created in the LabView environment.

3. Mathematical model

In Fig. 2 there is presented physical concept of the experimental rig described in the Section 2. The body (trolley, motor, disc, unbalanced mass and bracket) of total mass m moves along axis x and is connected to the support by the use of springs of total stiffness k. It is assumed that in the position x=0 the spring force is equal to zero. The damper of ratio c models damping in the springs as well as in linear bearing of the cart. At the position x=0 there is a gap x_I between two bumpers on the right side of the system. On the cart there is mounted a disk of angular position ωt, where ω represents the angular frequency of forcing and t denotes time. On the radius e of the disk there is placed a weight of unbalanced mass m_0.

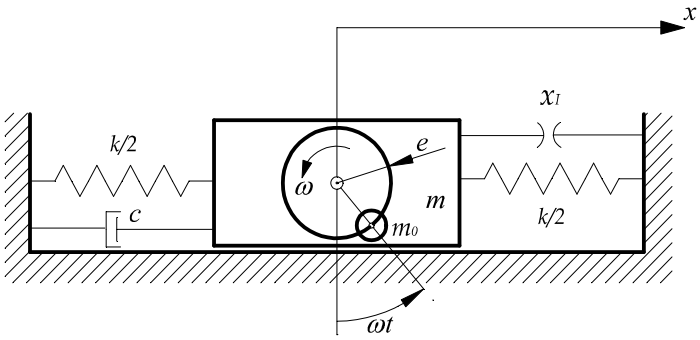

Figure 2. Physical model of the experimental stand

Mathematical model of the system presented in Fig. 2 has the following form

$$m\ddot{x} + kx + F_R(\dot{x}) + F_I(x, \dot{x}) = m_0 e\omega^2 sin\omega t\,, \tag{1}$$

where

$$F_R = c\dot{x} + T\frac{\dot{x}}{\sqrt{\dot{x}^2+\varepsilon^2}}\,, \tag{2}$$

$$F_I = \begin{cases} h^{\frac{3}{2}} \cdot k_I \left(1 + b\dot{h}\left|\dot{h}\right|^{n-1}\right) & \text{for } 1 + b\dot{h}\left|\dot{h}\right|^{n-1} \geq 0 \\ 0 & \text{for } 1 + b\dot{h}\left|\dot{h}\right|^{n-1} < 0 \end{cases}, \tag{3}$$

$$h = \begin{cases} x - x_I & \text{for } x \geq x_I \\ 0 & \text{for } x < x_I \end{cases}. \tag{4}$$

In Eqs. (1-4) F_R denotes resistance force acting on the cart and is not related to the impact phenomenon, while F_I stands for the impact force and h is penetration of the obstacle.

The resistance force F_R consists of linear damping force of coefficient c and Coulomb friction force of magnitude T, where special smooth approximation of sign function is applied and where ε is special parameter of regularization. It is assumed that friction force does not depend on normal loading of the linear bearing.

Impact force F_I is modelled based on Hertzian contact stiffness and damping [7-9], where k_I and b stand for the corresponding stiffness and damping coefficients. Additionally there is introduced a certain non-linearity in the impact damping by adding a parameter n, which in the original version of the model is equal to one.

Right-hand-side of Eq. (1) represents harmonic excitation generated by the unbalanced mass m_0. In this case it is taken into account only radial inertia force of the unbalance. Tangent inertia force related to angular acceleration of the disk is neglected as small when compared to the total excitation force. Therefore the presented model is valid for constant value of angular frequency of excitation ω or for small changes of this quantity as it is assumed during construction of bifurcation diagrams in Section 4.

4. Experiments and numerical simulations

Numerical simulations of the mathematical model presented in Section 3 are performed by the use of simulation models and corresponding scripts created by the use of Scilab environment and its module Xcos. The following parameters of the model are assumed to be known and fixed during the subsequent simulations: $m = 8.735$ kg, $m_0 e = 0.01805$ kg·m (based on relatively accurate direct measurements) and $\varepsilon = 10^{-6}$ m/s. Position of the obstacle x_I is measured accurately before each experiment by the use of the integrated Hall effect sensor. The remaining parameters are estimated based on the experimental data.

Identification of the parameters is based on the Nelder-Mead multi-dimensional optimization algorithm realized by *fminsearch* Scilab function. The minimized function is defined as follows

$$F_O(\boldsymbol{\mu}) = \frac{\int_{t_1}^{t_2}\left(x_{exp}(t) - x_{sim}(t)\right)^2 dt}{t_2 - t_1}, \tag{5}$$

where $x_{exp}(t)$ and $x_{sim}(t)$ are the corresponding position signals of the cart obtained experimentally and from the numerical simulation on the time interval $[t_1, t_2]$, while $\boldsymbol{\mu}$ is vector of estimated parameters.

There are well known the problems with local minima during the estimation of parameters of dynamical systems with the method described above, especially in the case of identification of large number of parameters in one step. In order to minimize that risk, the identification is performed in two stages. In the first one there is used experimental solution corresponding to free vibrations without impacts presented in Fig. 3. Initial part of the solution is cut off and initial conditions are read from the experimental data for the corresponding maximum of the position signal: $x(0) = 37.60$ mm and $\dot{x}(0) = 0$. Then the same initial conditions are used for numerical simulations during estimation of the parameters of the cart resistance model and the spring stiffness, leading to the results presented in Fig. 3. The following values of the parameters are obtained: c = 6.574 N·s/m, T = 0.6307 N and k = 1419 N/m, where the corresponding minimal value of the objective function is F_o = 0.0772 mm^2. In the next step the previously estimated parameters are assumed to be fixed and the parameters of the impact process are identified in the next experiment corresponding to the free vibrations with impacts presented in Fig. 4, where the obstacle position $x_I = -2.084$ mm is obtained precisely by the used of the integrated Hall effect sensor. As previously, the initial segment of the motion is cut off and the initial conditions are read from the experimental record at the corresponding extremum of the position signal: $x(0) = -36.02$ mm and $\dot{x}(0) = 0$. During the estimation process the following values of the parameters are obtained: k_I = 2.222·10^8 N/m$^{3/2}$, b = 0.8538 m^{-n}s^n and n = 0.1908, where the corresponding minimal value of the objective function is F_o = 0.0101 mm^2.

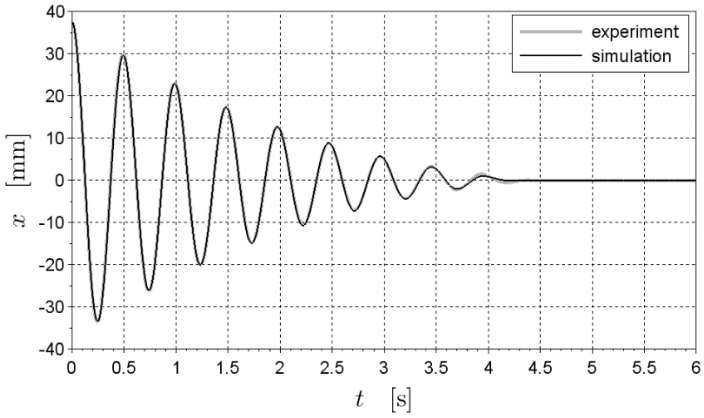

Figure 3. Result of the parameters' estimation (c = 6.574 N·s/m, T = 0.6307 N, k = 1419 N/m; F_o = 0.0772 mm^2) based on the experimental free vibrations without impacts

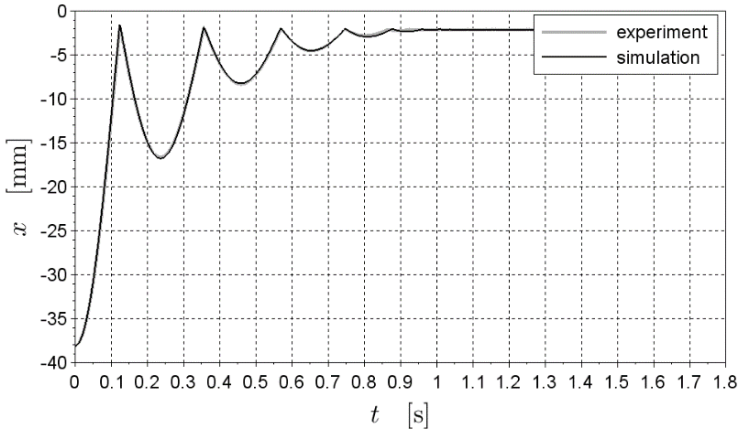

Figure 4. Result of the parameters' estimation (k_I = 2.222·108 N/m$^{3/2}$, b = 0.8538 m^{-n}s^{n}, n = 0.1908; F_o = 0.0101 mm^2) based on the experimental free vibrations with obstacle (x_I = -2.084 mm)

Figure 5 exhibits results of further experimental and numerical investigations of the system. In Fig. 5a there is presented time function of angular velocity of the forcing $\omega(t)$ applied in the experiment. The corresponding experimental bifurcation diagram is presented in Fig. 5b, where position of the system is sampled at instances when $\omega t = 2\pi i$ ($i \in \mathbb{Z}$). The so-defined points of Poincaré section are obtained by the use of cubic spline interpolation of the measured points, where sampling period is 0.5 ms. Position of the obstacle is set as $x_I = -2.086$ mm, so it is very close to the position of the stop during identification experiment presented in Fig. 4. Then the same input signal of forcing (see Fig. 5a) is applied in numerical model with the parameters obtained previously during experiments of free vibrations. The corresponding numerical bifurcation diagram is exhibited in Fig. 5c. One can observe quite good agreement between experimental data and numerical simulations. Since the position of the obstacle is smaller than zero, the initial part of the bifurcation diagram for lower excitation frequencies corresponds to the equilibrium position with the permanent contact between the moving body and the limier of motion. For larger amplitudes and higher frequencies of forcing the cart starts to detach the obstacle and initially periodic orbit is created. Then one can observe sophisticated bifurcation dynamics, chaotic windows, period doubling scenarios, etc. Experimental bifurcation diagram is slightly blurred because of some additional vibrations in the system not taken into account in the mathematical modelling. The quality of bifurcation diagrams, both experimental and numerical, may also be slightly decreased by too short time of the experiment (too high angular acceleration of forcing disk), limited by the parameters of the experimental equipment.

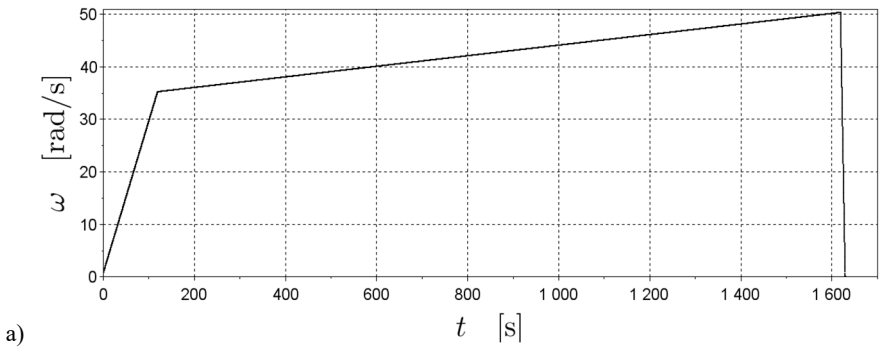

a)

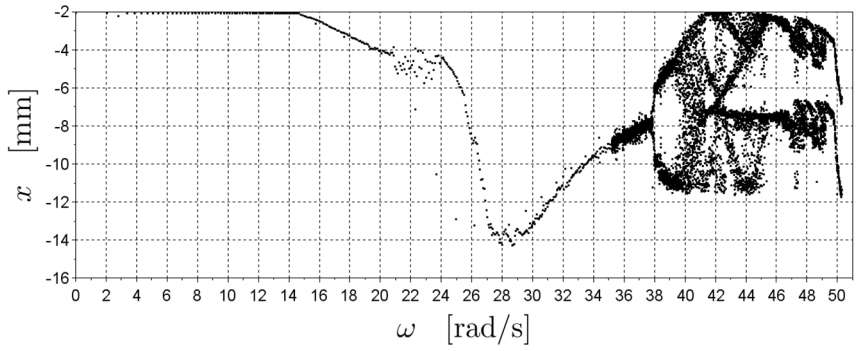

b)

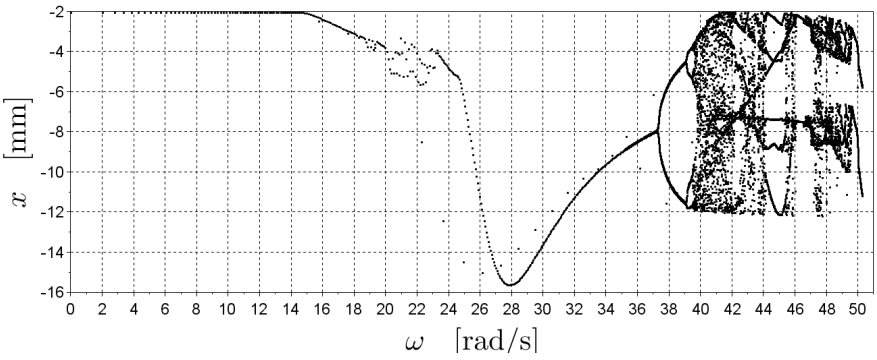

c)

Figure 5. The time function of angular velocity of the forcing $\omega(t)$ applied in the bifurcation diagrams' construction (a) and the corresponding experimental (b) and numerical (c) bifurcation diagrams

Fig. 6 exhibits experimental chaotic solution for the angular velocity of the forcing $\omega = 40.86$ rad/s corresponding to the bifurcation diagram in Fig. 5b but obtained from different experiment, where excitation frequency grows from 0 to 40.86 rad/s on the initial time interval [0, 120] and then is constant on the time interval [120, 1620]. There are presented time histories of displacement (a) and velocity

(b), phase portret (c) and the corresponding Poincaré section (d). Velocity is obtained by the use of numerical differentiation of displacement with the time step equal to the sampling period (0.5 ms) and no filtering.

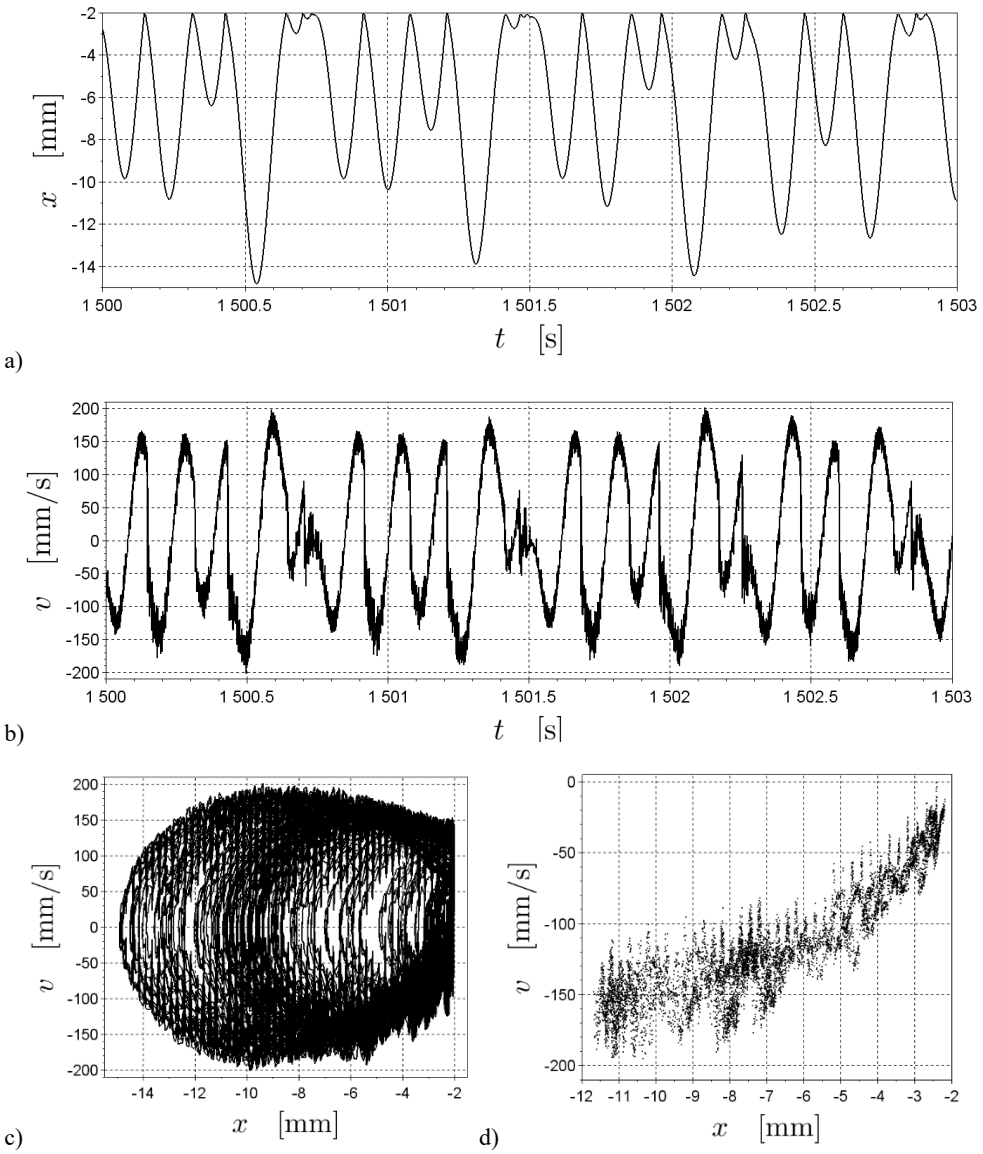

Figure 6. Experimental chaotic solution corresponding to the angular velocity of the forcing $\omega = 40.86$ [rad/s]: time histories of displacement (a) and velocity (b), phase portret (c) and the corresponding Poincaré section (d)

5. Concluding remarks

The paper presents results of preliminary investigations of one-degree-of-freedom impact oscillator, where the main goal is to build accurate mathematical model of the system, with special attention paid to resistance in the linear bearing and impact force, allowing to obtain good agreement between numerical simulations and experimental data. The presented results indicate that the assumed goal have been obtained. It is mainly because of introduction of special non-linearity in damping during contact with obstacle. It is interesting that identification process consists of two stages based on two simple experiments of free vanishing vibrations with and without impacts. The obtained parameters are then used in numerical simulations of more sophisticated bifurcation dynamics of the system, exhibiting very good agreement with experimental measurements, which can be treated as a successful validation of the model.

The observed system dynamics is very complicated but typical for classical one-degree-of-freedom impact oscillator with harmonic forcing. Measurement data is slightly blurred, which may indicate additional oscillations not taken into account in the model, because the measurement system is very accurate and with very low noise level (uncertainty is equal to 0.001 mm).

The developed mathematical and simulation model can serve as a convenient and efficient tool for prediction of bifurcation dynamics of the experimental rig. It is easier, more quickly and cheaper to perform firstly numerical simulations in order to find interesting bifurcation phenomena and then observe them in real system, than perform many time-consuming experimental investigations. Moreover the mathematical model allows for explanations of many non-linear dynamics phenomena observed experimentally, especially in the case when real data is blurred.

The presented work has a great potential of development. The project can be continued in the following directions: experimental and numerical investigations of a system of many-degrees-of-freedom (up to five) with double excitations (periodic, quasi-periodic and chaotic); energy flow investigations; experimental control of bifurcation scenarios; tests of different identification methods and different mathematical models of systems with impacts and linear bearings.

References

[1] Shaw, S.W., and Holmes, P. Periodically Forced Oscillator with Impacts: Chaos and Long-Period Motions. *Physical Review Letters* 51, 8 (1983), 623-626.

[2] Foale, S., and Bishop, S.R. Bifurcations in Impact Oscillations. *Nonlinear Dynamics* 6, (1994), 285-299.

[3] Budd, C., Dux, F., and Cliffe, A. The effect of frequency and clearance variations on single-degree-of-freedom impact oscillators. *Journal of Sound and Vibration* 184, 3 (1995), 475-502.

[4] Hinrichs, N., Oestreich, M., and Popp, K. Dynamics of Oscillators with Impact and Friction. *Chaos, Solitons & Fractals* 8, 4 (1997), 535-558.

[5] Peterka, F. Behaviour of impact oscillator with soft and preloaded stop. *Chaos, Solitons & Fractals* 18, (2003), 79-88.

[6] Ing, J., Pavlovskaia, E., Wiercigroch, M., and Banerjee, S. Experimental study of impact oscillator with one-sided elastic constraint. *Philosophical Transaction of the Royal Society A* 366, (2008), 679-704.

[7] Gilardi, G., and Sharf, I. Literature survey of contact dynamics modelling. *Mechanism and Machine Theory* 37, (2002), 1213-1239.

[8] Machado, M., Moreira, P., Flores, P., and Lankarani H.M. Compliant contact force models in multibody dynamics: Evolution of the Hertz contact theory. *Mechanism and Machine Theory* 53*,* (2012), 33-121.

[9] Hunt, K., and Erskine, C. Coefficient of restitution interpreted as damping in vibroimpact. *Journal of Applied Mechanics* 42, 2 (1975), 6 pages.

Krzysztof Witkowski, M.Sc. (Ph.D. student): Lodz University of Technology, Department of Automation, Biomechanics and Mechatronics, Stefanowski 1/15, 90-924 Łódź, Poland (krzys_wit@wp.pl), the author presented this contribution at the conference.

Grzegorz Kudra, Assistant Professor: Lodz University of Technology, Department of Automation, Biomechanics and Mechatronics, Stefanowski 1/15, 90-924 Łódź, Poland (grzegorz.kudra@p.lodz.pl).

Grzegorz Wasilewski, Ph.D.: Lodz University of Technology, Department of Automation, Biomechanics and Mechatronics, Stefanowski 1/15, 90-924 Łódź, Poland (grzegorz.wasilewski@p.lodz.pl).

Fryderyk Wiądzkowicz, B.A.: Lodz University of Technology, Department of Automation, Biomechanics and Mechatronics, Stefanowski 1/15, 90-924 Łódź, Poland (f.wiadzkowicz@gmail.com).

Jan Awrejcewicz, Professor: Lodz University of Technology, Department of Automation, Biomechanics and Mechatronics, Stefanowski 1/15, 90-924 Łódź, Poland (jan.awrejcewicz@p.lodz.pl).

Dynamics of a double physical pendulum with magnetic interaction

Mateusz Wojna, Grzegorz Wasilewski, Jan Awrejcewicz, Adam Wijata

Abstract: The paper is devoted to numerical and experimental investigations of a system consisting of the double physical pendulum with magnetic interaction caused by a pair of permanent magnets repelling each other. The poles of the magnets are oriented so that a repulsive force occurs between them. To the experimental rig of double physical pendulum system with the first body periodically forced a constructed magnetic interaction forces measurement system is added. The work consists of modeling, simulation and experimental measurements to validate the analytical predictions and the numerical simulation of the earlier introduced mathematical model. The parameters of the model are estimated matching the output signals from model and experiment. The analyzed system shows several types of non-linear effects. Few chaotic zones are detected numerically and confirmed experimentally.

1. Introduction

The paper is devoted to dynamics analysis of a unique dynamical system. The object of investigations is a double physical pendulum with magnetic interaction caused by two neodymium permanent magnets. First of the magnets is mounted on the end of pendulum, the second one – on the body of the setup. Magnets are in their nearby when pendulum is oriented downwards. Magnets are oriented so that repulsive force exists between them. In this paper mathematical model of this 2DOF system is presented. Additionally the system parameters identification and comparison between numerical simulations with experimental study are considered. Bifurcation analysis is also provided.

Described system is a unique construction. There is a lack of investigations about double pendulums with magnets in published paper works. There are papers describing systems only with single pendulums with magnets. A simple example of the EMS system is considered in [1]. The article contains of dynamical system with pendulum, permanent magnet and AC electromagnet. A magnet is placed on the end of the pendulum and additionally is its bob. There are presence and relative relations of chaos and parametric resonance investigated. Analytical results are confronted with numerical simulations and experimental studies.

Authors of [2] describe a system with single physical pendulum placed in magnetostatic field caused by two repelling permanent magnets, forced by sinusoidal signal. Dynamics of that system is experimentally investigated. There are results of numerical simulations also shown.

The measurement system contains of shaft encoder to measure angle position of pendulum as a function of time. Both experimental data and simulations indicates a presence of regular and chaotic behaviors of the system, depending on system parameters. As the parameters are defined: forcing frequency, relative magnets distance and relative magnets orientation in horizontal plane. Additionally there are magnitude jumps, hysteresis and bistable states observed.

In [3] system with physical pendulum is considered. On its end magnet is mounted, which interacts with another one mounted on the setup body. The magnets are in their nearby when a pendulum is vertically down placed. Authors show physical and mathematical model. The correctness of assumed model is proven by numerical simulations of bifurcation generated by estimation of coefficients for many various frequencies of forcing. In addition simulations show that estimated for one particular frequency coefficients could be used to predict behavior of the system in case of another forcing frequency.

Authors of [4] consider experimental and numerical analysis of the system with triple physical pendulum. Such construction with a possibility of recording multiple revolutions of every link of triple pendulum is a unique construction. The system is strongly nonlinear and there can be observed phenomena among others: regular and irregular behaviors, bifurcations, coexisting periodic, quasiperiodic, chaotic and hiperhaotic solutions. In considered system the motion of first link is forced by a specially constructed motor. The motor consists of two immovable stators and two rotors. Both parts of motor are symmetric and electrically coupled, but optical commutator is placed only on the one stator's plate. Such drive eliminates eventual misalignments of construction. There may be found description of forcing motor and entire measuring system also. Parameters of the system was identified by the sum of squares of deviations minimization of signals from the experiment and numerical simulation. A high compatibility of experimental and simulation results was obtained.

2. Mathematical model

In this section a mathematical model of considered system will be proposed. Fig. 1 presents a physical model of the system. Equations of motion consist of developed model of friction. Generally, equations of motion have following form:

$$\boldsymbol{M}(\boldsymbol{\psi})\begin{Bmatrix}\ddot{\psi}_1\\ \ddot{\psi}_2\end{Bmatrix}+\boldsymbol{N}(\boldsymbol{\psi})\begin{Bmatrix}\dot{\psi}_1^2\\ \dot{\psi}_2^2\end{Bmatrix}+\boldsymbol{r}(\boldsymbol{\psi},\dot{\boldsymbol{\psi}},\ddot{\boldsymbol{\psi}})+\begin{Bmatrix}M_1\sin\psi_1\\ M_2\sin\psi_2\end{Bmatrix}+\begin{Bmatrix}M_{1_{mag}}\\ M_{2_{mag}}\end{Bmatrix}=\begin{Bmatrix}M_e\\ 0\end{Bmatrix}. \tag{1}$$

Matrixes existing in (1) are described as follows

$$\boldsymbol{M}(\boldsymbol{\psi})=\begin{bmatrix}B_1 & N_{12}c_{12}\\ N_{12}c_{12} & B_2\end{bmatrix}, \tag{2}$$

$$\boldsymbol{N}(\boldsymbol{\psi}) = \begin{bmatrix} 0 & N_{12}s_{12} \\ -N_{12}s_{12} & 0 \end{bmatrix}, \tag{3}$$

$$\boldsymbol{r}(\boldsymbol{\psi}, \dot{\boldsymbol{\psi}}, \ddot{\boldsymbol{\psi}}) = \begin{bmatrix} M_{R1} - M_{R2} \\ M_{R2} \end{bmatrix}, \tag{4}$$

where

$$\begin{aligned} c_{ij} &= \cos(\psi_i - \psi_j), \\ s_{ij} &= \sin(\psi_i - \psi_j). \end{aligned} \tag{5}$$

Other quantities are expressed as follows

$$\begin{aligned} B_1 &= J_1 + e_1^2 m_1 + l_1^2 m_2, \\ B_2 &= J_2 + e_2^2 m_2, \\ N_{12} &= m_2 e_2 l_1, \\ M_1 &= m_1 g e_1 + m_2 g l_1, \\ M_2 &= m_2 g e_2. \end{aligned} \tag{6}$$

Torques of friction M_{Ri} in bearings are described in the following way

$$M_{Ri} = (T_i + \mu N_i)\frac{2}{\pi}\operatorname{atan}(\varepsilon\omega_{rel(i)})\left[(1-\mu')e^{-c'|\omega_{rel(i)}|} + \mu'\right] + c_i\omega_{rel(i)},\ i = 1,2. \tag{7}$$

Function $\frac{2}{\pi}\operatorname{atan}(\varepsilon\omega_{rel(i)})$ is used instead of function $\operatorname{sgn}(\omega_{rel(i)})$ in numerical simulations. In (7) T_i stands for drag torque independent of the load, μ is a coefficient of friction in the bearings giving a torque proportional to the radial loads N_i. Whereas μ' and c' are parameters of friction model according to Stribeck curve. Angular velocities $\omega_{rel(i)}$ follow

$$\begin{aligned} \omega_{rel(1)} &= \dot{\psi}_1, \\ \omega_{rel(2)} &= \dot{\psi}_2 - \dot{\psi}_1. \end{aligned} \tag{8}$$

Viscous friction coefficients c_i are assumed based on the value of one common coefficient c, i.e. we have

$$\begin{aligned} c_1 &= 2c, \\ c_2 &= c. \end{aligned} \tag{9}$$

Forcing torque $M_e = M_e(t, f)$ applied to the first link of pendulum is a rectangular time function with frequency f. Time series of this function is shown in Fig. 2. Moment of force due to magnets interaction $M_{i_{mag}}$ is described separately in the next section.

Reaction forces N_i in bearings in equation (7) are computed in the following way

$$\begin{aligned} N_1 &= \sqrt{N_{1n}^2 + N_{1t}^2}, \\ N_2 &= \sqrt{N_{2n}^2 + N_{2t}^2}. \end{aligned} \tag{10}$$

Here using indication from (5), components of reaction forces are as follows

$$\begin{aligned} N_{2n} &= m_2\left[g\cos\psi_2 + e_2\dot{\psi_2}^2 + l_1\left(\ddot{\psi}_1 s_{12} + \dot{\psi_1}^2 c_{12}\right)\right], \\ N_{2t} &= m_2\left[g\sin\psi_2 + e_2\ddot{\psi}_2 + l_1\left(\ddot{\psi}_1 c_{12} - \dot{\psi_1}^2 s_{12}\right)\right], \\ N_{1n} &= m_1\left(g\cos\psi_1 + e_1\dot{\psi_1}^2\right) + N_{2n}c_{12} - N_{2t}s_{12}, \\ N_{1t} &= m_1\left(g\sin\psi_1 + e_1\ddot{\psi}_1\right) + N_{2n}s_{12} + N_{2t}c_{12}. \end{aligned} \tag{11}$$

Whole mathematical modeling process has been conducted in *Wolfram Mathematica* software environment.

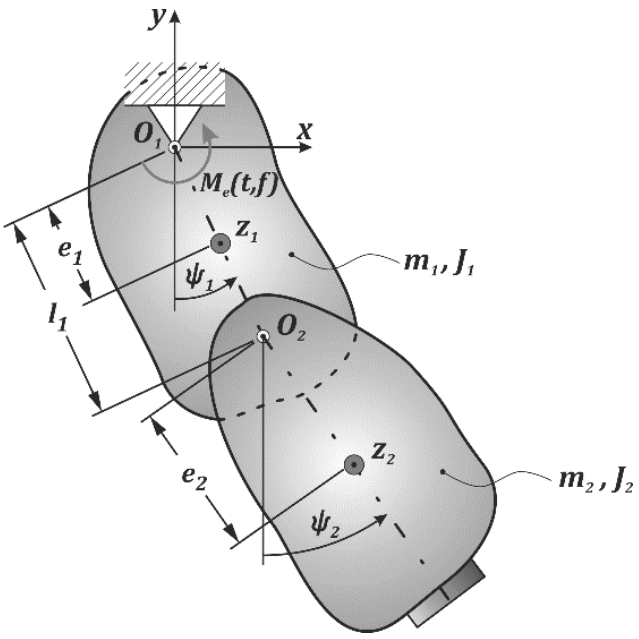

Figure 1. Physical model of the system

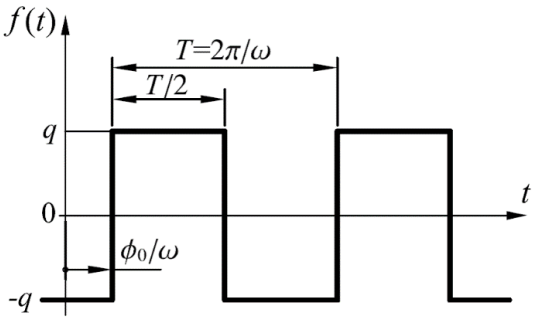

Figure 2. External forcing motor torque function

3. Magnetic interaction modeling

Above described mathematical model contains of a component due to magnets interaction. In this paper new approach of magnetic interaction modeling is proposed. Based on experimental data approximations curves of torque caused by repulsive magnets have been obtained. Considered approximations are the functions of two variables: angular position of first pendulum link and relative pendulum links angle. Fig. 3 shows the results of experimental studies. In order to describe magnetic interaction exponential function is proposed in the following form

$$M_{mag}(\psi_1, \psi_{rel}) = A(\psi_{rel}) \cdot e^{-\left(\frac{\psi_1 - B(\psi_{rel})}{C_1}\right)^2}, \tag{12}$$

where

$$\begin{aligned} &A(\psi_{rel}) = C_2 \cdot e^{-\left(\frac{\psi_{rel} - C_3}{C_4}\right)^2}, \\ &B(\psi_{rel}) = C_5 \cdot \psi_1 + C_6, \\ &C_1, C_2, C_3, C_4, C_5, C_6 \equiv const. \end{aligned} \tag{13}$$

It should be noticed that considered function has been developed separately for plus and minus values of torque taken from approximations curves shown in Fig. 3, and then expressions have been coupled into one expression by specially modified sgn function. Thus the magnetic interaction torque function is able to change its value sign. In magnetic interaction modeling process an assumption was taken that the direction of repulsive force is determined by the centers of the magnets. Such described torque due to magnets has been distributed into two links of pendulum components $M_{1,2_{mag}}$ based on the classical mechanics calculus.

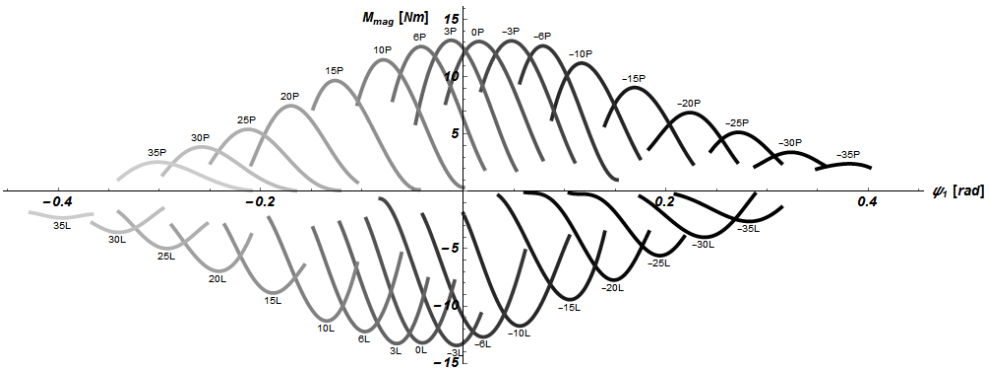

Figure 3. Torque due to magnets characteristics in function of an angle of the first pendulum link

4. Parameters identification

In considered mathematical model exist 15 parameters. Vector $\boldsymbol{W}$ containing of these parameters can be expressed as follows

$$\boldsymbol{W} = [g, l_1, m_1, m_2, e_1, e_2, J_1, J_2, T_1, T_2, c, \mu, \mu', c', \varepsilon]. \tag{13}$$

Values of such parameters as g, l_1, m_1, m_2 were determined independently by measuring. Other parameters were identified by comparing real time series of double pendulum without magnets with proposed mathematical model (excluding torque due to magnets). There has been a method of global minimum finding for the criterion-function used. Identification process has been conducted repeatedly, receiving many sets of parameters. The best correlation coefficient value was obtained based on set of time series containing of forced and free pendulum motion. The set of parameters used in numerical analysis is presented in Table 1.

Table 1. System parameters

Parameter [Unit]	Measured Value	Parameter [Unit]	Identified Value	Parameter [Unit]	Identified Value
$g\ [m/s^2]$	9.812	$e_1\ [m]$	$64.175 \cdot 10^{-3}$	$c\ [N \cdot m \cdot s]$	$0.759 \cdot 10^{-3}$
$l_1\ [m]$	0.174	$e_2\ [m]$	$88.292 \cdot 10^{-3}$	$\mu\ [m]$	$0.461 \cdot 10^{-3}$
$m_1\ [kg]$	4.275	$J_1\ [kg \cdot m^2]$	$45.381 \cdot 10^{-3}$	$\mu'\ [-]$	0.631
$m_2\ [kg]$	1.365	$J_2\ [kg \cdot m^2]$	$14.308 \cdot 10^{-3}$	$c'[s/rad]$	13.447
		$T_1\ [N \cdot m]$	$86.004 \cdot 10^{-3}$	$\varepsilon\ [s]$	1000
		$T_2\ [N \cdot m]$	$18.824 \cdot 10^{-3}$		

5. Numerical simulations and experimental data

Modeled system was investigated by numerical bifurcation analysis. As a bifurcation parameters was obtained a forcing frequency f. Bifurcation diagrams were prepared for increasing value of the parameter in range of $0.1 \div 3\ Hz$. Fig. 4 presents bifurcation diagrams for both links of pendulum. Diagrams show extensive zones of chaotic behaviors and relative narrow zones of regular motion. The most interesting range of frequency in the diagrams is $2 \div 3\ Hz$. For such range experimental bifurcation diagram has been also developed. Both simulation and experimental diagrams are juxtaposed in Fig. 5.

Numerical simulation shows at this range (see Fig. 5a) firstly occurrence of chaos for both links of pendulum. Leaving chaotic zone is sharp and an ordered single periodical behavior is stable for approximately $0.25\ Hz$. Order follows to next chaotic zone where the entry is also sharp.

Next period-halving bifurcations implies a tendency to move to regular dynamics. It should be emphasized that in very narrow range of frequency, four-periodic solutions exist.

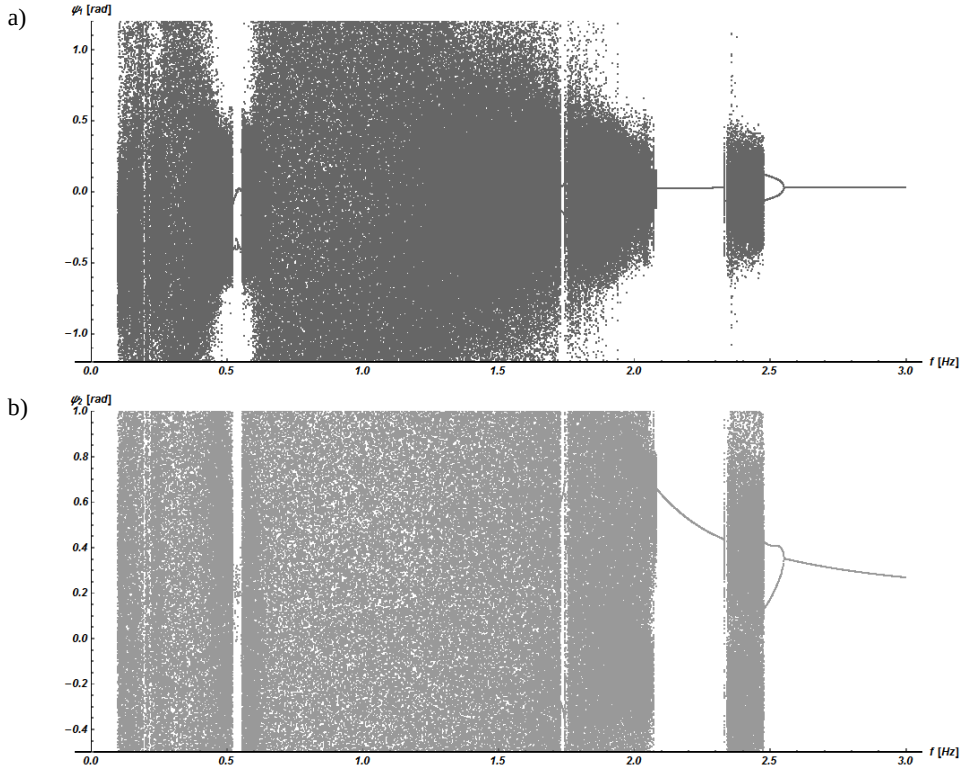

Figure 4. Bifurcation diagrams for increasing frequency in the range of (0.1 - 3) Hz: first (a) and second (b) link of pendulum

Experimentally obtained bifurcation diagrams has been compared to the simulation results. Fig. 5b presents wider first zone of regular motion than that obtained via numerical simulation. It is of worth mention that the values of angles in the first order zone (e.g. at 2.2 Hz) is very similar. Instead of sharp entering to the chaotic zone, experiment exhibits the period doubling bifurcations. Comparing to the simulations, the experimental chaotic zone in the neighborhood of frequency 2.4 Hz is narrower. It is worthy to highlight that this chaotic zone ends almost at the same value of frequency in both diagrams. Similarly to the simulation results the period-halving bifurcations exist, and four-periodic motion is visible. Period doubling bifurcations are robust. Regular motion zones are localized on the same value for both simulation and experimental diagrams. It should be mentioned that in the range of frequency $2.65 \div 2.7$ Hz there are period doubling bifurcations exhibited by the first pendulum link, while the second pendulum link angle does not tend to any stable configuration during the measurement time of evolution. It could mean that second link has much longer transitional state or there

is coexistence and interplay of regular (of the first link) and chaotic behavior of the second pendulum link.

To show similarities and to compare simulation and experimental results, the phase portraits for few forcing frequencies, are reported (see Fig. 6-8).

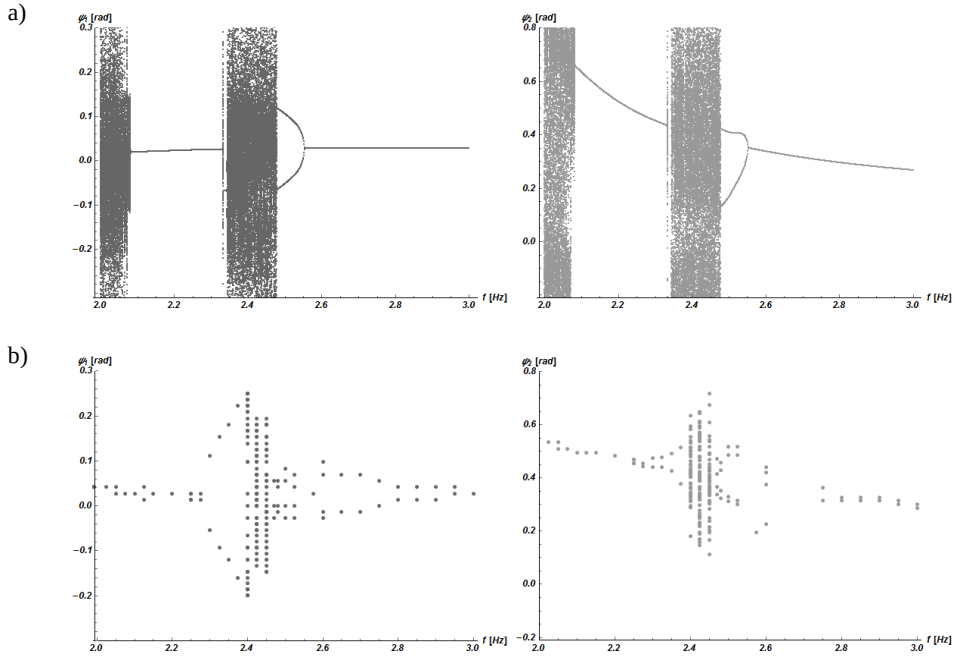

Figure 5. Bifurcation diagrams for increasing frequency in the range of (2 - 3) Hz for the first and second links of pendulum: numerical simulation (a) and laboratory experiment (b)

All of phase portraits shown in Fig. 6-8 have been constructed at the same condition, i.e. the initial condition are always the same and transitional processes minimally equal to 100s have been ignored.

Fig. 6 shows that for the bifurcation parameter $f = 2.2\ Hz$ both simulation and experimental results are qualitatively similar. There is a regular zone of the system behavior, and the ranges of angular displacements and velocities are very similar.

At frequency $f \cong 2.48\ Hz$, period doubling bifurcations appear. The bifurcation diagrams indicate an exit from the chaotic zone. Shapes of simulation and experimental phase portraits are similar, but not identical. It points out that applied mathematical model with the estimated parameters set should be verified and eventually improved.

The last shown set of phase portraits presents very good agreement between both numerical simulation and experimental measurements.

a)

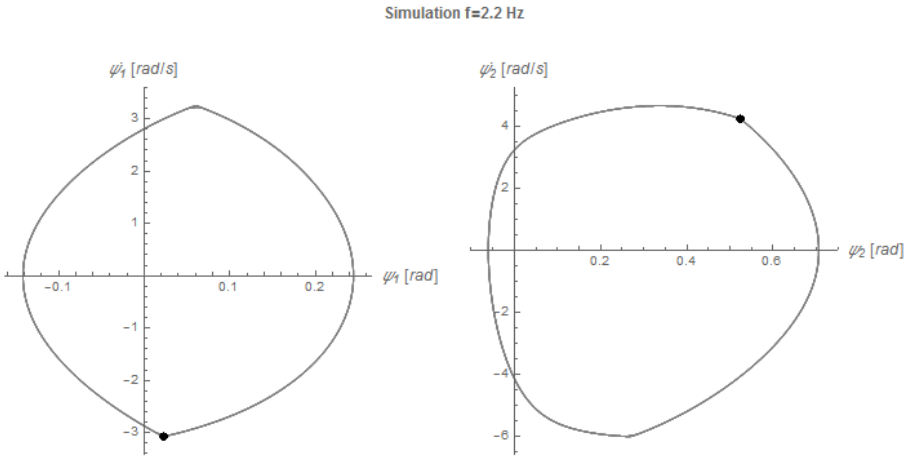

b)

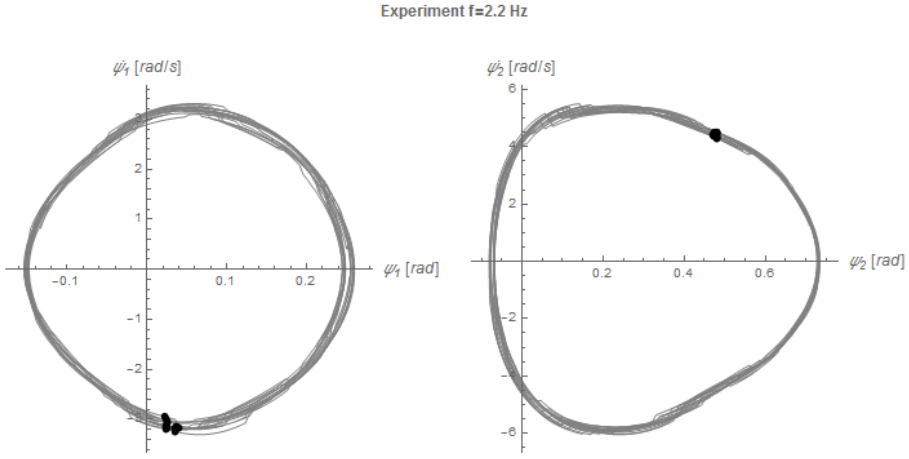

Figure 6. Phase portraits at f = 2.2 Hz:
numerical simulation (a) versus experimental results (b)

a)

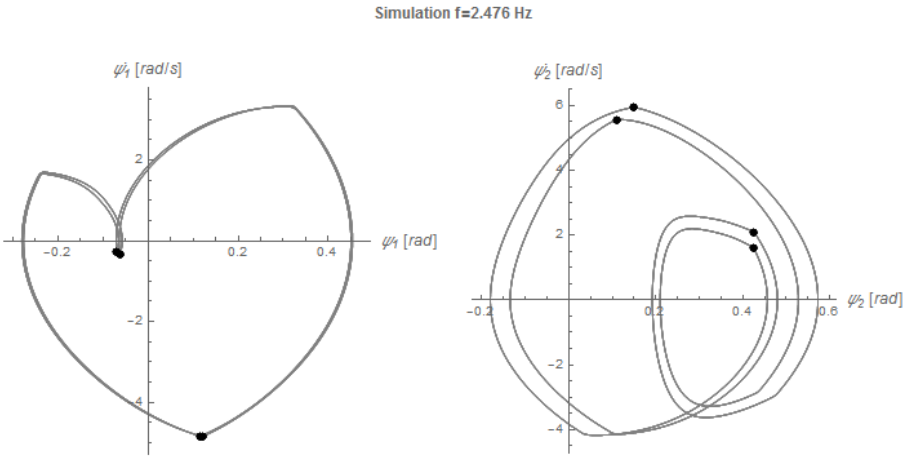

b)

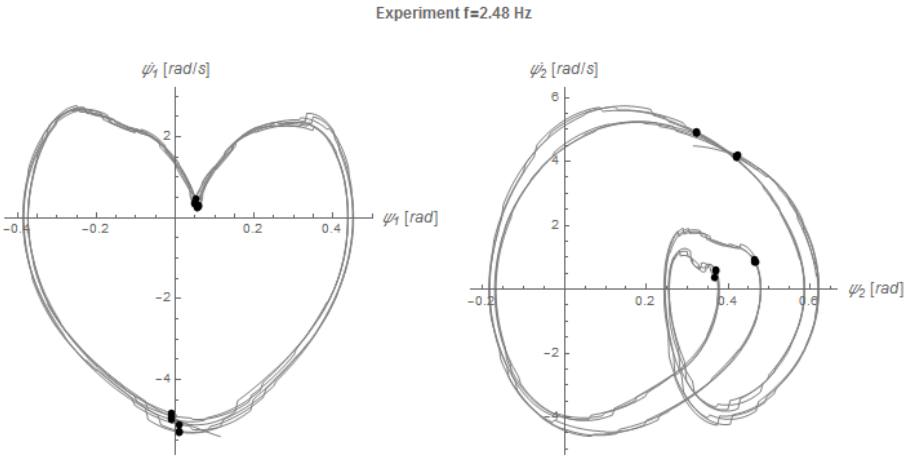

Figure 7. Phase portraits at f ≅ 2.48 Hz:
numerical simulation (a) versus experimental results (b)

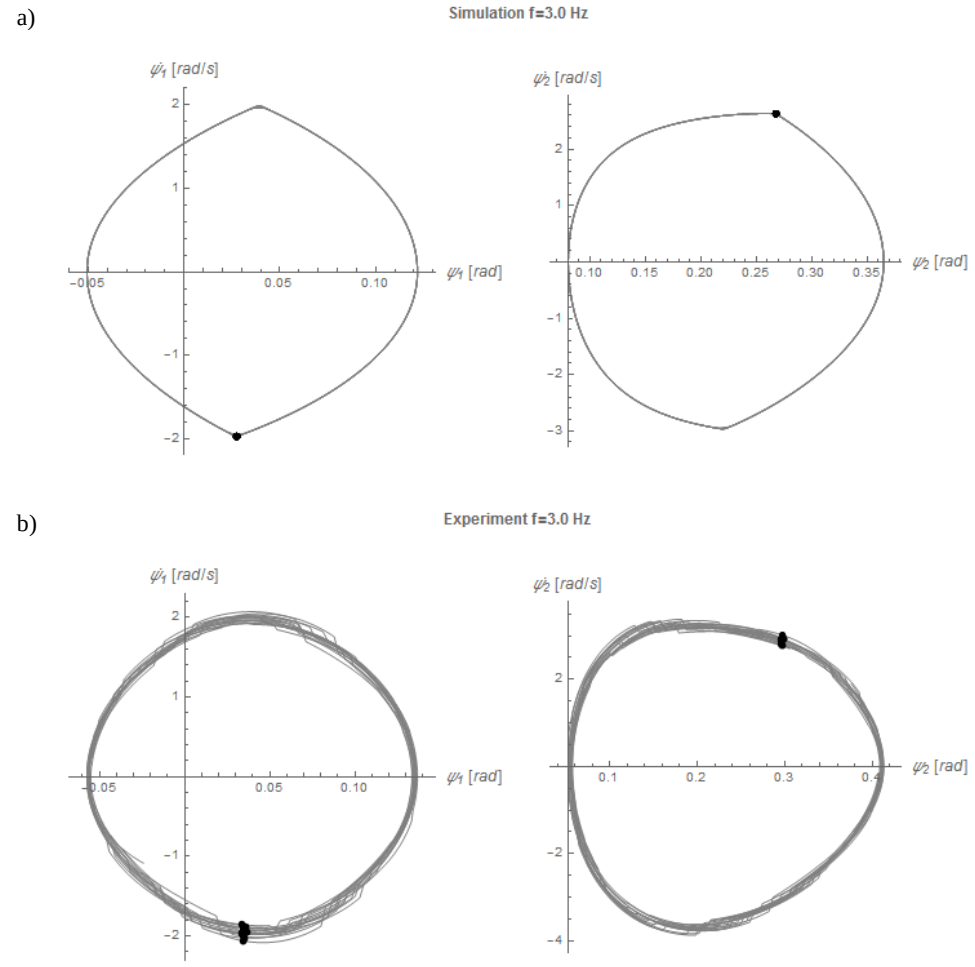

Figure 8. Phase portraits at f = 3.0 Hz:
numerical simulation (a) versus experimental results (b)

6. Concluding remarks

Both numerical and experimental studies of a system consisting of the double physical pendulum have been reported. There is a unique method of magnetic interaction modeling proposed and tested. Generally good agreement between both numerical simulation results and experimental measurements has been obtained and presented. Considered investigations point out that the proposed mathematical model of double physical pendulum with magnetic interaction with its parameters estimated experimentally can be applied as a tool for a first and quick searching for rich phenomena of nonlinear dynamics exhibited by a real constructed pendulum with neodymium magnets.

A few differences are also shown and discussed. First possible source of differences between results of numerical simulations and experimental observations is insufficiently complex mathematical model. It is worth to mention the fact that considered system often exhibited very long transitional processes, what also could be a reason for a few differences between simulation and experimental results. Additionally, the used as an identification method of global minimum finding does not belong to perfect ones in case of multi-dimensional problem.

References

[1] Khomeriki G., "Parametric resonance induced chaos in magnetic damped driven pendulum", Physics Letters A 380 (2016), 2382–2385.

[2] Siahmakoun A., French V. A., Patterson J., "Nonlinear dynamics of a sinusoidally driven pendulum in a repulsive magnetic field", American Journal of Physics 65, 393 (1997), 393-400.

[3] Tran V., Brost E., Johnston M., Jalkio J., "Predicting the behavior of a chaotic pendulum with a variable interaction potential", CHAOS 23, 033103 (2013).

[4] Awrejcewicz J., Supeł B., Lamarque C-H., Kudra G., Wasilewski G., Olejnik P., "Numerical and experimental study of regular and chaotic behavior of triple physical pendulum", International Journal of Bifurcation and Chaos, Vol. 18, No. 10 (2008), 2883-2915.

[5] Nana B., Yamagoue S.B., Tchitnga R., Woafo P., "Dynamics of a pendulum driven by a DC motor and magnetically controlled", Chaos, Solitons and Fractals 104 (2017), 18–27.

[6] Wasilewski G., „Analiza i sterowanie dynamiki nieliniowej podwójnego i potrójnego wahadła fizycznego", Ph.D. thesis, Lodz University of Technology, 2009, supervised by Awrejcewicz J., (in Polish).

Mateusz Wojna, B.A. (M.Sc. student): Lodz University of Technology, Faculty of Mechanical Engineering, Department of Automation, Biomechanics and Mechatronics, Stefanowskiego 1/15, 90-924, Lodz, POLAND (*mateuszwojna94@gmail.com*). The author gave a presentation of this paper during one of the conference sessions.

Grzegorz Wasilewski, Ph.D.: Lodz University of Technology, Faculty of Mechanical Engineering, Department of Automation, Biomechanics and Mechatronics, Stefanowskiego 1/15, 90-924, Lodz, POLAND (*grzegorz.wasilewski@p.lodz.pl*).

Jan Awrejcewicz, Professor: Lodz University of Technology, Faculty of Mechanical Engineering, Department of Automation, Biomechanics and Mechatronics, Stefanowskiego 1/15, 90-924, Lodz, POLAND (*jan.awrejcewicz@p.lodz.pl*).

Adam Wijata, M.Sc. (Ph.D. student): Lodz University of Technology, Faculty of Mechanical Engineering, Department of Automation, Biomechanics and Mechatronics, Stefanowskiego 1/15, 90-924, Lodz, POLAND (*adam.wijata@dokt.p.lodz.pl*).

Contact interaction of a nanoplate, reinforced by a local set of nanobeams located in a stationary temperature field

Alena A. Zakharova, Jan Awrejcewicz, Tatyana V. Yakovleva, Vadim S. Kruzhilin, Anton V. Krysko

Abstract: In this paper a mathematical model of nonlinear dynamics and contact interaction of a nanoplate, reinforced by a local set of nanobeams under conditions of external dynamic and temperature influences is constructed. The temperature field acts on the beams. In the constructed mathematical model the kinematic model of the first approximation is adopted: for nanoplates — Kirchhoff, and for nanobeams — Euler-Bernoulli. The contact interaction is taken into account by the Winkler model. The obtained mathematical model describes the composite elements work of micromechanical systems, and there are small gaps between these elements. Equations are derived from variation principles on the moment theory basis. The temperature field (two-dimensional) for nanobeams is determined separately from the heat equation by the finite differences method of the second and fourth accuracy order. Partial differential equations reduced to the Cauchy problem by the Faedo-Galerkin method in higher approximations, and the Cauchy problem is solved by several methods. The reliability of the obtained results is provided by comparison with the solution by other methods. The oscillations are investigated using qualitative methods of nonlinear dynamics: signals, phase portraits, Fourier power spectrum are analyzed; wavelet analysis and analysis of the signs of largest Lyapunov exponents by several methods (Rosenstein, Kantz, Wolf).

Keywords: Euler-Bernoulli nanobeam, Kirchhoff nanoplate, contact interaction, nonlinear dynamics, wavelet analysis.

1. Introduction

Nanoplates and nanobeams are components of modern electromechanical systems (MEMS, NEMS). Under conditions of external dynamic and temperature effects, the elements between there are small gaps, enter into a contact interaction, which leads to a strong nonlinearity (see the classification given by Lukash [1]). Therefore, an important issue is the study of the vibrations type and the contact interaction of nanoplates and nanobeams under the action of various real world loads. Recently, many attempts have been made to develop various theories allowing to model of scale effects in the continuum, such as the momentum theory of elasticity [2, 3], the nonlocal theory of elasticity [4], the gradient theory of elasticity [5], and the surface theory of elasticity [6]. In reference [7, 8], the nonlinear dynamics of a three-layer microplate is first studied. On the basis of the Kirchhoff theory of

plates and nonlinear deformations of von Kármán, nonlinear size-dependent, transverse and plane equations of motion have been derived. The model takes into account of the nonconservative damping force of a viscous type, as well as the external exciting load. The different arrangement effects of layers are investigated. In references [9-11] mathematical models have been constructed and layered beam nanostructures have been studied. A mathematical model of the contact interaction of plate-beam systems without taking into account nanoscale has been proposed in references [12-13]. The aim of this work is to study the nature of the three-layer packet oscillations consisting of two nanoplates, with two parallel nanobeams in between described by the momentum theory of elasticity.

2. Problem statement

A mathematical model of a three-layer nanosystem is constructed, which consists of two parallel nanoplates and between them there are two parallel nanobeams, which are symmetrical from the plates center (Fig. 1).

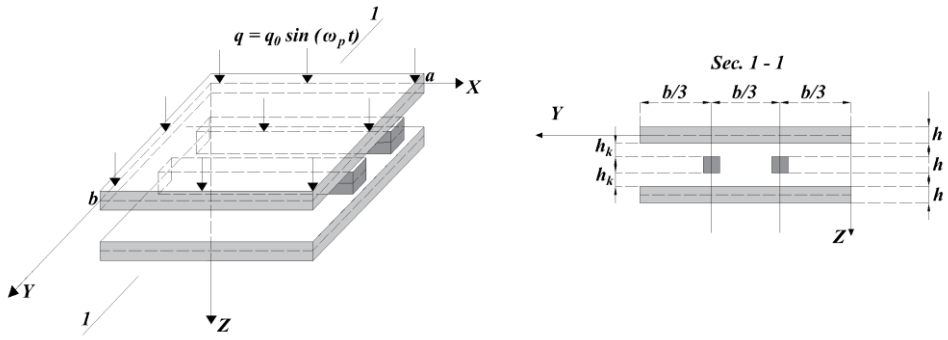

Fig. 1. Scheme of the studied plate-beams structure (b)

Between elements there are small gaps of equal value h_k. The upper nanoplate is affected by an external alternating distributed transverse load $q = q_0 \sin(\omega_p t)$, and the nanobeams are placed in a temperature field, i.e. before deformation, nanobeams are heated according to the corresponding law, which is determined from the solution of the two-dimensional heat equation. The material of nanoplates and nanobeams is isotropic, homogeneous and obeys the Hooke's law. Nanoplates and nanobeams are described by the first approximation kinematic hypotheses: Kirchhoff and Euler-Bernoulli, respectively. The contact interaction between nanoplates and nanobeams is taken into account by the Cantor model [14], and during the model derivation we have employed the appropriate hypotheses of the moment theory of elasticity [2, 3], the theory of plates [15] and beams, taking into

account the contact interaction [14]. The Hamilton-Ostragradsky functional yielded the variational equations, differential equations, boundary and initial conditions of dimensional-dependent plate-beam systems. They have the following form

$$\begin{cases} \ddot{w}_1 + \varepsilon\dot{w}_1 = q(t) + \left\{\dfrac{p_1}{12\gamma_1^2} + \dfrac{p_2}{2}\dfrac{\gamma_2^2}{\gamma_1^2}\right\}\left(\dfrac{1}{\lambda^2}\dfrac{\partial^4 w_1}{\partial x^4} + \lambda^2\dfrac{\partial^4 w_1}{\partial y^4} + 2\dfrac{\partial^4 w_1}{\partial x^2\partial y^2}\right) + \\ + K(w_1 - w_2 - h_k)\Psi_1 + K(w_1 - w_3 - h_k)\Psi_2, \\ \ddot{w}_2 + \varepsilon\dot{w}_2 = -\left[\left\{\dfrac{p_1}{12\gamma_1^2} + \dfrac{p_2}{2}\dfrac{\gamma_2^2}{\gamma_1^2}\right\}\dfrac{\partial^4 w_2}{\partial x^4} + K(w_1 - w_2 - h_k)\Psi_1 - K(w_2 - w_4 - h_k)\Psi_3\right] + \\ + \alpha\dfrac{\partial^2}{\partial x^2}\left(\int_{-h/2}^{h/2}\theta z dz\right), \\ \ddot{w}_3 + \varepsilon\dot{w}_3 = -\left[\left\{\dfrac{p_1}{12\gamma_1^2} + \dfrac{p_2}{2}\dfrac{\gamma_2^2}{\gamma_1^2}\right\}\dfrac{\partial^4 w_3}{\partial x^4} + K(w_1 - w_3 - h_k)\Psi_2 - K(w_3 - w_4 - h_k)\Psi_4\right] + \\ + \alpha\dfrac{\partial^2}{\partial x^2}\left(\int_{-h/2}^{h/2}\theta z dz\right), \\ \ddot{w}_4 + \varepsilon\dot{w}_4 = \left\{\dfrac{p_1}{12\gamma_1^2} + \dfrac{p_2}{2}\dfrac{\gamma_2^2}{\gamma_1^2}\right\}\left(\dfrac{1}{\lambda^2}\dfrac{\partial^4 w_4}{\partial x^4} + \lambda^2\dfrac{\partial^4 w_4}{\partial y^4} + 2\dfrac{\partial^4 w_4}{\partial x^2\partial y^2}\right) + \\ - K(w_2 - w_4 - h_k)\Psi_3 + K(w_3 - w_4 - h_k)\Psi_4, \end{cases} \tag{1}$$

$$\nabla^2(\theta) = 0,\ \theta(x,z), \tag{2}$$

$$\psi_1 = \frac{1}{2}\left[1 + sign(w_1 - h_k - w_2)\right], \psi_2 = \frac{1}{2}\left[1 + sign(w_1 - h_k - w_3)\right],$$

$$\psi_2 = \frac{1}{2}\left[1 + sign(w_2 - h_k - w_4)\right],\ \ \psi_3 = \frac{1}{2}\left[1 + sign(w_3 - h_k - w_4)\right],$$

where: $\gamma_1 = \dfrac{a}{h}, \gamma_2 = \dfrac{l}{h}$, $p_1 = \dfrac{1-\nu}{(1+\nu)(1-2\nu)}$, $p_2 = \dfrac{1}{2(1+\nu)}$, ν is Poisson ratio, w_1, w_4 stands for deflection functions of the upper and lower nanoplates, and w_2, w_3 denote the nanobeams deflection functions. Furthermore, we have also: K - the stiffness coefficient for the transverse compression of the structure in the contact area, h_k - the gap between the nanoplate and the nanobeam, $\theta\ (x,z)$ – the temperature increment for both beams; a, b – nanobeam size for *x* and *y*, respectively, a - nanobeams length of unit width, t – time, ε – attenuation coefficient, h – nanoplates thickness and height of nanobeams, g – acceleration of gravity, E – nanoplates and nanobeams elasticity modulus, $q(x,y,t)$ – transverse load acting on nanoplate, γ – material density of nanoplates and nanobeams. If

$w_1 > w_2 + h_k$ then contact exists between the upper nanoplate and nanobeams and $\Psi_1 = 1,$ otherwise $\Psi_1 = 0$ [14]. The values Ψ_2, Ψ_3, Ψ_4 are determined in a similar way. The parameter $l,$ presented in the higher order moment, is an additional independent material length parameter associated with the symmetric tensor of the rotation gradient. The latter must be taken into account in this model along with the usual Lamè parameters [16]. This is a direct consequence of the fact that in the moment theory of elasticity the strain energy density is a function of only the strain tensor and the symmetric curvature tensor. It does not depend explicitly on rotation (the asymmetric part of the strain gradient) and the asymmetric part of the curvature tensor [16].

The system of equations (1) is reduced to it counter part dimensionless form with the help of the following parameters:

$x = a\bar{x}$, $y = b\bar{y}$; $q = \bar{q}\dfrac{E(h)^4}{a^2 b^2}$, $\bar{t} = \dfrac{t}{\tau}$, $\tau = \dfrac{ab}{h}\sqrt{\dfrac{\gamma}{Eg}}$, $\lambda = \dfrac{a}{b} = 1$, $h_k = h\overline{h_k}$. For simplicity, the notation bar over the dimensionless parameters in the system of equations (1) is omitted.

Equations (1) are supplemented by the boundary conditions, i.e. hinged support along the contour for nanoplates and hinged support at the ends for nanobeams:

$$w_1 = 0;\ \frac{\partial^2 w_1}{\partial x^2} = 0;\ \text{at } x = 0;1; \qquad w_1 = 0;\ \frac{\partial^2 w_1}{\partial y^2} = 0;\ \text{at } y = 0;1$$

$$w_2 = 0;\ \frac{\partial^2 w_2}{\partial x^2} = 0;\ \text{at } x = 0;1; \qquad w_3 = 0;\ \frac{\partial^2 w_3}{\partial x^2} = 0;\ \text{at } x = 0;1; \tag{3}$$

$$w_4 = 0;\ \frac{\partial^2 w_4}{\partial x^2} = 0;\ \text{at } x = 0;1; \qquad w_4 = 0;\ \frac{\partial^2 w_4}{\partial y^2} = 0;\ \text{at } y = 0;1$$

In addition, the (1)-(2) boundary conditions of the first kind are added for the heat equation: The temperature distribution over the body surface S is set as following

$$(0 \le x \le a), (h/2 + h_k \le z \le 3h/2 + h_k)\ ,\ \theta = \varphi(x, z, t) : (x, z) \in S \tag{4}$$

As initial conditions we take the distribution of deflections, deflection velocities, and temperature increment at the initial instant of time $t = 0$:

$$w_m|_{t=0} = 0;\ \dot{w}_m|_{t=0} = 0,\ m=1,2,3,4, \quad \theta(x, z)|_{t=0} = 0 \tag{5}$$

In order to solve the problem (1)-(5), a combined approach is proposed. Equation (2) with boundary conditions (4) is solved by the finite differences method of the second and fourth accuracy order. Further, the temperature moments, which are substituted into equations (1) and (3), are calculated using the Newton-Cotes formulas. The resulting systems of constructively nonlinear partial

differential equations is reduced to a system of the second order ordinary differential equations by the Faedo-Galerkin method in higher approximations with respect to the space variables x and y. In this case, the approximating functions satisfying the boundary conditions (3) have the following form:

$$w_1 = \sum_{k=1}^{N}\sum_{j=1}^{N} A_{kj}(t)\sin(k\pi x)\sin(j\pi y), \qquad w_2 = \sum_{k=1}^{N} A_k(t)\sin(k\pi x),$$
$$w_3 = \sum_{k=1}^{N} A_k(t)\sin(k\pi x), \qquad w_4 = \sum_{k=1}^{N}\sum_{j=1}^{N} A_{kj}(t)\sin(k\pi x)\sin(j\pi y), \tag{6}$$

Due to the nonlinearity caused by the contact interaction between the elements, it is not possible to solve the obtained system analytically. Therefore, to confirm the results reliability, the solution was carried out by the finite differences method with approximation $0(h^2)$ and $0(h^4)$ and the Faedo-Galerkin method in higher approximations and the convergence of the methods for different number of terms in the series (6) and the different number of partitions in the finite differences method $0(h^2)$, $0(h^4)$ was investigated. Accuracy was established according to the Runge rule. Also, the solution essentially depends on the method and the solution step for time, therefore the Cauchy problem was solved by several numerical methods: the Runge-Kutta method of the second (RK2) and the 4th (RK4) orders, the fourth-order Kesh-Karp method (RKCK), the fourth-order Runge-Kutta-Felberg method (rkf45), the implicit Runge-Kutta method of the 2nd order (rk2imp) and the 4th (rk4imp) order, the eighth order Runge-Kutta Prince-Dormand (rk8pd). The convergence of these methods is investigated. Studies have shown that the fourth order Runge-Kutta method is optimal for solving a system describing the contact interaction of a plate-beam nanostructure under the action of an alternating load. Further investigation of the results was carried out by a qualitative method of the differential equations theory. For this purpose we analyzed the signals, Poincarè sections, phase portraits, Fourier power spectra, and we employed the wavelet analysis. The Morlet, Gauss 8, Haar wavelets we have been chosen as the mother wavelet transform. Preference is given to the Morlet wavelet, since it has better information at every time instant.

3. Numerical results

As an example, we study the contact interaction of a nanostructure consisting of two nanoplates, and between them there are symmetrically arranged nanobeams relative to the plates center. Preheating is not taken into account. Between nanoplates and nanobeams there are small gaps h_k=0.1. Let us study the oscillations nature of the multilayer nanosystem under the action of a transverse alternating load $q = q_0 \sin(\omega_p t)$ applied to the upper plate. The frequency of the external action ω_p =9 is larger than

the eigenfrequency of the nanobeam and nanoplates. Nanoscale coefficient is $\gamma_2 = 0.7$. When the load amplitude is q_0<200, the upper nanoplate performs periodic oscillations, the nanobeams and the lower nanoplate are at rest. When the loading amplitude is q_0=200, the upper nanoplate comes in contact with the nanobeams, the lower nanoplate is at rest. Both nanobeams perform synchronous, short-lived, damped oscillations. Further, with a load intensity q_0=250, all the elements of the nanosystem enter into the contact interaction, i.e. each nanobeam concerns both the upper and lower nanoplate. Table 1 shows the graph of the joint oscillations of all elements of the nanostructure at q_0=250 (a), Morlet 2D wavelet spectra for the upper (b) and lower nanoplates (e) and both beams (c, d). The upper nanoplate (w_1) oscillates throughout the considered time interval at the external excitation frequency ω_p =9, and on the time interval $t \in [1;40]$ on the wavelet spectrum exists frequency spectrum interval $\omega \in [0;4]$ (Table 1, b). Thus, at the moment of contact interaction, a burst of frequency characteristics occurs. The lower nanoplate (w_4) and both nanobeams (w_2, w_3) perform low-frequency ($\omega \in [0;3]$) oscillations in the time interval $t \in [1;40]$ (Table 1, c,d,e), then they decay as a result of the dissipation coefficient presence $\varepsilon = 0.1$. Oscillations of nanobeams are synchronous (Table 1, a). In view of the fact that the dissipative structure is considered and the dissipation coefficient for plates and beams is the same, its magnitude significantly affects the nature of the oscillations, and with its accepted value, the oscillations die out very quickly, but, nevertheless, these oscillations are chaotic.

Table 1. The vibration characteristics (see text for more details)

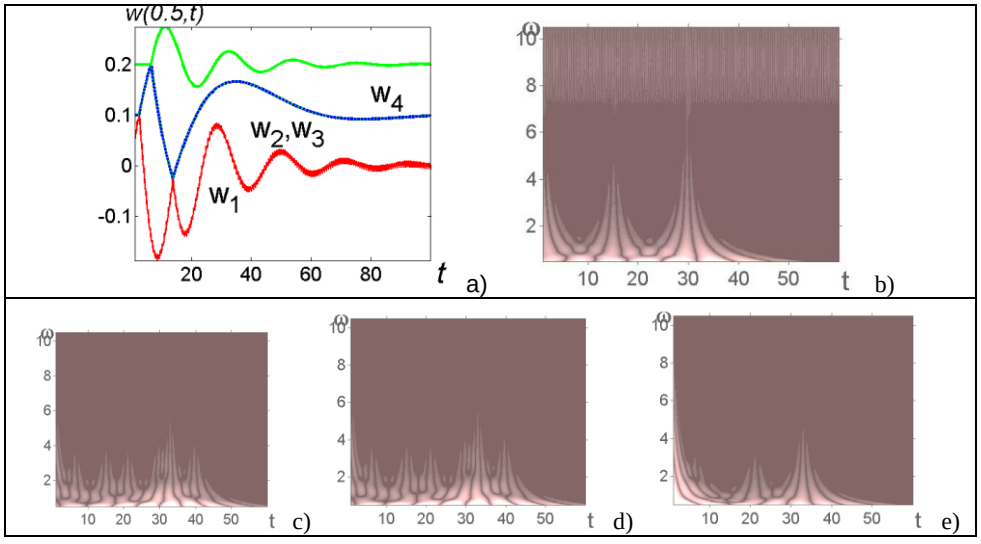

Acknowledgments

This work has been supported the Ministry of Education and Science of the Russian Federation by the Grant № 2.1642.2017

References

[1] Lukash, P.A. *Fundamentals of Nonlinear Construction Mechanics*. Moscow, Stroyizdat, 1978.

[2] Mindlin, R.D., Tiersten, H.F. Effects of couple-stresses in linear elasticity, *Arch. Ration.Mech. Anal*. 11 (1962) 415–448.

[3] Toupin, R.A. Elastic materials with couple-stresses, *Arch. Ration. Mech. Anal*. 11 (1962) 385–414.

[4] Eringen, C. Nonlocal polar elastic continua, *Int. J. Eng. Sci*. 10 (1972) 1–16.

[5] Aifantis, E.C. Strain gradient interpretation of size effects, *Int. J. Fract*. 95 (1999) 299–314.

[6] Gurtin, M.E., Weissmuller, J. Larche, F. The general theory of curved deformable interfaces in solids at equilibrium, *Philos. Mag. A* 78 (1998) 1093–1109.

[7] Ghayesh, M.H. Nonlinear dynamics of multi-layered microplates, *Journal of Computational and Nonlinear Dynamics*, 2017 (doi:10.1115/1.4037596).

[8] Ghayesh, M.H., Farokhi, H. Nonlinear dynamics of microplates, *International Journal of Engineering Science*, 86 (2015) 60-73.

[9] Awrejcewicz, J., Pavlov, S.P., Zhigalov, M.V., Krysko-jr., V.A. Chaotic dynamics of the size-dependent non-linear micro-beam model, *Communications in Nonlinear Science and Numerical Simulation*, 50, 2017, 16–28.

[10] Krysko, A.V., Awrejcewicz, J., Zhigalov, M.V., Pavlov, S.P., Krysko, V.A. Nonlinear behaviour of different flexible size-dependent beams models based on the modified couple stress theory. Part 1: Governing equations and static analysis of flexible beams. *International Journal of Non-Linear Mechanics*

[11] Krysko, A.V., Awrejcewicz, J., Zhigalov, M.V., Pavlov, S.P., Krysko, V.A. Nonlinear behaviour of different flexible size-dependent beams models based on the modified couple stress theory. Part 2. Chaotic dynamics of flexible beams. *International Journal of Non-Linear Mechanics*

[12] Awrejcewicz, J., Krysko-Jr., V.A., Yakovleva, T.V., Krysko, V.A. Noisy contact interactions of multi-layer mechanical structures coupled by boundary conditions. *Journal of Sound and Vibration* 369 (2016) 77–86.

[13] Awrejcewicz, J., Krysko-jr, V.A., Yakovleva, T.V., Krysko, V.A. Alternating chaos versus synchronized vibrations of interacting plate with beams. *International Journal of Non-Linear Mechanics* 88 (2017) 21–30.

[14] Kantor, B.Ya. *Contact Problems of the Nonlinear Theory of Rotation Shells*. Kiev, Science, 1990.

[15] Novozhilov, V.V. The theory of thin shells. Leningrad, Sudpromgiz, 1962.

[16] Yang, F., Chong, A.C.M., Lam, D.C.C., Tong, P. Couple stress based strain gradient theory for elasticity, *Int. J. Solids Struct*. 39 (2002) 2731–2743.

Alena A. Zakharova, Professor: Cybernetic Institute, National Research Tomsk Polytechnic University, Lenin Avenue 30, 634050 Tomsk, RUSSIAN FEDERATION (zaa@tpu.ru).

Jan Awrejcewicz, Professor: Lodz University of Technology, Faculty of Mechanical Engineering, Department of Automation, Biomechanics and Mechatronics, 1/15 Stefanowskego Str., 90-924, Lodz, POLAND (jan.awrejcewicz@p.lodz.pl).

Tatyana V. Yakovleva, Ph.D.: Department of Mathematics and Modeling, Saratov State Technical University, Politehnicheskaya 77, 410054 Saratov, and Cybernetic Institute, National Research Tomsk Polytechnic University, Lenin Avenue 30, 634050 Tomsk, RUSSIAN FEDERATION (Yantan1987@mail.ru).

Vadim S. Kruzhilin, B.A. (M.Sc. student): Department of Mathematics and Modeling, Saratov State Technical University, Politehnicheskaya 77, 410054 Saratov, RUSSIAN FEDERATION (mrkruzhilin@mail.ru).

Anton V. Krysko, Professor: Department of Applied Mathematics and Systems Analysis, Saratov State Technical University and Cybernetic Institute, National Research Tomsk Polytechnic University, Politehnicheskaya 77, 410054 Saratov, RUSSIAN FEDERATION (anton.krysko@gmail.com), the author presented this contribution at the conference.

The mathematical modelling of nonlinear vibration of rotors influenced by magnetic and electric effects

Jaroslav Zapoměl, Jan Kozánek, Petr Ferfecki

Abstract: The main parts of magnetorheological squeeze film dampers are two concentric rings separated by a gap filled with magnetorheological oil. Squeezing the oil film due to the rotor vibration produces the damping force. The magnetic flux generated in coils embedded in the damper housing passes through the lubricant and as its flow resistance depends on magnetic induction the change of the applied current can be used to control the damping force. The variation of the width of the damper gap changes the magnetic flux, which induces the electromotoric voltage and consequently reduces the applied current. As a result, the rotor vibration attenuation depends on a complex interaction between mutually coupled mechanical, hydraulic, magnetic, and electric transient phenomena. In the developed mathematical model the magnetorheological oil is represented by a bilinear material and the damper body by a set of meridian segments. Each segment is considered to be a divided core of an electromagnet with the gap filled with the magnetorheological oil. The pressure distribution in the lubricating film is governed by the Reynolds equation adapted to bilinear material. The goal of the carried out investigations was to learn more on nonlinear effects and a complex influence of the electromagnetic phenomena occurring in magnetorheological damping devices on the vibration attenuation of rotors.

1. Introduction

Unbalance is one of the principal sources of excitation of lateral vibrations of rotors. A frequently used technological solution consists in placing damping devices in the rotor supports. The analysis carried out in [1] shows that to achieve their optimum performance their damping effect must be adaptable to the speed of the rotor rotation.

A new approach to controlling the damping force is offered by magnetorheological squeeze film dampers. The principles of their work and practical experience with their applications can be found in a number of publications, e.g. in [2], [3]. Zapoměl et al. [4] developed the mathematical model of a short squeeze film magnetorheological damper, which is based on representing the magnetorheological oil by Bingham material. The efforts to increase stability of the computational procedures intended for dynamical analysis of rotor systems supported by magnetorheological squeeze film dampers arrived at the development of an enhanced model, in which the magnetorheological oil is represented by a bilinear material [5]. The determination of magnetic

induction in the lubricating film and the distribution of the magnetic flux in the damper body generated by electric current of constant magnitude was a subject of the study performed by Ferfecki et al. [6].

In this paper there is presented an extended mathematical model of a short magnetorheological squeeze film damper, which is based on assumptions of the classical theory of lubrication, on representing the magnetorheological oil by bilinear material and on taking into account the influence of the transient phenomena occurring in the electric circuit on attenuation of the rotors lateral vibration. The performed computational simulations contributed to better understanding of nonlinear effects related to behaviour of rotors supported by magnetorheological damping devices.

2. The damping forces produced by the magnetorheological squeeze film damper

The main parts of a magnetorheological squeeze film damper are two concentric rings separated by a thin layer of magnetorheological oil (Fig. 1). The inner ring is coupled with the shaft by a rolling element bearing and with the damper housing by a cage spring. The rotor lateral vibration arrives at squeezing the oil layer, which produces the damping force. The electric coils embedded in the damper body generate magnetic flux passing through the lubricant and as resistance against its flow depends on magnetic induction, the change of the applied current changes the damping effect.

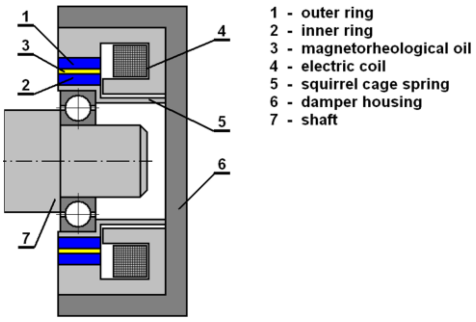

Figure 1. Scheme of the magnetorheological squeeze film damper.

The developed mathematical model of the damper is based on assumptions of the classical theory of lubrication. The magnetorheological oil is represented by bilinear material, the yielding shear stress of which is a function of magnetic induction. In addition, it is assumed that the damper parameters make it possible to consider it as short and that the damper is symmetric relative to its middle plane. In areas where the thickness of the oil film rises with time, a cavitation is assumed. In cavitated regions the pressure of the medium remains constant and equal to the pressure in the ambient space. The damper body is considered to be composed of a set of meridian segments and each segment as a divided core of an electromagnet with the gap filled with the magnetorheological oil.

The pressure distribution in the noncavitated part of the oil film is described by the Reynolds equation adapted to bilinear material [5]

$$\frac{\partial}{\partial Z}\left(\frac{1}{\eta_C}h^3 p'\right)=12\dot{h}, \quad \text{for} \quad 0\le Z\le Z_C, \tag{1}$$

$$\frac{\partial}{\partial Z}\left[\frac{1}{\eta}\left(h^3 p'+3h^2\tau_y+8\frac{\tau_C^3}{p'^2}-12\frac{\tau_y\tau_C^2}{p'^2}\right)-\frac{8}{\eta_C}\frac{\tau_C^3}{p'^2}\right]=12\dot{h}, \quad \text{for} \quad \dot{h}<0, \quad Z>Z_C, \tag{2}$$

$$Z_C=-\frac{\tau_C h^2}{6\eta_C\dot{h}}, \tag{3}$$

$$p'_C=-\frac{2\tau_C}{h}. \tag{4}$$

p is the pressure, p' stands for the pressure gradient in the axial direction, Z is the axial coordinate perpendicular to axes X, Y (Fig. 2), h is the film thickness, τ_y is the yielding shear stress, τ_c is the shear stress at the core border, η_C, η are the dynamic viscosities of the oil inside and outside the core area, respectively, Z_C defines the axial coordinate of the location where the core touches the rings surfaces, p'_C denotes the pressure gradient in the axial direction at location Z_C, and $(\dot{\cdot})$ denotes the first derivative with respect to time.

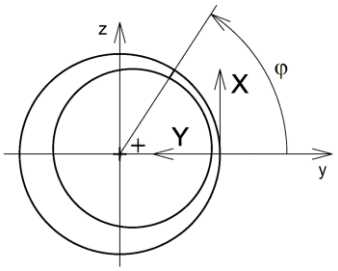

Figure 2. The coordinate systems.

The y and z components of the hydraulic force (F_{mry}, F_{mrz}) acting on the rotor journal are given by integration of the pressure distribution p_d in the damper gap

$$F_{mry}=-2R_D\int_0^{\frac{L_D}{2}}\int_0^{2\pi} p_d\,\cos\varphi\,\mathrm{d}\varphi\,\mathrm{d}Z, \tag{5}$$

$$F_{mrz}=-2R_D\int_0^{\frac{L_D}{2}}\int_0^{2\pi} p_d\,\sin\varphi\,\mathrm{d}\varphi\,\mathrm{d}Z \tag{6}$$

taking into account different pressure profiles in noncavitated and cavitated areas. R_D is the mean gap radius, L_D is the length of the damper, and φ is the circumferential coordinate.

As evident from (2), the pressure distribution in the damper gap depends on the yielding shear stress τ_y, the dependence of which on magnetic induction is approximated by a power function

$$\tau_y = k_y B^{n_y} \tag{7}$$

B is the magnetic induction and k_y and n_y are the material constants of the magnetorheological oil.

The idea of composing the body of meridian segments makes it possible to express magnetic induction in the oil film as a function of its thickness and magnitude of the applied current at any location around the damper circumference and along its length [6]

$$B = k_B \mu_0 \mu_{MR} \frac{I}{h}. \tag{8}$$

μ_0 is the vacuum permeability, μ_{MR} is the relative permeability of the magnetorheological oil, I is the applied current, k_B is the design parameter that is defined as a product of the number of the coil turns (N_C) and the magnetic efficiency. More details on its determination can be found in [6].

3. The influence of the electric and magnetic effects on the damping force

The electric current passing through the coil depends on the applied voltage, resistance of the electric circuit, and on the time variation of the generated magnetic flux. The variation is caused by changing the width of the damper gap due to the rotor lateral vibration

$$\frac{\mathrm{d}\Phi}{\mathrm{d}t} + RI = U \ . \tag{9}$$

Φ is the magnetic flux generated by the coil, R is resistance of the electric circuit, U is the applied voltage, and t is the time.

The total magnetic flux is given as a sum of magnetic fluxes passing through all meridian segments

$$\Phi = \sum_{i=1}^{N_S} \Phi_i \ , \tag{10}$$

N_s is the number of the meridian segments.

Utilizing the Hopkins law, it holds

$$N_C I = \Phi_i \frac{h_i}{\mu_{MR} S_i} \ . \tag{11}$$

The fraction on the right hand side of (11) is magnetic reluctance of the magnetic circuit related to the i-th meridian segment. It is assumed that magnetic reluctance of the steel part is negligible relative to that in the oil film. The area assigned to each segment through which the magnetic flux passes reads

$$S_i = R_D L_D \Delta\varphi \tag{12}$$

where $\Delta\varphi$ is the increment of the circumferential coordinate.

Next it is assumed that the segments are of the infinitesimal thickness. Then the introduction of

$$A = \int_0^{2\pi} \frac{\mathrm{d}\varphi}{h(\varphi)}, \tag{13}$$

expression Φ_i from (11) and utilization of (10) and (12) give the relation for the total magnetic flux

$$\Phi = \mu_{MR} N_C I R_D L_D A(t) \tag{14}$$

The differentiation of (14) with respect to time and its substitution into (9) yields the governing equation for the time history of the applied current in the electric circuit

$$\dot{I} + \left(\frac{\dot{A}}{A} + \frac{R}{\mu_{MR} N_C R_D L_D A} \right) I = \frac{U}{\mu_{MR} N_C R_D L_D A}. \tag{15}$$

4. The investigated rotor system

The studied rotor (Fig. 3) is rigid. It consists of a shaft and of one disc. At both its ends it is coupled with the rigid stationary part by two magnetorheological squeeze film dampers. The rotor rotates at constant angular speed, is loaded by its weight, and is excited by the disc unbalance. Both cage springs are prestressed to eliminate their deflection caused by the rotor weight. In addition, the whole system can be considered as symmetric relative to the disc middle plane.

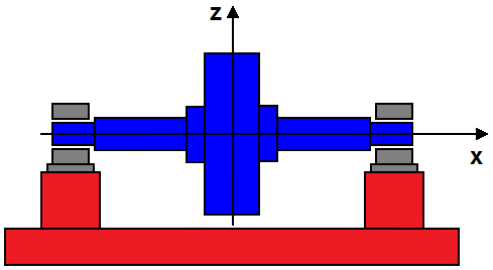

Figure 3. Scheme of the studied rotor system.

The task was to investigate influence of the electric circuit on the damping effect at different operating speeds by means of computational simulations.

In the computational model the rotor and the stationary part were considered to be absolutely rigid, the dampers were represented by springs and nonlinear force couplings, and the damping caused by the environment was assumed to be viscous and linear.

Because of the system symmetry, the lateral vibration of the rotor is governed by a set of two nonlinear motion equations

$$m_R \ddot{y} + b_P \dot{y} + 2 k_D y = 2 F_{mry} + m_R e_T \omega^2 \cos \omega t + F_{psy}, \tag{16}$$

$$m_R \ddot{z} + b_P \dot{z} + 2 k_D z = 2 F_{mrz} + m_R e_T \omega^2 \sin \omega t + F_{psz} - m_R g\,. \tag{17}$$

m_R is the rotor mass, b_P is the coefficient of external damping, k_D is the stiffness of the cage spring, ω is the angular speed of the rotor rotation, e_T is the eccentricity of the rotor unbalance, y, z are displacements of the rotor centre, F_{psy}, F_{psz} are the y and z components of the prestress force, g is the gravity acceleration, and $(\ddot{\cdot})$ denote the second derivatives with respect to time.

The motion equations are completed with equation (15) that describes the time history of the current affected by the magnetic and electric phenomena occurring in the electric circuit.

The governing equations were solved by means of the implicit Adams-Moulton method.

5. The results of the computational simulations

The technological parameters of the studied rotor are: the rotor mass 430 kg, the coefficient of linear damping of the rotor caused by the environment 100 Ns/m, the stiffness of one cage spring 2.0 MN/m, the eccentricity of the rotor unbalance 50 μm, the magnetorheological squeeze film damper length/diameter 50/150 mm, the width of the damper gap 1.0 mm, the oil dynamic viscosity not effected by a magnetic field 0.3 Pas, the oil dynamic viscosity in the core 300 Pas, the magnetorheological oil proportional and exponential constants 2000, 1.1, respectively, the oil relative permeability 5, the damper design parameter 60, and the resistance of the electric circuit 10 Ω.

A simple dynamical analysis shows that the critical speed of the undamped system (e.g. no lubricant is supplied to the magnetorheological squeeze film dampers) is 96.4 rad/s. Rising damping in the rotor supports shifts the critical velocity to higher values.

In the first analysis the rotor turns at constant angular velocity of 100 rad/s, which is close to the critical speed. The voltage is applied at the point of time of 0.1 s and increases linearly from 0 V to 10 V during the period of 10 ms. The time history of the corresponding current is drawn in Fig. 4 (left). The rotor vibration attenuation as a response on the voltage application is depicted in Fig. 4 (right). The steady state orbits before and after the manipulation can be seen in Fig. 5.

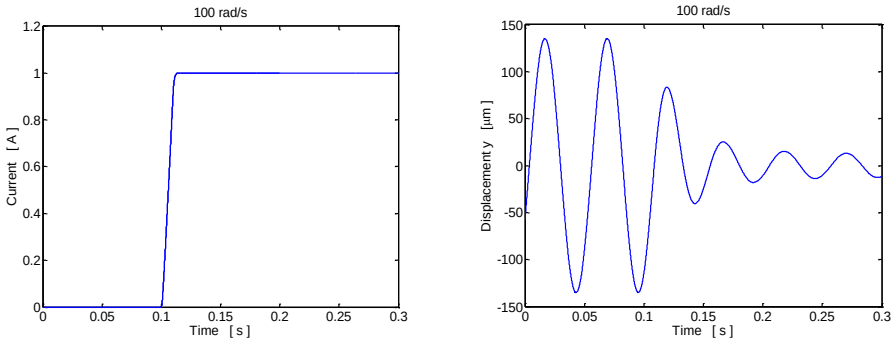

Figure 4. Time histories of the current (left) and of the rotor displacement in the horizontal direction (right).

In the second analysis the rotor rotates at speed of 300 rad/s higher than the critical one. The application of the voltage of 30 V at the moment of time of 0.1 s arrives only at a small reduction of amplitude of the rotor oscillations (Fig. 6, right). The corresponding time history of the applied current is evident from Fig. 6 (left).

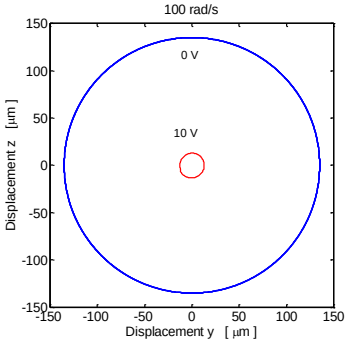

Figure 5. Steady state orbits of the rotor.

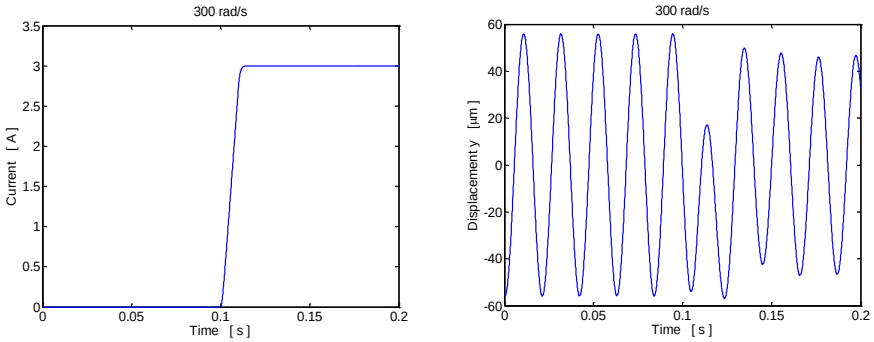

Figure 6. Time histories of the current (left) and of the rotor displacement in the horizontal direction (right).

The time history of the current is continuous and smooth. Some delay of its increase with respect to the voltage is evident. It is caused by induction of the electromotoric voltage due to the change of the magnetic flux.

6. Conclusions

This paper presents the enhanced mathematical model of a short magnetorheological squeeze film damper, in which the mutual interaction between the hydraulic forces, transient electromagnetic phenomena, and mechanical vibration is implemented. The model is based on assumptions of the classical theory of lubrication. The oil is represented by bilinear material. The pressure distribution in the full oil film in the damper gap is governed by the adapted Reynolds equation. The developed

mathematical model of the magnetorheological damper was implemented in the computational procedures for investigating lateral vibrations of rigid rotors. The results of the simulations show that the electromagnetic phenomena arrive at a time delay of the damping effect relative to the applied voltage. The implementation of the electromagnetic phenomena in the mathematical model of the magnetorheological squeeze film damper, its implementation into the computational procedures for analysis of lateral vibrations of rotors, and learning more on the influence of magnetorheological damping devices on behaviour of rotating machines are the principal contributions of this paper.

Acknowledgments

The research work reported in this article was made possible by the Czech Science Foundation (project no. 15-06621S) and the National Programme of Sustainability (project LQ1602 - IT4Innovations excellence in science). The support is highly acknowledged.

References

[1] Zapoměl, J., Ferfecki, P. and Kozánek, J. Determination of the transient vibrations of a rigid rotor attenuated by a semiactive magnetorheological damping device by means of computational modelling. *Appl. Comput. Mech.* 7 (2013), 223-234.

[2] Gong, X., Ruan, X., Xuan, S., Yan, Q. and Deng, H. Magnetorheological damper working in squeeze model. *Adv. Vib. Eng.* 6 (2014), 410158.

[3] Aravindhan, T. S. and Gupta, K. Application of magnetorheological fluid dampers to rotor vibration control. *Adv. Vib. Eng.* 5 (2006), 369-380.

[4] Zapoměl, J., Ferfecki, P. and Forte, P. A computational investigation of the transient response of an unbalanced rigid rotor flexibly supported and damped by short magnetorheological squeeze film dampers. *Smart Mater. Struct.* 21 (2012), 105011.

[5] Zapoměl, J., Ferfecki, P. and Forte, P. A new mathematical model of a short magnetorheological squeeze film damper for rotordynamic applications based on a bilinear oil representation - derivation of the governing equations. *Appl. Math. Model.* (2017), doi:10.1016/j.apm.2017.07.040.

[6] Ferfecki, P., Zapoměl, J. and Kozánek, J. Analysis of the vibration attenuation of rotors supported by magnetorheological squeeze film dampers as a multiphysical finite element problem. *Adv. in Eng. Soft.* 104 (2017), 1-11.

Jaroslav Zapoměl, Professor: Institute of Thermomechanics, Department of Dynamics and Vibrations, Dolejškova 1402/5, 182 00 Prague 8, Czech Republic (*zapomel@it.cas.cz*),
Department of Applied Mechanics, VŠB-Technical University of Ostrava, 17. listopadu 15/2172, 708 33 Ostrava-Poruba, Czech Republic (*jaroslav.zapomel@vsb.cz*).

Jan Kozánek, Research engineer: Institute of Thermomechanics, Department of Dynamics and Vibrations, Dolejškova 1402/5, 182 00 Prague 8, Czech Republic (*kozanek@it.cas.cz*).

Petr Ferfecki, Research engineer: VŠB-Technical University of Ostrava, Department of Applied Mechanics, 17. listopadu 15/2172, 708 33 Ostrava-Poruba, Czech Republic (*petr.ferfecki@vsb.cz*),
VŠB-Technical University of Ostrava, IT4Innovations National Supercomputing Center, 17. listopadu 15/2172, 708 33 Ostrava-Poruba, Czech Republic (*petr.ferfecki@vsb.cz*).

Contact force control for a high speed pantograph using co-simulations

Paweł Zdziebko, Adam Martowicz, Tadeusz Uhl

Abstract: Active control for operational conditions, which is performed for high speed pantographs is one of the promising solutions for improving the current collection quality in high speed railways. The present work deals with an exemplary configuration of a controller proposed to reduce the contact force deviation in the modeled slider-to-catenary interface. Adapted settings of the controller were proposed for different train speeds. The performance of the controller is analyzed with the use of a co-simulation tool to determine the pantograph-catenary interaction, presented recently by the authors in other works. It was achieved by computing statistical parameters of the contact force. The simulation algorithm considers the Finite Element nonlinear model of a catenary and Multibody pantograph model. Various control scenarios were successfully analyzed including disturbance from locomotive vibrations and aerodynamic forces fluctuations. Considering realistic scenarios for a rail vehicle ride, a significant parameter describing time-delays in the control loop was also investigated. The proposed control strategy revealed satisfactory reduction of the standard deviation for the contact force.

1. Introduction

The pantograph-catenary system is present in electrified railways. In the most basic configuration, a catenary consists of a contact, messenger wires (which are tensioned) and droppers. A pantograph is mounted on the roof of a train and its carbon strip is in a contact with catenary wire to provide energy delivery to a train. Exemplary configuration of this system is presented in Fig. 1.

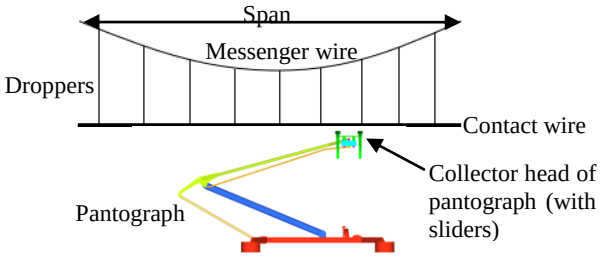

Figure 1. Pantograph-catenary system.

The contact interface is disturbed by many factors (e.g. wave reflections in catenary, vibrations generated by a rail vehicle or aerodynamic effects), especially at high speed run. Recently, many investigations have been performed on the influence of improvement of pantograph's suspension characteristic on the contact quality, e.g. [1]. The second strategy, which was lately studied, is active

control for improving pantograph-catenary dynamic interaction [2,3]. The present paper addresses a new approach in that field, which concerns simultaneously control of the nominal torque exerted by a pneumatic drive of a pantograph, depending on a speed of travel, and control of an additional drive (responsible for higher frequency control) mounted in parallel with nominal one. The analysis was performed employing the multi-domain co-simulation model presented previously by the authors [4].

The paper is organized as follows. After brief introductory Section 1, the following Section 2 introduces a pantograph model employed in the analysis. Subsequently, simulation algorithm is presented in Section 3. Next, two steps of the proposed control strategy and results are discussed in Section 4. Section 5 presents results for different control scenarios and, finally, Section 6 summaries the paper.

2. Pantograph model

The goal of the presented analysis is to investigate the performance of the proposed control strategy applied to a model, which represents the pantograph which is commonly used in Europe, i.e. 160ECT (produced by EC Engineering). Basic kinematic diagram of its mechanism is presented in Fig. 2.

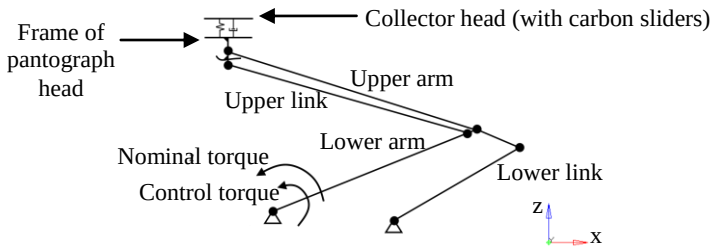

Figure 2. Kinematic diagram of pantograph.

Revolute joints that are present in the pantograph mechanism are depicted in the diagram by black circles (rotational axis is perpendicular to the ZX plane). Triangular icons denote mounting screws (to the frame). "Nominal torque" (marked in Fig. 2) is responsible for opening the pantograph and exerting nominal static contact force (CF) on the contact wire. This is completed by a pneumatic actuator (originally present in the pantograph), which can be controlled for low frequencies. On the other hand, the "control torque" may be assured by additional high frequency pneumatic actuator placed in parallel with nominal one.

3. Co-simulation environment

The numerical model, which is employed in the work is an extension of the multi-domain co-simulation approach presented in an extended form by the authors in [4]. The present development

involves adding a control module, which allows to test different control approaches. The main algorithm is presented Fig. 3.

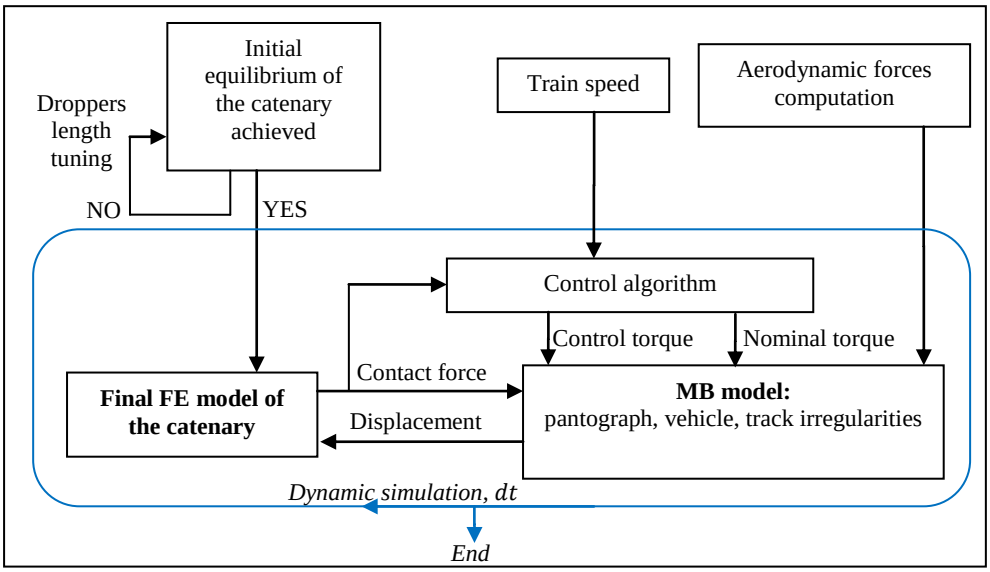

Figure 3. Co-simulation environment.

Simulations are carried out within the following computational environment. Initially, two separate models are created:

1. Employing the Finite Element Method (FEM), initial model of an overhead lines (catenary) is built. It is utilized to set final catenary model with appropriate amount of a pre-sag (considering gravity force and tension in cables), the model was built using Altair Hyper Mesh program (10 spans were modeled, each of them is 60 m long).
2. Fluid structure interaction (FSI) model of a pantograph. Computed aerodynamic forces acting on its parts are then transmitted into the MB model.

In the next step, when initial configuration of a catenary is set and aerodynamic forces are computed, the Multibody (MB) coupled track – rail vehicle – pantograph model is constructed. The pantograph – catenary interaction is simulated with given time step *dt* in the co-simulation between FEM and MB models. The simulation framework assumes that MB code is run first, and passes the position of the collector head (considering train speed and vibrations of a rail vehicle) into FEM catenary model. Next, dynamic solution of a catenary under actual position of a collector head is computed (employing MSC.Marc solver and considering the contact between these two parts) and reaction forces acting on the slider are then transmitted into MB code, where the track – rail vehicle – pantograph model is solved again, considering CF passed by catenary FEM model. Simultaneously, CF computed in FEM model is passed into the torque controller, which

generates adequate nominal and control torque for a pantograph depending on the velocity and measured actual contact force. The algorithm is iterated within a loop to cover the total simulation time (which is needed to run along 10 spans of catenary with individual speed). The obtained results are shown in the following and, then, briefly discussed. The proposed multi-domain co-simulation produces results based on real physical phenomena present in the modeled system. The method of simulation was validated according to the first step of validation process presented in the European Standard 50318 [5].

4. Control strategy

The goal of a control strategy is to improve the contact between pantograph slider and catenary wire. It is desired to reduce fluctuations of the contact force. Therefore, the standard deviation (STD) is used as a parameter to quantitatively characterize the CF, which should be minimized. Minimal and maximal values of the contact force also have a significant meaning, because they may cause detachments or excessive wear of sliders, respectively. Simplifying, the peak-to-peak (Peak-Peak) value is used as the other parameter describing the control strategy performance in this paper. Like it was suggested in [5] those statistical quantities are computed from the filtered course of the contact force corresponding to two central spans. An exemplary course of contact force is presented in Fig. 4.

According the European Standard 50367 [6], the mean contact force should be kept within specified limits, approximate ranges are presented in Fig.5. The mean contact force is assumed to be the next factor utilized in results analysis.

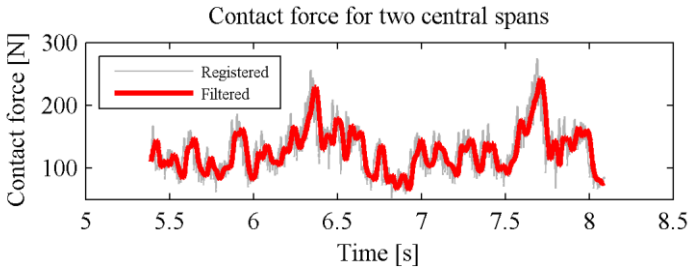

Figure 4. Exemplary course of the contact force.

4.1. Nominal torque control

The idea of „Nominal torque control" is very basic: the mean contact force is kept just above minimal accepted value (see Fig. 5). The FSI analysis have proved, that original torque setting in 160ECT pantograph causes contact force which is close to the maximum limit for all investigates speeds of travel. To gain confidence about FSI results correctness, the validation with experiment performed in a wind tunnel test rig was done. The results of validation are presented in Table 1. The achieved

numerical results – error of 0.4% - shows that prepared numerical model is correct and can be used for calculation of aerodynamic forces also for other flow speeds.

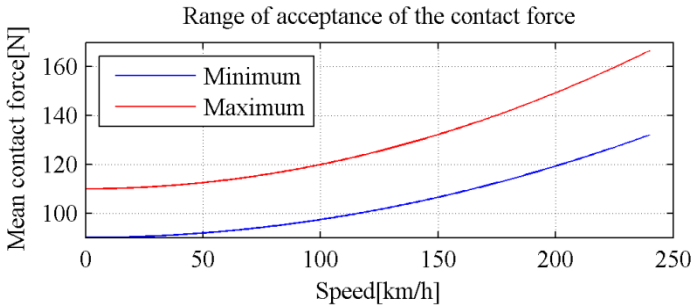

Figure 5. Acceptance ranges for mean contact force.

In "Nominal torque control" approach, the torque depicted as "Nominal" in Fig. 2 and is controlled to keep the mean contact force on the lowest possible level.

Table 1. Validation of FSI model.

	140 km/h	160km/h
Contact force – Experiment [N]	129.4	135.9
Contact force - FSI model [N]	128.9	135.37
error [%]	0.4	0.4

Schematic description of "Nominal torque control" approach is presented in Fig. 6. Through the preliminary calculations for different speeds, accepted values of minimal contact force were finally set and look-up table was created (realized by "Rule based controller"). For selected train speeds (which are easy to be measured) adequate value of "Nominal torque" is assigned.

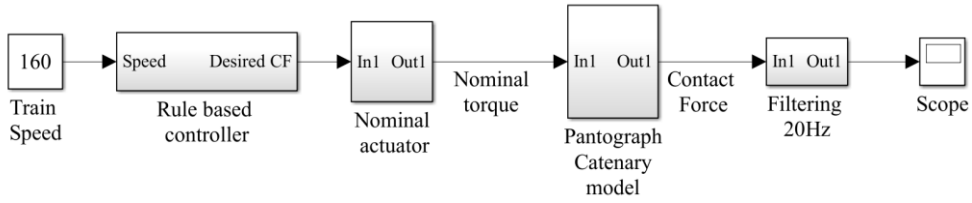

Figure 6. "Nominal torque control".

This approach is considered to be of easy implementation, does not need the contact force to be measured, but involves *a priori* knowledge of aerodynamic properties of the pantograph (collected form experiments or FSI analysis). In the analyzed case, the torque was respectively tuned to produce minimum allowed static contact force (compare "Static contact force" in Table 2 to the Fig. 5).

Table 2. Nominal torque control depending on train speed.

	Case 1: Initial case		Case 2: Nominal torque control	
Speed [km/h]:	Nominal torque:	Static contact force [N]	Controlled torque:	Static contact force [N]
140	100%	126.5	95.8%	105.7
160	100%	134.7	95.1%	109.5
180	100%	135.6	95.8%	114.4

The results of above mentioned control strategy are presented in Table 3.

Table 3. Results of contact force in "Nominal torque control".

	Speed: 140km/h		Speed: 160km/h		Speed: 180km/h	
	Case 1	Case 2	Case 1	Case 2	Case 1	Case 2
Mean [N]	126.4	105.7	134.7	109.4	135.6	114.4
STD [N]	19.9	16.7	36.2	31.7	37.2	33.2
Peak-Peak [N]	122.6	100.6	228.0	181.2	224.1	180.4

In Fig. 7, a percentage reduction of the most important statistical parameters of CF are presented (comparing to the initial Case 1). Despite its simplicity, the "Nominal torque control" approach can significantly reduce the STD (up to 16.4%) and Peak-to-Peak (up to 20.5%) of contact force, which indeed improves the dynamic interaction between pantograph and catenary.

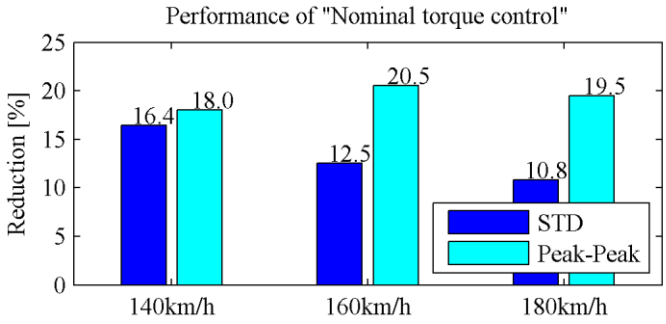

Figure 7. "Nominal torque control" performance.

4.2. Nominal and additional torque control

In the "Nominal and additional torque control" approach, the torque depicted as "Nominal" in Fig. 2 is controlled to keep the mean contact force on the lowest possible level like it was mentioned in Section 4.1. Moreover, additional "Control torque" is employed in this approach to react for instantaneous deviations of CF – which is assumed to be measurable (e.g. see [7]). Schematic description of "Nominal plus additional torque control" approach is presented in Fig. 8.

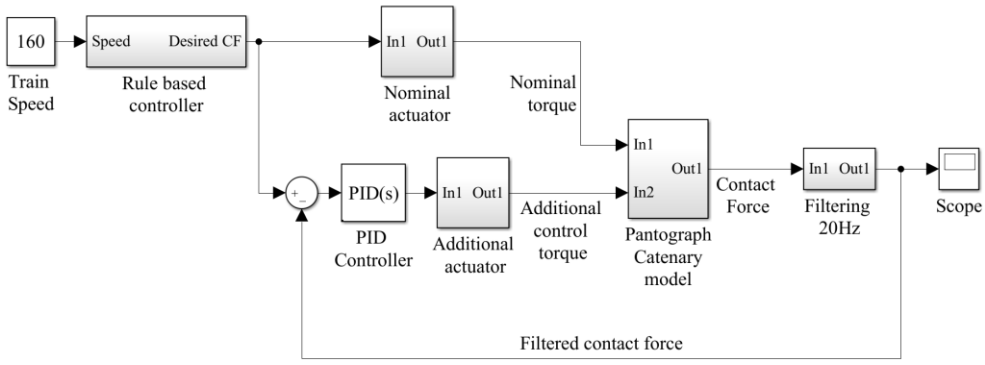

Figure 8. "Nominal and additional torque control" approach.

In this approach control is realized in a closed loop. Only proportional (P) and proportional-integral controllers were taken into consideration. According to [3] derivative term of PID controller is not necessary for pantograph active control. Different coefficients of proportional (Kp) and integral (Ki) terms were investigated. The results of the mean contact force, STD and Peak-to-Peak of CF calculated for train speed 160km/h are presented in Fig. 9-11. Notice, that different perspectives are used at graphs for better results presentation. Precise values were computed only for combinations of Kp and Ki depicted by dark points – areas between then is the field of further investigation.

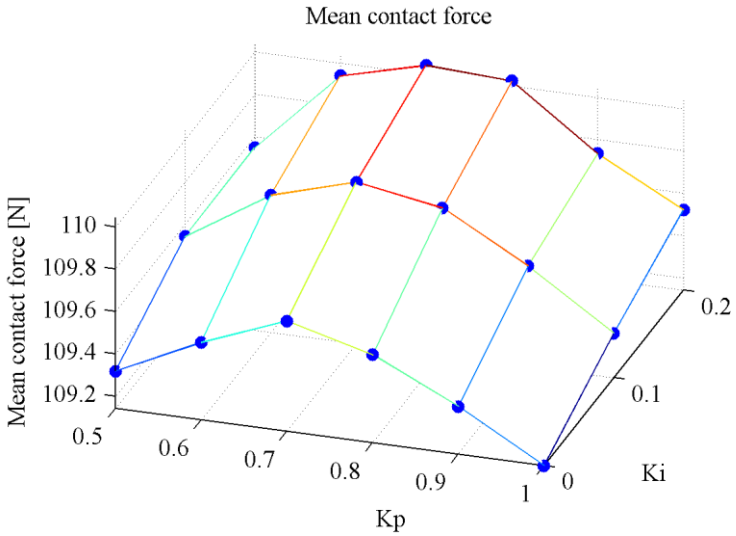

Figure 9. Mean contact force versus Kp and Ki.

The mean contact force in all analyzed cases is within the acceptance ranges, therefore it is assumed, that any of controller configuration significantly influences the mean contact force.

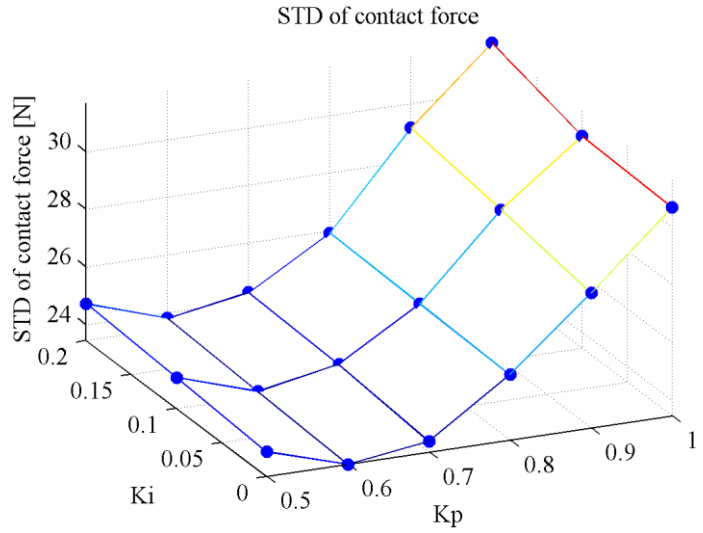

Figure 10. STD of contact force versus Kp and Ki.

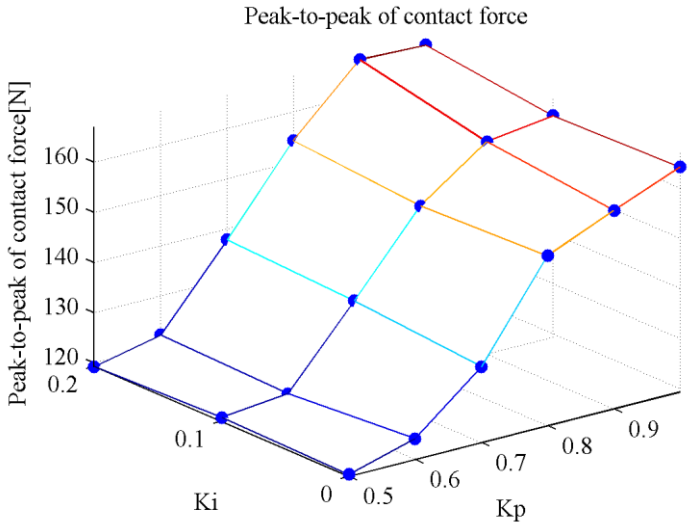

Figure 11. Peak-to-Peak of contact force versus Kp and Ki.

It can be observed, that integral term (Ki) has marginal meaning for control performance (in analyzed range) – and does not improve the contact quality in any case. Therefore, for the other speeds (140, 180 km/h) only proportional controllers were investigated.

The results for the „Nominal and additional torque control" approach employing proportional control are presented in Fig. 12-13.

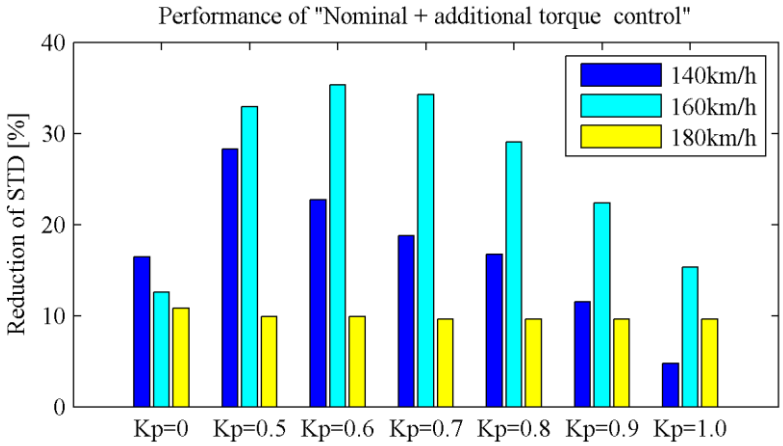

Figure 12. Reduction of STD in "Nominal and additional torque" control.

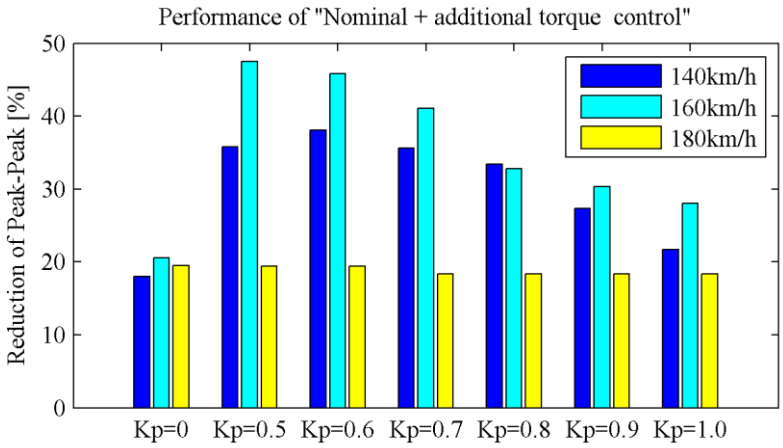

Figure 13. Reduction of Peak-to-Peak of CF in "Nominal plus additional torque" control.

It can be easily seen, that different settings of Kp are preferred for different speeds. Since, the STD of contact force is assumed to be more crucial than Peak-to-Peak, therefore following values of Kp: 0.6, 0.5, 0 are proposed to be adapted respectively for speeds 140, 160, 180 km/h.

5. Case study

For the case of train speed of 160km/h and for selected controller (Kp=0.6), which was assumed to generate the best performance for that train speed (highest reduction of STD of contact force),

the influence of: time delays in control rig, quality of track and fluctuations of aerodynamics effects on the controller performance was investigated.

Table 4 presents the results for different time delays. It can be observed, that time lag greater than 0.012s drastically decreases the robustness of controller, because applied control torque is finally set with a phase shift and deteriorate the system behavior. Time delays: 0.036 or 0.048 s even causes detachments of pantograph slider. From the other hand, the time delay is inevitable in the real implementation, so it may question the sense of additional torque controller implementation.

Table 4. Results of contact force for different time delays.

	Time delays				
	t=0s	0=0.012s	t=0.024s	t=0.036s	t=0.048s
Mean [N]	109.5	109.3	108.9	108.6	107.3
STD [N]	23.4	24.4	31.1	40.3	54.8
Min. [N]	51.2	48.8	44.2	-0.2	-8.8
Max. [N]	174.7	174.5	198.4	206.5	234.0
Peak-Peak [N]	123.5	125.7	154.2	206.6	242.8

Subsequently, the influence of different track quality classes on the contact force were investigated. Randomized track irregularities were modeled using the PSD formula described in [1]. The results proves good controller performance for various track quality, see Fig. 14.

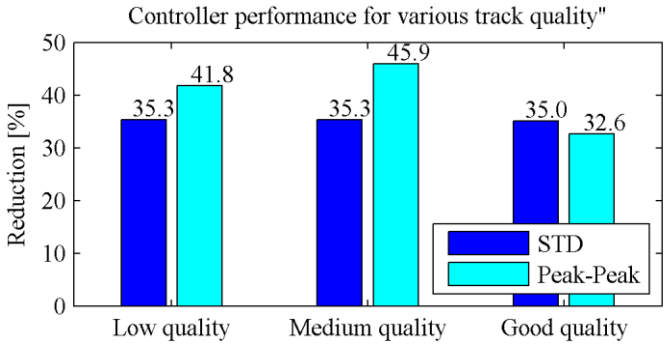

Figure 14. Controller performance for different track quality.

Employing the “Nominal and additional torque control”, the STD of CF is reduced by 35% or slightly greater in all analyzed cases of track quality. Reduction of Peak-to-Peak CF differs on the track quality class, but is also on very good level – see Fig. 14.

Wind fluctuations are the last factor that was investigated. Three different cases of the presence of wind fluctuations were considered: “nominal” – only air flow caused by train speed is present, “Wind-“, and “Wind+”. Two last cases represent the situation when additional wind blows from the

back or front of the pantograph, respectively (in range of 0-20km/h). Random wind speed was generated employing similar PSD formula like in the case of track irregularities. Generated wind speed profile is presented in Fig. 15.

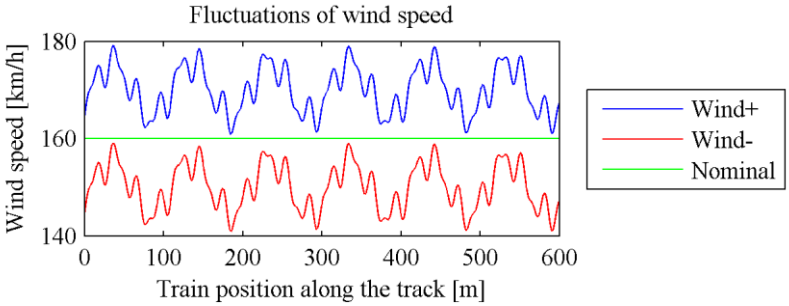

Figure 15. Wind speed history.

The results of the contact force for wind fluctuations are presented in Table 5.

Table 5. Results of contact force for different wind fluctuations.

	Wind		
Case:	Wind -	Nominal	Wind +
Mean [N]	107.8	109.5	110.4
STD [N]	23.2	23.4	23.6
Min. [N]	49.1	51.2	53.1
Max. [N]	172.0	174.7	174.9
Peak-Peak [N]	122.9	123.5	121.8

It can be observed that despite of marginal influence on the mean CF, wind fluctuations (in investigated variability) do not significantly influence the STD and other statistical parameters of CF. The proportional controller (with Kp=0.6) is considered to be resistant for wind fluctuations.

6. Conclusions

The main conclusions resulting from the paper are:

1. Lowering the nominal static pressure exerted by a pantograph on a catenary cable to minimal allowable level can be used to reduce the STD of contact force in dynamic train run.
2. The above-mentioned feature was employed to design the open-loop control scheme called “Nominal torque control”, which adapts the static pressure exerted by pneumatic drive of pantograph to produce minimal allowable contact force, independently for various speeds. In this control strategy, STD of CF is reduced by 10.8-16.4% depending on the train speed.
3. Additional fast pneumatic drive can be employed to reduce actual contact force deviation.

4. The previously stated idea (together with “Nominal torque control”) - called by the authors “Nominal and additional torque control” was also investigated in this paper. In this control strategy, STD of CF is reduced by 10.8-36%, depending on the train speed.
5. The performed analysis shows that different gain for proportional controller is favourable for different train speed: 0.5, 0.6 and 0 for speed of 140, 160 and 180 km/h respectively.
6. The results of controllers performance depend on the disturbance from many sources (time delays, track quality and wind fluctuations were analyzed).
7. The most crucial disturbance (among all the mentioned ones) is time delay in the control rig – lags greater than 0.012s causes significant deterioration of controller performance (results of CF are worse than in “no control” case).

Acknowledgments

The work was supported by the AGH Grant no. 15.11.130.627 and carried out employing the infrastructure of the Centre of Energy AGH (Czarnowiejska 36, 30-054 Kraków, Poland).

References

[1] Ambrosio, J., Pombo, J., and Pereira, M. Optimization of high-speed railway pantographs for improving pantograph-catenary contact. *Theoretical & Applied Mechanics Letters* 3 (2013).

[2] Song, Y., Ouyang, H., Liu, Z., Mei, G., Wang, H., and Lu, X. Active control of contact force for high-speed railway pantograph-catenary based on multi-body pantograph model. *Mechanism and Machine Theory* 115 (2017), 35-59.

[3] Sanchez-Rebollo, C., Jimenez-Octavio, J. R., and Carnicero, A. Active control strategy on a catenary–pantograph validated model. *Vehicle System Dynamics 51*, 4 (2013), 554-569.

[4] Zdziebko, P., Martowicz, A., and Uhl, T. Multi-domain simulation for a pantograph-catenary system investigation. *Proceedings of CMES - 2nd International Conference of Computational Methods in Engineering Science*, 2017 (to be published).

[5] European Standard PN-EN 50318, 2002.

[6] European Standard PN-EN 50367, 2012.

[7] Wagner, R., Dietmar, M., Viel, W., Saliger, F., Saliger, C., Horak, R., and Noack, T. A fibre optic sensor instrumented pantograph as part of a continuous structural health monitoring system for railway overhead lines. *7th European Workshop on Structural Health Monitoring*, 2014

Paweł Zdziebko, M.Sc. (Ph.D. student): AGH University of Science and Technology, Department of Robotics and Mechatronics, Al. A. Mickiewicza 30, 30-059 Krakow, Poland (*zdziebko@agh.edu.pl*). The author gave a presentation of this paper during one of the conference sessions.

Adam Martowicz, Ph.D.: AGH University of Science and Technology, Department of Robotics and Mechatronics, Al. A. Mickiewicza 30, 30-059 Krakow, Poland (*adam.martowicz@agh.edu.pl*).

Tadeusz Uhl, Professor: AGH University of Science and Technology, Department of Robotics and Mechatronics, Al. A. Mickiewicza 30, 30-059 Krakow, Poland (*tuhl@agh.edu.pl*).

Control optimization for a three-segmented hopping leg model of human locomotion

Ambrus Zelei, Bernd Krauskopf, Tamás Insperger

Abstract: The research of human and robotic legged locomotion applies dynamic models with a wide range of complexity and aims to answer many different questions. In our research we focus on the effect of kinematic parameters and foot placement techniques on the ground-foot impact intensity. Our method is to use the multibody dynamic model of a segmented leg. We obtain a quantitative measure for the foot collision intensity by analytic calculations. The pre-impact velocity conditions are obtained by a hopping three-segmented planar leg model that imitates pedal locomotion. The single legged model contains the foot, the shank, the thigh and a reaction wheel attached in the hip. Stable periodic motion, i.e. hopping was achieved by means of control torques in the ankle, the knee and the hip joint. Different control strategies are specified for the grounded and flight phase. The parameters of the linear feedback controller are tuned to optimise different cost functions, such as running speed, energy efficiency and impact intensity. We also investigate how the stability of periodic motion depends on the control gains.

1. Introduction

Understanding of human walking, running, jumping and the development of corresponding bipedal robots require thorough analysis of complex dynamic models. Although, there are many experimental and theoretical results, analysis of bipedal locomotion of humans and mobile robots are still in the center of interests of biomechanics. In this paper, we develop a segmented leg model, which can describe stable periodic motion associated with hopping.

1.1. Motivations

A yet unresolved issue is the effect of running kinematics and foot placement pattern on the ground-foot collision intensity. Depending on the form of running, high impacts and therefore high kinetic energy absorption may occur, which should actually be avoided in order to minimize the risk of injuries and also to increase energy efficiency during running [7,9,11,14]. The hopping leg model presented in this paper provides measures for the ground-foot collision, like kinetic energy absorption and effective mass. The model provides realistic pre-impact configuration.

In spite of the large number of publications, the mechanism of human balancing is still not entirely understood and is still a strongly researched area [1, 6]. A possible research goal is to discover and compare the energy consumption needed for balancing when standing still and during walking, running or hopping. The postural sway during standing still shows that certain energy input is required for the stabilization of the otherwise unstable upright standing position, similarly to the stabilization of an inverted pendulum via a feedback controller. Running, on the other hand, is a periodic motion for which the energy consumption can be divided into two parts: 1) the energy required for the recovery of dissipation and the energy loss due to dynamic reasons; and 2) the effort needed for the prevention of falling over. The energy required for the stabilization may actually be smaller in case of running than in case of standing still.

1.2. Models and results for ground-foot impact intensity

A mechanical model containing the foot and the shank was introduced in [11] for the investigation of the effect of the foot strike pattern. The foot-shank system falls vertically and the foot hits a fixed pin. The contact point position is characterized by the strike pattern s. A further developed but still two-segmented model was introduced in [9]. As an extension of the model in [11], a variable ankle angle and a horizontal velocity were introduced. Both [11] and [9] report that the effective mass and therefore the impact intensity is lower for forefoot-strike, when strike pattern is $s = 0.7 \dots 1$ than heel-strike, when $s = 0 \dots 0.2$.

Results in [14] showed that in addition to the strike pattern, the angle of the shank also strongly affects the properties of the ground-foot impact. The model in [14] involves the thigh and the total mass of the human body. The segments perform a rigid-body-like motion in the pre-impact phase with no relative motion of the body segments, which is not realistic.

A realistic pre-impact velocity condition can be obtained either from experiments or from a dynamic model that performs stable periodic running motion. In our previous work [3], we introduced such a dynamic model subjected to a torque control in order to perform further biomechanical analysis of human running performance. The advantage of this model over an experiment is that the control parameters can be tuned to optimize different cost functions, such as running speed, energy efficiency and impact intensity. Present paper reports new results about the detailed analysis of the model.

1.3. Existing segmented hopping leg models and related results

This subsection overviews a few models developed to perform stable periodic motion, like walking, hopping and running.

Many aspects of periodic motion of legged systems are detailed in [5], where several walking, running and hopping models are reviewed. The classical spring-loaded inverted pendulum (SLIP) model gives a fundamental background for hopping leg models. SLIP represents the body inertia as a point mass which bounces along on a single elastic massless leg. The supporting role of the leg in each stance phase is characterized by the SLIP.

Self-stable running-like locomotion is presented in [13] for a case where the inertia and dynamic effects of the segments are neglected and the body weight is modeled by a point mass in the hip. It is reported that the stable domain regarding landing angle and horizontal speed is larger than in case of SLIP model. The presence of massless segments leads to 1) smooth dynamics, i.e. there is no impulsive forces when the foot gets in contact with the ground; 2) the elimination of all inertial forces due to the inertia of the leg segments. These simplifications facilitates essential analytical and numerical results. Here, we extend this model in such way, that 1) the energy loss and impact forces are possible to be obtained, 2) the effects due to inertial forces are discovered. While the model in [13] is self-stable, in the extended model we use state feedback and control actions in order to achieve the stable hopping motion.

2. Dynamic model of the controlled hopping leg

The single-legged, planar mechanical model depicted in Fig. 1 is an extended combination of the ground-foot impact model in [14] and the self-stable hopping model in [13]. The new aspect is that a feedback controller is introduced to the model from [14], which was not actuated at all. In contrast with [13], self-stability without controller is not possible here, because the rigid body collision absorbs energy. Another extension is that the proposed control concept also involves a reaction wheel which is attached in the hip. The overall model consists of the equations of motion and the control algorithm similarly as in [3].

2.1. Mechanical structure

The three segments 1, 2 and 3 correspond to the foot, shank and thigh, respectively. Points A, B, C and D correspond to the tiptoe, the ankle, the knee and the hip, respectively. The reaction wheel plays the role of the upper body: the torque M_D that rotates the thigh has the reaction torque exerted on the wheel. The reaction wheel has mass m_r and moment of inertia J_r. The homogeneous, prismatic bars have masses m_i and lengths l_i, $i = 1 \dots 3$. The centre of gravity is located at point G. The segments are interconnected by torsional springs with stiffnesses k_B and k_C. Actuating torques M_B and M_C assist the motion according to the control, which will be introduced below.

The model has a total of 6 DoFs in the flight phase: $\mathbf{q}^\mathrm{f} = [x_\mathrm{A}, z_\mathrm{A}, \theta_1, \theta_{12}, \theta_{23}, \theta_\mathrm{r}]$, where

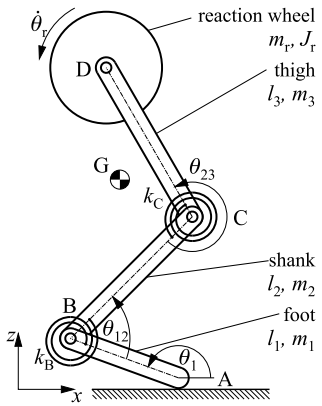

Figure 1. Segmented leg model

x_A and z_A are the Cartesian coordinates of the tiptoe. There are 4 DoFs in grounded phase: $\mathbf{q}^g = [\theta_1, \theta_{12}, \theta_{23}, \theta_r]$. In both phases, the equation of motion assumes the general form:

$$\mathbf{M}(\mathbf{q})\ddot{\mathbf{q}} + \mathbf{C}(\mathbf{q}, \dot{\mathbf{q}}) = \mathbf{Q}(\mathbf{q}, \dot{\mathbf{q}}) \,, \tag{1}$$

where $\mathbf{M} \in \mathbb{R}^{n \times n}$ is the mass matrix, $\mathbf{C} \in \mathbb{R}^n$ is the inertial force vector and $\mathbf{Q} \in \mathbb{R}^n$ general force contains the control torques. Here $\mathbf{q} = \mathbf{q}^f$ and $n = 6$ in flight-phase; while $\mathbf{q} = \mathbf{q}^g$ and $n = 4$ in ground-phase.

We assume that the ground-foot impact is completely inelastic, there is no rebound and the friction coefficient is high enough to prevent sliding of the foot. These assumptions allows us to constrain the tiptoe to the ground until the contact force is positive. See Section 3.1 for more details.

The non-linear spring characteristics, which is caused by the muscle-tendon dynamics, is not considered here in order to reduce the number of parameters. The torques exerted by the linear torsional springs of stiffness k_B and k_C are given by

$$k_B(\theta_{12} - \alpha_{12}) \qquad \text{and} \qquad k_C(\theta_{23} - \alpha_{23}) \,, \tag{2}$$

where α_{12} and α_{23} denotes the joint angle values that corresponds to unstretched springs.

The anatomical data adopted from [2] of a 24 years old average male with bodyweight of 73 kg and body height of 173.1 cm were considered (see Table 1).

2.2. Control

On the top of the spring torques, additional torques are exerted with respect to the control in equations (3) - (5) and (7) - (9). In our concept a control law is formulated that provides

Table 1. Inertial and geometric data of body segments

	mass	length/height	CoG mass moment of inertia
whole body	$m_\mathrm{b} = 73\,\mathrm{kg}$	$l_\mathrm{b} = 1.731\,\mathrm{m}$	-
trunk	$m_\mathrm{r} = 0.6028 m_\mathrm{b}$	-	$J_\mathrm{r} = 1.9778\,\mathrm{kgm}^2$
feet	$m_1 = 0.0274 m_\mathrm{b}$	$l_1 = 0.0885 l_\mathrm{b}$	$J_1 = 1/12 m_1 l_1^2$
shanks	$m_2 = 0.0866 m_\mathrm{b}$	$l_2 = 0.2470 l_\mathrm{b}$	$J_2 = 1/12 m_2 l_2^2$
thighs	$m_3 = 0.2832 m_\mathrm{b}$	$l_3 = 0.2320 l_\mathrm{b}$	$J_3 = 1/12 m_3 l_3^2$

periodic motion of the body. The motion of the segments is dictated by their dynamics, rather than having prescribed trajectories for the limb segments and a feedback control that forces the segment onto these prescribed trajectories. These two concepts are distinguished in [5]. Naturally, our control law needs the observation of the configuration of the segments and needs information about the actual flight/ground-phase of the leg.

2.2.1. Passive motion does not exist because of ground-foot impact

In general, the tiptoe touches the ground with non-zero velocity. This causes an impact and a certain kinetic energy loss, called *constrained motion space kinetic energy* (CMSKE) [9,14]. CMSKE is often used used as an energy efficiency indicator of passive walkers [4] because their energy loss is the foot impact only.

As a consequence, periodic hopping motion is not possible without some kind of energy input, which is provided by the muscles in humans and by motors in legged robots. An alternative possibility to avoid energy loss is to achieve zero-velocity collision, which means that the tiptoe velocity becomes zero at the instance of time when the foot touches down. However, impact-free motion does not guarantee periodicity, because the model can fall over, and using a controller is a more feasible approach.

2.2.2. Flight-phase

The vibrations of the leg segments are suppressed by M_B and M_C in the flight phase as (3) and (4) show. A proportional-derivative controller defined in (5) tries to keep the tiptoe (point A) at a specified horizontal position near to the centre of mass position x_G of the overall model in order to avoid falling over.

$$M_\mathrm{B}^\mathrm{f} = -D_\mathrm{B}\dot{\theta}_{12}\,, \tag{3}$$

$$M_\mathrm{C}^\mathrm{f} = -D_\mathrm{C}\dot{\theta}_{23}\,, \tag{4}$$

$$M_\mathrm{D}^\mathrm{f} = P(x_\mathrm{A} - (x_\mathrm{G} + x_\Delta)) + D(\dot{x}_\mathrm{A} - \dot{x}_\mathrm{G})\,. \tag{5}$$

Term x_Δ modifies the desired tiptoe position regarding the angular momentum Π_A calculated for point A. Furthermore, a constant K_v modifies the horizontal velocity:

$$x_\Delta = P_\Pi \, \Pi_\mathrm{A} - K_v \, . \tag{6}$$

2.2.3. Ground-phase

A certain part of the kinetic energy called CMSKE is absorbed in each stride because of the ground-foot impact. CMSKE is recovered by means of the control torques (7) and (8) exerted in the ankle and the knee. The goal is to keep the total mechanical energy E at the freely chosen desired energy level E_0. The mechanical power of these torques are positive only if the joints are in extension, so that $\dot{\theta}_{12}$ is positive and $\dot{\theta}_{23}$ is negative. Torque M^g_D in (9) prevents the continuous growth of the angular velocity $\dot{\theta}_\mathrm{r}$ of the reaction wheel.

$$M^\mathrm{g}_\mathrm{B} = P_E(E - E_0)\,\mathrm{sgn}(\dot{\theta}_{12}) \, , \tag{7}$$

$$M^\mathrm{g}_\mathrm{C} = P_E(E - E_0)\,\mathrm{sgn}(-\dot{\theta}_{23}) \, , \tag{8}$$

$$M^\mathrm{g}_\mathrm{D} = -P_\mathrm{r}\theta_\mathrm{r} - D_\mathrm{r}\dot{\theta}_\mathrm{r} \, . \tag{9}$$

2.2.4. Limitations

1) Depending on the configuration, bow and zigzag mode is possible, out of which only the latter is considered, because only this is possible for human leg. 2) There is no specific strategy for heel-strike yet. We consider hopping modes with ground-tiptoe contact only. 3) Since the segments are rigid, the behaviour of soft tissue is not possible yet. 4) As we mentioned earlier, the slip of the foot relative to the ground is not possible in this model. 5) The elastic-plastic behaviour of the ground is not considered.

3. Methods

Present work is based on numerical simulations of the hopping leg model, which was explained in Section 2. The most fundamental details are summarized in this Section.

3.1. Ground-foot impact intensity and energy loss

The foot touchdown is handled as an impulsive phenomenon, during which the velocity condition of the model goes under abrupt change. We assume that the ground-foot collision is instantaneous, which leads to infinitely large instantaneous forces over an infinitesimal time duration so that the net impulse due to the impact force is finite [9, 11]. Completely inelastic collision is also assumed, so that there is no rebound [9, 11, 14]. These assumptions lead us to consider the ground-foot contact as an instantly arising geometric constraint $\boldsymbol{\varphi}(\mathbf{q})$ as in [9, 14]. While velocity condition changes instantly, the configuration does not change.

Before foot touchdown, the system moves freely during flying phase. The new constraints $\boldsymbol{\varphi}(\mathbf{q}) = \mathbf{0}$ related to the ground contact arise at the time instant of the impact. The post-impact velocities are determined by the projection to the space of the admissible motion:

$$\dot{\mathbf{q}}^{+} = \mathbf{P}_a \dot{\mathbf{q}}^{-}, \tag{10}$$

where $\dot{\mathbf{q}}^{-} = \dot{\mathbf{q}}(t^{-})$ and $\dot{\mathbf{q}}^{+} = \dot{\mathbf{q}}(t^{+})$ are the pre- and post-impact generalized velocities respectively. $\mathbf{P}_{\mathrm{a}} = \mathbf{I} - \mathbf{P}_{\mathrm{c}}$ projects into the null-space of the constraint Jacobian $\boldsymbol{\Phi}_{\mathbf{q}} = \nabla_{\mathbf{q}}(\boldsymbol{\varphi})$, which is the subspace of the admissible motion. $\mathbf{P}_{\mathrm{c}} = \boldsymbol{\Phi}_{\mathbf{q}}^{\dagger}\boldsymbol{\Phi}_{\mathbf{q}}$ projects into the constrained subspace. The *generalised inverse* of the constraint Jacobian is calculated according to [10]:

$$\boldsymbol{\Phi}_{\mathbf{q}}^{\dagger} = \mathbf{M}^{-1}\boldsymbol{\Phi}_{\mathbf{q}}^{\mathrm{T}}(\boldsymbol{\Phi}_{\mathbf{q}}\mathbf{M}^{-1}\boldsymbol{\Phi}_{\mathbf{q}}^{\mathrm{T}})^{-1}. \tag{11}$$

The kinetic energy CMSKE related to the constrained motion vanishes when the foot touches the ground and can be calculated based on [8] as:

$$T_{\mathrm{c}} = \frac{1}{2}(\dot{\mathbf{q}}^{-})^{\mathrm{T}}\mathbf{P}_{\mathrm{c}}^{\mathrm{T}}\mathbf{M}\mathbf{P}_{\mathrm{c}}\dot{\mathbf{q}}^{-}. \tag{12}$$

Papers [9] and [8] showed that foot strike intensity can be characterised by the CMSKE which depends on the pre-impact configuration $\mathbf{q}^{-}$ and velocity $\dot{\mathbf{q}}^{-}$ and the *effective mass matrix* $\mathbf{M}_{\mathrm{e}} = \mathbf{P}_{\mathrm{c}}^{\mathrm{T}}\mathbf{M}\mathbf{P}_{\mathrm{c}}$. In this work the CMSKE is used for characterising the foot impact intensity: CMSKE is directly proportional to the impulse of the contact reaction force and also to the peak reaction force [8, 9].

3.2. Periodic paths and tuning of control parameters

Our goal is to find the control parameter set resulting stable periodic motion, while some cost function, like energy efficiency is minimized. We have 10 parameters in (3)-(9) collected in the vector $\mathbf{p} = [D_{\mathrm{B}}\,, D_{\mathrm{C}}\,, P\,, D\,, P_{\Pi}\,, K_v\,, P_E\,, E_0\,, P_{\mathrm{r}}\,, D_{\mathrm{r}}]$. Parameters $\mathbf{p}$ were tuned by trial-and-error method until periodic motion was possible to be found in [3] by means of *shooting method*.

For a given set of parameters $\mathbf{p}$, $\mathbf{x}_0^{*} = [\mathbf{q}_0^{*}\,, \dot{\mathbf{q}}_0^{*}]^{\mathrm{T}}$; $\mathbf{x}_0^{*} \in \mathbb{R}^{2n}$ is a periodic solution, if the system is in the same state at the beginning and at the end of the period, so that mapping $\mathbf{g}(\mathbf{x}_0, \mathbf{p})$ has a fix point or in other words $\mathbf{F}(\mathbf{x}_0^{*}, \mathbf{p}) = \mathbf{0}$, where

$$\mathbf{F}(\mathbf{x}_0, \mathbf{p}) = \mathbf{g}(\mathbf{x}_0, \mathbf{p}) - \mathbf{x}_0. \tag{13}$$

As Fig. 2 shows, the period starts at the beginning of the flight-phase and ends at the end of the ground-phase: event function $h_{\mathrm{g}\mapsto\mathrm{f}} = \lambda_{\mathrm{A}}$ crosses 0 in positive direction (λ_{A} is the vertical contact force magnitude). Transition from flight- to ground-phase occurs when

event function $h_{\mathrm{f}\mapsto\mathrm{g}} = z_{\mathrm{A}}$ crosses 0 in negative direction. Between flight- and ground phase a discontinuity mapping from $\mathbf{x}^-$ to $\mathbf{x}^+$ is realized by (10). Systems with such discontinuities are referred as *hybrid systems* in [12].

With a prosperous initial guess for $\mathbf{x}_0$, Newton-Raphson iteration provides the numerical approximation for $\mathbf{x}_0^*$ by finding the root of (13). The Jacobian $\mathbf{J} = \nabla_{\mathbf{x}_0}(\mathbf{F})$ is necessarily computed in the Newton-Raphson method, with which a possible approximation of the Jacobian $\mathbf{M} = \nabla_{\mathbf{x}_0}(\mathbf{g})$ of the mapping $\mathbf{g}$ can be computed as $\mathbf{M} = \mathbf{J} + \mathbf{I}$.

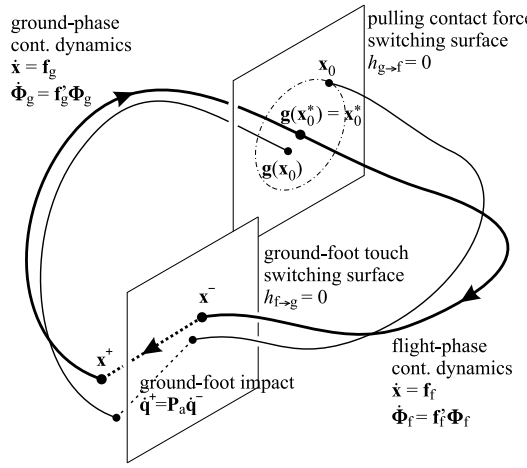

Figure 2. Schematic picture of a single period: flight-phase, ground-foot impact, ground-phase and ground foot detachment

The periodic orbit is stable, if a perturbed initial condition $\mathbf{x}_0$ is mapped ,,closer" to the periodic path. Due to the non-smoothness of our system, the accuracy of $\mathbf{M}$ is not sufficient for judging stability of the periodic path. Instead, the *flow Jacobian* is computed based on [12]. The following $2n + (2n)^2$ size ODE, which is referred as *first variational equation* in the literature, is solved during the continuous dynamics:

$$\dot{\mathbf{x}}(t) = \mathbf{f}(\mathbf{x}(t)); \quad \mathbf{x}(0) = \mathbf{x}_0, \tag{14}$$

$$\dot{\mathbf{\Phi}}(t) = \nabla_{\mathbf{x}}(\mathbf{f}(\mathbf{x}(t)))\,\mathbf{\Phi}(t); \quad \mathbf{\Phi}(0) = \mathbf{I}, \tag{15}$$

where $\mathbf{I}$ is $2n$ by $2n$ identity. Equations (14) and (15) can be applied with substitution $\mathbf{f} = \mathbf{f}_{\mathrm{f}}$ in flight-phase and $\mathbf{f} = \mathbf{f}_{\mathrm{g}}$ in ground-phase. Flow Jacobians $\mathbf{\Phi}_{\mathrm{f}}$ and $\mathbf{\Phi}_{\mathrm{g}}$ are obtained at the end of the flight- and ground-phase respectively. The Jacobian of the composite flow needs the Jacobian $\mathbf{S}$ of the discontinuity mapping, which is referred as *saltation matrix* in [12]. Finally the composite flow Jacobian, which can be reliably applied for determining stability of the periodic orbit, is obtained as $\tilde{\mathbf{\Phi}} = \mathbf{\Phi}_{\mathrm{g}} \mathbf{S} \mathbf{\Phi}_{\mathrm{f}}$.

The method described above makes possible to tune the parameters $\mathbf{p}$ in order to find the optimum for a certain cost function to be minimized. The cost function may be the norm of the largest eigenvalue of $\tilde{\mathbf{\Phi}}$, which characterizes stability. An other possible alternative for instance is to use T_c as cost function, which characterizes impact intensity. In order to find the minimum of the cost function, several numerical algorithms, like simplex method could be applied on the top of the above explained shooting method. The following sequence is repeated until the minimum of the cost function is found: the simplex method modifies $\mathbf{p}$, and the shooting method serves the solution $\mathbf{q}_0^*$ related to $\mathbf{p}$.

4. Results

Periodic paths was found for the control parameters that are collected in Table 2. Parameter E_0 was swept for $K_v = 0$ and 0.4 m fixed values. E_0 and K_v are responsible for the height and horizontal locomotion speed of the hopping motion respectively. Cases **A** and **B** are the smallest and largest possible E_0 values for $K_v = 0$ m without loosing stability, while Cases **C** and **D** are the same for $K_v = 0.4$ m. The stiffness parameters were set to $k_\mathrm{B} = 1200$ Nm and $k_\mathrm{C} = 1300$ Nm. The unstretchered angle of the springs are $\alpha_{12} = 80\,^\circ$ and $\alpha_{23} = 225\,^\circ$.

Table 2. Control parameters: E_0 and K_v are varied in the case examples, the rest are fixed

case	E_0 [J]	K_v [m]	D_B [Nms]	D_C [Nms]	P [N]	D [Ns]	P_Π $[(\mathrm{Ns})^{-1}]$	P_E [1]	P_r [Nm]	D_r [Nms]
A	752	0								
B	2970	0	15	20	950	50	0.01	0.2	4	15
C	1027	0.4								
D	3310	0.4								

4.1. Hopping motion with different speed and height

Hopping motion for four illustrative case examples are shown in Fig. 3. We found stable hopping motion from 0.018 to 2.141 m tiptoe elevation. The amplitude of the vertical centre of mass motion are 0.064 m in case **A**, 1.32 m in **B**, 0.071 m in **C** and 1.11 m in case **D**. The average locomotion v_x speed and the tiptoe elevation are plotted in the right panel of Fig. 3. A wide range of locomotion speed and hopping height is covered by tuning E_0 and K_v only, however we expect that the tuning of other control parameters provides larger stable domain.

4.2. Ground-foot impact intensity

The total kinetic energy T, the CMSKE (T_c) and the preserved part of the kinetic energy T_a are calculated for the ground-foot impact as Fig. 4 left panel shows. The normalized T_c and T_a on the right panel has a minimum value for the different values of the speed control

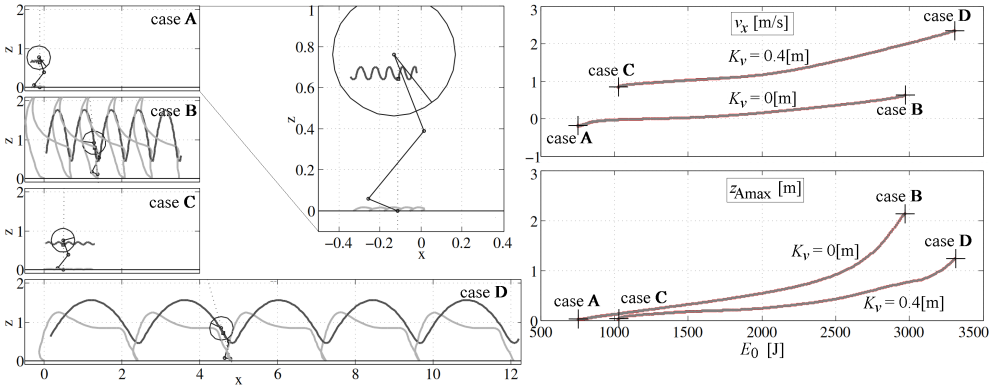

Figure 3. Results: the hopping motion with tiptoe and centre of mass path are illustrated in cases **A**, **B**, **C** and **D** in the left panel; the velocity v_x of the locomotion and the apex height z_{Amax} of the tiptoe path are plotted as the function of the desired energy level E_0.

parameter K_v. For $K_v = 0\,\mathrm{m}$ the optimal E_0 value is 821 J and 0.971 % of the kinetic energy is absorbed by the ground-foot impact. The optimum for $K_v = 0.4\,\mathrm{m}$ is $E_0 = 2230\,\mathrm{J}$ and the absorbed kinetic energy ratio is 2.09 %.

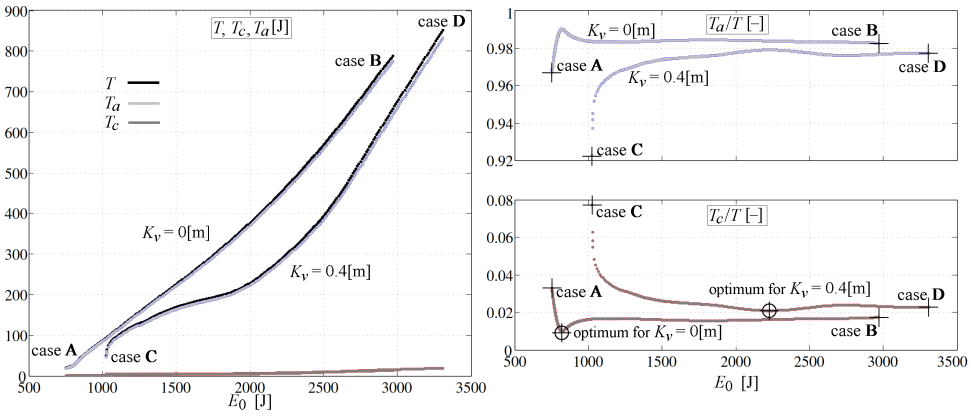

Figure 4. Results: the pre-impact kinetic energy T, the absorbed kinetic energy T_{c} related to the constrained subspace and the remaining kinetic energy T_{a} related to the admissible subspace are plotted in left panel; the normalized T_{c} and T_{a} are plotted in the right panel.

5. Conclusions and further steps

Stable periodic motion, i.e. running was achieved with the planar three-segmented leg model by means of control torques in the ankle and the knee joint and with a reaction wheel

placed at the hip. Wide range of locomotion velocity ($-0.2 \ldots 2.35\,\mathrm{m/s}$) and hopping motion height (tiptoe elevation: $0.018 \ldots 2.14\,\mathrm{m}$) were discovered, where the remaining fixed control parameters guaranteed stable operation. However, the currently fixed parameters will be tuned hereafter. The optimum of the hopping height was found, when the ground-foot impact intensity is the smallest and therefore the largest amount of kinetic energy is preserved.

We applied shooting method to obtain periodic orbits of the hybrid system. However, in future works, we plan to find and follow periodic orbits and their stability with advanced continuation methods. The model will be developed further in order to achieve more human-like motion; in particular, two legs and a more accurate model for the upper body can be considered. The model can also be used to investigate the effect of the terrain on the optimal motion, like inclination of the ground. Although some conclusion regarding human motion can be drawn from mathematically generated trajectories of the a model, a comparison with laboratory experiments with human subjects is also necessary. After refinement of the proposed mechanical model and the controller other performance measures of human running may become feasible.

References

[1] Chagdes, J., Rietdyk, S., Jeffrey, M., Howard, N., and Raman, A. Dynamic stability of a human standing on a balance board. journal of biomechanics. *Journal of Biomechanics 46*, 15 (2013), 2593–2602.

[2] de Leva, P. Adjustments to zatsiorsky-seluyanov's segment inertia parameters. *Journal of Biomechanics 29*, 9 (1996), 1223–1230.

[3] Fekete, L., Krauskopf, B., and Zelei, A. Three-segmented hopping leg for the analysis of human running locomotion. In *ENOC 2017 – 9th European Nonlinear Dynamics Conference* (Budapest, Hungary, 25-30, June 2017), pp. 1–2.

[4] Garcia., M., Chatterjee., A., Ruina, A., and Coleman, M. The simplest walking model: stability, complexity, and scaling. *Journal of Biomechanical Engineering 120* (1998), 281–288.

[5] Holmes, P., Full, R. J., Koditschek, D. E., and Guckenheimer, J. The dynamics of legged locomotion: Models, analyses, and challenges. *SIAM Rev. 48*, 2 (2006), 207–304.

[6] Insperger, T., and Milton, J. Sensory uncertainty and stick balancing at the fingertip. *Biological Cybernetics 108*, 1 (2016), 85–101. doi:10.1007/s00422-013-0582-2.

[7] Jungers, W. L. Barefoot running strikes back. *Nature, Biomechanics 463*, 7280 (2010), 433–434.

[8] Kövecses, J., and Font-Llagunes, J. M. An eigenvalue problem for the analysis of variable topology mechanical systems. *ASME Journal of Computational and Nonlinear Dynamics 4*, 3 (2009), 9 pages. doi:10.1115/1.3124784.

[9] Kövecses, J., and Kovács, L. L. Foot impact in different modes of running: mechanisms and energy transfer. *Procedia IUTAM 2* (Symposium on Human Body Dynamics, 2011), 101–108.

[10] Kövecses, J., Piedoboeuf, J.-C., and Lange, C. Dynamic modeling and simulation of constrained robotic systems. *IEEE/ASME Transactions on Mechatronics 2*, 2 (2003), 165–177.

[11] Lieberman, D. E., Venkadesan, M., Werbel, W. A., Daoud, A. I., D'Andrea, S., Davis, I. S., Mang'Eni, R. O., and Pitsiladis, Y. Foot strike patterns and collision forces in habitually barefoot versus shod runners. *Nature, Biomechanics 463*, 7280 (2010), 531–535.

[12] Piiroinen, P. T., and Dankowicz, H. J. Low-cost control of repetitive gait in passive bipedal walkers. *International Journal of Bifurcation and Chaos 15*, 6 (2005), 1959–1973.

[13] Rummel, J., and Seyfarth, A. Stable running with segmented legs. *Intl. Journal of Robotics Research 27*, 8 (2008), 919–934.

[14] Zelei, A., Bencsik, L., Kovács, L. L., and Stépán, G. Energy efficient walking and running - impact dynamics based on varying geometric constraints. In *12th Conference on Dynamical Systems Theory and Applications* (Lodz, Poland, 2-5, December 2013), pp. 259–270.

Ambrus Zelei, Ph.D. (Research Associate): Department of Applied Mechanics, Budapest University of Technology and Economics and MTA-BME Research Group on Dynamics of Machines and Vehicles, Muegyetem rkp. 3-5.,Budapest, 1111, Hungary (*zelei@mm.bme.hu*). The author gave a presentation of this paper during one of the conference sessions.

Bernd Krauskopf, Ph.D. (Professor): Department of Mathematics, University of Auckland, Private Bag 92019, Auckland 1142, New Zealand (*b.krauskopf@auckland.ac.nz*).

Tamás Insperger, Ph.D. (Associate Professor): Department of Applied Mechanics, Budapest University of Technology and Economics and MTA-BME Lendület Human Balancing Research Group, Muegyetem rkp. 3-5.,Budapest, 1111, Hungary (*insperger@mm.bme.hu*).

INDEX OF AUTHORS

Alber Oliver **9**
Alevras Panagiotis **25**
Anderson Kurt **253**
Andrianov Igor V. **35**
Angulo Fabiola **413**
Avanço Rafael **41**
Awrejcewicz Jan **35, 53, 61, 215, 231, 549, 559, 571**
Aydin Ersin **71**
Balthazar José **41**, **139, 279, 323**
Bhaskar Atul **151**, **299**
Bielski Włodzimierz **83**
Böhm Valter **485**
Buratowski Tomasz **105**
Burdzik Rafał **95**
Charlemagne Simon **269**
Ciszewski Michał **105**
Craig Nathan Paul **115**
De Melo Vinicius Yoshida **323**
Diskovsky Alexander A. **35**
Díaz-Marín Carlos D. **127**
Dobriyan Vitalyi **53**
Dos Santos Guilherme Pacheco **139**
Dutkiewicz Maciej **71**
Dzyubak Larysa **151**
Ďuriš Radislav **335**
Ehehalt Ulrich **9**
Erofeev Nikolay P. **53**
Ferfecki Petr **579**
Frączek Janusz **401**
Freitas Celso **241**
Freundlich Jan **161**
Gąsiorski Grzegorz **447**
Gidlewski Mirosław **173**
Giergiel Mariusz **105**

Grigg Harriet **115**
Grzelczyk Dariusz **215**
Gutschmidt Stefanie **435, 475**
Insperger Tamás **599**
Jackson Samuel **475**
Janzen Frederic Conrad **139, 279**
Jemioł Leszek **173**
Jenkins Alejandro **127**
Kędzia Piotr **183**
Kik Tomasz **193**
Kolíková Lenka **335**
Konieczny Łukasz **95**
Koruba Zbigniew **203**
Kosińska Angelika **215**
Kossoski Adriano **279**
Kozánek Jan **579**
Krauskopf Bernd **599**
Kruzhilin Vadim S. **571**
Krysko Anton V. **571**
Krysko Vadim A. **53**
Krzysztofik Izabela **223**
Kudra Grzegorz **231, 549**
Lacerda Juliana **241**
Laflin Jeremy **253**
Lamarque Claude Henri **269**
Latalski Jarosław **537**
Lentz Lukas **525**
Lenz Wagner Barth **279**
Litak Grzegorz **291**
Losyeva Nataliya **61**
López Montenegro Luis Eduardo **381**
Ludwicki Michał **231**
Łygas Krystian **291**
Macau Elbert **241**

Magnucki Krzysztof **183**
Mardaleishvili Nodar **345, 357, 369**
Markert Richard **9**
Martowicz Adam **587**
Mazur Olga **299**
Mikhlin Yuri **423**
Mirosław Tomasz **311**
Młyńczak Jakub **95**
Moseshvili Tamar **345, 357, 369**
Muñoz Guillermo **413**
Muñoz Loaiza Aníbal **381**
Nabarrete Airton **41**, **139, 279, 323**
Naď Milan **335**
Navarro Helio **41**
Nikabadze Mikhail **345, 357, 369**
Nowak Bogusław **95**
Olivar Tost Gerard **381**
Olutimo Akinwale **389**
Öztürk Baki **71**
Pękal Marcin **401**
Pérez Arnold **413**
Plaksiy Katarina Y. **423**
Pons Arion **435**
Przybylski Jacek **447**
Puzyrov Volodymyr **61**
Radkowski Stanisław **461**
Rahnejat Homer **25**
Rocha Rodrigo Tumolin **139, 279**
Roeser Dennis **475**
Rolník Ladislav **335**
Rozmus Jacek **95**
Sapieta Milan **505**
Sattel Thomas **475**
Saunders Tim **25**

Schmid Václav **505**
Schorr Philipp **485**
Selyutskiy Yury **497**
Słomczyński Maciej **461**
Smyczyński Mikołaj **183**
Soukup Josef **505**
Suetake Marcelo **41**
Sumi Susanne **485**
Svoboda Martin **505**
Szewc Michał **231**
Szlagowski Jan **311**
Szmidt Piotr **513**
Szmit Zofia **537**
Theodossiades Stephanos **25**
Tskhakaia Ketevan **345, 357, 369**
Ture Savadkoohi Alireza **269**
Tusset Angelo **41, 139, 279, 323**
Uhl Tadeusz **587**
Ulukhanian Armine **345, 357, 369**
Von Wagner Utz **525**
Warmiński Jerzy **537**
Wasilewski Grzegorz **549, 559**
Wegener Georg **9**
Wiądzkowicz Fryderyk **549**
Wijata Adam **559**
Witkowski Krzysztof **231, 549**
Wolszczak Piotr **291**
Wyględacz Bernard **193**
Wojna Mateusz **559**
Wojnar Ryszard **83**
Wojtyra Marek **401**
Wstawska Iwona **183**
Yakovleva Tatyana V. **571**
Zakharova Alena A. **571**

Zapoměl Jaroslav **579**
Zawadzki Adam **311**
Zdziebko Paweł **587**
Zebrowski Zbigniew **311**
Zelei Ambrus **599**
Zimmermann Klaus **485**
Żardecki Dariusz **173**